RISING STARS IN FOOD CHEMISTRY

EDITED BY: Fuguo Liu, Shuai Chen, Biao Yuan and Yahong Han

PUBLISHED IN: Frontiers in Nutrition

frontiers Research Topics

Frontiers eBook Copyright Statement

The copyright in the text of individual articles in this eBook is the property of their respective authors or their respective institutions or funders. The copyright in graphics and images within each article may be subject to copyright of other parties. In both cases this is subject to a license granted to Frontiers.

The compilation of articles constituting this eBook is the property of Frontiers.

Each article within this eBook, and the eBook itself, are published under the most recent version of the Creative Commons CC-BY licence. The version current at the date of publication of this eBook is CC-BY 4.0. If the CC-BY licence is updated, the licence granted by Frontiers is automatically updated to the new version.

When exercising any right under the CC-BY licence, Frontiers must be attributed as the original publisher of the article or eBook, as applicable.

Authors have the responsibility of ensuring that any graphics or other materials which are the property of others may be included in the CC-BY licence, but this should be checked before relying on the CC-BY licence to reproduce those materials. Any copyright notices relating to those materials must be complied with.

Copyright and source acknowledgement notices may not be removed and must be displayed in any copy, derivative work or partial copy which includes the elements in question.

All copyright, and all rights therein, are protected by national and international copyright laws. The above represents a summary only. For further information please read Frontiers' Conditions for Website Use and Copyright Statement, and the applicable CC-BY licence.

ISSN 1664-8714
ISBN 978-2-83250-466-6
DOI 10.3389/978-2-83250-466-6

About Frontiers

Frontiers is more than just an open-access publisher of scholarly articles: it is a pioneering approach to the world of academia, radically improving the way scholarly research is managed. The grand vision of Frontiers is a world where all people have an equal opportunity to seek, share and generate knowledge. Frontiers provides immediate and permanent online open access to all its publications, but this alone is not enough to realize our grand goals.

Frontiers Journal Series

The Frontiers Journal Series is a multi-tier and interdisciplinary set of open-access, online journals, promising a paradigm shift from the current review, selection and dissemination processes in academic publishing. All Frontiers journals are driven by researchers for researchers; therefore, they constitute a service to the scholarly community. At the same time, the Frontiers Journal Series operates on a revolutionary invention, the tiered publishing system, initially addressing specific communities of scholars, and gradually climbing up to broader public understanding, thus serving the interests of the lay society, too.

Dedication to Quality

Each Frontiers article is a landmark of the highest quality, thanks to genuinely collaborative interactions between authors and review editors, who include some of the world's best academicians. Research must be certified by peers before entering a stream of knowledge that may eventually reach the public - and shape society; therefore, Frontiers only applies the most rigorous and unbiased reviews.
Frontiers revolutionizes research publishing by freely delivering the most outstanding research, evaluated with no bias from both the academic and social point of view. By applying the most advanced information technologies, Frontiers is catapulting scholarly publishing into a new generation.

What are Frontiers Research Topics?

Frontiers Research Topics are very popular trademarks of the Frontiers Journals Series: they are collections of at least ten articles, all centered on a particular subject. With their unique mix of varied contributions from Original Research to Review Articles, Frontiers Research Topics unify the most influential researchers, the latest key findings and historical advances in a hot research area! Find out more on how to host your own Frontiers Research Topic or contribute to one as an author by contacting the Frontiers Editorial Office: frontiersin.org/about/contact

RISING STARS IN FOOD CHEMISTRY

Topic Editors:
Fuguo Liu, Northwest A&F University, China
Shuai Chen, Wuhan University, China
Biao Yuan, China Pharmaceutical University, China
Yahong Han, Huazhong Agricultural University, China

Citation: Liu, F., Chen, S., Yuan, B., Han, Y., eds. (2022). Rising Stars in Food Chemistry. Lausanne: Frontiers Media SA. doi: 10.3389/978-2-83250-466-6

Table of Contents

06 ***Editorial: Rising Stars in Food Chemistry***
Shuai Chen, Biao Yuan, Fuguo Liu and Yahong Han

09 ***Physicochemical Properties and Biological Activities of Silver Carp Scale Peptide and Its Nanofiltration Fractions***
Xiao-yan Zu, Ya-jing Zhao, Shi-ming Fu, Tao Liao, Hai-lan Li and Guang-quan Xiong

20 **Porphyra yezoensis *Sauces Fermented With Lactic Acid Bacteria: Fermentation Properties, Flavor Profile, and Evaluation of Antioxidant Capacity* in vitro**
Jie Yang, Tengqi Gao, Feng Ge, Hao Sun, Zihang Cui, Zhen Wei, Shujun Wang, Pau Loke Show, Yang Tao and Wenbin Wang

29 ***A Combined Proteomic and Metabolomic Strategy for Allergens Characterization in Natural and Fermented* Brassica napus *Bee Pollen***
Shuting Yin, Yuxiao Tao, Yusuo Jiang, Lifeng Meng, Liuwei Zhao, Xiaofeng Xue, Qiangqiang Li and Liming Wu

39 ***Advancement on Milk Fat Globule Membrane: Separation, Identification, and Functional Properties***
Cong Wang, Xinyu Qiao, Zengli Gao, Lianzhou Jiang and Zhishen Mu

47 ***Polysaccharide-Zein Composite Nanoparticles for Enhancing Cellular Uptake and Oral Bioavailability of Curcumin: Characterization, Anti-colorectal Cancer Effect, and Pharmacokinetics***
Lu Liu, Shufang Yang, Feng Chen and Ka-Wing Cheng

58 ***Determination of Tropomyosin in Shrimp and Crab by Liquid Chromatography–Tandem Mass Spectrometry Based on Immunoaffinity Purification***
Sufang Fan, Junmei Ma, Chunsheng Li, Yanbo Wang, Wen Zeng, Qiang Li, Jinru Zhou, Liming Wang, Yi Wang and Yan Zhang

67 ***Targeted Lipidomics Reveal the Effect of Perchlorate on Lipid Profiles in Liver of High-Fat Diet Mice***
Qiao Wang, Wanying Song, Yimei Tian, Peihao Hu, Xin Liu, Lin Xu and Zhiyong Gong

76 ***The Whitening, Moisturizing, Anti-aging Activities, and Skincare Evaluation of Selenium-Enriched Mung Bean Fermentation Broth***
Kang Wei, Congyin Guo, Jiangxiong Zhu, Yang Wei, Meirong Wu, Xiaodong Huang, Mu Zhang, Jide Li, Xueyun Wang, Yuanfeng Wang and Xinlin Wei

88 ***The Mechanism of Acrylamide-Induced Neurotoxicity: Current Status and Future Perspectives***
Mengyao Zhao, Boya Zhang and Linlin Deng

103 ***Extraction, Structural Characterization, and Immunomodulatory Activity of a High Molecular Weight Polysaccharide From* Ganoderma lucidum**
Guo Liu, Jun Zhang, Qixin Kan, Mingyue Song, Tao Hou, Siyu An, Hongyu Lin, Hongzhang Chen, Liuyun Hu, Jie Xiao, Yunjiao Chen and Yong Cao

115 ***The Positive Influence of Polyphenols Extracted From* Pueraria lobata *Root on the Gut Microbiota and Its Antioxidant Capability***
Xiao Xu, Ying Guo, Shaoqin Chen, Wenliang Ma, Xinlei Xu, Shuning Hu, Lifang Jin, Jianqiu Sun, Jian Mao and Chi Shen

126 ***Mediterranean Diet Combined With a Low-Carbohydrate Dietary Pattern in the Treatment of Overweight Polycystic Ovary Syndrome Patients***
Shanshan Mei, Jie Ding, Kaili Wang, Zhexin Ni and Jin Yu

138 ***Therapeutic Prospects of Polysaccharides for Ovarian Cancer***
Kaili Wang, Mengcheng Cai, Shuai Sun, Wen Cheng, Dongxia Zhai, Zhexin Ni and Chaoqin Yu

145 ***Influence of Carboxymethyl Cellulose on the Stability, Rheological Property, and* in-vitro *Digestion of Soy Protein Isolate (SPI)-Stabilized Rice Bran Oil Emulsion***
Wenguan Zhang, Jia Hao, Yanan Yuan and Duoxia Xu

156 ***A Novel Hyaluronic Acid-Black Rice Anthocyanins Nanocomposite: Preparation, Characterization, and Its Xanthine Oxidase (XO)-Inhibiting Properties***
Ya Liu and Bangzhu Peng

169 ***Nano-Sized Antioxidative Trimetallic Complex Based on Maillard Reaction Improves the Mineral Nutrients of Apple (*Malus domestica *Borkh.)***
Yu-zhang Yang, Qin-ping Wei, Jia Zhou, Min-ji Li, Qiang Zhang, Xing-liang Li, Bei-bei Zhou and Jun-ke Zhang

182 ***Limonin Isolated From Pomelo Seed Antagonizes Aβ25-35-Mediated Neuron Injury via PI3K/AKT Signaling Pathway by Regulating Cell Apoptosis***
Yuanxin Qiu, Jingxian Yang, Lukai Ma, Mingyue Song and Guo Liu

193 ***Ginsenosides Rb1 Attenuates Chronic Social Defeat Stress-Induced Depressive Behavior* via *Regulation of SIRT1-NLRP3/Nrf2 Pathways***
Ning Jiang, Yiwen Zhang, Caihong Yao, Hong Huang, Qiong Wang, Shuangxue Huang, Qinghu He and Xinmin Liu

205 ***Structural Characterization of* Gracilariopsis lemaneiformis *Polysaccharide and Its Property in Delaying Cellular Senescence***
Xiaomei Wang, Xiaogang Xu, Genxiang Mao, Yue Guo, Guangce Wang, Xue Sun, Nianjun Xu and Zhongshan Zhang

217 ***Comparison of the Fungal Community, Chemical Composition, Antioxidant Activity, and Taste Characteristics of Fu Brick Tea in Different Regions of China***
Yulian Chen, Jiaxu Chen, Ruyang Chen, Leike Xiao, Xing Wu, Lin Hu, Zongjun Li, Yuanliang Wang, Mingzhi Zhu, Zhonghua Liu and Yu Xiao

235 ***Regulatory Effect of Sea-Buckthorn Procyanidins on Oxidative Injury HUVECs***
Ximeng Lin, Michael Yuen, Tina Yuen, Hywel Yuen, Min Wang and Qiang Peng

244 ***Gut Microbiota of Individuals Could Be Balanced by a 14-Day Supplementation With* Laminaria japonica *and Differed in Metabolizing Alginate and Galactofucan***
Xueqian Zhang, Changyu Su, Cui Cao, Guiping Gong, Linjuan Huang, Zhongfu Wang, Shuang Song and Beiwei Zhu

255 ***Preparation, Characterization, and Antioxidant Properties of Phycocyanin Complexes Based on Sodium Alginate and Lysozyme***
Bian-Wen Qiao, Xin-Tong Liu, Chen-Xin Wang, Shuang Song, Chun-Qing Ai and Ying-Huan Fu

266 ***The Effect of Glycosylated Soy Protein Isolate on the Stability of Lutein and Their Interaction Characteristics***
Xia Wang, Shaojia Wang, Duoxia Xu, Jingwei Peng, Wei Gao and Yanping Cao

279 ***DHA Ameliorates Cognitive Ability, Reduces Amyloid Deposition, and Nerve Fiber Production in Alzheimer's Disease***
Min Xiao, Wei Xiang, Yashu Chen, Nan Peng, Xiubo Du, Shuhuan Lu, Yao Zuo, Boling Li, Yonggang Hu and Xiangyu Li

293 ***Pea Peptide Supplementation in Conjunction With Resistance Exercise Promotes Gains in Muscle Mass and Strength***
Shaohui Jia, Qiming Wu, Shue Wang, Juntao Kan, Zhao Zhang, Xiping Zhang, Xuejun Zhang, Jie Li, Wenhan Xu, Jun Du and Wei Wei

304 ***Rapid Determination of 103 Common Veterinary Drug Residues in Milk and Dairy Products by Ultra Performance Liquid Chromatography Tandem Mass Spectrometry***
Xiujuan Guo, Hao Tian, Fan Yang, Sufang Fan, Jingwen Zhang, Junmei Ma, Lianfeng Ai and Yan Zhang

frontiers | Frontiers in Nutrition

TYPE Editorial
PUBLISHED 27 September 2022
DOI 10.3389/fnut.2022.1019054

Check for updates

OPEN ACCESS

EDITED AND REVIEWED BY
Michael Rychlik,
Technical University of
Munich, Germany

*CORRESPONDENCE
Biao Yuan
yuanbiao@cpu.edu.cn
Fuguo Liu
fuguo@nwafu.edu.cn
Yahong Han
yahonghan2019@hotmail.com

SPECIALTY SECTION
This article was submitted to
Food Chemistry,
a section of the journal
Frontiers in Nutrition

RECEIVED 14 August 2022
ACCEPTED 16 September 2022
PUBLISHED 27 September 2022

CITATION
Chen S, Yuan B, Liu F and Han Y (2022)
Editorial: Rising stars in Food
Chemistry. *Front. Nutr.* 9:1019054.
doi: 10.3389/fnut.2022.1019054

COPYRIGHT
© 2022 Chen, Yuan, Liu and Han. This
is an open-access article distributed
under the terms of the Creative
Commons Attribution License (CC BY).
The use, distribution or reproduction
in other forums is permitted, provided
the original author(s) and the copyright
owner(s) are credited and that the
original publication in this journal is
cited, in accordance with accepted
academic practice. No use, distribution
or reproduction is permitted which
does not comply with these terms.

Editorial: Rising stars in Food Chemistry

Shuai Chen[1], Biao Yuan[2]*, Fuguo Liu[3]* and Yahong Han[4]*

[1]School of Public Health, Wuhan University, Wuhan, China, [2]Department of Food Quality and Safety/National R&D Center for Chinese Herbal Medicine Processing, China Pharmaceutical University, Nanjing, China, [3]College of Food Science and Engineering, Northwest A&F University, Xianyang, China, [4]Key Laboratory of Aquaculture Facilities Engineering, Ministry of Agriculture and Rural Affairs, College of Engineering, Huazhong Agricultural University, Wuhan, China

KEYWORDS

Food Chemistry, bioactive compounds, fermentation, delivery systems, food nutrition

Editorial on the Research Topic
Rising stars in Food Chemistry

Recognizing the future leaders of Food Chemistry is fundamental to safeguarding tomorrow's driving force in innovation. This collection showcased the high-quality work of internationally recognized researchers in the early stages of their careers. It includes the preparation of natural products and their health effects, the treatment of food by biological fermentation to enhance its function and activity, the delivery systems for bioactive compounds, food nutrition and toxicology, food safety and detection technology, *etc.*

Natural products have always been an important source of bioactive compounds that were usually used in food field. Polyphenols, polysaccharides, peptides and fatty acids were studied and discussed in this Research Topic. Firstly, scientists studied the extraction of polyphenols and their activity. For example, Xu et al. purified the polyphenol-rich extract from *Pueraria lobata* and investigated systematically its antioxidant activities and its effect on gut microbiota. Results showed that *P. lobata* extract consisted of a large amount of puerarin that exhibited strong antioxidant bioactivity, in addition, it had beneficial and prebiotic effects on the composition and structure of gut microbiota. Qiu et al. analyzed the phenols compositions of waste pomelo seed extract using UPLC-MS/MS and successfully obtained limonin with high concentration in pomelo seed. They illustrated the protect effect of nerve cells by activating the PI3K/Akt pathway and prevented mitochondrial damage from oxidative damage, and effectively reduced Aβ-induced neurotoxicity. Lin et al. used oxidative damaged human umbilical vein endothelial cells (HUVECs) as a model and investigated the regulatory effect of procyanidins from sea-buckthorn (SBP) on HUVECs. It provided a theoretical foundation for further research on natural bioactive compounds to exert antioxidant activity in the body. Secondly, the extraction and function of polysaccharides have also been studied, Wang, XU et al. found that the purified *G. lemaneiformis* polysaccharide (PGP) pretreatment could decrease senescence-associated β-galactosidase (SA-β-gal) positive cells and prevent the formation of senescence-associated heterochromatic foci (SAHF) induced by H_2O_2 in a dose-dependent manner. It is speculated that PGP

may delay aging by downregulating the expression of p21 and p53 genes. Liu, Zhang et al. screened a homogeneous and high molecular weight polysaccharide (named RGLP-1) with the greatest immune-regulatory activity *in vitro* after double purification with ultrafiltration membrane and Sephacryl S-500 HR and explored the structure-activity relationship of the polysaccharide from *Ganoderma lucidum*. Wang, Cai et al. reviewed effects of natural polysaccharides on inhibiting the cell proliferation and growth, regulating the tumor cell cycle, inducing apoptosis, suppressing the tumor cell migration and invasion, improving the immunomodulatory activities, and enhancing the efficacy of chemotherapy (cisplatin) in ovarian cancer. In recent years, peptides have attracted more and more attention from researchers. Jia et al. demonstrated that pea peptide combined with resistance exercise training markedly promoted skeletal muscle growth. Furthermore, they found that the oligopeptide with amino acid sequence of LDLPVL presented a more significant proliferation of C2C12 cells than other oligopeptides. Zu et al. explored the physicochemical properties and biological functions of silver carp scale peptide (SCSP), its molecular-weight fractions SCSP-I, II, and III obtained by nanofiltration were assessed for their solubility, emulsibility, free radical scavenging ability, effect on the proliferation of mouse B16 cells. This work provided a data base for the development of SCSP and increases the possibility of its application. Wang, Qiao et al. summarized the research progress of milk fat globule membrane (MFGM), including separation, identification, and functional properties. MFGM can be separated and prepared from fresh milk, cream, casein and cream whey. The composition of MFGM is complex, mainly composed of polar lipids and membrane-specific proteins. MFGM has good Emulsifying, foaming, and water holding properties, as well as various biological activities such as immunomodulatory activity, anti-enteritis activity, anti-tumor activity, and promoting cell growth and differentiation. This paper can provide some guidance for the development and utilization of MFGM. Fatty acids play an important role in metabolism and gut microbiota, Xiao et al. found that DHA significantly reduced the deposition of amyloid β-peptide in the brain and inhibited the production of nerve fibers, thereby increasing cognitive abilities in the mice with Alzheimer's disease. Zhang, Su et al. demonstrated that a 14-day Laminaria japonica supplementation, one of the most widely consumed commercial edible seaweeds, could balance firmicutes/bacteroidetes ratio and strengthen the utilization of alginate so to enhance the production of short chain fatty acid. Some related studies of other natural bioactive products are also included in this collection. Jiang et al. found that ginseng saponin Rb1 can effectively restore the depressive-like behavior in chronic social defeat stress (CSDS) induced model mice, mediated in part by the normalization of oxidative stress levels. The suppression of neuroinflammation is mediated by the regulation of SIRT1-NLRP3/Nrf2 pathways. Rb1 is a novel therapeutic candidate for treating depression.

Fermentation can also be used to produce bioactive compounds. Yang, Gao et al. used three lactic acid bacteria strains to ferment *Porphyra yezoensis* sauces, including *Lactobacillus fermentum*, *Lactobacillus casei*, *Streptococcus thermophilus*, and the mixed strains, analyzed the fermentation characteristics, antioxidant capacity *in vitro*, sensory properties, and flavoring substances of fermented *P. yezoensis* sauces. They found that the fermented *P. yezoensis* sauce possessed greater DPPH radical scavenging activity and ferric-reducing ability power than the unfermented P. yezoensis. In addition, the whitening, moisturizing, anti-aging activities, and skincare evaluation of selenium-enriched mung bean fermentation broth was investigated by Wei et al., and a clinical trial was conducted on 31 Chinese women aged 25–60 years, the test of the Se-MBFB mask showed that after 4 weeks of using the Se-MBFB facemask, the faces of the participants became whiter with reduced wrinkles and increased moisture content. Yin et al. identified two potential allergens, glutaredoxin and oleosin-B2, in Brassica napus bee pollen using mass spectrometry-based proteomics analyses, and used bioinformatics to predict their antigenic epitopes. Fermentation could potentially alleviate allergenicity, while also positively affecting nutritional properties of B. napus bee pollen.

Bioactive compounds have various health effects, however, their physicochemical properties are unstable and their bioavailability is low. Developing and fabricating the delivery systems can solve these problems. Liu and peng has prepared a high-performance hyaluronic acid-black rice anthocyanins (HAA) nanocomposite particles by a simple crosslinking method. HAA nanocomposite particles can effectively improve black rice anthocyanins' stability and activity, creating an ideal new material for inhibiting xanthine oxidase activity. Qiao et al. has prepared phycocyanin-sodium alginate/lysozyme complex (PC-SLC), the complex formed by the mass ratio of SA-LZM of 0.1 showed the highest PC encapsulation rate (89.9 ± 0.374%). Compared with free phycocyanin (PC), its thermal stability was obviously improved, and could exist stably in simulated gastric fluid for 2 h and be slowly digested in simulated intestinal fluid, which helped to promote the absorption of nutrients in the intestinal tract. Wang, Wang et al. analyze the stability and interaction mechanism of the complex glycosylated soy protein isolate prepared using soy protein isolate, inulin-type fructans and lutein. They showed that glycosylation reduced the fluorescence intensity and surface hydrophobicity of soy protein isolate but improved the emulsification process and solubility. Liu, Yang et al. developed curcumin-encapsulated zein/polysaccharide complex nanoparticles as a therapeutic agent against colorectal cancer (CRC), including gum Arabic-zein-curcumin (GA-Zein-CUR), hyaluronic acid-zein-curcumin (HA-Zein-CUR), and pectin-zein-curcumin (PC-Zein-CUR). Results showed that HA-Zein-CUR with

the highest encapsulation efficiency and loading capacity, inhibited cell viability and colony formation, exhibited higher cellular uptake of CUR, enhanced pharmacokinetic properties of intragastric administration, delivery and accumulation of curcumin in major organs/tissues, in particular CRC tumors and colon. Zhang, Hao et al. studied the impact of carboxymethyl cellulose (CMC) on the physicochemical stability, rheological property, and *in-vitro* digestion of soybean protein isolate (SPI)-stabilized rice bran oil (RBO) emulsions. RBO emulsions stabilized by SPI and various contents of CMC were prepared, it showed that the chemical stability, free fatty acids release rate and bioavailability of the emulsion added with CMC was improved compared with the SPI-stabilized RBO emulsion. Yang, Wei et al. developed an antioxidative trimetallic complex with high stability by interacting Ca^{2+}, Fe^{2+}, and Zn^{2+} with the biodegradable ligands from Maillard reaction and then investigated the effect of the complex on the mineral contents of apple. The results showed that mineral nutrients of Ca, Fe, and Zn in apple increased significantly through surface spraying of the metal–integrated complex, and the efficiency is much higher than the traditional inorganic salts and single chelated metals.

In addition to bioactive compounds, the proportion of carbohydrates and lipids in the diet also has a regulatory effect on human health. Mei et al. reported that the mediterranean diet / low-carbohydrate (MED/LC) diet model is a good treatment for overweight polycystic ovary syndrome (PCOS) patients, significantly restoring their menstrual cycle, improving their anthropometric parameters and correcting their disturbed endocrine levels, and its overall effectiveness is significantly better than the low-fat diet model systematically Chen et al. characterized the diversity of fungal communities, chemical composition, antioxidant activity, and taste quality of Fu brick tea samples from five different regions of China, and assessed the relationship between bioactive metabolites and fungal communities and the key chemical substances contributing to the variations in antioxidant activity and taste profile.

Food safety is also an important factor affecting human health. Zhao et al. reviewed the exposure to occupational, environmental, and daily acrylamide (ACR) contamination in food. Moreover, acrylamide metabolism and the potential mechanism of acrylamide-induced neurotoxicity were discussed, with particular focus on the axonal degeneration of the nervous system, nerve cell apoptosis, oxidative stress, inflammatory response, and gut-brain axis homeostasis. Perchlorate, commonly available in drinking water and food, acts on the iodine uptake by the thyroid affecting lipid metabolism. High-fat diets leading to various health problems continually raise public concern. In the study of Wang, Song et al., liver lipid metabolism profiles and metabolic pathways were investigated in C57BL/6J mice chronically exposed to perchlorate using targeted metabolomics. Perchlorate low, medium and high dose groups were identified with 11, 7 and 8 significantly altered lipid metabolites compared to the control group, respectively. The improvement of detection technology is an important guarantee to maintain food safety. Fan et al. developed and established a UPLC-MS/MS method for the detection of tropomyosin in shrimp and crab. While Guo et al. successfully developed a method for the identification and quantification of 103 common veterinary drug residues in milk and dairy products.

Overall, the collection highlighted research by leading scientists of the future across the entire breadth of Food Chemistry, and present advances in theory, experiment and methodology with applications to compelling problems.

Author contributions

SC, BY, FL, and YH prepared, checked and revised the manuscript, and approved the submitted version. All authors contributed to the article and approved the submitted version.

Funding

This study was supported by the Fundamental Research Funds for the Central Universities (2042021kf0042); the Beijing Engineering and Technology Research Center of Food Additives, Beijing Technology and Business University (BTBU); the Postdoctoral Innovative Research Position of Hubei Province; China Postdoctoral Science Foundation (2022M712473 and 2019M662659); Hubei Provincial Natural Science Foundation of China (2020CFB314); the National Natural Science Foundation of China (No. 31901699).

Conflict of interest

The authors declare that the research was conducted in the absence of any commercial or financial relationships that could be construed as a potential conflict of interest.

Publisher's note

All claims expressed in this article are solely those of the authors and do not necessarily represent those of their affiliated organizations, or those of the publisher, the editors and the reviewers. Any product that may be evaluated in this article, or claim that may be made by its manufacturer, is not guaranteed or endorsed by the publisher.

frontiers in Nutrition

ORIGINAL RESEARCH
published: 04 January 2022
doi: 10.3389/fnut.2021.812443

Physicochemical Properties and Biological Activities of Silver Carp Scale Peptide and Its Nanofiltration Fractions

Xiao-yan Zu[1], *Ya-jing Zhao*[1,2], *Shi-ming Fu*[1], *Tao Liao*[1], *Hai-lan Li*[1]* and *Guang-quan Xiong*[1]*

[1] *Institute of Agricultural Products Processing and Nuclear Agricultural Technology, Hubei Academy of Agricultural Sciences, Wuhan, China,* [2] *College of Petrochemical, Lanzhou University of Technology, Lanzhou, China*

OPEN ACCESS

Edited by:
Shuai Chen,
Wuhan University, China

Reviewed by:
Quancai Sun,
Jiangsu University, China
Tao Feng,
Shanghai Institute of Technology, China
Ru Liu,
Huazhong Agricultural University, China

***Correspondence:**
Hai-lan Li
hl.li@hotmail.com
Guang-quan Xiong
xiongguangquan@163.com

Specialty section:
This article was submitted to Food Chemistry, a section of the journal Frontiers in Nutrition

Received: *10 November 2021*
Accepted: *09 December 2021*
Published: *04 January 2022*

Citation:
Zu X-Y, Zhao Y-J, Fu S-M, Liao T, Li H-L and Xiong G-Q (2022) Physicochemical Properties and Biological Activities of Silver Carp Scale Peptide and Its Nanofiltration Fractions. Front. Nutr. 8:812443. doi: 10.3389/fnut.2021.812443

To explore the physicochemical properties and biological functions of silver carp scale peptide (SCSP), its molecular-weight fractions SCSP-I, II, and III obtained by nanofiltration were assessed for their solubility, emulsibility, free radical scavenging ability, effect on the proliferation of mouse B16 cells. The results showed that the solubility of each fraction of SCSP was higher than 90%, SCSP-II and III were higher than 95%. The antioxidant powers on •OH, O_2^-• and Fe^{3+} were ranked as SCSP-III > SCSP-II > SCSP-I > SCSP. All fractions of SCSP had no toxic or side effects in mouse B16 melanoma cells experiments *in vitro*. At a concentration of 0.01 mg/mL, the tyrosinase activity of B16 cells in the SCSP-II fraction was significantly lower than that of the α-arbutin ($P < 0.05$), at 65.37%. The molecular weight distribution of SCSP was 399–1404 Dalton and 13 peptide sequences were detected. Among them, SCSP-II contained many hydrophobic amino acids, and SCSP-III stood out for combining arginine with hydrophobic amino acids. This may be the reason why the low molecular-weight SCSPs show the strong antioxidant activity and strong tyrosinase inhibition. The work provides a data base for the development of SCSP and increases the possibility of its application.

Keywords: silver carp scale peptide, physicochemical properties, free radical scavenging, tyrosinase inhibition, amino acid sequence

INTRODUCTION

Silver carp (*Hypophthalmichthys molitrix*) is widely distributed in lakes and rivers across Asia. A fast-growing fish, it has high feed efficiency and high nutritional value, so it is one of the four major farmed freshwater fishes in China. In 2020, the aquaculture production of silver carp reached 3.81 million tons, second only to grass carp (Ministry of Agriculture Fishery Administration., 2021). During the processing of silver carp, many by-products are produced, including fish heads, bones, skins, and internal organs. Their weight accounts for approximately 50–70% of the total body weight of the fish, of which fish scales account for approximately 5% (1). For a long time, fish scales have been considered of low value, so the rate of fish scale utilization and processing has been low, resulting in the serious waste of biological resources.

The high-quality collagen that is enriched in fish scales can undergo the disintegration of molecular chains *via* hydrolysis, forming peptide mixtures between proteins and amino acids (2). Fish scale peptide is characterized by high solubility, good thermal stability, and easy absorption (3). And it can have multiple biological functions such as binding to mineral ions (4), inhibiting aging and antioxidation (5). Addition, according to Ma's conclusion that short peptides containing 2–10 amino acids have greater antioxidant potential and biological activity than their native proteins or peptides (6). The composition and proportion of hydrophobic amino acids (e.g., Pro, Ala, Val, Phe, Leu, Ile) in the sequence are also related to the antioxidant activity of polypeptides (7), the presence of hydrophobic amino acid residues can enhance the antioxidant capability of peptides, and the higher their content, the stronger the antioxidant activity (8).

Excellent biocompatibility and low immunogenicity enable the fish scale peptides to be used in biomedical fields, such as wound healing and medical dressings. Due to its strong antioxidant, moisturizing, and whitening properties, fish scale peptide has been approved for uses in cosmetics, health foods, and other products (9, 10). At present, the overuse of popular skin-whitening agents on the market, such as arbutin and hydroquinone, can cause permanent white patches on the skin (11). Therefore, it is imperative to find a safe and effective natural inhibitor of melanin synthesis.

In this paper, the physicochemical properties of silver carp scale peptide (SCSP) and its three molecular-weight fractions were studied. The amino acid sequences and molecular weights of the corresponding peptides were identified by mass spectrometry. Free radical scavenging assays, *in vitro* cell experiments, and a tyrosinase inhibition assay were carried out to verify their antioxidant and whitening effects. This study is expected to provide technical support for the development of SCSP as a consumer product.

MATERIALS AND METHODS

Materials

Silver carp scales were purchased from Liangzihu Aquatic Products Processing Co., Ltd. (Wuhan, China). Soybean oil (food grade) was from the COFCO Fulinmen Food Marketing Co., Ltd. (Wuhan, China). Alkaline protease (liquid, 2,400,000 U/mL) was from Genencor (China) Bioengineering Co., Ltd. 2, 2-Diphenyl-1-picrylhydrazyl (DPPH) was from Sigma Corporation (USA). B16-F1 mouse melanoma cells were from the China Center for Type Culture Collection (CCTCC, Hubei, Wuhan). 3-(4, 5-Dimethylthiazol-2-yl)-2, 5-diphenyltetrazolium bromide (MTT) was purchased from BioFroxx (Germany). Trypsin-EDTA (0.25%), fetal bovine serum, and penicillin-streptomycin were from GIBCO (New York, USA). Chromatographically pure acetonitrile was from Thermo Fisher Scientific Co., Ltd. (Shanghai, China). All other reagents used in the experiment were of analytically pure grade and were from Sinopharm Chemical Reagent Co., Ltd. (Shanghai, China).

Technical Route

In this study, decalcified silver carp scales were hydrolyzed with alkaline protease to obtain an enzymatic hydrolysate. After removing the enzymes, the enzymatic hydrolysate was separated by nanofiltration to prepare different molecular-weight fractions of SCSP. The physicochemical properties and biological activities of SCSP and its three molecular-weight fractions were studied. The technical flow chart is shown in **Figure 1**.

Preparation of SCSP and Its Nanofiltration Fractions

The decalcified silver carp scales were cleaned with deionized water to remove impurities and mixed with deionized water at a ratio of 1:50 (w/v), and 0.01 M sodium hydroxide (NaOH) was used to adjust the solution pH to 8.0. Then alkaline protease was added, and the mixture was mixed evenly and placed at 50°C to undergo enzymatic hydrolysis until all the solid scales had disappeared. The enzymatic hydrolysate was inactivated at 100°C for 10–15 min and then centrifuged at 5,000 rpm for 20 min to remove the impurities and enzymes to obtain the SCSP.

The SCSP was filtrated and separated with a nanofiltration membrane (S-UF3, Shanghai Langji membrane separation equipment Engineering Co., Ltd., China) with a molecular weight cut-off of 5,000 Dalton (Da), and the filtrate continued to be separated by a nanofiltration membrane with a molecular weight cut-off of 3,000 Da. The substances retained by the 5,000-Da nanofiltration membrane were the SCSP-I fraction, the substances retained by the 3000-Da nanofiltration membrane were the SCSP-II fraction, and the filtrate that passed through the 3,000-Da nanofiltration membrane was the SCSP-III fraction. The SCSP sample before nanofiltration and different molecular-weight fractions were freeze-dried for later use.

Determination of Solubility

The method of Adler-Nissen et al. (12) was used as a reference for the determination of collagen peptide solubility, with slight modifications. In 50 mL of distilled water, 5 mg of the freeze-dried SCSP, SCSP-I, SCSP-II, and SCSP-III samples were dissolved, and the pH values were, respectively, adjusted to 3.0, 4.0, 5.0, 6.0, 7.0 8.0, 9.0, and 10.0 with 6.0 M HCl or 6.0 M NaOH solution, followed by centrifugation at 4,000 rpm for 20 min. In 1 mL of the supernatant, the biuret method was used to determine the polypeptide contents. The solubility of SCSP and its fractions was calculated according to Equation (1), and the result is expressed as the nitrogen solubility index (NSI):

$$\text{NSI (\%)} = \frac{\text{N1}}{\text{N2}} \times 100\% \quad (1)$$

where N_1 is the polypeptide content in the supernatant, g/g; and N_2 is the total polypeptide content in the sample, g/g.

Determination of Emulsibility and Emulsifying Stability

Emulsibility was measured as described by Vioque et al. (13) with slight modifications. In 40 mL of distilled water, 2 g of SCSP, SCSP-I, SCSP-II, or SCSP-III freeze-dried powder was dissolved, and its pH was adjusted to 7.0, followed by adding 10 mL of soybean oil. The sample was homogenized in a high-speed homogenizer (FJ3000, Shanghai Specimen and Model Factory, China) for 2 min, the homogenized mixture was centrifuged at

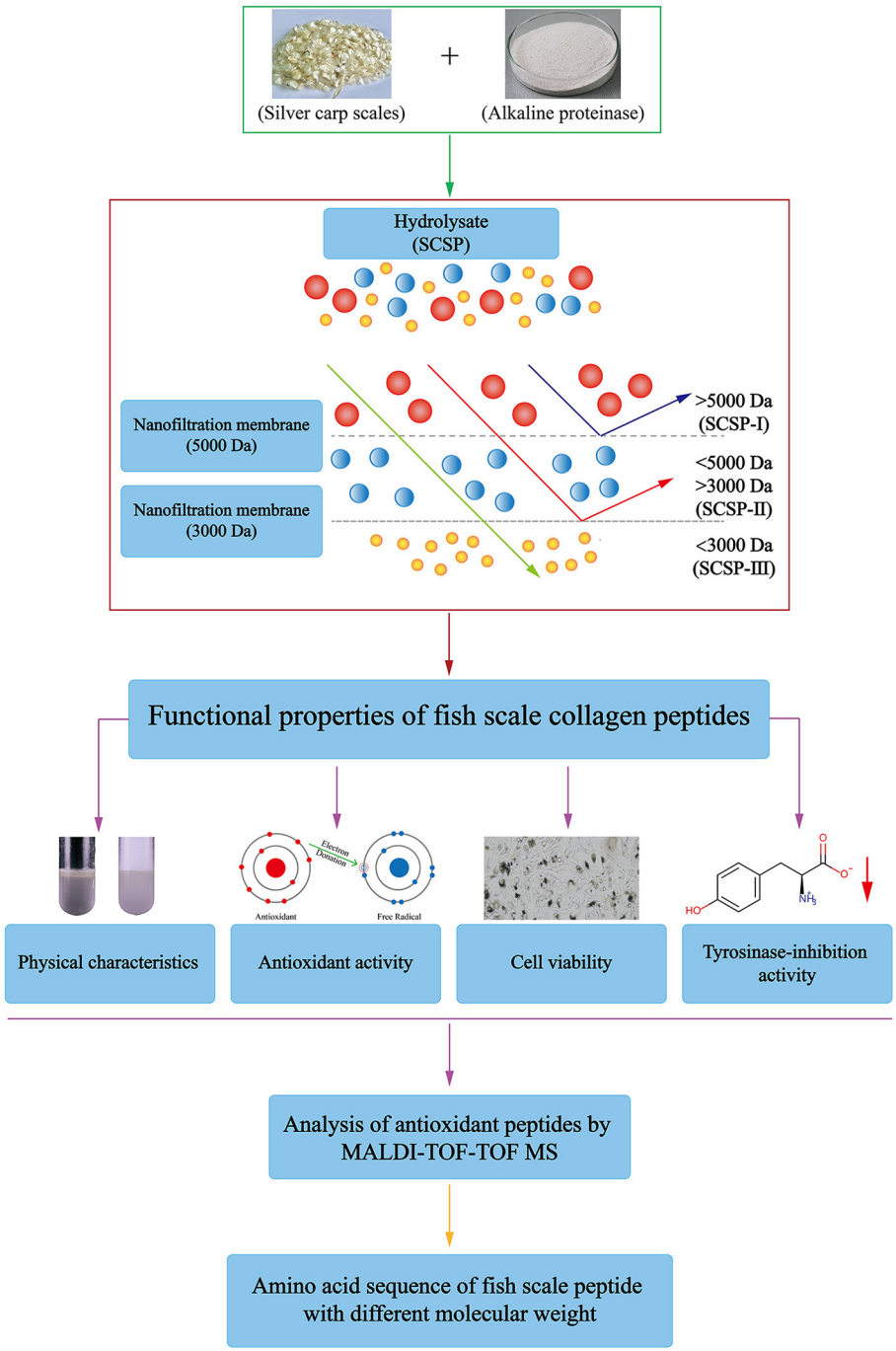

FIGURE 1 | Technical roadmap for the preparation and analysis of SCSPs.

1,000 rpm for 5 min, and the emulsifying activity index (EAI) was calculated according to Equation (2). After the measurement, the centrifuge tube was placed in a constant-temperature water bath (HH-6, Changzhou Zhiborui Instruments Manufacturing Co., Ltd., China) at 50°C for 30 min. After cooling to room temperature, the sample was centrifuged at 1,500 rpm for 10 min. According to Equation (3), the emulsifying stability index (ESI) was calculated.

$$\text{EAI}\ (\%) = \frac{\text{H1}}{\text{H}} \times 100\% \quad (2)$$

$$\text{ESI}\ (\%) = \frac{\text{H2}}{\text{H1}} \times 100\% \quad (3)$$

where H is the total height of the liquid in the centrifuge tube, cm; H_1 is the height of the emulsion layer, cm; and H_2 is the height of the emulsion layer after centrifugation, cm.

Measurement of Antioxidant Activity

The freeze-dried powders of SCSP, SCSP-I, SCSP-II, and SCSP-III were added to deionized water to prepare sample solutions of 1, 2, 4, 6, 8, and 10 mg/mL for the measurement of antioxidant activity.

Measurement of DPPH● Scavenging Activity

The method of Bougatef et al. (14) with slight modifications was used to measure DPPH● scavenging activity. In a test tube, 2.5 mL of SCSP, SCSP-I, SCSP-II, or SCSP-III sample solution of different concentrations was added, followed by adding 2.5 mL of DPPH solution (0.1 mmol/L) prepared in absolute ethanol. The mixture was shaken for 10 s and then left to react in the dark at room temperature for 30 min. Next, the absorbance of the solution was measured at 517 nm with an ultraviolet-visible spectrophotometer (UH5300, Hitachi High-Technologies Corporation, Japan). The blank control had 2.5 mL of distilled water. The DPPH radical scavenging rate of the sample solution was calculated according to Equation (4):

$$\text{DPPH radical scavenging activity (\%)} = \frac{A0 - A}{A0} \times 100\% \quad (4)$$

where A_0 represents the absorbance of the DPPH● ethanol solution without sample and A represents the absorbance of the DPPH● ethanol solution in the measured sample.

Measurement of ●OH Scavenging Activity

The method of Fu et al. (15) was used to determine the capability of SCSP to scavenge ●OH. In an Erlenmeyer flask, 1 mL of SCSP, SCSP-I, SCSP-II, or SCSP-III sample solution of different concentrations was added with a pipette, followed by adding 1 mL salicylic acid-ethanol solution (10 mmol/L), 1 mL $FeSO_4$ solution (10 mmol/L), 2 mL H_2O, and 5 mL H_2O_2 solution (10 mmol/L). The flask stood at 37°C for 15 min. The absorbance of the solution was measured at 510 nm with an ultraviolet-visible spectrophotometer. The hydroxyl radical scavenging rate of the sample solution was calculated according to Equation (5):

$$\text{OH radical scavenging activity (\%)} = \frac{A0 - A}{A0} \times 100\% \quad (5)$$

where A_0 represents the background absorbance and A represents the absorbance of the measured sample.

Measurement of Ferric-Reducing/Antioxidant Power

The method of Bougatef et al. (14) was used to measure the capability of the SCSP to reduce Fe^{3+}. After 1 mL of SCSP, SCSP-I, SCSP-II, or SCSP-III sample solution of different concentrations was mixed evenly with 1 mL (1%) $K_3[Fe(CN)_6]$ and 1 mL (0.2 mol/L) phosphate-buffered saline (PBS) buffer solution, the mixture was reacted in a constant-temperature water bath at 50°C for 20 min. After it had cooled to room temperature, 1 mL (10%) trichloroacetic acid solution was added to consume excess $K_3[Fe(CN)_6]$, and the sample was centrifuged at 4,000 rpm for 10 min. To 2.5 mL of the supernatant, 0.75 mL (0.1%) $FeCl_3$ solution and 2.5 mL of distilled water were added, the mixture was placed in a constant-temperature water bath at 50°C for 10 min until Prussian blue appears. Then the absorbance of the solution was measured at 700 nm.

Measurement of O_2^- Radical Scavenging Activity

The method of Wang et al. (16) with slight modifications was used to determine the O_2^-● scavenging activity. In an Erlenmeyer flask, 4.2 mL of different concentrations of SCSP, SCSP-I, SCSP-II, or SCSP-III sample solution was added by pipette, followed by adding 4.5 mL of Tris-HCl (0.1 mol/L, pH 8.2) buffer solution. The sample was mixed evenly and let stand in water bath at 25°C for 15 min, followed by quickly adding 0.3 mL (3 mmol/L) of pyrogallol (prepared with 10 mmol/L HCl). Then, the solution was mixed evenly. Distilled water instead of peptide solution served as the blank control. The absorbance was measured at 325 nm every 30 s for 4 min. The slope of absorbance over time was calculated. The O_2^-● scavenging rate of the solution was calculated according to Equation (6):

$$\text{Superoxide anion radical scavenging activity (\%)} = \frac{k0 - k}{k} \times 100\% \quad (6)$$

where k_0 represents the slope of the blank group and k represents the slope of the sample group.

Cell Viability Determination by MTT Assay and Cell Morphology Observation

The method of Huang et al. was used to measure cell viability (17). After the B16 melanoma cells in the logarithmic growth phase were inoculated in 96-well plates at 1×10^4 cells/well, they were cultured in an incubator (MCO-15AC, SANYO Electric Co., Ltd., Japan) with 5% CO_2 at 37°C for 12 h, and then the medium was changed. Among them, 100 μL of sample (0.01, 0.1, 0.5, or 1.0 mg/mL) was added to the medium of the experimental group. The positive control group received an equal volume of α-arbutin at the same concentration, the blank group an equal volume of medium. After cultivation for 48 h, 20 μL of 0.5% MTT was added to each well, and the cultivation continued for 2 more h. The supernatant was collected, followed by adding 200 μL of dimethyl sulfoxide, and the mixture was shaken for 10 min. The absorbance at 490 nm was measured with a microplate reader (Fluoroskan, Thermo Fisher Scientific Co., Ltd., UK). The cell viability was calculated by Equation (7):

$$\text{Cell viability (\%)} = \frac{A}{A0} \times 100\% \quad (7)$$

where A is the measured absorbance of the positive control group or the experimental group and A_0 is the absorbance of the blank group.

To observe the cell morphology, B16 melanoma cells in the logarithmic growth phase were cultured in a cell culture dish. After 12 h, the medium was changed, and 1.0 mg/mL α-arbutin, SCSP, SCSP-I, SCSP-II, or SCSP-III sample solution was added.

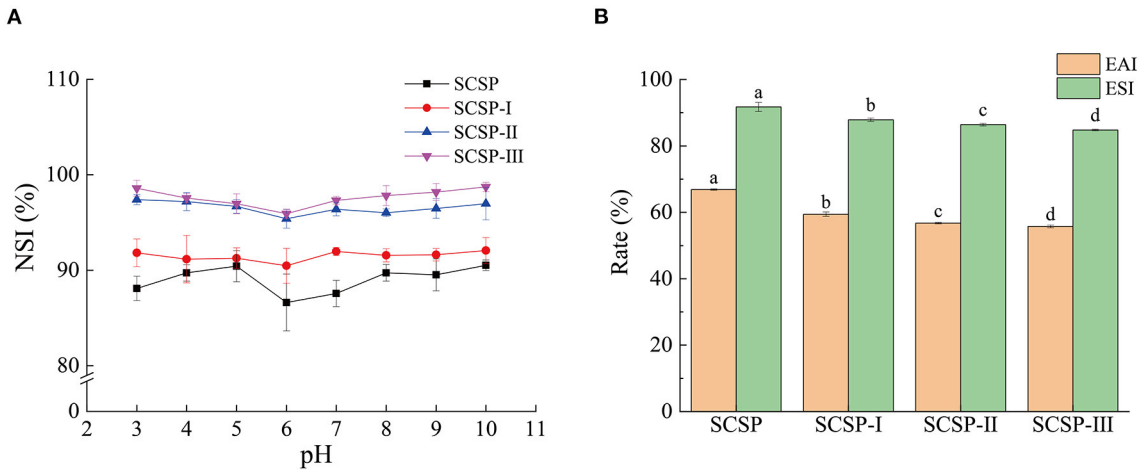

FIGURE 2 | Solubility **(A)**, emulsibility and emulsifying stability **(B)** of SCSPs. The 0.1 mg/mL and 50 mg/mL SCSPs were used in the tests of solubility and emulsibility, respectively. Different lowercase letters denote significant differences between SCSP, SCSP-I, SCSP-II, and SCSP-III groups ($P < 0.05$). All experiments were repeated three times. Data are expressed as mean ± standard deviation.

The cultivation continued for 48 more h, and then an inverted microscope (IX7, Olympus Co., Ltd., Japan) was used to observe and photograph the morphology of each group of cells.

Determination of Tyrosinase Activity

The method of Huang et al. (17) was used to determine the tyrosinase activity. The cell inoculation method, inoculation density, and sample loading method were the same as those of section 2.7. After the cells had been cultured for 48 h, the cells were disrupted with 90 μL of PBS (pH 6.8) buffer containing 1% Triton X-100, and the resulting sample was centrifuged at 1,000 rpm for 30 min in a centrifuge. Considering the toxicity of high concentration α-arbutin, low concentration SCSPs of 0.01 mg/ml were selected for tyrosinase activity inhibition test. To 90 μL of cell disruption solution, 10 μL of 1 mg/mL L-3, 4-dihydroxyphenylalanine (L-DOPA) was added, and the sample was cultured at 37°C for 90 min. The absorbance at 475 nm was measured with a microplate reader. The intracellular tyrosinase activity was calculated by Equation (8):

$$\text{Tyrosinase activity (\%)} = \frac{A}{A0} \times 100\% \quad (8)$$

where A is the measured absorbance of the positive control group or the experimental group and A_0 is the absorbance of the blank group.

Determination of Molecular Weight

Matrix-assisted laser desorption ionization time-of-flight mass spectrometry (MALDI-TOF-MS) (autoflexmaX, Bruker Co., Ltd., Germany) was used to analyze the molecular weight and molecular weight distribution range corresponding to each SCSP, SCSP-I, SCSP-II, or SCSP-III sample. The sample was mixed with 2,5-dihydroxybenzoic acid (20 mg/mL) in 50% acetonitrile/water (containing 0.1% trifluoroacetic acid) at a ratio of 1:1. After 1 μL of the sample mixture was placed in one well of a 384-well plate and naturally dried at room temperature, the sample plate was placed in the ion source for measurement. The final mass spectrum was obtained by accumulating 10 single-scan signals.

Determination of Amino Acid Sequence

The amino acid sequence of the peptides was determined by ultraperformance liquid chromatography-tandem mass spectrometry (UPLC-MS/MS) (Agilent6545Q-TOF, Waldbronn, Germany). The sequencing conditions were as follows: the sample volume was 5 μL, mobile phase A was 0.1% formic acid-acetonitrile, and mobile phase B was 0.1% formic acid-water. The gradient elution program was: 1–30% A (0–45 min), 30–90% A (45–50 min), 90% A (50–52 min), 90–1% A (52–55 min), and 1% A (55–60 min); the flow rate was 0.2 mL/min. Mass spectrometry conditions: the electrospray ion source was set to electrospray ionization positive ion scanning mode, the nebulizer and drying gas were high-purity nitrogen, the drying temperature was 200°C, the drying gas flow rate was 6.0 L/min. And the scanning range was controlled with the MS program with a mass-to-charge ratio (m/z) of 50–3000 and the MS/MS program with m/z = 50–2000. The data were analyzed using the Proteome Discoverer 2.4 software from Thermo Fisher (Thermo Fisher Scientific Co., Ltd., UK), and collagen peptides were classified by searching against the UniProt protein database (www.UniProt.org).

Data Analysis

IBM SPSS Statistics 20.0 (International Business Machines Corporation Co., Ltd., USA) was used for statistical analysis. Differences with $P < 0.05$ were considered statistically significant. Origin 9.1 software (Origin Lab Co., Ltd., USA) was used to draw graphs. All experiments were carried out in triplicate, and the data are expressed as mean ± standard deviation.

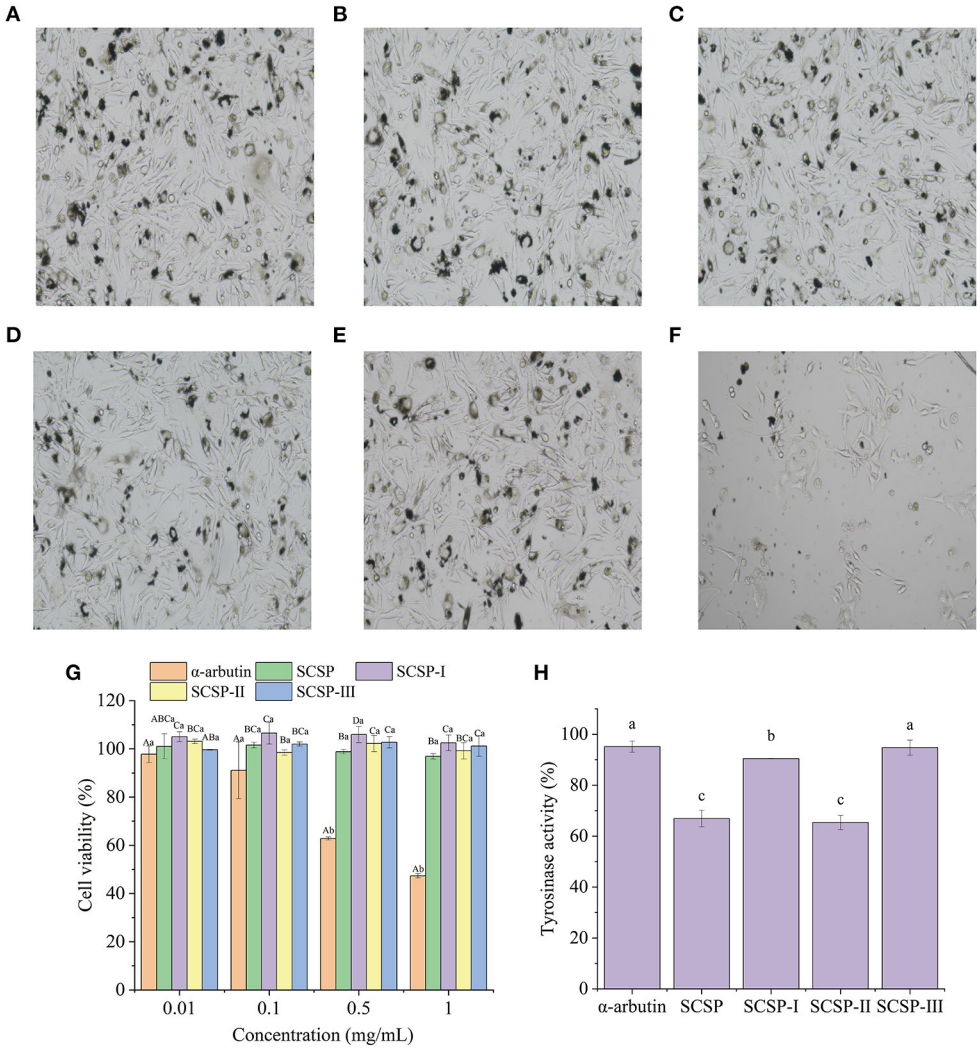

FIGURE 3 | Morphology of mouse B16 melanoma cells in the normal state (blank control) **(A)**, and under the action of 1.0 mg/mL SCSP **(B)**, SCSP-I **(C)**, SCSP-II **(D)**, SCSP-III **(E)**, and α-arbutin **(F)**. The proliferative activity **(G)** of mouse B16 melanoma cells under the action of SCSPs at 0.01, 0.1, 0.5, 1.0 mg/mL, respectively. The cell tyrosinase activity **(H)** under the action of 0.01 mg/mL SCSPs. In **(G)**, different capital letters denote significant differences between the SCSP, SCSP-I, SCSP-II, and SCSP-III groups at the same concentration ($P < 0.05$), and different lowercase letters denote significant differences between the same fractions of different concentrations ($P < 0.05$). In **(H)**, different lowercase letters denote significant differences between groups ($P < 0.05$). All experiments were repeated three times. Data are expressed as mean ± standard deviation.

RESULTS

Solubility, Emulsibility, and Emulsifying Stability of SCSPs

As shown in **Figure 2A**, at different pH values, the solubilities of SCSP and its three fractions were ranked as SCSP-III > SCSP-II > SCSP-I > SCSP. The solubility of each fraction was higher than 90%, SCSP-III and SCSP-II having solubilities higher than 95%. In addition, under different pH values, each fraction showed a similar trend of changes in solubility. When the pH was < 6, the solubility of each fraction decreased with increasing pH; when the pH was > 6, the solubility of each fraction slowly increased with increasing pH and eventually plateaued.

As shown in **Figure 2B**, the emulsibility and emulsifying stability significantly decreased with decreasing molecular weight ($P < 0.05$), emulsibility decreasing more significant than emulsifying stability. The emulsibility of SCSP was 66.89 ± 0.23%, and the emulsifying stability was as high as 91.74 ± 1.36% after the sample had stood for 30 min. The emulsibility and emulsifying stability of SCSP-III were only 55.77 ± 0.40% and 84.82 ± 0.23%, respectively.

Antioxidant Effects of SCSPs

As shown in **Figure 3A**, in the range of 1–10 mg/mL, the DPPH• scavenging rates of the SCSP and its three fractions all increased with increasing peptide concentration, and the increase in SCSP-I group was the most significant ($P < 0.05$). The O_2^-• and •OH

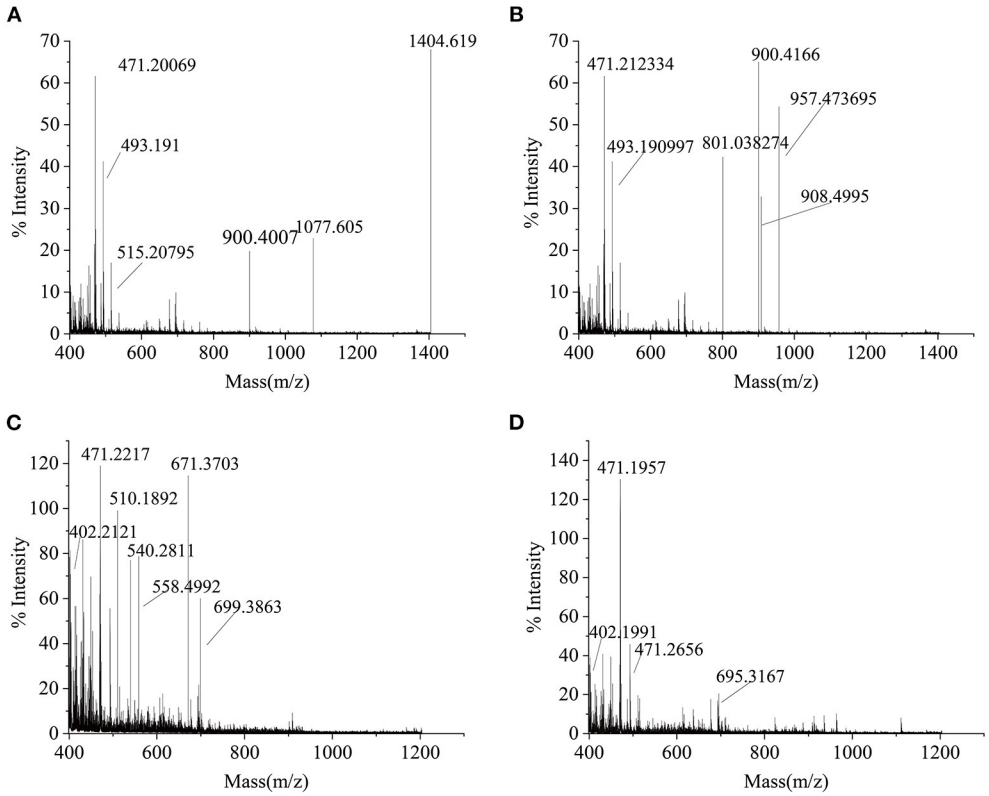

FIGURE 4 | Antioxidant capability of SCSPs. **(A)** DPPH• radical scavenging capability, **(B)** hydroxyl radical scavenging capability, **(C)** ferric-reducing/antioxidant power, **(D)** superoxide anion radical scavenging capability were measured under the action of SCSPs at 1, 2, 4, 6, 8, 10 mg/mL, respectively. Different capital letters denote significant differences between the SCSP, SCSP-I, SCSP-II, and SCSP-III groups at the same concentration ($P < 0.05$), and different lowercase letters denote significant differences between the same fractions with different concentrations ($P < 0.05$). All experiments were repeated three times. Data are expressed as mean ± standard deviation.

scavenging rates and the ferric-reducing/antioxidant power of each fraction showed an upward trend with increasing peptide concentration (**Figures 3B–D**). At the same concentration, the fractions with lower molecular weights had higher antioxidant capability (**Figures 3B–D**).

Effects of SCSPs on the Proliferation of Mouse B16melanoma Cells

Figures 4A–F shows the morphology of mouse B16 melanoma cells under the action of 1.0 mg/mL sample. The cells in each SCSP group displayed uniform adhesion and were mostly spindle-shaped, with normal morphology, clear cell edges, and high cell density (**Figures 4B–E**). The SCSP groups were not significantly different from the blank control group (**Figure 4A**). In the α-arbutin group (**Figure 4F**), there were many apoptotic cells and no complete cell structure, the intercellular spaces became larger, dendritic structures disappeared, and there were fewer cells. The cell morphology results supported the results of the MTT cell viability assay. As shown in **Figure 4G**, except for α-arbutin, each sample had similar effects on the proliferation of mouse B16 melanoma cells as its concentration changed ($P > 0.05$). There was no significant difference in the proliferation of mouse B16 cells when the α-arbutin concentration was in the range of 0.01–0.1 mg/mL ($P > 0.05$). But when the α-arbutin concentration was higher than 0.1 mg/mL, it significantly inhibited B16 cell proliferation ($P < 0.05$), such that the cell survival rate was only 47.34 ± 0.88% in 1.0 mg/mL α-arbutin.

Effects of SCSPs on the Tyrosinase Activity

Under the condition of 0.01 mg/mL, the effect of SCSPs on tyrosinase activity was studied with α-arbutin as positive control. As shown in **Figure 4H**, the inhibitory effect of each fraction on tyrosinase was higher than that of α-arbutin. Among them, the tyrosinase activity of the SCSP-II group was 65.37 ± 2.81%, which was significantly lower than that of the arbutin group ($P < 0.05$). Moreover, SCSP-II was seems to be safer to cells than α-arbutin. Tyrosinase is a key enzyme in the synthesis of melanin.

Molecular Weight Ranges of SCSPs

As seen in **Figure 5A**, the molecular weight distribution of peptides in the SCSP ranged from 399 to 1404 Da, of which m/z 471.20 and 1404.62 were relatively abundant. **Figure 5B** shows that the molecular weight of SCSP-I ranged from 399 to 957 Da, of which m/z 471.21, and 900.42 were relatively abundant. **Figure 5C** shows that the molecular weight of SCSP-II ranged

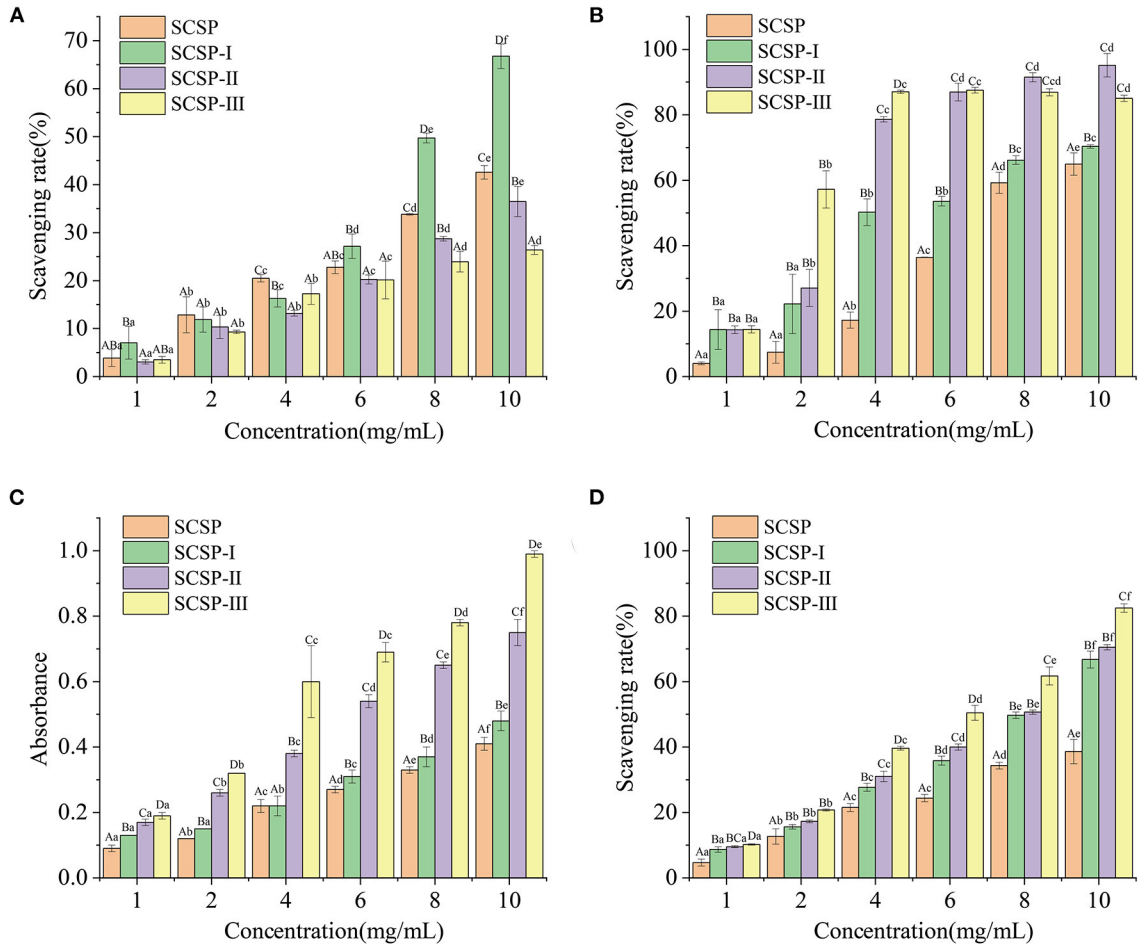

FIGURE 5 | MALDI-TOF-MS spectral profiles of SCSPs. **(A)** SCSP, **(B)** SCSP-I, **(C)** SCSP-II, **(D)** SCSP-III.

TABLE 1 | The peptide sequence and molecular weight of SCSPs.

No.	Sequence	Theo. MH+ [Da]	NF component	Confidence	XCor
a	GARGDKGETGEA	1,147	SCSP-I	High	3.30
b	SGPAGPRGPAGSSGPA	1,322	SCSP-I	High	3.24
c	GMRGPRGA	801	SCSP-I	High	2.53
d	GERGEQGPA	900	SCSP-I	High	1.90
e	AGDPGPV	612	SCSP-II	High	1.86
f	VAGGIL	529	SCSP-II	High	1.62
g	RGDVGPA	671	SCSP-II	High	1.60
h	GRVGPA	556	SCSP-II	High	1.59
i	GAQGPIGA	670	SCSP-II	High	1.50
j	GNPGPA	512	SCSP-II	High	1.23
k	GPAGPA	469	SCSP-III	High	2.15
l	GPSGPA	485	SCSP-III	High	1.73
m	GIAGPA	485	SCSP-III	High	1.57

The amino acids represented by capital letters in the table are as follows: A-Ala, G-Gly, R-Arg, D-Asp, K-Lys, E-Glu, S-Ser, M- Met, P-Pro, Q-Gln, V-Val, and I-Ile.

from 399 to 699 Da, of which m/z 471.22 and 671.37 were relatively abundant. **Figure 5D** shows that the molecular weight of SCSP-III ranged from 399 to 695 Da, in which m/z 471.20 were relatively abundant. The above results indicate that silver carp scales underwent complete enzymolysis under the action of alkaline protease.

Amino Acid Sequence of SCSPs

As shown in **Table 1**, a total of 13 peptides were identified in SCSP. The peptides contained many Gly, Ala, and Pro, and Gly accounted for approximately 33.30% of the total sequence. These types of amino acids are essential amino acids for the synthesis of collagen (18). According to the molecular weight ranges of the peptides in **Table 1**, **Figure 5**, the obtained peptides were classified into the fractions SCSP-I, SCSP-II, and SCSP-III. The content of hydrophobic amino acids in the peptides GPAGPA, GPSGPA, and GIAGPA was generally higher than those of other peptides. Correspondingly, the antioxidant activity of SCSP-III was also higher than those of other SCSPs.

DISCUSSION

Physical Properties of SCSPs

According to the test results, the smaller the molecular weight of the peptide is, the higher the solubility is. The balance of hydrophilic forces and hydrophobic forces is a key factor affecting the solubility of peptides. Peptides with smaller molecular weights are expected to obtain more polar residues -COOH, -NH2, -OH, etc. (19). These hydrophilic groups can form hydrogen bonds with H2O and increase the force between peptide molecules and solvent molecules, thereby increasing the solubility of the peptide. With the increase of pH value, the solubility of the same SCSP first decreases and then increases and there seems to be a turning point at pH 6 (**Figure 2A**). This is because the solubility of the peptide also depends on the net charge of the molecule. The peptide solution near the isoelectric point is neutral, and the interaction between the solute and the solvent is stronger than the electrostatic effect, leading to aggregation and precipitation between the peptide solute molecules and a reduction of the solubility (20). When the pH is away from the isoelectric point, under the combined action of intermolecular force and electrostatic force, the peptide solute can be effectively dispersed in the solvent system, and the solubility increases. In the experiment, the emulsibility and emulsifying stability decreased with decreasing molecular weight (**Figure 2B**). This may be because the low intermolecular cross-linking of low-molecular-weight peptides is not enough to form a stable dispersion system, resulting in the decreases in emulsibility and emulsifying stability (21).

Antioxidant Effects of SCSPs

On the case of DPPH results, there seems to be little correlations between DPPH clearance and peptide molecular weight, because that small-molecule peptides are mostly more polar and hydrophilic, making them less reactive with lipophilic DPPH• free radicals (22). This difference may also have been related to the highest histidine mass fraction (0.14%) in SCSP-I. Because histidine is an important active site of antioxidant peptides, it can act as a proton donor to combine with DPPH•, thus improving the efficiency of SCSP-I at free radical scavenging (23). **Figures 3B–D** shows that the antioxidant powers were ranked as SCSP-III > SCSP-II > SCSP-I > SCSP, which was different from the ordering of DPPH• scavenging rates. This may be because the polar molecules of low-molecular-weight peptides can provide many electrons, which can convert free radicals into stable products and terminate free-radical chain reactions (23, 24). Therefore, small-molecule peptides may exhibit better antioxidant properties in this respect.

Biological Activities of SCSPs

An increase in melanin can lead to hyperpigmentation disorders, forming dark spots, spots, and freckles (25). Therefore, tyrosinase inhibitors, as an effective component to promote skin whitening, have received extensive attention in the field of cosmetics (26). Choi et al. have shown that low concentrations of fish scale peptide can be absorbed by cells and can effectively inhibit the tyrosinase activity in melanoma cells (27), which is supported by the results of this work. The α-arbutin produces toxic and side effects at high concentrations, blocking cell activity and causing cell apoptosis (28). In contrast, the fractions of SCSP were highly safe to mouse B16 cells even at high concentrations.

Relations Between SCSP Biological Activity and Amino Acid Sequence

After enzymolysis, the resulting products were mostly small-molecule substances, and the signal intensity of small-molecule peptides after nanofiltration was significantly higher than that before nanofiltration, in line with the results of Cinq-Mars et al. (29). The primary structure and molecular weight of a peptide directly determines the strength of its antioxidant activity (21, 30).

In the work, the sequences of the SCSP-II and SCSP-III fractions were both shorter than 10 amino acids (**Table 1**), and compared with SCSP-I, the two had stronger antioxidant capability. These results are consistent with Ma's conclusion that short peptides have greater antioxidant activities (6). The content of hydrophobic amino acids in SCSP-III was higher than that of other SCSPs. This may be because hydrophobic amino acids act as hydrogen donors to interact with other amino acids to enhance the hydrophobic properties of the polypeptides (31), or act as hydrogen donors to react with metal ions and free radicals to reduce the oxidation rate (32), thereby enhancing their antioxidant capability.

The Gly, Ala, Ser, and Leu present in the fish scale peptides after nanofiltration can also enhance the peptides' tyrosinase inhibitory activity, thereby inhibiting the production of melanin and giving them a strong whitening effect (33). In addition, the combination of Arg or Phe residues and hydrophobic aliphatic residues (such as Val, Ala or Leu) can directly interact with tyrosinase to inhibit the formation of quinines (34). In RGDVGPA and GRVGPA of SCSP-II, Arg is combined with hydrophobic amino acids, which may be why SCSP-II showed strong tyrosinase inhibition (**Figure 4H**).

CONCLUSIONS

The solubility of each component of SCSP was higher than 90%, and the smaller the molecular weight, the higher the solubility. In terms of antioxidation, generally, the lower the

molecular weight of the peptide, the stronger the antioxidative activity. Among them, SCSP-III had a good scavenging effect on •OH and O_2^-• and had a strong ferric reducing/antioxidant power. Cell experiments *in vitro* showed that at a concentration of 0.01 mg/mL, SCSP-II had the strong inhibitory effect on tyrosinase, which was significantly better than that of α-arbutin. This peptide fraction was safe, exhibiting no toxic or side effects. The molecular weight distribution of SCSP was 399.83 ∼ 1404.62 Da by MALDI-TOF-MS, and 13 peptide sequences were detected by UPLC-MS/MS. The peptides GPAGPA, GPSGPA, and GIAGPA, with relatively high contents of hydrophobic amino acids, may underlie the strong antioxidant activity of SCSP-III. The combination of Arg and hydrophobic amino acids in RGDVGPA and GRVGPA may be the reason why the SCSP-II component strongly inhibits tyrosinase. The above results indicate that short peptides SCSP-II and SCSP-III have good biological activity and can replace α-arbutin for melanin inhibition and oxidation inhibition. At present, although the SCSP shows the possibility of replacing α-arbutin as a whitening agent, but the product forms and sensory qualities (such as color, taste and smell) need to be further studied before application.

DATA AVAILABILITY STATEMENT

The original contributions presented in the study are included in the article/supplementary material, further inquiries can be directed to the corresponding authors.

AUTHOR CONTRIBUTIONS

XYZ: writing—original draft, formal analysis, methodology, investigation, and funding acquisition. YJZ: data curation, visualization, and writing—review and editing. SMF: visualization and writing—review and editing. TL: investigation and writing—review and editing. HLL: conceptualization, writing—review and editing, project administration, and funding acquisition. GQX: supervision, visualization, and writing—review and editing. All authors contributed to the article and approved the submitted version.

FUNDING

This work was financed by the National Key Research and Development Program of China (2019YFD0902000).

REFERENCES

1. Faralizadeh S, Rahimabadi EZ, Bahrami SH, Hasannia S. Extraction, characterization and biocompatibility evaluation of silver carp (Hypophthalmichthys molitrix) skin collagen. *Sustain Chem Pharm.* (2021) 22:100454. doi: 10.1016/j.scp.2021.100454
2. Liu D, Nikoo M, Boran G, Zhou P, Regenstein JM. Collagen and gelatin. *Annu Rev Food Sci Technol.* (2015) 6:527–57. doi: 10.1146/annurev-food-031414-111800
3. Nagai T, Izumi M, Ishii M. Fish scale collagen. preparation and partial characterization. *Int J Food Sci Technol.* (2010) 39:239–44. doi: 10.1111/j.1365-2621.2004.00777.x
4. Huang CY, Wu CH, Yang JI, Li YH, Kuo JM. Evaluation of iron-binding activity of collagen peptides prepared from the scales of four cultivated fishes in Taiwan. *J Food Drug Anal.* (2015) 23:671–8. doi: 10.1016/j.jfda.2014.06.009
5. Kim SK, Kim YT, Byun HG, Nam KS, Joo DS, Shahidi F. Isolation and characterization of antioxidative peptides from gelatin hydrolysate of Alaska pollack skin. *J Agric Food Chem.* (2001) 49:1984–9. doi: 10.1021/jf000494j
6. Ma Y, Xiong YL, Zhai J, Zhu H, Dziubla T. Fractionation and evaluation of radical-scavenging peptides from *in vitro* digests of buckwheat protein. *Food Chemist.* (2010) 118:582–88. doi: 10.1016/j.foodchem.2009.05.024
7. Tang X, He Z, Dai Y, Xiong YL, Xie M, Chen J. Peptide fractionation and free radical scavenging activity of zein hydrolysate. *J Agric Food Chem.* (2010) 58:587–93. doi: 10.1021/jf9028656
8. Wu X, Cai L, Zhang Y, Mi H, Li J. Compositions and antioxidant properties of protein hydrolysates from the skins of four carp species. *Int J Food Sci Technol.* (2015) 50:2589–97. doi: 10.1111/ijfs.12927
9. Zhang JY, Deng H, Bai J, Zhou XH, Zhao YS, Zhu Y, et al. Health-promoting properties of barley: a review of nutrient and nutraceutical composition, functionality, bioprocessing, and health benefits. *Crit Rev Food Sci Nutr.* (2021).
10. Ogawa M, Portie RJ, Moody MW, Bell J, Schexnayder MA, Losso JN. Biochemical properties of bone and scale collagens isolated from the subtropical fish black drum (Pogonia cromis) and sheepshead seabream (Archosargus probatocephalus). *Food Chem.* (2004) 88:495–501. doi: 10.1016/j.foodchem.2004.02.006
11. Fisher AA. The safety of bleaching creams containing hydroquinone. *Cutis.* (1998) 61:303–4.
12. Adler-Nissen J. Enzymic hydrolysis of food proteins. *Can Med Assoc J.* (1986) 172:1783–5.
13. Vioque J, Sánchez-Vioque R, Clemente A, Pedroche J, Millán F. Partially hydrolyzed rapeseed protein isolates with improved functional properties. *J Am Oil Chem Soc.* (2000) 77:447–50. doi: 10.1007/s11746-000-0072-y
14. Bougatef A, Nedjar-Arroume N, Manni L, Ravallec R, Barkia A, Guillochon D, et al. Purification and identification of novel antioxidant peptides from enzymatic hydrolysates of (*Sardinella aurita*) by-products proteins. *Food Chem.* (2010) 118:559–65. doi: 10.1016/j.foodchem.2009.05.021
15. Fu R, Zhang Y, Guo Y, Chen F. Antioxidant and tyrosinase inhibition activities of the ethanol-insoluble fraction of water extract of sapium sebiferum (L) roxb leaves. *S Afr J Botany.* (2014) 93:98–104. doi: 10.1016/j.sajb.2014.04.003
16. Wang B, Li ZR, Chi CF, Zhang QH, Luo HY. Preparation and evaluation of antioxidant peptides from ethanol-soluble proteins hydrolysate of *Sphyrna lewini* muscle. *Peptides.* (2012) 36:240–50. doi: 10.1016/j.peptides.2012.05.013
17. Huang YC, Yang CH, Chiou YL. Citrus flavanone naringenin enhances melanogenesis through the activation of Wnt/β-catenin signalling in mouse melanoma cells. *Phytomedicine.* (2011) 18:1244–9. doi: 10.1016/j.phymed.2011.06.028
18. Li P, Wu G. Roles of dietary glycine, proline, and hydroxyproline in collagen synthesis and animal growth. *Amino Acids.* (2018) 50:29–38. doi: 10.1007/s00726-017-2490-6
19. Gbogouri GA, Linder M, Fanni J, Parmentier M. Influence of hydrolysis degree on the functional properties of salmon byproducts hydrolysates. *J Food Sci.* (2006) 69:C615–22. doi: 10.1111/j.1365-2621.2004.tb09909.x
20. Jongjareonrak A, Benjakul S, Visessanguan W, Nagai T, Tanaka M. Isolation and characterisation of acid and pepsin-solubilised collagens from the skin of Brownstripe red snapper (*Lutjanus vitta*). *Food Chem.* (2006) 93:475–84. doi: 10.1016/j.foodchem.2004.10.026
21. Jeon YJ, Byun HG, Kim SK. Improvement of functional properties of cod frame protein hydrolysates using ultrafiltration membranes. *Process Biochemist.* (1999) 35:471–8. doi: 10.1016/S0032-9592(99)00098-9
22. Zhu L, Chen J, Tang X, Xiong YL. Reducing, radical scavenging, and chelation properties of *in vitro* digests of alcalase-treated zein hydrolysates. *J Agric Food Chemist.* (2008) 56:3884. doi: 10.1021/jf801328j
23. Wu R, Wu C, Liu D, Yang X, Huang J, Zhang J, et al. Antioxidant and anti-freezing peptides from salmon collagen hydrolysate

prepared by bacterial extracellular protease. *Food Chem.* (2018) 248:346–52. doi: 10.1016/j.foodchem.2017.12.035
24. Park SH, Jo YJ. Static hydrothermal processing and fractionation for production of a collagen peptide with anti-oxidative and anti-aging properties. *Process Biochemist*. (2019) 83:176–82. doi: 10.1016/j.procbio.2019.05.015
25. Phanuwat P, Ninnaj C, Papassara S, Tanatorn S, Aphichart K. Inhibitory activities of protein hydrolysates from spotted Babylon snails on tyrosinase and melanogenesis. *J Aquat Food Product Technol.* (2018) 27:1–19. doi: 10.1080/10498850.2018.1499687
26. Karkouch I, Tabbene O, Gharbi D, Mlouka MAB, Elkahoui S, Rihouey C, et al. Antioxidant, antityrosinase and antibiofilm activities of synthesized peptides derived from Vicia faba protein hydrolysate: a powerful agents in cosmetic application. *Ind Crop Prod.* (2017) 109:310–9. doi: 10.1016/j.indcrop.2017.08.025
27. Choi HK, Lim YS, Kim YS, Park SY, Lee CH, Hwang KW, et al. Free-radical-scavenging and tyrosinase-inhibition activities of Cheonggukjang samples fermented for various times. *Food Chem.* (2008) 106:564–8. doi: 10.1016/j.foodchem.2007.06.024
28. Jiang L, Wang D, Zhang Y, Li J, Wu Z, Wang Z, et al. Investigation of the pro-apoptotic effects of arbutin and its acetylated derivative on murine melanoma cells. *Int J Mol Med.* (2018) 41:1048–54. doi: 10.3892/ijmm.2017.3256
29. Cinq-Mars CD, Hu C, Kitts DD, Li-Chan ECY. Investigations into inhibitor type and mode, simulated gastrointestinal digestion, and cell transport of the angiotensin I-converting enzyme-inhibitory peptides in Pacific hake (*Merluccius productus*) fillet hydrolysate. *J Agric Food Chem.* (2008) 56:410–9. doi: 10.1021/jf072277p
30. Suetsuna K, Ukeda H, Ochi H. Isolation and characterization of free radical scavenging activities peptides derived from casein. *J Nutr Biochem*. (2000) 11:128–31. doi: 10.1016/S0955-2863(99)00083-2
31. Chen HM, Muramoto K, Yamauchi F, Nokihara K. Antioxidant activity of designed peptides based on the antioxidative peptide isolated from digests of a soybean protein. *J Agric Food Chem.* (1996) 44:2619–23. doi: 10.1021/jf950833m
32. Mendis E, Rajapakse N, Kim SK. Antioxidant properties of a radical-scavenging peptide purified from enzymatically prepared fish skin gelatin hydrolysate. *J Agric Food Chem.* (2005) 53:581–7. doi: 10.1021/jf048877v
33. Park SY, Lee JO, Baek HE, Lee HG. Purification and characterization of antioxidant peptides from soy protein hydrolysate. *J Food Biochem.* (2010) 34:120–32. doi: 10.1111/j.1745-4514.2009.00313.x
34. Schurink M, van Berkel WJ, Wichers HJ, Boeriu CG. Novel peptides with tyrosinase inhibitory activity. *Peptides*. (2007) 28:485–95. doi: 10.1016/j.peptides.2006.11.023

Conflict of Interest: The authors declare that the research was conducted in the absence of any commercial or financial relationships that could be construed as a potential conflict of interest.

Publisher's Note: All claims expressed in this article are solely those of the authors and do not necessarily represent those of their affiliated organizations, or those of the publisher, the editors and the reviewers. Any product that may be evaluated in this article, or claim that may be made by its manufacturer, is not guaranteed or endorsed by the publisher.

Copyright © 2022 Zu, Zhao, Fu, Liao, Li and Xiong. This is an open-access article distributed under the terms of the Creative Commons Attribution License (CC BY). The use, distribution or reproduction in other forums is permitted, provided the original author(s) and the copyright owner(s) are credited and that the original publication in this journal is cited, in accordance with accepted academic practice. No use, distribution or reproduction is permitted which does not comply with these terms.

frontiers in Nutrition

ORIGINAL RESEARCH
published: 13 January 2022
doi: 10.3389/fnut.2021.810460

Porphyra yezoensis Sauces Fermented With Lactic Acid Bacteria: Fermentation Properties, Flavor Profile, and Evaluation of Antioxidant Capacity *in vitro*

Jie Yang*[1,2,3], *Tengqi Gao*[1], *Feng Ge*[1], *Hao Sun*[1], *Zihang Cui*[1], *Zhen Wei*[1,3], *Shujun Wang*[1,3], *Pau Loke Show*[4], *Yang Tao*[5] *and Wenbin Wang*[1,3]*

[1] *Jiangsu Key Laboratory of Marine Bioresources and Environment/Jiangsu Key Laboratory of Marine Biotechnology, Jiangsu Ocean University, Lianyungang, China,* [2] *Jiangsu Key Laboratory of High-Tech Research and Development of Veterinary Biopharmaceuticals, Jiangsu Agri-Animal Husbandry Vocational College, Taizhou, China,* [3] *Co-Innovation Center of Jiangsu Marine Bio-industry Technology, Jiangsu Ocean University, Lianyungang, China,* [4] *Department of Chemical and Environmental Engineering, Faculty of Science and Engineering, University of Nottingham Malaysia, Semenyih, Malaysia,* [5] *College of Food Science and Technology, Nanjing Agricultural University, Nanjing, China*

OPEN ACCESS

Edited by:
Biao Yuan,
China Pharmaceutical University, China

Reviewed by:
Ronghai He,
Jiangsu University, China
Xu-Cong Lv,
Fujian Agriculture and Forestry University, China

****Correspondence:***
Wenbin Wang
wenbin66@jou.edu.cn

Specialty section:
This article was submitted to Food Chemistry, a section of the journal Frontiers in Nutrition

Received: *07 November 2021*
Accepted: *20 December 2021*
Published: *13 January 2022*

Citation:
Yang J, Gao T, Ge F, Sun H, Cui Z, Wei Z, Wang S, Show PL, Tao Y and Wang W (2022) Porphyra yezoensis Sauces Fermented With Lactic Acid Bacteria: Fermentation Properties, Flavor Profile, and Evaluation of Antioxidant Capacity in vitro. Front. Nutr. 8:810460. doi: 10.3389/fnut.2021.810460

The demand for roasted seaweed sandwich (*Porphyra yezoensis*) product has risen in recent years. The product slicing process has created a huge number of scraps that are not utilized effectively. Three lactic acid bacteria (LAB) strains were used to ferment *P. yezoensis* sauces in this study, including *Lactobacillus fermentum*, *Lactobacillus casei*, *Streptococcus thermophilus*, and the mixed strains (1:1:1, v/v). The fermentation characteristics, antioxidant capacity *in vitro*, sensory properties, and flavoring substances of fermented *P. yezoensis* sauces were analyzed. After 21 days of fermentation, all LAB strains grew well in the *P. yezoensis* sauces, with protease activity increased to 6.6, 9.24, 5.06, and 5.5 U/mL, respectively. Also, the flavors of *P. yezoensis* sauces fermented with *L. casei* and *L. fermentum* were satisfactory. On this premise, gas chromatography-mass spectrometry (GC-MS) was used to investigate the changes in gustatory compounds in *P. yezoensis* sauces fermented with *L. casei* and *L. fermentum*. In general, 42 and 41 volatile flavor chemicals were identified after the fermentation of *L. casei* and *L. fermentum*. Furthermore, the fermented *P. yezoensis* sauce possessed greater DPPH scavenging activity and ferric-reducing ability power than the unfermented *P. yezoensis*. Overall, the flavor and taste of *P. yezoensis* sauce fermented by *L. casei* was superior.

Keywords: ***Porphyra yezoensis*** **sauce, lactic acid bacteria, volatile components, GC-MS, antioxidation**

INTRODUCTION

The East China Sea, South China Sea, Huanghai Sea, and other coastal regions produce *Porphyra yezoensis*. The protein level in dried *P. yezoensis* is 25–30%, while the carbohydrate amount is around 40% (1). It also contains vitamins like riboflavin and niacin (2). Moreover, *P. yezoensis* is rich in minerals that can assist youngsters and the elderly to absorb nutrition (3, 4).

Dietary *P. yezoensis* products are popular in Japan and Korea while Chinese consumers eat less *P. yezoensis* products. The local market of *P. yezoensis* products in China is underdeveloped with few product varieties and influential manufactors (5). One of the main reasons is that *P. yezoensis* processing are essential, whereas the products have a distinct flavor that some domestic consumers cannot tolerate. Currently, the primary domestic seaweed processing methods are drying and roasting. Thus, more processing methods of *P. yezoensis* are needed to boosting its economic value and increase the market of *P. yezoensis* products.

The slicing of roasted seaweed sandwich into small pieces generates a large number of wastes, which are rich in protein and maltose. The processing of sandwich seaweed filet to *Porphyra* sauce helps save waste. In addition, microbal fermentation, expecially lactic acid fermentation can preserve the nutritional value of *Porphyra* sauce, give it a unique taste and flavor, enrich its product form, and creat new opportunities for the *Porphyra* market. To our knowledge, the fermentation of *P. yezoensis* sauces has been poorly studied. Zhang et al. investigated the basic nutrient content of dried *Porphyra*, and fermented it with LAB and *Aspergillus oryzae* (6). Fan et al. utilized *A. oryzae* and *Rhodozyme* to co-ferment *Porphyra* and optimized the fermentation based on the protease activity and sensory index of *Porphyra* sauces (7).

LAB is a probiotic that may generate high quantities of amino acids in its fermentation *P. yezoensis* supernatant. It coud be a suitable species to ferment *Porphyra* sauces (8). This study chose *L. fermentum*, *L. casei*, and *S. thermophilus* to independently and co-ferment waste materials of roasted seaweed sandwich. The changes of fermentation characteristics and flavor profile were evaluated. Furthermore, the DPPH scavenging activity and ferric-reducing ability power (FRAP) of fermented *P. yezoensis* sauces were also investigated. The findings may help to produce probiotic fermented *P. yezoensis* sauces with excellent nutritional value and flavor.

MATERIALS AND METHODS

Bacterial Strains and Culture Conditions

S. thermophilus FJAT-46738, *L. fermentum* FJAT-46744, and *L. casei* FJAT-7928 were obtained from the Fujian Academy of Agricultural Sciences, China. The single colony of the three LAB strains were innoculted to 10 mL MRS broth, cultivated for 36 h at 40°C except for *L. fermentum* (37°C). These strains were cultured with the AnaeroPack System C-32 (Mitsubishi Gas Chemical Company, Inc. Tokyo).

Fermentation of *P. yezoensis* Sauce

The waste materials of roasted seaweed (*P. yezoensis*) sandwich was obtained from a local plant (Lianyungang Wende Food Co., Ltd. Lianyungang) in Lianyungang, Jiangsu, China. The seaweed sandwich scraps were crushed to a specific value (0.01 mm) by a beater. The aperture of the machine sieve hole should be kept at around 0.01 mm to promote the release of protein from the tissue (9). Ten grams of seaweed sandwich scrap powders and 15 mL water were mixed with a ratio (m/v) of 1:1.5 in 100 mL glass bottles with blue lid. The bottles were then sterilized at 121°C for 30 min in a autoclave. This process both softened the tissue of *P. yezoensis* and inactivated the residue bacteria. After cooling to room tempreature, the activated *L. fermentum*, *S. thermophilus*, *L. casei*, and their mixtures (1:1:1 v/v) were, respectively, added into the bottles at a ratio of 3% (v/v). The blue lid bottles were then tightened and statically fermented at 40°C. The viable bacteria level, pH, protease vitality, and sensory quality of the fermented products were measured at 0, 3, 7, 14, and 21 days.

Determination of Viable Cell and pH

One gram of fermented *P. yezoensis* sauces were weighed and serially diluted with sterile 0.9% (w/v) NaCl solution. One hundred microlilter of each dilutions were, respectively, spread on MRS agar plates with two replicates and incubated in AnaeroPack System C-32 at 40°C for 36 h. The cell counts were expressed as colony numbers (Log 10 CFU per g). The *P. yezoensis* sauce without fermentation was used as control. An appropriate amount of fermented *P. yezoensis* sauces were sampled and the pH was measured by a digital pH meter (Instrument & Electricity Scientific Instruments Company, Shanghai).

Sensory Evaluations

Ten grams of each fermented *P. yezoensis* sauce were placed in plastic cups with cup and individually tasted by the sensory panelists. The sensory panel consisted of 7 persons (2 males and 5 females, aged 19–24) from School of Food Science and Engineering, Jiangsu Ocean University. All of the members were well-tranined before sensory evaluation. The sensory descriptors agreed by the team members include intensities (seaweed flavor, sauce flavor and no fishy flavor), preferences (aroma, sour flavor, bitter flavor and aftertaste), and overall quality. The intensity, preference, and overall quality scales ranged from 0 (weak) to 10 (strong), 0 (bad or dislike) to 10 (good or like), and 0 (dislike) to 10 (like), respectively (10).

About 10 g fermented *P. yezoensis* sauces at 25°C was randomly taken in the training and evaluation process. Water and white bread were provided to the assessors to wash the palate. The training and evaluation were organized in conformity to the International Organization for Standardization (ISO, 1993) and conducted in a sensory laboratory that complies with the American Society for Testing and Materials (ASTM) criteria.

Determination of Protease Activity

The protease produced during the fermentation could effectively enhanced biological activity of the products (11). The formaldehyde method was used to determine the protease activity of *P. yezoensis* sauce (12). Ten grams of fermented *P. yezoensis* sauce in a 250 mL tapered container was added with 80 mL 55°C ddH_2O, and incubated in water bath at 55°C for 3 h. The samples were then boiled for 1 min to inactivate the inherent enzyme. The sample was cooled to room temperature and the volume was adjusted to 100 mL with ddH_2O, and filtered through filter paper. Ten milliliter of the filtrate in a 150 mL tapered bottle was added with 50 mL ddH_2O, 4–5 drops of phenolphthalein indicator, and titrated with 0.1 mol/L NaOH solution until the solution just turned red. The volume

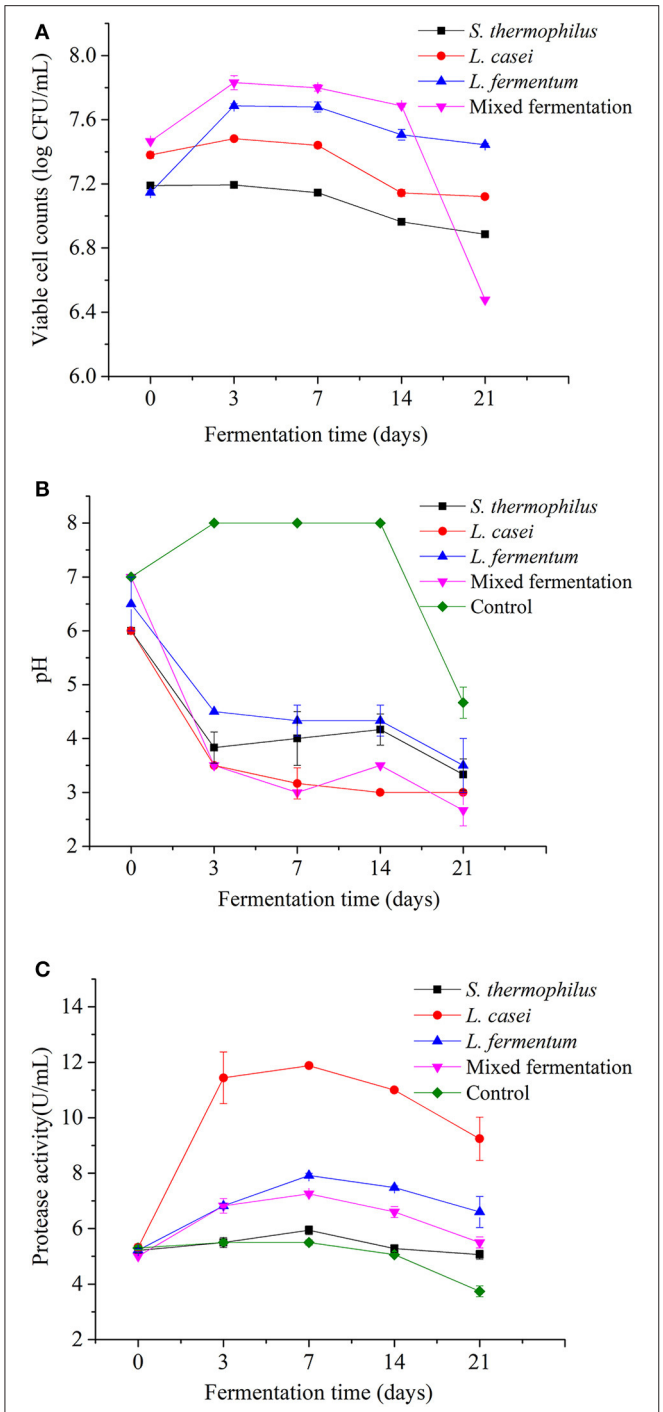

FIGURE 1 | Evolutions of viable cell counts **(A)**, pH value **(B)** and protease activity **(C)** of *Porphyra yezoensis* sauces during 21 days of LAB strains fermentation.

of consumed NaOH was recorded as V1. The sample in the tapered bottle was added with 10 mL formaldehyde, titrated with 0.1 mol/L NaOH to dark red as the endpoint. The volume of consumed NaOH was recorded as V2. The protease viability is then calculated as (Eq. 1):

$$\text{Protease viability} = \{[(V2 - V1) \times C \times 0.044]/[10 \times 10/100]\} \times 100/1 - W \quad (1)$$

where V1 is the volume of NaOH consumed by titration before adding formaldehyde, mL; V2 is the volume of NaOH consumed by titration after adding formaldehyde, mL; C is the concentration of standard NaOH, mol/L; W is the moisture content of fermented *P. yezoensis* sauces, mL.

GC-MS Analysis

Agilent 5977A series GC/MSD system (Agilent Technologies, CA) and Agilent HP-INNOWAX (30 m × 0.25 mm × 0.25 μm) were used to analyze the volatile compounds in the fermented *P. yezoensis* sauces. Two grams of sauce sample in a 20 mL headspace bottle was added with 3 mL of saturated sodium chloride solution (refrigerated at −20°C). The intake temperature was 250°C and the initial column temperature was 40°C. After incubation for 1 min, it was heated to 80°C at a rate of 4°C/min. This temperature was hold for 1 min, then heated to 160°C at a rate of 2°C/min, and finally heated to 220°C at a rate of 10°C/min. The temperature was then maintained for 10 min. Helium gas with high purity was used as the gas load and the flow rate was 1 mL/min. MS temperatures of the quaternary rod were 150°C. The ion source (230°C) was an electron-ion source with an electron energy of 70 eV and a scanning range of 35–350 *m/z*.

The semi-qualitative analysis was done with mass spectrometry in the computer spectral library (NIST/WILEY). The compound was identified when matched to a known volatile component with a score ≥80. The internal standard in this study was 2-octanol (concentration of 10 mg/L) (13, 14). The content of each volatile compound in the tested samples was calculated according to the following formula (Eq. 2).

$$C_X = M_X / M_{\text{intensor}} \times C_{\text{intensor}} (\text{mg/kg}) \quad (2)$$

where CX is the concentration of volatile compounds to be measured, MX is the peak area of the measured volatile compound, M_{intensor} is the peak area of the internal standard, C_{intensor} is the concentration of the internal standard.

The data of samples were sorted and drawn with Origin 2021 to analyze the changes in volatile profile (15).

Assay of DPPH Radical Scavenging and Ferric-Reducing Activity

Active ingredients of each *P. yezoensis* sauce (5 g) was extracted with 50 mL ddH_2O. Ultrasound (Wuxi Gangzheng Technology Co., Ltd. Wuxi) was utilized to disrupt the cell wall and assist the extraction. The ultrasound power was 880 W the ultrasonic duration was 30 min, and the ultrasonic temperature was 50°C. The sample was then centrifuged at 8,000 g for 15 min, and the supernatant was collected (16, 17). *P. yezoensis* sauce extract (1 mL) was mixed with 1 mL of DPPH solution (0.1 mM), and incubated at 37°C in the dark for 30 min prior to measuring the

absorbance at 517 nm (17). The scavenging activity of the DPPH radical was calculated as follows (Eq. 3).

$$\text{DPPH radical scavenging activity}(\%) = 1 - [(A_{\text{sample}} - A_{\text{control}})/A_{\text{blank}}] \times 100 \quad (3)$$

A_{control} was made by using absolute ethanol instead of DPPH ethanolic solution, and A_{blank} was prepared by replacing the polysaccharide sample solution with ddH_2O.

The Ferric-Reducing activity of fermented *P. yezoensis* sauces were determined by the FRAP assay with an commercial kits (Jiancheng Bioengineering Institute, Nanjing, China). The absorbance was recorded at 593 nm.

Statistical Analysis

All of the experiments were repeated triplicate. Data were expressed as the mean ± standard deviation. The data were analyzed by Excel, Origin 2021, and SPSS 20.0 software. Significance was defined at $p < 0.05$.

RESULTS

Growth of LAB and pH Changes

The changes of viable cell counts and pH value of *P. yezoensis* sauces fermented with *S. thermophilus*, *L. casei*, *L. fermentum*, and the mixed strains during 21 days of fermentation are shown in **Figure 1**. All the three LAB strains were able to grow in the rehydrated roasted seaweed sandwich scraps. The initial viable bacteria counts of *L. casei*, *L. fermentum*, *S. thermophilus* and the mixed fermentation group were 7.38 ± 0.02, 7.15 ± 0.01, 7.19 ± 0.01 and 7.47 ± 0.03 log CFU/mL, respectively. After 21 days of fermentation, the viable cell counts in *P. yezoensis* sauce fermented with *L. casei*, *L. fermentum*, *S. thermophilus* and the mixed strains were 7.1 ± 0.01, 7.4 ± 0.01, 6.9 ± 0.015 and 6.5 ± 0.01 CFU/mL, indicating that the *L. casei* and *L. fermentum* strains were able to adapt to the fermentation environment. The number of viable bacteria of *P. yezoensis* sauce fermented with the mixed strains was considerably low at the end of fermentation. This was possibly due to the low pH (2.7 ± 0.29), which was one of the important factors affecting the number of viable bacteria during lactic acid fermentation (18). After 3 days of fermentation, the viable cell count frist rose and then decreased in the fermented *P. yezoensis* sauces. In contrast, no viable bacteria were found in the unfermented *P. yezoensis* sauce that was previously sterilized.

The pH value of the *P. yezoensis* sauce decreased during fermentation with all the LAB strains (**Figure 1B**). The pH values of the three strains have generally decreased. From 0 to Day 3, the pH value of fermented *P. yezoensis* sauces decreased the fastest. The pH value of each strain steadily dropped over a period of 3–21 days. When compared to the other two bacteria, *L. casei* has always had the lowest pH value. A low pH would efficiently inhibit the multiplication of pathogenic bacteria in samples and extend the shelf life (19).

Determination of Protease Activity

Microbial fermentation might enhance the protease activity of the product (20). **Figure 1C** revealed that the protease activity of *P. yezoensis* sauces was initially around 5.20 U/mL and increased during all the fermentation processes. The protease activity increased to the peak at Day 7 and then decreased in the following fermentation period. Among all the groups, the protease activity of *P. yezoensis* sauces fermented by *L. casei* were the greatest (11.88 U/mL at day 7) at the same stage, which was partly consistent with the low pH value. After 21 days of fermentation, the protease activities of *P. yezoensis* sauces fermented by *L. fermentum*, *L. casei*, *S. thermophilus*, and the mixed strains were increased to 6.60, 9.24, 5.06, and 5.50 U/mL, respectively. Furthermore, the protease activity of all fermented *P. yezoensis* sauces were significantly increased ($p < 0.05$) than the control.

Sensory Evaluation

The intensities of all the sensory attributes of fermented *P. yezoensis* sauces showed an increasing trend within the first week and then decreased gradually (**Figure 2**). The sensory quality of *P. yezoensis* sauces fermented by *L. casei* was the best among all the samples at the same fermentation period, followed by *L. fermentum*, *S. thermophilus* and the mixed strains. The fishy flavor, bitter flavor, and sour tastes in all samples got intensified with time, and the scent of seaweed and sauce flavor were more apparent in the *L. casei* fermented *P. yezoensis* sauce. Moreover, the sensory properties of the *P. yezoensis* sauce fermented by *L. fermentum* were relatively stable, and no significant changes in the flavors werwe observed. The aroma value increased the maximum at Day 7, and then declined significantly. Besides, the sensory quality of *P. yezoensis* sauces fermented by *S. thermophilus* were relatively low, among which the bitter and fishy smells were stonger than the aroma and sauce flavors. Taking all the sensory results into account, *L. casei* was more suitable for the *P. yezoensis* sauce fermentation.

Analysis of Volatile Composition

According to the above results, *L. casei* and *L. fermentum* strains were preferred for fermenting *P. yezoensis* sauce. Thus, GC-MS was employed to investigate flavor alterations in *P. yezoensis* sauce fermented by *L. casei* and *L. fermentum*. **Figure 3** shows that during fermentation at 7 and 21 day, a total of 67 volatile compounds were detected from the *P. yezoensis* sauces. Specifically, 35, 41, and 42 volatile compounds were identified in the control group, *L. fermentum* group and *L. casei* group during fermentation, respectively. These volatile compounds mainly included aldehydes, alcohols, hydrocarbons, acids, phenols, ketones, esters, pyrazines, furans and benzodiazepines and others (**Supplementary Table 1**). At a given fermentation, the volatile profile changed with time due to the catabolic response of flavor precursor material (21). Alcohols presented the highest amount in all the 6 samples, accounting for 65.62%. Aldehydes and hydrocarbons accounted for 46.45 and 27.29% of the total volatile compounds, respectively. Alcohols and esters were mainly produced in the middle stage of fermentation, while hydrocarbons were produced in the later stage (22).

Assay of DPPH Radical Scavenging and Ferric-Reducing Activity

Polysaccharides, polyphenols, proteins, and porphyrins were the physiologically active compounds found in *P. yezoensis*, with anticancer, antioxidant, hypolipidemic, and anti-inflammatory properties (23, 24). Fermentation with LAB can increase the biological activity of food by bio-transforming active molecules (25). The antioxidant capacities of *P. yezoensis* sauces extract before and after fermentation with *L. casei* and *L. fermentum* are shown in **Figure 4**. The free radical scavenging capability and ferric reducing antioxidant capacity of unfermented *P. yezoensis* sauce were only 20.4% and 0.23, respectively. The antioxidant activity of all the tested extract from fermentated *P. yezoensis* sauces steadly increased during the 21 days of fermentation. For the *P. yezoensis* sauce fermented by *L. casei* for 21 days, the free radical scavenging capability and ferric reducing antioxidant capacity increased to 78% and 0.73, respectively. Similarly, *L. fermentum* fermented samples increased to 67.8% and 0.58, respectively.

DISCUSSION

As more people become aware of the health benefits of laver, the laver industrial development has become more diverse and extended (26). The waste from the manufacturing of roasted seaweed sandwich were used to prepare the fermented *P. yezoensis* sauce. The obtained results revealed that *L. casei* was capable to grow in the the *P. yezoensis* sauce. The resulting seaweed sauce was featured by high enzyme vitality, and pronounced taste and flavor. In addition, compared with the control group and *L. fermentum* fermentation, *L. casei* fermentation improved the antioxidant activity of the sauce significantly, which was in line with the finding reported by Zubaidah et al., who fermented cabbage by *L. casei* (27).

The GC-MS analysis revealed that 42, 41, and 35 volatile flavor compounds were detected in the *P. yezoensis* sauces fermentated by *L. casei*, *L. fermentum* and the control group, respectively. These volatile compounds were responsible for *P. yezoensis* sauce flavor. Aldehydes are generated by fat oxidation, providing a fat scent (28). In the *L. casei* fermentation group one aldehyde was detected at Day 7, and 8 aldehydes were found at Day 21. The portion of aldehyde in the total volatile components increased from 2.71% at Day 7 to 46.45% at Day 21. However, in the *L. fermentum* group, the relative amount of aldehydes dropped from 25.53 to 6.64% and the number of compounds dropped from 6 to 3. In the control group, the ratio of aldehyde species increased from 2.49 to 8.47%, and the number of aldehyde species increased from 2 to 5. The unsaturated aldehydes have attractive aromas (29). For example, benzaldehyde possesses pleasant fruity flavor, and furfural refers to thew sweet and almond scent. These

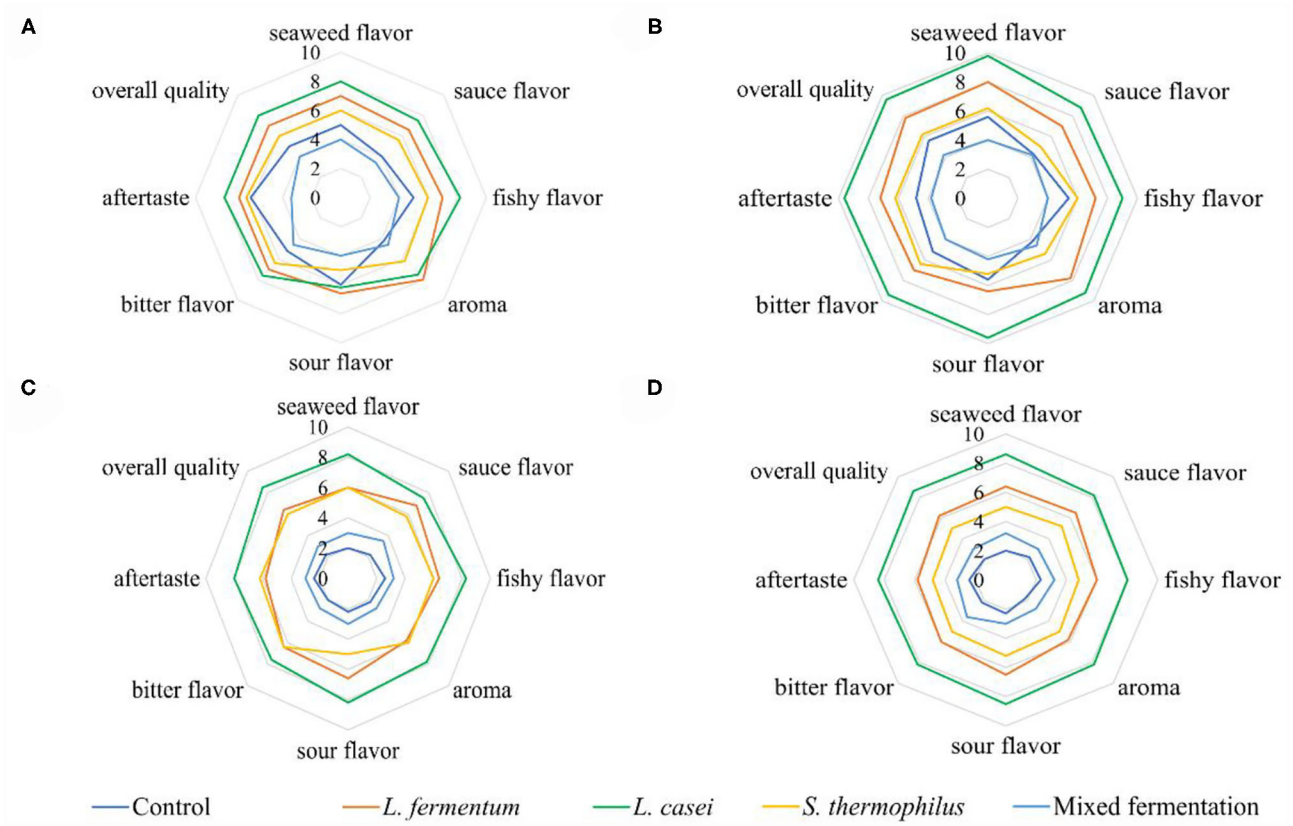

FIGURE 2 | Radiation map of sensory profile for fermented *P. yezoensis* sauces. **(A)** 3 days of fermentation, **(B)** 7 days of fermentation, **(C)** 14 days of fermentation, **(D)** 21 days of fermentation.

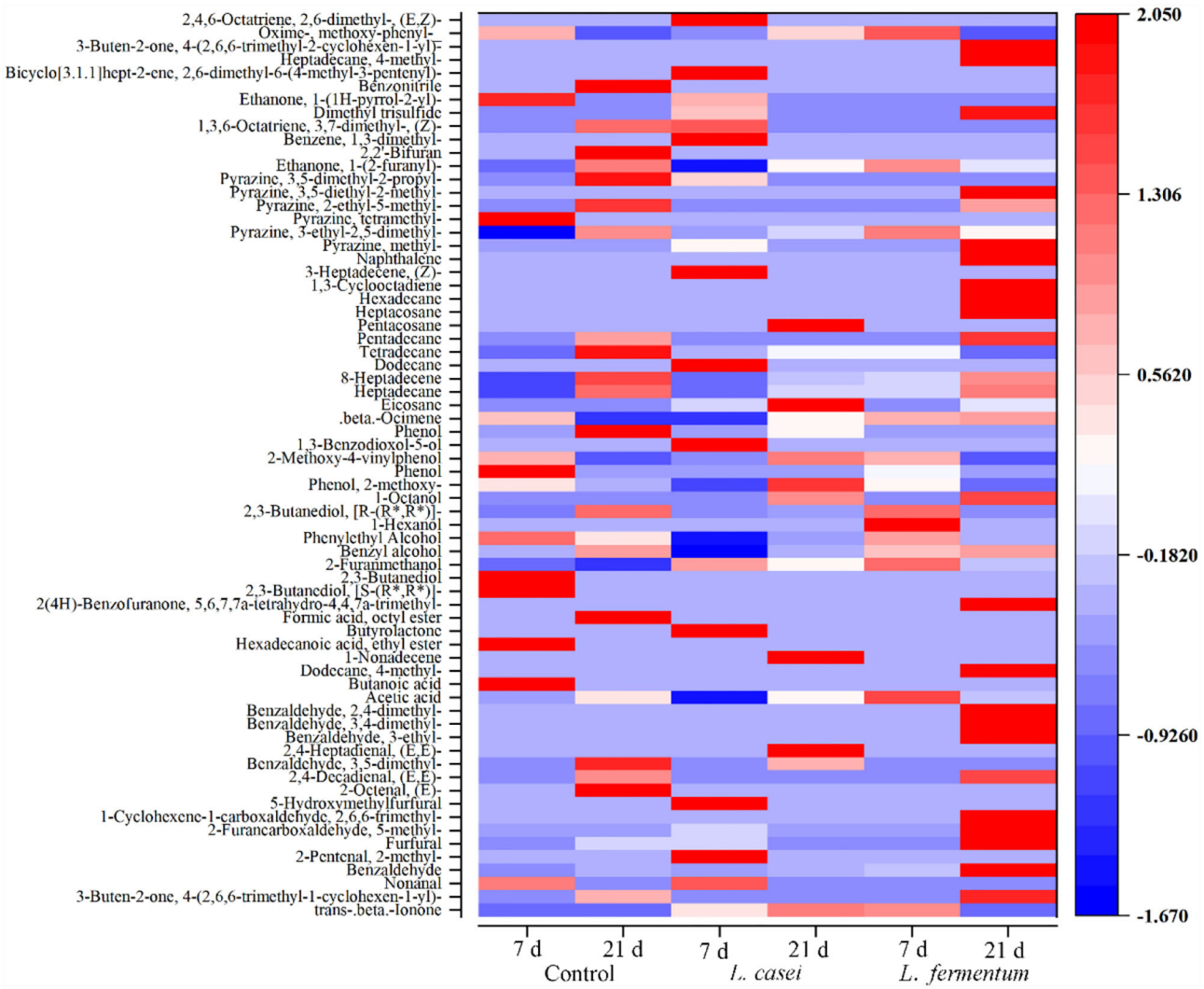

FIGURE 3 | Heat map of volatile substances of *P. yezoensis* sauces.

components can contribute to the enhancement of the sauce flavor (30).

Alcohols are produced by the microbial metabolism including the breakdown of unsaturated fatty acids and the reduction of base chemicals, which impart a clove scent (31). A total of 8 alcoholic compounds were detected from the six groups, including 2,3-Butanediol, [S-(R*,R*)], 2,3-butanediol, 2-furanmethanol, benzyl alcohol, phenylethyl alcohol and 2,3-Butanediol, [R-(R*,R*)], etc. The relative content of 2,3-Butanediol, [R-(R*,R*)] increased up to 40.91% at Day 7 of *L. casei* fermentation, and then decreased to 1.71% at Day 21 of fermentation, thus providing little contribution to the overall flavor.

Hydrocarbon compounds were identified in *P. yezoensis* sauces, including β-ocimene, eicosane, heptadecane, 8-heptadecene, tetradecane and others. Although alkyene compounds were regarded as odorless due to the cleavage of the alkoxygen radical, some olefins generated aldehydes and ketones under specific circumstances still can contribute to the overall flavor of *P. yezoensis* sauces (32). Several alkanes, when degraded under certain circumstances, generated a fishy odor (33). After 21 days of fermentation with *L casei*, the number of hydrocarbon species increased from 4 to 9, with the relative content of 8-heptadecene increased from 7.15 to 19.15%. During fermentation, the relative content of 8-heptadecene in unfermented group increased from 2.21 to 16.48%, but the relative content of 8-heptadecene during *L. fermentum* fermentation was no significant difference. It was widely established that 8-heptadecene tadecene was a distinctive flavor compound found in a wide variety of macroalgae (34).

P. yezoensis sauces contained a total of four acid compounds, namely acetic acid, butanoic acid, dodecane, 4-methyl, and 1-non-adecene. Among them, acetic acid is primarily an enzymatic response in the lipogenesis enzyme pathway, which has an oily fishy smell. Also, acetic acid may create ester bonds with sugar to enhance the flavor (35). The *L.*

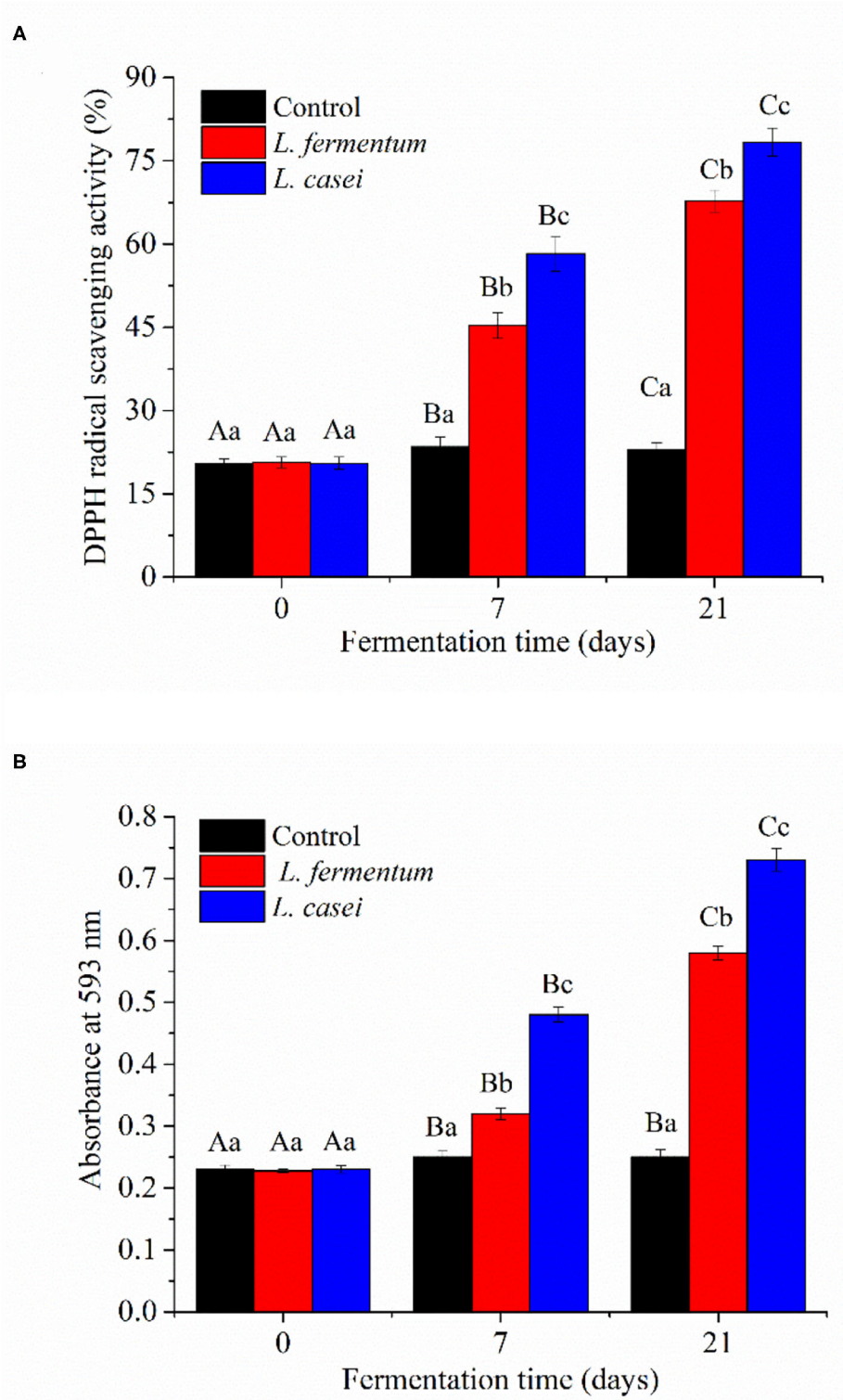

FIGURE 4 | DPPH radical scavenging activity **(A)** and FRAP **(B)** of *P. yezoensis* sauces during fermentation. Values with different letters within each samples indicated a significant difference in content ($p < 0.05$).

casei fermentation reduced the concentration of acetic acid, consequently atteunating the pungent smell of *P. yezoensis* sauces (36). At the same time, the release of acetic acid indicates that *L. casei* has the ability to metabolize lactic acid (37).

Esters are formed by esterifying carboxylic acid and alcoho, which are usually related with fruit or floral scents, and contributing to the flavor of food products (38, 39). Ketones with a unique fruit smell, can be generated by heat oxidation

or breakdown of amino acids (40). Pyrazines are nitrogen-containing heterocyclic compounds that are an intermediate in the Millard reaction (41). They often have a barbeque and nut flavor, an excellent dispersed fragrance, and an extreme deficient concentration. These volatile compounds were detected in *P. yezoensis* sauce fermented by *L. casei*. Therefore, it was determined that fermenting *P. yezoensis* sauce with *L. casei* produces the finest flavor.

CONCLUSION

In this study, three LAB strains fermented sandwich seaweed processing waste to prepare *P. yezoensis* sauce. The detection and analysis of the three LAB strains fermented *P. yezoensis* sauces revealed that the *L. casei* was able to adapt to the fermentation environment and had high protease vitality. Sensory evaluation results showed that fermentation of *L. casei* could enhanced the acceptability of *P. yezoensis* sauce. Following GC-MS detection, *P. yezoensis* sauce generated 42 volatile flavor compounds by fermentation of *L. casei*. These volatile chemicals are essential for *P. yezoensis* sauce taste. The antioxidant activity of *P. yezoensis* sauces fermented by *L. casei* was also higher. Overall, *L. casei* fermented *P. yezoensis* sauce had the best flavor and was appropriate for producing *P. yezoensis* sauce meals. The fermented *P. yezoensis* sauces has a distinctive taste and excellent nutritional value for the elderly, children and babies. This study can provide guidance for the development of LAB fermented *P. yezoensis* sauces in future studies.

DATA AVAILABILITY STATEMENT

The original contributions presented in the study are included in the article/**Supplementary Material**, further inquiries can be directed to the corresponding author/s.

AUTHOR CONTRIBUTIONS

JY performed the experiments, analyzed the data, and wrote the manuscript. TG and FG analyzed the data and wrote the manuscript. HS, ZC, and ZW analyzed and discussed the data. SW, PS, and YT provided samples and discussed the data. WW designed the research content, analyzed the data, and modified the manuscript. All authors have read and agreed to the published version of the manuscript.

FUNDING

This study was supported by the Project funded by Opening Foundation of Key Laboratory of high-tech veterinary biopharmaceutical research, Jiangsu province (No. NSFK201803), National Natural Science Foundation of China (Nos. 32100037 and 32172284), Natural Science Research General Project of Jiangsu Higher Education Institutions (No. 20KJB550008), China Postdoctoral Science Foundation (No. 2019M661767), Natural Science Foundation of Jiangsu Province (No. BK20201028), Jiangsu Planned Projects for Postdoctoral Research Funds (No. 2021K316C), Jiangsu Ocean University Research Funds (No. KQ17028), and Priority Academic Program Development of Jiangsu Higher Education Institutions (PAPD).

SUPPLEMENTARY MATERIAL

The Supplementary Material for this article can be found online at: https://www.frontiersin.org/articles/10.3389/fnut.2021.810460/full#supplementary-material

REFERENCES

1. Jin C, Wang J, Wang S, Xu X. *Porphyra* species: a mini-review of its pharmacological and nutritional properties. *J Med Food.* (2016) 19:111–9. doi: 10.1089/jmf.2015.3426
2. Watanabe F, Takenaka S, Katsura H, Miyamoto E, Nakano Y. Characterization of a vitamin B12 compound in the edible purple laver. porphyra yezoensis. *J Agric Chem Soc Japan.* (2000) 64:2712–5. doi: 10.1271/bbb.64.2712
3. Venkatraman KL, Syed AA, Indumathi P, Mehta A. Vitpor ai, a coagulation factor xiia inhibitor from *porphyra yezoensis*: *In vivo* mode of action and assessment of platelet function analysis. *Prot Pept Lett.* (2020) 27:243–50. doi: 10.2174/0929866526666191026111056
4. Qian L, Zhou Y, Ma JX. Hypolipidemic effect of the polysaccharides from *porphyra yezoensis*. *Int J Biol Macromol.* (2014) 68:48–9. doi: 10.1016/j.ijbiomac.2014.04.004
5. Tian Y, Jiang Y, Guo Y, Zhao Y, Li N, Yao L, et al. Research progress on nutritional quality and edible value of *Porphyra*. *J Food Saf Qual.* (2021) 12:4929–36. doi: 10.19812/j.cnki.jfsq11-5956/ts.2021.12.033
6. Zhang X, Luo J, Zhuo D, He Y, Zhou H, Ren D, et al. Fermentation technology of special *Porphyra haitanensis* sauce. *J Food Saf Qual.* (2020) 11:2609–16. doi: 10.19812/j.cnki.jfsq11-5956/ts.2020.08.047
7. Fan L, Shi X. Technology of fermentative *Porphyra* sauce. *Food Sci Technol.* (2015) 40:269–72. doi: 10.13684/j.cnki.spkj.2015.03.064
8. Uchida M, Miyoshi T, Yoshida G, Niwa K, Mori M, Wakabayashi H. Isolation and characterization of halophilic lactic acid bacteria acting as a starter culture for sauce fermentation of the red alga nori (*porphyra yezoensis*). *J Appl Microbiol.* (2014) 116:1506–20. doi: 10.1111/jam.12466
9. Ryu S. Study on manufactute of porphyran jam and eppiciency extraction method of porphyran from *Porphyra yezoensis*. *J Korean Appl Sci Technol.* (2013) 30:504–17. doi: 10.12925/jkocs.2013.30.3.504
10. Yuasa M, Shimada A, Matsuzaki A, Eguchi A, Tominaga M. Chemical composition and sensory properties of fermented citrus juice using probiotic lactic acid bacteria. *Food Biosci.* (2021) 39:100810. doi: 10.1016/j.fbio.2020.100810
11. Chen Y, Wang Y, Chen J, Tang H, Wang C, Li Z, et al. Bioprocessing of soybeans (*Glycine max* L.) by solid-state fermentation with *Eurotium cristatum* YL-1 improves total phenolic content, isoflavone aglycones, and antioxidant activity. *RSC Adv.* (2020) 10:16928–41. doi: 10.1039/C9RA10344A
12. Zhang S. Determination of the relationship between protease enzyme activity and number of psychrophilic bacteria in fresh milk in Harbin. *China Dairy Ind.* (2012) 40:41–9. doi: 10.3969/j.issn.1001-2230.2012.07.012
13. Apa B, Yha B, Rui M, Khe A, Lpt C, Mc A. Combination of solid phase microextraction and low energy electron ionization gas chromatography-quadrupole time-of-flight mass spectrometry to meet the challenges of flavour analysis. *Talanta.* (2021) 235:122793. doi: 10.1016/j.talanta.2021.122793

14. Augustini A, Sielemann S, Telgheder U. Strategy for the identification of flavor compounds in e-liquids by correlating the analysis of GCxIMS and GC-MS. *Talanta.* (2021) 230:122318. doi: 10.1016/j.talanta.2021.122318
15. Yang J, Lu J, Zhu Q, Tao Y, Zhu Q, Guo C, et al. Isolation and characterization of a novel *Lactobacillus plantarum* MMB-07 from traditional suanyu for *Acanthogobius hasta* fermentation. *J Biosci Bioeng.* (2021) 132:161–6. doi: 10.1016/j.jbiosc.2020.12.016
16. Tang WZ, Wang B, Wang MM, Wang MM. Ultrasound-assisted extraction of *Osmanthus fragrans* fruit oil and evaluation of its fatty acid composition, physicochemical properties and antioxidant activity. *J Appl Res Med Aroma.* (2021) 25:100331. doi: 10.1016/j.jarmap.2021.100331
17. Xu J, Xu L, Zhou Q, Hao S, Zhou T, Xie H. Enhanced in vitro antioxidant activity of polysaccharides from Enteromorpha prolifera by enzymatic degradation. *J Food Biochem.* (2016) 40:275–83. doi: 10.1111/jfbc.12218
18. Muhialdin BJ, Hussin A, K Adum H, Hamid AA, Jaafar AH. Metabolomic changes and biological activities during the lacto-fermentation of jackfruit juice using *lactobacillus casei* atcc334. *LWT-Food Sci Technol.* (2021) 141:110940. doi: 10.1016/j.lwt.2021.110940
19. Wang Y, Tao Y, Zhang X, Shao S, Han Y, Chu D, et al. Metabolic profile of ginkgo kernel juice fermented with lactic acid bacteria: a potential way to degrade ginkgolic acids and enrich terpene lactones and phenolics. *Process Biochem.* (2018) 76:25–33. doi: 10.1016/j.procbio.2018.11.006
20. Li W, Wang T. Effect of solid-state fermentation with *Bacillus subtilis* lwo on the proteolysis and the antioxidative properties of chickpeas. *Int J Food Microbiol.* (2020) 338:108988. doi: 10.1016/j.ijfoodmicro.2020.108988
21. Li S, Jin Z, Hu D, Yang W, Chen X. Effect of solid-state fermentation with *Lactobacillus casei* on the nutritional value, isoflavones, phenolic acids and antioxidant activity of whole soybean flour. *LWT Food Sci Technol.* (2020) 125:109264. doi: 10.1016/j.lwt.2020.109264
22. Song J, Bi J, Chen Q. Assessment of sugar content, fatty acids, free amino acids, and volatile profiles in jujube fruits at different ripening stages. *Food Chem.* (2019) 270:344–52. doi: 10.1016/j.foodchem.2018.07.102
23. Isaka S, Cho K, Nakazono S, Abu R, Ueno M, Kim D, et al. Antioxidant and anti-inflammatory activities of porphyran isolated from discolored nori (*porphyra yezoensis*). *Int J Biol Macromol.* (2015) 74:68–75. doi: 10.1016/j.ijbiomac.2014.11.043
24. Wang F, Kong LM, Xie YY, Wang C, Zhou T. Purification, structural characterization, and biological activities of degraded polysaccharides from *Porphyra yezoensis*. *J Food Biochem.* (2021) 45:e13661. doi: 10.1111/jfbc.13661
25. Li S, Tao Y, Li D, Wen G, Zhou J, Manickam S, et al. Fermentation of blueberry juices using autochthonous lactic acid bacteria isolated from fruit environment: fermentation characteristics and evolution of phenolic profiles. *Chemosphere.* (2021) 276:130090. doi: 10.1016/j.chemosphere.2021.130090
26. Cho TJ, Min SR. Health functionality and quality control of laver (*Porphyra*, *Pyropia*): current issues and future perspectives as an edible seaweed. *Marine Drugs.* (2020) 18:14. doi: 10.3390/md18010014
27. Zubaidah E, Arum MS, Widyaningsih TD, Rahayu AP. Sauerkraut with the addition of *lactobacillus casei*: effects of salt and sugar concentrations on fermentation and antioxidant activity. *Curr Nutr Food Sci.* (2020) 16:1265–9. doi: 10.2174/1573401316666200217112642
28. Widjaja R, Craske JD, Wootton M. Comparative studies on volatile components of non-fragrant and fragrant rices. *J Sci Food Agric.* (2015) 70:151–61. doi: 10.1002/(SICI)1097-0010(199602)70:2<151::AID-JSFA478>3.0.CO;2-U
29. Jiye A, Trygg J, Gullberg J, Johansson AI, Jonsson P, Antti H, et al. Extraction and GC/MS analysis of the human blood plasma metabolome. *Anal Chem.* (2005) 77:8086–94. doi: 10.1021/ac051211v
30. Cao R, Hu M, Zhao L, Wang L, Liu Q. Flavor characteristics of different crops of laver (*Porphyra yezoensis*) during one harvest cycle. *J Ocean U China.* (2021) 20:213–20. doi: 10.1007/s11802-021-4447-3
31. Lee SM, Seo BC, Kim YS. Volatile compounds in fermented and acid-hydrolyzed soy sauces. *J Food Sci.* (2006) 71:C146–56. doi: 10.1111/j.1365-2621.2006.tb15610.x
32. Giannetti V, Mariani MB, Mannino P. Volatile fraction analysis by HS-SPME/GC-MS and hemometric modeling for traceability of apples cultivated in the Northeast Italy. *Food Control.* (2017) 78:215–21. doi: 10.1016/j.foodcont.2017.02.036
33. Chakraborty K, Joseph D. Production and characterization of refined oils obtained from Indian oil sardine (*Sardinella longiceps*). *J Agric Food Chem.* (2015) 63:998–1009. doi: 10.1021/jf505127e
34. Murathan ZT, Zarifikhosroshahi M, Kafkas NE. Determination of fatty acids and volatile compounds in fruits of rosehip (*Rosa L.*) species by HS-SPME/GC-MS and Im-SPME/GC-MS techniques. *Turk J Agric For.* (2016) 40:269–79. doi: 10.3906/tar-1506-50
35. Lalel H, Singh Z, Tan SC. Glycosidically-bound aroma volatile compounds in the skin and pulp of 'kensington pride' mango fruit at different stages of maturity. *Postharvest Biol Tec.* (2003) 29:205–18. doi: 10.1016/S0925-5214(02)00250-8
36. Nishino N, Touno E. Ensiling characteristics and aerobic stability of direct-cut and wilted grass silages inoculated with *Lactobacillus casei* or *Lactobacillus buchneri*. *J Sci Food Agric.* (2005) 85:1882–8. doi: 10.1002/jsfa.2189
37. Li S, Chen C, Ji Y, Lin J, Chen X, Qi B. Improvement of nutritional value, bioactivity and volatile constituents of quinoa seeds by fermentation with *lactobacillus casei*. *J Cereal Sci.* (2018) 84:83–9. doi: 10.1016/j.jcs.2018.10.008
38. Jabalpurwala F, Gurbuz O, Rouseff R. Analysis of grapefruit sulphur volatiles using SPME and pulsed flame photometric detection. *Food Chem.* (2010) 120:296–303. doi: 10.1016/j.foodchem.2009.09.079
39. Xiao Y, Huang Y, Chen Y, Fan Z, Chen R, He C, et al. Effects of solid-state fermentation with *Eurotium cristatum* YL-1 on the nutritional value, total phenolics, isoflavones, antioxidant activity, and volatile organic compounds of black soybeans. *Agronomy.* (2021) 11:1029. doi: 10.3390/agronomy11061029
40. Sarnoski PJ, O'Keefe SF, Jahncke ML, Mallikarjunan P, Flick GJ. Analysis of crab meat volatiles as possible spoilage indicators for blue crab (*Callinectes sapidus*) meat by gas chromatography-mass spectrometry. *Food Chem.* (2017) 122:930–5. doi: 10.1016/j.foodchem.2010.03.069
41. Pini GF, Brito E, García NHP, Valente A, Augusto F. A headspace solid phase microextraction (HS-SPME) method for the chromatographic determination of alkylpyrazines in cocoa samples. *J Brazil Chem Soc.* (2004) 15:267–71. doi: 10.1590/S0103-50532004000200017

Conflict of Interest: The authors declare that the research was conducted in the absence of any commercial or financial relationships that could be construed as a potential conflict of interest.

Publisher's Note: All claims expressed in this article are solely those of the authors and do not necessarily represent those of their affiliated organizations, or those of the publisher, the editors and the reviewers. Any product that may be evaluated in this article, or claim that may be made by its manufacturer, is not guaranteed or endorsed by the publisher.

Copyright © 2022 Yang, Gao, Ge, Sun, Cui, Wei, Wang, Show, Tao and Wang. This is an open-access article distributed under the terms of the Creative Commons Attribution License (CC BY). The use, distribution or reproduction in other forums is permitted, provided the original author(s) and the copyright owner(s) are credited and that the original publication in this journal is cited, in accordance with accepted academic practice. No use, distribution or reproduction is permitted which does not comply with these terms.

frontiers in Nutrition

ORIGINAL RESEARCH
published: 28 January 2022
doi: 10.3389/fnut.2022.822033

A Combined Proteomic and Metabolomic Strategy for Allergens Characterization in Natural and Fermented *Brassica napus* Bee Pollen

Shuting Yin[1,2†], Yuxiao Tao[1†], Yusuo Jiang[2], Lifeng Meng[1], Liuwei Zhao[1], Xiaofeng Xue[1], Qiangqiang Li[1] and Liming Wu[1*]*

[1] Institute of Apicultural Research, Chinese Academy of Agricultural Sciences, Beijing, China, [2] College of Animal Science, Shanxi Agricultural University, Shanxi, China

OPEN ACCESS

Edited by:
Shuai Chen,
Wuhan University, China

Reviewed by:
Rui Fan,
Peking University, China
Liping Luo,
Nanchang University, China

***Correspondence:**
Qiangqiang Li
qiangqiangli1991@163.com
Liming Wu
apiswu@126.com

[†] These authors have contributed equally to this work

Specialty section:
This article was submitted to Food Chemistry, a section of the journal Frontiers in Nutrition

Received: 25 November 2021
Accepted: 03 January 2022
Published: 28 January 2022

Citation:
Yin S, Tao Y, Jiang Y, Meng L, Zhao L, Xue X, Li Q and Wu L (2022) A Combined Proteomic and Metabolomic Strategy for Allergens Characterization in Natural and Fermented Brassica napus Bee Pollen. Front. Nutr. 9:822033. doi: 10.3389/fnut.2022.822033

Bee pollen is consumed for its nutritional and pharmacological benefits, but it also contains hazardous allergens which have not been identified. Here, we identified two potential allergens, glutaredoxin and oleosin-B2, in *Brassica napus* bee pollen using mass spectrometry-based proteomics analyses, and used bioinformatics to predict their antigenic epitopes. Comparison of fermented (by *Saccharomyces cerevisiae*) and unfermented bee pollen samples indicated that glutaredoxin and oleosin-B2 contents were significantly decreased following fermentation, while the contents of their major constituent oligopeptides and amino acids were significantly increased based on metabolomics analyses. Immunoblot analysis indicated that the IgE-binding affinity with extracted bee pollen proteins was also significantly decreased after fermentation, suggesting a reduction in the allergenicity of fermented bee pollen. Furthermore, fermentation apparently promoted the biosynthesis of L-valine, L-isoleucine, L-tryptophan, and L-phenylalanine, as well as their precursors or intermediates. Thus, fermentation could potentially alleviate allergenicity, while also positively affecting nutritional properties of *B. napus* bee pollen. Our findings might provide a scientific foundation for improving the safety of bee pollen products to facilitate its wider application.

Keywords: ***Brassica napus* bee pollen, allergens, degradation and catabolism, fermentation, *Saccharomyces cerevisiae***

INTRODUCTION

Bee pollen, plant pollen grains collected by honeybees and aggregated by salivary gland secretions and flower nectar, has been widely considered a complete food of abundant nutrients and bioactive compounds (1). More than 200 nutrients and bioactive components, including proteins, amino acids, carbohydrates, lipids, vitamins, minerals, polyphenols, etc. have been identified in bee pollen and its consumption reportedly confers numerous benefits that are the subject of ongoing

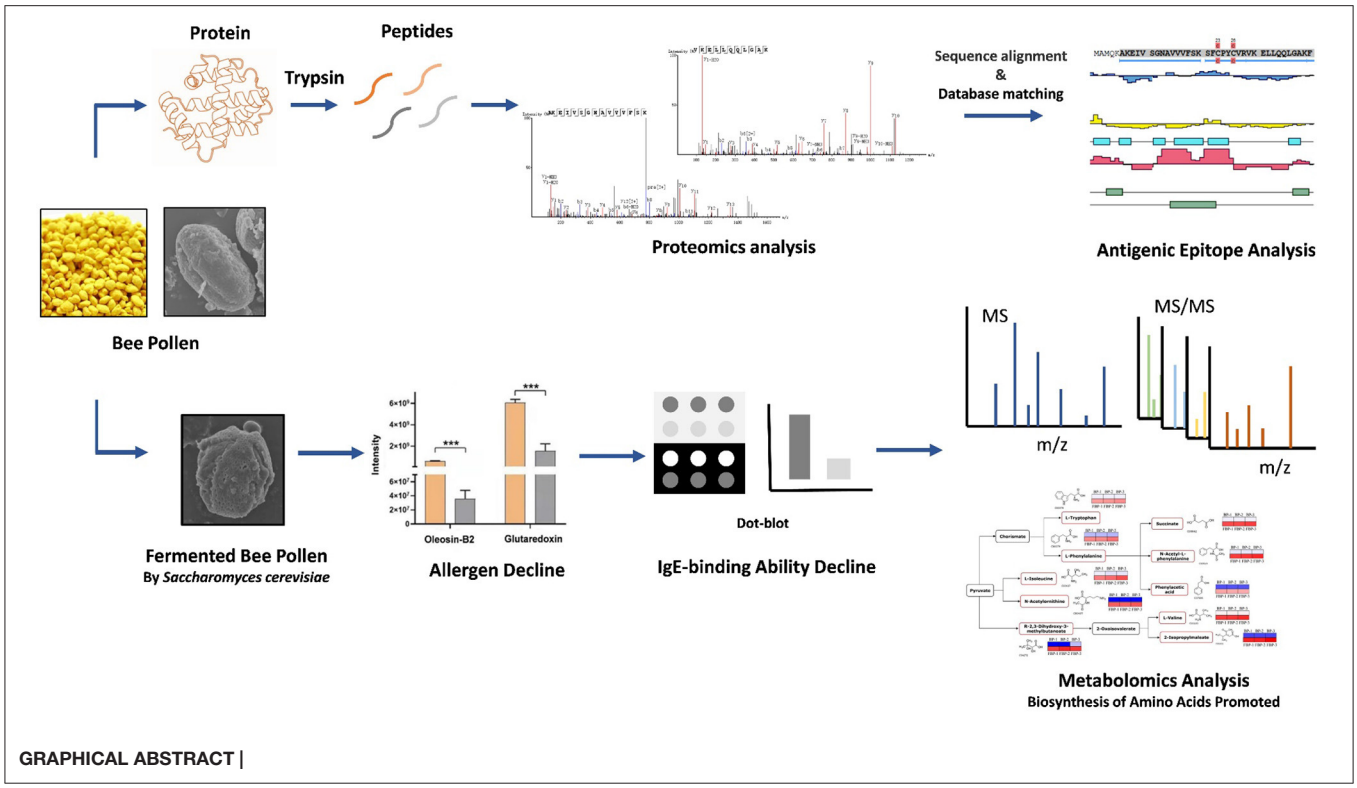

GRAPHICAL ABSTRACT |

investigation (2, 3). With increasing applications of bee pollen, for example in foods, cosmetics, and nutraceuticals, potential issues related to allergens require close scrutiny to ensure public safety. In general, patients with plant pollen allergies are also susceptible to bee pollen allergies, although some allergenic compounds in bee pollen are partially degraded or reduced by honeybee processing (4, 5).

Brassica napus bee pollen, which is produced worldwide, has potential sensitization hazards. Puumalainen et al. identified 2S albumins, or napins, as potential allergens in *B. napus* pollen (6). Another eight potential allergens of *B. napus* pollen were detected using immunoblot method although their primary structures have not been determined (7). However, the studies investigating allergens of bee pollen from *B. napus* remain limited, thereby resulting in a threat to its consumption.

Studies have shown that fermentation can reduce food allergens through hydrolysis (8), while improving nutritional and physicochemical characteristics of foods (9, 10). Reduction of protein allergens through fermentation has been reported for milk (11, 12), peanuts (13), soybeans (14, 15), and wheat (16, 17). Also, their nutritional properties were notably improved following fermentation, such as increasing the contents of free amino acids in milk (18), as well as improving the levels of phenolic compounds, bioactive peptides, and free amino acids in cereals (19). Fermentation was also found to improve the flavor and nutritional value of bee pollen in our previous research, such as increasing the contents of oligopeptides, fatty acids, phenolic compounds, etc. (20). However, it is unclear whether and how these effects are related to allergen degradation.

Therefore, this study aimed to identify the potential allergens in *B. napus* bee pollen using mass spectrometry-based proteomics analyses. We also conducted bioinformatic prediction of allergen epitopes for T and B cells. Furthermore, we explored the effects of fermenting *B. napus* bee pollen on its putative allergenic components, using proteomics, metabolomics, and immunoblot analyses. This research provides a scientific foundation for improving the safety of bee pollen products to facilitate its wider application.

MATERIALS AND METHODS

Reagents

HPLC-grade methanol and acetonitrile (ACN) were purchased from Fisher Scientific (Pittsburgh, PA). Ultrapure water was purified with a Millipore Milli-Q system (Millipore, Bedford, MA). Other chemicals were purchased from Sigma-Aldrich (St. Louis., MO) except modified sequencing grade trypsin, which was obtained from Promega (Madison, WI).

Sample Preparation

B. napus bee pollen samples were collected from the apiary of the Institute of Apicultural Research, Chinese Academy of Agricultural Sciences in April 2020. Samples were freeze-dried and ground into powder, and then subject to 7 kGy irradiation sterilization (IS) and stored at −80°C. The fermented bee pollen samples were prepared according to our previously reported method with several modifications (20). Briefly, 5 g sterilized bee pollen powder was mixed with 10 ml ultrapure water, then

combined with 150 mg active dry *S. cerevisiae* (Angel Yeast Co., Ltd., Yichang, Hubei Province, China). The mixture was incubated at 40°C for 48 h of fermentation. Fermented samples were again freeze-dried and stored at −80°C before analysis.

Bee Pollen Protein Pretreatment

For protein analyses, 100 mg of freeze-dried bee pollen powder was homogenized on ice for 30 min in 1 ml lysis buffer containing 8 mol/L urea, 2 mol/L thiourea, 4% 3-[(3-cholamidopropyl) dimethylammonio]-1-propanesulfonate acid (CHAPS), 20 mmol/L tris-base, and 30 mmol/L dithiothreitol (DDT). The homogenate was ultrasonicated for 90 s, then centrifugated at 12, 000 × g for 15 min at 4°C. The supernatant was collected and filtered using a Millipore 0.22 μm nylon filter, followed by addition of 5 ml ice-cold acetone for 60 min to precipitate the protein. The pellet was centrifuged at 13, 000 × g for 10 min at 4°C. The protein precipitates were collected and dried at 25 ± 2°C, then resuspended in 200 μl of 5 mol/L urea solution. Protein concentration was determined using bicinchoninic acid (BCA) protein assay kit (Beyotime biotechnology, China). Then, 100 μl protein solution was mixed with 400 μl 40 mmol/L NH_4HCO_3, incubated with 50 μl of 100 mmol/L DDT at 25 ± 2°C for 1 h, and alkylated with 250 μl 50 mM iodoacetamide (IAA) at 25 ± 2°C for 1 h in the dark. The acetylated protein solution was digested with modified sequencing grade trypsin by incubating at 37°C for 12 h. One microliter formic acid was added to terminate the enzymatic reaction. A Ziptip C18 column (Millipore) was used for peptide purification and enrichment. Peptide concentration was determined by Nanodrop2000, and normalized before LC-MS/MS analysis.

Proteomics-Based Allergen Identification

Peptide samples were analyzed using an Easy-nLC1000-LTQ-Orbitrap Elite mass spectrometer (ThermoScientific, USA) with Electrospray Ionization. Prior to analytical separation, the samples were loaded onto a trap column (100 μm × 2 cm, with 5 μm Aqua C18 beads, Thermo Fisher Scientific) in mobile phase A (0.1% formic acid in ultrapure water) at a flow rate of 5 μl/min for 2 min. Then, the peptides were separated on an analysis column (75 μm × 15 cm, with 3 μm, 100 Å, Aqua C18 beads, Thermo Fisher Scientific) in a 120 min-gradient: 0 min, 3% mobile phase B (0.1% formic acid in acetonitrile); 5 min, 8% B; 85 min, 20% B; 105 min, 30% B; 110 min, 90% B; 120, 90% B, at a flow rate of 350 nl/min. The mass spectrometer was operated in positive ionization mode. Analytical parameters were identical to those in previous study (21).

The original data were collected using Xcalibur (Version 2.2, Thermo Fisher Scientific), then imported to Peaks DB 7.5 software (Bioinformatics Solutions Inc., Waterloo, Canada) for qualitative and quantitative analysis. The *Brassica* protein databases were downloaded from NCBI and Uniprot for searching and matching protein sequences. Search parameters were set as follows: precursor ion mass tolerance, 15 ppm; fragment mass tolerance, 0.05 Da; enzyme, trypsin; maximum missed cleavages, 2; maximum variable PTM per peptide, 3; fixed modification, carbamidomethyl (C, +57.02 Da); variable modification: oxidation (M, +15.99 Da). Confidently identified proteins contained at least one unique peptide with at least two spectra. False discovery rate (FDR) was set to <1% using a fusion-decoy search strategy. Quantification of relative protein abundance was conducted with Peaks Q module by a label-free quantification (LFQ) method. Triplicates of each sample were analyzed and one sample was automatically selected as representative. The quantitative parameters included: retention time offset, 0.5 s; mass error tolerance, 15 ppm. Alignment of homologous protein sequences was performed using NCBI BLAST tools based on Allergen Online Database, with reference to FAO/WHO rules (22). Antigenic epitope analysis of the potential allergens was performed with DNAStar software.

UPLC-QTOF-MS/MS Metabolite Detection

For metabolite detection, 100 mg freeze-dried bee pollen powder was mixed with 100 μl of ultrapure water, followed by addition of 400 μl methanol. Samples were vortexed for 5 min and ultrasonicated for 10 min. After centrifugation at 13000 × g at 4°C for 15 min, supernatants were collected and filtered using an Agilent 0.22 μm nylon filter. Ten microliter of each sample was taken preparation of quality controls.

An Agilent 1,290 Infinity II series ultra-performance liquid chromatography (UPLC) system equipped with an Eclipse Plus C18 Rapid Resolution HD column (2.1 mm × 100 mm, 1.8 μm, Agilent Technologies, USA) was applied for sample separation. Mobile phases A and B were water and acetonitrile (both containing 0.1% formic acid), respectively. The gradient was set as follows: 0 min, 5% B; 2 min, 5% B; 20 min, 100% B; 25 min, 100% B; post time 5 min, with 5% B. The flow rate was 0.3 ml/min, and the injection volume was 1 μl.

An Agilent 6,545 ESI-Q-TOF system was used for MS acquisition in negative ionization mode. The mass spectrum parameters were identical to those in previous work (23). Nitrogen was used for drying, ionization, and collision. Reference ions were used to calibrate the mass accuracy. Reference ions 112.985587 and 1033.988109 were used for real-time calibration during acquisition. Detected compounds were analyzed using Agilent Mass Profiler Professional software. Metabolites were identified with the METLIN Database (DB). Metabolites with DB scores above 80 and mass error lower than 5 ppm (0.0005%) were screened as biomarkers for statistical analysis.

Immunoblot Analysis

Bee pollen protein was extracted using a commercial plant protein extraction kit (CWBIO Co., Ltd., Jiangsu, China). Three-hundred milligram bee pollen was added with 1.5 ml protein extraction reagent, and then centrifuged at 13, 000 g for 20 min at 4°C. The supernatant was assayed by a BCA protein assay kit (CWBIO Co., Ltd., Jiangsu, China) for protein concentration quantification, and then normalized to a concentration of 25 μg/μl. Then 2 μl was loaded onto a 5 cm × 5 cm nitrocellulose membrane. After drying the membrane, it was soaked in a 10 cm culture dish containing 5% BSA solution and incubated at 25 ± 2°C for 1 h. The membrane was then incubated at 25 ± 2°C in 5% BSA solution containing 1:1000 diluted human native IgE antibody for 1 h. The membrane was washed three

times with TBS-T solution for 5 min per wash, then incubated in 5% BSA solution containing HRP-labeled anti-human IgE mouse monoclonal antibody (1:1500) at 25 ± 2°C for 1 h. After washing as before, a DAB color developing kit was used following the manufacturer's instructions to reveal brown spots on the membrane. Dried, developed membrane images were captured by HP scanner (Color LaserJet Pro MFP M277dw). Image J software was used for grayscale processing, and relative quantification of dot intensity to evaluate protein binding affinity with human-specific IgE.

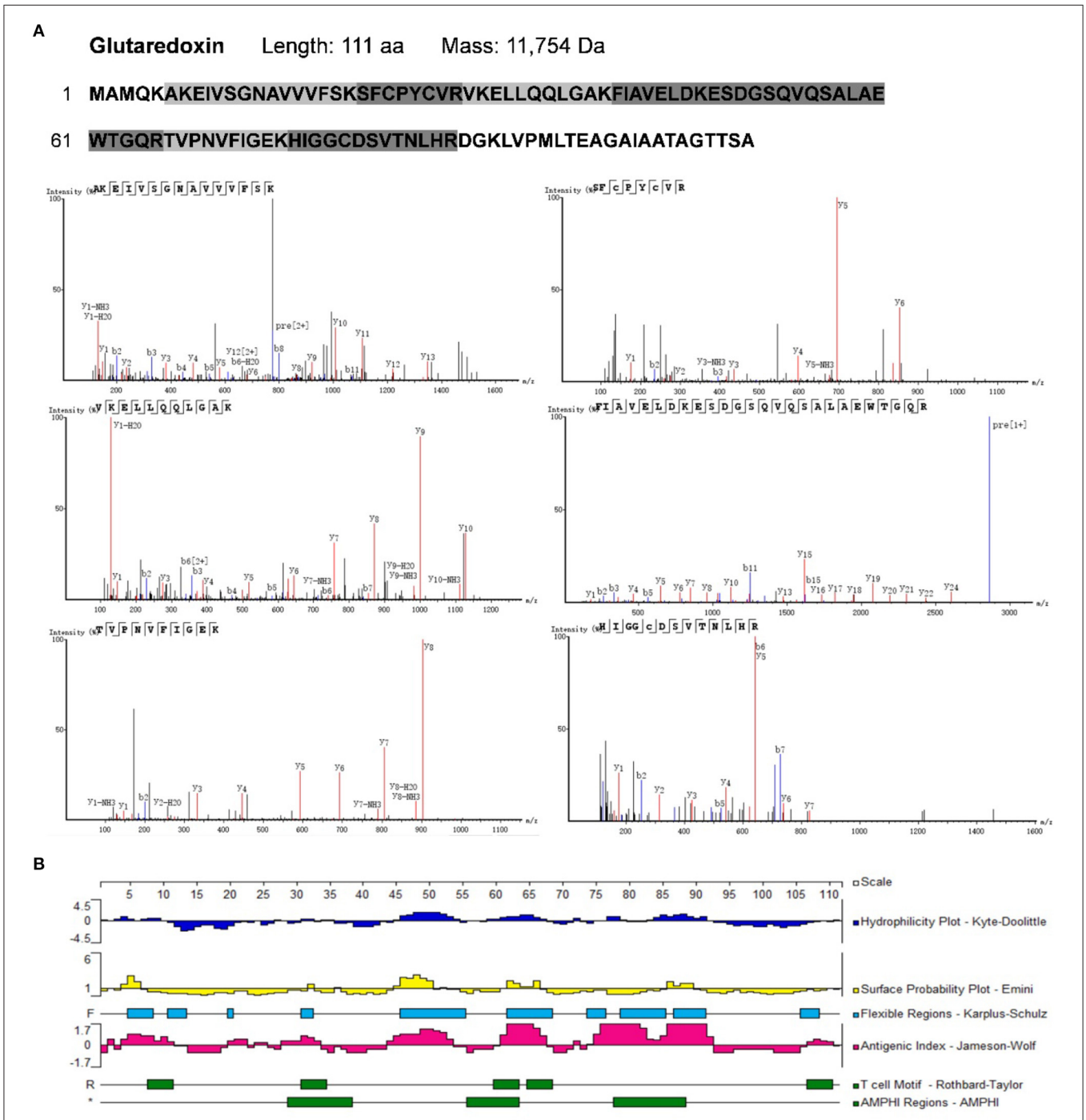

FIGURE 1 | (A) The amino acid sequence of glutaredoxin containing the shade parts which indicated the identified amino acid sequence fragments by proteomics analysis. The mass spectra of these identified amino acid sequence fragments were displayed. **(B)** Epitope prediction of Glutaredoxin for acting with T cells and B cells.

Statistics

SPSS 21.0 statistical software was used for *t*-test and analysis of variance (ANOVA), conducted at 95% probability level to identify significant differences in allergenic proteins, peptides, and amino acids among samples. Multi-experiment viewer (MEV) 4.9 software was used for heat-map analysis. MetaboAnalyst 4.0 and KEGG online websites were used for metabolic pathway analysis.

RESULTS AND DISCUSSION

Proteomics-Based Identification and Epitope Prediction of *B. napus* Bee Pollen Allergens

To identify potential allergens in *B. napus* bee pollen, we used a label-free proteomics strategy based on the NCBI and Uniprot protein databases for *Brassica*. We detected six unique peptides (AKEIVSGNAVVVFSK, VKELLQQLGAK, FIAVELDKESDGSQVQSALAEWTGQR, TVPNVFIGEK, SFCPYCVR, and HIGGCDSVTNLHR) assigned to glutaredoxin (Accession No.: A0A0D3C059) (**Figure 1**). Proteomics analysis showed that glutaredoxin contains 111 amino acids (MW = 11, 754 Da), and coverage of the detected peptides in the total amino acid sequence approached 75%. One unique peptide (TAGGVSLLQSPLR) assigned to oleosin-B2 (Accession No.: P29526) was also detected (**Figure 2**) with 183 amino acid sequence (MW = 18,149 Da) and 7% coverage of the detected peptide.

Sequence-based allergen prediction with the FAO/WHO method uses two specific comparison rules: (1) the word matching rule requires that proteins with more than six consecutive amino acids matching the sequence of a known allergen are thus considered potential allergens; (2) the sliding window matching rule requires proteins with more than 35% of any 80 consecutive amino acids that are consistent with those of a known allergen are also considered potential allergens (22, 24, 25). Redoxins represent a major class of allergens

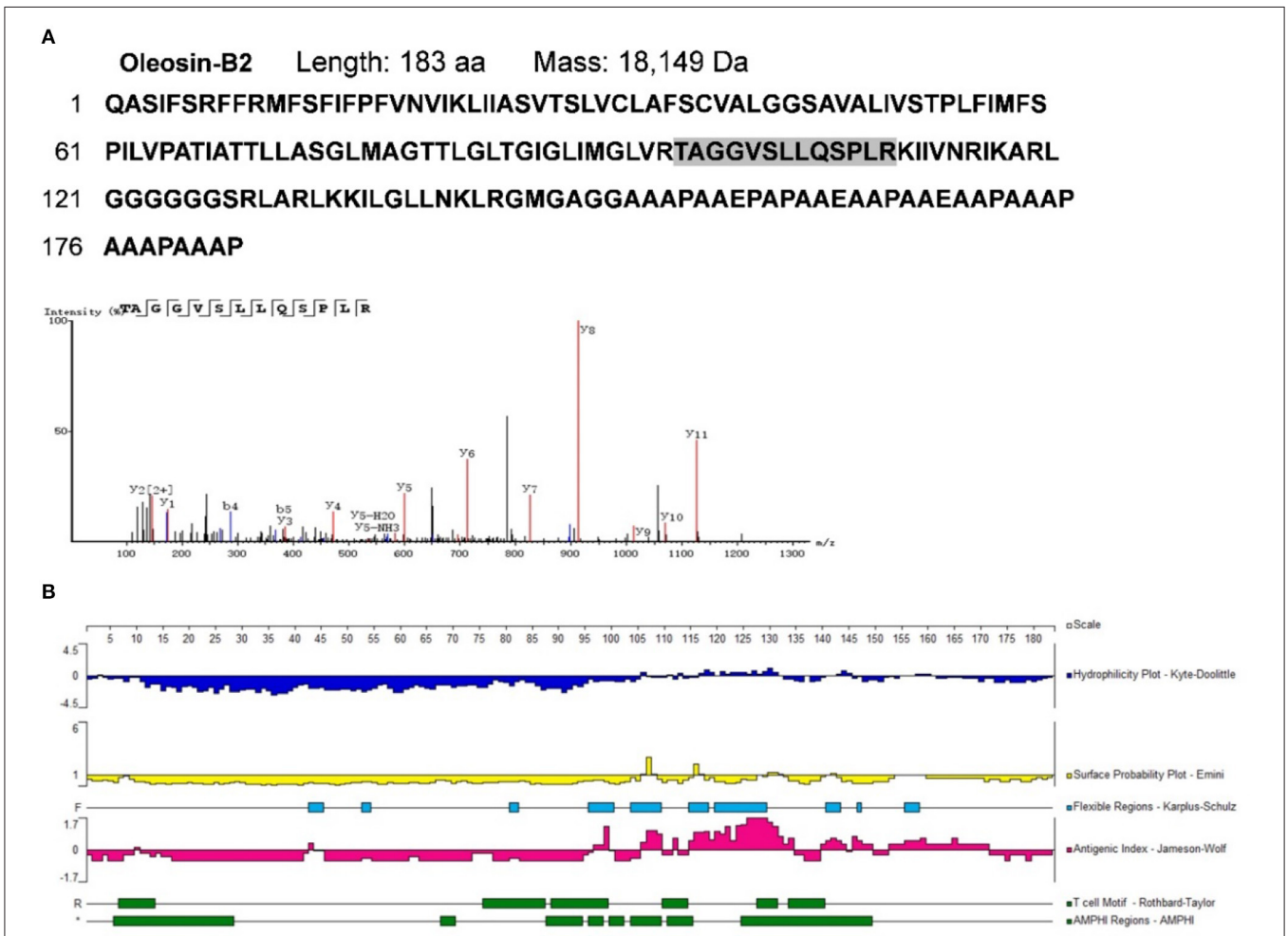

FIGURE 2 | (A) The amino acid sequence of oleosin-B2 containing the shade part which indicated the identified amino acid sequence fragment by proteomics analysis. The mass spectrum of the identified amino acid sequence fragment was displayed. **(B)** Epitope prediction of oleosin-B2 for acting with T cells and B cells.

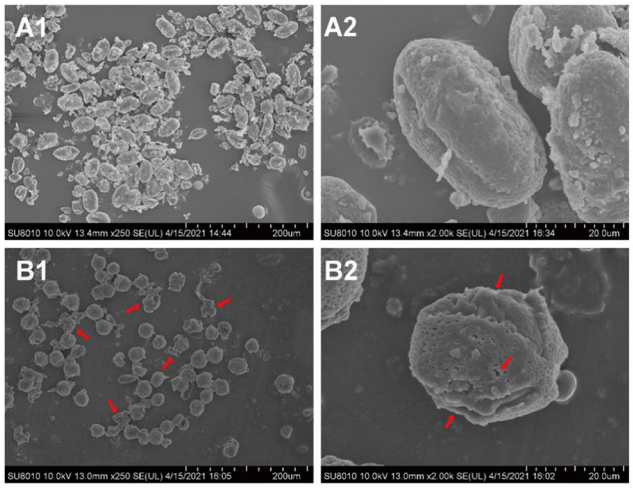

FIGURE 3 | The morphological changes of *B. napus* bee pollen grains before and after fermentation by *S. cerevisiae* using scanning electron microscope (SEM). **(A1)** Unfermented *B. napus* bee pollen (250×). **(A2)** Single unfermented *B. napus* bee pollen grain (2000×). **(B1)** Fermented *B. napus* bee pollen (250×). **(B2)** Single fermented *B. napus* bee pollen grain (2000×). The red arrows indicate the breakage of outer pollen wall and the exposure of intracellular substances through fermentation.

that are distributed across plants and animals, which include glutaredoxins—the thioredoxin superfamily disulfide reductases (26). As a member of thioredoxin superfamily, glutaredoxins contain a highly conserved active site C-X-X-C motifa — a major epitope region with high immunogenicity (27). Oleosins are considered typical allergens present in some allergenic plant-based foods (28). For instance, the oleosin Fag t 6 (18 kDa) from buckwheat seeds was reported to cause allergic symptoms (29). We performed the protein sequence alignment by a NCBI BLAST tool and found that oleosins-B2 has 42% homology similarity with the allergen oleosin Ara h 15 (17 kDa) from peanut. Thus, based on the FAO/WHO rules, we categorized both glutaredoxin and oleosin-B2 as potential allergens in *B. napus* bee pollen.

Previous research has led to the development of several algorithms that use the properties of amino acids (such as hydrophilicity, antigenicity, segmental mobility, flexibility, and accessibility) to predict B cell and T cell epitopes in protein sequences (30, 31). Here, we used the Protean module in DNAStar software to predict the epitopes of glutaredoxin and oleosin-B2. For glutaredoxin (**Figure 1B**), its potential B cell epitopes are distributed in residues 4–12, 19–23, 28–34, 44–54, 60–67, 71–82, 83–92, and 106–111, as determined by the Jameson-Wolf method. By contrast, the Rothbard-Taylor and AMPHI methods were used in conjunction to obtain the T cell epitopes of glutaredoxin located at residues 31–34 and 60–64. It showed that the predicted epitopes sites 28–34 or 31–34 were both close to the active center—C-X-X-C motifa.

For oleosin-B2 (**Figure 2B**), the Jameson-Wolf method identified putative B cell epitopes in residues 96–100, 106–110, 112–113, 115–135, 140–145, 146–150, and 152–172, while Rothbard-Taylor/AMPHI analyses identified T cell epitopes at amino acid positions 6–14, 88–94, 95–99, 110–115,127–132, and 134–141. Notably, antigenic regions highly overlapped with flexible regions on these peptides, indicating higher plasticity in epitope formation at these sites. Cumulatively, the findings showed that glutaredoxin and oleosin-B2 presented positive B cell and T cell epitopes, further verifying their allergenic properties.

Degradation of Glutaredoxin and Oleosin-B2 in *B. napus* Bee Pollen Through *S. cerevisiae* Fermentation

Fermentation is a widely used method to improve the flavor and nutritional properties of bee pollen, due to lysis of pollen walls and subsequent release of pollen cell contents (20). Scanning electron microscopy (SEM) showed that *B. napus* pollen spore morphology was substantially altered by fermentation with *S. cerevisiae* (**Figure 3**). Before fermentation, spores were oblong, with three shallow germination grooves on the surface, and closed germination holes. Typically, the pollen outer wall exhibits a net-like, meshed pattern. After fermentation, there were obviously fewer intact spores, and pollen grains were rounder than oblong. The outer wall mesh pattern was also enlarged and sparsely distributed. In addition, pollen walls were ruptured at the germination holes with obviously leaking contents. Some spores were severely fragmented or degraded into smaller, unrecognizable components through the fermentation process.

The major allergens in pollen are water-soluble proteins and glycoproteins located on the pollen wall (32). Enzymes secreted by yeast can destroy the pollen wall and degrade the allergens (33). Previous studies have shown that microbes can degrade allergenic proteins in food into small peptides or amino acids through fermentation, thereby reducing allergenicity (34, 35). We therefore compared the potential allergenic protein contents in *B. napus* bee pollen before and after fermentation, and found that the concentrations of glutaredoxin and oleosin-B2 were significantly lower in fermented samples compared with those of unfermented samples ($P < 0.001$) (**Figure 4A**). In addition, metabolomics analysis revealed that the contents of five oligopeptides, including Ile Ala Val, Glu Ile, Gln Leu, Phe Ile, and Val Val, substantially increased in fermented samples compared to unfermented samples (**Figure 4B**). Furthermore, the individual contents of L-valine, L-isoleucine, L-tryptophan, and L-phenylalanine were also increased in the fermented pollen samples (**Table 1**). Together, these five oligopeptides and four amino acids represent key constituent fractions of glutaredoxin and oleosin-B2, and the commensurate increase in their levels was closely correlated with the observed decreases in glutaredoxin and oleosin-B2, suggesting that yeast-based fermentation could degrade these putative allergens into oligopeptides and amino acids.

Fermentation Reduced Binding Affinity Between Fermented Pollen Proteins and IgE

We next used dot-blot assays to observe and quantify binding affinity between proteins extracted from fermented or

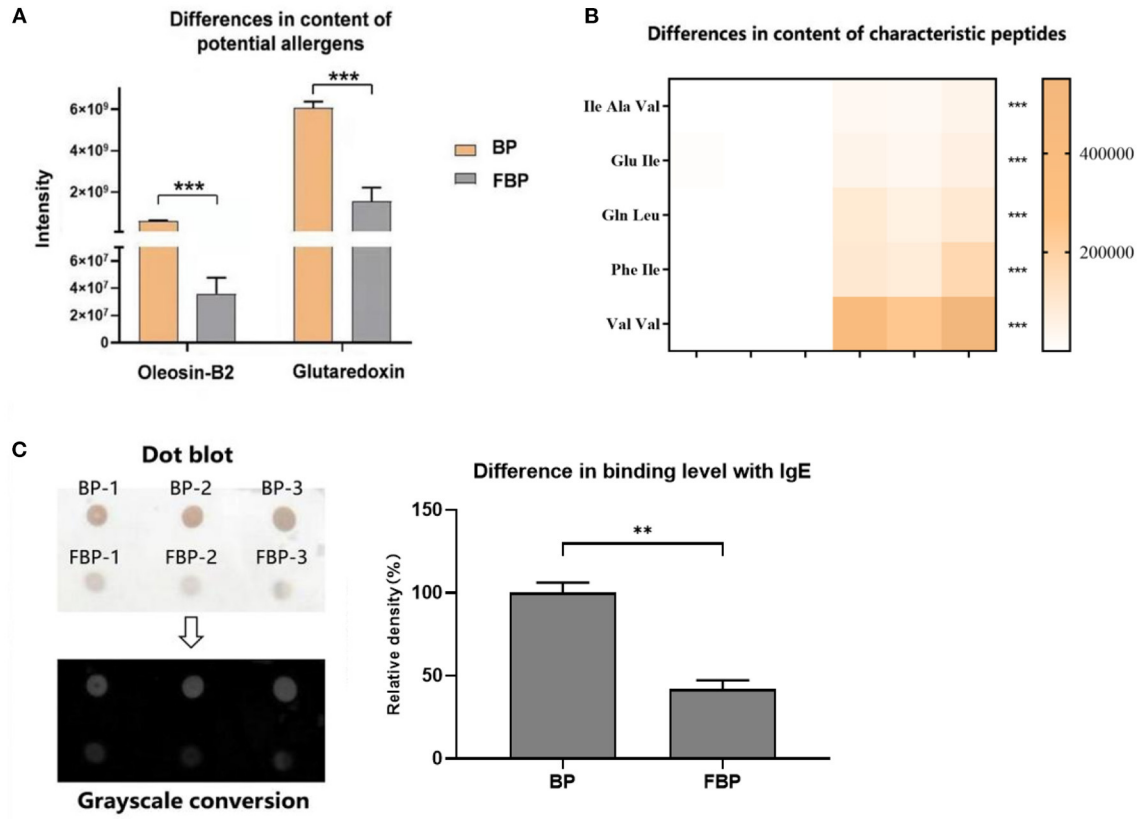

FIGURE 4 | (A) Differences in the content of potential allergens of *B. napus* bee pollen before and after fermentation by *S. cerevisiae*. BP means the unfermented *B. napus* bee pollen, and FBP means the *S. cerevisiae* fermented *B. napus* bee pollen. **(B)** Differences in the content of characteristic oligopeptides in bee pollen before and after fermentation. The color bar from blank to yellow represented the level of five oligopeptides from low to high in the bee pollen. **(C)** Difference in the binding level of *B. napus* bee pollen protein with human native immunoglobulin E (IgE) before and after fermentation detected using Dot-blot method. Three repeated experiments were conducted. The symbol of **means $P < 0.01$, and ***means $P < 0.001$.

unfermented *B. napus* bee pollen and human IgE. The results showed a coefficient of variation of <10% among replicate dots, suggesting low variability. After grayscale conversion and analysis of the integrated intensity of each dot, we found that fermented pollen proteins exhibited significantly lower binding affinity with IgE compared to that of unfermented pollen proteins ($P < 0.001$) (**Figure 4C**).

This finding was in agreement with reports showing that the majority of food allergies cause type I hypersensitivity, mediated by IgE, which induces degranulation of sensitized mast cells or basophils (36). When specific allergens first enter the human digestive tract, they are processed by dendritic cells, then delivered to Th2 cells. Th2 cells subsequently induce B proliferation by secreting IL-4, IL-13, and other cytokines, and produce IgE antibody. The Fc fragment of IgE binds to the Fc high-affinity receptor (FcεRI) on the surface of mast cells or basophils resulting in sensitization. Upon subsequent exposure to the same allergen, it specifically binds to IgE, inducing mast cells or basophils to release vasoactive amines and cytokines, heightening the allergic reaction (37). Food allergens include both linear and conformational epitopes to IgE. Conformational epitopes are easily denatured during food processing, whereas changes in linear epitopes require manipulation of specific residues in the peptide (38). Our results suggest that fermentation by yeast can potentially degrade allergens into peptides and single amino acids, thereby destroying linear epitopes of IgE, and ultimately resulting in decreased binding between allergens and IgE. This effect was consistent with the decrease in potentially allergenic proteins and increase in constituent fragments detected in the fermented bee pollen. Collectively, these results suggest that allergenicity of bee pollen could be reduced through fermentation by *S. cerevisiae*.

Intervention of *S. cerevisiae* in Amino Acid Metabolism

In addition to proteins, we detected the metabolites that accumulated to significantly different levels ($P < 0.05$; Fold Change>2) between fermented and unfermented bee pollen (**Table 1**). KEGG pathway enrichment analysis suggested that the most significantly enriched metabolites were involved in three main pathways: (1) biosynthesis of amino acids, (2) valine, leucine and isoleucine biosynthesis, and (3) phenylalanine

TABLE 1 | The metabolic pathway analysis base on the changed metabolites in fermented bee pollen by *S. cerevisiae*.

Pathway	Compound	KEGG ID	Formula	Mass	Score (DB)	FC ([Y] Vs [C])	Regulation	*P*-value
Biosynthesis of amino acids	L-Valine	C00183	C5 H11 N O2	117.0789	88	4.637	Up	***
	L-Isoleucine	C00407	C6 H13 N O2	131.0943	88	10.098	Up	***
	2,3-Dihydroxy-3-methylbutyric acid	C04272	C5 H10 O4	134.0582	99	37142.844	Up	**
	L-Tryptophan	C00078	C11 H12 N2 O2	204.0903	98	4.535	Up	***
	L-Phenylalanine	C00079	C9 H11 N O2	165.0794	99	68.297	Up	***
	N2-Acetyl-L-ornithine	C00437	C7 H14 N2 O3	174.1007	99	341288.970	Up	***
Valine, leucine and isoleucine biosynthesis	L-Isoleucine	C00407	C6 H13 N O2	131.0943	88	10.098	Up	***
	L-Valine	C00183	C5 H11 N O2	117.0789	88	4.637	Up	***
	2,3-Dihydroxy-3-methylbutyric acid	C04272	C5 H10 O4	134.0582	99	37142.844	Up	**
	2-Isopropylmaleate	C02631	C7 H10 O4	158.0576	99	33276.340	Up	***
Phenylalanine metabolism	Phenylacetic acid	C07086	C8 H8 O2	136.0520	85	5980.313	Up	***
	Succinic	C00042	C4 H6 O4	118.0271	98	9.355	Up	***
	N-Acetyl-L-phenylalanine	C03519	C11 H13 N O3	207.0894	99	16.499	Up	***
	L-Phenylalanine	C00079	C9 H11 N O2	165.0794	99	68.297	Up	***

*** means P < 0.01; *** means P < 0.001.*

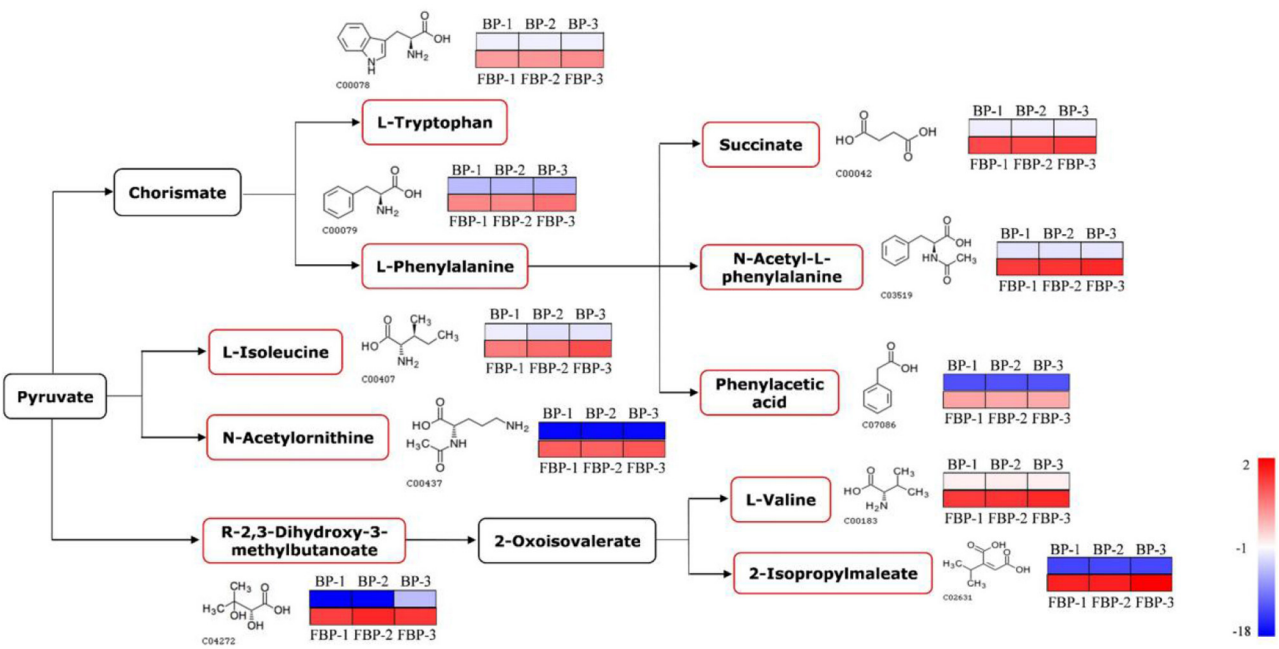

FIGURE 5 | The changed metabolic pathways due to *S. cerevisiae* fermentation in *B. napus* bee pollen based on KEGG pathway analysis. The red frame represented that the content of those highlighted metabolites was significantly increased in the fermented bee pollen compared to the unfermented bee pollen. The color bar from blue to red indicated the metabolite level from low to high.

metabolism (**Figure 5**). These metabolites were all found in higher concentrations in the fermented bee pollen, which suggested that fermentation promoted the biosynthesis of L-valine, L-isoleucine, L-tryptophan, and L-phenylalanine.

The branched-chain amino acids L-valine and L-isoleucine are essential to humans, which can maintain blood glucose level, supply energy, and protect muscle function (39–41). The aromatic amino acids L-tryptophan and L-phenylalanine,

which cannot be synthesized by humans but are essential for protein synthesis, are known to regulate the levels of insulin-like growth factor-1 and leptin (42). Additionally, 2,3-Dihydroxy-3-methylbutyric acid can be converted into 2-oxoisovalerate through dehydration, which is a substrate for L-valine and 2-isopropylmaleate production by transaminase. 2-Isopropylmaleate is involved in the synthesis of L-leucine, another branched-chain amino acid that promotes myofibrillar protein synthesis and metabolism (43). Fermentation apparently increased the contents of these essential amino acids and their precursors or intermediates in bee pollen, suggesting that this process improved nutritional properties while also reducing allergenicity of *B. napus* bee pollen.

CONCLUSION

Through proteomics analysis, we identified two putative allergenic proteins, glutaredoxin and oleosin-B2 in *B. napus* bee pollen, and predicted their antigenic epitopes to B and T cells. We also found differences in the levels of allergenic proteins, characteristic peptides, and predominant amino acids between unfermented and fermented bee pollen. Notably, glutaredoxin and oleosin-B2 contents were significantly lower, while their five major constituent oligopeptides and four amino acids were significantly higher in fermented bee pollen compared to that in unfermented pollen samples, which indicated fermentation by *S. cerevisiae* could degrade these two potential allergens. Immunoblot analysis showed that the IgE-binding affinity of fermented bee pollen protein extract also declined, suggesting an apparent decrease in allergenicity attributable to the fermentation process. Metabolomics analysis revealed that fermentation apparently promoted the biosynthesis of essential amino acids, implying that *S. cerevisiae* fermentation also exerted positive effects on the nutritional properties of *B. napus* bee pollen. The findings provide a scientific foundation for improving the safety of bee pollen products to facilitate its wider application.

DATA AVAILABILITY STATEMENT

The datasets presented in this study can be found in online repositories. The names of the repository/repositories and accession number(s) can be found at: http://proteomecentral.proteomexchange.org PXD030273; https://www.ebi.ac.uk/metabolights/ MTBLS3950.

AUTHOR CONTRIBUTIONS

SL and YT: writing-original draft preparation, investigation, and formal analysis. YJ, LM, LZ, and XX: validation. QL: writing-original draft preparation, conceptualization, methodology, writing-reviewing and editing, supervision, project administration, and funding acquisition. LW: supervision, project administration, and funding acquisition. All authors contributed to the article and approved the submitted version.

FUNDING

This work was supported by the National Natural Science Foundation of China (No. 32102605), and the Agricultural Science and Technology Innovation Program under Grant (CAAS-ASTIP-2020-IAR).

ACKNOWLEDGMENTS

We acknowledged the technical supports from the proteomics and metabolomics platform of the Institute of Apicultural Research, Chinese Academy of Agricultural Sciences.

REFERENCES

1. Li QQ, Wang K, Marcucci MC, Sawaya A, Hu L, Xue XF, et al. Nutrient-rich bee pollen: a treasure trove of active natural metabolites. *J Funct Foods.* (2018) 49:472. doi: 10.1016/j.jff.2018.09.008
2. Thakur M, Nanda V. Composition and functionality of bee pollen: a review. *Trends Food Sci Technol.* (2020) 98:82–106. doi: 10.1016/j.tifs.2020.02.001
3. Boroujeni ZA, Rezaei Z, Karampour NS. Biological and therapeutic properties of Bee pollen. *J Sci Food Agric.* (2018) 96:4303–9. doi: 10.1002/jsfa.7729
4. Jeong HC, Young SJ, Jae WO, Cheol HK, In GH. Bee pollen-induced anaphylaxis: a case report and literature review. *Allergy Asthma Immunol Res.* (2014) 7:513–7. doi: 10.4168/aair.2015.7.5.513
5. Mcnamara KB, Pien L. Exercise-induced anaphylaxis associated with the use of bee pollen. *Ann Allergy Asthma Immunol.* (2018) 122:118–9. doi: 10.1016/j.anai.2018.09.461
6. Puumalainen TJ, Poikonen S, Kotovuori A, Vaali K, Kalkkinen N, Reunala T, et al. Napins, 2S albumins, are major allergens in oilseed rape and turnip rape. *J Allergy Clin Immunol.* (2006) 117:426–32. doi: 10.1016/j.jaci.2005.10.004
7. Singh A, Shahi S, Katiyar RK, Gaur S, Jain V. Hypersensitivity to pollen of four different species of brassica: a clinico-immunologic evaluation in patients of respiratory allergy in India. *Asia Pac Allergy.* (2014) 4:197–205. doi: 10.5415/apallergy.2014.4.4.197
8. Pi XW, Yang Y, Sun Y, Cui Q, Cheng J. Recent advances in alleviating food allergenicity through fermentation. *Crit Rev Food Sci Nutr.* (2021) 1–14. doi: 10.1080/10408398.2021.1913093
9. Chen L, Song P, Jia F, Wang JS. Reducing the allergenicity from food by microbial fermentation. *Adv Mat Res.* (2012) 524–7:2302–5. doi: 10.4028/www.scientific.net/AMR.524-527.2302
10. Shady E-G, Aynur A, Imen H-S, Kamel EEM, Inga B, Yvan C, et al. Potential use of lactic acid bacteria for reduction of allergenicity and for longer conservation of fermented foods. *Trends Food Sci Technol.* (2011) 22:509–516. doi: 10.1016/j.tifs.2011.05.003
11. Zhao W, Shu Q, He G, Chen Q. Reducing antigenicity of bovine whey proteins by kluyveromyces marxianus fermentation combined with ultrasound treatment. *Food Chem.* (2020) 311:125893. doi: 10.1016/j.foodchem.2019.125893
12. Wroblewska B, Markiewicz LH, Szyc AM, Dietrich MA, Szymkiewicz A, Fotschki J. Lactobacillus casei lcY decreases milk protein immunoreactivity of fermented buttermilk but also contains ige-reactive proteins. *Food Res Int.* (2016) 83:95–101. doi: 10.1016/j.foodres.2016.02.016
13. Ekezie F, Cheng JH, Sun DW. Effects of nonthermal food processing technologies on food allergens: a review of recent research advances. *Trends Food Sci Technol.* (2018) 74:12–25. doi: 10.1016/j.tifs.2018.01.007

14. Lu QL, Zuo LL, Wu ZH Li X, Tong P, Wu Y, et al. Characterization of the protein structure of soymilk fermented by lactobacillus and evaluation of its potential allergenicity based on the sensitized-cell model. *Food Chem.* (2021) 366:130569. doi: 10.1016/j.foodchem.2021.130569
15. Yang H, Qu YZ, Li JT, Liu XQ, Wu RN, Wu JR. Improvement of the protein quality and degradation of allergens in soybean meal by combination fermentation and enzymatic hydrolysis. *LWT.* (2020) 128:109442. doi: 10.1016/j.lwt.2020.109442
16. Xin R, Jin H, Xing G, Zhang Q, Wei L, Dong M. Changes in soy protein immunoglobulin e reactivity, protein degradation, and conformation through fermentation with lactobacillus plantarum strains. *LWT.* (2019) 99:156–65. doi: 10.1016/j.lwt.2018.09.034
17. Fu W, Xue W, Liu C, Tian Y, Zhang K, Zhu Z. Screening of lactic acid bacteria and yeasts from sourdough as starter cultures for reduced allergenicity wheat products. *Foods.* (2020) 9:751. doi: 10.3390/foods9060751
18. Yao M, Luo Y, Shi J, et al. Effects of fermentation by Lactobacillus rhamnosus GG on the antigenicity and allergenicity of four cows' milk proteins. *Food Agric Immunol.* (2014) 25:545–55. doi: 10.1080/09540105.2013.852163
19. Gobbetti M, De Angelis M, Di Cagno R, Calasso M, Archetti G, Rizzello CG. Novel insights on the functional/nutritional features of the sourdough fermentation. *Int J Food Microbiol.* (2019) 302:103–13. doi: 10.1016/j.ijfoodmicro.2018.05.018
20. Yan S, Li QQ, Xue XF, Kai W, Zhao LW, Wu LM. Analysis of improved nutritional composition of bee pollen (Brassica campestris L) after different fermentation treatments. *Int J Food Sci.Technol.* (2019) 54:2169–81. doi: 10.1111/ijfs.14124
21. Meng L, Huo X, Mao F, Yu F, Li J. Proteomics reveals the molecular underpinnings of stronger learning and memory in eastern compared to western bees. *Mol Cell Proteomics.* (2018) 17:255–69. doi: 10.1074/mcp.RA117.000159
22. FAO/WHO. *Report of a Joint FAO/WHO Expert Consultation on Allergenicity of Foods Derived from Bio-technology Rome* (2003).
23. Li QQ, Sun M, Wan Z, Liang J, Wang K. Bee pollen extracts modulate serum metabolism in lipopolysaccharide-induced acute lung injury mice with anti-inflammatory effects. *J Agric Food Chem.* (2019) 67:7855–68. doi: 10.1021/acs.jafc.9b03082
24. Stadler MB, Stadler BM. Allergenicity prediction by protein sequence. *FASEB J.* (2003) 17:1141–3. doi: 10.1096/fj.02-1052fje
25. Li K, Issac P, Krishnan A. Predicting allergenic proteins using wavelet transform. *Bioinformatics.* (2004) 20:2572–8. doi: 10.1093/bioinformatics/bth286
26. Radauer C, Bublin M, Wagner S, Mari A, Breiteneder H. Allergens are distributed into few protein families and possess a restricted number of biochemical functions. *J Allergy Clin Immunol.* (2008) 121:847–852.e7. doi: 10.1016/j.jaci.2008.01.025
27. Foloppe N, Nilsson L. The glutaredoxin -C-P-Y-C- motif: influence of peripheral residues. *Structure.* (2004) 12:289–300. doi: 10.1016/j.str.2004.01.009
28. Majsiak E, Choina M, Miśkiewicz K, Doniec Z, Kurzawa R. Oleosins: A Short Allergy Review. *Adv Exp Med Biol.* (2020) 1324:51–5. doi: 10.1007/5584_2020_579
29. Chen F, Li H, Fan XJ, Li YL, Zhang CY, Zhu LX, et al. Identification of a novel major allergen in buckwheat seeds: fag t 6. *J Agric Food Chem.* (2021) 69:13315–22. doi: 10.1021/acs.jafc.1c01537
30. Pomés A. Relevant b cell epitopes in allergic disease. *Int Arch Allergy Immunol.* (2010) 152:1–11. doi: 10.1159/000260078
31. Zhang ZW, Zhang YG, Wang YL, Li P, Fang YZ, Jiang ST, et al. Screening and identification of b cell epitopes of structural proteins of foot-and-mouth disease virus serotype asia1. *Vet Microbiol.* (2010) 140:25–33. doi: 10.1016/j.vetmic.2009.07.011
32. Wang W, Milanesi C, Faleri C, Cresti M. Localization of group-1 allergen zea m 1 in the coat and wall of maize pollen. *Acta Histochemica.* (2006) 108:395–400. doi: 10.1016/j.acthis.2006.06.003
33. Zhang Z, Cao H, Chen C, Chen X, Wei Q, Zhao F. Effects of fermentation by ganoderma lucidum and saccharomyces cerevisiae on rape pollen morphology and its wall. *J Food Sci Technol.* (2017) 54:4026–34. doi: 10.1007/s13197-017-2868-1
34. Yang A, Zuo LL, Cheng Y, Wu Z, Li X, Tong P, et al. Degradation of major allergens and allergenicity reduction of soybean meal through solid-state fermentation with microorganisms. *Food Funct.* (2018) 9:1899–909. doi: 10.1039/C7FO01824J
35. Fu W, Liu C, Meng X, Tao S, Xue W. Co-culture fermentation of pediococcus acidilactici xz31 and yeast for enhanced degradation of wheat allergens. *Int J Food Microbiol.* (2021) 347:109190. doi: 10.1016/j.ijfoodmicro.2021.109190
36. Gould HJ, Sutton BJ, Beavil AJ, Beavil RL, Smurthwaite L. The biology of ige and the basis of allergic disease. *Annu Rev Immunol.* (2003) 21:579–628. doi: 10.1146/annurev.immunol.21.120601.141103
37. Christensen LH, Holm, J, Lund G, Riise E, Lund K. Several distinct properties of the ige repertoire determine effector cell degranulation in response to allergen challenge. *J Allergy Clin Immunol.* (2008) 122:298–304. doi: 10.1016/j.jaci.2008.05.026
38. Liu C, Krishna SS. Food allergen epitope mapping. *J Agric Food Chem.* (2018) 66:7238–48. doi: 10.1021/acs.jafc.8b01967
39. Zhang S, Zeng X, Man R, Mao X, Qiao S. Novel metabolic and physiological functions of branched chain amino acids: a review. *J Anim Sci.* (2017) 8:501–12. doi: 10.1186/s40104-016-0139-z
40. Horiuchi M, Takeda T, Takanashi H, Ozaki-Masuzawa Y, Taguchi Y, Toyoshima Y, et al. Branched-chain amino acid supplementation restores reduced insulinotropic activity of a low-protein diet through the vagus nerve in rats. *Nutr Metab.* (2017) 14:59. doi: 10.1186/s12986-017-0215-1
41. Samuelsson H, Moberg MW, Apró EB, Blomstrand E. Intake of branched-chain or essential amino acids attenuates the elevation in muscle levels of pgc-1α4 mrna caused by resistance exercise. *Am J Physiol Endocrinol Metab.* (2016) 311:E246. doi: 10.1152/ajpendo.00154.2016
42. Flynn NE, Shaw MH, Becker JT. Amino acids in health and endocrine function. *Adv Exp Med Biol.* (2020) 1265:97–109. doi: 10.1007/978-3-030-45328-2_6
43. Waskiw FM, Hannaian S, Duncan J, Kato H, Sawan SA, Locke M, et al. Leucine-enriched essential amino acids improve recovery from post-exercise muscle damage independent of increases in integrated myofibrillar protein synthesis in young men. *Nutrients.* (2020) 12:1061. doi: 10.3390/nu12041061

Conflict of Interest: The authors declare that the research was conducted in the absence of any commercial or financial relationships that could be construed as a potential conflict of interest.

Publisher's Note: All claims expressed in this article are solely those of the authors and do not necessarily represent those of their affiliated organizations, or those of the publisher, the editors and the reviewers. Any product that may be evaluated in this article, or claim that may be made by its manufacturer, is not guaranteed or endorsed by the publisher.

Copyright © 2022 Yin, Tao, Jiang, Meng, Zhao, Xue, Li and Wu. This is an open-access article distributed under the terms of the Creative Commons Attribution License (CC BY). The use, distribution or reproduction in other forums is permitted, provided the original author(s) and the copyright owner(s) are credited and that the original publication in this journal is cited, in accordance with accepted academic practice. No use, distribution or reproduction is permitted which does not comply with these terms.

frontiers in Nutrition

REVIEW
published: 28 January 2022
doi: 10.3389/fnut.2021.807284

Advancement on Milk Fat Globule Membrane: Separation, Identification, and Functional Properties

Cong Wang[1,2,3]*, *Xinyu Qiao*[1], *Zengli Gao*[2], *Lianzhou Jiang*[3] *and Zhishen Mu*[2]*

[1] Center of Experimental Instrument, School of Food Science and Technology, Dalian Polytechnic University, Dalian, China, [2] Inner Mongolia Mengniu Dairy Industry (Group) Co., Ltd., Hohhot, China, [3] College of Food Science, Northeast Agricultural University, Harbin, China

Dairy products have become more common in people's daily diets in recent years, and numerous useful components derived from milk are widely employed in the food industry. Milk fat globule membrane (MFGM) is a kind of film that encases milk fat globules, and has been shown to have a high nutritional value. In this work, the protein, lipid, carbohydrate, and other components of MFGM are discussed, and also common separation, preparation, and analysis technologies, physicochemical properties, and functional features of MFGM are reviewed, to provide some guidance for the development and utilization of MFGM.

Keywords: dairy industry, components, preparation, functionality, prosperity

OPEN ACCESS

Edited by:
Fuguo Liu,
Northwest A&F University, China

Reviewed by:
Xianghe Meng,
Zhejiang University of Technology, China
Jinxuan Cao,
Ningbo University, China
Xueying Mao,
China Agricultural University, China

***Correspondence:**
Cong Wang
yuanque@163.com
Zhishen Mu
muzhishen@163.com

Specialty section:
This article was submitted to Food Chemistry, a section of the journal Frontiers in Nutrition

Received: *02 November 2021*
Accepted: *06 December 2021*
Published: *28 January 2022*

Citation:
Wang C, Qiao X, Gao Z, Jiang L and Mu Z (2022) Advancement on Milk Fat Globule Membrane: Separation, Identification, and Functional Properties. Front. Nutr. 8:807284. doi: 10.3389/fnut.2021.807284

HIGHLIGHTS

- The identification of primary components of milk fat globule membrane (MFGM) was compared.
- The separation and preparation technologies of components in MFGM were illustrated.
- The bioactivities and applications of MFGM in functional food industry were reviewed.

INTRODUCTION

Milk fat in milk is secreted by breast cells and exists in the form of fat globules with a diameter of 0.2–15 μM. The milk fat globule membrane (MFGM) is a thin layer that surrounds the fat globules. The content of MFGM in milk was different, and the reports about MFGM accounted for 2–6% of fat globules (1, 2). These contents were reported due to the difference in collection season, collection stage, preparation method, and determination method of raw milk.

The structure of MFGM is constructed with three layers, and the thickness of MFGM is 10–50 nm (3). The inner membrane is a monolayer composed of proteins and polar lipids from the endoplasmic reticulum. It is the membrane that is covered by triglycerides when they are accumulated in the endoplasmic reticulum of breast epithelial cells and released into the cytoplasm in the way of budding and growth; the outer membrane is a double-layer membrane, which is composed of proteins and polar lipids from the plasma membrane at the top of the epithelial cells of the mammary gland (4), which is the fat globule in the cytoplasm. When released by mammary epithelial cells in the manner of budding expansion after reaching a specific size, this membrane is

covered. Furthermore, some cytoplasm may persist between the inner and outer membranes after lipoglobulin production.

The research heat was low from MFGM's initial report in 1936 until 1970. MFGM research has steadily increased since the 1970's. The current focus of MFGM research is on the following aspects: composition identification, separation and preparation methods, physical and chemical properties, and functional feature analysis. In recent years, the application of MFGM in the food industry has attracted more and more attention. In this article, the separation, preparation, composition, physicochemical properties, functional properties, and development prospects of MFGM are reviewed.

ISOLATION AND PREPARATION

Milk fat globule membrane can be separated and prepared from fresh milk, cream, casein, and butter whey. The yield of MFGM in the separation process is influenced by three primary elements: biological factors, such as raw milk type; physical factors, such as temperature; and chemical factors, such as salt ions. The findings suggest that the heat treatment temperature has a significant effect on the integrity and stability of MFGM in milk. The denaturation of protein in MFGM and its binding with whey protein is induced by heating the milk above 60°C (5). The freezing and thawing will lead to the instability of fat globules, which will cause serious damage to MFGM. The stability of MFGM is also affected by fast air intake during separation. The composition, physical, and chemical characteristics of MFGM isolation are also affected by the separation technique, the kind of raw materials, and the preparation of raw materials. Therefore, to avoid the effects of the above elements on MFGM, it is required to research and improve the separation procedure.

There are many reports on the preparation of MFGM with fresh milk as raw material, mainly including degreasing, cream cleaning, MFGM release, collection, drying, and other procedures (6). First, the milk is separated into cream and skimmed milk (7). The cream is washed with water or salt solution of 3–5 times volume for 2–3 times (3), to remove casein and whey protein in cream (8). The washed cream is cooled to 10°C and centrifuged to promote the separation of the fat phase and the water phase (9). The buttermilk and butter particles are obtained by filtering with a filter cloth. After adding water and melting at 40–60°C, the upper layer of centrifugation is butter, and the lower layer is butter whey. The mixture of butter whey and casein is used to obtain MFGM suspension. MFGM suspension is acidified, salted out, or ultracentrifuged to remove the residual lipids, and then dried to obtain MFGM (10). There are also some studies on the preparation of MFGM with casein powder as raw material, which is mainly divided into the following steps: dissolution, washing, centrifugal separation, and drying of casein powder (11). As a whole, the main process of separating MFGM from milk was shown in **Figure 1**.

In the preparation technologies of MFGM, in addition to physical separation methods, such as salt solution, a filtration device can also be used to remove whey protein and casein in milk (12). In the subsequent infiltration process, reverse osmosis water was added to keep the feed rate unchanged. The MFGM was separated from the reflux by acidification (13).

In the dairy industry, butter whey is usually selected as the main source of MFGM (4). In this process, whey protein and casein are mainly removed from raw materials (14). Since MFGM is similar to casein in size, casein must be removed before microfiltration. In industry, MFGM is usually prepared by a two-step method: first, rennet or casein is used, and then MFGM is obtained by microfiltration. It can be obtained by adding sodium citrate into the cheese milk to remove the casein by microfiltration and then centrifuging at high speed.

COMPOSITION OF MFGM

The composition of MFGM is complex, mainly composed of polar lipids and membrane-specific proteins. Due to different separation, purification, and analysis techniques, the composition of MFGM in the relevant literature is also quite different (15). At the same time, factors, such as lactation stage, season, feed, and fat globule size, also affect the content and composition of MFGM (16). There are many reports on the molecular types of protein components, lipid components, and polysaccharide components in MFGM, but there are great differences among them. The qualitative and quantitative analysis methods of these components are summarized in **Figure 2**.

Proteins in MFGM

According to the current publications, the protein content of milk MFGM is about 25–30%. Due to the different separation and preparation conditions and analysis methods of MFGM, the highest protein content in the industrial MFGM powder is about 60%. At the same time, the number of MFGM proteins reported in different studies was also different. Lu et al., identified 169 kinds of MFGM proteins in milk by the filter-aided sample preparation method (FASP) and Nano LC-MS/MS. In addition, 312, 554, 175, and 143 MFGM proteins were identified from human milk, cow milk, goat milk, and yak milk (17). Le et al., used polyacrylamide gel electrophoresis (SDS-PAGE) and liquid chromatography-tandem mass spectrometry (LC-MS/MS) to identify 225 proteins from milk-derived MFGM (2). Michael et al., identified 244 and 133 kinds of proteins in whey protein concentrate and casein concentrate by LC-MS/MS combined with the shotgun method (18).

Among the MFGM proteins, there are 8 kinds with the highest abundance, including MUC1 and MUC1 six glycoproteins, xanthine oxidoreductase (XDH/XO), mucin 15 (MUC15/PAS III), fatty acid transporter (CD36/PAS IV), lactophilic lipoprotein and lectin (pas6/7), and two non-glycosylated proteins: adipogenic differentiation-associated protein (ADPH) and fatty acid-binding protein (FABP).

Lipids in MFGM

The main lipids in MFGM are polar lipids and neutral lipids (15). The main polar lipids can be divided into five types: phosphatidylcholine (PC: 19.2–37.3%), phosphatidylethanolamine (PE: 19.8–42%), sphingomyelin

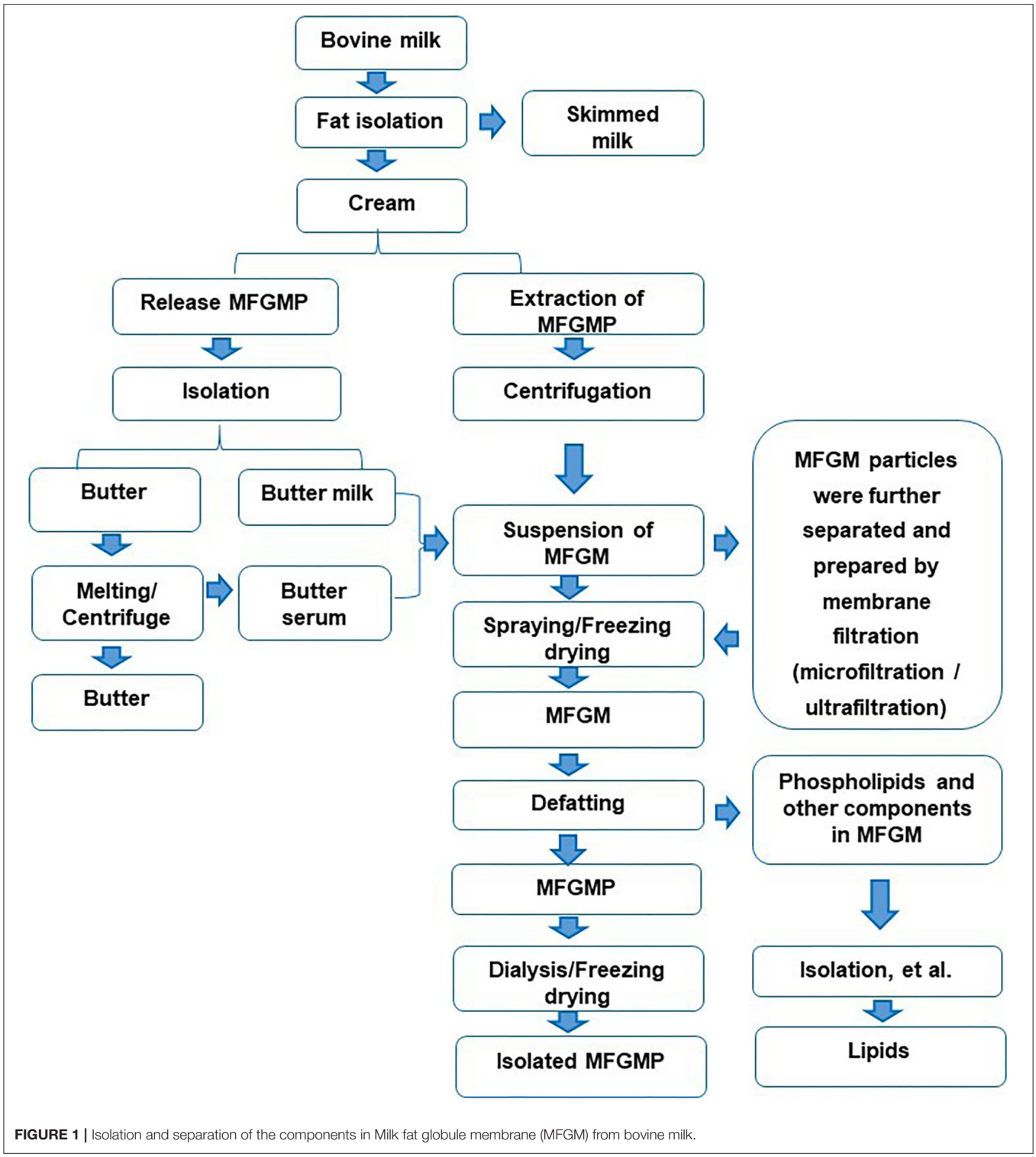

FIGURE 1 | Isolation and separation of the components in Milk fat globule membrane (MFGM) from bovine milk.

(SM: 18–34.1%), phosphatidylinositol (PI: 0.6–13.6%), and phosphatidylserine (PS: 1.9–16%) (19). Phosphatidylcholine and sphingomyelin are mainly located in the outer layer of the cell membrane. Phosphatidylethanolamine is mainly located in the outer layer of the cell membrane, and phosphatidylinositol and phosphatidylserine are concentrated in the phospholipid bilayer. Neutral lipids include triglyceride, diglyceride, monoglyceride, cholesterol, and other esters, of which triglyceride is the main part (accounting for 62% of the total lipid) (10). The content of neutral grease in MFGM is variable (56–80%), which largely depends on the separation method used in MFGM separation (20).

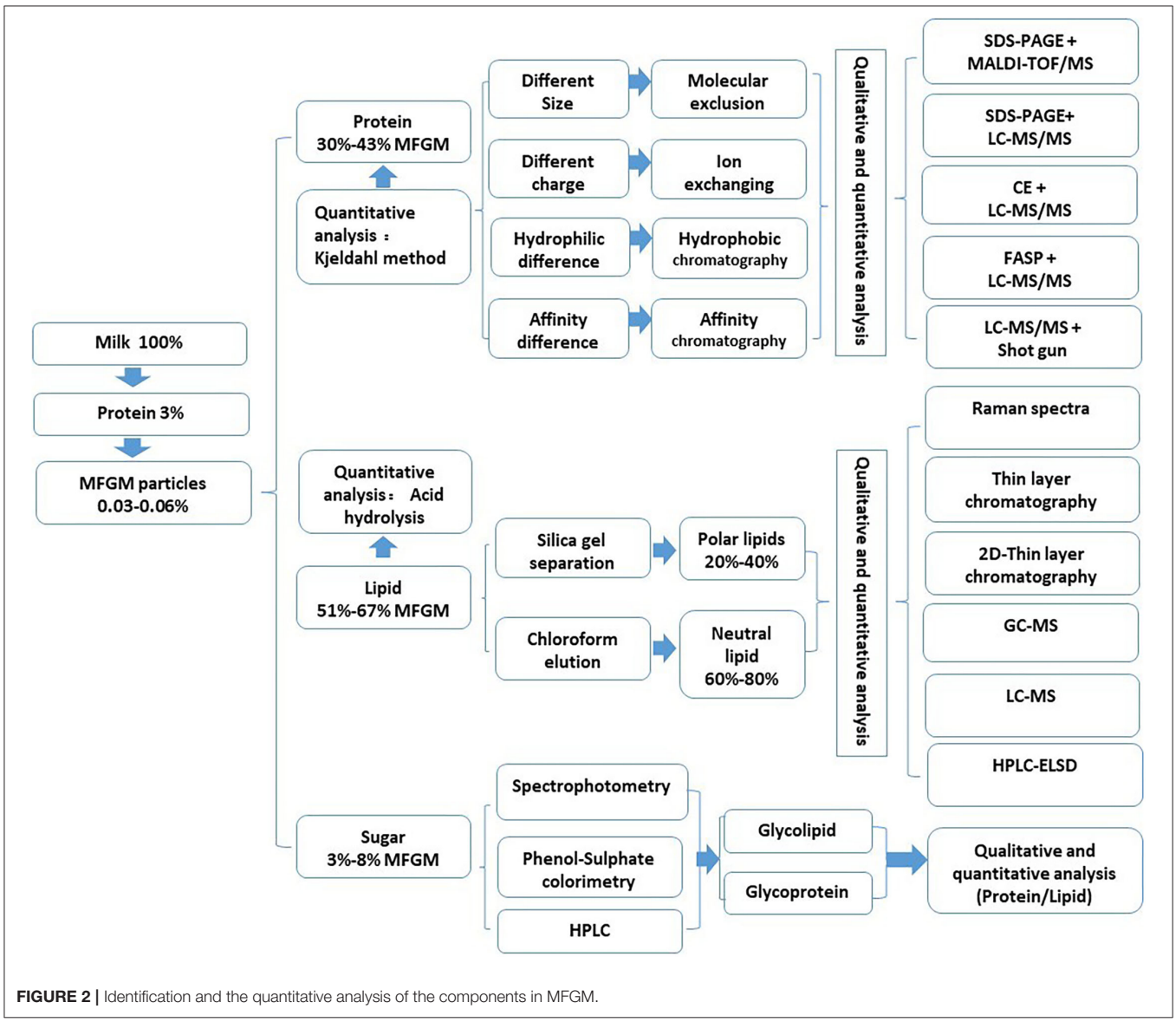

FIGURE 2 | Identification and the quantitative analysis of the components in MFGM.

Sugars in MFGM

The carbohydrate in MFGM is mainly combined with proteins or lipids and exists in the form of glycoprotein or glycolipid. Glycolipids can be divided into neutral glycolipids and acid glycolipids (gangliosides). Ceramide is sphingosine, which is linked to fatty acids by an amide bond. Neutral glycolipids are composed of one or more carbohydrate residues connected to ceramide in the lipid portion, including galactosylceramide, glucoceramide, and lacer. Acid glycolipids are composed of oligosaccharides linked by ceramide to at least one sialic acid and various other residues through glycosidic bonds. Glycoproteins include mucin, butyrophilin (BTN), fatty acid transporter (CD36), milk lectin PAS 6 (52 kDa), and PAS 7 (47 kDa) (21).

There are few reports about the content of polysaccharides in MFGM and the differences are large. He et al., determined the mass fraction of polysaccharides in yak MFGM by phenol sulfuric acid method, which was about 0.1 mg/g. Ji et al., determined the mass fraction of polysaccharides from five kinds of mammals, including cow milk (8.54 mg/g), camel milk (5.90 mg/g), buffalo milk (5.06 mg/g), yak MFGM (3.16 mg/g), and goat milk (2.96 mg/g). It can be seen that the mass fraction of polysaccharides in MFGM is related to many factors, such as mammalian species, separation, and analysis methods of MFGM.

FUNCTIONAL PROPERTIES OF MFGM

Emulsifying

Milk fat globule membrane and its components are amphiphilic, and they are considered to be excellent emulsifiers. The results indicated that the emulsion created with MFGM and MFGM protein had lower viscosity and smaller droplet size than the emulsion prepared with MFGM lipid. The results of heat

treatment showed that the emulsion prepared by MFGM was stable at the temperature range of 35–85°C, whereas the emulsion made from MFGM protein became unstable at temperatures above 65°C (22).

The emulsifying performance of MFGM is related to its composition, which is closely related to the raw materials and separation methods of MFGM. It was found that the MFGM rich material separated from the reconstituted milk by microfiltration had a better emulsifying performance by comparing the particle size distribution, viscosity, and stability of different emulsions (23, 24). The discovery of emulsifying properties of MFGM is also helpful to the food industry. Due to the poor bioavailability and absorption of β-carotene in the aqueous phase, its application in the food industry has been greatly restricted. MFGM can be used as an emulsifier to form emulsion with β-carotene, which can improve the dispersion and poor stability of β-carotene in water, so as to improve its bioavailability (25).

Foaming

Due to the emulsifying properties of MFGM and MFGM protein, adding an appropriate amount of MFGM and MFGM protein in whipping cream will cover fat droplets and form an aggregated network structure, which will cover the air mixed in the whipping process and increase the foaming rate. Within a certain time range, there is a positive correlation between the stirring time and the foaming rate.

Water Holding

Because of its high water-holding capacity, MFGM may prevent moisture loss and migration in the bread core, which reduces the problem of bread aging and hardening. It can also be used as a bread improver, which can not only increase the nutritional value of bread, but also improve the quality of bread.

BIOACTIVITIES OF MFGM

There are various functional components in MFGM. Reinhardt et al. discovered that 23% of MFGM proteins are involved in membrane or protein transport, 11% in fat transport or metabolism, 7% in protein synthesis, binding, or folding, 9% in carrier protein, 4% in immune protein, and 2% in β- and x-casein; the remaining 21% in protein function is unknown (26). These functions are mainly derived from the protein, lipid, and carbohydrate components of the MFGM, as shown in **Figure 3**. From the current situation reported, the functional characteristics of MFGM are mainly as follows.

Immunomodulatory Activity

Many components in MFGM have been proved to have many nutritional values. BTN has a positive impact on human central nervous system diseases. BTN has sequence homology with antibodies detected in autistic children's serum. It can participate in the immune regulation of autism, positively regulate autoimmune encephalomyelitis, and affect the pathogenesis of autism. Some studies have also shown that compared with infants who eat skimmed milk powder, MFGM as complementary food can regulate the metabolic abnormalities of malnourished infants, thus improving metabolic regulation and enhancing immunity (27).

Anti-intestinal Inflammatory Activity

Infants given commercially available formula had a greater incidence of acute otitis media, gastrointestinal, and respiratory tract infections within 1 year of birth, compared with breastfed infants, perhaps because of the absence of MFGM. Studies have shown that supplementing formula milk powder with bovine MFGM can help to reduce the incidence of acute otitis media in infants and the utilization rate of antipyretic drugs and has an immunomodulatory effect on the humoral response of pneumococcal vaccine (28).

In recent years, the research on the protective effect of milk agglutinin on the gastrointestinal tract has become a hot spot. Milk agglutinin can specifically bind with various rotaviruses, inhibit its replication, reduce the apoptosis of intestinal epithelial cells, and prevent rotavirus infection leading to gastroenteritis. Mexican newborn research discovered a link between milk lectin levels in breast milk and infant rotavirus infection.

In addition, glycoprotein, butyric glycoside, lactonectin, and mucus of MFGM have antiviral effects *in vitro*, whereas oligosaccharides can inhibit the binding of a variety of bacteria (including pneumococci) to mucosa (29). Mucin has been proved to reduce the adhesion of Yersinia enterocolitica to the intestinal mucus.

Antitumor Activity

In the milk of cattle, goat, buffalo, yak, and camel, MFGM of goat and buffalo showed a better effect in inducing apoptosis and reducing the activity of HT-29 cells (30). Colon cancer, breast cancer, and other malignancies are all inhibited by the lipid and protein components of MFGM. Studies have found that the FABP in MFGM can inhibit the growth of breast cancer cells *in vitro* at very low concentrations. Nerve sphingomyelin can induce cancer cells to stop growth, differentiation, and apoptosis through ceramide, sphingosine, and metabolites of colon cancer cells, which can effectively inhibit early and late colon cancer. In human breast cancer cells, the expression of milk agglutinin will be reduced the survival rate of cancer cells. Therefore, MFGM can be used as a nutritional supplement to inhibit the growth of cancer cells (31).

Promoting Cell Growth and Differentiation

Milk agglutinin can support the growth of epithelial cells. The purified MFGM protein can effectively promote cell growth and inhibit the apoptosis of C_2C1_2 cells by upregulating the expression of Akt and mTOR protein kinase. MFGM has the potential to aid in illness prevention and also newborn growth and development (32). Studies have shown that adding MFGM to the diet of infants aged 6–11 months can prevent diarrhea, and adding MFGM to the diet of preschool children can improve the fever of children's language function (33). Feeding SM supplemented milk to preterm newborns with birth weights $<$1,500 g can compensate for neural development deficits caused by inadequate breast milk, resulting in a favorable influence

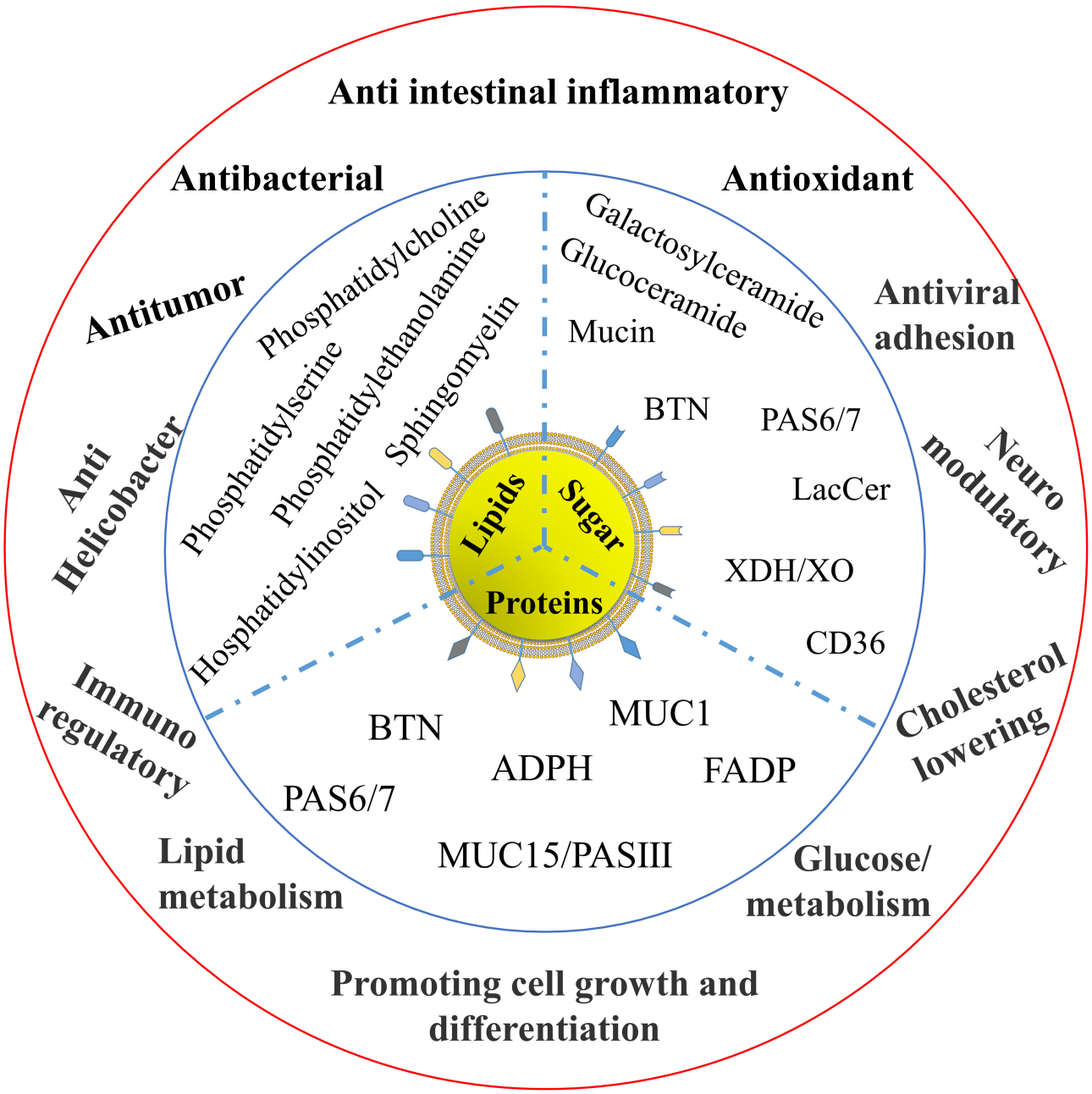

FIGURE 3 | Bioactivities of the components in MFGM.

on the infant's neural development (34). The combination of bovine MFGM and lactoferrin in the diet can not only better approach the bioactive components of breast milk, but also contribute to the cognitive, gastrointestinal, and respiratory health of infants (35).

Other Activities of MFGM

The MFGM differential proteins of yak and cow were shown to be involved in glycolipid metabolism, immunological regulation, antioxidant activity, anticancer, neuromodulation, antibacteria, and viral adhesion in marker-free proteomics. Both differential protein and protein-related genes predicted that yak and bovine MFGM protein had the biological function of regulating glucose and lipid metabolism. *In vitro* experiments confirmed that yak and bovine MFGM protein could reduce lipid accumulation and increase glucose uptake in HepG2 cells. The MFGM protein of yak and cattle has the higher lipid-lowering ability and increasing glucose uptake ability, which are respectively related to different MFGM proteins related to glucose and lipid metabolism in yak and cattle (36).

The elderly's feeling of balance, strength, and sensitivity can be improved by combining MFGM consumption with adequate exercise (37). Furthermore, the inclusion of MFGM may aid in the treatment of dyskinesia syndrome. Sphingolipids in MFGM can not only treat and improve cardiovascular diseases, but also participate in the inflammatory process of atherosclerosis and insulin resistance. Therefore, it can be inferred that dietary sphingolipids have great potential for the treatment of various aspects of metabolic syndromes, such as dyslipidemia, insulin resistance, and cardiovascular diseases.

PROSPECTIVE

With the deep understanding of the composition and properties of MFGM, the nutritional function, growth and development of different populations, disease prevention, and other functional characteristics of MFGM have been gradually discovered, but the nutritional and functional characteristics of specific components of MFGM still need to be studied further. At present, infant formula with MFGM concentrate has been launched in the market. Special medical purpose formula food, special food, and functional food containing MFGM still have a sizable market. Furthermore, the research heat of the MFGM is increasing, and the fine separation and preparation technology is improving.

AUTHOR CONTRIBUTIONS

CW, ZG, and LJ contributed to conception and design of the study. XQ organized the figures. ZM performed the statistical analysis. CW wrote the first draft of the manuscript. ZG and XQ wrote sections of the manuscript. All authors contributed to manuscript revision, read, and approved the submitted version.

FUNDING

This study was financially supported by the Basic Research Program of Liaoning Education Department (2017J080) and the National Natural Science Foundation of China (31371805).

SUPPLEMENTARY MATERIAL

The Supplementary Material for this article can be found online at: https://www.frontiersin.org/articles/10.3389/fnut.2021.807284/full#supplementary-material

REFERENCES

1. Smoczyński M, Staniewski B, Kiełczewska K. Composition and structure of the bovine milk fat globule membrane—some nutritional and technological implications. *Food Rev Int.* (2012) 28:188–202. doi: 10.1080/87559129.2011.595024
2. Le TT, Van Camp J, Dewettinck K. Milk fat globule membrane material: Isolation techniques, health-beneficial properties, and potential applications. *Stud Nat Prod Chem.* (2014) 7:347–82. doi: 10.1016/B978-0-444-63294-4.00012-7
3. Le TT, Van Camp J, Rombaut R, Van Leeckwyck F, Dewettinck K. Effect of washing conditions on the recovery of milk fat globule membrane proteins during the isolation of milk fat globule membrane from milk. *J Dairy Sci.* (2009) 92:3592–603. doi: 10.3168/jds.2008-2009
4. Guerin J, Burgain J, Gomand F, Scher J, Gaiani C. Milk fat globule membrane glycoproteins: valuable ingredients for lactic acid bacteria encapsulation? *Crit Rev Food Sci Nutr.* (2019) 59:639–51. doi: 10.1080/10408398.2017.1386158
5. He S, Li H, Ma Y. Composition and physiological characteristics of milk fat globule membrane. *China Dairy Industry.* (2009) 37:38–57. doi: 10.3389/fped.2018.00313
6. Dewettinck K, Rombaut R, Thienpont N, Le TT, Messens K, Van Camp J. Nutritional and technological aspects of milk fat globule membrane material. *Int Dairy J.* (2008) 18:436–57. doi: 10.1016/j.idairyj.2007.10.014
7. Li H, Xu W, Ma Y, Zhou S. Separation and purification of the bovine milk fat globule membrane protein and its effect on improvement of C_2C_{12} mouse skeletal muscle cell proliferation. *N J Chem.* (2017) 41:6530–9. doi: 10.1039/C7NJ00560A
8. Jukkola A, Partanen R, Xiang W, Heino A, Rojas OJ. Food emulsifiers based on milk fat globule membranes and their interactions with calcium and casein phosphoproteins. *Food Hydrocoll.* (2019) 94:30–7. doi: 10.1016/j.foodhyd.2019.03.005
9. Qu X, Hu H, Wang Y, Cao C, Li H, Liu X, et al. Proteomics analysis of milk fat globule membrane enriched materials derived from by-products during different stages of milk-fat processing. *LWT.* (2019) 116:108531. doi: 10.1016/j.lwt.2019.108531
10. Kanno C, Kim D-H. A simple procedure for the preparation of bovine milk fat globule membrane and a comparison of its composition, enzymatic activities, and electrophoretic properties with those prepared by other methods. *Agric Biol Chem.* (1990) 54:2845–54. doi: 10.1080/00021369.1990.10870405
11. Corredig M, Dalgleish DG. Isolates from industrial buttermilk: emulsifying properties of materials derived from the milk fat globule membrane. *J Agric Food Chem.* (1997) 45:4595–600. doi: 10.1021/jf970531f
12. Hansen SF, Hogan SA, Tobin J, Rasmussen JT, Larsen LB, Wiking L. Microfiltration of raw milk for production of high-purity milk fat globule membrane material. *J Food Eng.* (2020) 276:109887. doi: 10.1016/j.jfoodeng.2019.109887
13. Hansen SF, Petrat-Melin B, Rasmussen JT, Larsen LB, Ostenfeld MS, Wiking L. Placing pasteurisation before or after microfiltration impacts the protein composition of milk fat globule membrane material. *Int Dairy J.* (2018) 81:35–41. doi: 10.1016/j.idairyj.2017.12.015
14. Holzmüller W, Kulozik U. Isolation of milk fat globule membrane (MFGM) material by coagulation and diafiltration of buttermilk. *Int Dairy J.* (2016) 63:88–91. doi: 10.1016/j.idairyj.2016.08.002
15. El-Loly MM. Composition, properties and nutritional aspects of milk fat globule membrane-a review. *Pol J Food Nutr Sci.* (2011) 61:11. doi: 10.2478/v10222-011-0001-0
16. Ahn Y-J, Ganesan P, Kwak H-S. Composition, structure, and bioactive components in milk fat globule membrane. *Food Sci Anim Resourc.* (2011) 31:1–8. doi: 10.5851/kosfa.2011.31.1.001
17. Cebo C, Caillat H, Bouvier F, Martin P. Major proteins of the goat milk fat globule membrane. *J Dairy Sci.* (2010) 93:868–76. doi: 10.3168/jds.2009-2638
18. Affolter M, Grass L, Vanrobaeys F, Casado B, Kussmann M. Qualitative and quantitative profiling of the bovine milk fat globule membrane proteome. *J Proteomics.* (2010) 73:1079–88. doi: 10.1016/j.jprot.2009.11.008
19. Lopez C. Milk fat globules enveloped by their biological membrane: unique colloidal assemblies with a specific composition and structure. *Curr Opin Colloid Interface Sci.* (2011) 16:391–404. doi: 10.1016/j.cocis.2011.05.007
20. Truong T, Lopez C, Bhandari B, Prakash S. *Dairy Fat Products and Functionality*. Berlin: Springer (2020). doi: 10.1007/978-3-030-41661-4
21. Gupta VK, Tuohy MG, O'donovan A, Lohani M. *Biotechnology of Bioactive Compounds: Sources and Applications*. Hoboken, NJ: John Wiley & Sons (2015). doi: 10.1002/9781118733103
22. He S, Tang H, Yi H, Xu W, Ma Y, Wang R. Properties of emulsions from milk fat globule membrane and its components. *Int J Food Proper.* (2017) 20:1342–53. doi: 10.1080/10942912.2017.1343348

23. Phan TTQ, Asaduzzaman M, Le TT, Fredrick E, Van Der Meeren P, Dewettinck K. Composition and emulsifying properties of a milk fat globule membrane enriched material. *Int Dairy J.* (2013) 29:99–106. doi: 10.1016/j.idairyj.2012.10.014
24. Phan TTQ, Le TT, Van Der Meeren P, Dewettinck K. Comparison of emulsifying properties of milk fat globule membrane materials isolated from different dairy by-products. *J Dairy Sci.* (2014) 97:4799–810. doi: 10.3168/jds.2014-8030
25. He S, Ye A. Formation and gastrointestinal digestion of β-carotene emulsion stabilized by milk fat globule membrane. *J Food Process Eng.* (2019) 42:e13301. doi: 10.1111/jfpe.13301
26. Reinhardt TA, Lippolis JD. Bovine milk fat globule membrane proteome. *J Dairy Res.* (2006) 73:406–16. doi: 10.1017/S0022029906001889
27. Zhang X, Wu Y, Ye H, Feng C, Han D, Tao S, et al. Dietary milk fat globule membrane supplementation during late gestation increased the growth of neonatal piglets by improving their plasma parameters, intestinal barriers, and fecal microbiota. *RSC Adv.* (2020) 10:16987–98. doi: 10.1039/D0RA02618B
28. Timby N, Hernell O, Vaarala O, Melin M, Lönnerdal B, Domellöf M. Infections in infants fed formula supplemented with bovine milk fat globule membranes. *J Pediatr Gastroenterol Nutr.* (2015) 60:384–9. doi: 10.1097/MPG.0000000000000624
29. Da Silva RC, Colleran HL, Ibrahim SA. Milk fat globule membrane in infant nutrition: a dairy industry perspective. *J Dairy Res.* (2021) 88:105–16. doi: 10.1017/S0022029921000224
30. Ji X, Xu W, Cui J, Ma Y, Zhou S. Goat and buffalo milk fat globule membranes exhibit better effects at inducing apoptosis and reduction the viability of HT-29 cells. *Sci Rep.* (2019) 9:1–14. doi: 10.1038/s41598-019-39546-y
31. Motouri M, Matsuyama H, Yamamura J-I, Tanaka M, Aoe S, Iwanaga T, et al. Milk sphingomyelin accelerates enzymatic and morphological maturation of the intestine in artificially reared rats. *J Pediatr Gastroenterol Nutr.* (2003) 36:241–7. doi: 10.1097/00005176-200302000-00016
32. Hernell O, Lonnerdal B, Timby N. Milk fat globule membranes: effects on microbiome metabolome and infections in infants and children. *Nestle Nutr Inst Workshop Ser.* (2020) 94:133–40. doi: 10.1159/000505066
33. Zavaleta N, Kvistgaard AS, Graverholt G, Respicio G, Guija H, Valencia N, et al. Efficacy of an MFGM-enriched complementary food in diarrhea, anemia, and micronutrient status in infants. *J Pediatr Gastroenterol Nutr.* (2011) 53:561–8. doi: 10.1097/MPG.0b013e318225cdaf
34. Tanaka K, Hosozawa M, Kudo N, Yoshikawa N, Hisata K, Shoji H, et al. The pilot study: sphingomyelin-fortified milk has a positive association with the neurobehavioural development of very low birth weight infants during infancy, randomized control trial. *Brain Dev.* (2013) 35:45–52. doi: 10.1016/j.braindev.2012.03.004
35. Li F, Wu SS, Berseth CL, Harris CL, Richards JD, Wampler JL, et al. Improved neurodevelopmental outcomes associated with bovine milk fat globule membrane and lactoferrin in infant formula: a randomized, controlled trial. *J Pediatr.* (2019) 215:24–31.e28. doi: 10.1016/j.jpeds.2019.08.030
36. Zhao L, Du M, Gao J, Zhan B, Mao X. Label-free quantitative proteomic analysis of milk fat globule membrane proteins of yak and cow and identification of proteins associated with glucose and lipid metabolism. *Food Chem.* (2019) 275:59–68. doi: 10.1016/j.foodchem.2018.09.044
37. Yoshinaka Y, Soga S, Ota N, Yokoyama K, Yamada Y, Kimura M. Light rhythmic exercise with dietary milk fat globule membrane improves physical fitness in an elderly Japanese population: a double-blind randomized placebo-controlled trial. *Biosci Biotechnol Biochem.* (2018) 82:677–82. doi: 10.1080/09168451.2017.1412248

Conflict of Interest: CW is a full-time faculty in the Dalian Polytechnic University and she directed a research work funded by the Inner Mongolia Mengniu Dairy Industry (Group) Co., Ltd., in which ZG and ZM engaged.

The remaining authors declare that the research was conducted in the absence of any commercial or financial relationships that could be construed as a potential conflict of interest.

Publisher's Note: All claims expressed in this article are solely those of the authors and do not necessarily represent those of their affiliated organizations, or those of the publisher, the editors and the reviewers. Any product that may be evaluated in this article, or claim that may be made by its manufacturer, is not guaranteed or endorsed by the publisher.

Copyright © 2022 Wang, Qiao, Gao, Jiang and Mu. This is an open-access article distributed under the terms of the Creative Commons Attribution License (CC BY). The use, distribution or reproduction in other forums is permitted, provided the original author(s) and the copyright owner(s) are credited and that the original publication in this journal is cited, in accordance with accepted academic practice. No use, distribution or reproduction is permitted which does not comply with these terms.

frontiers in Nutrition

ORIGINAL RESEARCH
published: 02 March 2022
doi: 10.3389/fnut.2022.846282

Polysaccharide-Zein Composite Nanoparticles for Enhancing Cellular Uptake and Oral Bioavailability of Curcumin: Characterization, Anti-colorectal Cancer Effect, and Pharmacokinetics

Lu Liu[1,2,3], Shufang Yang[2,3], Feng Chen[2,3] and Ka-Wing Cheng[2,3]**

[1] Institute for Food and Bioresource Engineering, College of Engineering, Peking University, Beijing, China, [2] Shenzhen Key Laboratory of Marine Microbiome Engineering, Institute for Advanced Study, Shenzhen University, Shenzhen, China, [3] Institute for Innovative Development of Food Industry, Shenzhen University, Shenzhen, China

OPEN ACCESS

Edited by:
Yahong Han,
Huazhong Agricultural University,
China

Reviewed by:
Rui Fan,
Peking University, China
Rohitash Jamwal,
University of Rhode Island,
United States

***Correspondence:**
Feng Chen
sfchen@szu.edu.cn
Ka-Wing Cheng
kwcheng@szu.edu.cn

Specialty section:
This article was submitted to
Food Chemistry,
a section of the journal
Frontiers in Nutrition

Received: 31 December 2021
Accepted: 14 February 2022
Published: 02 March 2022

Citation:
Liu L, Yang S, Chen F and
Cheng K-W (2022)
Polysaccharide-Zein Composite
Nanoparticles for Enhancing Cellular
Uptake and Oral Bioavailability
of Curcumin: Characterization,
Anti-colorectal Cancer Effect,
and Pharmacokinetics.
Front. Nutr. 9:846282.
doi: 10.3389/fnut.2022.846282

Curcumin (CUR) has demonstrated promising potential as a therapeutic agent against colorectal cancer (CRC). However, its intrinsic shortcomings, including oxidative instability, sensitivity to gastrointestinal (GI) hydrolytic/enzymatic action, and susceptibility to biotransformation and systemic elimination, have greatly undermined its value for application in clinical settings. The development of carriers, in particular oral formulations, for its efficient delivery has remained an important direction in nutraceutical research. In the present work, CUR-encapsulated nanoparticles were fabricated with zein alone (Zein-CUR) and with zein and a polysaccharide (PS) [gum Arabic (GA), hyaluronic acid (HA) and pectin (PC), respectively] (PS-Zein-CUR). Their physicochemical and biological properties were evaluated in a series of *in vitro* and *in vivo* assays. Dynamic light scattering analysis showed an increase in the particle size of the nanoparticles from 129.0 nm (Zein-CUR) to 188.8–346.4 nm (PS-Zein-CUR). The three PS-Zein-CUR formulations had significantly higher (17–22%) CUR encapsulation efficiency (EE) than Zein-CUR. Among them, HA-Zein-CUR exhibited the highest EE and loading capacity. Zeta potential and FTIR spectra indicated the involvement of electrostatic and hydrophobic interactions and hydrogen bonds in the formation of the PS-Zein-CUR. In human CRC cell lines (HCT8, HCT29, and HCT116), the three PS-Zein-CUR and CUR all effectively inhibited cell viability and colony formation (HA-Zein-CUR > PC-Zein-CUR > GA-Zein-CUR/CUR). HA-Zein-CUR and PC-Zein-CUR also resulted in significantly higher cellular uptake of CUR than GA-Zein-CUR and CUR. Simulated GI-digestion assay demonstrated significantly improved controlled-release properties of these two formulations. Further pharmacokinetics and tissue distribution assays in a CRC subcutaneous xenograft model in nude mice corroborated the enhanced pharmacokinetic properties of intragastric administration of HA-Zein-CUR

compared with that of free CUR (3 times higher C_{max} and 9.18 times higher plasma AUC). HA-Zein-CUR also led to enhanced delivery and accumulation of CUR in major organs/tissues, in particular CRC tumors and colon. These results together support that HA-Zein-CUR has promising potential as an oral agent for the control of CRC.

Keywords: curcumin, polysaccharide-zein composite nanoparticles, cellular uptake, colorectal cancer, pharmacokinetics

INTRODUCTION

Curcumin (CUR), a natural polyphenol derived from turmeric (*Curcuma longa*), has been approved as a food additive in many countries. It has been reported to suppress the initiation, promotion, and/or progression of various types of cancers *via* multiple action mechanisms (1). In particular, its efficacy in colorectal cancer (CRC) control has been widely studied with promising results (2, 3). However, it has poor solubility and pH sensitivity, and is susceptible to biotransformation. These properties together with its sensitivity to the hydrolytic condition of the gastrointestinal (GI) tract have significantly compromised its oral bioavailability and limited its value for clinical applications (4). When administered orally to rats at a dose of 1 g/kg, 75% of CUR was excreted in the feces (5). In humans, oral administration of CUR at a dose of 2 g resulted in undetectable or extremely low serum levels (6). An array of carriers has been proposed to help overcome one or more of these shortcomings, and thus improve the efficacy of CUR in various disease models (7, 8).

Formulations for oral administration are among the most highly sought-after and have attracted a lot of research interest. In this regard, many studies have been centered on biocompatible, biodegradable, and highly safe natural molecules, such as proteins and polysaccharides (PS), for the fabrication of delivery systems for nutraceuticals (9, 10). As a major protein in corn, zein has been much appreciated for its low production cost besides being a renewable macromolecule. It is highly amphipathic and can easily self-assemble into nanoparticles by the antisolvent precipitation method, making it a favorable material for encapsulating hydrophobic bioactive compounds (11). Nonetheless, studies also showed that zein may form aggregates in the GI tract under near-isoelectric and high-ionic strength conditions, and may be partially digested by trypsin (12). Coating with PS, such as gum Arabic (GA), hyaluronic acid (HA), pectin (PC), chitosan, and alginate, has been proposed to be a promising approach to help overcome these limitations (13). These PS are capable of forming a core-shell structure with zein *via* crosslinking between the various functional groups on the macromolecules. Studies showed that PS-Zein had the advantages of convenient preparation, good dispersion and stability in aqueous solution, which make them ideal carriers to protect the encapsulated bioactive molecules from the chemical or biochemical insults of the external environment (14–16). However, most studies have focused on the fabrication and characterization of the physicochemical characteristics of PS-Zein. Information regarding the biological properties including bioactivity and pharmacokinetics of these promising nanocarriers remains limited.

The present study aimed to evaluate the potential of CUR-encapsulated PS-Zein nanoparticles (PS-Zein-CUR) as an oral agent for CRC therapy. Three common natural PS (GA, HA, and PC) which have wide applications in the food and pharmaceutical industries were chosen to fabricate the corresponding PS-Zein-CUR. Their physicochemical properties, anticancer effects, and cellular uptake in CRC cells were investigated. Furthermore, their simulated GI digestion (SGID) *in vitro* and pharmacokinetics and tissue distribution *in vivo* were also examined. A scheme of the experimental design is shown in **Figure 1**.

MATERIALS AND METHODS

Materials

Curcumin was obtained from Tianjin Guangfu Fine Chemical Research Institute (Tianjin, China). HA (100–300 kDa, ≥99%) was purchased from Xi'an XABC Biotech Co., Ltd., (Xi'an, China). GA (51198), PC (P9135), and zein (Z3625) were purchased from Sigma-Aldrich (St. Louis, MO, United States). HCT116, HCT8, and HT29 cells were obtained from the National Infrastructure of Cell Line Resource (Beijing, China).

Preparation of the Composite Nanoparticles

Zein-CUR and PS-Zein-CUR were prepared using an antisolvent coprecipitation method based on a previous study with some modifications (17). Briefly, zein (100 mg) and CUR (10 mg) were dissolved in 10 mL of aqueous ethanol (80%, v/v). The solution was slowly injected into 50 mL of distilled water or a PS solution (GA: 3 mg/mL; HA: 0.4 mg/mL; or PC: 0.6 mg/mL) with stirring at 600 rpm for 20 min. The mass ratios of PS to zein in the formulations were chosen based on a few recent reports (17–19). The ethanol was removed from the solution by rotary evaporation (45°C, −0.1 MPa). This was followed by centrifugation at 3,000 rpm for 10 min to remove the insoluble particles. The blank Zein/PS-Zein without CUR were also prepared with the same protocol.

Characterization of Composite Nanoparticles

After appropriate dilution, the composite nanoparticles were analyzed in a dynamic light scattering (DLS) particle analyzer (NanoBrook 90Plus, Brookhaven, GA, United States) to determine their particle size, polydispersity index (PDI), and

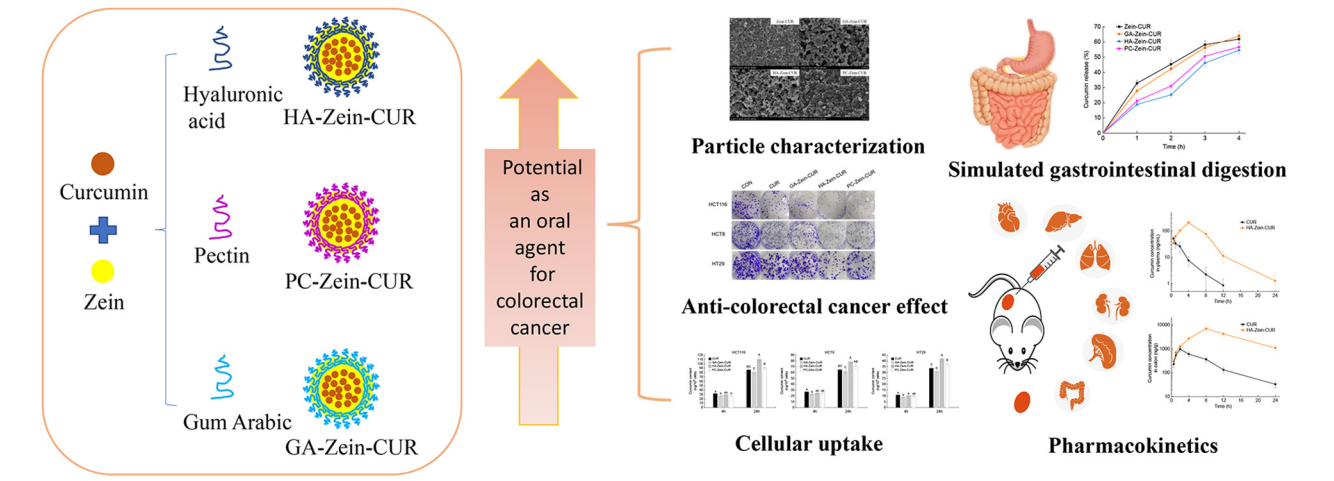

FIGURE 1 | Experimental scheme. The evaluation of the potential of PS-Zein-CUR an oral agent for CRC therapy: physicochemical properties, anti-CRC effects, cellular uptake, and gastrointestinal simulated digestion *in vitro* and pharmacokinetics and tissue distribution *in vivo*.

zeta potential. The turbidity of the nanoparticle suspensions was analyzed by measuring their optical density at 600 nm (OD_{600}) in a spectrophotometer (NP80 Touch, Implen, Munich, Germany). Their micromorphology was captured with a field-emission scanning electron microscope (FE-SEM) (SU8020, HITACHI, Tokyo, Japan), and their Fourier transform infrared (FTIR) spectra were recorded with an FTIR spectrometer (IS10, Nicolet, Wisconsin, WI, United States) in the wavenumber range of 400–4,000 cm^{-1}. Sixty-four scans at a resolution of $4cm^{-1}$ were performed for each sample. CUR in the nanoparticles was extracted with ethanol and quantified at 426 nm in a microplate reader (SpectraMaxTM i3X, Molecular Devices, Silicon Valley, CA, United States) using a standard curve. Encapsulation efficiency (EE) and loading capacity (LC) of the CUR-encapsulated nanoparticles were calculated using the following equations:

EE = encapsulated CUR (g)/total CUR (g) × 100%

LC = encapsulated CUR (g)/total mass of nanoparticles (g) × 100%

Cell Viability Assay

Cytotoxicity of CUR, PS-Zein and PS-Zein-CUR against CRC cells was assessed by using a CCK-8 kit (CK-04, Dojindo, Kumamoto, Japan). Briefly, cells were seeded in 96-well plates at a density of 5×10^3 cells per well. After 24 h of incubation at 37°C, the cells were treated with the above agents for 48 h, and then incubated with CCK-8 solution for 1 h. Absorbance was measured at 450 nm in a microplate reader. The IC_{50} values of the different treatments were determined using the logistic regression model in SPSS software.

Colony-Formation Assay

A thousand cells were seeded into each well of a 6-well plate and allowed to attach. After 48-h treatment with drugs or vehicles, the cells were cultured in media without drugs for 2 weeks. The colonies formed were fixed with methanol, stained with 0.1% crystal violet, and counted to obtain an average sum.

Cellular Uptake Analysis

Cells were seeded in 6-well plates at a density of 5×10^5 cells per well. After incubation with drugs for 4 and 24 h, respectively, the cells were harvested and washed twice with PBS. CUR was extracted from the cells with aqueous acetonitrile (70%) assisted with ultrasonication. The extract was centrifuged at 14,000 rpm for 10 min (4°C), and the supernatant was filtered through a 0.22-μm membrane prior to UPLC-MS analysis.

UPLC-MS Analysis of Curcumin

UPLC-MS analysis of CUR was conducted on a ACQUITY UPLC system coupled with a triple-quadrupole mass spectrometer (Waters, Milford, MA, United States) and equipped with a BEH reversed-phase C18 column (50 × 2.1 mm, 1.7 μm, Waters). The mobile phase consisted of acetonitrile (A) and water with 0.1% formic acid (B) at a flow rate of 0.3 mL/min. The injection volume was 1 μL. The gradient elution program was as follows: 0–6 min 40–100% A, 6–8 min, 100–40% A. MS/MS data acquisition was performed under positive electrospray ionization mode. Multiple Reaction Monitoring mode was employed to monitor CUR with precursor-to-product ion transition of *m/z* 369.28/145.13 and *m/z* 369.28/177.12. The MS parameters were set as follows: capillary voltage 3.0 Kv, desolvation gas flow 600 L/h, desolvation temperature 400°C, and cone voltage 20 V.

Simulated Gastrointestinal Digestion Assay

Simulated gastrointestinal digestion (SGID) assay was carried out by the method of Brodkorb et al. (20). Briefly, samples were diluted with an equal volume of simulated gastric fluid (SGF) and incubated in a shaking water bath (100 rpm, 37°C) for 2 h. The gastric chyme was then diluted with an equal volume

of simulated intestinal fluid (SIF) and incubated in a shaking water bath (100 rpm, 37°C) for a further 2 h. Samples were collected at 1, 2, 3, and 4 h during SGID and then centrifuged with Amicon Ultra centrifugal filters (MWCO 3 kDa). CUR was quantified by UPLC-MS.

Pharmacokinetics and Tissue Distribution Study

All animal experiments were approved by the Animal Ethical and Welfare Committee of Shenzhen University and carried out in accordance with the Regulations for the Administration of Affairs Concerning Experimental Animals of China. BALB/c nude mice (6-week-old, female) were purchased from Guangdong Medical Laboratory Animal Center (Foshan, China). The mice were kept under pathogen-free conditions and allowed to acclimatize for a week before experimentation. HCT116 cells (suspended in serum-free medium containing 50% Matrigel) were injected subcutaneously into the right flanks of the BALB/c nude mice at a density of 1×10^6 cells per mouse. Five days after implantation when the HCT116-derived xenografts were established, the mice were randomly divided into two groups (21 mice per group) for the following intragastric treatments, respectively: CUR (6 mg/kg, dissolved in 0.5% sodium carboxymethylcellulose) and HA-Zein-CUR (equivalent to 6 mg/kg CUR). Following administration, three mice were sacrificed at each of the designated time points (0.5, 1, 2, 4, 8, 12, and 24 h), and their blood, tumors, and organs (heart, lung, liver, colon, kidney, and spleen) were collected. The blood samples were centrifuged at 4,000 rpm at 4°C for 10 min to obtain plasma. Two hundred microliters of each plasma sample were used for extraction. The tumors and organs were washed and homogenized with precooled PBS in a TissueLyser (85300, Qiagen, Dusseldorf, Germany). Acetonitrile (3x, v/v) was used to extract CUR from plasma and tissue homogenates assisted with ultrasonication. After centrifugation at 14,000 rpm for 10 min (4°C), the supernatant was filtered through a 0.22-μm membrane and then analyzed by UPLC-MS.

Statistical Analysis

The data of the experiments are presented as mean ± SD. Significant differences among groups were identified by one-way ANOVA and the Duncan test. SPSS software was used for the analyses. $P < 0.05$ was considered to be statistically significant.

RESULTS AND DISCUSSION

Dynamic Light Scattering, Encapsulation Efficiency, and Loading Capacity Analysis of Curcumin-Loaded Composite Nanoparticles

The nanoparticle samples were subjected to DLS analysis of particle size, PDI, and zeta potential. As shown in **Figure 2A**, the incorporation of PS (GA, HA, or PC) significantly increased the turbidity (OD_{600}) of the Zein-CUR formulation. The adsorption of the anionic PS onto the surface of the cationic zein molecules also led to an increase in the particle size of the nanoparticles from 129.0 nm (Zein-CUR) to 188.8–346.4 nm (PS-Zein-CUR) (**Figure 2B**). HA-Zein-CUR and PC-Zein-CUR had significantly larger particle sizes than GA-Zein-CUR, which likely explained the higher turbidity of the former solutions than the latter (21). The particle size of PS-Zein-CUR was dependent on the inherent attribute of PS, such as electric charge (17). The PDI values of GA-Zein-CUR, HA-Zein-CUR, and PC-Zein-CUR were 0.13, 0.33, and 0.25, respectively, suggesting a narrower particle size distribution of GA-Zein-CUR than the other two formulations (**Figure 2C**). This is consistent with the results of a recent study that the presence of GA altered the polydispersity of Zein nanoparticles (22). It was also observed that the addition of PS greatly altered the surface charge density of the nanoparticles as evidenced by the reversal of the zeta potential from positive on Zein-CUR (34.1 mV) to negative on GA-Zein-CUR, HA-Zein-CUR, and PC-Zein-CUR (−30.0, −56.9 and −34.4 mV, respectively) (**Figure 2D**). The low negative zeta potentials (< −30 mV) also indicate that PS-Zein-CUR had good stability, especially HA-Zein-CUR, which was likely due to the capability of HA to introduce stronger electrostatic repulsive forces to the nanoparticles than GA and PC (23).

The EE and LC of the nanoparticles are presented in **Table 1**. The incorporation of the PS (GA, HA, or PC) significantly increased the EE of the Zein-CUR by 17 – 22%. A similar phenomenon was also reported for resveratrol-encapsulated Zein nanoparticles, whose EE was improved by chitosan coating (24). Meanwhile, LC of the formulations did not seem to have any particular trend. Only HA was able to moderately (9%) improve LC of the nanoparticles, while PC did not have any significant effect, and GA led to a significant reduction of LC by ∼50%. Taken together the EE and LC data, HA-Zein-CUR was thus considered to be the most effective carrier for CUR among the three formulations.

Spectroscopic Analysis of PS-Zein-CUR

Representative FE-SEM images of Zein-CUR and PS-Zein-CUR are shown in **Figure 3A**. The Zein-CUR appeared to be closely packed spheres, and the PS-Zein-CUR were in more loosely arranged bigger spheres. The GA-Zein-CUR seemed to have more uniform and smaller particle sizes than the HA-Zein-CUR and PC-Zein-CUR, which was consistent with the DLS data showed in **Figures 2B,C**. The generally bigger size and looser arrangement of the PS-Zein-CUR than the Zein-CUR was likely due to the intermolecular interactions of the PS molecules, in particularly hydrogen bonding among -COOH, $-NHCOCH_3$, and -OH groups (25, 26).

FTIR spectroscopy was subsequently performed to provide some theoretical grounds for the purported intermolecular interactions in the nanoparticle formulations. The FTIR spectra of CUR, PS, Zein, Zein-CUR, and PS-Zein-CUR are displayed in **Figure 3B**. The Zein-CUR showed characteristic peaks at 3,429, 1,649, and 1,539 cm^{-1}, which could be assigned to the vibration of hydroxyl, amide I, and amide II groups, respectively (27). It was noticed that the Zein and Zein-CUR exhibited almost identical IR spectra. This was likely due to the masking effect of the characteristic peaks of CUR (1,628, 1,601, and 1,510 cm^{-1})

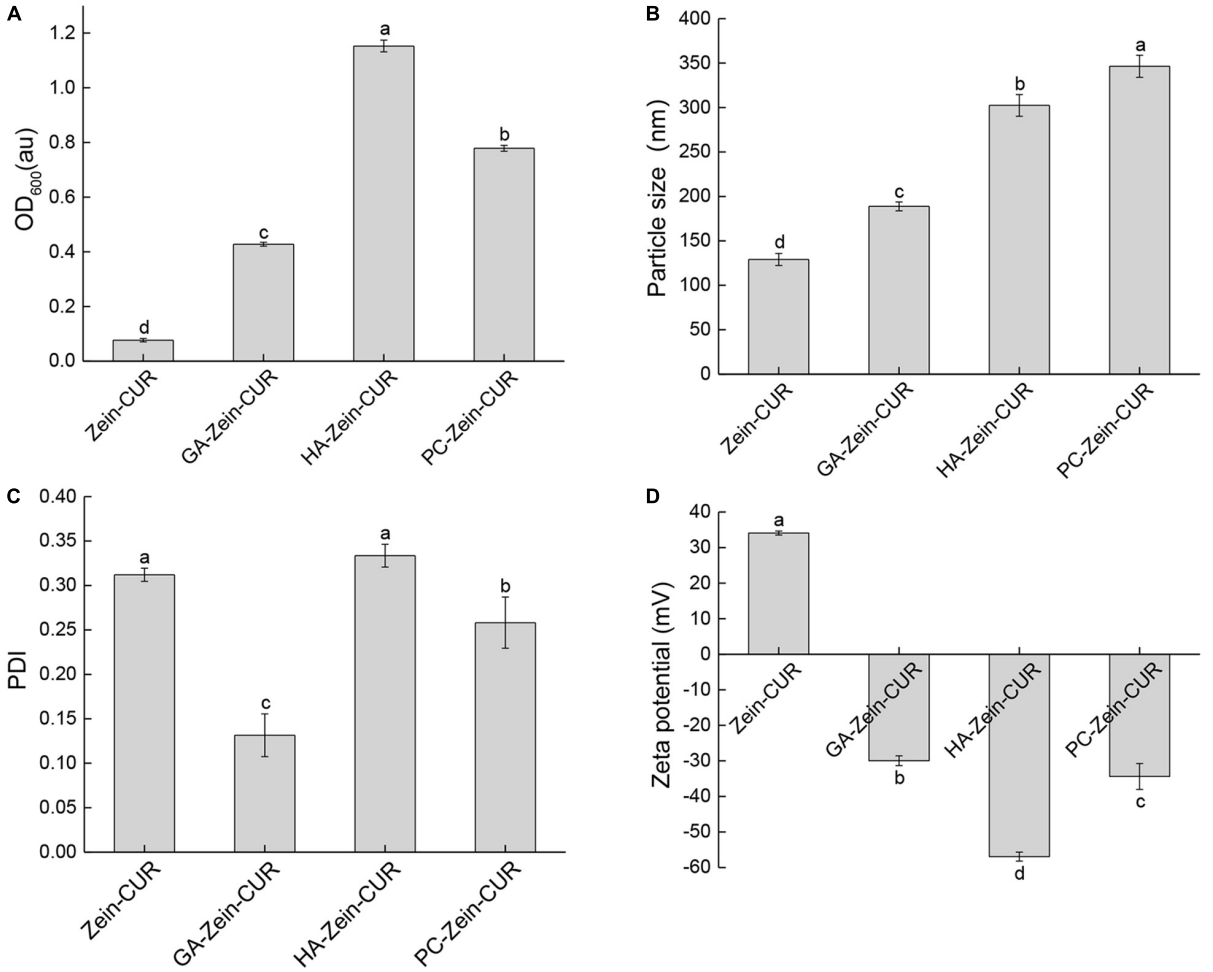

FIGURE 2 | Analysis of zein-curcumin (CUR) and polysaccharide (PS)-Zein-CUR suspensions. **(A)** Turbidity (OD_{600}), **(B)** particle size, **(C)** polydispersity index (PDI), and **(D)** zeta potential. Values are mean ± SD, $n = 3$. Bars marked with different letters indicate significant difference at $P < 0.05$.

TABLE 1 | Encapsulation efficiency (EE) and loading capacity (LC) of CUR-loaded composite nanoparticles.

	EE (%)	LC (%)
Zein-CUR	75.59 ± 2.57^{c}	6.87 ± 0.23^{B}
GA-Zein-CUR	92.94 ± 3.15^{b}	3.57 ± 0.12^{C}
HA-Zein-CUR	97.24 ± 2.23^{a}	7.48 ± 0.17^{A}
PC-Zein-CUR	95.05 ± 1.74^{ab}	6.79 ± 0.12^{B}

Values are mean ± SD, n = 3. Different letters in the same column indicate significant difference at P < 0.05.

by the amide I and amide II peaks of Zein. The identical IR spectra together with the almost complete disappearance of CUR's characteristic peaks at the regions of 813–1,429 cm^{-1} also suggests that CUR was well encapsulated and did not appreciably change the primary structure of Zein (28). The blue shift of the peaks corresponding to hydroxyl stretching vibration of the PS-Zein-CUR (3,430–3,439 cm^{-1}) relative to the Zein-CUR (3,429 cm^{-1}) may indicate the formation of hydrogen bonds between the hydroxyl groups of the PS and the amide groups of zein that resulted in lower bond energy than the original hydrogen bonds in the Zein-CUR formulation (29). Chen et al. also suggested that hydrogen bonding was a main driving force in the formation of zein-chitosan-quercetagetin nanoparticles (30). Meanwhile, the red shift of the amide I (1,635–1,648 cm^{-1}) and blue shift of the amide II peak (1,540–1,542 cm^{-1}) in the PS-Zein-CUR relative to those in the Zein-CUR (1,649 and 1,539 cm^{-1}, respectively) may arise as a result of hydrogen bond formation as well as hydrophobic interactions between zein and the PS molecules (31). Zein is known to have a high content of hydrophobic amino acids (32). The presence of GA, HA, or PC would change the hydrophilicity/hydrophobicity property of the surrounding environment of the zein polypeptides, and thus perturb their hydrophobic interaction (31). In addition, the disappearance of the asymmetric and symmetric COO- peaks of anionic PS (1,618–1,626 cm^{-1} and 1,403–1,420 cm^{-1}) in the PS-Zein-CUR also supports the occurrence of crosslinking between the PS and zein molecules (33). The C-O-C stretch peaks of the PS (1,016–1,066 cm^{-1}) was retained in the GA-Zein-CUR, but

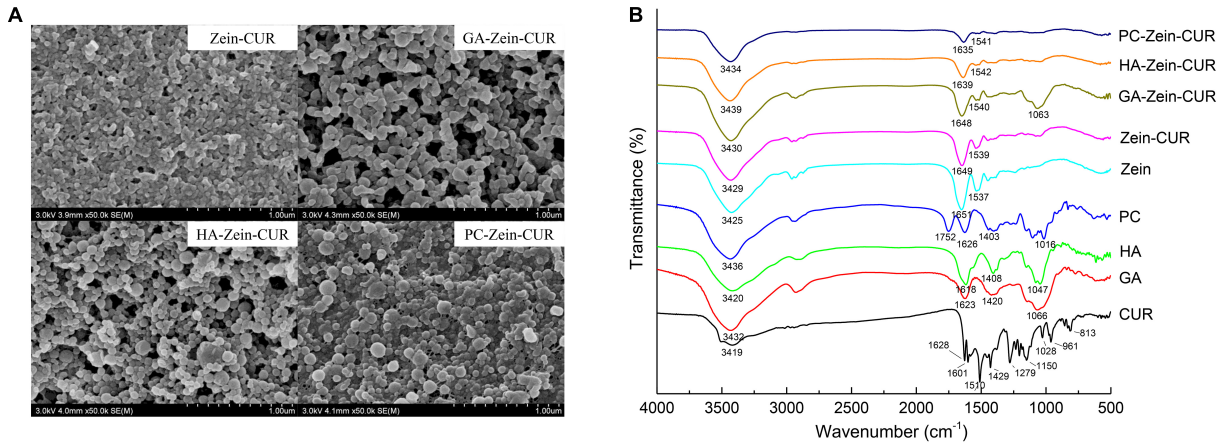

FIGURE 3 | Spectroscopic analysis of composite nanoparticles. **(A)** FE-SEM images (50,000× magnification) of Zein-CUR and PS-Zein-CUR. **(B)** FTIR spectra of CUR, PS, Zein, Zein-CUR, and PS-Zein-CUR.

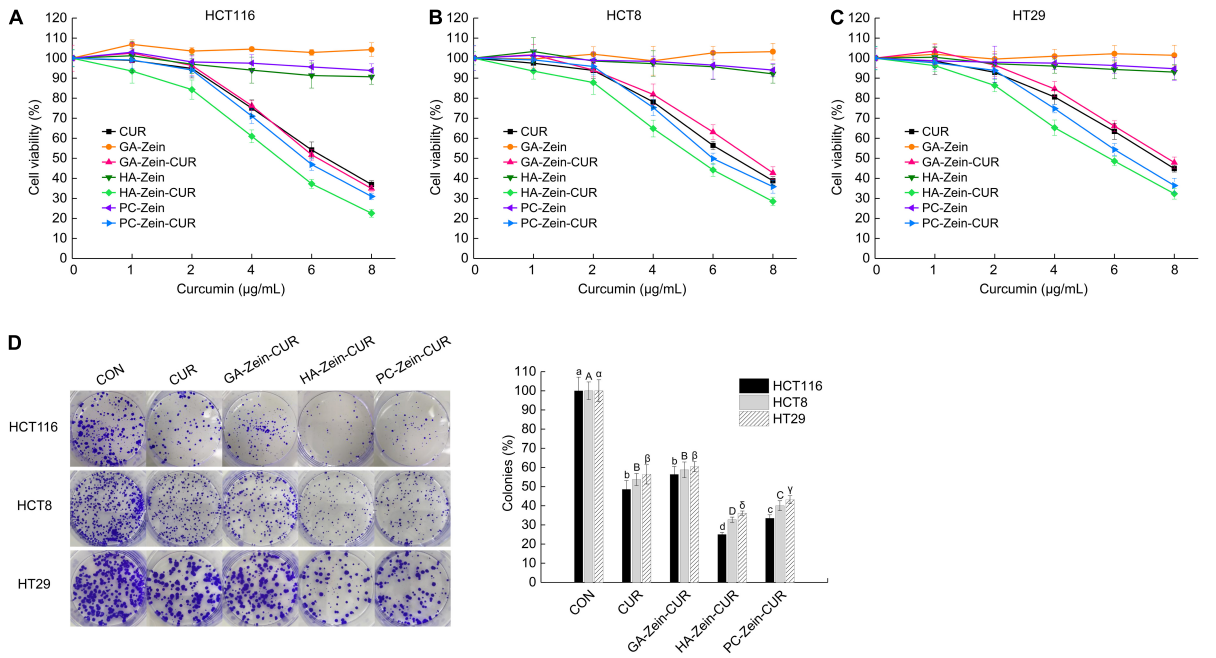

FIGURE 4 | Inhibitory effect of PS-Zein-CUR on CRC (HCT116, HCT8, and HT29) cell growth. Cells were treated with the indicated doses of CUR, PS-Zein, and PS-Zein-CUR for 48 h, respectively. **(A–C)** Cell viability measured by using a CCK-8 cell counting kit. **(D)** Left: images of colony formation assay; Right: quantitative analysis of colony formation expressed as percentage relative to vehicle control. Values are mean ± SD, $n = 3$. Bars marked with different letters indicate significant difference at $P < 0.05$.

nearly disappeared in the HA-Zein-CUR and PC-Zein-CUR. This might be attributed to the lower mass ratio of HA/PC to zein that led to a stronger shielding effect on the PS C-O-C groups.

Effect of Curcumin-Loaded Composite Nanoparticles on Human Colorectal Cancer Cells

The inhibitory effects of CUR, PS-Zein, and PS-Zein-CUR on the viability of human CRC cells were evaluated in HCT116, HCT8, and HT29 cell lines (**Figures 4A–C**). As expected, the blank PS-Zein did not show any significant inhibitory effect on CRC cell viability over the concentration range assayed. CUR and PS-Zein-CUR, on the other hand, all showed strong and dose-dependent growth inhibitory effects in the three cell lines. However, they did not seem to have any selective effect toward any of the three cell lines. As shown in **Table 2**, the order of their IC_{50} values in the three cell lines was CUR/GA-Zein-CUR > PC-Zein-CUR > HA-Zein-CUR, indicating significantly stronger cytotoxicity of HA-Zein-CUR than the other two formulations.

TABLE 2 | IC_{50} values of CUR and PS-Zein-CUR in HCT116, HCT8, and HT29 cells.

IC_{50} (μ_g/mL)	HCT116	HCT8	HT29
CUR	6.40 ± 0.68^{a}	6.73 ± 0.82^{A}	$7.55 \pm 1.12^{\alpha}$
GA-Zein-CUR	6.24 ± 0.59^{a}	$7.32 + 0.98^{A}$	$7.79 \pm 1.07^{\alpha}$
HA-Zein-CUR	4.61 ± 0.51^{b}	5.24 ± 0.63^{B}	$5.58 \pm 0.70^{\beta}$
PC-Zein-CUR	5.76 ± 0.54^{a}	6.19 ± 0.60^{AB}	$6.40 \pm 0.73^{\alpha}_^{\beta}$

Values are mean ± SD, n = 3. Different letters in the same column indicate significant difference at P < 0.05.

Based on the cell viability assay data, 4 μg/mL of CUR and PS-Zein-CUR (<IC_{50}) were selected to subsequently assess their inhibitory effect on colony formation of the CRC cells. The order of their inhibitory effect was HA-Zein-CUR > PC-Zein-CUR > CUR/GA-Zein-CUR (**Figure 4D**), which was consistent with the result of the cell viability assay. These data suggest that the encapsulation of CUR in PC-Zein and HA-Zein, but not GA-Zein, led to enhanced inhibitory effect on CRC cells. Considering the negligible cytotoxicity of the blank nanocarriers themselves toward the CRC cells, it was hypothesized that the differential inhibitory effects of CUR and the PS-Zein-CUR may be associated with their different cellular uptake efficiencies.

Results of the cellular uptake of CUR and PS-Zein-CUR are presented in **Figures 5A–C**. Compared with free CUR, PS-Zein-CUR did not promote (GA even decreased) the uptake or accumulation of CUR in the CRC cells after incubation for 4 h. However, after incubation for 24 h, HA-Zein-CUR significantly increased CUR content in HCT116, HCT8, and HT29 cells, and PC-Zein-CUR significantly increased it in HT29 cells, while GA-Zein-CUR did not result in any increase of CUR content in the three CRC cell lines. The different cellular uptake of CUR could be attributed to the time-dependent controlled release and internalization mechanisms of the PS-Zein-CUR, which depend on the inherent properties of the PS. The encapsulation of CUR in PS-Zein-CUR likely slowed down CUR degradation in the

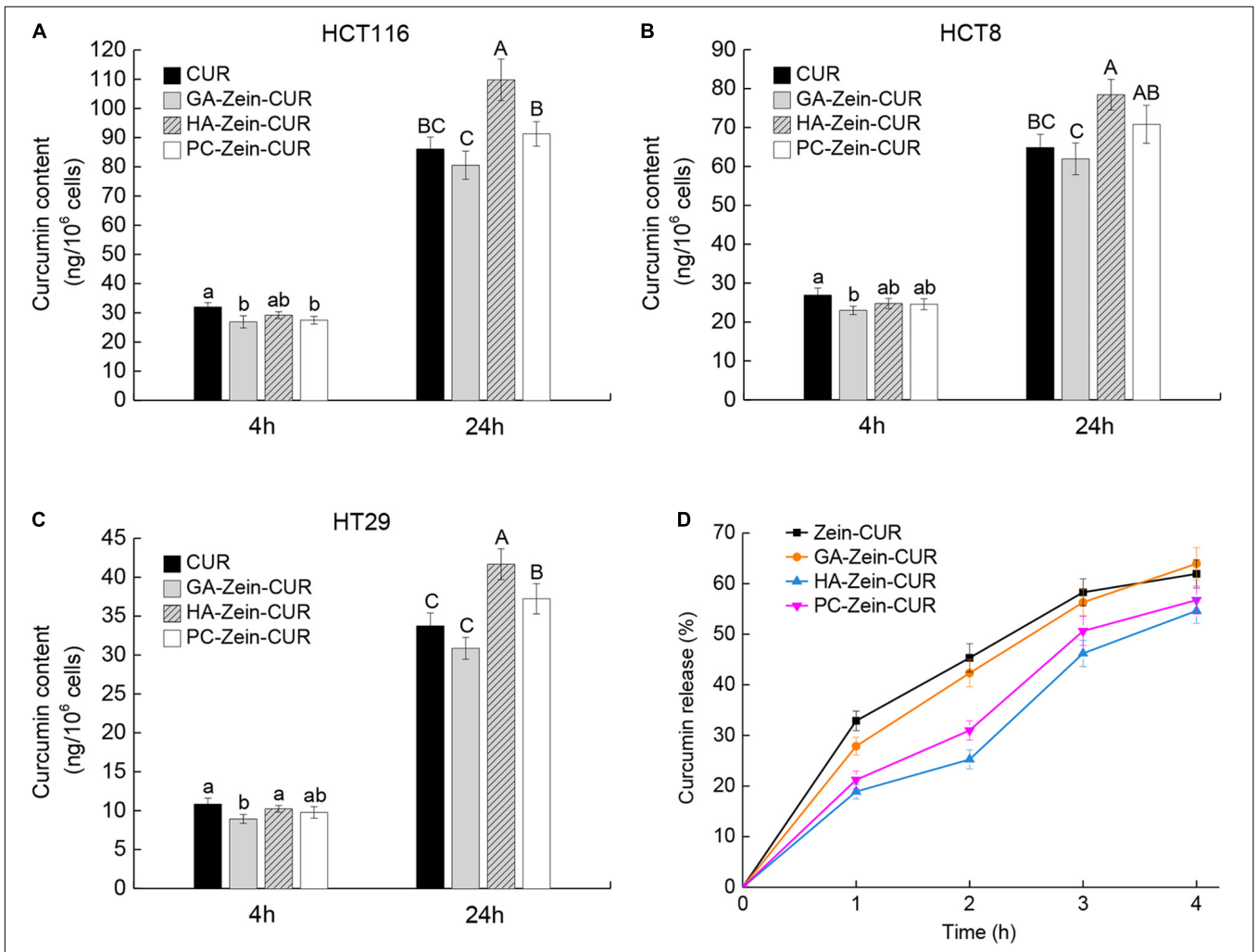

FIGURE 5 | Cellular uptake and simulated gastrointestinal digestion (SDIG) of PS-Zein-CUR. **(A–C)** CUR contents in CRC cells incubated, respectively with CUR and PS-Zein-CUR for 4 and 24 h. Values are mean ± SD, $n = 3$. Bars marked with different letters indicate significant difference at $P < 0.05$. **(D)** CUR release from Zein-CUR and PS-Zein-CUR during SDIG. Values are mean ± SD, $n = 3$.

culture medium (34). In addition, different from CUR, PS-Zein-CUR might enter the cells through endocytosis, which resulted in more efficient cellular uptake under the experimental conditions (35). In particular, specific ligand-receptor interactions between nanoparticles and cancer cells have been considered a promising strategy to enhance the cellular uptake of pharmaceuticals (36). HA has been reported to be capable of specifically interacting with certain proteins overexpressed in cancer cells, such as CD44, Rhamm, and TSG6, thus facilitating the targeting of HA-fabricated nanoparticles to cancer cells (37). Parashar et al. found that HA decorated poly caprolactone nanoparticles could increase the delivery efficiency of naringin to lung cancer cells by actively targeting the overexpressed CD44 (38).

Simulated GI Digestion of Curcumin-Loaded Nanoparticles

Prior to further evaluation of the pharmacokinetics of the CUR-loaded nanoparticles, their stability under simulated GI condition was assessed (**Figure 5D**). A high release rate (25.88%) of CUR from Zein-CUR was observed during the 1st h of the SGID. The release gradually slowed down toward later time points, reaching 61.93% at 4 h. GA-Zein-CUR exhibited similar release characteristics to Zein-CUR. In contrast, HA-Zein-CUR and PC-Zein-CUR had significantly lower release rates than Zein-CUR during the SGID. The much better CUR-retention capability of HA-Zein-CUR and PC-Zein-CUR (44.26 and 26.75% higher than Zein-CUR, respectively) could be attributed to the PS coating that protected zein from the hydrolytic action of pepsin (12). The difference in their release rates tended to get smaller in the intestinal digestion phase. This was mainly due to the accelerated release of CUR from HA-Zein-CUR and PC-Zein-CUR during 2–3 h upon transmit from the simulated gastric to intestinal condition, while the release rates of the other two formulations remained steady. These results indicate that HA-Zein-CUR and PC-Zein-CUR may help reduce the loss of CUR under gastric condition, and allow its controlled release during intestinal digestion.

Pharmacokinetics and Tissue Distribution of Free Curcumin and HA-Zein-CUR in Mice

Among the three PS-Zein-CUR, HA-Zein-CUR exhibited the best inhibitory effect and cellular uptake in the CRC cell lines. It also demonstrated better controlled release of CUR than GA- and PC-Zein-CUR during the SGID. These results support its good potential as an efficient oral delivery system for CUR in CRC treatment. Subsequently, a CRC (HCT116) xenograft model in nude mice was employed to further evaluate its pharmacokinetics (**Figure 6A** and **Table 3**). Following intragastric administration of HA-Zein-CUR, the plasma concentration of CUR increased gradually and reached 208.37 μg/L (C_{max}) at 4 h, which was threefold higher than that achieved with the administration of free CUR (76.73 ± 12.27 ng/g). T_{max} of free CUR was at 0.5 h. These data further supported the successful sustained-release behavior of HA-Zein-CUR, which was also consistent with the SGID data *in vitro*. Moreover, HA-Zein-CUR had a 1.70 times longer $t_{1/2}$ and 2.68 times longer mean residence time (MRT) than those of free CUR, indicating significantly slower systemic elimination of the former. The superior pharmacokinetic profile of CUR accomplished with HA-Zein-CUR when compared to that accomplished with free CUR was also reflected in the much higher (9.18 times) area under curve (AUC_{0-t}) of the former than the latter. In addition, according to the equation of a previous study (39), the relative bioavailability (RB) of HA-Zein-CUR compared to free CUR was calculated to be 10.18. This was higher than those of formulations such as MicroActive CUR (RB = 9.7) and Micronized CUR (RB = 9), which were reported to have significantly improved bioavailability over free CUR (40, 41). These data together therefore suggested that the formulation was able to substantially increase the oral bioavailability of CUR. Over the last decade, many formulations, such as liposomes, phytosomes, piperine complex, cyclodextrin inclusions and colloidal nanoparticles, have been developed to improve the bioavailability of CUR mainly *via* increasing its solubility and gastrointestinal stability (39). Compared with most

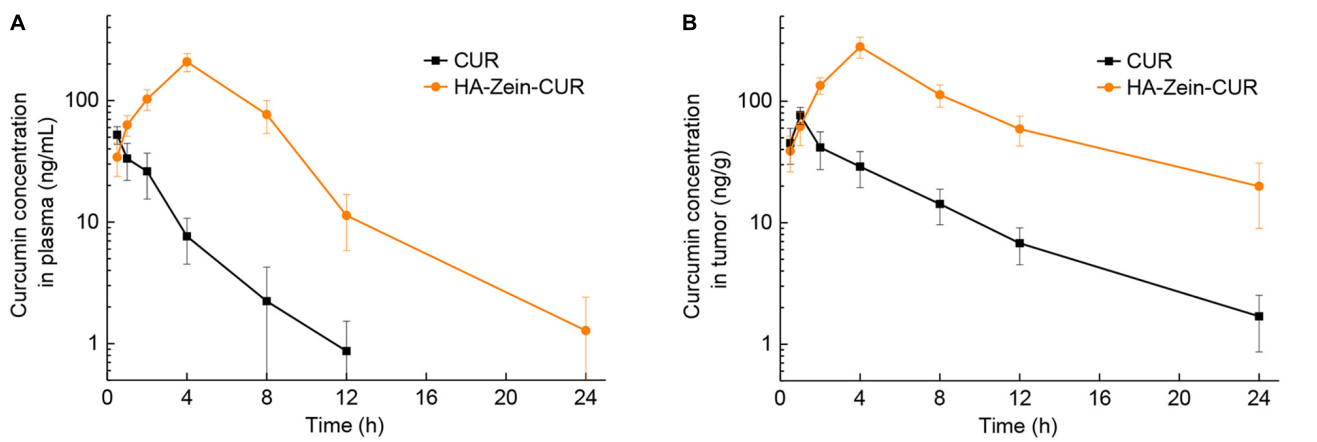

FIGURE 6 | Pharmacokinetics analysis of free CUR and HA-Zein-CUR in mice. **(A)** Plasma and **(B)** tumor concentration profiles of CUR in mice following intragastric administration of free CUR and HA-Zein-CUR, respectively. Values are mean ± SD, n = 3.

TABLE 3 | Pharmacokinetic parameters of free CUR and HA-Zein-CUR after intragastric administration in mice.

Parameter	CUR	HA-Zein-CUR
C_{max} (μg/L)	52.27 ± 8.66	208.37 ± 28.16
T_{max} (h)	0.50	4.00
$t_{1/2}$ (h)	2.07 ± 0.61	3.57 ± 0.94
MRT (h)	2.68 ± 0.43	5.92 ± 0.52
AUC_{0-t} (μg/L·h)	123.90 ± 8.32	1261.23 ± 75.24
AUC_{0-8} (μg/L·h)	126.50 ± 8.38	1281.35 ± 76.13
RB	1	10.18

Values are mean ± SD, n = 3. t of AUC_{0-t} is 24 h. RB, relative bioavailability.

existing formulations, our formulation was prepared using a simple antisolvent coprecipitation method and consisted of only natural macromolecules zein and HA, and thus had the advantage of easy preparation and high safety as an oral agent.

Having established the favorable pharmacokinetic behavior of the HA-Zein-CUR, we proceeded to examine its tissue distribution in the xenograft model. Compared to free CUR, intragastric administration of HA-Zein-CUR resulted in a significantly higher C_{max} of CUR in the tumors (280.33 ± 54.86 vs. 76.73 ± 12.27 ng/g) and a longer T_{max} (4 h vs. 1 h) (**Figure 6B**). A previous report also demonstrated that HA-Zein nanoparticles loaded with hydrophobic agents were capable of accumulating in colon carcinoma CT26 tumors although the test agent was given intravenously to the mice (42). Our data together with the literature therefore strongly support the favorable pharmacokinetic properties of the HA-Zein-CUR.

Measurement of the CUR levels in major organs after intragastric administration of HA-Zein-CUR or free CUR showed distinct delivery/accumulation of CUR between these two agents (**Figure 7**). For HA-Zein-CUR, C_{max} appeared at 4 h in all the organs assayed except colon. For free CUR, C_{max} occurred at more varied and earlier time points (0.5–2 h) in the different organs. It was also noted that the C_{max} values of both free CUR and HA-Zein-CUR in the colon were significantly higher than in other organs. Starting from the 2-h till the 24-h time point, HA-Zein-CUR exhibited much better delivery efficiency than free CUR. Remarkably, the C_{max} (7070.72 ± 1509.59 ng/g) in the colon achieved with HA-Zein-CUR was 6.19-fold higher than that achieved with free CUR. Even after 24 h, CUR concentration in the colon following administration of HA-Zein-CUR remained at 1101.44 ± 291.84 ng/g, which was 32.44-fold higher than that in the free CUR group. These data were also consistent with the time-course distribution analysis in the xenografts of the mice.

Curcumin has been reported to inhibit the proliferation of CRC cells *via* regulating multiple signaling pathways (43). Delivery of effective dosages to the tumor cells or target tissue *in vivo*, however, has remained a major challenge for the realization of the purported anticancer efficacy, and thus its application in clinical settings. The results from the pharmacokinetics and tissue distribution assay have provided strong evidence that the HA-Zein-CUR could deliver and sustain high levels of CUR in the subcutaneous CRC tumors. Its preferential distribution to the colon over other tissues/organs also indicates a promising therapeutic potential against orthotopic CRC tumors.

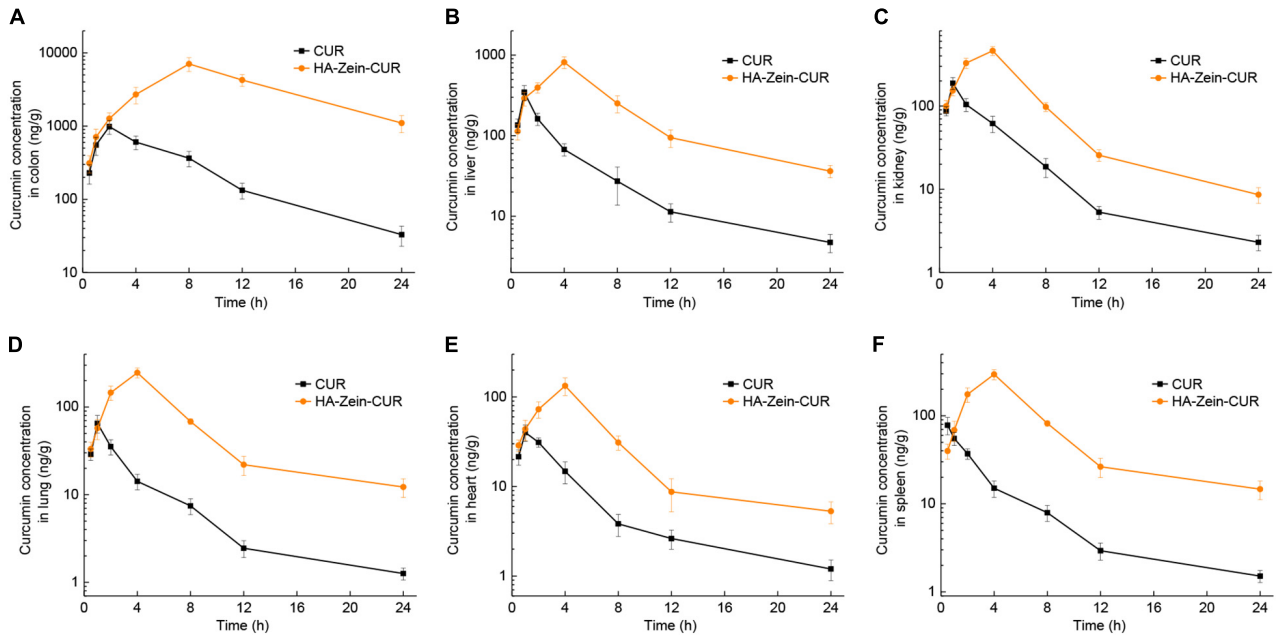

FIGURE 7 | Organ distribution of CUR in mice. Concentration profile of CUR in panel **(A)** colon, **(B)** liver, **(C)** kidney, **(D)** lung, **(E)** heart, and **(F)** spleen following intragastric administration of free CUR and HA-Zein-CUR, respectively. Values are mean ± SD, *n* = 3.

CONCLUSION

In conclusion, coating of Zein-CUR with GA, HA, and PC had significant and distinct effects on the physicochemical properties of the nanoparticles, including particle size, colloidal stability, EE, and LC. The controlled-release property and enhanced cellular uptake of the PS-Zein-CUR were translated into their significantly stronger activity against the growth of multiple CRC cell lines. Among them, HA-Zein-CUR was the most promising and its favorable pharmacokinetic behavior and distribution profile were further corroborated *in vivo*, in particular the multi-fold enhancement in its delivery to the tumors as well as the colon. The results from the SGID, cellular uptake, and pharmacokinetics and tissue distribution assays in the present study highlight that the HA-Zein-CUR represents a promising oral delivery system for further evaluation of the therapeutic value of CUR in diverse CRC models including subcutaneous xenograft and orthotopic models.

DATA AVAILABILITY STATEMENT

The raw data supporting the conclusions of this article will be made available by the authors, without undue reservation.

ETHICS STATEMENT

The animal study was reviewed and approved by the Animal Ethical and Welfare Committee of Shenzhen University.

AUTHOR CONTRIBUTIONS

LL and K-WC conceived and designed the experiments. LL and SY performed the experiments. LL, SY, and K-WC revised the manuscript. K-WC and FC acquired the funding and supervised the study. All authors contributed to the article and approved the submitted version.

FUNDING

This work was supported by the Guangdong Province Zhujiang Talent Program, China (No. 2019ZT08H476), the Shenzhen Science and Technology Program, China (No. KQTD20180412181334790), and the Innovation Team Project of Universities in Guangdong Province, China (No. 2020KCXTD023).

REFERENCES

1. Giordano A, Tommonaro G. Curcumin and cancer. *Nutrients.* (2019) 11:2376. doi: 10.3390/nu11102376
2. Howells LM, Iwuji COO, Irving GRB, Barber S, Walter H, Sidat Z, et al. Curcumin combined with FOLFOX chemotherapy is safe and tolerable in patients with metastatic colorectal cancer in a randomized Phase IIA trial. *J Nutr.* (2019) 149:1133–9. doi: 10.1093/jn/nxz029
3. Weng W, Goel A. Curcumin and colorectal cancer: an update and current perspective on this natural medicine. *Semin Cancer Biol.* (2020). (in press). doi: 10.1016/j.semcancer.2020.02.011
4. Ma Z, Wang N, He H, Tang X. Pharmaceutical strategies of improving oral systemic bioavailability of curcumin for clinical application. *J Control Release.* (2019) 316:359–80. doi: 10.1016/j.jconrel.2019.10.053
5. Holder GM, Plummer JL, Ryan AJ. The metabolism and excretion of curcumin (1,7-bis-(4-hydroxy-3-methoxyphenyl)-1,6-heptadiene-3,5-dione) in the rat. *Xenobiotica.* (1978) 8:761–8. doi: 10.3109/00498257809069589
6. Shoba G, Joy D, Joseph T, Majeed M, Rajendran R, Srinivas PSSR. Influence of piperine on the pharmacokinetics of curcumin in animals and human volunteers. *Planta Med.* (1998) 64:353–6. doi: 10.1055/s-2006-957450
7. Chen Y, Lu Y, Lee RJ, Xiang G. Nano encapsulated curcumin: and its potential for biomedical applications. *Int J Nanomed.* (2020) 15:3099–120. doi: 10.2147/ijn.S210320
8. Shen R, Lin D, Liu Z, Zhai H, Yang X. Fabrication of bacterial cellulose nanofibers/soy protein isolate colloidal particles for the stabilization of high internal phase pickering emulsions by anti-solvent precipitation and their application in the delivery of curcumin. *Front Nutr.* (2021) 8:734620. doi: 10.3389/fnut.2021.734620
9. Gaber M, Mabrouk MT, Freag MS, Khiste SK, Fang JY, Elkhodairy KA, et al. Protein-polysaccharide nanohybrids: hybridization techniques and drug delivery applications. *Eur J Pharm Biopharm.* (2018) 133:42–62. doi: 10.1016/j.ejpb.2018.10.001
10. Chen W, Ma S, Wang Q, McClements DJ, Liu X, Ngai T, et al. Fortification of edible films with bioactive agents: a review of their formation, properties, and application in food preservation. *Crit Rev Food Sci Nutr.* (2021):1–27. doi: 10.1080/10408398.2021.1881435
11. Wang Y, Padua GW. Nanoscale characterization of zein self-assembly. *Langmuir.* (2012) 28:2429–35. doi: 10.1021/la204204j
12. Tapia-Hernández JA, Rodríguez-Felix F, Juárez-Onofre JE, Ruiz-Cruz S, Robles-García MA, Borboa-Flores J, et al. Zein-polysaccharide nanoparticles as matrices for antioxidant compounds: a strategy for prevention of chronic degenerative diseases. *Food Res Int.* (2018) 111:451–71. doi: 10.1016/j.foodres.2018.05.036
13. Li M, Yu M. Development of a nanoparticle delivery system based on zein/polysaccharide complexes. *J Food Sci.* (2020) 85:4108–17. doi: 10.1111/1750-3841.15535
14. Chen S, Sun C, Wang Y, Han Y, Dai L, Abliz A, et al. Quercetagetin-loaded composite nanoparticles based on zein and hyaluronic acid: formation, characterization, and physicochemical stability. *J Agric Food Chem.* (2018) 66:7441–50. doi: 10.1021/acs.jafc.8b01046
15. Wei Y, Li C, Dai L, Zhang L, Liu J, Mao L, et al. The construction of resveratrol-loaded protein-polysaccharide-tea saponin complex nanoparticles for controlling physicochemical stability and in vitro digestion. *Food Funct.* (2020) 11:9973–83. doi: 10.1039/d0fo01741h
16. Liu F, Li R, Mao L, Gao Y. Ethanol-induced composite hydrogel based on propylene glycol alginate and zein: formation, characterization and application. *Food Chem.* (2018) 255:390–8. doi: 10.1016/j.foodchem.2018.02.072
17. Chen S, Han Y, Sun C, Dai L, Yang S, Wei Y, et al. Effect of molecular weight of hyaluronan on zein-based nanoparticles: fabrication, structural characterization and delivery of curcumin. *Carbohydr Polym.* (2018) 201:599–607. doi: 10.1016/j.carbpol.2018.08.116
18. Li J, Xu X, Chen Z, Wang T, Wang L, Zhong Q. Biological macromolecule delivery system fabricated using zein and gum arabic to control the release rate of encapsulated tocopherol during in vitro digestion. *Food Res Int.* (2018) 114:251–7. doi: 10.1016/j.foodres.2018.08.073
19. Huang X, Liu Y, Zou Y, Liang X, Peng Y, Mcclements DJ, et al. Encapsulation of resveratrol in zein/pectin core-shell nanoparticles: stability, bioaccessibility, and antioxidant capacity after simulated gastrointestinal digestion. *Food Hydrocoll.* (2019) 93:261–9. doi: 10.1016/j.foodhyd.2019.02.039
20. Brodkorb A, Egger L, Alminger M, Alvito P, Assunção R, Ballance S, et al. INFOGEST static in vitro simulation of gastrointestinal food digestion. *Nat Protoc.* (2019) 14:991–1014. doi: 10.1038/s41596-018-0119-1

21. Sun C, Dai L, Gao Y. Interaction and formation mechanism of binary complex between zein and propylene glycol alginate. *Carbohydr Polym.* (2017) 157:1638–49. doi: 10.1016/j.carbpol.2016.11.046
22. Song J, Sun C, Zhang J, Xiong Z, Fang Y. Fabrication, characterization, and formation mechanism of zein-gum arabic nanocomposites in aqueous ethanol solution with a high ethanol content. *J Agric Food Chem.* (2020) 68:13138–45. doi: 10.1021/acs.jafc.9b08179
23. Kumar V. Stability studies on nanomaterials used in drugs". In: Simon H editor. *Characterization and Biology of Nanomaterials for Drug Delivery*. London: Matthew Dean Press (2019). p. 425–44. doi: 10.1016/b978-0-12-814031-4.00015-5
24. Ren X, Hou T, Liang Q, Zhang X, Hu D, Xu B, et al. Effects of frequency ultrasound on the properties of zein-chitosan complex coacervation for resveratrol encapsulation. *Food Chem.* (2019) 279:223–30. doi: 10.1016/j.foodchem.2018.11.025
25. KjØNiksen AL, Hiorth M, Bo N. Association under shear flow in aqueous solutions of pectin. *Eur Polym J.* (2005) 41:761–70. doi: 10.1016/j.eurpolymj.2004.11.006
26. Tu L, Wu L, Zhang H, You W. A study on the nature of intermolecular links in the cryotropic weak gels of hyaluronan. *Carbohydr Polym.* (2012) 87:2076–85. doi: 10.1016/j.carbpol.2011.10.029
27. Hu K, Huang X, Gao Y, Huang X, Xiao H, McClements DJ. Core-shell biopolymer nanoparticle delivery systems: synthesis and characterization of curcumin fortified zein-pectin nanoparticles. *Food Chem.* (2015) 182:275–81. doi: 10.1016/j.foodchem.2015.03.009
28. Zhang D, Jiang F, Ling J, Ouyang XK, Wang YG. Delivery of curcumin using a zein-xanthan gum nanocomplex: fabrication, characterization, and in vitro release properties. *Colloids Surf B Biointerf.* (2021) 204:111827. doi: 10.1016/j.colsurfb.2021.111827
29. Hansen PE, Spanget-Larsen J. NMR and IR investigations of strong intramolecular hydrogen bonds. *Molecules.* (2017) 22:552. doi: 10.3390/molecules22040552
30. Chen S, Ma X, Han Y, Wei Y, Guo Q, Yang S, et al. Effect of chitosan molecular weight on zein-chitosan nanocomplexes: formation, characterization, and the delivery of quercetagetin. *Int J Biol Macromol.* (2020) 164:2215–23. doi: 10.1016/j.ijbiomac.2020.07.245
31. Wang Y, Padua GW. Formation of zein microphases in ethanol-water. *Langmuir.* (2010) 26:12897–901. doi: 10.1021/la101688v
32. Wang X, Fan M. Interaction behaviors and structural characteristics of zein/NaTC nanoparticles. *RSC Adv.* (2019) 9:5748–55. doi: 10.1039/C9RA00005D
33. Seok HY, Sanoj Rejinold N, Lekshmi KM, Cherukula K, Park IK, Kim YC. CD44 targeting biocompatible and biodegradable hyaluronic acid cross-linked zein nanogels for curcumin delivery to cancer cells: in vitro and in vivo evaluation. *J Control Release.* (2018) 280:20–30. doi: 10.1016/j.jconrel.2018.04.050
34. Wang YJ, Pan MH, Cheng AL, Lin LI, Lin JK. Stability of curcumin in buffer solutions and characterization of its degradation products. *J Pharm Biomed Anal.* (1997) 15:1867–76. doi: 10.1016/s0731-7085(96)02024-9
35. Pricci M, Girardi B, Giorgio F, Losurdo G, Ierardi E, Di Leo A. Curcumin and colorectal cancer: from basic to clinical evidences. *Int J Mol Sci.* (2020) 21:236421. doi: 10.3390/ijms21072364
36. Wang DD, Zhang XN. Advances in receptor modulation strategies for flexible, efficient, and enhanced antitumor efficacy. *J Control Release.* (2021) 333:418–47. doi: 10.1016/j.jconrel.2021.03.045
37. Zhang H, Huang S, Yang X, Zhai G. Current research on hyaluronic acid-drug bioconjugates. *Eur J Med Chem.* (2014) 86:310–7. doi: 10.1016/j.ejmech.2014.08.067
38. Parashar P, Rathor M, Dwivedi M, Saraf SA. Hyaluronic acid decorated naringenin nanoparticles: appraisal of chemopreventive and curative potential for lung cancer. *Pharmaceutics.* (2018) 10:33. doi: 10.3390/pharmaceutics10010033
39. Jamwal R. Bioavailable curcumin formulations: a review of pharmacokinetic studies in healthy volunteers. *J Integr Med.* (2018) 16:367–74. doi: 10.1016/j.joim.2018.07.001
40. Madhavi D, Kagan D. Bioavailability of a sustained release formulation of curcumin. *Integr Med.* (2014) 13:24–30.
41. Schiborr C, Kocher A, Behnam D, Jandasek J, Toelstede S, Frank J. The oral bioavailability of curcumin from micronized powder and liquid micelles is significantly increased in healthy humans and differs between sexes. *Mol Nutr Food Res.* (2014) 58:516–27. doi: 10.1002/mnfr.201300724
42. Seok H-Y, Rejinold NS, Lekshmi KM, Cherukula K, Park I-K, Kim Y-C. CD44 targeting biocompatible and biodegradable hyaluronic acid cross-linked zein nanogels for curcumin delivery to cancer cells: in vitro and in vivo evaluation. *J Control Release.* (2018) 280:20–30. doi: 10.1016/j.jconrel.2018.04.050
43. Ismail NI, Othman I, Abas F, Lajis NH, Naidu R. Mechanism of apoptosis induced by curcumin in colorectal cancer. *Int J Mol Sci.* (2019) 20:2454. doi: 10.3390/ijms20102454

Conflict of Interest: The authors declare that the research was conducted in the absence of any commercial or financial relationships that could be construed as a potential conflict of interest.

The reviewer RF declared a shared affiliation with one of the author LL at the time of the review.

Publisher's Note: All claims expressed in this article are solely those of the authors and do not necessarily represent those of their affiliated organizations, or those of the publisher, the editors and the reviewers. Any product that may be evaluated in this article, or claim that may be made by its manufacturer, is not guaranteed or endorsed by the publisher.

Copyright © 2022 Liu, Yang, Chen and Cheng. This is an open-access article distributed under the terms of the Creative Commons Attribution License (CC BY). The use, distribution or reproduction in other forums is permitted, provided the original author(s) and the copyright owner(s) are credited and that the original publication in this journal is cited, in accordance with accepted academic practice. No use, distribution or reproduction is permitted which does not comply with these terms.

frontiers in Nutrition

METHODS
published: 03 March 2022
doi: 10.3389/fnut.2022.848294

Determination of Tropomyosin in Shrimp and Crab by Liquid Chromatography–Tandem Mass Spectrometry Based on Immunoaffinity Purification

Sufang Fan[1†], Junmei Ma[1,2†], Chunsheng Li[3], Yanbo Wang[4], Wen Zeng[5], Qiang Li[1], Jinru Zhou[4], Liming Wang[1], Yi Wang[5] and Yan Zhang[1,2*]*

[1] Hebei Food Safety Key Laboratory, Key Laboratory of Special Food Supervision Technology for State Market Regulation, Hebei Food Inspection and Research Institute, Shijiazhuang, China, [2] Hebei Key Laboratory of Forensic Medicine, College of Forensic Medicine, Hebei Medical University, Shijiazhuang, China, [3] Biology Institute of Hebei Academy of Science, Shijiazhuang, China, [4] School of Food Science and Biotechnology, Zhejiang Gongshang University, Hangzhou, China, [5] Department of Chemical Engineering, Key Laboratory for Industrial Biocatalysis, Ministry of Education of China, Tsinghua University, Beijing, China

OPEN ACCESS

Edited by:
Biao Yuan,
China Pharmaceutical University, China

Reviewed by:
Xizhi Shi,
Ningbo University, China
Wentong Xue,
China Agricultural University, China

***Correspondence:**
Yan Zhang
snowwinglv@126.com
Yi Wang
wangyi671@mail.tsinghua.edu.cn

[†] These authors have contributed equally to this work and share first authorship

Specialty section:
This article was submitted to Food Chemistry, a section of the journal Frontiers in Nutrition

Received: 04 January 2022
Accepted: 02 February 2022
Published: 03 March 2022

Citation:
Fan S, Ma J, Li C, Wang Y, Zeng W, Li Q, Zhou J, Wang L, Wang Y and Zhang Y (2022) Determination of Tropomyosin in Shrimp and Crab by Liquid Chromatography–Tandem Mass Spectrometry Based on Immunoaffinity Purification. Front. Nutr. 9:848294. doi: 10.3389/fnut.2022.848294

A UPLC-MS/MS method was developed for the detection of tropomyosin (TM) in shrimp and crab. After simple extraction, the samples were purified by immunoaffinity column and then digested by trypsin. The obtained sample was separated by Easy-nLC 1000-Q Exactive. The obtained spectrums were analyzed by Thermo Proteome Discoverer 1.4 software and then ANIQLVEK with high sensitivity was selected as the quantitative signature peptide. Isotope-labeled internal standard was used in the quantitative analysis. The method showed good linearity in the range of 5–5,000 μg/L with a limit of quantification (LOQ) of 0.1 mg/kg. The average recoveries were 77.22–95.66% with RSDs ≤ 9.97%, and the matrix effects were between 88.53 and 112.60%. This method could be used for rapid screening and quantitative analysis of TM in shrimp and crab. Thus, it could provide technical support for self-testing of TM by food manufacturers and promote further improvement of allergen labeling in China.

Keywords: liquid chromatography-tandem mass spectrometry, tropomyosin, immunoaffinity purification, isotope-label, signature peptide

INTRODUCTION

Food allergy is an immunoglobulin E-mediated response to food protein, which can lead to anaphylaxis, a life-threatening reaction (1). More and more researchers are paying attention to food allergies for their lethal effects on allergic consumers (2, 3). It is reported that 5% of adults and 8% of young children suffer from food allergies, while more than 90% of food allergies are caused by milk, peanuts, eggs, soybeans, wheat, nuts, fish, and crustaceans (4–9). At the very top of the list of food allergens, shellfish is commonly identified as a cause of food hypersensitivity toward sensitized individuals (10). Allergy to crustacean aquatic products such as shrimp and crab can lead to allergic symptoms such as skin redness and swelling, asthma, and rhinitis, which is accompanied by collapse, shock, and can even be life-threatening, which seriously affects the health and quality of life of allergic people. Shellfish is responsible for approximately 16.1% of all food allergy cases (11, 12). The

allergen protein tropomyosin (TM) is a cross reacting allergen among crustaceans and has been shown to be the main allergen in species like shrimp, lobster, crab, and Antarctic krill (13, 14). Studies have shown that the sequence of TM is highly conserved in different shellfish species, that is, there are great similarities in the amino acid sequence of TM in different shrimp and crabs, and there are common epitopes in TM of different crustacean aquatic products (10, 15).

Current analytical methods have been used to determine TM in shellfish products, including enzyme-linked immunosorbent assay (ELISA) (16), quantum-dot-based fluorescent lateral flow immunoassay (LFIA) (17), real-time polymerase reaction (PCR) (18), surface plasmon resonance (SPR) sensor (10), fluorometric sandwich biosensor (12), and aptameric biosensor (19, 20). In recent years, mass spectrometry has been successfully used in the detection of allergens in food due to its high sensitivity and accuracy (21–23), particularly, high-performance liquid chromatography or nanoliquid chromatography–tandem mass spectrometry has been used to determine the intact protein or signature peptides after protein digestion (24, 25).

This experiment was designed to solve the problem of difficult detection of TM in shrimp and crab samples. For the first time, the antibody of TM was obtained and filled to the immunoaffinity column, which was used in the purification of TM. In this study, TM was extracted and purified. The antibody of TM was obtained by immunization, and the immune affinity column of TM was prepared. After simple extraction, the samples were purified by immunoaffinity column and then digested by trypsin. The obtained samples were injected into nanoliquid chromatography–quadrupole/electrostatic field orbitrap high-resolution mass spectrometer for analysis, and the characteristic peptides of TM were obtained after spectrum database retrieval. A liquid chromatography–tandem mass spectrometry method was established with the synthesized characteristic TM peptides as the standard, and the linear relationship, detection limit, method recovery, and other parameters of the established method were verified and applied to the actual sample detection so as to provide technical support for the accurate quantification of TM in shrimp and crab products.

MATERIALS AND METHODS

Chemicals and Reagents

Ammonium bicarbonate (NH_4HCO_3), dithiothreitol (DTT), and iodoacetamide (IAA) were supplied by Sigma-Aldrich (St. Louis, MO, USA). TM was prepared and purified in the laboratory. HPLC grade acetonitrile and formic acid were purchased from Merck (Darmstadt, Germany). Tryptase was got from AB Sciex. Distilled water (Watsons, Hong Kong, China) was used in the experiment. Two signature peptides and the internal standard of ANIQLVEK, IVELEEELR, and ANIQL ($^{13}C_6$,^{15}N)VEK were synthesized by Qiangyao Biotechnology Company (Shanghai, China). The purity of all the synthetic peptides was higher than 98%.

HAT, HT, Freund's complete adjuvant, Freund's incomplete adjuvant, PEG4000, and immunoglobulin subtype kit were purchased from Sigma; cell culture plate and DMEM medium were purchased from GIBCO company; HRP-labeled sheep anti-mouse IgG was purchased from Beijing ZhongShan Gold Bridge Biotechnology Limited Company (Beijing, China). Bovine serum albumen (BSA), ovalbumin (OVA), and fetal bovine serum were supplied by Shanghai Shenggong; caprylic acid and ammonium sulfate with analytical grade were obtained from Komil Chemical Reagent Limited Company (Tianjin, China). BALB/c mice aged 6 to 9 weeks were purchased from the Laboratory Animal Center of Hebei Medical University.

Instruments

Low protein adsorption sample bottles were supplied by Waters. Triple Quad 6500$^+$ liquid chromatography–tandem mass spectrometry equipped with MultiQuant 3.0.1 data processing system (AB Sciex, USA) was used for allergen quantification analysis. Orbitrap Fusion equipped with a nanoliquid chromatography system (Easy-nLC 1000) (Thermo Scientific, USA) was adopted for allergen identification.

Carbon dioxide incubator (Sanyo Company, Japan), purification table (Suzhou Purification Equipment limited company, China), inverted microscope (Olympus, Japan), electronic analytical balance (Mettler, Switzerland), liquid nitrogen tank (Chengdu Jinfeng Liquid Nitrogen Container limited company, China), high-speed refrigerated centrifuge (Beckman, Germany), electric thermostatic water bath (Shanghai Jinghong Equipment limited company, China), microplate reader (Bio-Tek, USA), vortex mixer (Shanghai Medical University Instrument Factory, China), and ultramicro nucleic acid protein tester (Thermo, USA) were used in our experiment.

Preparation of Standard Storage Solution

Proper amount of ANIQLVEK, IVELEEELR, and ANIQL ($^{13}C_6$,^{15}N)VEK were accurately weighed and dissolved in water to 10 ml, and 100 μmol/L mixed standard storage solution was prepared. An appropriate amount of TM was weighed and dissolved in a 10 ml volumetric flask, dissolving it in water to a constant volume, and then 100 μmol/L TM standard storage solution was made.

Purification of TM

Preparation of Acetone Powder

TM was extracted according to the method reported elsewhere (12). The head, tail, and shrimp lines of the white prawns were removed and buffer A (50 mmol/L KCl and 2 mmol/L $NaHCO_3$) was added at the ratio of 1:10 (g/ml). The samples were extracted at 4°C for 20 min, centrifuged at 4°C for 10,000 r/min for 20 min, and the precipitates were obtained. The precipitate was resuspended in buffer A of 10 times volume, centrifuged at 4°C for 10,000 r/min for 20 min, and the precipitates were obtained. The above steps were repeated five times. The precipitates were thoroughly washed with precooled acetone until they were colorless, filtered with six layers of gauze, and dried at room temperature. Impurities such as fat and fat-soluble pigment were removed and shrimp acetone powder was obtained.

Purification of TM

As described in the literature (12), 1 g acetone powder was weighed and dissolved in buffer B (0.02 mol/L Tris-HCl, 1 mol/L KCl, and 0.1 mmol/L DTT, pH 7.5) with a solid–liquid ratio of 1:5 (g/ml) and extracted for 72 h. The extract was filtered with six layers of gauze and the filtrate was obtained, which was heated for 20 min, centrifuged at 4°C for 10,000 r/min for 20 min after which the supernatant was obtained. Then 30% ammonium sulfate solution was added slowly, placed at 4°C for 1 h, centrifuged at 4°C for 10,000 r/min for 20 min, and the precipitates were got. Then 1 mol/L PBS was used to redissolve it, and 1 mol/L HCl solution was used to adjust the pH to 4.6. Precipitates were got after centrifugation at 4°C for 8,000 r/min for 10 min and PBS was used as the reconstitution solution. The protein content of the complex solution was determined by the BCA method.

Preparation and Identification of the Monoclonal Antibody

Three female BALB/c mice aged 6–8 weeks were selected for the antibody preparation. TM was diluted with normal saline and injected into the neck and back with an equal volume of Freund's complete adjuvant. The immunization was enhanced every 2 weeks. Freund's incomplete adjuvant of equal volume was added for the second and third immunization. Blood samples were collected after 7–10 days for the third immunization sessions, and indirect ELISA was used to detect the serum antibody titer.

SP2/0 myeloma was fused with spleen cells as described by Yang et al. (26). High-specificity and stable monoclonal cell strains against TM were repeatedly screened out by confirmation detections. The cell strains were cultured to achieve a certain quantity and then injected into atoleine-pretreated BALB/c mice to produce ascites fluids. The ascites fluids were purified according to the octanoic acid–ammonium sulfate method. The TM antibody was freeze-dried and stored at −20°C, and the antibody was thawed and diluted with PBS prior to use. All animal experiments were carried out according to the guidelines of the National Institutes of Health for Care and Use of Laboratory Animals and was approved by the Animal Ethical and Welfare Review Committee of Hebei Food Inspection and Research Institute.

The antibody subtypes were determined using Sigma's immunoglobulin subtype kit. Extract of shrimps, Argentine red shrimps, *Penaeus vannameri*, and bread crab were respectively coated and used to determine the crossreaction of monoclonal antibody by indirect ELISA. The ELISA procedure was as follows: appropriately diluted antigen with a concentration of 5 μg/ml was added to a 96-well ELISA plate (100μl/well) and coated overnight at 4°C, where carbonate buffer was used as the coating solution. After three washings, the wells were blocked with phosphate-buffered saline (PBS) containing 10% gelatin (300 μl/well) at 37°C for 2 h. After washing, 100 μl of the sample extract was added, and the plates were incubated at 37°C for 45 min. Blank control well (PBS) and negative well (negative serum) were set. After washing, 300 μl of 1:10,000 diluted HRP enzyme-labeled goat anti-mouse IgG was added to each well and placed at 37°C for 30 min. After washing, 100 μl of substrate-developing solution was added to each well and reacted at 37°C for 15 min away from light. The A450nm value was measured after the reaction was terminated by the stop buffer.

Preparation of Immunoaffinity Column

Refer to the instructions of CNBr-activated Sepharose 4B gel, and some modifications were made.

The first step is washing. A total of 2 g CNBr activated Sepharose 4B dry gel was suspended in 20 ml 1 mmol/L HCl to swell, and then the swollen gel was washed with 200 ml 1 mmol/L HCl and fully washed with 200 ml reaction buffer (0.1 mol/L $NaHCO_3$ pH 8.1).

The second step is coupling. The pretreated gel was quickly transferred to 10 ml of 2.7 mg/ml TM-antibody coupling buffer (0.1 mol/L$NaHCO_3$, 0.5 mol/L NaCl, pH 8.3), stirring overnight at 4°C with the purpose of conjugating TM monoclonal antibody to CNBr-activated Sepharose 4B adequately. The uncoupled antibodies were washed off with a coupling buffer of more than five times the volume of gel and all the eluents were collected. The content of uncoupled proteins in the eluent was determined by ultraviolet spectrophotometer, and the coupling rate was calculated.

The conjugation rate = 1-leached monoclonal antibodies/the added monoclonal antibodies. In the experiment, the conjugation rate between TM antibody and gel was 97.6%.

The third step is washing, where five times of the volume of 0.1 mol/L acetic acid buffer (pH 4.0, containing 0.5 mol/L NaCl) and 0.1 mol/L Tris-HCl (pH 8.0, containing 0.5 mol/L NaCl) were used to alternately wash the gel 4–6 times successively.

The last step is to install the column, where 1 ml column was used to prepare the immunoaffinity column and a sieve was placed into the column. PBS buffer solution (0.01 mol/L pH 7.4) was suspended and the coupling glue was loaded into the column until the glue height was 0.5 ml. PBS was balanced and the bottom of the mouth was sealed and stored in the refrigerator at 4°C.

Chromatographic and Mass Spectrometry Conditions

Easy-nLC 1000-Orbitrap Fusion Conditions

Allergen identification was carried out using Orbitrap Fusion high resolution mass spectrometery system equipped with a nanoliquid chromatography system (Easy-nLC 1000). Precolumn (C_{18}, 5 μm, 120A, 100 μm × 4 cm) and analytical column (C_{18}, 5 μm, 120A, 75 μm × 15 cm) were supplied by Beijing Lerunfeng Technology Co. LTD. Injection volume was 2 μl, the flow rate of the sample pickup was 20 μl/min, and the volume of sample loading was 20 μl. Mobile phase A was water with 0.1% formic acid and mobile phase B was acetonitrile. Precolumn equilibration was conducted by 8 μl mobile phase A and analytical column equilibration was carried out by 6 μl mobile phase A. Gradient elution was adopted, the elution program was set up with a linear gradient from 3% B to 7% B in 3 min, gradient to 22% B in 38 min, gradient to 35% in 48 min, ramped to 90% B in 50 min, then held at 90% B for 10 min, and the flow rate was 300 nl/min. It takes 70 min to complete one analysis.

All data were acquired in full-MS and data-dependent scan ($ddMS^2$) mode under the electrospray positive ion mode. Full MS conditions were set as follows: resolution, 1,20,000; AGC target was set as 2e5; and scan range was 350–1,500 m/z. $dd-MS^2$ conditions were set as follows: isolation mode was set as quadrupole; activation type was set as HCD; resolution, 15,000; and AGC target was set as 5.0e4. Isolate window was 1.6 m/z, fixed first mass was 100.0 m/z, and HCD collision energy was set as 30%.

Triple Quad 6500$^+$ Conditions

A Triple Quad 6500$^+$ liquid chromatography–tandem mass spectrometry was used for allergen quantification. A LC-30AD UPLC system equipped with binary solvent manager, sample manager, and column manager was adopted for the tryptic peptides separation (Shimadzu, Japan). The column was XBridge BEH C_{18} (2.5 μm, 2.1 mm × 100 mm, Waters). Then 0.1% formic acid (mobile A) and acetonitrile (mobile B) were used as mobile phase with a flow rate of 0.3 ml/min, the column temperature was set at 40°C, and the injection volume was 1 μl. Mobile phase B was maintained at 2% in the initial 1.0 min, linear gradient from 2 to 65% in 7.0 min, and then held at 65% for 2.0 min, returned back to 2% B in 0.01 min, and equilibrated at 2% B for 2.0 min.

The ESI source was used in data acquisition of the Triple Quad 6500$^+$ MS and multiple reaction monitoring (MRM) was used as scan mode. The capillary voltage was set as 5.5 kV, the pressure of atomizer (GS1) was set as 50 psi, the pressure of auxiliary gas (GS2) was set as 55 psi, the pressure of curtain gas was 30 psi, and the temperature of ion source (TEM) was 500°C.

Data Analysis

Raw data obtained from Orbitrap Fusion was analyzed by the software Thermo Proteome Discoverer 1.4, and the relative parameters were set as follows: MS1 precursor was adopted in precursor selection; minimum precursor mass was set as 350 Da; maximum precursor mass was set as 5,000 Da; the minimum peak count was 1; protein database, shrimp database, and crab database were downloaded from Uniprot (http://www.uniprot.org); trypsin was used in enzymatic hydrolysis; maximum missed cleavage site was set as 2; minimum peptide length was 6; maximum peptide length was set as 144; the precursor mass tolerance was 10 ppm; fragment mass tolerance was 0.02 Da; oxidation (+15.995 Da) was selected in dynamic modification; and carbamidomethyl (+57.021 Da) was chosen in static modification.

Sample Extraction and Purification

Solid samples were finely ground before extraction as reported before (27). Then 0.1 g of the homogenized sample was weighed, 10 ml distilled water was added, the sample was shaken for 1 h, and centrifuged for 10 min with 9,500 g. Then 3 ml extract was taken for subsequent purification treatment.

The immunoaffinity column was taken out and the plug was removed to allow the liquid to flow out by gravity. A total of 10 ml phosphate buffer was used to balance the immunoaffinity column when the fluid in the column was no longer dripping. A total of 3 ml extract was sampled after the phosphate buffer was close to the sieve plate. Then 10 ml phosphate buffer (PH 7.4) was added to wash the impurities in the affinity column after the level of the sample liquid entered the affinity column. After the level of the sample liquid entered the affinity column, 10 ml phosphate buffer (PH 7.4) was added to wash the impurities in the affinity column.

After leaching, phosphate buffer was removed clearly with washing ears ball or cylinder. A total of 2.7 ml elution buffer (0.1 M of glycine buffer, pH 2.5) was added as the eluent solution by gravity flow rate drop out and the flow rate should be less than one drop each second. After all the liquid falls into the sieve plate, the eluent in the column was brought out by the ear ball or needle. A total 300 μl neutralization buffer (1 M Tris, pH 9.0) was added to the eluent, quickly mixed with the liquid collected in the test tube for subsequent enzymatic hydrolysis treatment.

Enzymatic Digestion

Enzymatic digestion was conducted according to literature report (21). An aliquot of 500 μl sample solution was spiked with 25 μl of 25 nM stable isotope-labeled internal standard solution and then mixed with 10 μl of 500 mM DTT solution in a 60°C water bath for 30 min. An alkylation was performed with the addition of 30 μl 500 mM IAA solution at room temperature for 30 min in the dark. Thereafter, 100 μl 500 mM NH_4HCO_3 solution and 40 μl of 250 μg/ml trypsin were added and incubated overnight at 37°C in a water bath vibrator. Then, 20 μl 0.1% formic acid was added to terminate the digestion and 275 μl pure water was added to fill the volume to 1 ml. The sample was centrifuged at 14,000 g at room temperature for 20 min and the supernatant solution was collected for determination.

Statistical Analysis

The statistical significance was analyzed through one-way analysis of variance by IBM SPSS Statistics 26. All experiments were performed at least three times.

RESULTS AND DISCUSSION

Antibody Production and Characterization

The characteristics of the TM antibody were evaluated by indirect competition ELISA (28, 29). The serum titers of immunized mice were more than 1:4,00,000. Seven cell lines of anti-shrimp TM monoclonal antibody were screened, which were named as 1H1, 2C1, 2H11, 2F12, 3B2, 3H11, and 4B9, respectively. The protein concentration was measured by ultrafine nucleic acid protein analyzer and the titer was determined by indirect ELISA. The results showed that 2H11 had the highest titer, which was 1:1 million, the titer of 1H11, 3H11, and 4B9 was more than 1:250 000, and the titer of 2C1, 2F12, and 3B2 was more than 1:30 000. 2H11 was selected in the preparation of the subsequent immunoaffinity column.

The extracts of base shrimp, Argentine red shrimp, *P. vannamei*, and bread crab (labeled TMJ, TMA, TMN, TMM, respectively) and TM, 2H11 was diluted at 1:200, 1:50000, and 1:200000 times, respectively, and indirect ELISA was used to detect the crossreaction rate. The crossreaction rate was calculated by A450nm (sample)/A450nm (TM) × dilution ratio. The results were shown in **Table 1**. When the dilution factor

TABLE 1 | The results of crossreaction of antibody 1H11 with four analogs ($n = 3$).

Cross reactant	Dilution factor was 200		Dilution factor was 50,000		Dilution factor was 200,000	
	A_{450nm}	Cross reaction rate (%)	A_{450nm}	Cross reaction rate (%)	A_{450nm}	Cross reaction rate (%)
TM	2.706 ± 0.0096	100	2.607 ± 0.0076	100	1.560 ± 0.0038	100
TMJ	2.581 ± 0.0020	95.4 ± 0.223	2.020 ± 0.0062	77.5 ± 0.255	0.830 ± 0.0025	53.2 ± 0.083
TMA	2.454 ± 0.0098	90.7 ± 0.178	1.023 ± 0.010	39.2 ± 0.287	0.395 ± 0.0076	25.3 ± 0.425
TMN	2.488 ± 0.0080	91.9 ± 0.501	0.460 ± 0.0022	17.6 ± 0.0607	0.145 ± 0.0060	9.3 ± 0.364
TMM	2.342 ± 0.0040	86.5 ± 0.355	0.406 ± 0.0051	15.6 ± 0.234	0.123 ± 0.0050	7.9 ± 0.307

The results indicate with "mean ± SD".

TABLE 2 | The results of column capacity test with different sample loading quantity.

Sample loading quantity (μg)	40	50	60	80	100
Recovery (%)	95.8	96.3	96.5	95.2	79.1

was 200, the crossreaction rates were higher than 86.5%; when the dilution factor was 50,000, the crossreaction rate of TMJ and TMA was 77.5%, 39.2%, respectively, and the crossreaction rate of TMN and TMM was lower than 20%. When the dilution factor was 2,00,000, the crossreaction rate of TMJ was 53.2%, the crossreaction rate of TMA was 25.3%, and the crossreaction rate of TMN and TMM was lower than 10%. The results showed that when the dilution factor was low, the crossreaction rate was serious, which indicated the high homology of TM in different shrimp and crab. Significant differences existed in the crossreaction rates among different species at different dilution ratios, and the p-values were lower than 0.001.

Capacity Test of Immunoaffinity Column

To test the column capacity of self-made immunoaffinity column, we tested the recovery rate of different sample loading. As shown in **Table 2**, when the loading quantity of TM was in the range of 40–80 μg, the recovery rate was above 95%, and when the loading quantity reached 100 μg, the recovery rate was 79.1%. This is because the immunoaffinity column purification is based on the specific binding of antigen and antibody. Therefore, when the amount of antibody filled in the immunoaffinity column is fixed, the amount of antigen that can be adsorbed has an extreme limit. When all the specific binding sites of antibody are occupied, the specific binding of more antigens cannot be carried out. To ensure the purification effect, it is recommended that the sample quantity is not higher than 80 μg.

Selection and Synthesis of Signature Peptide for Allergen Protein

The selection of signature peptides is very important in the LC-MS/MS method development, which could influence the specificity and sensitivity of the method for the different ionization response of different peptides (24). Trypsin was used in enzymatic hydrolysis, where the cleavage site of trypsin was specifically at the C-terminal of lysine and arginine (30). When the length of peptide is lower than five amino acids, the analytical specificity is poor; when the peptides are too long, it is difficult and expensive to synthesize and the response of mass spectrometry is also unfavorable, so the peptide length is usually seven and 16 amino acids. To prevent possible chemical modifications, some susceptible amino acids, such as cysteine and methionine, should be avoided in the signature peptides selection. The selected peptide should be reproducibly observed and detectable in different states of samples, including the digested sample (31, 32).

Nanoliquid chromatography system tandem Orbitrap Fusion was used to analyze the peptide fragments after enzymolysis of TM. Raw data was analyzed by Thermo Proteome Discoverer 1.4. Twenty-eight peptides of TM were identified, and ANIQLVEK (AK-8), IVELEEELR (IR-9) were selected as signature peptides according to the principles selection.

Internal peptide (IP) was designed in our method. Based on the enzymatic digestion technique, homologous peptide was employed as the IP for measuring shrimp and crab allergen proteins. The isotopically labeled IP ANIQL ($^{13}C_6$, ^{15}N)VEK was designed and synthesized, in which all the carbon and nitrogen atoms in leucine (L) residues were labeled with ^{13}C and ^{15}N.

Optimization of MRM Conditions

To optimize the parameters of mass spectrometry, standard solutions of synthetic peptides were directly injected into mass spectrometry by the syringe pump. Full scan mode was used to find the precursor ion of peptide fragment, the declustering potential was also optimized, the product ions were confirmed in product scan mode, and the collision energy was optimized. Three product ions were selected for each precursor ion and precursor-to-product ion transitions were detected by multiple reaction monitoring (MRM) mode. AK-8 was selected as the quantitative peptide for TM. All parameters of MS are shown in **Table 3**. The chromatographic-mass spectrograms of signature peptides and internal standard of TM are shown in **Figure 1**.

Method Validation

Specificity of the Method

The specificity of the method means that the method should not be interfered with nontarget subjects. Both the peptide standards and the tryptic samples spiked with the internal standard were detected to investigate the specificity of the method. There were sharp and symmetric peaks in the synthetic peptide standards

TABLE 3 | Mass spectrometry parameters of signature peptides and the isotope-labeled internal standard of tropomyosin.

Allergen	Peptide	Q_1 (m/z)	Q_3 (m/z)	Fragmenter (V)	CE (eV)
Tropomyosin	ANIQLVEK[&]	457.769	729.451*	80	21.4
			616.366		21.4
			488.308		21.4
	IVELEEELR	565.309	917.457*	80	26.7
			788.415		26.7
			675.311		26.7
	ANIQL ($^{13}C_6$,^{15}N)VEK	461.500	736.400*	50	18.3
			623.300		19.0
			495.300		21.8

[&] *Marked for quantitative peptide.*
**Marked for quantitative ions.*

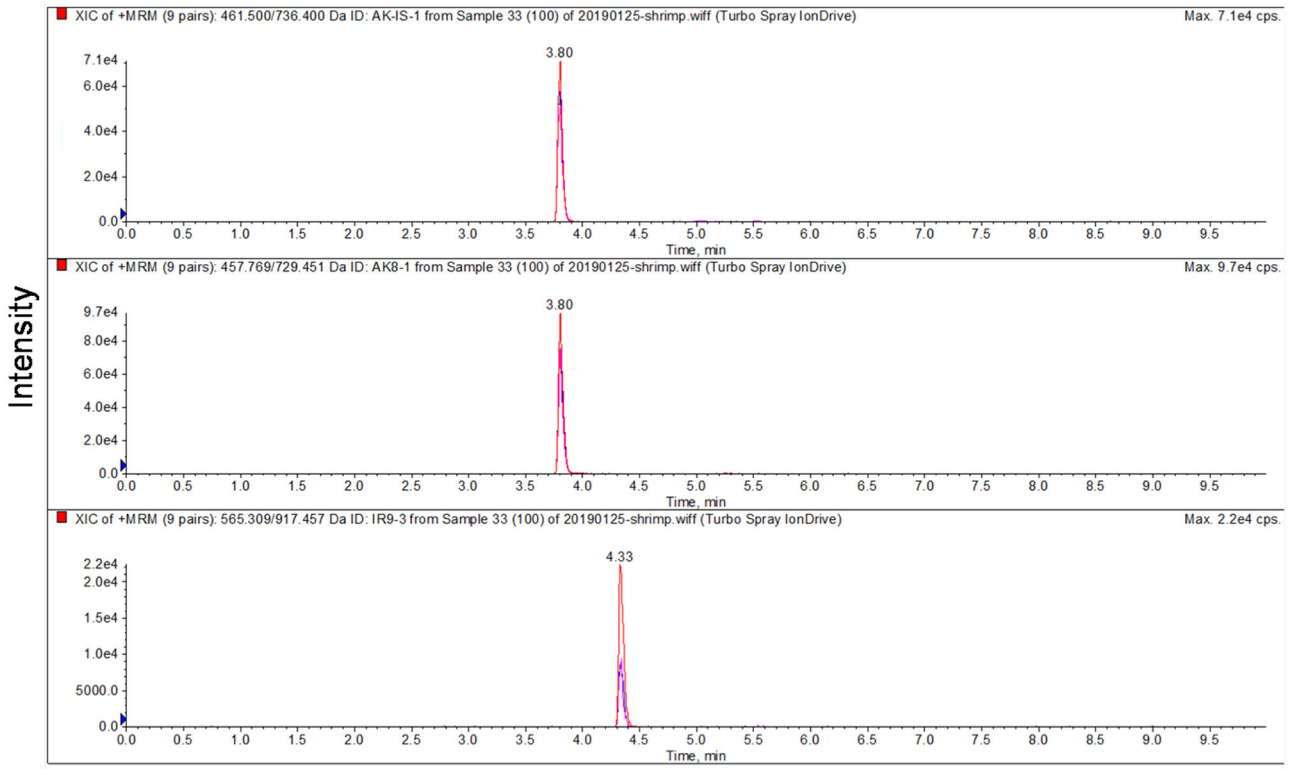

FIGURE 1 | Chromatographic-mass spectrograms of signature peptides and internal standard of tropomyosin.

and the selected signature peptide from tryptic samples, whereas there were no peaks in samples without tryptic digestion. There were no interferences from the matrix components on the retention time of the peptide standards, which indicated the perfect specificity of the method (32).

Matrix Effect

Matrix effect must be considered in mass spectrometry, which means the change in the analytical signal is caused by anything in the sample matrix (33). Signal suppression or enhancement of the analyte due to the coelution of matrix components could influence the accuracy of the method (34–36). Matrix effect could be caused by compounds brought from complex matrices of analytical samples, solvents, reagents, and materials used in sample preparation or solvents, buffers, and additives contained in the mobile phase. Postextraction addition, post-column infusion, and comparison of slopes of calibration curves are the main approaches to evaluate the matrix effect (37).

In this experiment, matrix effects were expressed as the ratio between the calibration curve slopes of matrix-matched and solvent-based standards. If the percentage of these slopes is larger than 100%, signal enhancement would occur, and when the percentage is lower than 100%, signal suppression may exist (38). In our test, the matrix effects of potato chips and sea bass

TABLE 4 | Linearity, LOD, and LOD of the method.

Matrix	Linear range (nmol/L)	Regression equation	R^2	Limit of detection (μg/g)	Limit of quantification (μg/g)
Potato chip	0.5∼400	Y = 0.33958X + 0.01748	0.99950	7.16	14.3
Sea bass	0.5∼400	Y = 0.36087X − 0.02017	0.99919	3.58	7.16

substrate without shrimp were tested, and the results showed that the matrix effects of potato chips and sea bass were 92.8 and 98.6%, respectively. Therefore, in the follow-up experiment, the matrix-matched standard curve was used in quantitative analysis to compensate for the matrix effect. In general, the internal standard method was not significantly influenced by the matrix effect.

Linear Range, Limit of Detection, and Limit of Quantification

In order to investigate the linearity, limits of detection (LODs) and limits of quantification (LOQs) of the method, potato chips and sea bass without shrimp were subject to method validation. The standard curves were fitted between the analyte/IP peptide area ratio (y) versus analyte/IS concentration ratio (x). The concentrations of synthetic peptides ranged from 0.5 to 400 nmol/L of TM in different matrices, with correlation coefficients (R^2) higher than 0.999 in all cases. Blank substrate of potato chips and sea bass without shrimp were used to test the LODs and LOQs using the spiked samples. The spike levels of target peptides with signal-to-noise ratio of three and 10 are defined as the LOD and LOQ of the method. The LOD and LOQ were expressed as TM contents, which were calculated based on the equimolar relationship between the protein and signature peptide. The LOD of TM in potato chips and sea bass substrate was 7.16 and 3.58 μg/g, respectively. The LOQ of TM in potato chips and sea bass substrate was 14.3 and 7.16 μg/g, respectively. Data of linear range, regression equation, LOD, and LOQ are presented in **Table 4**.

Method Recovery and Precision

Method accuracy was confirmed by spike samples, while the precision of the method was studied by carrying out five parallels of each spiking level. Precision of the method was expressed by relative standard deviation (RSD). The recoveries of TM for different matrices were calculated based on the samples spiked at three levels on LOQ, 3 LOQ, and 10 LOQ, from which the recovery of TM was determined in a range of 84.3–92.8% and RSDs were in the range of 1.32–5.24%. The data of recovery and precision were given in **Table 5**.

Sample Analysis

A total of 13 samples purchased from local supermarkets were used to determine the applicability of the method, including prawn, shrimp sticks, shrimp balls, crab stick, fish balls, etc. As shown in **Table 6**, TM was detected in *Penaeus vannamei* and China shrimp samples, with a concentration of 3,291 and 3,730 μg/g. TM was not detected in other samples. The results showed that the developed method could be used for the determination of TM in different kinds of food samples.

TABLE 5 | Recovery and precision of the method ($n = 5$).

Matrix	Spike level (μg/g)	Recovery (%)	RSD (%)
Potato chip	14.3	87.5	4.66
	42.9	92.7	1.32
	143	92.8	1.48
Sea bass	7.16	84.3	5.24
	21.5	89.9	2.32
	71.6	92.2	1.65

TABLE 6 | Results of real samples.

Sample	TM (μg/g)
Penaeus vannamei	3,291
China shrimp	3,730
Fresh shrimp slices	ND
Fresh shrimp strips	ND
Shrimp balls	ND
Lobster steak	ND
Lobster stick	ND
Crab king stick	ND
Crab chops	ND
Fish ball	ND
Cuttle ball	ND
Dragon prawn ball	ND

The Advantages of the Method

To compare relevant papers in the field, immunoaffinity purification was used in the procedure of sample pretreatment for first time. TM extraction, purification, antibody preparation, and the preparation of immunoaffinity column were finished by members of the research group. Signature peptides and isotope-labeled internal standard were used in the quantitative analysis. The method has the advantages of simple pretreatment, less interference, high specificity, and perfect accuracy and precision.

CONCLUSION

In this experiment, TM was extracted and purified, antibody of TM was made, and immunoaffinity column was filled. After simple extraction, the samples were purified by immunoaffinity column and then digested by trypsin. A new liquid chromatography–tandem mass spectrometry method at the peptide level was developed to determine TM, NIQLVEK (AK-8) was confirmed as the quantitative peptide and synthesized for the further process, and isotope-labeled internal standard was used in the quantitative analysis. The

specificity, linearity, sensitivity, matrix effect, accuracy, and precision of the method were investigated, and the developed method has been successfully used for the detection of TM in various food samples.

DATA AVAILABILITY STATEMENT

The raw data supporting the conclusions of this article will be made available by the authors, without undue reservation.

ETHICS STATEMENT

The animal study was reviewed and approved by Animal Ethical and Welfare Review Committee of Hebei Food Inspection and Research Institute.

AUTHOR CONTRIBUTIONS

YZ and YW conceived and designed the experiments. SF, JM, QL, CL, and JZ performed the experiments. YW analyzed the data. WZ and LW wrote the original draft. All authors have read and approved the manuscript.

FUNDING

This work was supported by Hebei Province High-Level Talent Funding Program (Project No. A201901008), Science and Technology Project of State Administration for Market Regulation (Project No. 2021MK023), and Research Project of Hebei Administration for Market Regulation (Project No. 2020ZD12).

REFERENCES

1. Waserman S, Shah A, Cruikshank H, Avilla E. Recognition and management of food allergy and anaphylaxis in the school and community setting. *Immunol Allergy Clin North Am*. (2022) 42:91–103. doi: 10.1016/j.iac.2021.09.008
2. Sung JS, Bong JH, Lee SJ, Jung JY, Kang MJ, Lee M, et al. One-step immunoassay for food allergens based on screened mimotopes from autodisplayed Fv-antibody library. *Biosens Bioelectron.* (2020) 202:113976. doi: 10.1016/j.bios.2022.113976
3. Morais S, Tortajada-Genaro LA, Maquieira Á, Martinez MG. Biosensors for food allergy detection according to specific IgE levels in serum. *Trends in Analytical Chemistry*. (2020) 127:115904. doi: 10.1016/j.trac.2020.115904
4. Palladino C, Breiteneder H. Peanut allergens. *Mol Immunol.* (2018) 100:58–70. doi: 10.1016/j.molimm.2018.04.005
5. Geiselhart S, Hoffmann-Sommergruber K, Bubin M. Tree nut allergens. *Mol Immunol.* (2018) 100:71–81. doi: 10.1016/j.molimm.2018.03.011
6. Manny E, Dominguez SA, Barrère V, Théolier J, Godefroy SB. Allergen action levels for food industries as risk management tools for a better use of precautionary allergen labelling. *Food Control.* (2022) 135:108773. doi: 10.1016/j.foodcont.2021.108773
7. Sealey-Voyksner J, Zweigenbaum J, Voyksner R. Discovery of highly conserved unique peanut and tree nut peptides by LC-MS/MS for multi-allergen detection. *Food Chem.* (2016) 194:201–11. doi: 10.1016/j.foodchem.2015.07.043
8. Shim JH, Reddy YVM, Park TJ, Park JP. Recent advances in analytical strategies and microsystems for food allergen detection. *Food Chem.* (2022) 371:131120. doi: 10.1016/j.foodchem.2021.131120
9. Korte R, Oberleitner D, Brockmeyer J. Determination of food allergens by LC-MS: Impacts of sample preparation, food matrix, and thermal processing on peptide detectability and quantification. *J Proteomics.* (2019) 196:131–40. doi: 10.1016/j.jprot.2018.11.002
10. Zhou JR, Wang YB, Qian YF, Zhang T, Zhang L, Fu LL. Quantification of shellfish major allergen tropomyosin by SPR biosensor with gold patterned biochips. *Food Control.* (2020) 107:106547. doi: 10.1016/j.foodcont.2019.02.041
11. Hajeb P, Selamat J. A contemporary review of seafood allergy. *Clin Rev Allergy Immunol.* (2012) 42:365–85. doi: 10.1007/s12016-011-8284-9
12. Wang YB Li LF, Li H, Peng YF, Fu LL. A fluorometric sandwich biosensor based on rationally imprinted magnetic particles and aptamer modified carbon dots for the detection of tropomyosin in seafood products. *Food Control.* (2022) 132:108552. doi: 10.1016/j.foodcont.2021.108552
13. Lopata AL, Kleine-Tebbe J, Kamath SD. Allergens and molecular diagnostics of shellfish allergy: part 22 of the series molecular allergology. *Allergo J Int.* (2016) 25:210–8. doi: 10.1007/s40629-016-0124-2
14. Vang B, Mæhre HK, Jensen I, Olsen RL. Detection of tropomyosin and determination of proteins in crustacean oils. *Food Chem.* (2013) 141:72–6. doi: 10.1016/j.foodchem.2013.02.125
15. Tsabouri S, Triga M, Makris M, Kalogeromitros D, Church M, Priftis KN. Fish and shellfish allergy in children: Review of a persistent food allergy. *Pediatr Allergy Immunol.* (2012) 23:608–15. doi: 10.1111/j.1399-3038.2012.01275.x
16. Zhang H, Lu Y, Ushio H, Shiomi K. Development of sandwich ELISA for detection and quantification of invertebrate major allergen tropomyosin by amonoclonal antibody. *Food Chem.* (2014) 150:151–7. doi: 10.1016/j.foodchem.2013.10.154
17. Wang YQ Li ZX, Lin H, Siddanakoppalu PN, Zhou JR, Chen GZ Yu ZW. Quantum-dot-based lateral flow immunoassay for the rapid detection of crustacean major allergen tropomyosin. *Food Control.* (2019) 106:106714. doi: 10.1016/j.foodcont.2019.106714
18. Eischeid AC, Kim BH, Kasko SM. Two quantitative real-time PCR assays for the detection of penaeid shrimp and blue crab, crustacean shellfish allergens. *J Agric Food Chem*. (2013) 61:5669–74. doi: 10.1021/jf3031524
19. Tabrizi MA, Sharmsipur M, Saber R, Sarkar S, Ebrahimi V. A high sensitive visible light-driven photoelectrochemical aptasensor for shrimp allergen tropomyosin detection using graphitic carbon nitride-TiO[[sb]]2[[/s]] nanocomposite. *Biosens Bioelectron.* (2017) 98:113–8. doi: 10.1016/j.bios.2017.06.040
20. Chinnappan R, Rahamn AA, AlZabn R, Kamath S, Lopata AL, Abu-Salah KM, et al. Aptameric biosensor for the sensitive detection of major shrimp allergen, tropomyosin. *Food Chem.* (2020) 314:126133. doi: 10.1016/j.foodchem.2019.126133
21. Ho CW, Hsu JL, Chen SH, Liasw ET, Liu S, Huang E S, et al. Development and validation of mass spectrometry-based method for detecting shrimp allergen tropomyosin. *LWT*. (2021) 152:112367. doi: 10.1016/j.lwt.2021.112367
22. Tolin S, Pasini G, Simonato B, Mainente F, Arrigoni, G. Analysis of commercial wines by LC-MS/MS reveals the presence of residual milk and egg white allergens. *Food Control.* (2012) 28:321–6. doi: 10.1016/j.foodcont.2012.05.015
23. Pilolli R, Chaudhari R, Palmisano F, Monaci L. Development of a mass spectrometry immunoassay for unambiguous detection of egg allergen traces in wines. *Anal Bioanal Chem.* (2017) 409:1581–9. doi: 10.1007/s00216-016-0099-3
24. Zhang JS, Lai SY, Zhang Y, Huang BF, Li D, Ren YP. Multiple reaction monitoring-based determination of bovine α-lactalbumin in infant formulas and whey protein concentrates by ultra-high performance liquid chromatography-tandem mass spectrometry using tryptic signature peptides and synthetic peptide standards. *Analytica Chimica Acta*. (2012) 727:47–53. doi: 10.1016/j.aca.2012.03.034
25. Sun LR, Lin H, Li ZX, Sun WH, Wang JH, Wu HY, et al. Development of a method for the quantification of fish major allergen parvalbumin in food matrix *via* liquid chromatography-tandem mass spectrometry with multiple reaction monitoring. *Food Chem.* (2019) 276:358–65. doi: 10.1016/j.foodchem.2018.10.014

26. Yang TB, Ren XF, Li YB, Chen FJ. Development of a sensitive monoclonal antibodybased ELISA for the detection of sulfamethazine in cow milk, honey, and swine urine. *Hybridoma.* (2010) 29:403–7. doi: 10.1089/hyb.2010.0048
27. Wang YB, Rao ZH, Zhou JR, Zheng L, Fu LL. A chiral assembly of gold nanoparticle trimer-based biosensors for ultrasensitive detection of the major allergen tropomyosin in shellfish. *Biosens Bioelectron.* (2019) 132:84–9. doi: 10.1016/j.bios.2019.02.038
28. Li YF, Lin ZZ, Hong CY, Huang ZY. Histamine detection in fish sample based on indirect competitive ELISA method using iron-cobalt co-doped carbon dots labeled histamine antibody. *Food Chem.* (2021) 345:128812. doi: 10.1016/j.foodchem.2020.128812
29. Li J, Ding Y, Chen H, Sun WL, Huang Y, Liu FQ, et al. Development of an indirect competitive enzyme-linked immunosorbent assay for propiconazole based on monoclonal antibody. *Food Control.* (2022) 134:108751. doi: 10.1016/j.foodcont.2021.108751
30. Chen Q, Zhang JS, Ke X, Lai SY Li D, Yang JC, et al. Simultaneous quantification of α-lactalbumin and β-casein in human milk using ultra-performance liquid chromatography with tandem mass spectrometry based on their signature peptides and winged isotope internal standards. *Biochim Biophys Acta.* (2016) 1864:1122–7. doi: 10.1016/j.bbapap.2016.06.006
31. Lutter P, Parisod V, Weymuth H. Development and validation of a method for the quantification of milk proteins in food products based on liquid chromatography with mass spectrometric detection. *J AOAC Int.* (2011) 94:1043–59. doi: 10.1093/jaoac/94.4.1043
32. Zhang JS, Lai SY, Cai ZX, Chen Q, Huang BF, Ren YP. Determination of bovine lactoferrin in dairy products by ultra-high performance liquid chromatography-tandem mass spectrometry based on tryptic signature peptides employing an isotope-labeled winged peptide as internal standard. *Anal Chim Acta.* (2014) 829:33–9. doi: 10.1016/j.aca.2014.04.025
33. Li HJ, Wu JS, Chen C, Xin W, Zhang W. Simultaneous determination of 74 pesticide residues in Panax notoginseng by QuEChERS coupled with gas chromatography tandem mass spectrometry. *Food Sci Hum Wellness.* (2021) 10:241–50. doi: 10.1016/j.fshw.2021.02.014
34. Keshavarz B, Jiang XY, Hsieh YHP, Rao QH. Matrix effect on food allergen detection-A case study of fish parvalbumin. *Food Chem.* (2019) 274:526–34. doi: 10.1016/j.foodchem.2018.08.138
35. Soliman M, Khorshid MA, Abo-Aly MM. Combination of analyte protectants and sandwich injection to compensate for matrix effect of pesticides residue in GC-MS/MS. *Microchem J.* (2020) 156:104852. doi: 10.1016/j.microc.2020.104852
36. Wang SC Qi PP, Di SS, Wang J, Wu SG, Wang XY, et al. Significant role of supercritical fluid chromatography-mass spectrometry in improving the matrix effect and analytical efficiency during multi-pesticides residue analysis of complex chrysanthemum samples. *Anal Chim Acta.* (2019) 1074:108–16. doi: 10.1016/j.aca.2019.04.063
37. Sovoboda P, Sander D, Plachká K, Nováková L. Development of matrix effect-free MISPE-UHPLC-MS/MS method for determination of lovastatin in Pu-erh tea, oyster mushroom, and red yeast rice. *J Pharm Biomed Anal.* (2017) 140:367–76. doi: 10.1016/j.jpba.2017.03.058
38. Ferrer C, Lozano A, Agüera A, Girón AJ, Fernández-Alba AR. Overcoming matrix effects using the dilution approach in multiresidue methods for fruits and vegetables. *J Chromatogr A.* (2011) 1218:7634–9. doi: 10.1016/j.chroma.2011.07.033

Conflict of Interest: The authors declare that the research was conducted in the absence of any commercial or financial relationships that could be construed as a potential conflict of interest.

Publisher's Note: All claims expressed in this article are solely those of the authors and do not necessarily represent those of their affiliated organizations, or those of the publisher, the editors and the reviewers. Any product that may be evaluated in this article, or claim that may be made by its manufacturer, is not guaranteed or endorsed by the publisher.

Copyright © 2022 Fan, Ma, Li, Wang, Zeng, Li, Zhou, Wang, Wang and Zhang. This is an open-access article distributed under the terms of the Creative Commons Attribution License (CC BY). The use, distribution or reproduction in other forums is permitted, provided the original author(s) and the copyright owner(s) are credited and that the original publication in this journal is cited, in accordance with accepted academic practice. No use, distribution or reproduction is permitted which does not comply with these terms.

frontiers in Nutrition

ORIGINAL RESEARCH
published: 14 March 2022
doi: 10.3389/fnut.2022.837601

Targeted Lipidomics Reveal the Effect of Perchlorate on Lipid Profiles in Liver of High-Fat Diet Mice

*Qiao Wang, Wanying Song, Yimei Tian, Peihao Hu, Xin Liu, Lin Xu and Zhiyong Gong**

Key Laboratory for Deep Processing of Major Grain and Oil (The Chinese Ministry of Education), College of Food Science and Engineering, Wuhan Polytechnic University, Wuhan, China

Perchlorate, commonly available in drinking water and food, acts on the iodine uptake by the thyroid affecting lipid metabolism. High-fat diets leading to various health problems continually raise public concern. In the present study, liver lipid metabolism profiles and metabolic pathways were investigated in C57BL/6J mice chronically exposed to perchlorate using targeted metabolomics. Mice were fed a high-fat diet and treated orally with perchlorate at 0.1 mg/kg bw (body weight), 1 mg/kg bw and 10 mg/kg bw daily for 12 weeks. Perchlorate induced disorders of lipid metabolism *in vivo* and hepatic lipid accumulation confirmed by serum biochemical parameters and histopathological examination. There were 34 kinds of lipid in liver detected by UHPLC-MS/MS and key metabolites were identified by multivariate statistical analysis evaluated with VIP > 1, p-value < 0.05, fold change > 1.2 or < 0.8. Perchlorate low, medium and high dose groups were identified with 11, 7 and 8 significantly altered lipid metabolites compared to the control group, respectively. The results of the metabolic pathway analysis revealed that the differential metabolites classified into different experimental groups contribute to the glycerophospholipid metabolic pathway. These findings provide insights into the effects of perchlorate on lipid metabolism during long-term exposure to high-fat diets and contribute to the evaluation of perchlorate liver toxic mechanisms and health effects.

Keywords: perchlorate, lipid metabolism, high-fat diet, targeted lipidomics, C57BL/6J mice

OPEN ACCESS

Edited by:
Shuai Chen,
Wuhan University, China

Reviewed by:
Guo Xiao-fei,
Qingdao University, China
Yong Chen,
Zhejiang Gongshang University, China
Hengye Chen,
South-Central University for Nationalities, China

***Correspondence:**
Zhiyong Gong
gongwhqg@163.com

Specialty section:
This article was submitted to Food Chemistry, a section of the journal Frontiers in Nutrition

Received: *16 December 2021*
Accepted: *08 February 2022*
Published: *14 March 2022*

Citation:
Wang Q, Song W, Tian Y, Hu P, Liu X, Xu L and Gong Z (2022) Targeted Lipidomics Reveal the Effect of Perchlorate on Lipid Profiles in Liver of High-Fat Diet Mice. Front. Nutr. 9:837601. doi: 10.3389/fnut.2022.837601

INTRODUCTION

Perchlorate, considered a persistent inorganic pollutant, is an anionic compound usually combined with potassium, sodium or ammonium (1). The presence of perchlorate in the environment is mainly through natural formation and artificial chemical synthesis, and this perchlorate contaminates the water and enters the food chain through plant absorption and enrichment (2). Since the 1990s, perchlorate has been found to be widely present in drinking water and foods which has been raised as a public health concern (3). Numerous studies have reported high detection frequencies of perchlorate in foods such as vegetables, fruits, milk and other foods in amounts deserving of attention (4–6). Approximately 83% of perchlorate is exposed to humans through foods (7). Upon entry into the body, perchlorate competitively inhibits iodine uptake by the thyroid and disrupts the synthesis of thyroid hormones (8), which play a pivotal role in regulating of lipid metabolism (9).

With the improvement of human nutrition, excessive fat intake is considered as a persistent public health problem. Long-term high-fat diet (HFD) can lead to weight gain and a series of adverse reaction, including obesity, hepatic steatosis, hyperlipidemia and hyperglycemia (10, 11).

In this case, toxicants contribute to oxidative stress *in vivo*, leading to further abnormalities in hepatic lipid metabolism. Experimentally, it has been shown that the administration of harmful substances (endotoxins or pro-oxidants) to obese mice can lead to severe liver damage and even death (12, 13).

In rodent studies, perchlorate interferes with endocrine function and causes disruptions in lipid metabolism, which in turn causes fat accumulation, weight gain, insulin resistance and abnormal glucose tolerance (14). Lipids have great biological importance in physiological activities such as forming cell membranes, storing energy and transmitting cellular signals, thus lipids largely reflect the metabolic status between health and disease (15). Disorders of lipid metabolism may lead to a range of diseases such as diabetes, obesity, atherosclerosis, coronary heart disease and brain damage (16). Further the liver is the most activated organ for lipid metabolism, and disorders of lipid metabolism may result in fat enrichment and degeneration within hepatocytes. Lipids of interest include phospholipids, cholesterol, sphingolipid and triglycerides.

To our knowledge, there is little published information on the chronic effects of perchlorate on hepatic lipid profiles following a high-fat diet. Studies using lipidomics to explore endocrine disruption by perchlorate have not been reported, but some studies suggest that exposure to exogenous pollutants is an important cause of disruption of lipid metabolism in the body and leads to obesity by affecting metabolic pathways (17). Therefore, the present study applied targeted metabolomics to profile hepatic lipid metabolism in mice with long-term perchlorate intervention. The aim of this work was to investigate the mechanism of hepatotoxicity of perchlorate on lipid metabolism and to contribute to the understanding of the health effects of perchlorate chronically.

MATERIALS AND METHODS

Chemicals and Reagents

Sodium perchlorate ($NaClO_4$) standard aqueous solution (10 mg/L) was purchased from O2SI Smart Solution (Charleston, SC, USA). All lipid standards and internal standards were purchased from Avanti Polar Lipids Inc. (Alabaster, AL, USA). Formic acid (≥95%) and chloroform were obtained from Sigma-Aldrich (St. Louis, MO, USA). Acetonitrile, methanol, isopropanol, *n*-Hexane were all HPLC grade, obtained from Thermo Fisher Scientific (Waltham, MA, USA). Sodium chloride, sodium sulfate and sodium hydroxide were supplied by Sinopharm Chemical Reagents Co., Ltd.

Animal Experiment

A total of 24 6-week-old male C57BL/6J mice (bw: 27–29 g) were purchased from Hubei Province Animal Research Center, Hubei, China. The study was approved by the Institutional Animal Care and Use Committee Tongji Medical College, Huazhong University of Science and Technology (IACUC Number: 2395).

All mice were housed in a specific-pathogen-free animal laboratory with a 12/12 h light-dark cycle (temperature 24 ± 1°C; relative humidity 55–65%). After 3 days of acclimatization, animals were randomly divided into one control group and three experimental groups of six mice each: low-dose group (LG, 0.1 mg/kg bw daily), middle-dose group (MG, 1 mg/kg bw daily), high-dose group (HG, 10 mg/kg bw daily) and control group (CG, received an equivalent volume of saline). Sodium perchlorate was dissolved in physiological saline and administered orally to the mice. High-fat feed and drinking water were supplied *ad libitum*, the high-fat feed consisted of 10.0% fat, 15.0% protein, 30.6% starch, 4.6% ash and 6.6% moisture. Mice were routinely fed for 12 consecutive weeks and weighed every 6 days. Blood samples and liver tissues were harvest after all mice sacrifice via cervical dislocation, liver weight and body weight were recorded. Liver coefficients were calculated according to the formula: Liver coefficient (%) = liver weight (g) / body weight (g) × 100%. All collected samples were stored at −80°C until assayed.

Determination of Biochemical Parameters

The serum of mice was separated from whole blood by centrifugation and measured using commercial ELISA kits (Nanjing Jiancheng Bioengineering Institute, China), to assess the serum biochemistry. Parameters included the liver function markers aspartate aminotransferase (AST), alanine aminotransferase (ALT), malondialdehyde (MDA); and indicators of lipid metabolism, total cholesterol (TC), total triglyceride (TG), high-density lipoprotein cholesterol (HDL-c), and low-density lipoprotein cholesterol (LDL-c).

Histological Analysis of Liver Section

Liver tissues were removed after the mice were sacrificed and fixed with 4% paraformaldehyde, embedded in paraffin, and processed for hematoxylin and eosin (H&E) staining using a standard protocol (18). The sections were observed and photographed with an inverted microscope at 400× magnification.

Pretreatment of Lipid Analysis

The pretreatment of liver was performed as previously described (19), with some modifications. 100 mg liver tissue sample was placed in a homogenate tube thawed on ice, 1 mL ice water was added and homogenized for 8 min. Then 0.1 mL homogenate was mixed with 1.2 mL methanol/chloroform (2:1, v/v, 0.1% MTBE) and 0.6 mL water vortexed for 1 min in 2 mL EP tube. The mixture was sonicated for 5 min and centrifuged at 10,000 g for 10 min at 4°C. The supernatant was collected and dried with nitrogen gas. Finally, the residue was reconstituted in 1 mL initial mobile phase and filtered through a 0.22 μm membrane for UHPLC-MS/MS analysis.

Quality control (QC) sample was prepared by mixing equal amounts (50 μL) of each extracted sample (24 in total). Moreover, the QC specimen was analyzed every six samples throughout the whole analysis procedure.

UPLC-MS/MS Analysis

Ultra-high performance liquid chromatography-tandem mass spectrometry analysis was performed as previously described (20). Briefly, UHPLC-MS/MS analysis was undertaken on QTRAP® 6,500+ LC-MS/MS system (AB Sciex, USA)

equipped with Acquity HSS T3 column (2.1 × 100 mm i.d., 1.8 μm, Waters, USA). The mobile phase was composed of water/methanol/acetonitrile (1/1/1, v/v/v) containing 10 mM ammonium formate and 0.1% formic acid (solvent A) and isopropanol (solvent B) at a flow speed of 0.4 mL/min. The gradient elution program was set as follows: solvent A initially at 80% declined to 10% within 12 min and held for 1 min, then decreased to 80% within 2 min and held for 1 min. The column temperature maintained at 45 °C and the injection volume was 10 μL.

Initially separated liver samples were scanned in a triple quadrupole containing ion trap. The system is equipped with ESI Turbo ion spray port, which can be operated by Analyst 1.6.3 software. The conditions used for the electrospray source were shown as follows: the ion source temperature, 550 °C; the ion spray voltage, 5,500 V in positive mode (or −4,500 V in negative model); the ion source gas I, 55 psi; the gas II, 55 psi; the curtain gas, 35 psi; the collision gas, medium; quantification of ion pairs corresponding to lipids by multiple reaction monitoring mode (MRM). Mass spectrometry information of the target lipid metabolites, including compound name, MRM transition, optimized dephasing potential (DP) and collision energy (CE) is shown in **Supplementary Table 1**. All targets were quantified separately using D31-PG(16:0/18:1), D31-PE(16:0/18:1), D31-PC(16:0/18:1), C17-Sphinganine and D5-TAG(17:0/17:1/17:0) as internal standards to quantify phosphatidylglycerol (PG), Lyso-phosphatidylcholine (LPC), phosphatidylcholine (PC), phosphatidylethanolamine (PE), sphingolipids (SM) and triglyceride (TAG), respectively.

Raw Data Processing and Metabolic Pathway Analysis

Raw mass-spectrometry data were processed with Software Analyst 1.6.3. The pooled sample was used as quality control (QC) to validate the reproducibility and stability of lipid metabolites in the positive and negative ion mode of the method and equipment. The quantification of target lipid metabolites was based on signal intensity relative to the corresponding internal standard by the multiple reaction monitoring mode (MRM) of triple quadrupole mass spectrometry. The integration and calibration of chromatographic peaks was performed with Multiquant Software version 3.0.2 (AB Sciex Inc.).

Quantitative data of lipid metabolites were analyzed by SIMCA-P software version 14.1 (Umetrics, Sweden) using an orthogonal partial least squares discriminant analysis (OPLS-DA) model for differential analysis to screen for potentially differential lipids. Lipid metabolites with VIP value > 1, p-value < 0.05 and FC > 1.2 or FC < 0.8 were defined as significantly different. Metabolic pathway analysis was performed with Metaboanalyst 5.0 (www.metaboanalyst.ca).

Statistical Analysis

All data were collected and computed into IBM SPSS Statistics 19 and expressed as mean ± standard deviation (SD). The difference between the experimental groups and the control group was highly significant by one-way ANOVA. P-values < 0.05 were considered statistically significant.

RESULTS AND DISCUSSION

Body Weight and Liver Coefficient

The weights of the mice were recorded every 6 days for total of 12 weeks, and fresh livers were weighed immediately upon harvest, individual ratio of liver to body weights were calculated. **Figure 1** shows changes in body weight and liver coefficient. Body weight trended to increase gradually over perchlorate exposure time. Within 1 week after the start of the experiment, there was almost no change in body weight between the groups, and the difference gradually appeared after 1 week, indicating that short-term exposure to perchlorate had less effect on the growth of mice, and this result was consistent with the previously reported (21). Compared with the CG group, the body weight of the LG group was significantly increased ($p < 0.05$) at the end of the experiment, but there was no significant difference in MG and HG groups **(Figure 1A)**. No significant differences were observed in liver coefficient between treatment groups and control group, whereas HG group showed a significantly decreased ($p < 0.05$), after mice were exposed to different doses of perchlorate **(Figure 1B)**. These results suggest that chronic high dose intake of perchlorate might have affected the liver coefficients.

Biochemical Parameters

The seven biochemical indicators in serum were divided into two subgroups according to their physiological meaning **(Table 1)**. AST, ALT and MDA as indicators of liver function, there was no significant difference between the perchlorate exposed groups and the control group. With the increase of perchlorate dose, the content of MDA increases correspondingly. MDA is generated by lipid peroxidation, so the change in MDA content reflects the extent of membrane damage (22). The lipid metabolic markers include serum TC, TG, HDL-c, LDL-c. Compared with those of the CG group, TC in MG and HG groups showed markedly increased, TG in HG group was increased and the difference was statistically. The high-fat diet resulted in elevated serum levels of TC, TG and LDL cholesterol and reduced levels of HDL cholesterol in mice (23). However, under the influence of perchlorate, LDL cholesterol levels did not change significantly, and HDL levels increased significantly in the experimental groups, which indicated that perchlorate caused lipid metabolism disturbance.

Histopathology Examination

Histopathological analysis was performed after oral administration of treatments in C57BL/6J mice for 12 weeks. Liver sections with H&E staining were imaged using an inverted fluorescence microscope **(Figure 2)**. In the 400X magnification images, vacuolization was observed in the liver sections of all groups. Small amounts of inflammatory cells were present in the CG and LG groups. In the MG group, inflammatory cells infiltrate of liver lobules and dilated congested central vein were observed. The same was more evident in the HG group. Combined with the results of serum biochemical parameters, it further demonstrates that perchlorate affects lipid accumulation and lipid metabolism disorders in the liver *in vivo*, which may

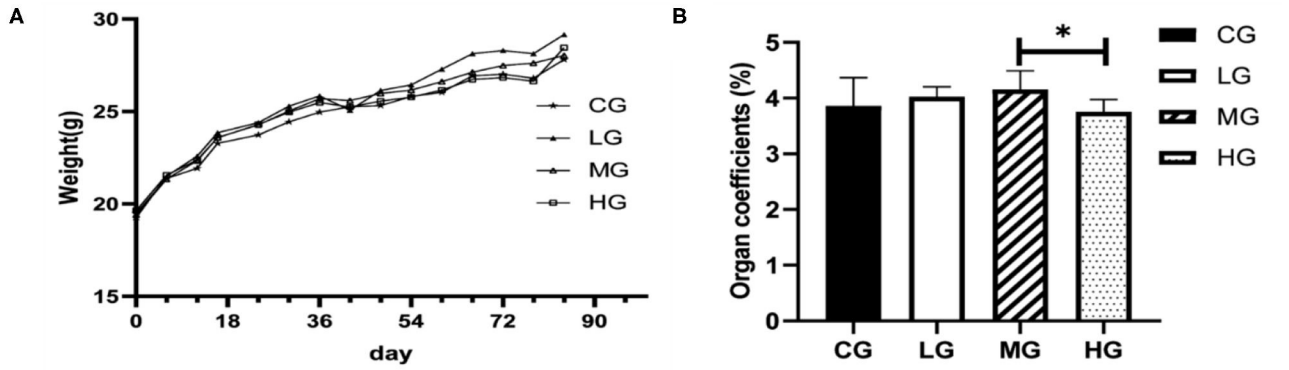

FIGURE 1 | Changes of body weights of the mice during the experiment **(A)**, liver coefficient **(B)** (*$P < 0.05$, $n = 6$).

TABLE 1 | Levels of serum biochemistry parameters in mice from experiment and control groups.

Parameter	CG	LG	MG	HG
AST (U/L)	26.75 ± 4.50	26.00 ± 1.63	25.75 ± 1.89	28.75 ± 2.06
ALT (U/L)	11.00 ± 0.82	10.50 ± 2.08	11.00 ± 3.16	11.50 ± 1.73
MDA (nmol/mL)	4.94 ± 1.77	5.19 ± 0.98	5.96 ± 2.32	6.47 ± 1.10
TC (mmol/L)	1.19 ± 0.11[a]	1.284 ± 0.04[a,b]	1.42 ± 0.13[b]	1.464 ± 0.23[b]
TG (mmol/L)	0.12 ± 0.03[a]	0.12 ± 0.01[a]	0.20 ± 0.05[a,b]	0.17 ± 0.23[b]
HDL-c (mmol/L)	1.21 ± 0.10[a]	1.27 ± 0.04[a,b]	1.35 ± 0.12[a,b]	1.49 ± 0.25[b]
LDL-c (mmol/L)	0.17 ± 0.04	0.20 ± 0.04	0.25 ± 0.07	0.18 ± 0.03

Mean ± standard deviation values in the same row for each parameters followed by different letters are significantly different ($p < 0.05$).

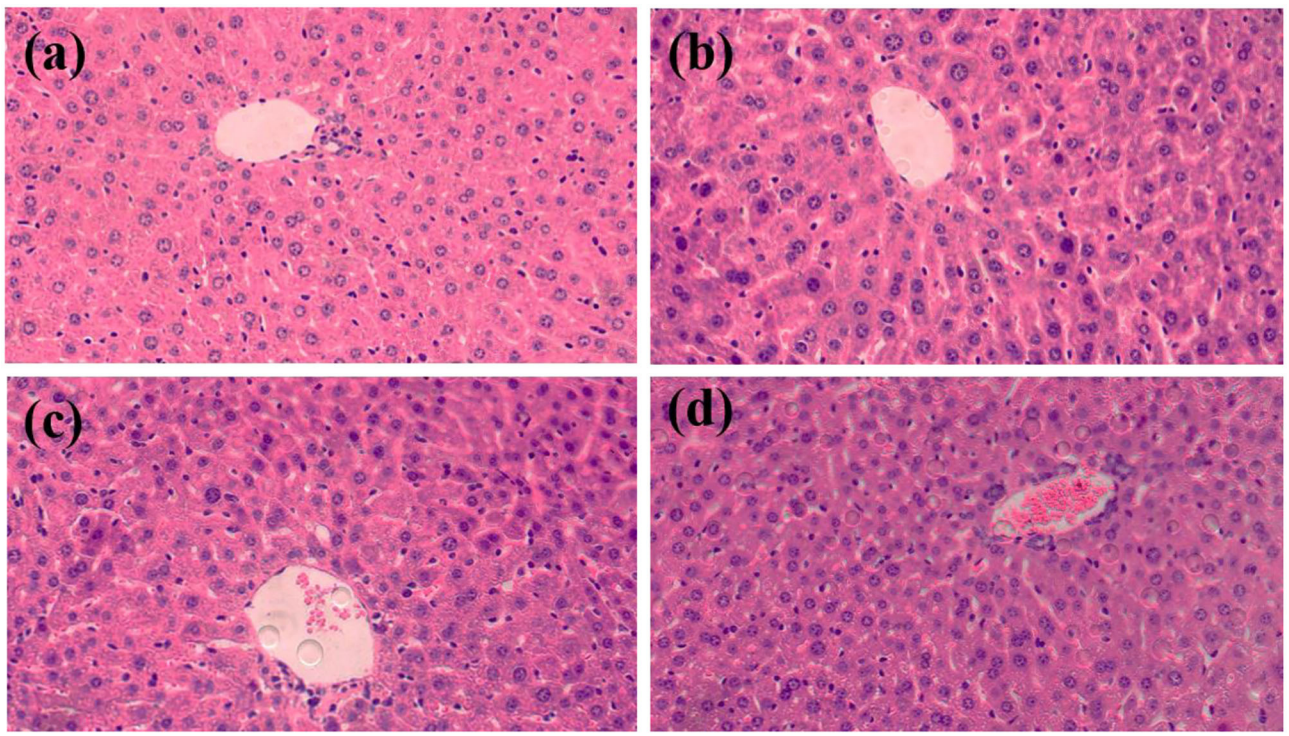

FIGURE 2 | Histopathological analysis of liver (HE, 400×). **(A)** CG, **(B)** LG, **(C)** MG, and **(D)** HG.

be associated with inflammation, obesity and other chronic diseases (24–26).

Quantification of Liver Lipid Metabolites

To investigate the effect of perchlorate on hepatic lipid metabolism in mice fed a high-fat diet, 34 common lipids were selected as targets for quantitative. These included 4 phosphatidylglycerols (PG), 8 phosphatidylcholines (PC), 3 lyso-phosphatidylcholines (LPC), 2 phosphatidylethanolamines (PE), 4 sphingolipids (SM) and 13 triglycerides (TAG). All mice liver samples were subjected to UHPLC-MS/MS analysis. Quantification of PGs, PCs, LPCs, PEs, SMs and TAGs by D31-PG (16:0/18:1), D31-PC (16:0/18:1), D31-PE (16:0/18:1), C17-sphinganine and D5-TAG (17:0/17:0/17:0), respectively. The relative standards deviation values of peak areas of lipids in all QC samples are required to be <10%. The content of all lipids in the liver of C57BL/6J mice is taken as a logarithm with a base of 10, as shown in the **Figure 3**.

In phospholipids metabolism **(Figure 3A)**, PG (16:0/16:0), PG (16:0/18:2), PG (18:0/18:1), PC (2:0/15:1) and PC (18:0/14:0) shown an increasing trend in the experimental groups with dose-effect relationship. PC (18:0/14:0) in the LG group was significantly decreased compared to the CG group ($p < 0.05$), and PG (18:0/18:1) in the HG group was very significantly elevated compared to the CG group ($p < 0.01$). However, LPC (20:0/0:0), LPC (20:1/0:0), PC (3:0/16:0), PC (6:0/13:1) and PE (20:3/15:0) formed a decreasing trend among the experimental groups, and all of them were significantly reduced in the HG groups compared to the CG group ($p < 0.01$), with PC (3:0/16:0) and PE (20:3/15:0) showing significance in all experimental groups and LPC (20:0/0:0)

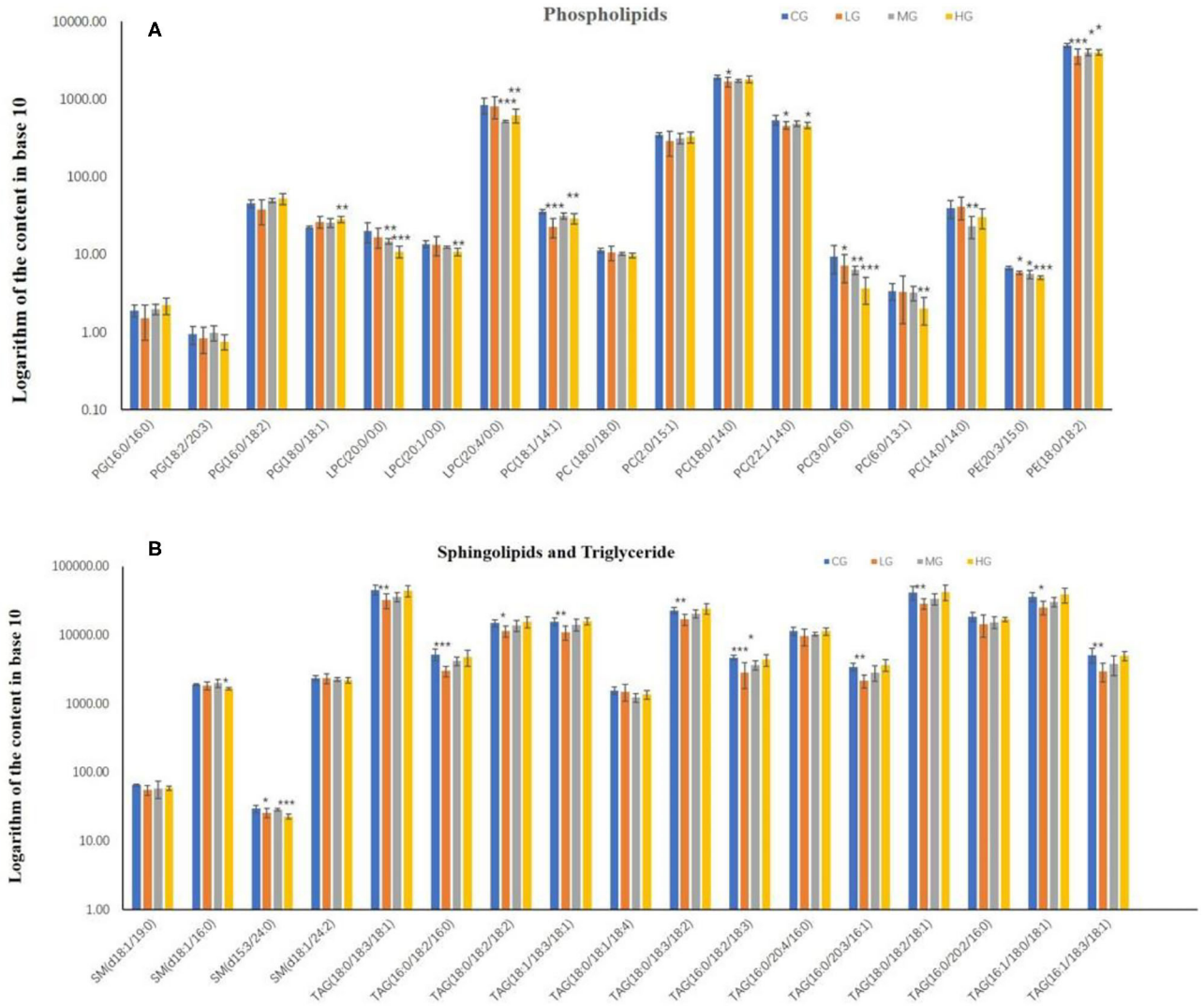

FIGURE 3 | The content of phospholipids **(A)** and sphingolipids and triglyceride **(B)** in the liver of mice in high-dose group (HG), middle-dose group (MG), low-dose group (LG) and control group (CG) ($^{*}P < 0.05$, $^{**}P < 0.01$, $^{***}P < 0.001$, compared with the control group, $n = 6$).

showing significance in the MG group ($p < 0.01$). Moreover, PC (18:1/14:1), PC (22:1/14:1) and PE (18:0/18:2) were decreased in experimental groups compared to the CG group, with the exception of PC (18:1/14:1) and PC (22:1/14:0) in the MG group, which showed significant differences in all groups ($p < 0.05$).

In sphingolipids and triglyceride metabolism **(Figure 3B)**, 4 types of sphingolipids were lowered in the experimental groups in comparison with the CG group, with significant differences both in the HG group for SM (d18:1/16:0) and in the LG and HG groups for SM (d15:3/24:0). This result could indicate that the intake of perchlorate in high-fat dietary mice may reduce sphingolipids. Another aspect is that all triglyceride lipids showed an increasing trend in the experimental groups except for TAG (18:0/18:1/18:4). Furthermore, in contrast to the CG group, TAG (18:0/18:3/18:1), TAG (16:0/18:2/16:0), TAG (18:0/18:2/18:2), TAG (18:1/18:3/18:1), TAG (18:0/18:3/18:2), TAG (16:0/20:3/16:1), TAG (18:0/18:2/18:1), TAG (16:1/18:0/18:1) and TAG (16:1/18:3/18:1) significantly decreased in LG group, as well as TAG (16:0/18:2/18:3) in the LG and MG groups.

PC and PE account for more than 50% of the total phospholipid species in eukaryotic membranes and play a major role in the structure and function of biological membranes (27). PE is synthesized *in vivo* by methylation to 1-methylphosphatidylethanolamine (PMME), which is then methylated to produce dimethyl phosphatidylethanolamine (PDME), and PDME is synthesized under the action of enzymes to PC (28). The phospholipase PLA2 hydrolyzes PC to LPC, and LPC and PC can be interconverted (29). It has been demonstrated that PC mediates the promotion of cell proliferation, growth and programmed cell death (30). LPC is a pro-inflammatory mediator that promotes inflammation in acute injuries or chronic diseases (31). One study found that high-fat diet-induced obesity decreased LPC levels in the body (32), which is consistent with the reduction of LPC levels with increasing perchlorate levels in the present study, showing that perchlorate exacerbates the symptoms of high-fat diet-induced obesity. PGs, a surface-active lipid *in vivo*, showed an increasing trend in our study, implying that the increased dose of perchlorate exposure may promote the formation of phosphatidylglycerols. Triglycerides are closely related to metabolic diseases such as atherosclerosis, hyperlipidemia and obesity (33, 34). Most of the triglycerides in the experiment showed significant changes reflecting that the metabolic homeostasis of high-fat mice was disturbed by perchlorate intake, with a dose-effect relationship.

Metabolite Screening

Hepatic lipid metabolism is influenced by multiple factors, analysis of variable importance is carried out as a key step in the profiling analysis of the effects of perchlorate on lipid metabolism in mice fed a high-fat diet. To this end, the study analyzed the differential metabolites by establishing the OPLS-DA model. Different experimental groups were examined in comparison with the control group, and differential lipid metabolites were identified for VIP values > 1, statistically significant P values < 0.05 and fold change > 1.2 or <0.8 (35). A total of 21 lipid metabolites were identified among the experimental groups, including 10 types of phospholipids, 1 type of sphingolipid and 10 types of triglycerides. In addition, 11, 7 and 8 differential lipid metabolites were identified in the LG, MG and HG groups, respectively **(Table 2)**. Also, TAG(16:0/18:2/18:3) and TAG(18:0/18:3/18:1) were selected in both the LG and MG groups, and LPC(20:4/0:0), LPC(20:0/0:0) and PC(3:0/16:0) were selected in both the MG and HG groups. By the results, the differential lipid metabolites were primarily phospholipids and triglycerides, as well as the lipids identified were mostly different in the three experimental groups. It can be inferred that perchlorate mainly affected phospholipid metabolic pathway and triglyceride metabolic pathway, and that mice may be more sensitive to perchlorate dose in long-term lipid metabolism. It is noteworthy that in the above results total serum triglycerides were significantly increased in the experimental groups, which is consistent with other environmental pollutants (e.g., perfluorinated compounds, BPA, PCBs, etc.) that affect the lipid metabolism leading to fat accumulation (14), while the identified triglycerides in the liver were down-regulated. This may be due to the effect of high-fat diet on the liver by perchlorate, which in turn reduces total lipid accumulation in the liver by accordingly diminishing the hepatic triglyceride concentration as a protection action (36). The mechanism of this result deserve more work for further study.

TABLE 2 | Potential differential metabolites identified significantly different in liver in each group.

Group	Compound name	VIP	*P*-value	FC	Regulation
LG	PC (18:1/14:1)	1.35	0.000	0.63	Down
	PE (18:0/18:2)	1.31	0.000	0.74	Down
	TAG (16:0/18:2/18:3)	1.30	0.000	0.60	Down
	TAG (16:1/18:3/18:1)	1.27	0.000	0.58	Down
	TAG (16:0/20:3/16:1)	1.24	0.002	0.63	Down
	TAG (18:0/18:3/18:2)	1.20	0.004	0.74	Down
	TAG (18:0/18:2/18:2)	1.17	0.014	0.76	Down
	TAG (18:1/18:3/18:1)	1.16	0.002	0.70	Down
	TAG (16:0/18:2/16:0)	1.16	0.001	0.57	Down
	TAG (16:1/18:0/18:1)	1.09	0.015	0.71	Down
	TAG (18:0/18:3/18:1)	1.07	0.005	0.71	Down
MG	LPC (20:4/0:0)	1.60	0.000	0.62	Down
	LPC (20:0/0:0)	1.58	0.000	0.74	Down
	PC (3:0/16:0)	1.44	0.001	0.67	Down
	TAG (16:0/18:2/18:3)	1.21	0.007	0.77	Down
	PC (14:0/14:0)	1.18	0.005	0.60	Down
	TAG (18:0/18:3/18:1)	1.15	0.035	0.79	Down
	TAG (18:0/18:1/18:4)	1.11	0.006	0.78	Down
HG	LPC (20:0/0:0)	1.60	0.000	0.54	Down
	PE (20:3/15:0)	1.57	0.000	0.75	Down
	PC (3:0/16:0)	1.54	0.000	0.39	Down
	SM (d15:3/24:0)	1.44	0.000	0.77	Down
	PG (18:0/18:1)	1.43	0.001	1.27	Up
	LPC (20:1/0:0)	1.41	0.000	0.79	Down
	PC (6:0/13:1)	1.29	0.001	0.59	Down
	LPC (20:4/0:0)	1.20	0.000	0.74	Down

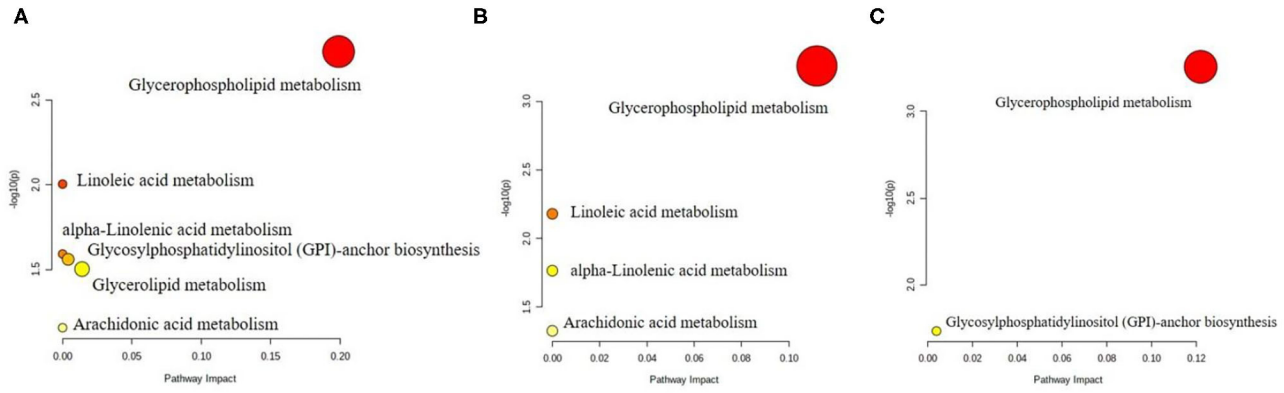

FIGURE 4 | Pathway analysis of differential lipid metabolites in liver from the **(A)** LG group, **(B)** MG group, and **(C)** HG group.

Metabolic Pathway Analysis

Analysis of the key metabolic pathways included enrichment analysis and topology analysis conducted by Metaboanalyst 5.0 program. Overrepresentation analysis and path topology analysis were tested for hypergeometry and relative intermediacy, respectively. The pathway database was selected from the Rattus norvegicus (rat) in Metaboanalyst 5.0. The path impact on the horizontal axis was the calculated impact value from the path topology analysis, and the –log(p) on the vertical axis was the negative logarithmic shift of the *p*-value calculated in the path enrichment analysis **(Figure 4)**. The pathways analysis revealed a significant enrichment of glycerophospholipid metabolism pathway in all LG, MG and HG groups, suggesting that perchlorate affects the targets of hepatic lipid metabolism in mice fed a high-diet mainly by regulating glycerophospholipid metabolism. In addition, there may be effects on the metabolic pathways such as linoleic acid metabolism, alpha-linolenic acid metabolism, arachidonic acid metabolism and glycosylphosphatidylinositol (GPI)-anchor biosynthesis.

Glycerophospholipids are the most abundant phospholipids *in vivo* and they regulate intracellular molecular signaling pathways via hydrolysis by phospholipases and binding to G protein-coupled receptors on biological membranes, which in turn are involved in various processes such as inflammation, immunity and tumor growth (37). In the above findings, the different glycerophospholipids in the experimental groups contributed higher values in the multivariate analysis, and the changes in lipid metabolic pathways in high-fat mice chronically under the influence of diverse doses of perchlorate directed to the glycerophospholipid metabolic pathway. The results suggest that the effect of perchlorate on lipid metabolism *in vivo* is mainly in the glycerophospholipid metabolic pathway and that the lipids in the glycerophospholipid pathway regulated by perchlorate at doses of 0.1 mg/kg bw, 1 mg/kg bw and 10 mg/kg bw per day are different.

CONCLUSION

In summary, the study investigated lipid metabolism in high-fat C57BL/6J mice chronically exposed to perchlorate. On the basis of growth parameters, serum biochemical parameters, histopathological examination and lipid quantification, long-term perchlorate exposure exhibited effects on disorders of serum and hepatic lipid metabolism and lipid accumulation in the liver of mice. Taking advantage of targeted lipidomics, it was found that perchlorate had a significant effect on glycerophospholipid metabolic pathways in mice on a high-fat diet. Investigators should consider the combined effects of perchlorate on metabolic damage *in vivo* in the future. Other small molecule metabolomics, proteomics, transcriptomics, genomics and molecular biology techniques should be applied to enhance the understanding of the toxicological mechanisms of perchlorate. This study lays the foundation for the identification of the effects of perchlorate on lipid metabolism and metabolic pathways.

DATA AVAILABILITY STATEMENT

The original contributions presented in the study are included in the article/**Supplementary Material**, further inquiries can be directed to the corresponding author.

ETHICS STATEMENT

The animal study was reviewed and approved by the Institutional Animal Care and Use Committee Tongji Medical College, Huazhong University of Science and Technology.

AUTHOR CONTRIBUTIONS

WS, YT, and PH carried out animal experiment, histopathological examination, and sample processing. XL and LX completed targeted lipidomics analysis. The study was

designed by QW and ZG. The manuscript was written by QW and WS. All authors contributed to the article and approved the submitted version.

FUNDING

This research was supported by the National Natural Science Foundation of China (No. 32172313), the National Key Research and Development Program of China (No. 2017YFC1600500), and the Open Foundation of Hubei Key Laboratory for Processing and Transformation of Agricultural Products (Wuhan Polytechnic University) (No. 2020HBSQGDKFB04).

SUPPLEMENTARY MATERIAL

The Supplementary Material for this article can be found online at: https://www.frontiersin.org/articles/10.3389/fnut.2022.837601/full#supplementary-material

REFERENCES

1. Tian Y, Xu H, Liu S, Fang M, Wu Y, Gong Z. Study on the bioaccessibility and bioavailability of perchlorate in different food matrices *in vitro*. *Food Chem*. (2020) 333: 127470. doi: 10.1016/j.foodchem.2020.127470
2. Wang Z, Forsyth D, Lau PY, Pelletier L, Gaertner D. Estimated dietary exposure of Canadians to perchlorate through the consumption of fruits and vegetables available in Ottawa markets. *J Agr Food Chem*. (2009) 57: 9250–5. doi: 10.1021/jf901910x
3. Urbansky ET. Perchlorate as an environmental contaminant. *Environ Sci Pollut Res*. (2002) 9: 187–92. doi: 10.1007/BF02987487
4. Chang WH, Chen HL, Lee CC. Dietary exposure assessment to perchlorate in the Taiwanese population: a risk assessment based on the probabilistic approach. *Environ Pollut*. (2020) 267: 115486. doi: 10.1016/j.envpol.2020.115486
5. Lee JW, Oh SH, Oh JE. Monitoring of perchlorate in diverse foods and its estimated dietary exposure for Korea populations. *J Hazard Mater*. (2012) 243: 52–8. doi: 10.1016/j.jhazmat.2012.09.037
6. Liao Z, Cao D, Gao Z, Zhang S. Occurrence of perchlorate in processed foods manufactured in China. *Food Control*. (2020) 107:106813. doi: 10.1016/j.foodcont.2019.106813
7. Oh SH, Lee JW, Mandy P, Oh JE. Analysis and exposure assessment of perchlorate in Korean dairy products with LC-MS/MS. *Environ Health Toxicol*. (2011) 26:e2011011. doi: 10.5620/eht.2011.26.e2011011
8. Massimo T, Aldo P, Antonio D, Eleonora F, Patrizia A, Paolo V, et al. Relative potencies and additivity of perchlorate, thiocyanate, nitrate, and iodide on the inhibition of radioactive iodide uptake by the human sodium iodide symporter. *Thyroid*. (2004) 14: 1012–9. doi: 10.1089/thy.2004.14.1012
9. Lee J, Ha J, Jo K, Lim DJ, Lee JM, Chang SA, et al. High normal range of free thyroxine is associated with decreased triglycerides and with increased high-density lipoprotein cholesterol based on population representative data. *J Clin Med*. (2019) 8: 758. doi: 10.3390/jcm8060758
10. Liu C, Ma J, Sun J, Cheng C, Feng Z, Jiang H, et al. Flavonoid-rich extract of paulownia fortunei flowers attenuates diet-induced hyperlipidemia, hepatic steatosis and insulin resistance in obesity mice by AMPK pathway. *Nutrients*. (2017) 9:959. doi: 10.3390/nu9090959
11. Wang S, Moustaid-Moussa N, Chen L, Mo H, Shastri A, Su R, et al. Novel insights of dietary polyphenols and obesity. *J Nutr Biochem*. (2014) 25: 1–18. doi: 10.1016/j.jnutbio.2013.09.001
12. Ito K, Kiyosawa N, Kumagai K, Manabe S, Matsunuma N, Yamoto T. Molecular mechanism investigation of cycloheximide-induced hepatocyte apoptosis in rat livers by morphological and microarray analysis. *Toxicology*. (2006) 219: 175–86. doi: 10.1016/j.tox.2005.11.017
13. Yang SQ, Lin HZ, Mandal AK, Huang J, Diehl AM. Disrupted signaling and inhibited regeneration in obese mice with fatty livers: implications for nonalcoholic fatty liver disease pathophysiology. *Hepatology*. (2001) 34: 694–706. doi: 10.1053/jhep.2001.28054
14. Holtcamp W. Obesogens: an environmental link to obesity. *Environ Health Persp*. (2014) 120: 62–8. doi: 10.1289/ehp.120-a62
15. Gross RW and Han X. Unlocking the complexity of lipids: using lipidomics to identify disease mechanisms, biomarkers and treatment efficacy. *Future Lipidol*. (2006) 1: 539–47. doi: 10.2217/17460875.1.5.539
16. Rao MA, Hatcher JF, Dempsey RJ. Lipids and lipidomics in brain injury and diseases. *AAPS PharmSci*. (2006) 8:E314. doi: 10.1007/BF02854902
17. Lustig RH. Childhood obesity: behavioral aberration or biochemical drive? Reinterpreting the First Law of Termodynamics. *Nat Clin Pract Endocrinol Metab*. (2006) 2: 447–58. doi: 10.1038/ncpendmet0220
18. Alday-Parejo B, Richard F, Worthmuller J, Rau T, Galvan JA, Desmedt C, et al. MAGI1, a new potential tumor suppressor gene in estrogen receptor positive breast cancer. *Cancers*. (2020) 12:223. doi: 10.3390/cancers12010223
19. Liu Y, Wang R, Zheng K, Xin Y, Jia S, Zhao X. Metabonomics analysis of liver in rats administered with chronic low-dose acrylamide. *Xenobiotica*. (2020) 50: 894–905. doi: 10.1080/00498254.2020.1714791
20. Chen JX, Han YS, Zhang SQ, Li ZB, Chen J, Yi WJ, et al. Novel therapeutic evaluation biomarkers of lipid metabolism targets in uncomplicated pulmonary tuberculosis patients. *Signal Transduct Target Ther*. (2021) 6:22. doi: 10.1038/s41392-020-00427-w
21. Yu KO, Narayanan L, Mattie DR, Godfrey RJ, Todd PN, Sterner TR, et al. The pharmacokinetics of perchlorate and its effect on the hypothalamus-pituitary-thyroid axis in the male rat. *Toxicol Appl Pharmacol*. (2002) 182:148–59. doi: 10.1006/taap.2002.9432
22. Hu Y, Liu S, Zhu BM. CRISPR/Cas9-induced loss of keap1 enhances anti-oxidation in rat adipose-derived mesenchymal stem cells. *Front Neurol*. (2019) 10:1311. doi: 10.3389/fneur.2019.01311
23. Yang D, Hu C, Deng X, Bai Y, Cao H, Guo J, et al. Therapeutic effect of chitooligosaccharide tablets on lipids in high-fat diets induced hyperlipidemic rats. *Molecules*. (2019) 24:514. doi: 10.3390/molecules24030514
24. Varghese M, Griffin C, McKernan K, Eter L, Lanzetta N, Agarwal D, et al. Sex differences in inflammatory responses to adipose tissue lipolysis in diet-induced obesity. *Endocrinology*. (2019) 160:293–312. doi: 10.1210/en.2018-00797
25. Akmatov MK, Ermakova T, Holstiege J, Steffen A, Stillfried D, Batzing J. Comorbidity profile of patients with concurrent diagnoses of asthma and COPD in Germany. *Sci Rep*. (2020) 10: 17945. doi: 10.1038/s41598-020-74966-1
26. Ding Y, Haks MC, Forn-Cuni G, He J, Nowik N, Harms AC, et al. Metabolomic and transcriptomic profiling of adult mice and larval zebrafish leptin mutants reveal a common pattern of changes in metabolites and signaling pathways. *Cell Biosci*. (2021) 11:126. doi: 10.1186/s13578-021-00642-0
27. Federica G, Smith TK. The Kennedy pathway *de novo* synthesis of phosphatidylethanolamine and phosphatidylcholine. *IUBMB Life*. (2010) 62: 414–28. doi: 10.1002/iub.354
28. Haberl EM, Pohl R, Rein-Fishboeck L, Horing M, Krautbauer S, Liebisch G, et al. Hepatic lipid profile in mice fed a choline-deficient, low-methionine diet resembles human non-alcoholic fatty liver disease. *Lipids Health Dis*. (2020) 19:250. doi: 10.1186/s12944-020-01425-1
29. Sahu PK, Tomar RS. The natural anticancer agent cantharidin alters GPI-anchored protein sorting by targeting Cdc1-mediated remodeling in endoplasmic reticulum. *J Biol Chem*. (2019) 294:3837–52. doi: 10.1074/jbc.RA118.003890
30. Ridgway ND. The role of phosphatidylcholine and choline metabolites to cell proliferation and survival. *Crit Rev Biochem Mol Biol*. (2013) 48:20–38. doi: 10.3109/10409238.2012.735643
31. Liu-Wu Y, Hurt-Camejo E, Wiklund O. Lysophosphatidylcholine induces the production of IL-1β by human monocytes. *Atherosclerosis*. (1998) 137:351–7. doi: 10.1016/S0021-9150(97)00295-5
32. Rai S, Bhatnagar S. Novel lipidomic biomarkers in hyperlipidemia and cardiovascular diseases: an integrative biology analysis. *OMICS*. (2017) 21:132–42. doi: 10.1089/omi.2016.0178

33. Chaix A, Zarrinpar A, Miu P, Panda S. Time-restricted feeding is a preventative and therapeutic intervention against diverse nutritional challenges. *Cell Metab.* (2014) 20:991–1005. doi: 10.1016/j.cmet.2014.11.001
34. Tan T, Lai CJ, Zeng L, Liu EH, Li P. Enzymatic hydrolysis-based absolute quantification of triacylglycerols in plant oil by use of a single marker. *Anal Bioanal Chem*. (2014) 406:4921–9. doi: 10.1007/s00216-014-7899-0
35. Ou M, Li C, Tang D, Xue W, Xu Y, Zhu P, et al. Genotyping, generation and proteomic profiling of the first human autosomal dominant osteopetrosis type II-specific induced pluripotent stem cells. *Stem Cell Res Ther*. (2019) 10:251. doi: 10.1186/s13287-019-1369-8
36. Aragones G, Suarez M, Ardid-Ruiz A, Vinaixa M, Rodriguez MA, Correig X, et al. Dietary proanthocyanidins boost hepatic NAD(+) metabolism and SIRT1 expression and activity in a dose-dependent manner in healthy rats. *Sci Rep*. (2016) 6:24977. doi: 10.1038/srep24977
37. Makide K, Uwamizu A, Shinjo Y, Ishiguro J, Okutani M, Inoue A, et al. Novel lysophosphoplipid receptors: their structure and function. *J Lipid Res*. (2014). 55:1986–95. doi: 10.1194/jlr.R046920

Conflict of Interest: The authors declare that the research was conducted in the absence of any commercial or financial relationships that could be construed as a potential conflict of interest.

Publisher's Note: All claims expressed in this article are solely those of the authors and do not necessarily represent those of their affiliated organizations, or those of the publisher, the editors and the reviewers. Any product that may be evaluated in this article, or claim that may be made by its manufacturer, is not guaranteed or endorsed by the publisher.

Copyright © 2022 Wang, Song, Tian, Hu, Liu, Xu and Gong. This is an open-access article distributed under the terms of the Creative Commons Attribution License (CC BY). The use, distribution or reproduction in other forums is permitted, provided the original author(s) and the copyright owner(s) are credited and that the original publication in this journal is cited, in accordance with accepted academic practice. No use, distribution or reproduction is permitted which does not comply with these terms.

frontiers in Nutrition

ORIGINAL RESEARCH
published: 18 March 2022
doi: 10.3389/fnut.2022.837168

The Whitening, Moisturizing, Anti-aging Activities, and Skincare Evaluation of Selenium-Enriched Mung Bean Fermentation Broth

Kang Wei[1], Congyin Guo[2], Jiangxiong Zhu[2], Yang Wei[1], Meirong Wu[2], Xiaodong Huang[3], Mu Zhang[3], Jide Li[3], Xueyun Wang[4], Yuanfeng Wang[2] and Xinlin Wei[1]**

[1] School of Agriculture and Biology, Shanghai Jiao Tong University, Shanghai, China, [2] College of Life Sciences, Shanghai Normal University, Shanghai, China, [3] Shanghai Yuemu Cosmetics Co., Ltd., Shanghai, China, [4] Enshi Selenium Impression Agricultural Technology Co., Ltd., Shadi Township, Enshi, China

OPEN ACCESS

Edited by:
Yahong Han,
Huazhong Agricultural University, China

Reviewed by:
Michael Murkovic,
Graz University of Technology, Austria
Haixia Chen,
Tianjin University, China

***Correspondence:**
Xinlin Wei
foodlab2010@163.com
Yuanfeng Wang
yfwang@shnu.edu.cn

Specialty section:
This article was submitted to Food Chemistry, a section of the journal Frontiers in Nutrition

Received: 16 December 2021
Accepted: 21 January 2022
Published: 18 March 2022

Citation:
Wei K, Guo C, Zhu J, Wei Y, Wu M, Huang X, Zhang M, Li J, Wang X, Wang Y and Wei X (2022) The Whitening, Moisturizing, Anti-aging Activities, and Skincare Evaluation of Selenium-Enriched Mung Bean Fermentation Broth. Front. Nutr. 9:837168. doi: 10.3389/fnut.2022.837168

Selenium-enriched mung bean (Se-MB) is a combination of mung bean (MB) and selenium (Se), which have a variety of potential biological activities. However, little is known about the skincare activity of Se-MB. The chemical composition of Se-MB fermentation broth (Se-MBFB) was analyzed to investigate the whitening, moisturizing, and anti-aging activities of Se-MBFB. The tyrosinase inhibition, anti-melanogenic in melanocytes (B16F10 cells), and moisturizing effect in human dermal fibroblasts (HDFs) were analyzed. Besides, the free radical scavenging activity of Se-MBFB was assessed *in vitro*. To verify the *in vivo* effects and the potential of practical applications of Se-MBFB, a clinical trial was conducted on the participants: 31 Chinese women aged 25–60 years, with no pigmentation disorder, no illness, no history of hypersensitivity reaction, and no use of skincare product on the face. The participants used an Se-MBFB masque for 15-20 min after cleaning the face. The measurement points were Week 0, 2, and 4 (W0, W2, and W4) after using the masque, and target sites were cheek and canthus. The following parameters were recorded on the target sites at each visit: melanin index, skin color, cuticle moisture content, transepidermal water loss, and crow's feet. The results demonstrated that Se-MBFB was rich in polyphenols, peptides, and γ-aminobutyric acid (GABA), displayed significant free radical scavenging and tyrosinase inhibiting activities, decreased the synthesis of melanin, and upregulated the aquaporin-3 (AQP3) expression. The test of the Se-MBFB mask showed that after 4 weeks of using the Se-MBFB facemask, the faces of the participants became whiter with reduced wrinkles and increased moisture content. Se-MB possessed the excellent whitening, moisturizing, and antioxidant efficacy, which could lay a scientific foundation for utilization and development of skincare products of Se-MB and its related industrial cosmetics products.

Keywords: Se-enriched mung bean fermentation broth, chemical composition, whitening, moisturizing, anti-aging, facemask

INTRODUCTION

The skin is the largest tissue that is thin and wide in humans, with a surface of about 2 m^2 and 4 kg (1). The skin is mainly composed of the epidermis and dermis, separated by the junction of the two parts. Skin is essential to human health as it is the body's first line of defense against harmful external physical, chemical, and biological invasions, as well as other functions, such as controlling body temperature. In addition, skin is not only regarded as a physical barrier, but also a dynamic tissue with its metabolism and the interaction between internal and external cells (1). As external environment changes, coupled with a fast-paced lifestyle, environmental pollution, abuse of hormone products, contamination of pesticide residue, and increased mental stresses, a series of skin-related problems have increasingly occurred, including dryness, roughness, aging, and dull skin tone, leading to the chronic sub-health of the skin (2). Previous studies have shown that natural active substances from plants could effectively improve skin health. Chowdhury found that polyphenols like EGCG could increase extracellular matrix deposition of elastin and collagen and may improve skin properties (3). Kang reported that marigold methanol extract with high levels of polyphenols has significant skin anti-aging potential (4). Amakye et al. reported that two peptides obtained from soybean, Trp-Pro-Lys (WPK) and Ala-Tyr-Leu-His (AYLH), have better anti-aging effects compared with oyster peptides and sea cucumber peptides (5).

Selenium (Se), as an essential micronutrient for human health with many physiological activities, possesses a superior antioxidant and detoxifying effect on the skin. Se is one of the four internationally recognized antioxidants that promotes the breakdown of peroxides and protects hemoglobin in cells from oxidative damage (6). Burke et al. found that selenomethionine has been shown to protect subjects from acute skin damage following UVB exposure (7). Michaelssons et al. have demonstrated that a good clinical result was obtained after supplementation of Se in male acne patients (8). Organic Se exhibits more biological activity, relatively less toxicity and side effects than inorganic Se, whereas plants or soil microorganisms can transform inorganic Se into organic Se (9).

Mung bean (*Phaseolus radiatus* L.) is one of the important legumes widely planted in temperate and subtropical regions. Studies have shown that mung bean (MB) possesses a variety of potential bioactivities like hypolipidemic, antioxidant, anti-tumor, antibacterial, and immune enhancement (10), which could be attributed to the various nutrients (including protein, lipids, minerals, vitamins, and carotene) and functional bioactive ingredients (such as alkaloids, flavonoids, coumarins, and functional oligosaccharides) in MBs (10–12). Since both Se and MB possess vital effects on human health, Se-MBs can optimize the physiological and pharmacological functions of two components. However, most people currently consume MBs as food, and after passing through the human digestive system, many active ingredients (such as polyphenols) are metabolized and destroyed by several digestive enzymes, leading to the loss of their biological activity. Besides, the biological value of the nutrients in MB may be limited by some of the anti-nutritional factors it contains (13). For instance, phytic acid in MB can combine several important divalent cations, such as zinc, iron, magnesium, and calcium to form insoluble complexes to limit the absorption and utilization of minerals in the small intestine (14). Fortunately, these disadvantages can be reduced or eliminated through various processing methods, such as sprouting, fermentation, etc. (13).

Since the cell walls of Se-MB are difficult to break (the main components are cellulose and pectin), the various active substances in the cells cannot be fully utilized. Biological fermentation can be used to rupture the cell walls of tissues and break down macromolecular substances into small molecular substances, thereby releasing a variety of nutrients or active substances (15). However, one major drawback of current biological activity research of MB is that there is rare research on skin protection activity, which limits the research of MB. In this study, we used *Lactobacillus helveticus* and *bifidobacterial* to prepare Se-MBFB by fermenting selenium-enriched mung beans. The chemical composition was analyzed by measuring the content of total polyphenols, total flavonoids, peptides, and free amino acids to explore the whitening, moisturizing, and anti-aging activity of Se-MBFB. Besides, we use the Se-MBFB in the preparation of facial masks, which provides a reference for the development of Se-MB and its related industrial cosmetics products.

MATERIALS AND METHODS

Materials and Reagents

Se-MBs (Se content: 2.83 ± 0.13 mg/kg) were derived from En Shi City (Hubei Province, China). The mouse melanoma cell line (B16F10) and human foreskin fibroblasts (HFF-1) were purchased from the National Collection of Authenticated Cell Cultures (Shanghai, China). Se standard solution was provided by the Shanghai Institute of Measurement and Testing Technology (Shanghai, China). The 0.25% Trypsin-EDTA, fetal bovine serum (FBS), DMEM, and RPMI 1640 culture mediums were obtained from Gibco Co. (California). The Se-MBFB facemask was commissioned to be produced by Shanghai Guzidi Industrial Co., Ltd (Shanghai, China), its formula is listed in **Supplementary Table S1**, the addition of other raw materials except Se-MBFB was to improve the experience of the subjects and did not have any efficacy. The reverse transcription and real-time PCR kits were purchased from Takara (Otsu, Japan). Tyrosinase, L-3,4-dihydroxyphenylalanine (L-DOPA) was obtained from Shanghai Baomanbio Technology Co., Ltd (Shanghai, China). 2,2-diphenyl-1-picrylhydrazyl (DPPH) was provided by Seebio Biotech Co., Ltd (Shanghai, China). 2,2-azino-bis-(3-ethyl-benzothiazoline-6-sulfonic acid) (ABTS) and vitamin C (Vc) were obtained from Sinopharm Chemical Reagent Co., Ltd (Shanghai, China). *Lactobacillus helveticus* and *Bifidobacteria* (*HN019*™) were obtained from Shanghai University (China). All other chemicals and solvents were of analytical grade.

Preparation of Se-MBFB

The Se-MBFB was prepared as described earlier by Song with modification (16). Se-MBs were treated with 75% (w/w) or (w/v) aqueous ethanol solution for 1 to 2 s, washed three times with sterile distilled water, and then soaked for 24 h until sprouted to 5–6 mm. A total of 60–70% sterile distilled water, 10% Se-MBs (after pretreatment), and 2% of *Lactobacillus helveticus* and *Bifidobacteria* (*HN019*^{TM}) (1:1) liquid were added into the fermenter, and the nitrogen was used to remove oxygen in the fermenter. The fermentation was conducted at 37°C for 48–50 h, with stirring for 2 min per 8 h to make fermentation uniform. After the end of the fermentation, the fermentation broth was filtered with a microporous membrane and stored at 4°C, and the Se-MBFB was obtained.

Determination of Main Active Ingredients in Se-MBFB

Total Amino Acid Composition Analysis

A total amino acid composition of free peptides and protein hydrolysate was determined as described earlier by Shazly et al. with slight modifications (17). A total of 1 mL of Se-MBFB was mixed with 2 mL of 6 mol/L HCl and 20 μL of phenol and then blown with nitrogen for 5 min. Thereafter, the mixture was hydrolyzed at 110 ± 1°C for 22 h, cooled to room temperature, and centrifuged (12,000 rpm, 4°C, 25 min). A total of 600 μL supernatant was dried with nitrogen and dissolved in 400 μL of HCl (0.02 mol/L). After filtration with 0.22 μm membrane, the supernatant was analyzed with an L-8900 automatic amino acid analyzer (Hitachi, Tokyo, Japan).

Free Amino Acids Composition Analysis

A total of 1 mL of Se-MBFB was mixed with 500 μL of 0.1 M HCl and 500 μL 10% trichloroacetic acid solution, and then reacted at 4°C for 0.5 h and centrifuged for 25 min (12,000 rpm, 4°C). A total of 200 μL supernatant was filtered with 0.22 μm membrane and determined with L-8900 automatic amino acid analyzer (Hitachi, Tokyo, Japan).

Determination of Chemical Composition

The content of polysaccharides was determined by the phenol sulfuric acid method, and glucose was used as a standard. The content of polyphenols was measured by Folin-Ciocalteu's reagent method according to the Chinese National Standard. The content of flavonoids was estimated according to the Chinese National Standard with rutin as a standard. The peptide content was determined by the Biuret method (18). The protein content was measured according to the Bradford method based on the standard curve of BSA (19). The peptide molecular weight was determined by the HPLC system (20). The total selenium content was determined by the Ventura method (21).

Whitening Activity Assays *in vitro*

Inhibitory Effect on the Tyrosinase Activity

The composition of the reaction system with a total volume of 4 mL was as follows: 1 mL of L-DOPA as the enzyme-substrate (1.5 mg/mL, dissolved in pH 6.8 PBS), various concentrations (0.25, 0.5, 1, 2, 4, 8%) of Se-MGFBs, 0.5 mL of tyrosinase solution (200 U/mL, dissolved in pH 6.8 PBS) pre-stored at 37°C to maintain the optimum enzyme activity, and corresponding volume of PBS solution (pH 6.8). Then L-DOPA, Se-MGFBs, and tyrosinase were mixed and pre-incubated at 37°C for 10 min. After that, L-DOPA was added and incubated at 37°C for 5 min and then measured under 475 nm. The PBS was used instead of the sample solution as a negative control, and Vc was used as a positive control. The inhibition activity of the tyrosinase enzyme was calculated as follows:

$$\text{Tyrosinase inhibition (\%)} = (1 - \text{OD475}_{\text{sample}}/\text{OD475}_{\text{negative}}) \times 100\% \quad (1)$$

Effect on Melanin Formation

The murine B16F10 melanoma cell line was maintained in RPMI1640 medium supplemented with 5% fetal bovine serum and Gentamicin (50 μg/mL) at 37°C in a humidified atmosphere containing 5% CO_2.

Cell Viability Assay

Cell viability was determined using the MTT assay. Briefly, the B16F10 cells were seeded at a density of 2×10^4 cells/well in a 96-well tissue culture plate. After 24 h of incubation, the cells were treated with various concentrations (0.5, 1, 2, 4, 8, and 16%) of Se-MGFBs for 24 h. After media removal, fresh media containing MTT solution (1 mg/mL) was added and incubated for 4 h at 37°C. Subsequently, the formazan crystals formed were dissolved in 150 μL DMSO and vibrated at a low speed for 15 min, then the absorbance was measured at 570 nm using the AMR-100 microplate reader (Olympus, Tokyo, Japan), and the group without samples was regarded as the control.

$$\text{Cell viability (\%)} = \text{OD570}_{\text{sample}}/\text{OD570}_{\text{control}} \times 100\% \quad (2)$$

Inhibition Assay of Melanin Production

The melanin content in murine melanoma cells was measured using a previously described method with slight modifications (22). Briefly, B16F10 cells were cultured at a density of 5×10^4 cells/well in a 6-well plate for 24 h, then the cells were treated with Se-MBFBs (2, 4, 8%). After 48 h of incubation, the cells were harvested and washed twice with PBS. The pelleted cells were dissolved in 200 μL of NaOH (1 mol/L), incubated at 100°C for 2 h, and then measured at an absorbance of 405 nm. The group without samples was regarded as control, Kojic acid (25 μg/mL) was a positive control, and the group without cells was regarded as blank. The relative content of melanin was calculated according to the following formula:

$$\text{Relative content of melanin (\%)} = (\text{OD405}_{\text{sample}}/\text{OD405}_{\text{blank}}) \times 100\% \quad (3)$$

Moisturizing Activity Assays *in vitro*

HFF-1 cells were maintained in DMEM medium supplemented with 10% FBS and cultured in a carbon dioxide incubator with constant temperature (5% CO_2, 37°C).

Cell Viability Assay

The cell viability was determined using different concentrations of sample (0.78, 1.56, 3.13, 6.25, 12.5, 25%) according to the description by Section Cell Viability Assay).

Cell Moisturizing Gene Expression Assay

The HFF-1 cells were cultured at a density of 2×10^4 cells/well in a 12-well plate for 48 h, then the cells were treated with Se-MBFBs (1.56, 3.13, 6.25%). After 48 h of incubation, the cells were harvested and washed once with PBS, then total mRNA in HFF-1 cells was extracted by RNA Extraction kit according to the manufacturer's instructions, then total mRNA was reverse transcribed into cDNA according to the Reverse transcription kit instructions. The mRNA expression level was detected by SYBR qPCR Master Mix (Thermofisher, Beijing, China) according to the light quantitative PCR kit instructions. The specific primers used were as follows: AQP3, 5′-CCTTTGGCTTTGCTGTCACTC-3′(F), 5′-ACGGGGTTGTTGTAAGGGTCA-3′(R); GAPDH, 5′-AAGAAGGTGGTGAAGCAGG-3′(F), 5′-AGGTGGAGGAGTGGGTGTCG-3′(R). The gene GAPDH was employed as an internal reference and the relative mRNA level of target genes was calculated by using the $2^{-\Delta\Delta Ct}$ method.

Anti-aging Assays *in vitro*

DPPH Radical Scavenging Assay

Different concentrations of Se-MBFB (1, 2, 4, 8, and 16%) were mixed with 2 mL of 0.1 mM DPPH (dissolved in 95% ethanol solution) at room temperature for 30 min. The absorbance value was determined at 517 nm and recorded as A1. The sample solution was replaced by an equal volume of 95% ethanol and distilled water, and their absorbance values were recorded as A0 and A2, separately, and Vc was used as a positive control. The DPPH radical scavenging rate of the sample was calculated as follows:

$$\text{DPPH radical scavenging rate (\%)} = [A0 - (A1 - A2)]/A0 \times 100\% \quad (4)$$

ABTS Radical Scavenging Assay

A total of 10 mL ABTS (7 mmol/L) solution and equal volume $K_2S_2O_8$ (2.45 mmol/L) solution were mixed and kept in the dark for 12–16 h at room temperature, then diluted 40–50 times with 95% ethanol to make the absorbance reach 0.70 ± 0.02 at 734 nm and obtain ABTS test solution. A total of 4.0 mL ABTS test solution was added into Se-MBFBs (1, 2, 4, 8, and 16%) with different concentrations and incubated at room temperature for 10 min, the absorbance at 734 nm was measured and recorded as A1. The absorbance value of 95% ethanol instead of sample solution was recorded as A0, and Vc was used as a positive control. The ABTS radical scavenging rate of the sample was calculated as follows:

$$\text{ABTS radical scavenging rate (\%)} = (1 - A1/A0) \times 100\% \quad (5)$$

Safety Evaluation

According to the Safety and Technical Standards for Cosmetics (STSC, version in 2015, China), heavy metal content analysis, skin sensitization test, acute eye/corrosion irritation test, and dermal irritation/corrosion test were performed following the criteria to evaluate its safety.

Whitening, Moisturizing, and Antioxidant Activities *in vivo*

A total of 31 female volunteers have been enrolled upon inclusion/exclusion criteria screening by the investigator, they were aged between 25 and 60 years (tested by Intertek Shanghai Healthcare and Beauty Product Clinical Research Service Lab). Volunteers were excluded if they had pigmentation disorders, acute or chronic illness, and history of hypersensitivity reaction to any ingredient of the tested products. Also, volunteers who have used a whitening, moisturizing, or antioxidant product on the investigated areas within the month before the study and/or during the experiment were also excluded. Besides, volunteers under medical treatment for skin disease in the past and/or present with a therapy that may influence the results of the study were excluded. Before the start of the test, all subjects were given test instructions and signed informed consent.

The test environment was conducted under a condition with constant temperature and humidity (temperature: 21.0 ± 1.0°C; humidity: 50.0 ± 10.0%). The volunteer's face was cleaned with sterile pure water, then they sat quietly for 30 min. After that, various indicators of the face were analyzed and tested. The volunteers used Se-MBFB masque on their face every 2 d, 15–20 min each time, then cleaned their face with sterile pure water. The study lasted for 4 weeks, with visits at weeks 0, 2, and 4 (W0, W2, and W4). Clinical assessments and instrumental measurements were performed at every visit, and target sites were cheek and canthus, the following parameters were recorded on the target sites at each visit: Melanin index (Mexameter, Courage & Khazaka, Germany) and skin color (L^*b^* system; chroma meter CR-400, Japan). Cuticle moisture content (Corneometer, Courage & Khazaka, Germany) and transepidermal water loss (Tewameter, Courage & Khazaka, Germany). Also, the center, right, and left sides of the face were photographed separately using the VISIA-CR (Canfield, OH) imaging station, and crow's feet were determined by Primos (LMI Technologies Gmbh, Canada). Besides, a study that included 26 healthy female volunteers aged 25–35 was performed to evaluate the short-acting moisturizing effect. The cuticle moisture content of the forearm was assessed by Corneometer (Courage & Khazaka, Germany) after using the mask 1 h, 6 h, and 8 h. All tests are conducted in accordance with the instructions of the instrument.

Statistical Analysis

The data were expressed as the mean ± standard deviation (SD; $n = 3$) and analyzed using the GraphPad Prism 8.0 Software (GraphPad Software, Inc., San Diego, CA, USA). Analysis of variance (one-way, ANOVA) was performed using SPSS software (version 20.0). Since sample variance was homogeneous, Duncan's test (parametric) was used to identify

statistically different samples. A value of $p < 0.05$ was considered significant.

RESULTS

Chemical Composition Analysis of Main Active Ingredients in Se-MBFB

The total selenium content of Se-MBFB is 0.003 ± 0.001 (ppm). **Table 1** presents the experimental data on some main active components content. As shown in **Table 1**, the content of polyphenols was the highest, followed by the peptides, proteins, and flavonoids, and the polysaccharides content was the lowest. Our results indicated that Se-MB contained functional active polyphenols which were strongly released and produced a high content of new functional active peptides (6.90 mg/mL). In addition, the molecular weight of most active peptides was small (**Supplementary Figure S1**).

The Amino Acids Composition Analysis

The amino acid compositions of free amino acids and peptides in Se-MBFB are presented and summarized in **Figure 1** and **Table 2**. Briefly, 13 free amino acids with small molecular weight were obtained from Se-MBFB (**Figure 1A**), and γ-aminobutyric acid (GABA), Glu, Arg, Ala, and Gly had the top five amino acid contents. Among them, GABA was the dominant amino acid among the free amino acids in Se-MBFB, and its content was much higher than other amino acids (94.81%). Free peptides and protein hydrolysate were composed of 17 amino acids (**Figure 1B**), including 7 essential amino acids. Among them, Glu, Lys, Arg, Gly, and Ala were the top five amino acids.

TABLE 1 | Chemical composition of Se-MBFB.

Sample	Unit (mg/mL)				
	Polysaccharides	Polyphenols	Flavonoids	Peptides	Proteins
Se-MBFB	0.26 ± 0.02	26.11 ± 0.56	0.52 ± 0.02	6.90 ± 0.61	3.24 ± 0.32

Evaluation of Whitening, Moisturizing, and Antioxidant Activities of Se-MBFB *in vitro*

Whitening Activity

Just as shown in **Figure 2A**, the Se-MBFB exhibited an outstanding tyrosinase inhibition rate, notably lower than Vc but more than 80% at high concentration. Se-MBFB could inhibit the activity of tyrosinase in a dose-dependent manner, which implies that Se-MBFB may be a promising new skin whitening ingredient.

The viabilities of cells treated with Se-MBFB (0.5–16%) were determined using the MTT assay. The outcome demonstrated that there was no significant cytotoxic effect under 16% of Se-MBFB (**Figure 2B**). Three doses of Se-MBFB (2, 4, and 8%) were

TABLE 2 | The amino acids of free amino acid and peptides in Se-MBFB (nmol%).

Category	Free amino acid	Amino acid of free peptides and protein hydrolysate
Asp	0.14	3.44
Thr	0.1	1.73
Ser	0.04	1.30
Glu	3.77	47.00
Gly	0.17	4.22
Ala	0.24	3.87
Cys	–	0.14
Val	0.17	1.45
Met	–	0.30
Ile	–	0.71
Leu	–	0.85
Tyr	0.03	0.55
Phe	0.07	3.54
Lys	0.13	23.07
His	0.05	1.38
Arg	0.29	4.38
Pro	–	2.07
GABA	94.81	–

'–'Indicated that the content was lower than the detection limit and not detected.

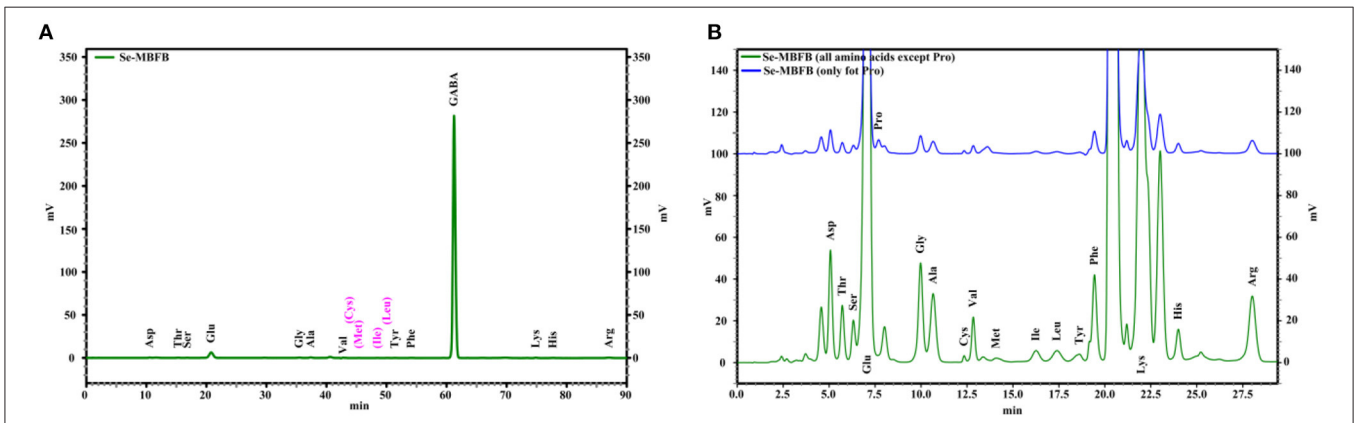

FIGURE 1 | The IC chromatograms of the amino acids of free amino acid **(A)** and free peptides and protein hydrolysate **(B)** in Se-MBFB.

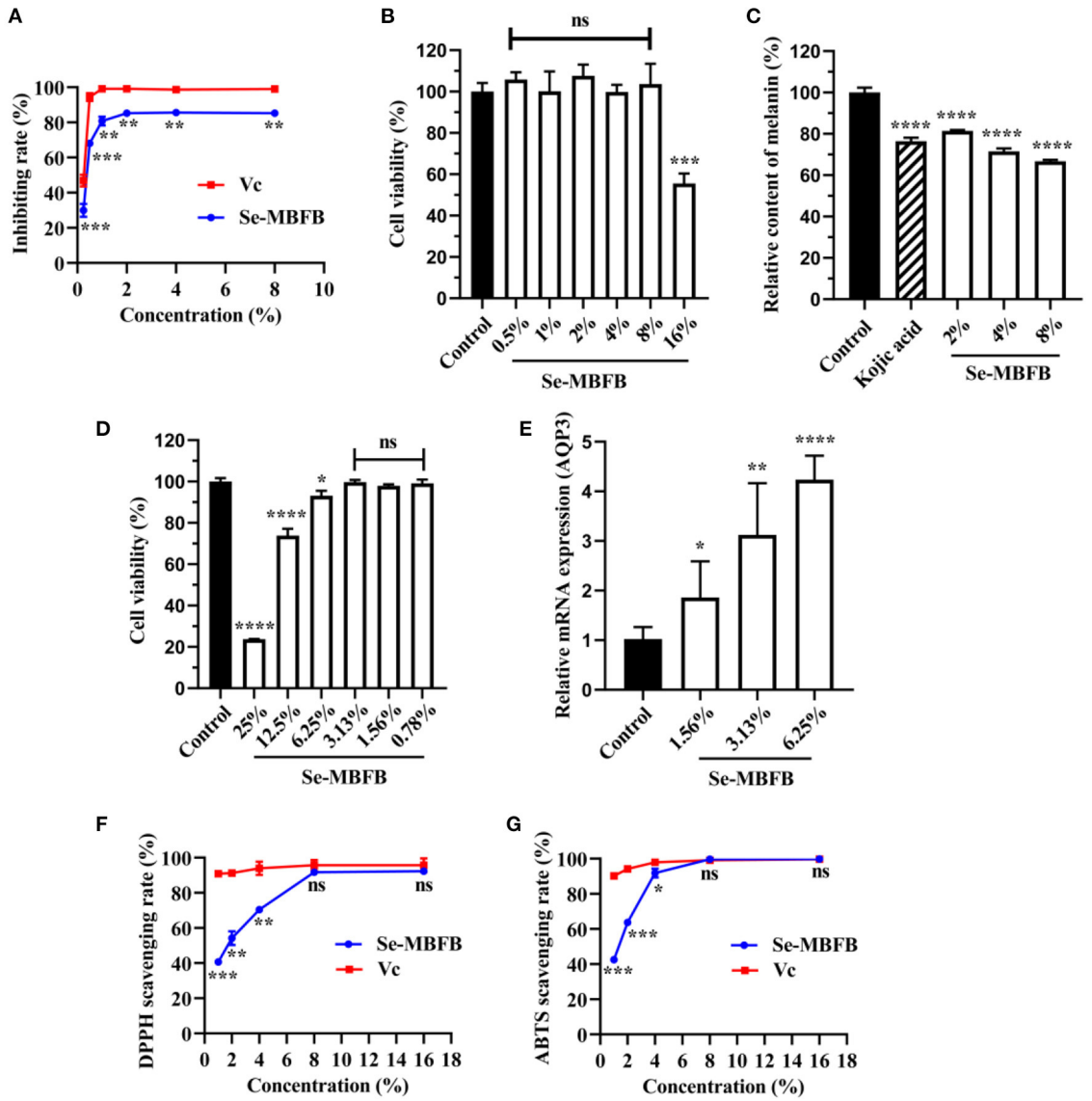

FIGURE 2 | (A) Comparison of tyrosinase inhibition rates between Se-MBFB and Vc; **(B)** effects of Se-MBFB on B16-F10 cell viability; **(C)** effects of Se-MBFB on melanin synthesis in B16-F10 cells; **(D)** effects of Se-MBFB on HDF cell viability; **(E)** effect of Se-MBFB on expression of AQP3 in HDF cells; **(F)** effect of Se-MBFB on DPPH free radical scavenging activity; **(G)** effect of Se-MBFB on ABTS free radical scavenging activity. A significant difference was presented with $p < 0.05$ compared with control or Vc group, '*' represented $p < 0.05$, '**' represented $p < 0.01$, '***' represented $p < 0.001$, and '****' represented $p < 0.0001$.

used to investigate the effect of Se-MBFB on melanin production. The melanin synthesis assay displayed that Se-MBFB showed a consistent and significant reduction in the melanin content of B16F10 mouse melanoma cells in a dose-dependent manner (**Figure 2C**). The data showed that melanin content of cells treated with Se-MBFB was even lower than Kojic acid, further indicating that Se-MBFB has a potential whitening effect.

Moisturizing Activity

The viabilities of cells treated with Se-MBFB (0.78–25%) were determined using the MTT assay. The experimental results showed that the Se-MBFB affected the cell viability of HDF cells in a dose-dependent manner (**Figure 2D**). The concentrations of 6.25, 12.5, and 25% were significantly cytotoxic to cells, but considering the small effect of 6.25% of Se-MBFB on cell viability (>95%) and the potential moisturizing effect of higher concentrations, 6.25, 3.13, and 1.56% of Se-MBFB were used to investigate the moisturizing effect of Se-MBFB. The result exhibits that Se-MBFB prominently and dose-dependently promoted the expression of the moisturizing related gene, AQP3 (**Figure 2E**). It can be inferred that the Se-MBFB has potential moisturizing effects.

Anti-aging Activity

Since excessive free radicals can damage cells and accelerate the aging process of the human body (23), DPPH and ABTS scavenging assays were conducted to evaluate the anti-aging activity of the Se-MBFB. The results demonstrated that DPPH and ABTS radicals were eliminated dose-dependently by Se-MBFB (**Figures 2F,G**). Compared with Vc, the Se-MBFB possessed similar inhibition activity at high concentrations (no significant difference between them), which reveals that the Se-MBFB may have effective anti-aging activity.

Safety Evaluation of Se-MBFB

No potential irritant was presented by heavy metal analysis (**Supplementary Table S2**), skin sensitization test (**Supplementary Table S3**), acute eye/corrosion irritation test (**Supplementary Table S4**), and dermal irritation/corrosion test (**Supplementary Table S5**), suggesting the potential of Se-MBFB for the development of safe facial skincare products.

Whitening, Moisturizing, and Anti-aging Activities of Se-MBFB Facemask *in vivo*

Whitening Efficacy Evaluation

Over the study duration, L* and ITA° values were markedly increased (**Figures 3A,C**), and the MI value was remarkably decreased after treatment with Se-MBFB facemask (**Figure 3D**). Although the b* value was decreased, while there was no significant difference between W0 and W2 or W4 (**Figure 3B**). Compared with W0, there were significant changes in pigmentation level of hyperpigmented spots: L* and ITA° increased at W2 and W4, and MI decreased greatly at W2 and W4. In addition, photographs taken by VISIA-CR at every visit demonstrated the changes in skin features, a gradual skin lightening color is depicted on the face (**Figure 4**). Thus, the Se-MBFB played a good role in whitening by making it less pigmented and melanogenesis.

Moisturizing Efficacy Evaluation

Over the 4-week study, cuticle moisture content was increased significantly and transepidermal water loss was decreased significantly (**Figures 3E,F**), while there was no significant change in skin color uniformity (**Figure 3H**). CORNE values at W2 and W4 were increased and TEWL values were significantly decreased compared with W0, indicating the Se-MBFB facemask can increase moisture in the skin and improve the skin barrier to prevent water loss in the skin. In addition, cuticle moisture content values increased significantly in the treated area (**Figure 3G**). From 1 h until the end of the study at 8 h, the hydration of the sample and control areas was decreased, respectively. However, cuticle moisture content values of the sample areas were more than the control areas, which suggests that the Se-MBFB facemask has a favorable effect on short-acting moisturizing.

Anti-aging Activity Evaluation

On dermatome assessment of wrinkles (**Figures 3I–L**), the number of wrinkles, wrinkle volume, area, and length at W2 and W4 were significantly decreased compared with W0. Furthermore, the wrinkles of female volunteers were improved over time by using a facemask (**Figure 5**). These results prove that the Se-MBFB facemask possesses a good anti-aging effect.

DISCUSSION

Skin, as the body's first barrier, is an important part of maintaining human life and health. To the best of our knowledge, skin is extremely susceptible to damage caused by environmental factors. In addition to the aging factors brought about by age, stress response, pollution, sunlight, and ultraviolet radiation are all important causes of wrinkles in the skin (2). The aging of the social population and the deterioration of the environment will lead to increasingly serious aging of people's skin. Therefore, people will increasingly need long-lasting, efficient, regulatory, and preventive skincare products. Due to the few side effects and good curative effects of natural plants, skincare activities derived from natural plants have received extensive attention in recent years. In this study, we found that natural Se-MBFB had good whitening, moisturizing, and anti-aging effects on skincare with excellent safety. In addition, the facemask prepared by it also exerted good whitening, moisturizing, and anti-aging effects in human skin tests.

As a kind of legume food, MB contains rich nutrients, especially protein. It was reported that MB has been confirmed as an effective source of essential amino acids (deficient in many grains) (24). Thus, far, MB and its extracts have shown good biological activities. It was reported that the fermented MB had a greater effect on the regulation of blood glucose than the non-fermented MB (13). MB processed by boiling and sprouting showed higher hypolipidemic potential (13). Notably, the anti-melanogenesis become one of the hot spots of MB activity in recent years (13). In addition, the polysaccharides, polyphenols, and peptides contained in the mung bean exhibit antioxidative activity, which can improve the body's health. The health benefits of Se have been widely confirmed. It is worth noting that Se is a good antioxidant and anti-aging active substance (25). Therefore, Se-MB exhibited the synergistic health-promoting effects of Se and MB. The results showed that Se-MBFB showed significant whitening, moisturizing, and anti-aging properties after bio-fermentation with a dose-dependent effect. Similarly, Norlaily et al. found the content of free amino acids and soluble phenolic acid in the fermented MB has increased obviously, along with a significant increase in the content of GABA. Furthermore, the fermented MBs have better antioxidant immunomodulatory (26). However, Norlaily et al.'s research focused on the suppression of cancer by fermented mung beans and found that the active substances are mainly phenolic acids and free amino acids. Our studies have revealed the potential of fermented MB as a functional food to maintain skin health, which may be attributed to the polyphenols, polysaccharides, and peptides with a small molecular weight in the MB fermentation broth, as well as the rich amino acid composition (especially GABA).

Tyrosinase, as an oxidoreductase that is widely present in the human body, is the main rate-limiting enzyme in the process of

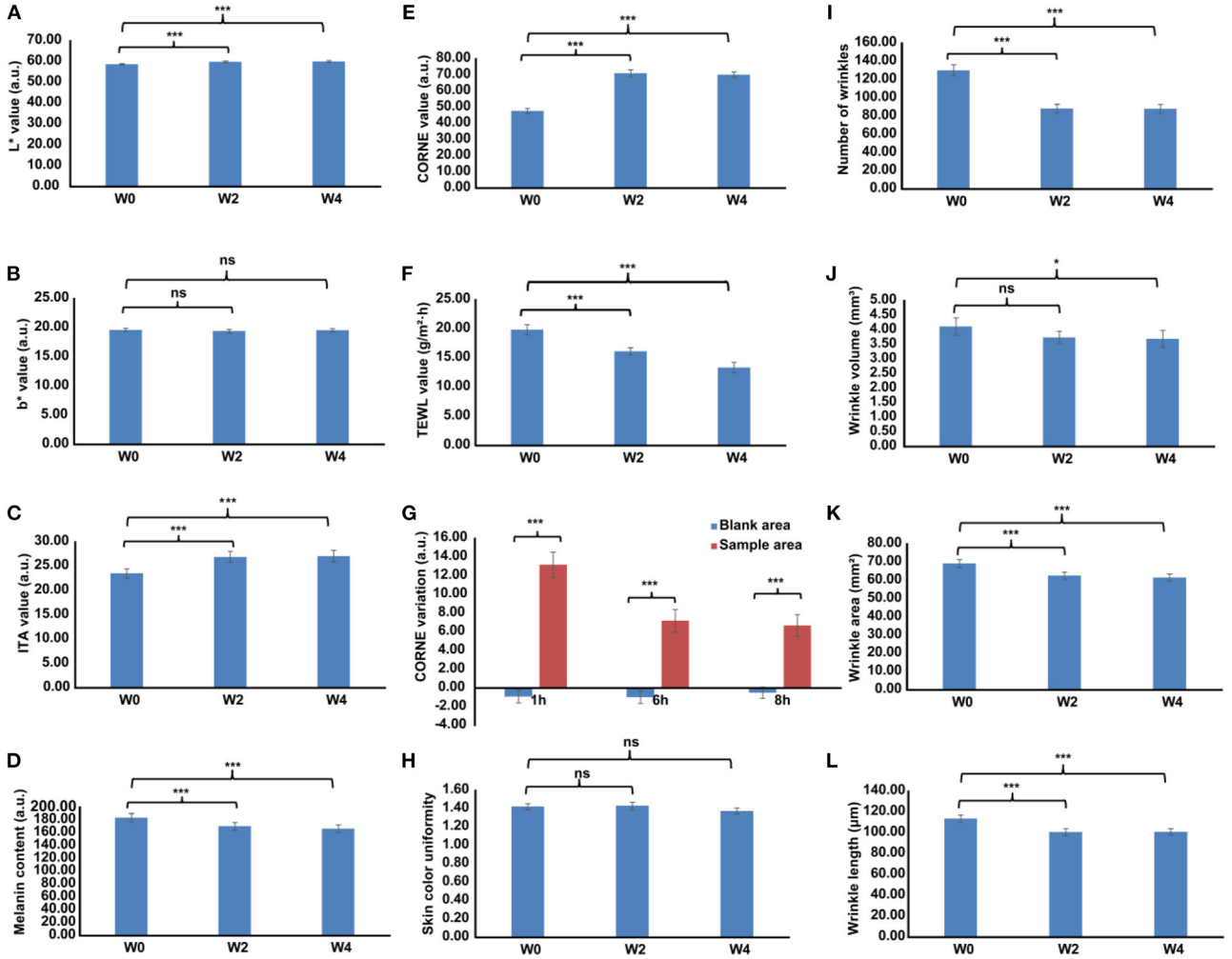

FIGURE 3 | The whitening, moisturizing, and anti-aging activities of Se-MBFB facemask at 0, 2, and 4 weeks, differences adjusted by start values at W0. **(A)** L* value on the cheek areas; **(B)** b* value on the cheek areas; **(C)** ITA° value on the cheek areas; **(D)** melanin index on the cheek areas; **(E)** CORNE value on the cheek areas; **(F)** TEWL value on the cheek areas; **(G)** TEWL variation value on the forearm areas; **(H)** skin color uniformity value on face; **(I)** number of wrinkles on the canthus areas; **(J)** wrinkle volume on the canthus areas; **(K)** wrinkle area on the canthus areas; **(L)** wrinkle length on the canthus areas. L*, skin clarity; b*, skin yellowness; ITA°, individual typology angle; and MI, melanin index; CORNE, cuticle moisture content; TEWL, transepidermal water loss. A significant difference was presented with $p < 0.05$ compared with W0, 'ns' represented $p > 0.05$, '*' represented $0.01 \leq p < 0.05$, '**' represented $0.001 \leq p < 0.01$, and '***' represented $p < 0.001$.

melanin synthesis. Inhibition of tyrosinase activity will reduce the efficiency of catalyzing the synthesis of melanin, resulting in reduced melanin production (27). A previous study showed that the tyrosinase inhibitory ability of the ethanol extract of MB is the highest among the 16 kinds of legume ethanol extracts, and the extract also demonstrates a significant inhibitory effect on melanin production in B16F1 melanoma cells (28). In addition, the proanthocyanidins and condensed tannins in the seed coat of MB show a good inhibitory effect on the tyrosinase activity and melanogenesis of B16 mouse melanoma cells (29). In line with these studies, it was found that Se-MBFB showed a good inhibitory effect on tyrosinase activity and prevents melanin production in a dose-dependent manner, which was also confirmed by the Se-MBFB mask test. Combining these results, it was speculated that this might be related to the presence of some special phenolic compounds in MBs. It was reported that the two pure phenolic compounds isolated from the ethyl acetate extract of MB—vitexin and isovitexin—had excellent inhibitory effects on melanogenesis (30). Furthermore, based on molecular docking, previous studies have reported that proanthocyanidins or condensed tannins in the seed coat of MB could interact with tyrosinase driven by hydrogen bonds and hydrophobic forces, which might exert a crucial role in inhibiting the production of melanin (29).

AQP3, located in the basal layer, is an internal membrane protein responsible for transporting water and uncharged molecules on the cell membrane (31). It was reported that AQP3 could bring water, glycerol, and triglycerides from the sebaceous glands into the epidermis from the circulation, thereby preventing the epidermis from drying, which was very crucial

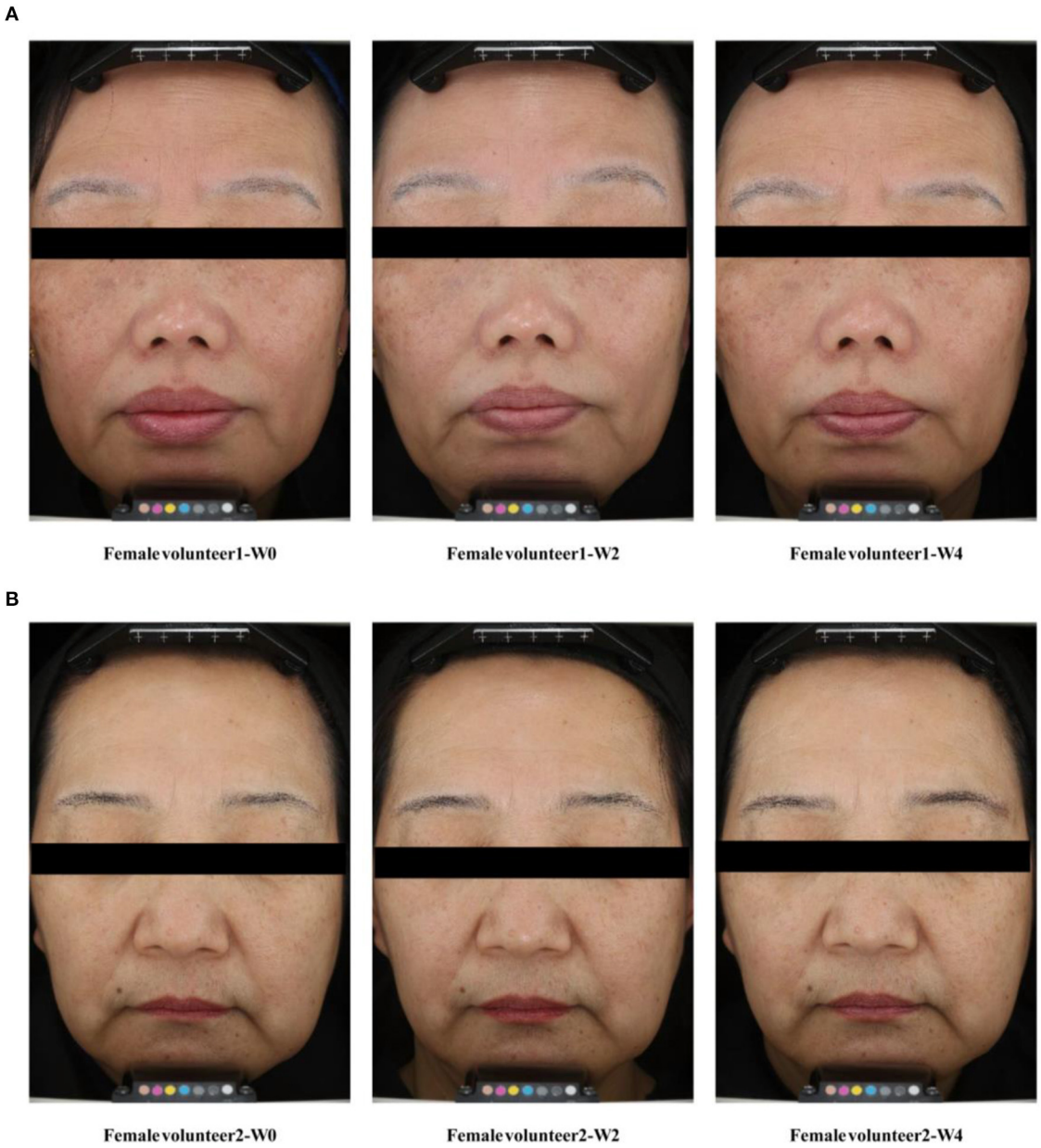

FIGURE 4 | VISIA-CR facial image legend. **(A)** Case 1: Facial condition of volunteer 1 at 0, 2, and 4 weeks; **(B)** Case 2: Facial condition of volunteer 2 at 0, 2, and 4 weeks.

for repairing the skin barrier and moisturizing of the epidermis (31). Free radicals are the normal product of the human body's oxidative metabolism. Nevertheless, excessive free radicals will attack normal cells, cause destructive damage to cells, and ultimately produce irreversible death, which leads to skin aging (32). To date, the moisturizing and anti-aging effects of phenolic substances have been proven. Myung et al. reported that phenolics can prevent wrinkle formation by reducing the levels of matrix metalloproteinase and inflammatory cytokines and increasing the expression of moisturizing factors and antioxidant genes (33). A previous study has reported that phenolic substances could significantly improve skin's fine lines and wrinkles, pigmentation, elasticity, firmness, and light damage (34). The moisturizing and anti-aging effects of small molecule peptides have also been reported (23). Studies have shown that the Glu content in peptides is positively correlated with the inhibition of lipid oxidation. Glu residue is a good metal chelator and free based scavenger attributing to its binding capacity of metal ions (35). Polar amino acids including Lys, Arg, and Gly residues in peptides may play a critical role in the free radical scavenging activity because of their carboxyl and amino groups in the side chains (36). Ala is a hydrophobic amino acid, and

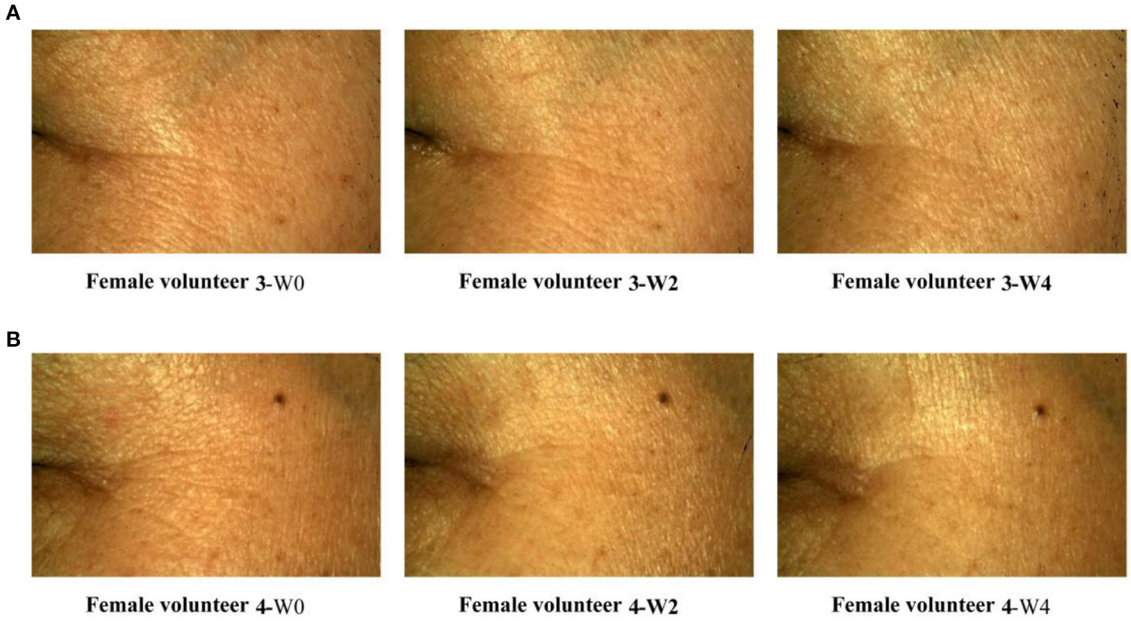

FIGURE 5 | Primos crow's feet image legend. **(A)** Case 1: the crow's feet of volunteer 3 were observed at 0, 2, and 4 weeks; **(B)** Case 2: the crow's feet of volunteer 4 were observed at 0, 2, and 4 weeks.

studies have shown that a higher content of hydrophobic amino acid can promote free radical scavenging and metal chelating activities of protein hydrolysate components (37). In this study, the results indicated that free peptides and protein hydrolysate in Se-MBFB might have good antioxidant activity. Although there are related studies on the AQP3 moisturizing gene, the relevant action mechanism is still unclear (31).

As for the anti-aging capacity of Se-MBFB, it was observed that higher phenols and peptides could scavenge free radicals, thereby reducing skin wrinkles and delaying aging, which confirmed that excessive free radicals could accelerate aging to a certain extent (23). In addition to phenols and peptides, the moisturizing and anti-aging effects of amino acids cannot be ignored. The unbalanced ratio of amino acids (components of protein) will lead to a decrease in skin protein synthesis. Furthermore, epidermal keratinocytes need amino acids to synthesize some antimicrobial peptides and kill pathogens (38). Amino acid substitution is indispensable in the skin because the shedding of stratum corneum cells will lose amino acids. GABA is a non-protein amino acid, which shows an obvious promoting-effect of skin healing, anti-wrinkle, and preventing skin aging, as well as inhibiting nerve activity, which can slow down the excitement of the sensory central nervous system, and prevent it from affecting the muscles, thereby improving expression lines and tightening the skin (39). In this study, GABA in Se-MBFB accounted for 94.81% of free amino acids, which provides effective anti-aging activity of Se-MBFB. Glu is the main constituent amino acid of peptides in Se-MBFB, which can be converted into GABA by Glutamate decarboxylase with anti-aging effects under certain conditions (40). Arg is a dibasic amino acid and the main component of keratin. It can accelerate the synthesis of human collagen tissue, promote wound healing, and has a significant moisturizing effect (41). Ala is a humectant added to some skincare products, which has a certain effect on the water retention of the stratum corneum. Gly is the constituent amino acid of the endogenous antioxidant reducing glutathione, which can condense with salicylaldehyde to inhibit the formation of hydroxyl free radicals in the body to achieve an antioxidant effect and better prevent skin aging (42). Due to their small molecular weight, these amino acids are easier to penetrate the epidermis of the skin and enter the dermis, thereby improving skin health (1).

The application of MB to the production of facial masks has been studied. Similarly, Husni et al. used MB in the production of facial masks because of its antioxidant activity (43). Husni et al. focused on optimizing the formulation of the mask and its physical properties while our study focuses on the activity of the mask. In this study, a mask with Se-MBFB as the main functional substance was designed. An Se-MBFB mask exerted a good anti-wrinkle effect, whitening effect, and moisturizing effect in volunteer trials, laying the foundation for the promotion and application of Se-MBFB.

CONCLUSION

In this study, we prepared Se-MBFB through fermentation and conducted *in vitro* tests to reveal that Se-MBFB possessed good whitening, moisturizing, and antioxidant activities, and there were no safety hazards. The whitening effect was mainly reflected in the good inhibitory effect of Se-MBFB on tyrosinase activity. Phenols, peptides, and free amino acids were the main active substances of Se-MBFB for anti-aging and moisturizing.

Moreover, an Se-MBFB facemask was prepared and a series of skin test experiments on it were designed, which further confirmed the skincare activity of Se-MBFB. Our results provide a good reference for the functional development and economic benefit improvement of Se-MB related agricultural products.

DATA AVAILABILITY STATEMENT

The raw data supporting the conclusions of this article will be made available by the authors, without undue reservation.

ETHICS STATEMENT

The studies involving human participants were reviewed and approved by Intertek Shanghai Healthcare and Beauty Product Clinical Research Service Lab. The patients/participants provided their written informed consent to participate in this study.

AUTHOR CONTRIBUTIONS

KW: conceptualization and writing—original draft preparation. CG: figure preparation and data acquisition. JZ: writing—original draft preparation and figure preparation. YaW: investigation, methodology, and revision. MW: data acquisition. XH and MZ: methodology. XuW and JL: software. YuW: revision. XiW: supervision, reviewing, and editing. All authors contributed to the article and approved the submitted version.

FUNDING

This study was funded by projects commissioned by enterprises and institutions (2019310031001329) of Shanghai Yuemu Cosmetics Co., Ltd., Shanghai, China. The authors are grateful for financially sponsored by Program of Shanghai Academic/Technology Research Leader (20XD1433500), Shanghai Agricultural Leading Talent Program, the National Natural Science Foundation of China (No. 32172223), and the National Key R&D Program of China (No. 2018YFC1604401).

SUPPLEMENTARY MATERIAL

The Supplementary Material for this article can be found online at: https://www.frontiersin.org/articles/10.3389/fnut.2022.837168/full#supplementary-material

REFERENCES

1. Solano F. Metabolism and functions of amino acids in the skin. *Adv Exp Med Biol*. (2020) 1265:187–99. doi: 10.1007/978-3-030-45328-2_11
2. Taylor SE, Repetti RL, Seeman T. Health psychology: what is an unhealthy environment and how does it get under the skin? *Annu Rev Psychol.* (1997) 48:411–47. doi: 10.1146/annurev.psych.48.1.411
3. Chowdhury A, Nosoudi N, Karamched S, Parasaram V, Vyavahare N. Polyphenol treatments increase elastin and collagen deposition by human dermal fibroblasts; implications to improve skin health. *J Dermatol Sci.* (2021) 102: 94–100. doi: 10.1016/j.jdermsci.2021.03.002
4. Amakye WK, Hou C, Xie L, Lin X, Gou N, Yuan E, et al. Bioactive anti-aging agents and the identification of new anti-oxidant soybean peptides. *Food Biosci.* (2021) 42:101194. doi: 10.1016/j.fbio.2021.101194
5. Kang CH, Rhie SJ, Kim YC. Antioxidant and skin anti-aging effects of marigold methanol extract. *Toxicol Res.* (2018) 34:31–9. doi: 10.5487/TR.2018.34.1.031
6. Lv J, Ai P, Lei S, Zhou F, Chen S, Zhang Y. Selenium levels and skin diseases: systematic review and meta-analysis. *J Trace Elem Med Biol.* (2020) 62:126548. doi: 10.1016/j.jtemb.2020.126548
7. Burke KE, Burford RG, Combs GF. French IW, Skeffington DR. The effect of topical L-selenomethionine on minimal erythema dose of ultraviolet irradiation in humans. *Photodermatol Photoimmunol Photomed.* (1992) 9:52–7. doi: 10.1016/S0190-9622(08)80809-2
8. Michalsson G, Edqvist LE. Erythrocyte glutathione peroxidase activity in acne vulgaris and the effect of selenium and vitamin E treatment. *Acta Derm Venereol.* (1984) 64:9–14. doi: 10.1097/00006534-198604000-00106
9. Zhu J, Du M, Wu M, Yue P, Yang X, Wei X, et al. Preparation, physicochemical characterization and identification of two novel mixed ACE-inhibiting peptides from two distinct tea alkali-soluble protein. *Eur Food Res Technol.* (2020) 246:1483–94. doi: 10.1007/s00217-020-03505-z
10. Kundu A, Paul S, Dey A, Pal A. High throughput sequencing reveals modulation of microRNAs in Vigna mungo upon Mungbean Yellow Mosaic India Virus inoculation highlighting stress regulation. *Plant Sci.* (2017) 257:96–105. doi: 10.1016/j.plantsci.2017.01.016
11. Wei Y, Sun C, Dai L, Zhan X, Gao Y. Structure, physicochemical stability and *in vitro* simulated gastrointestinal digestion properties of β-carotene loaded zein propylene glycol alginate composite nanoparticles fabricated by emulsificationevaporation method. *Food Hydrocolloids*. (2018) 81:149–58. doi: 10.1016/j.foodhyd.2018.02.042
12. Wei Y, Tong Z, Dai L, Wang D, Lv P, Liu J, et al. Influence of interfacial compositions on the microstructure, physiochemical stability, lipid digestion and β -carotene bioaccessibility of Pickering emulsions. *Food Hydrocolloids*. (2020) 104:105738. doi: 10.1016/j.foodhyd.2020.105738
13. Hou D, Yousaf L, Xue Y, Hu J, Wu J, Hu X, et al. Mung bean (*Vigna radiata* L.): bioactive polyphenols, polysaccharides, peptides, and health benefits. *Nutrients.* (2019) 11:1238–66. doi: 10.3390/nu11061238
14. Sandberg AS. Bioavailability of minerals in legumes. *Br J Nutr.* (2002) 88:S 281–5. doi: 10.1079/BJN/2002718
15. Li L, Wang L, Fan W, Jiang Y, Zhang C, Li J, et al. The application of fermentation technology in traditional Chinese medicine: a review. *Am J Chin Med*. (2020) 48:899–921. doi: 10.1142/S0192415X20500433
16. Song YS, Frias, J, Martinez-Villaluenga C, Vidal-Valdeverde C, Mejia EG. Immunoreactivity reduction of soybean meal by fermentation, effect on amino acid composition and antigenicity of commercial soy products. *Food Chem*. (2008) 108:571–81. doi: 10.1016/j.foodchem.2007.11.013
17. Shazly AB. He Z, El-Aziz MA, Zeng M, Zhang S, Qin F, et al. Fractionation and identification of novel antioxidant peptides from buffalo and bovine casein hydrolysates. *Food Chem*. (2017) 232:753–62. doi: 10.1016/j.foodchem.2017.04.071
18. Xu J, Lv J. Determination of content of peptides in milk protein hydrolysates. *Food Sci Technol.* (2010) 35:275–8. doi: 10.13684/j.cnki.spkj.2010.12.051
19. Bradford MM. A rapid and sensitive method for the quantitation of microgram quantities of protein utilizing the principle of protein-dye binding. *Anal Biochem.* (1976) 72:248–54. doi: 10.1016/0003-2697(76)90527-3
20. Frenz J, Quan CP, Hancock WS, Bourell J. Characterization of a tryptic digest by high-performance displacement chromatography and mass spectrometry. *J Chromatogr A*. (1991) 557:289–305. doi: 10.1016/S0021-9673(01)87139-9
21. Ventura MG, Stibilj V, Freitas MC, Pacheco AM. Determination of ultratrace levels of selenium in fruit and vegetable samples grown and consumed in Portugal. *Food Chem*. (2009) 115:200–6. doi: 10.1016/j.foodchem.2008.10.089
22. Kim IS, Yoon SJ, Park YJ, Lee HB. Inhibitory effect of ephedrannins A and B from roots of Ephedra sinica STAPF on melanogenesis. *Biochim Biophys Acta Gen Subj.* (2015) 1850:1389–96. doi: 10.1016/j.bbagen.2015.04.001

23. Hekimi S, Lapointe J, Wen Y. Taking a "good" look at free radicals in the aging process. *Trends Cell Biol.* (2011) 21:569–76. doi: 10.1016/j.tcb.2011.06.008
24. Spallhalz JE, Boylan LM, Larsen HS. Advances in understanding selenium's role in the immune system. *Ann N Y Acad Sci*. (1990) 5871:123–39. doi: 10.1111/j.1749-6632.1990.tb00140.x
25. Nair RM, Yang RY, Easdown WJ, Thavarajah D, Keatinge JD. Biofortification of mungbean (*Vigna radiata*) as a whole food to enhance human health. *J Sci Food Agric.* (2013) 93:1805–13. doi: 10.1002/jsfa.6110
26. Ali NM, Yeap SK, Yusof HM, Beh BK, Ho WY, Koh SP, et al. Comparison of free amino acids, antioxidants, soluble phenolic acids, cytotoxicity and immunomodulation of fermented mung bean and soybean. *J Sci Food Agric.* (2016) 96:1648–58. doi: 10.1002/jsfa.7267
27. Tang H, Cui F, Liu L, Li Y. Predictive models for tyrosinase inhibitors: challenges from heterogeneous activity data determined by different experimental protocols. *Comput Biol Chem.* (2018) 73:79–84. doi: 10.1016/j.compbiolchem.2018.02.007
28. Jeong YM, Ha JH, Noh GY, Park SN. Inhibitory effects of mung bean (*Vigna radiata* L.) seed and sprout extracts on melanogenesis. *Food Sci Biotechnol.* (2016) 25:567–73. doi: 10.1007/s10068-016-0079-6
29. Chai WM, Ou-Yang C, Huang Q, Lin MZ, Wang YX, Xu KL, et al. Antityrosinase and antioxidant properties of mung bean seed proanthocyanidins: novel insights into the inhibitory mechanism. *Food Chem.* (2018)260:27–36. doi: 10.1016/j.foodchem.2018.04.001
30. Yao Y, Cheng X, Wang L, Wang S, Ren G. Mushroom tyrosinase inhibitors from mung bean (*Vigna radiatae* L.) extracts. *Int J Food Sci Nutr.* (2012) 63:358–61. doi: 10.3109/09637486.2011.629177
31. Schrader A, Siefken W, Kueper T, Breitenbach U, Gatermann C, Sperling G, et al. Effects of glyceryl glucoside on AQP3 expression, barrier function and hydration of human skin. *Skin Pharmacol Physiol.* (2012) 25:192–9. doi: 10.1159/000338190
32. Francisco L, Pinto D, Rosseto H, Toledo L, Santos R, Tobaldini-Valerio F, et al. Evaluation of radical scavenging activity, intestinal cell viability and antifungal activity of Brazilian propolis by-product. *Food Res Int.* (2018) 105:537–47. doi: 10.1016/j.foodres.2017.11.046
33. Myung DB, Han HS, Shin JS, Ji YP, Lee KT. Hydrangenol isolated from the leaves of hydrangea serrata attenuates wrinkle formation and repairs skin moisture in UVB-irradiated hairless mice. *Nutrients.* (2019) 11:2345. doi: 10.3390/nu11102354
34. Chaudhuri RK, Bojanowski K. Bakuchiol: a retinol-like functional compound revealed by gene expression profiling and clinically proven to have anti-aging effects. *Int J Cosmet Sci.* (2014) 36:221–30. doi: 10.1111/ics.12117
35. Torres-Fuentes C, Alaiz M, Vioque J. Iron-chelating activity of chickpea protein hydrolysate peptides. *Food Chem.* (2012) 134:1585–8. doi: 10.1016/j.foodchem.2012.03.112
36. Yang XR, Zhang L, Ding DG, Chi CF, Wang B, Huo JC. Preparation, identification, and activity evaluation of eight antioxidant peptides from protein hydrolysate of hairtail (*Trichiurus japonicas*) muscle. *Mar Drugs.* (2019) 17:23. doi: 10.3390/md17010023
37. Pownall TL, Udenigwe CC, Aluko RE. Amino acid composition and antioxidant properties of pea seed (*Pisum sativum* L.) enzymatic protein hydrolysate fractions. *J Agric Food Chem.* (2010) 58:4712–8. doi: 10.1021/jf904456r
38. Park K, Lee S, Lee YM. Sphingolipids and antimicrobial peptides: function and roles in atopic dermatitis. *Biomol Ther.* (2013) 21:251–7. doi: 10.4062/biomolther.2013.058
39. Denda M, Inoue K, Inomata S, Denda S. Gamma-Aminobutyric acid (A) receptor agonists accelerate cutaneous barrier recovery and prevent epidermal hyperplasia induced by barrier disruption. *J Invest Dermatol.* (2002) 119:1041–7. doi: 10.1046/j.1523-1747.2002.19504.x
40. Ito K, Tanaka K, Nishibe Y, Hasegawa J, Ueno H. GABA-synthesizing enzyme, GAD67, from dermal fibroblasts: evidence for a new skin function. *Biochim Biophys Acta Gen Subj*. (2007) 1770:291–6. doi: 10.1016/j.bbagen.2006.09.017
41. Re R, Pellegrini N, Proteggente A, Pannala A, Yang M, Rice-Evans C. Antioxidant activity applying an improved ABTS radical cation decolorization assay. *Free Rad Biol Med.* (1999) 26:1231–7. doi: 10.1016/S0891-5849(98)00315-3
42. Li P, Wu G. Roles of dietary glycine, proline, and hydroxyproline in collagen synthesis and animal growth. *Amino Acids*. (2018) 50:29–38. doi: 10.1007/s00726-017-2490-6
43. Husni1 P, Dewi EM. Formulation of peel-off gel mask containing mung bean (*Vigna radiata* (L.) Wilczek) extract. *Indones J Pharm.* (2019) 1:7–12. doi: 10.24198/idjp.v1i2.19894

Conflict of Interest: MZ and JL were employed by Shanghai Yuemu Cosmetics Co., Ltd. XuW was employed by Enshi Selenium Impression Agricultural Technology Co., Ltd. Shadi Township.

The authors declare that this study received funding from Shanghai Yuemu Cosmetics Co., Ltd., Shanghai, China. They instructed and assisted in the production method of Se-MBFM in this study.

The remaining authors declare that the research was conducted in the absence of any commercial or financial relationships that could be construed as a potential conflict of interest.

Publisher's Note: All claims expressed in this article are solely those of the authors and do not necessarily represent those of their affiliated organizations, or those of the publisher, the editors and the reviewers. Any product that may be evaluated in this article, or claim that may be made by its manufacturer, is not guaranteed or endorsed by the publisher.

Copyright © 2022 Wei, Guo, Zhu, Wei, Wu, Huang, Zhang, Li, Wang, Wang and Wei. This is an open-access article distributed under the terms of the Creative Commons Attribution License (CC BY). The use, distribution or reproduction in other forums is permitted, provided the original author(s) and the copyright owner(s) are credited and that the original publication in this journal is cited, in accordance with accepted academic practice. No use, distribution or reproduction is permitted which does not comply with these terms.

frontiers in Nutrition

REVIEW
published: 25 March 2022
doi: 10.3389/fnut.2022.859189

The Mechanism of Acrylamide-Induced Neurotoxicity: Current Status and Future Perspectives

Mengyao Zhao[1,2], Boya Zhang[1] and Linlin Deng[1]*

[1] State Key Laboratory of Bioreactor Engineering, School of Biotechnology, East China University of Science and Technology, Shanghai, China, [2] Shanghai Collaborative Innovation Center for Biomanufacturing Technology (SCICBT), Shanghai, China

Acrylamide (ACR), a potential neurotoxin, is produced by the Maillard reaction between reducing sugars and free amino acids during food processing. Over the past decade, the neurotoxicity of ACR has caused increasing concern, prompting many related studies. This review summarized the relevant literature published in recent years and discussed the exposure to occupational, environmental, and daily ACR contamination in food. Moreover, ACR metabolism and the potential mechanism of ACR-induced neurotoxicity were discussed, with particular focus on the axonal degeneration of the nervous system, nerve cell apoptosis, oxidative stress, inflammatory response, and gut-brain axis homeostasis. Additionally, the limitations of existing knowledge, as well as new perspectives, were examined, specifically regarding the connection between the neurotoxicity caused by ACR and neurodegenerative diseases, NOD-like receptor protein 3 (NLRP3) inflammasome-related neuroinflammation, and microbiota-gut-brain axis signaling. This review might provide systematic information for developing an alternative pathway approach to assess ACR risk.

Keywords: acrylamide, neurotoxicity, oxidative stress, apoptosis and autophagy, inflammation, gut-brain axis

OPEN ACCESS

Edited by:
Shuai Chen,
Wuhan University, China

Reviewed by:
Marta Kopańska,
University of Rzeszów, Poland
Yuchen Zhu,
China Agricultural University, China
Yuan Yuan,
Jilin University, China
Yahui Guo,
Jiangnan University, China

****Correspondence:***
Mengyao Zhao
myzhao@ecust.edu.cn

Specialty section:
This article was submitted to Food Chemistry, a section of the journal Frontiers in Nutrition

Received: *21 January 2022*
Accepted: *28 February 2022*
Published: *25 March 2022*

Citation:
Zhao M, Zhang B and Deng L (2022) The Mechanism of Acrylamide-Induced Neurotoxicity: Current Status and Future Perspectives. Front. Nutr. 9:859189. doi: 10.3389/fnut.2022.859189

INTRODUCTION

For decades, acrylamide (ACR) has been widely used in the paper industry, as well as for wastewater treatment and soil conditioning. It is also used in medicine and the textile industry, mainly to synthesize high molecular polymers, such as poly-ACR (1). In 1994, ACR was listed as a class 2A substance by the International Agency for Research on Cancer (IARC) ("most likely carcinogenic

Abbreviations: ACR, acrylamide; ASC, apoptosis-associated speck-like protein containing CARD; Bax, BCL2-associated X protein; Bcl-2, B-cell lymphoma-2; BDNF, brain-derived neurotrophic factor; Caspase-1, cysteinyl aspartate specific proteinase 1; DAMPs, damage-associated molecular patterns; DNA, deoxyribonucleic acid; EFSA, European Food Safety Authority; ERK, extracellular regulated protein kinases; EU, European Union; GA, glycidamide; GSDMD, gasdermin D; GSDME, gasdermin E; GSH, glutathione; Hb, hemoglobin; IARC, International Agency for Research on Cancer; IL-1β, interleukin-1β; IL-6, interleukin-6; IL-18, interleukin-18; JECFA, Joint FAO/WHO Expert Committee on Food Additives; JNK, c-Jun N-terminal kinase; LC3-II, microtubule associated protein 1 light chain 3-II; LPS, lipopolysaccharide; MAPK, mitogen-activated protein kinase; MDA, malondialdehyde; Nrf2, nuclear factor E2-related factor-2; NF-κB, nuclear factor-kappa B; NO, nitric oxide; NLR, nod like receptor; NLRP3, NOD-like receptor protein 3; 8-OHdG, 8-hydroxy-2-deoxyguanosine; PAMPs, pathogen-associated molecular patterns; PRRs, pattern recognition receptors; ROS, reactive oxygen species; SCFA, short-chain fatty acids; SD, Sprague Dawley; TNF-α, tumor necrosis factor-α; WHO, World Health Organization.

to humans") (2). In 2002, Swedish scientists first discovered the presence of ACR in heat-processed foods rich in asparagine, raising widespread concern (3, 4). In the same year, two articles on the formation mechanism of ACR were published in Nature, confirming that the Maillard reaction was primarily responsible for ACR formation in heat-processed foods, causing concern regarding ACR exposure *via* normal dietary intake (5, 6). In 2015, the European Food Safety Authority (EFSA) issued a survey report on the ACR content in 43,419 food products. The results showed that the average ACR content in fried potato products was as high as 1.0 mg/kg, while the highest ACR content in coffee was 4.5 mg/kg (7). Moreover, the European Commission set the residue limits of ACR in potato crisps at 750 μg/kg and roast coffee and coffee substances at 400–850 μg/kg (8). Therefore, ACR toxicity and its risk to human health require urgent attention due to its abundance in food products and the environment (9).

Acrylamide is responsible for developmental genotoxicity, neurotoxicity, and potentially carcinogenicity, of which neurotoxicity has been confirmed *via* human and animal experiments (10). Therefore, neurotoxicity is closely connected with human health. For decades, results showed similar phenotypical neurotoxicity in various laboratory animals, including dogs, cats, guinea pigs, rabbits, and rodents when repeatedly exposed to ACR levels ranging between 0.5 and 50 mg/kg/day (11–13). These neurological disorders may be caused by covalent adduct formation between highly nucleophilic cysteine and ACR at the active location of the presynaptic neuron. This process deactivates neurons and impacts neurotransmitter transfer, leading to neurotoxicity (14). Moreover, oxidative stress serves as a biochemical and physiological activation signal and is, directly and indirectly, related to the neurotoxicity caused by ACR (15, 16). Although the potential molecular mechanism reported in recent years as underlying ACR-related neurotoxicity is multifaceted, a complete characterization and summary of the comprehensive mechanical system and its impact are still required.

Therefore, this review summarizes the relevant literature published in recent years, discusses the primary potential mechanisms, and provides insight into the axonal degeneration of the nervous system, nerve cell apoptosis, oxidative stress, inflammatory response, and gut-brain axis homeostasis. Furthermore, the existing challenges and research aspects showing potential for examining ACR-induced neurotoxicity are discussed. This review may provide a more complete theoretical foundation to uncover the ACR toxicity mechanism while improving its subsequent adverse impact. This paper offers a fresh perspective on neurotoxicity while furnishing guidance regarding health safety development.

EXPOSURE TO ACRYLAMIDE

Occupational and Environmental Exposure

As a raw material used during industrial production, ACR often enters the water, soil, atmosphere, and other environmental media, damaging human health and severely affecting the nervous system (17). Occupational exposure is one of the main ACR exposure pathways. As early as the 1950s, it was reported that several workers exposed to ACR showed symptoms of poisoning, such as weakness, numbness, leg weakness, and unsteady gait. In recent years, occasional studies have examined ACR neurotoxicity, primarily acute occupational ACR poisoning during construction, coal mining, flocculator manufacturing, and tunnel construction (18). In addition to occupational exposure, ACR exposure can occur *via* drinking water, especially when public drinking water sources are treated using polyacrylamide as a flocculant (19), leading to high ACR concentrations in tap water (20, 21). Moreover, residual ACR is present in cosmetics, packaging materials, and cigarettes, while exposure can also occur *via* direct skin contact and alimentary contact (22–24). **Table 1** summarizes the environmental and occupational characteristics of ACR exposure, including routes, estimated doses, typical cases, and threshold values. In summary, extensive research has been conducted involving the potentially harmful effect of ACR in occupational settings and daily life. However, additional studies are necessary to fully understand the chronic toxic effect of ACR and improve risk assessment to protect public health.

Foodborne Exposure

Consumers can be directly exposed to ACR *via* the oral intake of high-carbohydrate foods, such as potato chips, baked cereals, and bread (18). As early as 2010, the JECFA presented data regarding the ACR detected in 12,582 food samples from 31 countries, which included fried potatoes, bread, biscuits, coffee, and other food products. The results indicated the presence of ACR in almost all the analyzed food samples, with the highest levels in fried potato products and coffee (21). In 2011, the JECFA evaluated the dietary intake of ACR in eight representative countries. The findings showed that the average daily intake of the general population was about 1 μg/kg b.w., with the highest consumption at about 4 μg/kg b.w. (25). Moreover, young people tend to consume food products high in carbohydrates more frequently. The average exposure of adolescents aged 10–18 is 0.4–0.9 μg/kg b.w./day, and the high-level exposure is 0.9–2.0 μg/kg b.w./day. For children aged 3–10 the average exposure is 0.9–1.6 μg/kg b.w./day, while the high-level exposure can reach 1.4–3.2 μg/kg b.w./day. Based on body weight, the intake of ACR in children is two to three times higher than that of adults (7). In 2015–2017, a survey report by EFSA showed that the average ACR content in fried potatoes and coffee products remained high at 1 and 5 mg/kg, respectively (7). In 2017, the EU set the benchmark levels for the presence of ACR in food products, with that of French fries (ready-to-eat) at 500 μg/kg and potato dough products at 750 μg/kg. The benchmark level for roasted coffee was 400 μg/kg, while that of instant coffee was 850 μg/kg (26). Therefore, ACR toxicity and its risk to human health require urgent attention due to its abundance in food products and high exposure frequency.

The Metabolic Pathway of Acrylamide

Acrylamide is a small-molecule hydrophilic substance. It is absorbed *via* the gastrointestinal tracts of humans and animals

TABLE 1 | A summary of the occupational and environmental exposure to ACR.

	Exposure route	Typical cases	Estimated exposure dose	Threshold value
Occupational exposure	Construction, coal mining, flocculator manufacturing, tunnel construction (18)	In 2001, the hemoglobin (Hb) adduct levels of tunnel workers exposed to ACR were measured, representing the blood biomarker for ACR exposure (120)	17.7 nmol/g globin (163 workers)	~0.02–0.07 nmol/g globin
		Two workers developed peripheral neuropathy after ACR monomer exposure in a closed environment without sufficient ventilation (121)	/	0.1 mg/mL (EU) (122)
Environmental exposure	Drinking water (19)	In the United Kingdom, ACR was found in tap water in an area where polyacrylamide was used for water treatment (20)	0.75 μg/L	<0.5 μg/L (WHO) (21)
		Plymouth, United Kingdom uses polyacrylamide to treat public drinking water. High ACR concentrations were found in drinking water samples (123)	4.5 μg/L	
	Cosmetics (24)	ACR in cosmetics is absorbed through the skin	1 μg/kg b.w./day	<5 mg/kg (American Cosmetic Raw Material Evaluation Committee) (24) Body care products<0.1 ppm Other cosmetic products <0.5 ppm (102)
	Packaging materials (22)	ACR is widely used as a papermaking additive in many paper packages. Tests show that ACR exposure from paper packaging poses a safety risk (124)	0.5–8.8 mg/kg	/
	Cigarettes (7)	Zhang et al. examined 51 local volunteers and further correlated the exposure model with the daily intake of ACR (23)	Non-smokers 1.08 ± 0.51 μg/kg b.w./day Smokers 4.18 ± 1.13 μg/kg b.w./day	/

and passively diffused to the entire body. ACR can also pass through the blood-brain barrier to directly exert its toxic effect on the nervous system (27). ACR follows two main metabolic pathways in the body (**Figure 1**). (1) Briefly, an enzymatic reaction occurs when catalyzed by the cytochrome P450 enzyme system, CYP2E1, converting ACR into glycidamide (GA) (28). Studies have found that GA can combine with purine bases on deoxyribonucleic acid (DNA) molecules to form DNA adducts, inhibit the release of neurotransmitters, cause nerve terminal degeneration, damage nerve structures, and display distinct cumulative effects. In addition, the ability of GA to form Hb and DNA adducts is more significant than ACR. Therefore, it is believed that this pathway is the main route of ACR-induced neurotoxicity (29, 30). (2) ACR undergoes biotransformation and is catalyzed by glutathione S-transferase in the liver, combining with glutathione to generate N-acetyl-S-cysteine. It is further degraded into mercapturic ACR acids, which are excreted in the urine. This pathway is mainly responsible for ACR detoxification (31). Glutathione consumption reduces antioxidant levels, leading to excessive active oxygen accumulation and causing oxidative stress and neurotoxicity (32). Various reviews elaborate on the metabolic pathways of ACR. Those published by Koszucka et al. (27), Rifai et al. (28), and Fang et al. (30) are recommended for more details.

Model and Dosage

Previous studies involving ACR neurotoxicity mostly used a dose of 5–50 mg/kg/day during animal experiments in the in vivo model, with an average dose range of 1–5 mM in various cell lines. Toxic relationship and mechanism investigation mainly established between exposure to high concentrations (>2 mM *in vitro* or 20 mg/kg body weight *in vivo*) of ACR and neurotoxicity.

Barber and LoPachin exposed Sprague Dawley (SD) rats to a dose of 50 mg/kg/day for 28 days to explore ACR neurotoxicity, revealing that the mice displayed significant weight loss and abnormal gait (33). Yu et al. exposed male Wistar rats to doses of 20 and 40 mg/kg/days for 8 weeks, revealing the same phenomenon (34). In 2011, another study exposed adult male SD rats to 50 mg/kg/day ACR for 10 days. The results showed that ACR toxicity was associated with selective nerve terminal damage in the central and peripheral nervous systems (35). Santhanasabapathy and Vasudevan exposed adult Swiss albino male mice to a dose of 20 mg/kg/day for 4 weeks, indicating that ACR promoted microglial and astrocyte activation (36). Recently Guo and Cao exposed adult male SD rats to 40 mg/kg/day ACR for 4 weeks, showing the death of hippocampal neurons and neurotoxicity caused by oxidative stress (37). Moreover, the ACR exposure dose is relatively high in most *in vitro* studies. Human embryonic stem cells (H1hESC) were exposed to 2.5 mM and 5 mM for 24 h, demonstrating that ACR inhibited neuron differentiation based on the oxidative stress response (38). Similarly, Li and Sun exposed rat adrenal pheochromocytoma cells (PC12) to 5 mM ACR for 24 h, revealing oxidative stress-induced cytotoxicity (39). Triningsih and Yang used 5 mM 24 h ACR treatment to explore the

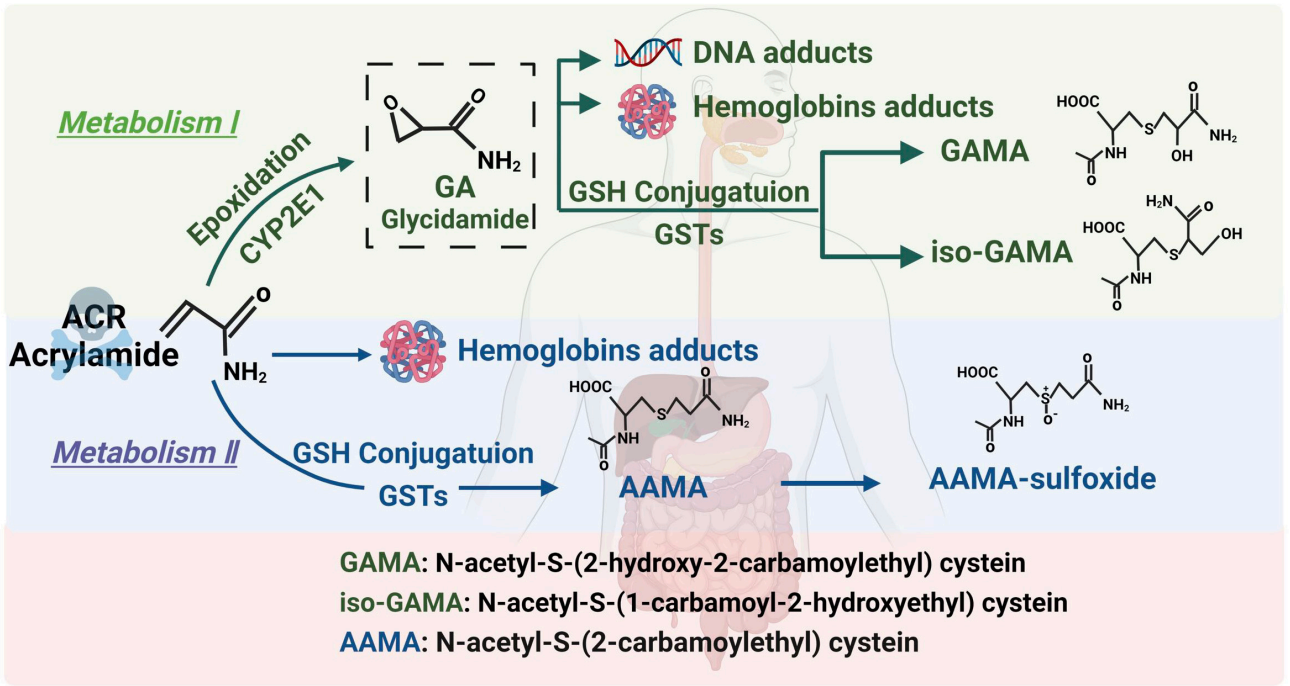

FIGURE 1 | The metabolic pathway of ACR.

relationship between ACR neurotoxicity and autophagy in PC12 cells (40).

Exposure to high ACR concentrations can produce central-peripheral signal transduction obstacles and influence neural development in occupationally exposed humans and laboratory animals (41–43). However, dietary intake is the main source of ACR exposure in humans (4). Several *in vivo* studies established models with a dose below 5 mg/kg/day and exposure times exceeding 60 days to investigate the neurotoxic effect and mechanism of foodborne ACR exposure. For example, SD rats provided with treated drinking water containing ACR dosages of 0, 0.5, or 5 mg/kg/day for 12 months displayed gait abnormality and cognitive dysfunction (44). Zhao et al. orally exposed C57BL/6 male mice to a low ACR dose of 5 mg/kg/day for 60 day (sub-chronic toxicity) to explore its neurotoxicity. This group displayed a slight gait abnormality at the end of the intonation period (45). Similarly, doses (about 1–5 μM) closer to chronic foodborne exposure are relatively rare in *in vitro* exposure models. Zong et al. demonstrated that ACR exposure increased the expression of cytokines and inflammatory markers in BV-2 microglial cells after treatment with a low ACR dose of 5 μM (46). Currently, extensive research has focused on the high-dose neurotoxicity, while chronic foodborne exposure of ACR has not received enough attention. In addition, health risk assessments require information regarding the relationship between exposure, internal brain dosage, and the observed toxic effects. Therefore, further research is needed to clarify and assess the risk of foodborne ACR neurotoxicity.

MECHANISMS OF ACRYLAMIDE-INDUCED NEUROTOXICITY

Axonal Degeneration

Early research suggests that ACR-induced neurotoxicity may be related to nerve-ending damage in the peripheral and central nervous systems (47). Studies have shown that ACR can change the β-actin, β-tubulin, and other cytoskeletal proteins, destroying the neuron structures to cause neurotoxicity. Subsequent morphological, electrophysiological, and electrochemical research shows that nerve endings represent the primary target of ACR toxicity (48). With the passage of exposure time, the damage is gradually aggravated and eventually leads to axonal degeneration. Chronic ACR poisoning can cause selective peripheral and central nerve fiber degeneration, which initially occurs at the ends of long and large nerve fibers, followed by progressive, continuous proximal axon degeneration (49). Further studies show that ACR affects the levels of actin, motor proteins, and other neuronal proteins, resulting in an insufficient supply of adenosine triphosphate, impairing axonal transport functionality (50).

With the development of mass spectrometry and nuclear magnetic resonance technology, researchers found that ACR, as an electrophilic reagent, can quickly attack the sulfhydryl group on proteins and react with molecular DNA while adduct formation may be a reason for its neurotoxicity (51). In

addition, ACR can also attack protein sites containing thiols, interfere with the presynaptic nitric oxide (NO) signaling pathway, damage presynaptic nerve endings, disturb nerve signal transmission, and produce neurotoxicity (52). Moreover, phosphorylated Tau agglomeration causes cytoskeletal instability and neuronal malfunction or even death (53). According to recent research, ACR induces Tau tubulin hyperphosphorylation and brain-derived neurotrophic factor (BDNF) reduction in rat hippocampi, resulting in synaptic damage and spatial cognitive impairment (54). Furthermore, chronic ACR exposure leads to motor dysfunction by significantly degenerating dopaminergic and acetyl cholinergic neurons (55). Kopańska et al. believed that the cholinergic anti-inflammatory pathway was closely related to ACR-induced neurotoxicity. ACR decreased cholinergic conduction and acetylcholine secretion, inhibiting the cholinergic anti-inflammatory pathway and causing a potential systemic inflammatory reaction (56). Moreover, it is worth noting that the cognitive impairment caused by neuron degeneration is a precursor of Alzheimer's disease (57), while the loss of dopaminergic neurons in the brain is related to Parkinson's disease, indicating that ACR may be a risk factor for the pathological development of neurodegenerative diseases (58).

Apoptosis and Autophagy

As a common form of programmed cell death, apoptosis plays a vital role in neurodegenerative diseases (59). Neurocytes, including neurons, astrocytes, and microglia, are essential in maintaining brain function (60). Astrocytes mainly support neurotrophic functionality (61). As the resident immune cells in the central nervous system (62), microglial activation is crucial for collective immune monitoring, but excessive activation leads to the release of pro-inflammatory factors (63). Neurons represent the main executors of nerve impulses and, if damaged, cause cognitive impairment and motor dysfunction (64). Early studies have indicated that ACR can induce the apoptosis of various neurocytes, such as human neuroblastoma SH-SY5Y cells, astrocytoma U1240-MG cells, and rat stellate cells (65, 66). Therefore, ACR may damage brain homeostasis and cause neurotoxicity by inducing nerve cell apoptosis.

Liu et al. conducted a mechanism investigation and found that ACR caused mitochondrial malfunctioning in human astrocytoma cells and BV-2 mouse microglia, activated caspase-9 and its downstream pathway, up-regulated the BCL2-associated X protein (Bax)/B-cell lymphoma-2 (Bcl-2) ratio, and induced mitochondrial-dependent apoptosis and neurotoxicity (67). Moreover, other signaling pathways are also involved in ACR-induced apoptosis. Mitogen-activated protein kinase (MAPK), a serine-threonine protein kinase, can control many cell activities, such as apoptosis and the proliferation and expression of signal-regulated protein kinase [extracellular regulated protein kinases (ERK), c-Jun N-terminal kinase (JNK), and p38 protein] genes (68, 69). The inactivation of ERK and activation of JNK and p38 are essential for inducing apoptosis. Tabeshpour et al. found that intraperitoneal ACR injection reduced the p-ERK/ERK ratio while increasing the Bax/Bcl-2, p-JNK/JNK, and p-p38/p38 ratios in the cerebral cortexes of rats, indicating that the MAPK signaling pathway promoted ACR-induced apoptosis (70). Additionally, nuclear factor-κB (NF-κB) regulates a variety of target genes, such as proliferation and apoptosis, while the NF-κB signal is prone to crosstalk and affects several signaling pathways (71). ACR can promote apoptosis *via* the MAPK-driven NF-κB signaling pathway, ultimately resulting in cytotoxicity (72). The nuclear factor E2-related factor-2 (Nrf2) family represents a transcriptional factor that regulates the redox state of cells and participates in the coordination of adaptive responses to various stimuli (73). Pan et al. found that ACR activated the Nrf2 and MAPK pathways in PC12 cells. The MAPK served as an upstream regulator to control the nuclear translocation of Nrf2, exhibiting an antioxidative effect (74). It is worth noting that MAPK could control both the Nrf2 and NF-κB cascades as an upstream factor and facilitate dual-direction regulation (75). Consequently, crosstalk between the NF-κB, MAPK, and Nrf2 signaling pathways is vital during ACR-induced apoptosis and neurotoxicity.

Lysosome-mediated protective autophagy is essential for maintaining intracellular redox balance and is crucial for clearing damaged cell proteins and organelles, as well as regulating cell death and survival (76). However, high ACR doses may inhibit autophagy. For example, Liu et al. revealed that sub-chronic exposure to ACR could block autophagy flow by inhibiting lysosomal protease D in the hippocampus, decreasing the inflammasome clearance, and inducing local inflammation (44), which might be a decisive factor in ACR neurotoxicity. Song et al. reported that ACR caused autophagic marker microtubule-associated protein 1 light chain 3-II (LC3-II) and p62 accumulation, suggesting that ACR might inhibit cellular autophagy (77). However, autophagy flow is a finely regulated process and includes (1) autophagosome formation, (2) autophagosome and lysosome fusion, and (3) autolysosome degradation (78). Moreover, the crosstalk affiliation between apoptosis and autophagy is critical for brain health maintenance and central nervous system pathogenesis (79, 80). A study by Deng et al. confirmed the immunofluorescence and co-localization positions and co-expressed intensity of key autophagic markers during the three-autophagic process. The ACR-induced autophagosome accumulation could probably be ascribed to blocked autophagic flux, preventing the autophagosomes from combining with lysosomes. Additional information substantiating the connection between cellular apoptosis and autophagic flux showed that restricting the protective autophagy caused by ACR further promoted the initiation of apoptosis (**Figure 2**)(81).

Oxidative Stress

The brain is more vulnerable to oxidative stress than other organs (82, 83), and most neurocyte components can be oxidized and damaged (84). Recent studies have shown that oxidative stress may be involved in the occurrence and development of neurodegenerative and chronic diseases (such as stroke, diabetes, Parkinson's, Alzheimer's, and other diseases) (85). Although reactive oxygen species (ROS) are produced during the normal physiological process, excessive production inhibits antioxidant reductase activity and disrupts redox balance, leading to oxidative stress damage (36). ACR-induced neurotoxicity

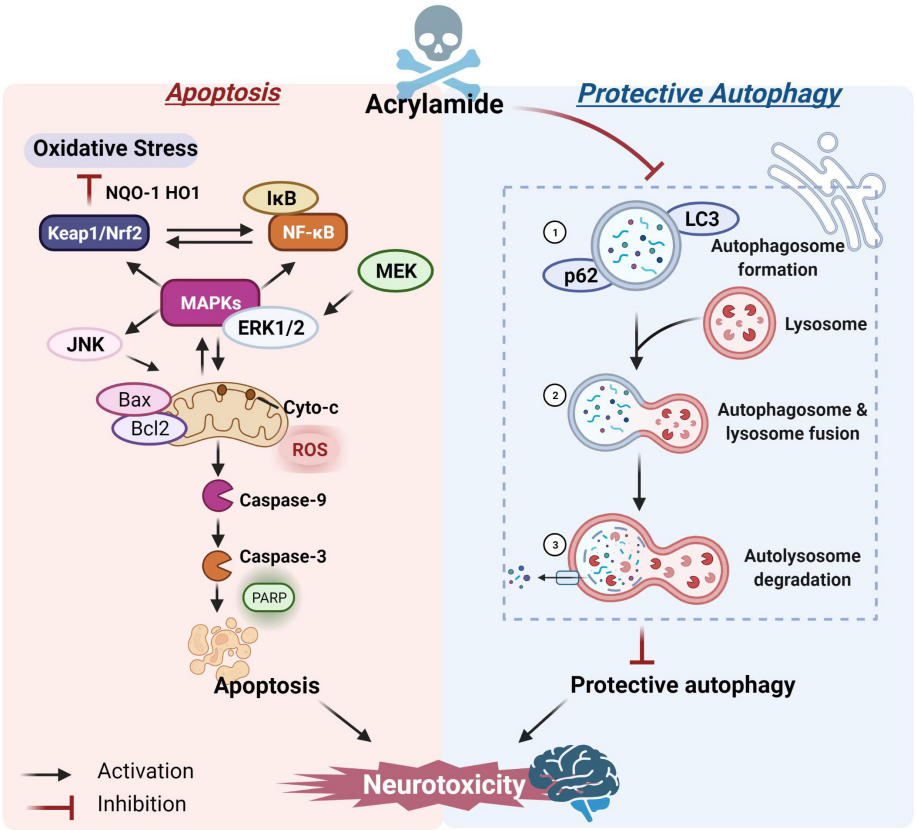

FIGURE 2 | The potential mechanism of ACR-induced apoptosis and autophagy.

typically manifests as intracellular glutathione depletion (86), indicating that oxidative stress may play a significant role in ACR neurotoxicity.

Mitochondria are essential organelles for intracellular energy metabolism and redox system regulation. Zhao et al. indicated that ACR disrupted the activity of the mitochondrial electron transport chain complexes, I, III, IV, and V, resulting in mitochondrial membrane swelling, the collapse of inner membrane potential, obvious electron transfer disorder, and electron leakage, leading to ROS accumulation (87). Liu et al. also found that ACR significantly increased the ROS level in the BV-2 microglial cell line, leading to oxidative stress, mitochondrial damage, and functionality loss while increasing the expression of caspase-dependent apoptosis-related genes (67). Damage to the mitochondrial structure and functional loss are hallmarks of endogenous apoptosis, activating the Bcl-2 protein family (88, 89). These results suggest that ACR-mediated mitochondrial dysfunction and oxidative stress injury are crucial factors leading to caspase-cascade activation and cellular apoptosis. Moreover, subsequent studies have revealed ACR-induced crosstalk in multiple signaling pathways during oxidative stress response and mitochondrial dysfunction. The Nrf2/NF-κB pathway in astrocytes and microglia was sequentially activated, gradually causing glutathione consumption, ROS accumulation, mitochondrial damage, and neuroinflammation (16).

Oxidative stress is deemed a significant predisposing factor in the pathogenesis of ACR-induced neurotoxicity, of which an increase in ROS accumulation or induced oxidative stress in the brain is only phenotypical. Of fundamental importance is linking these redox shifts to various signaling pathways and explaining how the changes occur. For example, research should explore (1) how oxidative stress arises *via* ACR in the brain, (2) how it is neutralized, (3) which typical signaling or genetic factors may trigger ACR-induced neurotoxicity development, and (4) how this impacts inflammation or autoimmunity in the central nervous system. Consequently, novel, more precise, and effective therapies can then be established to better understand how oxidative stress drives the underlying neurotoxic mechanisms.

Inflammation

The immune system recognizes external stimuli like pathogen-associated molecular patterns (PAMPs) and damage-associated molecular patterns (DAMPs) *via* pattern recognition receptors (PRRs). Furthermore, cellular PRRs, such as the nucleotide oligomerization domain (NOD)-like receptor (NLR), can activate the downstream immune-inflammatory response. Of these, NOD-like receptor protein 3 (NLRP3) in the NOD subfamily has been widely studied due to its unique response mechanism to a variety of stimuli (90). Research has shown that misfolded proteins like α-synuclein and β-amyloid can activate NLRP3

inflammasomes in the microglia, which may participate in neurodegenerative disease development, such as Parkinson's and Alzheimer's diseases (91). Mild cognitive impairment and the early symptoms of Alzheimer's disease are similar to that of chronic neurotoxicity induced by ACR, suggesting the involvement of NLRP3 inflammasomes.

The primary manifestation of immune inflammation involves inflammatory factor secretion, such as tumor necrosis factor-α (TNF-α), interleukin-6 (IL-6), interleukin-18 (IL-18), and interleukin-1β (IL-1β) (92). Previous research by Zhao et al. found increased TNF-α, IL-6, and IL-1β levels in the primary microglia during the later stage of ACR exposure, further confirming the involvement of the immune-inflammatory response in ACR-induced neurotoxicity (16). Recent studies have shown that the NLRP3 inflammasome level was up-regulated in the hippocampi of rats after oral ACR administration, further increasing the expression levels of pro-inflammatory cytokines, IL-1β, IL-6, and IL-18 (46). Liu reported that inflammatory factors were released *via* the microglial activation facilitated by persistent ACR exposure. NLRP3 inflammasome activation increased the level of IL-1β, raising the levels of other inflammatory factors directly responsible for neuronal injury in the cerebrums of rats (44). Moreover, treatment with the NLRP3 inhibitor (MCC950) or NLRP3 siRNA safeguarded BV-2 microglial cells against the cytotoxicity produced by ACR while reversing NLRP3 inflammasome activation and the subsequent inflammatory response (93). Similarly, in mice exposed to MCC950, NLRP3 knockout intervention provided protection against the neurotoxic damage caused by ACR by restricting Nrf2 antioxidant pathway activation and neuroinflammation (93). Therefore, NLRP3 inflammasomes participate in the neurotoxicity facilitated by ACR and show promise as a target to improve therapeutic strategies.

Microbiota-Gut-Brain Axis Homeostasis

The brain-gut axis, which is linked by the immune system, is closely associated with mental disease and neurodevelopmental disorders (94). The mechanism underlying the influence of the intestinal barrier and intestinal flora on brain function may include synapse formation regulation (95), neuronal signaling activation, ROS formation inhibition (96), and blood-brain barrier function regulation *via* secondary metabolites (97).

Recent studies suggest that brain-gut axis homeostasis may be another important cause of ACR-induced neurotoxicity. ACR can facilitate circadian cognitive damage and spatial memory impairment by downregulating the protein expression of the circadian rhythm protein (Clock) and BDNF in mice (98). Moreover, ACR increases intestinal permeability, decreases tight junction protein (Occludin) expression, and increases the lipopolysaccharide (LPS) content in the intestine and serum, while the expression of pro-inflammatory cytokines, IL-6, and IL-1β are significantly up-regulated (98). Excessive LPS and inflammatory factors in the blood can induce an immune-inflammatory response, destroy the close blood-brain barrier connection, and aggravate neurogenic inflammation, damaging the neurons and leading to memory impairment (98). Therefore, ACR may interfere with the communication between the intestine and brain *via* the brain-gut axis, leading to circadian rhythm dysfunction, further promoting neurotoxicity development. In addition, ACR can change the diversity of flora in rat feces, reduce the abundance of some beneficial bacteria, and significantly increase the abundance of pathogenic bacteria, resulting in an intestinal flora imbalance and reduced short-chain fatty acids (SCFA) production, further stimulating neurotoxicity (99).

The brain-gut axis attracts increasing attention for the physiological and biological exploration of neurodegenerative, age-related, and neurodevelopmental diseases. Considering the close relationship between ACR toxicity and induced neurodegenerative disorders, the underlying neurotoxic mechanism *via* brain-gut axis homeostasis requires further investigation.

CONCLUSION: THE ROLE OF MULTIPLE SIGNALING PATHWAYS IN ACRYLAMIDE-INDUCED NEUROTOXICITY

Acrylamide neurotoxicity has attracted extensive research attention globally. These reports confirmed that exposure to ACR can lead to neurological disorders like gait abnormality, cognitive impairment, and learning deficiencies. The representative effects and signaling pathways of the neurotoxicity caused by ACR are listed in **Table 2**. Developing research has gradually proposed a hypothesis regarding the neurotoxic mechanism of ACR and can be summarized as follows (**Figure 3**): (1) Axonal degeneration, neuronal deficits, and DNA-protein adduct formation are primarily responsible for ACR-induced neurological disorders. (2) Oxidative stress is a typical response caused by ACR and may be associated with mitochondrial malfunction resulting from ACR in conjunction with calcium dyshomeostasis. (3) Multiple neural pathways involving apoptosis, autophagy, and inflammation are attributed to ACR-induced neurotoxicity. (4) Brain-intestinal axis homeostasis and circadian rhythms also participate in ACR-induced neurotoxicity.

FUTURE PERSPECTIVES

Studies are increasingly concentrating on the neurological impact and various underlying mechanisms of ACR. However, despite extensive research involving multiple models, fundamental questions persist, requiring resolution. This section discusses future research from three perspectives, requiring further attention. These insights may further prompt the development of alternative approaches examining ACR risk factors.

Acrylamide and Neurodegenerative Diseases

As early as 2008, Lopachin et al. suggested that the onset and progression of some neuropathogenic processes, like Parkinson's and Alzheimer's diseases and amyotrophic lateral sclerosis, are

TABLE 2 | A summary of the representative neurotoxic effect of ACR in different models.

No.	Model	ACR dose	Time	Endpoint	Potential mechanism	References
1	PC12 cells	0.6 mM 1.25 mM 2.5 mM 5 mM	24 h	Oxidative stress	ROS↑ MDA↑ GSH↓; HO-1, NQO-1↑. NF-κB (IκBα, p65), ERK1/2, JNK, p38↑. The MAPK pathway is an upstream NF-κB and Nrf2 pathway regulator.	(32)
				Inflammation	TNF-α, IL-6, COX-2↑	
2	Zebrafish (*Danio rerio*)	0.75 mM	3 days	Oxidative stress	ROS↑ MDA↑ GSH↓. Zebrafish exhibit gait abnormalities and negative scototaxis.	(125)
3	H1 hESC cells	2.5 mM 5 mM	24 h	Apoptosis Oxidative stress	SOX2, TUJ1, GFAP, CTIP2, SOX9↓. MAPK, Nrf2↑. FTL, GCLC, GCLM, SLC7A11, HMOX1↑. Caspase-6, caspase-9, c-FOS↑. Stimulated Tau hyperphosphorylation and suppressed neuronal differentiation.	(38)
4	PC12 cells	0.6 mM 1.25 mM 2.5 mM 5 mM	24 h	Apoptosis	Pro-caspase-3, pro-caspase-9, Bcl-2↓. JNK, p-38, Bax, Bax/Bcl-2, cleavage-caspase-9, cleavage-caspase-3↑. Vacuole formation and structural rarefaction cause abnormal mitochondria.	(74)
				Oxidative stress	ROS↑ MDA↑ GSH↓. Nrf2, MAPKs↑. The generation of GSH is reduced *via* Nrf2 knockdown, while the MDA levels are increased.	
5	BV-2 cells	0.5 mM 1 mM 2 mM	24 h	Apoptosis	BDNF, Bcl-2/Bax, p-Akt / Akt↓. Cyto-c, cleavage-caspase-9, cleavage-caspase-3, PARP↑. Decreases mitochondrial respiration and anaerobic glycolysis.	(67)
				Inflammation	iNOS, NO↑.	
6	Male SD rats	0.5 mg/kg/day 5 mg/kg/day	12 months	Inflammation	IL-6, TNF-α, IL-10↑. SYN1, SYP, PSD95↓. NLRP3, caspase-1, IL-1ß↑. Chronic ACR exposure induces neuron lesions and synaptic impairment and activates NLRP3 inflammasomes.	(44)
				Oxidative stress	MDA↑.	
7	PC12 cells	5 mM	24 h	Autophagy	Becline-1, LC3-II, p62↑. ACR induces neurotoxicity *via* activation of PKCs (α, δ) and ERK and inhibition of AMPK.	(40)
8	Male C57BL/6 mice	20 mg/kg/day	4 weeks	Autophagy	ATG4B, LC3-II, Cathepsin D, LAMP2a ↑. Trx-1 siRNA enhances ACR-induced autophagy by regulating ITGAV.	(126)
	PC12 cells	1 mM, 2 mM 4 mM, 8 mM	24 h			
9	Male C57/BL6J mice	Drinking water containing 0.003% ACR	16 weeks	Brain-gut axis inflammation	Bmal1, Clock, SNAP-25, PSD-95, ZO-1, Occludin↓. IL-10, COX-2, TNF-α, COX-2↑. ACR potentially suppresses circadian, impacting cognitive function in the brain.	(98)
10	Male SD rats	50 mg/kg/day	3–28 days	Neurotransmitter dysfunction	Neurological toxicity and weight loss. ACR-cysteine adduct (CEC), 7S SNARE core complex↑. ACR can facilitate adduct formation in the presence of SNARE and NSF proteins (both containing cysteine residues).	(33)
11	Male Wistar rats	20 mg/kg/day 40 mg/kg/day	8 weeks	Axon degeneration	Abnormal gait and nerve damage. The calibers of myelinated axons↓. NF-L, NF-M↑. Accumulation of neurofilaments (NFs).	(34)

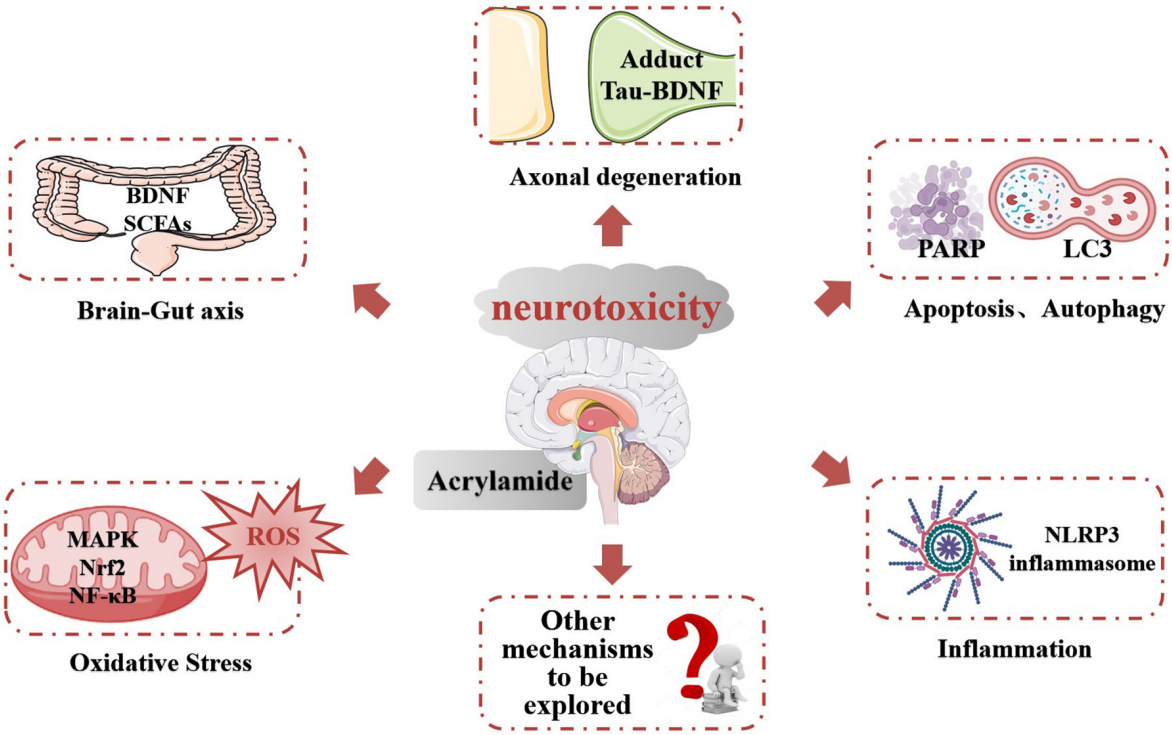

FIGURE 3 | The potential mechanism of ACR-induced neurotoxicity.

accelerated by environmental exposure to some type-2 alkenes, such as ACR (100). Moreover, a recent epidemiological study involving 2,534 elderly non-smoking Chinese men indicated that ACR exposure was related to a mild cognitive decrease and a higher risk of poor cognition in four years (101). Extensive research has shown that the various neurotoxic syndromes due to ACR exposure and neurodegenerative diseases, including biochemical changes and neuropathic events in the brain and spinal cord, are similar (102, 103). The inflammatory response and oxidative stress, as well as the related activated signaling pathways present in both neurodegenerative diseases and ACR-induced neurotoxicity, were investigated to clarify the underlying mechanism (13, 104, 105). Therefore, a close connection may exist between the neurotoxicity caused by ACR and neurodegenerative diseases.

However, despite existing comparative studies, some fundamental questions remain. (1) Discoveries regarding ACR-related neurotoxic mechanisms require further investigation based on the neuropathological process of neurodegenerative diseases. (2) How ACR promotes the neuropathological process of neurodegenerative diseases and whether ACR can induce the expression of neurodegenerative pathogenic factors like β-amyloid protein aggregation in the brain remain unclear. However, this presents a fascinating research topic for the future. (3) Clarification is required regarding the existence of a shared target or signaling connection during ACR-induced neurotoxicity and pathological neurodegenerative processing, such as innate immune receptors, toll-like receptor-4, and NLRP3, as well as their signaling interaction. Therefore, more evidence is required. (4) These challenges necessitate a more in-depth understanding of the mechanisms underlying the neurotoxicity caused by ACR. The knowledge regarding the mechanism can be used to develop novel strategies or inhibitors to reduce and block the targets required to manifest adverse ACR effects.

Nucleotide Oligomerization Domain-Like Receptor Protein 3 Inflammasome-Related Immune Inflammation

Several studies have clarified the role of inflammation in the neurotoxicity caused by ACR (36, 72), revealing a connection with NLRP3 inflammasomes (93). However, the specific regulatory role and mechanism of NLRP3 inflammasomes in ACR-induced neurotoxicity require further clarification (**Figure 4**).

Canonical NLRP3 inflammasomes contain effector protein caspase-1, adaptor protein ASC (a speck-like protein containing a CARD, associated with adaptor molecule apoptosis), and sensory protein NLRP3 (106), while it requires priming and activation to become operational. The priming process includes pro-IL-18, pro-IL-1β, and NLRP3 expression, the initiation of which occurs *via* the NF-κB signaling pathway (107, 108). The activation process allows inflammasome complex assembly, facilitating pro-caspase-1 cleavage to obtain active caspase-1. Then, mature IL-18

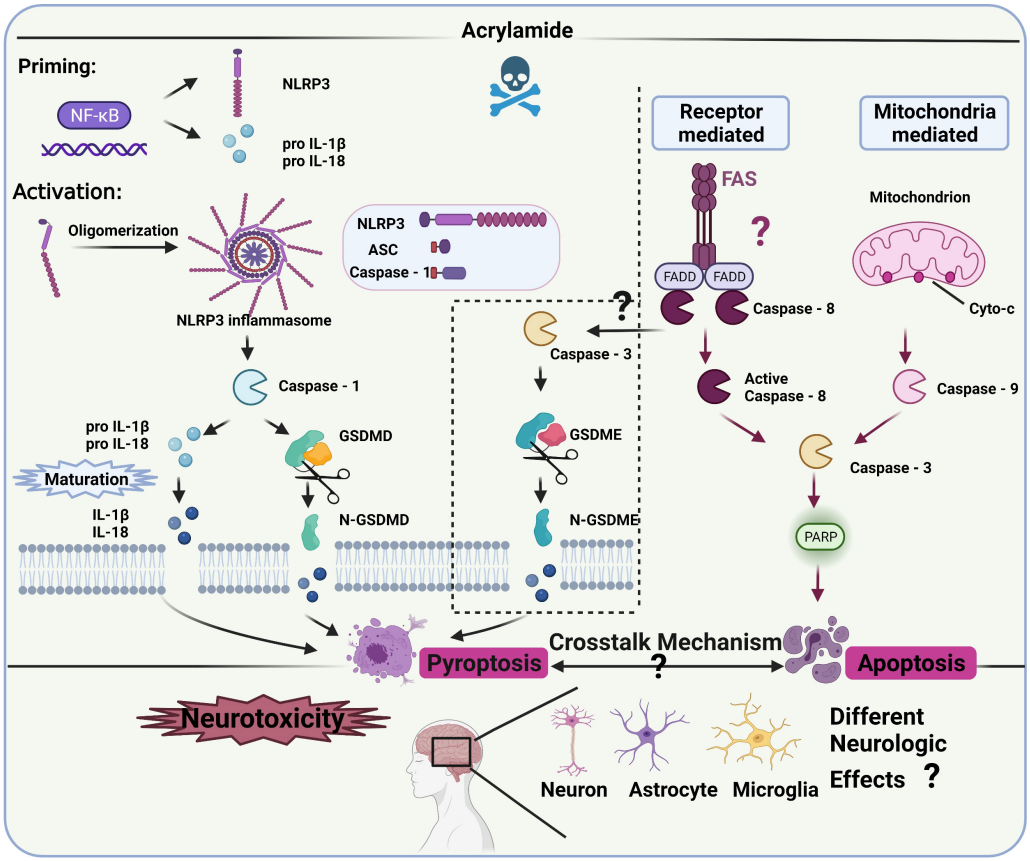

FIGURE 4 | NLRP3 inflammasomes and the related pathway in ACR-induced neurotoxicity.

and IL-1β are released *via* pro-IL-18 and pro-IL-1β cleavage (44). Additionally, the N-terminal domain of gasdermin D (GSDMD) is released *via* activated caspase-1 cleavage, forming pores in the plasma membrane to rapidly release mature IL-18 and IL-1β, which may cause pyroptosis (109). Besides the canonical pathway, caspase-3 and gasdermin E (GSDME) can also facilitate the release of mature IL-18 and IL-1β while inducing inflammatory cell death, known as alternative pyroptosis in many neurodegenerative diseases and inflammatory response models (110, 111). However, whether the activated caspase-3-IL-1β/IL-18-GSDME signaling contributes to ACR-induced pyroptosis and neurotoxicity remains unknown. Therefore, the pyroptosis-related pathway representing the main signal cascade (NLRP3-ASC-caspase-1-IL-1β/IL-18-GSDMD or caspase-3-IL-1β/IL-18-GSDME) induced by ACR and its neurological impact requires exploration. Furthermore, future studies should also investigate which cascade is activated first during ACR exposure and whether the activation is time-dependent. Additionally, both pyroptosis and apoptosis are involved in programmed cell death but are differentiated *via* morphology (112). ACR can induce pyroptosis and apoptosis with phenotypical traits (109), while caspase-3 represents the effector protein in both the mitochondrially mediated apoptosis pathway and caspase-3-IL-1β/IL-18-GSDME cascade. How ACR dosage, period, and various other factors affect the functionality of caspase-3, as well as the synergistic effect of pyroptosis and apoptosis on the neurological mechanism, require further exploration.

Given the role of inflammasome signaling in the ACR-induced neurotoxic conditions mentioned above, researchers should explore the crucial biomarkers in the pathways to develop specific inhibitors against ACR-induced neurotoxicity. In this case, the correlation between oxidative stress and neuroinflammation should be further refined. For example, how the specific modification of cellular oxidative stress impacts neuroinflammation warrants further attention. Clarification is necessary regarding the connection between mitochondrial dysfunction and inflammasome signaling and whether ion efflux and energy metabolism contribute to this association. Moreover, the potential biomarkers in the NLRP3-related pathway like NLRP3, ASC, caspase-1, GSDMD, and the alternative pyroptosis pathway like caspase-3 and GSDME, should be further confirmed *in vitro* and *in vivo*. An adequate transgenic model must be employed to further verify the NLRP3-related biomarkers and investigate their mechanistic role.

Microglial cells (such as the BV-2 cell line) are generally considered central neuron system immune cells and are activated during the inflammatory response. However, future studies

should compare the functional response diversity of neurons, astrocytes, and microglia using different *in vitro* neurocyte models to verify the pathways involved in neuroinflammation while assessing their contribution to ACR neurotoxicity. Another challenge involves achieving cell-cell communication between neurons and glia, specifically concerning the microglia-astrocyte-neuron impact on the neuroinflammation produced by ACR. This interaction may be explained using a co-cultural model.

Microbiota-Gut-Brain Axis Signaling

The gut-brain axis is deemed an essential pathway for physiological regulation and communication, while gut microbiota are seemingly crucial in this interactive relationship (113). Several pathways are involved in microbiota-gut-brain axis signaling and include the immune system, neurochemical signaling host recruitment, the vagus nerve and direct enteric nervous system routes, and bacterial metabolite production (114–117).

Altered gut microbial profiles and signaling have been described in various neurological disorders, such as Parkinson's and Alzheimer's diseases (118, 119). Although the similar neurological impact has prompted some studies to investigate the connection between ACR-induced neurotoxicity and microbiota-gut-brain axis signaling in recent years, systematic studies involving this topic are still lacking. In general, the hypothetical effect of microbiota-gut-brain axis signaling induced by ACR occurs *via* the gut bacterial metabolites of a defective gut barrier, leading to a systematic inflammatory response. This process impairs the blood-brain barrier, ultimately leading to neural damage and deterioration (**Figure 5**).

However, these hypotheses should be investigated further. (1) Screening and identifying the microbiome of a specific type of putative bacterium (biomarkers) related to ACR-induced neurotoxicity deserves further attention. (2) Further exploration is required regarding potential neurotoxic molecule production, such as amyloid proteins, LPS, and additional secondary metabolites that can reach the central neuron system *via* systemic circulation to activate microglia and ROS signaling. Furthermore, research should clarify whether ACR exposure can modulate the metabolism of normal functional neurotransmitters, such as serotonin and tryptophan, and whether the behavior impacted by ACR-induced gut microbiota and those relying on intact serotonergic neurotransmission overlaps. The underlying crosstalk mechanisms require further elucidation and may be associated with the gut microbial capacity to regulate the metabolism of the host tryptophan in conjunction with the kynurenine pathway. (3) The communication between the brain and the gut during ACR exposure requires clarification. The release of cytokines *via* the immune response represents the most common assumption during the gut-brain communication mechanism. Other influencing routes include the vagus nerve, hypothalamic-pituitary-adrenal axis, and secondary microbial metabolites, while neuromodulators and neurotransmitters may also be involved. However, the details regarding the signaling pathways and crucial biomarkers for communication require further investigation. (4) Limited epidemiological-related data is available, and it is unclear whether any common changes in the gut microbiota are evident in high-risk individuals during ACR exposure. Moreover, whether common microbiota biomarkers are evident in high-risk exposed individuals and

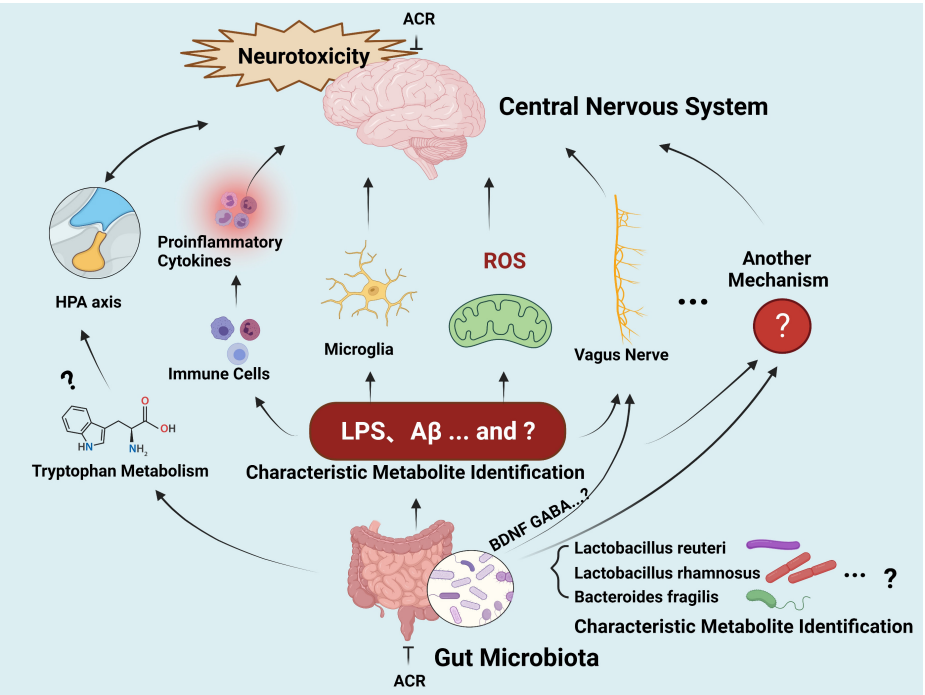

FIGURE 5 | The gut-brain axis in ACR-induced neurotoxicity.

neurodegenerative disease patients requires elucidation. During the extended journey from the gut microbiota to the brain, many connections are still unidentified. If this challenge can be resolved, the microbiota-gut-brain axis can facilitate new therapeutic strategies for ACR-induced neurotoxicity and various neurological conditions.

AUTHOR CONTRIBUTIONS

MZ: conceptualization, original draft preparation, writing – review and editing, project administration, and funding acquisition. BZ: original draft preparation, especially in summarizing the table and creating the flow chart of the signaling pathways, and writing – review and editing. LD: writing – review and editing and validation. All authors read and approved the final manuscript.

FUNDING

The National Natural Science Foundation for Young Scientists of China (No. 31801668), The Fundamental Research Funds for the Central Universities (No. 222201814036), The Shanghai PuJiang Program (No. 18J1401900), and The National Key R&D Program of China (No. 2019YFD090180302).

REFERENCES

1. Smith EA, Oehme FW. Acrylamide and polyacrylamide: a review of production, use, environmental fate and neurotoxicity. *Rev Environ Health.* (1991) 9:215–28. doi: 10.1515/reveh.1991.9.4.215
2. Zhang Y, Zhang Y. Formation and reduction of acrylamide in Maillard reaction: a review based on the current state of knowledge. *Crit Rev Food Sci Nutr.* (2007) 47:521–42. doi: 10.1080/10408390600920070
3. Capuano E, Fogliano V. Acrylamide and 5-hydroxymethylfurfural (HMF): a review on metabolism, toxicity, occurrence in food and mitigation strategies. *LWT Food Sci Technol.* (2011) 44:793–810. doi: 10.1016/j.lwt.2010.11.002
4. Tareke E, Rydberg P, Karlsson P, Eriksson S, Tornqvist M. Analysis of acrylamide, a carcinogen formed in heated foodstuffs. *J Agric Food Chem.* (2002) 50:4998–5006. doi: 10.1021/jf020302f
5. Mottram DS, Wedzicha BL, Dodson AT. Acrylamide is formed in the Maillard reaction. *Nature.* (2002) 419:448–9. doi: 10.1038/419448a
6. Stadler RH, Blank I, Varga N, Robert F, Hau J, Guy PA, et al. Acrylamide from Maillard reaction products. *Nature.* (2002) 419:449–50. doi: 10.1038/419449a
7. Panel. Scientific Opinion on acrylamide in food. *EFSA J.* (2015) 13:4104. doi: 10.2903/j.efsa.2015.4104
8. Powers SJ, Mottram DS, Curtis A, Halford NG. Acrylamide levels in potato crisps in Europe from 2002 to 2016. *Food Addit Contam Part A Chem Anal Control Expo Risk Assess.* (2017) 34:2085–100. doi: 10.1080/19440049.2017.1379101
9. Pundir CS, Yadav N, Chhillar AK. Occurrence, synthesis, toxicity and detection methods for acrylamide determination in processed foods with special reference to biosensors: a review. *Trends Food Sci Technol.* (2019) 85:211–25. doi: 10.1016/j.tifs.2019.01.003
10. Exon JH. A review of the toxicology of acrylamide. *J Toxicol Environ Health B Crit Rev.* (2006) 9:397–412. doi: 10.1080/10937400600681430
11. Barber DS, Stevens S, LoPachin RM. Proteomic analysis of rat striatal synaptosomes during acrylamide intoxication at a low dose rate. *Toxicol Sci.* (2007) 100:156–67. doi: 10.1093/toxsci/kfm210
12. Baydar T, Erkekoglu P, Sipahi H, Ahin G. Aflatoxin M1 and Ochratoxin contents of infant formulas and baby foods commonly consumed in Ankara. In: *Proceedings of the 10th International Congress of Toxicology* (2014). Available online at: https://www.researchgate.net/publication/264755252_Aflatoxin_M1_and_Ochratoxin_contents_of_infant_formulas_and_baby_foods_commonly_consumed_in_Ankara
13. LoPachin RM. The changing view of acrylamide neurotoxicity. *Neurotoxicology.* (2004) 25:617–30. doi: 10.1016/j.neuro.2004.01.004
14. LoPachin RM, Gavin T, DeCaprio A, Barber DS. Application of the hard and soft, acids and bases (HSAB) theory to toxicant–target interactions. *Chem Res Toxicol.* (2011) 25:239–51. doi: 10.1021/tx2003257
15. Zamani E, Shokrzadeh M, Ziar A, Abedian-Kenari S, Shaki F. Acrylamide attenuated immune tissues' function via induction of apoptosis and oxidative stress: Protection by l-carnitine. *Hum Exp Toxicol.* (2018) 37:859–69. doi: 10.1177/0960327117741753
16. Zhao M, Lewis Wang FS, Hu X, Chen F, Chan HM. Acrylamide-induced neurotoxicity in primary astrocytes and microglia: roles of the Nrf2-ARE and NF-kappaB pathways. *Food Chem Toxicol.* (2017) 106(Pt A):25–35. doi: 10.1016/j.fct.2017.05.007
17. Friedman M. Chemistry, biochemistry, and safety of acrylamide. A review. *J Agric Food Chem.* (2003) 51:4504–26. doi: 10.1021/jf030204
18. Pennisi M, Malaguarnera G, Puglisi V, Vinciguerra L, Vacante M, Malaguarnera M. Neurotoxicity of acrylamide in exposed workers. *Int J Environ Res Public Health.* (2013) 10:3843–54. doi: 10.3390/ijerph10093843
19. Backe WJ, Yingling V, Johnson T. The determination of acrylamide in environmental and drinking waters by large-volume injection - hydrophilic-interaction liquid chromatography and tandem mass spectrometry. *J Chromatogr A.* (2014) 1334:72–8. doi: 10.1016/j.chroma.2014.02.005
20. Brown L, Rhead MM, Hill D, Bancroft KCC. Qualitative and quantitative studies on the in situ adsorption, degradation and toxicity of acrylamide by the spiking of the waters of two sewage works and a river. *Water Res.* (1982) 16:579–91. doi: 10.1016/0043-135490078-1
21. Who. Evaluation of certain contaminants in food. *World Health Organiz Tech Rep Ser.* (2011) 959:1–166.
22. Smith EA, Prues SL, Oehme FW. Environmental degradation of polyacrylamides. II. Effects of environmental (outdoor) exposure. *Ecotox Environ Saf.* (1997) 37:76–91. doi: 10.1006/eesa.1997.1527
23. Zhang Y, Wang Q, Zhang G, Jia W, Ren Y, Wu Y. Biomarker analysis of hemoglobin adducts of acrylamide and glycidamide enantiomers for mid-term internal exposure assessment by isotope dilution ultra-high performance liquid chromatography tandem mass spectrometry. *Talanta.* (2018) 178:825–33. doi: 10.1016/j.talanta.2017.09.092
24. Lu X. Research progress of acrylamide in cosmetics and its detection. *China Med Pharm.* (2014). 4:52–55.
25. Viswanath P. Evaluation of certain contaminants in food. In: *Proceedings of the 72nd Report of the Joint FAO/WHO Expert Committee on Food Additives.* Geneva: Medknow Publications and Media Pvt. Ltd (2012).
26. Mesias M, Nouali A, Delgado-Andrade C, Morales FJ. How far is the spanish snack sector from meeting the acrylamide regulation 2017/2158? *Foods.* (2020) 9:247. doi: 10.3390/foods9020247
27. Koszucka A, Nowak A, Nowak I, Motyl I. Acrylamide in human diet, its metabolism, toxicity, inactivation and the associated European Union legal regulations in food industry. *Crit Rev Food Sci Nutr.* (2020) 60:1677–92. doi: 10.1080/10408398.2019.1588222
28. Rifai L, Saleh FAA. Review on acrylamide in food: occurrence, toxicity, and mitigation strategies. *Int J Toxicol.* (2020) 39:93–102. doi: 10.1177/1091581820902405
29. Mucci LA, Wilson KA. Acrylamide intake through diet and human cancer risk. *J Agr Food Chem.* (2008) 56:6013–9. doi: 10.1021/jf703747b
30. Fang C, Hu X, Liu Y, Wang P, Li D. *Metabolism of Acrylamide: Interindividual and Interspecies Differences as Well as the Application as Biomarkers.* (Vol. 17). (2015). 2488645 p. doi: 10.1145/2488608.2488645
31. Kirman CR, Gargas ML, Deskin R, Tonner-Navarro L, Andersen ME. A physiologically based pharmacokinetic model for acrylamide and its

metabolite, glycidamide, in the rat. *J Toxicol Environ Health A.* (2003) 66:253–74. doi: 10.1080/15287390306368
32. Pan X, Wu X, Yan D, Peng C, Rao C, Yan H. Acrylamide-induced oxidative stress and inflammatory response are alleviated by N-acetylcysteine in PC12 cells: Involvement of the crosstalk between Nrf2 and NF-kappaB pathways regulated by MAPKs. *Toxicol Lett.* (2018) 288:55–64. doi: 10.1016/j.toxlet.2018.02.002
33. Barber DS, LoPachin RM. Proteomic analysis of acrylamide-protein adduct formation in rat brain synaptosomes. *Toxicol Appl Pharmacol.* (2004) 201:120–36. doi: 10.1016/j.taap.2004.05.008
34. Yu S, Zhao X, Zhang T, Yu L, Li S, Cui N, et al. Acrylamide-induced changes in the neurofilament protein of rat cerebrum fractions. *Neurochem Res.* (2005) 30:1079–85. doi: 10.1007/s11064-005-7413-3
35. Zhang L, Gavin T, Barber DS, LoPachin RM. Role of the Nrf2-ARE pathway in acrylamide neurotoxicity. *Toxicol Lett.* (2011) 205:1–7. doi: 10.1016/j.toxlet.2011.04.011
36. Santhanasabapathy R, Vasudevan S, Anupriya K, Pabitha R, Sudhandiran G. Farnesol quells oxidative stress, reactive gliosis and inflammation during acrylamide-induced neurotoxicity: behavioral and biochemical evidence. *Neuroscience.* (2015) 308:212–27. doi: 10.1016/j.neuroscience.2015.08.067
37. Guo J, Cao X, Hu X, Li S, Wang J. The anti-apoptotic, antioxidant and anti-inflammatory effects of curcumin on acrylamide-induced neurotoxicity in rats. *BMC Pharmacol Toxicol.* (2020) 21:62. doi: 10.1186/s40360-020-00440-3
38. Bu Q, Huang Y, Li M, Dai Y, Fang X, Chen K, et al. Acrylamide exposure represses neuronal differentiation, induces cell apoptosis and promotes tau hyperphosphorylation in hESC-derived 3D cerebral organoids. *Food Chem Toxicol.* (2020) 144:111643. doi: 10.1016/j.fct.2020.111643
39. Li L, Sun HY, Liu W, Zhao HY, Shao ML. Silymarin protects against acrylamide-induced neurotoxicity via Nrf2 signalling in PC12 cells. *Food Chem Toxicol.* (2017) 102:93–101. doi: 10.1016/j.fct.2017.01.021
40. Triningsih D, Yang JH, Sim KH, Lee C, Lee YJ. Acrylamide and its metabolite induce neurotoxicity via modulation of protein kinase C and AMP-activated protein kinase pathways. *Toxicol In Vitro.* (2021) 72:105105. doi: 10.1016/j.tiv.2021.105105
41. Lakshmi D, Gopinath K, Jayanthy G, Anjum S, Prakash D, Sudhandiran G. Ameliorating effect of fish oil on acrylamide induced oxidative stress and neuronal apoptosis in cerebral cortex. *Neurochem Res.* (2012) 37:1859–67. doi: 10.1007/s11064-012-0794-1
42. Mehri S, Abnous K, Khooei A, Mousavi SH, Shariaty VM, Hosseinzadeh H. Crocin reduced acrylamide-induced neurotoxicity in Wistar rat through inhibition of oxidative stress. *Iran J Basic Med Sci.* (2015) 18:902–8.
43. Prasad SN, Muralidhara. Mitigation of acrylamide-induced behavioral deficits, oxidative impairments and neurotoxicity by oral supplements of geraniol (a monoterpene) in a rat model. *Chem Biol Interact.* (2014) 223:27–37. doi: 10.1016/j.cbi.2014.08.016
44. Liu Y, Zhang X, Yan D, Wang Y, Wang N, Liu Y, et al. Chronic acrylamide exposure induced glia cell activation, NLRP3 infl-ammasome upregulation and cognitive impairment. *Toxicol Appl Pharmacol.* (2020) 393:114949. doi: 10.1016/j.taap.2020.114949
45. Zhao M, Deng L, Lu X, Fan L, Zhu Y, Zhao L. The involvement of oxidative stress, neuronal lesions, neurotransmission impairment, and neuroinflammation in acrylamide-induced neurotoxicity in C57/BL6 mice. *Environ Sci Pollut Res Int.* (2022). doi: 10.1007/s11356-021-18146-2
46. Zong C, Hasegawa R, Urushitani M, Zhang L, Nagashima D, Sakurai T, et al. Role of microglial activation and neuroinflammation in neurotoxicity of acrylamide in vivo and in vitro. *Arch Toxicol.* (2019) 93:2007–19. doi: 10.1007/s00204-019-02471-0
47. LoPachin RM Jr., Lehning EJ. Acrylamide-induced distal axon degeneration: a proposed mechanism of action. *Neurotoxicology.* (1994) 15:247–59. doi: 10.1016/0028-390890123-6
48. Von Burg R, Penney DP, Conroy PJ. Acrylamide neurotoxicity in the mouse: a behavioral, electrophysiological and morphological study. *J Appl Toxicol.* (1981) 1:227–33. doi: 10.1002/jat.2550010409
49. Spencer PS, Schaumburg HH. Nervous system degeneration produced by acrylamide monomer. *Environ Health Perspect.* (1975) 11:129–33. doi: 10.1289/ehp.7511129
50. An L, Li G, Si J, Zhang C, Han X, Wang S, et al. Acrylamide retards the slow axonal transport of neurofilaments in rat cultured dorsal root ganglia neurons and the corresponding mechanisms. *Neurochem Res.* (2016) 41:1000–9. doi: 10.1007/s11064-015-1782-z
51. LoPachin RM, Barber DS, He D, Das S. Acrylamide inhibits dopamine uptake in rat striatal synaptic vesicles. *Toxicol Sci.* (2006) 89:224–34. doi: 10.1093/toxsci/kfj005
52. Mohr S, Stamler JS, Brüne B. Mechanism of covalent modification of glyceraldehyde-3-phosphate dehydrogenase at its active site thiol by nitric oxide, peroxynitrite and related nitrosating agents. *FEBS Lett.* (1994) 348:223–7. doi: 10.1016/0014-579300596-6
53. L'Episcopo F, Drouin-Ouellet J, Tirolo C, Pulvirenti A, Giugno R, Testa N, et al. GSK-3beta-induced Tau pathology drives hippocampal neuronal cell death in Huntington's disease: involvement of astrocyte-neuron interactions. *Cell Death Dis.* (2016) 7:e2206. doi: 10.1038/cddis.2016.104
54. Yan D, Yao J, Liu Y, Zhang X, Wang Y, Chen X, et al. Tau hyperphosphorylation and P-CREB reduction are involved in acrylamide-induced spatial memory impairment: Suppression by curcumin. *Brain Behav Immun.* (2018) 71:66–80. doi: 10.1016/j.bbi.2018.04.014
55. Murray SM, Waddell BM, Wu CW. Neuron-specific toxicity of chronic acrylamide exposure in *C. elegans*. *Neurotoxicol Teratol.* (2020) 77:106848. doi: 10.1016/j.ntt.2019.106848
56. Kopańska M, Łagowska A, Kuduk B, Banaś-Ząbczyk A. Acrylamide neurotoxicity as a possible factor responsible for inflammation in the cholinergic nervous system. *Int J Mol Sci.* (2022) 23:2030. doi: 10.3390/ijms23042030
57. Janoutova J, Sery O, Hosak L, Janout V. Is mild cognitive impairment a precursor of alzheimer's disease? Short Review. *Cent Eur J Public Health.* (2015) 23:365–7. doi: 10.21101/cejph.a4414
58. Benedetto A, Au C, Avila DS, Milatovic D, Aschner M. Extracellular dopamine potentiates mn-induced oxidative stress, lifespan reduction, and dopaminergic neurodegeneration in a BLI-3-dependent manner in *Caenorhabditis elegans*. *PLoS Genet.* (2010) 6:182–8. doi: 10.1371/journal.pgen.1001084
59. Unver-Saraydin S, Saraydin D, Sahin Inan ZD. A study of digital image analysis on the acrylamide derivative monomers induced apoptosis in rat cerebrum. *Microsc Res Tech.* (2020) 83:436–45. doi: 10.1002/jemt.23431
60. Barres BA. The mystery and magic of glia: a perspective on their roles in health and disease. *Neuron.* (2008) 60:430–40. doi: 10.1016/j.neuron.2008.10.013
61. Sofroniew MV, Vinters HV. Astrocytes: biology and pathology. *Acta Neuropathol.* (2010) 119:7–35. doi: 10.1007/s00401-009-0619-8
62. Graeber MB, Streit WJ. Microglia: biology and pathology. *Acta Neuropathol.* (2010) 119:89–105. doi: 10.1007/s00401-009-0622-0
63. Block ML, Zecca L, Hong JS. Microglia-mediated neurotoxicity: uncovering the molecular mechanisms. *Nat Rev Neurosci.* (2007) 8:57–69. doi: 10.1038/nrn2038
64. Xiao JW, Guo CL, Niu KL, Zhong-Sheng LI, Meng HL, Bin LI. Effects of Schwan cells on damage and repair of motor neuron induced by acrylamide. *J J Toxicol.* (2011) 25:328–31.
65. Lee JG, Wang YS, Chou CC. Acrylamide-induced apoptosis in rat primary astrocytes and human astrocytoma cell lines. *Toxicol In Vitro.* (2014) 28:562–70. doi: 10.1016/j.tiv.2014.01.005
66. Henn A, Lund S, Hedtjarn M, Schrattenholz A, Porzgen P, Leist M. The suitability of BV2 cells as alternative model system for primary microglia cultures or for animal experiments examining brain inflammation. *ALTEX.* (2009) 26:83–94. doi: 10.14573/altex.2009.2.83
67. Liu Z, Song G, Zou C, Liu G, Wu W, Yuan T, et al. Acrylamide induces mitochondrial dysfunction and apoptosis in BV-2 microglial cells. *Free Radic Biol Med.* (2015) 84:42–53. doi: 10.1016/j.freeradbiomed.2015.03.013
68. Cuadrado A, Nebreda AR. Mechanisms and functions of p38 MAPK signalling. *Biochem J.* (2010) 429:403–17. doi: 10.1042/BJ20100323
69. Wagner EF, Nebreda AR. Signal integration by JNK and p38 MAPK pathways in cancer development. *Nat Rev Cancer.* (2009) 9:537–49. doi: 10.1038/nrc2694
70. Tabeshpour J, Mehri S, Abnous K, Hosseinzadeh H. Role of oxidative stress, MAPKinase and apoptosis pathways in the protective effects of

thymoquinone against acrylamide-induced central nervous system toxicity in rat. *Neurochem Res.* (2020) 45:254–67. doi: 10.1007/s11064-019-02908-z
71. Taniguchi K, Karin M. NF-kappaB, inflammation, immunity and cancer: coming of age. *Nat Rev Immunol.* (2018) 18:309–24. doi: 10.1038/nri.2017.142
72. Yan D, Pan X, Yao J, Wang D, Wu X, Chen X, et al. MAPKs and NF-kappaB-mediated acrylamide-induced neuropathy in rat striatum and human neuroblastoma cells SY5Y. *J Cell Biochem.* (2019) 120:3898–910. doi: 10.1002/jcb.27671
73. Hayes JD, Dinkova-Kostova AT. The Nrf2 regulatory network provides an interface between redox and intermediary metabolism. *Trends Biochem Sci.* (2014) 39:199–218. doi: 10.1016/j.tibs.2014.02.002
74. Pan X, Yan D, Wang D, Wu X, Zhao W, Lu Q, et al. Mitochondrion-Mediated Apoptosis Induced by Acrylamide is Regulated by a Balance Between Nrf2 Antioxidant and MAPK Signaling Pathways in PC12 Cells. *Mol Neurobiol.* (2017) 54:4781–94. doi: 10.1007/s12035-016-0021-1
75. Pan X. *The role and Mechanism of MAPKs, Nrf2 and NF-κB Signaling pathWay in Acrylamide Neurotoxicity*. Master's thesis. Wuhan: Huazhong University of Science and Technology (2016).
76. Aldawood N, Alrezaki A, Alanazi S, Amor N, Alwasel S, Sirotkin A, et al. Acrylamide impairs ovarian function by promoting apoptosis and affecting reproductive hormone release, steroidogenesis and autophagy-related genes: An in vivo study. *Ecotoxicol Environ Saf.* (2020) 197:110595. doi: 10.1016/j.ecoenv.2020.110595
77. Song D, Xu C, Holck AL, Liu R. Acrylamide inhibits autophagy, induces apoptosis and alters cellular metabolic profiles. *Ecotoxicol Environ Saf.* (2021) 208:111543. doi: 10.1016/j.ecoenv.2020.111543
78. Yorimitsu T, He C, Wang K, Klionsky DJ. Tap42-associated protein phosphatase type 2A negatively regulates induction of autophagy. *Autophagy.* (2009) 5:616–24. doi: 10.4161/auto.5.5.8091
79. Ghavami S, Sharma P, Yeganeh B, Ojo OO, Jha A, Mutawe MM, et al. Airway mesenchymal cell death by mevalonate cascade inhibition: integration of autophagy, unfolded protein response and apoptosis focusing on Bcl2 family proteins. *Biochim Biophys Acta.* (2014) 1843:1259–71. doi: 10.1016/j.bbamcr.2014.03.006
80. Wu H, Che X, Zheng Q, Wu A, Pan K, Shao A, et al. Caspases: a molecular switch node in the crosstalk between autophagy and apoptosis. *Int J Biol Sci.* (2014) 10:1072–83. doi: 10.7150/ijbs.9719
81. Deng L, Zhao M, Cui Y, Xia Q, Jiang L, Yin H, et al. Acrylamide induces intrinsic apoptosis and inhibits protective autophagy via the ROS mediated mitochondrial dysfunction pathway in U87-MG cells. *Drug Chem Toxicol.* (2021) 21:1–12. doi: 10.1080/01480545.2021.1979030
82. Foyet HS, Tchinda Deffo S, Koagne Yewo P, Antioch I, Zingue S, Asongalem EA, et al. Ficus sycomorus extract reversed behavioral impairment and brain oxidative stress induced by unpredictable chronic mild stress in rats. *BMC Complement Altern Med.* (2017) 17:502. doi: 10.1186/s12906-017-2012-9
83. da Silva AI, Monteiro Galindo LC, Nascimento L, Moura Freitas C, Manhaes-de-Castro R, Lagranha CJ, et al. Fluoxetine treatment of rat neonates significantly reduces oxidative stress in the hippocampus and in behavioral indicators of anxiety later in postnatal life. *Can J Physiol Pharmacol.* (2014) 92:330–7. doi: 10.1139/cjpp-2013-0321
84. Chen Z, Zhong C. Oxidative stress in Alzheimer's disease. *Neurosci Bull.* (2014) 30:271–81. doi: 10.1007/s12264-013-1423-y
85. Patil SP, Jain PD, Sancheti JS, Ghumatkar PJ, Tambe R, Sathaye S. Neuroprotective and neurotrophic effects of Apigenin and Luteolin in MPTP induced parkinsonism in mice. *Neuropharmacology.* (2014) 86:192–202. doi: 10.1016/j.neuropharm.2014.07.012
86. Kopańska M, Lukáč N, Kapusta E, Formicki G. Acrylamide influence on activity of acetylcholinesterase, thiol groups, and malondialdehyde content in the brain of swiss mice. *J Biochem Mol Toxicol.* (2015) 29:472–8. doi: 10.1002/jbt.21717
87. Zhao M, Wang P, Zhu Y, Liu X, Hu X, Chen F. The chemoprotection of a blueberry anthocyanin extract against the acrylamide-induced oxidative stress in mitochondria: unequivocal evidence in mice liver. *Food Funct.* (2015) 6:3006–12. doi: 10.1039/c5fo00408j
88. Zhang P, Pan H, Wang J, Liu X, Hu X. Telomerase activity-independent function of telomerase reverse transcriptase is involved in acrylamide-induced neuron damage. *Biotech Histochem.* (2014) 89:327–35. doi: 10.3109/10520295.2013.855323
89. Cosentino K, Garcia-Saez AJ. Mitochondrial alterations in apoptosis. *Chem Phys Lipids.* (2014) 181:62–75. doi: 10.1016/j.chemphyslip.2014.04.001
90. Swanson KV, Deng M, Ting JP. The NLRP3 inflammasome: molecular activation and regulation to therapeutics. *Nat Rev Immunol.* (2019) 19:477–89. doi: 10.1038/s41577-019-0165-0
91. Singhal G, Jaehne EJ, Corrigan F, Toben C, Baune BT. Inflammasomes in neuroinflammation and changes in brain function: a focused review. *Front Neurosci.* (2014) 8:315. doi: 10.3389/fnins.2014.00315
92. Tschopp J, Schroder K. NLRP3 inflammasome activation: the convergence of multiple signalling pathways on ROS production? *Nat Rev Immunol.* (2010) 10:210–5. doi: 10.1038/nri2725
93. Sui X, Yang J, Zhang G, Yuan X, Li W, Long J, et al. NLRP3 inflammasome inhibition attenuates subacute neurotoxicity induced by acrylamide in vitro and in vivo. *Toxicology.* (2020) 432:152392. doi: 10.1016/j.tox.2020.152392
94. Luna RA, Foster JA. Gut brain axis: diet microbiota interactions and implications for modulation of anxiety and depression. *Curr Opin Biotechnol.* (2015) 32:35–41. doi: 10.1016/j.copbio.2014.10.007
95. Cryan JF, O'Mahony SM. The microbiome-gut-brain axis: from bowel to behavior. *Neurogastroenterol Motil.* (2011) 23:187–92. doi: 10.1111/j.1365-2982.2010.01664.x
96. Jiang Y, Li L, Liu B, Zhang Y, Chen Q, Li C. Vagus nerve stimulation attenuates cerebral ischemia and reperfusion injury via endogenous cholinergic pathway in rat. *PLoS One.* (2014) 9:e102342. doi: 10.1371/journal.pone.0102342
97. Braniste V, Al-Asmakh M, Kowal C, Anuar F, Abbaspour A, Toth M, et al. The gut microbiota influences blood-brain barrier permeability in mice. *Sci Transl Med.* (2014) 6:263ra158. doi: 10.1126/scitranslmed.3009759
98. Tan X, Ye J, Liu W, Zhao B, Shi X, Zhang C, et al. Acrylamide aggravates cognitive deficits at night period via the gut-brain axis by reprogramming the brain circadian clock. *Arch Toxicol.* (2019) 93:467–86. doi: 10.1007/s00204-018-2340-7
99. Quigley EMM. Microbiota-Brain-Gut Axis and Neurodegenerative Diseases. *Curr Neurol Neurosci Rep.* (2017) 17:94. doi: 10.1007/s11910-017-0802-6
100. Lopachin RM, Gavin T, Barber DS. Type-2 alkenes mediate synaptotoxicity in neurodegenerative diseases. *Neurotoxicology.* (2008) 29:871–82. doi: 10.1016/j.neuro.2008.04.016
101. Liu ZM, Tse LA, Chen B, Wu S, Chan D, Kowk T, et al. Dietary acrylamide exposure was associated with mild cognition decline among non-smoking Chinese elderly men. *Sci Rep.* (2017) 7:6395. doi: 10.1038/s41598-017-06813-9
102. Erkekoglu P, Baydar T. Acrylamide neurotoxicity. *Nutr Neurosci.* (2014) 17:49–57. doi: 10.1179/1476830513Y.0000000065
103. LoPachin RM, Gavin T. Molecular mechanism of acrylamide neurotoxicity: lessons learned from organic chemistry. *Environ Health Perspect.* (2012) 120:1650–7. doi: 10.1289/ehp.1205432
104. Heneka MT, Kummer MP, Latz E. Innate immune activation in neurodegenerative disease. *Nat Rev Immunol.* (2014) 14:463–77. doi: 10.1038/nri3705
105. Libby P, Everett BM. Novel Antiatherosclerotic Therapies. *Arterioscler Thromb Vasc Biol.* (2019) 39:538–45. doi: 10.1161/ATVBAHA.118.310958
106. Hanamsagar R, Torres V, Kielian T. Inflammasome activation and IL-1beta/IL-18 processing are influenced by distinct pathways in microglia. *J Neurochem.* (2011) 119:736–48. doi: 10.1111/j.1471-4159.2011.07481.x
107. Afonina IS, Zhong Z, Karin M, Beyaert R. Limiting inflammation-the negative regulation of NF-kappaB and the NLRP3 inflammasome. *Nat Immunol.* (2017) 18:861–9. doi: 10.1038/ni.3772
108. Wu AG, Zhou XG, Qiao G, Yu L, Tang Y, Yan L, et al. Targeting microglial autophagic degradation in NLRP3 inflammasome-mediated neurodegenerative diseases. *Ageing Res Rev.* (2021) 65:101202. doi: 10.1016/j.arr.2020.101202
109. Deng L. *Study on the Mechanism Of Acrylamide-Induced Neurotoxicity*. [Master's thesis]. Shanghai: East China University of Science and Technology (2021).

110. Wang Y, Yin B, Li D, Wang G, Han X, Sun X. GSDME mediates caspase-3-dependent pyroptosis in gastric cancer. *Biochem Biophys Res Commun.* (2018) 495:1418–25. doi: 10.1016/j.bbrc.2017.11.156
111. Xia W, Li Y, Wu M, Jin Q, Wang Q, Li S, et al. Gasdermin E deficiency attenuates acute kidney injury by inhibiting pyroptosis and inflammation. *Cell Death Dis.* (2021) 12:139. doi: 10.1038/s41419-021-03431-2
112. Fink SL, Cookson BT. Apoptosis, pyroptosis, and necrosis: mechanistic description of dead and dying eukaryotic cells. *Infect Immun.* (2005) 73:1907–16. doi: 10.1128/IAI.73.4.1907-1916.2005
113. Foster JA, McVey-Neufeld KA. Gut-brain axis: how the microbiome influences anxiety and depression. *Trends Neurosci.* (2013) 36:305–12. doi: 10.1016/j.tins.2013.01.005
114. Chen J, Li Y, Tian Y, Huang C, Li D, Zhong Q, et al. Interaction between Microbes and host intestinal health: modulation by dietary nutrients and gut-brain-endocrine-immune axis. *Curr Protein Pept Sci.* (2015) 16:592–603. doi: 10.2174/1389203716666150630135720
115. El Aidy S, Dinan TG, Cryan JF. Immune modulation of the brain-gut-microbe axis. *Front Microbiol.* (2014) 5:146. doi: 10.3389/fmicb.2014.00146
116. Forsythe P, Bienenstock J, Kunze WA. Vagal pathways for microbiome-brain-gut axis communication. *Adv Exp Med Biol.* (2014) 817:115–33. doi: 10.1007/978-1-4939-0897-4_5
117. Kuwahara A, Matsuda K, Kuwahara Y, Asano S, Inui T, Marunaka Y. Microbiota-gut-brain axis: enteroendocrine cells and the enteric nervous system form an interface between the microbiota and the central nervous system. *Biomed Res.* (2020) 41:199–216. doi: 10.2220/biomedres.41.199
118. Hu X, Wang T, Jin F. Alzheimer's disease and gut microbiota. *Sci China Life Sci.* (2016) 59:1006–23. doi: 10.1007/s11427-016-5083-9
119. Sun MF, Shen YQ. Dysbiosis of gut microbiota and microbial metabolites in Parkinson's Disease. *Ageing Res Rev.* (2018) 45:53–61. doi: 10.1016/j.arr.2018.04.004
120. Hagmar L, Tornqvist M, Nordander C, Rosen I, Bruze M, Kautiainen A, et al. Health effects of occupational exposure to acrylamide using hemoglobin adducts as biomarkers of internal dose. *Scand J Work Environ Health.* (2001) 27:219–26. doi: 10.5271/sjweh.608
121. Mulloy KB. Two case reports of neurological disease in coal mine preparation plant workers. *Am J Industr Med.* (1996) 30:56–61. doi: 10.1002/(sici)1097-0274(199607)30:13.0.Co;2-q
122. Skowron J. [Priority: safe working conditions]. *Med Pr.* (2019) 70:497–509. doi: 10.13075/mp.5893.00832
123. Brown L, Rhead M. Liquid chromatographic determination of acrylamide monomer in natural and polluted aqueous environments. *The Analyst.* (1979) 104:391–9. doi: 10.1039/an9790400391
124. Yang F, Li Z, Bian Z, Tang G, Fan Z, Wang Y, et al. Environmentally friendly method for the determination of acrylamide and trimethylolpropane in paper packaging materials by liquid chromatography with tandem mass spectrometry. *J Sep Sci.* (2014) 37:3625–31. doi: 10.1002/jssc.201400504
125. Faria M, Valls A, Prats E, Bedrossiantz J, Orozco M, Porta JM, et al. Further characterization of the zebrafish model of acrylamide acute neurotoxicity: gait abnormalities and oxidative stress. *Sci Rep.* (2019) 9:7075. doi: 10.1038/s41598-019-43647-z
126. Wang W, Huang L, Thomas ER, Hu Y, Zeng F, Li X. Notoginsenoside R1 protects against the acrylamide-induced neurotoxicity via upregulating Trx-1-Mediated ITGAV expression: involvement of autophagy. *Front Pharmacol.* (2020) 11:559046. doi: 10.3389/fphar.2020.559046

Conflict of Interest: The authors declare that the research was conducted in the absence of any commercial or financial relationships that could be construed as a potential conflict of interest.

Publisher's Note: All claims expressed in this article are solely those of the authors and do not necessarily represent those of their affiliated organizations, or those of the publisher, the editors and the reviewers. Any product that may be evaluated in this article, or claim that may be made by its manufacturer, is not guaranteed or endorsed by the publisher.

Copyright © 2022 Zhao, Zhang and Deng. This is an open-access article distributed under the terms of the Creative Commons Attribution License (CC BY). The use, distribution or reproduction in other forums is permitted, provided the original author(s) and the copyright owner(s) are credited and that the original publication in this journal is cited, in accordance with accepted academic practice. No use, distribution or reproduction is permitted which does not comply with these terms.

frontiers in Nutrition

ORIGINAL RESEARCH
published: 25 March 2022
doi: 10.3389/fnut.2022.846080

Extraction, Structural Characterization, and Immunomodulatory Activity of a High Molecular Weight Polysaccharide From *Ganoderma lucidum*

Guo Liu[1,2†], Jun Zhang[1†], Qixin Kan[1], Mingyue Song[1], Tao Hou[1], Siyu An[1], Hongyu Lin[1], Hongzhang Chen[3], Liuyun Hu[3], Jie Xiao[1], Yunjiao Chen[1]* and Yong Cao[1]*

[1] Guangdong Provincial Key Laboratory of Nutraceuticals and Functional Foods, College of Food Science, South China Agricultural University, Guangzhou, China, [2] College of Horticulture, South China Agricultural University, Guangzhou, China, [3] Infinitus China Co., Ltd., Guangzhou, China

OPEN ACCESS

Edited by:
Biao Yuan,
China Pharmaceutical University, China

Reviewed by:
Tao Feng,
Shanghai Institute of Technology, China
Xiao Xu,
Shaoxing University, China

***Correspondence:**
Yunjiao Chen
yunjiaochen@scau.edu.cn
Yong Cao
caoyong2181@scau.edu.cn

† These authors have contributed equally to this work

Specialty section:
This article was submitted to Food Chemistry, a section of the journal Frontiers in Nutrition

Received: 30 December 2021
Accepted: 18 February 2022
Published: 25 March 2022

Citation:
Liu G, Zhang J, Kan Q, Song M, Hou T, An S, Lin H, Chen H, Hu L, Xiao J, Chen Y and Cao Y (2022) Extraction, Structural Characterization, and Immunomodulatory Activity of a High Molecular Weight Polysaccharide From Ganoderma lucidum. Front. Nutr. 9:846080. doi: 10.3389/fnut.2022.846080

Ganoderma lucidum polysaccharides (GLP) exhibited excellent immunomodulatory activity. Unfortunately, the structure and immunomodulatory activity of GLP are still unclear. GLP was separated into two fractions [high Mw Restriction Fragment Length Polymorphism (RGLP) and low Mw EGLP] using 10 kDa cut-off ultrafiltration membrane. Although the RGLP content was low in GLP, the immunomodulatory activity in RGLP was significantly higher than that of EGLP. Moreover, RGLP was further separated *via* the Sephacryl column to obtain RGLP-1 showed the best immunomodulatory activity in the macrophage RAW264.7 model. Structural analysis revealed that RGLP-1 was 3,978 kDa and mainly consisted of glucose. Periodate oxidation, Smith degradation, and methylation results indicated that RGLP-1 is a β-pyran polysaccharide mainly with 1→3, 1→4, 1→6, and 1→3, 6 glycosyl bonds at a molar ratio of 40.08: 8.11: 5.62: 17.81. Scanning electron microscopy, atomic force microscopy, and Congo red experiments revealed that RGLP-1 intertwined with each other to form circular aggregates and might possess a globular structure with triple-helix conformation in water. Overall, these results provide RGLP-1 as a potential functional food ingredient or pharmaceutical for immunomodulatory.

Keywords: *Ganoderma lucidum*, high molecular weight polysaccharides, purification, structure, immunomodulatory activity

INTRODUCTION

Ganoderma lucidum (*G. lucidum*) is both food and traditional Chinese medicine (1). It has a long history of being used as soup, tea, and liquor food raw material in Shandong, Anhui, and other regions of China. There are a large number of commercially available functional foods with *G. lucidum* as raw materials in Asian counties (2, 3). Until now, the number of functional foods products containing *G. lucidum* has reached about 1,060 according to the published data from Chinese Administration for Market Regulation. The annual sale of *G. lucidum* products exceeded $2.5 billion in 2013 (4). In recent decades, *G. lucidum* exhibits valuable biological activities, such as immunomodulatory, antitumor, antioxidant, antiaging, anti-inflammatory,

and hypoglycemic effects (5, 6). In modern pharmacological and functional food investigations, a number of bioactive compounds were separated from *G. lucidum*, including polysaccharides, triterpenoids, protein, sterols, nucleosides, and alkaloids (7–9). Polysaccharides stand for one of the most abundant components in *G. lucidum,* contributing to a major active ingredient with numerous healthy benefits, particularly for the prevention and treatment of immunomodulation (10) and antitumor properties (11, 12). It has been reported that the biological activity of *G. lucidum* polysaccharides (GLP) relies on their chemical composition (13).

Currently, there is no general agreement on the relationships between the structural features and biological activities of GLP (2). The structure of polysaccharides is complex and diverse, which is determined by molecular weight, monosaccharide composition, glycoside bond structure, configurations of main and branch chains, and branch type (14). Expectedly, the bioactivity depended on molecular size and chemical structures (15). A study reported that a heteroglycans (PL-1) with a molecular weight of 8.3 kDa isolated from fruiting bodies of *G. lucidum* had an immune-stimulating activity in mice (16). Researchers purified a homogeneous polysaccharide with an average molecular weight of 44.4 kDa from *G. lucidum* fruiting bodies and found that this polysaccharide exhibited excellent antitumor and immunomodulatory activities using a mouse model (17). A homogeneous *Ganoderma atrum* polysaccharide (PSG-1) with an average molecular weight of 1,013 kDa has strong immunomodulatory, antitumor, and antioxidant activities (1, 18, 19). A water-soluble polysaccharide (GSP-6B) with a molecular mass of 1,860 kDa was isolated from the fruiting bodies of *Ganoderma sinense*, an *in vitro* immunomodulating activity assay revealed that GSP-6B could significantly induce the release of IL-1β and TNF-α in human peripheral blood mononuclear cells in a dose-dependent manner, suggesting that GSP-6B had the potential as adjuvant therapy medicines against tumors (20). To sum up, it has been reported that both high and low *Ganoderma* polysaccharides have immunomodulatory activity. A previous study showed that high molecular weight was probably not necessary to obtain immunoregulatory activities (21). On the contrary, a recent study has shown that bioactivities of polysaccharides are closely correlated to their molecular weight, the larger the molecular weight of GLP, the higher the bioactivity function (2). To date, this query that what molecular weight of polysaccharide has the best immunomodulatory activity has been controversial, the relationship between the molecular weight of GLP and immunobiological activity is still unclear.

In this work, GLP was obtained using a novel continuous phase transition extraction technology. We then used ultrafiltration purification and RAW264.7 macrophages model *in vitro* to investigate the immunobiological activity. Fraction Restriction Fragment Length Polymorphism (RGLP) with the greatest immunobiological activity was further purified by Sephacryl S-500 HR column chromatography. The structure characterization of sub-fraction RGLP-1 was investigated systematically by high-performance gel permeation chromatography (HPGPC), gas chromatography–mass spectroscopy (GC–MS), methylation analysis, Fourier transform-infrared spectroscopy (FT-IR), Congo red test, circular dichroism (CD), scanning electron microscopy (SEM), and atomic force microscopy (AFM). Therefore, these should all help further clarify the structure-effective relationship of GLP. Further, RGLP-1 was potential commercial functional food ingredient for immunoregulation.

MATERIALS AND METHODS

Materials and Chemicals

The fruiting bodies of *G. lucidum* were supplied by Infinitus China Co., Ltd. (Guangzhou, China) and cut into small pieces (sieved through 3 mesh screens). The *G. lucidum* pieces were dried at 60°C in the oven and stored at room temperature until analysis. A multifunctional continuous phase transition extraction apparatus was supplied by Guangdong Provincial Key Laboratory of Nutraceuticals and Functional Foods.

Cut-off ultrafiltration membrane (10 kDa, Vivaflow 50) and Sephacryl S-500 HR were purchased from Sartorius Life Sciences (Goettingen, Sartorius) and GE Healthcare Life Sciences (Uppsala, Sweden), respectively. Macrophage RAW264.7 cells line was purchased from the Chinese Academy of Sciences Cell Bank. Dextrans with different molecular weights (5, 25, 50, 80, 150, 270, 410, 670, and 1,800 kDa) and the monosaccharide standards (xylose, fructose, galactose, arabinose, mannose, and glucose) were acquired from Sigma-Aldrich (MO, United States). Dulbecco's modified Eagle's minimum (DMEM), penicillin, 3-(4, 5-dimethylthiazol-2-yl)-2, 5-diphenyltetrazolium bromide (MTT), streptomycin, fetal bovine serum (FBS), and dimethyl sulfoxide (DMSO) were obtained from Gibco (Carlsbad, California, United States). All of the other reagents were analytical grade.

Extraction and Separation of Polysaccharides

The extraction of crude GLP was performed using a continuous phase transition extraction apparatus on a pilot scale. Air-dried fruiting bodies of *G. lucidum* pieces (2.0 kg) were placed in a 3 L extraction kettle. The extraction conditions were as follows: solvent, distilled water; temperature, 100°C; time, 4 h; flow rate, 28 L/h. The aqueous extracts were concentrated using the continuous phase transition extraction device and mixed with anhydrous ethanol (1:4, v/v) at 4°C overnight. The precipitation was collected by centrifugation at 2,620 G for 10 min and freeze-dried to obtain the crude GLP.

The GLP was dissolved in 500 ml of distilled water and centrifuged at 2,620 G for 10 min before loading on a 10 kDa cut-off ultrafiltration membrane. GLP solution sample was injected into the cut-off ultrafiltration membrane at a rate of 1 ml/min by a constant current pump for ultrafiltration separation. In this way, an eluted fraction (EGLP, Mw < 100 kDa) and a retained (RGLP, Mw > 100 kDa) fraction were obtained according to molecular weight. Then EGLP and RGLP fractions were lyophilized and stored at −20°C.

The RGLP was further purified by Sephacryl S-500 HR column (2.6 × 60 cm), pre-equilibrated with deionized water, and eluted with 0.2 mol/L NaCl at a rate of 0.8 ml/min (8 ml/tube). The main fraction was collected, dialyzed, and lyophilized to afford one white fluffy polysaccharide RGLP-1. The polysaccharide content was determined by the phenol-sulfuric acid method.

Study on the Immunostimulatory Activity of Polysaccharides

Culture Cell

RAW264.7 cell lines were cultured in DMEM supplemented with 10% heat-inactivated FBS containing 100 μg/ml of penicillin and 100 μg/ml of streptomycin at 37°C under humidified air with 5% CO_2. Cells in the exponential growth phase were used for experiments.

Cell Viability Analysis

The effect of polysaccharide GLP, EGLP, and RGLP on the viability of RAW264.7 cells was determined by MTT assay. The cells were seeded at a density of 1×10^5 cells/ml in a 96-well plate for 24 h at 37°C in a humidified atmosphere with 5% CO_2, and then were cultured with different concentrations of polysaccharides (1, 2, 5, 10 μg/ml) for 24 h. Each concentration was repeated in three wells. After incubation, MTT was added to each well 20 μl to a final concentration of 0.5 mg/ml. After 4 h incubation, the produced formazan crystals were dissolved in DMSO (150 μl/well). The absorbance was measured at 570 nm, and the cell proliferation index was calculated according to the formula:

Cell proliferation index (%) = $(A_1/A_0) \times 100\%$. A_0 is the absorbance of a blank treatment group. A_1 is the absorbance of a sample treatment group.

Phagocytic Activity Assay

The phagocytic activity of GLP, EGLP, and RGLP in RAW264.7 cells was measured by a neutral red assay. RAW264.7 cells were seeded at 2×10^4 cells/well in a 96-well plate and incubated for 24 h. Various final concentration of GLP, RGLP, and EGLP (1, 2, 5, 10 μg/ml), DMEM medium and LPS (1 μg/ml) were added into each well. After 24 h incubation in the condition of 37°C and 5% CO_2, culture media were removed and 100 μl/well of 0.1% neutral red was added and incubated for 4 h, the plate was washed with PBS for three times, 100 μl of cell lying solution (ethanol and acetic acid mixed in equal volume) was added into each well and shaken for 10 min. The absorbance was evaluated in a microplate reader at 540 nm, and the phagocyte phagocytosis rate was calculated according to the equation:

Phagocyte phagocytosis index (%) = $(A_1/A_0) \times 100\%$. A_0 is the absorbance of a blank treatment group. A_1 is the absorbance of a sample treatment group.

Determination of Nitric Oxide, Tumor Necrosis Factor-α, and Interleukin-6

The RAW264.7 cells were seeded into 96-well plates at a density of 2×10^4 cells/well and cultured for 24 h with GLP, EGLP, and RGLP at various concentrations as mentioned earlier. Equal volume of medium or LPS (1 μg/ml) was added as the control and positive group, respectively. Then, the cell culture supernatants were collected and levels of nitric oxide (NO), tumor necrosis factor-α (TNF-α), and interleukin 6 (IL-6) were measured by the Nitric Oxide Assay kit (Beyotime, Shanghai, China) and TNF-α, IL-6 enzyme-linked immunoassay kits (Neobioscience, Shenzhen, China).

Characterization of RGLP-1

Ultraviolet Absorption Spectroscopy Analysis

To detect the purity of the RGLP-1, the UV spectra of RGLP-1 were investigated using an UV spectrophotometer (UV-1700, Shimadzu, Japan) scanned in the 200–400 nm region according to a published method with minor modification (22). Briefly, 1.0 mg/ml RGLP-1 was prepared with distilled water, the solution was transferred in a quartz cuvette.

Determination of Molecular Weight

The molecular weight of RGLP-1 was measured using HPGPC (23) performed on an analytic HPLC system (Shimadzu) equipped with a TSK G-6000 PWXL column (7.8 × 300 mm) connected to TSK G-3000 PWXL column (7.8 × 300 mm, Tosoh Biosep, Japan) and a RID-10A refractive index detector (Shimadzu). The injection volume was 20 μl. The 0.02 mol/L Na_2SO_4 solution was used as mobile phase at a flow rate of 0.6 ml/min at 35°C. The average molecular weight of RGLP-1 was calculated by the calibration curve established by a series of dextran standards (5, 25, 40, 80, 270, 410, 670, 1,500, and 1,800 kDa).

Monosaccharide Composition

To determine the monosaccharide composition, RGLP-1 was first hydrolyzed using a reported procedure as previously described method (24). The RGLP-1 was hydrolyzed by 4 ml of 2 mol/L trifluoroacetic acid (TFA) at 110°C for 6 h. Acetylation was carried out with 10 mg of hydroxylamine hydrochloride and 1 ml of pyridine for 30 min at 90°C. Next, 1 ml of acetic anhydride was added with continuous heating. The hydrolysis products were converted into their acetylated derivatives and analyzed by GC-MS spectrometer (TSQ 8000, Thermo Fisher, Waltham, MA, United States) equipped with a TG-5MS capillary column (60 m × 0.25 mm × 0.50 μm). Five monosaccharides (fucose, mannose, rhamnose, galactose, and glucose) were used as the external standards to identify the composition of the polysaccharides.

The temperature program of the column was set as follows: initial temperature of 160°C for 2 min, then increased to 200°C at the rate of 5°C/min and held for 5 min. Subsequently, the temperature increased from 200 to 230°C at 2°C/min and was maintained for 10 min. Helium was used as the carrier gas at a constant flow rate of 0.8 ml/min. The injection temperature and detector temperature were both 250°C. The injection volume was 1 μl and the split ratio was 10: 1 (25).

Periodate Oxidation—Smith Degradation

The samples were treated using a modified method (26). Briefly, the RGLP-1 (10 mg) was dissolved in 12.5 ml of distilled water, and 12.5 ml of sodium periodate (30 mmol/L) was then added.

The solution was kept in the dark at 4°C, and 0.1 ml of aliquots were withdrawn at 6–12 h intervals, diluted to 25 ml with distilled water, and read using a spectrophotometer at 223 nm, until the optical density value became stable. Glycol (2 ml) was used to stop periodate oxidation. The solution of periodate product (2 ml) was titrated to calculate the production of formic acid by 0.01 mol/L sodium hydroxide, and the rest was extensively dialyzed against tap water and distilled water for 48 h. The residues were concentrated and reduced with sodium borohydride (35 mg). The solution was placed at room temperature for 24 h, neutralized to pH 5.5 with 50% acetic acid, dialyzed as described earlier, and concentrated to a volume of 10 ml followed by freeze-drying. Subsequent treatments were performed as described previously. The residues (10 mg) were hydrolyzed with trifluorocetic acid and then were acetylated with hydroxylamine hydrochloride, pyridine, and acetic anhydride.

Methylation Analysis

The polysaccharide was methylated by a published method with some modification (27). The dried RGLP-1 (10 mg) was dissolved in 5 ml DMSO with heated or sonicated for 1 h to ensure a completed solution. Sodium hydroxide (200 mg) and iodine methane (2.5 ml) were added to the solution with stirring for 12 h in a dark place. This methylation procedure was conducted three times and stopped by the addition of 2 ml distilled water. The methylated polysaccharide was extracted three times with 5 ml trichloromethane. The trichloromethane extract was then evaporated to dryness. The dried methylated polysaccharide was hydrolyzed with trifluorocetic as described earlier. The hydrolysate was dissolved in 4 ml distilled water and the pH value in solution should be adjusted to 10–12 by 10% sodium hydroxide solution. Then, the hydrolysate solution was reduced by sodium borohydride (100 mg). After 12 h, the pH value in solution should be adjusted to 5.5 by 50% acetic acid and evaporated to dryness. The following procedure of acetylation was described as earlier.

Fourier Transform Infrared Spectra Analysis

The infrared profile of RGLP-1 was determined using the KBr disc method. The KBr-disk was monitored in the range of 400–4,000 cm^{-1} with a Fourier transform infrared (FT-IR) spectrophotometer (Vertex70, Bruker, Ettlingen, Germany). The experimental parameters setting of resolution was 4 cm^{-1} and the scans number was 16 times.

Scanning Electron Microscope Observation

Morphological alterations of RGLP-1 were observed using an EVO18 scanning electron microscope (ZEISS, Germany) at an accelerating voltage of 10.0 kV. The dried sample was coated with a gold film before testing, and scanned at the magnification of 250×, 500×, 1,000×, and 2,000×.

Atomic Force Microscopy Observation

The dried sample was dissolved to 10 μg/ml deionized water. About 10 μl of polysaccharides solution was dropped onto a mica plate and dried at room temperature for 12 h. The AFM (Multimode 8 instrument, United States) was operated in the tapping mode. The images were captured by NanoScope software.

Congo Red Test

The helical structure of RGLP-1 was determined *via* Congo red test according to a reported method with minor modification (28). In brief, 2.0 ml polysaccharide sample (1 mg/ml) was mixed with 2.0 ml of a Congo red solution (80 μmol/L). Then, the mixtures were gradually added with a 1 mol/L NaOH solution to form the final NaOH concentrations of 0–0.5 mol/L. The mixtures were equilibrated for 10 min at room temperature. The maximum absorption wavelength of Congo red and Congo red-polysaccharide mixture was measured by an ultraviolet-visible spectrophotometer (UV-1700, Shimadzu, Japan) in the range of 400–600 nm.

Circular Dichroism Analysis

The CD spectra of RGLP-1 (1 ml of 1 mg/ml polysaccharide solution was mixed with 1 ml deionized water) and RGLP-1-Congo red complex (1 ml of 1 mg/ml polysaccharide solution was mixed with 1 ml of 80 μmol/L Congo red) were obtained on a chirascan CD spectrometer (Applied Photophysics Ltd., United Kingdom) with a scan rate of 100 nm/min and a bandwidth of 1 nm and a time constant of 1 s at 25°C. Data were collected from 190 to 260 nm with three scans averaged.

Statistical Analysis

All experimental data were expressed as the mean ± *SD*. The significance of the difference was evaluated by multiple comparison analyses with Duncan's tests (SPSS 21.0 software). A value of $P < 0.05$ was considered to be defined as statistically significant.

RESULTS AND DISCUSSION

Extraction, Purification, and Molecular Weight Distribution of *Ganoderma lucidum* Polysaccharides

Crude GLP with a yield of 7.13% was isolated from *G. lucidum* through hot water extraction using continuous phase transition extraction technology followed by ethanol precipitation and lyophilization. The molecular weight distribution of the crude GLP was determined by HPGPC as illustrated in **Figure 1A**. HPGPC chromatograms profiles of GLP exhibited two main populations at the retention time of 32 min and 34 min. The percentage of the two populations with low molecular weight was 95.26%, implying that GLP mainly contained polysaccharides with low molecular weight. In crude GLP, two small populations at the retention time of 18.5 and 24 min were also found which only accounted for 4.74%. GLP was then purified by a 10 kDa cut-off ultrafiltration membrane into two fractions, including EGLP (**Figure 1B**) and RGLP (**Figure 1C**). According to the calibration curve (log Mw = 12.671–0.292t, $R^2 = 0.9989$). EGLP consisted of two main fractions with an average molecular weight of 3,288 and 948 Da. In the RGLP fraction, one main population at 3,473 kDa was obtained representing 95% according to the area normalization method in **Figure 1C**. A previous study reported that the crude polysaccharides had three major fractions (PS-F1, PS-F2, and PS-F3), PS-F1 contained large polysaccharides

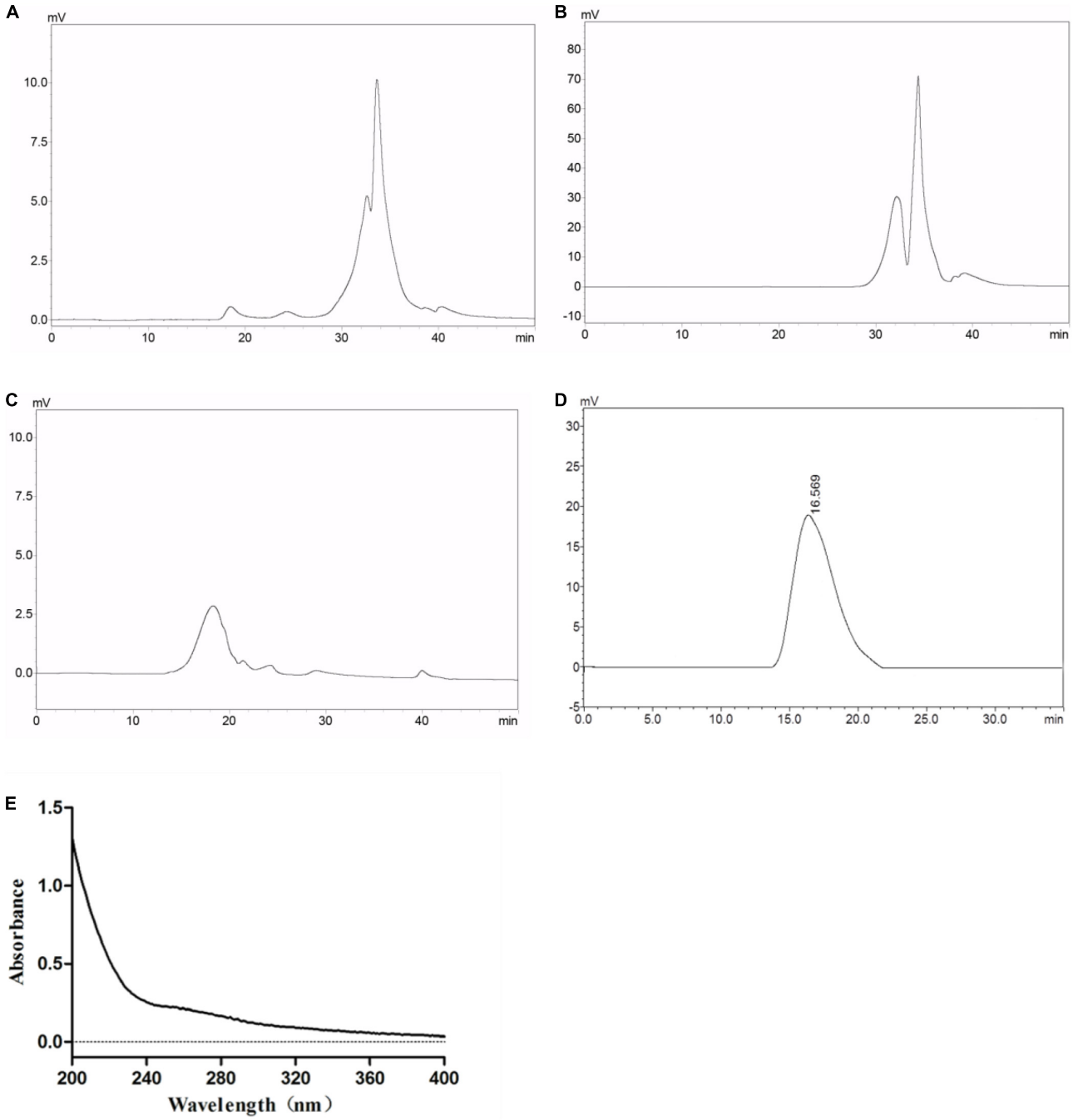

FIGURE 1 | Average molecular weight distribution of **(A)** GLP, **(B)** EGLP, **(C)** RGLP, **(D)** RGLP-1 and ultraviolet absorption spectrum **(E)** of RGLP-1.

which are over 2,000 kDa, and PS-F2 (6–52 kDa) and PS-F3 (2–4 kDa) contained smaller molecule polysaccharide (29). Different molecular weight distributions may be due to the difference between the extraction process and the alcohol precipitation process.

Restriction Fragment Length Polymorphism with higher immunomodulatory activity was further purified through the Sephacryl S-500 HR column. A novel purified fraction of RGLP-1 was obtained and the molecular weight of RGLP-1 was determined by HPGPC in **Figure 1D**. It could be seen that RGLP-1 exhibited a narrow and symmetrical peak, of which the baseline was stable, indicating that RGLP-1 was a homogeneous polysaccharide after purification by cut-off ultrafiltration membrane and Sephacryl gel column. According to the calibration curve, the molecular weight of RGLP-1 was exactly 3,978 kDa. RGLP-1 contained 96.23% (w/w) of total sugar by the

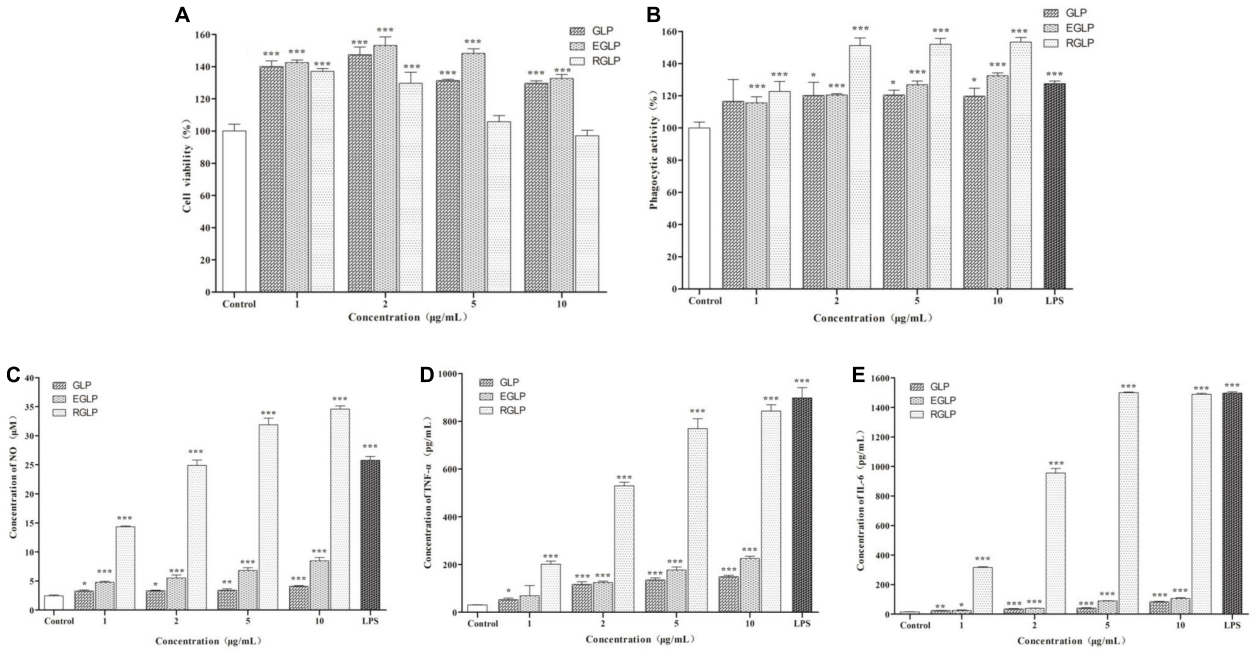

FIGURE 2 | The effect of polysaccharides on cell viability **(A)**, phagocytic ability **(B)**, NO **(C)**, TNF-α **(D)**, and IL-6 **(E)** of RAW 264.7 cells. ***Statistically significant at $P < 0.001$. **Statistically significant at $P < 0.01$. *Statistically significant at $P < 0.05$.

phenol–sulfuric acid method. UV absorption spectrum of RGLP-1 showed no absorption peak at 260 or 280 nm in **Figure 1E**, indicating that RGLP-1 was absent of nucleic acids and protein.

In vitro Immunostimulatory Activities

Effects of *Ganoderma lucidum* Polysaccharides, EGLP, and RGLP on the Proliferation of Macrophages

In this study, the RAW264.7 macrophage cells model was used to perform the immunomodulatory activity of GLP, EGLP, and RGLP. For each sample, four concentrations (1, 2, 5, and 10 μg/ml) were selected.

The MTT assay indicated that GLP, EGLP, and RGLP had no cytotoxic effect on macrophage RAW264.7 cells at a concentration range of 1–10 μg/ml in **Figure 2A**. At the concentration of 2 μg/ml, EGLP had the best proliferative effect of RAW264.7 cells. RGLP had the best proliferation on RAW264.7 cells in the concentration of 1 μg/ml and the viability showed a slight decline when the concentrations increased further from 1 to 10 μg/ml. Therefore, the selected concentration of GLP, EGLP, and RGLP for immunological activity assay should fall below 10 μg/ml.

Effect of *Ganoderma lucidum* Polysaccharides, EGLP, and RGLP on the Phagocytosis of Macrophages

Phagocytosis is one of the most prominent characteristics of macrophage activation and is an important barrier to the host innate immune system (30). As shown in **Figure 2B**, LPS (1 μg/ml) as the positive control could significantly promote RAW264.7 cells to uptake neutral red significantly ($p < 0.001$). As expected, compared with the control, GLP, EGLP, and RGLP also enhanced the phagocytic ability significantly at the concentration range of 1–10 μg/ml. The extent of stimulation followed the order: RGLP > EGLP > GLP. The phagocytic ability in RGLP at the concentration range of 2–10 μg/ml was significantly higher than that of LPS ($p < 0.01$).

Effects of *Ganoderma lucidum* Polysaccharides, EGLP, and RGLP on the Production of NO and Cytokines From RAW264.7 Macrophages

Activated macrophages secrete NO and cytokines, such as TNF-α and IL-6, which play an important role in immunomodulation (31). The results showed that compared with the control group, GLP, EGLP, and RGLP could significantly stimulate the NO production in a dose-dependent manner ($p < 0.001$) in **Figure 2C**. NO production in RGLP was higher than those of GLP and EGLP groups.

Besides, the expressions of TNF-α and IL-6 were in a dose-dependent manner with the increase of the GLP, EGLP, and RGLP concentration in **Figures 2D,E**. When the concentration of GLP, EGLP, and RGLP was 10 μg/ml, the relative expression content of TNF-α reached the maximal, respectively, was 4.85, 7.66, and 27.50 times higher than that of the control group. Like the result of TNF-α, the relative expression content of IL-6 of GLP, EGLP, and RGLP also reached the maximal at the concentration of 10 μg/ml, which was 5.55, 6.98, and 98.56 times higher than that of the control group. The amount of NO, TNF-α, and IL-6 stimulated by each fraction followed the order: RGLP > EGLP > GLP. Overall, these results suggested that GLP, EGLP, and RGLP may potentially enhance macrophage-mediated immune response, especially RGLP.

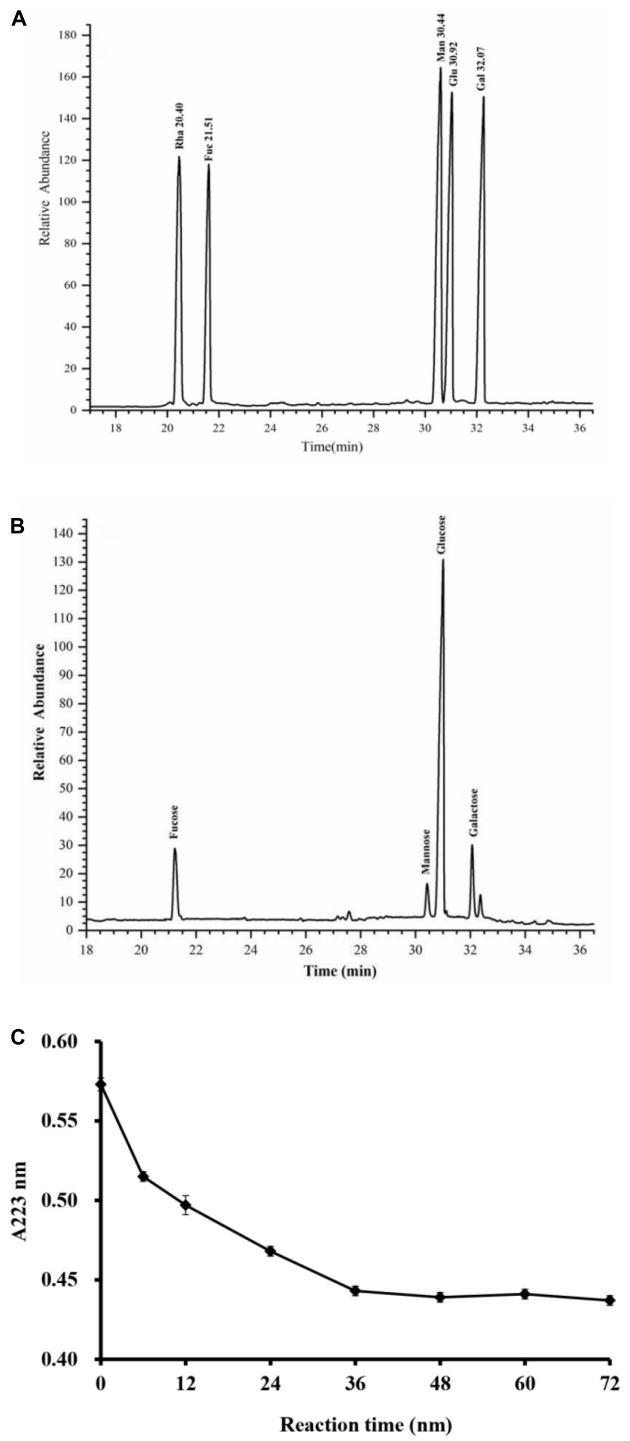

FIGURE 3 | GC–MS chromatograms of monosaccharide standards **(A)** and RGLP-1 **(B)**; The periodic acid consumption of RGLP-1 **(C)**.

Structural Analysis

Monosaccharide Composition

As shown in **Figure 3**, the monosaccharide composition of RGLP-1 was composed of fucose, mannose, glucose, and galactose at a molar ratio of 0.13: 0.05: 0.72: 0.10. These results suggested that RGLP-1 is a heteropolysaccharide, glucose had the highest proportion and may be the backbone of the chain of RGLP-1. A previous study found that GLP-3 was purified from *Ganoderma leucocontextum* by ultrafiltration and column chromatography consisted of arabinose, xylose, mannose, glucose, and galactose in a molar ratio of 2.4: 3.3: 0.8: 92.7: 0.8 (32). In addition, the purified GLP consist of glucose, galactose, arabinose, xylose, and mannose with molar ratios of 0.793: 0.964: 2.944: 0.167: 0.384: 7.94 and linked by β-glycosidic linkages (33). Although the heterogeneous polysaccharides were obtained after separation from *G. lucidum*, there were significant differences in the types and amount of monosaccharides. This is likely because of the differences in varieties of raw materials, extraction process, and purification method.

Periodate Oxidation and Smith Degradation Analysis

Periodate oxidation results are shown in **Figure 3C**. About 1 mol of hexose residue consumed 0.358 mol of periodate and produced 0.016 mol of formic acid. A small amount of formic acid formation suggested that RGLP-1 contains a small amount of (1→) or (1→6) linkage. The molar amount of periodate consumed by RGLP-1 was far less than the sample consumption, it indicated that there is a large proportion of (1→3) linkage in RGLP-1. The molar amount of periodate consumed by RGLP-1 was far more than two times the molar amount of formic acid, revealing that RGLP-1 also contains (1→2) or (1→4) linkage.

Then RGLP-1 structure was further analyzed by Smith degradation by GC–MS. The glycerol, erythritol, mannose, glucose, and galactose absorption peak were found. Glycerol indicated that (1→2), (1→4), or (1→6) linkage existed. Erythritol is a chemical indicative of (1→4) or (1→6) linkage, suggesting that (1→4) or (1→6) linkage existed. The presence of a lot of mannose, glucose, and galactose demonstrated that some of the linkages, such as (1→3), (1→3,6), (1→2,3), (1→2,4), (1→3,4), and (1→2,3,4), were existed (34–36). This finding is consistent with a previous study that GCPB-2 (GLP fraction) may have (1→2), (1→4), (1→6) glycosidic bonds by periodate oxidation and Smith degradation analysis (36). More precise glycosidic bonds were confirmed in the methylation analysis.

Methylation Analysis

The methylation analysis was performed to determine the glycosidic linkages of RGLP-1. Based on the retention time and standard data in the CCRC spectral database, RGLP-1 exhibited 12 main peaks as summarized in **Table 1**.

According to the retention time, the 12 peaks were identified as 2,4,6-Me_3-Glcp, 2,3,4,6-Me_4-Glcp, 2,4-Me_2-Glcp, 2,3,6-Me_3-Glcp, 2,3,4-Me_3-Glcp, 2,3,4-Me_3-Glcp, 2,4,6-Me_3-Galp, 4,6-Me_2-Galp, 2,3,4,6-Me_4-Galp, 2,3,4-Me_3-Galp, 2,3-Me_2-Galp, 2,4,6-Me_3-Manp, and 3,4,6-Me_3-Manp with a molar ratio of 34.54:22.40:17.81:8.11:4.12:4.13:2.16:2.12:1.50:1.14:1.41:0.56.

The results suggested that RGLP-1 contained 12 linkage forms: (1→3)-linked glucose, (1→)-linked glucose, (1→3,6)-linked glucose, (1→4)-linked glucose, (1→6)-linked glucose, (1→3)-linked galactose, (1→2,3)-linked galactose, (1→)-linked galactose, (1→6)-linked galactose, (1→4,6)-linked galactose,

TABLE 1 | GC–MS analysis of the methylated products of RGLP-1.

Retention time (min)	Methylated sugar	Linkage	Molar ratio
20.31	2,3,4-Me_3-Galp	1,6-	1.50
21.12	2,4,6-Me_3-Manp	1,3-	1.41
21.64	2,3,4,6-Me_4-Glcp	T-	22.40
22.19	2,3,4,6-Me_4-Galp	T-	2.12
24.39	3,4,6-Me_3-Manp	1,2-	0.56
24.57	2,4,6-Me_3-Glcp	1,3-	34.54
24.87	2,3,6-Me_3-Glcp	1,4-	8.11
25.16	2,4,6-Me_3-Galp	1,3-	4.13
25.64	2,3,4-Me_3-Glcp	1,6-	4.12
27.72	4,6-Me_2-Galp	1,2,3-	2.16
29.12	2,3-Me_2-Galp	1,4,6-	1.14
29.45	2,4-Me_2-Glcp	1,3,6-	17.81

(1→3)-linked mannose, and (1→2)-linked mannose. These results indicated that (1→3)-linked glucose, (1→3,6)-linked glucose, and (1→4)-linked glucose was the main chain of RGLP-1 with a small amount of (1→6) linkage. The above results also agreed with the result from the periodate oxidation–Smith degradation. This result was consistent with a previous study that the main chain of water-soluble β-glucan from *G. lucidum* is 1, 3-linked Glcp (37).

The presence of terminal residues (T-Glcp and T-Galp) and branching points [(1→3, 6)-linked-Glcp and (1→4, 6)-linked-Galp] indicated that RGLP-1 contained both linear and branched polysaccharides. The ratio between terminal residues and the branching points was 1.16, suggesting that the number of terminal units was slightly more than that of branching points. Moreover, the degree of branching (DB) value of RGLP-1 was 45.63% calculated by the equation DB = (NT + NB)/(NT + NB + NL), where NT is the numbers of the terminal residues (T-Glcp and T-Galp), where NB is the numbers of the branch residues [(1→3, 6)-linked-Glcp and (1→4, 6)-linked-Galp], and where NL is the linear residues (1,3-Glcp, 1,4-Glcp, 1,6-Glcp, 1,3-Galp, 1,3-Galp, 1,6-Galp).

Fourier Transform-Infrared Spectroscopy Analysis

The FT-IR spectrum of RGLP-1 exhibited typical signals for polysaccharides in the range 4,000–400 cm^{-1}, and the characteristic absorption peak was apparent in **Figure 4**. A strong band at 3,408.06 cm^{-1} was the –OH group. The band at 2,939.40 cm^{-1} was due to the C–H stretching vibration (38). The absorbance at 1,656.77 cm^{-1} indicated the presence of the bound water (39). The four peaks at 1,544.91, 1,429.19, 1,377.11 and 1,313.46 cm^{-1} can be assigned to methyl C–H wagging vibrations (40). The region around 1,045–1,080 cm^{-1} indicated the presence of a pyranose ring structure. Moreover, the band at 885.28 cm^{-1} is the characteristic absorption of β-linkage pyranose (36). The spectra indicated that RGLP-1 had the typical groups of sugars.

Scanning Electron Microscopy Observation

Restriction Fragment Length Polymorphism-1 units formed filiform-shaped chains with uneven diameters at the ends, generating a fibrous structure with characteristic interconnection or aggregates in **Figures 5A–D**. When this specific filiform-shaped surface was enlarged to × 2,000 times, the surface was smooth and dense with many spiral folds. This finding is similar to the morphology analysis of purified *Dendrobium*

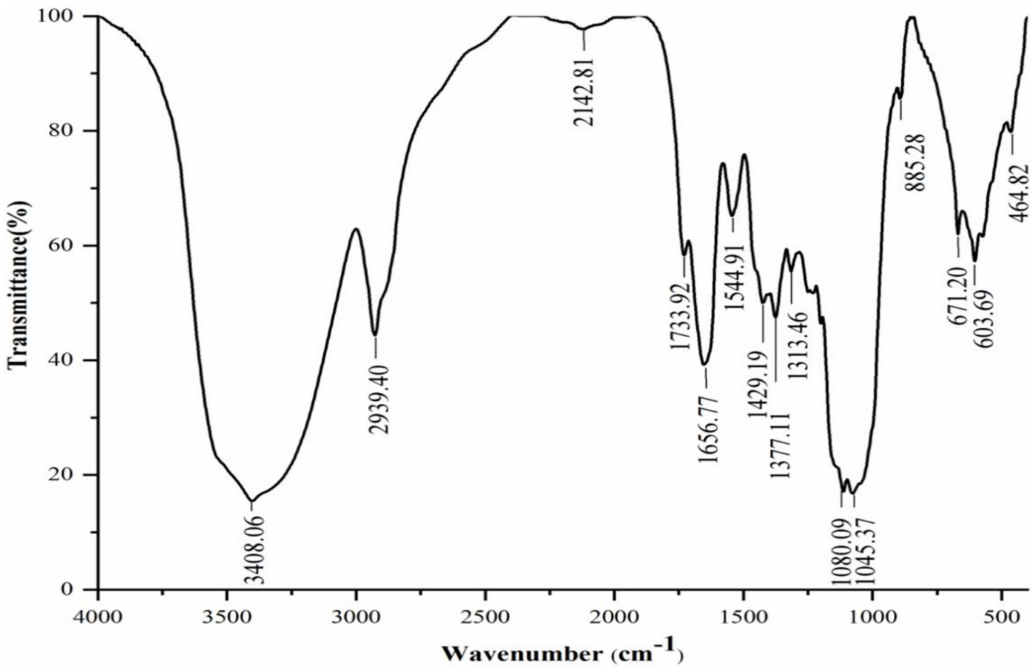

FIGURE 4 | IR spectra of RGLP-1.

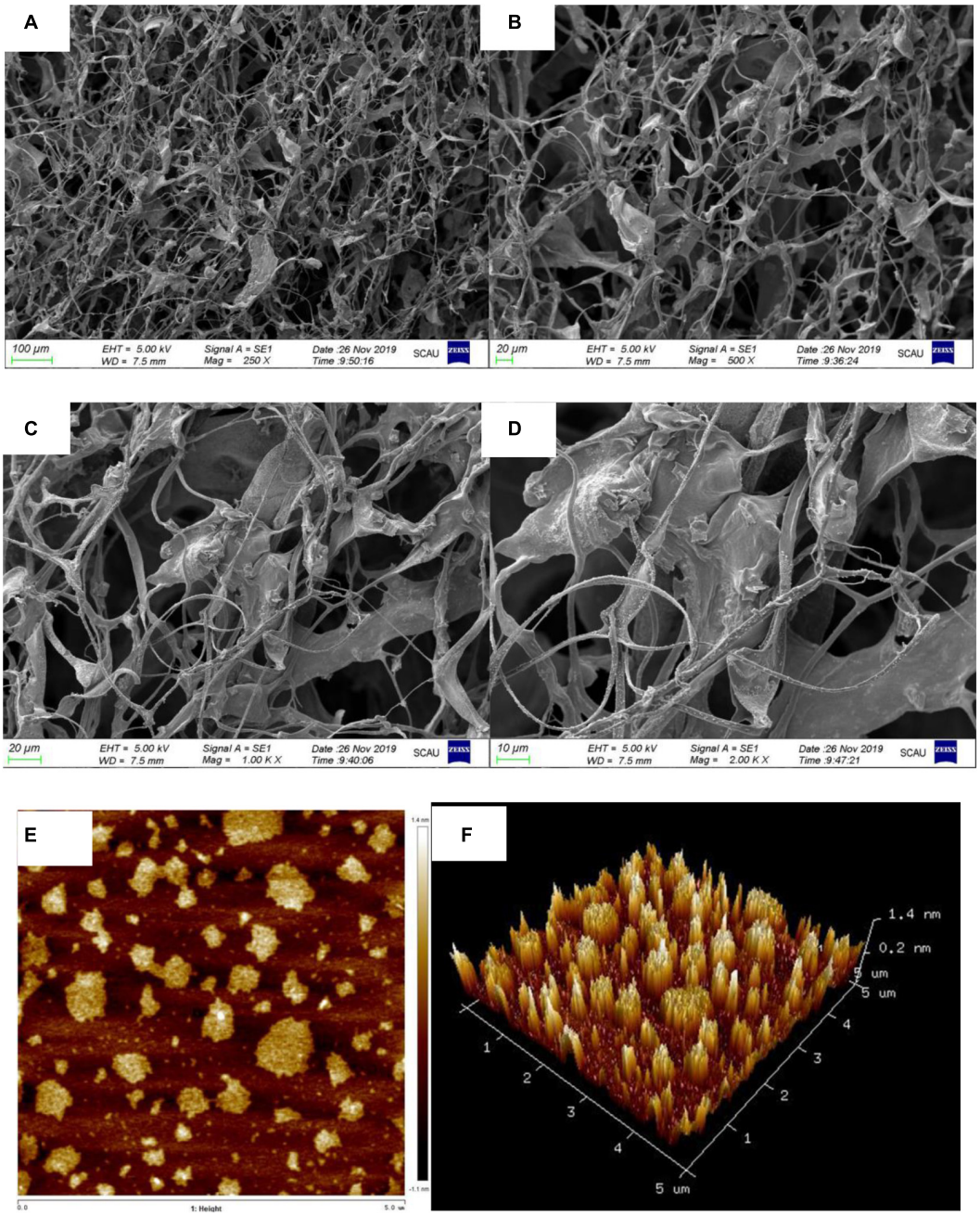

FIGURE 5 | SEM image with different magnifications ×250 **(A)**; ×500 **(B)**; ×1,000 **(C)**; ×2,000 **(D)**; AFM height analysis images **(E)**; and three dimensional image **(F)** of RGLP-1.

aphyllum polysaccharide (41). It indicated that RGLP-1 with higher molecular weight showed a strong intermolecular interaction and existed crosslinking which might be related to its complex structure.

Atomic Force Microscopy Analysis

Atomic force microscopy is a powerful technique to characterize soft biological surfaces, has gradually been used to analyze the surface of biological macromolecules (42, 43). The AFM diagrams of RGLP-1 are presented in **Figures 5E,F**, respectively. It is clear that the polysaccharide displayed irregular globular-like or curly structure. The diameters of the molecules were ranging from 110.2 to 706.9 nm and the heights were in the range of 0.9–6.0 nm. Normally, the height of a single polysaccharide chain is 0.1–1 nm. We speculate that the branched molecular chains of RGLP-1 were intertwined with each other to form circular aggregates. The hydroxyl groups in the RGLP-1 molecule may be the most important factor for the strong intramolecular

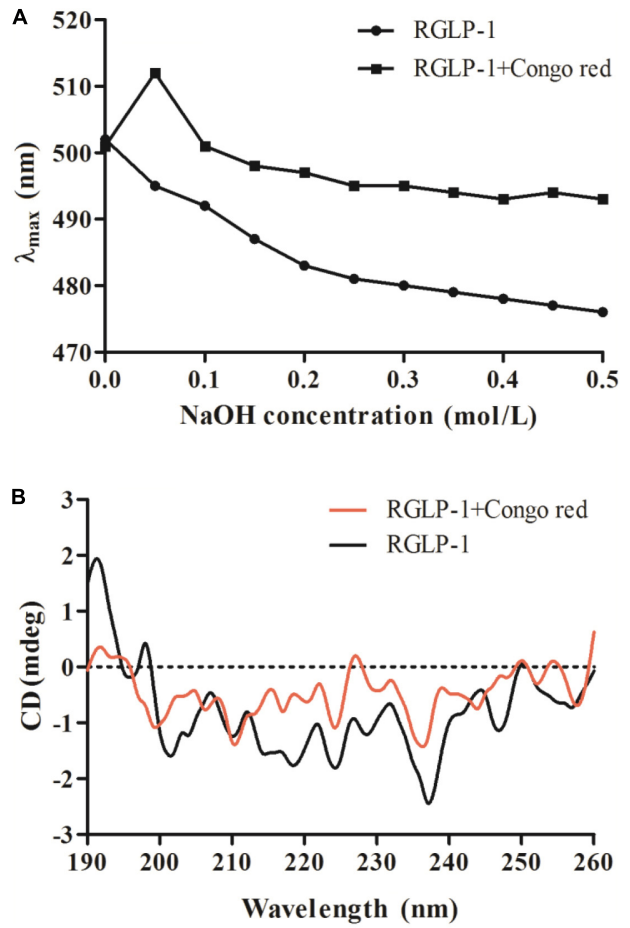

FIGURE 6 | Maximum absorption wavelength of RGLP-1 and RGLP-1 + Congo red at different concentrations of NaOH **(A)**; CD spectrogram **(B)** of RGLP-1.

and intermolecular interaction to form aggregates on the mica sheet (44).

Congo Red Test

Generally, triple-helix polysaccharides combined with Congo red will lead to the redshift of the maximum absorption wavelength (λ_{max}) of the Congo red-polysaccharide complex. Therefore, the existence of triple-helix structure of polysaccharides can be determined by Congo-red experiment. It was reported that original blackberry fruiting polysaccharide had triple-helical conformation using the Congo-red method (45). It was apparently observed that the interaction of Congo red-RGLP-1 polysaccharide complex undergo a distinct bathochromic shift from 501 to 512 nm in 0.05 mol/L NaOH solution in **Figure 6A**, the maximum absorption wavelength decreased with the increase of NaOH concentration, which indicated that RGLP-1 had a triple-helix structure. The recent study also reported that triple-helix structure existed in GLP-3 purified from *G. leucocontextum* (32).

Circular Dichroism Analysis

To further investigate the conformational structure information of RGLP-1, the CD spectroscopy was obtained in the range of 190–260 nm. As shown in **Figure 6B**. RGLP-1 had a positive cotton effect at 192 and 197 nm indicating that the polysaccharide was ordered. In addition, the negative cotton peak at 202 nm in the spectra indicating that RGLP-1 was existed by ordered helical structure in water solution. When Congo red was presented, the signals in the CD spectra had shifted. In comparison with the maximum peak of RGLP-1, the positive cotton effect of the Congo red-polysaccharide complex weakened a lot and the negative cotton effect disappeared. This result further proved that RGLP-1 has a triple-helical structure, which was consistent with the Congo red experimental analysis.

CONCLUSION

In summary, we screened a homogeneous and high molecular weight polysaccharide (RGLP-1) with the greatest immunoregulatory activity *in vitro* after double purification with ultrafiltration membrane and Sephacryl S-500 HR. RGLP-1 had a relative molecular weight of 3,978 kDa. RGLP-1 was composed of fucose, mannose, glucose, and galactose at a molar ratio of 0.13: 0.05: 0.72: 0.10, the majority of which was (1→3)-β-Glcp and (1→3, 6)-β-Glcp residues with triple-helix conformation. RGLP-1 showed a strong intermolecular interaction and diameters of the molecules was ranging from 110.2 to 706.9 nm and heights in the range of 0.9–6.0 nm. Thus, these findings explored the structure-activity relationship of GLP and suggested that RGLP-1 could be a complementary dietary bioactive component for immunoregulation.

DATA AVAILABILITY STATEMENT

The original contributions presented in the study are included in the article/supplementary material, further inquiries can be directed to the corresponding author/s.

AUTHOR CONTRIBUTIONS

GL: data curation, formal analysis, investigation, writing—review, and editing, validation. JZ: data curation, formal analysis, investigation, and roles and writing—original draft. QK: data curation, formal analysis, writing—review, and editing. MS: data curation, formal analysis, and investigation. TH: data curation, formal analysis, and investigation. SA: data curation and formal analysis. HL: investigation and methodology. HC and LH: formal analysis, methodology, and resources. JX: writing—review and editing. YJC: investigation, writing—review and editing, and supervision. YNC: project administration, funding acquisition, writing—reviewing and editing, investigation, supervision, and resources. All authors contributed to the article and approved the submitted version.

FUNDING

This study was supported by the Scientific Research Project from Guangdong Province Department of Education (No. 2013gjhz0003), the Guangdong Province Engineering Research Center for Bioactive Natural Products (2016B090920093), the Guangdong Provincial Key Laboratory of Nutraceuticals and Functional Foods (2018B030322010), and the Program for Guangdong Introducing Innovative and Entrepreneurial Teams (2019ZT08N291).

ACKNOWLEDGMENTS

We would like to extend our appreciation to Infinitus China Co., Ltd.

REFERENCES

1. Xiang Q, Yu Q, Wang H, Zhao M, Liu S, Nie S, et al. Immunomodulatory activity of *Ganoderma atrum* polysaccharide on purified T lymphocytes through Ca2+/CaN and mitogen-activated protein kinase pathway based on RNA sequencing. *J Agr Food Chem.* (2017) 65:5306–15. doi: 10.1021/acs.jafc.7b01763
2. Lu J, He R, Sun P, Zhang F, Linhardt RJ, Zhang A. Molecular mechanisms of bioactive polysaccharides from *Ganoderma lucidum* (Lingzhi), a review. *Int J Biol Macromol.* (2020) 150:765–74. doi: 10.1016/j.ijbiomac.2020.02.035
3. Liu Y, Zhang J, Tang Q, Yang Y, Guo Q, Wang Q, et al. Physicochemical characterization of a high molecular weight bioactive β-d-glucan from the fruiting bodies of *Ganoderma lucidum*. *Carbohydr Polym.* (2014) 101:968–74. doi: 10.1016/j.carbpol.2013.10.024
4. Li J, Zhang J, Chen H, Chen X, Lan J, Liu C, et al. Complete mitochondrial genome of the medicinal mushroom *Ganoderma lucidum*. *PLoS One.* (2013) 8:e72038. doi: 10.1371/journal.pone.0072038
5. Li J, Gu F, Cai C, Hu M, Fan L, Hao J, et al. Purification, structural characterization, and immunomodulatory activity of the polysaccharides from *Ganoderma lucidum*. *Int J Biol Macromol.* (2020) 143:806–13. doi: 10.1016/j.ijbiomac.2019.09.141
6. Chen M, Xiao D, Liu W, Song Y, Zou B, Li L, et al. Intake of *Ganoderma lucidum* polysaccharides reverses the disturbed gut microbiota and metabolism in type 2 diabetic rats. *Int J Biol Macromol.* (2020) 155:890–902. doi: 10.1016/j.ijbiomac.2019.11.047
7. Zeng X, Li P, Chen X, Kang Y, Xie Y, Li X, et al. Effects of deproteinization methods on primary structure and antioxidant activity of *Ganoderma lucidum* polysaccharides. *Int J Biol Macromol.* (2019) 126:867–76. doi: 10.1016/j.ijbiomac.2018.12.222
8. Boh B, Berovic M, Zhang J, Zhi-Bin L. *Ganoderma lucidum* and its pharmaceutically active compounds. *Biotechnol Annu Rev.* (2007) 13:265. doi: 10.1016/S1387-2656(07)13010-6
9. Yeh CH, Chen HC, Yang JJ, Chuang WI, Sheu F. Polysaccharides PS-G and protein LZ-8 from Reishi (*Ganoderma lucidum*) exhibit diverse functions in regulating murine macrophages and T lymphocytes. *J Agric Food Chem.* (2010) 58:8535–44. doi: 10.1021/jf100914m
10. Wang C, Shi S, Chen Q, Lin S, Wang R, Wang S, et al. Antitumor and immunomodulatory activities of *Ganoderma lucidum* polysaccharides in glioma-bearing rats. *Integr Cancer Ther.* (2018) 17:674–83. doi: 10.1177/1534735418762537
11. Sohretoglu D, Huang S. *Ganoderma lucidum* polysaccharides as an anti-cancer agent. *Anticancer Agents Med Chem.* (2018) 18:667. doi: 10.2174/1871520617666171113121246
12. Zhang H, Nie S, Cui SW, Xu M, Ding H, Xie M. Characterization of a bioactive polysaccharide from *Ganoderma atrum*: re-elucidation of the fine structure. *Carbohydr Polym.* (2017) 158:58–67. doi: 10.1016/j.carbpol.2016.11.088
13. Bohn JA, BeMiller JN. (1→3)-β-d-glucans as biological response modifiers: a review of structure-functional activity relationships. *Carbohyd Polym.* (1995) 28:3–14. doi: 10.1016/0144-8617(95)00076-3
14. Sun L, Wang C, Shi Q, Ma C. Preparation of different molecular weight polysaccharides from *Porphyridium cruentum* and their antioxidant activities. *Int J Biol Macromol.* (2009) 45:42–7. doi: 10.1016/j.ijbiomac.2009.03.013
15. Benner R, Opsahl S. Molecular indicators of the sources and transformations of dissolved organic matter in the Mississippi river plume. *Org Geochem.* (2001) 32:597–611. doi: 10.1016/S0146-6380(00)00197-2
16. Bao XF, Wang XS, Dong Q, Fang JN, Li XY. Structural features of immunologically active polysaccharides from *Ganoderma lucidum*. *Phytochemistry.* (2002) 59:175–81. doi: 10.1016/s0031-9422(01)00450-2
17. Wang Y, Fan X, Wu X. *Ganoderma lucidum* polysaccharide (GLP) enhances antitumor immune response by regulating differentiation and inhibition of MDSCs via a CARD9-NF-kappaB-IDO pathway. *Biosci Rep.* (2020) 40:BSR20201170. doi: 10.1042/BSR20201170
18. Zhang S, Nie S, Huang D, Huang J, Feng Y, Xie M. A polysaccharide from *Ganoderma atrum* inhibits tumor growth by induction of apoptosis and activation of immune response in CT26-bearing mice. *J Agric Food Chem.* (2014) 62:9296–304. doi: 10.1021/jf503250d
19. Yu Q, Nie SP, Li WJ, Zheng WY, Yin PF, Gong DM, et al. Macrophage immunomodulatory activity of a purified polysaccharide isolated from *Ganoderma atrum*. *Phytother Res.* (2013) 27:186–91. doi: 10.1002/ptr.4698
20. Han XQ, Chung LCB, Dong CX, Yang YH, Ko CH, Gar-Lee YG, et al. Isolation, structure characterization, and immunomodulating activity of a hyperbranched polysaccharide from the fruiting bodies of *Ganoderma sinense*. *J Agric Food Chem.* (2012) 60:4276–81. doi: 10.1021/jf205056u
21. Ferreira SS, Passos CP, Madureira P, Vilanova M, Coimbra MA. Structure–function relationships of immunostimulatory polysaccharides: a review. *Carbohydr Polym.* (2015) 132:378–96. doi: 10.1016/j.carbpol.2015.05.079
22. Liu G, Ye J, Li W, Zhang J, Wang Q, Zhu XA, et al. Extraction, structural characterization, and immunobiological activity of ABP Ia polysaccharide from *Agaricus bisporus*. *Int J Biol Macromol.* (2020) 162:975–84. doi: 10.1016/j.ijbiomac.2020.06.204
23. Wang Q, Liu F, Chen X, Yang Z, Cao Y. Effects of the polysaccharide SPS-3-1 purified from *Spirulina* on barrier integrity and proliferation of Caco-2 cells. *Int J Biol Macromol.* (2020) 163:279–87. doi: 10.1016/j.ijbiomac.2020.06.203
24. Zhang J, Wen C, Qin W, Qin P, Zhang H, Duan Y. Ultrasonic-enhanced subcritical water extraction of polysaccharides by two steps and its characterization from *Lentinus edodes*. *Int J Biol Macromol.* (2018) 118:2269–77. doi: 10.1016/j.ijbiomac.2018.07.098
25. Lin L, Zhuang M, Zou L, Lei F, Yang B, Zhao M. Structural characteristics of water-soluble polysaccharides from *Rabdosia serra* (MAXIM.) HARA leaf and stem and their antioxidant capacities. *Food Chem.* (2012) 135:730–7. doi: 10.1016/j.foodchem.2012.05.029
26. Xia Y, Wang T, Yu S, Liang J, Kuang H. Structural characteristics and hepatoprotective potential of *Aralia elata* root bark polysaccharides and their effects on SCFAs produced by intestinal flora metabolism. *Carbohydr Polym.* (2019) 207:256–65. doi: 10.1016/j.carbpol.2018.11.097
27. Rong Y, Yang R, Yang Y, Wen Y, Liu S, Li C, et al. Structural characterization of an active polysaccharide of longan and evaluation of immunological activity. *Carbohydr Polym.* (2019) 213:247–56. doi: 10.1016/j.carbpol.2019.03.007
28. Cao J, Lv Q, Zhang B, Chen H. Structural characterization and hepatoprotective activities of polysaccharides from the leaves of *Toona sinensis* (A. Juss) Roem. *Carbohydr Polym.* (2019) 212:89–101. doi: 10.1016/j.carbpol.2019.02.031
29. Wang CL, Pi CC, Kuo CW, Zhuang YJ, Khoo KH, Liu WH, et al. Polysaccharides purified from the submerged culture of *Ganoderma formosanum* stimulate macrophage activation and protect mice against *Listeria monocytogenes* infection. *Biotechnol Lett.* (2011) 33:2271–8. doi: 10.1007/s10529-011-0697-2
30. PeNarando J, Aranda E, RodrIguez-Ariza A. Immunomodulatory roles of nitric oxide in cancer: tumor microenvironment says "no" to antitumor immune response. *Transl Res.* (2019) 210:99–108. doi: 10.1016/j.trsl.2019.03.003

31. Wang N, Jia G, Wang X, Liu Y, Li Z, Bao H, et al. Fractionation, structural characteristics and immunomodulatory activity of polysaccharide fractions from asparagus (*Asparagus officinalis* L.) skin. *Carbohydr Polym.* (2021) 256:117514. doi: 10.1016/j.carbpol.2020.117514
32. Gao X, Qi J, Ho CT, Li B, Mu J, Zhang Y, et al. Structural characterization and immunomodulatory activity of a water-soluble polysaccharide from *Ganoderma leucocontextum* fruiting bodies. *Carbohydr Polym.* (2020) 249:116874. doi: 10.1016/j.carbpol.2020.116874
33. Shao BM, Dai H, Xu W, Lin ZB, Gao XM. Immune receptors for polysaccharides from *Ganoderma lucidum*. *Biochem Biophys Res Commun.* (2004) 323:133–41. doi: 10.1016/j.bbrc.2004.08.069
34. Guo MZ, Meng M, Duan SQ, Feng CC, Wang CL. Structure characterization, physicochemical property and immunomodulatory activity on RAW264.7 cells of a novel triple-helix polysaccharide from *Craterellus cornucopioides*. *Int J Biol Macromol.* (2019) 126:796–804. doi: 10.1016/j.ijbiomac.2018.12.246
35. Jiang J, Kong F, Li N, Zhang D, Yan C, Lv H. Purification, structural characterization and in vitro antioxidant activity of a novel polysaccharide from Boshuzhi. *Carbohydr Polym.* (2016) 147:365–71. doi: 10.1016/j.carbpol.2016.04.001
36. Huang Y, Li N, Wan JB, Zhang D, Yan C. Structural characterization and antioxidant activity of a novel heteropolysaccharide from the submerged fermentation mycelia of *Ganoderma capense*. *Carbohydr Polym.* (2015) 134:752–60. doi: 10.1016/j.carbpol.2015.08.067
37. Wang Y, Liu Y, Yu H, Zhou S, Zhang Z, Wu D, et al. Structural characterization and immuno-enhancing activity of a highly branched water-soluble beta-glucan from the spores of *Ganoderma lucidum*. *Carbohydr Polym.* (2017) 167:337–44. doi: 10.1016/j.carbpol.2017.03.016
38. Zeng Y, Yang H, Ou X, Su H, Zong M, Yang J, et al. Fungal polysaccharide similar with host *Dendrobium officinale* polysaccharide: preparation, structure characteristics and biological activities. *Int J Biol Macromol.* (2019) 141:460–75. doi: 10.1016/j.ijbiomac.2019.08.238
39. Zhu Z, Liu R, Si C, Zhou F, Wang Y, Ding L, et al. Structural analysis and anti-tumor activity comparison of polysaccharides from *Astragalus*. *Carbohyd Polym.* (2011) 85:895–902. doi: 10.1016/j.carbpol.2011.04.020
40. Xu L, Lu Y, Cong Y, Zhang P, Han J, Song G, et al. Polysaccharide produced by *Bacillus subtilis* using burdock oligofructose as carbon source. *Carbohydr Polym.* (2019) 206:811–9. doi: 10.1016/j.carbpol.2018.11.062
41. Liu H, Ma J, Gong F, Wei F, Zhang X, Wu H. Structural characterisation and immunomodulatory effects of polysaccharides isolated from *Dendrobium aphyllum*. *Int J Food Sci Tech.* (2018) 53:1185–94. doi: 10.1111/ijfs.13695
42. Zhang J, Chen M, Wen C, Zhou J, Gu J, Duan Y, et al. Structural characterization and immunostimulatory activity of a novel polysaccharide isolated with subcritical water from *Sagittaria sagittifolia* L. *Int J Biol Macromol.* (2019) 133:11–20. doi: 10.1016/j.ijbiomac.2019.04.077
43. Zheng X, Sun H, Wu L, Kong X, Song Q, Zhu Z. Structural characterization and inhibition on alpha-glucosidase of the polysaccharides from fruiting bodies and mycelia of *Pleurotus eryngii*. *Int J Biol Macromol.* (2020) 156:1512–9. doi: 10.1016/j.ijbiomac.2019.11.199
44. Kong L, Yu L, Feng T, Yin X, Liu T, Dong L. Physicochemical characterization of the polysaccharide from *Bletilla striata*: effect of drying method. *Carbohydr Polym.* (2015) 125:1–8. doi: 10.1016/j.carbpol.2015.02.042
45. Dou Z, Chen C, Fu X. The effect of ultrasound irradiation on the physicochemical properties and α-glucosidase inhibitory effect of blackberry fruit polysaccharide. *Food Hydrocolloid.* (2019) 96:568–76. doi: 10.1016/j.foodhyd.2019.06.002

Conflict of Interest: HC and LH were employed by Infinitus China Co., Ltd.

The remaining authors declare that the research was conducted in the absence of any commercial or financial relationships that could be construed as a potential conflict of interest.

Publisher's Note: All claims expressed in this article are solely those of the authors and do not necessarily represent those of their affiliated organizations, or those of the publisher, the editors and the reviewers. Any product that may be evaluated in this article, or claim that may be made by its manufacturer, is not guaranteed or endorsed by the publisher.

Copyright © 2022 Liu, Zhang, Kan, Song, Hou, An, Lin, Chen, Hu, Xiao, Chen and Cao. This is an open-access article distributed under the terms of the Creative Commons Attribution License (CC BY). The use, distribution or reproduction in other forums is permitted, provided the original author(s) and the copyright owner(s) are credited and that the original publication in this journal is cited, in accordance with accepted academic practice. No use, distribution or reproduction is permitted which does not comply with these terms.

frontiers in Nutrition

ORIGINAL RESEARCH
published: 29 March 2022
doi: 10.3389/fnut.2022.868188

The Positive Influence of Polyphenols Extracted From *Pueraria lobata* Root on the Gut Microbiota and Its Antioxidant Capability

Xiao Xu[1,2], Ying Guo[1], Shaoqin Chen[1], Wenliang Ma[1], Xinlei Xu[1], Shuning Hu[1], Lifang Jin[1], Jianqiu Sun[1], Jian Mao[1,2] and Chi Shen[1]**

[1] School of Life Sciences, Shaoxing University, Shaoxing, China, [2] National Engineering Research Center for Cereal Fermentation and Food Biomanufacturing, Jiangnan University, Wuxi, China

Pueraria lobata, an edible food and medicinal plant, is a rich source of bioactive components. In this study, a polyphenol-rich extract was isolated from *P. lobata*. Puerarin was identified, and the high antioxidant bioactivity of the *P. lobata* extract was evaluated using the methods of 2,2-diphenyl-1-picrylhydrazyl (DPPH), 2,2′-azinobis-(3-ethylbenzthiazoline-6-sulphonate) (ABTS), and hydroxyl free radical scavenging ratio. Additionally, the IC_{50} values of DPPH, ABTS, and hydroxyl radical scavenging activities were 50.8, 13.9, and 100.4 μg/ml, respectively. Then, the *P. lobata* extract was administered to C57Bl/6J mice and confirmed to have a superior effect on enhancing the antioxidant status including improving superoxide dismutase activity, glutathione peroxidase peroxide activity, total antioxidant capacity activity, and malondialdehyde contents *in vivo*. Furthermore, the *P. lobata* extract had beneficial and prebiotic effects on the composition and structure of gut microbiota. Results showed that the *P. lobata* extract significantly increased the abundance of beneficial bacteria, involving *Lactobacillaceae* and *Bacteroidetes*, and decreased the abundance of *Ruminococcaceae*, *Prevotellaceae,* and *Burkholderiaceae*. Overall, our results provided a basis for using the *P. lobata* extract as a promising and potential functional ingredient for the food industry.

Keywords: ***Pueraria lobata*, antioxidant, polyphenols, gut microbiota, mice model**

OPEN ACCESS

Edited by:
Fuguo Liu,
Northwest A&F University, China

Reviewed by:
Jiarun Han,
Zhejiang Gongshang University, China
Daoyuan Ren,
Shaanxi Normal University, China

***Correspondence:**
Jian Mao
maojian@jiangnan.edu.cn
Chi Shen
acha@139.com

Specialty section:
This article was submitted to Food Chemistry, a section of the journal Frontiers in Nutrition

Received: *02 February 2022*
Accepted: *28 February 2022*
Published: *29 March 2022*

Citation:
Xu X, Guo Y, Chen S, Ma W, Xu X, Hu S, Jin L, Sun J, Mao J and Shen C (2022) The Positive Influence of Polyphenols Extracted From Pueraria lobata Root on the Gut Microbiota and Its Antioxidant Capability. Front. Nutr. 9:868188. doi: 10.3389/fnut.2022.868188

INTRODUCTION

Pueraria is a typical representative genus comprising over 20 species of herbs, which are highly found in China, Japan, and Korea. Among them, kudzu [*Pueraria montana* var. *lobata* (Willd.)] was first documented in a Chinese Materia Medica named Shen Nong Ben Cao Jing written in the Western Han Dynasty, and its medical properties have a long history of wide application in traditional Chinese medicine, as well as being developed as a royal special food for edible uses in Japanese cuisine (1, 2). *Pueraria lobata* has also been utilized to manage cardiovascular diseases, alcohol-induced liver injury, and many chronic diseases. Likewise, being an herbal, foodstuff could be widely used in nutritious foods and dietary supplements. According to preliminary statistics, the total area of cultivated and wild *P. lobata* in China is 400,000 hectares, with an annual production

of more than 1.5 million tons. In the future decade, the global demand for kudzu is estimated to increase sharply to 50 million tons per year.

Polyphenols derived from food and medicinal plants have been known to prevent many chronic diseases, such as diabetes, atherosclerosis, and obesity (3). The major constituents of kudzu (the root of *P. lobata*) were high levels of starch, but recent studies showed that the extracts of *P. lobata* contained rich polyphenols, such as puerarin, genistin, daidzin, and daidzein. The high levels of polyphenolic compounds in *P. lobata* have recently attracted much attention due to the functional properties of lowering cholesterol, inhibiting cancer cell proliferation and tumor growth, and modulating the immune system (4). Some studies focus on the protective effect of puerarin on alcoholic liver disease, for instance, reducing the production of free radicals, improving the activities of antioxidant enzymes, stimulating AMPK and Nrf2 signaling pathways, inhibiting the mTOR, regulating the activities of ethanol dehydrogenase and aldehyde dehydrogenase, as a result of keeping the balance of cellular redox state, and promoting liver energy metabolism dysfunction. In the process of oxidative stress on the diet-induced obesity model, daidzein in *P. lobata* is associated with reduction of apoptosis and stearoyl-CoA desaturase 1, which is a key enzyme relative to obesity (5). Furthermore, *P. lobata* has been demonstrated to possess the capability of regulating inflammatory factors and pathways, resulting in exhibiting potential anti-inflammatory activity. Some studies also found that the biological properties of antioxidant and antimicrobial activities displayed by the *P. lobata* extract were attributed to the existence of phenolic compounds (6, 7).

The gut microbiota is a microbial community in the intestinal with over 100 trillion microorganisms, which is the largest and most complex ecosystem in the human body, and has been shown the participation in the body's nutrient metabolism, immune system, and overall health of the host (8). A healthy gut, as a result of stable gut microbiota and diverse ecosystem, played an active influence in regulating metabolic pathways and resisting pathogen invasion (9). In contrast, if the gut ecosystem was broken and suffered from an imbalance of gut microbiota, a great deal of host health problems would be induced ceaselessly, including obesity, metabolic syndrome, diabetes, and intestinal bowel disease (10–12). In recent studies, the gut microbiota has been widely considered as a key role in the modulation of transformation of nutrients and compounds in the dietary supplements. Likewise, bioactive components in functional foods give an effect on gut microbiota. In fact, a novel potential therapy, based on altering the gut microbiota, aroused worldwide concern, especially in the treatment of preventing metabolic disorders (13). The abundance and diversity of gut microbiota could be examined using next-generation sequencing analysis of 16S rRNA amplicons to get knowledge about the profile of microbial characterization influenced by bioactive components. Liu et al. found that the promotion of *Bacteroides vulgatus*, *Parabacteroides distasonis*, *Prevotella,* and *Bifidobacterium* is a master regulator of anti-obesity properties (14). Additionally, the abundance of the *Prevotella* and *Akkermansia* genus could be increased by the flavan-3-ols, which was reported to be reversely linked to body weight gain and adipose tissue inflammation. Therefore, it is notable that the presence of specific gut bacterial species would participate in the improvement of the healthy gut ecosystem and cellular antioxidant state.

Pervious study suggested that *P. lobata* extract was closely related to antioxidant, antiproliferative, and anti-inflammation effects *via* cell models (15). However, few studies paid attention to elucidate the relationship and mechanism of the effect of *P. lobata* extract on the antioxidant activities and the composition of gut microbiota. In addition, there is a need to characterize a functional *P. lobata* extract and demonstrate its bioactive properties *in vitro* and *in vivo*. Therefore, in this study, we had a polyphenol-rich *P. lobata* extract, investigated the antioxidant *in vitro* and *in vivo*, as well as profiled the specific gut microbiota modulated by the polyphenol-rich extract. The health benefits of *P. lobata* extract could be better understood according to the direct comparison of microbial composition and structure *via* treated by *P. lobata* extract.

MATERIALS AND METHODS

Materials and Chemicals

Pueraria lobata was purchased from a local market (Hangzhou, China). Then, the fruiting bodies of *P. lobata* root were grounded into powder and stored at a low-temperature refrigerator before being used. The antioxidant indicator kits of superoxide dismutase activities (SOD), glutathione peroxidase peroxide (GSH-Px) activities, total antioxidant capacity (T-AOC) activities, and malondialdehyde (MDA) contents were obtained from the Nanjing Jiancheng Bioengineering Institute (Nanjing, China). The other chemicals and solvents were of liquid chromatography grade and purchased from Fisher Scientific or Beijing Solarbio Science & Technology Limited Company (Beijing, China).

Polyphenol-Rich Extract

The extraction method of *P. lobata* root was conducted according to a previous study with some modifications (16). In brief, *P. lobata* powder (10 g) was mixed with chilled acetone (200 ml) with ultra-sonicated for 30 min and then centrifuged for 20 min with the speed of 14,000 × *g* at 4°C. Then, the supernatant was removed, and the remaining pellet was re-extracted with another chilled acetone (200 ml). The pooled extracts were evaporated to dryness at 35°C. The macroporous resin column was used for the preliminary purification. The solution was then reconstituted in the solution of methanol, dried, and stored at −20°C before the test. The residue in this study referred to the *P. lobata* extract.

Determination of Total Phenolic Content

The total phenolic content of the *P. lobata* extract was measured based on the method described previously with some minor modifications (17). The *P. lobata* extract was dissolved in methanol to a concentration of 0.25 mg/ml. Gallic acid standards or the samples (20 μL) and diluted Folin–Ciocalteu reagent were incubated at room temperature for 1 min, followed by terminating reaction with sodium carbonate (75 mg/ml). Molecular Devices SpectraMax microplate spectrophotometer (San Jose, CA, United States) was used to record the absorbance

at 760 nm. Total phenolic contents were expressed as μmol gallic acid equivalents/mg polyphenol-rich *P. lobata* extract.

High-Performance Liquid Chromatography Analysis

The chromatographic analysis of the *P. lobata* extract was performed using a high-performance liquid chromatography (HPLC) system (Waters, Milford, MA, United States) (18, 19). The mobile phases were prepared as follows: water with 0.1% formic acid and acetonitrile with 0.1% formic acid. The gradient procedure was as follows: 0–3 min, 5% B, 3–42 min, 5%–35% B, 42–46 min, 35%–90% B, 46–50 min, 90% B, 50–56 min, 90%–5% B. The column was maintained at 30°C. The flow rate was set at 0.8 ml/min. The *P. lobata* extract was separated using an Agilent ZORBAX Eclipse Plus C18 (250 mm × 4.6 mm, 5.0 μm particle size). The detection of the *P. lobata* extract was recorded using an ultraviolet detector at 280 nm wavelength.

Antioxidant Activities

2,2-Diphenyl-1-Picrylhydrazyl Free Radical Scavenging Activity

The 2,2-diphenyl-1-picrylhydrazyl (DPPH) assay solution was performed according to a previous study prepared by mixing samples or blank solution (20 μl) with 50% ethanol solution containing DPPH solution (180 μl) (20). The mixture was incubated at room temperature for 60 min in the dark. The absorbance was measured at 517 nm. The results were described using the DPPH scavenging ratio, which was calculated as follows:

$$\text{The DPPH scavenging ratio (\%)} = [1 - A_{\text{sample}}/A_{\text{control}}] \times 100$$

A_{control} is the absorbance measured for blank, and A_{sample} is the absorbance measured for the *P. lobata* extract. Ascorbic acid (vitamin C) was selected as the positive control.

2,2′-Azinobis-(3-Ethylbenzthiazoline-6-Sulphonate) Free Radical Scavenging Activity

The 2,2′-azinobis-(3-ethylbenzthiazoline-6-sulphonate) (ABTS) scavenging activity was measured based on the method studied described previously with minor modification (21). $ABTS^{\cdot+}$ was generated by mixing 7 mM of ABTS solution with a 2.45 mM of the aqueous solution of $K_2S_2O_8$ and reacting for 12 h at room temperature in the dark. The $ABTS^{\cdot+}$ reaction solution (100 μl) with an absorbance of 0.70 cm^{-1} at 734 nm was used, and 100 μl of samples or blank solution was mixed and reacted for 60 min in the dark. The absorbance was recorded at 734 nm. The results were shown by the $ABTS^{\cdot+}$ scavenging ratio, which was calculated as follows:

$$ABTS^{\cdot+}\text{ scavenging ratio (\%)} = [1 - A_{\text{sample}}/A_{\text{control}}] \times 100$$

A_{control} is the absorbance of water and A_{sample} is the absorbance of samples. Ascorbic acid (vitamin C) was used as a positive control.

Hydroxyl Radical Scavenging Activity

The hydroxyl radical scavenging activity was measured based on the method reported in a previous study (21). In brief, the *P. lobata* extract solution (100 μl) was mixed with 100 μl of 6 mM ferrous sulfate solution and 6 mM salicylic acid ethanol solution. The mixtures were mixed with 1 ml of 0.1% hydrogen peroxide and reacted for 30 min in the dark. The absorbance was recorded at 510 nm, and the results were displayed by the hydroxyl radical scavenging ratio.

Mice Animal Design

The animal experimental protocols were approved and authorized by the Institutional Animal Care and Use Committee of China Pharmaceutical University (SYXK-2020-0023). The experimental test was designed according to the study with minor modifications (22). Twelve specific pathogen-free male C57BL/6 mice (6 weeks of age, around 18 g) were purchased from the Model Animal Research Center of Nanjing University. The mice were divided randomly into two groups after acclimatization for 1 week. In brief, except for daily gavage with water, the two-group mice were separately fed by the normal diet with or without *P. lobata* extract (200 mg/kg/day). The body weight of each mouse was measured daily. Also, the feces were collected at the end of the feeding duration and the experimental period. The feces of two experimental groups were immediately frozen in liquid nitrogen and stored at −80°C before the sequence analysis. All the animals were sacrificed using isoflurane as an anesthetic. Livers from each mouse were excised and collected for biochemical assays.

The Antioxidant Status of Mice Liver

The biochemical parameters of liver samples from the mice, including SOD, GSH-Px activity, T-AOC, and MDA activity, were prepared according to the study and determined by using commercial kits following the manufacturer's instructions (23).

The Sequencing of Gut Microbiota

Total genome DNA was extracted from the fecal samples of the control and the *P. lobata* extract groups using a QIAamp DNA stool kit, and the DNA concentration and purity were monitored on 1% agarose gels, and then diluted to 1 ng/μl for amplicon generation. The 16S V3-V4 rDNA genes were amplified using the specific primer with the barcode. All PCR reactions were carried out with the high-fidelity PCR master mix, forward and reverse primers, and template DNA. Thermal cycles were conducted as the following: initial denaturation at 98°C for 1 min, 30 cycles of denaturation at 98°C for 10 s, annealing at 50°C for 30 s, and elongation at 72°C for 5 min. Then, the PCR products were mixed and purified using the Axygen AxyPrep DNA Gel Extraction Kit. Finally, the sequencing libraries were generated using the NEBNext® Ultra™ DNA Library Prep Kit following the manufacturer's instructions and then sequenced on an Illumina MiSeq platform (San Diego, CA, United States).

Gut Microbiota Data Analysis

The paired-end reads from the original DNA fragments from the control and the *P. lobata* extract groups were merged using the Flash software. The aired-end reads were assigned by the different barcodes. Then, the Upare software package was used to perform the sequences. The alpha and beta diversities were also analyzed by the In-house Perl scripts. The sequences with ≥97% similarity were assigned to the same operational taxonomic units (OTUs).

The observed species were used to estimate the amount of unique OTUs, as well as the rarefaction curves were generated based on these three metrics. The cluster analysis was illustrated using the principal component analysis and the principal coordinate analysis (PCoA). The Stamp software was utilized to study the differences in the abundances of individual taxonomy. The Linear discriminant analysis Effect Size (LEfSe) was used for the quantitative analysis of biomarkers among different groups. The 16S rRNA raw sequence data generated were deposited into the National Center for Biotechnology Information Sequence Read Archive Sprout and available under the accession number of PRJNA805070[1].

Statistical Analysis

The SPSS software (version 24.0) and excel (version 2020) were used for statistical analysis. The Student's *t*-test was used to assess the mean difference between the *P. lobata* extract and the control groups. A *p*-value of <0.05 or <0.01 was considered statistically significant. The results were expressed as the mean ± standard deviation.

RESULTS AND DISCUSSION

Identification of Polyphenolic Compounds in the *P. lobata* Extract

Pueraria lobata has been in the Chinese List of Food and Medicine Homologous Substance since 2002 and is currently regarded as a functional food in the food industry due to possessing a great number of bioactive compounds such as isoflavones, polysaccharides, terpenoids, and amino acids. It has been reported that the antioxidant activity of the *P. lobata* extract was well correlated with the content of phenolic compounds (24). Although other antioxidants were probably present in the *P. lobata* extract, phenolic compounds made a significant contribution to the antioxidant activity. The polyphenol-rich *P. lobata* extract (EPM) was eluted by gradient elution HPLC (**Figure 1**). The yield content of this *P. lobata* extract is 1.2%. The total phenolic content of this extract was 67.3 mg gallic acid equivalents/g dry weight.

Effect of the *P. lobata* Extract on Antioxidant Activity Analysis

Effect of the *P. lobata* Extract on 2,2-Diphenyl-1-Picrylhydrazyl Radical Scavenging Activity

The scavenging activity of DPPH free radical is widely used to evaluate the free radical scavenging capability of natural bioactive compounds (20). All the *P. lobata* extract fractions tested exhibited strong antioxidant activities in this assay in a dose-dependent manner (**Figure 2A**). For instance, the DPPH free radical scavenging ratio of the *P. lobata* extract was 62.3, 78.8, 85.2, and 88.0% at the concentrations of 100, 200, 300, and 400 μg/ml, respectively. Additionally, the IC_{50} values of DPPH radical scavenging activity by the *P. lobata* extract fraction were 50.8 μg/ml. As well, there were differences in the scavenging ratios exhibited by the different concentrations of the *P. lobata* extract fractions. The antioxidant activity of the *P. lobata* extract was still considerably lower than that of vitamin C at the same concentration. Cherdshewasart et al. found that the same concentration of puerarin (IC_{50} value 93.26 μg/ml) exhibited insignificant antioxidant activity evaluated by DPPH activity as compared with vitamin C (IC_{50} value 72.33 μg/ml) (24). The mechanism of the *P. lobata* extract scavenging DPPH radical could be through providing protons to reduce oxidative free radicals, besides preventing chain reactions of free radicals (25). These findings suggested that the *P. lobata* extract owned a robust antioxidative capacity of scavenging free radicals.

Effect of the *P. lobata* Extract on 2,2′-Azinobis-(3-Ethylbenzthiazoline-6-Sulphonate) Radical Scavenging Activity

ABTS free radicals can be inhibited by diverse antioxidant compounds sourced from foods, resulting in the reduced formation of nitrogen-centered $ABTS^{\cdot+}$ cation (26). The *P. lobata* extract scavenged ABTS free radicals in a dose-dependent manner (**Figure 2B**). For the *P. lobata* extract fraction, the scavenging capabilities were 79.6, 90.7, 96.0, and 97.2% at the concentrations of 100, 200, 300, and 400 μg/ml, respectively. Additionally, the IC_{50} values of ABTS radical scavenging activity by the *P. lobata* extract fraction were 13.9 μg/ml. In addition, the scavenging ability of the *P. lobata* extract was slightly higher than that of ascorbic acid when the concentration of the *P. lobata* extract was over 250 μg/ml. Wang et al. showed that polysaccharides extracted from *P. lobata* exerted a comparative activity to scavenge $ABTS^{\cdot+}$ (27). This capacity of the *P. lobata* extract fraction to scavenge $ABTS^{\cdot+}$ was similar to that result obtained from DPPH radical scavenging assay. All these findings suggested that the *P. lobata* extract, rich in polyphenols, had excellent abilities of scavenging free radicals.

Effect of the *P. lobata* Extract on Hydroxyl Radical Scavenging Activity

The antioxidant activities of the *P. lobata* extract were further tested and confirmed by measuring the activity to cleanse hydroxyl radicals. Hydroxyl radicals could attack the biological molecules, interference with normal cellular functions, leading to cause human adverse physical reactions (28). Similar to the results shown above, the *P. lobata* extract (100–400 μg/ml) dose-dependently cleansed hydroxyl radical, which suggested that the *P. lobata* extract could inhibit the production of hydroxyl radical and effectively diminish the oxidative damage in human bodies (**Figure 2C**). For the *P. lobata* extract fraction, the scavenging activities were 49.7, 70.6, 84.5, and 88.8% at the concentrations of 100, 200, 300, and 400 μg/ml, respectively. In addition, the IC_{50} values of hydroxyl radical scavenging activity by the *P. lobata* extract fraction were 100.4 μg/ml. For comparison, the scavenging capacity of the *P. lobata* extract was higher than that of positive control when the concentration was higher than 225 μg/ml. Consistently, Jin

[1]https://dataview.ncbi.nlm.nih.gov/object/PRJNA805070

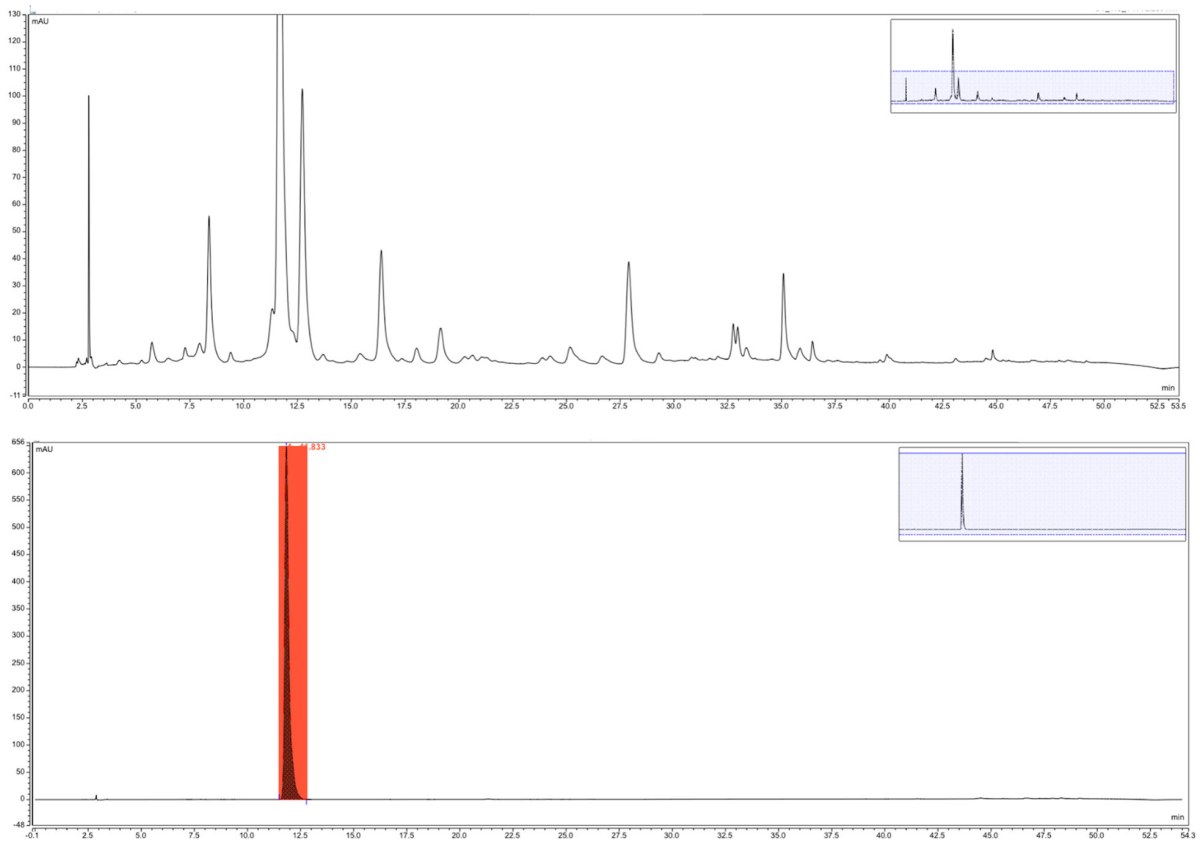

FIGURE 1 | Phenolic high-performance liquid chromatography (HPLC) spectra of the *Pueraria lobata* extract and compound puerarin.

et al. reported that the polyphenols in *P. lobata* riched in daidzein, genistein, B-2-*O*-glucopyranoside, (+)-puerarol, and puerarin could exhibit strong scavenging hydroxyl radical ratios (29). These results denoted that the *P. lobata* extract did excellently in scavenging oxidants through the series of analyses *in vitro*.

Effect of the *P. lobata* Extract on the Antioxidant Status of Mice Liver *in vivo*

As the mechanisms of antioxidant evaluation methods *in vitro* and *in vivo* were different, in order to determine the potential antioxidative activities comprehensively, mice model was used, and the SOD, GSH-Px activity, T-AOC, and MDA contents in the mice liver were measured, which could be mirrored the cellular antioxidant status as key indicators (**Table 1**) (30). The main endogenous antioxidant enzymes including SOD, GSH-PX, T-AOC, and MDA in the body system were a protective mechanism, and these compounds could prevent oxidative stress and cell damage (31). Puerarin was reported to possess the potential antioxidative activities both *in vitro* and *in vivo*. The antioxidant effect *in vivo* was partly responded *via* increasing the activities of antioxidant enzymes, for instance, increasing GSH and the ratio of GSH/GSSG in rat liver, as well as reducing the related activity of caspase-3 relative to cell apoptosis (23).

There was an insignificant difference in the body weight between the control and the *P. lobata* extract groups during the feeding period. The GSH-Px activity in the liver in the *P. lobata* extract group was significantly increased by 21.6% compared with that in the control group ($p < 0.05$). As for the SOD activity, T-AOC and MDA parameters in the mice liver of the *P. lobata* extract group were significantly increased by 25.7, 13.6, and 33.9%, respectively ($p < 0.05$), compared with control. As a result, our study noted that the *P. lobata* extract could enhance the activities of antioxidant enzymes in the liver and inhibit the oxidative damage inside the body, which was evidenced for potentially affecting positively the protection of the liver. Similar findings have been reported by Senevirathne et al. (32). Polyphenols extracted from foods or medical herbs have been also demonstrated a strong ability to scavenge free radicals and terminate oxidative reactions, thereby in consideration of their antioxidant capacities (33, 34). Previously, dietary polyphenol-rich supplementation of barley bran and cranberry (*Vaccinium macrocarpon*) peel could help to boost the antioxidant status of serum and liver based on the mice model evaluation (35, 36). Notably, the results indicated that the enhanced antioxidant capacities of polyphenol-rich extract of *P. lobata in vitro* could be further verified in this mice liver model *via* increasing the activities of SOD, GSH-Px, and MDA, as well as did better in T-AOC than those in the control.

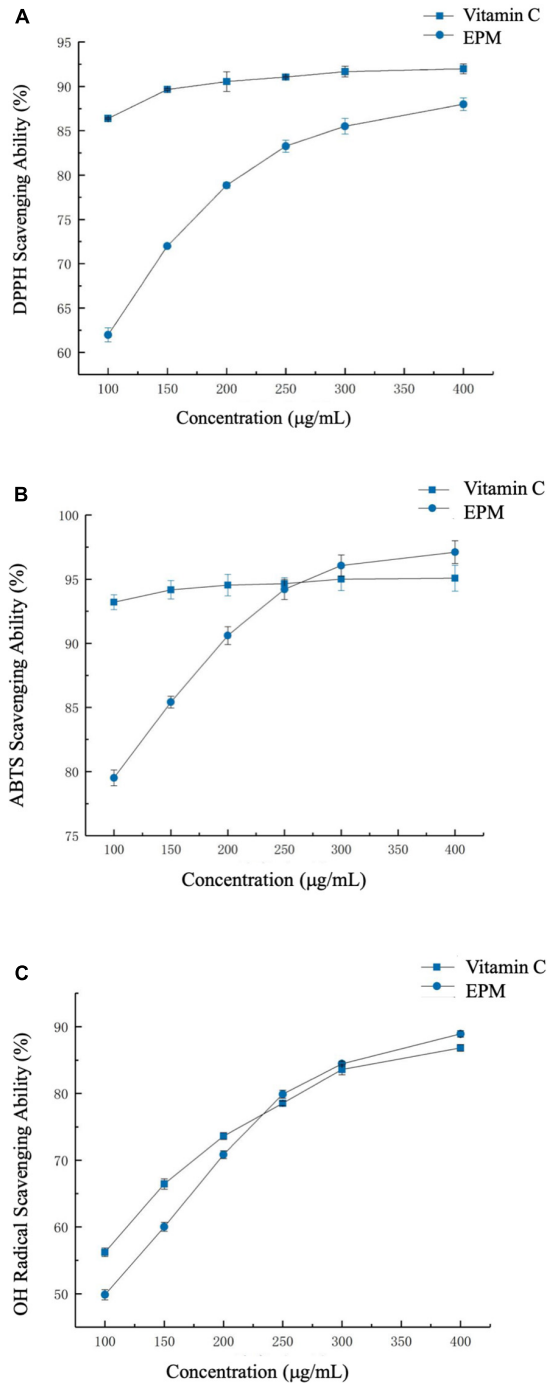

FIGURE 2 | The antioxidant activities of the *Pueraria lobata* extract. **(A)** 2,2-Diphenyl-1-picrylhydrazyl (DPPH) scavenging activity, **(B)** 2,2′-azinobis-(3-ethylbenzthiazoline-6-sulphonate) (ABTS) scavenging activity, and **(C)** hydroxyl radical scavenging activity. CTL, normal control group; EPM, *P. lobata* extract group.

Effect of the *P. lobata* Extract on the Gut Microbiota

The *P. lobata* extract was proved to possess the antioxidant bioactivities using *in vitro* and *in vivo* methodologies, and to further investigate the potential effect on the gut microbes, the *in vivo* evaluation of the *P. lobata* extract on the composition and structure of the gut microbiota was performed (**Figure 3A**). Gut microbiota is responsible for the production of human functional compounds, vitamins, and metabolization of the dietary compound and has a potential beneficial protection against the unhealthy pathogens. Numerous studies showed that any imbalanced status about the composition and structure of gut microbiota would potentially cause the development of colonic dysbiosis, which is powerfully associated with several pathologies and human chronic diseases, including intestinal bowel disease, colon cancer, and obesity (37–39). Polyphenols derived from foods and medicine plants have the capability to reduce bacterial metabolizing enzymes, thereby reducing the colonic tumor incidence and improving cell metabolism; as well, the growth of harmful microbiome could be inhibited, and the abundance of the health-benefit microbiome was enhanced, such as *Lactobacillus* and *Bifidobacterium* species (40). The link of the antioxidant effect of polyphenols *in vivo* and hinder the bacterial proliferation, and the growth of enterpathogenic bacteria was also discussed in several studies (41, 42).

We performed the high-throughput sequencing of the 16S rDNA region to determine the gut microbial community treated by the *P. lobata* extract. The sequencing depth reads of the control and the *P. lobata* extract groups were in the range of 272,642 base pairs (bp) and 295,776 bp, respectively. The data indicated that most of the species in the gut microbiota were captured, and the output of these data was valid. Considering the bacterial change at the phylum level, the microbiome of the control and the *P. lobata* extract groups mainly consisted of *Actinobacteria, Bacteroidetes, Cyanobacteria, Deferribacteres, Epsilonbacteraeota, Firmicutes, Patescibacteria, Proteobacteria, Tenericutes, and Verrucomicrobia* (**Figure 3B**). The ratios of *Actinobacteria* and *Bacteroidetes* in the *P. lobata* extract group were 1.39-fold and 1.20-fold higher than those in the control group, respectively. However, the ratios of *Cyanobacteria, Firmicutes,* and *Proteobacteria* decreased by 15.5, 44.7, and 28.1% compared with the control group, respectively. The ratio of *Bacteroidetes* and *Firmicutes* phyla consisted of more than 90% population in the gut microbiota, and they would play an important role in human health (43). The *Bacteroidetes* was considered to have an effect to modulate the immune responses and activate the immune lymphocyte T cells (44). In summary, the supplementation of the *P. lobata* extract contributed to the functional differences of mice gut microbiota.

TABLE 1 | Effects of the *Pueraria lobata* extract on the activities of SOD, GSH-Px, T-AOC, and MDA in the liver of mice, respectively.

	SOD (U/mg Prot)	GSH-Px (U/mg Prot)	T-AOC (U/mg Prot)	MDA (mmol/g Prot)
Control	121.2 a	93.1 a	0.81 a	6.2 a
Pueraria lobata extract	152.4 b	113.2 b	0.92 b	8.3 b

The different small letters, respectively, showed significantly different differences between groups ($p < 0.05$).
SOD, superoxide dismutase activities; GSH-Px, glutathione peroxidase peroxide; T-AOC, total antioxidant capacity; MDA, malondialdehyde.

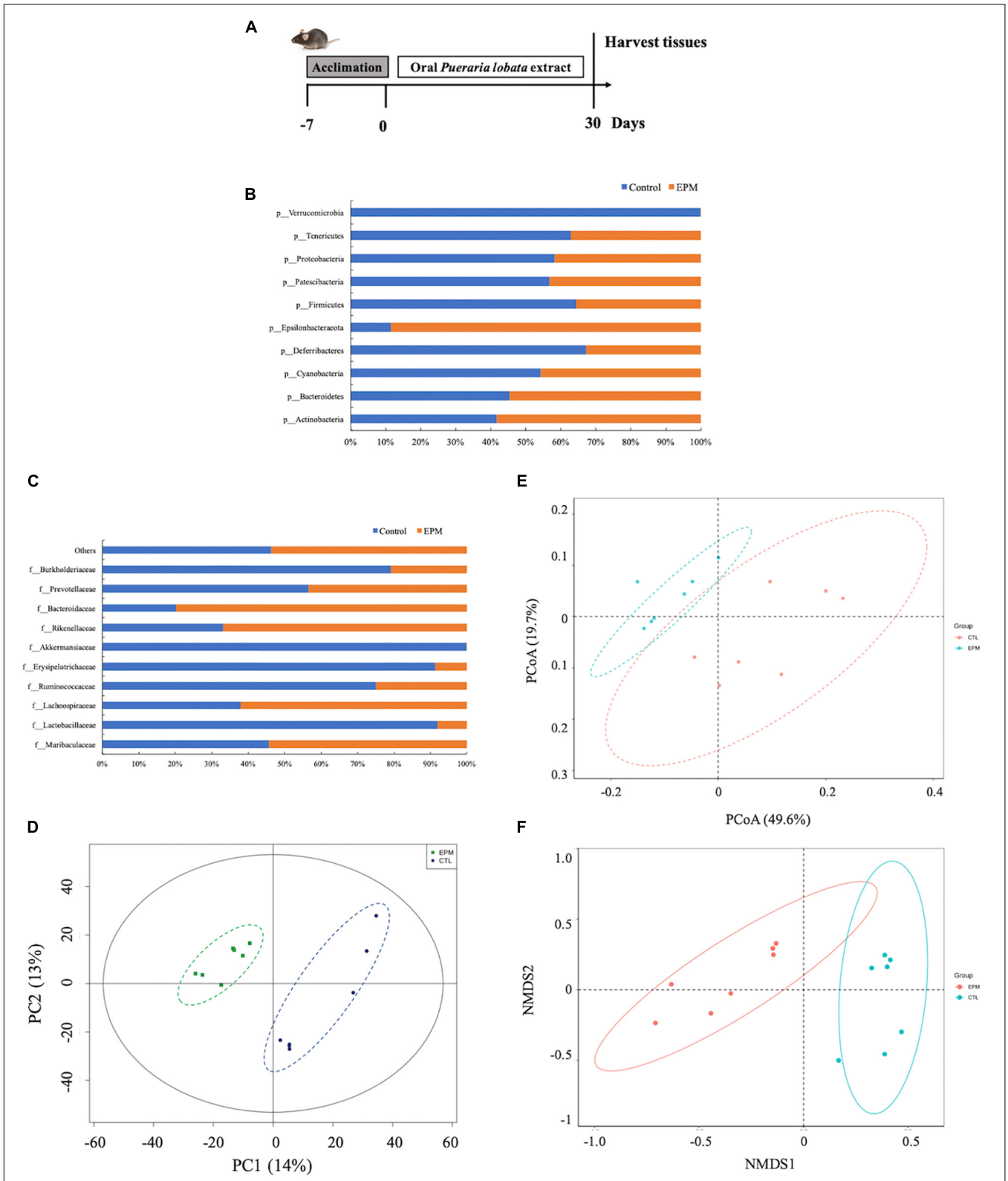

FIGURE 3 | (A) Animal design and the antioxidant of the *Pueraria lobata* extract *in vivo*. **(B)** Gut bacterial taxonomic profiling of the control and the *P. lobata* extract groups at the phylum level. **(C)** Gut bacterial taxonomic profiling of the control and the *P. lobata* extract groups at the class level. **(D)** PCA, **(E)** PCoA, and **(F)** NMDS plots of weighted UniFrac and Unweighted UniFrac distance analyses of beta-diversity among samples showing a higher similarity among the bacterial community between the control group and the *P. lobata* extract group.

All the 10 most abundant or representative families were *Muribaculaceae, Lachnospiraceae, Lactobacillaceae, Ruminococcaceae, Akkermansiaceae, Erysipelotrichaceae, Rikenellaceae, Bacteroidaceae, Prevotellaceae,* and *Burkholderiaceae* (**Figure 3C**). The ratios of *Lactobacillaceae, Rikenellaceae*, and *Bacteroidetes* in the *P. lobata* extract group were 1.64-fold, 2.02-fold, and 3.96-fold higher than those in the control group, respectively. However, the ratio of *Ruminococcaceae, Prevotellaceae*, and *Burkholderiaceae* decreased by 66.8, 23.3, and 73.6% than those in the control group. Interestingly, the *P. lobata* extract almost decreased over 90% of *Erysipelotrichaceae* and *Akkermansiaceae* at the family level, which could be useful when these two families of microbiome were overgrown and overproduced in the gut. These results noted that the *P. lobata* extract would be a useful ingredient to restore the balance of the gut ecosystem.

When searching how the *P. lobata* extract and control differ in terms of the composition and structure of gut microbiota profiles, a distance square matrix was calculated to reflect the dissimilarity between the two groups (weighted UniFrac and unweighted UniFrac distances) (**Figure 3D**). The QIIME software could calculate both weighted and unweighted UniFrac distance, which are phylogenetic measures of beta diversity. We used unweighted UniFrac distance for the PCoA, and the PCoA could help to get principal coordinates and visualize them from complex, multidimensional data (**Figure 3E**). The results demonstrated that the bacterial communities of the *P. lobata* extract were significantly different from those of the control group. A long-distance between these groups was observed, pointing out that the *P. lobata* extract modulated the bacterial gut microbiome. This distance difference was also significantly evident in the non-metric multidimensional scaling, which displayed the differences among gut microbiota of the *P. lobata* extract and control groups (**Figure 3F**).

Altogether, the metagenomics showed the modulation of gut microbiota by the consumption of the *P. lobata* extract group *via* the changing of the abundance of *Firmicutes and Bacteroidetes* phyla and the decrease of *Ruminococcaceae, Verrucomicrobiae*, and *Prevotellaceae* phyla in mice gut (**Figures 4A,B**). Chen et al. administered 12.5 mg/kg polysaccharides extracted in *P. lobata* to both normal mice and antibiotic-associated diarrhea mice for 2 weeks (45). They showed that the *P. lobata* extract fractions significantly increased the abundance of beneficial bacteria, involving *Oscillospira* and *Anaerotruncus*, whereas relieving colonic pathological changes and gut microbiota dysbiosis additionally. Thus, *P. lobata* polyphenol extract may be a promising source of the phenolic compound that exerts prebiotic effects *in vivo* for human health. In addition to taxonomic composition, the functional profiles were predicted by PICRUSt, and the functional differences are shown in **Figure 5**. The LEfSe result could illustrate biological explanations to establish the biological consistency and estimation of predicted biomarkers (46). In the treatment of *P. lobata,* the phenolic-rich extracts induced functional differences of microbial communities consisted of cellular process and signaling, circulatory system, and neurodegenerative diseases. This was in consistent with the previous studies that the Puerarin, the main bioactive compound found in *P. lobata*, was found to be beneficial to the neurodegenerative diseases *in vitro* and *in vivo* (47, 48). A similar study found that the bioactive compound puerarin had an obvious anti-inflammatory effect using mice model, and it repaired intestinal mucosal integrity *via* regulating

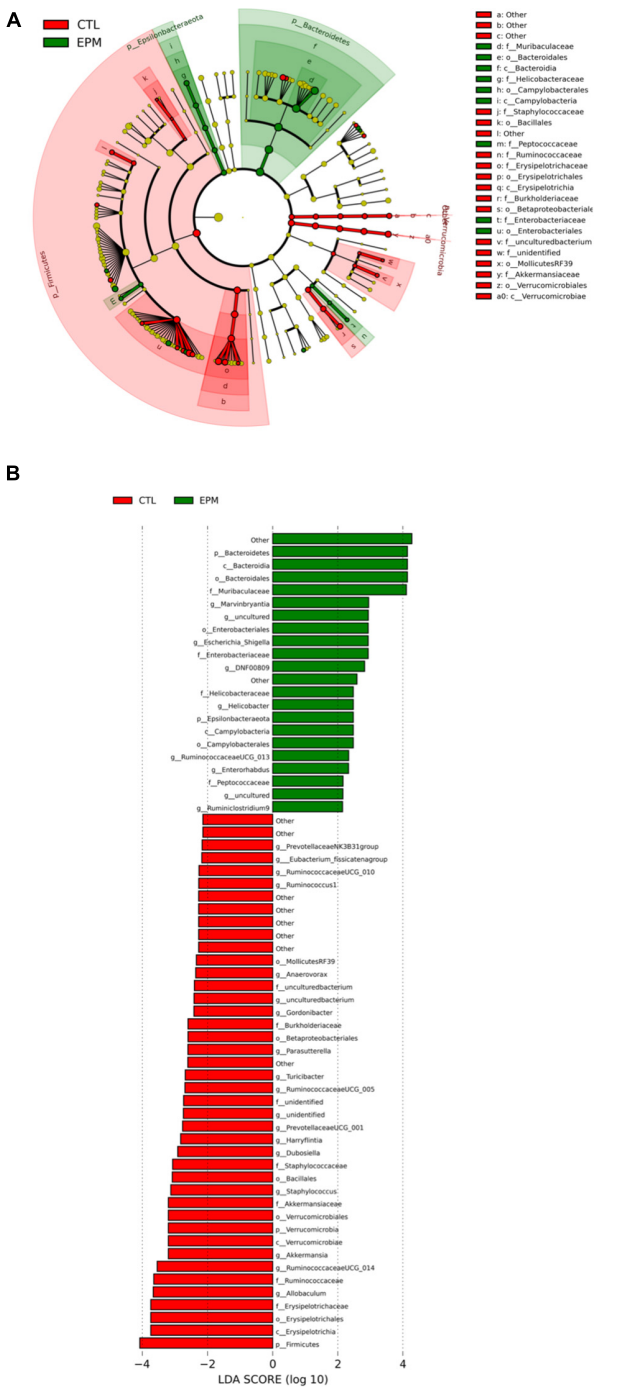

FIGURE 4 | Linear discriminant analysis Effect Size (LEfSe) plot of microbial communities affected by the *Pueraria lobata* extract diet. (Red) CTL; (Green) EPM. The brightness of each dot was proportional to its effect size **(A)**. The taxa had a significant LDA threshold value of > 2 were shown **(B)**. CTL, normal control group; EPM: *P. lobata* extract group.

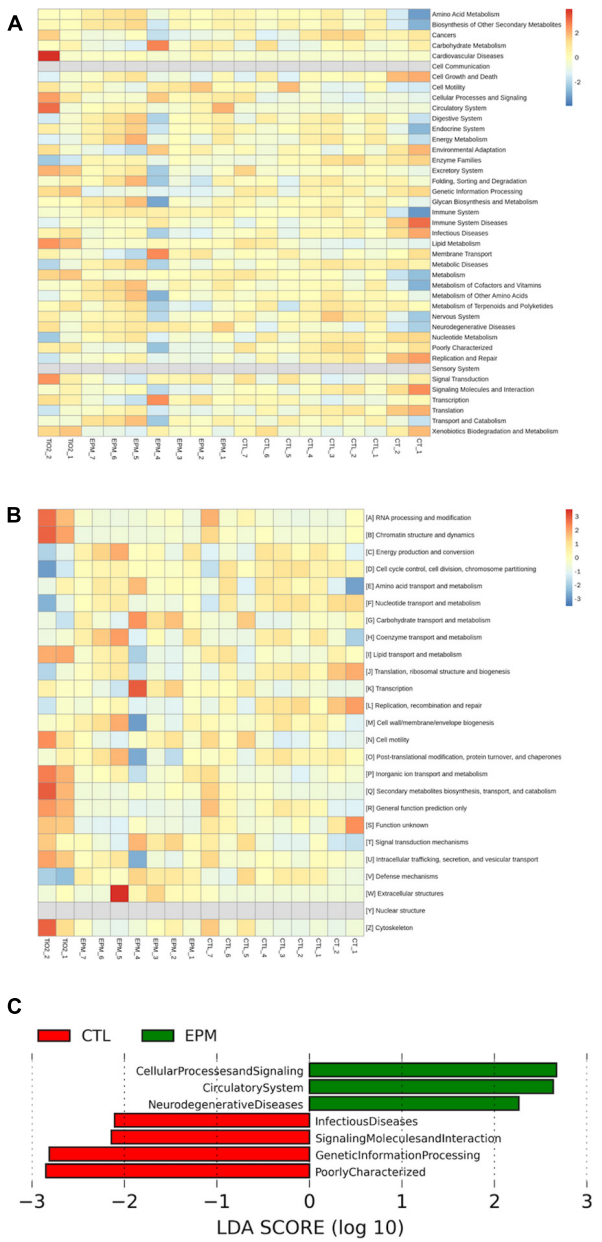

FIGURE 5 | Effect of the normal control group and the *Pueraria lobata* extract on differential operational taxonomic units (OTUs) and predicted microbial community functions by PICRUSt. **(A)** Kyoto Encyclopedia of Genes and Genomes (KEGG) heat map analysis. **(B)** Cluster of orthologous groups of proteins (COG) heat map analysis. **(C)** PICRUSt function prediction. CTL, normal control group; EPM, *P. lobata* extract group.

the abundance and kinds of the disorder gut microbiota, increasing the express of tight binding proteins ZO-1 and occludin, and these bacterial *Ruminococcaceae, Lachnospiraceae, Eubacterium_xylanophilum, and Ruminococcus_1* were the key species related (49). This study provides new insight into the potential application of *P. lobata* to be developed as a functional ingredient, which would have a beneficial effect on gut health. The physiological effects of fermentation of *P. lobata* on the potential colon health will be further investigated.

CONCLUSION

In this study, we purified the polyphenol-rich extract from *Pueraria lobata* and investigated systematically its antioxidant activities and its effect on gut microbiota. The *P. lobata* extract consisted of a large amount of puerarin that exhibited strong antioxidative capabilities *in vitro* and *in vivo*. Moreover, it had a positive effect on the structure and composition of gut microbiota. In summary, the phenolic-rich extract of *P. lobata* has considerable potential for utilization as a natural antioxidative food additive, as well as a type of gut microbiota-modulating health-promoting food ingredient. Therefore, we suggested that the *P. lobata* extract could be utilized as a promising supplement for functional foods that contributed to the prevention of various human chronic diseases.

DATA AVAILABILITY STATEMENT

The datasets presented in this study can be found in online repositories. The names of the repository/repositories and accession number(s) can be found in the article/supplementary material.

ETHICS STATEMENT

The animal study was reviewed and approved by the Institutional Animal Care and Use Committee of China Pharmaceutical University.

AUTHOR CONTRIBUTIONS

XX conceived the project idea and obtained the funding. XX and CS assigned the project, performed the research, and wrote the manuscript. YG, SC, WM, and XLX finished all the research. JM, JS, and CS revised the manuscript. XX, SH, LJ, and JM participated in the method and review. All authors approved the final version of the manuscript.

FUNDING

This study was financially supported by the Natural Science Foundation of Zhejiang Province, China (LQ21C200003), Natural Science Foundation of Shaoxing University (2019LG1012), and Scientific Research Start-Up Fund of Shaoxing University (20195015).

ACKNOWLEDGMENTS

We acknowledge the Institutional Animal Care and Use Committee of China Pharmaceutical University for the support of animal experiments in our study.

REFERENCES

1. Fang Q. Some current study and research approaches relating to the use of plants in the traditional Chinese medicine. *J Ethnopharmacol.* (1980) 2:57–63. doi: 10.1016/0378-8741(80)90031-8
2. Wong KH, Li GQ, Li KM, Razmovski-Naumovski V, Chan K. Kudzu root: traditional uses and potential medicinal benefits in diabetes and cardiovascular diseases. *J Ethnopharmacol.* (2011) 134:584–607. doi: 10.1016/j.jep.2011.02.001
3. Tome-Carneiro J, Visioli F. Polyphenol-based nutraceuticals for the prevention and treatment of cardiovascular disease: review of human evidence. *Phytomedicine.* (2016) 23:1145–74. doi: 10.1016/j.phymed.2015.10.018
4. Xu L, Zheng N, He Q, Li R, Zhang K, Liang T. Puerarin, isolated from *Pueraria lobata* (Willd.), protects against hepatotoxicity via specific inhibition of the TGF-β1/Smad signaling pathway, thereby leading to anti-fibrotic effect. *Phytomedicine.* (2013) 20:1172–9. doi: 10.1016/j.phymed.2013.06.008
5. Park HJ, Jeon YK, You DH, Nam MJ. Daidzein causes cytochrome c-mediated apoptosis via the Bcl-2 family in human hepatic cancer cells. *Food Chem Toxicol.* (2013) 60:542–9. doi: 10.1016/j.fct.2013.08.022
6. Son E, Yoon J-M, An B-J, Lee YM, Cha J, Chi G-Y, et al. Comparison among activities and isoflavonoids from *Pueraria thunbergiana* aerial parts and root. *Molecules.* (2019) 24:912. doi: 10.3390/molecules24050912
7. Lim DW, Lee C, Kim I-H, Kim YT. Anti-inflammatory effects of total isoflavones from *Pueraria lobata* on cerebral ischemia in rats. *Molecules.* (2013) 18:10404–12. doi: 10.3390/molecules180910404
8. Gagniere J, Raisc JH, Veziant J, Barnich N, Bonnet R, Buc E, et al. Gut microbiota imbalance and colorectal cancer. *World J Gastroenterol.* (2016) 24:501–18. doi: 10.3748/wjg.v22.i2.501
9. Flint HJ, Scott KP, Louis P, Duncan SH. The role of the gut microbiota in nutrition and health. *Nat Rev Gastroenterol Hepatol.* (2012) 9:577–89. doi: 10.1038/nrgastro.2012.156
10. Morgan XC, Tickle TL, Sokol H, Gevers D, Devaney KL, Ward DV, et al. Dysfunction of the intestinal microbiome in inflammatory bowel disease and treatment. *Genome Biol.* (2012) 13:R79. doi: 10.1186/gb-2012-13-9-r79
11. Kostic AD, Xavier RJ, Gevers D. The microbiome in inflammatory bowel disease: current status and the future ahead. *Gastroenterology.* (2014) 146:1489–99. doi: 10.1053/j.gastro.2014.02.009
12. Everard A, Belzer C, Geurts L, Ouwerkerk JP, Druart C, Bindels LB, et al. Cross-talk between *Akkermansia muciniphila* and intestinal epithelium controls diet-induced obesity. *Proc Natl Acad Sci USA.* (2013) 110:9066–71. doi: 10.1073/pnas.1219451110
13. Laparra JM, Sanz Y. Interactions of gut microbiota with functional food components and nutraceuticals. *Pharmacol Res.* (2010) 61:219–25. doi: 10.1016/j.phrs.2009.11.001
14. Liu Z, Chen Q, Zhang C, Ni L. Comparative study of the anti-obesity and gut microbiota modulation effects of green tea phenolics and their oxidation products in high-fat-induced obese mice. *Food Chem.* (2022) 367:130735. doi: 10.1016/j.foodchem.2021.130735
15. Choi Y-H, Hong SS, Shin YS, Hwan BYG, Park S-Y, Lee D. Phenolic compounds from *Pueraria lobata* protect PC12 cells against a beta-induced toxicity. *Arch Pharm Res.* (2010) 33:1651–4. doi: 10.1007/s12272-010-1014-7
16. Okarter N, Liu C-S, Sorrells ME, Liu RH. Phytochemical content and antioxidant activity of six diverse varieties of whole wheat. *Food Chem.* (2010) 33:249–57. doi: 10.1016/j.foodchem.2009.06.021
17. Alvarez-Parrilla E, de la Rosa LA, Amarowicz R, Shahidi F. Antioxidant activity of fresh and processed jalapeño and serrano peppers. *J Agric Food Chem.* (2011) 59:163–73. doi: 10.1021/jf103434u
18. Wagle A, Seong SH, Jung HA, Choi JS. Identifying an isoflavone from the root of *Pueraria lobata* as a potent tyrosinase inhibitor. *Food Chem.* (2019) 276:383–9. doi: 10.1016/j.foodchem.2018.10.008
19. Bing J, Xiao X, McClements DJ, Biao Y, Chongjiang C. Protein corona formation around inorganic nanoparticles: food plant proteins-TiO2 nanoparticle interactions. *Food Hydrocol.* (2021) 115:106594. doi: 10.1016/j.foodhyd.2021.106594
20. Biao Y, Jiannan H, Yaolan C, Shujie C, Dechun H, Julian Mcclements D, et al. Identification and characterization of antioxidant and immune-stimulatory polysaccharides in flaxseed hull. *Food Chem.* (2020) 315:126266. doi: 10.1016/j.foodchem.2020.126266
21. Xu X, Hu W, Zhou S, Tu C, Xia X, Zhang J, et al. Increased phenolic content and enhanced antioxidant activity in fermented glutinous rice supplemented with fu brick tea. *Molecules.* (2019) 24:671. doi: 10.3390/molecules2404067
22. Hu Q, Yuan B, Wu X, Du H, Gu M, Han Y, et al. Dietary intake of *Pleurotus eryngii* ameliorated dextran-sodium-sulfate-induced colitis in mice. *Mol Nutr Food Res.* (2019) 63:e1801265. doi: 10.1002/mnfr.201801265
23. Liu C-M, Ma J-Q, Sun Y-Z. Protective role of puerarin on lead-induced alterations of the hepatic glutathione antioxidant system and hyperlipidemia in rats. *Food Chem Toxicol.* (2011) 49:3119–27. doi: 10.1016/j.fct.2011.09.007
24. Cherdshewasart W, Sutjit W. Correlation of antioxidant activity and major isoflavonoid contents of the phytoestrogen-rich *Pueraria mirifica* and *Pueraria lobata* tubers. *Phytomedicine.* (2008) 15:38–43. doi: 10.1016/j.phymed.2007.07.058
25. Huang DJ, Ou BX, Prior RL. The chemistry behind antioxidant capacity assays. *J Agric Food Chem.* (2005) 53:1841–56. doi: 10.1021/jf030723c
26. Re R, Pellegrini N, Proteggente A, Pannala A, Yang M, Rice-Evans C. Antioxidant activity applying an improved ABTS radical cation decolorization assay. *Free Radic Biol Med.* (1999) 26:1231–7. doi: 10.1016/s0891-5849(98)00315-3
27. Wang Z-B, Chen B-B, Luo L, Yan J-K. Fractionation, physicochemical characteristics and biological activities of polysaccharides from *Pueraria lobata* roots. *J Taiwan Inst Chem Eng.* (2016) 67:54–60. doi: 10.1016/j.jtice.2016.07.029
28. Treml J, Smejkal K. Flavonoids as potent scavengers of hydroxyl radicals. *Compr Rev Food Sci Food Saf.* (2016) 15:720–38. doi: 10.1111/1541-4337.12204
29. Jin SE, Son YK, Min B-S, Jung HA, Choi JS. Anti-inflammatory and antioxidant activities of constituents isolated from *Pueraria lobata* roots. *Arch Pharm Res.* (2012) 35:823–37. doi: 10.1007/s12272-012-0508-x
30. Olawole TD, Okundigie MI, Rotimi SO, Okwumabua O, Afolabi IS. Preadministration of fermented sorghum diet provides protection against hyperglycemia-induced oxidative stress and suppressed glucose utilization in alloxan-induced diabetic rats. *Front Nutr.* (2018) 5:16. doi: 10.3389/fnut.2018.00016
31. Duangjan C, Rangsinth P, Zhang S, Gu X, Wink M, Tencomnao T. *Vitis vinifera* leaf extract protects against glutamate-induced oxidative toxicity in HT22 hippocampal neuronal cells and increases stress resistance properties in *Caenorhabditis elegans*. *Front Nutr.* (2021) 8:634100. doi: 10.3389/fnut.2021.634100
32. Senevirathne M, Ahn C-B, Je J-Y. Hepatoprotective effect of chitooligosaccharides against tert-butylhydroperoxide-induced damage in chang liver cells. *Carbohydr Polym.* (2011) 83:995–1000. doi: 10.1016/j.carbpol.2010.09.016
33. RiceEvans CA, Miller NJ, Paganga G. Structure-antioxidant activity relationships of flavonoids and phenolic acids. *Free Radic Biol Med.* (1996) 20:933–56. doi: 10.1016/0891-5849(95)02227-9
34. RiceEvans CA, Miller J, Paganga G. Antioxidant properties of phenolic compounds. *Trends Plant Sci.* (1997) 2:152–9. doi: 10.1016/S1360-1385(97)01018-
35. Zavodnik I, Buko V, Lukivskaya O, Lapshina E, Ilyich T, Belonovskaya E, et al. Cranberry (*Vaccinium macrocarpon*) peel polyphenol-rich extract attenuates rat liver mitochondria impairments in alcoholic steatohepatitis in vivo and after oxidative treatment in vitro. *J Funct Foods.* (2019) 57:83–94. doi: 10.1016/j.jff.2019.04.001
36. Zhang Y, Yin L, Huang L, Tekliye M, Xia X, Li J, et al. Composition, antioxidant activity, and neuroprotective effects of anthocyanin-rich extract from purple highland barley bran and its promotion on autophagy. *Food Chem.* (2021) 339:127849. doi: 10.1016/j.foodchem.2020.127849
37. Round JL, Mazmanian SK. The gut microbiota shapes intestinal immune responses during health and disease. *Nat Rev Immunol.* (2009) 9:313–23. doi: 10.1038/nri2515
38. Louis P, Hold GL, Flint HJ. The gut microbiota, bacterial metabolites and colorectal cancer. *Nat Rev Microbiol.* (2014) 12:661–72.
39. Tremaroli V, Backhed F. Functional interactions between the gut microbiota and host metabolism. *Nature.* (2012) 12:242–9. doi: 10.1038/nature11552

40. Loo YT, Howell K, Chan M, Zhang P, Ng K. Modulation of the human gut microbiota by phenolics and phenolic fiber-rich foods. *Compre Rev Food Sci Food Saf.* (2020) 19:1268–98. doi: 10.1111/1541-4337.12563
41. Yin J, Ren W, Wei B, Huang H, Li M, Wu X, et al. Characterization of chemical composition and prebiotic effect of a dietary medicinal plant *Penthorum chinense* Pursh. *Food Chem.* (2020) 319:126568. doi: 10.1016/j.foodchem.2020.126568
42. Gowd V, Bao T, Wang L, Huang Y, Chen S, Zheng X, et al. Antioxidant and antidiabetic activity of blackberry after gastrointestinal digestion and human gut microbiota fermentation. *Food Chem.* (2018) 269:618–27. doi: 10.1016/j.foodchem.2018.07.020
43. Turnbaugh PJ, Ley RE, Mahowald MA, Magrini V, Mardis ER, Gordon JI. An obesity-associated gut microbiome with increased capacity for energy harvest. *Nature.* (2006) 444:1027–31. doi: 10.1038/nature05414
44. Picard C, Fioramonti J, Francois A, Robinson T, Neant F, Matuchansky C. Review article: bifidobacteria as probiotic agents – physiological effects and clinical benefits. *Aliment Pharm Ther.* (2005) 22:495–512. doi: 10.1111/j.1365-2036.2005.02615.x
45. Chen R, Liu B, Wang X, Chen K, Zhang K, Zhang L, et al. Effects of polysaccharide from *Pueraria lobata* on gut microbiota in mice. *Int J Biol Macromol.* (2020) 158:740–9. doi: 10.1016/j.ijbiomac.2020.04.201
46. Liu J, Liu L, Zhang G, Peng X. *Poria cocos* polysaccharides attenuate chronic nonbacterial prostatitis by targeting the gut microbiota: comparative study of *Poria cocos* polysaccharides and finasteride in treating chronic prostatitis. *Int J Biol Macromol.* (2021) 189:346–55. doi: 10.1016/j.ijbiomac.2021.08.139
47. Zou Y, Hong B, Fan L, Zhou L, Liu Y, Wu Q, et al. Protective effect of puerarin against beta-amyloid-induced oxidative stress in neuronal cultures from rat hippocampus: involvement of the GSK-3 beta/Nrf2 signaling pathway. *Free Radic Res.* (2013) 47:55–63. doi: 10.3109/10715762.2012.742518
48. Mahdy HM, Mohamed MR, Emam MA, Karim AM, Abdel-Naim A, Khalifa AE. The anti-apoptotic and anti-inflammatory properties of puerarin attenuate 3-nitropropionic-acid induced neurotoxicity in rats. *Can J Physiol Pharmacol.* (2014) 92:252–8. doi: 10.1139/cjpp-2013-0398
49. Li B, Liu M, Wang Y, Gong S, Yao W, Li W, et al. Puerarin improves the bone micro-environment to inhibit OVX-induced osteoporosis via modulating SCFAs released by the gut microbiota and repairing intestinal mucosal integrity. *Biomed Pharmacother.* (2020) 132:110923. doi: 10.1016/j.biopha.2020.110923

Conflict of Interest: The authors declare that the research was conducted in the absence of any commercial or financial relationships that could be construed as a potential conflict of interest.

Publisher's Note: All claims expressed in this article are solely those of the authors and do not necessarily represent those of their affiliated organizations, or those of the publisher, the editors and the reviewers. Any product that may be evaluated in this article, or claim that may be made by its manufacturer, is not guaranteed or endorsed by the publisher.

Copyright © 2022 Xu, Guo, Chen, Ma, Xu, Hu, Jin, Sun, Mao and Shen. This is an open-access article distributed under the terms of the Creative Commons Attribution License (CC BY). The use, distribution or reproduction in other forums is permitted, provided the original author(s) and the copyright owner(s) are credited and that the original publication in this journal is cited, in accordance with accepted academic practice. No use, distribution or reproduction is permitted which does not comply with these terms.

frontiers | Frontiers in Nutrition

BRIEF RESEARCH REPORT
published: 04 April 2022
doi: 10.3389/fnut.2022.876620

Mediterranean Diet Combined With a Low-Carbohydrate Dietary Pattern in the Treatment of Overweight Polycystic Ovary Syndrome Patients

Shanshan Mei[1,2†], Jie Ding[2†], Kaili Wang[2†], Zhexin Ni[2] and Jin Yu[2,3*]*

[1] Shanghai University of Traditional Chinese Medicine, Shanghai, China, [2] Department of Gynecology of Traditional Chinese Medicine, Changhai Hospital of PLA Military Medical University, Shanghai, China, [3] International Peace Maternity and Child Health Hospital, School of Medicine, Shanghai Jiao Tong University, Shanghai, China

Objectives: To determine the therapeutic effect of a Mediterranean diet (MED) combined with a low-carbohydrate (LC) dietary model in overweight polycystic ovary syndrome (PCOS) patients.

Methods: In this 12-week randomized controlled clinical trial, 72 overweight patients with PCOS were randomly assigned to one of two energy-restricted dietary models: the MED/LC diet or the Low fat (LF) diet. After the intervention, the number of the two groups returned to normal menstruation was counted. Body weight, body mass index (BMI), waist circumference, waist-hip ratio (WHR), body fat percentage (BF%), serum fasting insulin(FINS), fasting plasma glucose(FPG), insulin resistance index (HOMA-IR), quantitative insulin sensitivity index (QUIKI), total cholesterol (TC) and high density lipoprotein cholesterol (HDL-C), low density lipoprotein cholesterol (LDL-C), triglyceride (TG), total testosterone (TT), luteinizing hormone (LH), follicle-stimulating hormone (FSH), and prolactin (PRL) were compared between 2 groups before and after intervention.

Results: MED/LC group had more significant reduction trend in weight (−6.10 ± 1.52 kg vs −4.79 ± 0.97 kg, $P < 0.05$), BMI (−2.12 ± 0.57 kg/m^2 vs −1.78 ± 0.36 kg/m^2, $P < 0.05$), WC (−6.12 ± 5.95 cm vs −3.90 ± 1.58 cm, $P < 0.05$), WHR (−0.06 ± 0.02 vs −0.03 ± 0.02, $P < 0.05$), BF% (−2.97% ± 1.78% vs −1.19% ± 0.91%, $P < 0.05$), TT (−0.20 ± 0.24 ng/mL vs 0.08 ± 0.11 ng/Ml, $P < 0.001$), LH (−5.28 ± 3.31 mIU/mL vs −3.39 ± 3.64 mIU/mL, $P < 0.05$), and LH/FSH (−1.18 ± 0.75 vs -0.66 ± 1.05, $P < 0.05$) compared with the LF group. In addition, FPG (0.05 ± 0.38 mmol/mL vs -0.50 ± 1.01 mmol/mL, $P < 0.001$), FINS (−4.88 ± 6.11 μU/mL vs −8.53 ± 5.61 μU/mL, $P < 0.01$), HOMA-IR index (−1.11 ± 1.51 vs −2.23 ± 0.25, $P < 0.05$), and QUIKI index (0.014 ± 0.016 vs 0.028 ± 0.019, $P < 0.05$) decreased significantly in the MED/LC group compared with the LF group. Comparing the changes in lipid parameters between the two groups (LF vs MED/LC), significant differences in TG (−0.33 ± 0.32 mmol vs −0.76 ± 0.97 mmol, $P < 0.05$), TC (−0.40 ± 1.00 mmol vs −1.45 ± 2.00 mmol, $P < 0.05$), and LDL-C (−0.41 ± 1.05 mmol vs −0.73 ± 0.76 mmol, $P < 0.05$) were observed.

Conclusion: The results of this study suggest that the MED/LC diet model is a good treatment for overweight PCOS patients, significantly restoring their menstrual cycle,

OPEN ACCESS

Edited by:
Shuai Chen,
Wuhan University, China

Reviewed by:
Jie Qiao,
Shanghai Jiao Tong University, China
Elnaz Daneshzad,
Tehran University of Medical Sciences, Iran

****Correspondence:***
Zhexin Ni
nizxzg@163.com
Jin Yu
395005545@163.com

† These authors have contributed equally to this work

Specialty section:
This article was submitted to Food Chemistry, a section of the journal Frontiers in Nutrition

Received: *15 February 2022*
Accepted: *07 March 2022*
Published: *04 April 2022*

Citation:
Mei S, Ding J, Wang K, Ni Z and Yu J (2022) Mediterranean Diet Combined With a Low-Carbohydrate Dietary Pattern in the Treatment of Overweight Polycystic Ovary Syndrome Patients. Front. Nutr. 9:876620. doi: 10.3389/fnut.2022.876620

improving their anthropometric parameters and correcting their disturbed endocrine levels, and its overall effectiveness is significantly better than the LF diet model. Therefore, this study recommends that the MED/LC diet model can be used in the clinical treatment of patients with overweight PCOS.

Keywords: mediterranean diet, low-carbohydrate diet, polycystic ovary syndrome, overweight mediterranean diet, overweight

INTRODUCTION

Polycystic ovary syndrome (PCOS) is a common group of endocrine metabolic disorders in women of reproductive age, characterised by polycystic ovarian changes, sporadic ovulation and menstrual disorders (1). Based on conservative estimates, the prevalence of PCOS in women of reproductive age is 6–15%, whereas insulin resistance (IR) is present in 50–70% of patients with PCOS, with obese PCOS patients accounting for approximately 75% of IR patients (2). PCOS causes reproductive endocrine disorders in the near term, which can lead to metabolic syndromes in the long term, such as fatty liver, type 2 diabetes, cardiovascular risk, and increased risk of endometrial cancer (3). Amongst these disorders, IR is an important mechanism causing abnormal glucolipid metabolism and reproductive dysfunction (4), whereas obesity increases IR and compensatory hyperinsulinemia (HI), which in turn increases adipogenesis and decreases lipolysis, promotes ovarian androgen production and exacerbates ovarian androgen hypersecretion disorder, thereby further amplifying reproductive endocrine disorders and metabolic problems in patients with PCOS (5).

Pharmacological treatment; lifestyle management such as diet and exercise and psychological modification have been recommended as the first line of treatment for PCOS at all times (6), with dietary modification playing an important role in the treatment of patients with PCOS patients. Based on previous reports, the diet of patients with PCOS tends to be high in carbohydrates and fat, which to a certain extent increases the IR and lipid inflammatory environment of patients (7) and promotes the progression of the disease. Therefore, calorie-restricted dietary regimens have been recognised as important dietary options for patients with PCOS (8), and corresponding studies on the effects of dietary modification on PCOS are found, such as low-fat (LF) diet, low-carbohydrate (LC) diet, top hypertension diet, pulse-based diet, high-protein diet, ketogenic diet and other dietary models (9–11). At present, considerable research has been conducted to demonstrate that LF diets can effectively reduce central obesity in patients by affecting their insulin levels and lipid metabolism (12, 13). LC diet has also been shown to improve insulin sensitivity and promote normal lipid metabolism (14), however, effective comparisons of dietary regimens and strategies for optimal dietary combinations are not yet well researched.

The Mediterranean diet (MED) model has been studied and discussed in many fields in recent years as a respected dietary structure (15, 16). Its nutritional structure is modelled by emphasising a high intake of vegetables, fruits, fish, seafood, legumes, and nuts, with whole grains generally recommended as staple foods, and cooking with vegetable oils (containing unsaturated fatty acids) instead of animal oils (containing saturated fatty acids), with olive oil being particularly advocated. This diet is more liberal with regard to fat intake, and cereals have a moderating effect on IR as good-quality carbohydrates (17). Based on previous studies, the MED model can reduce the secretion of pro-inflammatory adipocytokines by reducing visceral fat, with a diet structure based on plant-based food intake, and phenolic compounds of plant origin can modulate insulin action and metabolism in insulin-sensitive tissues, with potential preventive or therapeutic effects on IR and IR-related diseases. The increased intake of seafood suggested in the protocol can remarkably increase the levels of n-3 long-chain polyunsaturated fatty acids in human and the circulating levels of insulin-sensitive hormone lipocalin to a certain extent, and the regular intake of seafood can reduce energy intake by 4–9% compared with the regular intake of terrestrial meat, which could be effective in preventing obesity and maintaining energy balance (18, 19). By contrast, the extent to which the MED model is effective has not been supported by additional data in studies of dietary models of PCOS. Thus, this study aimed to combine the MED model with a LC dietary model based on energy restriction, compared with a LF dietary model, investigate whether this novel dietary model could provide significant improvements in reproductive endocrine and metabolic levels in overweight patients with PCOS through a 12-week strict dietary intervention and provide better supplements and recommendations for the behavioural treatment of PCOS in clinical practice.

MATERIALS AND METHODS

Study Design

This study is an open-label, parallel-group randomised controlled trial design for a 12-week intervention with a 4-week follow-up. The study protocol was approved by the by the Ethics Committee of Changhai Hospital of PLA Military Medical University. The study protocol was in accordance with all the principles of the World Medical Association Declaration of Helsinki. Written

Abbreviations: PCOS, polycystic ovary syndrome; IR, insulin resistance; HI, hyperinsulinemia; LF, low fat; MED, Mediterranean diet; LC, low carbohydrate; HP, high protein; SFAs, saturated fatty acids; BMI, body mass index; WHR, waist-to-hip ratio; BF%, body fat percentage; TT, total testosterone; LH, luteinising hormone; FSH, follicle-stimulating hormone; LH/FSH, ratio of luteinising hormone to follicle-stimulating hormone; PRL, prolactin; FPG, fasting plasma glucose; FINS, fasting insulin; HOMA-IR, homeostatic model assessment of insulin resistance; QUIKI, quantitative insulin sensitivity check index; TC, total cholesterol; TG, triglyceride; HDL-C, high-density lipoprotein cholesterol; LDL-C, low-density lipoprotein cholesterol.

informed consent was signed by participants prior to their inclusion in the study. The trial was registered at https://ClinicalTrials.gov/, No. CHiECRCT-20160050. Participants had basic information collected through a questionnaire at the beginning of the study, including age, height, weight, medical history, blood pressure, and heart rate. They were randomly assigned to one of two calorie-restricted diets throughout the study period: a LF diet or a Mediterranean/low-carbohydrate (MED/LC) diet. Items collected before and after the intervention included fasting weight on the day of collection, body mass index (BMI), waist circumference (WC), hip circumference (HC), body fat percentage (BF%), fasting plasma glucose (FPG), fasting insulin (FINS), total testosterone (TT), luteinising hormone (LH), follicle-stimulating hormone (FSH), oestradiol (E2), prolactin (PRL), progesterone (P), triglycerides (TG), total cholesterol (TC), high-density lipoprotein cholesterol (HDL-C), and low-density lipoprotein cholesterol (LDL-C).

Participants

The 72 participants in this study were successively drawn from patients with PCOS, who were attending the Department of Traditional Chinese Medicine and Gynecology at the Changhai Hospital of PLA Military Medical University from 2018 to 2020, with all data collection completed in February 2021. The inclusion criteria were as follows: (a) diagnosis of PCOS according to the Rotterdam criteria (20), (b) age 16–45 years, and (c) BMI consistent with an overweight diagnosis of BMI $\geq$24.0 kg/m^2. The exclusion criteria were as follows: (a) combination of other endocrine etiological disorders (congenital adrenal hyperplasia, Cushing's syndrome, androgen-secreting tumours, hyperprolactinemia, diabetes mellitus, thyroid, adrenal, and other endocrine disorders) according to the Rotterdam criteria; (b) combination of cardiovascular and cerebrovascular diseases, haematological disorders, hepatic and renal insufficiency, and other serious diseases; (c) pregnant women, breastfeeding women, and pregnancy preparation or no contraception during the intervention period; (d) suffering from mental illness or cancer; and (e) have taken non-progesterone hormonal medication or insulin sensitisers or medication affecting lipid metabolism (fish oil, etc.) within 3 months. The exclusion and detachment criteria were as follows: (a) poor compliance during the intervention and non-cooperation with treatment and (b) incomplete observation case information. Participant groupings were randomly assigned by an associate in the department based on a computer-generated random number table.

Diet Intervention

Both diets aimed at moderate long-term metabolic improvement and restricted the intake of sweets and foods containing trans fatty acids. The participants were divided into two groups, and they joined separate diet management groups, where a professional dietitian recommended 7-day recipes. The LF group had less than 30% of total dietary calories from fat, less than 40 g of fat intake throughout the day and up to 10% saturated fat (21). They do not consume fatty foods such as fatty meats, butter, offal, fried foods, preserved foods, poultry skin, fish roe, shrimp roe, and crabmeat, and they increased the intake of cereals, vegetables, and fruits as appropriate (**Supplementary Table 1**). In the MED/LC group, which is a combination of MED and LC diet, according to the definition of a LC diet (22), the participants had a maximum carbohydrate intake of less than 20%, a maximum carbohydrate intake of 100 g throughout the day and an increased intake of protein and fat. In combination with the MED group, participants were advised to consume whole grain as a staple food, a high intake of extra virgin olive oil, vegetables (including green leafy vegetables, fruit, cereals, nuts, and legumes), moderate intake of fish and other meat, dairy products, and a low intake of eggs (23) (**Supplementary Table 2**). The average daily total calorie baseline was maintained for both dietary groups.

Treatment Adherence

Participants were provided with a daily food recommendation every 7 days via the Chinese social networking software WeChat and were instructed to record their daily food intake from the beginning to the end of the dietary intervention period using the Chinese dietary app Boohee software to calculate the corresponding calories. Participants were asked to perform only daily basal activity during the intervention period and were prohibited from taking any other nutritional supplements. Participants were contacted via WeChat at the end of each week to review the programme, monitor for adverse events and provide counselling support to facilitate the effectiveness of the intervention. All outcome assessments were performed at week 12, and data were collected when normal menstrual cycles returned.

Anthropometric Measurements and Body Composition Analysis

The height of each participant was measured using an ultrasonic height-measuring device with an accuracy of 1 cm (BXT-15A, BAXIT, Germany), and the weight and BF% were measured using a body composition analyser with an accuracy of 0.1 kg (T6100A, TEZEWA, United States). In addition, the BMI was automatically read by an app connected to the instrument (kg/m^2). WC and HC were measured by a fixed researcher using a soft ruler with an accuracy of 1 mm. WC was measured as the midpoint of the line between the lowest point of the rib and the upper edge of the iliac crest, and HC was measured as the horizontal circumference of the most prominent part of the hip towards the back. The waist-to-hip ratio (WHR) was calculated as WC (cm)/HC (cm).

Blood Exams and Biochemical Assessment

Fasting blood samples were obtained in the morning at 2–5 days of the menstrual cycle (or progesterone withdrawal bleeding) from the median cubital vein, and the hormonal and glucose parameters were detected. Blood samples were collected in BD vacutainers tubes (SSTTM II Advance, REF 367958) and centrifuged at 3,500 rpm for 15 min at 4°C, and then serum and plasma were frozen at −80°C. FINS, FSH, LH, E2, TT,

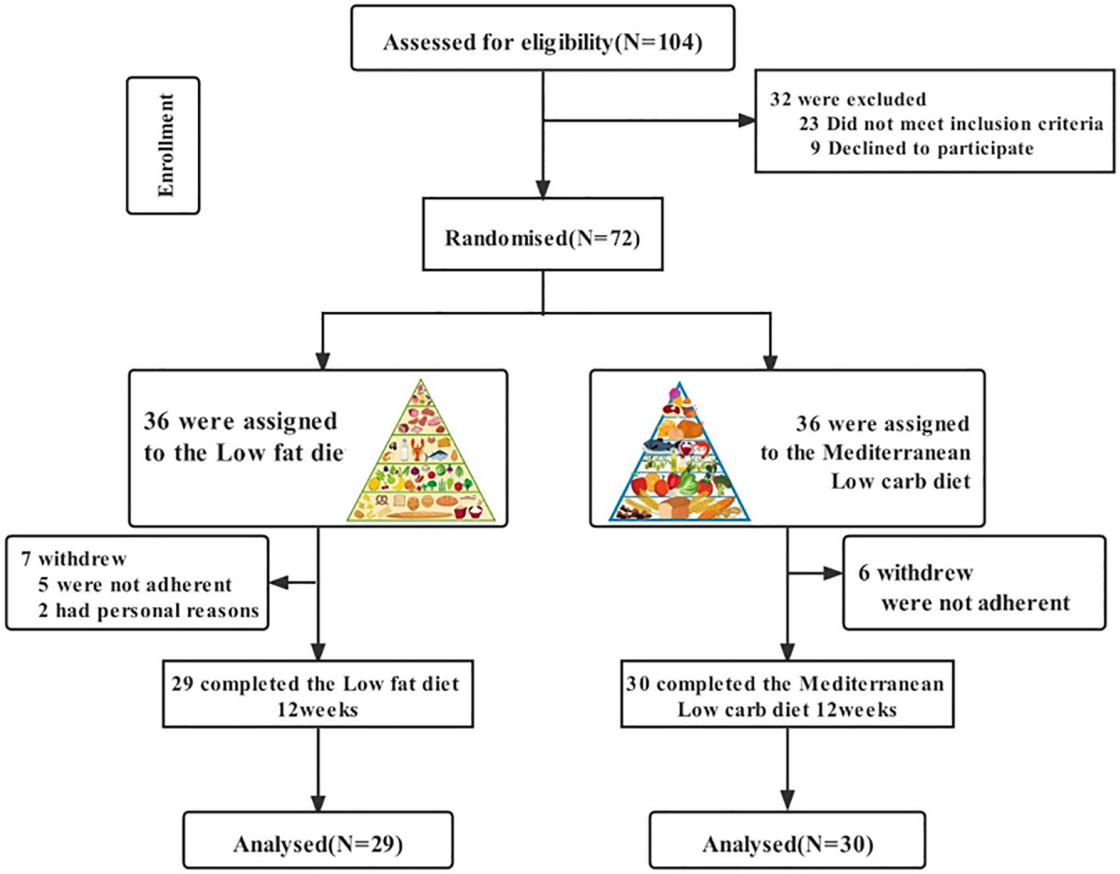

FIGURE 1 | Flow chart from the study design.

PRL, and P were measured by enzyme-linked immunosorbent assay (Elisa Kit, CUSABIO, Wuhan, China). FPG, TC, TG, HDL-C, and LDL-C were measured by coupled enzyme assay (Sigma, United States). The HOMA-IR index was calculated as FINS (μU/mL) × FPG (mmol/L)/22.5, and the QUIKI index was calculated as 1/(log(FINS(μU/mL))+ log(FPG(mg/dL))).

Statistical Analysis

The Shapiro–Wilk test was used to test whether the data conformed to a normal distribution. Data that conformed to a normal distribution were expressed as mean ± standard deviation (mean ± SD), and data before and after the intervention were counted using paired *t*-tests and between two groups using independent sample *t*-tests. Data that did not conform to a normal distribution were presented as median (25th–75th percentile) and analysed using the Mann–Whitney U test to compare the parameters before and after 12 weeks. All data analyses were performed using SPSS, version 26 (SPSS Inc., Chicago, IL, United States). All data graphs were produced and analysed using GraphPad Prism (version 9.0.0). Differences were considered statistically significant when $P < 0.05$. For the treatment of missing values, these values were not included in this analysis.

RESULTS

Participants' Characteristics

Figure 1 shows a flow chart of participants' progress through the various stages of the study. We recruited a total of 104 patients, of whom 16 were taking hormone medication five had abnormal liver function, two were on insulin sensitisers, six were preparing for pregnancy and three were resistant to diet modification. We included 72 patients in the study programme, of which some patients in both groups did not complete the study cycle because they were unable to adhere to the diet programme or for personal reasons (change of pregnancy plans or outright discontinuation of the study programme), resulting in 29 final completers in the LF diet group and 30 final completers in the MED/LC diet group. No side effects were observed during the dietary intervention in patients with PCOS throughout the study. Based on the initial randomisation, no differences were observed between the LF and MED/LC groups at baseline with regard to age, anthropometrics, sex hormone levels, and blood biochemistry (**Table 1**).

Dietary Intake

Differences in total nutrient intake were calculated on three randomly selected days based on participants' dietary records

throughout the intervention (**Figure 2**). No statistically significant differences were found between the two groups with regard to total energy and cholesterol intake. The MED/LC group had a relatively lower carbohydrate intake ($P < 0.001$), a relatively higher total protein and fat intake ($P < 0.001$), and a significant difference in saturated fatty acid intake ($P < 0.001$) compared with the LF group (**Table 2**).

Menstruation Situation

At the end of the study, the number of patients who returned to normal menstruation in the two groups was counted. 72.4% (21/29) of patients in the LF group returned to normal menstrual cycles, whereas 86.7% (26/30) of patients in the MED/LC group returned to normal menstrual cycles, with no significant difference between the two groups ($P = 0.174 > 0.05$).

Anthropometric and Body Composition Measurements

Combining the data before and after the dietary intervention in both groups, a decrease in weight, BMI, WC, WHR, and BF% in both groups was observed, with statistically significant differences ($P < 0.05$ or $P < 0.001$; **Table 3**), indicating that both interventions had effective management effects. **Figure 3** shows the data before and after the two groups showed that the MED/LC group had more significant reduction trend in weight (−6.10 ± 1.52 kg vs −4.79 ± 0.97 kg), BMI (−2.12 ± 0.57 kg/m^2 vs −1.78 ± 0.36 kg/m^2), WC (−6.12 ± 5.95 cm vs −3.90 ± 1.58 cm), WHR (−0.06 ± 0.02 vs −0.03 ± 0.02), and BF% (−2.97% ± 1.78% vs. −1.19% ± 0.91%) compared with the LF group.

Gonadal Parameters

With regard to sex hormones (**Table 4**), significant changes in TT, LH, and LH/FSH were observed before and after the dietary intervention in both groups ($P < 0.05$ or $P < 0.001$), whereas FSH and PRL were basically unchanged compared with baseline values ($P > 0.05$).

As shown in **Figure 4**, the trend of hormonal changes in the two groups was compared, and a decrease in TT (−0.20 ± 0.24 ng/mL vs. 0.08 ± 0.11 ng/mL) was found in the MED/LC group compared with the LF group ($P < 0.001$). In addition, a decrease in LH (−5.28 ± 3.31 mIU/mL vs. −3.39 ± 3.64 mIU/mL) and LH/FSH (−1.18 ± 0.75 vs −0.66 ± 1.05) was found, and the differences were statistically significant ($P < 0.05$). However, the change in PRL between the two groups was not statistically significant ($P > 0.05$).

Metabolic Parameters

After the intervention in both groups (**Table 5**), FINS, HOMA-IR index, QUIKI index and lipid parameters, including TG, TC, and LDL-C, decreased significantly ($P < 0.05$ or $P < 0.001$), but HDL-C levels did not change significantly ($P > 0.05$). The reduction in blood glucose in the MED/LC group after the intervention was statistically significant ($P < 0.05$). In the MED/LC group, FPG (0.05 ± 0.38 mmol/mL vs -0.50 ± 1.01 mmol/mL, $P < 0.001$), FINS (−4.88 ± 6.11 μU/mL vs −8.53 ± 5.61 μU/mL, $P < 0.01$), HOMA-IR index (−1.11 ± 1.51 vs −2.23 ± 0.25), and QUIKI index (0.014 ± 0.016 vs 0.028 ± 0.019) decreased compared with the LF group (**Figure 5**), and all differences were statistically significant ($P < 0.05$). Comparing the changes in lipid parameters between the two groups (LF vs MED/LC), significant differences in TG (−0.33 ± 0.32 mmol vs −0.76 ± 0.97 mmol), TC (−0.40 ± 1.00 mmol vs −1.45 ± 2.00 mmol), and LDL-C (−0.41 ± 1.05 mmol vs −0.73 ± 0.76 mmol; $P < 0.05$) were observed, but no significant difference in HDL-C was found between the two groups ($P > 0.05$).

TABLE 1 | Baseline characteristics of the study participants.

Characteristic	LF group (N = 29)	MED/LC group (N = 30)	*P*-value
Age (years)	28.07 ± 7.126	27.97 ± 5.295	0.95
Height (m)	1.64 ± 0.05	1.64 ± 0.05	0.87
Weight (kg)	79.76 ± 9.71	79.34 ± 7..94	0.85
BMI (kg/m^2)	29.57 ± 2.48	29.37 ± 2.22	0.75
Waist circumference (cm)	96.66 ± 9.98	96.05 ± 10.27	0.82
Hip circumference (cm)	105.3(101.95–114.75)	105.15(101.48–110.13)	0.59*
WHR	0.90 ± 0.05	0.91 ± 0.05	0.25
body fat percentage (BF%)	37.28 ± 5.19	37.41 ± 7.03	0.94
TT (ng/ml)	0.85(0.80–0.94)	0.89(0.80–1.02)	0.28*
LH (mIU/ml)	8.11(6.87–11.09)	9.07(7.12–11.28)	0.51*
FSH (mIU/ml)	4.58 ± 1.36	4.70 ± 1.28	0.75
LH/FSH ratio	1.82(1.55–2.52)	2.02(1.64–2.27)	0.58*
PRL (ng/ml)	11.28(7.91–15.39)	12.36(9.36–16.57)	0.41*
FPG (mmol/ml)	5.12(4.77–5.44)	5.32(4.95–5.62)	0.22*
FINS (μU/ml)	18.90(14.80–23.45)	19.80(14.93–27.40)	0.53*
HOMA-IR index	4.00(3.39–5.43)	4.90(3.70–6.75)	0.19*
QUIKI index	0.307 ± 0.014	0.304 ± 0.013	0.30
TG (mmol)	1.48(1.17–2.60)	1.67(1.02–2.14)	0.92*
TC (mmol)	4.99(4.20–5.40)	5.05(4.50–5.76)	0.50*
HDL-C (mmol)	1.21(0.96–1.37)	1.09(0.95–1.25)	0.28*
LDL-C (mmol)	2.86(2.21–3.60)	3.06(2.66–3.52)	0.30*

*BMI, body mass index; WHR, waist-to-Hip Ratio; BF%, body fat percentage TT, total testosterone; LH, luteinizing hormone; FSH, follicle stimulating hormone; LH/FSH, ratio of luteinizing hormone to follicle stimulating hormone; PRL, prolactin; FPG, fasting plasma glucose; FINS, fasting insulin; HOMA-IR, homeostatic model assessment of insulin resistance; QUIKI, quantitative insulin sensitivity check index; TC, total cholesterol; TG, triglyceride; HDL-C, high-density lipoprotein cholesterol; LDL-C, low-density lipoprotein cholesterol. P Comparison between two groups has been assessed using independent t-test. Results are expressed as mean ± SD. *P Comparison between two groups has been assessed using Mann–Whitney tests. Results are expressed as median (25th–75th percentile).*

DISCUSSION

This study was the first to use the MED combined with a LC diet for 12 weeks of strict dietary management in overweight patients with PCOS. It also compared the effects of the MED/LC diet and the LF diet on anthropometric indicators, reproductive endocrine levels, degree of IR and lipid metabolism levels in

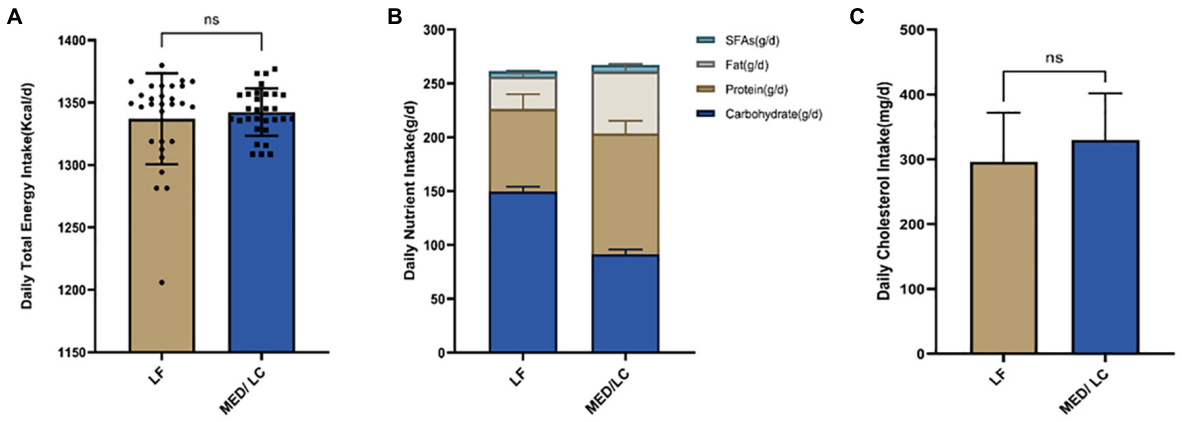

FIGURE 2 | Intake of energy and nutrients between the diet intervention groups. **(A)** Baseline for daily total energy intake remained the same for both groups($P > 0.05$). **(B)** The Mediterranean/low-carbohydrate (MED/LC) diet more greatly decreased the intake of carbohydrate and more greatly increased the intake of protein, fat and saturated fatty acids (SFAs). **(C)** No difference in daily cholesterol intake between the two groups($P > 0.05$). Analysis of variance with a covariance (ANCOVA) test was used. LF, low fat diet.

patients with PCOS; recorded the number of people who returned to normal menstrual cycles during management in both groups and investigated the degree of rationality and effectiveness of the two dietary regimens.

Polycystic ovary syndrome is a common gynaecological endocrine metabolic disorder in adolescent and fertile women. IR is a metabolic abnormality characteristic of PCOS, and it leads to compensatory elevation of body insulin levels and the development of HI, which exacerbates hyperandrogenaemia, anovulation and polycystic ovary formation (24). Most patients with PCOS are formally obese, and obesity is an important cause of IR in patients with PCOS. Clinical management of PCOS is still mostly limited to pharmacological treatment. As research into the mechanisms of IR in patients with PCOS progresses, including its effects on glucose and lipid metabolism and the warning of long-term complications such as cardiovascular disease and endometrial cancer, considerable attention should be given to lifestyle interventions as a safe, effective and closely related daily treatment management modality (25). As the first line of treatment for PCOS, the management of dietary behaviour plays an important role in the efficacy of the disease, and no standardised dietary protocols are available at present. In an earlier clinical study, the average daily total energy intake of patients with PCOS was higher than that of the common people, and limiting their total energy intake ameliorated their weight, androgen secretion and insulin index (26). Subsequently, overweight patients with PCOS have a predominance of visceral adiposity, and they are evidently and centrally obese. In addition, adipose tissue secretes a variety of adipokines, including leptin, lipocalin, resistin and visceral adiponectin to promote the development of PCOS. The formation of obesity is strongly related to the daily preference for high-fat foods (27). The development of obesity is strongly associated with the daily preference for high-fat foods. Therefore, some researchers have developed a LF diet model with no energy restriction and a low glycaemic index diet model to compare the improvement of obesity and reproductive endocrinology in patients with PCOS and found that both dietary models improved obesity in patients with PCOS but not reproductive endocrinology (28). In the pathogenesis of PCOS, IR plays a crucial role as a central mechanism for the sensitivity of body's glucose metabolism, usually manifested by poor glucose tolerance and reduced insulin sensitivity (29). Therefore, controlling the level of carbohydrate content in the daily dietary intake of patients with PCOS plays an important role. Jafari-Maram et al. found diets lower in carbohydrate and higher in protein and fat were not associated with overweight, obesity and cardiovascular risk factors (30). In a meta-analysis of intervention studies in patients with PCOS using an unrestricted energy LC diet model, LC significantly reduced BMI, androgen and IR levels and improved lipid metabolism in eight relevant RCTs compared with standard dietary regimens (31). Thus, a LC diet is recommended. The MED model, a dietary model that has emerged in recent years, is based on a rich variety of plant foods, including a large number of vegetables, fruits, grains and cereals, legumes, nuts and seeds, with fat accounting

TABLE 2 | Dietary intakes of study participants throughout the study.

	LF Group (N = 29)	MED/LC Group (N = 30)	*P*-value
Total energy (Kcal/day)	1348.79(1318.94–1363.40)	1342.34(1333.90–1356.91)	0.69*
Carbohydrate (g/day)	149.61(145.39–153.60)	91.73(88.44–95.23)	<0.001*
Protein (g/day)	76.64 ± 13.62	112.35 ± 11.72	<0.001
Fat (g/day)	29.79 ± 3.02	57.51 ± 6.56	<0.001
SFAs (g/day)	5.26 ± 0.54	6.08 ± 0.94	<0.001
Cholesterol (mg/day)	296.27 ± 75.64	329.97 ± 71.59	0.08

*SFAs, saturated fatty acids; LF, low fat diet; MED/LC, Mediterranean/low-carbohydrate diet. P Comparison of between-group changes (independent t-test). Data are expressed as mean ± SD. *P Comparison of between-group changes (Mann–Whitney tests). Results are expressed as median (25th–75th percentile).*

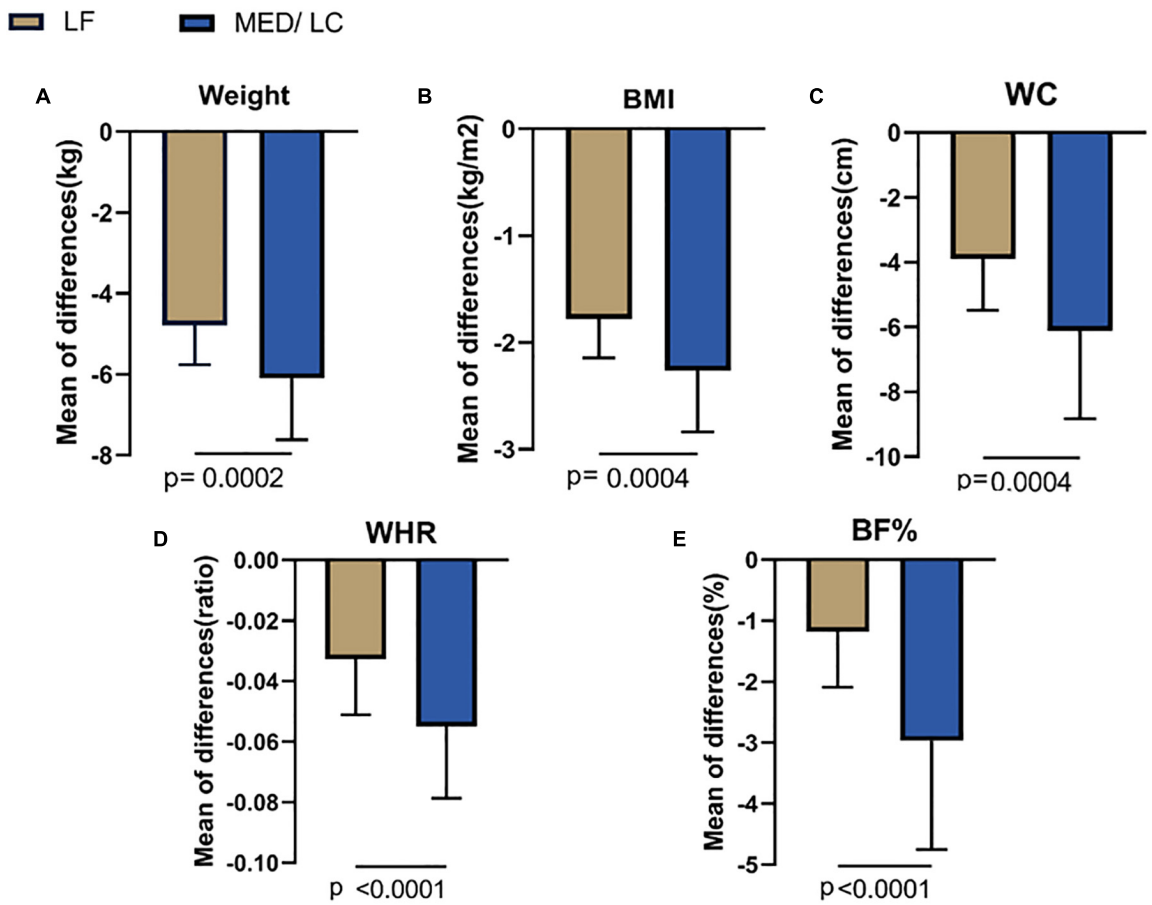

FIGURE 3 | Comparison of changes in anthropometric variables between two groups. **(A)** The MED/LC diet resulted in more weight loss than the LF diet. **(B)** MED/LC diet reduced body mass index (BMI) more than LF diet. **(C)** The MED/LC diet resulted in more waist circumference (WC) loss than the LF diet. **(D)** MED/LC diet reduced waist-to-hip ratio (WHR) more than LF diet. **(E)** The MED/LC diet resulted in more body fat percentage (BF%) loss than the LF diet. Data are mean (± SD). Analysis of variance with a covariance (ANCOVA) test was used.

TABLE 3 | Anthropometric measurements and body composition at baseline and after the intervention.

	LF group (n = 29)			MED/LC group (n = 30)		
	LF before	**LF after**	***P*-value**	**MED/LC before**	**MED/LC after**	***P*-value**
Weight (kg)	76.8(71.85–86.55)	72.5(67.5–81.35)	0.046*	79.34 ± 7.94	73.24 ± 7.12	<0.001
BMI (kg/m^2)	29.57 ± 2.48	27.78 ± 2.39	<0.001	29.37 ± 0.41	27.11 ± 1.86	<0.001
WC (cm)	96.66 ± 9.98	92.75 ± 9.20	<0.001	96.05 ± 10.27	89.93 ± 9.65	<0.001
WHR	0.90 ± 0.05	0.87 ± 0.05	<0.001	0.91 ± 0.05	0.86 ± 0.05	<0.001
BF (%)	37.28 ± 5.19	36.10 ± 5.30	<0.001	37.41 ± 7.03	34.44 ± 7.67	<0.001

*BMI, body mass index; WC, waist circumference; WHR, waist-to-hip Ratio; BF%, body fat percentage; P Comparison of within-group changes (Paired sample t-test). Dates are expressed as mean ± SD. *P Comparison of within-group changes (Mann–Whitney tests). Results are expressed as median (25th–75th percentile).*

for up to 35% of total dietary energy and less than 7–8% of saturated fatty acids. It has a refined broad framework for the composition of the diet, and it is widely used in metabolic and cardiovascular diseases (32), but its application in PCOS is less common. The MED model can effectively modify IR (33). Therefore, in this study, we used the MED structural model combined with the LC diet model, which was compared with the LF diet model, to provide a 12-week dietary intervention for overweight patients with PCOS based on restricted total energy intake, and we found that at the end of the intervention, both dietary models had an effect on the anthropometric indicators of patients with PCOS, reproductive endocrine levels, the degree of IR and lipid metabolism-related indicators. The MED/LC group showed more significant improvements in weight, BMI, WC, WHR, and BF% than the LF diet group. The primary issue for overweight patients with PCOS is weight and body fat

TABLE 4 | Serum sex hormone levels at baseline and after the intervention.

	LF group (n = 29)			MED/LC group (n = 30)		
	LF before	**LF after**	***P*-value**	**MED/LC before**	**MED/LC after**	***P*-value**
TT (ng/ml)	0.85(0.80–0.94)	0.80(0.71–0.89)	0.03*	0.89(0.80–1.02)	0.72(0.51–0.84)	<0.001*
LH (mIU/ml)	8.11(6.87–11.09)	5.26(2.57–6.89)	<0.001*	9.07(7.12–11.28)	3.59(1.85–5.48)	<0.001*
FSH (mIU/ml)	4.58 ± 1.36	4.40 ± 1.63	0.54	4.72(3.92–5.76)	4.39(3.79–4.96)	0.50*
LH/FSH ratio	1.82(1.55–2.52)	1.24(0.71–1.77)	0.001*	2.03 ± 0.56	0.85 ± 0.09	<0.001
PRL (ng/ml)	11.28(7.91,15.39)	13.52(8.93–17.75)	0.32*	12.36(9.36–16.57)	12.56(9.48–15.51)	0.9*

*TT, total testosterone; LH, luteinizing hormone; FSH, follicle stimulating hormone; LH/FSH, ratio of luteinizing hormone to follicle stimulating hormone; PRL, prolactin; P Comparison of within-group changes (Paired sample t-test). Data are expressed as mean ± SD. *P Comparison of within-group changes (Mann–Whitney tests). Results are expressed as median (25th–75th percentile).*

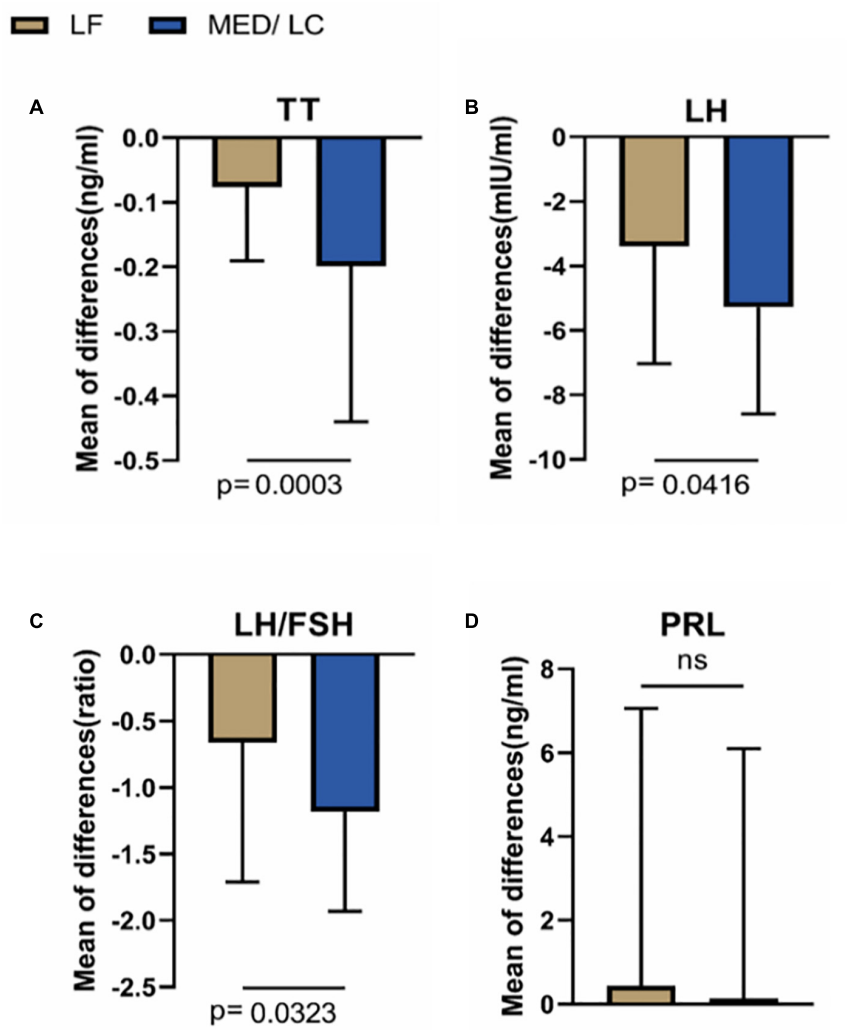

FIGURE 4 | Comparison of changes in serum sex hormone levels between two groups. **(A)** The MED/LC diet resulted in more total testosterone (TT) loss than the LF diet. **(B)** MED/LC diet reduced luteinizing hormone (LH) more than LF diet. **(C)** The MED/LC diet resulted in more ratio of luteinizing hormone to follicle-stimulating hormone (LH/FSH) loss than the LF diet. **(D)** Prolactin (PRL) changes of MED/LC diet and LF diet had no difference. Data are mean(±SD). Analysis of variance with a covariance (ANCOVA) test was used.

loss; therefore, the MED/LC regimen is effective for overweight patients with PCOS, surpassing the LF regimen to a certain extent. With regard to reproductive endocrine levels, TT, LH, and LH/FSH all decreased to a certain extent in the LF group after the intervention, but the decrease was more prominent after the MED/LC intervention. In addition, with regard to FSH and PRL

TABLE 5 | Glucolipid metabolism index at baseline and after the intervention.

	LF group (n = 29)			MED/LC group (n = 30)		
	LF before	**LF after**	***P*-value**	**MED/LC before**	**MED/LC after**	***P*-value**
FPG (mmol/ml)	5.17 ± 0.47	5.22 ± 0.47	0.491	5.32(4.95–5.62)	4.97(4.45–5.38)	0.017*
FINS (μU/ml)	18.90(14.80–23.45)	13.49(9.75–19.45)	0.006*	21.7 ± 7.62	13.18 ± 5.58	<0.001
HOMA-IR	4.00(3.39–5.43)	3.06(2.24–4.33)	0.013*	5.17 ± 1.7	2.94 ± 1.36	<0.001
QUIKI	0.307 ± 0.014	0.321 ± 0.020	<0.001	0.304 ± 0.013	0.332 ± 0.024	<0.001
TG (mmol)	1.48(1.17–2.60)	1.10(0.88–1.94)	0.039*	1.67(1.02–2.14)	1.03(0.76–1.33)	0.003*
TC (mmol)	4.95 ± 1.02	4.55 ± 0.82	0.037	5.05(4.50–5.76)	4.05(2.98–4.82)	<0.001*
HDL-C (mmol)	1.21(0.96–1.37)	1.27(1.05–1.34)	0.355*	1.09(0.95–1.25)	1.14(0.95–1.28)	0.383*
LDL-C (mmol)	2.84 ± 0.88	2.43 ± 0.83	0.046	3.06(2.66–3.52)	2.44(1.91–2.91)	<0.001*

*FPG, fasting plasma glucose; FINS, fasting insulin; HOMA-IR, homeostatic model assessment of insulin resistance; QUIKI, quantitative insulin sensitivity check index; TC, total cholesterol; TG, triglyceride; HDL-C, high-density lipoprotein cholesterol; LDL-C, low-density lipoprotein cholesterol; P Comparison of within-group changes (Paired sample t-test). Data are expressed as mean ± SD. *P Comparison of within-group changes (Mann–Whitney tests). Results are expressed as median (25th–75th percentile).*

levels, a slight change was observed in both groups. The decrease in these indicators is important for follicular development and the recovery of ovulatory cycles in patients with PCOS. The decline in TT is particularly important. Hyperandrogenaemia, a representative pathological mechanism in PCOS, is a pathological increase in androgens that activates the earliest stages of follicular growth, thereby stimulating the growth of small sinus follicles, leading to the recruitment of small follicles and the formation of polycystic ovaries. Moreover, a high androgen level increases the expression of granulosa cell androgen receptors and FSH receptors, promoting granulosa cell and follicular membrane cell proliferation and cortical thickening, with ovulatory disturbances and secondary menstrual disorders (34). Therefore, a decrease in androgens would play a direct role in restoring ovulation. In previous studies, the LF diet alone did not significantly improve reproductive endocrine disorders in overweight patients with PCOS (28), whereas the LF diet model in this study showed good improvement. The present study controlled the total energy intake by setting the LF diet model, which had an important effect on the metabolic level to a certain extent. This result suggests that the restriction of total energy intake is important in the development of dietary intervention, regardless of the changes in the composition of the diet. Comparing the number of people who returned to normal menstrual cycles between the two groups, the return to normal menstrual cycles was greater than 50% in the LF and MED/LC groups (72.4 vs. 86.7%), with no significant difference between the two groups, indicating that both dietary regimens were effective in restoring ovulation in overweight patients with PCOS. In the dietary regimen of this study, the LF group was set up with an average daily fat intake of less than 40 g, thereby significantly increasing the ratio of carbohydrate to protein intake compared with the MED/LC group with regard to dietary structure. When comparing the reduction in the degree of IR, we found that the FPG in the LF group was higher than that before the intervention, which may be related to the higher proportion of carbohydrate intake in this model. Therefore, the total energy intake and the total fat intake were controlled during the 12 weeks of the protocol, and the FINS, HOMA-IR, and QUIKI indices still showed a decreasing trend to a certain extent, indicating that our LF diet in the presence of calorie restriction can still alleviate the degree of IR, although the carbohydrate intake ratio was correspondingly higher. The results of a previous study found little difference in changes in blood glucose and HI-related indicators after a high-fat diet versus a high-carbohydrate diet, but the metabolic pattern shifted to impaired insulin sensitivity during the high-fat diet (35). This finding suggests that the intake of fat content has a profound effect on the IR status, which could explain the corresponding improvement in IR in our LF diet model. However, the MED/LC group significantly controlled carbohydrate intake compared with the LF group. Combining the two dietary models, the MED/LC group significantly increased protein intake compared with the LF group, whereas fat intake did not significantly exceed the standard diet (the standard for a LF diet is a total daily intake of <50 g, and the fat intake in this study was at 57.51 ± 6.56 g). Therefore, the MED/LC diet model in this study is similar to the high-protein (HP) diet model to a certain extent. In an earlier trial of a dietary intervention for PCOS, researchers found significant improvements in anthropometric indicators and testosterone levels and a slight difference in lipid levels in patients with PCOS compared with the standard ratio dietary model after intervention with a dietary model that simply increased the protein/carbohydrate ratio (36). In studies of metabolic-related diseases, calorie-restricted HP diet model can relieve hyperglycaemia and IR status by modifying intestinal flora (37, 38), and the results of the present study suggest that a similar mechanism may exist in the MED/LC model. Comparing the relevant metabolic indices before and after the intervention of the two dietary models in this study, the decrease in IR-related indices (FPG, FINS, HOMA-IR index, and QUIKI index) and lipid profile (TG, TC, and LDL-C) after the MED/LC diet intervention was significant compared with the LF group, which indicated that the MED/LC diet model has an advantage over the LF diet model with regard to calorie restriction. The MED/LC group had an advantage over the LF group with regard to improvement in all PCOS-related indicators, which was also related to the difference in the specific refinement of food between the two groups. The MED diet recommends a whole-grain diet as the staple food,

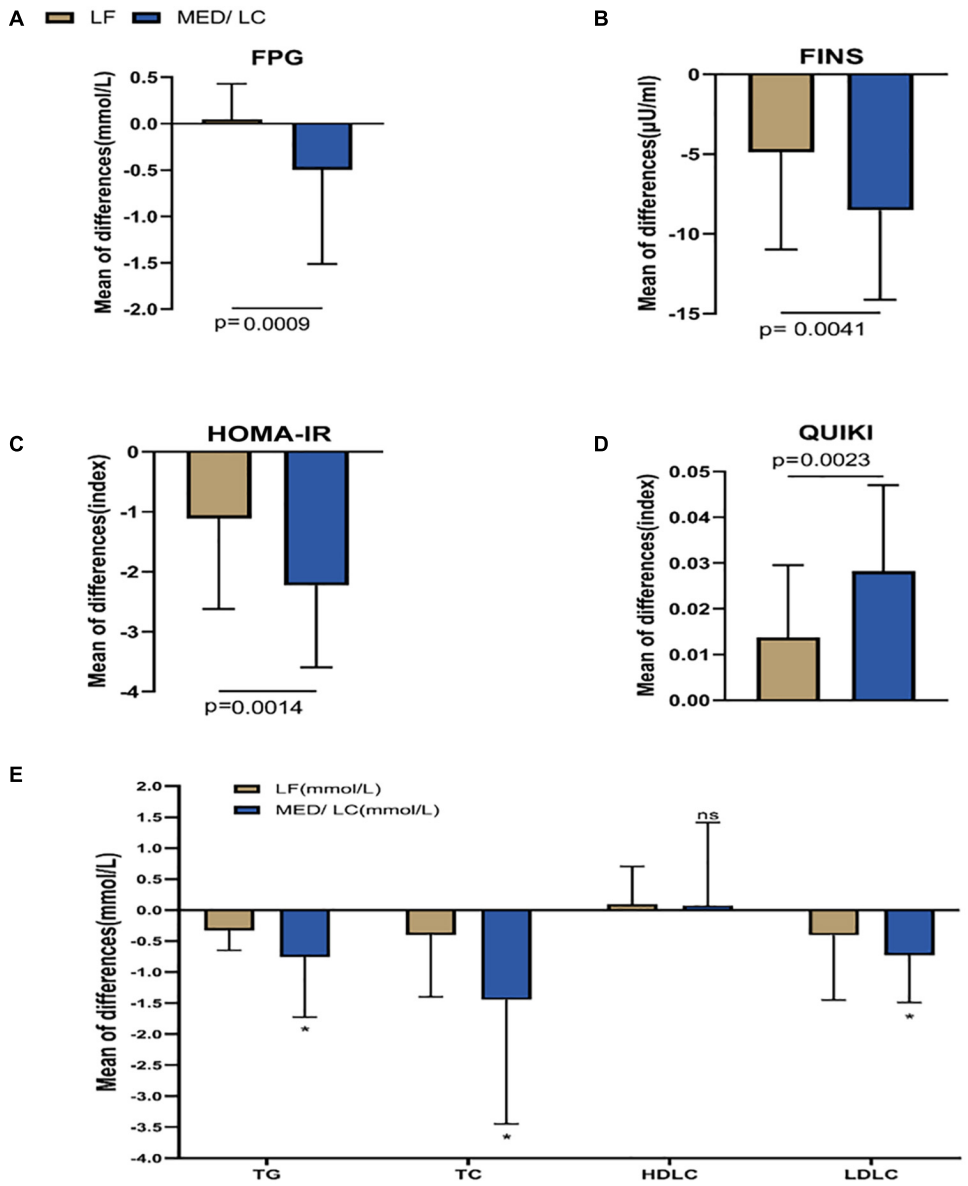

FIGURE 5 | Comparison of changes in metabolic parameters between two groups. **(A)** Change in fasting plasma glucose (FPG) in the MED/LC diet compared to the LF diet. **(B)** Change in fasting insulin (FINS) in the MED/LC diet compared to the LF diet. **(C)** Change in homeostatic mode assessment of insulin resistance (HOMA-IR) in the MED/LC diet compared to the LF diet. **(D)** Change in quantitative insulin sensitivity check index (QUIKI) in the MED/LC diet compared to the LF diet. **(E)** Change in blood lipid level in the MED/LC diet compared to the LF diet. TC, total cholesterol; TG, triglyceride; HDL-C, high-density lipoprotein cholesterol; LDL-C, low-density lipoprotein cholesterol. Data are mean (± SD). Analysis of variance with a covariance (ANCOVA) test was used. *$P < 0.05$. ns: $P > 0.05$.

and the LF model does not emphasise restricting the type of staple food, which may also have some effect. Based on previous studies, the dietary fibre content of cereals is higher than that of refined carbohydrates (e.g., rice and noodles), and the higher the dietary fibre intake, the lower the body weight, glycaemic load and triglyceride and cholesterol levels (39), which would better explain the advantages of the MED/LC dietary model. The MED/LC group is more finely structured than the LF group and is more useful for clinicians to understand its specific application. The strength of this study lies in the combination of the MED diet model and the LC diet model, with specific dietary interventions based on calorie restriction and a comparison with the LF group. Analysis of the results shows that the MED/LC diet model with calorie restriction has a greater advantage in the improvement of all indicators in overweight patients with PCOS, and it provides a better reference for the intervention criteria of the PCOS diet structure. In addition, the MED/LC diet model has a more specific reference for the arrangement

of the diet structure, which also facilitates clinical application. Few prospective controlled studies have used the MED diet model for the treatment of PCOS. One single-arm study of the MED diet model combined with a ketogenic diet model showed that the combined diet model was effective in improving PCOS anthropometric indicators, reproductive endocrine levels and IR levels (40). However, the ketogenic diet is not long lasting because of potential negative effects on the kidneys and adverse effects such as decreased insulin sensitivity after withdrawal of ketones (41), which also has some reference value for our study. Notably, this study still has significant limitations similar to other studies of lifestyle interventions. First, patient adherence to the dietary intervention in this study was highly problematic, with PCOS patients having difficulty adhering to a single dietary model for 12 consecutive weeks. Second, this study was a single-centre trial, and the participants were all Chinese patients. The development of the diet plan considered certain regional characteristics, and the generalised type of diet may have some limitations for various food cultures. Third, the treatment period was only 12 weeks, without long-term intervention and follow-up, and some statistical biases against long-term effects were found. Therefore, this study could establish a relatively advantageous dietary model as a model reference for clinicians in the treatment of PCOS with regard to dietary interventions.

CONCLUSION

This study evaluated the effectiveness of the MED diet model in combination with the LC diet model in the treatment of overweight patients with PCOS, based on restricting total energy intake, compared with the LF diet model.

The results of the study showed that the LF and MED/LC dietary models were effective in modifying anthropometric parameters, reproductive endocrine levels, IR levels and lipid levels in patients with PCOS, with the MED/LC dietary model being more effective and the recovery of menstrual cycles being approximately the same in both groups. Therefore, the MED/LC diet model was recommended for the treatment of overweight patients with PCOS.

DATA AVAILABILITY STATEMENT

The raw data supporting the conclusions of this article will be made available by the authors, without undue reservation.

ETHICS STATEMENT

The studies involving human participants were reviewed and approved by the Ethics Committee of Changhai Hospital of PLA Military Medical University. The patients/participants provided their written informed consent to participate in this study.

AUTHOR CONTRIBUTIONS

SM and JD collected the data and thesis writing. KW conducted the statistical analyses. ZN revised the final version. JY proposed the research ideas and designed the research plans. All authors contributed to the article and approved the submitted version.

FUNDING

This work was supported by the National Natural Science Foundation of China (grant numbers 81973896 and 81603646) and China Postdoctoral Science Foundation (grant number 2020M681337).

ACKNOWLEDGMENTS

We gratefully acknowledge the enthusiastic support of the women who volunteered to participate in the present study. We thank our consulting dietitians and nutrition students who provided professional technical support of nutrition.

SUPPLEMENTARY MATERIAL

The Supplementary Material for this article can be found online at: https://www.frontiersin.org/articles/10.3389/fnut.2022.876620/full#supplementary-material

REFERENCES

1. Zhang J, Bao Y, Zhou X, Zheng L. Polycystic ovary syndrome and mitochondrial dysfunction. *Reprod Biol Endocrinol.* (2019) 17:67. doi: 10.1186/s12958-019-0509-4
2. Skiba MA, Islam RM, Bell RJ, Davis SR. Understanding variation in prevalence estimates of polycystic ovary syndrome: a systematic review and meta-analysis. *Hum Reprod Update.* (2018) 24:694–709. doi: 10.1093/humupd/dmy022
3. Zeng X, Xie Y-J, Liu Y-T, Long S-L, Mo Z-C. Polycystic ovarian syndrome: correlation between hyperandrogenism, insulin resistance and obesity. *Clin Chim Acta.* (2020) 502:214–21. doi: 10.1016/j.cca.2019.11.003
4. Ding H, Zhang J, Zhang F, Zhang S, Chen X, Liang W, et al. Resistance to the insulin and elevated level of androgen: a major cause of polycystic ovary syndrome. *Front Endocrinol (Lausanne).* (2021) 12:741764. doi: 10.3389/fendo.2021.741764
5. Glueck CJ, Goldenberg N. Characteristics of obesity in polycystic ovary syndrome: etiology, treatment, and genetics. *Metabolism.* (2019) 92:108–20. doi: 10.1016/j.metabol.2018.11.002
6. Hoeger KM, Dokras A, Piltonen T. Update on pcos: consequences, challenges, and guiding treatment. *J Clin Endocrinol Metab.* (2021) 106:e1071–83. doi: 10.1210/clinem/dgaa839
7. Afrin S, AlAshqar A, El Sabeh M, Miyashita-Ishiwata M, Reschke L, Brennan JT, et al. Diet and nutrition in gynecological disorders: a focus on clinical studies. *Nutrients.* (2021) 13:1747. doi: 10.3390/nu13061747
8. Shang Y, Zhou H, He R, Lu W. Dietary modification for reproductive health in women with polycystic ovary syndrome: a systematic review and meta-analysis. *Front Endocrinol (Lausanne).* (2021) 12:735954. doi: 10.3389/fendo.2021.735954

9. Katcher HI, Kunselman AR, Dmitrovic R, Demers LM, Gnatuk CL, Kris-Etherton PM, et al. Comparison of hormonal and metabolic markers after a high-fat, western meal versus a low-fat, high-fiber meal in women with polycystic ovary syndrome. *Fertil Steril.* (2009) 91:1175–82. doi: 10.1016/j.fertnstert.2008.01.035
10. Barrea L, Marzullo P, Muscogiuri G, Di Somma C, Scacchi M, Orio F, et al. Source and amount of carbohydrate in the diet and inflammation in women with polycystic ovary syndrome. *Nutr Res Rev.* (2018) 31:291–301. doi: 10.1017/S0954422418000136
11. Cincione RI, Losavio F, Ciolli F, Valenzano A, Cibelli G, Messina G, et al. Effects of mixed of a ketogenic diet in overweight and obese women with polycystic ovary syndrome. *Int J Environ Res Public Health.* (2021) 18:12490. doi: 10.3390/ijerph182312490
12. Moran LJ, Brown WJ, McNaughton SA, Joham AE, Teede HJ. Weight management practices associated with pcos and their relationships with diet and physical activity. *Hum Reprod.* (2017) 32:669–78. doi: 10.1093/humrep/dew348
13. Panjeshahin A, Salehi-Abargouei A, Anari AG, Mohammadi M, Hosseinzadeh M. Association between empirically derived dietary patterns and polycystic ovary syndrome: a case-control study. *Nutrition.* (2020) 79–80:110987. doi: 10.1016/j.nut.2020.110987
14. Goldenberg JZ, Day A, Brinkworth GD, Sato J, Yamada S, Jönsson T, et al. Efficacy and safety of low and very low carbohydrate diets for type 2 diabetes remission: systematic review and meta-analysis of published and unpublished randomized trial data. *BMJ.* (2021) 372:m4743. doi: 10.1136/bmj.m4743
15. Chicco F, Magrì S, Cingolani A, Paduano D, Pesenti M, Zara F, et al. Multidimensional impact of Mediterranean diet on IBD patients. *Inflamm Bowel Dis.* (2021) 27:1–9. doi: 10.1093/ibd/izaa097
16. Salas-Salvadó J, Díaz-López A, Ruiz-Canela M, Basora J, Fitó M, Corella D, et al. Effect of a lifestyle intervention program with energy-restricted Mediterranean diet and exercise on weight loss and cardiovascular risk factors: one-year results of the predimed-plus trial. *Diabetes Care.* (2019) 42:777–88. doi: 10.2337/dc18-0836
17. Malin SK, Kullman EL, Scelsi AR, Haus JM, Filion J, Pagadala MR, et al. A whole-grain diet reduces peripheral insulin resistance and improves glucose kinetics in obese adults: a randomized-controlled trial. *Metabolism.* (2018) 82:111–7. doi: 10.1016/j.metabol.2017.12.011
18. Hussain T, Tan B, Yin Y, Blachier F, Tossou MCB, Rahu N. Oxidative stress and inflammation: what polyphenols can do for us? *Oxid Med Cell Longev.* (2016) 2016:7432797. doi: 10.1155/2016/7432797
19. Liaset B, Øyen J, Jacques H, Kristiansen K, Madsen L. Seafood intake and the development of obesity, insulin resistance and type 2 diabetes. *Nutr Res Rev.* (2019) 32:146–67. doi: 10.1017/S0954422418000240
20. Rotterdam ESHRE/ASRM-Sponsored PCOS Consensus Workshop Group. Revised 2003 consensus on diagnostic criteria and long-term health risks related to polycystic ovary syndrome. *Fertil Steril.* (2004) 81:19–25. doi: 10.1016/j.fertnstert.2003.10.004
21. Baker B. Weight loss and diet plans. *Am J Nurs.* (2006) 106:52–9; quiz 60.
22. Oh R, Gilani B, Uppaluri KR. *Statpearls: Low Carbohydrate Diet.* Treasure Island, FL: StatPearls Publishing (2021).
23. Davis C, Bryan J, Hodgson J, Murphy K. Definition of the Mediterranean diet; a literature review. *Nutrients.* (2015) 7:9139–53. doi: 10.3390/nu7115459
24. Escobar-Morreale HF. Polycystic ovary syndrome: definition, aetiology, diagnosis and treatment. *Nat Rev Endocrinol.* (2018) 14:270–84. doi: 10.1038/nrendo.2018.24
25. Teede HJ, Misso ML, Costello MF, Dokras A, Laven J, Moran L, et al. Recommendations from the international evidence-based guideline for the assessment and management of polycystic ovary syndrome. *Fertil Steril.* (2018) 110:364–79. doi: 10.1016/j.fertnstert.2018.05.004
26. Thomson RL, Buckley JD, Noakes M, Clifton PM, Norman RJ, Brinkworth GD. The effect of a hypocaloric diet with and without exercise training on body composition, cardiometabolic risk profile, and reproductive function in overweight and obese women with polycystic ovary syndrome. *J Clin Endocrinol Metab.* (2008) 93:3373–80. doi: 10.1210/jc.2008-0751
27. Barber TM, Franks S. Obesity and polycystic ovary syndrome. *Clin Endocrinol (Oxf).* (2021) 95:531–41. doi: 10.1111/cen.14421
28. Wong JMW, Gallagher M, Gooding H, Feldman HA, Gordon CM, Ludwig DS, et al. A randomized pilot study of dietary treatments for polycystic ovary syndrome in adolescents. *Pediatr Obes.* (2016) 11:210–20. doi: 10.1111/ijpo.12047
29. Diamanti-Kandarakis E, Dunaif A. Insulin resistance and the polycystic ovary syndrome revisited: an update on mechanisms and implications. *Endocr Rev.* (2012) 33:981–1030. doi: 10.1210/er.2011-1034
30. Jafari-Maram S, Daneshzad E, Brett NR, Bellissimo N, Azadbakht L. Association of low-carbohydrate diet score with overweight, obesity and cardiovascular disease risk factors: a cross-sectional study in Iranian women. *J Cardiovasc Thorac Res.* (2019) 11:216–23. doi: 10.15171/jcvtr.2019.36
31. Zhang X, Zheng Y, Guo Y, Lai Z. The effect of low carbohydrate diet on polycystic ovary syndrome: a meta-analysis of randomized controlled trials. *Int J Endocrinol.* (2019) 2019:4386401. doi: 10.1155/2019/4386401
32. Lăcătuşu C-M, Grigorescu E-D, Floria M, Onofriescu A, Mihai B-M. The Mediterranean diet: from an environment-driven food culture to an emerging medical prescription. *Int J Environ Res Public Health.* (2019) 16:942. doi: 10.3390/ijerph16060942
33. Mirabelli M, Chiefari E, Arcidiacono B, Corigliano DM, Brunetti FS, Maggisano V, et al. Mediterranean diet nutrients to turn the tide against insulin resistance and related diseases. *Nutrients.* (2020) 12:1066. doi: 10.3390/nu12041066
34. Wang J, Wu D, Guo H, Li M. Hyperandrogenemia and insulin resistance: the chief culprit of polycystic ovary syndrome. *Life Sci.* (2019) 236:116940. doi: 10.1016/j.lfs.2019.116940
35. Wallenius V, Elebring E, Casselbrant A, Laurenius A, le Roux CW, Docherty NG, et al. Glycemic control and metabolic adaptation in response to high-fat versus high-carbohydrate diets-data from a randomized cross-over study in healthy subjects. *Nutrients.* (2021) 13:3322. doi: 10.3390/nu13103322
36. Sørensen LB, Søe M, Halkier KH, Stigsby B, Astrup A. Effects of increased dietary protein-to-carbohydrate ratios in women with polycystic ovary syndrome. *Am J Clin Nutr.* (2012) 95:39–48. doi: 10.3945/ajcn.111.020693
37. Dong TS, Luu K, Lagishetty V, Sedighian F, Woo S-L, Dreskin BW, et al. A high protein calorie restriction diet alters the gut microbiome in obesity. *Nutrients.* (2020) 12:3221. doi: 10.3390/nu12103221
38. Yu Z, Nan F, Wang LY, Jiang H, Chen W, Jiang Y. Effects of high-protein diet on glycemic control, insulin resistance and blood pressure in type 2 diabetes: a systematic review and meta-analysis of randomized controlled trials. *Clin Nutr.* (2020) 39:1724–34. doi: 10.1016/j.clnu.2019.08.008
39. Reynolds A, Mann J, Cummings J, Winter N, Mete E, Te Morenga L. Carbohydrate quality and human health: a series of systematic reviews and meta-analyses. *Lancet.* (2019) 393:434–45. doi: 10.1016/S0140-6736(18)31809-9
40. Paoli A, Mancin L, Giacona MC, Bianco A, Caprio M. Effects of a ketogenic diet in overweight women with polycystic ovary syndrome. *J Transl Med.* (2020) 18:104. doi: 10.1186/s12967-020-02277-0
41. Paoli A. Ketogenic diet for obesity: friend or foe? *Int J Environ Res Public Health.* (2014) 11:2092–107. doi: 10.3390/ijerph110202092

Conflict of Interest: The authors declare that the research was conducted in the absence of any commercial or financial relationships that could be construed as a potential conflict of interest.

The reviewer JQ declared a shared affiliation with the author JY to the handling editor at the time of review.

Publisher's Note: All claims expressed in this article are solely those of the authors and do not necessarily represent those of their affiliated organizations, or those of the publisher, the editors and the reviewers. Any product that may be evaluated in this article, or claim that may be made by its manufacturer, is not guaranteed or endorsed by the publisher.

Copyright © 2022 Mei, Ding, Wang, Ni and Yu. This is an open-access article distributed under the terms of the Creative Commons Attribution License (CC BY). The use, distribution or reproduction in other forums is permitted, provided the original author(s) and the copyright owner(s) are credited and that the original publication in this journal is cited, in accordance with accepted academic practice. No use, distribution or reproduction is permitted which does not comply with these terms.

frontiers | Frontiers in Nutrition

MINI REVIEW
published: 07 April 2022
doi: 10.3389/fnut.2022.879111

Therapeutic Prospects of Polysaccharides for Ovarian Cancer

Kaili Wang†, Mengcheng Cai†, Shuai Sun, Wen Cheng, Dongxia Zhai, Zhexin Ni and Chaoqin Yu**

Department of Traditional Chinese Gynecology, The First Affiliated Hospital of Naval Medical University, Shanghai, China

OPEN ACCESS

Edited by:
Shuai Chen,
Wuhan University, China

Reviewed by:
Ting Zhu,
Qingdao University, China
Zhi-Hong Zhang,
Jiangsu University, China
Ping Zheng,
Peking Union Medical College Hospital, China
Ping Zhou,
Chinese Academy of Medical Sciences and Peking Union Medical College, China

***Correspondence:**
Zhexin Ni
nizxzg@163.com
Chaoqin Yu
chqyu81@163.com

†These authors have contributed equally to this work and share first authorship

Specialty section:
This article was submitted to Food Chemistry, a section of the journal Frontiers in Nutrition

Received: *18 February 2022*
Accepted: *11 March 2022*
Published: *07 April 2022*

Citation:
Wang K, Cai M, Sun S, Cheng W, Zhai D, Ni Z and Yu C (2022) Therapeutic Prospects of Polysaccharides for Ovarian Cancer. Front. Nutr. 9:879111. doi: 10.3389/fnut.2022.879111

Ovarian cancer (OC) is ranked as the leading cause of death among cancers of the female reproductive tract. First-line platinum treatment faces the severe challenges associated with the patient relapse and poor prognosis. Thus, it is imperative to develop natural antitumor drugs for OC with high efficacy. Natural polysaccharides have significant biological activities and antitumor effects. Our work has demonstrated that polysaccharides play key roles by inhibiting the cell proliferation and growth, regulating the tumor cell cycle, inducing apoptosis, suppressing the tumor cell migration and invasion, improving the immunomodulatory activities, and enhancing the efficacy of chemotherapy (cisplatin) in OC, which provide powerful evidence for the application of polysaccharides as novel anticancer agents, supplementary remedies, and adjunct therapeutic agents alone or in combination with cisplatin for preventing and treating the OC.

Keywords: polysaccharides, anticancer, ovarian cancer, combination treatment, platinum, drug resistance

INTRODUCTION

Ovarian cancer (OC) is the leading cause of death due to female gynecological cancers, is characterized by high lethality and a high death incidence ratio (1, 2), and its early detection is not readily achieved (3, 4). Among all malignant gynecological lesions, the fatality rate ranks first, posing a great threat to the health of patients. Currently, chemotherapy is one of the major treatments for OC, and platinum-related chemotherapy is the first-line treatment for OC (1, 2). However, most chemotherapeutic agents inhibit cancer cells but also exhibit undesirable side effects on normal tissues, resulting in a decline in patient immune function and causing serious effects on the human body, and the treatment is expensive (3, 4). To improve the efficacy of chemotherapy, it is imperative to identify and develop natural antitumour drugs with high efficacy and low toxicity (1, 5–7). In addition, cisplatin resistance and sensitivity are gradually becoming severe problems in OC treatment; these issues mainly account for the patient relapse and poor prognosis, and ∼65–80% of patients experience recurrence within the first 5 years (1, 6). Therefore, it is critical to develop novel agents and therapeutic strategies to enhance the clinical efficacy and inhibit drug resistance when treating OC.

Polysaccharides are natural polymers formed by covalently linking multiple monosaccharides through glycosidic bonds and have minor side-effects, which are one of the four basic substances that constitute life and are widely distributed in microorganisms, plants, and animals (8, 9).

Their structures and molecular size always in range from linear to highly branched (10, 11), which include storage polysaccharides and structural polysaccharides (8); and natural polysaccharides display both branched and linear polymer architectures, such as starch, glycogen, cellulose, and chitin (8, 10, 11). In clinic, polysaccharides from medicinal plants mainly include ginseng polysaccharide, astragalus polysaccharide, Ganoderma lucidum polysaccharide, lotus polysaccharide, lentinus edodes polysaccharide, and Ruminococcus mushroom polysaccharide, which have attracted a lot of attention due to their significant anti-tumour bioactivities (8, 12).

An increasing number of studies have suggested that polysaccharides have a wide range of biological activities and pharmacological effects *via* immunoregulation (13–15), anticancer activity (16, 17), and antioxidation (14, 17). Polysaccharides not only regulate the metabolism and immune function, but also have antitumour, antiviral, antioxidation, antiaging, and hypoglycaemic effects (8, 9, 12). Because of the significant antitumour activity, high efficacy, low toxicity, wide availability, and low price, polysaccharides have received increasing attention from researchers worldwide (18, 19). Although polysaccharides have been widely studied by researchers, it has not been clearly determined whether polysaccharides can be used to treat OC as candidate drugs or adjuvant agents combined with cisplatin chemotherapy, and no summarized reports or analyses have been conducted to assess the therapeutic prospects of polysaccharides as a treatment.

Therefore, based on the literature, we summarized and analyzed the pharmacological effects and mechanisms of polysaccharides in OC to provide a theoretical basis for subsequent preparation, development, clinical research, and applications. Moreover, we systematically explored and discussed the therapeutic effects and clinical prospects of polysaccharides in pretreating and treating OC, which has further provided powerful support and evidence.

EFFECTS OF POLYSACCHARIDES ON OC

Effects of Polysaccharides on Cell Proliferation and Apoptosis

Apoptosis is a form of programmed death that is highly regulated and plays an important role in cancer treatment, and it is a popular target of many treatment strategies (7, 20). The occurrence, development, and regression of OC are closely related to apoptosis, and inducing apoptosis in cancer cells is a research hot spot and a vital strategy for tumor treatment (2, 21). The previous studies (**Figure 1**) have shown that the natural polysaccharides exert anticancer effects on OC models by regulating the tumor cell cycle, inhibiting cell proliferation, and inducing the apoptosis *in vitro* and *in vivo* (22–28).

The BPP is a natural polysaccharide found in *Balanophora polyandra* that can inhibit the proliferation and growth of ovarian tumors formed by SKOV3 (human ovarian carcinoma cells) cells *in vitro* and in rats with OC. These results suggest that BPP regulates the S phase of cell cycle arrest by decreasing the expression levels of cyclin A and cyclin-dependent kinase 2 (CDK2). The BPP triggers the apoptosis in OC cells in a concentration-dependent manner, and this induction of apoptosis involves the downregulation of B-cell lymphoma-2 (BCL-2) in A2780 and OVSAHO cells (22). In addition, the noted antitumour effects of BPP are related to the tumor suppressor gene-53 (also known as P53) pathway (22).

The APS is a natural antioxidant polysaccharide obtained from *Astragalus membranaceus* that exerts antiproliferative and proapoptotic effects on OC. APS inhibits not only proliferation, but also invasion and migration in OC cells. APS treatment induces apoptosis in OC cells by downregulating the expression of miR-27a, which was confirmed by RNA sequencing and overexpression/knockdown cells. F-box and WD-40 domain repeat-containing protein 7 (FBXW7) is a direct target of miR-27a and can reverse the antitumor effect of APS, indicating that APS induces apoptosis in OVCAR-3 cells *via* the FBXW7/miR-27 pathway (24).

Polygala tenuifolia polysaccharide (PTP) is a natural polysaccharide isolated from the roots of *Polygala tenuifolia* that plays a key role in inhibiting OC. On the one hand, PTP significantly suppresses the growth of SKOV3 cells *in vitro* and in OC model rats, inhibits the proliferation of SKOV3 cells in a concentration-dependent manner (23, 29), decreases tumor growth in nude mice, rapidly exhausts glutathione (GSH) level (23), and promotes the production of intracellular reactive oxygen species (ROS) (23, 30). On the other hand, PTP inhibits the proliferation of OVCAR-3 cells, induces cell death by arresting the cell cycle at the G0/G1 phase, and suppresses the growth in OC cells (27, 28). These effects on human OC may be associated with the increased expression of mitochondrial proteins (BCL2-associated X [BAX] protein, caspase-3/9, and cytochrome c), nuclear factor kappa B (NF-κB), and the programmed cell death pathway (27, 28).

Furthermore, MDP-A1 and MDP-A2 are acidic polysaccharides, isolated from the rhizome of *Menispermum dauricum* (MW 9.1×10^4 – 5.8×10^4 Da), significantly inhibit the proliferation of human SKOV3 cells in a concentration-dependent manner, increase the number of apoptotic cells, and reduce the expression of caspase-3 and caspase-8; these effects were further observed in mice (25). In addition, PPC has negligible cytotoxicity on fibroblasts, is a type of polysaccharide–protein complex, and can induce the death in tumor cells through apoptosis and necrosis (26), which may be addressed with chemical modifications.

Overall, these findings suggest that various polysaccharides from natural plants can inhibit cell growth and proliferation and induce apoptosis in OC cells *via* the mitochondrial apoptosis pathway, the FBXW7/miR-27 pathway, the NF-κB and programmed cell death pathways, and oxidative stress regulation and the P53 pathway and they may be beneficial as potential therapeutic agents for the treatment of OC.

Effects of Polysaccharides on Cell Migration and Invasion

Cancer cell migration and invasion in tissue and the vasculature are the initial and dynamic steps that play an important

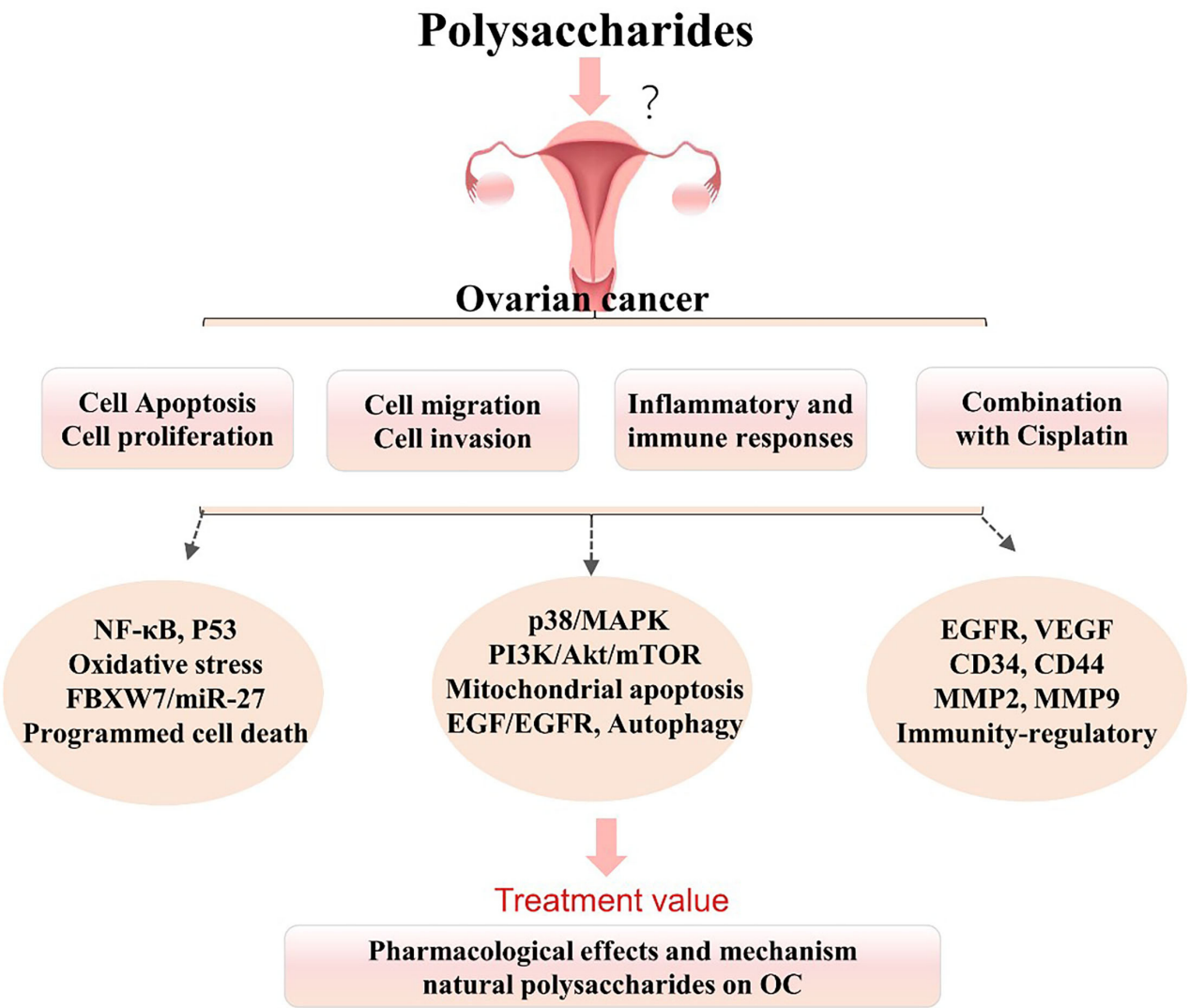

FIGURE 1 | Summarized effects and mechanisms underlying natural polysaccharides in the treatment of ovarian cancer (OC). Polysaccharides play vital roles in the treatment of OC *via* multiple pathways and molecules, but it remains uncertain whether polysaccharides can be used in the clinical treatment of OC. It is uncertain or not completely verified. BAX, BCL2-associated X protein; EGFR, epidermal growth factor receptor; FBXW7, F-box, and WD-40 domain protein 7; MMP-2/9, matrix metalloproteinase 2/9; MAPK, mitogen-activated protein kinase; NF-κB, nuclear factor kappa B; OC, ovarian cancer; PI3K, phosphatidylinositol 3-kinase; P53, tumor suppressor gene-53; VEGF, vascular endothelial growth factor.

role in the tumor progression and cancer metastasis (31, 32). Thus, it is crucial to develop novel treatment strategies to inhibit tumor cell migration and invasion, and get prevention from this life-threatening phenomenon (31, 32). In addition to suppressing tumor cell growth and proliferation (22, 24), natural polysaccharides inhibit OC tumor cell migration and invasion (33–35).

The *Bangia fuscopurpurea* (BFP) polysaccharide is a novel polysaccharide extracted from *Bangia fuscopurpurea* that has been confirmed to increase the accumulation of ROS, reduce mitochondrial membrane potential, and thus induce apoptosis in A2780 OC cells. Moreover, BFP polysaccharide inhibits the migration and invasion of OC cells. Further results show that BFP polysaccharide induces cell death by activating the autophagy (Beclin1-LC3-P62) pathway and promotes the mitochondrial apoptosis pathway by downregulating BCL2 expression, upregulating BAX protein expression, and increasing cytochrome C release in A2780 cells (34). These findings demonstrate that BFP polysaccharide may be useful for developing functional foods for adjuvant anticancer treatment.

The SIP-SII is a sulfated derivative polysaccharide from *Sepiella maindroni* that significantly inhibits the tumor growth and metastasis (35). First, the migration and invasion of SKOV-3 cells are notably inhibited by SIP-SII. Second, SIP-SII is transported and located on the cell membrane, downregulates the expression of epidermal growth factor receptor (EGFR) and

matrix metalloproteinase 2 (MMP-2), attenuates EGF-induced EGFR phosphorylation, and suppressed OC cell migration. Additionally, SIP-SII significantly inhibited the p38/mitogen-activated protein kinase (MAPK) and phosphatidylinositol 3-kinase (PI3K)/Akt/mTOR signaling pathways in SKOV-3 cells. These findings demonstrate that SIP-SII has potential inhibitory effects on tumor metastasis in OC, which are associated with regulating the p38/MAPK and PI3K/Akt/mTOR signaling pathways (35).

The CPPA is an acidic polysaccharide isolated from *Codonopsis pilosula* that inhibits the proliferation of HO-8910 cells (human epithelial OC cells) *in vitro*. CPPA treatment significantly inhibits invasion, migration, and adhesion in tumor cells by down regulating the CD44 expression (33), indicating that CPPA may be a potential candidate for the prevention of tumor metastasis. In addition, APS and BPP inhibit migration and invasion in OC cells *via* the FBXW7/miR-27a and P53-mediated pathways (22, 24).

In summary, these results (**Figure 1**) further suggest that polysaccharides not only play vital roles in the induction of OC cells, but also show marked regulatory effects on tumor metastasis (cell migration and invasion) in OC. These polysaccharides have great potential as novel agents against tumor metastasis *via* the p38/MAPK and PI3K/Akt/mTOR signaling pathways, the mitochondrial apoptosis pathway, the EGF-EGFR and MMP2 pathways, and the FBXW7/miR-27a and P53 pathways.

Effects of Polysaccharides on Inflammatory and Immune Responses

Inflammatory and immune responses play vital roles at different stages of tumor development, such as initiation, invasion, proliferation, malignant conversion, and metastasis (36, 37). Therefore, it is of great importance to develop new agents with immunomodulatory activities to improve the efficacy of chemotherapy (cisplatin). Recent studies indicate that various polysaccharides have antioxidant and immunoregulatory effects on OC (29, 33, 38–40).

The PSP is a polysaccharide extracted from fresh purslane that significantly inhibits superoxide anion, 2,2-Diphenyl-1-picrylhydrazyl (DPPH) free radical, hydroxyl radicals, and nitric oxide (NO) in a dose-dependent manner. The PSP effectively increased splenocyte, thymocyte, and T and B lymphocyte proliferation and also improved the function of red blood cells. These findings support the use of polysaccharides to treat OC, and these effects are mediated by scavenging accumulating free radicals and enhancing immunity (29).

Polygala tenuifolia polysaccharide is known to inhibit the growth and proliferation of OC cells (23, 29, 30), which are at least partially related to inflammation and the immune response. First, PTP increases serum vascular endothelial growth factor (VEGF) and EGFR levels and downregulates the transcript and protein levels of EGFR, VEGF, and CD34 *in vivo* (29). Moreover, PTP regulates the NF-κB pathway in SKOV3 cells (27, 28). *In vivo* and *in vitro* evidence suggests that PTP is a powerful adjuvant therapy for patients with OC at an advanced stage.

BPS is a polysaccharide isolated from basil that can inhibit the invasion of SKOV3 cells. In contrast, coadministration of BSP and curcumin significantly suppressed the invasion of SKOV3 cells and immature and mature human monocyte-derived dendritic cells (DCs) and reduced the mRNA and protein expression of CD44 and MMP-9 in SKOV3 cells, indicating that curcumin and BPS regulated the invasion of SKOV3 cells and DCs by distinctly downregulating osteopontin (OPN), CD44, and MMP-9 expression. Moreover, CAPP also inhibited the invasion, migration, and adhesion of tumor cells by regulating CD44 (33, 40). *Ganoderma lucidum* and polysaccharides enhance immune functions and inhibit cancer cell growth (41).

Therefore, curcumin and these polysaccharides (CAPP, PSP, and BPS) may be suitable candidates for OC immunotherapy (**Figure 1**). These results suggest that these polysaccharides can be used as adjunct supplementary agents in chemotherapy and immunotherapy to threaten OC *via* immunoregulation. However, the underlying mechanisms and pathways of polysaccharide-related immunotherapy remain unclear.

EFFECTS OF COMBINATION TREATMENT WITH POLYSACCHARIDES AND CISPLATIN ON OC

Ovarian cancer is characterized by high lethality and an impressive death-to-incidence ratio. Currently, platinum-based therapies are the first-line treatment of OC (1, 6), but platinum sensitivity and drug resistance are huge challenges in the clinical treatment of OC, causing the majority of patients to relapse and have a poor prognosis. Thus, it is of great importance to develop new adjunct agents and supplemental therapies for OC by enhancing therapeutic effects and inhibiting drug resistance in combination with platinum. Recent studies (**Figures 1**, **2**) have shown that polysaccharides can increase sensitivity and ameliorate resistance to cisplatin treatment of OC and thus have great potential to enhance chemosensitivity (39–43).

The APS is a natural polysaccharide that not only exerts antiproliferative and proapoptotic effects on various cancers (24), but also enhances the sensitivity of cancer cells to chemotherapeutic drugs (42). Treatment with APS and cisplatin synergistically enhanced the inhibitory effects of cisplatin on cell viability and promoted cisplatin-induced apoptosis. The enhanced effects mainly stemmed from the regulation of BCL2, BAX, and caspase 3 expressions *via* the c-Jun amino terminal kinase (JNK1/2) signaling pathway, which was further confirmed by related inhibitors (42).

The DDAP is a novel polymeric platinum compound that conjugates the platinum analog to aspartate chondroitin, which is regarded as a combined complex of polysaccharides and platinum. On the one hand, DDAP improves platinum solubility, enhances drug delivery, and increases cellular uptake of DDAP in platinum-resistant OC cells, which reduces systemic toxicity and produces more efficacious outcomes. On the other hand, DDAP significantly inhibits cell growth, especially at lower doses, induces apoptosis, and arrests cells in the S-phase (43). The related mechanisms may be associated with the caspase

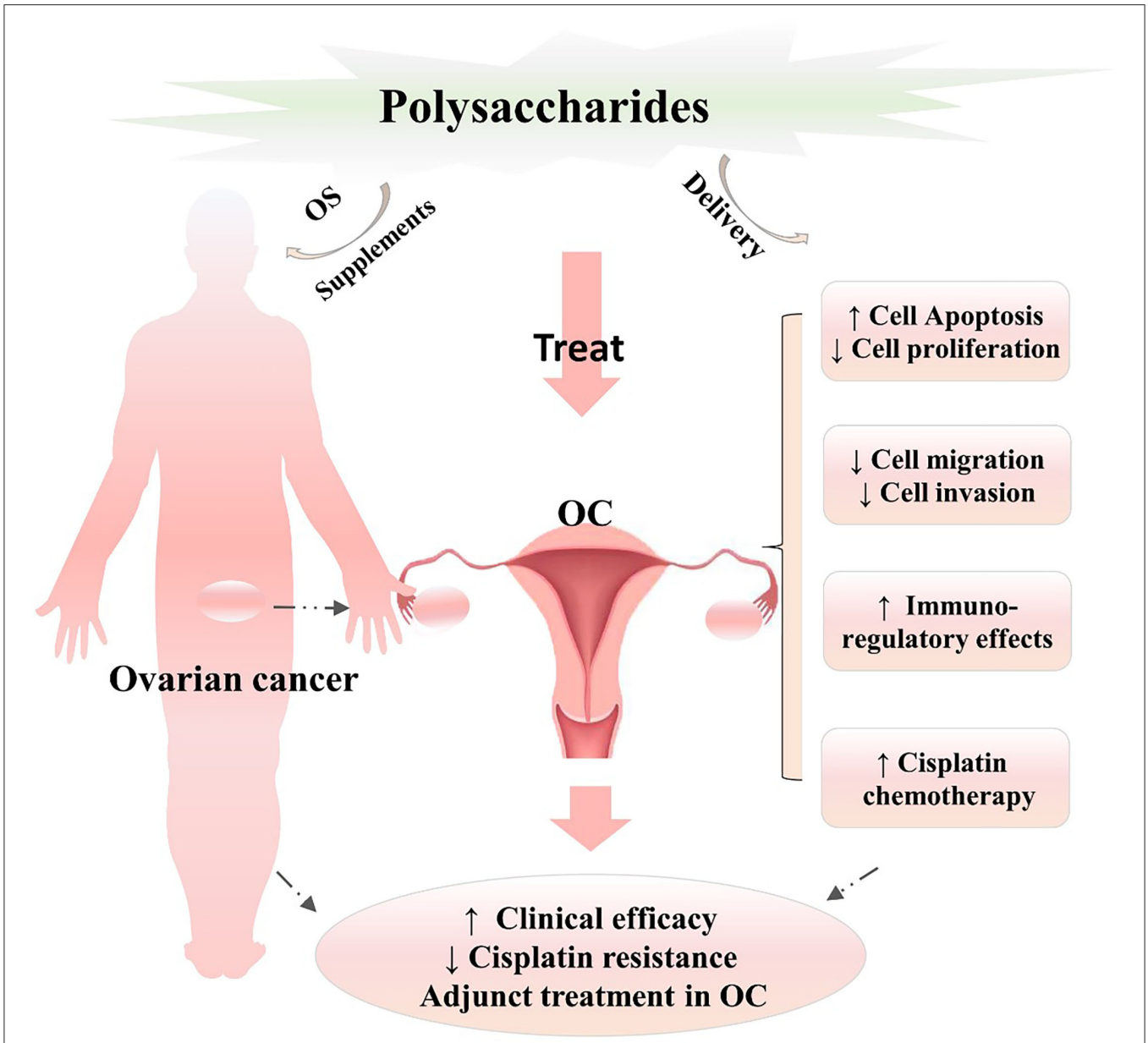

FIGURE 2 | Analysis of the therapeutic prospects of natural polysaccharides in the treatment of OC. Polysaccharides play vital roles in inhibiting cell proliferation and growth, regulating the tumor cell cycle, inducing cell apoptosis, suppressing tumor cell migration and invasion, improving immunomodulatory activities, and enhancing the efficacy of chemotherapy in OC and can be developed as adjunct agents or supplementary treatments in combination with cisplatin, which needs to further develop in the process of polysaccharide healthcare products in future work. OC, ovarian cancer; ↑, significantly enhance or improve; ↓ significantly downregulate or inhibit.

3 pathway, the upregulation of p21, and the maintenance of cyclin A (43).

The PS_K is protein-bound polysaccharides collected by Coriolus versicolour QUEL that has similar activities as superoxide dismutase (SOD) (39); the coadministration of PS_K and cisplatin can prevent cisplatin-associated cytotoxicity in NRK-49F cells. Cisplatin increases lipid peroxides, decreases SOD activity at the IC_{50}, and markedly inhibits proliferation in each cell line. When administered with PS_K, these effects were augmented in H4-II-E and OC cells but diminished in the NRK-49F cell line, indicating that cisplatin combined with PS-K has more significant anticancer effects on OC patients than monotherapy (39).

In addition, *Ganoderma lucidum* enhances immune functions and exerts its antitumour effects on various cancers (41). Polysaccharides and triterpenes are biologically active constituents of *Ganoderma lucidum*; thus, polysaccharides of *Ganoderma lucidum* have great potential in suppressing

cell growth, inducing apoptosis in OVCAR-3 cells, inhibiting the disruption of cell cycle progression by downregulating cyclin D1, and regulating antioxidative/detoxification activity *via* the nuclear factor E2-related factor 2 (Nrf2)-mediated signaling pathway, such as the antioxidant NAD(P)H, SOD, catalase, quinone oxidoreductase 1 (NQO1), and glutathione S-transferase P1 (41). These chemopreventive effects provide powerful support for the use of *Ganoderma lucidum*, and these polysaccharides can be developed as adjunct supplementary agents in combination with cisplatin chemotherapy and have great clinical prospects in OC treatment.

CONCLUSIONS AND PROSPECTS

Ovarian cancer is ranked first among female gynecological cancers (1). Because patients relapse and develop resistance to first-line cisplatin chemotherapy (6, 44, 45), enhancing the clinical efficacy (sensitivity), and ameliorating cisplatin drug resistance are increasingly major problems. Fortunately, natural active polysaccharides provide an alternative OC treatment as adjunct therapeutic agents or in combination with cisplatin. In the present work (**Figure 2**), we systematically explored and analyzed the therapeutic effects and clinical prospects of polysaccharide pretreatment and treatment as OC therapies, further providing powerful support and evidence for this viewpoint. In addition, hyaluronan, a high-MW polysaccharide, can be used for magnetic resonance imaging (MRI) visualization of hyaluronidase in OC (46); glycosaminoglycan motifs may form a new class of biomarkers for OC, as indicated here for the GD3G7 epitope in OC tissue (47).

Taken together, the currently available data and results (**Figure 2**) suggest that natural polysaccharides have significant biological activities and pharmacological effects and play vital roles in inhibiting the cell proliferation and growth, regulating the tumor cell cycle, inducing cell apoptosis, suppressing tumor cell migration and invasion, improving immunomodulatory activities, and enhancing the efficacy of chemotherapy (cisplatin) in OC. However, because of the lack of clinical testing and clinical data to further support the clinical therapeutic efficacy and safety of natural polysaccharides in OC, further clinical trials and evidence are essential. At present, functional drug delivery systems combining polysaccharides and cisplatin are rare in the clinic, and active polysaccharide-enriched supplements are limited in the market. Some polysaccharide complexes with biological functions, which have health and medical value and broad prospects, need to be further developed.

AUTHOR CONTRIBUTIONS

KW and MC designed the review. KW, MC, and SS wrote the manuscript. WC, DZ, and KW helped in creating the figures and revising the manuscript. ZN and CY were mainly responsible for supervising the work and managing related projects. All authors discussed, edited, approved the final version, and agreed to be accountable for the content of this work.

FUNDING

This work was funded by the National Natural Science Foundation of China (82074206 and 81973896), the Shanghai 3-Year Action Plan for Traditional Chinese Medicine [ZY(2018-2020)-FWTX-1107], the Leading Project of Traditional Chinese Medicine of Shanghai Science and Technology Committee (19401930200), and the China Postdoctoral Science Foundation (2020M681337).

REFERENCES

1. Matulonis UA, Sood AK, Fallowfield L, Howitt BE, Sehouli J, Karlan BY. Ovarian cancer. *Nat Rev Dis Primers.* (2016) 2:16061. doi: 10.1038/nrdp.2016.61
2. Natanzon Y, Goode EL, Cunningham JM. Epigenetics in ovarian cancer. *Semin Cancer Biol.* (2018) 51:160–9. doi: 10.1016/j.semcancer.2017.08.003
3. Siegel RL, Miller KD, Jemal A. Cancer statistics 2019. *CA Cancer J Clin*. (2019) 69:7–34. doi: 10.3322/caac.21551
4. Zhang M, Cheng S, Jin Y, Zhao Y, Wang Y. Roles of CA125 in diagnosis, prediction, and oncogenesis of ovarian cancer. *Biochim Biophys Acta Rev Cancer.* (2021) 1875:188503. doi: 10.1016/j.bbcan.2021.188503
5. Al-Jorani K, Rüther A, Haputhanthri R, Deacon GB, Li HL, Cullinane C, et al. ATR-FTIR spectroscopy shows changes in ovarian cancer cells after incubation with novel organoamidoplatinum(ii) complexes. *Analyst.* (2018) 143:6087–94. doi: 10.1039/C8AN01558A
6. Bogani G, Lopez S, Mantiero M, Ducceschi M, Bosio S, Ruisi S, et al. Immunotherapy for platinum-resistant ovarian cancer. *Gynecol Oncol.* (2020) 158:484–8. doi: 10.1016/j.ygyno.2020.05.681
7. Wong RS. Apoptosis in cancer: from pathogenesis to treatment. *J Exp Clin Cancer Res.* (2011) 30:87. doi: 10.1186/1756-9966-30-87
8. Xie JH, Jin ML, Morris GA, Zha XQ, Chen HQ, Yi Y, et al. Advances on bioactive polysaccharides from medicinal plants. *Crit Rev Food Sci Nutr.* (2016) 56(Suppl. 1):S60–84. doi: 10.1080/10408398.2015.1069255
9. Zheng B, Zhou X, Hu X, Chen Y, Xie J, Yu Q. Advances in the regulation of natural polysaccharides on human health: the role of apoptosis/autophagy pathway. *Crit Rev Food Sci Nutr*. (2021). doi: 10.1080/10408398.2021.1995844. [Epub ahead of print].
10. Caputo HE, Straub JE, Grinstaff MW. Design, synthesis, and biomedical applications of synthetic sulphated polysaccharides. *Chem Soc Rev.* (2019) 48:2338–65. doi: 10.1039/C7CS00593H
11. Yuan D, Li C, Huang Q, Fu X, Dong H. Current advances in the anti-inflammatory effects and mechanisms of natural polysaccharides. *Crit Rev Food Sci Nutr*. (2022). doi: 10.1080/10408398.2022.2025535. [Epub ahead of print].
12. Guo T, Akan OD, Luo F, Lin Q. Dietary polysaccharides exert biological functions via epigenetic regulations: advance and prospectives. *Crit Rev Food Sci Nutr*. (2021). doi: 10.1080/10408398.2021.1944974. [Epub ahead of print].
13. Sun XB, Matsumoto T, Yamada H. Purification of immune complexes clearance enhancing polysaccharide from the leaves of panax ginseng, and its biological activities. *Phytomedicine.* (1994) 1:225–31. doi: 10.1016/S0944-7113(11)80069-3
14. Sun Y. Structure and biological activities of the polysaccharides from the leaves, roots and fruits of Panax ginseng C.A. Meyer: an overview. *Carbohydrate Polymers.* (2011) 85:490–9. doi: 10.1016/j.carbpol.2011.03.033
15. Vinay DS, Ryan EP, Pawelec G, Talib WH, Stagg J, Elkord E, et al. Immune evasion in cancer: mechanistic basis and therapeutic strategies. *Semin Cancer Biol.* (2015) 35:S185–98. doi: 10.1016/j.semcancer.2015.03.004

16. Ooi VE, Liu F. Immunomodulation and anti-cancer activity of polysaccharide-protein complexes. *Curr Med Chem.* (2000) 7:715–29. doi: 10.2174/0929867003374705
17. Yu Y, Shen M, Song Q, Xie J. Biological activities and pharmaceutical applications of polysaccharide from natural resources: a review. *Carbohydr Polym.* (2018) 183:91–101. doi: 10.1016/j.carbpol.2017.12.009
18. Prateeksha, Sharma VK, Liu X, Oyarzún DA, Abdel-Azeem AM, Atanasov AG, et al. Microbial polysaccharides: an emerging family of natural biomaterials for cancer therapy and diagnostics. *Semin Cancer Biol.* (2021). doi: 10.1016/j.semcancer.2021.05.021. [Epub ahead of print].
19. Wang XY, Zhang DD, Yin JY, Nie SP, Xie MY. Recent developments in *Hericium erinaceus* polysaccharides: extraction, purification, structural characteristics and biological activities. *Crit Rev Food Sci Nutr.* (2019) 59:S96–115. doi: 10.1080/10408398.2018.1521370
20. Lopez J, Tait SW. Mitochondrial apoptosis: killing cancer using the enemy within. *Br J Cancer.* (2015) 112:957–62. doi: 10.1038/bjc.2015.85
21. Emmings E, Mullany S, Chang Z, Landen CN Jr., Linder S, Bazzaro M. Targeting mitochondria for treatment of chemoresistant ovarian cancer. *Int J Mol Sci.* (2019) 20:229. doi: 10.3390/ijms20010229
22. Qu J, He Y, Shi Y, Gai L, Xiao L, Peng F, et al. Polysaccharides derived from *Balanophora polyandra* significantly suppressed the proliferation of ovarian cancer cells through P53-mediated pathway. *J Cell Mol Med.* (2020) 24:8115–25. doi: 10.1111/jcmm.15468
23. Xin T, Zhang F, Jiang Q, Chen C, Huang D, Li Y, et al. Extraction, purification and antitumor activity of a water-soluble polysaccharide from the roots of *Polygala tenuifolia*. *Carbohydr Polym.* (2012) 90:1127–31. doi: 10.1016/j.carbpol.2012.06.058
24. Guo Y, Zhang Z, Wang Z, Liu G, Liu Y, Wang H. Astragalus polysaccharides inhibit ovarian cancer cell growth via microRNA-27a/FBXW7 signaling pathway. *Biosci Rep.* (2020) 40:BSR20193396. doi: 10.1042/BSR20193396
25. Lin M, Xia B, Yang M, Gao S, Huo Y, Lou G. Anti-ovarian cancer potential of two acidic polysaccharides from the rhizoma of *Menispermum dauricum*. *Carbohydr Polym.* (2013) 92:2212–7. doi: 10.1016/j.carbpol.2012.12.013
26. Fiołka MJ, Lewtak K, Rzymowska J, Grzywnowicz K, Hułas-Stasiak M, Sofińska-Chmiel W, et al. Antifungal and anticancer effects of a polysaccharide-protein complex from the gut bacterium Raoultella ornithinolytica isolated from the earthworm *Dendrobaena veneta*. *Pathog Dis.* (2013) 69:46–61. doi: 10.1111/2049-632X.12056
27. Zhang F, Song X, Li L, Wang J, Lin L, Li C, et al. Polygala tenuifolia polysaccharide PTP induced apoptosis in ovarian cancer cells via a mitochondrial pathway. *Tumour Biol.* (2015) 36:2913–9. doi: 10.1007/s13277-014-2921-x
28. Zhang F, Song X, Li L, Wang J, Lin L, Li C, et al. Polygala tenuifolia polysaccharide (PTP) inhibits cell proliferation by repressing Bmi-1 expression and downregulating telomerase activity. *Tumour Biol.* (2015) 36:2907–12. doi: 10.1007/s13277-014-2920-y
29. Yao H, Cui P, Xu D, Liu Y, Tian Q, Zhang F. A water-soluble polysaccharide from the roots of *Polygala tenuifolia* suppresses ovarian tumor growth and angiogenesis *in vivo*. *Int J Biol Macromol.* (2018) 107(Pt. A):713–8. doi: 10.1016/j.ijbiomac.2017.09.043
30. Yan YY, Yuan S, Ma HH, Zhang XF. Structural modification and biological activities of carboxymethyl Pachymaran. *Food Sci Nutr.* (2021) 9:4335–48. doi: 10.1002/fsn3.2404
31. Duff D, Long A. Roles for RACK1 in cancer cell migration and invasion. *Cell Signal.* (2017) 35:250–255. doi: 10.1016/j.cellsig.2017.03.005
32. Zhang Y, Zou X, Qian W, Weng X, Zhang L, Zhang L, et al. Enhanced PAPSS2/VCAN sulfation axis is essential for Snail-mediated breast cancer cell migration and metastasis. *Cell Death Differ.* (2019) 26:565–79. doi: 10.1038/s41418-018-0147-y
33. Xin T, Zhang F, Jiang Q, Chen C, Huang D, Li Y, et al. The inhibitory effect of a polysaccharide from Codonopsis pilosula on tumor growth and metastasis *in vitro*. *Int J Biol Macromol.* (2012) 51:788–93. doi: 10.1016/j.ijbiomac.2012.07.019
34. Wu J, Lin C, Chen X, Pan N, Liu Z. Polysaccharides isolated from Bangia fuscopurpurea induce apoptosis and autophagy in human ovarian cancer A2780 cells. *Food Sci Nutr.* (2021) 9:6707–19. doi: 10.1002/fsn3.2621
35. Jiang W, Cheng Y, Zhao N, Li L, Shi Y, Zong A, et al. Sulfated polysaccharide of Sepiella Maindroni ink inhibits the migration, invasion and matrix metalloproteinase-2 expression through suppressing EGFR-mediated p38/MAPK and PI3K/Akt/mTOR signaling pathways in SKOV-3 cells. *Int J Biol Macromol.* (2018) 107(Pt. A):349–62. doi: 10.1016/j.ijbiomac.2017.08.178
36. Grivennikov SI, Greten FR, Karin M. Immunity, inflammation, and cancer. *Cell.* (2010) 140:883–99. doi: 10.1016/j.cell.2010.01.025
37. Taniguchi, K. and Karin M, NF-κB, inflammation, immunity and cancer: coming of age. *Nat Rev Immunol.* (2018) 18:309–24. doi: 10.1038/nri.2017.142
38. YouGuo C, ZongJi S, XiaoPing C. Evaluation of free radicals scavenging and immunity-modulatory activities of Purslane polysaccharides. *Int J Biol Macromol.* (2009) 45:448–52. doi: 10.1016/j.ijbiomac.2009.07.009
39. Kobayashi Y, Kariya K, Saigenji K, Nakamura K. Enhancement of anti-cancer activity of cisdiaminedichloroplatinum by the protein-bound polysaccharide of Coriolus versicolor QUEL (PS-K) *in vitro*. *Cancer Biother.* (1994) 9:351–8. doi: 10.1089/cbr.1994.9.351
40. Lv J, Shao Q, Wang H, Shi H, Wang T, Gao W, et al. Effects and mechanisms of curcumin and basil polysaccharide on the invasion of SKOV3 cells and dendritic cells. *Mol Med Rep.* (2013) 8:1580–6. doi: 10.3892/mmr.2013.1695
41. Hsieh TC, Wu JM. Suppression of proliferation and oxidative stress by extracts of *Ganoderma lucidum* in the ovarian cancer cell line OVCAR-3. *Int J Mol Med.* (2011) 28:1065–9. doi: 10.3892/ijmm.2011.788
42. Li C, Hong L, Liu C, Min J, Hu M, Guo W. Astragalus polysaccharides increase the sensitivity of SKOV3 cells to cisplatin. *Arch Gynecol Obstet.* (2018) 297:381–86. doi: 10.1007/s00404-017-4580-9
43. Zheng H, Hu W, Yu D, Shen DY, Fu S, Kavanagh JJ, et al. Diammine dicarboxylic acid platinum enhances cytotoxicity in platinum-resistant ovarian cancer cells through induction of apoptosis and S-phase cell arrest. *Pharm Res.* (2008) 25:2272–82. doi: 10.1007/s11095-008-9621-4
44. Bowtell DD, Böhm S, Ahmed AA, Aspuria PJ, Bast RC Jr., Ramos P, et al. Rethinking ovarian cancer II: reducing mortality from high-grade serous ovarian cancer. *Nat Rev Cancer.* (2015) 15:668–79. doi: 10.1038/nrc4019
45. Morand S, Devanaboyina M, Staats H, Stanbery L, Nemunaitis J. Ovarian cancer immunotherapy and personalized medicine. *Int J Mol Sci.* (2021) 22:6532. doi: 10.3390/ijms22126532
46. Shiftan L, Israely T, Cohen M, Frydman V, Dafni H, Stern R, et al. Magnetic resonance imaging visualization of hyaluronidase in ovarian carcinoma. *Cancer Res.* (2005) 65:10316–23. doi: 10.1158/0008-5472.CAN-04-3947
47. Vallen MJ, Massuger LF, ten Dam GB, Bulten J, van Kuppevelt TH. Highly sulfated chondroitin sulfates, a novel class of prognostic biomarkers in ovarian cancer tissue. *Gynecol Oncol.* (2012) 127:202–9. doi: 10.1016/j.ygyno.2012.06.022

Conflict of Interest: The authors declare that the research was conducted in the absence of any commercial or financial relationships that could be construed as a potential conflict of interest.

Publisher's Note: All claims expressed in this article are solely those of the authors and do not necessarily represent those of their affiliated organizations, or those of the publisher, the editors and the reviewers. Any product that may be evaluated in this article, or claim that may be made by its manufacturer, is not guaranteed or endorsed by the publisher.

Copyright © 2022 Wang, Cai, Sun, Cheng, Zhai, Ni and Yu. This is an open-access article distributed under the terms of the Creative Commons Attribution License (CC BY). The use, distribution or reproduction in other forums is permitted, provided the original author(s) and the copyright owner(s) are credited and that the original publication in this journal is cited, in accordance with accepted academic practice. No use, distribution or reproduction is permitted which does not comply with these terms.

frontiers | Frontiers in Nutrition

ORIGINAL RESEARCH
published: 11 April 2022
doi: 10.3389/fnut.2022.878725

Influence of Carboxymethyl Cellulose on the Stability, Rheological Property, and *in-vitro* Digestion of Soy Protein Isolate (SPI)-Stabilized Rice Bran Oil Emulsion

Wenguan Zhang, Jia Hao, Yanan Yuan and Duoxia Xu*

Beijing Key Laboratory of Flavor Chemistry, Beijing Laboratory for Food Quality and Safety, Beijing Advanced Innovation Center for Food Nutrition and Human Health (BTBU), Beijing Engineering and Technology Research Center of Food Additives, School of Food and Health, Beijing Higher Institution Engineering Research Center of Food Additives and Ingredients, Beijing Technology and Business University, Beijing, China

In this study, carboxymethyl cellulose (CMC) was added to soybean protein isolate (SPI)-stabilized rice bran oil (RBO) emulsion to improve its physicochemical stability and free fatty acid (FFA) release characteristics. RBO emulsions stabilized by SPI and various contents of CMC were prepared and assessed by measuring zeta potential, particle size, transmission, and microstructure, the rheological properties were analyzed by dynamic shear rheometer. In addition, its chemical stability was characterized by a storage experiment, and the FFA release was explored by a simulated gastrointestinal tract (GIT) model. It showed that the negative charge of the droplets of RBO emulsion was increased with increasing CMC content. The decrease in transmission of SPI-stabilized RBO emulsion with increasing CMC content was due to the droplets not being free to move by the special network interaction and an increase in the viscosity. According to the determination of the reactive substances of lipid hydroperoxide and thiobarbituric acid during 30 days storage at 37°C, the chemical stability of the emulsion added with CMC was enhanced compared with the SPI-stabilized RBO emulsion. *In-vitro* digestion studies not only evaluated the structural changes of RBO emulsions at different stages, but also found that RBO emulsion with CMC showed a higher level of free fatty acids release in comparison with that without CMC. It indicated that the utilization of CMC can improve the bioavailability of RBO emulsions.

Keywords: rice bran oil (RBO), emulsion, carboxymethyl cellulose (CMC), physicochemical stability, rheological properties, *in vitro* digestion

OPEN ACCESS

Edited by:
Fuguo Liu,
Northwest A&F University, China

Reviewed by:
Jianhua Yi,
Shaanxi University of Science and Technology, China
Lei Dai,
Qingdao Agricultural University, China

****Correspondence:***
Duoxia Xu
xdxbtbu@126.com

Specialty section:
This article was submitted to Food Chemistry, a section of the journal Frontiers in Nutrition

Received: *18 February 2022*
Accepted: *10 March 2022*
Published: *11 April 2022*

Citation:
Zhang W, Hao J, Yuan Y and Xu D (2022) Influence of Carboxymethyl Cellulose on the Stability, Rheological Property, and in-vitro Digestion of Soy Protein Isolate (SPI)-Stabilized Rice Bran Oil Emulsion. Front. Nutr. 9:878725. doi: 10.3389/fnut.2022.878725

INTRODUCTION

In the recent years, rice bran oil (RBO) is now widely used in food processing. It suggests that RBO can promote human health, reduce human serum cholesterol, regulate human brain function, and may have certain preventive and therapeutic effects on vascular headaches and autonomic nervous dysfunction (1, 2). RBO with high content of unsaturated fatty acids in which the ratio of linoleic acid to oleic acid is close to 1:1 (3). It also contains a range of natural antioxidants,

namely, vitamin E, oryzanol, squalene, active lipase, sitosterol, and other functional components (4–6). Compared with other vegetable oils, RBO has a relatively long shelf life due to high levels of natural antioxidants (7).

Therefore, there is interest in developing an RBO delivery system to benefit from its ideal nutritional and functional characteristics. RBO is highly lipid-soluble and can be incorporated into foods in the form of oil-in-water emulsions as an oil phase. However, the studies on RBO were mainly focused on refining, detection of active substances, and improvement of production process and storage methods, while the research on its delivery system and *in-vitro* digestion characteristics was limited. Studies have shown that the addition of surfactants (Twain 80 and Span80 mixture) can improve the oxidation stability of oil in RBO oil phase emulsion (8). The effect of natural emulsifier type on the stability of RBO emulsions found that the emulsion formed by a polysaccharide (modified starch and Arabia gum) has better thermal stability, salt stability, and pH stability than that of whey protein isolate emulsion. This may be due to the difference in colloidal interaction between oil droplets (9). Moreover, it was also reported that RBO-in-water pickering emulsions prepared by cellulose nanocrystals as stabilizers, gum Arabia and nonionic surfactant as emulsifiers showed gel-like behavior and high oxidative stability (10).

Soybean protein isolate (SPI), as the most important nutritional ingredient in soybean, is a high-quality vegetable protein of edible origin and contains eight essential amino acids required by the human body (11). It also has many important functional properties such as emulsifying, solubility, and gelation (12–14). These properties can significantly reduce the interfacial tension of oil-water or air-water further improve food functional properties, such as improving taste and storage property, increasing elasticity, water retention, and oil absorption. When it is used as an emulsifier in emulsion, it is reported that the protein only forms a thin interface layer around the lipid droplet. Therefore, the main stabilization mechanism is electrostatic exclusion. However, when repulsive electrostatic interaction decreases or attractive hydrophobic interaction increases, it tends to unstable aggregation. It is said that the stability mechanism of the protein-polysaccharide system is a steric hindrance and electrostatic repulsion. After adding polysaccharides, a thick interface layer can be formed around the droplet (15). Therefore, protein-polysaccharide encapsulated lipid droplets are more stable to changes in environmental conditions than protein encapsulated lipid droplets (16).

Carboxymethyl cellulose (CMC) is an anionic linear polymer. The Food and Agriculture Organization (FAO) and the WHO have approved the use of pure CMC in food as a good emulsion stabilizer and thickener, which can maintain the stability of food quality, prevent oil-water stratification, and prolong storage time. Previous studies had applied it to the production of ice cream and found that CMC could increase the emulsifying ability of protein and reduce fat agglomeration, which played a certain role in the homogenization of ice cream liquid (17, 18). Recently, CMC was reported as an oral delivery system. In contrast to all other polysaccharides, CMC has a hydrophilic character because of its carboxylate groups. These carboxylate groups are responsible for *in-situ* gelations, bioadhesion, sensitivity to environmental stimuli, and controlled drug release (19). Studies have shown that the addition of CMC into SPI-stabilized emulsion can effectively reduce the release of VD3 in the simulated *in-vitro* digestion process due to the cross-linked by CMC and Ca^{2+} had polysaccharide protection (20).

Therefore, the purpose of this study is to investigate the effects of different concentrations of CMC on the physicochemical stability and *in-vitro* digestion characteristics of SPI-stabilized RBO emulsion. The RBO emulsion was assessed by zeta potential, particle size, transmission, microstructure, and rheological behavior. The microstructural changes of RBO emulsions at different phases of *in-vitro* digestion and the FFA release in the small intestine stage were also evaluated. Ultimately, our goal is to apply plant protein-polysaccharide to improve the physicochemical stability and digestion capacity of RBO and extend the application of RBO in the food industry.

MATERIALS AND METHODS

Materials

Soy protein isolate (SPI) was obtained from Shanghai YUANYE Biotechnology Corporation Ltd. (Shanghai, China). CMC was purchased from Changshu WEALTHY Technology Corporation Ltd. (Changshu, China). Rice bran oil (RBO) was purchased from Jinlongyu (Qinhuangdao, China). Mucin from the porcine stomach (CAS#84082-64-4, BR), pepsin from porcine gastric mucosa (CAS#9001-75-6, 10,000 U/g), bile salt from pigs (CAS#8008-63-7, more than 60% cholic acid content), and lipase from porcine pancreas (CAS#9001-62-1, BR, 30,000 U/g) were purchased from Shanghai YUANYE Biotechnology Corporation Ltd. (Shanghai, China). All other chemicals were of analytical grade.

Preparation of Emulsions

Soy protein isolate (SPI) (1.5 wt%) and CMC (3 wt%) were first dissolved in the 10.0 mM phosphate buffer at pH 6.0, 0.02% sodium azide was added to prevent microbial growth. The solutions were kept overnight to ensure complete dissolution and dispersion. Then, RBO (10 wt%) was added to the SPI solution by using an Ultra-Turrax (B25 model, Shanghai Beierte experimental Equipment Co., Ltd) to prepare crude emulsion at 19,000 rpm for 3 min, which was subsequently homogenized using a microfluidizer processor (M-110PS model, Microfluidics International Corporation, Newton, MA) at 50 MPa for three times. Then, the SPI-RBO emulsion and CMC were homogenized with the ratio of 2:1 by using an Ultra-Turrax (B25 model, Shanghai Beierte experimental Equipment Corporation Ltd.) at 19,000 rpm for 3 min. Finally, the pH was adjusted to pH 3.5 using 1.0 M HCl or NaOH. Thus, final emulsions contained 1 wt% SPI, 6.67 wt% rice bran oil and various contents of CMC (0–0.625 wt%), respectively.

Zeta Potential and Particle Size Measurements

Zeta potential and particle size of the samples were analyzed according to the method of Xu et al. (21). The zeta potential

of SPI-RBO emulsions stabilized with different concentrations of CMC was determined by Zetasizer Nano-ZS90 (Malvern Instruments, Worcestershire, UK). Emulsions were diluted (1:400) with buffer solution (pH 3.5) before analysis to minimize multiple scattering effects. The data were collected over 11 continuous readings after the samples were equilibrated at 25°C for about 120 s.

To determine the average droplet size of emulsions, diluted samples (1:400) were loaded into the instrument at a fixed detector angle of 90°. Droplet size was described as cumulative mean diameter (size, μm).

Physical Stability Measurements

The physical stability of SPI-RBO emulsions stabilized with different concentrations of CMC was measured by using LUMiSizer (LUM GmbH, Berlin, Germany). The instrumental parameters of the measurement were as follows: volume, 0.4 ml of dispersion; 4,000 rpm; time interval, 60 s; temperature, 25°C; and the number of scanning times, 255.

Microstructure Analysis

The microstructure of emulsion samples was observed by confocal laser microscopy (FV1200, Olympus, Japan) after emulsions were diluted 4 times. In this experiment, samples were mixed with Nile Red (λex: 488 nm) to stain oil phase (RBO) and with Nile Blue A (λex: 640 nm) to stain proteins. Microstructure pictures were taken using a 10X eyepiece with a 60X objective lens (oil immersion). They were magnified 16 times by the software of the instrument (FV10i-Oil, Olympus, Japan).

Shear Rheological Properties

The shear rheological properties were measured by a dynamic shear rheometer (MCR 301, WESP, Graz, Austria). It was equipped with cone-plate geometry (CP50-1). SPI-stabilized RBO emulsions with different concentrations of CMC were loaded into the rheometer measurement platform and equilibrated at 25°C for 2 min before making measurements. Shear stress and viscosity profiles were then performed in the range of 2–200 s^{-1}.

Rice Bran Oil Oxidation Measurements

Rice bran oil oxidative stability was determined by storing SPI-stabilized RBO emulsions with 0.5 wt% CMC in test tubes in the dark at 37°C for 30 days. Lipid hydroperoxides and thiobarbituric acid reactive substances (TBARSs) were determined according to the method of Long et al. (22). In short, hydroperoxide and TBARS were extracted using isooctane/isopropanol (3:1, v/v) mixture and TBA reagent, respectively. The absorbance of hydroperoxides was measured at 510 nm and the absorbance of TBARS was measured at 532 nm using a UV-vis scanning spectrophotometer, respectively (Shimadzu UVmini-1240, Kyoto, Japan). The cumene hydroperoxide calibration curve was used to determine hydroperoxide concentrations. The standard curve made for 1,1,3,3-tetra ethoxy propane was used to determine TBARS concentrations.

In-vitro Digestion

Soy protein isolate-stabilized RBO emulsions with and without 0.5 wt% CMC were passed through an *in-vitro* digestion model. The simulated gastrointestinal tract model followed the method which involved mouth, stomach, and small intestine phases (23).

Simulated mouth phase: 3 g mucin was dissolved in 100 ml ultrapure water as the simulated saliva solution, and then adjusting the pH to 6.8. Initial emulsion samples were diluted in 1 mM, pH 3.5 phosphate buffer at a ratio of 1:5 (v/v) and then were mixed with simulated saliva solution at the ratio of 1:1 (v/v). The mixture was continuously shaken at 100 rpm for 10 min in a 37°C water bath.

Simulated stomach phase: the simulated gastric juice was prepared by dissolving 0.32 g pepsin, 0.2 g NaCl, and 0.7 ml HCl (12.0 M) in a volumetric flask (100 ml) with ultrapure water. Simulated stomach solution was then added to the saliva sample from the previous experiment at the ratio of 1:1 (v/v) and the mixture (pH 2.5) was stirred for 2 h (37°C, 100 rpm).

Simulated small intestine: 3 ml simulated intestinal fluid, 7 ml bile salt solution (53.6 mg/ml), 5 ml freshly prepared lipase solution (24 mg/ml) were successively added to a simulated stomach sample (60 g), respectively. The automatic titration unit (AT710S, KEM, Japan) was used to monitor the pH and maintain it at pH 7.0 by titrating 0.2 M NaOH solution into the reaction vessel for 2 h at 37°C.

Free Fatty Acid Release

The rate of free fatty acids (FFAs) released was calculated using the following formula:

$$FFA\ (\%) = \frac{\left(V_{NaOH} \times m_{NaOH} \times M_{Lipid}\right)}{W_{Lipid} \times 2} \times 100\%$$

Here V_{NaOH} is the volume of NaOH required to neutralize the produced FFA (in L), m_{NaOH} is the molarity of the added NaOH solution (0.2 M), W_{Lipid} is the total weight of lipid initially present in the reaction vessel (0.2 g), and M_{Lipid} is the mean relative molecular weight of RBO (273.64 g/mol).

Microstructure During *in-vitro* Digestion

The microstructure of SPI-stabilized emulsions with different concentrations of CMC was observed by confocal laser microscopy (FV1200, Olympus, Japan) after passing through an *in-vitro* digestion. All the microstructure pictures were taken using a 10X eyepiece with a 60X objective lens (oil immersion). The images were magnified 16 times by the software of confocal laser microscopy (FV10i-Oil, Olympus, Japan).

Statistical Analysis

All the experiments were done in triplicate using freshly prepared RBO emulsions. Results are reported as the calculated mean and SD of replicates. Data were analyzed of variance (ANOVA) using the software package Origin 8.5.

RESULTS AND DISCUSSION

Effect of the CMC Concentration on the Physical Stability of SPI-RBO Emulsions

Zeta Potential and Particle Size

Zeta potential represents the stability of emulsion by reflecting the electrostatic interaction between droplets (24). The zeta potential of SPI-RBO emulsions stabilized with different concentrations of CMC at pH 3.5 was shown in **Figure 1A**. It showed that the net charge on the SPI-coated RBO droplets without CMC was around 24.4 ± 1.5 mV. The isoelectric point of SPI is about pH 4.5 (25), hence the SPI-coated RBO droplets were positively charged at pH 3.5, the electrical charge on the RBO droplets became less positive with the increase of CMC content, which indicated that the negatively charged CMC molecules absorbed to the surface of the positively charged RBO emulsion droplets forming SPI-CMC membranes (26). As an anionic polysaccharide, CMC contains a large number of negatively charged carboxyl groups, which can be combined with positively charged groups in 7S-β subunit and 11S-B polypeptide chains of SPI, such as amino groups, through electrostatic attraction (27). A small amount of CMC with 0.125 and 0.25 wt% decreased the zeta potential values of RBO emulsions to almost zero. It indicated that CMC at a lower concentration might bind to one or more RBO droplets and was not enough to form strong electrostatic repulsion interaction between droplets. At high contents of CMC (0.375–0.625 wt%), the emulsion droplets became negatively charged and finally the charge reached a plateau at −18.7 ± 1.3 mV when CMC concentration was 0.5 wt%, indicating that the droplets had become saturated with CMC or the increase of electrostatic repulsion force prevents the further adsorption of CMC (26). The ability of charged CMC to be adsorbed to the surface of charged emulsion droplets has been well evaluated (28).

The droplet size of SPI-RBO emulsions stabilized with different concentrations of CMC at pH 3.5 was shown in **Figure 1B**. It was shown that the droplet size of the SPI-RBO emulsion was about 1.2 μm. The smaller particle size may be due to the positive charge of the particle, which generates strong electrostatic repulsion. At lower CMC contents (0.125 and 0.25 wt%), there were significant increases in size (29.9 and 31.5 μm). This phenomenon may be attributed to the fact that there were insufficient CMC molecules present to completely cover SPI-coated oil droplet surfaces. As a result, CMC could bind to the surfaces of more than one cationic oil droplet leading to charge neutralization and bridging flocculation. With the further addition of CMC more than 0.25 wt%, there was a large decrease in the droplet size of RBO emulsion. When CMC content was more than 0.5 wt%, the droplet size of RBO emulsion reached a plateau and showed 1.0 μm. It indicated the interaction of CMC with SPI-coated RBO droplets and corresponded to the droplet charge given in **Figure 1A**. With the increase of CMC content, it would be enough to cover the RBO droplet's surface and form a thick interfacial layer. It was by other reports that CMC can interact with proteins by electrostatic interactions to form complexes (29). Therefore, the increased strong steric resistance and electrostatic repulsion between droplets can inhibit flocculation and reduce the particle size of droplets.

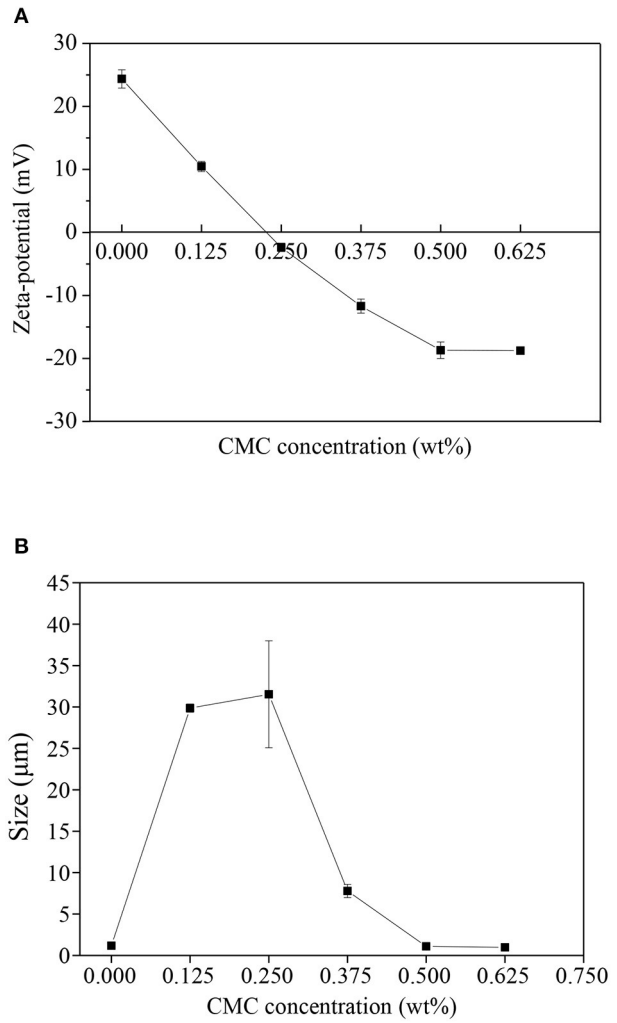

FIGURE 1 | Effect of the different concentrations of carboxymethyl cellulose (CMC) on the zeta potential **(A,B)** particle size of SPI (1 wt%) stabilized rice bran oil (RBO) (6.67 wt%) emulsions at pH 3.5, 25°C. Error bars are SDs of mean values.

Physical Stability

According to our previous study (30), the more change of the transmission with the centrifugation is, the less stable the emulsion is. **Figures 2A–F** exhibits the original transmission profiles of SPI-coated RBO emulsions stabilized with different concentrations of CMC ranging from 0 to 0.625 wt%. The positions in the transmission profiles at about 105 and 130 mm corresponded to the filling height and cell bottom, respectively. It was obvious that with increasing the CMC content from 0 to 0.625 wt%, the last integral transmissions were lower along the sample length, indicating that emulsions were more stable. It can be seen in **Figures 2A–F** that a sharp front moved toward the

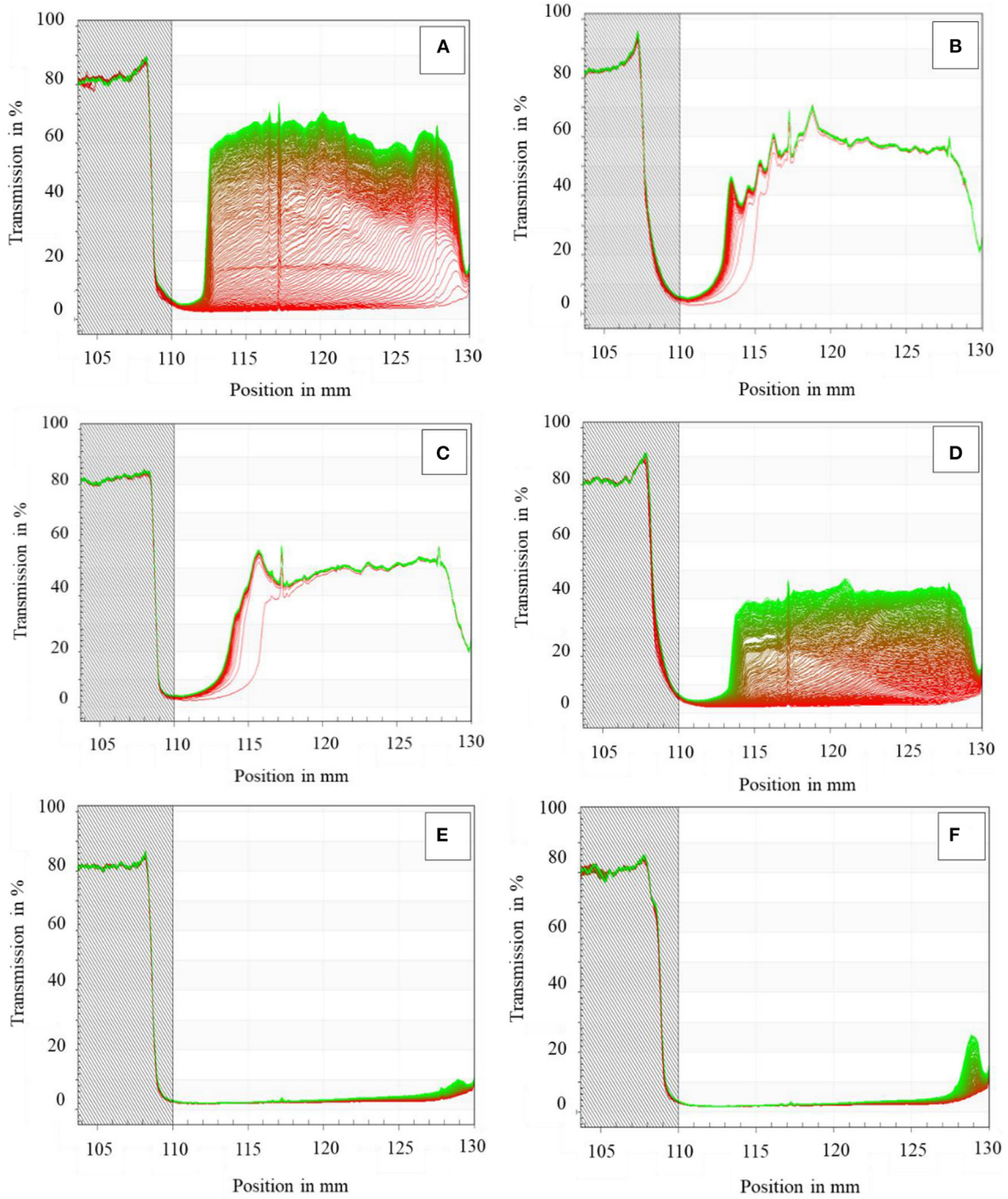

FIGURE 2 | Physical stability tested by LUMiSizer (original transmission) of the SPI-stabilized rice bran oil emulsions with different concentrations of CMC at pH 3.5, 25°C [**(A)** 0 wt% CMC; **(B)** 0.125 wt% CMC; **(C)** 0.25 wt% CMC; **(D)** 0.375 wt% CMC; **(E)** 0.5 wt% CMC; and **(F)** 0.625 wt% CMC].

cell top during centrifugation, which means that RBO droplets of all the emulsions were moving as a collective (zone creaming). **Figure 2A** shows the original transmission of sample position of emulsion without CMC, presenting the obvious creaming compared with other emulsions. It was also found that the first profiles of emulsions stabilized with 0.125 wt% CMC (**Figure 2B**) and 0.25 wt% CMC (**Figure 2C**) exhibited higher transmission along the sample length, which might be due to the flocculation of large particles in emulsions during centrifugation. As the amount of CMC increased from 0.375 wt% (**Figure 2D**) to 0.5 wt% (**Figure 2E**), the last profile of all emulsions was lower than that without CMC along the sample length, which indicated that the

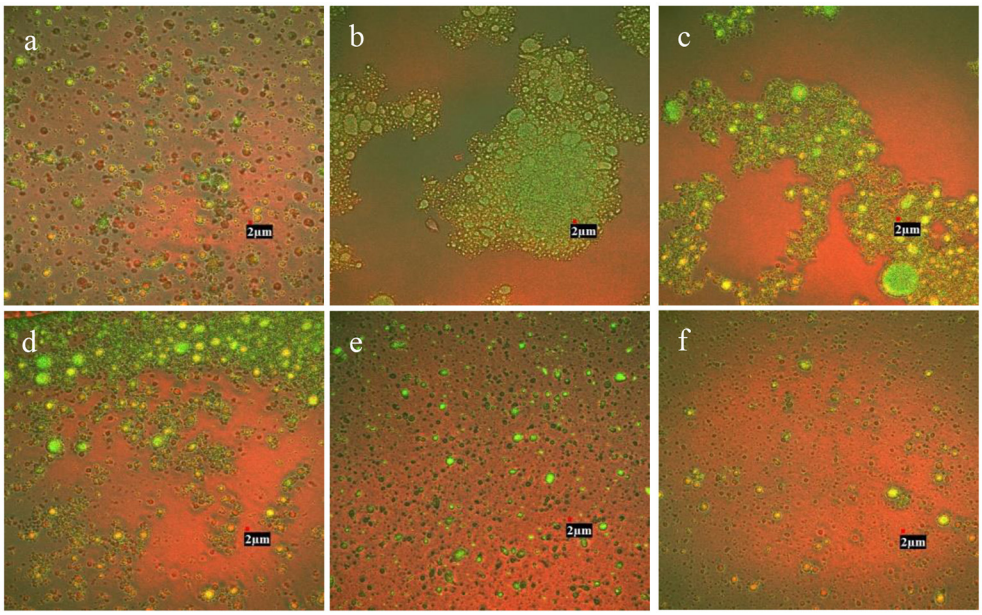

FIGURE 3 | The confocal laser scanning microscopy images of the SPI-stabilized rice bran oil emulsions with different concentrations of CMC at pH 3.5, 25°C [**(A)** 0 wt% CMC; **(B)** 0.125 wt% CMC; **(C)** 0.25 wt% CMC; **(D)** 0.375 wt% CMC; **(E)** 0.5 wt% CMC; and **(F)** 0.625 wt% CMC]. All the photos were magnified at 30,000X.

stability of emulsion increases with the increase of CMC addition, which may be due to enhanced steric hindrance and droplet network in RBO emulsion. The transmission peak of emulsion stabilized with 0.625 wt% CMC (**Figure 2F**) was higher and wider than that with 0.5 wt% CMC, indicating that the former was less stable than the latter. This might be depletion flocculation caused by the addition of excessive CMC (31).

Microstructure Analysis

Confocal laser scanning microscopy analysis demonstrated the microstructure of RBO emulsions stabilized with different concentrations of CMC (**Figure 3**). The green area represented RBO phase enrichment and the red area presented the SPI enrichment phase region. It was found that emulsion stabilized with 0.125 wt% CMC and 0.25 wt% CMC appeared extensive droplet flocculation compared with RBO emulsion without CMC. It might be due to the net charges of the particles in these two emulsions approaching zero, resulting in weakening the electrostatic repulsion. On the other hand, the concentrations of CMC were relatively low and the space resistance was relatively small. Combined with the above reasons, aggregation was more likely to occur between particles. The result was also consistent with the conclusion of particle size measurement (**Figure 1A**). As can be seen from **Figure 3D**, the particles in the emulsion with 0.375 wt% CMC exhibited slight flocculation, which might be the consequence of the enhancement of electrostatic repulsion and steric resistance. In the emulsion containing 0.5 or 0.625 wt% CMC, the droplet showed a relatively uniform distribution compared with the emulsion containing 0.125 wt% CMC, and the presence of CMC did not lead to flocculation in the emulsion. This might be because the particles in emulsions were negatively charged in this circumstance, increasing electrostatic repulsion between the particles. At the same time, the increase of CMC concentration also increased the spatial resistance between particles. Finally, the particles were uniformly dispersed and not easy to aggregate. Ultimately this indicated that RBO emulsions stabilized with 0.5 wt% CMC and 0.625 wt% CMC were more stable than others, which was in accordance with the result of physical stability and droplet size of RBO emulsions stabilized with different concentrations of CMC.

Shear Rheological Properties

Flow curves and the apparent viscosity of SPI-stabilized RBO emulsions with different concentrations of CMC with the shear rate in the range of 2 to 200 s^{-1} were characterized, as shown in **Figure 4**. In the RBO emulsions stabilized with different concentrations of CMC, significantly higher shear stress was observed with increasing concentrations of CMC, except for the RBO emulsion stabilized with 0.375 wt% CMC (**Figure 4A**). This might be because the additional amount of CMC just reached saturation, that is, each CMC molecule was wrapped on the surface of SPI-RBO particles under the action of electrostatic attraction, and the newly formed particles had a smooth surface and were similar in structure to RBO emulsion without CMC. The result was insistent with the particle size and zeta potential results.

The effect of different concentrations of CMC on the apparent viscosity of RBO emulsions was exhibited in **Figure 4B**. It showed that the apparent viscosity of all RBO emulsions decreased appreciably with the shear rate increased, indicating that the addition of CMC promoted SPI-RBO emulsions to become pseudoplastic fluid. This shear-thinning behavior could be that

the internal structure of the RBO emulsion opens with increasing the shear rate, and the molecules were linearly aligned in the direction of the shear rate (32). When the shear rate was greater, the viscosity curve tended to be flat with increasing shear rate, indicating that it was close to Newtonian fluid. The viscosity of SPI-RBO emulsions with 0.5 wt% CMC was significantly higher than that of SPI-RBO emulsion alone, which may be due to the larger particle size, forming a specific spatial structure, thus increasing the viscosity value. It was worthy to mention that the viscosity of RBO emulsion stabilized with 0.375 wt% CMC was close to that of RBO emulsion without CMC. The structural similarity of the particles in the two RBO emulsions might be the cause of this phenomenon (33, 34).

Chemical Stability

To measure the differences in oxidative stability between SPI-RBO emulsions without and with 0.5 wt% CMC, these emulsions were stored at 37°C in the dark for 30 d to accelerate oxidation rates. **Figure 5A** shows the content of lipid hydroperoxides in SPI-RBO emulsions without and with 0.5 wt% CMC during the incubation. SPI-RBO emulsions showed a more dramatic increase in lipid hydroperoxide formation than that stabilized with 0.5 wt% CMC. Lipid hydroperoxides increased slightly from day 0 to 8 in the SPI-RBO emulsions with and without 0.5 wt% CMC. After that, fast increases in lipid hydroperoxide formation were found, with the largest increase in lipid hydroperoxide at day 16. The concentrations of lipid hydroperoxides in the SPI-RBO stabilized without and with 0.5 wt% CMC were 5,548.9 and 5,066.7 μmol lipid hydroperoxides/l, respectively. After that, lipid hydroperoxides of both the RBO emulsions decreased obviously. It could be due to the oxidation of lipid hydroperoxides into the secondary lipid oxidation products.

In addition, secondary lipid oxidation product TBARS was also determined for the monitoring of oxidative stability of SPI-RBO emulsions during storage. The results of TBARS concerning SPI-RBO emulsions without and with 0.5 wt% CMC are given in **Figure 5B**. It was found that the content of TBARS in the SPI-RBO emulsion was more than that in the emulsion stabilized with 0.5 wt% CMC after storing 30 days, indicating that CMC could reduce the accumulation of TBARS. No obvious change in the content of TBARS (≈ 0.6 μg/ml) was observed in both RBO emulsions after storage of 16 d. However, the TBARS of RBO emulsion was increased obviously at day 22 in RBO emulsion without CMC. The TBARS concentration in RBO emulsion without CMC was 0.71 μg/ml TBARS. It shows that in the absence of CMC, more primary oxidation products decompose to form secondary oxidation products. After that, the RBO oxidation product of emulsions tended to decrease, which might be due to the additional by-products. Overall, the RBO emulsion stabilized with 0.5 wt% CMC was more effective in inhibiting the lipid oxidation compared to the single SPI-coated RBO emulsion, which might have two possible explanations. First, the carboxyl group in CMC interacts with the amino group in SPI to form SPI-CMC complex, which can be functioned as an emulsifier to form a layer of hydrated interfacial film on the surface of RBO, which improves the surface viscosity and density of droplets, thus improving the stability of emulsions (26, 35). Second, the steric hindrance effect produced by macromolecules reduces the contact between oxygen, transition metals, and RBO, thus reducing the release of free radicals and delaying the oxidative decomposition of RBO. In general, the composite membrane structure formed by SPI and CMC could slow down oil oxidation. It was consistent with the study of Ma et al. (36).

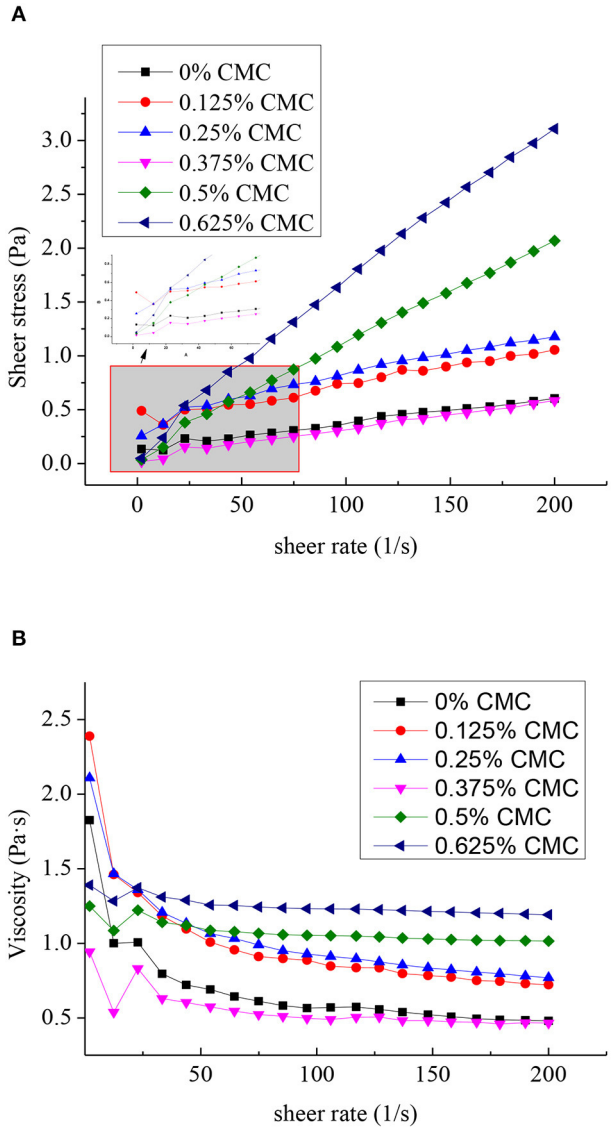

FIGURE 4 | Flow curves **(A)** and the apparent viscosity **(B)** of the SPI-stabilized rice bran oil emulsions with different concentrations of CMC (shear rate ranging from 2 to 200 s^{-1} at pH 3.5, 25°C).

In-vitro Digestion

Figure 6 shows the FFA release profiles of RBO emulsions stabilized with and without 0.5 wt% CMC during intestinal digestion. In the first 30 min, the FFA release rate of the two emulsions was very fast and reached a plateau at about

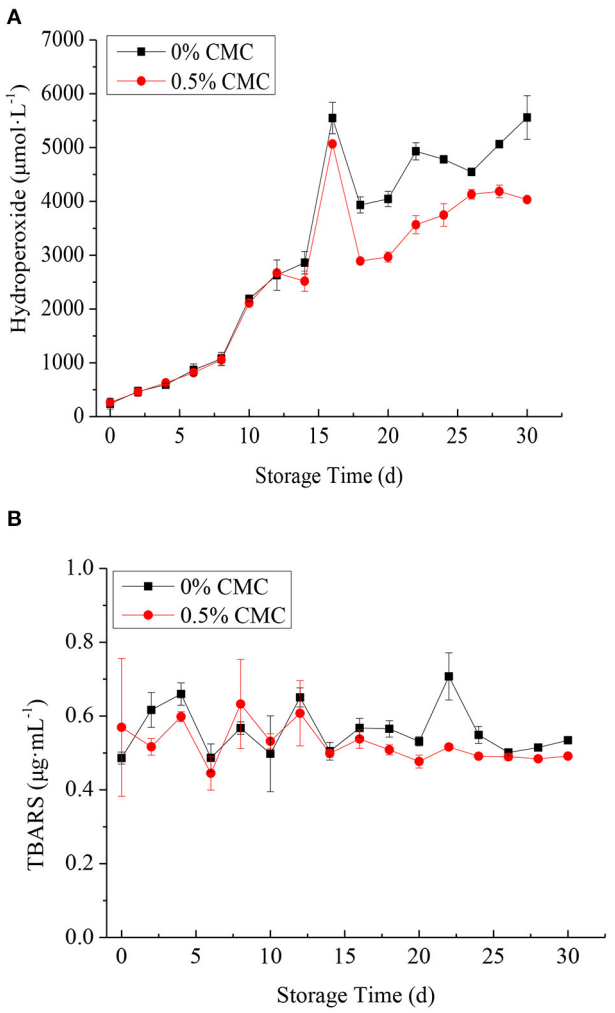

FIGURE 5 | The formation of lipid hydroperoxides (μmol/l emulsion) **(A)** and thiobarbituric acid reactive substances (TBARS) (μg/ml emulsion) **(B)** in SPI-stabilized rice bran oil emulsions with 0.5 wt% CMC during the incubation at 37°C. Data points represent means ($n = 3$) ± SDs.

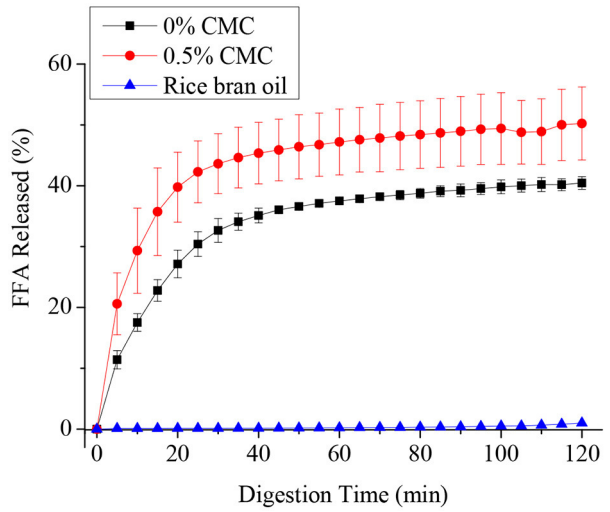

FIGURE 6 | Free fatty acids (FFAs) released from SPI-stabilized rice bran oil emulsions with 0.5 wt% CMC and pure rice bran oil after passing through an *in-vitro* digestion model (oral, gastric, and intestinal phases).

40 min. The reason for this phenomenon might be that with the progress of enzymatic hydrolysis reaction, the concentration of substrate decreased and the reaction site was gradually saturated by lipase. When the concentration of digestive products increased, its competitive inhibition became stronger, or enzyme activity decreased.

It can be seen that the RBO emulsions without CMC have a higher FFA release rate than pure rice bran oil, their final percentage of FFA release was around 30 and 1%, respectively. While around 50% FFA was released after digestion in the SPI-RBO emulsions stabilized with 0.5 wt% CMC. This result indicated that RBO digestion was appreciably improved by the emulsification of SPI. Emulsion stabilized by CMC could further accelerate the release of fatty acid and improve the digestibility of RBO. Compared with a single aqueous phase or an organic phase, lipase can play a better catalytic role on the oil-water interface, because the aqueous phase can disperse enzyme molecules and maintain the dominant conformation of enzyme protein, while the organic phase can open the lid structure on the enzyme active center, allowing substrate molecules to enter the enzyme active center, thus activating the enzyme (37). Hydrophilic groups and lipophilic groups in SPI can accelerate the combination of lipase and lipid droplets to degrade fat. Therefore, the free fatty acid release rate of SPI-RBO emulsion was higher than that of pure RBO, while CMC contains a large number of hydrophilic groups such as hydroxyl and carboxyl, which can optimize the catalysis of lipase and accelerate the release of FFA (38, 39).

Structural Changes During *in-vitro* Digestion

Figure 7 shows the microstructure of SPI-RBO emulsions with and without 0.5 wt% CMC during different stages of *in-vitro* digestion. First, there was no significant difference occurred in the simulated oral phase between both emulsions. It can be seen that mucin had no obvious effect on inducing emulsifier bridging or depletion flocculation in the simulated oral phase, which might be due to the short reaction time and mild reaction conditions, such as moderate pH (40, 41).

However, after the stomach, the droplets began to show obvious flocculation and aggregation. It could be attributed to the fact that the pepsin could hydrolyze SPI to destroy the structure of the original emulsifier, and the oil phase was driven by hydrophobic action to flocculate and deposit again. In addition, due to the strong acidity of gastric juice and the high ionic strength environment, interfacial layer hydrolysis and lower electrostatic repulsion force would increase the possibility of droplet flocculation (42–44).

After digestion in the simulated small intestine phase, droplets in both RBO emulsions were less compared with the original

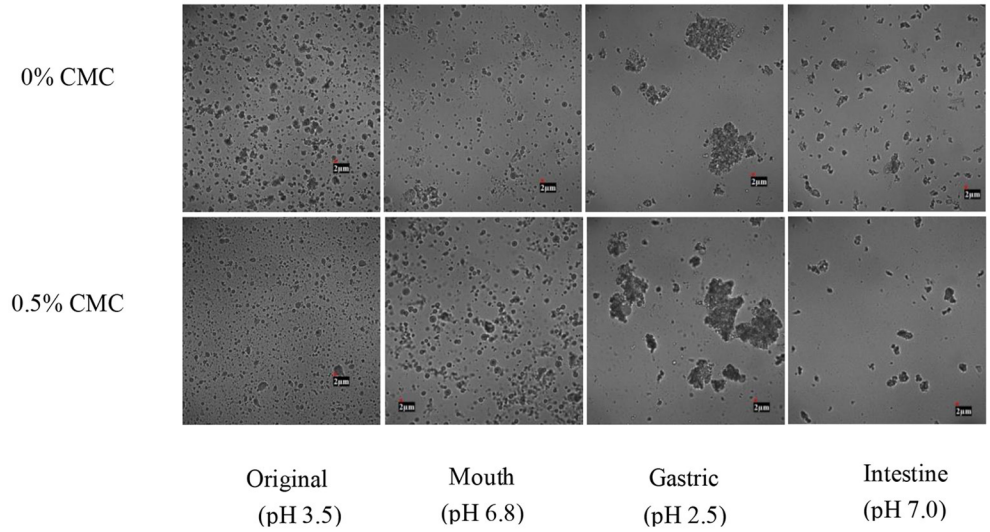

FIGURE 7 | The microstructures of different stages of SPI-stabilized rice bran oil emulsions with 0.5 wt% CMC after passing through an *in-vitro* digestion model (original, oral, gastric, and intestinal phases).

ones, indicating that some droplets were degraded and utilized. This was because lipase on the surface of the oil had a digestive effect on emulsified lipid. The lipase adhered to the surface of the lipid droplet and degraded triacylglycerol into free amino acids and triacylglycerol, thus changing the interfacial properties of the emulsion (45). SPI-RBO emulsion without CMC still contained relatively large droplets than that with 0.5 wt% CMC, which indicated that RBO emulsion with 0.5 wt% CMC had undergone more thorough degradation. The reason might be that the addition of CMC, especially hydrophilic groups, such as hydroxyl and carboxyl, accelerated the adsorption rate of lipase, thus making fatty acids easier to be released (46–48).

CONCLUSION

This study had characterized the impact of CMC on the physicochemical stability, rheological property, and *in-vitro* digestion of SPI-RBO emulsions. It is concluded that 0.5 wt% negatively charged CMC can be uniformly coated on a positively charged SPI-RBO droplet at pH 3.5, and the emulsion exhibited a smaller particle size, uniform distribution, and improved physical stability. The stable structure of the emulsion is formed by electrostatic interaction and steric hindrance between CMC and SPI on the droplet surface. Compared with SPI-RBO emulsion, adding CMC can effectively reduce the oxidation products produced during long-term storage. In addition, *in-vitro* digestion experiments showed that the FFA release rate of CMC-stabilized SPI-RBO emulsion added with 0.5 wt% was significantly higher than that of pure RBO and SPI-RBO emulsion, indicating that CMC had the potential to improve RBO bioaccessibility and was beneficial to the use of bioactive substances in RBO. To sum up, the use of CMC-stabilized SPI-RBO emulsion can improve the theoretical basis for the development of functional factors delivery system in food production.

DATA AVAILABILITY STATEMENT

The original contributions presented in the study are included in the article/**Supplementary Material**, further inquiries can be directed to the corresponding author.

AUTHOR CONTRIBUTIONS

WZ: methodology, formal analysis, writing–review, and editing. JH: methodology and review. YY: methodology, investigation, and validation. DX: conceptualization, writing–review and editing, project administration and supervision, and funding acquisition. All authors contributed to the article and approved the submitted version.

FUNDING

This study was funded by the National Natural Science Foundation of China (32072216), the Graduate Innovation Project of School of Food and Health in 2021 of Beijing Technology and Business University. CIFST - Abbott Foundation of Food Nutrition and Safety (No. 2021-F04).

SUPPLEMENTARY MATERIAL

The Supplementary Material for this article can be found online at: https://www.frontiersin.org/articles/10.3389/fnut.2022.878725/full#supplementary-material

REFERENCES

1. Lichtenstein AH, Ausman LM, Carrasco W, Gualtieri LJ, Jenner JL, Ordovas JM. Rice bran oil consumption and plasma lipid levels in moderately hypercholesterolemic humans. *Arterioscler. Thromb. Vasc. Biol.* (1994) 14:549–56. doi: 10.1161/01.atv.14.4.549
2. Nicolosi RJ, Ausman LM, Hegsted DM. Rice bran oil lowers serum total and low density lipoprotein cholesterol and apo b levels in nonhuman primates. *Atherosclerosis.* (1991) 88:133–42. doi: 10.1016/0021-9150(91)90075-e
3. Reena MB, Lokesh BR. Effect of blending and lipase catalyzed interesterification reaction on the cholesterol lowering properties of palm oil with rice bran oil in rats. *Int J Food Sci Tec.* (2012) 47. doi: 10.1111/j.1365-2621.2011.02827.x
4. Hoed VV, Depaemelaere G, Ayala JV, Santiwattana P, Verhe R, Greyt WD. Influence of chemical refining on the major and minor components of rice brain oil. *J Am Oil Chem Soc.* (2006) 83:315–21. doi: 10.1007/s11746-006-1206-y
5. Juliano C, Cossu M, Alamanni MC, Piu L. Antioxidant activity of gamma-oryzanol: mechanism of action and its effect on oxidative stability of pharmaceutical oils. *Int J Pharm.* (2005) 299:146–54. doi: 10.1016/j.ijpharm.2005.05.018
6. Piironen V, Lindsay DG, Miettinen TA, Toivo J, Lampi AM. Plant sterols: biosynthesis, biological function and their importance to human nutrition. *J Sci Food Agric.* (2000) 80:939–66. doi: 10.1002/(sici)1097-0010(20000515)80:7<939::aid-jsfa644>3.3.co;2-3
7. Thanonkaew A, Wongyai S, Decker EA, McClements DJ. Formation, antioxidant property and oxidative stability of cold pressed rice bran oil emulsion. *J Food Sci Tech Mys.* (2015) 52:6520–8. doi: 10.1007/s13197-015-1743-1
8. Hoang HN, Choi K, Kim DE, Kang W, Ko S. Improvement of oxidative stability of rice bran oil emulsion by controlling droplet size. *J Food Process Pres.* (2013) 37:139–51. doi: 10.1111/j.1745-4549.2011.00633.x
9. Ratchanee C, Anuvat J, Kamolwan J, Thepkunya H, Onanong N, McClements DJ. Influence of biopolymer emulsifier type on formation and stability of rice bran oil-in-water emulsions: whey protein, gum arabic, and modified starch. *J Food Sci.* (2011) 76:E165–72. doi: 10.1111/j.1750-3841.2010.01959.x
10. Angkuratipakorn T, Sriprai A, Tantrawong S, Chaiyasit W, Singkhonrat J. Fabrication and characterization of rice bran oil-in-water Pickering emulsion stabilized by cellulose nanocrystals. *Colloid Surface.* (2017) 522:310–9. doi: 10.1016/j.colsurfa.2017.03.014
11. Liu C, Wang X, Ma H, Zhang Z, Gao W, Xiao L. Functional properties of protein isolates from soybeans stored under various conditions. *Food Chem.* (2008) 111:29–37. doi: 10.1016/j.foodchem.2008.03.040
12. García MC, Torre M, Marina ML, Laborda F. Composition and characterization of soybean and related products. *Crit Rev Food Sci.* (1997) 37:361–91. doi: 10.1111/j.1745-4514.2010.00469.x
13. Petruccelli S, Anon MC. Relationship between the method of obtention and the structural and functional properties of soy protein isolates 2 surface properties. *J Agr Food Chem.* (1994) 42:2170–6. doi: 10.1021/jf00046a018
14. Wagner JR, Jacques G. Surface functional properties of native, acid-treated, and reduced soy glycinin 2 emulsifying properties. *J Agr Food Chem.* (1999) 47:2181–7. doi: 10.1021/jf9809784
15. Chen W, Yuan S, Shen J, Chen Y, Xiao Y. A composite hydrogel based on pectin/cellulose via chemical Cross-Linking for Hemorrhage. *Front. Bioeng. Biotechnol.* (2021) 8:1582. doi: 10.3389/fbioe.2020.627351
16. Lam RSH, Nickerson MT. Food proteins: a review on their emulsifying properties using a structure-function approach. *Food Chem.* (2013) 141:975–84. doi: 10.1016/j.foodchem.2013.04.038
17. Bahramparvar M, Razavi SMA, Khodaparast MHH. Rheological characterization and sensory evaluation of a typical soft ice cream made with selected Food Hydrocolloidoids. *Food Sci Technol Int.* (2010) 16:79–88. doi: 10.1177/1082013209353244
18. Moore LJ, Shoemaker CF. Sensory textural properties of stabilized ice cream. *J Food Sci.* (1981) 46:399–402.
19. Hossieni-Aghdam SJ, Foroughi-Nia B, Zare-Akbari Z, Mojarad-Jabali S, Motasadizadeh H, Farhadnejad H. Facile fabrication and characterization of a novel oral pH-sensitive drug delivery system based on CMC hydrogel and HNT-AT nanohybrid. *Int J Biol Macromol.* (2017) 107:2436–49. doi: 10.1016/j.ijbiomac.2017.10.128
20. Zhang A, Chen S, Wang Y, Wang X, Xu N, Jiang L. Stability and in vitro digestion simulation of soy protein isolate-vitamin D3 nanocomposites. *LWT - Food Sci Technol.* (2020) 117:108647. doi: 10.1016/j.lwt.2019.108647
21. Xu, D., Gao, Q., Ma, N., Hao, J., Yuan, Y., Zhang, M., et al. Structures and physicochemical characterization of enzyme extracted oil bodies from rice bran. *LWT - Food Sci Technol.* (2021) 135: 109982. doi: 10.1016/j.lwt.2020.109982
22. Long Z, Casimir C A. Oxidative stability of structured lipid-based infant formula emulsion: Effect of antioxidants. *Food Chem.* (2015) 178:1–9. doi: 10.1016/j.foodchem.2015.01.073
23. Diez-Sánchez E, Quiles A, Hernando I. Interactions between blackcurrant polyphenols and food macronutrients in model systems: In Vitro digestion studies. *Foods.* (2021) 10:847. doi: 10.3390/foods10040847
24. Sun C, Gunasekaran S, Richards MP. Effect of xanthan gum on physicochemical properties of whey protein isolate stabilized oil-in-water emulsions. *Food Hydrocolloid.* (2007) 21:555–64. doi: 10.1016/j.foodchem.2016.05.187
25. Wang D, Sun XS, Yang G, Wang Y. Improved water resistance of soy protein adhesive at isoelectric point. *Transactions of the ASABE.* (2009) 52:173−7.
26. Huan Y, Zhang S, Vardhanabhuti B. Influence of the molecular weight of carboxymethylcellulose on properties and stability of whey protein-stabilized oil-in-water emulsions. *J Dairy Sci.* (2016) 99:3305–15. doi: 10.3168/jds.2015-10278
27. Renkema JMS, Knabben JHM, Vliet TV. Gel formation by β-conglycinin and glycinin and their mixtures. *Food Hydrocolloid.* (2001) 15:407–14.
28. Surh J, Decker EA, McClements DJ. Influence of pH and pectin type on properties and stability of sodium-caseinate stabilized oil-in-water emulsions. *Food Hydrocolloid.* (2006) 20:607–18. doi: 10.1016/j.foodhyd.2005.07.004
29. Owens C, Griffin K, Khouryieh H, Williams K. Creaming and oxidative stability of fish oil-in-water emulsions stabilized by whey protein-xanthan-locust bean complexes: impact of pH. *Food Chem.* (2018) 239:314–22. doi: 10.1016/j.foodchem.2017.06.096
30. Xu D, Qi Y, Wang X, Li X, Wang S, Cao Y. The influence of flaxseed gum on the microrheological properties and physicochemical stability of whey protein stabilized β-carotene emulsions. *Food Funct.* (2017) 8:415–23. doi: 10.1039/c6fo01357k
31. Yerramilli M, Ghosh S. Long-term stability of sodium caseinate-stabilized nanoemulsions. *J Food Sci Tech Mys.* (2017) 54:82–92. doi: 10.1007/s13197-016-2438-y
32. Torres LG, Iturbe R, Snowden MJ, Chowdhry BZ, Leharne SA. Preparation of o/w emulsions stabilized by solid particles and their characterization by oscillatory rheology. *Colloid Surface a.* (2007) 302:439–48. doi: 10.1016/j.colsurfa.2007.03.009
33. Kinsella JE, Damodaran S, German B. Physicochemical and functional properties of oilseed proteins with emphasis on soy proteins. *New Protein Foods Seed Storage Proteins.* (1985) 79:107–79.
34. Wang X, Li X, Xu D, Liu G, Xiao J, Cao Y. Influence of unadsorbed emulsifiers on the rheological properties and structure of heteroaggregate of whey protein isolate coated droplets and flaxseed gum coated droplets. *Food Hydrocolloid.* (2018) 80:42–52. doi: 10.1016/j.foodhyd.2018.01.041
35. Grotenhuis ET, Paques M, Aken GAV. The application of diffusing-wave spectroscopy to monitor the phase behavior of emulsion-polysaccharide systems. *J Colloid Interf Sci.* (2000) 227:495–504. doi: 10.1006/jcis.2000.6888
36. Ma N, Gao Q, Li X, Xu D, Yuan Y, Cao Y. Enhancing the physicochemical stability and digestibility of DHA emulsions by encapsulation of DHA droplets in caseinate/alginate honeycomb-shaped microparticles. *Food Funct.* (2020) 11:2080–93. doi: 10.1039/c9fo02947h
37. Brzozowski AM, Derewenda U, Derewenda ZS, Dodson GG, Lawson DM, Turkenburg JP, et al. model for interfacial activation in lipases from the structure of a fungal lipase-inhibitor complex. *Nature.* (1991) 351:491–4. doi: 10.1038/351491a0
38. Golding M, Wooster TJ. The influence of emulsion structure and stability on lipid digestion. *Curr Opin Colloid in.* (2010) 15:90–101. doi: 10.1016/j.cocis.2009.11.006
39. Xu D, Cao Y, Yuan F, Gao Y. Influence of whey protein–beet pectin conjugate on the properties and digestibility of β-carotene emulsion during in vitro digestion. *Food Chem.* (2014) 156:374–9. doi: 10.1016/j.foodchem.2014.02.019

40. Chang Y, McClements DJ. Characterization of mucin-lipid droplet interactions: influence on potential fate of fish oil-in-water emulsions under simulated gastrointestinal conditions. *Food Hydrocolloid.* (2016) 56:425–33. doi: 10.1016/j.foodhyd.2015.12.034
41. Liu F, Ma C, Zhang R, Gao Y, McClements DJ. Controlling the potential gastrointestinal fate of beta-carotene emulsions using interfacial engineering: impact of coating lipid droplets with polyphenol-protein-carbohydrate conjugate. *Food Chem.* (2017) 221:395–403. doi: 10.1016/j.foodchem.2016.10.057
42. Fave G. Physicochemical properties of lipids: new strategies to manage fatty acid bioavailability. *Cell Mol Biol.* (2004) 50:815–31.
43. Maldonado-Valderrama J, Woodward NC, Gunning AP, Ridout MJ, Husband FA, Mackie AR. Interfacial characterization of β-lactoglobulin networks: displacement by bile salts. *Langmuir.* (2008) 24:6759–67. doi: 10.1021/la800551u
44. Mun S, Decker EA, McClements DJ. Influence of emulsifier type on in vitro digestibility of lipid droplets by pancreatic lipase. *Food Res Int.* (2007) 40:770–81. doi: 10.1016/j.foodres.2007.01.007
45. Hu M, Li Y, Decker EA, McClements DJ. Role of calcium and calcium-binding agents on the lipase digestibility of emulsified lipids using an in vitro digestion model. *Food Hydrocolloid.* (2010) 24:719–25. doi: 10.1016/j.foodhyd.2010.03.010
46. Dickinson E. Mixed biopolymers at interfaces: competitive adsorption and multilayer structures. *Food Hydrocolloid.* (2011) 25:1966–83. doi: 10.1016/j.foodhyd.2010.12.001
47. Juan MRP, Pilosof AMR. Protein–polysaccharide interactions at fluid interfaces. *Food Hydrocolloid.* (2011) 25:1925–37. doi: 10.1016/j.foodhyd.2011.02.023
48. Park C, Jimenez-Flores R, Maleky F. Quantifications of oleocolloid matrices made of whey protein and oleogels. *Foods.* (2020) 9:1697–708. doi: 10.3390/foods9111697

Conflict of Interest: The authors declare that the research was conducted in the absence of any commercial or financial relationships that could be construed as a potential conflict of interest.

Publisher's Note: All claims expressed in this article are solely those of the authors and do not necessarily represent those of their affiliated organizations, or those of the publisher, the editors and the reviewers. Any product that may be evaluated in this article, or claim that may be made by its manufacturer, is not guaranteed or endorsed by the publisher.

Copyright © 2022 Zhang, Hao, Yuan and Xu. This is an open-access article distributed under the terms of the Creative Commons Attribution License (CC BY). The use, distribution or reproduction in other forums is permitted, provided the original author(s) and the copyright owner(s) are credited and that the original publication in this journal is cited, in accordance with accepted academic practice. No use, distribution or reproduction is permitted which does not comply with these terms.

frontiers | Frontiers in Nutrition

ORIGINAL RESEARCH
published: 14 April 2022
doi: 10.3389/fnut.2022.879354

A Novel Hyaluronic Acid-Black Rice Anthocyanins Nanocomposite: Preparation, Characterization, and Its Xanthine Oxidase (XO)-Inhibiting Properties

*Ya Liu and Bangzhu Peng**

College of Food Science and Technology, Huazhong Agricultural University, Wuhan, China

To promote the normal metabolism of human uric acid, high-performance hyaluronic acid-black rice anthocyanins (HAA) nanocomposite particles were successfully prepared by a simple crosslinking method as a novel xanthine oxidase inhibitor. Its structure and properties were characterized by scanning electron microscopy (SEM), transmission electron microscopy (TEM), Fourier transform infrared spectrometry (FT-IR), and X-ray diffraction (XRD). SEM and TEM electron microscopy showed an obvious double-layer spherical structure with a particle size of ∼298 nm. FT-IR and XRD analysis confirmed that black rice anthocyanins (ATC) had been successfully loaded into the hyaluronic acid (HA) structure. Nanocomposite particles (embedded form) showed higher stability in different environments than free black rice ATC (unembedded form). In addition, the preliminary study showed that the inhibition rate of the nanocomposite particles on Xanthine oxidase (XO) was increased by 40.08%. These results indicate that HAA nanocomposite particles can effectively improve black rice ATC's stability and activity, creating an ideal new material for inhibiting XO activity that has a broad application prospect.

Keywords: uric acid, black rice anthocyanins, hyaluronic acid, xanthine oxidase, inhibition

OPEN ACCESS

Edited by:
Shuai Chen,
Wuhan University, China

Reviewed by:
Hongshun Yang,
National University of Singapore, Singapore
Haixia Yang,
China Agricultural University, China

***Correspondence:**
Bangzhu Peng
bzpeng@mail.hzau.edu.cn

Specialty section:
This article was submitted to Food Chemistry, a section of the journal Frontiers in Nutrition

Received: *19 February 2022*
Accepted: *25 March 2022*
Published: *14 April 2022*

Citation:
Liu Y and Peng B (2022) A Novel Hyaluronic Acid-Black Rice Anthocyanins Nanocomposite: Preparation, Characterization, and Its Xanthine Oxidase (XO)-Inhibiting Properties. Front. Nutr. 9:879354. doi: 10.3389/fnut.2022.879354

INTRODUCTION

Uric acid ($C_5H_4N_4O_3$) is the final product of the metabolism of endogenous purines and exogenous purines *in vivo* and is a heterocyclic organic compound (1). When the level of uric acid in the blood is too high, it will accumulate in the form of urate in joints, cartilage, and other body tissues, causing swelling and deformation of organ tissues, resulting in gout arthritis and eventually the development of hyperuricemia. Xanthine oxidase (XO) is an important enzyme for regulating uric acid synthesis and metabolism (2). It is a molybdate protease composed of two completely symmetrical subunits. The catalytic center includes a molybdenum center, two iron-sulfur centers, and a xanthine adenine dinucleotide. The molybdenum center is the key site for the catalytic production of uric acid. The drugs that inhibit the production of uric acid are mainly XO inhibitors, so they are also one of the most promising therapeutic targets. Allopurinol and other commonly used traditional therapeutic drugs greatly impact human health due to their long curative effect and strong side effects (3, 4). Therefore, it is important to search for high efficiency and low toxicity in nutritional regulatory factors.

Black rice is a medicinal, edible rice formed by the long-term cultivation of gramineous plant rice. It has a long cultivation history and is an ancient and valuable rice variety in China (5, 6). Modern medicine has confirmed that black rice has the effects of nourishing the yin and kidney, invigorating the spleen, warming the liver, improving eyesight, and promoting blood circulation (7). This is mainly ascribed to the rich anthocyanins (ATC) in black rice skin. In recent years, the physiological functions of black rice ATC, such as alleviating liver injury, lowering blood lipids, acting as an anticancer agent, controlling diabetes, and preventing myocardial injury (8, 9), have been widely studied, and related literature reports that ATC have a strong inhibitory effect on XO activity (10). However, the instability and low bioavailability of black rice ATC limit their application in food ingredients. Although ATC can be directly absorbed by intestinal epithelial cells (11), they are easily degraded by the digestive environment of the small intestine. They are usually transferred to the colon with a low absorption rate (12). Thus, there is a considerable demand to develop a technology that can effectively improve ATC's bioavailability and physiological activity.

Nanoembedding technology has improved ATC stability by embedding ATC from light, heat, pH, and other environmental effects (13, 14). Hyaluronic acid (HA) is a polysaccharide in the extracellular and loose connective tissue of mammalian bone marrow cells. It is an ideal carrier for preparing nanomaterials because of its good biocompatibility and biodegradability (15–17). The hydrophobic drugs doxorubicin and camptothecin were loaded into HA to improve the water solubility and bioavailability of the drug (18, 19). Therefore, nanomaterials combined with HA and black rice ATC could be developed into a new type of health care substance, effectively improving the low stability of black rice ATC and enhancing the inhibition of XO activity.

The commonly used method for synthesizing nanomaterials is mainly chemical modification (20). Still, this method is more complicated and usually involves the addition of organic solvents, which have certain hidden dangers to human health when applied to food ingredients. Therefore, based on the group and charge characteristics of HA and black rice ATC, a simple crosslinking method was used to prepare hyaluronic acid-black rice anthocyanins (HAA) nanocomposite particles (21). The method is simple and has higher safety than the conventional chemical modification method. The nanocomposite particles were characterized by a Malven Zetasizer Nano-ZS (Nano-ZS), scanning electron microscopy (SEM), transmission electron microscopy (TEM), Fourier transform infrared spectroscopy (FT-IR), and X-ray diffraction (XRD). Then, the stability, *in vitro* release, and *in vitro* simulated digestion were evaluated to determine the effectiveness and applicability of HAA. For the first time, synthetic HAA was used as an inhibitor to improve the inhibitory effect on XO. This paper could also provide a reference for the development of novel enzyme inhibitors related to nanotechnology and provide a theoretical basis for the research and application of inhibiting XO activity in the fields of medicine and functional food.

MATERIALS AND METHODS

Materials

A black rice-derived mixture of anthocyanins with a purity >25% (mainly containing Cyanidin-3-glucoside) was obtained from Xi 'an Xiaocao Plant Technology Co., Ltd. (Xi 'an, China). Hyaluronic acid (HA) (purity >95%) was purchased from Henan Sanhua Biological Technology Co., Ltd. (China). Xanthine oxidase (Cat. NO. X1875, from bovine milk, ≥0.4 units/mg protein, 5U) and xanthine (purity ≥99%) were purchased from Sigma–Aldrich Co. Ltd. (St. Louis, USA). Other chemicals were all analytical grade and were purchased from Sinopharm Chemical Reagent Co., Ltd. (Shanghai, China). All experimental water was deionized water.

Preparation of HAA Nanocomposite Particles

The HA/ATC mass ratio (8–12: 1), reaction pH (2.8–4.8), and stirring time (1–5 h) were considered as the experimental factors for the preparation of HAA nanocomposite particles. The nanocomposite particles were prepared according to a previously reported method (22) with slight modifications. HA (18 mg) was dissolved in 10 mL of deionized water and stirred continuously until a clear and transparent solution was obtained. Then, under the action of magnetic stirring, 2 mL black rice ATC solution was slowly added into HA solution with a syringe and mixed evenly. The pH was adjusted to 4.3 with dilute hydrochloric acid (1.0 M). After ultrasonic treatment for 5 min (power 200 W, frequency 59 kHz, working for 10 s, intermittent 5 s), magnetic stirring was performed for 3 h to obtain a uniform pink suspension. Finally, the suspension was dried in a vacuum freeze to obtain HAA nanocomposite particles. All the above experiments were carried out in a dark environment.

Encapsulation Efficiency (EE) Calculation

Black rice ATC's EE (%) was determined using the methods described previously (14, 23). The nanocomposite particles were centrifuged at 8,000 rpm for 30 min, and the free black rice ATC content in the supernatant was determined by the pH differential method. The samples were diluted with pH 1.0 (0.025 M) and pH 4.5 (0.4 M) buffers, and the absorbance was determined with distilled water as a blank at 510 and 700 nm, respectively. The black rice ATC content was calculated by the equivalent of cyanidin-3-glucoside (C3G) according to the equation (1):

$$c = \frac{(\mathrm{ApH1.0} - \mathrm{ApH4.5}) \times \mathrm{Mw} \times \mathrm{DF} \times 1000}{\mathrm{Ma} \times \mathrm{L}} \quad (1)$$

where ApH1.0 and ApH4.5 are the maximum absorbance of pH 1.0 and pH 4.5 buffer dilution samples, respectively. Mw is the molecular equivalent (449.2 g/mol) of C3G. DF is the dilution factor; Ma is the extinction coefficient (26,900 mol/L*cm); L is the optical diameter (1 cm); and 1,000 is the conversion factor.

The encapsulation efficiency of the black rice ATC was calculated according to the equation (2):

$$\mathrm{EE}(\%) = \frac{\mathrm{ATC0} - \mathrm{ATCt}}{\mathrm{ATC0}} \times 100 \quad (2)$$

where ATC0 is the initial content of black rice ATC in the nanocomposite particles, and ATCt is the content of free black rice ATC in the supernatant.

Characterization of HAA Nanocomposite Particles

The particle size, zeta potential, and polydispersity index (PDI) of HAA nanocomposite particles were analyzed using a Malven Zetasizer Nano-ZS (Nano-ZS) (Malvern Inst. Ltd., UK) at 25°C. Scanning electron microscopy (SEM) (SU8010, Hitachi Ltd., Japan) and transmission electron microscopy (TEM) (H-7650, Hitachi, Tokyo, Japan) were used to determine the surface morphology of the samples. X-ray diffractometry (XRD) (D8 Advance, Brucker, Karlsruhe, Germany) was used to scan and determine the structure and composition of the nanocomposite particles at room temperature. The FT-IR spectra of nanocomposite particles were determined by Fourier Transform Infrared Spectrometer (FT-IR) (IS50, USA) scanning in the range from 4,000 cm^{-1} to 400 cm^{-1}.

Stability Analysis

The nanocomposite particles were stored for 6 days at 25°C and protected from light under 0.1, 0.25, 0.5, and 1.0 mg/mL ascorbic acid (AA) conditions. Samples were taken every day to detect the retention rate of black rice ATC. Sampling and detecting the retention rate of black rice ATC at appropriate intervals at three conventional temperatures of 4°C (cooling temperature), 25°C (room temperature), and 40°C (accelerated heating) (13). The nanocomposite particles were exposed to light and stored at 25°C for 10 days, and the retention rate of black rice ATC was measured every other day. The retention rate of black rice ATC was calculated by the pH differential method according to the equation (3, 24):

$$R(\%) = \frac{Ct}{C0} \times 100 \quad (3)$$

where R represents the black rice ATC retention rate (%) (defined as the percentage of ATC content change); Ct represents the black rice ATC content sampled at time t (mg/L); and C0 represents the initial black rice ATC content (mg/L).

In vitro Simulation Analysis

The *in vitro* sustained release analysis of nanocomposite particles referred to a slightly modified version of the previous method (25). The lyophilized nanocomposite particle powder was suspended in phosphate-buffered saline (PBS) buffer (0.1 M, pH 7.4) to fully dissolve it, transferred to an 8–14 kDa dialysis bag, sealed and put into a vial containing 50 mL PBS buffer, and shaken at 100 rpm (37°C). Then, 3 mL of the fluid outside the dialysis bag was removed at a fixed point, and fresh buffer solution with the same temperature and amount was immediately added. The drug release amount and cumulative drug release percentage were calculated, and the sustained release curves of the nanocomposite particles were plotted *in vitro*.

The *in vitro* simulated digestion of nanocomposite particles was evaluated according to a previous method (26) with slight modifications. Simulated oral digestion: 1 mL of activated saliva (6.5 mg α-amylase and 0.5 mg $CaCl_2$ dissolved in ultra-pure water at pH 6.75) was added to a conical flask containing a 10 mL sample and digested at 100 rpm for 10 min (37°C). Simulated gastric digestion: After 10 min of simulated oral digestion according to the above steps, the oral digestive juice was adjusted to pH 2.0 with 6 M HCl, and then 1 mL of activated gastric juice (0.3 g of pepsin dissolved in 0.1 M HCl at pH 2.0), mixed well, and then shaken for 2 h. Simulated intestinal digestion: After oral and gastric simulated digestion according to the above steps, the gastric digestive juice was adjusted to pH 7.5 with 0.9 M $NaHCO_3$, and then 10 mL of activated intestinal juice was added (3.8 g of pig bile salt and 0.6 g of trypsin were dissolved in 0.1 M $NaHCO_3$ at pH 7.5) and mixed well, followed by shaking for 2 h. The retention rate of black rice ATC at different stages of simulated digestion *in vitro* was determined according to the method described in section stability analysis.

Inhibitory Activity of Nanocomposite Particles on XO *in vitro*

To compare and analyze the inhibitory activities of nanocomposite particles on XO *in vitro*, the inhibition experiment was carried out according to a previous report with slight modifications (27). Briefly, a series of mixtures consisting of a standard concentration of XO (0.012 U/mL), PBS buffer (0.05 M, pH 7.5), and the samples were incubated in a 25°C constant temperature water bath for 30 min. Then, 1 mL xanthine (0.2 mg/mL) was added to start the reaction. Then, the time/kinetics software UV–Visible spectrophotometer (U3010, Hitachi Ltd., Japan) was used to determine the absorbance of uric acid at 290 nm in the reaction system and to determine the catalytic activity of uric acid produced by XO in the presence of nanocomposite particles with different concentrations. Then, the relative inhibition rate of the sample to XO was calculated according to the equation (4):

$$I(\%) = \left(1 - \frac{B}{A}\right) \times 100 \quad (4)$$

where B represents the enzyme reaction activity in the presence of inhibitor, and A represents the enzyme reaction activity in the absence of inhibitor.

Statistical Analysis

All data are expressed as the means ± standard deviations of triplicate determinations. One-way analysis of variance (ANOVA) and Duncan's test ($P < 0.05$) were performed by SPSS 26.0 (IBM Inc., Armonk, NY, USA) to compare the differences between groups. Origin 8.0 (Origin Lab Inc., Massachusetts, USA) was used to draw relevant charts.

RESULTS AND DISCUSSION

Preparation and Characterization of HAA Nanocomposite Particles

Nano-ZS Analysis

HA and black rice ATC will interact when mixed. The Malven Zetasizer Nano-ZS was used to determine the influence of

TABLE 1 | Average particle size, zeta potential, PDI, and EE (%) of HAA nanocomposite particles.

Samples	Particle size (nm)	zeta potential (mV)	PDI	EE (%)
9:1-pH 4.3–3 h	298.56 ± 5.51	−32.51 ± 0.99	0.343 ± 0.02	86.04 ± 0.5

different factors on the particle size, zeta potential and PDI value of the prepared HAA nanocomposite particles. The effect of the mass ratio of HA to black rice ATC on HAA nanocomposite particles is shown in **Supplementary Table 1**. With the increase contents of HA, the particle size of HAA decreased first and then increased gradually, and the zeta potential showed a downward trend, indicating that a large proportion of HA did not conform to the basic characteristics of nanocomposite particles. This may be because: the ionic interactions between black rice ATC and HA would be strengthened to a certain extent with the increase contents of HA (14), resulting in a tighter combination of the two. Further increasing the HA content exceeded the binding limit with black rice ATC, too much water-soluble carrier attached to the surface of the nanocomposite particles or float around, leading to the gradual increase of the particle size. The effect of pH on the nanocomposite particles is shown in **Supplementary Table 2**. With the increase of pH, the particle size and PDI of the nanocomposite particles decreased relatively, and zeta potential relatively increased, but as the pH continued to increase, the zeta potential decreased. This may be because the small pH (pH < 3) increased the repulsive force between the positive charge density of black rice ATC and the -NH_2 groups, which destabilized the polymer network and induced the swelling of the particles. The electrostatic force between the positive charge of black rice ATC and anionic polysaccharides at pH values of about 3 and 4 was strong, resulting in a close binding between the two. As the pH value continued to increase, the electrostatic force between HA and black rice ATC weakened, and PDI increased, resulting in condensation. The effect of stirring time on the nanocomposite particles is shown in **Supplementary Table 3**. With the increase of stirring time, the particle size of the nanocomposite particles gradually decreased and was evenly dispersed. However, as the stirring time continued to increase, the particle size and PDI value increased sharply. This may be due to the dynamic formation process of HAA nanocomposite particles. Appropriate stirring time was conducive to the dispersion of solutes and the uniform particle size of nanocomposite particles. Excessive stirring destroyed the interaction between HA and black rice ATC, increasing the frequency of collisions and aggregations in the system, thus affecting the morphology and homogeneity of the nanocomposite particles. Further experimental results and range analysis are shown in **Supplementary Tables 4**, **5**, and the stirring time had the greatest influence on the particle size and zeta potential of HAA nanocomposite particles. Based on the analysis results of particle size and zeta potential, the stirring time 3 h, pH 4.3, and HA:ATC mass ratio 9:1 were considered optimal conditions for preparing HAA nanocomposite particles.

To further characterize the preparation conditions of the HAA nanocomposite particles, verification experiments were carried out, and the results are shown in **Table 1**. The prepared nanocomposite particles showed a suitable particle size. Generally, since 50–500 nm nanocomposites are optimal for epithelial cells (28), HAA nanocomposite particles are favorable for absorption by intestinal epithelial cells. In addition, the PDI value of the nanocomposite particles prepared under the process conditions was acceptable. The zeta potential value can reflect nanoparticles' physical and chemical characteristics and biological stability in solution. The zeta value of the nanocomposite particles prepared in this experiment was larger, indicating that the state of the nanoparticles in the system was relatively stable. Moreover, the higher encapsulation efficiency is conducive to improving the utilization of small molecule active substances. It is speculated that the electrostatic attraction between the black rice ATC cation and the carboxyl groups on HA would enhance the encapsulation of black rice ATC. It may also be because the dense network formed by hydrogen bonds between black rice ATC and HA contributed to the improvement of embedding efficiency, which has a better protective effect on black rice ATC (24).

Morphological Analysis

TEM and SEM were used to evaluate the morphology of HAA nanocomposite particles, which is helpful to explain the microstructure and aggregation characteristics of HAA. As shown in **Figures 1A,B**, the synthesized HAA nanocomposite particles had a clear structure without obvious agglomeration phenomena, which is similar to other biopolymer-based nanomaterials. As shown in **Figures 1C,D**, the nanocomposite particles were evenly dispersed, with a single spherical shape and an average particle size of 200 nm. However, it should be noted that there was a difference between the particle size measured by the Malvern particle size analyzer and the transmission electron microscope, which may be due to the loss of water during freeze-drying. In general, the average particle size determined by the Malvern particle size analyzer is closer to the size of the nanoparticle in the systemic circulation system, which is more suitable for the absorption and utilization of the biological environment (29). In addition, compared with HA alone (**Figure 1E**), an obvious double-layer structure could be found after the nanocomposite particles formed, which could intuitively reflect that the black rice ATC had been successfully loaded into the network structure of HA.

Structural Analysis

As shown in **Figure 2**, the diffraction peaks of black rice ATC were mostly sharp, and characteristic peaks were observed at 2θ values of 15.47°, 23.36°, 31.71°, and 45.55°, which indicated that black rice ATC was highly crystalline. Two relatively wide diffraction peaks were detected at 2θ values of 11.31° and 19.73°, indicating that HA was semicrystalline. The diffraction peak intensity of the synthesized nanocomposite particles was significantly reduced, showing the characteristics of amorphous polymers. The results showed that the crystal structure of the black rice ATC molecule in the nanocomposite

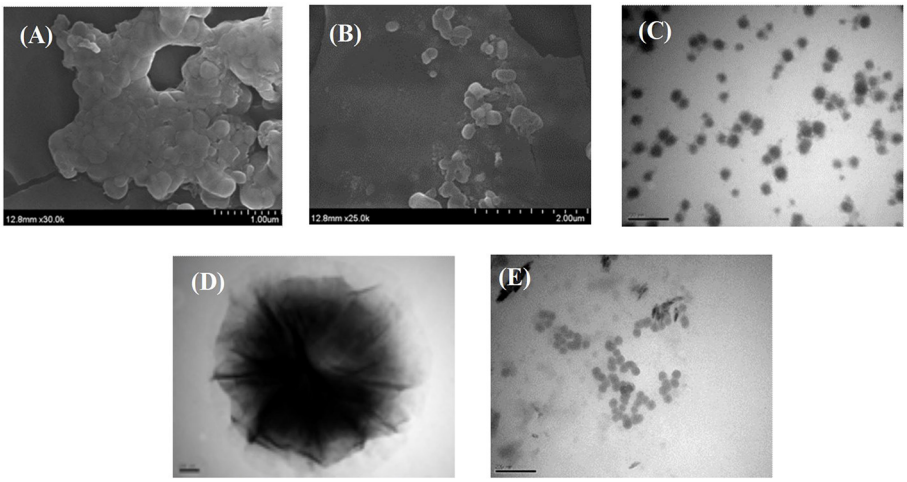

FIGURE 1 | SEM images of HAA nanocomposite particles **(A,B)**, TEM images of HAA nanocomposite particles **(C,D)**, and HA **(E)**.

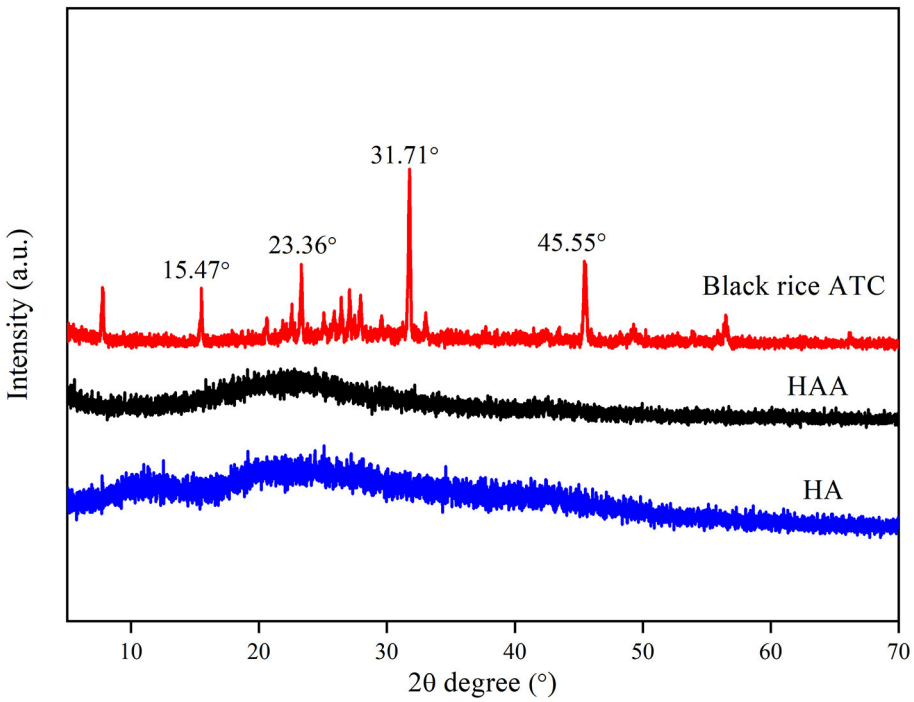

FIGURE 2 | XRD spectra of HA, black rice ATC, and HAA nanocomposite particles.

particles was covered, and that the diffraction peak intensity was significantly reduced, which may be related to the newly formed intermolecular hydrogen bond between black rice ATC and HA.

Spectral Analysis

The averaged and smoothed FT-IR spectra of HA, black rice ATC, and HAA nanocomposite particles are shown in **Figure 3**, and the characteristic peak positions of HA, black rice ATC and HAA are shown in **Supplementary Table 6** (30, 31). The positions of the characteristic peaks were determined according to previously methods (23, 32, 33). The peaks of black rice ATC at 1,641 and 1,444 cm^{-1} corresponded to the stretching vibrations of C=C and C=O in the aromatic ring skeleton, respectively. A band at 1,326 cm^{-1} corresponded to C-O angular deformations of phenols (13), and 1,245 cm^{-1} was the stretching vibration peak caused by the benzopyran aromatic ring, which was a typical flavonoid structure peak. The peaks

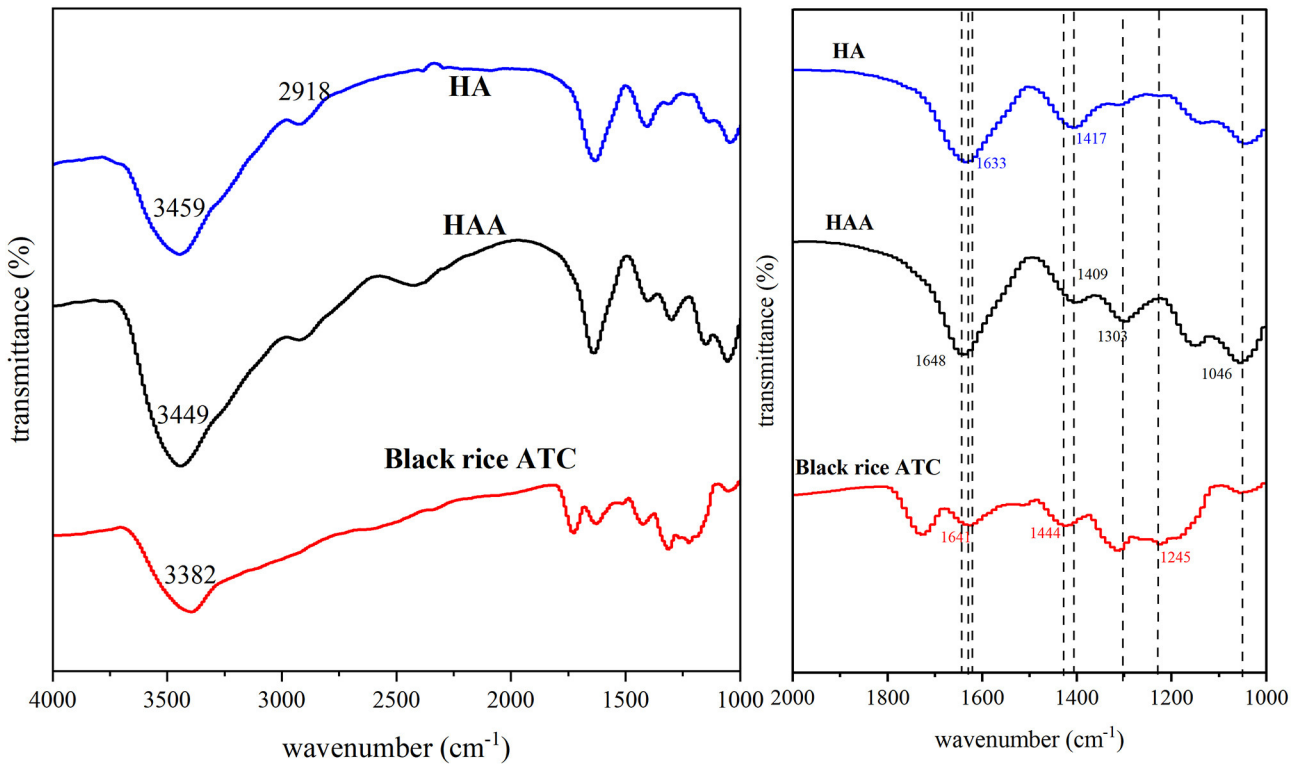

FIGURE 3 | The averaged and normalized FT-IR spectra of HA, black rice ATC, and HAA nanocomposite particles.

of HA at 1,633 and 1,417 cm^{-1} belonged to the -COO^- group of carboxylic acid salt. In the spectral bands of the synthesized nanocomposite particles, the stretching vibration of C=O (1,648 cm^{-1}) showed a blueshift absorption peak, and the stronger stretching vibration at 1,303 cm^{-1} was attributed to the introduction of black rice ATC, while the absorption peak at 1,046 cm^{-1} was stronger than that of HA, indicating hydrogen bond formation. Moreover, there was a shift in O-H stretching vibrations from 3,382 to 3,449 cm^{-1}, revealing hydrogen bonding between black rice ATC and HA (34). The characteristic peak of ATC disappeared at 1,245 cm^{-1} in HAA, indicating that HA had successfully embedded black rice ATC. In addition, the COO^- characteristic peak of HA at 1,417 cm^{-1} was shifted to 1,409 cm^{-1} in HAA, indicating the electrostatic interaction between -COOH of HA and -OH of black rice ATC. The above results all confirmed the successful combination of HA and black rice ATC.

Stability Analysis

Affected by its own structure, ATC are often unstable to the external environment and are easily degraded. The expectation that HA would stabilize black rice ATC by providing a barrier is supported by studies examining free black rice ATC and HAA storage. The stability analysis of free black rice ATC and HAA nanocomposite particles under different environmental stresses and storage conditions is shown below.

Effect of Ascorbic Acid Treatment

AA is a common additive in food. Relevant studies have shown that a certain amount of AA has a degradation effect on ATC, mainly due to the effect of hydrogen peroxide (H_2O_2). H_2O_2 is an auto oxidizing product of AA that opens the ring of ATC and leads to the oxidation of flavonoid salts into colorless products, leading to ATC degradation (35–37). As shown in **Figure 4**, the retention rates of free black rice ATC at different AA concentrations gradually decreased with the extension of storage days, and the retention rates after 6 days were 60.39, 51.08, 32.24, and 24.49%, respectively. However, HAA nanocomposite particles showed significant protection against ATC degradation at the same AA concentration. The retention rates were increased by 32.27, 31.5, 48.42, and 54.84%, respectively, which was in accordance with previously reported studies (13). The encapsulation of nanocomposite particles provided a physical barrier to prevent direct contact between black rice ATC and AA, thus improving stability. The higher retention rate of HAA nanocomposite particles was also attributed to the higher encapsulation efficiency.

Effect of Thermal Treatment

ATC are sensitive to temperature. The stability analysis of free black rice ATC and HAA under different conventional temperatures is shown in **Figure 5**. The black rice ATC retention rates of HAA nanocomposite particles stored at 4°C for 18 days, 25°C for 6 days, and 40°C for 3 days were 87.18, 73.68, and

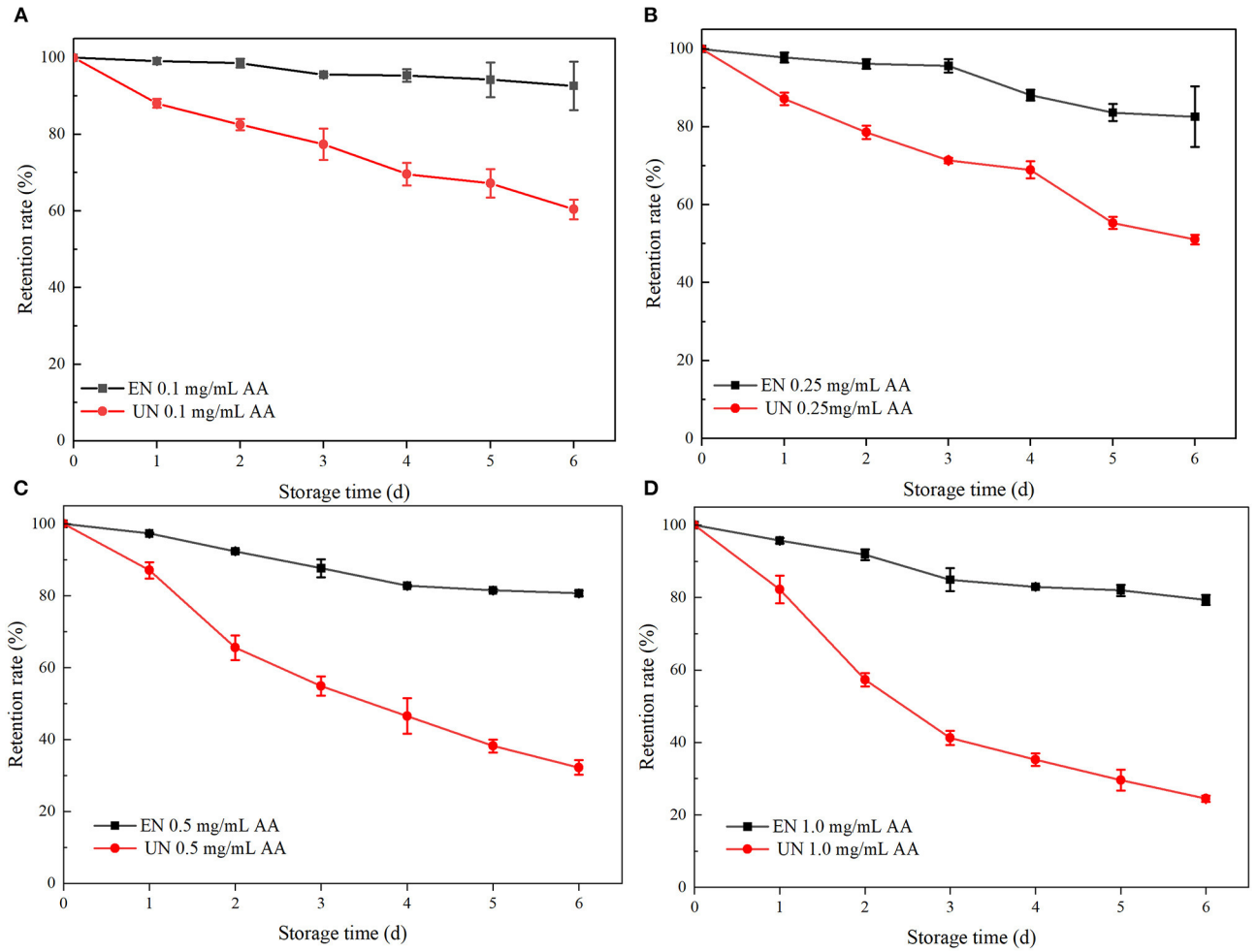

FIGURE 4 | The stability of black rice ATC at different ascorbic acid (AA) concentrations [**(A)** 0.1 mg/mL AA, **(B)** 0.25 mg/mL AA, **(C)** 0.5 mg/mL AA, and **(D)** 1.0 mg/mL AA]. EN and UN represent HAA nanocomposite particles (embedded form) and black rice ATC (unembedded form), respectively.

71.71%, respectively, while the free black rice ATC stored at 4, 25, and 40°C for the same time were only 75.09, 44.68, and 33.37%, respectively. The HAA nanocomposite particles showed better thermal stability than free black rice ATC did. After the interaction of HA with black rice ATC, black rice ATC was not reduced to a colorless chalcone structure and methanol pseudoalkaline form, which prevented the hydration of black rice ATC and thus maintained thermal stability. Generally, water-soluble carbohydrates can significantly improve the thermal stability of ATC by reducing the water activity around ATC (38). Our experimental results show that the nanocomposite particles can effectively reduce the degradation of black rice ATC caused by temperature factors, providing new insight for improving the stability of black rice ATC at different storage temperatures and expanding its wide application in food.

Effect of Light Treatment

Light is an important factor affecting the degradation of ATC. As shown in **Figure 6A**, after 10 days of light treatment, the retention rate of free black rice ATC was 23.28%, while the retention rate of HAA nanocomposite particles increased by 43.63%, showing an obvious protective effect. ATC are prone to discoloration and degradation during exposure to light (39). As shown in **Figure 6B**, with the prolongation of light, the color of free black rice ATC changed from pink to light yellow and finally to dark yellow. In contrast, the color change of HAA nanoparticles was less obvious, indicating that HAA effectively protected the degradation of black rice ATC under light and improved its stability. The color changes of free black rice ATC and HAA nanocomposite particles were consistent with the change trend of black rice ATC retention rate, which indicated that HA embedding can effectively reduce the degradation of black rice ATC and improve the light stability.

The above conclusion could be explained from the strong interaction between HA and black rice ATC observed in XRD and FT-IR spectra. We believe that the stability of the HAA nanocomposite particles is due to the high permeability barrier

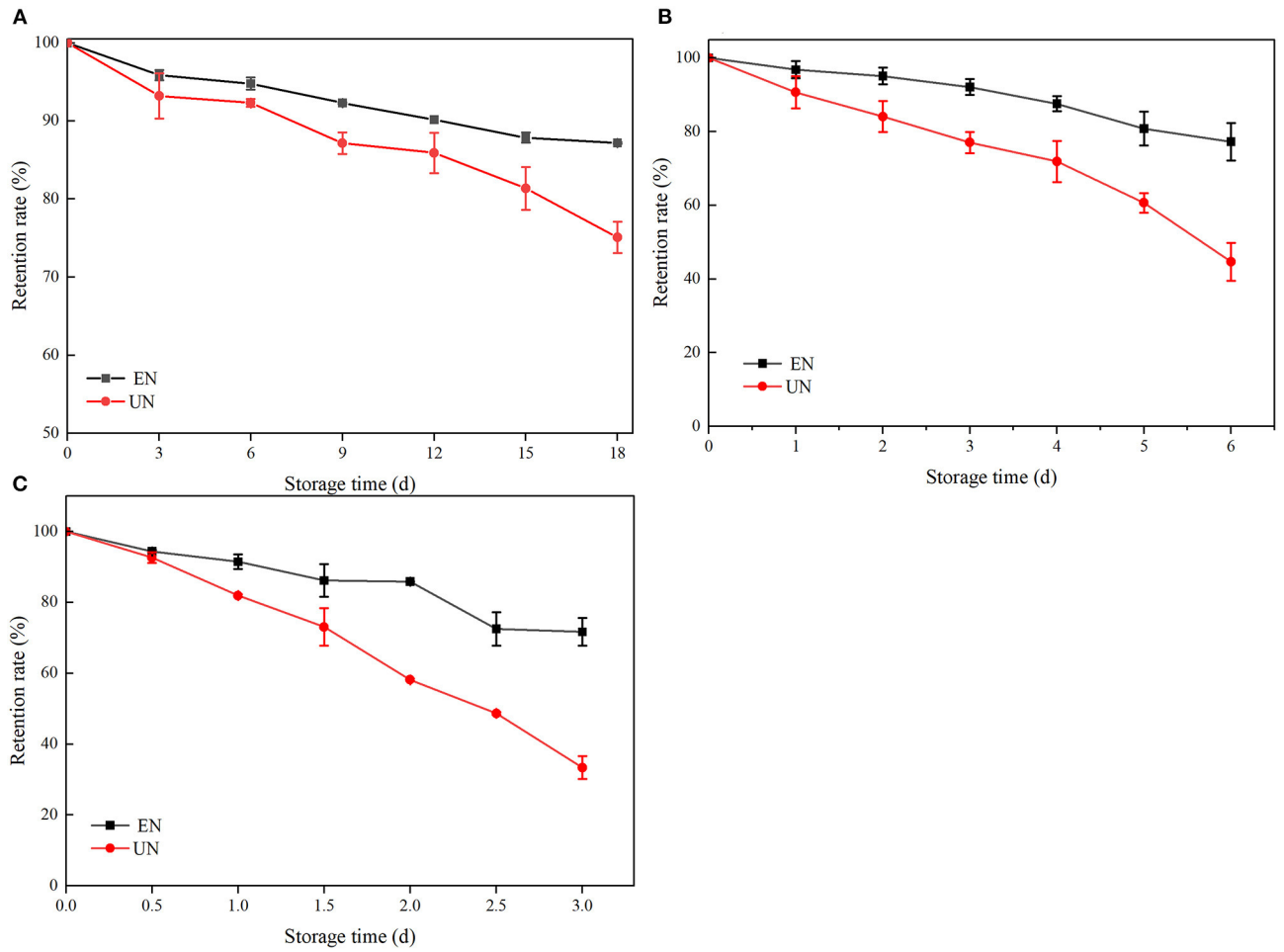

FIGURE 5 | The stability of black rice ATC at different temperatures [**(A)** 4°C, **(B)** 25°C, and **(C)** 40°C].

of the HA carrier in the outer layer to polar oxidants (such as ascorbic acid) and degradation under heat and light.

In vitro Simulation Analysis

Analysis of Sustained Release *in vitro*

The release characteristics of HAA nanocomposite particles embedded with black rice ATC are not only affected by gastrointestinal environment, but also related to the encapsulation material. Before simulating gastrointestinal digestive environment, exploring *in vitro* release characteristics of HAA nanocomposite particles embedded with HA is crucial to understand whether the nanocomposite particles can play an active role *in vivo* and *in vitro*, which can reflect the release of bioactive substances in the human digestive tract. As shown in **Figure 7**, free black rice ATC was released rapidly in the first 12 h and reached 60% at 4 h, showing sudden release behavior. In comparison, the release rate of HAA was faster in the first 12 h and then leveled off, and the total release reached 60% after 60 h. Therefore, the nanocomposite particles showed significant *in vitro* sustained release characteristics. This phenomenon may be that the interaction force between black rice ATC and HA made free black rice ATC not easy to diffuse, or the protective layer after HA embedded black rice ATC delayed the release of ATC. Similar studies have also pointed out that sustained release can reduce the degradation of active compounds, thus increasing the absorption and bioavailability of more active compounds in the gastrointestinal tract (40).

Analysis of Simulated Digestion *in vitro*

Based on the sustained-release characteristics of HAA nanoparticles *in vitro*, the effect of the simulated gastrointestinal digestive environment after the release of the HAA nanocomposite particles was further analyzed (**Figure 8**).

In the digestion process, the bioavailability of ATC will be affected due to factors such as pH value and digestive enzymes. The stability of the HAA nanocomposite particles and free black rice ATC was evaluated during the simulated digestion process *in vitro*. As a whole, the black rice ATC content was not significantly affected by oral and gastric simulated digestion environments, which was similar to the effect of *in vitro* simulated digestion on

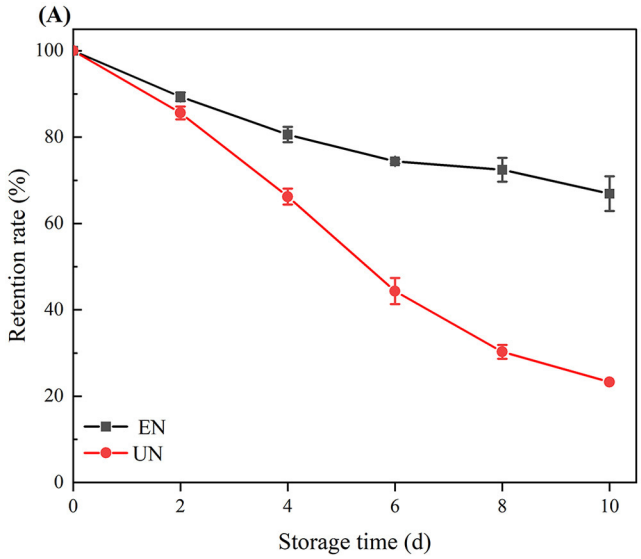

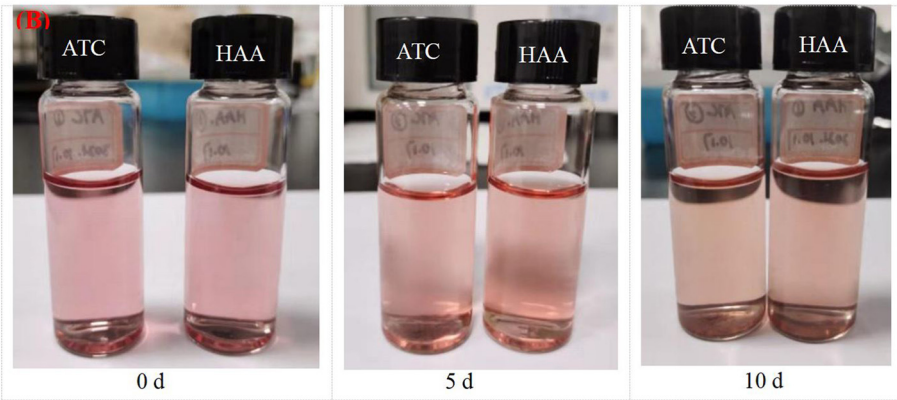

FIGURE 6 | (A) The stability of black rice ATC under 10 days of light; **(B)** Photographs of free ATC and HAA under 10 days of light.

ATC content from other extracts (14) and was also related to the better stability of ATC under acidic conditions (41). In addition, oral digestive enzymes and gastric digestive enzymes did not exert significant metabolic activity on ATC (42). In contrast, simulated intestinal digestion resulted in a sharp decrease in the ATC content of free black rice ATC and HAA nanocomposite particles. After 2 h of intestinal digestion, the ATC content of free black rice ATC and nanocomposite particles decreased to 16.46 and 24.73%, respectively. This phenomenon may be related to the effect of the intestinal pH value on the structural integrity of black rice ATC. Also, bile salts in intestinal juice gradually replaced the polysaccharides adsorbed on the surface, destroying the structure of HAA, and rapidly degrading black rice ATC (43). The retention rate of black rice ATC in HAA nanocomposite particles was always higher than that of free black rice ATC during the whole simulated digestion process *in vitro*, which may be because the black rice ATC was embedded in HA, which modified the degradation of black rice ATC in the simulated gastrointestinal tract. The results showed that nanoembedding technology could reduce the degradation of active compounds and improve the bioavailability of more active compounds in gastrointestinal digestion and absorption. However, the actual human digestive process is much more complicated, and its digestion and absorption mechanisms still need further study.

Evaluation of XO Activity *in vitro*

XO is a key enzyme that produces uric acid in the human body and is a common drug target. Inhibiting XO activity becomes the main way to reduce the production of uric acid. ATC has a strong inhibitory effect on XO activity *in vitro* (10). To further test whether the synthesized HAA nanocomposite particles improved the inhibitory effect on XO activity, the activity of producing uric acid catalyzed by XO in the reaction system was detected *in vitro*. According to the mass ratio of HA and black rice ATC of 9:1, the inhibitory effects on XO activity were detected, and the results are shown in **Figure 9**. The *in vitro* inhibitory rate of black rice ATC (0.2 mg/mL) was 16.34%, indicating that black rice ATC had a certain inhibitory effect on XO. The inhibitory rate of HA (1.8 mg/mL) on XO was 40%, indicating that HA also had a certain inhibitory effect on

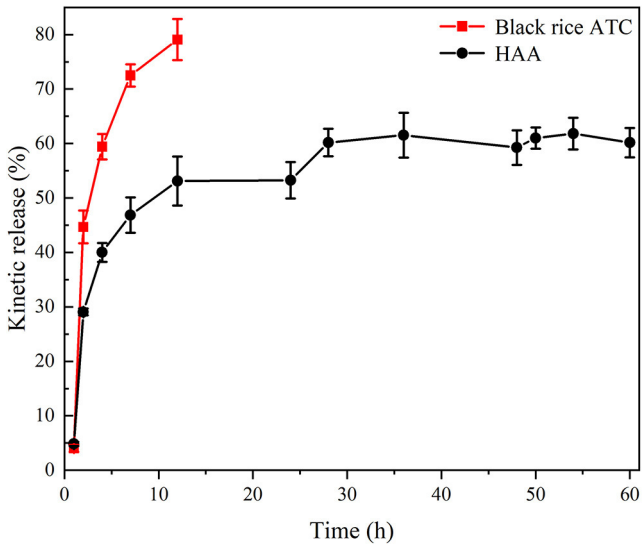

FIGURE 7 | *In vitro* sustained-release diagram of black rice ATC and HAA nanocomposite particles.

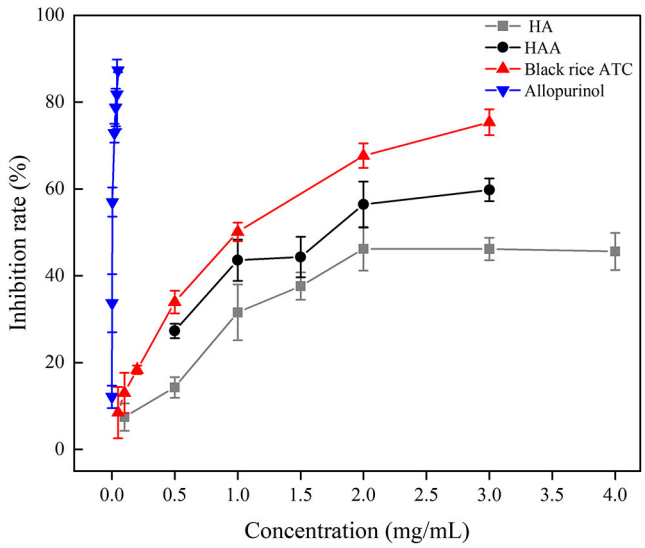

FIGURE 9 | The inhibitory effect of black rice ATC, HA, and HAA nanocomposite particles on XO.

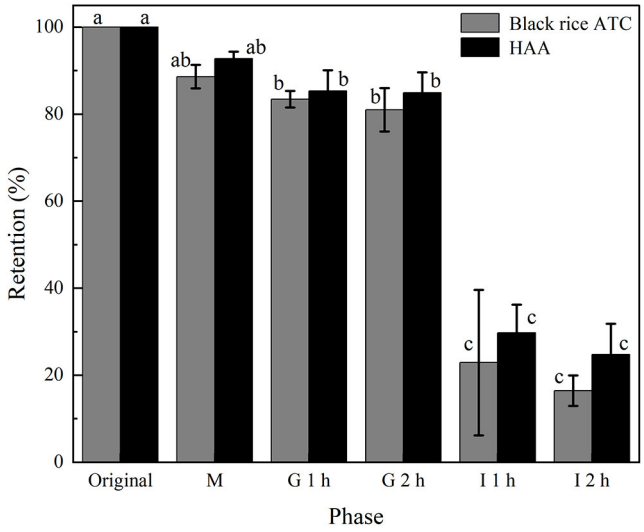

FIGURE 8 | ATC content changes of free black rice ATC and HAA nanocomposite particles during simulated digestion *in vitro*.

XO. When HAA nanocomposite particles were used as inhibitors to inhibit XO activity, the inhibitory rate of HAA nanocomposite particles (2.0 mg/mL) on XO activity *in vitro* reached 56.42%, the inhibitory effect improved with increasing concentration. HA and black rice ATC have a synergistic effect of inhibiting XO activity effectively. Although the inhibitory effect of HAA on XO was not as strong as that of allopurinol, our results suggested that HAA is a promising XO inhibitor. In addition, many studies have found that allopurinol has strong toxicity and side effects, which can cause symptoms such as inflammatory cell infiltration of the renal interstitium and renal duct dilatation. The above results confirmed the effectiveness and applicability of HAA nanocomposite particles prepared by a simple cross-linking method in inhibiting XO, which provided a new idea for inhibiting the production of uric acid.

DISCUSSION

The pH effect and molecular groups during simple crosslinking are a reasonable explanation for the preparation of HAA nanocomposite particles. Hyaluronic acid is a unique negatively charged acidic mucopolysaccharide, which differs from other acidic mucopolysaccharides in that the acid group is carboxyl instead of sulfuric acid (44). The surface of ATC is positively charged at pH 3 and 4 (45), and the presence of carboxyl functional groups in polysaccharides ensures strong electrostatic interaction and hydrogen bonding with ATC. The particle size of the nanocomposite particles increased with the increase of polysaccharide (**Supplementary Table 1**). With the increase of HA, too much water-soluble carrier adhered and aggregated, resulting in a gradual increase of the particle size. In addition, the free NH^{3+} in the polysaccharide structure increased, resulting in greater repulsion and larger diameter of nanoparticles (46). The surface of ATC is positively charged when the pH value is about 3 and 4, and the electrostatic force closely bound with HA. The electrostatic force weakened as the pH increased, resulting in intermolecular repulsion, particle size dispersion and agglomeration (**Supplementary Table 2**). The interaction between HA and black rice ATC groups was well-reflected in XRD and FT-IR spectra. The intensity of the characteristic absorption peaks of HA and black rice ATC and the changes of functional groups are attributed to the combination between the phenolic hydroxyl group of black rice ATC and COO- on HA, resulting in hydrogen bond formation and electrostatic force

generation, which makes the formation of black rice ATC load HA nanocomposites possible. However, the structural interaction form between HA and black rice ATC and the cross-linking mechanism still need to be further studied in the future.

ATC are easily affected by external environment and undergo degradation, which affects bioavailability. HA improved the environmental stress and storage stability of black rice ATC by providing a covering layer and weakening environmental damage, and significantly inhibited AA, heat, and light-induced degradation of ATC. This also benefits from the stabilizing force formed between HA and black rice ATC. Therefore, HA is a good candidate material to study the inhibition of black rice ATC degradation. This study improves the stability of black rice ATC in different environments and expands their wide application in food.

ATC are also easily degraded *in vivo*, and their bioavailability *in vivo* is affected not only by gastrointestinal digestive environment, but also by encapsulation materials (40). Some encapsulation materials can affect the utilization of encapsulated active compounds *in vivo*, affect their effective release ability in the gastrointestinal tract, and limit their absorption (47). The nanocomposite particles formed by HA-encapsulated black rice ATC had significant slow-release properties, which would not affect the release of black rice ATC, but also reduced the effect of black rice ATC on the environment *in vivo* and avoided rapid degradation. Excluding the effect of embedding materials, free black rice ATC were rapidly degraded during the entire digestion process, and HAA nanocomposite particles significantly reduced the effect of black rice ATC on gastrointestinal digestive environment due to their good barrier ability, confirming the embedding protective effect of nanocomposites. This conclusion also confirmed the previous results that ATC could improve the stability of the external environment. In conclusion, the encapsulation of nanocomposite particles not only enhances the stability of black rice ATC *in vitro*, but also improves its absorption and bioavailability *in vivo* to a certain extent, indicating that the biological function of black rice ATC may be enhanced. Compared with free black rice ATC, HAA nanoparticles had a synergistic effect on XO *in vitro*. However, the binding characteristics of HA and black rice ATC synergistically inhibiting XO and their respective contributions to XO need further study. Moreover, the scope and limitations of the synergistic effect of HA and ATC still need to be further studied.

CONCLUSIONS

This study proposed a novel and efficient simple cross-linking method to prepare HAA nanocomposite particles to inhibit XO activity. Compared with the conventional chemical modification method, this method is simple to operate and does not require the addition of any organic solvents. The introduction of HA enhanced the stability of black rice ATC under different environmental stress (AA) and storage conditions (thermal and light). It delayed the release of black rice ATC *in vitro* (the total release amount of black rice ATC reached 60% at 60 h, with significant, sustained-release characteristics). The bioavailability of active compounds in *in vitro* digestion and absorption was improved. In addition, compared with free black rice ATC, the inhibition rate of XO activity was increased by 40.08%. This discovery indicates that HAA nanocomposite particles have the potential to stabilize and enhance the physiological activity of black rice ATC, which is of great significance for the development of novel nanocomposite materials for inhibiting XO activity. However, in this study, the preparation and characterization of the nanocomposite particles and the inhibition of XO were verified *in vitro*. Whether the black rice ATC and the HAA nanocomposite particles can play a good role in inhibiting XO activity and lowering uric acid *in vivo* remains to be further determined, which needs to be analyzed by animal experiments in later experiments.

DATA AVAILABILITY STATEMENT

The original contributions presented in the study are included in the article/**Supplementary Material**, further inquiries can be directed to the corresponding authors.

AUTHOR CONTRIBUTIONS

YL: conceptualization, methodology, data curation, formal analysis, writing—original draft, and writing—review and editing. BP: resources, writing—original draft, writing—review and editing, supervision, project administration, and funding acquisition. All authors contributed to the article and approved the submitted version.

FUNDING

This research was financed by the National Natural Science Foundation of China (Grant No. 31972063).

SUPPLEMENTARY MATERIAL

The Supplementary Material for this article can be found online at: https://www.frontiersin.org/articles/10.3389/fnut.2022.879354/full#supplementary-material

REFERENCES

1. Tung YT, Chang ST. Inhibition of xanthine oxidase by Acacia confusa extracts and their phytochemicals. *J Agric Food Chem.* (2010) 58:781–6. doi: 10.1021/jf901498q
2. Yee HS, Fong NT. A review of the safety and efficacy of acarbose in diabetes mellitus. *Pharmacother J Hum Pharmacol Drug Ther.* (1996) 16:792–805.
3. Hare JM, Mangal B, Brown J, Fisher C Jr, Freudenberger R, Colucci WS, et al. Impact of oxypurinol in patients with symptomatic heart failure.

Results of the OPT-CHF study. *J Am Coll Cardiol.* (2008) 51:2301–9. doi: 10.1016/j.jacc.2008.01.068
4. Stamp LK, Haslett J, Frampton C, White D, Gardner D, Stebbings S, et al. The safety and efficacy of benzbromarone in gout in Aotearoa New Zealand. *Intern Med J.* (2016) 46:1075–80. doi: 10.1111/imj.13173
5. Ito VC, Lacerda LG. Black rice (Oryza sativa L.): a review of its historical aspects, chemical composition, nutritional and functional properties, and applications and processing technologies. *Food Chem.* (2019) 301:125304. doi: 10.1016/j.foodchem.2019.125304
6. Kong S, Lee J. Antioxidants in milling fractions of black rice cultivars. *Food Chem.* (2010) 120:278–81. doi: 10.1016/j.foodchem.2009.09.089
7. Ling WH, Wang LL, Ma J. Supplementation of the black rice outer layer fraction to rabbits decreases atherosclerotic plaque formation and increases antioxidant status. *J Nutr.* (2002) 132:20–6. doi: 10.1093/jn/132.1.20
8. Hu C, Zawistowski J, Ling WH, Kitts DD. Black rice (*Oryza sativa* L. indica) pigmented fraction suppresses both reactive oxygen species and nitric oxide in chemical and biological model systems. *J Agric Food Chem.* (2003) 51:5271–7. doi: 10.1021/jf034466n
9. Hui C, Bin Y, Xiaoping Y, Long Y, Chunye C, Mantian M, et al. Anticancer activities of an anthocyanin-rich extract from black rice against breast cancer cells *in vitro* and *in vivo*. *Nutr Cancer.* (2010) 62:1128–36. doi: 10.1080/01635581.2010.494821
10. Yang Y, Zhang ZC, Zhou Q, Yan JX, Zhang JL, Su GH. Hypouricemic effect in hyperuricemic mice and xanthine oxidase inhibitory mechanism of dietary anthocyanins from purple sweet potato (*Ipomoea batatas* L.). *J Funct Foods.* (2020) 73:104151. doi: 10.1016/j.jff.2020.104151
11. Liu YX, Zhang D, Wu YP, Wang D, Wei Y, Wu JL, et al. Stability and absorption of anthocyanins from blueberries subjected to a simulated digestion process. *Int J Food Sci Nutr.* (2014) 65:440–8. doi: 10.3109/09637486.2013.869798
12. Gonzalez-Barrio R, Borges G, Mullen W, Crozier A. Bioavailability of anthocyanins and ellagitannins following consumption of raspberries by healthy humans and subjects with an ileostomy. *J Agric Food Chem.* (2010) 58:3933–9. doi: 10.1021/jf100315d
13. Ge J, Yue PX, Chi JP, Liang J, Gao XL. Formation and stability of anthocyanins-loaded nanocomplexes prepared with chitosan hydrochloride and carboxymethyl chitosan. *Food Hydrocoll.* (2018) 74:23–31. doi: 10.1016/j.foodhyd.2017.07.029
14. He B, Ge J, Yue PX, Yue XY, Fu RY, Liang J, et al. Loading of anthocyanins on chitosan nanoparticles influences anthocyanin degradation in gastrointestinal fluids and stability in a beverage. *Food Chem.* (2017) 221:1671–7. doi: 10.1016/j.foodchem.2016.10.120
15. Choi KY, Saravanakumar G, Park JH, Park K. Hyaluronic acid-based nanocarriers for intracellular targeting: interfacial interactions with proteins in cancer. *Colloids Surf B Biointerfaces.* (2012) 99:82–94. doi: 10.1016/j.colsurfb.2011.10.029
16. Guo CJ, Yin JG, Chen DQ. Co-encapsulation of curcumin and resveratrol into novel nutraceutical hyalurosomes nano-food delivery system based on oligo-hyaluronic acid-curcumin polymer. *Carbohydr Polym.* (2018) 181:1033–7. doi: 10.1016/j.carbpol.2017.11.046
17. Toole BP. Hyaluronan: from extracellular glue to pericellular cue. *Nat Rev Cancer.* (2004) 4:528–39. doi: 10.1038/nrc1391
18. Camacho KM, Kumar S, Menegatti S, Vogus DR, Anselmo AC, Mitragotri S. Synergistic antitumor activity of camptothecin-doxorubicin combinations and their conjugates with hyaluronic acid. *J Control Release.* (2015) 210:198–207. doi: 10.1016/j.jconrel.2015.04.031
19. Zhu MQ, Ge LU, Qiu LP. Preparation and characterization of hyaluronic acid copolymeric micelles. *Chem Ind Eng Prog.* (2016) 35:283–6. doi: 10.16085/j.issn.1000-6613.2016.s2.048
20. Chytil M, Pekar M. Effect of new hydrophobic modification of hyaluronan on its solution properties: evaluation of self-aggregation. *Carbohydr Polym.* (2009) 76:443–8. doi: 10.1016/j.carbpol.2008.11.003
21. Jeong SH, Sun JY, Kim HE. Dual-crosslinking of hyaluronic acid-calcium phosphate nanocomposite hydrogels for enhanced mechanical properties and biological performance. *Macromol Mater Eng.* (2017) 302:1700160. doi: 10.1002/mame.201700160
22. Xiong Q, Wang YW, Wan JY, Yuan P, Chen HL, Zhang LK. Facile preparation of hyaluronic acid-based quercetin nanoformulation for targeted tumor therapy. *Int J Biol Macromol.* (2020) 147:937–45. doi: 10.1016/j.ijbiomac.2019.10.060
23. Cui HJ, Si X, Tian JL, Lang YX, Gao NX, Tan H, et al. Anthocyanins-loaded nanocomplexes comprising casein and carboxymethyl cellulose: stability, antioxidant capacity, and bioaccessibility. *Food Hydrocoll.* (2022) 122:107073. doi: 10.1016/j.foodhyd.2021.107073
24. Jeong D, Na K. Chondroitin sulfate based nanocomplex for enhancing the stability and activity of anthocyanin. *Carbohydr Polym.* (2012) 90:507–15. doi: 10.1016/j.carbpol.2012.05.072
25. Liang HS, Zhou B, He L, An YP, Lin LF, Li Y, et al. Fabrication of zein/quaternized chitosan nanoparticles for the encapsulation and protection of curcumin. *RSC Adv.* (2015) 5:13891–900. doi: 10.1039/C4RA14270E
26. Faller ALK, Fialho E, Liu RH. Cellular antioxidant activity of feijoada whole meal coupled with an *in vitro* digestion. *J Agric Food Chem.* (2012) 60:4826–32. doi: 10.1021/jf300602w
27. Zhang C, Zhang GW, Pan JH, Gong DM. Galangin competitively inhibits xanthine oxidase by a ping-pong mechanism. *Food Res Int.* (2016) 89:152–60. doi: 10.1016/j.foodres.2016.07.021
28. Liang TS, Zhang ZT, Jing P. Black rice anthocyanins embedded in self-assembled chitosan/chondroitin sulfate nanoparticles enhance apoptosis in HCT-116 cells. *Food Chem.* (2019) 301:125280. doi: 10.1016/j.foodchem.2019.125280
29. Zhu KK, Ye T, Liu JJ, Peng Z, Xu SS, Lei JQ, et al. Nanogels fabricated by lysozyme and sodium carboxymethyl cellulose for 5-fluorouracil controlled release. *Int J Pharm.* (2013) 441:721–7. doi: 10.1016/j.ijpharm.2012.10.022
30. Ren ZY, Li ZM, Chen ZZ, Zhang YY, Lin XR, Weng WY, et al. Characteristics and application of fish oil-in-water pickering emulsions structured with tea water-insoluble proteins/κ-carrageenan complexes. *Food Hydrocoll.* (2021) 114:106562. doi: 10.1016/j.foodhyd.2020.106562
31. Yang Z, Yang HJ, Yang HS. Effects of sucrose addition on the rheology and microstructure of κ-carrageenan gel. *Food Hydrocoll.* (2018) 75:164–73. doi: 10.1016/j.foodhyd.2017.08.032
32. Lan S, Wu XM, Li LL, Li MM, Guo FY, Gan SC. Synthesis and characterization of hyaluronic acid-supported magnetic microspheres for copper ions removal. *Colloids Surf A Physicochemical Eng Aspects.* (2013) 425:42–50. doi: 10.1016/j.colsurfa.2013.02.059
33. Sow LC, Yang HS. Effects of salt and sugar addition on the physicochemical properties and nanostructure of fish gelatin. *Food Hydrocoll.* (2015) 45:72–82. doi: 10.1016/j.foodhyd.2014.10.021
34. Cai XR, Du XF, Cui DM, Wang XN, Yang ZK, Zhu GL. Improvement of stability of blueberry anthocyanins by carboxymethyl starch/xanthan gum combinations microencapsulation. *Food Hydrocoll.* (2019) 91:238–45. doi: 10.1016/j.foodhyd.2019.01.034
35. Chung C, Rojanasasithara T, Mutilangi W, Mcclements DJ. Enhanced stability of anthocyanin-based color in model beverage systems through whey protein isolate complexation. *Food Res Int.* (2015) 76:761–8. doi: 10.1016/j.foodres.2015.07.003
36. Guldiken B, Gibis M, Boyacioglu D, Capanoglu E, Weiss J. Impact of liposomal encapsulation on degradation of anthocyanins of black carrot extract by adding ascorbic acid. *Food Funct.* (2017) 8:1085–93. doi: 10.1039/C6FO01385F
37. Chung C, Rojanasasithara T, Mutilangi W, Mcclements DJ. Enhancement of colour stability of anthocyanins in model beverages by gum arabic addition. *Food Chem.* (2016) 201:14–22. doi: 10.1016/j.foodchem.2016.01.051
38. Sadilova E, Stintzing FC, Kammerer DR, Carle R. Matrix dependent impact of sugar and ascorbic acid addition on color and anthocyanin stability of black carrot, elderberry and strawberry single strength and from concentrate juices upon thermal treatment. *Food Res Int.* (2009) 42:1023–33. doi: 10.1016/j.foodres.2009.04.008
39. Sari P, Wijaya CH, Sajuthi D, Supratman U. Colour properties, stability, and free radical scavenging activity of jambolan (Syzygium cumini) fruit anthocyanins in a beverage model system: natural and copigmented anthocyanins. *Food Chem.* (2012) 132:1908–14. doi: 10.1016/j.foodchem.2011.12.025
40. Oliveira A, Pintado M. *In vitro* evaluation of the effects of protein–polyphenol–polysaccharide interactions on (+)-catechin and cyanidin-3-glucoside bioaccessibility. *Food Funct.* (2015) 6:3444–53. doi: 10.1039/C5FO00799B

41. Woodward G, Kroon P, Cassidy A, Kay C. Anthocyanin stability and recovery: implications for the analysis of clinical and experimental samples. *J Agric Food Chem.* (2009) 57:5271–8. doi: 10.1021/jf900602b
42. Huang HZ, Sun YJ, Lou ST, Li H, Ye XQ. *In vitro* digestion combined with cellular assay to determine the antioxidant activity in Chinese bayberry (*Myrica rubra Sieb*. et Zucc.) fruits: A comparison with traditional methods. *Food Chem.* (2014) 146:363–70. doi: 10.1016/j.foodchem.2013.09.071
43. Feng J, Wu YH, Zhang LX, Li Y, Liu SB, Wang H, et al. Enhanced chemical stability, intestinal absorption, and intracellular antioxidant activity of cyanidin-3- O-glucoside by composite nanogel encapsulation. *J Agric Food Chem.* (2019) 67:10432–47. doi: 10.1021/acs.jafc.9b04778
44. Gupta RC, Lall R, Srivastava A, Sinha A. Hyaluronic acid: molecular mechanisms and therapeutic trajectory. *Front Vet Sci.* (2019) 6:192. doi: 10.3389/fvets.2019.00192
45. Lee JY, Jo YU, Shin H, Lee J, Chae SU, Bae SK, et al. Anthocyanin-fucoidan nanocomplex for preventing carcinogen induced cancer: enhanced absorption and stability. *Int J Pharm.* (2020) 586:119597. doi: 10.1016/j.ijpharm.2020.119597
46. Tan C, Selig MJ, Abbaspourrad A. Anthocyanin stabilization by chitosan-chondroitin sulfate polyelectrolyte complexation integrating catechin co-pigmentation. *Carbohydr Polym.* (2018) 181:124–31. doi: 10.1016/j.carbpol.2017.10.034
47. Robert P, Gorena T, Romero N, Sepulveda E, Chavez J, Saenz C. Encapsulation of polyphenols and anthocyanins from pomegranate (*Punica granatum*) by spray drying. *Int J Food Sci Technol.* (2010) 45:1386–94. doi: 10.1111/j.1365-2621.2010.02270.x

Conflict of Interest: The authors declare that the research was conducted in the absence of any commercial or financial relationships that could be construed as a potential conflict of interest.

Publisher's Note: All claims expressed in this article are solely those of the authors and do not necessarily represent those of their affiliated organizations, or those of the publisher, the editors and the reviewers. Any product that may be evaluated in this article, or claim that may be made by its manufacturer, is not guaranteed or endorsed by the publisher.

Copyright © 2022 Liu and Peng. This is an open-access article distributed under the terms of the Creative Commons Attribution License (CC BY). The use, distribution or reproduction in other forums is permitted, provided the original author(s) and the copyright owner(s) are credited and that the original publication in this journal is cited, in accordance with accepted academic practice. No use, distribution or reproduction is permitted which does not comply with these terms.

frontiers | Frontiers in Nutrition

ORIGINAL RESEARCH
published: 25 April 2022
doi: 10.3389/fnut.2022.848857

Nano-Sized Antioxidative Trimetallic Complex Based on Maillard Reaction Improves the Mineral Nutrients of Apple (*Malus domestica* Borkh.)

*Yu-zhang Yang, Qin-ping Wei, Jia Zhou, Min-ji Li, Qiang Zhang, Xing-liang Li, Bei-bei Zhou and Jun-ke Zhang**

Institute of Forestry and Pomology, Beijing Academy of Agriculture and Forestry Sciences, Beijing, China

OPEN ACCESS

Edited by:
Fuguo Liu,
Northwest A&F University, China

Reviewed by:
Parmanand Malvi,
Yale University, United States
Biao Yuan,
China Pharmaceutical University, China

***Correspondence:**
Jun-ke Zhang
zhangjunke@baafs.net.cn

Specialty section:
This article was submitted to Food Chemistry, a section of the journal Frontiers in Nutrition

Received: *05 January 2022*
Accepted: *07 March 2022*
Published: *25 April 2022*

Citation:
Yang Y-z, Wei Q-p, Zhou J, Li M-j, Zhang Q, Li X-l, Zhou B-b and Zhang J-k (2022) Nano-Sized Antioxidative Trimetallic Complex Based on Maillard Reaction Improves the Mineral Nutrients of Apple (Malus domestica Borkh.). Front. Nutr. 9:848857. doi: 10.3389/fnut.2022.848857

The metallic complex is widely used in agricultural applications. Due to the oxidation of the metal and environmental unfriendliness of ligand, maintaining an efficient mineral supply for plants without causing environmental damage is difficult. Herein, an antioxidative trimetallic complex with high stability was synthesized by interacting Ca^{2+}, Fe^{2+}, and Zn^{2+} with the biocompatible ligands from the Maillard reaction. The composite structure elucidation was carried out by transmission electron microscopy (TEM), scanning electron microscopy (SEM), X-ray photoelectron spectroscopy (XPS), and Fourier transform infrared (FTIR). Thermal stability was measured by thermogravimetric (TG). Antioxidative activities were evaluated by ferric reducing antioxidant power and radical scavenging activity assays. The three metals were successfully fabricated on the Maillard reaction products (MRPs) with contents of Ca (9.01%), Fe (8.25%), and Zn (9.67%). Microscopy images revealed that the three metals were uniformly distributed on the MRPs with partial aggregation of <30 nm. FTIR and XPS results revealed that the metals were interacted with MRPs by metal–O and metal–N bonds. TG and antioxidative activity assays showed that the trimetallic complex meets the requirements of thermodynamics and oxidation resistance of horticultural applications. Additionally, the results of the exogenous spraying experiment showed that the trimetallic complex significantly increased the mineral contents of the "Fuji" apple. By treatment with the complex, the concentrations of Ca, Fe, and Zn were increased by 85.4, 532.5, and 931.1% in the leaf; 16.0, 225.2, and 468.6% in the peel; and 117.6, 217.9, and 19.5% in the flesh, respectively. The MRP-based complexes offered a higher growth rate of the mineral content in apples than ones based on sugars or amino acids. The results of the spraying experiment carried out in 2 years show that the method has high reproducibility. This study thus promotes the development of green metallic complexes and expands the scope of agrochemical strategy.

Keywords: trimetallic complex, Maillard reaction, antioxidative activity, fruit quality, mineral nutrients

INTRODUCTION

Mineral nutrients, generally deemed metal elements, benefit the storage, disease prevention, bioactivity, and internal quality of fruits (1–4). However, metal ions form insoluble metal oxides and consequently tend to persist in soil rather than be absorbed by plants (5, 6), and the characteristics of facile oxidation and precipitation of metal elements are amplified in the alkaline and calcareous environment which covers more than 30% of the global land surface (7, 8). Supplements and improvement in the content of mineral nutrients of fruits are subject to soil conditions; therefore, it requires human management in the orchards. Existing strategies take advantage of extraneous spraying of mineral nutrients. However, the application of soluble minerals is inefficient because a significant portion of metal ions is oxidized before they go into the plants. Conventional approaches for augmenting the stability of mineral elements rely on the use of metallic complex which is structured with synthetic or biological ligands (9–11). The ligands offer oxygen- or nitrogen-containing groups to form coordination bonds with metal ions to improve ion stability. Although metallic complexes can address these problems to a certain extent, many metallic complexes are either inefficient or costly and may adversely affect the environment (12–14). Therefore, developing biodegradable, eco-friendly, and absorption-promoted ligands of mineral elements are desirable for biological applications.

Antioxidative materials have attracted tremendous research interest in the field of food and medical engineering owing to their ability to construct carrier structures that can protect and deliver payloads into specific receptors (15–17). Of these, Maillard reaction products (MRPs) produced through the Maillard reaction (MR), which is a non-enzymatic browning reaction and widespread in food processing involving carbonyl and amino compounds (18–20), are efficient ligands for capturing metal ions for application in food additives and drug delivery (21, 22). The complicated structures of MRPs supply numerous binding sites with metal ions under mild conditions, thus offering a potential method for simultaneously capturing multiple metals, such as Ca^{2+}, Fe^{2+}, Zn^{2+}, Cu^{2+}, and Mg^{2+}, to improve their solubility (23). Previously, we have proved that the alkaline stability of Fe^{2+} can be improved by MRPs (24). The polymerized fraction of MRPs generated under alkaline conditions has the capability to turn the interaction of MRPs and Fe^{2+} from low binding affinity to high binding affinity by constructing more Fe–N bonds. Moreover, MRPs have been proven to be antimicrobial and biodegradable for biological applications (25–29). Thus, we suggested that MRPs have great potential in agricultural applications because they are not only an antioxidative ligand that can capture metals and prevent their oxidation but also a biocompatible carrier that guarantees sustained mineral supply for plants.

In contrast, the efficient transport of minerals to plants requires further resolution. Minerals move passively through the transpiration flux from the roots. However, fruits have a low transpiration surface in relation to their volume, and their mobility of nutrients through the phloem, which transports sugars from leaves to developing fruits, is ineffective (30). The limited mobility makes it necessary that spraying minerals on plants are applied directly since apparent mineral nutrients are not easily re-translocated from other organs to the fruit (31–34). Many studies have been carried out to study the spray effect of metal salts (35–37), metal oxides (38, 39), and metal complexes (40–43) on plant growth. Ca sprays are more effective than soil applications at allocating and increasing the Ca content in the apple fruits and could help reduce the incidence of Ca-related disorders (44, 45). Zn sprays enhance the fruit Zn content and result in the higher activities of carbohydrate metabolism-related enzymes, contributing to the accumulation of carbohydrates (46). Fe sprays increase the concentrations in leaves and decrease the fruit firmness and total phenolic compounds (40, 47), while they are considered a highly effective method for preventing and amending iron chlorosis (48). Although the impact of exogenous mineral treatments on fruits has been studied and utilized extensively, there is still a lack of research focusing on mineral nutrition. Mineral resources of metal salts, which could increase mineral nutrients in fruits, are restricted by oxidation in general use. Fertilizers consisting of the individual metal complex are expected to be more effective than the ones based on unchelated metal salts due to their improved stability and biocompatibility endowed by organic ligands. However, few studies have focused on the effect of poly-metal complex fertilizers on plant growth or fruit quality, successfully improving the contents of various mineral nutrients in fruits through surface treatment remains a challenge.

Given that the total area harvested worldwide of apple exceeds 4.6 mha, with a production of over 86.4 million tons (49), an ideal metallic complex designed to improve the nutrient content of apples can significantly enhance cultivation efficiency and subsequently increase economic value and stimulate the vitality of the market (50). Furthermore, the development and application of an innovative fertilizer with improved stability and reduced cost are desired in agriculture fields. Herein, by fusion of synthetic organic chemistry and plant physiology, we reported the synthetic method of MRP-based antioxidative complexes of Ca, Fe, Zn, and the trimetallic complex and investigated the effects of the complexes on apple mineral nutrients by exogenous treatments. This study provides a novel strategy for integrating metals into one complex. It will serve as a basis for developing effective fertilizers for improving the content of fruit mineral nutrients.

MATERIALS AND METHODS

Materials

Glucose and L-lysine were purchased from Macklin Co., Ltd (Shanghai, China). Ferrous sulfate heptahydrate ($FeSO_4{\cdot}7H_2O$), calcium chloride ($CaCl_2$), and zinc sulfate heptahydrate ($ZnSO_4{\cdot}7H_2O$) were purchased from the Aladdin Co., Ltd (Shanghai, China). Ethanol, *n*-hexane, and ammonium hydroxide (20%, NH_4OH) were purchased from Sinopharm Chemical Reagent Co., Ltd (Shanghai, China). Tripyridyltriazine (TPTZ), 1,1-diphenyl-2-picryl-hydrazil (DPPH), and 2,2′-azinobis(3-ethylbenothiazoline-6-sulphonic acid) diammonium salt (ABTS) were obtained from Solarbio Science and Technology

Co., Ltd (Beijing, China). Other chemicals were of analytical grade and supplied by Zhongxingweiye Chemicals Co., Ltd (Beijing, China). All chemicals were used as received. Distilled water was self-made.

Synthesis of Metallic Complexes

Metallic complexes were prepared by reacting metal inorganic salts with glucose and lysine under a thermal process. In brief, to prepare Ca complex (MRPs–Ca), a solution of lysine (7.3 g, 50 mmol) in distilled water (150 ml) was heated to 50°C, followed by a solution of glucose (9.0 g, 50 mmol, 100 ml) was added. After given reaction time at 90°C, $CaCl_2$ (5.0 g, 45 mmol) was added to the solution. After 6 h stirring, the solution was cooled down to room temperature, then NH_4OH (5 ml) was added to precipitate unreacted Ca. Prior to filtration, the solution was kept stirring until NH_4OH was volatilized completely. The filtrate was freeze-dried and then washed with the solution of ethanol and *n*-hexane (100 ml, $V_{ethanol}$:$V_{n-hexane}$ =3:1) for 3 times. The final product was obtained after filtration and desiccation under 50°C for 12 h. Fe complex (MRPs–Fe) and Zn complex (MRPs–Zn) were prepared following the method with $FeSO_4 \cdot 7H_2O$ (10.0 g, 40 mmol) and $ZnSO_4 \cdot 7H_2O$ (12.0 g, 42 mmol), respectively. The trimetallic complex (MRPs–Ca/Fe/Zn) was prepared by adding $FeSO_4 \cdot 7H_2O$ (10.0 g, 40 mmol), $ZnSO_4 \cdot 7H_2O$ (12.0 g, 42 mmol), and $CaCl_2$ (5.0 g, 45 mmol) into the Maillard reaction system at optimized periods (discussed later). The MRPs were prepared without metal salts.

Measurement of Reaction Degrees

The reaction degree of glucose-lysine interaction was monitored by the absorbance of the solutions at a wavelength λ of 420 nm. UV spectra were recorded using a Purkinje General TU-1901 spectrophotometer.

Characterization of Metallic Complexes

The metal contents of the complexes were measured by inductively coupled plasma optical emission spectrometry (ICP-OES) at 25 ± 0.1°C using an Agilent 5110. The size and morphology of the complexes were characterized by transmission electron microscopy (TEM) using an FEI Tecnai G2 F20. The size distribution was determined by measuring at least 50 microspheres from TEM images followed by statistical treatment. The microstructures of the samples were observed by scanning electron microscopy (SEM) with a SEU8010. The zeta potentials of the complexes were measured using a Zetasizer nano. Samples were mixed in absolute ethanol with a concentration of 0.1% (w/v) and immediately transferred into the quartz cuvette for determination. Fourier transform infrared (FTIR) spectra were recorded in the range of 400–4,000 cm^{-1} using a Perkin-Elmer Spectrum 400 spectrometer. The powder samples were dried and ground with potassium bromide in a volume ratio of 1:100. The elemental composition and chemical status of the electrodes were analyzed by X-ray photoelectron spectroscopy (XPS, EscaLab 250, Thermo Fisher Scientific) with a monochromatic Al Kα as the excitation source. The energy calibration was made against the C 1s peak. Thermogravimetric (TG) analyses were performed with a NETZSCH STA 449F3 at the heating rate of 10°C·min^{-1} from 30 to 500°C in a dynamic nitrogen atmosphere.

Measurement of Antioxidative Activity

The antioxidant capacity by ferric reducing antioxidant power (FRAP) assay is based on the reduction of Fe(III)-tripyridyltriazine (TPTZ) to a blue-colored Fe(II)-TPTZ. The FRAP reagent was prepared with 2.5 ml of 20 mM $FeCl_3 \cdot 6H_2O$, 25 ml 0.3 mM acetate buffer, and 2.5 ml of a 10 mM 2,4,6-tripyridyl-s-triazine (TPTZ) solution in 40 mM HCl. Vitamin C was used as a standard, the FRAP reagent was used as blank control, and the sample was prepared at a concentration of 1 mg·ml^{-1} (**Supplementary Figure 1**). Notably, 30 μl of the sample with 5-fold dilution, standard, and blank reagent were mixed with 500 μl of FRAP reagent and 2,000 μl of distilled water, respectively. After 30 min incubation at 37°C, the absorbance of the solutions at a wavelength λ of 593 nm was recorded using a Purkinje General TU-1901 spectrophotometer. Calibration was performed with vitamin C solution.

$$\text{Ferric reducing antioxidant power \%} = \left(\frac{A_{\text{sample}} - A_{\text{control}}}{A_{\text{sample}}}\right) 100\% \quad (1)$$

The radical scavenging activity was determined by the decolorization of 1,1-diphenyl-2-picryl-hydrazil (DPPH). The DPPH regent was prepared at a concentration of 0.12 mM and protected from light. Vitamin C was used as a standard, the DPPH reagent was used as blank control, and the sample was prepared at a concentration of 1 mg·ml^{-1} (**Supplementary Figure 1**). An aliquot of 1 ml of DPPH reagent was added to 100 μl of the sample with 5-fold dilution and 2 ml of distilled water. The solution was allowed to stand at room temperature in the dark for 30 min. The absorbance of the solutions at a wavelength λ of 515 nm was recorded using a Purkinje General TU-1901 spectrophotometer. The antiradical activity was expressed as a percentage of the disappearance of the initial purple color. Calibration was performed with vitamin C solution.

$$\text{DPPH radical scavenging activity \%} = \left(\frac{A_{control} - A_{sample}}{A_{control}}\right) 100\% \quad (2)$$

The radical cation decolorization activity was determined based on 2,2′-azinobis(3-ethylbenothiazoline-6-sulphonic acid) diammonium salt (ABTS). The ABTS regent was prepared at a concentration of 7 mM with 2.45 mM potassium persulfate and kept in the dark at room temperature for 12 h. Vitamin C was used as a standard, the DPPH reagent was used as blank control, and the sample was prepared at a concentration of 1 mg·ml^{-1} (**Supplementary Figure 1**). An aliquot of 1 ml of the solution was mixed with 30 μl of the sample and 2 ml of distilled water for 45 s. The absorbance of the solutions at a wavelength λ of 734 nm was recorded using a Purkinje General TU-1901 spectrophotometer.

The antiradical activity was expressed as the percentage of the disappearance of the initial blue color. Calibration was performed with vitamin C solution.

$$\text{ABTS radical scavenging activity \%} = \left(\frac{A_{control} - A_{sample}}{A_{control}}\right) 100\% \quad (3)$$

Plant Materials

The spraying experiment was conducted in an orchard located in Beijing, China (39° 57′ 59″ N, 116°13′ 22″ E). Six-year-old trees of apple (*Malus domestica* cultivars "Fuji") were chosen based on the uniformity of tree size. Trees were not treated with growth regulators or phytohormone-containing preparations. Control of pathogens and pests was performed according to the recommendations for integrated apple production.

Treatments and Experiment Layout

The concentration of solution for spray was based on the mass fraction of the metal element. The control treatment was sprayed with water. Low (L), medium (M), and high (H) concentrations of MRPs–Ca/Fe/Zn were sprayed at a given period (**Table 1**). For uniform coverage, 10 L solution was applied per tree, 0.2% tween-20 (v/v) was added to the solutions as a surfactant. The leaves and fruits without any covers were sprayed on the surfaces with machines backpack up to runoff in the morning (8:00–10:00 a.m.). Each treatment consisted of 3 replicates with 3 trees. Ten fruit samples were randomly harvested from each tree. Leaf samples were collected from the middle part of the new branches of the year.

Determination of Fruit Quality

To measure the weight (g), the fruits immediately after harvest were recorded using a digital balance. Flesh firmness was determined using a force gauge (GY-1, WDGage, China) on the two opposite sides of the fruit without skin.

To evaluate fruit soluble solid contents (SSCs) and titratable acidity (TA), a sample of juice was taken from one piece of each fruit. SSCs were determined using a digital refractometer (PAL-BX/ACID12, Atago, Japan) and expressed as a percentage. TA was determined by titrating 3 ml of juice in 27 ml distilled H_2O with 0.1 N NaOH to pH 8.1 and expressed as % malic acid.

To assess the mineral composition, 5 g leaves were washed with distilled water, and 5 g peels and 10 g longitudinal slices were obtained from each fruit, respectively. The samples were dried in an oven at 105°C for 30 min for deactivation of enzymes and then at 75°C for 48 h for dehydration. Ash was produced at 500°C for 8 h, then dissolved in 5 ml of 1N HCl, and filtered through a filter paper. Concentrations of Ca, Fe, and Zn were determined using an atomic absorption spectrophotometer (Z-2000, Hitachi, Japan) at 422.7, 248.3, and 213.9 nm, respectively.

To determine the total N content, the Kjeldahl method was used. The content of N was determined using a continuous flow analysis system (AA3, SEAL, Germany) at 660 nm.

Statistical Analysis

Statistical analysis was performed using SPSS (version 11.0, SPSS Inc., Chicago, USA). The data were subjected to the analysis of variance and expressed as the mean ± standard error (SE) ($n = 3$). Mean comparisons were performed using the least significant difference (LSD) test at a significance level of $P < 0.05$.

RESULTS AND DISCUSSION

Synthesis of the Trimetallic Complexes

The complexes were synthesized under heating conditions in the presence of glucose and lysine, a classical MR with high reactivity (51). To obtain high coordination ability with metal ions, a time-based synthetic process was studied. Superfluous metal salts were added into the system at different periods of the MR system, and metal combination rates were determined by checking the mass percentages of the final products. Prior to that, ammonia water was used to remove unreacted metals. Since

TABLE 1 | The design of the spray treatment of MRPs- Ca/Fe/Zn.

Treatment	Concentration[a]	Period				
		May 15th	June 15th	July 16th	August 15th	December 17th
T1	L	√				√
T2	L	√		√		√
T3	L	√	√	√	√	√
T4	M	√				√
T5	M	√		√		√
T6	M	√	√	√	√	√
T7	H	√				√
T8	H	√		√		√
T9	H	√	√	√	√	√
Control[b]		√	√	√	√	√

[a] *The concentration was calculated by mass fraction of the metal element. L (Ca: 0.27%, Fe: 0.25%, and Zn: 0.29%); M (Ca: 0.54%, Fe: 0.5%, and Zn: 0.58%); H (Ca: 0.9%, Fe: 0.83%, and Zn: 0.97%).*

[b] *The control was performed by distilled water.*

the reason for the interactions of metals and MRPs was different, the reaction process and coordination were different. As shown in **Figure 1**, the introduction of metals depressed the degree of MR. In the presence of metals, the degree increased when Ca^{2+} was added at an earlier or later stage; however, there was no significant change in the Ca content of MRPs–Ca whenever Ca^{2+} was added into the system (**Supplementary Table 1**). In contrast, premature addition of Fe^{2+} and Zn^{2+} caused a lower degree of MR, suggesting that Fe^{2+} and Zn^{2+} have inhibitory effects on the MR. However, higher Fe and Zn contents of MRPs–Fe and MRPs–Zn were achieved by adding inorganic salts in the initial periods. Therefore, to load more metals, the MRPs–Ca, MRPs–Fe, and MRPs–Zn were synthesized by adding the relevant salts after 3, 1, and 1 h of MR, respectively. The addition of Ca^{2+} and SO_4^{2-} in the system at different periods helped prepare soluble substances. Ultimately, MRPs–Ca/Fe/Zn was synthesized with 9.01%, 8.25%, and 9.67% contents of Ca, Fe, and Zn, respectively.

Structure of the Trimetallic Complexes

The TEM images (**Figure 2A**) illustrate that MRPs–Ca/Fe/Zn was amorphous owing to the glycosylated MRP structure. Metal ions were dispersed on film-like MRPs with partial aggregation of <30 nm. The elemental mapping images clearly demonstrate that Ca, Fe, and Zn were uniformly distributed in MRPs–Ca/Fe/Zn, indicating that the three metals were successfully integrated into the MRPs (**Figure 2B**). The SEM images (**Figure 2C** and **Supplementary Figure 2**) show that the morphology of the MRPs turned from a quasi-circular spheroid with a smooth

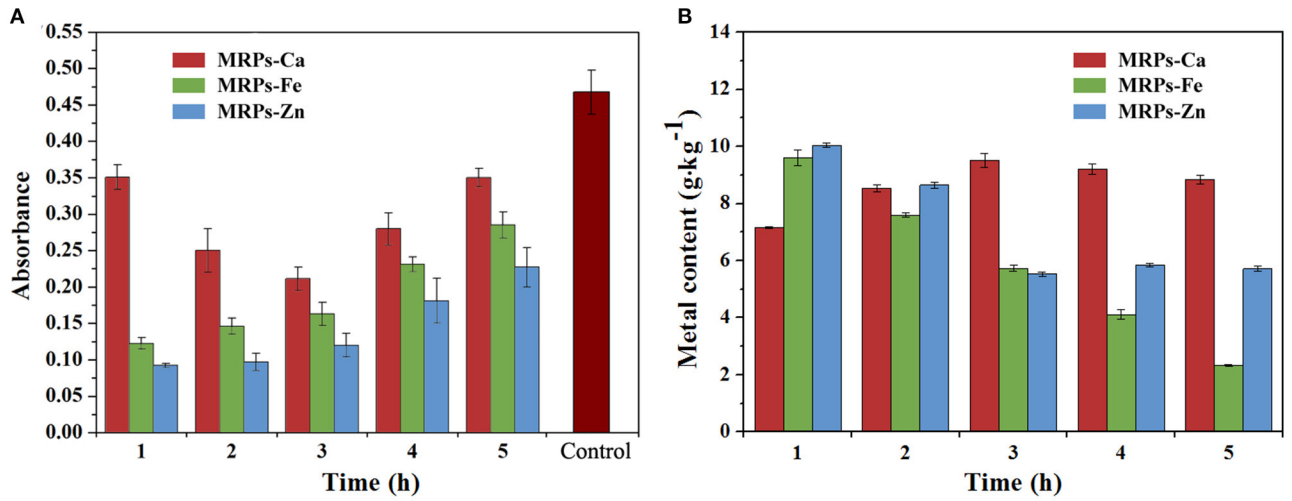

FIGURE 1 | Reaction degrees of the Maillard reaction (MR) **(A)** and metal contents of Maillard reaction products (MRPs)–Ca, MRPs–Fe, and MRPs–Zn **(B)**. The horizontal axis presents the reaction time of the MR when the metal is added. The control is MR without metals.

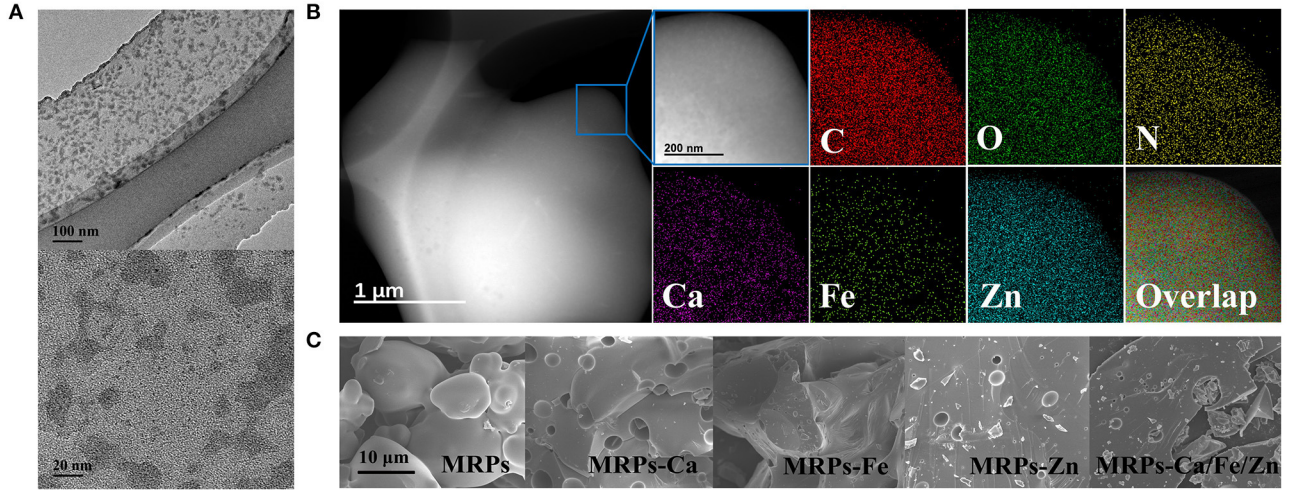

FIGURE 2 | Transmission electron microscopy (TEM) images of MRPs–Ca/Fe/Zn **(A)**. STEM images and corresponding elemental mapping analysis of MRPs–Ca/Fe/Zn **(B)**. Scanning electron microscopy (SEM) images of MRPs, MRPs–Ca, MRPs–Fe, MRPs–Zn, and MRPs–Ca/Fe/Zn **(C)**.

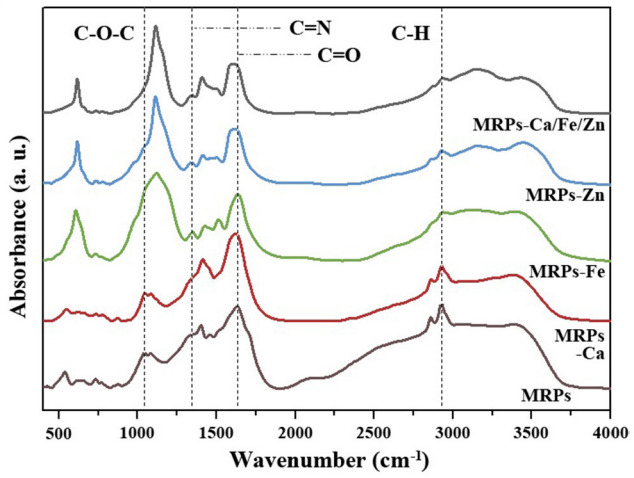

FIGURE 3 | Fourier transform infrared (FTIR) spectra of MRPs, MRPs–Ca, MRPs–Fe, MRPs–Zn, and MRPs–Ca/Fe/Zn.

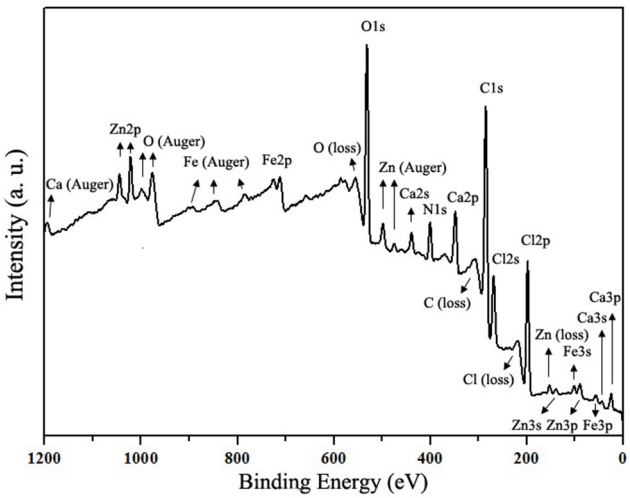

FIGURE 4 | X-ray photoelectron spectroscopy (XPS) spectrum of MRPs–Ca/Fe/Zn.

surface into a blocky structure with non-homogeneous defects by interacting with the metals. The ζ-potential of the MRPs changed from 0.02 to −4.06, 1.38, 3.11, and 1.30 for the MRP-based Ca, Fe, Zn, and Ca/Fe/Zn complexes, respectively (**Supplementary Figure 3** and **Supplementary Table 2**).

The FTIR spectra of MRPs–Ca, MRPs–Fe, MRPs–Zn, and MRPs–Ca/Fe/Zn significantly differed from the raw materials (**Supplementary Figures 4, 5**), indicating the formation of the complexes. **Figure 3** shows that all complexes contained huge amounts of –OH groups and intermolecular hydrogen bonds based on the broad peaks observed at 3,000–3,600 cm^{-1}. Moreover, the spectra suggest that the complexes contain crystalline water. The peak of the C–H vibration centered at 2,927 cm^{-1} of the MRPs was weakened by interaction with metal ions. The peak at 1,629 cm^{-1} of the MRPs, which could be regarded as the C=O of the carboxyl group, was red-shifted in MRPs–Ca, MRPs–Zn, and MRPs–Ca/Fe/Zn, indicating the formation of O–metal bonds (52). The similarity in the spectra of MRPs–Ca and MRPs was caused by the equal reaction degrees, which correspond to the insignificant influence of Ca^{2+} on the MR. The peaks at 607 and 1,121 cm^{-1} in MRPs–Fe, MRPs–Zn, and MRPs–Ca/Fe/Zn, attributable to SO_4^{2-}, were prominent, making the peaks of the C–O–C of the aromatic alkoxy at ∼1,042 cm^{-1} to appear as shoulders (53). The coexistence of Ca^{2+} and SO_4^{2-} confirmed that the metal was prevented from precipitating. Consequently, the interaction of metal ions and MRPs was confirmed, and the trimetallic complex was successfully obtained.

The full-scan XPS spectrum of MRPs–Ca/Fe/Zn is shown in **Figure 4**. The complex contained C, O, N, Ca, Fe, Zn, and Cl. The prominent peaks of C 1s and O 1s at a binding energy of ∼285 and 532 eV, respectively, were originated from the MRPs on the surface. Besides, the intensities of photoelectron lines of Cl were relatively higher, indicating the Cl^- preferred to combine on the surface. The deconvoluted high-resolution XPS spectra are illustrated in **Figure 5**. The three C 1s peaks at 284.2, 285.4, and 287.5 eV were assigned to the carbon as C–C/C–H, C–O/C–N, and C=O, respectively. The deconvoluted O 1s was fitted with three components at 530.7, 531.7, and 532.6 eV belonging to metal–O, O–H, and surf–O/C–O, respectively (24, 54). The N 1s peak can be deconvoluted into two peaks at 399.2 and 401.1 eV, which assigned, respectively, to pyridinic-N/metal–N and C–N/N–H (24, 55). The spectrum of Ca shows the $2p_{3/2}$ and $2p_{1/2}$ at 347.1 and 350.6 eV, respectively, and the binding energies of Ca $2p_{3/2}$ peak can be deconvoluted into 346.8 and 347.6 eV, suggesting the interaction between COO^- and Ca^{2+} (56). The peaks of Fe $2p_{3/2}$ and $2p_{1/2}$ were split into independent satellite peaks due to the major component of Fe(II), indicating that the Fe^{2+} were prevented from oxidation by the MRPs (57). The peak of Zn $2p_{3/2}$ at 1,021.8 eV was deconvoluted into 1,021.6 and 1,022.4 eV, which were, respectively, assigned to Zn–O and Zn–Cl (54, 58). This revealed that $ZnCl_2$ was generated due to the metathetical reaction in the presence of $CaCl_2$, thus $ZnCl_2$ was recommended for the preparation of MRPs–Ca/Fe/Zn.

Thermal Stability of the Trimetallic Complexes

The TG analysis presented in **Figure 6** shows the different mass losses of the complexes. The loss below 130°C was attributed to dehydration and dissociation of molecules from the sample surface (59). In practice, the use of glucose and lysine units rendered the complexes hydrophilic and hygroscopic, and careful preservation is recommended. The losses of MRPs, MRPs–Ca, and MRPs–Ca/Fe/Zn accelerated from 130°C, but no obvious acceleration was observed for MRPs–Fe and MRPs–Zn until 251°C and 293°C, respectively. The huge losses incurred from 375°C in MRPs and MRPs–Ca were due to the decomposition of the MRP molecules and release of methane (60); the loss in MRPs–Fe occurred at 472°C (**Supplementary Figure 6**). However, MRPs–Zn and

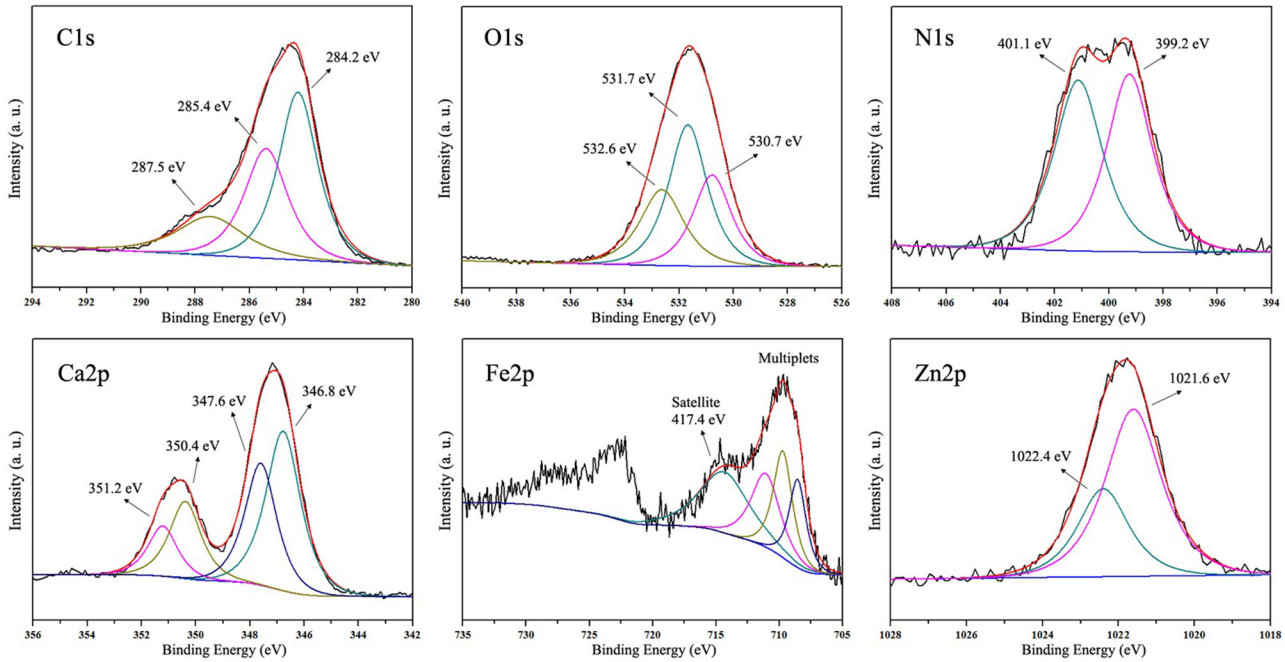

FIGURE 5 | The deconvoluted high-resolution XPS spectra of MRPs–Ca/Fe/Zn.

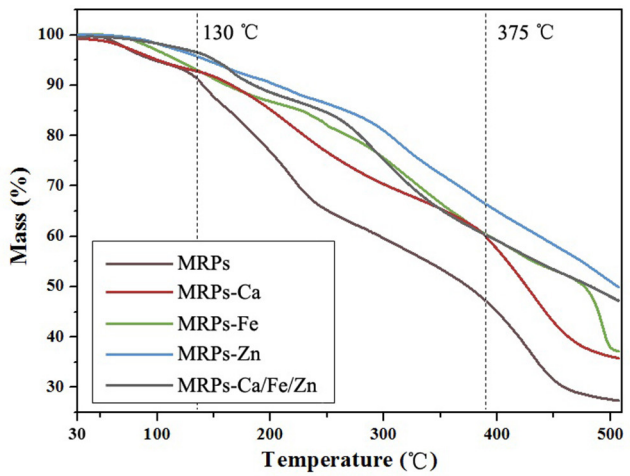

FIGURE 6 | Thermogravimetric (TG) plots of MRPs, MRPs–Ca, MRPs–Fe, MRPs–Zn, and MRPs–Ca/Fe/Zn.

MRPs–Ca/Fe/Zn underwent an insignificant loss process instead of severe ones. Overall, the complexes are competent in the normal environment of agricultural application.

Antioxidative Activity of the Trimetallic Complexes

Antioxidant assays were performed to determine the complexes' ability to resist oxidative stress and scavenge reactive oxygen species and thus assess their biocompatibilities. ABTS, DPPH, and FRAP assays exhibited a similar law of antioxidant activities among the metallic complexes. As shown in **Figure 7** and **Supplementary Table 3**, the activities of the MRPs were slightly lower than the standard and decreased on interaction with metal ions. The decreases in MRPs–Fe and MRPs–Zn were due to not only the introduction of metals but also the lower degree of the MR. Fortunately, the sharp loss due to Zn^{2+} could be restored by constructing a trimetallic complex. Distinctively, the activity of MRPs–Fe was higher than that of others in the FRAP assay. This is because the FRAP assay based on the reduction of Fe (III) to Fe (II) relies on the number of ferrous ions captured by TPTZ; a large number of ferrous ions from MRPs–Fe improved the association of TPTZ with Fe (II), resulting in the improved activity of FRAP. Overall, the complexes were endowed with considerable antioxidative activity by MRPs; thus, they have great potential in biological applications.

Effect of the Trimetallic Complexes on Apple

A field experiment was performed by spraying the solution of the complexes on apple trees with different concentrations and periods (**Table 1**). With the advantages associated with the complex structures, including high hydrophilicity due to the glycosylated coating and antioxidation due to protection from the MRPs, metal ions become highly stable under aqueous conditions. No oxidation or precipitation occurred during the spray. It is propitious for improving the efficiency of agrochemicals and reducing fertilizer consumption. Pretreatments showed that no damages were observed on the fruit surfaces (**Supplementary Figure 7**) under the high

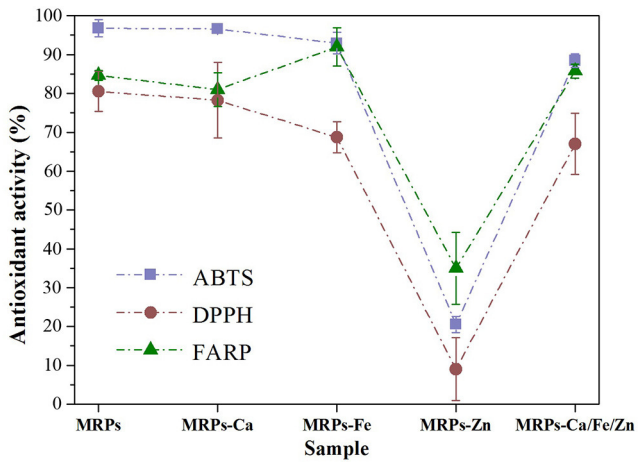

FIGURE 7 | Antioxidative activity analysis of MRPs, MRPs–Ca, MRPs–Fe, MRPs–Zn, and MRPs–Ca/Fe/Zn.

concentration treatments of MRPs–Ca, MRPs–Fe, MRPs–Zn, and MRP–Ca/Fe/Zn, suggesting that the complexes had certain biocompatibility (61). Given that we are focusing on the poly-metal complex fertilizer, the solutions of MRP–Ca/Fe/Zn were prepared for further experiments.

Figure 8 and **Supplementary Table 4** show the SSCs and TA contents of the treated fruits. The SSCs can be slightly increased by increasing the concentration of the trimetallic complex, but the index decreases with an increase in the number of sprays. It is reported that the spray treatment by $CaCl_2$ can result in a reduction in SSCs, even if the Ca content of a mature apple is increased (62). In contrast, foliar treatment with sugar alcohol zinc lead to increased sugar concentration, probably attributed to the significant effect of sugar alcohol zinc on sucrose synthase activity which regulates sugar accumulation (63). Therefore, the effect of MRPs–Ca/Fe/Zn on SSCs could be bidirectional, and excessive treatment would lead to a decrease in the content. For TA, majority treatments can decrease TA contents compared with the control, and the contents decreased with increasing concentration and number of sprays of MRPs–Ca/Fe/Zn. The treatment of T9 decreased the TA content from 0.26 to 0.19%. This trend of change is consistent with the reported studies (64, 65), but it is shown that the single application of amino acid triggers increasing in TA (65), suggesting that the reduction of TA is associated with mineral content. However, it also reported that the SSCs and TA are almost unchanged under the treatment of the chelated-metal or nanochelated-metal (66), indicating that the effect of MRPs–Ca/Fe/Zn was attributable to not only the concentration and period of application but also the complicated metabolic mechanism and environmental conditions (67).

As shown in **Supplementary Table 4**, the weight and firmness show no obvious regularity and did not differ among the treatments, indicating that MRPs–Ca/Fe/Zn hardly improved the two indices of the "Fuji" apple. It is known that the fruit concentration of Ca is positively correlated with firmness owing to the cell wall resistance that can be elevated by increasing the Ca level (68, 69). The slight decrease of firmness could be the reason that the MRP-based complex affected the fruit starch degradation pattern which has strong negative correlations with fruit firmness (70, 71).

The results of N content analysis are shown in **Figure 9** and **Supplementary Table 5**. The N contents of fleshes, peels, and leaves increased following the order of T1–T9, indicating that the MRPs containing N groups were absorbed into the plants. Compared with the control, MRPs–Ca/Fe/Zn sprays enhanced flesh N concentrations on average by 6.2, 49.6, and 99.2% of T3, T6, and T9, respectively. The growth rates in fleshes were high than that in peels and leaves, indicating that the trimetallic complex can improve the accumulation of N in the fruit flesh. The results were inconsistent with the N contents regulated by inorganic calcium salt (45), demonstrating the promotion effect of MRPs to the accumulation of N content. However, the mechanism remains unclear.

Figure 10 and **Supplementary Table 6** compare the contents of Ca, Fe, and Zn contents of fleshes, peels, and leaves of the harvested fruit. The results were in agreement with the mineral spray treatment taken on pear (47), grape (40), pomegranate (3), and orange (72). Overall, the metal contents increased with the increasing concentration and treating time of the complexes. Compared with the control, the enhanced mineral contents of T1–T9 were attributed to the additional metal absorbed into the plant by the MRPs. The rise of the mineral contents in leaves was higher than the other two parts owing to the higher rate of water supply and nutrient transport than the rest of the plant (73). Although the report shows that increasing Fe rates decreased leaf Zn contents due to the internal disturbance in the nutritional balance (41), the MRPs–Ca/Fe/Zn could drive the two contents' growth simultaneously. The rises in Fe and Zn contents in the peel were higher than those in the flesh, indicating that most of the two minerals were detained in the peel. However, the reverse order of Ca suggests that Ca passed through the skin and into the flesh with enhanced delivery efficiency. According to previous studies (45, 74, 75), Ca lacks the effectiveness to penetrate the fruit epidermis, the spraying of $CaCl_2$ or $CaCO_3$ hardly affects the concentration of flesh, and several treatments are needed to increase the concentration of Ca in the peel. Therefore, considering the results in this study, MRPs could improve the mobility and transportation of Ca to penetrate the plant cell. However, an insufficient amount of MRPs–Ca/Fe/Zn (T1, T4, T5, and T7) could decrease the Ca concentration in fleshes, as well as in peels, it implies that the combined effect of polymetallic foliar fertilizer might reduce the absorb efficiency of calcium, thus increase in dosage is recommended.

Notably, T9 of MRPs–Ca/Fe/Zn (Ca: 9.01%, Fe: 8.25%, and Zn: 9.67%) provided the following increments in Ca, Fe, and Zn contents: 85.4, 532.5, and 931.1% in the leaf; 16.0, 225.2, and 468.6% in the peel; and 117.6, 217.9, and 19.5% in the flesh, respectively. Therefore, the increase in mineral content did not directly relate to the metal content of the complex. Although the impact of the treatment on Ca in peel and Zn in flesh is subtle, none of the nutritional concentrations were negatively altered by the treatment relative to the control. Higher increments correlated with the efficiencies of absorption and

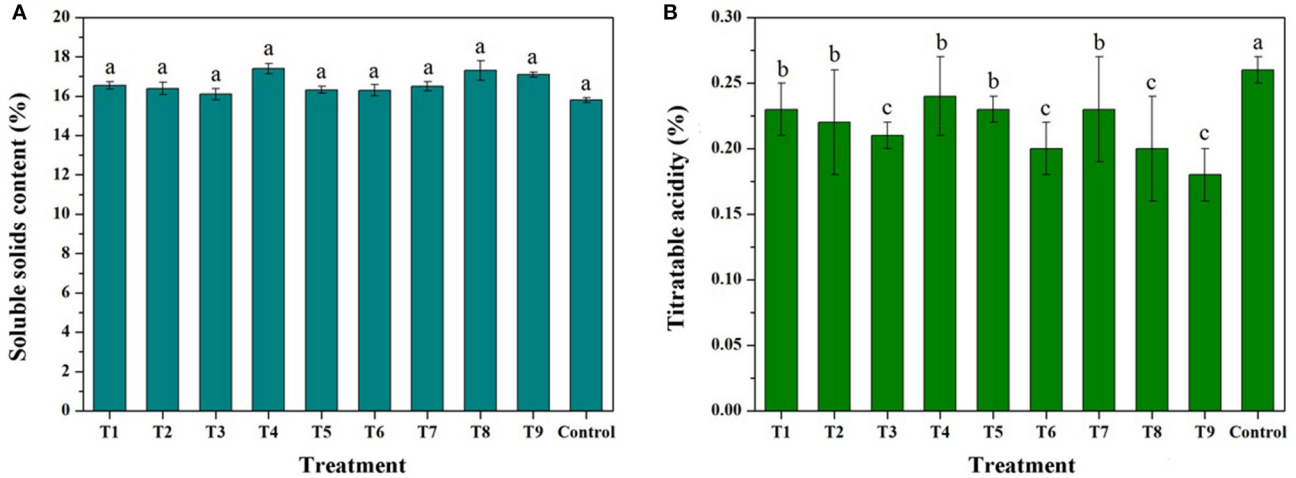

FIGURE 8 | Effects of MRPs–Ca/Fe/Zn on soluble solid contents (SSCs) **(A)** and titratable acidity (TA) **(B)** of the fruits.

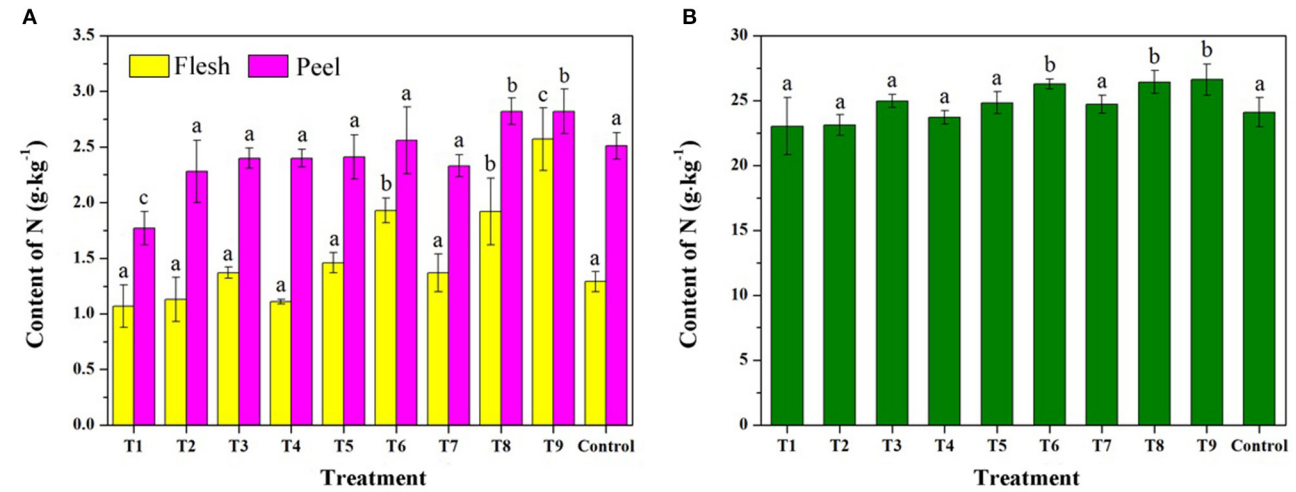

FIGURE 9 | Effects of MRPs–Ca/Fe/Zn on N contents of fleshes **(A)**, peels **(A)**, and leaves **(B)**.

metabolism; the modified metal provided more nutrients for these processes. Both sugar- and amino-based metallic materials have better efficiency for promoting the mineral absorption of apple than inorganic salts (62, 63, 76). It is noteworthy relative to the unchelated metals, chelated metal complex with improved stability can be conducive to mineral biofortification in fruits, although the mechanism is still unclear. Remarkably, the MRP-based complexes, in which the chelated ligands were derived from the reaction of sugar and amino acid, could lead to a higher growth rate of the mineral content in apples. These results indicate that the antioxidative ligands significantly contributed to the process of Ca, Fe, and Zn uptake by plants. Therefore, although the improvements in Ca, Fe, and Zn by MRPs–Ca/Fe/Zn were not identical, the bio-utilization of minerals would profit from the modified metals, which are coordinated with glycosylated compounds, resulting in uniform dispersion at minimal scale while being transported into the plant at highly active rates.

An identical treatment was carried out in the next year to test and verify the reliability and reproducibility of the method by introducing only the T9 in view of the highest efficiency. The effect on Ca, Fe, and Zn of the samples from 2020 to 2021 is compared in **Table 2**. Although the contents of Ca in flesh, Zn and Fe in the peel, and Zn in leaf were lower than those in 2020, these data did not differ significantly. The reason for the discrepancy might be due to the differences in plant growth conditions (soil and/or environmental) of the 2 years. Taking into account the data in the 2 years, we can attribute that this method for improving mineral concentration in cultivar apple is effective and reproductive.

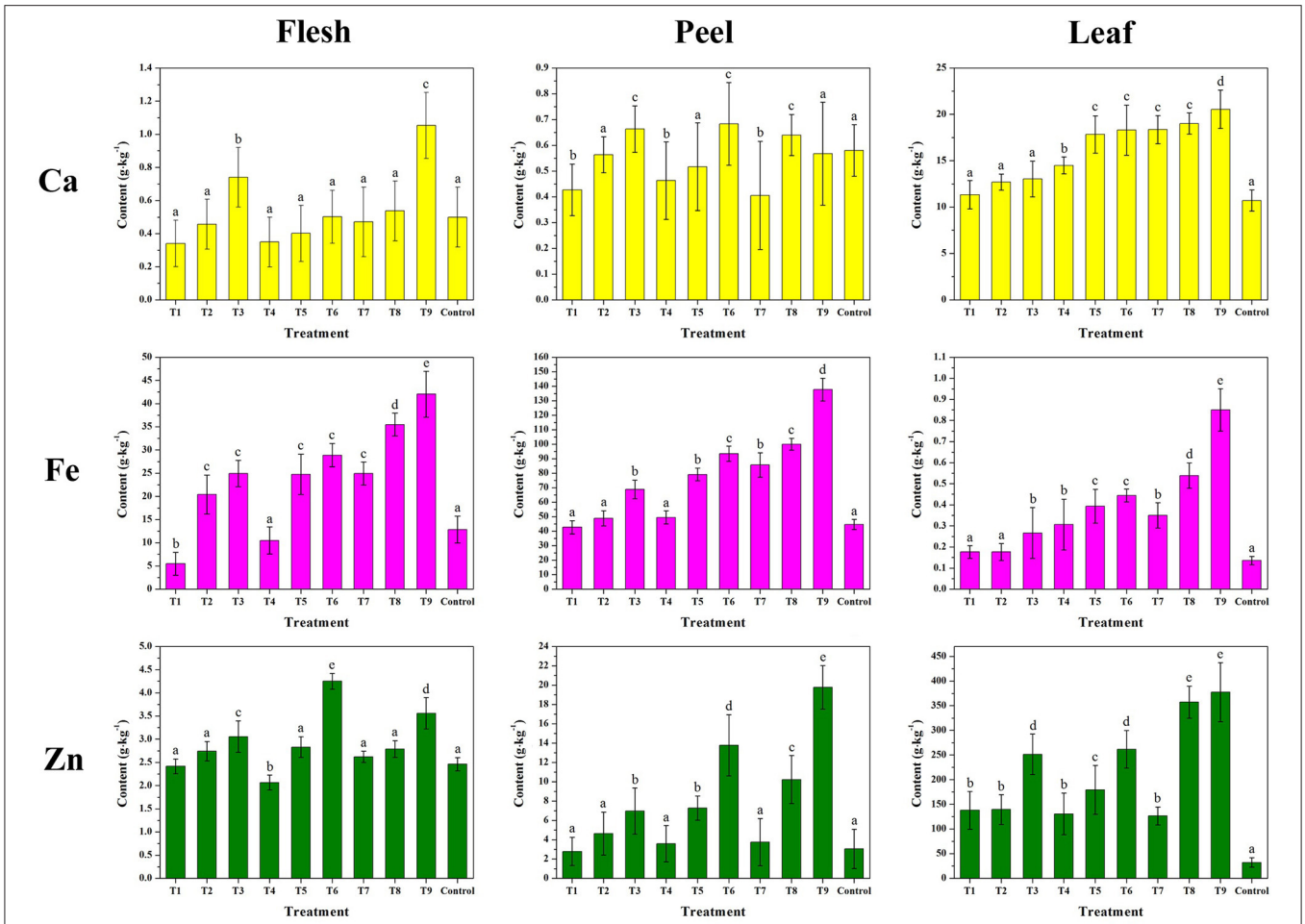

FIGURE 10 | Effects of MRPs–Ca/Fe/Zn on the mineral nutrients of fleshes, peels, and leaves of "Fuji" apple.

TABLE 2 | Content of mineral nutrients of the "Fuji" samples in 2 years.

Content (g·kg^{-1})	Flesh		Peel		Leaf	
	2020	2021	2020	2021	2020	2021
Ca	1.05 ± 0.2	0.97 ± 0.15	0.57 ± 0.23	0.73 ± 0.63	20.54 ± 2.08	22.13 ± 2.74
Fe	42.06 ± 4.95	55.65 ± 3.88	137.72 ± 7.85	124.53 ± 3.44	0.85 ± 0.1	1.12 ± 0.31
Zn	3.56 ± 0.34	4.12 ± 1.14	19.78 ± 2.26	16.85 ± 2.09	377.59 ± 59.8	356.46 ± 36.76

CONCLUSION

We developed a new approach to integrate Ca, Fe, and Zn with the biodegradable ligand which is derived from the thermal reaction of saccharide and amino acids. The metals are evenly distributed over the ligands with insignificant aggregation. The resultant complexes possess desirable stability and antioxidation to prevent metals from oxidizing, thereby enhancing stability under aqueous conditions and mineral transport efficiency into plants. The biological assay showed that mineral nutrients of Ca, Fe, and Zn in apple simultaneously and remarkably increased through surface spraying of the metal–integrated complex, and the efficiency is much higher than the traditional inorganic salts and single chelated metals. The proposed method will inspire new insights and methodologies to develop green agricultural technology.

DATA AVAILABILITY STATEMENT

The original contributions presented in the study are included in the article/**Supplementary Material**,

further inquiries can be directed to the corresponding author.

AUTHOR CONTRIBUTIONS

Y-ZY: writing—original draft, formal analysis, methodology, investigation, and funding acquisition. Q-PW: conceptualization, supervision, and funding acquisition. JZ: data curation, investigation, visualization, and writing—review and editing. M-JL and B-BZ: writing—review and editing. QZ: investigation and writing—review and editing. X-LL: supervision and visualization. J-KZ: supervision, project administration, and writing—review and editing. All authors contributed to the article and approved the submitted version.

FUNDING

This study was supported by the National Key Research and Development Program of China (No. 2020YFD1000201), the National Natural Science Foundation of China (No. 22005037), and the Agriculture Research System of China (CARS-27) for the funding.

SUPPLEMENTARY MATERIAL

The Supplementary Material for this article can be found online at: https://www.frontiersin.org/articles/10.3389/fnut.2022.848857/full#supplementary-material

REFERENCES

1. Anino SV, Salvatori DM, Alzamora SM. Changes in calcium level and mechanical properties of apple tissue due to impregnation with calcium salts. *Food Res Int.* (2006) 39:154–64. doi: 10.1016/j.foodres.2005.07.003
2. Chardonnet CO, Charron CS, Sams CE, Conway WS. Chemical changes in the cortical tissue and cell walls of calcium-infiltrated 'Golden Delicious' apples during storage. *Postharvest Biol Technol.* (2003) 28:97–111. doi: 10.1016/S0925-5214(02)00139-4
3. Chater JM, Garner LC. Foliar nutrient applications to 'Wonderful' pomegranate (*Punica granatum* L) I. Effects on fruit mineral nutrient concentrations and internal quality. *Sci Hortic.* (2019) 244:421–7. doi: 10.1016/j.scienta.2018.04.022
4. Neilsen G, Neilsen D, Dong SF, Toivonen P, Peryea F. Application of $CaCl_2$ sprays earlier in the season may reduce bitter pit incidence in 'Braebum' apple. *Hortscience.* (2005) 40:1850–3. doi: 10.21273/HORTSCI.40.6.1850
5. López-Rayo S, Nadal P, Lucena JJ. Novel chelating agents for iron, manganese, zinc, and copper mixed fertilisation in high pH soil-less cultures. *J Sci Food Agric.* (2016) 96:1111–20. doi: 10.1002/jsfa.7183
6. Morgan B, Lahav O. The effect of pH on the kinetics of spontaneous Fe(II) oxidation by O_2 in aqueous solution – basic principles and a simple heuristic description. *Chemosphere.* (2007) 68:2080–4. doi: 10.1016/j.chemosphere.2007.02.015
7. Hansen NC, Hopkins BG, Ellsworth JW, Jolley VD. Iron nutrition in field crops. In: Barton LL, Abadia J, editor, *Iron Nutrition in Plants and Rhizospheric Microorganisms*. Dordrecht: Springer Netherlands (2006). p. 23–59. doi: 10.1007/1-4020-4743-6_2
8. Stumm W, Lee GF. Oxygenation of ferrous iron. *Indus Eng Chem.* (1961) 53:143–6. doi: 10.1021/ie50614a030
9. Alcaniz S, Jorda JD, Cerdan M. Effectiveness of iron ethylenediamine-*N*,*N*'-bis(hydroxyphenylacetic) acid (*o*,*o*-EDDHA/Fe^{3+}) formulations with different ratios of meso and *d*,*l*-racemic isomers as iron fertilizers. *J Agric Food Chem.* (2017) 65:253–9. doi: 10.1021/acs.jafc.6b03274
10. Cieschi MT, Lucena JJ. Iron and humic acid accumulation on soybean roots fertilized with leonardite iron humates under calcareous conditions. *J Agric Food Chem.* (2018) 66:13386–96. doi: 10.1021/acs.jafc.8b04021
11. Garcia AC, Vavrusova M, Skibsted LH. Calcium d-saccharate: aqueous solubility, complex formation, and stabilization of supersaturation. *J Agric Food Chem.* (2016) 64:2352–60. doi: 10.1021/acs.jafc.6b00166
12. Bucheli-Witschel M, Egli T. Environmental fate and microbial degradation of aminopolycarboxylic acids. *FEMS Microbiol Rev.* (2001) 25:69–106. doi: 10.1111/j.1574-6976.2001.tb00572.x
13. Kovács K, Czech V, Fodor F, Solti A, Lucena JJ, Santos-Rosell S, Hernández-Apaolaza L. Characterization of Fe–leonardite complexes as novel natural iron fertilizers. *J Agric Food Chem.* (2013) 61:12200–10. doi: 10.1021/jf404455y
14. Molassiotis AN, Dimassi K, Diamantidis G, Therios I. Changes in peroxidases and catalase activity during in vitro rooting. *Biol Plant.* (2004) 48:1–5. doi: 10.1023/B:BIOP.0000024267.68394.96
15. An Z, Yan J, Zhang Y, Pei R. Applications of nanomaterials for scavenging reactive oxygen species in the treatment of central nervous system diseases. *J Mater Chem B.* (2020) 8:8748–67. doi: 10.1039/D0TB01380C
16. Chen K, Qian Y, Wu S, Qiu X, Yang D, Lei L. Neutral fabrication of UV-blocking and antioxidation lignin-stabilized high internal phase emulsion encapsulates for high efficient antibacterium of natural curcumin. *Food Funct.* (2019) 10:3543–55. doi: 10.1039/C9FO00320G
17. Zhai Y, Zhou K, Xue Y, Qin F, Yang L, Yao X. Synthesis of water-soluble chitosan-coated nanoceria with excellent antioxidant properties. *RSC Adv.* (2013) 3:6833–8. doi: 10.1039/c3ra22251a
18. Gerrard JA. Protein-protein crosslinking in food: methods, consequences, applications. *Trends in Food Sci Technol.* (2002) 13:391–9. doi: 10.1016/S0924-2244(02)00257-1
19. Liu FG, Ma CC, Gao YX, McClements DJ. Food-grade covalent complexes and their application as nutraceutical delivery systems: a review. *Compr Rev Food Sci Food Saf.* (2017) 16:76–95. doi: 10.1111/1541-4337.12229
20. Lund MN, Ray CA. Control of Maillard reactions in foods: Strategies and chemical mechanisms. *J Agric Food Chem.* (2017) 65:4537–52. doi: 10.1021/acs.jafc.7b00882
21. Lesmes U, McClements DJ. Controlling lipid digestibility: response of lipid droplets coated by beta-lactoglobulin-dextran Maillard conjugates to simulated gastrointestinal conditions. *Food Hydrocoll.* (2012) 26:221–30. doi: 10.1016/j.foodhyd.2011.05.011
22. Roncero-Ramos I, Pastoriza S, Navarro MP, Delgado-Andrade C. Assessing the effects of model Maillard compound intake on iron, copper and zinc retention and tissue delivery in adult rats. *Food Funct.* (2016) 7:164–70. doi: 10.1039/C5FO00790A
23. Nooshkam M, Varidi M, Verma DK. Functional and biological properties of Maillard conjugates and their potential application in medical and food: a review. *Food Res Int.* (2020) 131:18. doi: 10.1016/j.foodres.2020.109003
24. Yang YZ, Li MJ, Li XL, Zhou BB, Wei QP, Zhang JK. Preparation of soluble ferrous complex with high alkaline stability by reducing iron nanoparticle in Maillard reaction. *Chem Pap.* (2021) 75:3227–39. doi: 10.1007/s11696-021-01503-3
25. Chevalier F, Chobert JM, Genot C, Haertle T. Scavenging of free radicals, antimicrobial, and cytotoxic activities of the Maillard reaction products of beta-lactoglobulin glycated with several sugars. *J Agric Food Chem.* (2001) 49:5031–8. doi: 10.1021/jf010549x
26. Delgado-Andrade C, Seiquer I, Nieto R, Navarro MaP. Effects of heated glucose–lysine and glucose–methionine model-systems on mineral solubility. *Food Chem.* (2004) 87:329–37. doi: 10.1016/j.foodchem.2003.12.002
27. Li D, Na X, Wang H, Xie Y, Cong S, Song Y, et al. Fluorescent carbon dots derived from maillard reaction products: their properties, biodistribution, cytotoxicity, and antioxidant activity. *J Agric Food Chem.* (2018) 66:1569–75. doi: 10.1021/acs.jafc.7b05643
28. Yilmaz Y, Toledo R. Antioxidant activity of water-soluble Maillard reaction products. *Food Chem.* (2005) 93:273–8. doi: 10.1016/j.foodchem.2004.09.043

29. Yu X, Jing Y, Yan F. Chitooligosaccharide–lysine Maillard reaction products: preparation and potential application on fresh-cut kiwifruit. *Food Bioprocess Technol.* (2019) 12:1133–43. doi: 10.1007/s11947-019-02284-0
30. Ferguson IB. Calcium in plant senescence and fruit ripening. *Plant Cell Environ.* (1984) 7:477–89. doi: 10.1111/j.1365-3040.1984.tb01438.x
31. Hill J. The remobilization of nutrients from leaves. *J Plant Nutr.* (1980) 2:407–44. doi: 10.1080/01904168009362788
32. Alcaraz-López C, Botía M, Alcaraz CF, Riquelme F. Effects of foliar sprays containing calcium, magnesium and titanium on plum (*Prunus domestica* L) fruit quality. *J Plant Physiol.* (2003) 160:1441–6. doi: 10.1078/0176-1617-00999
33. Serrano M, Martinez-Romero D, Castillo S, Guillen F, Valero D. Effect of preharvest sprays containing calcium, magnesium and titanium on the quality of peaches and nectarines at harvest and during postharvest storage. *J Sci Food Agric.* (2004) 84:1270–6. doi: 10.1002/jsfa.1753
34. Wójcik P, Lewandowski M. Effect of calcium and boron sprays on yield and quality of "Elsanta" strawberry. *J Plant Nutr.* (2003) 26:671–82. doi: 10.1081/PLN-120017674
35. Alcaraz-López C, Botía M, Alcaraz CF, Riquelme F. Effect of foliar sprays containing calcium, magnesium and titanium on peach (*Prunus persica* L) fruit quality. *J Sci Food Agric.* (2004) 84:949–54. doi: 10.1002/jsfa.1703
36. Vithana MDK, Singh Z, Johnson SK. Levels of terpenoids, mangiferin and phenolic acids in the pulp and peel of ripe mango fruit influenced by pre-harvest spray application of $FeSO_4$ (Fe^{2+}), $MgSO_4$ (Mg^{2+}) and $MnSO_4$ (Mn^{2+}). *Food Chem.* (2018) 256:71–6. doi: 10.1016/j.foodchem.2018.02.087
37. Rossi L, Fedenia LN, Sharifan H, Ma X, Lombardini L. Effects of foliar application of zinc sulfate and zinc nanoparticles in coffee (*Coffea arabica* L) plants. *Plant Physiol Biochem.* (2019) 135:160–6. doi: 10.1016/j.plaphy.2018.12.005
38. Ranjbar S, Ramezanian A, Rahemi M. Nano-calcium and its potential to improve 'Red Delicious' apple fruit characteristics. *Hortic Environ Biote.* (2020) 61:23–30. doi: 10.1007/s13580-019-00168-y
39. Zahedi SM, Karimi M, da Silva JAT. The use of nanotechnology to increase quality and yield of fruit crops. *J Sci Food Agric.* (2020) 100:25–31. doi: 10.1002/jsfa.10004
40. Ma J, Zhang M, Liu Z, Chen H, Li YC, Sun Y, et al. Effects of foliar application of the mixture of copper and chelated iron on the yield, quality, photosynthesis, and microelement concentration of table grape (*Vitis vinifera* L). *Sci Hortic.* (2019) 254:106–15. doi: 10.1016/j.scienta.2019.04.075
41. El-Shazly SM, Dris R. Response of 'Anna' apple trees to foliar sprays of chelated iron, manganese and zinc. *J Food Agric Environ.* (2004) 2:126–30.
42. Hoseinabadi H, Taghavi T, Solgi M, Askari M, Rahemi A. Vinegar and iron chelate spray affected vegetative growth and yield of grape cv. thompson seedless. *J Hortic.* (2018) 5:3. doi: 10.4172/2376-0354.1000241
43. Taghavi T, Hoseinabadi H, Solgi M, Askari M, Rahemi A. Influence of vinegar and chelated iron field sprays on mineral nutrients and fruit quality of grapes (cv. 'Thompson seedless'). *Mitt Klosterneuburg.* (2020) 70:75–86.
44. Blanco A, Fernández V, Val J. Improving the performance of calcium-containing spray formulations to limit the incidence of bitter pit in apple (Malus x domestica Borkh). *Sci Hortic.* (2010) 127:23–8. doi: 10.1016/j.scienta.2010.09.005
45. Yu XM, Wang JZ, Nie PX, Xue XM, Wang GP, An M. Control efficacy of Ca-containing foliar fertilizers on bitter pit in bagged 'Fuji' apple and effects on the Ca and N contents of apple fruits and leaves. *J Sci Food Agric.* (2018) 98:5435–43. doi: 10.1002/jsfa.9087
46. Zhang Y, Yan Y, Fu C, Li M, Wang Y. Zinc sulfate spray increases activity of carbohydrate metabolic enzymes and regulates endogenous hormone levels in apple fruit. *Sci Hortic.* (2016) 211:363–8. doi: 10.1016/j.scienta.2016.09.024
47. Ozturk B, Karakaya O, Erdem H, Küçüker E, Özkan Y, Yildiz K. The effects of foliar iron treatments (+Fe) on fruit quality of different pear cultivars. *Erwerbs-Obstbau.* (2019) 61:373–8. doi: 10.1007/s10341-019-00442-4
48. Ferreira CMH, López-Rayo S, Lucena JJ, Soares EV, Soares HMVM. Evaluation of the efficacy of two new biotechnological-based freeze-dried fertilizers for sustainable fe deficiency correction of soybean plants grown in calcareous soils. *Front Plant Sci.* (2019) 10:1335. doi: 10.3389/fpls.2019.01335
49. Food and Agriculture Organization of the United Nations (2020). *FAOSTAT Database*. Available online at: http://www.fao.org/faostat/en/#data
50. Cruz-Hernandez A, Paredes-López O. Fruit quality: new insights for biotechnology. *Crit Rev Food Sci Nutr.* (2012) 52:272–89. doi: 10.1080/10408398.2010.499844
51. Mondaca-Navarro BA, Ávila-Villa LA, González-Córdova AF, López-Cervantes J, Sánchez-Machado DI, Campas-Baypoli ON, et al. Antioxidant and chelating capacity of Maillard reaction products in amino acid-sugar model systems: applications for food processing. *J Sci Food Agric.* (2017) 97:3522–9. doi: 10.1002/jsfa.8206
52. Liang S, Huang Y, Shim YY, Ma X, Reaney MJT, Wang Y. Novel flaxseed gum nanocomposites are slow release iron supplements. *J Agric Food Chem.* (2018) 66:5167–77. doi: 10.1021/acs.jafc.8b01347
53. Yang YZ, Li MJ, Zhou BB, Zhang Q, Li XL, Zhang JK, et al. Synthesis, characterization, and evaluation of bioactivity of novel Fe(II) nano-complexes based on sucrose, glucose, and fructose. *Chem Pap.* (2019) 73:321–9. doi: 10.1007/s11696-018-0582-8
54. Baek JH, Park JY, Kang JS, Kim D, Koh SW, Kang Y. Fabrication and thermal oxidation of zno nanofibers prepared *via* electrospinning technique. *Bull Korean Chem Soc.* (2012) 33:2694–8. doi: 10.5012/bkcs.2012.33.8.2694
55. Yu Y, Xiao D, Ma J, Chen C, Li K, Ma J, et al. The self-template synthesis of highly efficient hollow structure Fe/N/C electrocatalysts with Fe–N coordination for the oxygen reduction reaction. *RSC Adv.* (2018) 8:24509–16. doi: 10.1039/C8RA03672A
56. Xu M, Pan G, Cao Y, Guo Y, Chen H, Wang Y, et al. Surface analysis of stearic acid modification for improving thermal resistant of calcium phosphate coated iron oxide yellow pigments. *Surf Interface Anal.* (2020) 52:626–34. doi: 10.1002/sia.6803
57. Grosvenor AP, Kobe BA, Biesinger MC, McIntyre NS. Investigation of multiplet splitting of Fe 2p XPS spectra and bonding in iron compounds. *Surf Interface Anal.* (2004) 36:1564–74. doi: 10.1002/sia.1984
58. Winiarski J, Tylus W, Winiarska K, Szczygieł I, Szczygieł B. XPS and FT-IR characterization of selected synthetic corrosion products of zinc expected in neutral environment containing chloride ions. *J Spectrosc.* (2018) 2018:1–14. doi: 10.1155/2018/2079278
59. Li D, Xie Y, Na X, Li Y, Dai C, Li Y, et al. Insights into melanoidin conversion into fluorescent nanoparticles in the Maillard reaction. *Food Funct.* (2019) 10:4414–22. doi: 10.1039/C9FO90059D
60. Rubinsztain Y, Ioselis P, Ikan R, Aizenshtat Z. Investigations on the structural units of melanoidins. *Org Geochem.* (1984) 6:791–804. doi: 10.1016/0146-6380(84)90101-3
61. Cakmak I, Kutman UB. Agronomic biofortification of cereals with zinc: a review. *Eur J Soil Sci.* (2018) 69:172–80. doi: 10.1111/ejss.12437
62. Wójcik P, Skorupinska A, Gubbuk H. Impacts of pre- and postbloom sprays of tryptophan on calcium distribution within 'Red Jonaprince' apple trees and on fruit quality. *Hortscience.* (2016) 51:1511–6. doi: 10.21273/HORTSCI11216-16
63. Zhang Y, Fu C, Yan Y, Fan X, Wang Y, Li M. Foliar application of sugar alcohol zinc increases sugar content in apple fruit and promotes activity of metabolic enzymes. *Hortscience.* (2014) 49:1067–70. doi: 10.21273/HORTSCI.49.8.1067
64. Zhang Y, Fu C, Yan Y, Wang Y, Li M, Chen M, et al. Zinc sulfate and sugar alcohol zinc sprays at critical stages to improve apple fruit quality. *HortTechnology.* (2013) 23:490–7. doi: 10.21273/HORTTECH.23.4.490
65. Aglar E, Yildiz K, Ozkan Y, Ozturk B, Erdem H. The effects of aminoethoxyvinylglycine and foliar zinc treatments on pre-harvest drops and fruit quality attributes of Jersey Mac apples. *Sci Hortic.* (2016) 213:173–8. doi: 10.1016/j.scienta.2016.10.026
66. Rasouli M, Koushesh Saba M. Pre-harvest zinc spray impact on enzymatic browning and fruit flesh color changes in two apple cultivars. *Sci Hortic.* (2018) 240:318–25. doi: 10.1016/j.scienta.2018.06.053
67. Wang Y, Liu L, Wang Y, Tao H, Fan J, Zhao Z, et al. Effects of soil water stress on fruit yield, quality and their relationship with sugar metabolism in 'Gala' apple. *Sci Hortic.* (2019) 258:108753. doi: 10.1016/j.scienta.2019.108753
68. Fallahi E, Conway WS, Hickey KD, Sams CE. The role of calcium and nitrogen in postharvest quality and disease resistance of apples. *HortSci.* (1997) 32:831–5. doi: 10.21273/HORTSCI.32.5.831
69. Solhjoo S, Gharaghani A, Fallahi E. Calcium and potassium foliar sprays affect fruit skin color, quality attributes, and mineral nutrient concentrations of 'Red Delicious' apples. *Int J Fruit Sci.* (2017) 17:358–73. doi: 10.1080/15538362.2017.1318734

70. Fallahi E, Richardson DG, Westwood MN, Chaplin MH. Relationships among mineral nutrition, ethylene and post-harvest physiology in apples on six rootstocks. *Sci Hort.* (1985) 25:163–75. doi: 10.1016/0304-4238(85)90087-1
71. Fallahi E, Arzani K, Fallahi B. Long-term leaf mineral nutrition in 'Pacific Gala' apple (Malus×domestica Borkh) as affected by rootstock type and irrigation system during six stages of tree development. *J Hort Sci Biotechnol.* (2013) 88:685–92. doi: 10.1080/14620316.2013.11513025
72. Zheng YQ, Yang Q, Jia XM, Liu YM, He S, Deng L, et al. $Ca(NO_3)_2$ canopy spraying during physiological fruit drop period has a better influence on the tree character and fruit quality of Newhall navel orange (*Citrus sinensis Osbeck*). *J Integr Agr.* (2017) 16:1513–9. doi: 10.1016/S2095-3119(16)61603-9
73. Hocking B, Tyerman SD, Burton RA, Gilliham M. Fruit calcium: transport and physiology. *Front Plant Sci.* (2016) 7:17. doi: 10.3389/fpls.2016.00569
74. Fallahi E, Eichert T. Principles and practices of foliar nutrients with an emphasis on nitrogen and calcium sprays in apple. *Horttechnology.* (2013) 23:542–7. doi: 10.21273/HORTTECH.23.5.542
75. Val J, Monge E, Risco D, Blanco A. Effect of pre-harvest calcium sprays on calcium concentrations in the skin and flesh of apples. *J Plant Nutr.* (2008) 31:1889–905. doi: 10.1080/01904160802402757
76. Wójcik P, Filipczak J, Wójcik M. Effects of prebloom sprays of tryptophan and zinc on calcium nutrition, yielding and fruit quality of 'Elstar' apple trees. *Sci Hortic.* (2019) 246:212–6. doi: 10.1016/j.scienta.2018.10.071

Conflict of Interest: The authors declare that the research was conducted in the absence of any commercial or financial relationships that could be construed as a potential conflict of interest.

Publisher's Note: All claims expressed in this article are solely those of the authors and do not necessarily represent those of their affiliated organizations, or those of the publisher, the editors and the reviewers. Any product that may be evaluated in this article, or claim that may be made by its manufacturer, is not guaranteed or endorsed by the publisher.

Copyright © 2022 Yang, Wei, Zhou, Li, Zhang, Li, Zhou and Zhang. This is an open-access article distributed under the terms of the Creative Commons Attribution License (CC BY). The use, distribution or reproduction in other forums is permitted, provided the original author(s) and the copyright owner(s) are credited and that the original publication in this journal is cited, in accordance with accepted academic practice. No use, distribution or reproduction is permitted which does not comply with these terms.

frontiers | Frontiers in Nutrition

ORIGINAL RESEARCH
published: 12 May 2022
doi: 10.3389/fnut.2022.879028

Limonin Isolated From Pomelo Seed Antagonizes Aβ25-35-Mediated Neuron Injury via PI3K/AKT Signaling Pathway by Regulating Cell Apoptosis

Yuanxin Qiu[1,3], Jingxian Yang[1,2], Lukai Ma[1], Mingyue Song[4] and Guo Liu[4]**

[1] School of Food Science and Engineering, Zhongkai University of Agricultural Engineering, Guangzhou, China, [2] Guangdong Meizhou Vocational and Technical College, Meizhou, China, [3] Guangdong Provincial Key Laboratory of Lingnan Specialty Food Science and Technology, Guangzhou, China, [4] Guangdong Provincial Key Laboratory of Nutraceuticals and Functional Foods, College of Food Science, South China Agricultural University, Guangzhou, China

OPEN ACCESS

Edited by:
Biao Yuan,
China Pharmaceutical University, China

Reviewed by:
Yueliang Zhao,
Shanghai Ocean University, China
Yingbin Shen,
Guangzhou University, China

***Correspondence:**
Yuanxin Qiu
65518987@qq.com
Guo Liu
liuguo@scau.edu.cn

Specialty section:
This article was submitted to Food Chemistry, a section of the journal Frontiers in Nutrition

Received: 18 February 2022
Accepted: 15 April 2022
Published: 12 May 2022

Citation:
Qiu Y, Yang J, Ma L, Song M and Liu G (2022) Limonin Isolated From Pomelo Seed Antagonizes Aβ25-35-Mediated Neuron Injury via PI3K/AKT Signaling Pathway by Regulating Cell Apoptosis. Front. Nutr. 9:879028. doi: 10.3389/fnut.2022.879028

Pomelo seed as a by-product from pomelo consumption is rich in bioactive compounds, however, a huge volume of pomelo seed was disposed as wastes, the comprehensive utilization of pomelo seed could not only generate valued-added products/ingredients, but also decrease the environmental pollution. In this study, the main active substance limonin in pomelo seed was considered as a high-value bioactive compound. The purification of limonin from pomelo seed was investigated, and the neuroprotective and mechanism were characterized. The UPLC-MS/MS results indicated that 29 compounds in pomelo seed were identified, including 14 flavonoids, 3 limonids, 9 phenols and 3 coumarins. Moreover, high purity of limonin was obtained by crystallization and preparative-HPLC. Furthermore, limonin pretreatment can antagonize the cell damage mediated by $A\beta_{25-35}$ in a concentration-dependent relationship. The regulation of Bax/Bcl-2, expression of caspase-3 protein and the activation of PI3K/Akt signaling pathway were observed in the cells pretreated with limonin. Treatment of PC12 cells with PI3K inhibitor LY294002 weakened the protective effect of limonin. These results indicated that limonin prevented $A\beta_{25-35}$-induced neurotoxicity by activating PI3K/Akt, and further inhibiting caspase-3 and up-regulating Bcl-2. This study enables comprehensive utilization of pomelo seed as by-product and offers a theoretical principle for a waste-to-wealth solution, such as potential health benefits of food ingredient and drug.

Keywords: pomelo seed, limonin, PC12 cells, neuroprotective activity, PI3K/AKT

INTRODUCTION

Pomelo [*Citrus grandis (L.)* Osbeck], known as shaddock and pummel, is one of the most important commercially fruit crops. Pomelo belongs to the citrus genus in the Rutaceae family, which is widely cultivated in Asia and some other countries around the world (1–3). Its cultivation and consumption can date back to more than 4,000 years (4). In 2018, a total of 9.4 million metric tons

of pomelo was reportedly produced in global according to the Food and Agricultural Organization of the United Nations database (5). Pomelo seeds, as the main by-product of pomelo, account for ∼10.3% of the entire pomelo (6). In China, pomelo seeds are used in the treatment of hernias, cold lungs, coughs, yellowing, and breast hyperplasia due to its phytochemicals (6, 7). However, only small amounts of pomelo seeds are currently used as raw materials for traditional Chinese medicine due to their bitter taste. As a result, most of these pomelo seeds are discarded. Thus, the overall health benefits and economic value of pomelo seeds have not been fully appreciated. Most pomelo seeds go into landfill, which caused a serious environmental problem. Limonoids, flavonoids and polyphenols are the major chemical components in pomelo seeds. Previous studies have shown that these compounds have a variety of biological activities, such as anti-oxidation and anti-inflammatory effects, scavenging free radicals, inhibiting cancer cell growth and enhancing the activity of nerve growth factors (8–10). Therefore, pomelo seed extracts have great potential as a dietary nutritional supplement.

Limonin, as a triterpenoid compound, is the most prevalent member of limonoids in the citrus genus. It shows a broad-spectrum of biological activity, especially neuroprotective effects (11). Some previous study reported that limonin exhibited remarkable neuroprotective activity against glutamate-induced neurotoxicity *in vivo* (12) and *in vitro* (13). Triterpenoid derivatives are also considered to be important active substances with anti-β amyloid deposition (14). A recent study revealed that limonin could improve neurodegenerative lesions in rats by improving memory and the ability to learn (15).

The average age of the world population has been increasing in the last few decades, which also increases the possibility of the elderly to suffer from dementia. Alzheimer's disease (AD) accounts for 50–70% of all dementia (16). Currently, the most acceptable hypotheses include the cholinergic hypothesis, the β-amyloid hypothesis, and the Tau protein hypothesis (17). Among them, amyloid beta (Aβ) is the main component of senile plaques which are composed of 36–43 amino acid residues (18). A large amount of medical evidence shows that Aβ plays an indispensable role in the pathogenesis of AD. Aβ oligomers, such as $A\beta_{25-35}$ fragments, can lead to neuronal dysfunction (19–21) by causing mitochondrial dysfunction, imbalance of Ca^{2+}, and the occurrence of neuronal oxidative stress damage. Additionally, a potential toxic substance can cause neuronal dysfunction and neuron loss by severely damaging synaptic structure and function (22). $A\beta_{25-35}$ fragments have shown neurotoxicity in cell culture (23). Therefore, $A\beta_{25-35}$ has been widely used to establish *in vitro* AD experimental models. Although drugs such as donepezil can be used for the treatment of AD, these drugs usually have serious side effects such as drowsiness, restlessness, arrhythmia, and epilepsy. This drives people to pursue natural nutritional supplements with low side effects. To date, there are only a few reports on the mechanism of limonin and its effect on nerve cells. Further studies can help understand this mechanism and lead to better nutrition intervention for neurodegenerative diseases.

In the present study, the main bioactive compounds in pomelo seed were identified using the UPLC-MSMS system. Then, the neuroprotective effect of limonin isolated from pomelo seed was investigated using an apoptosis model of PC12 cells induced by $A\beta_{25-35}$. This study enables comprehensive utilization of the waste pomelo seed resources and proves the neuroprotective effect of limonin in the current scientific literature.

MATERIALS AND METHODS

Materials and Chemicals

The pomelo seeds were obtained from Meizhou, Guangdong province, China. Chromatographic grade acetonitrile was obtained from Merck (Merck KGaA, Darmstadt, Germany), trifluoroacetic acid, ethanol, formic acid, ethyl acetate, dichloromethane and isopropanol were obtained from Guangzhou Chemical Reagent Factory (Guangzhou, China). RPMI-1640 cell medium, fetal bovine serum and penicillin were all purchased from Sigma-Aldrich (St. Louis, MO, USA). Fluo-3/AM and LY294002 (the inhibitor of PI3K) were acquired from Shanghai Beyotime Biotechnology (S1056, Beyotime, China) and Selleck Chemicals (S1105, Selleck, USA), respectively.

Extraction and Identification of Bioactive Compounds

Subcritical equipment (Henan Subcritical Biotechnology, China) was used to remove grease of pomelo seeds with n- butane. The conditions were as follows: material liquid ratio 1: 4 (g/mL), extraction time 50 min, extraction temperature 50°C, and extraction 2 times.

The defatted pomelo seed (dried, 1.2 kg) was extracted three times with 70% ethanol at 50°C for 4 h. The ethanol extracts were analyzed by the UPLC-MSMS system (Thermo Fisher Scientific, USA). Chromatography was carried out on Zorbax Eclipse C18 (1.8 μm*2.1*100 nm, Agilent technologies, USA) at 30°C. The mobile phase contained 0.1% formic acid-water (A) and acetonitrile (B). The flow rate was 0.3 mL/min and injection volume was 2 μL. The gradient conditions were set as follows: 0–5% (B) in 0 to 2 min, 2–30% (B) in 2–6 min, 30% (B) in 6–7 min, 30–78% (B) in 7–12 min, 78% (B) in 12–14 min, 78–95% (B) in 14–17 min, 95% (B) in 17–20 min, 95–5% (B) in 20–21 min, and 5% (B) in 21–25 min.

The mass spectra were performed in positive electrospray ionization (ESI) modes, and the optimal conditions were set as follows: heater temperature 325°C; sheath gas flow rate 45 arb; auxiliary gas flow rate 15 arb; purge gas flow rate 1 arb; electrospray voltage 3.5 KV; capillary temperature 330°C; S-Lens RF Level 55%. Scanning mode was primary full scanning (Full Scan, m/z 100–1,500) and data-dependent secondary mass spectrometry scanning (dd-MS2, TopN = 10). Resolution was 120,000 (primary mass spectrometry) and 60,000 (secondary mass spectrometry). Collision mode was high-energy collision dissociation (HCD).

Purification of Limonin

The ethanol extracts (118 g) was obtained after drying under vacuum condition at 50°C in a water bath, and then further extracted with ethyl acetate. These extracts were once again concentrated in a vacuum evaporator. The extracts was resolved using dichloromethane and isopropanol (1:2 v/v), then

recrystallized at 4°C for 8 h. The recrystallization operation was performed three times until pure white crystals were obtained. The obtained filtrates were concentrated and recrystallized to obtain the mother liquor. The preparative-HPLC (Yilite,China) was used later for separation and the analytical-HPLC (1100, Agilent technologies, USA) for analysis to give compound (101 mg). The preparative-HPLC conditions contained water (A) and acetonitrile (B). The flow rate was 3 mL/min and injection volume was 500 μL. The gradient conditions were set as follows: 0–10% (B) in 0 to 5 min, 10–45% (B) in 5–10 min, 45% (B) in 10–30 min. The purification of limonin was calculated by area normalization method.

Test of Neuroprotective Effect on PC12 Cells

Cell Culture and Treatment

$A\beta_{25-35}$ (HY-P0128, MCE, China) stock solution (180 μmol/L) was prepared as follows: $A\beta_{25-35}$ was dissolved in distilled water, and aliquots were stored at −20°C and incubated at 37°C for 7 days before usage. Highly differentiated rat pheochromocytoma PC12 cells (iCell-r024, iCell Bioscience Inc, China) were cultured at 37°C with 5% CO_2 in RPMI-1640 medium with 1% penicillin and 10% fetal bovine serum.

Cell Counting Kit-8 (CCK-8) was applied to determine the final dosage of $A\beta_{25-35}$ and limonin for cell treatment. Results showed that treating cells for 48 h with 20-μM of $A\beta_{25-35}$ significantly inhibited PC12 cell growth. Therefore, 20 μM $A\beta_{25-35}$ was chosen as the cell injury model concentration.

Cells were divided into the following groups: control, $A\beta_{25-35}$, $A\beta_{25-35}$+12.5 μg/mL limonin, $A\beta_{25-35}$+25 μg/mL limonin, $A\beta_{25-35}$+50 μg/mL limonin, $A\beta_{25-35}$+LY294002, and $A\beta_{25-35}$+LY294002+50 μg/mL limonin. In the control group, only cell culture medium was added. In $A\beta_{25-35}$ group, the cells were treated with 20 μM $A\beta_{25-35}$ for 48 h. In the sample groups, the cells were pre-treated with various concentrations of limonin for 1 h. After that, 20 μM $A\beta_{25-35}$ was added and cultured for 48 h. In $A\beta_{25-35}$+LY294002 and $A\beta_{25-35}$+LY294002+50 μg/mL limonin groups, the cells were treated with LY294002 for 1 h before the addition of $A\beta_{25-35}$ and limonin, and then incubated for 48 h.

Cell Viability Assay

CCK-8 assay was used to determine cell viability. The PC12 cells were seeded into 96-well plates at a density of 1×10^4 cells/well and then incubated with $A\beta_{25-35}$, limonin and LY294002 for 48 h. After incubation, 20 μL of CCK-8 reagent was added and incubated for 2 h. Next, the upper medium was removed and absorbance was measured at 450 nm using a Microplate Reader (DR-200Bs, Diatek, China).

Lactic Dehydrogenase (LDH) Cytotoxicity Assay

PC12 cells were inoculated into a 6-well plate and cultured for 24 h, and then processed in different groups and incubated for a certain amount of time. After the incubation, cells were collected and washed twice with phosphate buffered saline (PBS). The LDH ratio of each group was measured using a LDH kit (A020-1-2, NanJing JianCheng Bioengineering Institute, China).

Ca^{2+} Concentration Assay

The intracellular Ca^{2+} concentration assay was used as previously described method with some modifications (24). Briefly, at the end of incubation, 5 μmol/L Fluo-3/AM working solution (prepared in DMSO) was added to each well and incubation continued in the dark; then the Fluo-3/AM working solution was removed, and the cells were washed with Hank's balanced salt solution without Ca^{2+} buffer. This step was repeated until Fluo-3/AM was fully converted, and the fluorescence intensity was detected by a flow cytometer (AriaIII, BD, USA).

Reactive Oxygen Species (ROS) Activity Assay

Intracellular ROS levels were detected using a reactive oxygen species detection kit (S0033, Bryotime, China). Briefly, after different treatments, cells were collected and 10 μM 2,7-Dichlorodihydrofluorescein diacetate (DCFH-DA) working solution diluted with serum-free medium was added, mixed well and incubated at 37°C in the dark for 30 min. Then, the cells were washed three times with PBS and analyzed by flow cytometry.

Measurement of Mitochondrial Membrane Potential (MMP)

Mitochondrial membrane potential was detected using a MMP detection Kit (C2006, Beyotime, China). Briefly, after different treatments, cells were harvested and 1 mL JC-1 solution was added and incubated at 37°C for 20 min. After the incubation, cells were washed three times with PBS, resuspended, and analyzed by flow cytometry.

Apoptosis Assay

Apoptosis was measured using Annexin V-FITC Apoptosis Detection Kit (AO2001-02P-G, Sungene Biotech, China). Briefly, after different treatments, cells were harvested, binding buffer (300 μL) diluted with PBS was added, and then 5 μL of PI and 5 μL Annexin V-FITC were added and incubated in the dark for 15 min, followed by measurement using flow cytometry: FITC excitation 494 nm, emission 520 nm; PI excitation 493 nm, emission 636 nm.

Western Blot Analysis

Western blotting assay was used to analyze changes of cell signaling. Briefly, at the end of incubation, the cells were harvested and Protein Extraction Kit (AS1011, ASPEN, China) was used to extract total cell proteins by following the manufacturer's instructions. BCA Protein Concentration Determination Kit (AS1086, ASPEN, China) was used to determine the total protein concentration. Protein samples were then separated on 12% SDS-PAGE and transferred to PVDF membranes (IPVH00010, Millipore, USA). β-actin served as an internal control. After blocking with 5% skimmed milk at room temperature for 1 h, the blocking solution was removed, and the membranes were washed with TBST buffer. PVDF membranes were then incubated with primary antibodies overnight at 4°C, and then washed three times with TBST buffer, and further incubated with secondary antibodies. The freshly prepared ECL mixed solution (A : B = 1 : 1) was used for membrane exposure

in a dark room. The optical densities of the target bands were analyzed using the commercial AlphaEaseFC software.

Statistical Analysis

All the data were analyzed using SPSS 25.0 software and are expressed as mean ± standard (SD). The differences between treatments were assessed by one-way ANOVA. P-value < 0.05 was considered statistically significant.

RESULTS

Ethanol Extract Identification Using UPLC-MSMS

The ethanol extract from the pomelo seed was identified using UPLC-MSMS. The TIC chromatograms of the various compounds of ethanol extract from the pomelo seed was shown in **Figure 1**. These results indicated that a total of 29 compounds had been identified by LC-ESI/MS and their retention times (t_R), MS, and MS/MS fragmentation ions are shown in **Table 1**, including 14 flavonoids, 3 limonids, 9 phenols, 3 coumarin and its derivatives. The two peaks with the highest response values were selected for analysis. Results showed that the compound (t_R =0.85) exhibited quasi-molecular ion peaks $[M+H]^+$ at m/z 144.1019 in the MS spectra, using Agilent qualitative analysis software to collect the molecular information of the component ions. The molecular formula of this component was $C_7H_{13}NO_2$. Meanwhile, different levels of collision energy were used to obtain appropriate MS/MS information, and the characteristic fragment ions were at m/z 84.08133 (C_5H_9N) and m/z 98.09681 ($C_6H_{11}N$). Through the secondary mass spectrum, using the Thermo mzCloud online database, the compound was preliminarily identified as DL-Stachydrine. Another substance was identified in the same way; the molecular formula was $C_{26}H_{35}O_8$, ion m/z 471.2009 $[M+H]^+$, and the characteristic fragment ions were at m/z 425.1951 ($C_{25}H_{33}O_6$) and m/z 95.0496 ($C_5H_7O_2$); this compound was tentatively identified as limonin. The TIC ion chromatogram showed that the response value of limonin was very high.

Purification of Limonin

Limonin was principally recovered by isolation and purification. In this study, limonin was obtained with a purity of 99.13% after recrystallization and pre-HPLC in **Figure 1C**. The limonin was identified by HPLC and comparison with authentic standards retention time (t_R) in **Figure 1B**.

Morphological Changes of PC12 Cells

The morphological changes of PC12 cells are shown in **Figure 2**. The cells in the control group adhered well and grew like a spindle with a clear cell outline. After treatment with $A\beta_{25-35}$, the shape of the cells changed significantly, most of the cell protrusions were broken and the edges blurred. While pre-treatment of limonin significantly alleviated the injuries caused by $A\beta_{25-35}$ and maintained normal cell morphology.

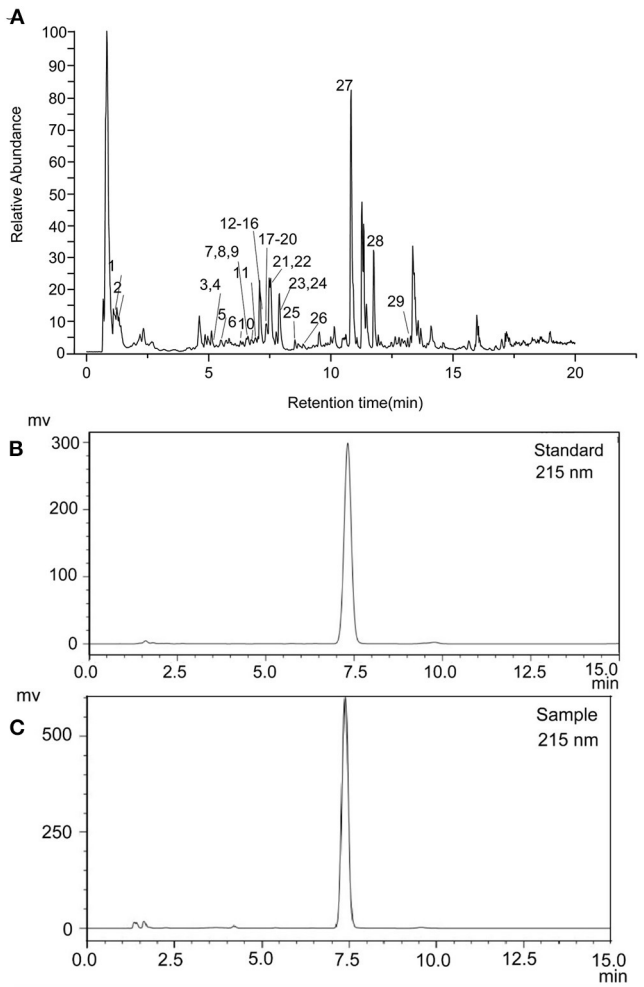

FIGURE 1 | Total ion current chromatograms of pomelo seed extract detected in positive ion mode **(A)**. HPLC chromatogram of limonin standard **(B)** and sample **(C)**.

LDH Release

As shown in **Figure 3**, when compared to the control group cells, treatment of cells with 20 μM $A\beta_{25-35}$ for 48 h resulted in a significant inhibition of cell viability and a significant increase in the release of LDH ($P < 0.0001$). Pre-treatment of cells with limonin reduced $A\beta_{25-35}$-mediated cell injury and the release of LDH ($p < 0.0001$). In the $A\beta_{25-35}$ + limonin group at doses of 12.5, 25, 50 μg/mL, the release of LDH declined from 192.59% to 85.19%. The results showed that as the concentration of limonin increased so did the protective effect on PC12 cells. The highest protection was observed when 50 μg/mL of limonin was utilized ($p < 0.0001$).

$[Ca^{2+}]I$ Release

As shown in **Figure 4A**, when compared to the control group cells, for the PC12 cells that were treated with $A\beta_{25-35}$, the content of $[Ca^{2+}]i$ increased significantly from 3.26 to 40.37%,

TABLE 1 | The characteristic components and their recognition results filtered by frequency in principal component analysis.

Peak number	Proposed compounds	Retention time (min)	Molecular formula	Molecular mass	Mass-to charge ratio	Deviation (ppm)	MS/MS fragment ions relative abundance (100%)
1	Phloroglucinol	1.237	$C_6 H_6 O_3$	126.03176	127.03905[M+H]$^+$	0	109.02875, 99.04456, 81.03412
2	2-Hydroxycinnamic acid	1.267	$C_9 H_8 O_3$	164.04742	165.05470[M+H]$^+$	0	119.04931
3	4-Methylumbelliferyl-α-D-glucopyranoside	5.477	$C_{16} H_{18} O_8$	338.09993	339.10715[M+H]$^+$	0	147.04401
4	Esculetin	5.481	$C_9 H_6 O_4$	178.02658	179.03383[M+H]$^+$	0	133.00283
5	Luteolin-3',7-Diglucoside	5.546	$C_{27} H_{30} O_{16}$	610.15343	611.16071[M+H]$^+$	0	450.11090,288.05798
6	5,7-Dihydroxy-4-methylcoumarin	6.378	$C_{10} H_8 O_4$	192.04235	193.04962[M+H]$^+$	0	178.02595,165.05472,149.0232
7	Isoferulic acid	6.556	$C_{10} H_{10} O_4$	194.05793	195.06532[M+H]$^+$	0	177.05458,163.03891,149.09610,145.00284
8	Vanillin	6.607	$C_8 H_8 O_3$	152.04735	153.05463[M+H]$^+$	0	125.05981
9	Eriodictyol	6.633	$C_{15} H_{12} O_6$	288.06308	289.07031[M+H]$^+$	−1	153.01820,123.04420,187.03896,179.03381,265.04933,243.0975
10	Quercetin	6.737	$C_{15} H_{10} O_7$	302.04244	303.4971[M+H]$^+$	0	274.0467,229.0941,165.01823,153.0181,137.02327
11	Ferulic acid	6.947	$C_{10} H_{10} O_4$	194.05792	195.06522[M+H]$^+$	0	177.05455,163.03893,149.05969,145.02837,117.03369
12	Keracyanin	7.028	$C_{27} H_{30} O_{15}$	594.1583	595.16553[M+H]$^+$	0	576.8625,552.69696,450.11115,449.10754,129.05479
13	Rhoifolin	7.041	$C_{27} H_{30} O_{14}$	578.16333	579.17072[M+H]$^+$	0	434.11575,271.05991,151.10870
14	Prunin	7.091	$C_{21} H_{22} O_{10}$	434.12077	435.12802[M+H]$^+$	−1	273.0753,153.01814
15	Naringeninchalcone	7.092	$C_{15} H_{12} O_5$	272.06802	273.0752[M+H]$^+$	−1	153.01822,107.04946
16	Naringin	7.092	$C_{27} H_{32} O_{14}$	580.17873	581.18579[M+H]$^+$	0	273.07538
17	Kaempferol	7.103	$C_{15} H_{10} O_6$	286.04735	287.05466[M+H]$^+$	−1	241.04906,213.05424,165.01826,153.01825,121.02847
18	Kaempferol-7-O-glucoside	7.107	$C_{21} H_{20} O_{11}$	448.10019	449.10751[M+H]$^+$	0	287.0548
19	Isorhamnetin	7.188	$C_{16} H_{12} O_7$	316.05789	317.06522[M+H]$^+$	−1	302.0418,285.03909,274.04694,153.01814
20	Hesperetin	7.195	$C_{16} H_{14} O_6$	302.07875	303.08599[M+H]$^+$	0	285.07520,177.05446,153.0180,
21	Sinapinic acid	7.463	$C_{11} H_{12} O_5$	224.06842	225.07561[M+H]+	0	207.0653,192.04147,147.04395
22	Naringenin	7.533	$C_{15} H_{12} O_5$	272.06803	271.06122[M+H]$^+$	−1	255.06500,179.03391,153.001823,147.044005,119.0494
23	Sinapyl aldehyde	7.636	$C_{11} H_{12} O_4$	208.07347	209.08075 [M+H]$^+$	0	177.05412, 191.07382, 121.06431
24	4-Coumaric acid	7.776	$C_9 H_8 O_3$	164.04728	165.05455[M+H]$^+$	0	147.0439,119.04929
25	Pinocembrin	8.616	$C_{15} H_{12} O_4$	256.07329	257.08054[M+H]$^+$	−1	153.01816,131.04918
26	Betaxolol	8.861	$C_{18} H_{29} N O_3$	307.21442	308.22171[M+H]$^+$	−1	116.1071, 72.0806, 98.0964
27	Limonin	10.568	$C_{26} H_{30} O_8$	470.19365	471.20099[M+H]$^+$	0	425.19510,95.04965
28	Obacunone	11.759	$C_{26} H_{30} O_7$	454.19857	455.20581[M+H]$^+$	−1	161.05966, 409.20065
29	Nootkatone	13.036	$C_{15} H_{22} O$	218.16692	219.17418[M+H]$^+$	0	163.11166

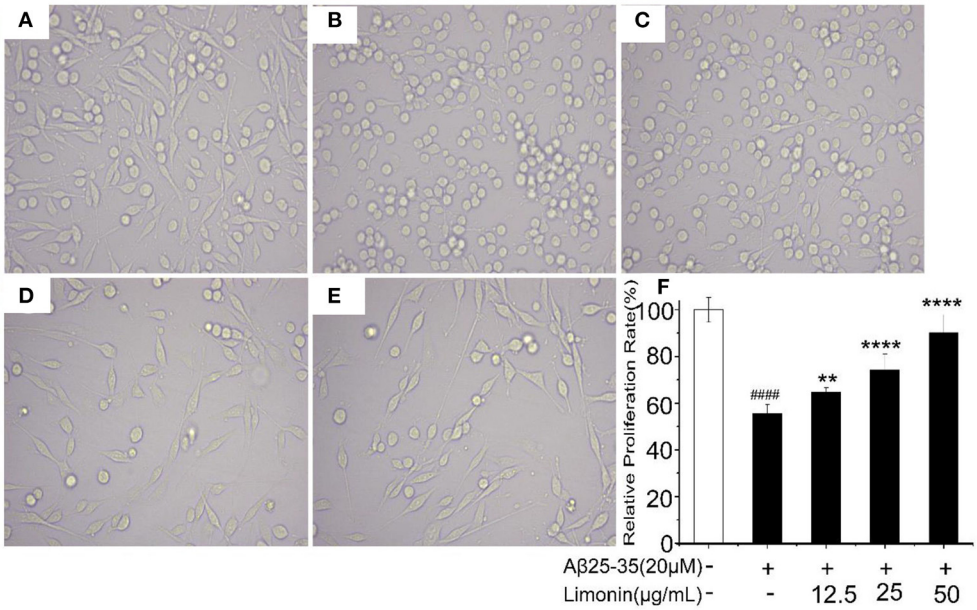

FIGURE 2 | Morphological changes of PC12 cells with different treatments. **(A)** Control group; **(B)** $A\beta_{25-35}$ group; **(C)** $A\beta_{25-35}$ +12.5 μg/mL limonin group; **(D)** $A\beta_{25-35}$ +25 μg/mL limonin group; **(E)** $A\beta_{25-35}$ +50 μg/mL limonin group; **(F)** Cell viability determination by CCK-8 assay. ####$p < 0.0001$ compared with the control group; **$p < 0.01$ and ****$p < 0.0001$ compared with the $A\beta_{25-35}$ group.

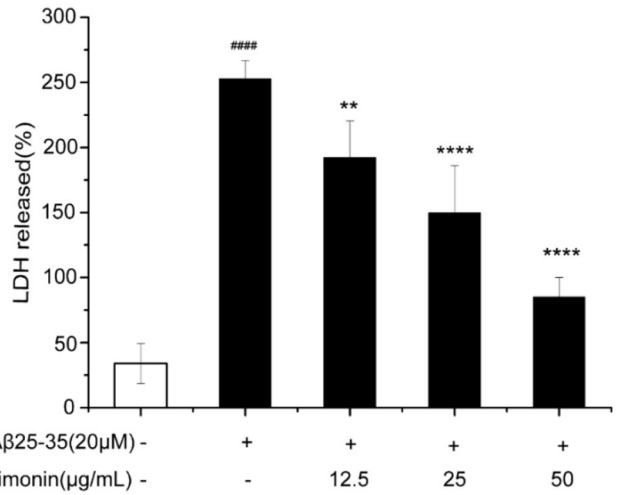

FIGURE 3 | Lactic dehydrogenase (LDH) activity was measured using an LDH assay kit. ####$p < 0.0001$ compared with the control group; **$p < 0.01$ and ****$p < 0.0001$ compared with the $A\beta_{25-35}$ group.

indicating that the Ca^{2+} in the cells were overloaded. The pre-treatment of limonin induced a statistically significant decrease ($p < 0.0001$) of intracellular Ca^{2+} concentration when compared to the $A\beta_{25-35}$ group. In the $A\beta_{25-35}$ + limonin group at doses of 12.5, 25, 50 μg/mL, the concentration of Ca^{2+} declined from 25.3% to 6.55%, indicating that limonin could antagonize the release of Ca^{2+} in $A\beta_{25-35}$-treated PC12 cells. Additionally, there was a dose-dependent relationship between the decline in the concentration of intracellular Ca^{2+} and the concentration of limonin utilized for the treatment of cells ($p < 0.0001$).

ROS Content in PC12 Cells

Figure 4B showed that the level of ROS significantly increased ($p < 0.0001$) in PC12 cells that were exposed to $A\beta_{25-35}$, compared to the control group cells. Pre-treatment with limonin for 24 h prior to the addition of 20 μM of $A\beta_{25-35}$ to the cells resulted in decreased content of ROS ($p < 0.0001$). In the $A\beta_{25-35}$ + limonin group at a dose of 12.5 to 50 μg/mL, the fluorescence intensity of ROS decreased from 2263.67 to 780.00 with increasing concentration of limonin, indicating that limonin can significantly reduce ROS level in $A\beta_{25-35}$-treated PC12 cells. When the concentration of limonin was at 50 μg/mL, compared to the $A\beta_{25-35}$ group, the fluorescence intensity of ROS showed a significant decrease ($p < 0.0001$).

MMP in PC12 Cells

The change of MMP in PC12 cells was measured by the JC-1 staining assay in **Figure 4C**. Compared to the control group, MMP significantly decreased after treatment with 20 μM of $A\beta_{25-35}$ ($P < 0.0001$), which was confirmed by the increase of red JC-1 staining in the cells of the Q3 area. The pre-treatment of limonin significantly reversed the decrease of MMP caused by $A\beta_{25-35}$ treatment ($P < 0.0001$). In the $A\beta_{25-35}$ + limonin group at low, medium and high doses, the change of MMP was dose-dependent with the concentration of limonin.

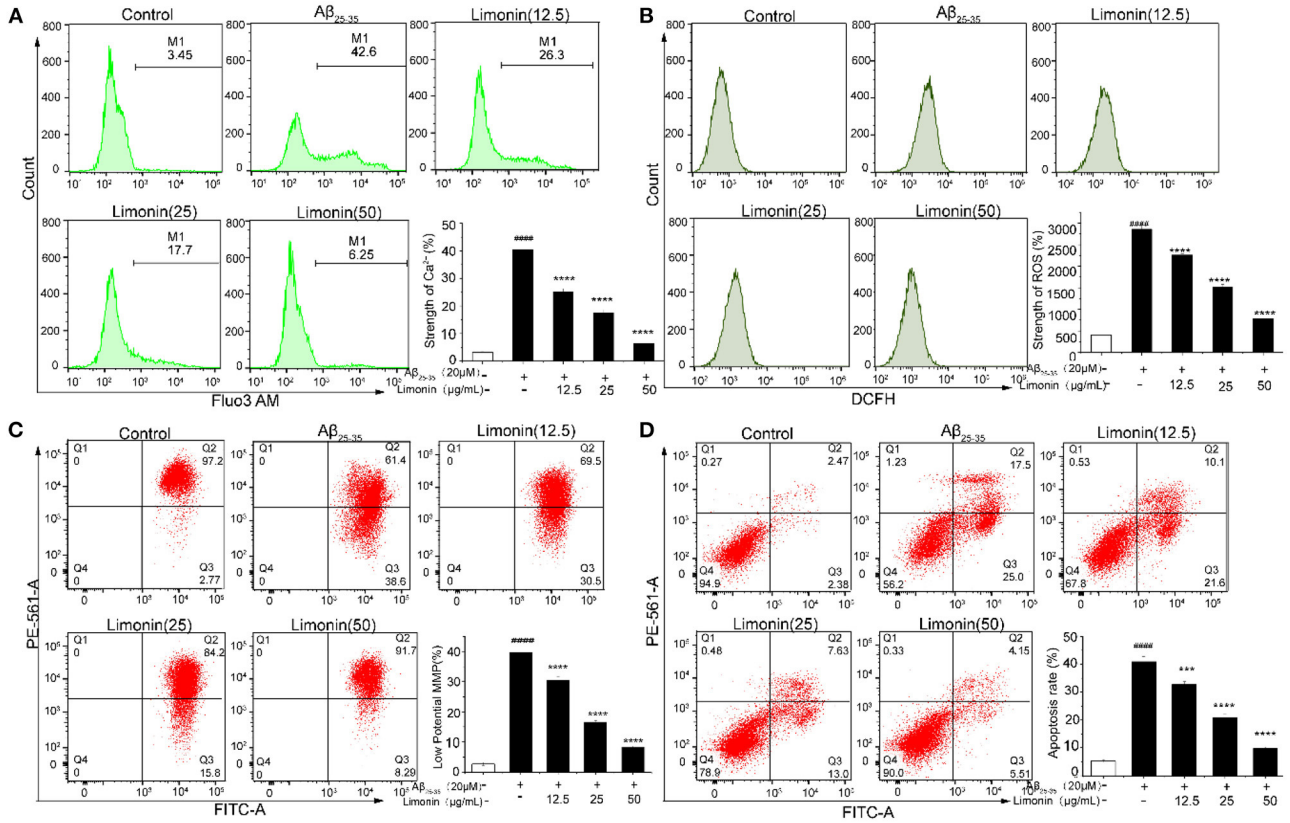

FIGURE 4 | The effect of limonin on $[Ca^{2+}]i$, ROS, MMP and apoptosis of PC12 cells induced by $A\beta_{25-35}$ treatment, analyzed with flow cytometer. **(A)** $[Ca^{2+}]i$ release; **(B)** reactive oxygen species (ROS) levels; **(C)** mitochondrial membrane potential (MMP); **(D)** apoptosis. ####$p < 0.0001$ compared with the control group; ***$p < 0.001$ and ****$p < 0.0001$ compared with the $A\beta_{25-35}$ group.

Apoptosis of PC12 Cells

To elucidate whether $A\beta_{25-35}$ induced death of PC12 cells is via an apoptotic-like mechanism, Annexin V-FITC/PI double staining method combined with flow cytometry technology was used to analyze the apoptosis of cells. As shown in **Figure 4D**, the total apoptotic rate of the control group was 4.85%, while 20 μM $A\beta_{25-35}$ significantly increased the early and late apoptosis of PC12 cells, and the total apoptotic rate reached 42.5% ($P < 0.0001$). After pre-protecting PC12 cells with different concentrations of limonin (12.5, 25, and 50 μg/mL), the total apoptotic rate of PC12 cells decreased to 31.7, 20.63, and 9.66%, respectively, compared with the $A\beta_{25-35}$ group, indicating that limonin could significantly inhibit $A\beta_{25-3}$-induced apoptosis of PC12 cells in a concentration-dependent manner.

The Activation of Bax/Bcl-2 and Caspase-3 in PC12 Cells

Bcl-2 and Caspase family proteins are related to cell apoptosis. In the current study, Western blot was used to determine Bax, Bcl-2 and Caspase-3 proteins under different treatment conditions. As shown in **Figure 5A**, when compared to control cells, PC12 cells that were treated with $A\beta_{25-35}$ for 48 h showed a significant decrease in the expression of Bcl-2, a significant increase in the expression of Bax and an increase in the ratio of Bax/Bcl-2 ($P < 0.0001$). Meanwhile, cleaved caspase-3 was also up-regulated ($P < 0.0001$), indicating that PC12 cells were undergoing apoptosis. In the limonin pre-treatment group, the expression of Bax was down-regulated, Bcl-2 was up-regulated, and cleaved caspase-3 was down-regulated, indicating the antagonistic effect of limonin on $A\beta_{25-35}$-mediated cell growth inhibition. As compared to the LY294002 inhibitor group, limonin was found to antagonize the inhibitor's regulation of apoptotic proteins, thereby preventing the occurrence of apoptosis programs.

PI3K/Akt Signal Pathway Activation in PC12 Cells

In order to explore the potential intracellular signaling mechanism of limonin antagonizing $A\beta_{25-35}$-induced death of PC12 cells, the changes in PI3K/Akt activation were evaluated. As shown in **Figure 5B**, compared to the control cells, the levels of p-Akt protein in $A\beta_{25-35}$ -treated PC12 cells were down-regulated and p-Akt/Akt ratio was significantly decreased ($P < 0.0001$). On the contrary, the expression level of p-Akt protein and the

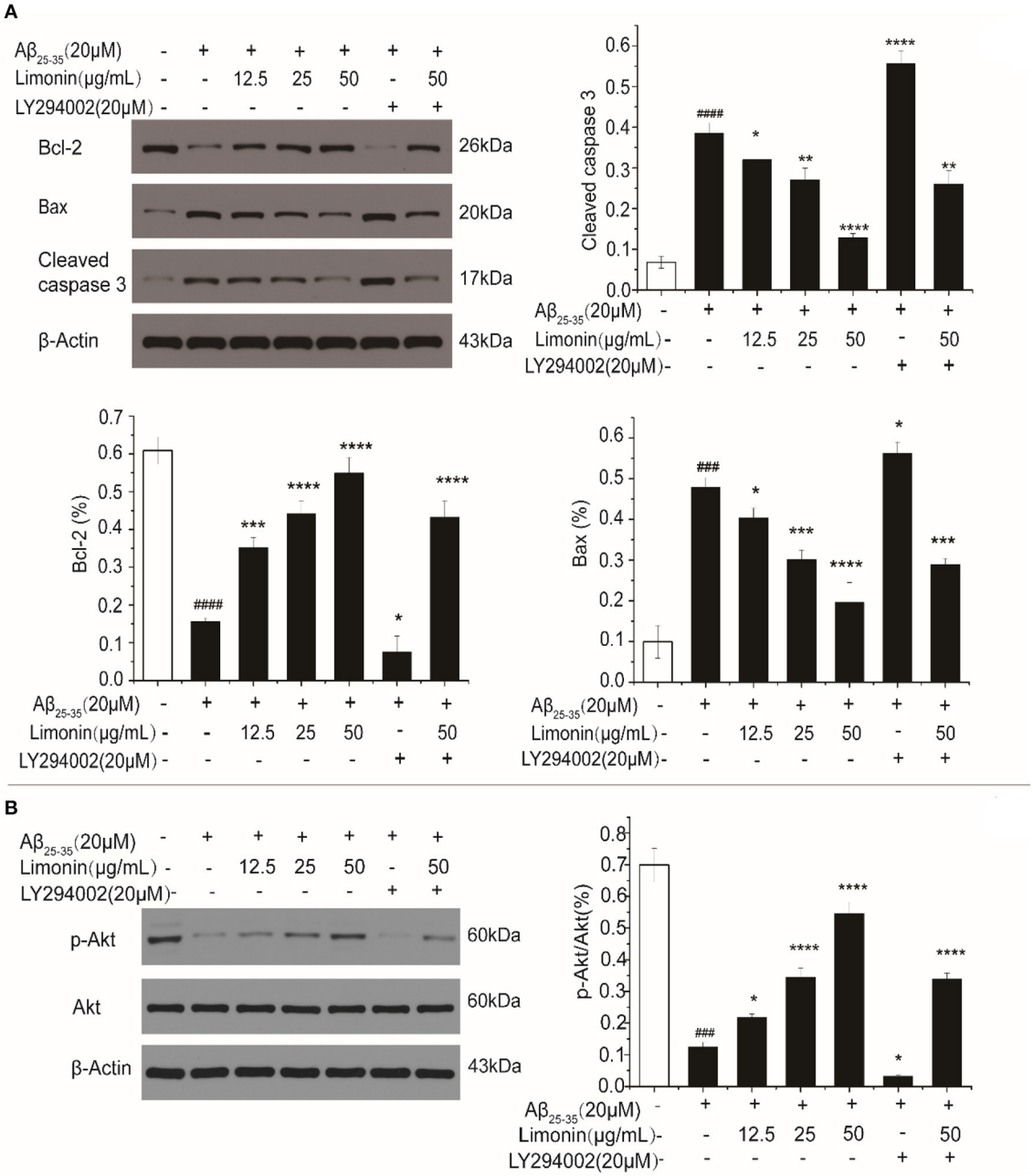

FIGURE 5 | The expression levels of Bax/Bcl-2 and Caspase-3 **(A)**, as well as p-Akt **(B)** in PC12 cells determined by Western blot. The values represent the mean ± SD ($n = 3$ in each group). ###$p < 0.001$ and ####$p < 0.0001$ compared with the control group; *$p < 0.05$, **$p < 0.01$, ***$p < 0.001$ and ****$p < 0.0001$ compared with the $A\beta_{25-35}$ group.

ratio of p-Akt/Akt in limonin treated PC12 cells were increased, indicating that limonin promoted the activation of Akt to form p-Akt, which then stimulated the biological activity of the PI3K/Akt signaling pathway in PC12 cells. LY294002 is a specific inhibitor of this pathway. LY294002 was added 1 h before limonin pre-treatment. It was found that the inhibitor LY294002 reversed the upregulation of p-Akt by limonin, indicating that limonin plays a role in activating the PI3K pathway.

DISCUSSION

In order to improve the utilization rate of pomelo seed, more high value-added products have to be found and applied. Firstly, the identification of chemical components of pomelo seeds extracts was investigated using UPLC-MS/MS. This study found that pomelo seeds are rich in active substances, such as limonoids, flavonoids, phenolic compounds, coumarin derivatives, among

others. The main ingredient limonin was successfully obtained with a purity of 99.13% via using crystallization and preparative-HPLC technologies. This high purity sample was helpful to understand the action mechanism of limonin directly and ensure the correctness of results.

In previous studies, limonin was shown to be able to improve the learning and memory ability of naturally aging rats, increase the anti-oxidant capacity of brain tissue, and have an effect of delaying brain aging (25, 26). The main clinical manifestations of AD are slowness of action and memory decline (27), thus the study of limonin is of great significance for exploring the prevention and dietary health care of AD. In the current study, an *in vitro* experiment was conducted to explore the role of limonin in antagonizing the neurotoxicity of PC12 cells mediated by $A\beta_{25-35}$. The experimental data showed that $A\beta_{25-35}$ significantly inhibited cell viability and increased lactate release. LDH represents the structural integrity of cell membrane to a certain extent (28). The increase in the content of LDH in the culture medium indicated that the cell membrane was damaged. Pre-treating cells with limonin could inhibit the neurotoxicity caused by treatment with $A\beta_{25-35}$. These results showed that limonin could protect PC12 cells from $A\beta_{25-35}$-mediated cytotoxicity and damage.

Precipitation of Aβ could increase the level of Ca^{2+} in the brain neurons of AD patients, reduce the excitability threshold of neurons, and cause neuronal function damage (29). We observed the protective effect of limonin pre-treatment by a significant decrease of Ca^{2+}, compared with $A\beta_{25-35}$ treatment group. ROS was closely related to AD pathological Aβ deposition, Tau protein phosphorylation, and inflammation (30). Mitochondria are the main source to generate ROS, thus mitochondrial dysfunction could easily lead to production and accumulation of ROS and cause cell oxidative damage (31). In PC12 cells treated with $A\beta_{25-35}$, a significant increase in ROS and a decrease in MMP were observed, indicating a mitochondrial system dysfunction. On the contrary, limonin treatment significantly reduced the excessive production of ROS, reversed the trend of MMP decline, and ultimately protected PC12 from $A\beta_{25-35}$-mediated oxidative stress and damage. This study has shown that limonin participated in the elimination of ROS, thereby inhibiting the occurrence of peroxidation and maintaining the integrity of cell membranes.

The neurotoxicity caused by abnormal deposition of Aβ could cause apoptosis of nerve cells, which is the main cause of AD (32). In PC12 cells treated with $A\beta_{25-35}$, the apoptotic rate was found to increase significantly, while the apoptotic rate significantly decreased after limonin treatment, indicating that limonin could reverse the occurrence of cell apoptosis. In the past, studies on cell apoptosis mainly focused on DNA degradation by enzymes into oligonucleotide fragments during cell apoptosis (33). In recent years, there has been more interest in investigating the early processes of cell apoptosis. Caspase participates in the process of specific enzymolysis and mediates the apoptosis signal transduction pathway. The roles of Caspase-3 and Bcl-2 have attracted much attention. Bcl-2 and Bax are a pair of homologous genes with opposite functions. In $A\beta_{25-35}$ treatment group, Bcl-2 expression was down regulated; Bax and Caspase-3 protein expression was up-regulated. It is generally believed that the role of Bcl-2 is upstream of the activation of Caspase-3. Caspase-3 is a protease for enzymatic hydrolysis of downstream substrates of each apoptotic pathway. Therefore, inhibiting the activation of Caspase-3 can lead to suppression of cell apoptosis. When the expression of Bcl-2 decreased, the cells will undergo apoptosis. The results of the limonin pre-treatment group showed that the changes of the above-mentioned proteins caused by $A\beta_{25-35}$ were reversed, and apoptosis was thereby prevented by limonin. It could be speculated that limonin inhibited the cascade of Bcl-2 and Caspase family proteins, and ultimately prevented cell apoptosis. This conclusion can also be verified by the results with LY294002.

PI3K/Akt is an important signal transduction pathway for anti-apoptosis and plays an important role in promoting cell survival. The protective effect of some drugs was exerted by regulating the Bcl-2 signal pathway and affecting the phosphorylation of Akt (34, 35). A large amount of literature showed that the PI3K/Akt pathway is closely related to neurological diseases such as AD and Parkinson disease. Qi et al. reported that schisandrin and nootkatone showed a neuroprotective effect via PI3K/Akt pathway, inhibiting inflammation and apoptosis (36). Lou et al. reported that linarin prevented $A\beta_{25-35}$ from inducing neurotoxicity via PI3K/Akt pathway (37). Akt is a serine/threonine protein kinase that promotes cell survival after nerve injury through PI3K signal transduction pathways. Akt activates to form p-Akt, which can phosphorylate multiple downstream targets (38). Therefore, the PI3K/Akt signaling pathway plays an anti-apoptotic effect through the apoptosis pathway and affects downstream anti-apoptotic molecules. In this study, after treatment with $A\beta_{25-35}$, the expression of p-Akt was significantly down-regulated, and the ratio of p-Akt/Akt decreased. With pre-treatment by limonin, the expression of p-Akt and the ratio of p-Akt/Akt were significantly increased. However, when the PI3K/Akt inhibitor LY294002 was added, the protective effect of limonin was attenuated, indicating that limonin exerted neuroprotective effects by affecting the PI3K/Akt pathway.

CONCLUSIONS

In conclusion, to begin with, the phenols compositions of waste pomelo seed extract were analyzed using UPLC-MS/MS. Besides, limonin with high concentration in pomelo seed was successfully obtained with a purity of 99.13% via using crystallization and preparative-HPLC technologies. Finally, limonin can protect nerve cells by activating the PI3K/Akt pathway. This activation also prevented mitochondrial damage, protected nerve cells from oxidative damage, and effectively reduced Aβ-induced neurotoxicity. This information provides a practical insight to produce valuable products from discarded pomelo seed, possessing potential to increase the economic profit and resource utilization rate while reducing environmental waste.

DATA AVAILABILITY STATEMENT

The original contributions presented in the study are included in the article/**Supplementary Material**, further inquiries can be directed to the corresponding author/s.

AUTHOR CONTRIBUTIONS

YQ: data curation, formal analysis, investigation, roles/writing—original draft, validation, project administration, supervision, and resources. JY: data curation, formal analysis, investigation, and roles/writing—original draft. LM: data curation, formal analysis, investigation, writing—review and editing, and validation. MS: formal analysis, writing—review and editing, and validation. GL: data curation, formal analysis, writing—reviewing and editing, investigation, supervision, and project administration. All authors contributed to the article and approved the submitted version.

FUNDING

This study was supported by the Guangdong Provincial Key Laboratory of Lingnan Specialty Food Science and Technology (2021B1212040013), and the Guangdong Province Key Field R&D Program Project (2019B020212002). We thank Zhongkai University of Agricultural Engineering for providing experimental conditions.

SUPPLEMENTARY MATERIAL

The Supplementary Material for this article can be found online at: https://www.frontiersin.org/articles/10.3389/fnut.2022.879028/full#supplementary-material

REFERENCES

1. Wu H, Lei Y, Zhu R, Zhao M, Lu J, Xiao D, et al. Preparation and characterization of bioactive edible packaging films based on pomelo peel flours incorporating tea polyphenol. *Food Hydrocolloid.* (2019) 90:41–9. doi: 10.1016/j.foodhyd.2018.12.016
2. Huang R, Cao M, Guo H, Qi W, Su R, He Z. Enhanced ethanol production from pomelo peel waste by integrated hydrothermal treatment, multienzyme formulation, fed-batch operation. *J Agric Food Chem.* (2014) 62:4643–51. doi: 10.1021/jf405172a
3. Van Hung P, Yen Nhi NH, Ting LY, Lan Phi NT, Abdullah AL, Al Loman A. Chemical composition and biological activities of extracts from pomelo peel by-products under enzyme and ultrasound-assisted extractions. *J Chem.* (2020) 2020:1–7. doi: 10.1155/2020/1043251
4. Puglisi I, De Patrizio A, Schena L, Jung T, Evoli M, Pane A, et al. Two previously unknown phytophthora species associated with brown rot of Pomelo (*Citrus grandis*) fruits in Vietnam. *PloS ONE.* (2017) 12:e172085. doi: 10.1371/journal.pone.0172085
5. Xiao L, Ye F, Zhou Y, Zhao G. Utilization of pomelo peels to manufacture value-added products: a review. *Food Chem.* (2021) 351:129247. doi: 10.1016/j.foodchem.2021.129247
6. Wu Z, Li H, Luo Y, Chen G, Li J, Wang Y, et al. Insights into the structural characterisations, bioactivities and their correlations with water-soluble polysaccharides extracted from different pomelo (*Citrus maxima* Merr.) tissues. *Int J Food Sci Tech.* (2020) 55:3091–103. doi: 10.1111/ijfs.14573
7. Wandee Y, Uttapap D, Mischnick P. Yield and structural composition of pomelo peel pectins extracted under acidic and alkaline conditions. *Food Hydrocolloid.* (2019) 87:237–44. doi: 10.1016/j.foodhyd.2018.08.017
8. Breksa AR, Manners GD. Evaluation of the antioxidant capacity of limonin, nomilin, limonin glucoside. *J Agric Food Chem.* (2006) 54:3827–31. doi: 10.1021/jf060901c
9. Shi Y, Xia H, Wu C, Li C, Duan C, Che C, et al. Novel nortriterpenoids with new skeletons and limonoids from the fruits of Evodia rutaecarpa and their bioactivities. *Fitoterapia.* (2020) 142:104503. doi: 10.1016/j.fitote.2020.104503
10. Shi Y, Zhang Y, Li H, Wu C, El-Seedi HR, Ye W, et al. Limonoids from Citrus: chemistry, anti-tumor potential, other bioactivities. *J Funct Foods.* (2020) 75:104213. doi: 10.1016/j.jff.2020.104213
11. Fan S, Zhang C, Luo T, Wang J, Tang Y, Chen Z, et al. Limonin: a review of its pharmacology, toxicity, and pharmacokinetics. *Molecules.* (2019) 24:3679. doi: 10.3390/molecules24203679
12. Yoon JS, Sung SH, Kim YC. Neuroprotective limonoids of root bark of *Dictamnus dasycarpus*. *J Nat Prod.* (2008) 71:208–11. doi: 10.1021/np070588o
13. Yoon JS, Yang H, Kim SH, Sung SH, Kim YC. Limonoids from *Dictamnus dasycarpus* protect against glutamate-induced toxicity in primary cultured rat cortical cells. *J Mol Neurosci.* (2010) 42:9–16. doi: 10.1007/s12031-010-9333-1
14. Zeb A, Son M, Yoon S, Kim JH, Park SJ, Lee KW. Computational simulations identified two candidate inhibitors of Cdk5/p25 to abrogate tau-associated neurological disorders. *Comput Struct Biotec.* (2019) 17:579–90. doi: 10.1016/j.csbj.2019.04.010
15. Lin ZL, Hu WM, Tang L, Zhang L, Zhang LJ, Hu ZH, et al. Effect of limonin on learning and memory ability and antioxidant capacity of natural apolexis rats. *Chin J Food Hyg.* (2016) 28:22–27. doi: 10.13590/j.cjfh.2016.01.005
16. Liu J, Zuo X, Han J, Dai Q, Xu H, Liu Y, et al. MiR-9-5p inhibits mitochondrial damage and oxidative stress in AD cell models by targeting GSK-3beta. *Biosci Biotechnol Biochem.* (2020) 84:2273–80. doi: 10.1080/09168451.2020.1797469
17. Ahmad SI, Ali G, Muhammad T, Ullah R, Umar MN, Hashmi AN. Synthetic beta-hydroxy ketone derivative inhibits cholinesterases, rescues oxidative stress and ameliorates cognitive deficits in 5XFAD mice model of AD. *Mol Biol Rep.* (2020) 47:9553–66. doi: 10.1007/s11033-020-05997-0
18. Nam G, Hong M, Lee J, Lee HJ, Ji Y, Kang J, et al. Multiple reactivities of flavonoids towards pathological elements in Alzheimer's disease: structure-activity relationship. *Chem Sci.* (2020) 11:10243–54. doi: 10.1039/D0SC02046J
19. Liu Y, Chen Z, Li B, Yao H, Zarka M, Welch J, et al. Supplementation with γ-glutamylcysteine (γ-GC) lessens oxidative stress, brain inflammation and amyloid pathology and improves spatial memory in a murine model of AD. *Neurochem Int.* (2021) 144:104931. doi: 10.1016/j.neuint.2020.104931
20. Tang Y, Xiong R, Wu AG, Yu CL, Zhao Y, Qiu WQ, et al. Polyphenols derived from lychee seed suppress Aβ (1-42)-induced neuroinflammation. *Int J Mol Sci.* (2018) 19:2109. doi: 10.3390/ijms19072109
21. Wang H, Lu B, Chen J. Knockdown of lncRNA SNHG1 attenuated Abeta25-35-inudced neuronal injury via regulating KREMEN1 by acting as a ceRNA of miR-137 in neuronal cells. *Biochem Biophys Res Commun.* (2019) 518:438–44. doi: 10.1016/j.bbrc.2019.08.033
22. Lee SJ, Nam E, Lee HJ, Savelieff MG, Lim MH. Towards an understanding of amyloid-beta oligomers: characterization, toxicity mechanisms, and inhibitors. *Chem Soc Rev.* (2017) 46:310–23. doi: 10.1039/C6CS00731G
23. Palop JJ, Mucke L. Amyloid-beta-induced neuronal dysfunction in Alzheimer's disease: from synapses toward neural networks. *Nat Neurosci.* (2010) 13:812–8. doi: 10.1038/nn.2583
24. Smith-Swintosky VL, Mattson MP. Glutamate, beta-amyloid precursor proteins, and calcium mediated neurofibrillary degeneration. *J Neural Transm Supp.* (1994) 44:29. doi: 10.1007/978-3-7091-9350-1_3
25. Tekupalli R, Anand S, Ramachandregowda S, Kariyappa AS, Gopinath MM. Neuroprotective effects of mangrove plants. In: Patra JK, Mishra RR, Thatoi H, editors. *Biotechnological Utilization of Mangrove Resources*. Salt Lake: Academic Press (2020). p. 261–73.

26. Almaliti J, Nada SE, Carter B, Shah ZA, Tillekeratne LM. Natural products inspired synthesis of neuroprotective agents against H_2O_2-induced cell death. *Front Mol Neurosci.* (2013) 23:1232–7. doi: 10.1016/j.bmcl.2013.01.013
27. Bocharova O, Pandit NP, Molesworth K, Fisher A, Mychko O, Makarava N, et al. Alzheimer's disease-associated β-amyloid does not protect against herpes simplex virus 1 infection in the mouse brain. *J Biol Chem.* (2021) 297:100845. doi: 10.1016/j.jbc.2021.100845
28. Yu X, Li Y, Mu X. Effect of quercetin on PC12 Alzheimer's disease cell model induced by A β 25-35 and its mechanism based on sirtuin1/Nrf2/HO-1 pathway. *BioMed Res Int.* (2020) 2020:8210578. doi: 10.1155/2020/8210578
29. Callens M, Kraskovskaya N, Derevtsova K, Annaert W, Bultynck G, Bezprozvanny I, et al. The role of Bcl-2 proteins in modulating neuronal Ca^{2+} signaling in health and in Alzheimer's disease. *BBA Mol Cell Res.* (2021) 1868:118997. doi: 10.1016/j.bbamcr.2021.118997
30. Toglia P, Cheung KH, Mak DO, Ullah G. Impaired mitochondrial function due to familial Alzheimer's disease-causing presenilins mutants via Ca^{2+} disruptions. *Cell Calcium.* (2016) 59:240–50. doi: 10.1016/j.ceca.2016.02.013
31. Sousa CA, Soares EV. Mitochondria are the main source and one of the targets of Pb (lead)-induced oxidative stress in the yeast *Saccharomyces cerevisiae*. *Appl Microbiol Biot.* (2014) 98:5153–60. doi: 10.1007/s00253-014-5631-9
32. Nam Y, Joo B, Lee J, Han K, Ryu K, Koh YH, et al. ALWPs improve cognitive function and regulate aβ plaque and tau hyperphosphorylation in a mouse model of Alzheimer's disease. *Front Mol Neurosci.* (2019) 12:192. doi: 10.3389/fnmol.2019.00192
33. Semick SA, Bharadwaj RA, Collado-Torres L, Tao R, Shin JH, Deep-Soboslay A, et al. Integrated DNA methylation and gene expression profiling across multiple brain regions implicate novel genes in Alzheimer's disease. *Acta Neuropathol.* (2019) 137:557–69. doi: 10.1007/s00401-019-01966-5
34. Jimenez S, Torres M, Vizuete M, Sanchez-Varo R, Sanchez-Mejias E, Trujillo-Estrada L, et al. Age-dependent accumulation of soluble amyloid beta amyloid β (Aβ) oligomers reverses the neuroprotective effect of soluble amyloid precursor protein-α (sAPPα) by modulating phosphatidylinositol 3-Kinase (PI3K)/Akt-GSK-3β pathway in Alzheimer mouse model. *J Biol Chem.* (2011) 286:18414–25. doi: 10.1074/jbc.M110.209718
35. Yang E, Zha J, Jockel J, Boise LH, Thompson CB, Korsmeyer SJ. Bad, a heterodimeric partner for Bcl-XL and Bcl-2, displaces Bax and promotes cell death. *Cell.* (1995) 80:285–91. doi: 10.1016/0092-8674(95)90411-5
36. Qi Y, Cheng X, Gong G, Yan T, Du Y, Wu B, et al. Synergistic neuroprotective effect of schisandrin and nootkatone on regulating inflammation, apoptosis and autophagy via the PI3K/AKT pathway. *Food Funct.* (2020) 11:2427–38. doi: 10.1039/C9FO02927C
37. Lou H, Fa NP, Perez RG, Lou H. Neuroprotective effects of linarin through activation of the PI3K/Akt pathway in amyloid-β-induced neuronal cell death. *Bioorg Med Chem.* (2011) 19:4021–7 doi: 10.1016/j.bmc.2011.05.021
38. Hu ZY, Huang WY, Zhang L, Huang B, Chen SC, Li XL. Expression of AKT and p-AKT protein in lung adenocarcinoma and its correlation with PD-L1 protein and prognosis. *Ann Transl Med.* (2020) 8:1172. doi: 10.21037/atm-20-5865

Conflict of Interest: The authors declare that the research was conducted in the absence of any commercial or financial relationships that could be construed as a potential conflict of interest.

Publisher's Note: All claims expressed in this article are solely those of the authors and do not necessarily represent those of their affiliated organizations, or those of the publisher, the editors and the reviewers. Any product that may be evaluated in this article, or claim that may be made by its manufacturer, is not guaranteed or endorsed by the publisher.

Copyright © 2022 Qiu, Yang, Ma, Song and Liu. This is an open-access article distributed under the terms of the Creative Commons Attribution License (CC BY). The use, distribution or reproduction in other forums is permitted, provided the original author(s) and the copyright owner(s) are credited and that the original publication in this journal is cited, in accordance with accepted academic practice. No use, distribution or reproduction is permitted which does not comply with these terms.

frontiers | Frontiers in Nutrition

ORIGINAL RESEARCH
published: 12 May 2022
doi: 10.3389/fnut.2022.868833

Ginsenosides Rb1 Attenuates Chronic Social Defeat Stress-Induced Depressive Behavior *via* Regulation of SIRT1-NLRP3/Nrf2 Pathways

*Ning Jiang[1,2], Yiwen Zhang[1], Caihong Yao[1], Hong Huang[1], Qiong Wang[2,3], Shuangxue Huang[2], Qinghu He[2] and Xinmin Liu[1,2]**

[1] Research Center for Pharmacology and Toxicology, Institute of Medicinal Plant Development, Chinese Academy of Medical Sciences, Peking Union Medical College, Beijing, China, [2] Hunan University of Chinese Medicine, College of Traditional Chinese Medicine, Changsha, China, [3] Affiliated TCM Hospital, School of Pharmacy, Sino-Portugal TCM International Cooperation Center, Southwest Medical University, Luzhou, China

OPEN ACCESS

Edited by:
Shuai Chen,
Wuhan University, China

Reviewed by:
Zhifang Deng,
Huazhong University of Science and Technology, China
Mi Mi Tang,
Central South University, China
Wei Jie Xie,
Shanghai Jiao Tong University, China

***Correspondence:**
Xinmin Liu
liuxinmin@hotmail.com

Specialty section:
This article was submitted to Food Chemistry, a section of the journal Frontiers in Nutrition

Received: 03 February 2022
Accepted: 29 March 2022
Published: 12 May 2022

Citation:
Jiang N, Zhang Y, Yao C, Huang H, Wang Q, Huang S, He Q and Liu X (2022) Ginsenosides Rb1 Attenuates Chronic Social Defeat Stress-Induced Depressive Behavior via Regulation of SIRT1-NLRP3/Nrf2 Pathways. Front. Nutr. 9:868833. doi: 10.3389/fnut.2022.868833

Ginsenoside Rb1, a diol-type ginseng saponin, has various positive effects on the central nervous system. This study aimed to evaluate the antidepressant effects of Rb1 on chronic social defeat stress (CSDS) induced behavioral deficits and the exact neural cascades linked with inflammatory processes. The results of behavioral tests such as social interaction, tail suspension, and forced swimming revealed that oral treatment of Rb1 (35 and 70 mg/kg) alleviates depression-like behavior. Rb1 treatment increased antioxidant enzyme activity (SOD and CAT) and reduced lipid peroxidation (LPO) content in the hippocampus. Rb1 also suppressed the production of inflammatory cytokines (TNF-α, IL-18, and IL-1β) as well as microglial activation (Iba1) in response to CSDS. Moreover, Rb1 administration considerably reduced the protein expression of NLRP3 (inflammasome) and promoted the protein expressions of Nrf2, HO-1 and Sirtuin1(SIRT1) activation in the hippocampus. Our findings showed that Rb1 effectively restores the depressive-like behavior in CSDS-induced model mice, mediated in part by the normalization of oxidative stress levels. The suppression of neuroinflammation is mediated by the regulation of SIRT1-NLRP3/Nrf2 pathways. Our results asserted that the Rb1 is a novel therapeutic candidate for treating depression.

Keywords: ginsenoside Rb1, depression, CSDS, mice, neuroinflammation

INTRODUCTION

Depression is an affective mental disorder, mainly characterized by significant and persistent depression, anhedonia, hopelessness, and worthlessness, accompanied by a syndrome of neurotic dysfunction (1). According to the World Health Organization (WHO), in 2008, depression ranked as the third most severe complication. It will rise to first place by 2030. Furthermore, the high rate of suicide and self-injury of depression seriously harms patients' physical and mental health, work, study, life, and social interaction and causes great social and financial load (2, 3). Even though a variety of antidepressants are now available to treat depression, the first choice drugs, such as

selective 5-HT reuptake inhibitors (SSRIs), have a minimal potential therapeutic ratio, a long list of adverse effects, poorer clinical compliance, and a high rate of recurrence after drug withdrawal (4). Hence, developing candidate therapeutic approaches with greater potency and comparatively less side effects are vital to prevent and treat depression.

Depression's pathogenesis is extremely complex and enigmatic. Multiple studies have reported that neuro-inflammation is due to the elevated pro-inflammatory cytokines in the brain. In recent years it has been considered a key factor in developing depression (5). Clinical studies demonstrated increased pro-inflammatory cytokine levels in the peripheral circulation and some brain regions in patients with depression (6). In animal models, recent findings have shown that inflammation plays a role in the progression of depressive and anxiety-like behavior in response to stress stimuli such as chronic unpredictable mild stress and social defeat stress (CSDS) (7).

NLRP3 inflammasome is a multimeric protein complex containing cytosolic NLRP3, the adaptor protein ASC, and Caspase-1 that triggers innate immune responses plays an important role in the maturation and release of inflammatory factors (8). The NLRP3 inflammasome is activated by numerous divergent invading pathogens and cellular damages such as ROS, mitochondrial DNA, ATP, and subsequent excretion of pro-inflammatory cytokines such as IL-18 and IL-1β into the extracellular matrix and prolonged immunological reactions that finally result in neurotransmitter dysfunction, oxidative damage to neurons, etc. (9). The NLRP3 inflammasome was found to be increased in the depression patient's peripheral blood mononuclear cells (PBMCs) (10). In animal models of depression, the depression-like phenotype is accompanied by NLRP3 inflammasome activation in the brain. Additionally, numerous pieces of evidence suggest a significant association between the NLRP3 inflammasome activation in the stress responses and depression's underlying causes, and inhibition of it exerts as a promoting therapeutic target for depressive disorders (11, 12).

Several studies have shown that increased reactive oxygen species (ROS) overcome the antioxidant defense system, resulting in oxidative stress, which plays a role in the pathophysiology of various disorders, including depression (13). ROS plays a crucial role in activating inflammasome, and pretreatment with various ROS scavengers represses NLRP3 inflammasome activation in response to a series of agonists (14, 15). The major transcriptional factor governing inflammation and oxidative stress in depression is nuclear factor E2-related factor 2 (Nrf2) (16). Under oxidative stress, Nrf2 is transported to the nucleus and binds to antioxidant response elements (ARE) to regulate the production of antioxidant enzymes such as HO-1 (17). The Nrf2/HO-1 signaling pathway plays an important role in anti-inflammatory activities. The upregulation of Nrf2/HO-1 and downregulation of IL-1β, IL-6, TNF-α in microglia have improved depressive-like behavior (18, 19). Furthermore, recent research has shown that Nrf2 regulates NLRP3 activation in LPS-induced depression, and the Nrf2/NLRP3 pathway is closely linked to the development of depression (20, 21).

Sirtuin1(SIRT1) is a NAD-dependent histone deacetylase belonging to the class III histone deacetylase family. SIRT1 is widely distributed in the brain. High levels in the hippocampus and cortex play a pivotal role in cellular events such as aging, inflammation, homeostasis, metabolic activities, and cellular survival (22). SIRT1 has recently been linked to major depressive disorder (23). Several studies in animal models also support the important role of SIRT1 in preventing and treating depression. Some previous studies have demonstrated that inflammatory cytokine expression is inhibited by SIRT1 via mediating initiation and progression of inflammation (e.g., deacetylating NF-kB) and ultimately preventing behavioral deficits (depressive and anxiety disorders) caused by chronic stress in rodents (24, 25). A recent study reported that an elevated expression of SIRT1 overcomes LPS-associated acute depressive-like behavior via suppressing microglial NLRP3 multiprotein oligomers known as Inflammasome (20).

Ginsenoside Rb1 (diol-type ginseng saponins) is considered the main active component of *Panax ginseng*. *Panax ginseng* is a traditional herb native to China, Siberia, and Korea. This herb has been widely used as a tonic for more than 2000 years in Far East countries. In Southeast Asian countries, it is used as a traditional remedy for preventing and treating neuropsychiatric diseases, such as depression (26). Our recent work showed that Rb1 can significantly ameliorate depressive-like behavior induced by chronic social defeat stress and modulates the BDNF-Trkb signaling pathway (27). Ginsenoside Rb1 demonstrated substantial antidepressant effects in rats by modulation of amino-acidergic and monoaminergic receptors and their associated neurotransmitters, induced microglial activation, and improved adult hippocampal neurogenesis in mice subjected to chronic mild stress (28). Unfortunately, very little is known about Rb1's antidepressant-like effect on behavioral impairments caused by CSDS, or on the exact neuronal processes underlying, or about Rb1's significance to the neuroprotective effect of slowing the inflammatory process in depression. Given these facts, the existing study aimed to examine the antidepressant effect of Rb1 in CSDS-associated depression-like behavior by assessing the behavioral changes and relations between neuroinflammatory parameters, such as microglia activation and the NLRP3 signaling pathway, as well as oxidative stress and the Nrf2/HO-1 signaling pathway in the hippocampus. Moreover, the expression of hippocampal SIRT1 was also estimated for unraveling possible mechanisms.

MATERIALS AND METHODS

Materials

Ginsenoside Rb1 (Rb1, purity > 98%) was provided by Chengdu Ruifensi Biological Technology Co., Ltd, China. Imipramine (IMI) was acquired from Sigma-Aldrich USA).

Animals

Vital River Co., Ltd. (Certificate No. SCXK 2016–0006, Beijing, China) supplied 6-8 weeks old male C57BL/6J mice ($n = 60$, weight: 20-22 g); and 12-months old retired breeders male CD-1 mice ($n = 70$, weight: 20-22 g). All mice were housed in

standard animal housing conditions, including a humidity of 55%, a 20-22°C temperature, a 12-h:12 h light/dark cycle, and unlimited access to water and food. The animal experiments were performed with proper approval (Approval No. SYXK 2017-0020) and agreed with the requirements outlined by the Animal Research Committee of Peking Union Medical College's Institute of Medicinal Plant Development. After 1 week of adaptation, the male mice were randomly divided into control, model, and treatment groups, i.p., imipramine (15 mg/kg), and Rb1 (35 and 70 mg/kg) (27). Rb1 and imipramine were suspended in distilled water using ultrasound. Except for the control group, the animals were subjected to a CSDS treatment followed by a series of behavioral assessments over the next four weeks. Imipramine (15 mg/kg) and Rb1 were administered orally for 32 days (**Figure 1**).

CSDS Procedure

The CSDS mouse model was developed according to the previously reported procedure with slight changes (7, 29, 30). Shortly after an intrusion into their cage, CD1 mice were used to observe the aggressive behavior of CSDS-induced mice (31). C57BL/6 mice were physically defeated for 28 days by being exposed to aggressive CD1 mice for 5 min each day. The C57BL/6 mice were placed in the same cage as the aggressor mouse the next day, isolated by a clear porous organic acrylic plate (thickness = 4 mm), and subjected to continuous psychological stress for the next 24 h, including frightening auditory, olfactory, and visual stimuli. Porous transparent organic acrylic sheets were placed to isolate the control mice in the same cage.

Behavioral Testing

Social Interaction Test

As previously reported, the **Social Interaction Test** (SIT) was carried out with minor modifications. A two-stage SIT was utilized to assess social avoidance behavior, and a video recording was made by 2-stage SIT (32). Each C57 mouse was caged in the arena and permitted to move freely for 150 s without a CD1 aggressor mouse in the interaction zone (IZ) in the first stage. The mice were taken out of the arena for 30 s at the end of the first phase, followed by cleaning the arena. After that, a CD1 mouse was caged using a transparent plastic box and released into the arena with the test mouse. The second step was then carried out for 150 s, and the same metrics were recorded again. Time spent in the IZ, both with and without the target, has been followed.

Open Field Test

On day 36, a computer-aided recorder was employed to monitor the mice's locomotor activity (LMA) using the open field test. A video recorder was placed on the top of a 75 cm diameter, 40 cm high metal container. Four mice were caged in the center of each box and permitted to roam free for 5 min for every test.

Tail Suspension Test

As per prior reports, mice were used in the tail suspension experiment (33, 34). Adhesive tape (about 1 cm from the tail tip) was used to suspend the mouse for 6 min. Following 2 min habituation, the immobility time was recorded during the final 4 min using Tail Suspension Real-Time Analysis (System-2.0).

Forced Swimming Test

The FST test was performed according to the earlier reported procedure (35). At about 25°C, the mice were placed in an acrylic tube (diameter = 14 cm and a height = 20 cm) confined to a depth of 15 cm for 6 min. For the last 4 min of a 6 min examination, Tail Suspension Real-Time Analysis (System-2.0) was used to take a video of immobility time.

Measurement of the Oxidative Stress and Inflammatory Factors

The hippocampus were homogenized with cold saline (10 volumes). The Pierce BCA Assay kits were used to determine protein concentration, while BSA was used as a reference. The CAT and SOD activity and LPO level in the hippocampus of mice were measured and estimated using commercial assay kits (Jiancheng Biology, China), following manufacturer instructions. One unit of SOD activity was defined as the amount that reduced the absorbance by 50% at 450 nm. The CAT activity was calculated according to the amount of the yellow complex produced by the reaction between H2O2 and ammonium molybdate at 405 nm. LPO were measured using the thiobarbituric acid reactive substance (TBARS) method as previously described in 535 nm. The adduct was maximally absorbed at a wave length of 586 nm. The LPO content and SOD and CAT activities in serum are expressed as μmol/l, U/ml, and U/ml, respectively (36). The levels of proinflammatory mediators, such as tumor necrosis factor α (TNF-α), interleukin 18 (IL-18), and interleukin 1β (IL-1β), in the serum were determined with commercial enzyme-linked immunosorbent assay (ELISA) kits for mice (Clound-clone, China) according to the manufacturer's instructions.

Western Blotting

Western blotting was performed with minor modifications as previously described (37). Following the approved operating conditions, cells were separated and loaded onto Millipore PFDF membranes (Bedford, MA, USA). After 2 h of blocking in 5% nonfat milk in Tris-buffered saline with Tween-20 (TBST), the membranes were treated with the primary antibodies described below overnight at 4°C: SIRT1 (ab189494, 1:1,000), NLRP3 (Q8R488, 1:1,000), cleaved Caspase-1 (89332s, 1:1,000), ASC (ab180799, 1:1,000), IL-1β (YT5201, 1:1,000), HO-1 (43966s, 1:1,000), Nrf2 (ab137550, 1:1,000), β-actin (4967s, 1:1,000). The membranes were treated for another 1 h at room temperature with a horseradish peroxidase-conjugated secondary antibody. ECL Prime Kit was used to visualize the protein bands, and ImageJ 1.46r software (NIH, USA, RRID: SCR_003070) was utilized to quantify them.

Immunohistochemistry

Following the behavioral tests, the animals were sedated with pentobarbital sodium and then transcranial perfused with 4% paraformaldehyde in 0.01 M phosphate buffer for 24 h after the last session. All the immunohistochemistry procedures were conducted according to our previous method (38). Every Iba-1^{+} cell within the DG was counted, and each group's fluorescence intensity was evaluated through ImageJ software

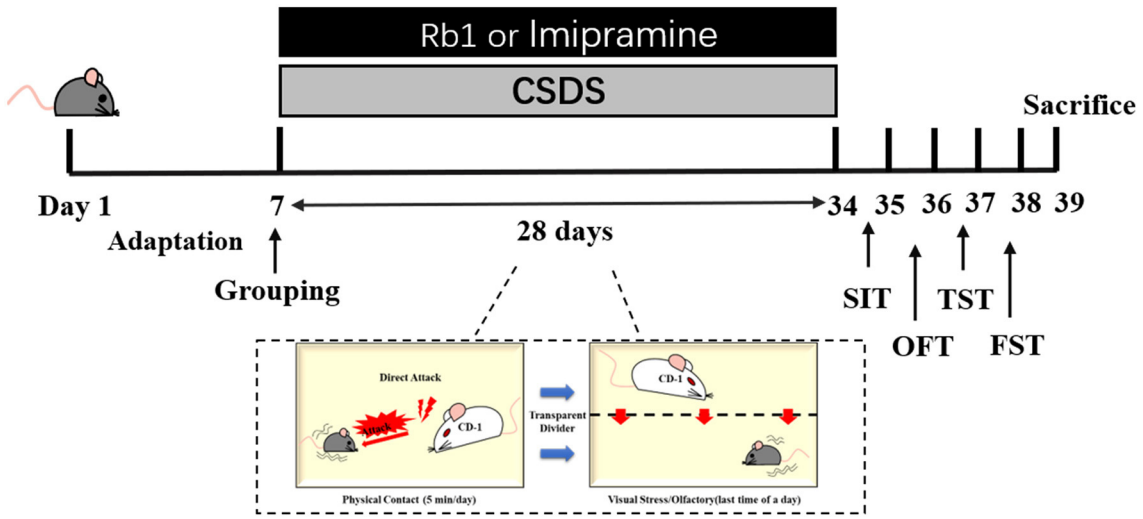

FIGURE 1 | Illustrates the experimental protocol utilized in the present study.

(Media Cybernetics, USA). A total of five mice were selected per group for the assessment.

Statistical Analysis

The SPSS Statistics version 21.0 (Chicago, USA) was employed to analyze the obtained results. The differences in the mean values were calculated using one-way ANOVA. A significant difference (LSD) test was employed for one-way ANOVA analyses, followed by a *post-hoc* test. The obtained results were indicated as the mean ± SEM. The p-value < 0.05 was regarded as statistically significant.

RESULT

Impact of Rb1 on Depressive-Like Behavior in CSDS Mice

There were no significant variations in the locomotor activities of all groups in the OFT, as indicated in **Figures 2A,B**. The underlined data suggested that the locomotor activities were unaffected by the drug or the CSDS treatment. According to the SIT, after 4 weeks of CSDS treatment, the social interaction ratio in CSDS mice was lowered than in the control mice ($p < 0.01$; **Figures 2C,D**). Rb1 treatment (35 and 70 mg/kg) or positive control drug imipramine (15 mg/kg) considerably reverse the decrease after 28 days of treatment (all $p < 0.01$). In TST and FST, the CSDS model group had a significantly longer immobility time, as shown in **Figures 2E,F** ($p < 0.01$). Rb1 (35 and 70 mg/kg) or imipramine (15 mg/kg) administration completely abolished the increase in immobility time induced by CSDS ($p < 0.05$).

Rb1 Attenuates the Inflammatory Cytokines Production and Oxidative Stress in the Hippocampus of CSDS Mice

The hippocampus of the CSDS model group showed a substantial elevation in hippocampal inflammatory markers such as TNF-α, IL-18, and IL-1β (**Figures 3A-C**; $p < 0.01$). Rb1 therapy, on the other hand, considerably reduced the CSDS-induced elevation in the underlined markers ($p < 0.05$). Relative to the control group, the CSDS group had noticeably lowered SOD and CAT activity in the hippocampus but greatly increased LPO levels (**Figures 3D-F**; all $p < 0.01$). Rb1 (35 and 70 mg/kg) or imipramine (15 mg/kg) therapy, on the other hand, increased SOD and CAT activity whilst substantially lowering the high content of LPO in the hippocampus ($p < 0.05$).

Effects of Rb1 on the SIRT1 Expression in the Hippocampus in CSDS Mice

IHC results showed that SIRT1 expression in the DG regions was decreased following a 28-day CSDS, while this decrease was reversed by Rb1 treatment (**Figure 4A**). The model group's relative fluorescence intensity in the DG areas was dramatically reduced, as seen in **Figure 4B** ($p < 0.01$). Conversely, Rb1 (35 and 70 mg/kg) exposure significantly increased the relative fluorescence intensity of SIRT1in the CSDS mice ($p < 0.05$, $p < 0.01$). Furthermore, Western blotting revealed that the amount of SIRT1protein was found to be considerably lowered in the hippocampus of mice (exposed to CSDS) than that of control mice (**Figure 4C**; $p < 0.01$). However, the Rb1 therapy prevented the lowered expression of SIRT1.

Rb1 Alleviates NLRP3 Inflammasome and Reduces Microglial Stimulation in the Hippocampus in CSDS Mice

The hippocampal expressions of cleaved Caspase-1, NLRP3, ASC, and IL-1β were considerably higher in the CSDS-exposed group than in the control group (**Figures 5A–D,G**; $p < 0.05$). In contrast, the expression of these proteins was dramatically reduced after treatment with Rb1. Immunohistochemistry for Iba1 revealed obvious alterations in the morphology of microglia in the dentate gyrus (DG) following CSDS. Iba1-positive

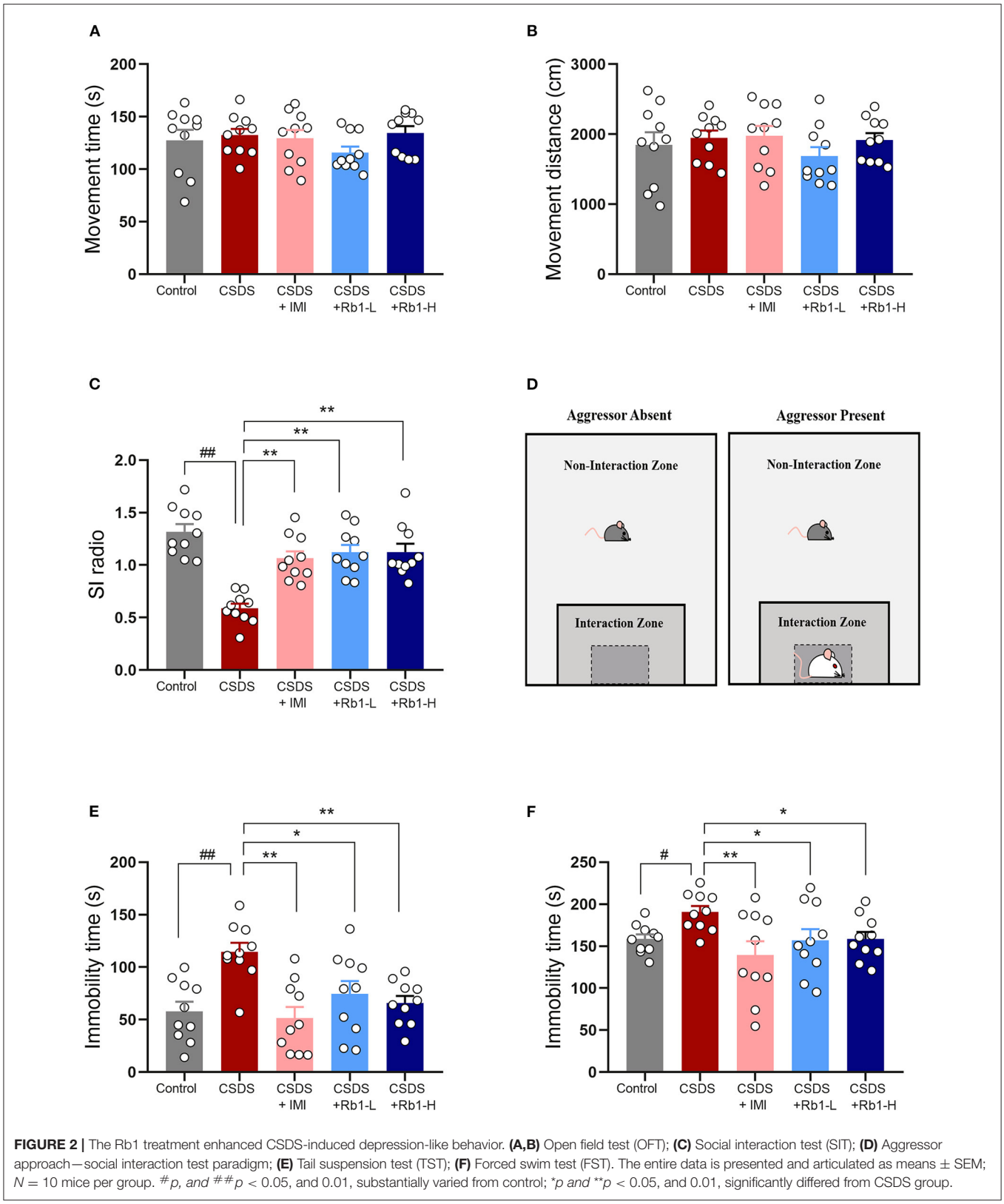

FIGURE 2 | The Rb1 treatment enhanced CSDS-induced depression-like behavior. **(A,B)** Open field test (OFT); **(C)** Social interaction test (SIT); **(D)** Aggressor approach—social interaction test paradigm; **(E)** Tail suspension test (TST); **(F)** Forced swim test (FST). The entire data is presented and articulated as means ± SEM; $N = 10$ mice per group. $^{\#}p$, *and* $^{\#\#}p < 0.05$, and 0.01, substantially varied from control; $^{*}p$ *and* $^{**}p < 0.05$, and 0.01, significantly differed from CSDS group.

microglia in the DG of non-stressed mice possessed fewer and scattered processes, while CSDS-treated mice had larger cell bodies with thick and condensed processes (**Figures 5E,F**). Relative to the other groups, the number of Iba1-immunoreactive cells in the DG elevated substantially post CSDS procedure (**Figure 5G**; $p < 0.01$). Rb1 inhibited microglia over-activation

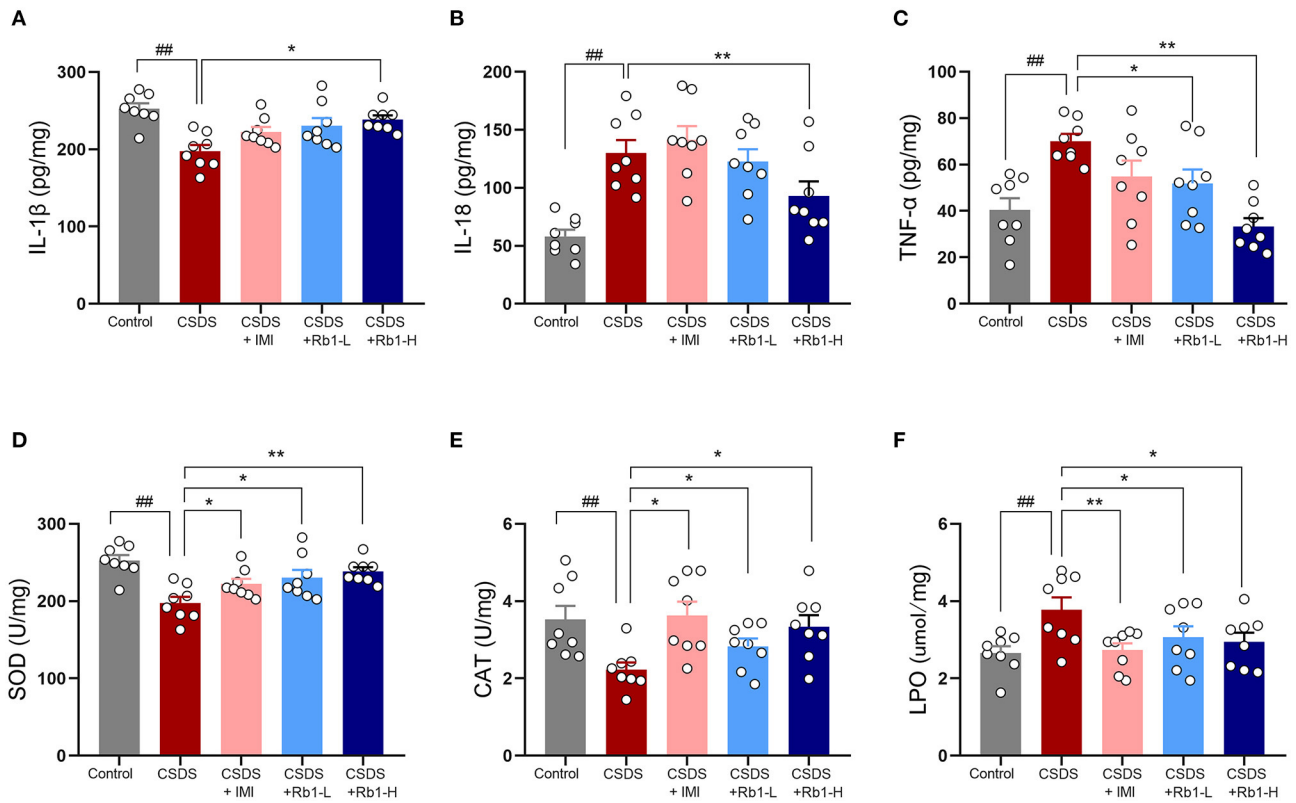

FIGURE 3 | Ginsenosides Rb1 and their effects on inflammatory and oxidative stress markers in CSDS mice; **(A)** Expression of IL-1β; **(B)** Expression of IL-6; **(C)** Expression of TNF-α; **(D)** SOD activity; **(E)** CAT-related activities; **(F)** Activity at the LPO level in the hippocampus. The entire data has been presented are means ± SEM; $N = 10$ mice per group. $^{\#\#}p < 0.01$, considerably differed from control; $^{*}p$ *and* $^{**}p < 0.05$, and 0.01, significantly varied from CSDS group.

by suppressing the translational level of ASC-1, NLRP3, and cleaved caspase-1.

Impact of Rb1 on the HO-1 and Nrf2 Protein Expression

The expression of Nrf2 and HO-1 was substantially decreased in CSDS rats' hippocampus compared to the control rats (**Figures 6A,B**; $p < 0.01$). However, Rb1 (35 and 70 mg/kg) considerably reversed the decrease in the HO-1 expression ($p < 0.05$). Rb1 therapy at 70 mg/kg led to a significant elevation in the expression of Nrf2.

DISCUSSION

In the current investigation, it has been revealed that Rb1 improves the behavioral deficit in CSDS mice, suggesting that it has antidepressant properties. In the hippocampus, the CSDS-induced neuroinflammatory response and oxidative stress were both ameliorated by Rb1 administration. Furthermore, Rb1 treatment considerably reduced the translational level of NLRP3 (inflammasome) and triggered translational levels of Nrf2, HO-1, and SIRT1 activation.

The CSDS depression model is frequently used and shown to be helpful in the evaluation of chronic stress-related depression (39). In the current study, we discovered that 4-week CSDS exposure significantly caused a persistent set of depression-like phenotypes such as despair and social-avoidance behaviors, as shown by deficits in SIT but prolonged immobility time in TST and FST, as indicated earlier (40, 41). More importantly, we observed that Rb1 at doses of 35 and 70 mg/kg (ip) in mice produced a significant increase of social interaction ratio in SIT and reduction of immobility time in the TST and FST. At the same time, Rb1 treatment did not lead to any significant abnormalities in locomotor activity even at the higher dose (70 mg/kg), indicating that this compound was well tolerated. The improvement of these behavioral deficits was not due to locomotor abnormality. Our observations were tested using standard behavioral tests, which quantitatively supported our findings and showed consistency with present findings. These results imply that ginsenoside Rb1 has antidepressant-like properties in CSDS depressed mice.

A strong relationship between neuroinflammation and depression has been revealed in recent decades. Inflammatory responses associated with central and peripheral pro-inflammatory cytokines secreting microglia (activation) and ROS and RNS generation are triggered by chronic stress and eventually result in depression (42). Microglia are significantly stimulated in the CNS and peripheral blood of animal models

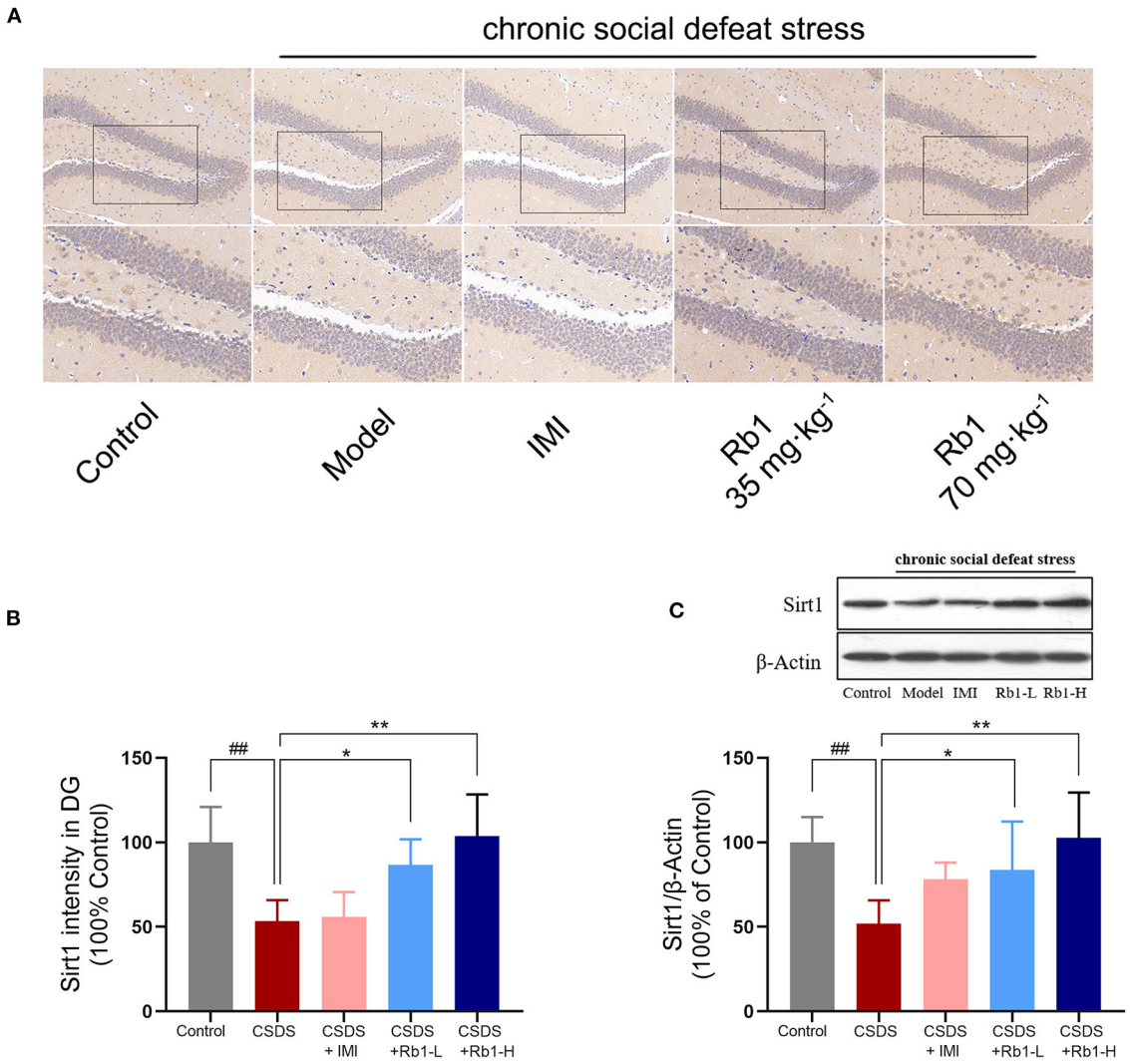

FIGURE 4 | In CSDS mice, ginsenosides Rb1 increased SIRT1 expression in the hippocampus. **(A)** SIRT1 expression in the rat hippocampal DG area, as seen by IHC staining. region (200, bar = 100 μm; 400, bar = 50 μm); **(B)** The mean fluorescence intensities of SIRT1 in the DG region; **(C)** Western blotting for detecting the SIRT1 expression in the hippocampus. The entire data has been presented are means ± SEM; $N = 4$ mice per group. $^{\#\#}p < 0.01$, considerably varied from control; $^{*}p$ and $^{**}p < 0.05$, and 0.01, considerably varied from CSDS group.

of depression such as CSDS and CUMS, and pro-inflammatory cytokines including TNF-α, IL-1 β, and IL-6 are also significantly elevated in the brain, according to a preclinical study (43). In agreement, we found that CSDS significantly promoted the Iba-1 activation and increased the levels of TNF-α IL-1 βin in the hippocampus of mice. At the same time, Rb1 administration could reverse these effects that have been considerably associated with the attenuation of microglia activation and an elevation of pro-inflammatory cytokines.

Rb1 therapy had an inhibitory impact on NLRP3 inflammasome stimulation in CSDS mice, according to our findings. NLRP3 inflammasome is a key constituent of the innate immune response. It consists of multiple proteins, including NLRP3 (nucleoside-bound oligomeric nod-like receptor), ASC (apoptosis-related spotted protein), and caspase-1 (cysteine aspartic protease) (44). Activation of NLRP3 inflammasome mainly occurs in macrophages and microglia. The activated NLRP3 inflammasome causes the hydrolysis of the inactive pro-caspase-1 protein, which is then cleaved into active caspase-1 that converts IL-1β and IL-18 precursor proteins into mature IL-1β and IL-18 (45). The underlined signals are received by other associated cells, resulting in the amplification of the signal cascade, which finally leads to pathogenic alterations involved in depression. Microglia positive expression level and pro-inflammatory factor expression level are increased under chronic stress, and NLRP3-inflammasome inhibitor can inhibit chronic stress-induced behavioral abnormalities (46). Numerous studies have linked chronic social defeat stress-induced depression to

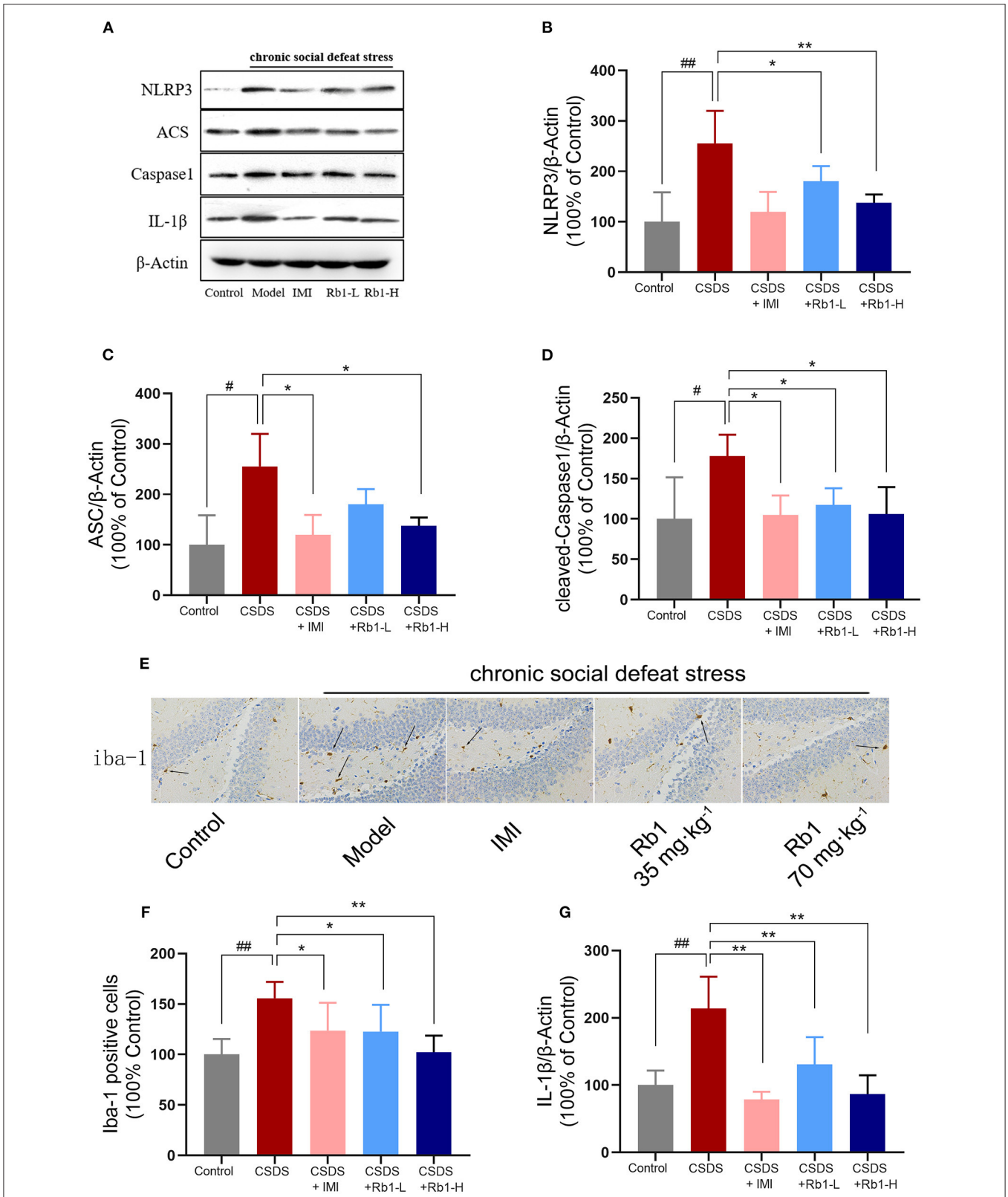

FIGURE 5 | In the hippocampus of CSDS mice, ginsenosides Rb1 reduced the NLRP3 inflammasome and microglial activation. Western blots analysis demonstrates **(A)** results of protein expression in the hippocampus of CSDS mice; **(B)** NLRP3; **(C)** ASC; **(D)** Cleaved Caspase-1; **(G)** IL-1β; **(E)** Immunohistochemical staining of Iba-1 in the hippocampus of CSDS mice (×400); **(F)** The number of Iba-1 positive cells. The entire data has been presented are means ± SEM; $N = 4$ mice per group. $^{\#}p$, and $^{\#\#}p < 0.05$, and 0.01, significantly different from control; $^{*}p$ and $^{**}p < 0.05$, and 0.01, considerably varied from CSDS group.

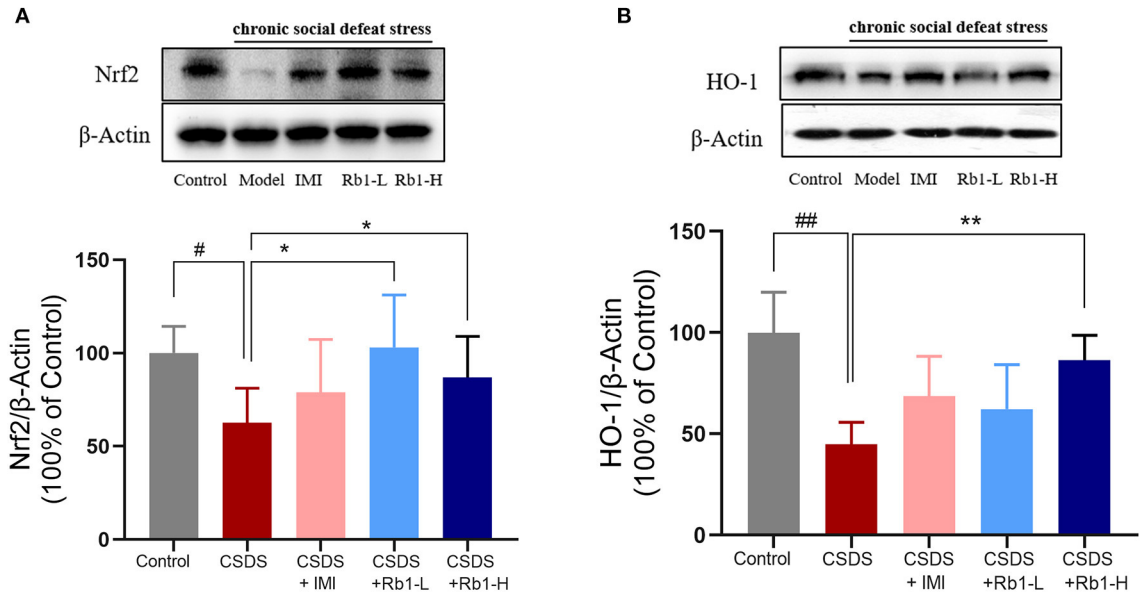

FIGURE 6 | Ginsenosides Rb1 induced NRF2 and HO-1 upregulation in the hippocampus of CSDS mice. Western blots analysis illustrates **(A)** NRF2; **(B)** HO-1. The entire data has been presented are means ± SEM; $N = 4$ mice/group. $^{\#}p$, and $^{\#\#}p < 0.05$, and 0.01, accordingly, considerably different from control; $^{*}p$, and $^{**}p < 0.05$, and 0.01, significantly varied from CSDS group.

an NLRP3 inflammasome-dependent inflammatory response in mice, as well as the suppression of the NLRP3 inflammasome by long-term antidepressant medication treatment (47). In this study, it has been revealed that the translational level of NLPR3, ASC, and cleaved caspase1 was considerably increased in CSDS mice, which was associated with increased production of inflammatory mediators and microglial activation. The underlined data showed consistency with the earlier research. However, Rb1 exposure considerably reduced the NLRP3-mediated inflammatory response and restored depression-like behavioral responses in CSDS animals. Previous studies reported that Rb1 inhibited inflammation and improved insulin signaling in adipose tissue by suppressing endoplasmic reticulum (ER) stress-associated NLRP3 inflammation activation (48). As a result, ginsenoside Rb1's putative antidepressant-like mechanisms may be linked to its positive effect in inflammation (CSDS-induced) in the hippocampus, which arises through suppressing of NLRP3 inflammasome stimulation.

Under normal settings, the dynamic balance between ROS and antioxidants is maintained; nevertheless, when the body is stressed, hyperactivation of active oxygen free radicals occurs, resulting in an imbalance of an organism's oxidation system. These effects cause mitochondrial damage, elevated levels of NO, MDA, and cytokine, a decrease in antioxidant activity (such as SOD, CAT, and GSH), hippocampus neuronal damage, apoptotic process, and depression, or worsening of the depression course (49, 50). Herein, MDA levels in the hippocampus of CSDS mice were found considerably higher, while CAT, SOD, and GSH levels were affectedly lowered. The underlined data showed consistency with the earlier studies. In contrast, Rb1 significantly increased the expression of antioxidant enzymes while reducing the content of the metabolite of lipid peroxidation (LPO), indicating a protective effect of Rb1 against oxidative stress impairment.

Furthermore, dysregulated redox-sensitive signaling plays a significant role in the immunological imbalance that often occurs with depression (51). An essential antioxidant cascade is Nrf2/HO-1, which contributes to maintaining redox balance and reducing oxidative damage by stimulating the expression of downstream antioxidant enzymes indicated as a candidate target for therapeutic approaches of depression (52). Depression-like symptoms can be alleviated by increasing the expression of Nrf2/HO-1 and decreasing the expression of IL-1β, IL-6, and TNF-α in the microglial cells. In addition, it has been postulated that CMS and CSDS depression models may reduce the expression of the Nrf2-system (Nrf2 and HO-1) (53). In agreement, our results of western blot revealed that the expression of Nrf2 and HO-1 were downregulated in the hippocampus of mice post 28 days of CSDS. Rb1 therapy, on the other hand, slightly improved the reduced expression of Nrf2 and its target proteins, such as HO-1. Ginsenoside Rb1 has been shown to have a neuroprotective impact by reducing oxidative stress in the CNS (54). Rb1 can enhance the expression of Nrf2 and HO-1 in the hippocampus of rats *in vivo* and *in vitro*. Its primary action mechanism is to activate Nrf2/HO-1, Nrf2/ARE signaling pathway, increase SOD and CAT activity, up-regulate endothelial nitric oxide synthase (eNOS), GSH, and HO-1 levels, reduce ROS and MDA content, thus improving intracellular redox status, reducing the expression of pro-apoptotic genes and inflammatory factor release in neuronal cells of rats, so as to alleviate damage of rat neuronal cells

induced by oxidative stress (55, 56). These findings imply that Rb1 may stimulate the Nrf2/HO-1 signaling cascade, which in turn modulates the production of downstream antioxidants, potentially contributing to its antidepressant-like effects. These findings supported the use of Rb1 to reduce oxidative stress in CSDS-induced depressive behavior.

Moreover, we found that Rb1 treatment could upregulate the expression of SIRT1 in the hippocampus of depressive mice (CSDS-induced). Sirtuin 1 (SIRT1) has been linked to oxidative stress in neuroinflammation is involved in aberrant mood behavior in response to stressful situations like depression (25). SIRT1 can regulate several transcription factors, including NF-κB and TNF-α, and have a key role in regulating inflammatory processes and oxidative stress (57). Furthermore, SIRT1 is linked to the stimulation of the NLRP3 inflammasome (58). Salvianolic Acid B improved CUMS-induced depressive-like behavior by reducing the inflammatory process oxidative stress and stimulating the SIRT1 signaling cascade, according to Liao et al. (59). Rg1 exhibits antidepressant effects in CSDS mice via SIRT1 signaling cascades, according to prior research (7). In recent decades, it has been revealed that melatonin inhibits acute depressive-like behavior (LPS-induced) and microglial NLRP3 Inflammasome stimulation via the SIRT1/Nrf2 cascade. Here, our data showed that Rb1 significantly increased the expression of SIRT1. Meanwhile, the mediation effects of Rb1 were accompanied by the upregulation of Nrf2/HO-1 and downregulation of NLRP3 inflammasome, as well as the improvement in depressive-like behavior in mice (exposed to CSDS). It has been reported that ginsenoside Rb1 attenuates oxidative damage through the SIRT1 signaling pathways *in vitro* experiments (60). Ginsenoside Rb1 inhibited the expression of pro-inflammatory cytokines such as IL-1β, TNF-α, and IL-6 in I/R injury rats *via* activating of TLR4/MyD88 and SIRT1 signaling cascades (61). The underlined results revealed that Rb1 induced SIRT expression, which in turn regulates NLRP3 inflammasome activation and the Nrf2/HO-1 cascade and suppresses the elevated oxidative stress and inflammation, that results in reducing depressive-like behavior. Despite the interesting findings, limitations still exist in the current study. More studies are required to confirm whether Rb1 attenuates chronic social defeat stress-induced depressive behaviors through SIRT1 pathway by using SIRT1 inhibitor or knocking down Sirt1 *in vitro* and *in vivo* experiments.

In summary, our findings suggested that administering Rb1 can rescue the depressive-like behavior such as social avoidance and behavioral despair of the CSD-induced mice model. Rb1 attenuates pro-inflammatory cytokines production and inhibits the activation of NLRP3 inflammasome. Moreover, RbI normalized oxidative stress imbalance followed by the Nrf2/HO-1 and SIRT1 activation. The underlined findings shed light on the molecular mechanisms by which Rb1 attenuates neuroinflammation. Moreover, this study highlights Rb1 as a candidate novel therapeutic agent for the prevention and treatment of depression.

DATA AVAILABILITY STATEMENT

The original contributions presented in the study are included in the article/supplementary materials, further inquiries can be directed to the corresponding author/s.

ETHICS STATEMENT

The animal experiments were carried out with proper approval (approval no. SYXK 2017-0020) and in agreement with the requirements outlined by the Animal Research Committee of Peking Union Medical College's Institute of Medicinal Plant Development.

AUTHOR CONTRIBUTIONS

NJ and XL designed the research. NJ, CY, HH, and YZ conducted the experiments. NJ, CY, and YZ performed the data analysis. NJ, YZ, QW, SH, QH, and XL wrote and amended the manuscript. XL and SH supervised the study and contributed to project administration. All authors approved the final version.

FUNDING

This work was supported by the International Cooperative Project of Traditional Chinese Medicine (GZYYG2020023), the Innovation Fund for Medical Sciences (CIFMS) grant (2021-1-I2M-034) and the Space Medical Experiment Project of the China Manned Space Program (HYZHXM05003).

REFERENCES

1. Xu P, Wang K, Lu C, Dong L, Chen Y, Wang Q, et al. Effects of the chronic restraint stress induced depression on reward-related learning in rats. *Behav Brain Res.* (2017) 321:185–92. doi: 10.1016/j.bbr.2016.12.045
2. Mcdonnell C. The burden of depression. *Nature.* (2014) 515:163. doi: 10.1038/515163a
3. Malhi GS, Mann JJ. Depression. *Lancet.* (2018) 392:2299–312. doi: 10.1016/S0140-6736(18)31948-2
4. Berwian IM, Walter H, Seifritz E, Huys QJ. Predicting relapse after antidepressant withdrawal - a systematic review. *Psychol Med.* (2017) 47:426–37. doi: 10.1017/S0033291716002580
5. Majd M, Saunders EFH, Engeland CG. Inflammation and the dimensions of depression: a review. *Front Neuroendocrinol.* (2020) 56:100800. doi: 10.1016/j.yfrne.2019.100800
6. Li W, Ali T, He K, Liu Z, Shah FA, Ren Q, et al. Ibrutinib alleviates LPS-induced neuroinflammation and synaptic defects in a mouse model of depression. *Brain Behav Immun.* (2021) 92:10–24. doi: 10.1016/j.bbi.2020.11.008
7. Jiang N, Lv J, Wang H, Huang H, Wang Q, Lu C, et al. Ginsenoside Rg1 ameliorates chronic social defeat stress-induced depressive-like behaviors and hippocampal neuroinflammation. *Life Sci.* (2020) 252:117669. doi: 10.1016/j.lfs.2020.117669
8. Xu Y, Sheng H, Bao Q, Wang Y, Lu J, Ni X. NLRP3 inflammasome activation mediates estrogen deficiency-induced depression- and anxiety-like behavior

and hippocampal inflammation in mice. *Brain Behav Immun.* (2016) 56:175–86. doi: 10.1016/j.bbi.2016.02.022
9. Heneka MT, Mcmanus RM, Latz E. Inflammasome signalling in brain function and neurodegenerative disease. *Nat Rev Neurosci.* (2018) 19:610–21. doi: 10.1038/s41583-018-0055-7
10. Alcocer-Gómez E, De Miguel M, Casas-Barquero N, Núñez-Vasco J, Sánchez-Alcazar JA, Fernández-Rodríguez A, et al. NLRP3 inflammasome is activated in mononuclear blood cells from patients with major depressive disorder. *Brain Behav Immun.* (2014) 36:111–7. doi: 10.1016/j.bbi.2013.10.017
11. Fleshner M, Frank M, Maier SF. Danger signals and inflammasomes: stress-evoked sterile inflammation in mood disorders. *Neuropsychopharmacology.* (2017) 42:36–45. doi: 10.1038/npp.2016.125
12. Inserra A, Rogers GB, Licinio J, Wong ML. The microbiota-inflammasome hypothesis of major depression. *Bioessays.* (2018) 40:e1800027. doi: 10.1002/bies.201800027
13. Ali T, Hao Q, Ullah N, Rahman SU, Shah FA, He K, et al. Melatonin act as an antidepressant *via* attenuation of neuroinflammation by targeting Sirt1/Nrf2/HO-1 signaling. *Front Mol Neurosci.* (2020) 13:96. doi: 10.3389/fnmol.2020.00096
14. Wu X, Zhang H, Qi W, Zhang Y, Li J, Li Z, et al. Nicotine promotes atherosclerosis *via* ROS-NLRP3-mediated endothelial cell pyroptosis. *Cell Death Dis.* (2018) 9:171. doi: 10.1038/s41419-017-0257-3
15. Yang M, Lv H, Liu Q, Zhang L, Zhang R, Huang X, et al. Colchicine alleviates cholesterol crystal-induced endothelial cell pyroptosis through activating AMPK/SIRT1 pathway. *Oxid Med Cell Longev.* (2020) 2020:9173530. doi: 10.1155/2020/9173530
16. Zborowski VA, Heck SO, Vencato M, Pinton S, Marques LS, Nogueira CW. Keap1/Nrf2/HO-1 signaling pathway contributes to p-chlorodiphenyl diselenide antidepressant-like action in diabetic mice. *Psychopharmacology (Berl).* (2020) 237:363–74. doi: 10.1007/s00213-019-05372-3
17. Guo C, Yang L, Wan CX, Xia YZ, Zhang C, Chen MH, et al. Anti-neuroinflammatory effect of Sophoraflavanone G from Sophora alopecuroides in LPS-activated BV2 microglia by MAPK, JAK/STAT and Nrf2/HO-1 signaling pathways. *Phytomedicine.* (2016) 23:1629–37. doi: 10.1016/j.phymed.2016.10.007
18. Bian H, Wang G, Huang J, Liang L, Zheng Y, Wei Y, et al. Dihydrolipoic acid protects against lipopolysaccharide-induced behavioral deficits and neuroinflammation via regulation of Nrf2/HO-1/NLRP3 signaling in rat. *J Neuroinflammation.* (2020) 17:166. doi: 10.1186/s12974-020-01836-y
19. Park BK, Kim NS, Kim YR, Yang C, Jung IC, Jang IS, et al. Antidepressant and anti-neuroinflammatory effects of bangpungtongsung-san. *Front Pharmacol.* (2020) 11:958. doi: 10.3389/fphar.2020.00958
20. Arioz BI, Tastan B, Tarakcioglu E, Tufekci KU, Olcum M, Ersoy N, et al. Melatonin attenuates LPS-induced acute depressive-like behaviors and microglial NLRP3 inflammasome activation through the SIRT1/Nrf2 pathway. *Front Immunol.* (2019) 10:1511. doi: 10.3389/fimmu.2019.01511
21. Tao W, Hu Y, Chen Z, Dai Y, Hu Y, Qi M. Magnolol attenuates depressive-like behaviors by polarizing microglia towards the M2 phenotype through the regulation of Nrf2/HO-1/NLRP3 signaling pathway. *Phytomedicine.* (2021) 91:153692. doi: 10.1016/j.phymed.2021.153692
22. Tang X, Zhao Y, Zhou Z, Yan J, Zhou B, Chi X, et al. Resveratrol mitigates sevoflurane-induced neurotoxicity by the SIRT1-dependent regulation of BDNF expression in developing mice. *Oxid Med Cell Longev.* (2020) 2020:9018624. doi: 10.1155/2020/9018624
23. Lei Y, Wang J, Wang D, Li C, Liu B, Fang X, et al. SIRT1 in forebrain excitatory neurons produces sexually dimorphic effects on depression-related behaviors and modulates neuronal excitability and synaptic transmission in the medial prefrontal cortex. *Mol Psychiatry.* (2020) 25:1094–111. doi: 10.1038/s41380-019-0352-1
24. Abe-Higuchi N, Uchida S, Yamagata H, Higuchi F, Hobara T, Hara K, et al. Hippocampal sirtuin 1 signaling mediates depression-like behavior. *Biol Psychiatry.* (2016) 80:815–26. doi: 10.1016/j.biopsych.2016.01.009
25. Lu G, Li J, Zhang H, Zhao X, Yan LJ, Yang X. Role and possible mechanisms of sirt1 in depression. *Oxid Med Cell Longev.* (2018) 2018:8596903. doi: 10.1155/2018/8596903
26. Xin C, Quan H, Kim JM, Hur YH, Shin JY, Bae HB, et al. Ginsenoside Rb1 increases macrophage phagocytosis through p38 mitogen-activated protein kinase/Akt pathway. *J Ginseng Res.* (2019) 43:394–401. doi: 10.1016/j.jgr.2018.05.003
27. Jiang N, Huang H, Zhang Y, Lv J, Wang Q, He Q, et al. Ginsenoside Rb1 produces antidepressant-like effects in a chronic social defeat stress model of depression through the BDNF-Trkb signaling pathway. *Front Pharmacol.* (2021) 12:680903. doi: 10.3389/fphar.2021.680903
28. Zhang L, Tang M, Xie X, Zhao Q, Hu N, He H, et al. Ginsenoside Rb1 induces a pro-neurogenic microglial phenotype *via* PPARγ activation in male mice exposed to chronic mild stress. *J Neuroinflammation.* (2021) 18:171. doi: 10.1186/s12974-021-02185-0
29. Golden SA, Covington HE, 3rd, Berton O, Russo SJ. A standardized protocol for repeated social defeat stress in mice. *Nat Protoc.* (2011) 6:1183–91. doi: 10.1038/nprot.2011.361
30. Monleon S, Duque A, Vinader-Caerols C. Inhibitory avoidance learning in CD1 mice: Effects of chronic social defeat stress. *Behav Processes.* (2015) 115:64–9. doi: 10.1016/j.beproc.2015.03.003
31. Sial OK, Warren BL, Alcantara LF, Parise EM, Bolaños-Guzmán CA. Vicarious social defeat stress: bridging the gap between physical and emotional stress. *J Neurosci Methods.* (2016) 258:94–103. doi: 10.1016/j.jneumeth.2015.10.012
32. Bo J, Fang W, Si Y, Peng F, Zhi-Fang D, Jun-Li X, et al. SKF83959 produces antidepressant effects in a chronic social defeat stress model of depression through BDNF-TrkB pathway. *Int J Neuropsychopharmacol.* (2015) 18:pyu096. doi: 10.1093/ijnp/pyu096
33. Steru L, Chermat R, Thierry B, Simon P. The tail suspension test: a new method for screening antidepressants in mice. *Psychopharmacology.* (1985) 85:367–70. doi: 10.1007/BF00428203
34. Jiang N, Zhang BY, Dong LM, Lv JW, Lu C, Wang Q, et al. Antidepressant effects of dammarane sapogenins in chronic unpredictable mild stress-induced depressive mice. *Phytother Res.* (2018) 32:1023–9. doi: 10.1002/ptr.6040
35. Sun XP, Shi Z, Pan RL, Qin C, Zhang YL, Li YH, et al. Antidepressant-like effects and mechanism of action of SYG in depression model in rats. *Neuro Endocrinol Lett.* (2014) 35:129–36. doi: 10.1016/S2212-5671(14)00446-8
36. Lu C, Lv J, Dong L, Jiang N, Wang Y, Wang Q, et al. Neuroprotective effects of 20(S)-protopanaxatriol (PPT) on scopolamine-induced cognitive deficits in mice. *Phytother Res.* (2018) 32:1056–63. doi: 10.1002/ptr.6044
37. Wang H, Lv J, Jiang N, Huang H, Wang Q, Liu X. Ginsenoside Re protects against chronic restraint stress-induced cognitive deficits through regulation of NLRP3 and Nrf2 pathways in mice. *Phytother Res.* (2021) 35:2523-35. doi: 10.1002/ptr.6947
38. Yang Y, Li S, Huang H, Lv J, Chen S, Pires Dias AC, et al. Comparison of the protective effects of Ginsenosides Rb1 and Rg1 on improving cognitive deficits in SAMP8 mice based on anti-neuroinflammation mechanism. *Front Pharmacol.* (2020) 11:834. doi: 10.3389/fphar.2020.00834
39. Yin YQ, Zhang C, Wang JX, Hou J, Yang X, Qin J. Chronic caffeine treatment enhances the resilience to social defeat stress in mice. *Food Funct.* (2015) 6:479–91. doi: 10.1039/C4FO00702F
40. Xu D, Sun Y, Wang C, Wang H, Wang Y, Zhao W, et al. Hippocampal mTOR signaling is required for the antidepressant effects of paroxetine. *Neuropharmacology.* (2018) 128:181–95. doi: 10.1016/j.neuropharm.2017.10.008
41. Jiang N, Lv JW, Wang HX, Wang Q, Lu C, Yang YJ, et al. Antidepressant-like effects of 20(S)-protopanaxadiol in a mouse model of chronic social defeat stress and the related mechanisms. *Phytother Res.* (2019) 33:2726–36. doi: 10.1002/ptr.6446
42. Park SE, Dantzer R, Kelley KW, Mccusker RH. Central administration of insulin-like growth factor-I decreases depressive-like behavior and brain cytokine expression in mice. *J Neuroinflammation.* (2011) 8:12. doi: 10.1186/1742-2094-8-12
43. Duan CM, Zhang JR, Wan TF, Wang Y, Chen HS, Liu L. SRT2104 attenuates chronic unpredictable mild stress-induced depressive-like behaviors and imbalance between microglial M1 and M2 phenotypes in the mice. *Behav Brain Res.* (2020) 378:112296. doi: 10.1016/j.bbr.2019.112296
44. Chen M, Li J, Peng J, Huang Y, Ouyang W, Liu X, et al. Linarin ameliorates innate inflammatory response in an experimental dry eye model via modulation of the NLRP3 inflammasome. Digital Chin Med. (2021) 4:42–53. doi: 10.1016/j.dcmed.2021.03.006

45. Latz E, Xiao TS, Stutz A. Activation and regulation of the inflammasomes. *Nat Rev Immunol.* (2013) 13:397–411. doi: 10.1038/nri3452
46. Hung WL, Ho CT, Pan MH. Targeting the NLRP3 inflammasome in neuroinflammation: health promoting effects of dietary phytochemicals in neurological disorders. *Mol Nutr Food Res.* (2020) 64:e1900550. doi: 10.1002/mnfr.201900550
47. Li Y, Song W, Tong Y, Zhang X, Zhao J, Gao X, et al. Isoliquiritin ameliorates depression by suppressing NLRP3-mediated pyroptosis *via* miRNA-27a/SYK/NF-κB axis. *J Neuroinflammation.* (2021) 18:1. doi: 10.1186/s12974-020-02040-8
48. Chen W, Wang J, Luo Y, Wang T, Li X, Li A, et al. Ginsenoside Rb1 and compound K improve insulin signaling and inhibit ER stress-associated NLRP3 inflammasome activation in adipose tissue. *J Ginseng Res.* (2016) 40:351–8. doi: 10.1016/j.jgr.2015.11.002
49. Vaváková M, Duračková Z, Trebatická J. Markers of oxidative stress and neuroprogression in depression disorder. *Oxid Med Cell Longev.* (2015) 2015:898393. doi: 10.1155/2015/898393
50. Juszczyk G, Mikulska J, Kasperek K, Pietrzak D, Mrozek W, Herbet M. Chronic stress and oxidative stress as common factors of the pathogenesis of depression and alzheimer's disease: the role of antioxidants in prevention and treatment. *Antioxidants.* (2021) 10:1439. doi: 10.3390/antiox10091439
51. Weyand CM, Shen Y, Goronzy JJ. Redox-sensitive signaling in inflammatory T cells and in autoimmune disease. *Free Radic Biol Med.* (2018) 125:36–43. doi: 10.1016/j.freeradbiomed.2018.03.004
52. Cigliano L, Spagnuolo MS, Boscaino F, Ferrandino I, Monaco A, Capriello T, et al. Dietary supplementation with fish oil or conjugated linoleic acid relieves depression markers in mice by modulation of the Nrf2 pathway. *Mol Nutr Food Res.* (2019) 63:e1900243. doi: 10.1002/mnfr.201900243
53. Gao W, Wang W, Liu G, Zhang J, Yang J, Deng Z. Allicin attenuated chronic social defeat stress induced depressive-like behaviors through suppression of NLRP3 inflammasome. *Metab Brain Dis.* (2019) 34:319–29. doi: 10.1007/s11011-018-0342-z
54. Liu X, Gu X, Yu M, Zi Y, Yu H, Wang Y, et al. Effects of ginsenoside Rb1 on oxidative stress injury in rat spinal cords by regulating the eNOS/Nrf2/HO-1 signaling pathway. *Exp Ther Med.* (2018) 16:1079–86. doi: 10.3892/etm.2018.6286
55. Peng H, You L, Yang C, Wang K, Liu M, Yin D, et al. Ginsenoside Rb1 attenuates triptolide-induced cytotoxicity in HL-7702 cells *via* the activation of Keap1/Nrf2/ARE pathway. *Front Pharmacol.* (2021) 12:723784. doi: 10.3389/fphar.2021.723784
56. Lin Z, Xie R, Zhong C, Huang J, Shi P, Yao H. Recent progress (2015-2020) in the investigation of the pharmacological effects and mechanisms of ginsenoside Rb(1), a main active ingredient in Panax ginseng Meyer. *J Ginseng Res.* (2022) 46:39–53. doi: 10.1016/j.jgr.2021.07.008
57. Yu X, Hu Y, Huang W, Ye N, Yan Q, Ni W, et al. Role of AMPK/SIRT1-SIRT3 signaling pathway in affective disorders in unpredictable chronic mild stress mice. *Neuropharmacology.* (2020) 165:107925. doi: 10.1016/j.neuropharm.2019.107925
58. Hu T, Lu XY, Shi JJ, Liu XQ, Chen QB, Wang Q, et al. Quercetin protects against diabetic encephalopathy via SIRT1/NLRP3 pathway in db/db mice. *J Cell Mol Med.* (2020) 24:3449–59. doi: 10.1111/jcmm.15026
59. Liao D, Chen Y, Guo Y, Wang C, Liu N, Gong Q, et al. Salvianolic acid B improves chronic mild stress-induced depressive behaviors in rats: involvement of AMPK/SIRT1 signaling pathway. *J Inflamm Res.* (2020) 13:195–206. doi: 10.2147/JIR.S249363
60. Fan C, Ma Q, Xu M, Qiao Y, Zhang Y, Li P, et al. Ginsenoside Rb1 attenuates high glucose-induced oxidative injury *via* the NAD-PARP-SIRT axis in rat retinal capillary endothelial cells. *Int J Mol Sci.* (2019) 20:4936. doi: 10.3390/ijms20194936
61. Cheng Z, Zhang M, Ling C, Zhu Y, Ren H, Hong C, et al. Neuroprotective effects of ginsenosides against cerebral ischemia. *Molecules.* (2019) 24:1102. doi: 10.3390/molecules24061102

Conflict of Interest: The authors declare that the research was conducted in the absence of any commercial or financial relationships that could be construed as a potential conflict of interest.

Publisher's Note: All claims expressed in this article are solely those of the authors and do not necessarily represent those of their affiliated organizations, or those of the publisher, the editors and the reviewers. Any product that may be evaluated in this article, or claim that may be made by its manufacturer, is not guaranteed or endorsed by the publisher.

Copyright © 2022 Jiang, Zhang, Yao, Huang, Wang, Huang, He and Liu. This is an open-access article distributed under the terms of the Creative Commons Attribution License (CC BY). The use, distribution or reproduction in other forums is permitted, provided the original author(s) and the copyright owner(s) are credited and that the original publication in this journal is cited, in accordance with accepted academic practice. No use, distribution or reproduction is permitted which does not comply with these terms.

frontiers | Frontiers in Nutrition

ORIGINAL RESEARCH
published: 16 May 2022
doi: 10.3389/fnut.2022.876992

Structural Characterization of *Gracilariopsis lemaneiformis* Polysaccharide and Its Property in Delaying Cellular Senescence

Xiaomei Wang[1†], Xiaogang Xu[2†], Genxiang Mao[2], Yue Guo[1], Guangce Wang[3], Xue Sun[4], Nianjun Xu[4*] and Zhongshan Zhang[1*]*

[1] Key Laboratory of Vector Biology and Pathogen Control of Zhejiang Province, Huzhou University, Huzhou, China, [2] Key Lab of Geriatrics & Geriatrics Institute of Zhejiang Province, Department of Geriatrics, Zhejiang Hospital, Hangzhou, China, [3] CAS and Shandong Province Key Laboratory of Experimental Marine Biology, Center for Ocean Mega-Science, Institute of Oceanology, Chinese Academy of Sciences, Qingdao, China, [4] National Engineering Research Laboratory of Marine Biotechnology and Engineering, Key Laboratory of Aquacultural Biotechnology, Ministry of Education, Collaborative Innovation Center for Zhejiang Marine High-Efficiency and Healthy Aquaculture, Key Laboratory of Marine Biotechnology of Zhejiang Province, Ningbo University, Ningbo, China

The sulfated polysaccharide was isolated from the purified *G. lemaneiformis* polysaccharide (PGP), and its property in delaying H_2O_2-induced 2BS cellular senescence was studied. The results showed that PGP was a linear polysaccharide containing alternating α-(1→ 3)- and β-(1→ 4)-galactopyranose units. Most of the sulfate groups are at C6 of the -(1→ 4)-α-D-Galp, and a small part of them are at C3 and C6. PGP pretreatment could decrease SA-β-gal-positive cells and prevent the formation of senescence-associated heterochromatic foci (SAHF) induced by H_2O_2 in a dose-dependent manner. It is speculated that PGP may delay aging by downregulating the expression of p21 and p53 genes. The finding provides new insights into the beneficial role of *G. lemaneiformis* polysaccharide (GP) on retarding senescence process.

Keywords: *G. lemaneiformis*, polysaccharide, cellular senescence, SA-β-gal, p53-p21 pathway

OPEN ACCESS

Edited by:
Shuai Chen, Wuhan University, China

Reviewed by:
Bo Jin, Zhejiang Chinese Medical University, China
Zhipeng Tao, Massachusetts General Hospital and Harvard Medical School, United States

***Correspondence:**
Zhongshan Zhang
01959@zjhu.edu.cn
Genxiang Mao
maogenxiang@163.com
Nianjun Xu
xunianjun@nbu.edu.cn

† These authors have contributed equally to this work and share first authorship

Specialty section:
This article was submitted to Food Chemistry, a section of the journal Frontiers in Nutrition

Received: *16 February 2022*
Accepted: *19 April 2022*
Published: *16 May 2022*

Citation:
Wang X, Xu X, Mao G, Guo Y, Wang G, Sun X, Xu N and Zhang Z (2022) Structural Characterization of Gracilariopsis lemaneiformis Polysaccharide and Its Property in Delaying Cellular Senescence. Front. Nutr. 9:876992. doi: 10.3389/fnut.2022.876992

INTRODUCTION

Cellular senescence is a physiological stress response of mammalian cells which results in the development of senescent cells with distinct physical, molecular, and metabolic signatures (1). In fact, aging is a key cellular program that can be induced and plays an important role in permanently limiting the reproduction of damaged and defective cells (2). Human embryonic fibroblasts can be cultured *in vitro* for about 50 generations. With the increase of generations, cell division and proliferation are slow and gradually show the characteristics of cell aging. The main result is that the cell volume increases, cell heterogeneity increases, and chromosome aberration and lysosome increase (3). Growth arrest is not only a prominent manifestation of cell aging but also an important factor causing biological aging. Therefore, the aging response can be prematurely induced in cells through the application of endogenous and exogenous stimuli *in vitro* and *in vivo*. H_2O_2 has been the most commonly used inducer for stress-induced premature senescence, which shares the features of replicative senescence (4). Oxidative stress-induced premature aging has been a good tool for *in vitro* aging research.

Gracilariopsis lemaneiformis, a kind of delicious seafood, is rich in active ingredients, including vitamins, polysaccharides, nicotinic acid, proteins, and dietary fiber (5). It was indicated that *G. lemaneiformis* polysaccharides (GPs) possess various biological activities, such as antitumor, antioxidant, and immune regulatory (6–11). Till present, the primary method of polysaccharide extraction is using hot water. However, there is a disadvantage of high energy consumption and long extraction time (12). Acid can effectively degrade the glycosidic bonds of polysaccharides and improve the yield of small molecular polysaccharides (13). Hydrochloric acid and citric acid are the most commonly used as medium at present.

In this study, a model *in vitro* was established that the human embryonic lung diploid cells (2BS) were treated with a sub-lethal dosage of H_2O_2 to study the protective potential of PGP against cellular senescence. Alterations in cellular morphology, senescence-associated β-galactosidase (SA-β-gal) activity, cell cycle, and molecular expression were evaluated to illustrate the possibly associated molecular mechanisms.

MATERIALS AND METHODS

Samples

G. lemaneiformis was collected from Xiapu County farm, Fujian Province. It was cleaned repeatedly and removed sediment and other sundries in the laboratory, then grounded and crushed after natural drying, and sealed for standby after 200 mesh screening.

Extraction and Purification of GP

A solution of 50 g seaweed powder in 1,000 ml distilled water was added to 0.15 g cellulose and stirred at 50°C for 3 h. Later, 25 g citric acid monohydrate was added for reaction at 95°C for 2 h. The extraction solution was filtered and centrifuged at 5,000 r/min for 15 min. The supernatant was adjusted to pH 7 with 10% ammonia and then concentrated and dialyzed. The extract solution was added to ethanol, and the precipitate was dried to obtain GP.

A solution of GP in distilled water was purified by gel chromatography on a Sephadex G-100 column (50 cm × 2.6 cm) eluted with tap water (0.2 ml/min). The fraction obtained was dialyzed and freeze-dried to yield a purified polysaccharide (PGP).

Structural Analysis

Routine component, including total sugar and sulfate content, was detected according to the previous method (14–16). Infrared spectrums were measured by a Nicolet Avatar 360 with KBr disks. Molecular weight and monosaccharide composition were determined by High Performance Gel Permeation Chromatography (HPGPC) and Gas Chromatography—Mass Spectrometry (GC-MS). ^{1}H and ^{13}C NMR spectra (e.g., 2D COSY, TOCSY, and DEPT) of samples were recorded using an AVANCE 600 MHz with a triple resonance probe.

Cell Viability Assay

2BS cells were cultured as a monolayer in Dulbeo's Modification of Eagle's Medium (DMEM) supplemented with 10% Fetal Bovine Serum (FBS) in a 37°C, 5% CO_2 humidified incubator. For drug administration, the culture medium was removed and PGP at indicated concentrations (e.g., 10, 50, 100, and 200 μg/ml) was added into each well for 2 h incubation, followed by treatment with 200 μM H_2O_2 for 1 h to induce premature senescence. Then, the H_2O_2-containing medium was replaced with a fresh medium for an additional 48 h before harvest. Cell viability was assessed by the Cell Counting Kit-8 assay, as described previously (17). Each compound was tested in triplicate and the experiments were repeated three times.

SA-β-Gal and DAPI Staining

Detection of *SA-β-Gal*-positive cells was performed, as described previously, according to the indications provided with the staining kit (18). All the experiments were repeated three times, and one of the representative results was shown. DNA was visualized by 4',6-diamidino-2-phenylindole (DAPI) (1 μg/ml) after fixation with 4.0% paraformaldehyde (PFA) (19).

Western Blot Analysis

An equal number of 2BS cells from the different groups were lysed using a sample buffer. Western blotting was performed, as described previously, according to the standard procedures. The sample was separated by 10% Sodium Dodecyl Sulfate PolyAcrylamide Gel Electrophoresis (SDS-PAGE) and transferred to nitrocellulose membranes. After being blocked in evaporated non-fat milk for 4 h, the membranes were incubated with 1% Bovine Serum Albumin (BSA) solution dissolving primary anti-bodies (p53, p21). Protein bands were visualized using horseradish peroxidase-conjugated secondary antibodies. Protein bands were quantified by densitometry and normalized to glyceraldehyde-3-phosphate dehydrogenase (GAPDH).

Statistical Analysis

All the data were presented as mean ± SD. A value of $p < 0.05$ was considered statistically significant. Differences between groups were evaluated by one-way ANOVA followed by Duncan's multiple range tests.

RESULTS

Chemistry of PGP

The soluble polysaccharide of *G. lemaneiformis* (GP) obtained by acid extraction was a non-gelling polysaccharide. Gel chromatography on dextran G100 separated the sulfated polysaccharide from GP into one peak, named PGP (**Figure 1A**). The latter was eluted as a single symmetrical peak corresponding to an average molecular weight of 2.7×10^3 Da, as determined by the high Performance Liquid Chromatography (HPLC) method. A lack of absorption at 280 nm indicated that PGP contained no protein.

The PGP contained 92.65% of total sugar and 5.37% of sulfate on the basis of fraction dry weight. Sugar compositional analysis revealed that PGP consists of polysaccharides containing a high amount of galactose together with a smaller amount of glucose unit.

Figure 1B exhibits the major functional groups and the chemical bonds of PGP. As shown, the broad absorption at 3,420 cm^{-1} was corresponded to the O–H stretching vibration,

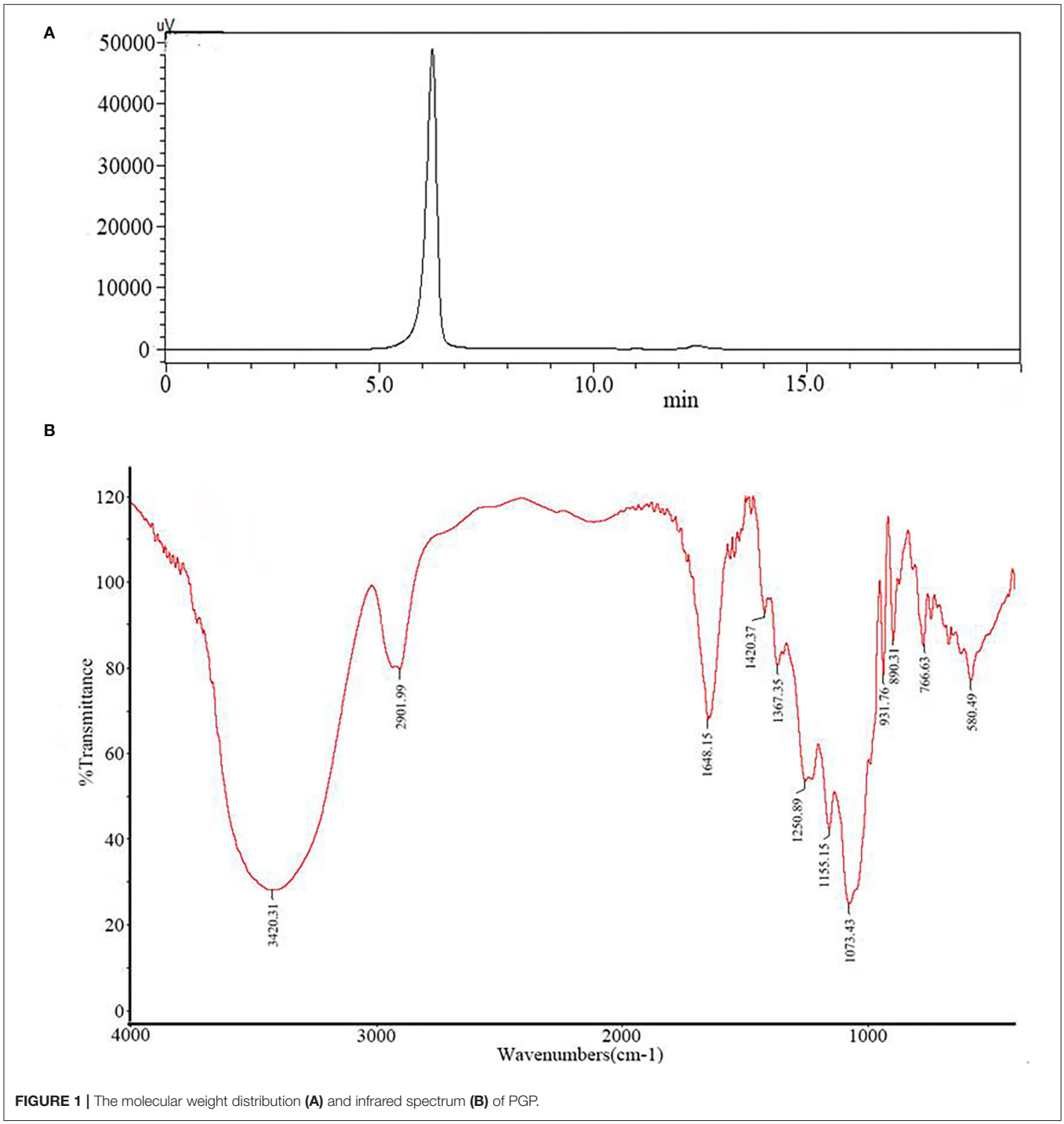

FIGURE 1 | The molecular weight distribution **(A)** and infrared spectrum **(B)** of PGP.

and the strong band at 2,902 cm^{-1} was ascribed to stretching vibrations of C–H. Two bands at 1,648 and 1,420 cm^{-1} were assigned to the absorbance of the deprotonated COO– group (20). These characteristics indicated that PGP was a typical acidic polysaccharide, which agreed with the content of uronic acid (9.84%). The bands at 1,250 and 931 cm^{-1} can be attributed to the S=O vibration of the sulfate groups and the C–O–C of 3,6-anhydro-a-L-galp (21). The peak at 820 cm^{-1} indicated that sulfate groups were located in position C6 of the galactose ring (22).

Structure of PGP

Methylation analysis of the sulfated PGP demonstrated the presence of a variety of methylated derivatives. In fact, methylation of sulfated polysaccharides does not always yield reliable proportions of methylated alditol acetates (23, 24). As shown in **Table 1**, it was probable that there was incomplete methylation. The peak type was relatively simple. The terminal group only exists in the form of Gal-(1→ indicating that galactose is the main terminal residue of PGP. The absence of other branched end residues indicated that most of the

TABLE 1 | Analysis of PGP methylation.

RT	Methylated sugar	Mass fragments (m/z)	Molar ratios	Type of linkage
17.661	2,3,4,6-Me_4-Galp	43,71,87,101,117,129,145,161,205	0.10	Gal-(1→
21.247	2,3,6-Me_3-Galp	43,87,99,101,113,117,129,131,161,173,233	0.34	→ 4)-Galp-(1→
21.549	2,4,6-Me_3-Galp	43,71,85,87,99,101,117,129,161	0.42	→ 3)-Galp-(1→
22.362	2,4-Me_2-Galp	43,71,87,99,101,117,129,139,159,173,189	0.14	→ 3,6)-Galp-(1→

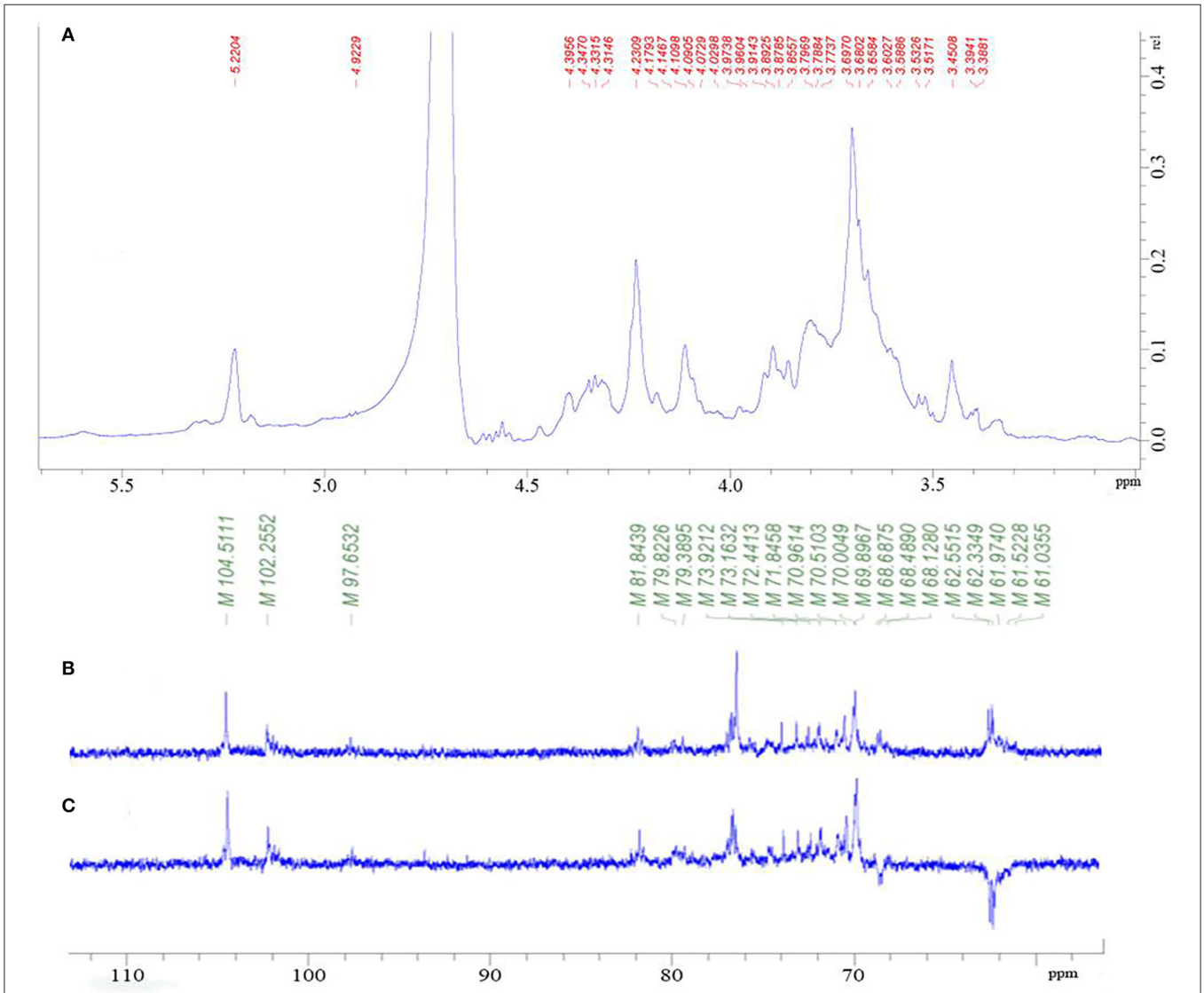

FIGURE 2 | ^{1}H NMR spectrum of PGP **(A)**; ^{13}C-NMR spectrum of PGP **(B)**; DEPT135 spectrum **(C)** of PGP.

branched chains may be degraded by citric acid. The proportion of 1→ 3 Gal and 1→ 4 Gal was similar, indicating that there was a common disaccharide unit in red algae. → 3,6)-Galp-(1→ indicated that there were substituted sulfate and galactose residues at C-6.

The NMR analysis was employed to determine the saccharide backbone structure and also to determine the sulfation pattern of the sulfated galactan. From **Figure 2A**, the proton signal of the sugar ring is mainly concentrated in δ 3.2–4.0. Furthermore, the signal peaks of end group proton (δ 5.22, 4.92, 4.40, and 4.35) were concentrated in the area of δ 4.3–5.5. The signals from an anomeric proton at δ 5.15 and 5.22 were assigned to 3,6-α-L-anhydrogalactose (LA) and α-L-galactose-6-sulfate (L-6S), respectively. However, it was obvious that the signal of δ

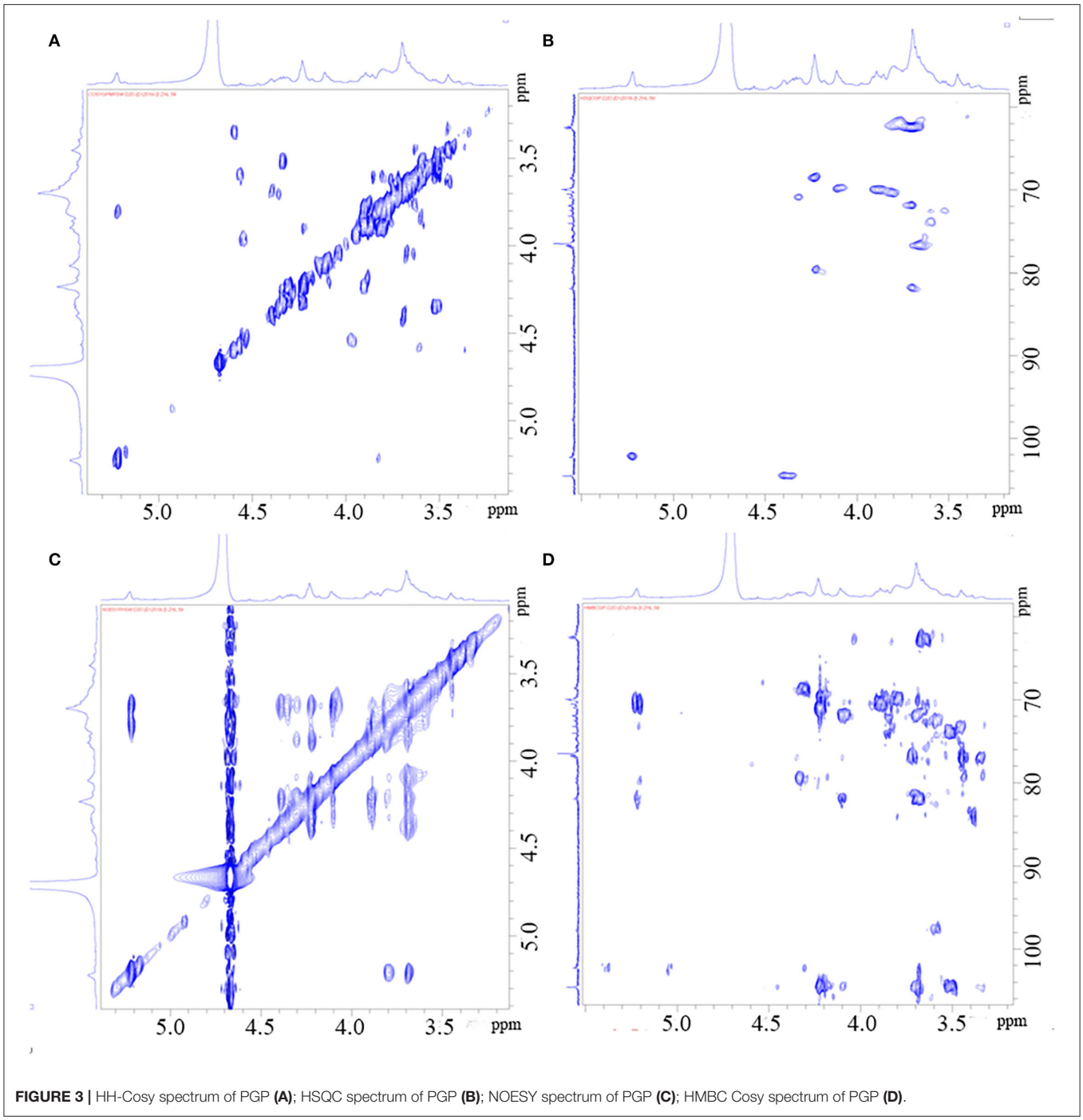

FIGURE 3 | HH-Cosy spectrum of PGP **(A)**; HSQC spectrum of PGP **(B)**; NOESY spectrum of PGP **(C)**; HMBC Cosy spectrum of PGP **(D)**.

5.22 was much greater than δ 5.15, indicating the C-6 position of (1→ 4)-α-L-galactose was mainly substituted by the sulfate group but not LA.

As shown in **Figure 2**, there were several main anomeric carbon signal peaks (δ 104.51, 102.26, and 97.65) of NMR carbon spectrum signal mainly located in δ 93–105. Among them, δ 104.51 and 102.26 were mainly β isomeric carbon, and δ 97.65 was mainly α isomeric carbon and β reductive terminal heterocarbon signal. The strong signal δ 70 also showed the existence of 6-OSO_3-α-L-galactose. Dept135 spectrum showed that δ 68.66, 62.54, 62.37, and 62.28 were inverted peaks, indicating the chemical shift of C6, and the peak at δ 68.66 migrates to the low field, indicating the substitution of C6.

Through the HSQC spectrum, it could be observed that δ 102.4 was the heterocephalic carbon signal. The corresponding heterocephalic hydrogen signal in HSQC spectrum was δ 5.22. We could infer that H1–H5 were, respectively, δ 5.22, 3.80,

TABLE 2 | Glycosidic bond signal attribution of PGP.

Glycosyl residues	H1 C1	H2 C2	H3 C3	H4 C4	H5 C5	H6a C6	H6b
→ 4)-α-D-Galp-(1→	5.22	3.8	3.9	4.23	4.32	3.68	ns
	102.4	70.45	70.05	79.55	70.93	62.44	
→ 3)-β-D-Galp-(1→	4.4	3.68	3.7	4.1	3.65	4.21	ns
	104.56	71.89	81.89	69.85	76.55	68.55	
→ 3,6)-β-D-Galp-(1→	4.4	3.68	3.7	4.1	3.65	4.21	ns
	104.56	71.89	81.89	69.85	76.55	68.55	
α-D-Galp-(1→	5.21	3.95	3.51	3.6	3.45	3.65	ns
	102.9	70.26	72.35	72.6	74.5	62.19	

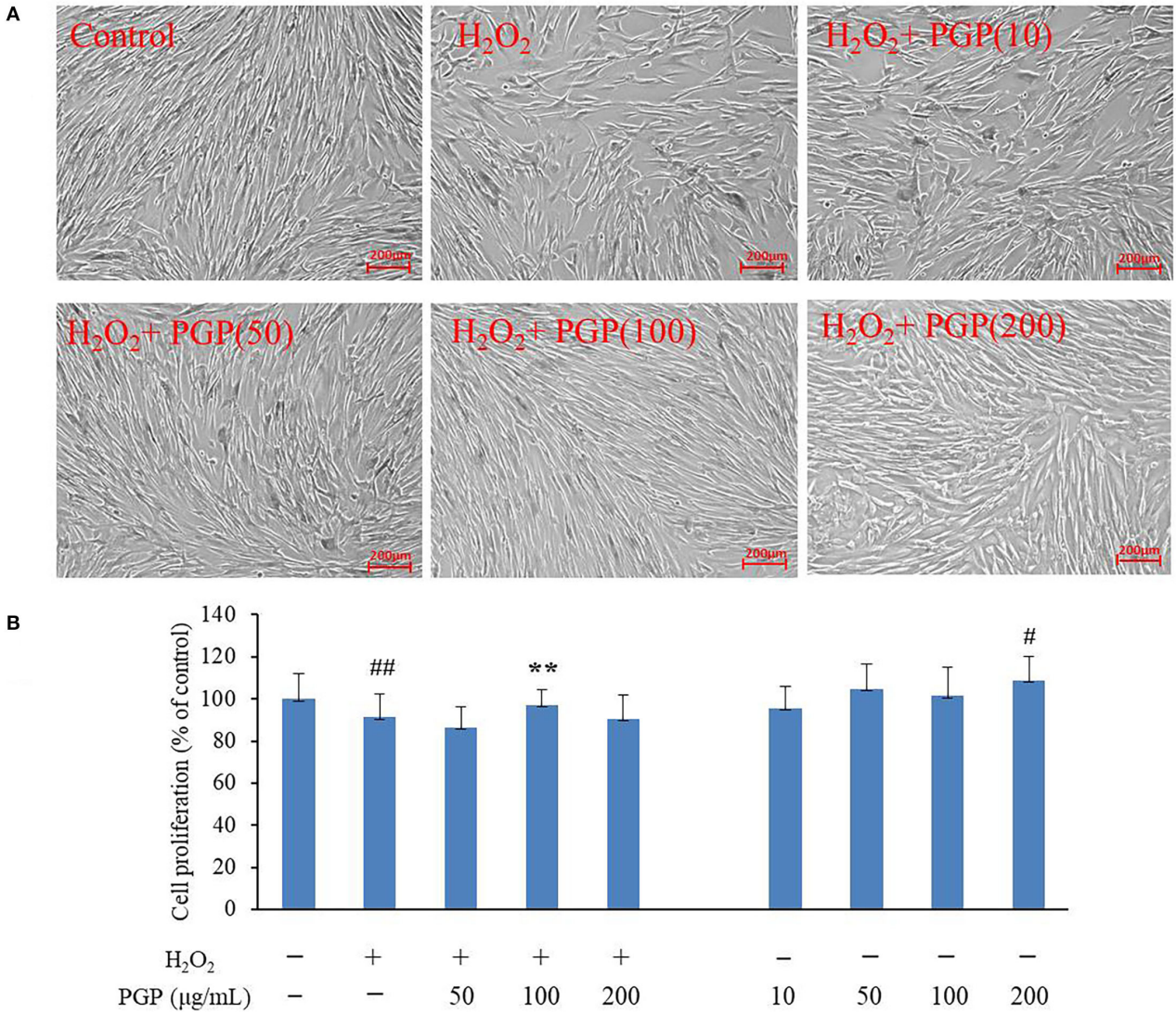

FIGURE 4 | The effect of PGP on cell morphology **(A)** and cell viability in H_2O_2-treated young 2BS cells at PD28 **(B)** (**$p < 0.01$ vs. H_2O_2 alone group; ##$p < 0.01$ vs. control group). Young 2BS cells at PD28 were incubated with 200 μM H_2O_2 at 37°C in the culture medium for 2 h. Then, H_2O_2-containing medium was replaced with fresh medium containing 10, 50, 100, and 200 μg/ml of PGP for additional 72 h before being morphologically observed at the magnification of 10×. Figures are representative of three independent experiments. #$p < 0.05$ vs. control group.

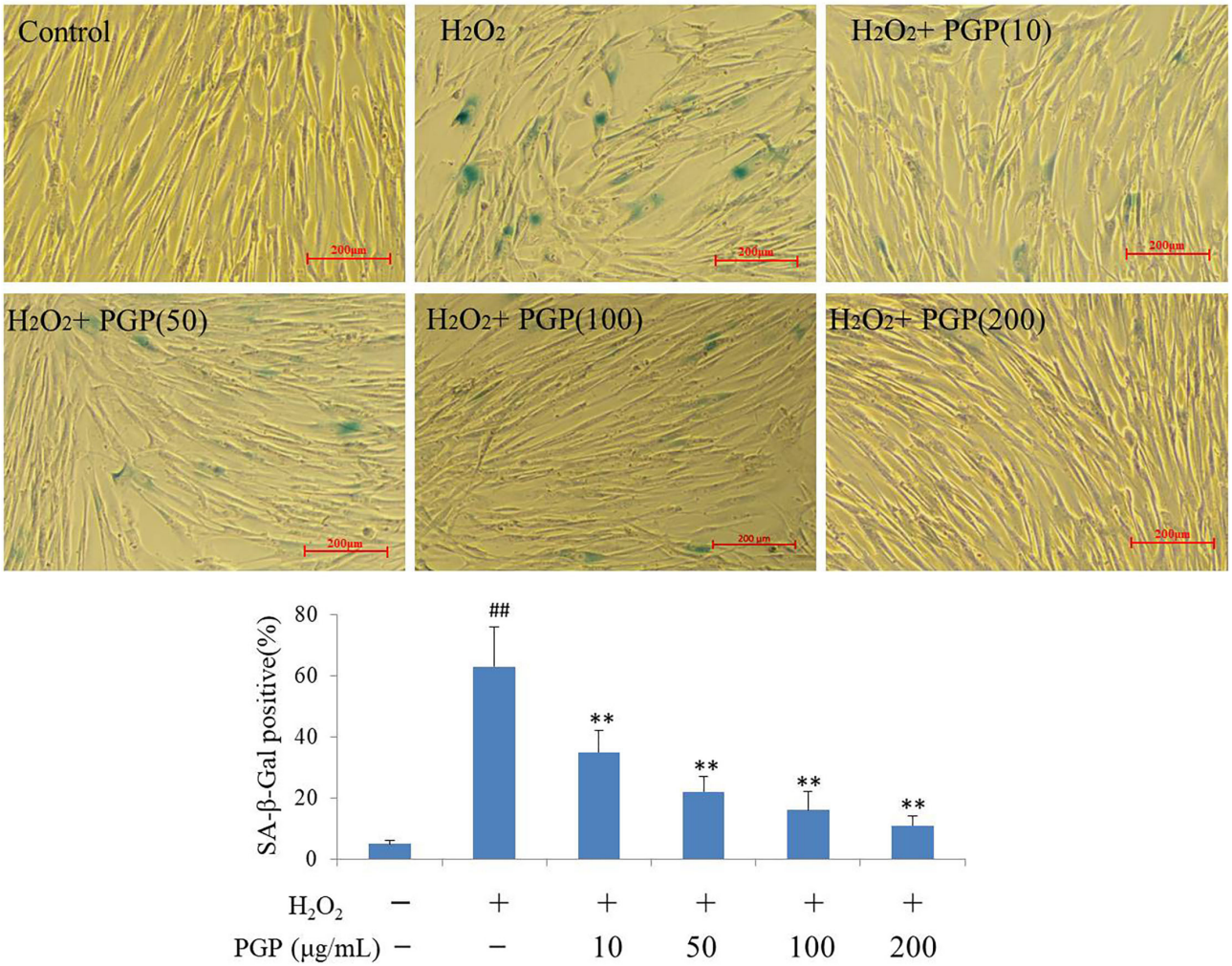

FIGURE 5 | The SA-β-Gal staining of young 2BS cells treated with H_2O_2 followed by PGP (**$p < 0.01$ vs. H_2O_2 alone group; ##$p < 0.01$ vs. control group). PD28 2BS cells were seeded in 24-well plates for 20 h before quick exposure to H_2O_2 as stated above. The cells were then incubated in fresh medium without or with PGP for additional 5 days. Cells were photographed at the magnification of 10×. The percentage of SA-β-gal-positive cells out of the total cells was counted and the average data were obtained from three independent experiments.

3.90, 4.23, 4.32, and 3.68. The corresponding C1–C5 is δ 102.40, 70.45, 70.05, 79.55, and 70.93. Therefore, the signal should be attributed to the glycosidic bond → 4)-α-Galp-(1→ . In the HMBC spectrum (**Figure 3**), we assigned the glycosidic bond signals of polysaccharides according to the one-dimensional and two-dimensional NMR spectrum. The isomeric hydrogen of → 4)-α-D-Galp has a correlation signal peak with its own C4, indicating the presence of → 4)-α-D-Galp-(1→ 4)-α-D-Galp-(1→ link mode. The isomeric hydrogen of → 3,6)-β-D-Galp-(1→ and H3 of → 3)-β-D-Galp-(1→ has a relevant signal peak, indicating the presence of → 3,6)-β-D-Galp-(1→ 3)-β-D-Galp-(1→ 3)-β-D-Galp-(1→ . The isomeric carbon of → 3)-β-D-Galp-(1→ and H4 of → 4)-α-D-Galp-(1→ has a relevant signal peak, indicating the presence of → 3)-β-D-Galp-(1→ 4)-α-D-Galp-(1→ . We combined the HMBC and NOESY spectra to assign all glycosidic bond signals, as shown in **Table 2**.

From the above results, it could be seen that PGP is a linear polysaccharide containing alternating α-(1→ 3)- and β-(1→ 4)-galactopyranose units. Most of the sulfate groups are at C6 of the -(1→ 4)-α-D-Galp, and a small part of them are etherified at C3 and C6. The methoxy signal of each type of sugar was weak, indicating that some residues were methylated. The fine structure needs to be further analyzed.

Cell Morphology and Viability

The MTT assay was performed to test the possible cytotoxic effects of different concentrations of PGP on cell growth. The results showed that an apparent reduction of cell proliferation was not observed upon drug treatment until the dose reached 200 μg/ml (**Figure 4**). It could be seen that normal young 2BS cells grow in a spindle shape and arrange regularly. They had vigorous vitality, more division phases, and clear cell boundaries. Instead, the activity of 2BS cells in the H_2O_2

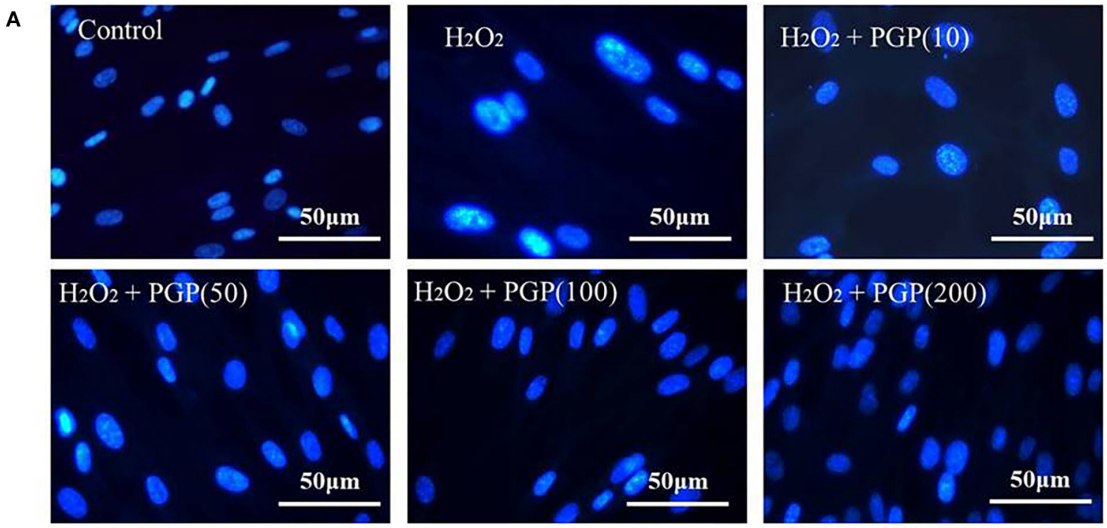

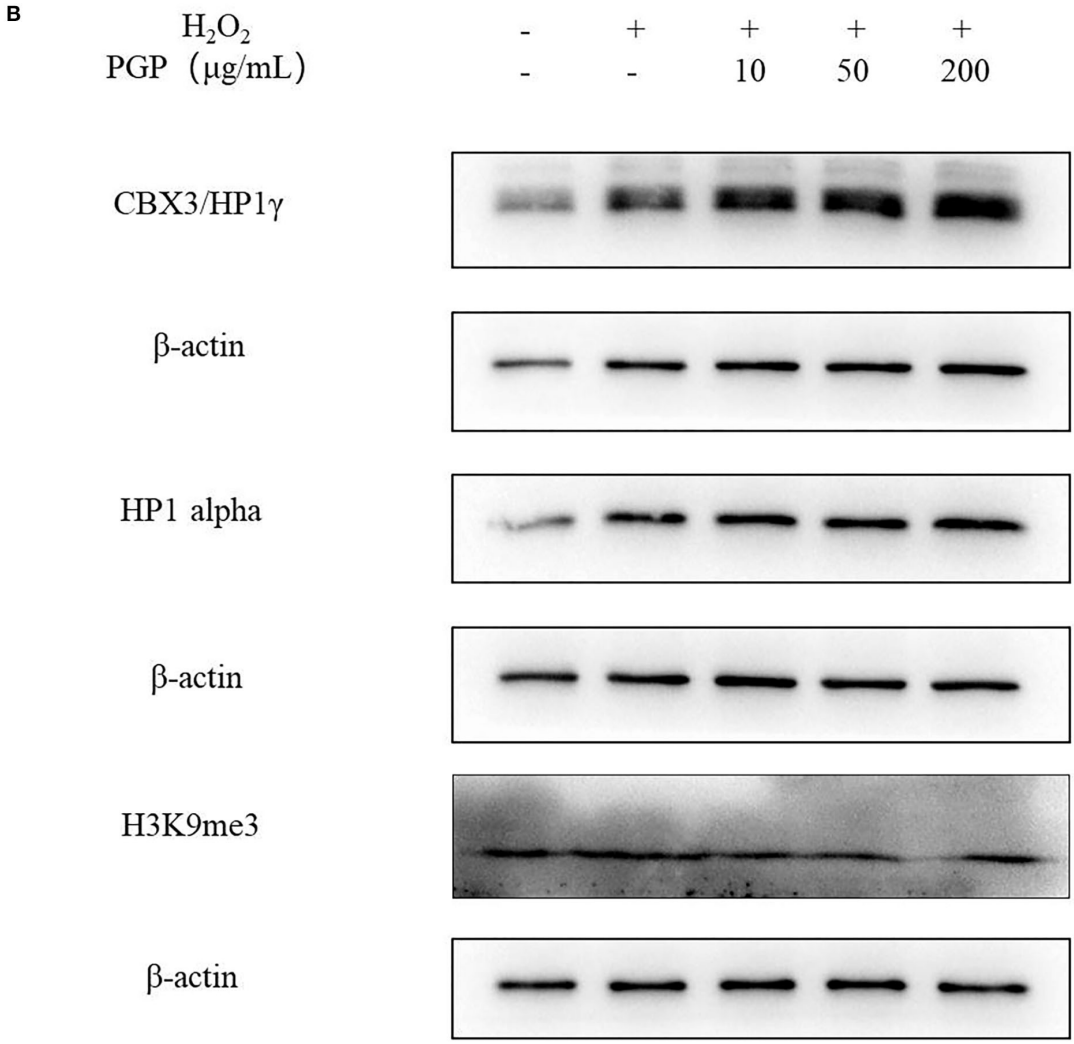

FIGURE 6 | Senescence-associated heterochromatic foci (SAHF) formation **(A)** and the expression levels of three proteins (HP1a, HP1g, and H3k9me3) **(B)** in the nucleus of senescent 2BS cells visualized by DAPI staining. Permeabilize the cells by incubating the coverslips in 0.2% (v/v) Triton-X 100 in PBS (pH 7.3) for 5 min at room temperature. Stain SAHF by incubating the coverslips with 0.15 μg/ml final concentration of DAPI diluted in 3% (w/v) BSA in PBS, pH 7.3 for 3 min. After the slides have dried, observe SAHF using a fluorescent microscope.

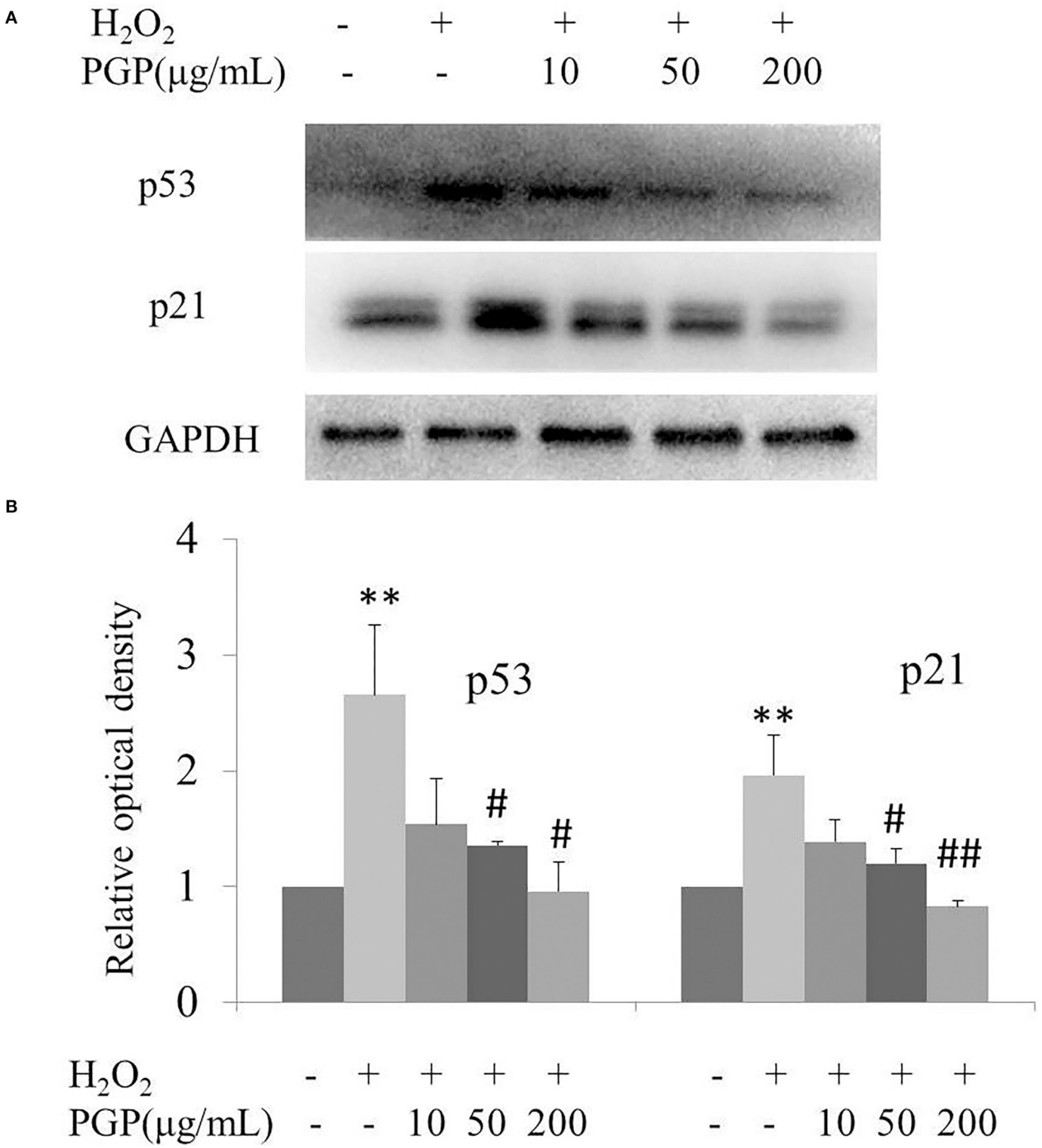

FIGURE 7 | The expression of senescence-associated proteins **(A)** and relative optical density of P53 and P21 in H_2O_2-treated young 2BS cells incubated with various concentrations of PGP (**$p < 0.01$ vs. control group; #$p < 0.05$ vs. H_2O_2 alone group; ##$p < 0.01$ vs. H_2O_2 alone group). Bars represent relative protein levels counted as *D1/D0* (the value for control was set as 1.0), where *D0* and *D1* stand for the optical density of GAPDH ladder and sample ladder, respectively. The optical density for each ladder was calculated using the ImageJ software. Data were obtained from three independent experiments.

treatment group is significantly decreased about 20%. The growth of cells is stagnant. The cell body becomes larger and the shape is flat. The arrangement is irregular, which was similar to replicative aging cells. The cytoplasmic area becomes larger, more particles or vacuoles can be seen in the cytoplasm, and the boundary is fuzzy (4). After the administration of PGP, the cells showed faint senescent morphology characteristics and displayed a fusiform appearance with oval nuclei, which could

improve the cell senescence caused by H_2O_2 treatment in a dose-dependent manner. It was found that an exposure of 2BS cells to PGP (100 μg/ml) caused a significant livability increase of ∼16% ($p < 0.01$).

SA-β-Gal Activity

The SA-β-gal stain is widely used to detect the signal of cellular senescence. The assay utilizes a fluorimetric substrate and cell-derived extract samples to determine quantitatively the enzymatic activity (25). As shown in **Figure 5**, the cells would be dyed blue-green in the process of cell replicative aging. At this time, SA-β-gal-positive rate increased gradually. The Young cells showed the lighter SA-β-Gal staining, and slender fibrous cells accounted for the vast majority. Cells in H_2O_2 treatment groups showed the deep SA-β-Gal staining, the increased cell volume, and the irregular shape. The SA-β-Gal-positive cells were significantly lower in cells supplemented with PGP at the concentration of 200 μg/ml (11.7%), compared to cells cultured with H_2O_2 (63.3%) ($p < 0.01$).

DAPI Staining

At the chromatin level, the occurrence of cell senescence is often accompanied by extensive changes in chromatin structure, with dot-like aggregation of heterochromatin structure and inhibition of the expression of cell proliferation-related genes. This characteristic phenomenon is called senescence-associated heterochromatic foci (SAHF) (26). Due to the consistent localization of HP1, H3K9me2/3, and SAHF, they have become the marker proteins of aging-related heterochromatin aggregation. This provides a method for researchers to judge whether cells have entered the aging state, that is, to observe the distribution of HP1 (or H3K9me2/3) and chromatin in the nucleus at the same time by the immunofluorescence method (27). From **Figure 6**, after DAPI staining, the cells in the H_2O_2 treatment group showed an obvious aging state with enlarged nucleoli compared with the control group. This indicated that the cells had entered the aging state. PGP pretreatment could prevent the formation of SAHF induced by H_2O_2 in a dose-dependent manner. When the doses were increased to 100 and 200 μg/ml, SAHF was significantly reduced to the level close to the control group. Western blotting showed that the expression levels of three proteins (i.e., HP1α, HP1γ, and H3k9me3) were upregulated in the model group. The sample PGP could downregulated the marker protein. These results clearly indicated that PGP was able to influence the cell cycle, leading to improved cell proliferation and delaying premature senescence induced by H_2O_2.

The Expression of Senescence-Associated Molecular Markers

The results of this experiment showed that the intracellular p53 and p21 of 2BS at the protein level were significantly increased after H_2O_2 treatment. PGP could decrease the expression of p53 and p21 in a dose-dependent manner, of which the most significant downregulated levels of p53 and p21 were treated with the concentration of 200 μg/ml (**Figure 7**). It was speculated that PGP may delay aging by downregulating the expression of p21 and p53.

DISCUSSION

Acid extraction is performed to obtain polysaccharides with dilute hydrochloric acid or rare organic acid as solvent. The activity was better, and the yield of polysaccharides is in high quantity (28). However, the glycosidic bond is easy to break under acidic conditions, which will affect the activity and structure of polysaccharides, but some novel polysaccharide chains can be obtained to increase the diversity of polysaccharide structure. The outer epidermis of *G. lemaneiformis* is hard which is difficult to obtain a higher yield of polysaccharides. Therefore, searching for ways to be more efficient to extract polysaccharides had become the investigations of many researchers. At present, solvent (e.g., water) extraction, physical-assisted (ultrasonic, microwave, etc.) extraction, and enzymatic hydrolysis extraction had become the main extraction methods of GP (29). There were many related reports before, but there was a less in-depth exploration of structural analysis. The polysaccharide obtained by *G. lemaneiformis* with citric acid at a lower concentration had been reported, which had a high molecular weight (30). In our study, the concentration of citric acid was increased to obtain polysaccharides with lower molecular weight. From the results, the expected polysaccharide with lower molecular weight was obtained. After separation and purification, we obtained the polysaccharide with good water solubility. The isolation of this sulfated polysaccharide from *G. lemaneiformis* added a new type of polysaccharide to this group of red seaweeds.

Senescent cells have become an emerging target for the disease of aging (31). H_2O_2 was known to induce cellular senescence showing multiple changes. Based on this study, we have employed low-passage cells and the appropriate H_2O_2 concentration to induce premature senescence was determined to be 200 mM. Senescent cells acquire a typical flat and enlarged shape and show the increased levels of a group of senescence biomarkers, including SA-β-Gal activity, and the protein abundance of p21 and p53 (32, 33). Studies suggested that the long-term supplementation of SHQA also notably delayed the growth arrest and lessened the raise of senescence biomarkers, including p53, p21, and SA-β-Gal. Consistently, we observed that upon exposure to low-dose H_2O_2, the abundance of SA-β-Gal-positive cells was elevated in 2BS; meanwhile, the pretreatment of PGP significantly suppressed their elevations, which suggested the ability of PGP to repress the oxidative stress-induced senescence in 2BS.

The p53-p21 pathway is a relatively recognized aging-related signal pathway. Inactivation of p53 or p21 gene can prolong the replicative life of cells, indicating that this signal pathway is closely related to cell aging (34). p53 and p21 are cell cycle regulators directly related to aging (35). When cells encounter some external stimuli, it is found that the expression of p53 will be rapidly upregulated with stress, so as to further activate p21, inhibit the phosphorylation of p21 protein, block the normal

cell cycle, and then lead to cell aging. The target molecule of p53 is p21, which is a cyclin-dependent protein kinase inhibitor that inhibits cell cycle and can make cells enter an irreversible growth arrest state (36). In this study, the partial inhibitory effects of PGP on 2BS may be due to the contribution of the p53-p21 pathway.

CONCLUSION

The polysaccharides isolated from *G. lemaneiformis* were slightly methylated agarans, with a low 3,6-anhydrogalactose content, bearing sulfated mainly at the 6-position of (1→ 4)-α-D-Galp. Our studies demonstrated that H_2O_2 caused cell cycle arrest accounting for inhibition of cell proliferation, resulting in SA-β-gal activity elevation and SAHF formation. Pretreatment with PGP protected against H_2O_2-induced cellular senescence. The anti-aging effect of PGP may be involved in potentiating the p53-p21 pathway. These results suggested the promising role of PGP as an attractive food with the potential to retard senescence and senescence-related diseases.

DATA AVAILABILITY STATEMENT

The original contributions presented in the study are included in the article/supplementary material, further inquiries can be directed to the corresponding author/s.

AUTHOR CONTRIBUTIONS

XW: visualization, investigation, and validation. XX and GM: feeding cells and supporting partial data. GW and XS: methodology, data analysis, drawing charts, and writing—original and editing. YG: conceptualization, methodology, and writing —review. NX: investigation and formal analysis. ZZ: funding acquisition and supervision. All authors have read and agreed to the publishing of the current version of the manuscript.

FUNDING

This study was supported by the Zhejiang Province Basic public welfare research project (LGN21D060001) and the National Natural Science Foundation of China (31700307 and 81771520).

REFERENCES

1. Hernandez-Segura A, Nehme J, Demaria M. Hallmarks of cellular senescence. *Trends Cell Biol.* (2018) 28:436–53. doi: 10.1016/j.tcb.2018.02.001
2. Tokmakov AA, Sato KI. Activity and intracellular localization of senescence-associated β-galactosidase in aging Xenopus oocytes and eggs. *Exp Gerontol.* (2019) 119:157–67. doi: 10.1016/j.exger.2019.02.002
3. Wang Y, Gao JJ, Wu F, Lai CY, Li YQ, Zhang GQ, et al. Biological and epigenetic alterations of mitochondria involved in cellular replicative and hydrogen peroxide-induced premature senescence of human embryonic lung fibroblasts. *Ecotoxicol Environ Saf.* (2021) 216:112204. doi: 10.1016/j.ecoenv.2021.112204
4. Toussaint O, Medrano EE, Zglinicki T. Cellular and molecular mechanisms of stress-induced premature senescence (SIPS) of human diploid fibroblasts and melanocytes. *Exp Gerontol.* (2000) 35:927–45. doi: 10.1016/S0531-5565(00)00180-7
5. Luo HT, Wang Q, Zhang CW, Zhang L, Yang YF. Bioaccumulation and release of heavy metals during growth and decomposition of cultivated *Gracilaria lemaneiformis*. *Mar Pollut Bull.* (2021) 173:113130. doi: 10.1016/j.marpolbul.2021.113130
6. Jiang WT, Fu YT, Yang F, Yang YF, Liu T, Zheng WJ, et al. *Gracilaria lemaneiformis* polysaccharide as integrin-targeting surface decorator of selenium nanoparticles to achieve enhanced anticancer efficacy. *ACS Appl Mater Inter.* (2014) 6:13738–48. doi: 10.1021/am5031962
7. Kang YN, Wang ZJ, Xie DS, Sun X, Yang WG, Zhao XD, et al. Characterization and potential antitumor activity of polysaccharide from *Gracilariopsis lemaneiformis*. *Mar Drugs.* (2017) 15:100–13. doi: 10.3390/md15040100
8. Liao XB, Yang LW, Chen MZ, Yu J, Zhang SM, Ju YY. The hypoglycemic effect of a polysaccharide (glp) from *Gracilaria lemaneiformis* and its degradation products in diabetic mice. *Food Funct.* (2015) 6:2542–49. doi: 10.1039/C4FO01185F
9. Liu QM, Yang Y, Maleki SJ, Alcocer MJC, Xu SS, Shi CL. Anti-food allergic activity of sulfated polysaccharide from *Gracilaria lemaneiformis* is dependent on immunosuppression and inhibition of p38 mapk. *J Agric Food Chem.* (2016) 64:4536–44. doi: 10.1021/acs.jafc.6b01086
10. Wen LR, Zhang YL, Sunwaterhouse DX, You LJ, Fu, X. Advantages of the polysaccharides from *Gracilaria lemaneiformis* over metformin in antidiabetic effects on streptozotocin-induced diabetic mice. *RSC Adv.* (2017) 7:9141–51. doi: 10.1039/C6RA26970B
11. Xu JT, Gao KS. Growth, pigments, UV-absorbing compounds and agar yield of the economic red seaweed *Gracilaria lemaneiformis* (Rhodophyta) grown at different depths in the coastal waters of the South China Sea. *J Appl Phycol.* (2007) 20:231–36. doi: 10.1007/978-1-4020-9619-8_29
12. Qiu SM, Aweya JJ, Liu XJ, Liu Y, Tang SJ, Zhang WC, et al. Bioactive polysaccharides from red seaweed as potent food supplements: a systematic review of their extraction, purification, and biological activities. *Carbohydr Polym.* (2022) 275:118696. doi: 10.1016/j.carbpol.2021.118696
13. Trygg J, Beltrame G, Yang BR. Rupturing fungal cell walls for higher yield of polysaccharides: acid treatment of the basidiomycete prior to extraction. *Innov Food Sci Emerg Technol.* (2019) 57:102206. doi: 10.1016/j.ifset.2019.102206
14. Jain VM, Karibasappa GN, Dodamani AS, Mali GV. Estimating the carbohydrate content of various forms of tobacco by phenol-sulfuric acid method. *J Educ Health Promot.* (2017) 6:90–95. doi: 10.4103/jehp.jehp_41_17
15. He YL, Ye M, Jing LY, Du ZZ, Surahio M, Xu HM. Preparation, characterization and bioactivities of derivatives of an exopolysaccharide from *Lachnum*. *Carbohydr Polym.* (2015) 117:788–96. doi: 10.1016/j.carbpol.2014.10.046
16. Yaphe W, Arsenault GP. Improved resorcinol reagent for the determination of fructose, and of 3,6-anhydrogalactose in polysaccharides. *Anal Biochem.* (1965) 13:143–48. doi: 10.1016/0003-2697(65)90128-4
17. Zhang ZS, Wang XM, Su HL, Pan YL, Han JF, Zhang TS, et al. Effect of sulfated galactan from *Porphyra haitanensis* on H_2O_2-induced premature senescence in WI38 cells. *Int J Biol Macromol.* (2018) 106:1235–39. doi: 10.1016/j.ijbiomac.2017.08.123
18. Huang TT, Rivera-Pérez JA. Senescence-associated β-galactosidase activity marks the visceral endoderm of mouse embryos but is not indicative of senescence. *Genesis.* (2014) 52:300–308. doi: 10.1002/dvg.22761
19. Schmid I, Uittenbogaart C, Jamieson BD. Live-cell assay for detection of apoptosis by dual-laser flow cytometry using Hoechst 33342 and 7-amino-actinomycin D. *Nat Prot.* (2007) 2:187–90. doi: 10.1038/nprot.2006.458
20. Manrique GD, Lajolo FM. FT-IR spectroscopy as a tool for measuring degree of methyl esterification in pectins isolated from ripening papaya fruit. *Postharvest Biol Technol.* (2002) 25:99–107. doi: 10.1016/S0925-5214(01)00160-0
21. Yamaguchi T, Takamura H, Matoba T, Terao J. Antioxidative activity of heterocyclic compounds found in coffee volatiles produced by Maillard reaction. *J Agric Food Chem.* (2002) 50:5480–84. doi: 10.1021/jf025616h

22. Maciel JS, Chaves LS, Souza BWS, Teixeira DIA, Freitas ALP, Feitosa JPA, et al. Structural characterization of cold extracted fraction of soluble sulfated polysaccharide from red seaweed *Gracilaria birdiae*. *Carbohydr Polym*. (2008) 71:559–65. doi: 10.1016/j.carbpol.2007.06.026
23. Patankar MS, Oehninger S, Barnett T, Williams RL, Clark GF. A revised structure for fucoidan may explain some of its biological activities. *J Biol Chem.* (1993) 268:21770–76. doi: 10.1016/S0021-9258(20)80609-7
24. Pereira MS, Mulloy B, Mourao PAS. Structure and anticoagulant activity of sulfated fucans. *J Biol Chem.* (1999) 274:7656–67. doi: 10.1074/jbc.274.12.7656
25. Ravelojaona V, Robert AM, Robert L. Expression of senescence- associated β-galactosidase (SA-β-Gal) by human skin fibroblasts, effect of advanced glycation end-products and fucose or rhamnose-rich polysaccharides. *Arch Gerontol Geriatr.* (2009) 48:151–54. doi: 10.1016/j.archger.2007.12.004
26. Narita M, Nuñez S, Heard E, Narita M, Lin AW, Hearn SA, et al. Rb-mediated heterochromatin formation and silencing of E2F target genes during cellular senescence. *Cell.* (2003) 113:703–16. doi: 10.1016/S0092-8674(03)00401-X
27. Funayama R, Saito, Tanobe H, Ishikawa F. Loss of linker histone H1 in cellular senescence. *J. Cell Biol.* (2006) 175:869–80. doi: 10.1083/jcb.200604005
28. Li X, Xie QT, Huang SM, Shao P, You LJ, Pedisic S. Digestion & fermentation characteristics of sulfated polysaccharides from *Gracilaria chouae* using two extraction methods *in vitro* and *in vivo*. *Food Res Int.* (2021) 145:110406. doi: 10.1016/j.foodres.2021.110406
29. Long XS, Hu X, Liu SC, Pan C, Chen SJ, Li LH, et al. Insights on preparation, structure and activities of *Gracilaria lemaneiformis* polysaccharide. *Food Chem.* (2021) 12:100153. doi: 10.1016/j.fochx.2021.100153
30. Ren YL, Zheng GQ, You LJ, Wen LR, Li C, Fu X, et al. Structural characterization and macrophage immunomodulatory activity of a polysaccharide isolated from *Gracilaria lemaneiformis*. *J Funct Foods.* (2017) 33:286–96. doi: 10.1016/j.jff.2017.03.062
31. Gruber HE, Ingram JA, Davis DE, Hanley EN. Increased cell senescence is associated with decreased cell proliferation *in vivo* in the degenerating human annulus. *Spine J.* (2009) 9:210–15. doi: 10.1016/j.spinee.2008.01.012
32. Veroutis D, Kouroumalis A, Lagopati N, Polyzou A, Chamilos C, Papadodima S, et al. Evaluation of senescent cells in intervertebral discs by lipofuscin staining. *Mech Ageing Dev.* (2021) 199:111564. doi: 10.1016/j.mad.2021.111564
33. Ben-Porath I, Weinberg RA. The signals and pathways activating cellular senescence. *Int J Biochem Cell Biol.* (2005) 37:961–76. doi: 10.1016/j.biocel.2004.10.013
34. Jin H, Lian N, Zhang F, Chen L, Chen Q, Lu C, et al. Activation of PPARγ/P53 signaling is required for curcumin to induce hepatic stellate cell senescence. *Cell Death Dis.* (2016) 7:e2189–99. doi: 10.1038/cddis.2016.92
35. Yang JF, Lu YC, Yang PP, Chen QF, Wang Y, Ding Q, et al. MicroRNA-145 induces the senescence of activated hepatic stellate cells through the activation of p53 pathway by ZEB2. *J Cell Physiol.* (2019) 234:7587–99. doi: 10.1002/jcp.27521
36. Zhang RG, Chen W, Adams PD. Molecular dissection of formation of senescence-associated heterochromatin foci. *Mol Cell Biol.* (2007) 27:2343–58. doi: 10.1128/MCB.02019-06

Conflict of Interest: The authors declare that the research was conducted in the absence of any commercial or financial relationships that could be construed as a potential conflict of interest.

Publisher's Note: All claims expressed in this article are solely those of the authors and do not necessarily represent those of their affiliated organizations, or those of the publisher, the editors and the reviewers. Any product that may be evaluated in this article, or claim that may be made by its manufacturer, is not guaranteed or endorsed by the publisher.

Copyright © 2022 Wang, Xu, Mao, Guo, Wang, Sun, Xu and Zhang. This is an open-access article distributed under the terms of the Creative Commons Attribution License (CC BY). The use, distribution or reproduction in other forums is permitted, provided the original author(s) and the copyright owner(s) are credited and that the original publication in this journal is cited, in accordance with accepted academic practice. No use, distribution or reproduction is permitted which does not comply with these terms.

frontiers | Frontiers in Nutrition

ORIGINAL RESEARCH
published: 17 May 2022
doi: 10.3389/fnut.2022.900138

Comparison of the Fungal Community, Chemical Composition, Antioxidant Activity, and Taste Characteristics of Fu Brick Tea in Different Regions of China

Yulian Chen[1,2†], Jiaxu Chen[1,3†], Ruyang Chen[1], Leike Xiao[1], Xing Wu[1], Lin Hu[1], Zongjun Li[1], Yuanliang Wang[1], Mingzhi Zhu[4,5], Zhonghua Liu[4,5] and Yu Xiao[1,4]**

[1] College of Food Science and Technology, Hunan Agricultural University, Changsha, China, [2] College of Animal Science and Technology, Hunan Agricultural University, Changsha, China, [3] Longping Branch Graduate School, Hunan University, Changsha, China, [4] Key Laboratory of Ministry of Education for Tea Science, College of Horticulture, Hunan Agricultural University, Changsha, China, [5] National Research Center of Engineering Technology for Utilization of Botanical Functional Ingredients, Hunan Agricultural University, Changsha, China

OPEN ACCESS

Edited by:
Biao Yuan,
China Pharmaceutical University,
China

Reviewed by:
Xin Zhang,
Ningbo University, China
Xiong Gao,
Guangdong Academy of Sciences,
China
Qing Xiao,
Rutgers, The State University
of New Jersey, United States

***Correspondence:**
Mingzhi Zhu
mzzhucn@hotmail.com
Yu Xiao
xiaoyu@hunau.edu.cn;
yuxiao_89@163.com

† These authors have contributed equally to this work

Specialty section:
This article was submitted to Food Chemistry, a section of the journal Frontiers in Nutrition

Received: 20 March 2022
Accepted: 26 April 2022
Published: 17 May 2022

Citation:
Chen Y, Chen J, Chen R, Xiao L, Wu X, Hu L, Li Z, Wang Y, Zhu M, Liu Z and Xiao Y (2022) Comparison of the Fungal Community, Chemical Composition, Antioxidant Activity, and Taste Characteristics of Fu Brick Tea in Different Regions of China. Front. Nutr. 9:900138. doi: 10.3389/fnut.2022.900138

In this study, the fungal community structure, metabolites, antioxidant ability, and taste characteristics of five Fu brick tea (FBT) from different regions of China were determined and compared. A total of 69 operational taxonomic units (OTUs) were identified and assigned into 5 phyla and 27 genera, with *Eurotium* as the predominant genus in all samples. Hunan (HN) sample had the strongest fungal diversity and richness, followed by Guangxi (GX) sample, and Zhejiang (ZJ) sample had the lowest. GX sample had higher amounts of gallic acid (GA), total catechins, gallocatechin (GC), and epicatechin gallate (ECG) as well as antioxidant activity than the other samples. The levels of total phenolics, total flavonoids, epigallocatechin (EGC), catechin, epicatechin (EC), thearubigins (TRs), and theaflavins (TFs) were the highest in the ZJ sample. Guizhou (GZ) and Shaanxi (SX) samples contained the highest contents of epigallocatechin gallate (EGCG) and gallocatechin gallate (GCG), respectively. Total phenolics, GA, EC, CG, and TFs were positively associated with most of fungal genera. Total phenolic content (TPC), total flavonoid content (TFC), and most of catechins contributed to the antioxidant activities of FBT. HN sample had the strongest sourness and sweetness, ZJ sample had the strongest saltiness, SX sample had the strongest umami, and GZ sample had the strongest astringency, which was ascribed to the varied metabolites. This work reveals that FBT in different regions vary greatly in fungal community, metabolites, antioxidant activity, and taste characteristics, and provides new insight into the quality characteristics formation of FBT in different regions.

Keywords: Fu brick tea, fungal community, chemical compositions, antioxidant activity, taste characteristics

INTRODUCTION

Conventional tea can be traditionally categorized into six types according to oxidation and fermentation degree: non-oxidized green tea, slightly oxidized white tea, lightly oxidized yellow tea, partially oxidized oolong tea, fully oxidized black tea, and post-fermented dark tea. As one of the important commercial dark tea varieties, Fu brick tea (FBT) is a special post-fermented dark tea manufactured from raw matured leaves of *Camellia sinensis* var. *sinensis* through the following steps: steaming, piling, tea brick pressing, fungal fermentation, and drying (1), in which fungal fermentation played a critical role in the formation of its quality characteristics. FBT has attracted people's interest throughout China, Korea, and Japan due to its unique sensory attributes and health-promoting effects, including anti-obesity, anti-hyperlipidemic, anti-proliferative, and antidysenteric effects (2–4). The main production regions of FBT are Shaanxi (SX) province, Hunan (HN) province, Guizhou (GZ) province, Zhejiang (ZJ) province, and Guangxi Zhuang Autonomous Region (GX) in China (**Figure 1**), especially in Hunan and Shaanxi provinces.

The special taste and health benefits of FBT are closely associated with the formation of metabolites during fungal fermentation. Fungal community and its relationship to metabolites formation have been previously investigated (5–8). In the past few years, the biotransformation of chemical constituents related to FBT quality during microbial fermentation has been identified; these constituents include free amino acids, polyphenolic compounds (phenolic acids, catechins and their derivatives, flavonoids, and tea pigments, etc.), purine alkaloids, and terpenoids (9). They are formed due to a sequence of biochemical reactions including oxidation, structural modification, methylation, degradation, condensation, and glycosylation catalyzed by extracellular enzymes from functional core microorganisms (10). Previous studies have revealed that *Eurotium*, *Aspergillus*, and *Penicillium* are the dominant genera during FBT manufacturing (11). The raw materials, processing and cultivation conditions of diverse FBT during manufacturing are different, which might greatly influence their microbial composition and caused the different quality characteristics. It was previously reported that the fungal community composition of various FBT vary greatly (12), which might lead to the great differences of chemical components in FBT. Different filamentous have significant effects on transformation ability of phenolic acid, catechines, flavonoids, and anthocyanins. For instance, both *A. niger* and *E. cristatum* reduces galloyl catechins and increase theabrownins (TBs), while *E. cristatum* contribute to the accumulation of B-ring fission derivatives of degalloyl catechins (13) and *A. niger* contribute to the accumulation of A-ring fission derivatives of degalloyl catechins in the fermentation (9). Therefore, it is of significant importance for analyzing the fungal community to enhance our understanding of the mechanisms on quality characteristics formation of FBT in different regions. High-throughput sequencing is a rapid, sensitive, and comprehensive technique that provides thousands of reads in a run and accurately describes microbial diversity in food matrices, which received great attention in the last years and become the main method to analysis of microbial composition. However, systematic study on the fungal community by using this approach, and analyze its influence on the metabolites formation of FBT in different regions of China is still lacking.

Numerous literatures have concentrated on the *in vitro* antioxidant activities of FBT and its association with chemical metabolites (14–16). It is suggested that the antioxidant capacity is recently attributed to flavonols and flavones, tea pigments, caffeine, alkaloids, terpenoids, polysaccharides as well as catechins and their derivatives (3, 14–16). For instance, tea catechins, especially epigallocatechin gallate (EGCG), have been extensively investigated for their excellent antioxidant activity. Likewise, both kaempferol-3-O-glucoside in flavonoids and TBs in tea pigments have significant impact on antioxidant capacity (14). Moreover, it is of great importance to mention that the antioxidant activity in FBT has been reported to be superior compared with other teas (16). FBT in different regions might have diverse antioxidant capacity due to their different metabolites, which have not yet been clearly studied. In addition, previous studies reported that FBT shows strong smoothness, sweetness, and mellowness attributes but with low levels of bitter and astringent. The distinctive taste phenotype of FBT is caused by differences in the contents of various metabolites (5, 8, 12). For instance, catechins, flavonols, and flavones and caffeine are key contributors to the bitterness and astringency of FBT infusion, which greatly influences tea quality (8, 12). The taste profile was mainly detected by an E-tongue sensor system, which simulates human tongue and exhibits good reproducibility, high sensitivity, and low detection limits of tastes compared with the human sense of taste (17). As an emerging technique, E-tongue has been increasingly used to describe the taste characteristics of dry-cured pork, fruit juice, and tea infusion (18, 19). To date, detailed and clear data on the diversity of antioxidant activity and taste quality of FBT produced from different regions of China is rare studied, and their association with bioactive metabolites is not available.

Therefore, the present work aims to investigate the structure and diversity of fungal communities by using Illumina Miseq sequencing of ITS2 region and illustrate the function of microorganisms in the conversion of chemical constituents. Network correlation analysis was used to evaluate the effect of metabolites on the antioxidant activity *in vitro*. The E-tongue system was also employed to detect the taste attributes of five FBT and clarify the key chemical substances contributing to variations in the taste profile. This study is of significant importance for providing valuable information to enhance our understanding of the mechanisms on quality characteristics formation of FBT in different regions of China.

MATERIALS AND METHODS

Materials and Chemical Reagents

Catechin, epicatechin gallate (ECG), EC epicatechin (EC), epigallocatechin (EGC), gallocatechin (GC), catechin gallate (CG), EGCG, and gallocatechin gallate (GCG) were acquired from Sigma-Aldrich Co. (St. Louis, MO, United States). High-Performance Liquid Chromatography (HPLC)-grade methanol

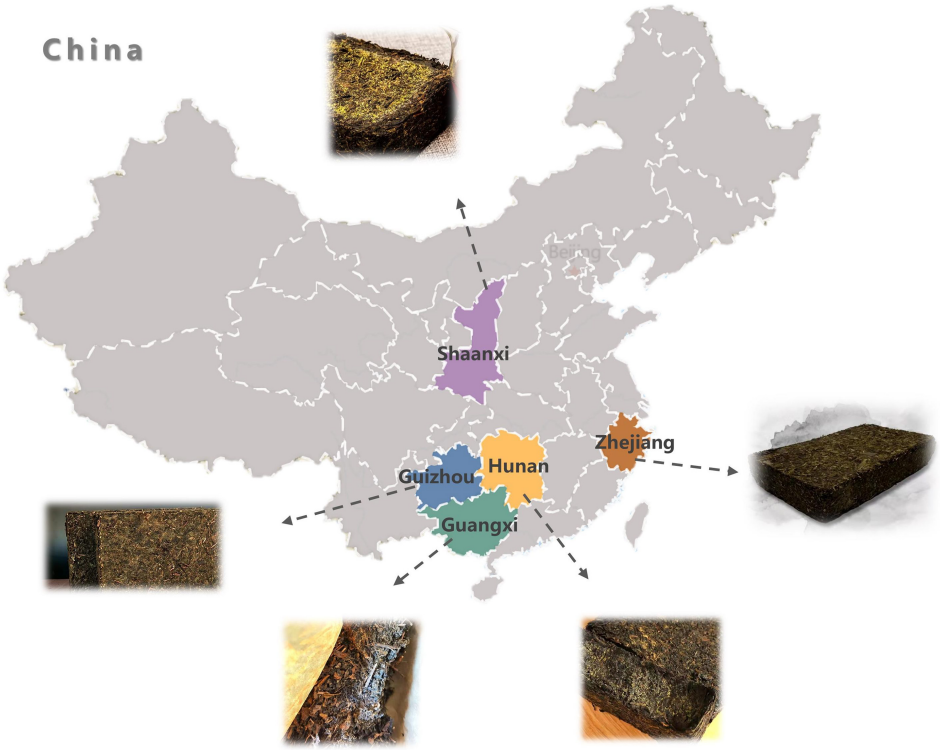

FIGURE 1 | The five Fu brick teas were collected from different provinces of China.

was obtained from Merck (Darmstadt, Germany). All other chemicals and reagents were of analytical grade. FBT is mainly consumed in Shaanxi province, Hunan province, Guizhou province, Zhejiang province, and Guangxi Zhuang Autonomous Region in China. From these main producing areas, five FBT samples were collected from large factories and named as SX (Shaanxi Xianxi Lamu Tea Co., Ltd.), HN (Anhua Yuntiange Tea Industry Co., Ltd.), GZ (Guizhou Fanjin Tea Industry Co., Ltd.), ZJ (Zhejiang Wuyi Luotuo Jiulong Brick Tea Co., Ltd.), and GX (Guangxi Jinhua Tea Co., Ltd.). All tea samples used in this study were produced in 2018.

DNA Extraction and ITS2 Sequencing

Microbial genomic DNA was extracted from FBT samples by using E.Z.N.A. Stool DNA Kit (D4015, Omega, Inc., United States) based on the manufacturer's instructions. Nuclear-free water was used for blank and elution buffer (50 μL) was used to elute the total DNA. The ITS2 gene was amplified by PCR with forward primers fITS7 (5′-GTGARTCATCGAATCTTTG-3′) and ITS4 (5′-TCCTCCGCTTATTGATATGC-3′). The amplification process was conducted in a reaction mixture (25 μL) with 2.5 μL of each primer, 12.5 μL PCR Premix, 25 ng of template DNA, and PCR-grade water to adjust the volume. The PCR conditions were as follows: initial denaturation for 30 s at 98°C; 35 cycles of denaturation for 10 s at 98°C, annealing for 30 s at 54°C/52°C, and an extension for 45 s at 72°C; and final extension for 10 min at 72°C. The PCR products were extracted from 2% agarose gel, purified by AMPure XT beads (Beckman Coulter Genomics, Danvers, MA, United States), and quantified by Qubit (Invitrogen, United States). After sequencing with the amplicon pools, the size and quantity of the amplicon library were estimated on Agilent 2100 Bioanalyzer (Agilent, United States) and with the Library Quantification Kit for Illumina (Kapa Biosciences, Woburn, MA, United States), respectively. Combined PhiX Control library (v3) (Illumina) and amplicon library (expected at 30%) together. The libraries were sequenced in 250PE MiSeq runs, and one library was sequenced using standard Illumina sequencing primers by both protocols without the need for a third (or fourth) index read.

Determination of Total Phenolic Content, Total Flavonoid Content, Theaflavins, Thearubigins, and Theabrownins

Total phenolic content in tea samples was determined using Folin-Ciocalteu method in accordance with literature (20). The content was calculated based on standard curve with gallic acid (GA) and expressed as milligram of GA equivalent per gram of tea sample (mg GAE/g d.w.). Total flavonoid content was evaluated using aluminum nitrate colorimetry in accordance with the method of Xiao et al. (21). The result was calculated based on standard curve with rutin and expressed as grams of rutin equivalent per gram of dry tea sample (g RE/g d.w.). The contents of TFs, TRs, and TBs in the tea samples were systematically measured using the method in literature (22).

Determination of Gallic Acid and Catechins by High-Performance Liquid Chromatography

FBT samples were freeze-dried and crushed using an electric grinder (FW 100, Beijing Yongguangming Medical Instrument Co., Ltd., Beijing, China). About 1 g of tea sample was placed in an extraction bottle and added with deionized water [1:40 (w/v)]. The sample was subjected to thermal extraction at 95°C for 30 min, with shaking every 5 min. The blend was centrifuged for 15 min at 10,000 × g after cooling, and the supernatant was collected. After the volume was adjusted to 50 mL, the sample was stored in darkness for future use.

The contents of catechin, GA, GCG, EGC, GC, EC, EGCG, ECG, and CG in the tea samples were analyzed using HPLC (23). A 0.45 μm PVDF membrane was used to filter the sample extracts. The filtrate (10 μL) was added into the Agilent 1260 Infinity II LC system (Agilent, Santa Clara, United States) for analysis of GA and catechins. An Agilent 5 TC-C18 (2) reverse-phase column (Eclipse Plus, Agilent Technologies, United States) (5 μm particle size; 4.6 mm × 250 mm) was also used. Water containing 0.1% (v/v) formic acid (mobile phase A) and acetonitrile (mobile phase B) were used for chromatographic elution as follows: 0–40 min, 10–35% B; 40–42 min, 35–10% B. The flow rate was kept at 0.8 mL/min for a total running time of 42 min at 25°C. The sample was monitored at 210 nm and subjected to a photodiode array detector (Agilent G7114A variable wavelength detector; Agilent, Santa Clara, United States). The identification and quantification of catechin, GA, GCG, EGC, GC, EC, EGCG, ECG, and CG were performed by comparing their UV spectra and retention times with their authentic standards. The contents were calculated as mg/100 g of dry weight tea samples. Total catechins were the summation of GCG, catechin, EGC, GC, EC, EGCG, ECG, and CG contents.

Evaluation of Antioxidant Activities

Several assays with different mechanisms were conducted to assess the antioxidant activities of the FBT samples. ABTS radical cation scavenging activity (ABTS), DPPH radical scavenging activity (DPPH), reducing power (RP), and hydroxyl radical scavenging ability (HAS) were performed according to our previous study (24). An array of vitamin C concentration were carried out to plot the calibration curve, and the results were expressed as milligram of vitamin C per gram dry weight FBT flour (mg VCE/g d.w.). Ferric reducing antioxidant power (FRAP) was conducted using the method reported by Xiao et al. (20). Various concentrations of $FeSO_4$ solution were used to plot the calibration curve. The FRAP values were presented as millimole Fe (II) equivalents per gram dry weight sample.

Electronic Tongue Analysis

The electronic tongue analysis of FBT samples from different regions in China was performed using TS-sa402b (INSENT Inc., Japan), which has imitated lipid membrane sensors with a wide area of selection. Every sample was infused with 200 mL of distilled boiled water (40°C) to homogenize (10,000 r/min) for 1 min. The tea infusion was then centrifuged at 3,000 rpm for 10 min at 4°C, and the supernatant was filtered through three layers of gauze. The determination process contained three steps: 30 s of sample detection, 30 s of aftertaste detection and 120 s of cleaning. Each FBT infusion was detected four times, and the average value of the last three cycles was determined, which were analyzed using TS-sa402b Library search software (INSENT, Japan) to characterize the taste quality of FBT samples.

Statistical Analysis

All measurements were conducted in triplicate, and data were presented as mean value ± standard deviation (*SD*) and analyzed by ANOVA. The significance of differences ($p < 0.05$) between the average values was determined by Duncan's multiple range test using SPSS version 16.0 (SPSS Inc., Chicago, United States). Data graphs were plotted by OriginPro 8.1 statistical software (OriginLab Co., United States). With regard to the ITS2 sequencing data, mixed sample amplicons were paired-end sequenced on an Illumina MiSeq platform according to the manufacturer's protocol from LC-Bio. Raw tags were quality-controlled filtered under specific conditions using fqtrim (V 0.94). Chimeric sequences were filtered using Vsearch software (v2.3.4). The representative sequences of operational taxonomic units (OTUs) were obtained by clustering ≥97% similarity using Vsearch (v2.3.4). Alpha diversity was determined by Chao1, Observed species, Goods coverage, Shannon, and Simpson indices using QIIME (Version 1.8.0). Beta diversity was estimated using (PCoA) and clustered using QIIME software (Version 1.8.0).

RESULTS AND DISCUSSION

Comparison of Fungal Communities of Fu Brick Tea Produced in Different Regions

Diversity of Fungal Communities

A total of 1,667,155 effective reads were generated from the five FBT samples in quadruplicate analysis after filtering quality and removing chimera, with a mean sequence number of 83,358 for each sample (20 samples; 79,869–86,727 reads per sample). On the basis of the 97% similarity threshold, these high-quality sequences were clustered into 69 OTUs for all samples, from the range of 4–19 OTUs per sample. The rarefaction curves for Shannon diversity reached saturation (**Supplementary Figure 1**), suggesting that the sequencing dataset was adequate to distinguish the species richness in the five regional FBT samples. The diversity and richness of the fungal communities was measured by alpha diversity analysis using ACE, Chao1 (community richness), goods coverage (sequencing depth), Shannon (evenness), and Simpson (richness) indices (**Supplementary Table 1**). The goods coverage of all the samples was >99.99%, confirming that the sequencing depth was sufficient to saturate the fungal diversity and most fungal microbes had already been captured, consistent with the rarefaction curves. As shown in **Supplementary Table 1**, no significant differences were observed in the Shannon and Simpson indices (the diversity of detected fungal community) among SX, GZ, and ZJ samples and between HN and GX samples

($p > 0.05$). The fungal diversity of HN and GX samples was higher than that of SX, GZ, and ZJ samples. In addition, the ACE and Chao1 indexes of the HN sample was higher than those of the other samples, consistent with the differences in the observed OTUs and indicating HN sample shows the highest fungal richness. The results implied that the fungal diversity and richness of the HN sample was the best, followed by GX, and the ZJ sample was the lowest. Rank-abundance curves revealed that a large proportion of the sequences were classified as rare microorganisms represented by only a few sequences, especially for ZJ sample (**Supplementary Figure 2**). The beta diversity results of NMDS analysis were analyzed based on unweighted uniFrac to estimate the distribution of fungal communities in the five FBT samples. As shown in **Supplementary Figure 3**, the fungal community structure of the GX sample had the highest level of similarity, while the GZ sample had the lowest. Venn diagram analysis was used to present the number of features that are common and unique to each sample/group of different FBT samples. Only 4 of the identified OTUs were shared in all groups. Eight of 36 OTUs, 6 of 49 OTUs, 6 of 37 OTUs, and 12 of 42 OTUs were shared between the HN sample and the SX, GX, ZJ, and GZ samples, respectively. Six of 34 OTUs, 7 of 22 OTUs, and 5 of 35 OTUs were shared between the SX sample and GX, ZJ, and GZ samples, respectively. Seven of 33 OTUs and 7 of 44 OTUs were shared between the GX sample and ZJ and GZ samples, respectively. Seven of 32 OTUs were shared between ZJ and GZ samples (**Figure 2A**). These results clearly demonstrated that fungal communities of FBT produced in different regions are greatly different.

Composition of Fungal Communities in Fu Brick Tea

Ribosomal Database Project (RDP) and unite databases were used for species classification and subsequent analysis to ensure the complete and accurate annotation results at the 70% threshold to investigate the taxonomic composition of microbial community and diversity among the five FBT samples. The detected fungal communities were subdivided into 5 phyla, 15 classes, 20 orders, 23 families, 27 genus, and 33 species. As the taxonomical granularity increased, the percentages of unclassified fungal ITS rRNA gene sequences increased to 1.86 at the species level. As shown in **Figure 2B**, Ascomycota was the only predominant phylum in all sequences, making up 99.97–100% of the total relative abundance. Basidiomycota, Chytridiomycota, and Zygomycota, even if they were also detected, accounted for a low percentage of the total effective sequences. At the genus level (**Figure 2C**), *Eurotium* and *Aspergillus* had more than 99.97% of all valid reads. *Eurotium* was predominant in all samples and represented the largest fraction, with average relative abundance of up to 88.84%, consistent with previous reports (24, 25). *Eurotium* is widely regarded as the main fungus in the fermentation of FBT (26), which has been reported as the key contributor in the formation of the special chemical components of FBT (5). *E. cristatum* could secrete many extracellular enzymes that have the great potential to transform chemical compounds in tea leaves into other components. For instance, previous studies reported that *E. cristatum* played an important role in the significant increase of TBs, soluble carbohydrates and three purine alkaloids (27). In addition, *E. cristatum* transformed phenolic compounds that leading into stronger red and yellow color of tea infusion (28). When the fungal composition was analyzed at the genus level with the dominant group removed (**Figure 2D**), *Aspergillus* was overwhelmingly dominant in all samples (SX 98.55%, HN 99.81%, GZ 98.59%, ZJ 94.17%, and GX 99.91%, respectively). *Aspergillus* is a genus of filamentous and saprophytic fungi that are widely distributed in nature and contains more than 250 species (29). Numerous previous studies have indicated that the quality formation of FBT was also closely related to the metabolism of *Aspergillus* genus. For instance, Zhao et al. reported that *Aspergillus* produced a variety of enzymes (pectinesterase, endo-1,4-β-xylanase, catalases, catalase-peroxidases, alkaline protease, and peroxiredoxins) that contributed to the oxidation of tea polyphenols and degradation of plant cell wall (30). Furthermore, the genus *Aspergillus* make great contribution to the enhancement of taste by secreting enzymes like proteases, α-amylases glucoamylases, xylanases, and other hemicellulose to decompose complex carbohydrates, proteins and lipid into small molecules in FBT and produce unique flavor (31, 32). Besides, it was found that *Saccharomycopsis* and *Debaryomyces* were more abundant in the ZJ sample than that in other regions, and *Monascus* and *Wallemia* were the two genera that only existed in the ZJ sample. Among them, the genus *Debaryomyces* has been considered to be an essential candidate microorganism in a fermentation starter for artificial fermentation of FBT, as it has a distinguished influence on the metabolites biotransformation during the manufacturing process. Their enzyme activities enhance the quality of FBT by producing the sweet substance xylitol, vitamins, and other organic acids, contributing to richer taste and flavor (33). Some species of *Monascus* genus have been widely used in tea fermentation owing to their abilities to decrease hydrogen peroxide and to bio-convert tea polyphenols into TFs and TRs during the fermentation process, exhibiting a strong antioxidant activity by preventing oxidative stress-induced diseases (34). The genus *Wallemia* was also identified as the core functional microorganisms that associated with the metabolic variations of volatile components during the pile-fermentation of FBT, and may play an important role in contributing the stale and betelnut aroma in dark tea (35). To better understand differences and similarities among different samples, we carried out Z-value transformation on the basis of the heat map and did cluster analysis on fungal genera (**Figure 3**). Among the 27 detected genera, eight were found in the GZ sample but not in the other samples. These unique genera were *Marasmius*, *Alternaria*, *Penicillium*, *Saccharomycetales Incertae sedis* unclassified, *Mortierella*, *Sporobolomyces*, *Eurotiomycetes* unclassified, and *Monosporascus*. Only one unique genus was found in the SX sample, namely, *Chaetothyriales* unclassified, and it also had the least number of genus-level community composition. LEfSe analysis was carried out to determine the specific fungal taxa that can distinguish FBT samples from different regions. LDA emphasized that about 11 fungal clades, whose abundance in a given regional variety differed from those in the other samples, exhibited statistically significant differences (**Figure 4A**). LEfSe was used to illustrate differentiating

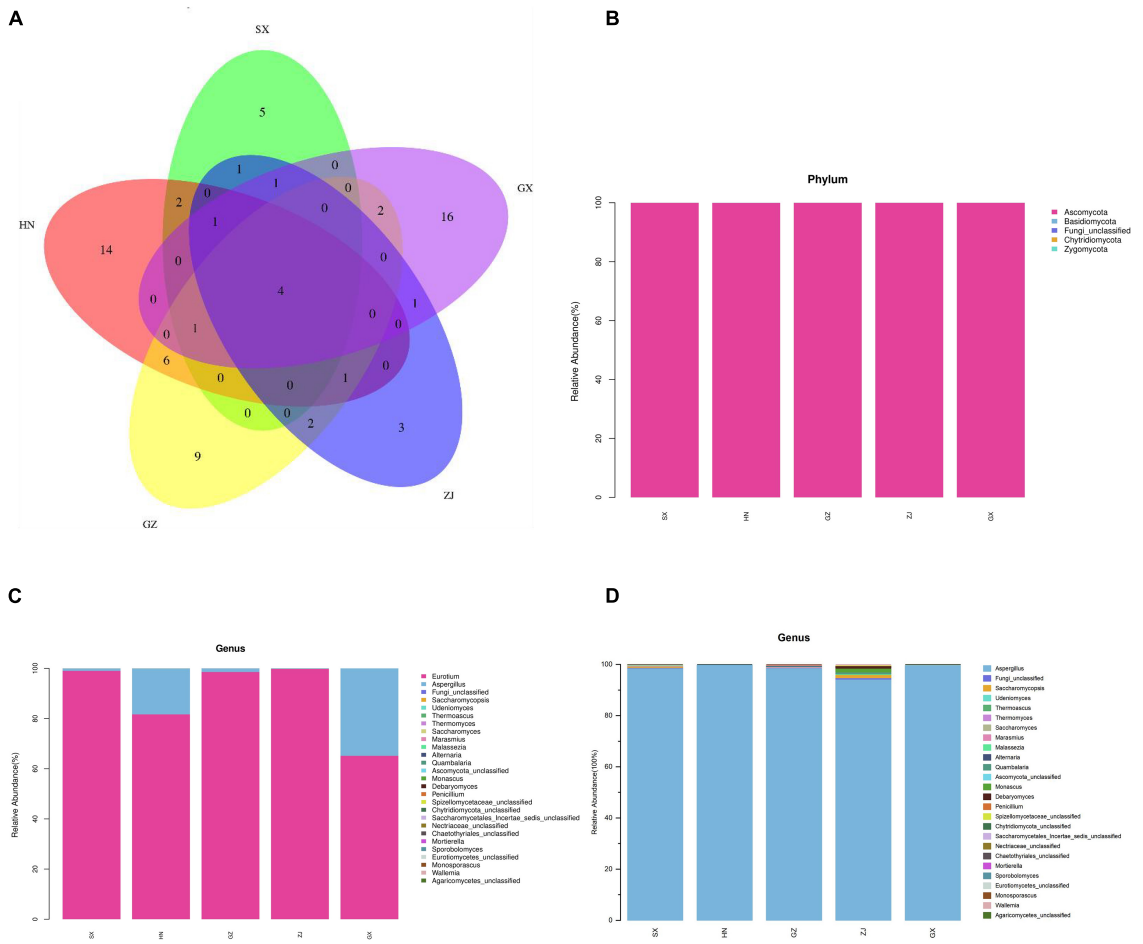

FIGURE 2 | The Venn diagram analysis of fungal community compositions of five Fu brick teas in different regions **(A)**. The average relative abundance of fungal communities **(B)** at phylum level; **(C)** at genus level; **(D)** genus level with the highest abundance group removed] of FBT samples.

taxa on the phylogenetic tree of the fungal community in the FBT samples from the domain to the species level (**Figure 4B**). No distinguishable fungal taxa were detected in GZ and SX samples. However, three residual samples appeared as differentially abundant fungi belong to one class (Saccharomycetes), one order (Saccharomycetales), 3 genera (*Eurotium*, *Aspergillus*, *Thermoascus*), and 6 species (*Eurotium amstelodami*, *Aspergillus vitricola*, *A. penicillioides*, *A.* sp. FLS 2010, *Thermoascus aurantiacus*, and *Eurotium* unclassified). The GX sample had the largest number of discriminate taxa, involving class Saccharomycetes, order Saccharomycetales, and genera *Aspergillus*, *Eurotium*, and *Thermoascus*, which were all statistically different and distinctive. *Eurotium* and *Aspergillus* were significantly enriched in HN and ZJ samples, respectively.

Main Metabolites of Fu Brick Tea From Different Regions

The TPC and TFC of the five FBT samples from different regions were evaluated (**Figures 5A,B**). The TPC and TFC in the ZJ sample were the highest (57.64 mg GAE/g d.w. and 76.24 g RE/g d.w., respectively). The GZ sample had the lowest TPC and TFC, which were 1.80 and 1.99 times lower than those in the ZJ sample. The HN sample contained higher TFC (55.28 g RE/g d.w.) and lower TPC (32.54 mg GAE/g d.w.) than the SX sample. The different results of FBT samples were partly due to their diverse fungal community composition. In this study, network correlation analysis revealed that TPC and TFC were significantly positively associated with *Monascus*, *Debaryomyces*, *Wallemia*, and *Quambalaria.* TFC was also found to be strongly correlated with *Monascus*, *Wallemia*, *Thermomyces*, and *Quambalaria* (**Figure 6**). Previous studies have also reported that the TPC was highly positively related to *Cyberlindnera*, *Wallemia*, *Penicillium*, *Ascomycota* unclassified, and *Eucasphaeria*, while negatively correlated with *Aspergillus* during manufacturing process of FBT (36). The TFC were significantly positively ($p < 0.05$) associated with *Candida*, *Cyberlindnera*, *Debaryomyces*, and *Penicillium*, while were negatively correlated with *Chlamydomonas* during the pile-fermentation period (37). Changes of phenolics and flavonoids are connected with the action of extracellular microbial enzymes, such as glucansucrase and cellulase, secreted by microorganisms

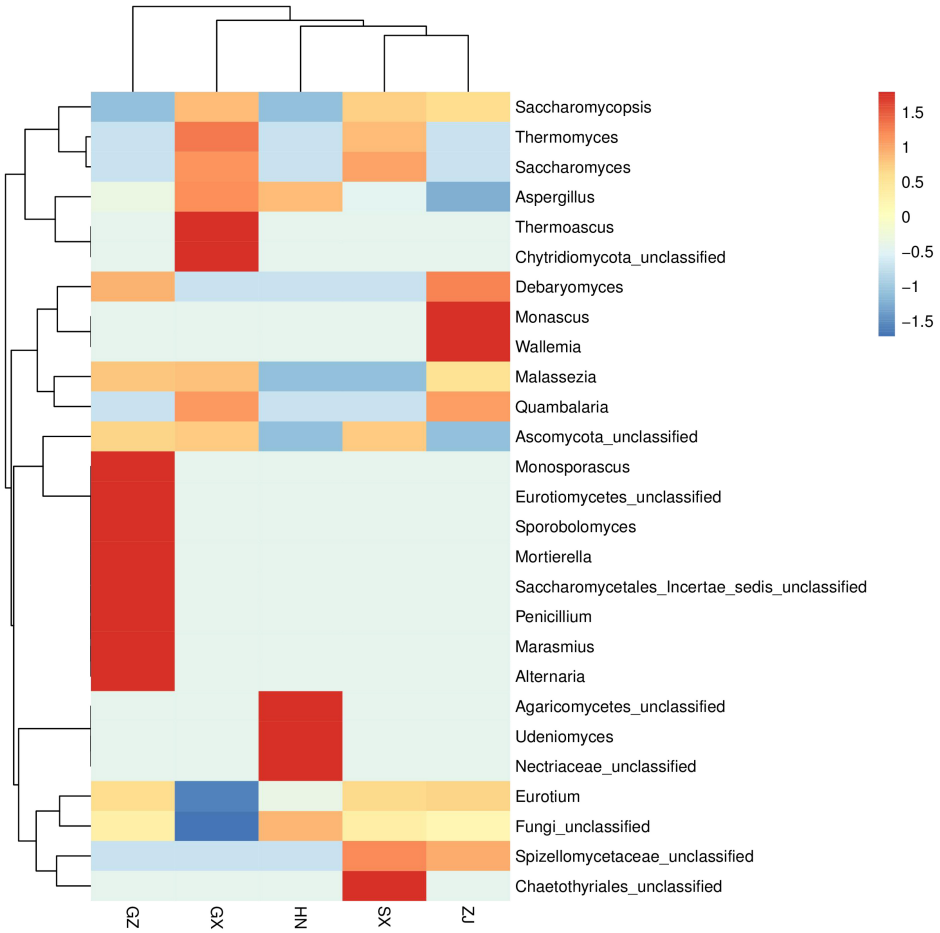

FIGURE 3 | Cluster analysis on fungal genera in five Fu brick teas in different regions.

including *Chlamydomonas*, *Penicillium*, and *Aspergillus* (9). Moreover, *A. pallidofulvus* and *A. sesamicola* make contribution to the accumulation of several flavonoids during fermentation (38, 39). It has been illustrated that the genus *Debaryomyces* increase both TPC and TFC during pile-fermentation probably attributed to the tannase secreted by the microbe, which could hydrolyze the ester and phenol condensation bonds in gallic tannin to produce simple catechins and GA, and also virtually hydrolyze the acetal bonds of EGCG to produce GA and EGC (40). The *Thermomyces* genus was reported to be one of the high-temperature resistant genera and occur when the humidity and temperature sharply increased during the early and mid-periods of pile-fermentation. Three non-volatile compounds (L-Tyrosine, L-Phenylalanine and GA) and six volatile compounds (2-ethylhexanol, rose oxide, safranal, α-ionone, β-Ionone, and ionone) were found to be significantly or highly significantly positively correlated with *Thermomyces*, contributing to the unique taste and flavor of dark tea (37, 41). However, the TFC in FBT declined significantly during manufacturing (36), which could be caused by moisture and heat reaction apart from the influence of microorganisms. The quality of FBT was mainly affected by raw materials and processing technology. Nevertheless, the degradation of TPC, TFC, and flavonoid glycosides during microbial fermentation might contribute to the taste characteristics and special aroma of dark tea (42).

As the main component of tea polyphenols (accounting for approximately 60–80%), catechins are divided into ester and non-ester catechins, and the molecular structure of the former has 1–2 more galloyl groups than the latter, and their content has a certain influence on the characteristic flavor and bioactivities of teas (9). The galloyl moiety of catechins is an essential donor to strong bitterness and astringency, while non-gallated catechins are not astringent (43). Therefore, GA, EGC, GC, EC, catechin, GCG, EGCG, CG, and ECG were identified and quantified by HPLC analysis to better understand the difference in the GA and catechins content of FBT produced from different regions (**Table 1**). The level of GA in the GX sample was significantly higher than that in the other samples ($p < 0.05$). GA and its derivatives are abundant in dark tea and exhibit anti-inflammatory, anti-mutagenic, and antioxidant activities as well as cardiovascular protective effects (44). In the present research, GA was positively associated with *Monascus*, *Debaryomyces*, *Wallemia*, and *Quambalaria* (**Figure 6**). Previous studies reported that the formation of GA

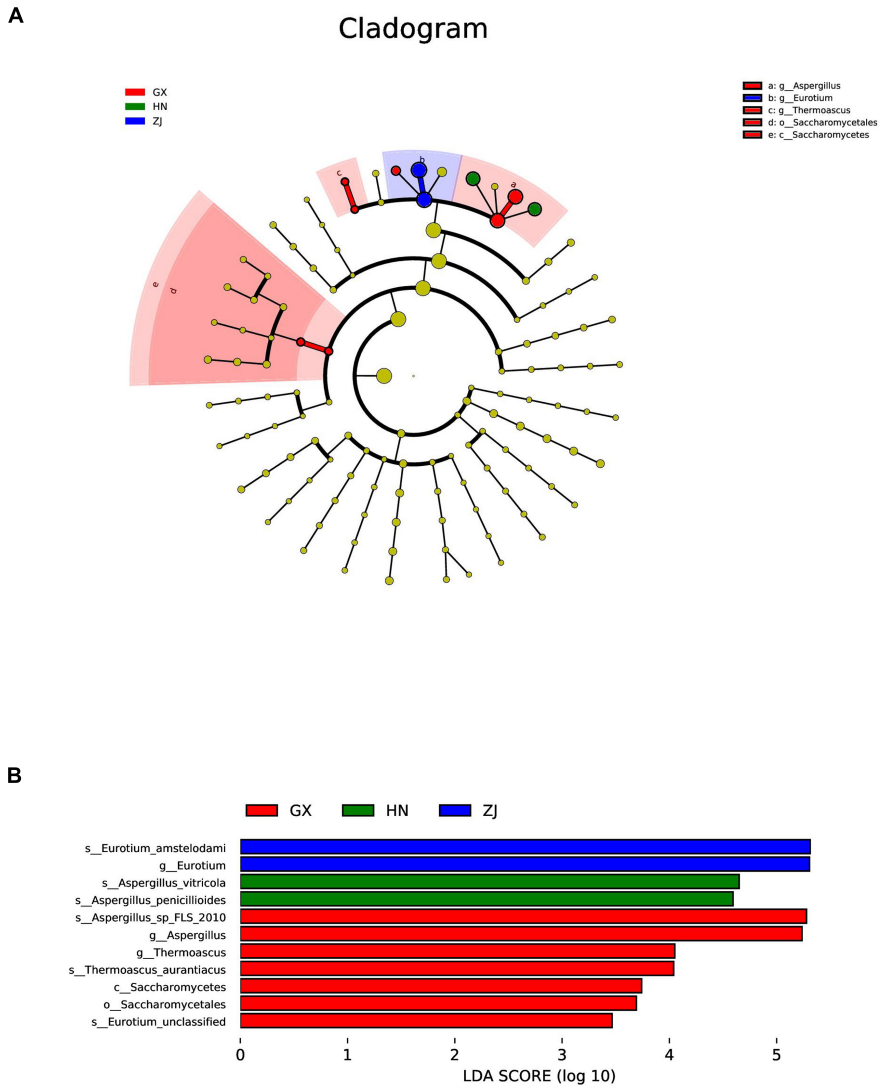

FIGURE 4 | Cladogram **(A)** and linear discriminant analysis (LDA) score **(B)** showed the significant abundance differences of fungal taxa by LEfSe analysis. The node size represents the difference in relative abundance.

probably resulted from moisture and heat reaction in the early stage and microbial metabolism is the main contributor at the later stage (33) during FBT manufacturing. In the early stage, the galloylated catechins underwent a gradual decomposition through hydrolysis by the effect of moisture and heat treatment, then corresponding degalloyl catechins along with GA were produced (28). Among them, EGCG is one of the most abundant and active galloylated catechins and was reported to be the main pathway for GA biosynthesis (45). In addition, the microbial tannase contributed to the formation of GA through the degradation of gallotannins like 3-O-galloylquinic acid or 1-galloylglucose and 1,2-digalloylglucose (6). Zhao et al. found that the content of EGCG and ECG decreased from 47.3 ± 2.42 and 39.94 ± 2.59 mg/g to 0.08 ± 0.15 and 0.48 ± 0.3 2 mg/g, respectively, after fermentation (30). By contrast, they found that the level of GA increased more than 11 times. Except for GA, the contents of total catechins, GC, and ECG were the highest in the GX sample. Tea samples produced from GZ and SX had the highest contents of EGCG (690.3 ± 0.89 mg/100 g) and GCG (82.48 ± 2.68 mg/100 g), respectively. The ZJ sample had higher amounts of non-galloylated catechins, including EGC, catechin, and EC, which could be attributed to the hydrolysis of galloylated EGCG, CG, and ECG; the lower bitterness and astringency in the ZJ sample could be explained at the same time (46). Interestingly, our results showed that GA, EGC, GC, EC, catechin, CG ECG, and total catechins were closely correlated with *Quambalaria* (**Figure 6**). As shown in **Figure 6**, catechin was positively related to the genus *Debaryomyces*, *Monascus*, *Wallemia* and *Quambalaria*. EGCG was significantly positively correlated with *Alternaria*, *Penicillium*, *Marasmius*, *Udeniomyces*, etc. ECG was positively associated with *Thermoascus*, *Saccharomycopsis*, *Saccharomyces*,

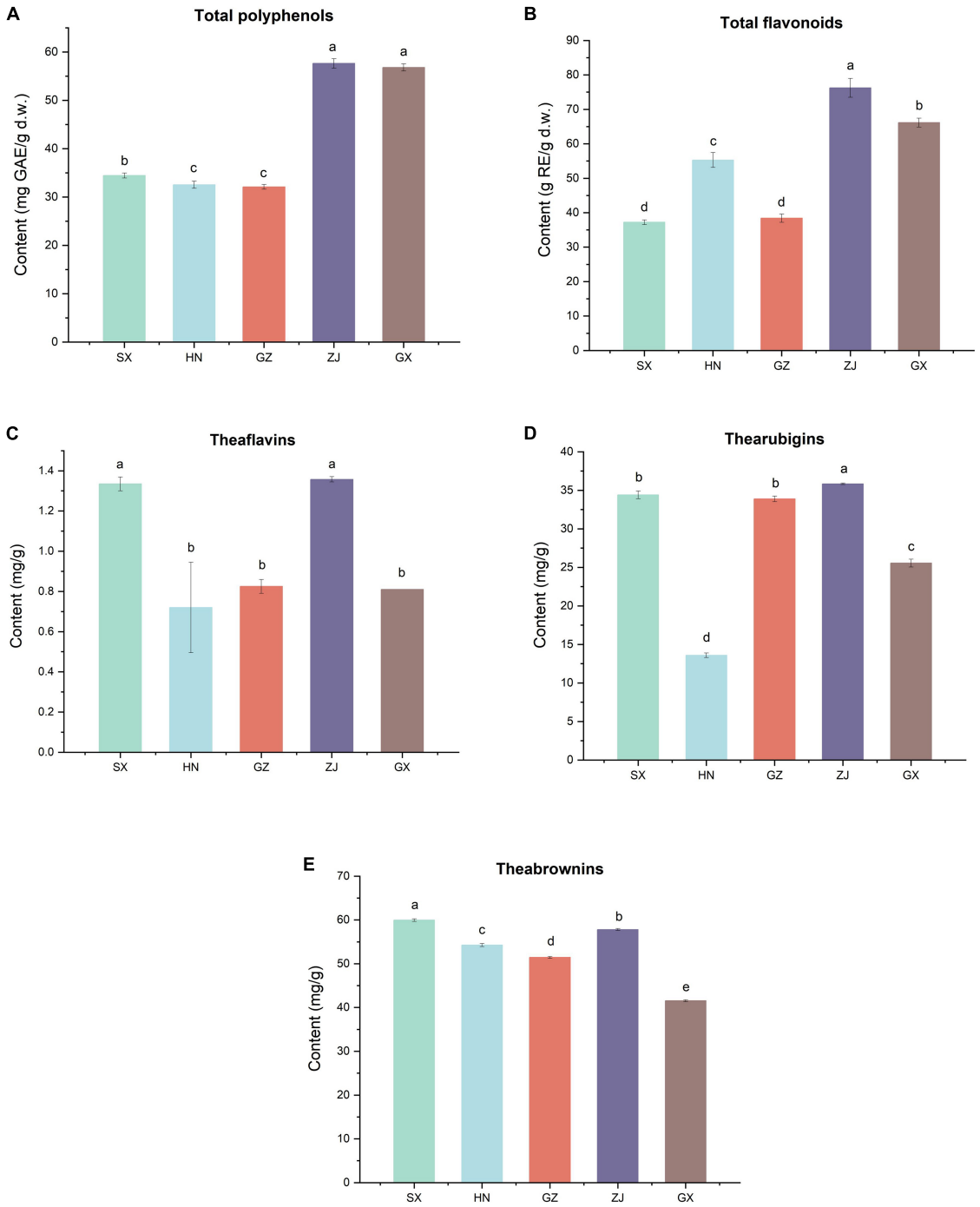

FIGURE 5 | Contents of **(A)** total polyphenols, **(B)** total flavonoids, **(C)** theaflavins, **(D)** thearubigins and **(E)** theabrownins of five Fu brick teas in different regions.

Thermomyces, *Quambalaria*, etc. This result was comparable to the results from previous studies. For instance, it has been reported that the catechin was positively associated with *Candida*, *Cyberlindnera*, *Debaryomyces,* and *Penicillium* (37). ECG was significantly positively correlated with *Candida*, *Wallemia*, *Penicillium*, and *Psychrobacter*, while negatively correlated with *Carnobacterium* and *Aspergillus* (36). EGCG was significantly associated with *Penicillium* and *Alternaria*, while negatively associated with *Burkholderia-Caballeronia-Paraburkholderia* and *Aspergillus* (12, 36, 47). GCG was significantly correlated with *Wallemia*, *Penicillium*, *Cyberlindnera*, and *Candida* (36). During microbial fermentation process, the formation of GA and non-gallyolated catechins are resulted from the gradual hydrolysis of gallyolated catechins and polymeric catechins in FBT. At

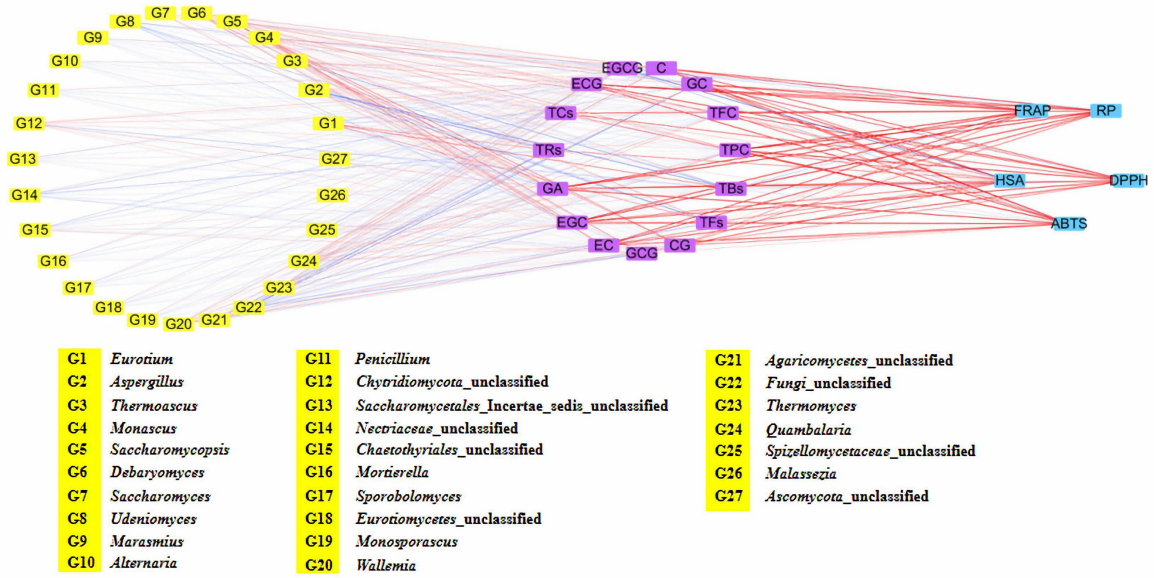

FIGURE 6 | Network visualized the relationship between main metabolites and fungal community, as well as antioxidant activity and main metabolites of five Fu brick teas in different regions.

TABLE 1 | Contents of gallic acid and catechins of five Fu brick teas in different regions.

Compounds	Contents (mg/100 g)				
	SX	HN	GZ	ZJ	GX
GA	181.5 ± 1.37^{c}	123.0 ± 2.10^{d}	117.3 ± 2.75^{d}	310.2 ± 4.47^{b}	416.4 ± 4.47^{a}
GC	113.0 ± 2.06^{c}	19.61 ± 1.28^{d}	114.7 ± 0.97^{c}	171.4 ± 2.95^{b}	190.0 ± 2.19^{a}
EGC	60.67 ± 0.63^{c}	7.03 ± 2.21^{d}	179.9 ± 0.46^{b}	574.6 ± 4.93^{a}	575.3 ± 6.18^{a}
Catechin	17.01 ± 0.22^{c}	16.49 ± 0.55^{c}	10.68 ± 2.15^{d}	40.63 ± 0.03^{a}	28.86 ± 1.40^{b}
EC	25.48 ± 0.26^{e}	29.19 ± 0.42^{d}	53.31 ± 0.77^{c}	246.7 ± 0.66^{a}	163.4 ± 0.56^{b}
EGCG	58.63 ± 1.13^{e}	664.9 ± 1.91^{b}	690.3 ± 0.89^{a}	134.7 ± 1.58^{d}	403.5 ± 5.61^{c}
GCG	82.48 ± 2.68^{a}	9.41 ± 1.82^{d}	35.63 ± 0.81^{c}	38.20 ± 0.44^{c}	71.78 ± 3.52^{b}
ECG	12.65 ± 0.35^{d}	5.88 ± 0.09^{e}	24.64 ± 0.44^{c}	74.60 ± 2.33^{b}	115.0 ± 2.79^{a}
CG	9.31 ± 0.25^{c}	10.03 ± 0.44^{c}	6.38 ± 0.18^{d}	67.90 ± 0.62^{a}	18.92 ± 0.39^{b}
Total catechins	379.2 ± 2.63^{e}	762.5 ± 4.90^{d}	1115.5 ± 3.21^{c}	1348.7 ± 4.30^{b}	1566.8 ± 11.47^{a}

GA, gallic acid; GC, gallocatechin; EGC, epigallocatechin; EC, epicatechin; EGCG, epigallocatechin gallate; GCG, gallocatechin gallate; ECG, epicatechin gallate; CG, catechin gallate. Each tea sample was determined with three replications. Letters indicate Duncan's pairwise differences among different samples ($p < 0.05$).

the same time, non-galloylated catechins are further degraded into phenolic acids or converted into complex phenolic tea pigments under the chemical reactions, such as oxidation and polymerization, leading to their decrease (48). For this reason, several catechin derivatives were newly formed in FBT, involving 2S, 3R-6-methoxycar-bonylgallocatechin (MCGE) and 2R, 3R-6-methox-ycarbonylgallocatechin-3-O-gallate (EGCGD) (4). Besides, due to the strong microbial action and hydrolysis during the fermentation of FBT, chemical reactions, such as oxidation and isomerization of catechins, occur, and a large amount of ester catechins are degraded into simple catechins. Larger amount of non-ester catechins to ester catechins leads to less astringent and more mellow taste (49).

Tea pigments such as TBs, TFs, and TRs are the water-soluble oxidation products of polyphenols in tea infusion and significantly contribute to the characteristic taste and color of FBT (46). TFs are primary transitional metabolites, which have been presumed to be produced initially by the oxidative polymerization of tea polyphenols, especially catechins, and were further polymerized into TBs with other compounds (such as polysaccharides, proteins, and caffeine) during pile fermentation (50). The level of TFs was the highest in the ZJ sample (1.36 ± 0.01 mg/g) and was almost equivalent to that in SX sample (1.34 ± 0.03 mg/g). Nevertheless, no statistically significant differences were found in the level of TFs among HN, GZ, and GX samples (**Figure 5C**). A significant positive correlation ($p < 0.05$) existed between the levels of TFs and the genera of *Eurotium*, *Monascus*, *Debaryomyces*, *Chaetothyriales* unclassified, *Wallemia*, and *Spizellomycetaceae* unclassified (**Figure 6**). Lee et al. used *Monascus* as the

strain to ferment tea for thirty days, the content of TFs in tea increased almost nine times compared with unfermented tea (34). It has also been reported that tea fermentation with inoculated *Debaryomyces hansenii* improved TFs (51). In addition, studies indicated there were other microorganisms including *A. pallidofulvus*, *A. sesamicola*, and *Penicillium manginii* also had significantly ($p < 0.05$) positive influence on TFs (10). Although the content of TFs in tea leaves is lower than that of TRs and TBs, it is an important factor that affects the brightness, taste intensity, and freshness of tea infusion. The ZJ sample also contained the highest level of TRs (35.84 ± 0.11 mg/g), which was 1.44, 1.95, and 10.28 mg/g higher in SX, GZ, and GX samples, respectively. The TRs content (13.60 ± 0.29 mg/g) was the lowest in the HN sample (**Figure 5D**). The level of TRs was positively associated with *Eurotium* and *Debaryomyces* but negatively correlated with *Aspergillus*, *Udeniomyces*, *Nectriaceae* unclassified, *Agaricomycetes* unclassified, and Fungi unclassified (**Figure 6**). *A. pallidofulvus* and *A. sesamicola* were also reported to have significant ($p < 0.05$) negative effects on TRs (10). TRs are one of the main substances that contribute to the red color and taste intensity of tea infusion. Importantly, TRs play a role similar to insulin or insulin-like growth factor in human cells and can become a new alternative for the treatment of overweight and obesity; it functions by activating lipolysis via mitochondrial uncoupling capacity and inactivating phosphoenolpyruvate carboxykinase (PEPCK) promoter as the major enzyme of gluconeogenesis through Forkhead box protein O1a (FOXO1a) phosphorylation (52). With the increasing oxidation degree of tea polyphenols, TRs and TFs are further oxidized and polymerized to TBs under the synergistic action of polyphenol oxidase (PPO), peroxidase (POD), and laccase produced by microorganisms, such as the genera *Aspergillus*, *Pseudomonas*, *Eurotium*, *Debaryomyces*, *Lichtheimia*, *Blastobotrys*, *Rosellinia*, *Geotrichum*, *Lichtheimia*, and *Rasamsonia* (9). The content of TBs was the highest in the SX sample (59.96 ± 0.29 mg/g) and was 1.04–1.44 folds higher than that in the four other samples, followed by ZJ sample (**Figure 5E**). This result was comparable to the results from Wang et al. (53), who determined that the levels of TBs, TFs, and TRs in the fermented tea were 98.67 ± 6.55, 0.98 ± 0.13, and 25.39 ± 10.56, respectively. The TBs content had a strong positive correlation with *Eurotium* but was extremely ($p < 0.01$) negatively correlated with *Thermoascus*, *Chytridiomycota* unclassified, *Thermomyces*, and *Malassezia*. Diverse strains isolated from fermentation of dark tea have been applied for producing TBs involving *E. cristatum, A. niger*, *A. tubingensis*, *A. marvanovae*, *A. fumigatus*, *Rhizomucor pusillus*, and *R. tauricus* (21, 53, 54). *A. sesamicola* was also thought to had highly significant ($p < 0.01$) negative effects on TBs (53). TBs are characteristic constituents in microbial-fermented tea that can regulate fatty acid metabolism and attenuate hypercholesterolemic capacities (55, 56). Previous research confirmed the gradual decrease in tea polyphenols and the accumulation of TBs when catechins were finally converted into TBs during the pile-fermentation process (50). This finding is consistent with the present results that GX sample had the highest TBs content and the lowest total catechin content. In addition, TFs, TRs, and TBs were significantly ($p < 0.05$) negatively associated with *Aspergillus*, with correlation coefficients (r) of −0.597, −0.660, and −0.715, respectively, which might be caused by few enzymes discharged from *Aspergillus*; these enzymes include proteases, hemicellulases, α-amylases, and cellulases, which could catalyze tea polyphenols, especially catechins and tea pigments.

Antioxidant Activities of Fu Brick Tea in Different Regions

FBT from different regions had diverse *in vitro* antioxidant activities. Five regular antioxidant capacity methods with disparate working mechanisms were used to assess the antioxidant activity of the five FBT samples (**Figure 7**). The GX sample had relatively stronger antioxidant capacity measured using ABTS (84.50 mg VCE/g d.w.), DPPH (210.14 mg VCE/g d.w.), RP (76.85 mg VCE/g d.w.), and FRAP (1.13 mmol Fe(II)/g d.w.) assays compared with tea samples from the other regions. Despite the lower HSA of GX sample than the ZJ sample, no statistically significant differences were detected among the samples. FBT produced in SX exhibited significant ($p < 0.05$) higher antioxidant activity measured using the five methods than HN and GZ samples. DPPH had no significant ($p > 0.05$) difference between SX and HN samples. The HN sample demonstrated the lowest value in ABTS (38.06 mg VCE/g d.w.), RP (39.24 mg VCE/g d.w.), FRAP (0.56 mmol Fe(II)/g d.w.), and HSA (52.80 mg VCE/g d.w.). Principal component analysis (PCA) was further carried out to detect cluster formation and reveal relationships among tea samples, bioactive composition, and antioxidant properties. As shown in **Figure 8A**, the PCA score plot indicated that tea samples from different regions were clearly distinguished from one another. The ZJ sample in the upper right part of **Figure 8A** was positively related to PC1 and PC2. This sample can be considered as having relatively higher antioxidant activity and higher content of polyphenolic metabolites. Loading plots (**Figure 8B**) were constructed to distinguish the most significant contributors. ABTS, DPPH, RP, and FRAP were found to be in a similar manner loaded on PC1, indicating that the four properties were connected with antioxidant activity. Moreover, most polyphenolic compounds had high loading on PC1 except for EGCG and TBs, which indicated that polyphenols were good antioxidants. According to literature, the reason behind the discrepancy in antioxidant capacity might be based on the presence of polyphenolic constituents, such as tea polyphenols, flavonoids, catechins, TFs, TRs, etc. in different FBT samples (57). Network correlation analysis was conducted to confirm the relationship between the antioxidant activity and polyphenolic components of tea products (**Figure 6**). The ABTS, DPPH, RP, and FRAP showed highly significant positive correlations with TPC and TFC ($|r| > 0.805$ and $p < 0.01$), while no significant ($p > 0.05$) correlation was found between HSA and TFC. Numerous studies have linked the increase in the antioxidant activity in tea with phenolic compounds (58, 59). The antioxidant activity of phenolic constituents mainly depends on the quantity of OH-groups and their position. The OH-groups on the 3′−, 4′−, and 5′− position

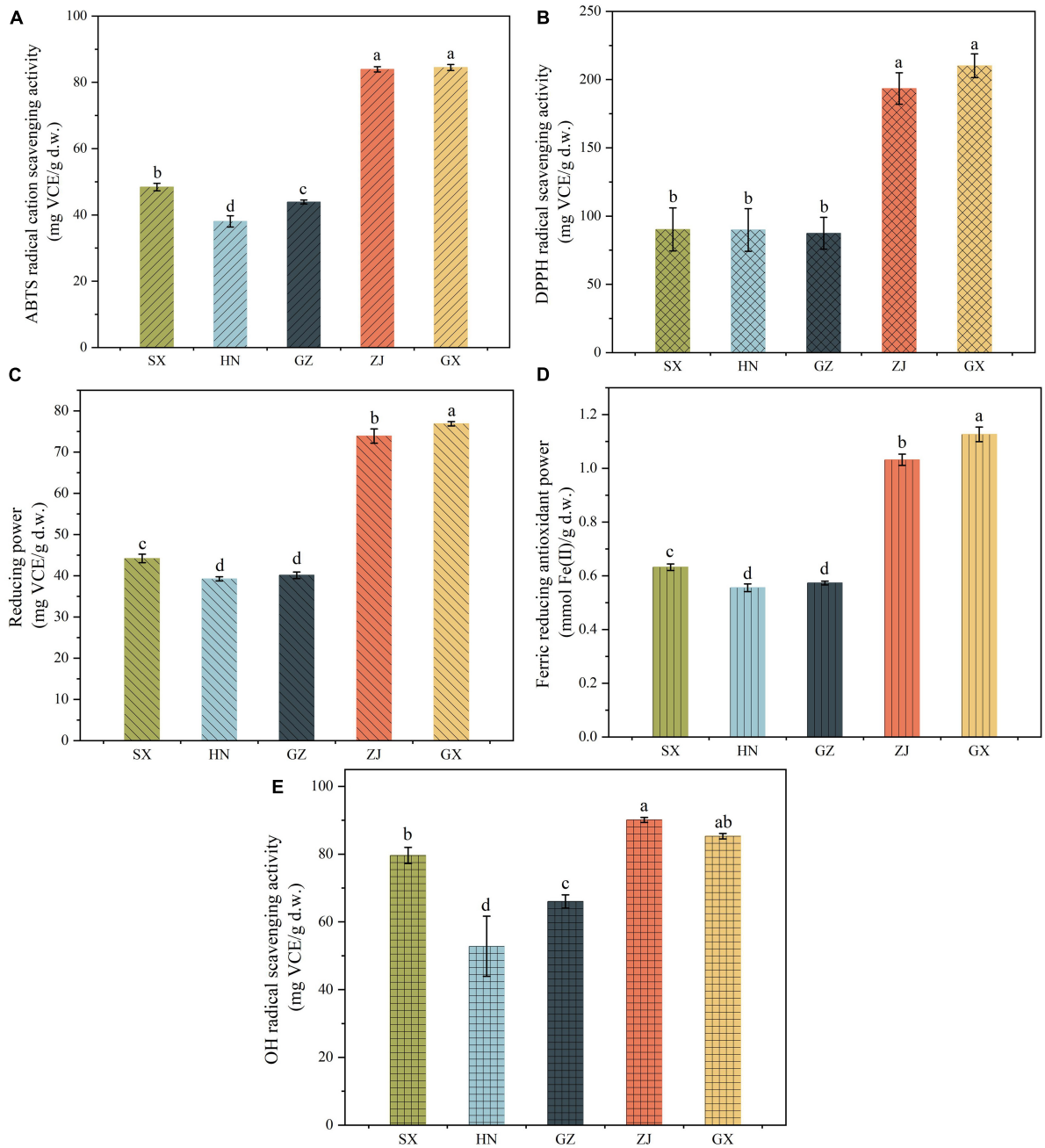

FIGURE 7 | Antioxidant activity of five Fu brick teas in different regions. ABTS radical cation scavenging activity **(A)**, DPPH radical scavenging activity **(B)**, reducing power **(C)**, OH radical scavenging ability **(D)** and ferric reducing antioxidant power **(E)**. Data were recorded as the mean value ± standard deviation of three replicates. Mean values marked by the different letters among the samples denoted significant difference ($p < 0.05$).

of the B-ring of flavonols and flavones enhance the antioxidant capacity of these substances compared with phenolics with one hydroxy group (12). The glycosylation of flavonoids by microbial enzymatic biotransformation during fermentation contributes to the antioxidant activity of FBT. GA and its derivatives have great antioxidant and antimicrobial capacity, which might be due to the methylization and glycosylation of GA by microbial enzymatic activity (60). As predicted, an extremely high correlation was observed between the results obtained of the five antioxidant activity assays involving ABTS, DPPH, RP, FRAP, and HSA and the GA content, with correlation coefficients of $r = 0.952$, $r = 0.947$, $r = 0.965$, $r = 0.979$, $r = 0.778$, respectively ($p < 0.01$). *In vitro* antioxidant activity in microbial enzymatically fermented teas including oolong tea, black tea, dark tea, and white tea was positively related to the high level of catechins (15, 61). All the five antioxidant activity methods exhibited the highly significant

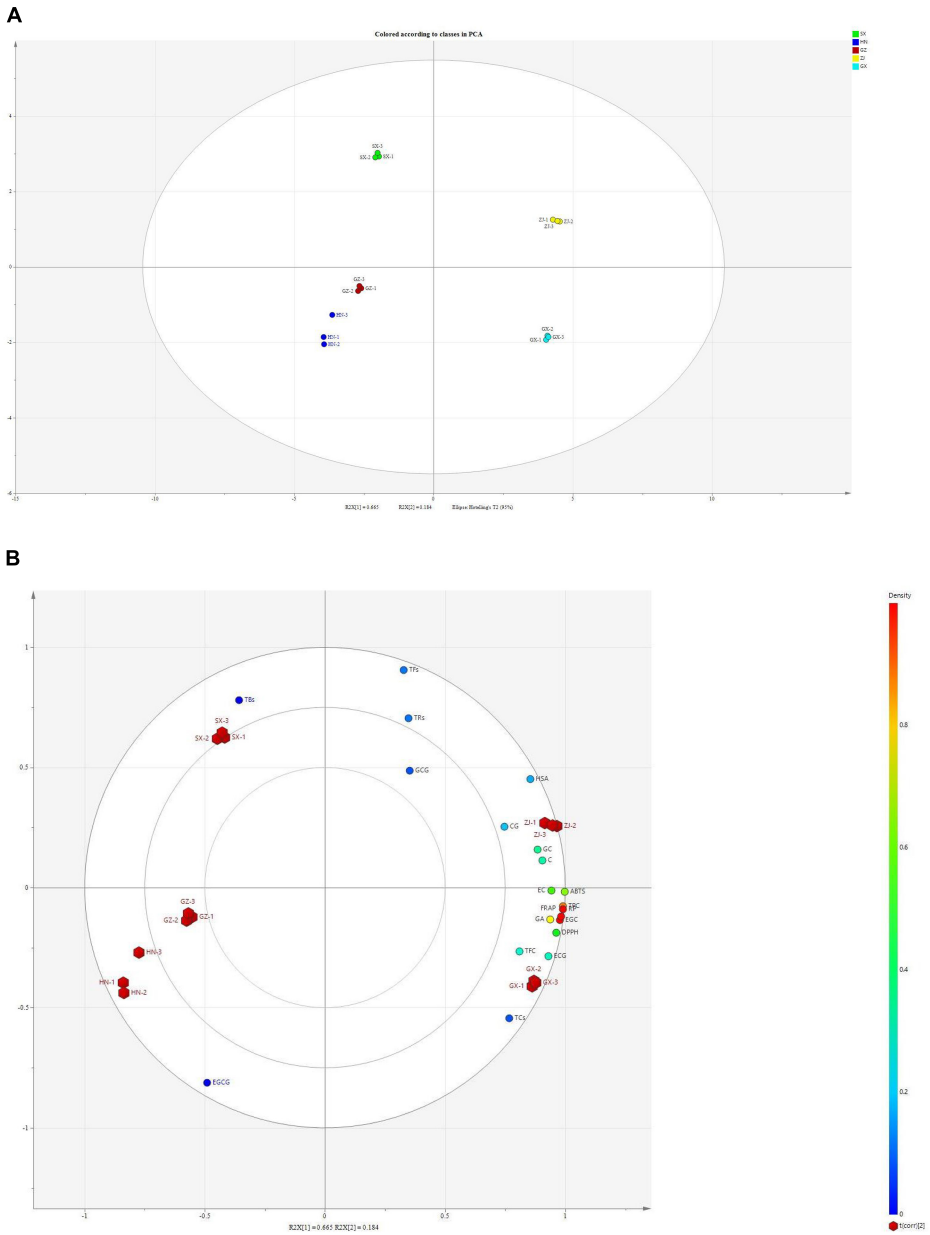

FIGURE 8 | Principal component analysis score **(A)** and loading plot **(B)** assessing the metabolites and antioxidant activity of five Fu brick teas in different regions.

($p < 0.01$) positive correlation with total catechins. Additionally, the antioxidant effects displayed the highest correlation with EGC among all types of catechins ($r > 0.780$). This remarkable antioxidant capacity of EGC can be ascribed to the higher extent of hydroxylation of the B ring and/or hydroxyl group at the C-3 position of the basic catechin structure, thereby improving the radical scavenging ability (62). Hence, catechins are potent antioxidants and play a protective role of dark tea in disease states related to reactive oxygen species (ROS). HSA showed significant positive correlation with TFs and TRs; no significant ($p > 0.05$) correlation was found between the four other *in vitro* antioxidant capacity assays and the two tea pigments. However, FRAP, ABTS, DPPH, and HSA had significant ($p < 0.05$) or highly significant ($p < 0.01$) negative correlation with TFs in dark tea in previous study (63). TFs was reported that can decrease the concentration of malondialdehyde and the activity of lactate acid dehydrogenase to improve superoxide dismutase capacity; as such, they are beneficial to increase the antioxidant activity (64). Moreover, colorless flavanols can be partially biotransformed into TFs and TRs under enzymatic oxidation by endogenous polyphenol oxidases and peroxidases, which contribute to the aroma and color of tea infusion (65). No significant ($p > 0.05$) correlation was observed between *in vitro* antioxidant activity and TBs (**Figure 6**). However, other reports noted that dark

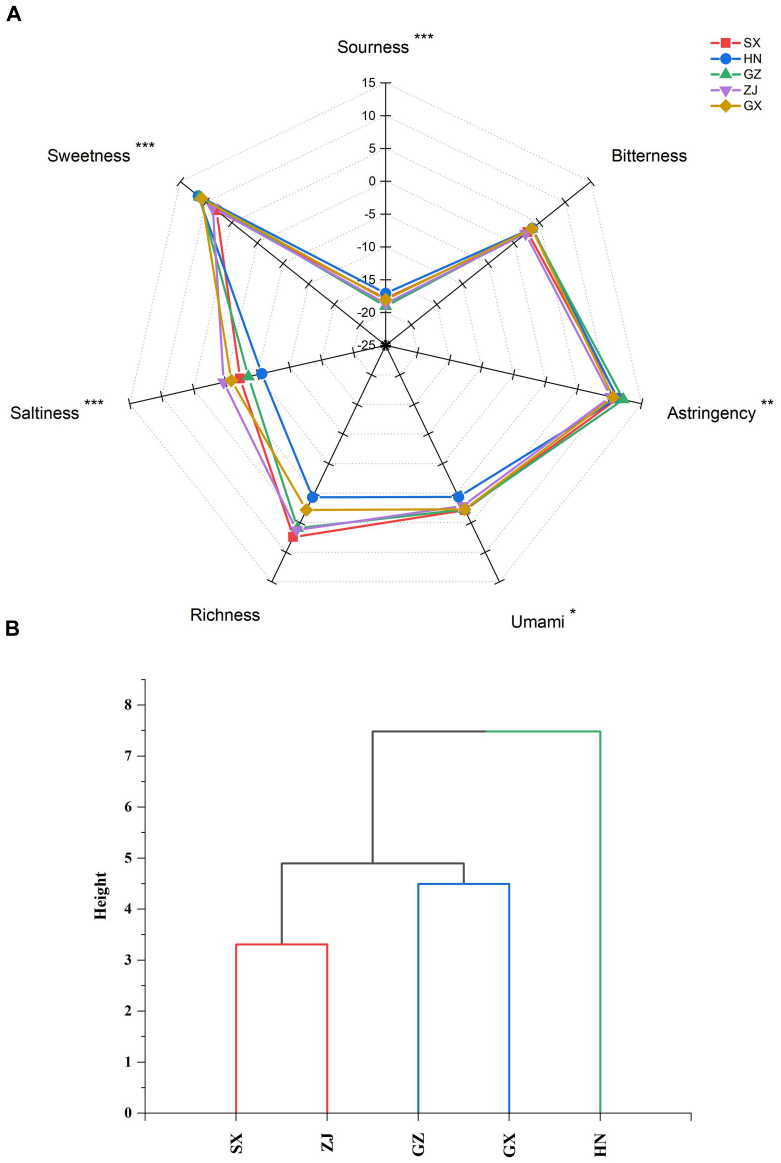

FIGURE 9 | Spider plot **(A)** and dendrogram plot **(B)** of the taste characteristics of five Fu brick teas in different regions evaluated by E-tongue. $^{*}p < 0.05$, $^{**}p < 0.01$, $^{***}p < 0.001$

tea with higher TBs content exhibited stronger superoxide radical scavenging activity (54). Tea pigments are non-enzymatic scavengers that have effective free radical scavenging capacities and kinetics and are similar to polyphenols (66). Hence, TPC, TFC, GA, GC, EGC, catechin, EC, ECG, CG, and tea pigments contributed to the antioxidant capacities of FBT in this study.

Phenolic compounds, particularly gallic acid and catechins, exhibited greatly positive relationship with antioxidant activities in microbial fermented dark teas (e.g., Pu-erh tea, Fu brick tea, Liubao tea) (3, 14). Fungal communities influenced the metabolites of FBT during fermentation, thus leading to the variant antioxidant activity of FBT. Previous studies reported that TPC, TFC, and TFs are the main contributors to the strong antioxidant activity of dark tea (14). The TPC, TFC, and TFs in the ZJ sample is higher compared with SX, HN, and GZ samples might possibly be due to the higher abundance of *Monascus*, *Debaryomyces*, *Wallemia*, and *Quambalaria* (**Figure 6**), thus, ZJ sample was noted with stronger antioxidant activities than the SX, HN, and GZ samples. Furthermore, previous studies reported that GA has been considered to be one of the key antioxidants in dark tea (67), similar result was also found in this study. For instance, it was found that GA and all antioxidant assays were highly positively correlated (**Figure 6**), higher GA in ZJ and GX samples is one of an important reason for their higher antioxidant activity compared with the other three FBT. Besides, the characteristics of gallic acid, catechins,

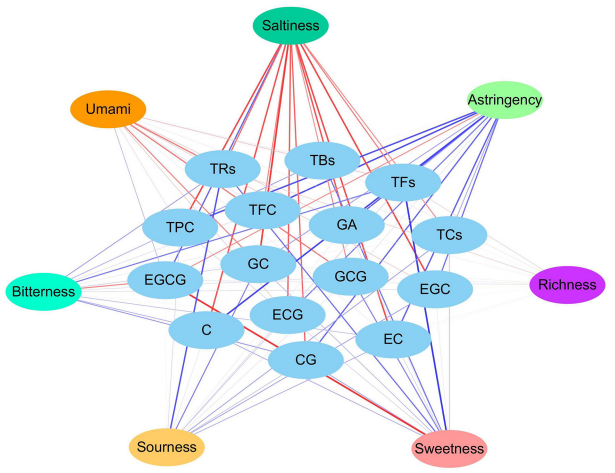

FIGURE 10 | Network correlation analysis of the taste profile and the main metabolites.

and tea pigments, which can act synergistically, additively or antagonistically should also be considered for the observed antioxidant activity of different FBT.

Taste Characteristics of Different Fu Brick Tea Samples and Their Relationship to Metabolites

Differences in the taste quality attributes of dark tea were investigated by E-tongue and presented in the spider plot (**Figure 9A**). The HN sample had the strongest sourness and sweetness; the ZJ sample had the strongest saltiness; the SX sample had the strongest umami; and the GZ sample had the strongest astringency among the FBT samples from different regions. No statistically significant difference ($p > 0.05$) in bitterness and richness was found among the FBT samples. The taste attributes of the FBT samples were clustered into three groups: HN, SX-ZJ, and GZ-GX (**Figure 9B**). The cluster of SX-ZJ samples demonstrated close taste characteristics. The GZ sample indicated similar taste attributes to the GX sample. The distinctive taste phenotype of FBT could be due to differences in the levels of various metabolites. Hence, network correlation analysis was performed to better understand the association between taste profiles and main constituents of dark tea (**Figure 10**). The bitterness of the FBT samples was positively related to EGCG ($|r| = 0.576$, $p < 0.05$) but negatively correlated with TFs ($|r| = 0.616$, $p < 0.05$), indicating that EGCG is the main contributor to the bitter taste of FBT. EGCG belongs to ester-type catechins and is thought to be the main source of bitterness in tea. The acceptance of green tea is related to bitterness genes, and that bitter taste is mainly linked with EGCG content (68), consistent with our research. Caffeine and several amino acids (arginine, alanine, etc.) also result in the bitter taste of tea infusion (8). Furthermore, the astringency of FBT had the most significant correlation with EGCG ($|r| = 0.526$ and $p < 0.05$). The amount of catechins in tea infusion greatly contributes to the bitterness and astringency of tea. However, previous studies reported that the level of catechins was sharply reduced under the action of enzymes during microbial fermentation (69). This finding may explain the decrease in bitterness and astringency and the increase in the mellow taste of FBT compared with green tea (8, 9, 25). The sweetness in tea was significantly ($p < 0.05$) negatively associated with GCG and tea pigments (TBs, TRs, and TFs). Sweet taste was related to soluble sugars including monosaccharides (most commonly glucose, galactose, fructose), polysaccharides, oligosaccharides, and a small number of other sugars (35). Sweetness is not the main taste of tea leaves, but it can harmonize the bitterness and astringency in tea soup. From our results, a negative relationship was found between sourness and the contents of GC and TRs. Tea contains a variety of organic acids (up to 3% of dry matter) mainly including GA, citric acid, ascorbic acid, malic acid, fatty acid, oxalic acid, etc. Most of the acid substances in tea are esterified with other compounds, such as alcohols, through processing, and the remaining part enters the tea soup to play a flavoring role (34). For example, soluble fruit acid is viscous and can increase the concentration of tea soup, making the tea taste richer and have better sense of hierarchy. Moreover, the main compounds responsible for the umami taste in tea infusion are amino acids such as theanine, glutamic acid, glutamine, aspartic acid, asparagine, etc., of which theanine and glutamate have the most remarkable effect (40). Interestingly, though the saltiness in FBT almost exhibited significant ($p < 0.05$) or highly significant ($p < 0.01$) positive correlations to all metabolites measured, the salty taste is mainly the result of the action of monovalent ions, such as potassium and sodium, and the corresponding negative ions, which are very low in content and are often masked by other tastes. Despite the lack of significant ($p > 0.05$) difference between richness and the 15 metabolites in our result, tea polyphenols and tea polysaccharides in tea infusion mainly contributed to richness (17). In fact, the taste characteristics of different FBT samples are not only depended by main metabolites catechins, tea polyphenols and tea pigments investigated in this study, some of other metabolites such as amino acids, soluble proteins, peptides, fatty acids, polysaccharides, etc. might also contributed to the taste attributes of FBT. These metabolites can act synergistically, additively or antagonistically with catechins to affect the taste attributes of FBT. Further research is essential to perform on identification of these compounds and their relationship with fungal community, as well as clarify their contribution to the taste characteristics of FBT.

CONCLUSION

This study systematically characterized the diversity of fungal communities, chemical composition, antioxidant activity, and taste quality of FBT samples from five different regions of China. The relationship between bioactive metabolites and fungal communities and the key chemical substances contributing to the variations in antioxidant activity and taste profile were assessed. Results showed a total of 69 OTUs, which assigned into 5 phyla, 15 classes, 20 orders, 23 families, 27 genus, and 33 species,

with *Eurotium* as predominant genus. The HN sample had the strongest fungal diversity and richness, followed by GX, and the ZJ sample had the lowest. Additionally, 15 metabolites (including total phenolics, total flavonoids, GA, 8 catechins, total catechins and 3 tea pigments) were evaluated. Higher contents of total phenolics, total flavonoids, TFs, TRs, catechin, EC, and CG were found in the ZJ sample. Higher levels of TBs and GCG were found in the SX sample. Higher contents of GA, GC, EGC, ECG, and total catechins were found in the GX sample. TPC, GA, EC, CG, and TFs were positively associated with most genera, while TFC, catechins, and TBs were negatively correlated. The antioxidant activities of FBT exhibited significant ($p < 0.05$) differences in the ABTS, DPPH, RP, FRAP, and HSA of the FBT samples from different regions. The GX sample had relatively stronger antioxidant capacity. The network correlation analysis uncovered that TPC, TFC, and most catechins contributed to the antioxidant activities in FBT. The taste phenotypes of FBT were classified into HN, SX-ZJ, and GZ-GX. The HN sample had the strongest sourness and sweetness; the ZJ sample showed the strongest saltiness; the SX sample showed the strongest umami; and the GZ sample showed the strongest astringency. This study provides insights into the fungal community in FBT and demonstrates the potential role of fungal community in metabolite formation to improve the quality characteristics of FBT products.

DATA AVAILABILITY STATEMENT

The raw data supporting the conclusions of this article will be made available by the authors, without undue reservation.

AUTHOR CONTRIBUTIONS

YC: methodology, writing—original draft, and investigation. JC: writing—original draft, data curation, and investigation. RC: methodology and investigation. XW, LH, and LX: investigation. ZL and YW: resources. ZL: conceptualization. MZ: supervision, methodology, and writing—review and editing. YX: project administration, supervision, funding acquisition, conceptualization, investigation, data curation, validation, formal analysis, methodology, writing—original draft, writing—review, and editing. All authors have read and agreed to the published version of the manuscript.

FUNDING

This work was financially supported by Natural Science Foundation of Hunan Province (No. 2020JJ5243), the Science and Technology Innovation Program of Hunan Province (Nos. 2020RC2055 and 2021NK4260), Natural Science Foundation of China (Nos. 32002095 and 32172217), and Excellent Youth Foundation of Education Department of Hunan Province (No. 19B269).

ACKNOWLEDGMENTS

We thank the Key Technologies Research and Development Program of Hunan Province (Nos. 2020NK2030 and 2020WK2017), the Hunan Provincial Natural Science Foundation of China (No. 2019JJ50238), and the Changsha City Outstanding Innovative Youth Training Program (No. kq2107015).

SUPPLEMENTARY MATERIAL

The Supplementary Material for this article can be found online at: https://www.frontiersin.org/articles/10.3389/fnut.2022.900138/full#supplementary-material

REFERENCES

1. Chen GJ, Peng YJ, Xie MH, Xu WQ, Chen CX, Zeng XX, et al. A critical review of Fuzhuan brick tea: processing, chemical constituents, health benefits and potential risk. *Crit Rev Food Sci Nutr.* (2021) 1–18. doi: 10.1080/10408398.2021.2020718 [Epub ahead of print].
2. Du Y, Yang WR, Yang CC, Yang XB. A comprehensive review on microbiome, aromas and flavors, chemical composition, nutrition and future prospects of Fuzhuan brick tea. *Trends Food Sci Technol.* (2021) 119:452–66. doi: 10.1016/j.tifs.2021.12.024
3. Ma BS, Wang JC, Xu CC, Wang ZY, Yin DF, Zhou BX, et al. Interrelation analysis between phenolic compounds and in vitro antioxidant activities in Pu-erh tea. *LWT Food Sci Technol.* (2022) 158:113117. doi: 10.1016/j.lwt.2022.113117
4. Lin FJ, Wei XL, Liu HY, Li H, Xia Y, Wu DT, et al. State-of-the-art review of dark tea: from chemistry to health benefits. *Trends Food Sci Technol.* (2021) 109:126–38. doi: 10.1016/j.tifs.2021.01.030
5. Zhang C, Guo J, Zhang Z, Tian S, Liu Z, Shen C. Biochemical components and fungal community dynamics during the flowering process of Moringa-Fu brick tea, a novel microbially fermented blended tea. *LWT Food Sci Technol.* (2021) 140:110822. doi: 10.1016/j.lwt.2020.110822
6. Xu J, Hu FL, Wang W, Wan XC, Bao GH. Investigation on biochemical compositional changes during the microbial fermentation process of Fu brick tea by LC-MS based metabolomics. *Food Chem.* (2015) 186:176–84. doi: 10.1016/j.foodchem.2014.12.045
7. Li Q, Li Y, Luo Y, Zhang Y, Chen Y, Lin H, et al. Shifts in diversity and function of the bacterial community during the manufacture of Fu brick tea. *Food Microbiol.* (2019) 80:70–6. doi: 10.1016/j.fm.2019.01.001
8. Li Q, Jin Y, Jiang R, Xu Y, Zhang Y, Luo Y, et al. Dynamic changes in the metabolite profile and taste characteristics of Fu brick tea during the manufacturing process. *Food Chem.* (2021) 344:128576. doi: 10.1016/j.foodchem.2020.128576
9. Zhu MZ, Li N, Zhou F, Ouyang J, Lu DM, Xu W, et al. Microbial bioconversion of the chemical components in dark tea. *Food Chem.* (2020) 312:126043. doi: 10.1016/j.foodchem.2019.126043
10. Zhou BX, Ma CQ, Ren XY, Xia T, Li XHLC-MS. /MS-based metabolomic analysis of caffeine-degrading fungus *Aspergillus sydowii* during tea fermentation. *J Food Sci.* (2020) 85:477–85. doi: 10.1111/1750-3841.15015
11. Zhao XX, Wang YR, Cai WC, Yang MJ, Zhong XD, Guo Z, et al. High-throughput sequencing-based analysis of microbial diversity in rice Wine Koji from different areas. *Curr Microbiol.* (2020) 77:882–9. doi: 10.1007/s00284-020-01877-9
12. Li MY, Xiao Y, Zhong K, Gao H. Study on taste characteristics and microbial communities in Pingwu Fuzhuan brick tea and the correlation between microbiota composition and chemical metabolites. *J Food Sci Technol.* (2022) 59:34–45. doi: 10.1007/s13197-021-04976-y

13. Xie HF, Kong YS, Li RZ, Nothias L-F, Melnik A, Zhang H, et al. Feature-based molecular networking analysis of the metabolites produced by in vitro solid-state fermentation reveals pathways for the bioconversion of epigallocatechin gallate. *J Agric Food Chem.* (2020) 68:7995–8007. doi: 10.1021/acs.jafc.0c02983
14. Lv HP, Zhang Y, Shi J, Lin Z. Phytochemical profiles and antioxidant activities of Chinese dark teas obtained by different processing technologies. *Food Res Int.* (2017) 100:486–93. doi: 10.1016/j.foodres.2016.10.024
15. Tang GY, Zhao CN, Xu XY, Gan RY, Cao SY, Shang A, et al. Phytochemical composition and antioxidant capacity of 30 Chinese teas. *Antioxidants.* (2019) 8:180. doi: 10.3390/antiox8060180
16. Cao SY, Li BY, Gan RY, Mao QQ, Wang YF, Shang A, et al. The in vivo antioxidant and hepatoprotective actions of selected Chinese teas. *Foods.* (2020) 9:262. doi: 10.3390/foods9030262
17. Cheng LZ, Wang YF, Zhang JR, Xu LR, Zhou H, Wei K, et al. Integration of non-targeted metabolomics and E-tongue evaluation reveals the chemical variation and taste characteristics of five typical dark teas. *LWT Food Sci Technol.* (2021) 150:111875. doi: 10.1016/j.lwt.2021.111875
18. Tian X, Li ZJ, Chao YZ, Wu ZQ, Zhou MX, Xiao ST, et al. Evaluation by electronic tongue and headspace-GC-IMS analyses of the flavor compounds in dry-cured pork with different salt content. *Food Res Int.* (2020) 137:109456. doi: 10.1016/j.foodres.2020.109456
19. Vitalis F, Tjandra Nugraha D, Aouadi B, Aguinaga Bósquez JP, Bodor Z, Zaukuu J-LZ, et al. Detection of monilia contamination in plum and plum juice with NIR spectroscopy and electronic tongue. *Chemosensors.* (2021) 9:355. doi: 10.3390/chemosensors9120355
20. Xiao Y, Wu X, Yao XS, Chen YL, Ho CT, He C, et al. Metabolite profiling, antioxidant and α-glucosidase inhibitory activities of buckwheat processed by solid-state fermentation with *Eurotium cristatum* YL-1. *Food Res Int.* (2021) 143:110262. doi: 10.1016/j.foodres.2021.110262
21. Xiao Y, He C, Chen YL, Ho CT, Wu X, Huang YX, et al. UPLC–QQQ–MS/MS-based widely targeted metabolomic analysis reveals the effect of solid-state fermentation with *Eurotium cristatum* on the dynamic changes in the metabolite profile of dark tea. *Food Chem.* (2022) 378:131999. doi: 10.1016/j.foodchem.2021.131999
22. Jiang YW, Hua JJ, Wang B, Yuan HB, Ma HL. Effects of variety, season, and region on theaflavins content of fermented Chinese Congou black tea. *J Food Q.* (2018) 2018:5427302. doi: 10.1155/2018/5427302
23. Li YJ, Zhang S, Sun YM. Measurement of catechin and gallic acid in tea wine with HPLC. *Saudi J Biol Sci.* (2020) 27:214–21. doi: 10.1016/j.sjbs.2019.08.011
24. Chen YL, Wang YL, Chen JX, Tang H, Wang CH, Li ZJ, et al. Bioprocessing of soybeans (*Glycine max* L.) by solid-state fermentation with *Eurotium cristatum* YL-1 improves total phenolic content, isoflavone aglycones, and antioxidant activity. *RSC Adv.* (2020) 10:16928–41. doi: 10.1039/C9RA10344A
25. Mao Y, Wei BY, Teng JW, Huang L, Xia N. Analyses of fungal community by Illumina MiSeq platforms and characterization of *Eurotium* species on Liupao tea, a distinctive post fermented tea from China. *Food Res Int.* (2017) 99:641–9. doi: 10.1016/j.foodres.2017.06.032
26. Mo HZ, Zhang H, Li YQ, Zhu Y. Antimicrobial activity of the indigenously microbial fermented Fuzhuan brick-tea. *J Biotechnol.* (2008) 136:S722–722. doi: 10.1016/j.jbiotec.2008.07.1719
27. Xiao Y, Zhong K, Bai JR, Wu YP, Gao H. Insight into effects of isolated *Eurotium cristatum* from Pingwu Fuzhuan brick tea on the fermentation process and quality characteristics of Fuzhuan brick tea. *J Sci Food Agric.* (2020) 100:3598–607. doi: 10.1002/jsfa.10353
28. Zhu YF, Chen JJ, Ji XM, Hu X, Ling TJ, Zhang ZZ, et al. Changes of major tea polyphenols and production of four new B-ring fission metabolites of catechins from post-fermented Jing-Wei Fu brick tea. *Food Chem.* (2015) 170:110–7. doi: 10.1016/j.foodchem.2014.08.075
29. Samson RA, Visagie CM, Houbraken J, Hong S-B, Hubka V, Klaassen CHW, et al. Phylogeny, identification and nomenclature of the genus *Aspergillus*. *Stud Mycol.* (2014) 78:141–73. doi: 10.1016/j.simyco.2014.07.004
30. Zhao M, Su XQ, Nian B, Chen LJ, Zhang DL, Duan SM, et al. Integrated meta-omics approaches to understand the microbiome of spontaneous fermentation of traditional Chinese pu-erh tea. *Msystems.* (2019) 4:e00680–19. doi: 10.1128/mSystems.00680-19
31. Ward OP, Qin WM, Dhanjoon J, Ye J, Singh A. Physiology and biotechnology of *Aspergillus*. *Adv Appl Microbiol.* (2005) 58:1–75. doi: 10.1016/S0065-2164(05)58001-8
32. Li Z, Huang L, Xia N, Teng J, Wei B, Peng D. Amount of Eurotium sp. in Chinese Liupao tea and its relationship with tea quality. *J Appl Microbiol.* (2020) 128:1658–68. doi: 10.1111/jam.14589
33. Xu A, Wang Y, Wen J, Liu P, Liu Z, Li Z. Fungal community associated with fermentation and storage of Fuzhuan brick-tea. *Int J Food Microbiol.* (2011) 146:14–22. doi: 10.1016/j.ijfoodmicro.2011.01.024
34. Lee YK, Lee SI, Kim JS, Yang SH, Lee I, Kim SD, et al. Antioxidant activity of green tea fermented with *Monascus pilosus*. *J Appl Biol Chem.* (2012) 55:19–25. doi: 10.3839/jabc.2011.054
35. Li Q, Hong X, Zheng XX, Xu YQ, Lai XM, Teng CQ, et al. Characterization of key aroma compounds and core functional microorganisms in different aroma types of Liupao tea. *Food Res Int.* (2022) 152:110925. doi: 10.1016/j.foodres.2021.110925
36. Li Q, Huang JN, Li YD, Zhang YY, Luo Y, Chen Y, et al. Fungal community succession and major components change during manufacturing process of Fu brick tea. *Sci Rep.* (2017) 7:6947. doi: 10.1038/s41598-017-07098-8
37. Hu S, He C, Li YC, Yu Z, Chen YQ, Wang YM, et al. Changes of fungal community and non-volatile metabolites during pile-fermentation of dark green tea. *Food Res Int.* (2021) 147:110472. doi: 10.1016/j.foodres.2021.110472
38. Wang ZH, Zheng CQ, Ma CQ, Ma BS, Wang JC, Zhou BX, et al. Comparative analysis of chemical constituents and antioxidant activity in tea-leaves microbial fermentation of seven tea-derived fungi from ripened Pu-erh tea. *LWT Food Sci Technol.* (2021) 142:111006. doi: 10.1016/j.lwt.2021.111006
39. Ma Y, Ling TJ, Su XQ, Jiang B, Nian B, Chen LJ, et al. Integrated proteomics and metabolomics analysis of tea leaves fermented by *Aspergillus niger*, *Aspergillus tamarii* and *Aspergillus fumigatus*. *Food Chem.* (2021) 334:127560. doi: 10.1016/j.foodchem.2020.127560
40. Bajpai B, Patil S. Induction of tannin acyl hydrolase (EC 3.1.1.20) activity in some members of fungi imperfecti. *Enzyme Microb Technol.* (1997) 20:612–4. doi: 10.1016/s0141-0229(96)00206-2
41. Hu S, He C, Li YC, Yu Z, Chen YQ, Wang YM, et al. The formation of aroma quality of dark tea during pile-fermentation based on multi-omics. *LWT Food Sci Technol.* (2021) 147:111491. doi: 10.1016/j.lwt.2021.111491
42. Castiglioni S, Damiani E, Astolfi P, Carloni P. Influence of steeping conditions (time, temperature, and particle size) on antioxidant properties and sensory attributes of some white and green teas. *Int J Food Sci Nutr.* (2015) 66:491–7. doi: 10.3109/09637486.2015.1042842
43. Obanda M, Owuor PO, Mang'oka R. Changes in the chemical and sensory quality parameters of black tea due to variations of fermentation time and temperature. *Food Chem.* (2001) 75:395–404. doi: 10.1016/S0308-8146(01)00223-0
44. Li HS, Fang QY, Nie QX, Hu JL, Yang C, Huang T, et al. Hypoglycemic and hypolipidemic mechanism of tea polysaccharides on type 2 diabetic rats via gut microbiota and metabolism alteration. *J Agric Food Chem.* (2020) 68:10015–28. doi: 10.1021/acs.jafc.0c01968
45. Tanaka T, Umeki H, Nagai S, Shii T, Matsuo Y, Kouno I. Transformation of tea catechins and flavonoid glycosides by treatment with Japanese post-fermented tea acetone powder. *Food Chem.* (2012) 134:276–81. doi: 10.1016/j.foodchem.2012.02.136
46. Zheng WJ, Wan XC, Bao GH. Brick dark tea: a review of the manufacture, chemical constituents and bioconversion of the major chemical components during fermentation. *Phytochem Rev.* (2015) 14:499–523. doi: 10.1007/s11101-015-9402-8
47. Zeng Q, Lv SH, Li X, Hu X, Liang Y, Fan C, et al. Bioactive ingredients and microbial diversity of Fuzhuan tea produced from different raw materials. *Food Sci.* (2020) 41:69–77. doi: 10.7506/spkx1002-6630-20190927-333
48. Ge YH, Bian XQ, Sun BQ, Zhao M, Ma Y, Tang YP, et al. Dynamic profiling of phenolic acids during Pu-erh tea fermentation using derivatization liquid chromatography-mass spectrometry approach. *J Agric Food Chem.* (2019) 67:4568–77. doi: 10.1021/acs.jafc.9b00789
49. Guo X, Ho CT, Schwab W, Wen Z, Zhu H, Liu Q, et al. Qualitative and quantitative changes of non-volatile compounds and taste profiles in Wuyi rock tea during the manufacturing processes. *J Food Bioact.* (2021) 14:14270. doi: 10.31665/JFB.2021.14270
50. Wang QP, Gong JS, Chisti Y, Sirisansaneeyakul S. Production of theabrownins using a crude fungal enzyme concentrate. *J Biotechnol.* (2016) 231:250–9.
51. Sansone C, Rita Massardo D, Pontieri P, Maddaluno L, De Stefano M, Maurizio Tredici S, et al. Isolation of a psychrotolerant Debaryomyces hansenii strain

fromfermented tea plant (*Camellia sinensis*) leaves. *J Plant Interact.* (2007) 2:169–74. doi: 10.1080/17429140701585169
52. Susanto H, Kharisma VD, Listyorini D, Taufiq A, Sunaryono, Aulanni'am A. Effectivity of black tea polyphenol in adipogenesis related IGF-1 and its receptor pathway through in silico based study. *J Phys.* (2018) 1093:012037. doi: 10.1088/1742-6596/1093/1/012037
53. Wang QP, Gong JS, Chisti Y, Sirisansaneeyakul S. Fungal isolates from a pu-erh type tea fermentation and their ability to convert tea polyphenols to theabrownins. *J Food Sci.* (2015) 80:M809–17. doi: 10.1111/1750-3841.12831
54. Wang YW, Zhang MY, Zhang ZZ, Lu HQ, Gao XL, Yue PX. High-theabrownins instant dark tea product by *Aspergillus niger* via submerged fermentation: α-glucosidase and pancreatic lipase inhibition and antioxidant activity. *J Sci Food Agric.* (2017) 97:5100–6. doi: 10.1002/jsfa.8387
55. Huang FJ, Zheng XJ, Ma XH, Jiang RQ, Zhou WY, Zhou SP, et al. Theabrownin from Pu-erh tea attenuates hypercholesterolemia via modulation of gut microbiota and bile acid metabolism. *Nat Commun.* (2019) 10:4971–87. doi: 10.1038/s41467-019-12896-x
56. Yue SJ, Zhao D, Peng CX, Tan C, Wang QP, Gong JS. Effects of theabrownin on serum metabolites and gut microbiome in rats with a high-sugar diet. *Food Funct.* (2019) 10:7063–80. doi: 10.1039/c9fo01334b
57. Dai WD, Qi DD, Yang T, Lv HP, Guo L, Zhang Y, et al. Non-targeted analysis using ultraperformance liquid chromatography-quadrupole time-of-flight mass spectrometry uncovers the effects of harvest season on the metabolites and taste quality of tea (*Camellia sinensis* L.). *J Agric Food Chem.* (2015) 63:9869–78. doi: 10.1021/acs.jafc.5b03967
58. Shannon E, Jaiswal AK, Abu-Ghannam N. Polyphenolic content and antioxidant capacity of white, green, black, and herbal teas: a kinetic study. *Food Res.* (2018) 2:1–11. doi: 10.26656/fr.2017.2(1).117
59. Rice-evans CA, Miller NJ, Bolwell PG, Bramley PM, Pridham JB. The relative antioxidant activities of plant-derived polyphenolic flavonoids. *Free Radic Res.* (1995) 22:375–83. doi: 10.3109/10715769509145649
60. Anissi J, Hassouni ME, Ouardaoui A, Sendide K. A comparative study of the antioxidant scavenging activity of green tea, black tea and coffee extracts: a kinetic approach. *Food Chem.* (2014) 150:438–47. doi: 10.1016/j.foodchem.2013.11.009
61. Seyoum A, Asres K, El-Fiky FK. Structure-radical scavenging activity relationships of flavonoids. *Phytochem.* (2006) 67:2058–70. doi: 10.1016/j.phytochem.2006.07.002
62. Dufresne CJ, Farnworth ER. A review of latest research findings on the health promotion properties of tea. *J Nutr Biochem.* (2001) 12:404–21. doi: 10.1016/S0955-2863(01)00155-3
63. Zhou BX, Ma BS, Ma CQ, Xu CC, Wang JC, Wang ZY, et al. Classification of Pu-erh ripened teas and their differences in chemical constituents and antioxidant capacity. *LWT Food Sci Technol.* (2022) 153:112370. doi: 10.1016/j.lwt.2021.112370
64. Zhang L, Ho CT, Zhou J, Santos JS, Armstrong L, Granato D. Chemistry and biological activities of processed *Camellia sinensis* teas: a comprehensive review. *Compr Rev Food Sci Food Saf.* (2019) 18:1474–95. doi: 10.1111/1541-4337.12479
65. Obanda M, Owuor PO, Mang'oka R, Kavoi M. Changes in thearubigen fractions and theaflavins levels due to variations in processing conditions and their effects on black tea liquor brightness and total colour. *Food Chem.* (2004) 85:163–73. doi: 10.1016/S0308-8146(02)00183-8
66. Zhou BX, Ma CQ, Ren XY, Xia T, Zheng CQ, Liu XH. Correlation analysis between filamentous fungi and chemical compositions in a type pu-erh tea after a long-term storage. *Food Sci Nutr.* (2020) 8:2501–11. doi: 10.1002/fsn3.1543
67. Yao YN, Wu MY, Huang YJ, Li CK, Pan X, Zhu W, et al. Appropriately raising fermentation temperature beneficial to the increase of antioxidant activity and gallic acid content in *Eurotium cristatum*-fermented loose tea. *LWT Food Sci Technol.* (2017) 82:248–54. doi: 10.1016/j.lwt.2017.04.032
68. Yu P, Yeo ASL, Low MY, Zhou WB. Identifying key non-volatile compounds in ready-to-drink green tea and their impact on taste profile. *Food Chem.* (2014) 155:9–16. doi: 10.1016/j.foodchem.2014.01.046
69. Yi T, Zhu L, Peng WL, He XC, Chen HL, Li J, et al. Comparison of ten major constituents in seven types of processed tea using HPLC-DAD-MS followed by principal component and hierarchical cluster analysis. *LWT Food Sci Technol.* (2015) 62:194–201. doi: 10.1016/j.lwt.2015.01.003

Conflict of Interest: The authors declare that the research was conducted in the absence of any commercial or financial relationships that could be construed as a potential conflict of interest.

Publisher's Note: All claims expressed in this article are solely those of the authors and do not necessarily represent those of their affiliated organizations, or those of the publisher, the editors and the reviewers. Any product that may be evaluated in this article, or claim that may be made by its manufacturer, is not guaranteed or endorsed by the publisher.

Copyright © 2022 Chen, Chen, Chen, Xiao, Wu, Hu, Li, Wang, Zhu, Liu and Xiao. This is an open-access article distributed under the terms of the Creative Commons Attribution License (CC BY). The use, distribution or reproduction in other forums is permitted, provided the original author(s) and the copyright owner(s) are credited and that the original publication in this journal is cited, in accordance with accepted academic practice. No use, distribution or reproduction is permitted which does not comply with these terms.

frontiers | Frontiers in Nutrition

BRIEF RESEARCH REPORT
published: 17 May 2022
doi: 10.3389/fnut.2022.850076

Regulatory Effect of Sea-Buckthorn Procyanidins on Oxidative Injury HUVECs

*Ximeng Lin[1], Michael Yuen[2], Tina Yuen[2], Hywel Yuen[2], Min Wang[1] and Qiang Peng[1]**

[1] College of Food Science and Engineering, Northwest A&F University, Yangling, China, [2] Puredia Limited, Xining, China

As society develops and aging populations increase, the incidence of arteriosclerosis, a seriously harmful cardiovascular disease (CVD) which mostly results from endothelial cellular oxidative damage, has continuously risen. Procyanidins from sea-buckthorn is a powerful antioxidant, although its protective effect on the cardiovascular system is not yet clearly understand. In this study, oxidative damaged HUVECs induced by palmitate acid (PA) were used as a model and the regulatory effect of procyanidins from sea-buckthorn (SBP) on HUVECs were investigated. The results showed SBP can be used for 12 h by HUVECs and had no detective cytotoxicity to them under 400 μg/L. Also, different concentrations of SBP can increase mitochondrial membrane potential and NO level and decrease LDH leakage in a dose-effect relationship, indicating SBP can improve oxidative damage. In addition, western blots and qPCR results showed SBP regulation on oxidative injured HUVECs is probably through p38MAPK/NF-κB signal pathway. This study revealed the molecular mechanism of procyanidins in decreasing endothelial oxidative damage, providing a theoretical foundation for further research on natural bioactive compounds to exert antioxidant activity in the body and prevent and improve cardiovascular diseases.

Keywords: ***Hippophae*** **rhamnoides, proanthocyanidins, antioxidant, cardiovascular disease, HUVECs**

OPEN ACCESS

Edited by:
Shuai Chen,
Wuhan University, China

Reviewed by:
Wei Jie Xie,
Shanghai Jiao Tong University, China
Yu Li,
Anhui Agricultural University, China
Weiqing Lan,
Shanghai Ocean University, China

Correspondence:
Qiang Peng
pengqiang@nwsuaf.edu.cn

Specialty section:
This article was submitted to Food Chemistry, a section of the journal Frontiers in Nutrition

Received: *07 January 2022*
Accepted: *05 April 2022*
Published: *17 May 2022*

Citation:
Lin X, Yuen M, Yuen T, Yuen H, Wang M and Peng Q (2022) Regulatory Effect of Sea-Buckthorn Procyanidins on Oxidative Injury HUVECs. Front. Nutr. 9:850076. doi: 10.3389/fnut.2022.850076

INTRODUCTION

Sea-buckthorns are precious deciduous shrubs, belonging to *Hippophae* genus in *Elaeagnaceae*. Procyanidins, as important bioactive compounds among vitamins, carotenoids, and flavonoids (1, 2), are multimeric compounds formed by the condensation of flavanols and widely exist in many plants with lower contents (3). From previous studies on procyanidins extracted from other plants, researchers found procyanidins are functionally bioactive polymers and they have antioxidant, anticancer, cardiovascular, and cerebrovascular disease prevention effects and anti-inflammatory and immunomodulatory activities (4, 5). However, studies on procyanidins from sea-buckthorns have rarely been reported.

Vascular endothelial cells (VECs) are a monolayer of cells that continuously cover the surface of the entire vascular cavity, which constitutes the starting barrier of blood vessels, and has the function of regulating blood flow, participating in substance exchange, preventing lipid leakage, inhibiting platelet aggregation, and preventing thrombosis (6–8). As society develops, CVD has gradually become the main disease that endangers health and causes atherosclerosis. Due to the pathogenesis complexity of AS, it has attracted more research attention. The trigger of AS is structural destruction and dysfunction of vascular endothelial cells (9). Although there are many

factors leading to vascular endothelial cells' injury, oxidative damage of vascular endothelial cells is considered an important causative factor and has obtained more attention. Recent studies have proved procyanidins can prevent and improve oxidative injury of vascular endothelial cells, especially oligomeric procyanidins (10, 11). Also, medical and toxicology-related experiments have shown natural procyanidins have non-carcinogenic, non-toxic, and non-teratogenic advantage compared with synthetic compounds. However, whether procyanidins can prevent oxidative injury of VECs and how their protection works in resisting oxidative damage is still unclear.

In this study, oxidative damaged HUVECs cells induced by PA were used as a model. The prevention effect of procyanidins in sea-buckthorn (SBP) on oxidative damaged HUVECs were investigated through cell viability, SBP absorption, Mitochondrial membrane potential ($\Delta\psi m$) determination, LDH leakage, and NO level detection. Moreover, western blot and qPCR were used to study the relative mRNA and proteins of SBP improved HUVECs oxidative injury.

METHODS

Materials and Chemicals

Cyanthox, Procyanidins from sea-buckthorn (SBP), was provided by Puredia Limited Co. (Qinghai, China). SBP yield was 9.1% compared with sea-buckthorn powder. The purity of SBP was 91.5% compared with standard procyanidins (95%). LC-MS/MS revealed SBP mainly contained four compounds: (-)-epicatechin gallate ($C_{22}H_{18}O_{10}$), procyanidin B ($C_{30}H_{26}O_{12}$), (+)-gallocatechin-(+)-catechin ($C_{30}H_{26}O_{13}$), and (+)-gallocatechin dimer ($C_{30}H_{26}O_{14}$).The antibodies of LOX-1, ICAM-1, p-NF-κB, and p-p38 were purchased from Cell Signaling Technology (Shanghai, China). PA was provided by Sinopharm Chemical Reagent Co. (China). All other chemicals and solvents used in this study were of analytical grade.

Cell Culture

HUVECs cells were purchased from ATCC. The cells were cultured in H-DMEM medium (Gibco Co., China) with 10% FBS (BioInd Co., Israel),100 U/mL penicillin (Erye Pharma Co., China), and 100 μg/mL streptomycin (NanJing SunShine Biotechnology Co., China) at a 37°C and in a 5% CO_2 incubator. Between 3 and 10 passages of HUVECs were used in this study.

Cell Viability Assay

HUVECs (5×10^4 cells/mL) were cultured in a 96-well plate for 24 h and treated with different concentrations of SBP (25, 50, 100, 200, 400, 600, and 800 μg/L) for 12 h. Afterwards, the cells were added to 10 μL CCK-8 (EnoGene Co., China) and kept for 1 h. The cell viability was determined by a multifunctional enzyme marker at a wavelength of 450 nm and expressed as relative percentage of blank control.

Abbreviations: SBP, procyanidins from sea-buckthorn; SB203580 (SB), a p38 enzyme inhibitor; CVD, cardiovascular disease; HUVECs, Human umbilical vein endothelial cells; NO, nitric oxide.

SBP Absorption Detection in HUVECs

HUVECs (5×10^4 cells/mL) were cultured in a 96-well plate for 24 h and then treated with 100 μg/L SBP for 1, 2, 4, 8, and 12 h. The mediums were collected and centrifuged (3000 rpm/min) for 10 min. Sulfuric acid-vanillin colorimetry was used for SBP absorption detection. The results were calculated by a formula adjusted by different concentrations of standard catechins. SBP dissolved in DMSO as blank control.

SBP Effect on HUVECs Cell Morphology

HUVECs were incubated in 6-well plate for 24 h and then treated with 25 and 100 μg/L SBP for 30 min. Afterwards, the cells were treated with 100 μmol/L PA for 24 h. The cells morphology was observed by inverted fluorescence microscope.

ROS Level Measurement

1.0×10^5/mL HUVECs were cultured in 12-well plate for 24 h. Then the cells were co-cultured with 25, 50, and 100 μg/L SBP for 12 h. Subsequently, the cells were co-incubated with 100 μmol/L PA for 12 h. Measurement of ROS level in each group was followed by ROS kit (Beijing Solarbio Science & Technology Co., China).

Mitochondrial Membrane Potential ($\Delta\psi m$) Determination

$\Delta\psi m$ was measured by JC-1 mitochondrial membrane potential detection kit (Beyotime Biotechnology Co., China). The cultured cells were continuously incubated in H-DMEM for 3 h. Afterwards, the cells were treated with 25, 50, and 100 μg/L SBP for 30 min and then incubated with 100 μmol/L PA for 6 h. $\Delta\psi m$ was measured at 590 nm after the cells were incubated with 1 mL JC^{-1} for 20 min.

LDH Leakage Detection

HUVECs were cultured with H-DMEM for 3 h. The cells were pre-treated with 25, 50, and 100 μg/L SBP for 30 min and then treated with 100 μmol/L PA for 12 h. LDH cytotoxicity test kit (Nanjing Jiancheng Bioengineering Institute, China) was used for LDH leakage analysis.

Assay for NO Detection

HUVECs were divided into six groups: blank, model, 25 μg/LSBP, 100 μg/LSBP, SB, SB, and SBP. NO detection kit (Beyotime Biotechnology Co., China) was used for NO content analysis after being cultured for 12 h.

Western Blot and qPCR Analysis

HUVECs were divided into the same six groups: blank, model, SBP (25 and 100 μg/L), SB, SB, and SBP. After being cultured for 12 h, the cells were collected for western blot and PCR analysis. The relative proteins (LOX-1, ICAM-1, p-NF-κB, and p-p38) and the relative mRNAs (LOX-1, ICAM, NF-κB, eNOS, and iNOS) were analyzed.

Statistical Analysis

All data were triplicate determinations expressed as means ± SD and analyzed with variance (ANOVA) followed by Duncan's multiple-range test. SPSS version 26.0 was used for statistical analysis and the definition of statistical significance was $p < 0.05$.

RESULTS

Cell Viability Analysis

The cell viability of different concentrations of SBP treatment was shown in **Figure 1A**. Compared with blank control, HUVECs viability did not significantly change after SBP treatment under 400 μg/L. However, when SBP treatment was above 600 μg/L, the cell viability changed extremely ($p < 0.01$). Thus, SBP concentration under 400 μg/L was selected for the following experiments.

SBP Absorption of HUVECs Analysis

SBP absorption of HUVECs at different time points was displayed in **Figure 1B**. With extended time, SBP concentration in the medium decreased. After 100 μg/L SBP incubated with HUVECs for 1 h, SBP concentration had significantly decreased. Also, after co-incubation for 12 h, SBP concentration, decreasing to 26.3 μg/L, was 70% of the original concentration. The concentration of SBP dissolved in DMSO also lacked a significant difference after 12 h. This indicated SBP can gradually be absorbed and metabolized by HUVECs and did not degrade when incubated with HUVECs. Therefore, the longest time of SBP and HUVECs co-incubation is 12 h in the following experiments.

Analysis of SBP Effect on HUVECs Cellular Morphology

Normally, HUVECs cells will adherently grow, and their morphology is of a flat cobblestone shape. After PA treatment, cellular morphology became round and their adherent growth ability was weaker. However, when pretreated with different concentrations of SBP (25 and 100 μg/L), their morphology gradually recovered. In addition, many cobblestone shape cells can be observed in the image of 100 μg/L SBP treatment group (**Figure 1C**).

ROS Level Analysis

From **Figure 1D**, compared to blank control group, 100 μmol/L PA significantly increased ROS level in HUVECs cells, which determined PA stimulation can induce cellular oxidative stress. However, different concentrations of SBP treatment significantly decreased ROS level ($p < 0.01$) and the reduction effect increased with SBP concentration increase. This meant SBP can effectively prevent HUVECs oxidative damage induced by high level lipid.

Δψm Determination

HUVECs oxidative damage will cause cellular mitochondria dysfunction, resulting in Δψm decrease. In **Figure 1E**, when HUVECs were stimulated by 100 μmol/L PA for 12 h, its Δψm significantly decreased to 0.73 compared with blank control ($p < 0.01$). Oppositely, SBP co-incubation can significantly recover HUVECs Δψm (0.90), meaning SBP can significantly prohibit Δψm decrease of HUVECs induced by PA and improve oxidative damage situation.

LDH Leakage Analysis

LDH is a glycolytic enzyme, widely existing in the cell matrix. Once LDH leakage occurs, it means cell membranes in cells or tissues have been attacked by ROS, resulting in oxidative damage. In **Figure 1F**, compared with blank control (88.7 U/L), PA can extremely increase LDH level to 641.5 U/L in medium ($p < 0.01$), indicating PA-induced oxidative damage caused LDH leakage in cell matrix. However, different concentrations of SBP can reduce LDH viability in medium and have a positive dose-effect relationship. Especially, 100 μg/L SBP extremely slowed down LDH leakage of cell matrix (216.3 U/L), indicating SBP can significantly decrease HUVECs oxidative damage induced by PA, which corresponded with the results above.

NO Content Analysis

NO, one of the most important products of HUVECs, plays a necessary role in maintaining vasodilation capacity. However, one cause of vascular disease is insufficient NO production resulting from endothelial oxidative damage. From **Figure 1G**, PA stimulation significantly decreased NO level (12.0 μmol/mL) while SBP pre-treatment can significantly improve NO level in HUVECs, especially the 100 μg/L SBP treatment (21.5 μmol/mL). This indicated that SBP can efficiently recover insufficient NO production in HUVECs induced by PA stimulation, resulting in improved endothelial oxidative damage and dysfunction. Compared with PA group, SB had a similar effect as SBP. However, incubation with SB and SBP did not have a superimposed effect on NO production. This meant the SBP effect on NO production is probably through p38MAPK/NF-κB signal pathway regulation.

Relative Proteins Expression Analysis

Western blots results (**Figure 2**) showed that PA could significantly increase LOX-1 expression while SBP and SB could slightly decrease its expression. ICAM-1 expression increased induced by PA, but higher concentration of SBP can obviously prohibit its expression, while SB had no significant effect on its expression. For p-NF-κB and p-p38 expression, PA treatment can significantly induce phosphorylation of NF-κB and p38, while higher concentrations of SBP can significantly inhibit activation of p38MAPK/NF-κB signal pathway. These results determined SBP can reduce HUVECs oxidative damage induced by PA probably through the regulation of p38MAPK/NF-κB signal pathway.

Relative mRNA Expression Analysis

Compared with blank control (**Figure 3**), PA stimulation significantly increased mRNAs expression of LOX-1, ICAM-1, NF-κB, and iNOS (average 3–4 times of blank control), while eNOS mRNA expression significantly decreased (about 53% of blank control). However, SBP treatment obviously inhibits this up or down regulation and has a positive does-effect relationship.

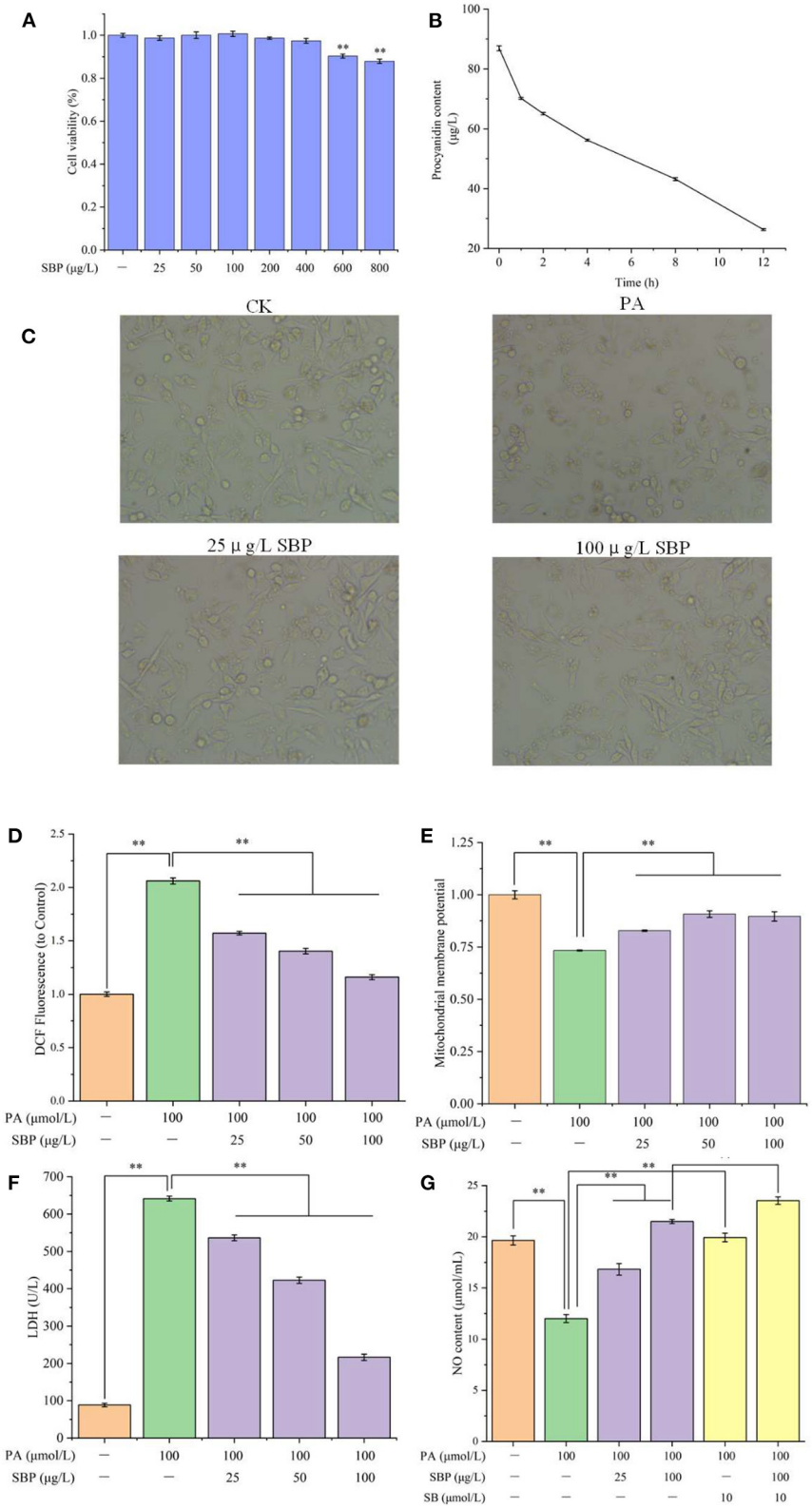

FIGURE 1 | Cell viability of HUVECs with different concentrations of SBP **(A)**, SBP absorption in HUVECs **(B)**, HUVECs cellular morphology under different treatments **(C)**, Mitochondrial membrane potential of different treatments **(D)**, LDH leakage of different treatments **(E)**, NO content of different treatments **(F)**, ROS content of different treatments **(G)**. The results were expressed as the mean ± SD ($n = 5$). $^{**}p < 0.01$.

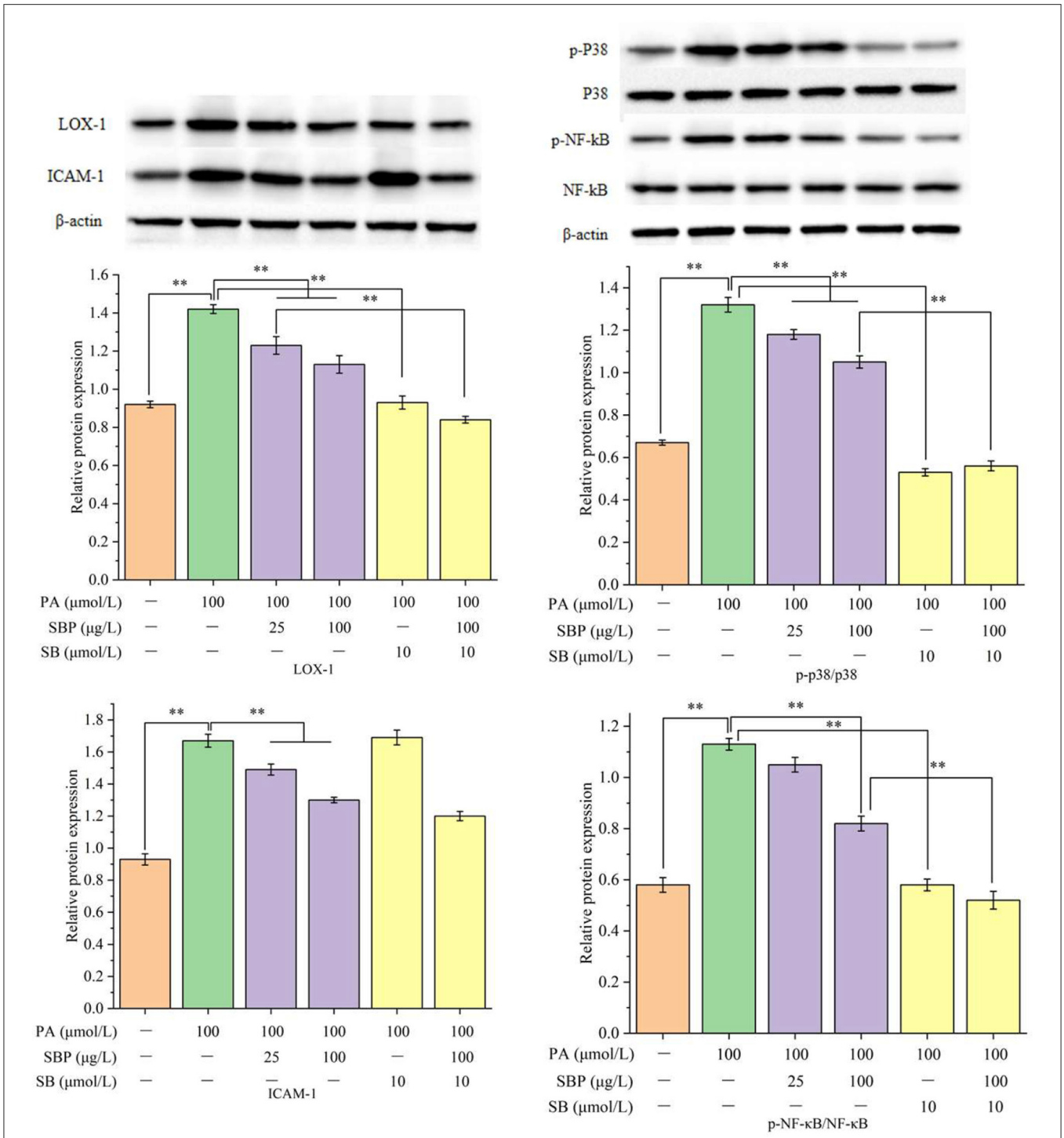

FIGURE 2 | Relative proteins expression (LOX-1, ICAM-1, p-p38/p38, and pNF-κB/NF-κB) under different treatments of SBP and SB. The results were expressed as the mean ± SD ($n = 3$). $^{**}p < 0.01$.

Moreover, SB treatment significantly inhibited all tested mRNAs expression which indicated SBP regulation of these mRNAs expression probably has a relationship with p38MAPK/NF-κB signal pathway. This is consistent with western blot analysis.

DISCUSSION

Endothelial cells' dysfunction is one of the main factors of many chronic diseases, especially CVD and related complications (12).

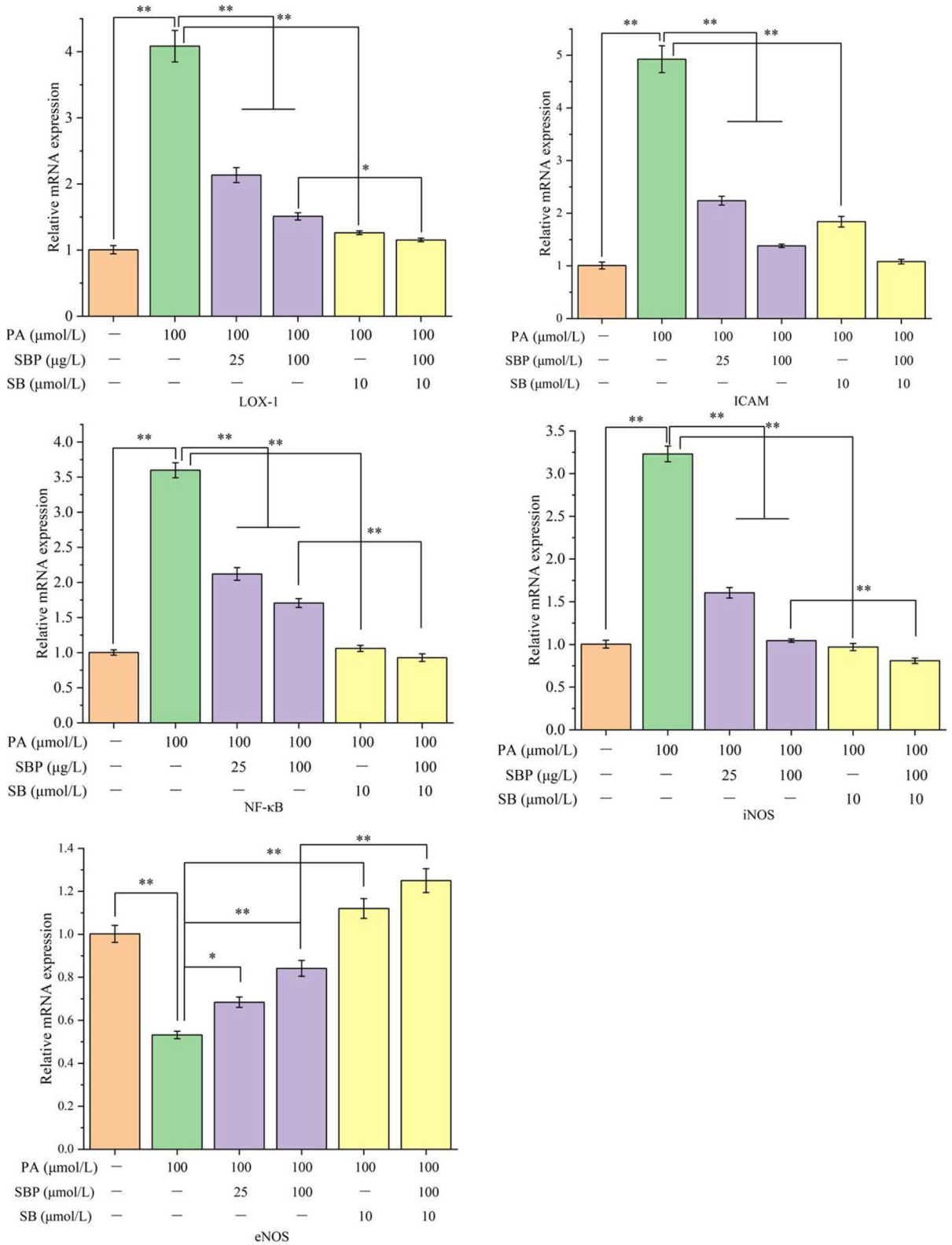

FIGURE 3 | Relative mRNA expression (LOX-1, ICAM, NF-κB, iNOS, and eNOS) under different treatments of SBP and SB. The results were expressed as the mean ± SD ($n = 3$). *$p < 0.05$ and **$p < 0.01$.

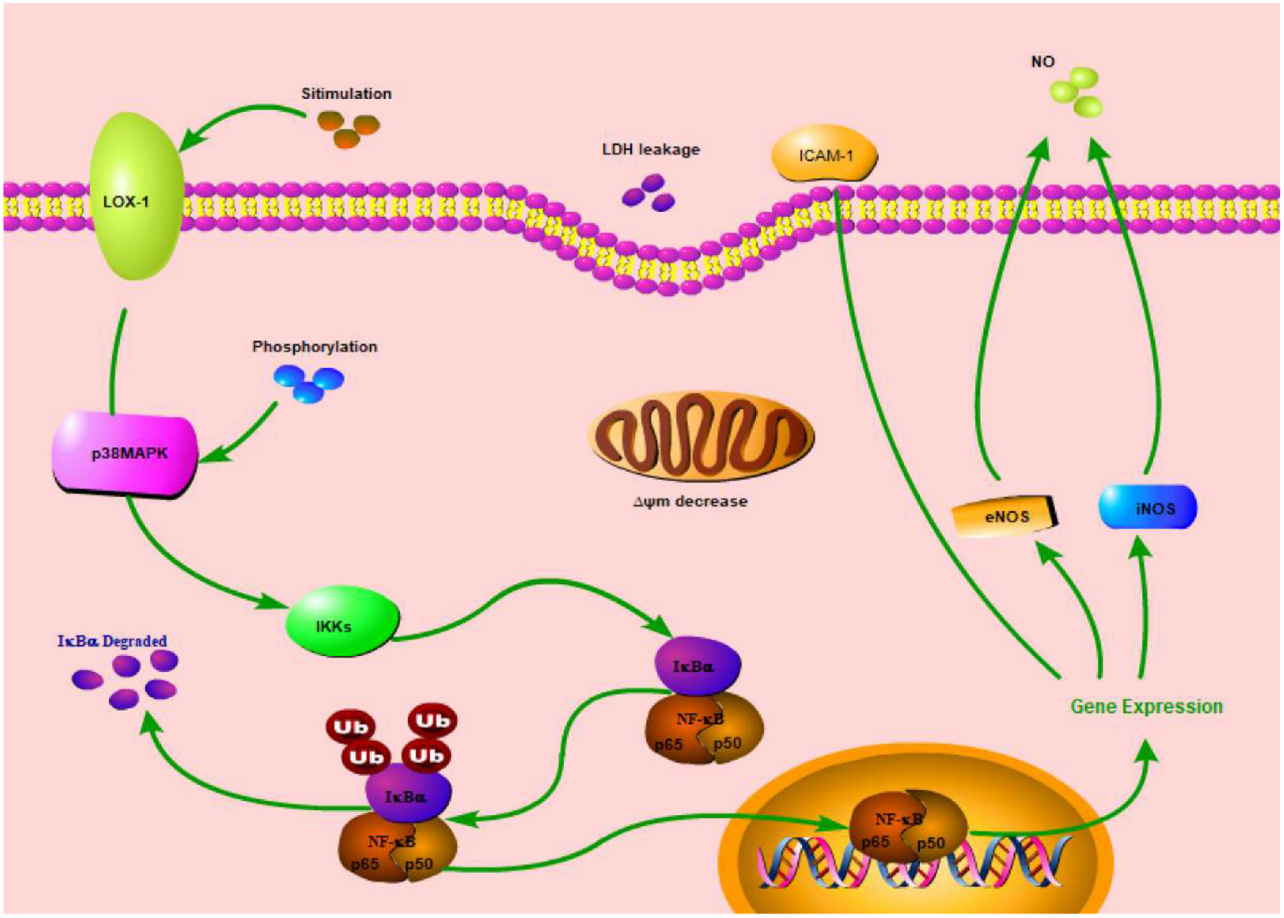

FIGURE 4 | Simplified p38MAPK/NF-κB signal pathway diagram.

Clinical studies have shown that oxidative stress induced by high sugar or high fat leads to endothelial cells' oxidative damage, which is significantly positively correlated with endothelial cells' dysfunction and CVD (13). Therefore, efficient improvement of oxidative injury of endothelial cells can prevent and reduce the possibility of CVD. Many studies *in vitro* and *in vivo* have proved polyphenolic compounds can effectively scavenge excessive free radicals and reduce chronic diseases caused by oxidative injury, such as diabetes, cancer, and CVD (11, 14). As a polyphenolic compound, procyanidins are equipped with powerful free radical scavenging ability, which has a positive relationship with its concentration (10).

From the results above, SBP can reduce LDH leakage caused by cell membrane damage, resulting in preventing oxidative injury. Δψm is the main bioenergy parameter to measure the electron transport capacity of mitochondria, directly controlling the ATP synthesis, respiration rate, and reactive oxygen species production of cells (15). High lipid induced oxidative stress of HUVECs leads to mitochondria damage, mainly manifested as the Δψm decrease. Pretreatment with SBP can obviously recover Δψm, protect mitochondria, and improve oxidative injury. Hence, in PA induced oxidative damaged endothelial cell model, SBP revealed a great ability for improving oxidative damage. However, how SBP exerts its oxidative ability still needs to be investigated.

In this study, we also investigated SBP effect on p38MAPK/NF-κB signal pathway. The results revealed SBP effect on related indexes (LOX-1, ICAM-1, NF-κB, eNOS, and iNOS) expression was associated with p38MAPK/NF-κB signal pathway (**Figure 4**), but ICAM-1 protein expression had no relation with this pathway.

MAPK family is a signal for intracellular and extracellular signaling which can affect a series of biological functions during cellular growth and development. In mammalian cells, extracellular-signal regulated kinase (ERK), c-Jun N-terminal kinase (JNK), and p38MAP kinases are three MAPK family members which have been clearly characterized (16). Lipid induction can activate signal pathways in cells, such as protein kinase pathway, tyrosine protein kinase pathway, and MAPK pathways, resulting in vascular endothelial cell dysfunction or apoptosis (17). p38MAPK is a main MAPK signal pathway, closely associated with cellular inflammation and oxidative stress

in HUVECs cells. In an oxidative stress situation, MKK3/6 respectively activates p38α/β and then makes p38 phosphorylate (18, 19). Afterwards, MAPK cascade reaction activates NF-κB. NF-κB is a main regulatory factor of inflammation which can regulate many genes' expression related to AS (20). In this study, SBP significantly inhibited phosphorylation of p38MAPK and NF-κB, indicating SBP probably prevents oxidative damage induced by PA through inhibition of p38MAPK/NF-κB signal pathway activation.

Endothelial cell apoptosis has been determined as a main characteristic of AS occurrence (21–23). LOX-1 expression can up-regulate the expression of pro-apoptotic factor (Bax) and down-regulate the expression of anti-apoptotic factor (Bcl-2), leading to endothelial cells' apoptosis (17). Research has proven NF-κB activation has to be regulated by LOX-1 system (24). This study showed mRNA and protein expression of LOX-1 in model group were both higher than blank control group, while its expression decreased after treatment with p38 prohibitor, indicating a protective effect of SBP on HUVECs is probably through the prevention of p38MAPK/NF-κB signal pathway activity.

NO content in endothelial cells is one important index to evaluate function of the cells (25). Oxidative stress can cause endothelial cells' dysfunction, resulting in a decrease of NO level and then insufficient diastolic capacity of blood vessels. NO is catalytically produced by nitric oxide synthase (NOS) and exerts significant function in the AS process. NOS contains neuronal NOS (nNOS), endothelial NOS (eNOS), and inducible NOS (iNOS). Normally, NO is catalytically produced by eNOS and can prevent CVD. When cells are in oxidative stress or inflammation, NO is catalytically produced by iNOS. Some studies found iNOS expression and NO content of serum in AS mice were higher than those in blank group, while some research found some anti-inflammatory medicine can down-regulate iNOS expression and decrease NO content, thus inhibiting inflammation (26). Hence, these results indicate NO has two sides for AS processing. NO produced by eNOS can protect cells while NO produced by iNOS can promote AS formation. In the model group of this study, eNOS expression decreased while iNOS expression increased and NO content decreased at the same time compared to blank group, indicating PA has a stronger effect on NO produced by eNOS than that by iNOS. Also, after treatment with SB, NO content and iNOS expression significantly decreased compared with model group. This meant the process of NO production also has a connection with p38MAPK/NF-κB signal pathway.

ICAM-1 expression has a close relationship with p38MAPK signal pathway (27). In this study, SB can significantly decrease ICAM mRNA expression, but has no significant influence on ICAM protein expression, indicating SBP regulation of ICAM is only associated with p38MAPK/NF-κB signal pathway at the transcriptional level while its regulation of ICAM after transcription is probably through other ways. Moreover, SB treatment decreased protein and mRNA expression of NF-κB. SB inhibition is similar to SBP inhibition, which indicated SBP regulation of NF-κB expression is also through p38MAPK/NF-κB signal pathway.

SBP regulation on oxidative damaged HUVECs induced by PA is probably achieved by inhibiting p38MAPK/NF-κB signal pathway activity, but this still needs further determination.

DATA AVAILABILITY STATEMENT

The original contributions presented in the study are included in the article/supplementary materials, further inquiries can be directed to the corresponding author/s.

AUTHOR CONTRIBUTIONS

XL: conceptualization. MY: methodology. TY: software. HY, MW, and QP: validation. QP: funding acquisition. All authors have read and agreed to the published version of the manuscript.

FUNDING

This research was financially supported by the Science and Technology Project of Xining (No. 2021-Y-15), Beijing Engineering and Technology Research Center of Food Additives, Beijing Technology & Business University (BTBU), and Yulin City Science and Technology Plan Project (No. CXY-2020-074).

REFERENCES

1. Mihalcea L, Turturica M, Barbu V, Ionita E, Patrascu L, Cotarlet M, et al. Transglutaminase mediated microencapsulation of sea buckthorn supercritical CO2 extract in whey protein isolate and valorization in highly value added food products. *Food Chem.* (2018) 262:30–8. doi: 10.1016/j.foodchem.2018.04.067
2. Xiao PT, Liu SY, Kuang YJ, Jiang ZM, Lin Y, Xie ZS, et al. Network pharmacology analysis and experimental validation to explore the mechanism of sea buckthorn flavonoids on hyperlipidemia. *J Ethnopharmacol.* (2021) 264:113380. doi: 10.1016/j.jep.2020.113380
3. Ashwin K, Pattanaik AK, Howarth GS. Polyphenolic bioactives as an emerging group of nutraceuticals for promotion of gut health: a review. *Food Biosci.* (2021) 44:101376. doi: 10.1016/j.fbio.2021.101376
4. Elejalde E, Villaran MC, Alonso RM. Grape polyphenols supplementation for exercise-induced oxidative stress. *J Int Soc Sports Nutr.* (2021) 18:3. doi: 10.1186/s12970-020-00395-0
5. Cory H, Passarelli S, Szeto J, Tamez M, Mattei J. The role of polyphenols in human health and food systems: a mini-review. *Front Nutr.* (2018) 5:87. doi: 10.3389/fnut.2018.00087
6. Lum H, Malik AB. Mechanisms of increased endothelial permeability. *Can J Physiol Pharmacol.* (1996) 74:787–800. doi: 10.1139/y96-081
7. Wu WZ, Hu DJ, Wang ZY, Liao LS, Li CC. Endothelial progenitor cell impairment mediated vasodilation dysfunction via diminishing nitric oxide production in postmenopausal females. *Mol Med Rep.* (2019) 19:2449–57. doi: 10.3892/mmr.2019.9888
8. Karki P, Birukov KG. Lipid mediators in the regulation of endothelial barriers. *Tissue Barriers.* (2018) 6:138–48. doi: 10.1080/21688370.2017.1385573
9. Ross R, Glomset JA. The pathogenesis of atherosclerosis (first of two parts). *N Engl J Med.* (1976) 295:369–77. doi: 10.1056/NEJM197608122950707

10. Zhu Y, Yuen M, Li W, Yuen H, Wang M, Smith D, et al. Composition analysis and antioxidant activity evaluation of a high purity oligomeric procyanidin prepared from sea buckthorn by a green method. *Curr Res Food Sci.* (2021) 4:840–51. doi: 10.1016/j.crfs.2021.11.008
11. Li W, Liu J, Guan R, Chen J, Yang D, Zhao Z, et al. Chemical characterization of procyanidins from Spatholobus and their antioxidative and anticancer activities. *J Func Foods.* (2015) 12:468–77. doi: 10.1016/j.jff.2014.11.009
12. Zhou H, You P, Liu H, Fan J, Tong C, Yang A, et al. Artemisinin and Procyanidins loaded multifunctional nanocomplexes alleviate atherosclerosis via simultaneously modulating lipid influx and cholesterol efflux. *J Controlled Release.* (2022) 341:828–43. doi: 10.1016/j.jconrel.2021.12.021
13. Venkata S, Zeeshan F, Ahmad KL, Saif H. Therapeutic potential of dietary phenolic acids. *Adv Pharmacol Sci.* (2015) 2015:823539. doi: 10.1155/2015/823539
14. Zhou HC, Lin YM, Wei SD, Tam NF. Structural diversity and antioxidant activity of condensed tannins fractionated from mangosteen pericarp. *Food Chem.* (2011) 129:1710–20. doi: 10.1016/j.foodchem.2011.06.036
15. Fang C, Zhang B, Han L, Gao C, Wang M. D-Fagomine attenuates high glucose-induced endothelial cell oxidative damage by upregulating the expression of PGC-1α. *J Agric Food Chem.* (2018) 66:2758–64. doi: 10.1021/acs.jafc.7b05942
16. Johnson GL, Lapadat R. Mitogen-activated protein kinase pathways mediated by ERK. JNK, and p38 protein kinases. *Science.* (2002) 298:1911–2. doi: 10.1126/science.1072682
17. Li D, Mehta JL. Upregulation of endothelial receptor for oxidized LDL (LOX-1) by oxidized LDL and implications in apoptosis of human coronary artery endothelial cells evidence from use of antisense LOX-1 mRNA and chemical inhibitors. *Arterioscler Thromb Vasc Biol.* (2000) 20:1116–22. doi: 10.1161/01.ATV.20.4.1116
18. Remy G, Risco AM, Inesta-Vaquera FA, Gonzalez-Teran B, Sabio G, Davis RJ, et al. Differential activation of p38MAPK isoforms by MKK6 and MKK3. *Cell Signal.* (2010) 22:660–7. doi: 10.1016/j.cellsig.2009.11.020
19. Zhong Y, Liu T, Guo Z. Curcumin inhibits ox-LDL-induced MCP-1 expression by suppressing the p38MAPK and NF-κB pathways in rat vascular smooth muscle cells. *Inflamm Res.* (2012) 61:61–7. doi: 10.1007/s00011-011-0389-3
20. Mallavia B, Recio C, Oguiza A, Ortiz-Munoz G, Lazaro I, Lopez-Parra V, et al. Peptide inhibitor of NF-κB translocation ameliorates experimental atherosclerosis. *Am J Pathol.* (2013) 182:1910–21. doi: 10.1016/j.ajpath.2013.01.022
21. Claise C, Edeas M, Chaouchi N, Chalas J, Capel I, Kalimouttou S, et al. Oxidized-LDL induce apoptosis in HUVEC but not in the endothelial cell line EA. Hy 926. *Atherosclerosis.* (1999) 147:95–104. doi: 10.1016/S0021-9150(99)00170-7
22. Huang CS, Lin AH, Liu CT, Tsai CW, Chang IS, Chen HW, et al. Isothiocyanates protect against oxidized LDL-induced endothelial dysfunction by upregulating Nrf2-dependent antioxidant and suppressing NF-κB activation. *Mol Nutr Food Res.* (2013) 57:1918–30. doi: 10.1002/mnfr.201300063
23. Thomas JP, Geiger PG, Girotti A. Lethal damage to endothelial cells by oxidized low density lipoprotein: role of selenoperoxidases in eytoprotection against lipid hydroperoxide and iron-mediated reactions. *J Lipid Res.* (1993) 34:479–90. doi: 10.1016/S0022-2275(20)40739-4
24. Kataoka H, Kume N, Miyamoto S, Minami M, Morimoto M, Hayashida K, et al. Oxidized LDL modulates Bax/Bcl-2 through the lectinlike Ox-LDL recepter-1 in vascular smooth muscle cells. *Arterioscler Thromb Vasc Biol.* (2001) 21:955–60. doi: 10.1161/01.ATV.21.6.955
25. Davignon J, Ganz P. Role of endothelial dysfunction in atherosclerosis. *Circulation.* (2004) 109:27–32. doi: 10.1161/01.CIR.0000131515.03336.f8
26. Xu X, Gao X, Potter BJ, Cao JM, Zhang C. Anti-LOX-1 rescues endothelial function in coronary arterioles in atherosclerotic ApoE knockout mice. *Arterioscler Thromb Vasc Biol.* (2007) 27:871–7. doi: 10.1161/01.ATV.0000259358.31234.37
27. Ma I, Liu X, Zhao Y, Chen B, Li X, Qi R. Ginkgolide B reduces LOX-1 expression by inhibiting Akt phosphorylation and increasing Sirt1 expression in oxidized LDL-stimulated human umbilical vein endothelial cells. *PLoS ONE.* (2013) 8:e74769. doi: 10.1371/journal.pone.0074769

Conflict of Interest: MY, TY, and HY were employed by Puredia Limited.

The remaining authors declare that the research was conducted in the absence of any commercial or financial relationships that could be construed as a potential conflict of interest.

Publisher's Note: All claims expressed in this article are solely those of the authors and do not necessarily represent those of their affiliated organizations, or those of the publisher, the editors and the reviewers. Any product that may be evaluated in this article, or claim that may be made by its manufacturer, is not guaranteed or endorsed by the publisher.

Copyright © 2022 Lin, Yuen, Yuen, Yuen, Wang and Peng. This is an open-access article distributed under the terms of the Creative Commons Attribution License (CC BY). The use, distribution or reproduction in other forums is permitted, provided the original author(s) and the copyright owner(s) are credited and that the original publication in this journal is cited, in accordance with accepted academic practice. No use, distribution or reproduction is permitted which does not comply with these terms.

frontiers | Frontiers in Nutrition

ORIGINAL RESEARCH
published: 18 May 2022
doi: 10.3389/fnut.2022.881464

Gut Microbiota of Individuals Could Be Balanced by a 14-Day Supplementation With *Laminaria japonica* and Differed in Metabolizing Alginate and Galactofucan

Xueqian Zhang[1], Changyu Su[2], Cui Cao[3], Guiping Gong[1,3], Linjuan Huang[1,3], Zhongfu Wang[1,3], Shuang Song[2,4]* and Beiwei Zhu[2,4]*

[1] College of Food Science and Technology, Northwest University, Xi'an, China, [2] National Engineering Research Center of Seafood, School of Food Science and Technology, Dalian Polytechnic University, Dalian, China, [3] Shaanxi Natural Carbohydrate Resource Engineering Research Center, College of Food Science and Technology, Northwest University, Xi'an, China, [4] National & Local Joint Engineering Laboratory for Marine Bioactive Polysaccharide Development and Application, Dalian Polytechnic University, Dalian, China

OPEN ACCESS

Edited by:
Biao Yuan,
China Pharmaceutical University, China

Reviewed by:
Yujiao Sun,
Shaanxi University of Science and Technology, China
Jialin Qu,
Dalian Medical University, China
Gaoxing Ma,
Nanjing University of Finance and Economics, China

***Correspondence:**
Zhongfu Wang
wangzhf@nwu.edu.cn
Shuang Song
songs1008@163.com

Specialty section:
This article was submitted to Food Chemistry, a section of the journal Frontiers in Nutrition

Received: 22 February 2022
Accepted: 21 March 2022
Published: 18 May 2022

Citation:
Zhang X, Su C, Cao C, Gong G, Huang L, Wang Z, Song S and Zhu B (2022) Gut Microbiota of Individuals Could Be Balanced by a 14-Day Supplementation With Laminaria japonica and Differed in Metabolizing Alginate and Galactofucan. Front. Nutr. 9:881464. doi: 10.3389/fnut.2022.881464

Laminaria japonica is rich in alginate (Alg) and galactofucan (GF) which have both been reported to regulate gut microbiota composition. To reveal the effect of *L. japonica* on human gut microbiota, the fecal microbiota of 12 volunteers before and after 14-day *L. japonica* intake was sequenced and compared, and the capabilities of the gut microbiota to utilize Alg and GF were also investigated. The 16S rRNA gene sequencing results demonstrated that *Firmicutes/Bacteroidetes* ratio could be balanced by *L. japonica* supplementation. The ability of gut microbiota to utilize Alg was significantly enhanced by *L. japonica* supplementation. Furthermore, the multiple linear regression analysis suggested that bacteria from *Bacteroidaceae* and *Ruminococcaceae* were positively correlated with Alg utilization while those from *Erysipelotrichaceae*, *Bacteroidaceae,* and *Prevotellaceae* participated in GF degradation. Moreover, the production of acetic acid and the total short-chain fatty acids (SCFAs) in fermentation were consistent with the consumption of Alg or GF, and propionic acid content was positively correlated with Alg consumption. In addition, the percentage of monosaccharides in the consumed GF after the fermentation suggested that gut microbiota from individuals could consume GF with different monosaccharide preferences. These findings shed a light on the impacts of dietary *L. japonica* on human health.

Keywords: ***Laminaria japonica*, polysaccharide, fermentation, alginate, fucoidan, gut microbiota**

INTRODUCTION

Laminaria japonica, one of the most widely consumed commercial edible seaweeds in the world (1, 2), has a high production in China, Japan, and Korea (3–5). It is rich in dietary fiber, such as alginate (Alg) and fucoidan, and their contents generally vary from 30 to 40% and 5 to 10% of the seaweed dry weight, respectively (6). Alg is an acidic polysaccharide composed of 1,4-linked β-D-mannuronate (M) and 1,4-linked α-L-guluronate (G) (7). Fucoidan is a class of

sulfated polysaccharides in brown algae containing fucose and varying greatly in their structural characteristics (8). Galactofucan (GF) found in *Laminaria japonica* is a type of fucoidan, consisting of fucose and galactose residues (9).

Both Alg and fucoidan are indigestible fibers that could modulate the composition and/or activity of microorganisms in the large intestine, thus conferring a beneficial physiological effect on the host (10). For instance, Alg could prevent high-fat diet-induced metabolic syndrome and increase the abundance of *Bacteroides* (11), and relieve hyperglycemia in type 2 diabetic mice by enriching *Bacteroides, Lactobacillus, Akkermansia, Alloprevotella, Weissella,* and *Enterorhabdus*, and decreasing *Turicibacter* and *Helicobacter* in the intestinal tracts of mice (12). Furthermore, fucoidan shows a therapeutic effect on metabolic syndrome and the improvement of gut dysbiosis in association with an increase of *Akkermansia* population in the gut microbes of high-fat diet mice (13). More recently, researchers have suggested that fucoidan could improve insulin resistance in diet-induced obese mice by remodeling gut microbiota (14). It could be concluded that both Alg and fucoidan could modulate gut microbiota in animal models, suggesting the benefits of *L. japonica* consumption on the ecosystem of the intestinal tract. Therefore, it is necessary to evaluate the effect of *L. japonica* in human dietary intervention studies. In addition, more and more pieces of evidence demonstrate that the utilization of dietary fibers by gut microbiota could produce short-chain fatty acids (SCFAs) and other metabolites to benefit the host. However, bacteria responsible for the breakdown and utilization of Alg and fucoidan are largely unknown.

The present study aimed to evaluate the effects of dietary *L. japonica* supplementation on the gut microbiota of normal humans and the capabilities of the gut microbiota to utilize Alg and GF, and reveal bacteria involved in the utilization of Alg and GF. The microbial communities from twelve volunteers before and after the 14-day supplementation with *L. japonica* were compared. Furthermore, the fermentation of Alg and GF from *L. japonica* and SCFAs production by these fecal microbiota communities from different individuals were assessed.

MATERIALS AND METHODS

Materials

Instant shredded kelp was provided by Sichuan Jixiangju Food Co., Ltd. (Sichuan, China). Dried *L. japonica* was obtained from Fujian Yida Food Co., Ltd. (Fujian, China). Alg was purchased from Qingdao Bright Moon Seaweed Group Co., Ltd. Its molecular weight was determined as 1,311 kDa according to the reported method (15). GF was prepared from *L. japonica* according to our previous method and its monosaccharide composition was fucose (Fuc): xylose (Xyl): galactose (Gal): glucose (Glc): galacturonic acid (GalA): manmose (Man) = 9.8: 1.0: 16.4: 1.8: 6.0: 12.7 as reported by us previously (15), and the average molecular weight of GF was determined as 627 kDa. Peptone and yeast extract were purchased from Oxoid (Thermo Co., Ltd, Massachusetts, USA). Monosaccharide standards, such as rhamnose (Rha), Xyl, Gal, GalA, Glc, glucuronic acid (GlcA), Man, arabinose (Ara), and Fuc were purchased from Sigma Chemical Co. (St. Louis, MO, USA). The ingredients of bacterial media were purchased from Qingdao Hope Bio-Technology Co., Ltd. All other chemical reagents with analytical grades used in this study were purchased from Sinopharm Chemical Reagent Co., Ltd. (Shanghai, China).

Subjects and Diet

In this study, 12 subjects were chosen from six male and six female volunteer students (aged 20–22 years old) of the School of Food Science and Technology, Dalian Polytechnic University. The volunteers consumed *L. japonica* 50 g/day for 14 days. The participants had no gastrointestinal disease or antibiotics treatment for at least 3 months. The study was supported by the Ethics Committee of Dalian Polytechnic University and all volunteers provided a well-informed and signed consent before entering the trial. The general characteristics of the 12 individuals during intervention are shown in **Supplementary Table S1**. The body mass index (BMI) of volunteers was 18.5–23.9 which is in the healthy weight range. The volunteers were asked not to take any medication that could affect the gastrointestinal tract during the trial.

High-Throughput Sequencing Analysis

The fecal samples obtained from the 12 normal volunteers before (Be) and after (Af) 14-day dietary intake of *L. japonica* were labeled as Be.1, Be.2, Be.3 to Be.12 and Af.1, Af.2, Af.3 to Af.12, respectively. The PowerFecal^{TM} DNA Isolation Kit (MO BIO, USA) was applied to isolate the genomic DNA from the feces, and the analysis of all the DNA samples was conducted by Novogene Bioinformatics Technology Co., Ltd. (Beijing, China). For each sample, the V3-V4 region of 16S rRNA was chosen for amplification using the forward primer 515F and the reverse primer 806R and sequenced by Ion S5TMXL platform. The analysis was based on sequenced reads and operational taxonomic units (OTUs).

In vitro Fermentation of Alg and GF

Preparation of Growth Medium

The preparation of growth medium was performed according to the method reported previously (16). Briefly, 1 L of the basal nutrient medium was composed of 2 g peptone, 2 g yeast extract, 0.02 g hemin, 0.5 g L -cysteine, 0.5 g bile salts, 0.1 g NaCl, 0.04 g K_2HPO_4, 0.04 g KH_2PO_4, 0.01 g $MgSO_4{\cdot}7H_2O$, 0.01 g $CaCl_2{\cdot}6H_2O$, 2 g $NaHCO_3$, 1 mg resazurin, 2 ml Tween-80, and 10 μl vitamin K. The whole substrates were dissolved in distilled water and autoclaved at 121°C for 15 min.

Preparation of Human Fecal Slurry and *in vitro* Fermentation

A total of 24 fecal samples as mentioned in Section High-Throughput Sequencing Analysis were used *in vitro* fermentation. Then, 1 g of feces from the donor was diluted in a 9-ml modified physiological saline solution containing 9 g/L of NaCl and blended using a magnetic stirrer to yield 10% (w/v) fecal slurry. Then, the fecal slurry was centrifuged at 4°C (500 rpm, 5 min). After that, 1.0 ml of the fecal suspension was added to 9.0 ml of the basal nutrient medium containing 3 g/L of Alg or

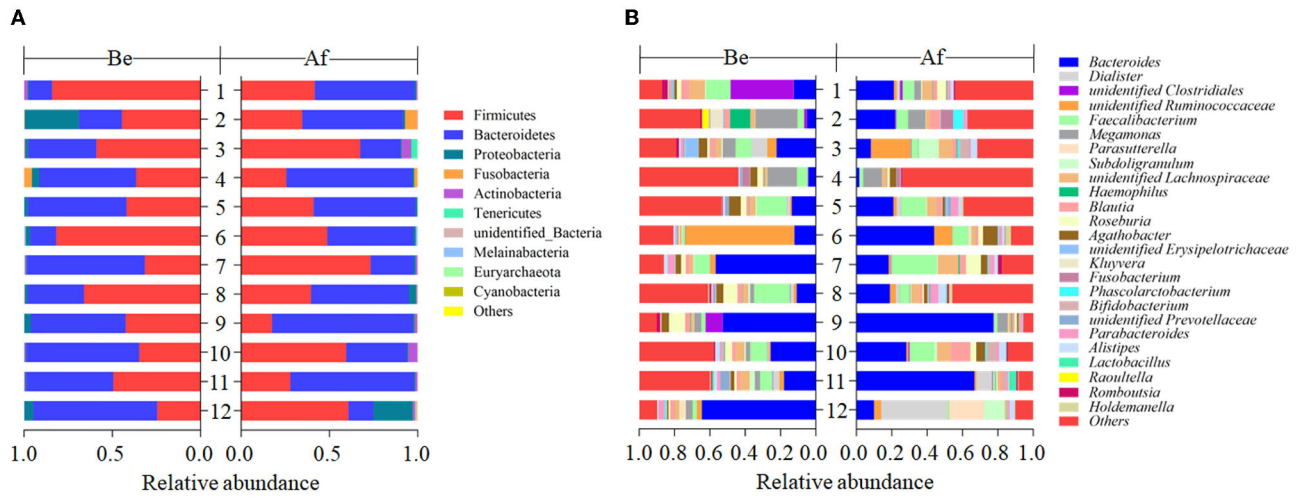

FIGURE 1 | The compositions of fecal gut microbiota before (Be) and after (Af) the 14-day dietary *Laminaria japonica* intake at the phylum level **(A)** and genus level **(B)**.

3 g/L of GF. All samples were incubated at 37°C in an anaerobic incubator (Electrotek, UK), and 1.5 ml fermentation samples were collected at 0 and 48 h and then stored at −80°C for further analysis. Each experiment was independently replicated 3 times.

Measurement of Residual Carbohydrates

The results were expressed as the proportion of residual Alg or GF (%) based on the contents of carbohydrates before and after fermentation. Residual Alg content was measured by using the *meta*-hydroxydiphenyl colorimetric method with Alg as standard (17) and residual GF content was determined using the phenol-sulfuric acid method with Gal as standard (18), respectively.

Determination of Contents of SCFAs

The contents of SCFAs, such as acetic acid, propionic acid, and butyric acid were measured according to the procedure reported with some modifications (19). Briefly, 500 μl of the fermentation broth was transferred into a 2-ml centrifuge tube, and the solution was acidified by adding 10 μl of sulfuric acid (50%, v/v). Subsequently, 900 μl of diethyl ether and 100 μl of 500 μg/ml 2-ethylbutyric acid (internal standard) solution were added to the sample. The solution was then mixed through vortex oscillation 2 times for 3 min. After being centrifuged (12,000 rpm, 15 min), the supernatant was transferred into a tube with 250 mg of Na_2SO_4. The mixed solution was centrifuged at 4°C and the supernatant was loaded by the GC (2010-plus, Shimadzu) equipped with a flame ionization detector (FID), and a Rtx®-Wax column (30 m × 0.25 mm × 0.25 μm) was used. For GC analysis, the initial column temperature was 100°C with a 1-min hold, then programmed to 180°C at a temperature ramp of 5°C/min and maintained for 4 min; the injector temperature was 250°C; the flow rates of hydrogen, air, and nitrogen make up gas were 40, 300, and 3 ml/min, respectively.

Analysis of Monosaccharide Composition

The monosaccharide composition analysis of GF after 48 h fermentation was performed as the previous method with a little modification (20). In brief, after dialyzed and dried, the sample was dissolved in 2 ml of 2 M trifluoroacetic acid (TFA) at 121°C for 2 h. Then, excess TFA was removed with deionized water by reduced pressure distillation. The residue was re-dissolved in 500 μl of Na_2CO_3 (0.5 mol/L) solution and maintained at 30°C for 45 min. After the reduction using sodium borohydride, acetic acid was added to the solution. Sodium in the obtained solution was removed by passing through a cation exchange column. Excess borohydride was decomposed by co-distillation with methanol. The resultant solution was heated at 85°C for 2 h to convert the aldose salt to lactone. The reagent of pyridine and n-propylamine (1 ml each) were added to dissolve the residue and then kept at 55°C for 30 min to react. Then, the solution was dried in vacuum. After adding 1 ml pyridine and 1 ml acetic anhydride, the solution was kept at room temperature overnight. The resulting solution was extracted 3 times using dichloromethane. Neutral sugars and uronic acids were subsequently determined by GC using the method reported previously (21).

Statistic Analysis

A multivariate linear regression model was used to investigate the associations between Alg or GF utilization and bacterial OTUs. The relative abundances of bacterial OTUs with an abundance larger than 5% in at least one sample were included in the regression model as confounding factors. Data were analyzed using SPSS version 20.0 software (SPSS Inc., Chicago, IL, USA). All the data were presented as means ± standard derivation (SD). Comparison between two groups/samples was performed using Student's *t*-test. The comparison of multiple samples was conducted by one-way analysis of variance (ANOVA) procedure followed by the Tukey's Honestly Significant Difference (HSD) test. Correlations were analyzed using Pearson's correlation. The values of $p < 0.05$ were regarded as statistically significant. $^{*}p < 0.05$, $^{**}p < 0.01$, and $^{***}p < 0.001$.

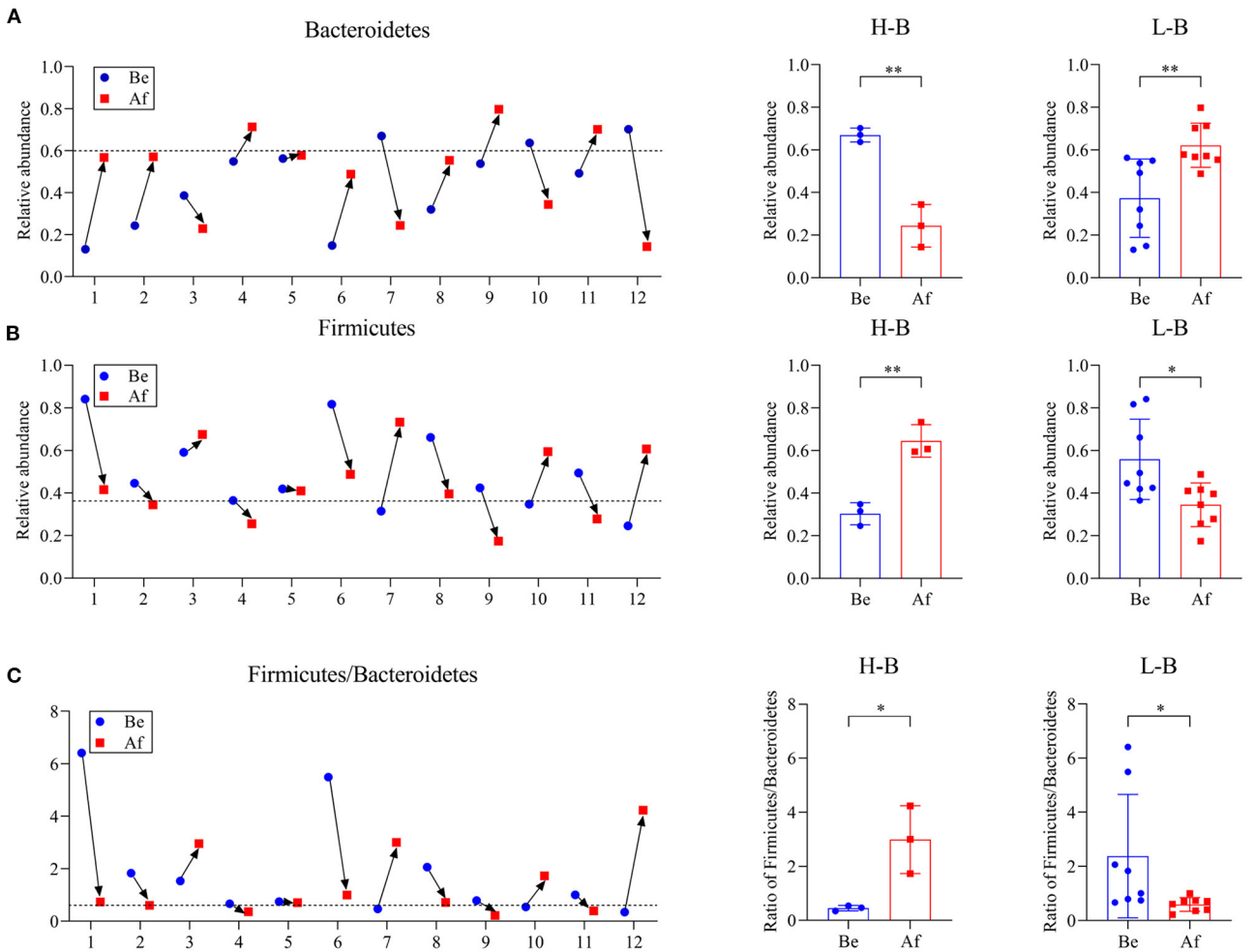

FIGURE 2 | The phylum *Bacteroidetes* abundance **(A)**, phylum *Firmicutes* abundance **(B),** and *Firmicute/Bacteroidetes* ratio **(C)** in individuals Be and Af the 14-day dietary *L. japonica* intake and the comparations of microbiota abundance in the H-B group and the L-B group. H-B group, original *Bacteroidetes* abundance higher than 0.6; L-B group, original Bacteroidetes abundance lower than 0.6. $^{*}p < 0.05$ and $^{**}p < 0.01$.

RESULTS AND DISCUSSION

Effects of *L. Japonica* Supplementation on Normal Human Gut Microbiota Structures

The effects of a 14-day supplementation with *L. japonica* on gut microbiota structures were evaluated by comparing the gut microbes of the volunteers before (Be group) and after (Af group) the dietary intervention. The gut microbiota compositions in most of the individuals varied obviously after supplementation with *L. japonica* both at phylum (**Figure 1A**) and genus (**Figure 1B**) levels. Then, the changes of *Bacteroidetes* and *Firmicutes* were observed at the individual level. The change directions of *Bacteroidetes* (**Figure 2A**) and *Firmicutes* (**Figure 2B**) in these 12 individuals were not consistent. However, interestingly, those with the original *Bacteroidetes* abundance higher than 0.6 (Nos. 7, 10, and 12), grouped as H-B, all down-adjusted the *Bacteroidetes* after the intake of *L. japonica* while those with *Bacteroidetes* lower than 0.6 (Nos. 1, 2, 4, 5, 6, 8, 9, and 11), grouped as L-B, demonstrated an opposite trend, except No. 3. Further significance analysis excluding No. 3 indicated that *L. japonica* intake could significantly reduce *Bacteroidetes* in the H-B group but increase *Bacteroidetes* in the L-B group. Moreover, the original Firmicutes abundance of more than 0.36 showed a reduced population after the intervention of *L. japonica*. Further analysis demonstrated that the modulation of *Firmicutes* in the H-B group and the L-B group was opposite to *Bacteroidetes*. Similar patterns were observed in *Firmicures/Bacteroidetes* (divided based on the line at 0.6) (**Figure 2C**). Previous studies have established the correlation of an increase in the *Firmicutes*-to-*Bacteroidetes* ratio to the higher energy harvesting from diet and the pathology of obesity (22–24). Dietary fiber was effective to downregulate the *Firmicutes*-to-*Bacteroidetes* ratio in obese patients and thus attenuated obesity (25–28). However, in the model of dextran sulfate sodium (DSS)-induced inflammatory mice, supplementation with polysaccharides could

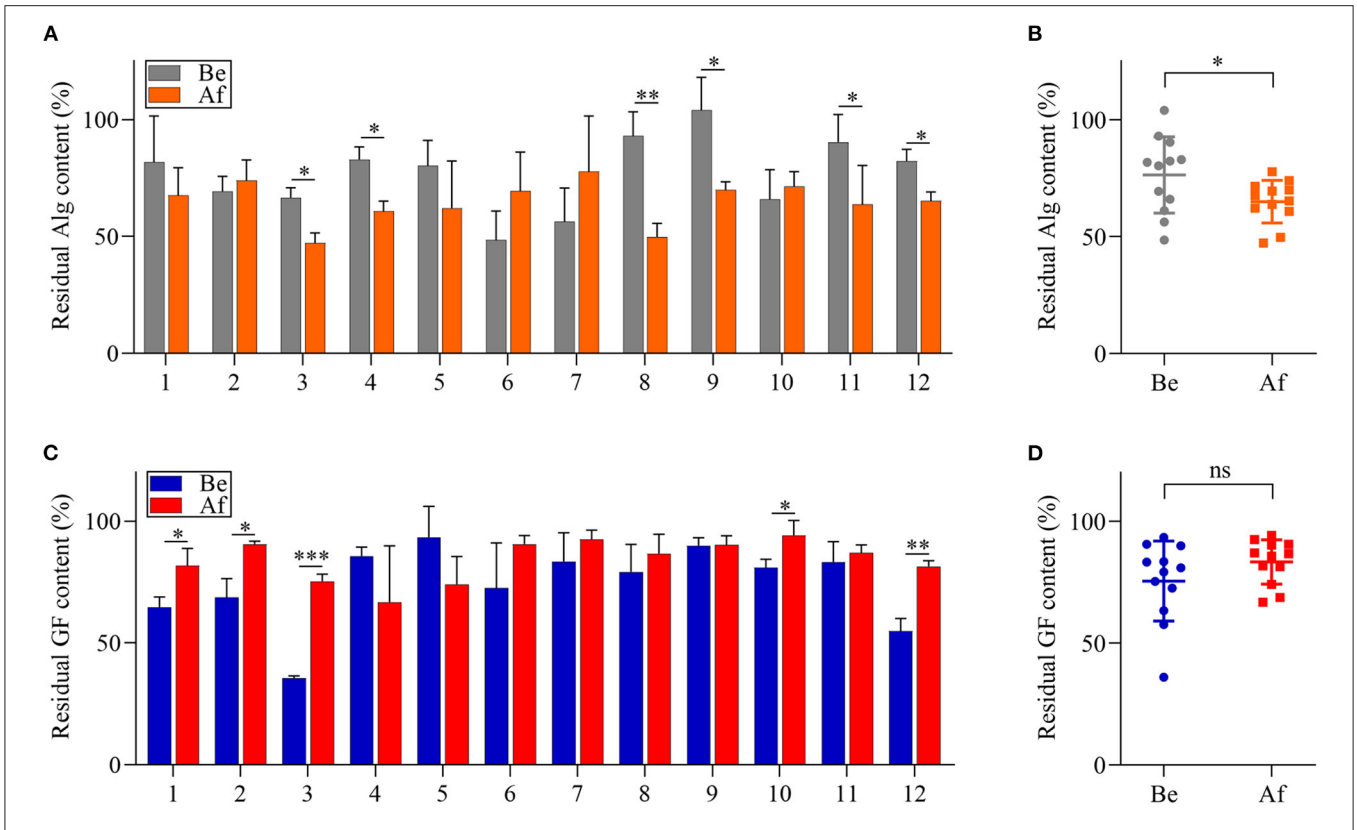

FIGURE 3 | The comparisons of alginate (Alg) and galactofucan (GF) utilization by fecal microbiota collected Be and Af *L. japonica* intake in individuals **(A,C)** and in groups **(B,D)**. $^{*}p < 0.05$, $^{**}p < 0.01$, $^{***}p < 0.001$; ns, no significant difference.

TABLE 1 | A multiple linear regression analysis between bacterial OTUs (%) and alginate (Alg) or galactofucan (GF) consumption (%).

	Variable	B	*p*	Tolerance	Family	Species
Alg	Intercept	0.356	0.000			
(R = 0.908)	OTU_{18}	−4.450	0.000	0.841	Lachnospiraceae	*Roseburia inulinivorans*
	OTU_{200}	3.841	0.000	0.899	Bacteroidaceae	*Bacteroides massiliensis*
	OTU_{75}	−3.222	0.004	0.960	Muribaculaceae	*Unidentified*
	OTU_{28}	1.064	0.013	0.947	Ruminococcaceae	*Ruminococcus bromii*
	OTU_{7}	0.288	0.043	0.958	Ruminococcaceae	*Unidentified*
GF	Intercept	0.177	0.011			
(R = 0.798)	OTU_{66}	7.744	0.001	0.972	Erysipelotrichaceae	*Unidentified*
	OTU_{1060}	5.714	0.010	0.967	Bacteroidaceae	*Bacteroides dorei*
	OTU_{589}	3.774	0.019	0.969	Prevotellaceae	*Unidentified*
	OTU_{18}	−2.565	0.044	0.990	Lachnospiraceae	*Roseburia inulinivorans*

R, correlation coefficient; B, unstandardized coefficients.

upregulate the *Firmicutes*-to-*Bacteroidetes* ratio and alleviate intestinal inflammation (29). In the present study, *L. japonica* supplementation balanced the population of *Firmicutes* to *Bacteriodetes* ratio in individuals, which may be associated with the intake of dietary fiber in *L. japonica*. The different changed directions of the microbiota abundance between the H-B group and the L-B group may be explained by the variation among inter-individuals.

Effects of *L. Japonica* Supplementation on the Capabilities of Fecal Microbiota to Metabolize Alg and GF

The utilization of Alg and GF by the fecal microbiota of 12 volunteers before and after the 14-day *L. japonica* intake was evaluated by determining the remaining sugar contents after 48 h of fermentation. As shown in **Figure 3A**, the residual content of Alg differed greatly among the samples in both the Be group

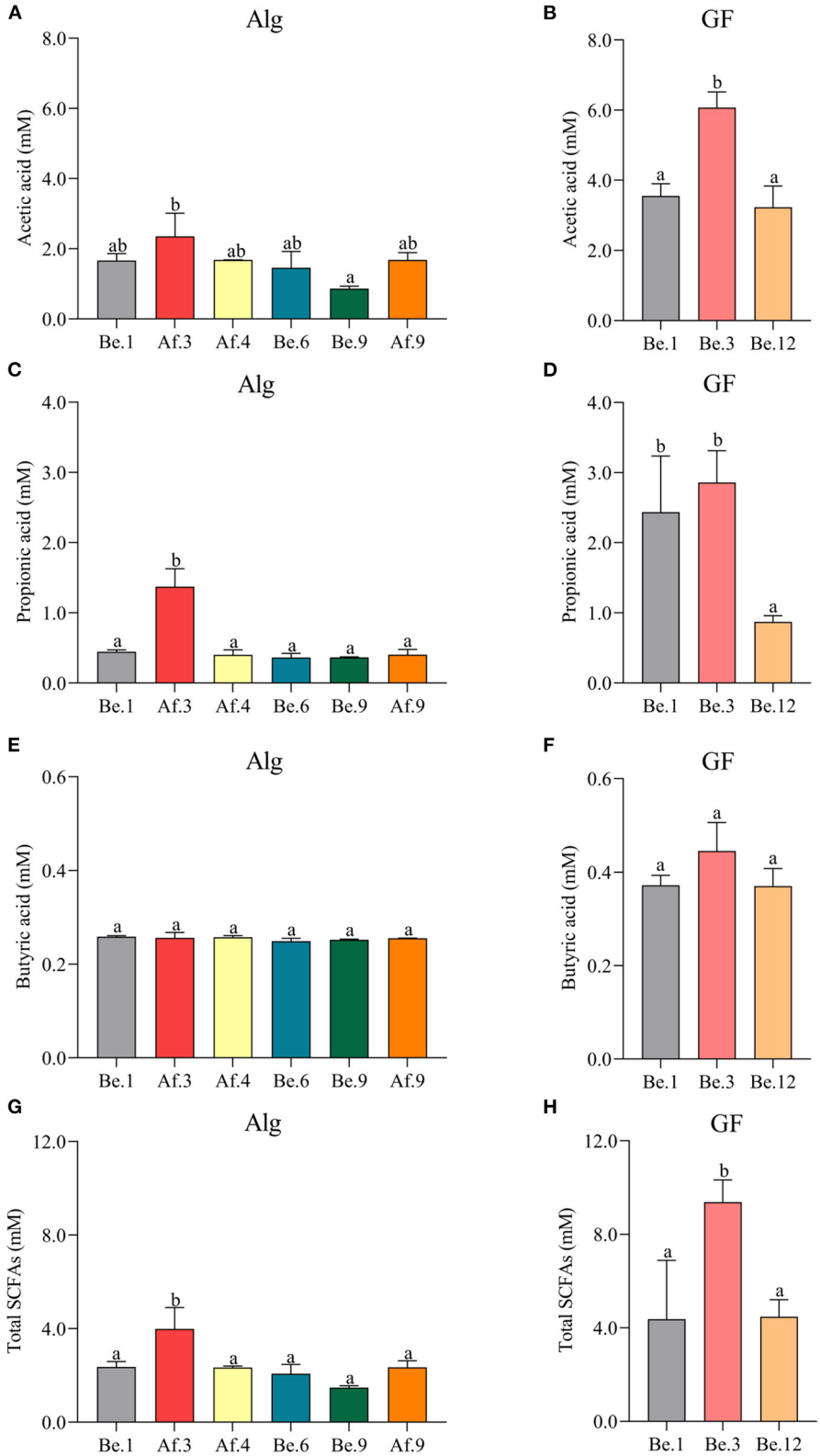

FIGURE 4 | The productions of acetic acid **(A,B)**, propionic acid **(C,D)**, butyric acid **(E,F)**, and total short-chain fatty acids (SCFAs) **(G,H)** after the fermentation of Alg and GF for 48 h. Graph bars marked with different letters on top represent statistically significant results ($p < 0.05$) based on one-way analysis of variance (ANOVA) followed by the Tukey's Honestly Significant Difference (HSD) test, whereas bars labeled with the same letter correspond to results that show no statistically significant differences.

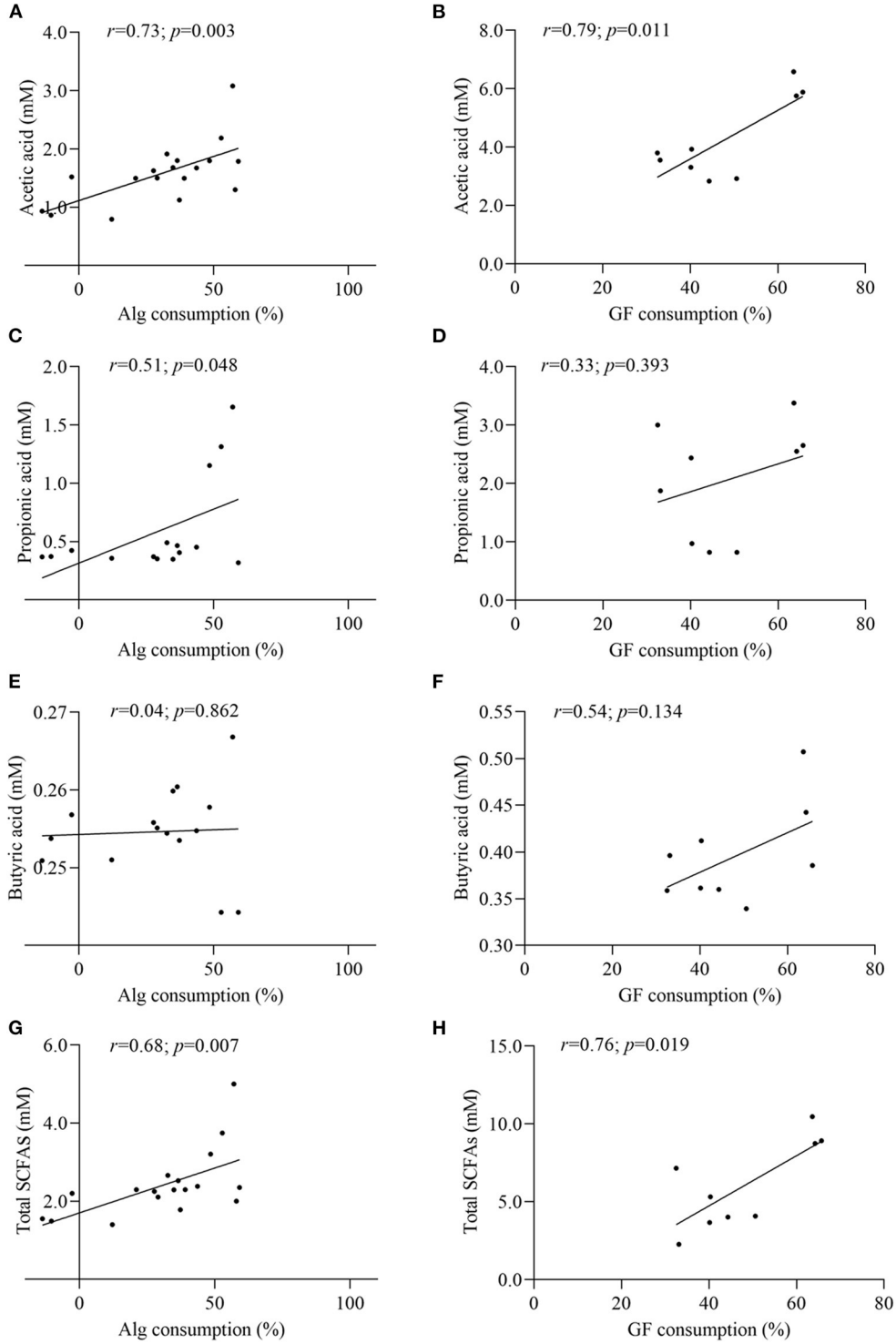

FIGURE 5 | Correlation analysis between Alg and GF consumption with the contents of acetic acid **(A,B)**, propionic acid **(C,D)**, butyric acid **(E,F)**, and total SCFAs **(G,H)**.

and the Af group. However, for one-half of the participants, the Alg content after fermentation in the Af group was significantly lower than that in the Be group. Moreover, **Figure 3B** showed that there was a significant difference between the Be group and the Af group in residual Alg content, indicating that *L. japonica* intake could enhance the capability of fecal microbiota

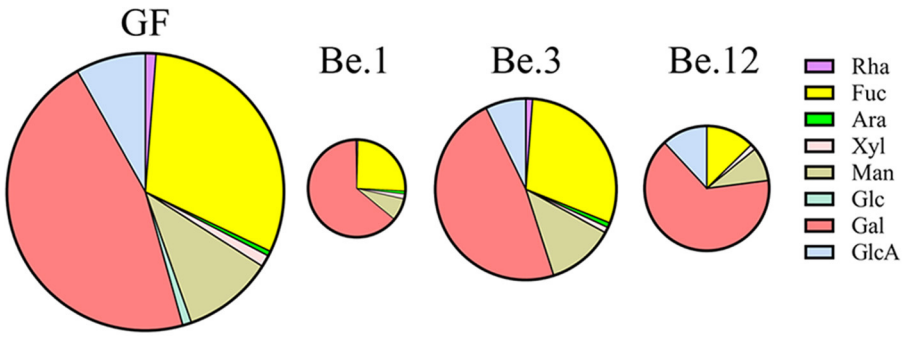

FIGURE 6 | The percentage of monosaccharides in the consumed GF after fermentation by different fecal samples. Be.1, Be.3, and Be.12 were fecal samples obtained from the volunteer Nos. 1, 3, and 12 before the 14-day dietary intake of *L. japonica*, respectively.

to metabolize Alg. Unlike Alg consumption, the GF content after fermentation in the Af group did not show more utilization by fecal microbiota than that in the Be group (**Figure 3C**) and no significant change in the GF utilization between the Be group and the Af group was observed (**Figure 3D**). It has been well documented that some dietary fibers could regulate the gut microbiota community when these microbiota consuming fibers. As the major component of *L. japonica*, Alg (30–40% of dry weight) (30) was supposed to show a far more important effect on gut microbiota than GF. Moreover, the degradation rates of Alg and GF by gut microbiota differed because of their different chemical structures, and obviously, Alg was favored more by gut microbiota than GF. Of note, *L. japonica* intake enhanced the Alg fermentation ability of fecal bacteria in Nos. 3, 4, 8, 9, 11, and 12. Of the individuals with the greatest consumption of Alg, Nos. 4, 8, 9, and 11 showed increased *Bacteroidetes* but No. 3 and 12 showed a reduction in *Bacteroidetes* (**Figure 2A**). Altogether, these results implied the discrepancy of Alg or GF utilization efficacy among individuals after *L. japonica* intake. This finding was consistent with the previous report that the fecal microbiota from different individuals differed in their ability to utilize polysaccharides (31). Previous studies have demonstrated that chondroitin sulfate could be readily metabolized to varying extents by diverse microbial consortiums (32). Recent studies revealed that the regulation results of gut microbiota by resistant starch varied greatly due to inter-individual differences in gut microbiota populations (33). These studies suggest that the beneficial outcomes of polysaccharides are influenced by the inter-individual variation of microbiome structure.

Gut Microbiota Involved in the Fermentation of Alg and GF

The multiple linear regression analysis is a regression model with more than one independent variable which is applied to determine the correlations among variables having cause-effect relationships and to make predictions for the topic by using the relationships (31, 34, 35). To identify the determinants of bacterial OTUs to Alg or GF utilization, the association of fecal bacterial OTUs with the consumption of the Alg or GF was analyzed by multiple linear regression analysis. The results are shown in **Table 1**, and the multiple linear regression equation was obtained as follows: the consumption of Alg = $0.356–4.450OTU_{18} + 3.841OTU_{200}$-$3.222OTU_{75} + 1.064OTU_{28} + 0.288OTU_{7}$, with a correlation coefficient of 0.908, and the consumption of GF = $0.177 + 7.744OTU_{66} + 5.714OTU_{1060} + 3.774OTU_{589}$-$2.565OTU_{18}$, with a correlation coefficient of 0.798. Totally, 5 OTUs and 4 OTUs were the significant variables attributed to Alg and GF utilization, respectively. The multiple linear regression analysis showed that the consumption of Alg was positively related ($B > 0$) with *Bacteroide smassiliensis* (OTU_{200}), *Ruminococcus bromii* (OTU_{28}), and a genus of *Ruminococcaceae* (OTU_{7}), and negatively related ($B < 0$) with OTU_{18} (*Roseburia inulinivorans*) and a genus of *Muribaculaceae* (OTU_{75}). The consumption of GF had a positive correlation with a genus of *Erysipelotrichaceae* (OTU_{66}), *Bacteroides dorei* (OTU_{1060}), and a genus of *Prevotellaceae* (OTU_{589}), and a negative correlation with *R. inulinivorans* (OTU_{18}). *Bacteroides massiliensis* and a genus of *Erysipelotrichaceae* (OTU_{66}) were the most powerful bacteria to metabolize Alg and GF, respectively. In addition, a multi-collinearity analysis demonstrated no interaction among these variables (tolerance > 0.1). *Bacteroidaceae* and *Prevotellaceae*, which are reported as the major gut microbiota families participating in the degradation of numerous polysaccharides (36–38), also play important roles in the utilization of Alg and GF. Moreover, it has been reported that most of the Alg-active bacteria are from *Bacteroides* (39), and *Bacteroides* could also be enriched by fucoidan (13), suggesting their possible participation in GF degradation in the gut. In addition, the members of the *Ruminococcaceae* family could also take part in the Alg utilization, as indicated by its potential power to degrade indigestible polysaccharides (40, 41). *Erysipelotrichaceae*, which is involved in the fermentation of plant polysaccharides (42), also demonstrated its attribution in GF consumption. Nevertheless, although *Roseburia* and *Muribaculaceae* are associated with carbohydrate metabolism (43, 44), they had an unexpected negative association with the consumption of Alg and/or GF. Notably, the bacteria members contributing to the degradation of Alg and GF were discrepant, indicating that different carbohydrate-active enzymes (CAZymes) were involved in the metabolism of the

2 polysaccharides. The inhomogeneity of the regulation on these microbiotas by *L. japonica* supplementation suggested the bacteria members participating in the polysaccharide degradation varied in individuals.

SCFAs Production in the Fermentation of Alg and GF

In the light of the fact that gut microbiota variation will lead to the distinct metabolic functions for Alg and GF, SCFAs, the most important microbial metabolites of dietary polysaccharides, produced by human microbiota from different individuals were compared and the correlation analysis between SCFAs and the Alg or GF consumption was further conducted. Fecal samples with the highest (Af.3) or lowest (Be.9) Alg utilization capabilities and those with more (Af.4 and Af.9) or less (Be.1 and Be.6) *Bacteroidetes* were chosen for the assay of SCFAs production. As shown in **Figures 4A,B**, among these samples, Af.3 and Be.3 produced the most acetic acid in the fermentation of Alg and GF, respectively, and of note, they were the most potent to degrade Alg and GF (as shown in Section Effects of *L. Japonica* Supplementation on the Capabilities of Fecal Microbiota to Metabolize Alg and GF), respectively. Moreover, Af.3 and Be.3 showed a comparatively high production of propionic acid in Alg and GF fermentation, respectively (**Figures 4C,D**). However, no significant differences among individuals were observed in the butyric acid concentration for both Alg and GF fermentation (**Figures 4E,F**). In addition, Af.3 and Be.3, which afforded the most acetic acid, produced the highest amounts of the total SCFAs in the fermentation of Alg and GF, respectively (**Figures 4G,H**). Subsequently, the correlation analysis showed that the production of the acetic acid and the total SCFAs were positively correlated with the consumption of both Alg and GF (**Figure 5**), and the production of propionic acid was positively associated with the utilization of Alg. It is well known that acetic acid and propionic acid are both beneficial for host health (45). For instance, acetic acid can serve as an energy source for gut microbiota (46) and peripheral tissues (47). Propionic acid can be converted into glucose by intestinal gluconeogenesis, leading to satiety and decreased hepatic glucose production (48). The differences in the productions of SCFAs among the fecal samples were related to the abilities of the gut microbiota to degrade Alg or GF, and SCFAs production was greatly correlated with Alg or GF utilization. Considering the important roles of SCFAs in host health, individuals with more powerful gut microbiota to utilize Alg and GF could benefit more from *L. japonica* consumption. Thus, for a great number of normal humans, a 14-day supplementation with *L. japonica* could strengthen the capability of gut microbiota to metabolize Alg in *L. japonica*, so to enhance their benefits from *L. japonica* consumption.

Preferences of Gut Microbiota on the Monosaccharide of GF

It has been well documented that the polysaccharides are metabolized by some CAZymes which are specialized to catalyze certain types of glycosic linkage (49). Due to the substrate specificity of these enzymes in the microbiota, the percentage of monosaccharides in the consumed GF after fermentation could reflect the utilization preferences of gut microbiota. Be.1, Be.3, and Be.12 with higher GF consumption (35.25, 64.54, and 45.09%, respectively) were chosen for monosaccharide composition analysis. As shown in **Figure 6**, GF was mainly composed of Fuc and Gal with the percentages of 30.83 and 46.18%, respectively. After 48 h of fermentation, the percentage of Gal consumption in Be.1 and Be.12 accounted for 65.79 and 70.23%, larger than that in the original GF. Of note, Be.3, with the most amount of GF consumption, demonstrates a relative ratio of Fuc and Gal similar to that of original GF. The above results demonstrated that Gal residues in GF were more ready to be utilized by intestinal microbiota in Be.1 and Be.12 so as to benefit the growth of beneficial bacteria in the gut. It has been reported that monosaccharides linked to a side chain were more susceptible to being broken down into monomers or dimmers compared with those linked to the backbone (50). It could be hypothesized that Gal residues in GF were possibly linked to the side chains of GF or the glycosidic linkages to Gal were easy to be broken down, resulting in the higher consumption rate of Gal. Whereas, gut microbes of Be.3 may degrade GF by consuming Gal and Fuc residues in GF. The above results indicated that GF could be fermented by specific intestinal microbiota and utilized with a different strategy.

CONCLUSION

The present study demonstrated that a 14-day *L. japonica* supplementation could balance *Firmicutes*/*Bacteroidetes* ratio. The Alg utilization capability was significantly enhanced by *L. japonica* supplementation for half of the volunteers. Gut bacteria from *Bacteroidaceae* and *Ruminococcaceae* were positively correlated with Alg utilization while those from *Erysipelotrichaceae*, *Bacteroidaceae*, and *Prevotellaceae* contributed to the degradation of GF. Of note, the production of acetic acid and the total SCFAs in fermentation were consistent with the consumption of Alg and GF, and the production of propionic acid was positively correlated with the utilization of Alg. Thus, *L. japonica* supplementation could strengthen the Alg utilization so to enhance SCFAs production. In addition, gut microbiota communities showed different monosaccharide preferences in GF consumption. The present study promoted the understanding of the impacts of dietary *L. japonica* on human health.

DATA AVAILABILITY STATEMENT

The datasets presented in this study can be found in online repositories. The names of the repository/repositories and accession number(s) can be found below: NCBI; PRJNA835688

ETHICS STATEMENT

The studies involving human participants were reviewed and approved by Ethics Committee of Dalian Polytechnic University. The patients/participants provided their written informed consent to participate in this study.

AUTHOR CONTRIBUTIONS

XZ: investigation, data curation, and writing-original draft. CS: formal analysis. CC: data curation. GG: methodology. LH: writing-review and editing. ZW: project administration and supervision. SS: conceptualization, writing- original draft, supervision, project administration, and funding acquisition. BZ: project administration. All authors contributed to the article and approved the submitted version.

FUNDING

This work was funded by the National Key Research and Development Program of China (No. 2019YFD0902005).

SUPPLEMENTARY MATERIAL

The Supplementary Material for this article can be found online at: https://www.frontiersin.org/articles/10.3389/fnut.2022.881464/full#supplementary-material

REFERENCES

1. Gao J, Lin L, Sun B, Zhao M. Comparison study on polysaccharide fractions from *Laminaria japonica*: structural characterization and bile acid binding capacity. *J Agric Food Chem.* (2017) 65:9790–8. doi: 10.1021/acs.jafc.7b04033
2. Peng Z, Liu M, Fang Z, Wu J, Zhang Q. Composition and cytotoxicity of a novel polysaccharide from brown alga (*Laminaria japonica*). *Carbohydr Polym.* (2012) 89:1022–6. doi: 10.1016/j.carbpol.2012.03.043
3. Wang J, Zhang Q, Zhang Z, Song H, Li P. Potential antioxidant and anticoagulant capacity of low molecular weight fucoidan fractions extracted from *Laminaria japonica*. *Int J Biol Macromol.* (2010) 46:6–12. doi: 10.1016/j.ijbiomac.2009.10.015
4. Gao J, Lin L, Sun B, Zhao M, A. comparison study on polysaccharides extracted from *Laminaria japonica* using different methods: structural characterization and bile acid-binding capacity. *Food Funct.* (2017) 8:3043–52. doi: 10.1039/C7FO00218A
5. Xing R, Liu S, Yu H, Chen X, Qin Y, Li K, et al. Extraction and separation of fucoidan from *Laminaria japonica* with chitosan as extractant. *Biomed Res Int*. (2013) 2013:193689. doi: 10.1155/2013/193689
6. Gotteland M, Riveros K, Gasaly N, Carcamo C, Magne F, Liabeuf G, et al. The pros and cons of using algal polysaccharides as prebiotics. *Front Nutr*. (2020) 7. doi: 10.3389/fnut.2020.00163
7. O'Sullivan L, Murphy B, McLoughlin P, Duggan P, Lawlor PG, Hughes H, et al. Prebiotics from marine macroalgae for human and animal health applications. *Mar Drugs.* (2010) 8:2038–64. doi: 10.3390/md8072038
8. Koh HSA, Lu J, Zhou W. Structure characterization and antioxidant activity of fucoidan isolated from *Undaria pinnatifida* grown in New Zealand. *Carbohydr Polym.* (2019) 212:178–85. doi: 10.1016/j.carbpol.2019.02.040
9. Usoltseva RV, Malyarenko OS, Anastyuk SD, Shevchenko NM, Silchenko AS, Zvyagintseva TN, et al. The structure of fucoidan from *Sargassum oligocystum* and radiosensitizing activity of galactofucans from some algae of genus *Sargassum*. *Int J Biol Macromol.* (2021) 183:1427–35. doi: 10.1016/j.ijbiomac.2021.05.128
10. Bindels LB, Delzenne NM, Cani PD, Walter J. Towards a more comprehensive concept for prebiotics. *Nat Rev Gastro Hepat.* (2015) 12:303–10. doi: 10.1038/nrgastro.2015.47
11. Ejima R, Akiyama M, Sato H, Tomioka S, Yakabe K, Kimizuka T, et al. Seaweed dietary fiber sodium alginate suppresses the migration of colonic inflammatory monocytes and diet-induced metabolic syndrome via the gut microbiota. *Nutrients*. (2021) 13. doi: 10.3390/nu13082812
12. Liu J, Wu S, Cheng Y, Liu Q, Su L, Yang Y, et al. *Sargassum fusiforme* alginate relieves hyperglycemia and modulates intestinal microbiota and metabolites in type 2 diabetic mice. *Nutrients.* (2021) 13:2887. doi: 10.3390/nu13082887
13. Shang Q, Song G, Zhang M, Shi J, Xu C, Hao J, et al. Dietary fucoidan improves metabolic syndrome in association with increased *Akkermansia* population in the gut microbiota of high-fat diet-fed mice. *J Funct Foods.* (2017) 28:138–46. doi: 10.1016/j.jff.2016.11.002
14. Zhang Y, Liu J, Mao G, Zuo J, Li S, Yang Y, et al. *Sargassum fusiforme* fucoidan alleviates diet-induced insulin resistance by inhibiting colon-derived ceramide biosynthesis. *Food Funct.* (2021) 12:8440–53. doi: 10.1039/D1FO01272J
15. Zhang T, Wu S, Ai C, Wen C, Liu Z, Wang L, et al. Galactofucan from *Laminaria japonica* is not degraded by the human digestive system but inhibits pancreatic lipase and modifies the intestinal microbiota. *Int J Biol Macromol.* (2021) 166:611–20. doi: 10.1016/j.ijbiomac.2020.10.219
16. Ding Y, Yan Y, Peng Y, Chen D, Mi J, Lu L, et al. *In vitro* digestion under simulated saliva, gastric and small intestinal conditions and fermentation by human gut microbiota of polysaccharides from the fruits of *Lycium barbarum*. *Int J Biol Macromol.* (2019) 125:751–60. doi: 10.1016/j.ijbiomac.2018.12.081
17. Blumenkrantz N, Asboe-Hansen G. New method for quantitative determination of uronic acids. *Anal Biochem.* (1973) 54:484–9. doi: 10.1016/0003-2697(73)90377-1
18. DuBois M, Gilles KA, Hamilton JK, Rebers PA, Smith F. Colorimetric method for determination of sugars and related substances. *Anal Biochem.* (1956) 28:350–6. doi: 10.1021/ac60111a017
19. Zhu Z, Zhu B, Sun Y, Ai C, Wu S, Wang L, et al. Sulfated polysaccharide from sea cucumber modulates the gut microbiota and its metabolites in normal mice. *Int J Biol Macromol.* (2018) 120:502–12. doi: 10.1016/j.ijbiomac.2018.08.098
20. Chen X, Tang R, Liu T, Dai W, Liu Q, Gong G, et al. Physicochemical properties, antioxidant activity and immunological effects *in vitro* of polysaccharides from *Schisandra sphenanthera* and *Schisandra chinensis*. *Int J Biol Macromol.* (2019) 131:744–51. doi: 10.1016/j.ijbiomac.2019.03.129
21. Gray GR, Ballou CE. Isolation and characterization of a polysaccharide containing 3-O-methyl-D-mannose from *Mycobacterium phlei*. *J Biol Chem.* (1971) 246:6835–42. doi: 10.1016/S0021-9258(19)45922-X
22. Turnbaugh PJ, Ley RE, Mahowald MA, Magrini V, Mardis ER, Gordon JI. An obesity-associated gut microbiome with increased capacity for energy harvest. *Nature.* (2006) 444:1027–31. doi: 10.1038/nature05414
23. Turnbaugh PJ, Hamady M, Yatsunenko T, Cantarel BL, Duncan A, Ley RE, et al. A core gut microbiome in obese and lean twins. *Nature.* (2009) 457:480–4. doi: 10.1038/nature07540
24. Turnbaugh PJ, Ridaura VK, Faith JJ, Rey FE, Knight R, Gordon JI. The effect of diet on the human gut microbiome: a metagenomic analysis in humanized gnotobiotic mice. *Sci Transl Med*. (2009) 1. doi: 10.1126/scitranslmed.3000322
25. Chen J, Liu J, Yan C, Zhang C, Pan W, Zhang W, et al. *Sarcodon aspratus* polysaccharides ameliorated obesity-induced metabolic disorders and modulated gut microbiota dysbiosis in mice fed a high-fat diet. *Food Funct.* (2020) 11:2588–602. doi: 10.1039/C9FO00963A
26. Liu M, Li X, Zhou S, Wang TTY, Zhou S, Yang K, et al. Dietary fiber isolated from sweet potato residues promotes a healthy gut microbiome profile. *Food Funct.* (2020) 11:689–99. doi: 10.1039/C9FO01009B
27. Shi L-l, Li Y, Wang Y, Feng Y. MDG-1, an *Ophiopogon* polysaccharide, regulate gut microbiota in high-fat diet-induced obese C57BL/6 mice. *Int J Biol Macromol.* (2015) 81:576–83. doi: 10.1016/j.ijbiomac.2015.08.057
28. Chen P, Chen X, Hao L, Du P, Li C, Han H, et al. The bioavailability of soybean polysaccharides and their metabolites on gut microbiota in the simulator of the human intestinal microbial ecosystem (SHIME). *Food Chem*. (2021) 36. doi: 10.1016/j.foodchem.2021.130233
29. Gou Y, Sun J, Liu J, Chen H, Kan J, Qian C, et al. Structural characterization of a water-soluble purple sweet potato polysaccharide and its effect on intestinal inflammation in mice. *J Funct Foods*. (2019) 61:103502. doi: 10.1016/j.jff.2019.103502
30. Liu Z, Zhang Y, Ai C, Wen C, Dong X, Sun X, et al. Gut microbiota response to sulfated sea cucumber polysaccharides in a differential

manner using an *in vitro* fermentation model. *Food Res Int*. (2021) 148. doi: 10.1016/j.foodres.2021.110562
31. Uyanik GK, Güler N, A. study on multiple linear regression analysis. *Procedia Soc Behav Sci.* (2013) 106:234–40. doi: 10.1016/j.sbspro.2013.12.027
32. Shang Q, Yin Y, Zhu L, Li G, Yu G, Wang X. Degradation of chondroitin sulfate by the gut microbiota of Chinese individuals. *Int J Biol Macromol.* (2016) 86:112–8. doi: 10.1016/j.ijbiomac.2016.01.055
33. Cherbuy C, Bellet D, Robert V, Mayeur C, Schwiertz A, Langella P. Modulation of the caecal gut microbiota of mice by dietary supplement containing resistant starch: impact is donor-dependent. *Front Microbiol*. (2019) 10:1234. doi: 10.3389/fmicb.2019.01234
34. Han X, Niu Y, Guo X, Hu Y, Yan W, He M. Age-related changes of intraocular pressure in elderly people in southern China: lingtou eye cohort study. *PLoS ONE.* (2016) 11:e0151766. doi: 10.1371/journal.pone.0151766
35. Orlandi M, Escudero-Casao M, Licini G. Nucleophilicity prediction via multivariate linear regression analysis. *J Org Chem.* (2021) 86:3555–64. doi: 10.1021/acs.joc.0c02952
36. Oliphant K, Allen-Vercoe E. Macronutrient metabolism by the human gut microbiome: major fermentation by-products and their impact on host health. *Microbiome*. (2019) 7. doi: 10.1186/s40168-019-0704-8
37. Kinross JM, Darzi AW, Nicholson JK. Gut microbiome-host interactions in health and disease. *Genome Med*. (2011) 3. doi: 10.1186/gm228
38. Cox LM, Cho I, Young SA, Anderson WHK, Waters BJ, Hung S-C, et al. The nonfermentable dietary fiber hydroxypropyl methylcellulose modulates intestinal microbiota. *FASEB J.* (2013) 27:692–702. doi: 10.1096/fj.12-219477
39. Fu T, Pan L, Shang Q, Yu G. Fermentation of alginate and its derivatives by different enterotypes of human gut microbiota: Towards personalized nutrition using enterotype-specific dietary fibers. *Int J Biol Macromol.* (2021) 183:1649–59. doi: 10.1016/j.ijbiomac.2021.05.135
40. Christopherson MR, Dawson JA, Stevenson DM, Cunningham AC, Bramhacharya S, Weimer PJ, et al. Unique aspects of fiber degradation by the ruminal ethanologen *Ruminococcus albus 7* revealed by physiological and transcriptomic analysis. *BMC Genom*. (2014) 15. doi: 10.1186/1471-2164-15-1066
41. Kim H, Lee I, Kwon Y, Kim BC, Ha S, Lee J-h, et al. Immobilization of glucose oxidase into polyaniline nanofiber matrix for biofuel cell applications. *Biosens Bioelectron.* (2011) 26:3908–13. doi: 10.1016/j.bios.2011.03.008
42. Hao YT, Wu SG, Jakovlic I, Zou H, Li WX, Wang GT. Impacts of diet on hindgut microbiota and short-chain fatty acids in grass carp (*Ctenopharyngodon idellus*). *Aquac Res.* (2017) 48:5595–605. doi: 10.1111/are.13381
43. David LA, Maurice CF, Carmody RN, Gootenberg DB, Button JE, Wolfe BE, et al. Diet rapidly and reproducibly alters the human gut microbiome. *Nature.* (2014) 505:559–63. doi: 10.1038/nature12820
44. Lagkouvardos I, Lesker TR, Hitch TCA, Galvez EJC, Smit N, Neuhaus K, et al. Sequence and cultivation study of *Muribaculaceae* reveals novel species, host preference, and functional potential of this yet undescribed family. *Microbiome*. (2019) 7. doi: 10.1186/s40168-019-0637-2
45. Zhou W, Yan Y, Mi J, Zhang H, Lu L, Luo Q, et al. Simulated digestion and fermentation *in vitro* by human gut microbiota of polysaccharides from bee collected pollen of Chinese wolfberry. *J Agric Food Chem.* (2018) 66:898–907. doi: 10.1021/acs.jafc.7b05546
46. Peng X, Li S, Luo J, Wu X, Liu L. Effects of dietary fibers and their mixtures on short chain fatty acids and microbiota in mice guts. *Food Funct.* (2013) 4:932–8. doi: 10.1039/c3fo60052a
47. Wong J, de Souza R, Kendall C, Emam A, Jenkins D, Wong J, et al. Colonic health: fermentation and short chain fatty acids. *J Clin Gastroenterol.* (2006) 40:235–43. doi: 10.1097/00004836-200603000-00015
48. Koh A, De Vadder F, Kovatcheva-Datchary P, Bäckhed F. From dietary fiber to host physiology: short-chain fatty acids as key bacterial metabolites. *Cell.* (2016) 165:1332–45. doi: 10.1016/j.cell.2016.05.041
49. Cockburn DW, Koropatkin NM. Polysaccharide degradation by the intestinal microbiota and its influence on human health and disease. *J Mol Biol.* (2016) 428:3230–52. doi: 10.1016/j.jmb.2016.06.021
50. Min F-F, Hu J-L, Nie S-P, Xie J-H, Xie M-Y. *In vitro* fermentation of the polysaccharides from *Cyclocarya paliurus* leaves by human fecal inoculums. *Carbohydr Polym.* (2014) 112:563–8. doi: 10.1016/j.carbpol.2014.06.027

Conflict of Interest: The authors declare that the research was conducted in the absence of any commercial or financial relationships that could be construed as a potential conflict of interest.

Publisher's Note: All claims expressed in this article are solely those of the authors and do not necessarily represent those of their affiliated organizations, or those of the publisher, the editors and the reviewers. Any product that may be evaluated in this article, or claim that may be made by its manufacturer, is not guaranteed or endorsed by the publisher.

Copyright © 2022 Zhang, Su, Cao, Gong, Huang, Wang, Song and Zhu. This is an open-access article distributed under the terms of the Creative Commons Attribution License (CC BY). The use, distribution or reproduction in other forums is permitted, provided the original author(s) and the copyright owner(s) are credited and that the original publication in this journal is cited, in accordance with accepted academic practice. No use, distribution or reproduction is permitted which does not comply with these terms.

frontiers | Frontiers in Nutrition

ORIGINAL RESEARCH
published: 24 May 2022
doi: 10.3389/fnut.2022.890942

Preparation, Characterization, and Antioxidant Properties of Phycocyanin Complexes Based on Sodium Alginate and Lysozyme

*Bian-Wen Qiao[1], Xin-Tong Liu[1], Chen-Xin Wang[1], Shuang Song[2], Chun-Qing Ai[2] and Ying-Huan Fu[2,3]**

[1] School of Food Science and Technology, Dalian Polytechnic University, Dalian, China, [2] National Engineering Research Center of Seafood, Dalian, China, [3] School of Light Industry and Chemical Engineering, Dalian Polytechnic University, Dalian, China

In this study, phycocyanin-sodium alginate/lysozyme complex (PC-SLC) was prepared for the first time and characterized by UV spectroscopy, Fourier transform infrared spectroscopy (FT-IR), and circular dichroism spectroscopy (CD). The stability of PC-SLC under light, temperature, pH and simulated gastrointestinal fluid was investigated. The scavenging ability of the complexes against DPPH and ABTS radicals was determined. The results showed that the complex formed by the mass ratio of SA-LZM of 0.1 showed the highest PC encapsulation rate (89.9 ± 0.374%). The combination of SA and LZM changed the secondary conformation of PC. The PC-SLC complex shows an irregular spherical structure and the spheres are clustered together. Compared with phycocyanin (PC), its thermal stability was obviously improved, but it was still greatly influenced by light. It could exist stably in simulated gastric fluid (SGF) for 2 h and be slowly digested in simulated intestinal fluid (SIF), which helped to promote the absorption of nutrients in the intestinal tract. Meanwhile, the complex PC-SLC showed high scavenging ability for DPPH and ABTS radicals. It can be concluded that the complexes have good antioxidant activity. This study provides an idea for the construction of PC delivery system and makes it more widely used in food industry and other fields.

Keywords: phycocyanin, antioxidation, stability, simulated digestion, electrostatic interactions

OPEN ACCESS

Edited by:
Shuai Chen,
Wuhan University, China

Reviewed by:
Sutapa Biswas Majee,
NSHM Knowledge Campus, India
Jing-Kun Yan,
Dongguan University of Technology, China

***Correspondence:**
Ying-Huan Fu
fuyh@dlpu.edu.cn

Specialty section:
This article was submitted to Food Chemistry, a section of the journal Frontiers in Nutrition

Received: *07 March 2022*
Accepted: *19 April 2022*
Published: *24 May 2022*

Citation:
Qiao B-W, Liu X-T, Wang C-X, Song S, Ai C-Q and Fu Y-H (2022) Preparation, Characterization, and Antioxidant Properties of Phycocyanin Complexes Based on Sodium Alginate and Lysozyme. Front. Nutr. 9:890942. doi: 10.3389/fnut.2022.890942

INTRODUCTION

Spirulina contains a variety of nutrients, such as vitamins, minerals, protein and γ-polyunsaturated fatty acids, such as linolenic acid (1). In addition, *spirulina* species has antiviral, antibacterial, antifungal and antiparasitic activities. *Spirulina* preparation can improve the intestinal environment by promoting the growth of *Lactobacillus*, *Bifidobacterium* and other intestinal beneficial bacteria (2). Recently, studies on *Spirulina* have shown that *Spirulina* contains many phenolic compounds, which usually have high antioxidant activity (3). Estrada et al. found that phycobiliprotein (PC) extracted from *Spirulina* also has good antioxidant activity (4).

Because PC contains all essential amino acids, it is often used as a nutritional supplement. The potential benefits of PC for human nutrition and health are significant (5). Because of its fluorescent properties, it is also used as a biochemical tracer in immunoassays for detailed knowledge of the

various stages involved in the immunoassay process in animals (6). As a water-soluble natural pigment, it is also widely used as food colorant, cosmetic additive and clinical diagnostic (7). In addition, PC can be used to treat oxidative stress-induced diseases because it has significant antioxidant, liver protection and free radical scavenging properties, such as preventing cisplatin induced nephrotoxicity by inhibiting oxidative stress (8). However, the sensitivity of PC to storage and processing conditions leads to variability, precipitation, and discoloration, which limits its application in different fields. Therefore, how to improve the stability of PC during transportation has been a popular research topic in the field of food.

The degradation of PC depends on the aggregation state of the protein, which is influenced by light, solution temperature, pH value and PC concentration (9, 10). Therefore, in the processing of PC as a natural pigment, it is very important to properly control temperature, pH value and light to improve its stability. At present, the stability of PC can be improved by adding stabilizers. Polysaccharides and polyols have been used to stabilize proteins and as stability agents in the food industry and pharmaceutical formulations due to their good food safety and non-cytotoxicity (11). Faieta et al. (12) showed that sucrose has a significant protective effect on PC. It was confirmed by circular dichroism that the loss of color of PC is closely related to the structural instability of the protein. In addition, microencapsulation technology can be used to improve the stability of PC. Das et al. (13) prepared polymer ultrafine particles by electrospray technology, while maintaining PC antioxidant activity and improving its heat resistance and stability.

Natural polysaccharide sodium alginate (SA) is widely used in the delivery systems of bioactive substances due to its good biocompatibility, low price and gel properties. Since the dissociation constants of mannuronic acid (M) and guluronic acid (G) monomers are 3.38 and 3.65, respectively, SA tends to be negatively charged in a wide pH range (14). Lysozyme (LZM) can be used as a model protein to study the interaction between protein and polysaccharide. Its isoelectric point is about 10.8, so they can form complexes through electrostatic attraction in a wide pH range. Therefore, in this study, we prepared phycocyanin sodium alginate/lysozyme (PC-SLC) complex, in which the main force is the electrostatic force between positively charged lysozyme and negatively charged sodium alginate. The purpose is to improve the processing and storage stability of PC by forming a complex, so the light, temperature, pH and gastrointestinal digestive fluid stability of the prepared PC-SLC were measured. The results showed that the formed complexes could improve the stability of PC. The complex PC-SLC has good antioxidant activity. This study provides an idea for constructing the capsule delivery system of algal cyanobacterial proteins, which is conductive to its application in food industry and other fields.

MATERIALS AND METHODS

Materials

PC was purchased from Binmei Biological Co., Ltd. (Zhejiang, China); LZM (molecular weight 14.7 kDa) was obtained from Shanghai Bioengineering Co. (Shanghai, China); SA was provided by Aladdin Industrial Co. (Shanghai, China); Other chemical reagents used were of analytical grade and commercially available.

Determination of Relative Molecular Mass of SA

High-performance gel-permeation chromatography (HPGPC) was used to determine the relative molecular mass of SA. The gel chromatography column was TSK-gel G5000PWxl (7.5 mm × 30.0 cm) with a column chamber temperature of 30°C. 0.1 mol/L ammonium acetate buffer solution (pH = 6) was used as the mobile phase with a flow rate of 0.4 ml/min. Using the mobile phase as the solvent of the standard dextran solution, which was injected in a volume of 10 μl. Drawing a linear regression equation with retention time t_R as the horizontal coordinate and lgMw as the vertical coordinate.

The prepared solution was filtered through a 0.22 μm filter membrane and the rest of the conditions were the same as those for the determination of the standards. It was measured the retention time of the sample peak and the relative molecular mass of the sample was calculated by substituting the retention time into the standard curve.

Preparation of Phycocyanin-Sodium Alginate/Lysozyme Complexes

The preparation of PC-SLC was based on a previously published method in the literature with slight modifications (15). Stock solutions of PC (0.24 mg/ml), LZM (10 mg/ml), and SA (1 mg/ml) were prepared with deionized-water. The PC stock solution (1 ml) was added dropwise to LZM solution (1 ml) and mixed well, then 1 ml SA stock solution was added dropwise to PC- LZM mixture with SA: LZM mass ratio of 0.1, and strirred at 25°C for 3 h to prepare the complex. The precipitate was collected by centrifugation at 7,800 g for 30 min and washed several times with deionized water until the washing solution contained no PC. The concentration of PC was tested according to the method in Determination of PC Concentration. Then the precipitate was collected by centrifugation and freeze-dried.

Determination of PC Concentration

PC concentration was determined according to the literature reported by Bennett and Bogorad (16) with slight modification. The supernatant after centrifugation was collected. Then absorbance values were measured using a microplate reader at 620 and 652 nm (Tecan). The calculation formula of PC concentration is as follows:

$$[PC] = \frac{OD_{620} - 0.474 \times OD_{652}}{5.34}$$

OD_{620}: the optical density at 620 nm; OD_{652}: the optical density at 652 nm;

The encapsulation efficiency (EE) was calculated according to the following formula:

$$EE\,(\%) = \frac{W_1}{W_2} \times 100$$

W_1: the mass of PC in embedding system; W_2: the mass of PC in feed.

The Characterization of the PC-SLC

UV–Visible Spectra

The supernatant after centrifugation was collected. UV-visible spectra were obtained using a Lambda 35 UV-visible spectrometer with a scan range of 200-700 nm (PerkinElmer, Japan).

Circular Dichroism Spectra

The precipitate after centrifugation of the complex solution is dissolved with deionized water and diluted. Circular dichroism spectra were collected on a Jasco J-1500 Spectropolarimeter from 320 to 190 nm with a scanning rate of 50 nm min^{-1}.

FT-IR

Dried samples were grounded in an agate mortar, mixed with KBr in the ratio of 1:50 (w/w), pressed into pellets and analyzed by FT-IR spectrometer (PerkinElmer) in the range of 4,000-400 cm^{-1}.

Scanning Electron Microscopy

A field-emission scanning electron microscopic image was collected using a JSM-7800F (Japan). The precipitate of the complex solution was collected after centrifugation and freeze-dried to obtain a solid powder. Three to five mg of the sample to be tested and dispersed evenly on a conductive adhesive on the sample stage. After vacuum gold plating, the morphology of the complex at magnifications of 5,000, 10,000, 30,000, and 50,000 was observed by SEM. The operating voltage is 3 Kv.

Stability Study of PC-SLC

pH Buffered Solutions

The stability test method of the complex PC-SLC at pH conditions was performed according to the method of Khan et al. (8) with slight modifications. Buffer solutions with different pH values (3, 5, 7.4, and 8) were prepared by mixing 0.2 mol/L aqueous disodium hydrogen phosphate and 0.1 mol/L aqueous citric acid while monitoring with a pH meter. The prepared PC-SLC was dissolved in different pH buffer solutions and then incubated at 25°C. At predetermined time intervals, 1 ml of supernatant was removed and supplemented with the same volume of fresh buffer solution. The absorbance of the supernatant was measured with a microplate reader (Tecan) at 620 and 652 nm. The cumulative release of PC was calculated with the following equation.

$$Cumulative\ PC\ release\ (\%) = \frac{W_t}{W_0} \times 100$$

W_t: the amount of PC released at time t; W_0: the amount of PC in the PC-SLC.

Thermal Stability

The method was modified with reference to the supplementary method published in literature (17). PC-SLC solid powder prepared was dissolved in disodium hydrogen phosphate-citrate buffer solution at pH 7.4 and incubated for 30 min (protected from light) at four different temperatures (37, 45, 53, 60 and 70°C). The cumulative release of PC was calculated by referring to the formula in pH buffered solutions.

Photostability

The photostability of PC-SLC was evaluated using UV lamp and cabinet. PC-SLC was dissolved in disodium hydrogen phosphate-citrate buffer pH 7.4. The solutions were mixed well and incubated under UVB light conditions and shaded conditions, respectively. At predetermined time intervals, 1 ml of supernatant was removed and supplemented with the same volume of fresh buffer solution. The cumulative release of PC was calculated by referring to the formula in pH buffered solutions.

In vitro Digestion Study

Based on the method described in literature (18), the *in vitro* gastrointestinal model composed of simulated gastric fluid (SGF) and simulated intestinal fluid (SIF) was used to evaluate the *in vitro* digestion of samples with some modifications.

16.4 ml of dilute hydrochloric acid (9.5-10.5% by volume) was added to 800 ml of water, and then 10 g of pepsin was added. After mixing, deionized water was added to make the volume up to 1 L to obtain simulated gastric fluid (SGF).

PC-SLC dissolved in deionized water was mixed with SGF and incubated in a thermostatic water bath at 37°C for 2 h. The sample solution (200 μl) was taken out every 30 min. The sample solution was filtered through a 0.45 μm filter membrane. The cumulative release was determined as before calculated using the formula in pH buffered solutions for the cumulative release of PC.

The pH of 13.6 mg/ml potassium dihydrogen phosphate solution (250 ml) was adjusted with NaOH (0.1 mol/L) to 6.8. It was mixed with 25 mg/ml trypsin solution (100 ml) and 150 ml distilled water was added to obtain the simulated intestinal fluid (SIF). Reference was made to the method of Li et al. (19) for the configuration of the simulated intestinal fluid.

PC-SLC dissolved in deionized water was mixed with SIF and incubated in a thermostatic water bath at 37°C for 6 h. The other steps remained the same as in the SGF.

Assay of Antioxidant Activity

Scavenging Activity of 2, 2'-azino-bis (3-ethylbenzothiazoline-6-sulfonic Acid Ammonium Salt) (ABTS) Radical

The ABTS free radical scavenging assay was modified from the method reported in the literature (20). ABTS (14 mmol/L) was mixed with $K_2S_2O_8$ (4.9 mmol/L) in equal volumes and kept away from light at room temperature for 12 h to obtain ABTS radical assay solution. The absorbance reached 0.70 ± 0.02 at 734 nm after ABTS radical assay solution dilution with 0.1 mol/L PBS buffer (pH = 7) before measurement. The sample (10 μl) and PBS (20 μl) were mixed with ABTS detection solution (70 μl), incubated for 6 min, and absorbance was measured at 734 nm. Vc was used as positive control. The ABTS free radical scavenging rate is calculated as follows:

$$Scavenging\ activity\ (\%) = \frac{A_0 - A}{A_0} \times 100$$

A_0: the absorbance of the control reaction; A: the absorbance value of the test samples.

Scavenging Activity of 1, 1-Diphenyl-2-picrylhydrazyl Radicals

The determination of DPPH radical scavenging activity was referred to Liang's method with some modifications (21). DPPH (1 mg) was dissolved in anhydrous ethanol (24 ml) and mixed thoroughly. DPPH solution (1 ml) was diluted by adding a certain volume (0.5 ml) of anhydrous ethanol solution, mixed thoroughly and then measured the absorbance value A_0 (between 0.6 and 1.0) at 519 nm. Add 1 ml of DPPH solution to the EP tube, add x μl of sample solution to the pre-test addition, add (500-x) μl of anhydrous ethanol solution, mix thoroughly, and measure the absorbance value at 519 nm after 30 min of standing. Vc was performed as positive control. The DPPH radical scavenging rate is calculated by the following equation:

$$Scavenging\ activity\ (\%) = \frac{A_0 - A}{A_0} \times 100$$

A_0: the absorbance of the control reaction; A: the absorbance value of the test samples.

Data Analysis

All data are shown as mean ± standard deviation (M ± SD) of three parallel samples ($n = 3$) within significance $P < 0.5$ after passing single factor analysis of variance SPSS 25.0 software. Significant differences between two groups of data were determined by *t*-test, and One-ANOVA was performed between multiple groups of data.

RESULTS AND DISCUSSION

Molecular Weight of SA

The HPGPC of SA is shown in **Figure 1**. The measured retention time of SA in the column was 13.76 min, and the molecular weight of SA was calculated as 4696.8 kDa from the plotted standard curve equation $lgMw = 0.2966t_R - 10.753$ ($R^2 = 0.9986$).

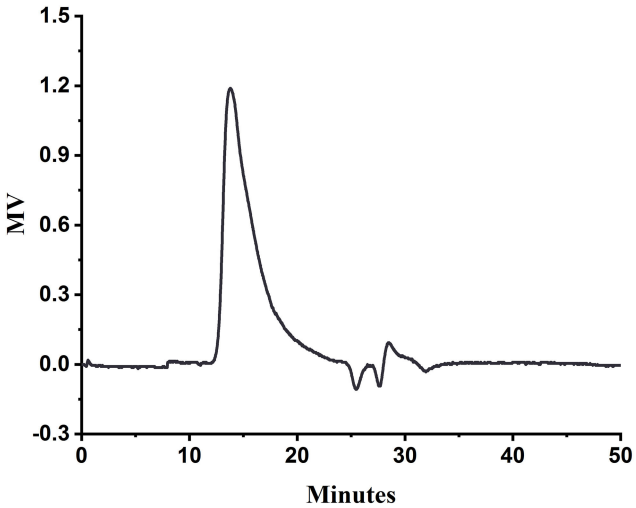

FIGURE 1 | HPGPC of SA.

Characterization of PC-SLC

LZM and SA solutions were prepared and mixed at a weight ratio of 10:1 to encapsulate PC to form PC-SLC complex solutions. The specific preparation process is shown in **Figure 2**.

As shown in **Figure 3**, when the weight ratio of SA to LZM was changed, there was a significant difference in the encapsulation efficiency of PC. The complex PC-SLC formed by the mass ratio of SA-LZM of 0.1 showed the highest encapsulation efficiency of PC (89.9 ± 0.374%). This may be due to the negative charge of PC and SA in aqueous solution, which can produce electrostatic interaction with LZM with opposite charge. It has been shown that electrostatic interactions between polysaccharides and proteins in a system can be achieved by changing the concentration and ratio of both. The results of Wang's study found that mixing different ratios of β-lactoglobulin with pectin in an aqueous system can lead to the formation of cohesions due to electrostatic interactions. It was found that increasing the mixing ratio of β-lactoglobulin could lead to the formation of cohesions with higher elasticity (22). When there was too much SA, there were more anions than cations in the whole system, the formation of PC-SLC may be hindered. Therefore, the follow-up experiments in this study were carried out with the weight ratio of SA to LZM of 1:10.

UV–Visible Spectroscopy Analysis

In this study, the supernatants centrifuged after the formation of PC, SA-LZM, and PC-SLC were measured separately by UV-visible spectroscopy. As shown in **Figure 4A**, the characteristic absorption peaks of PC appeared at 652 and 620 nm. For the same protein concentration, the lower absorption peak indicates less PC in the supernatant (23), which also indirectly indicates the higher encapsulation efficiency of PC. The weight ratio of SA to LZM is one of the important factors affecting the encapsulation rate of PC. The weakest PC characteristic peak was shown when the weight ratio of SA to LZM in the complex was 0.1. It is thus clear that the complex formed have the highest encapsulation efficiency for PC when the weight ratio of SA to LZM is 0.1.

CD Analysis

The CD spectrum of the complex PC-SLC is shown in **Figure 4B**. The LZM solution has one positive peak at 195 nm and two negative peaks at 208 and 222 nm. After the formation of the complex PC-SLC, the positive peak at 195 nm is slightly shifted and diminished toward the lower wave number and the negative peak at 208 nm is shifted toward the higher wave number. The obtained CD spectra were analyzed using secondary structure estimation software and the results are shown in **Table 1**. The results showed that the secondary structures of the complexes PC-SA/LZM formed with different weight ratios of SA/LZM were all changed compared to PC (24). Comparing the secondary structures of PC, SA/LZM with a weight ratio of 0.1 and the complex PC-SA/LZM formed from them, it is clear that the combination of SA and LZM resulted in changes in the secondary

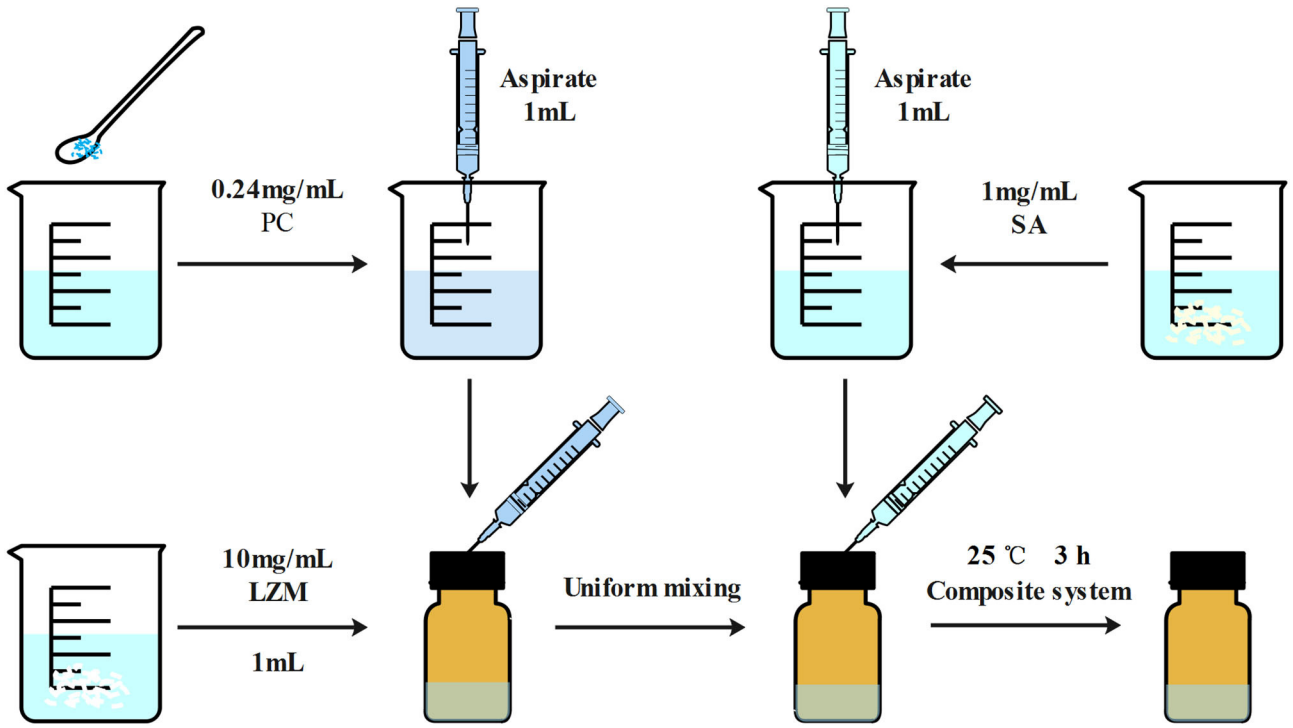

FIGURE 2 | Schematic diagram of the preparation of LZM and SA encapsulated PC particles. The main reason for the formation of particles is due to the electrostatic interactions between the macromolecules in the whole system.

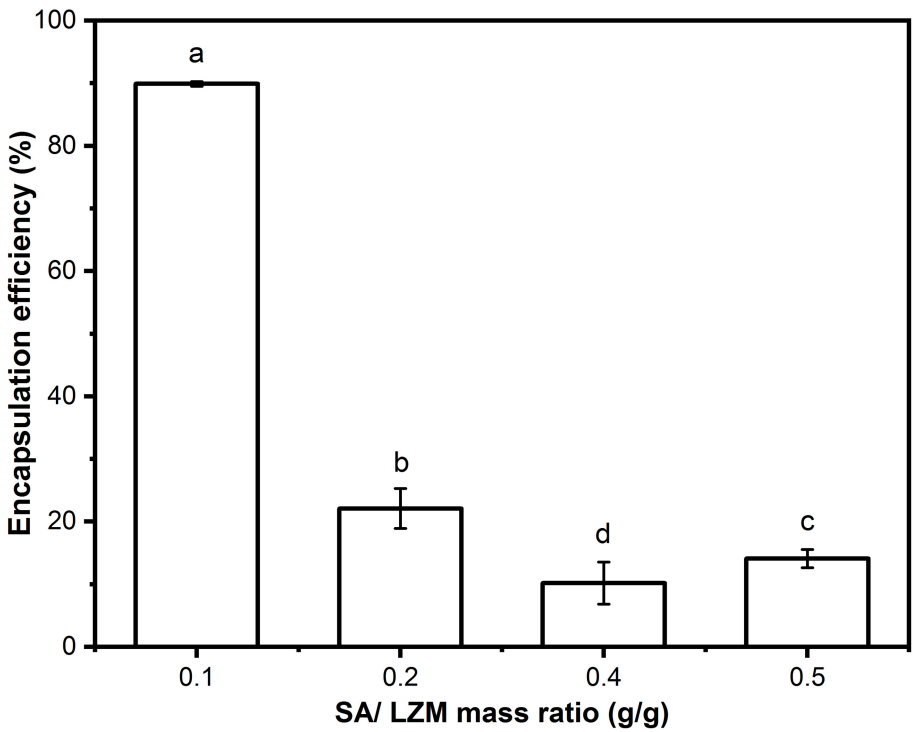

FIGURE 3 | Encapsulation efficiency of PC-SLC formed by different weight ratios of SA/LZM. Different letter a-d values indicate significant differences between the data ($p < 0.05$).

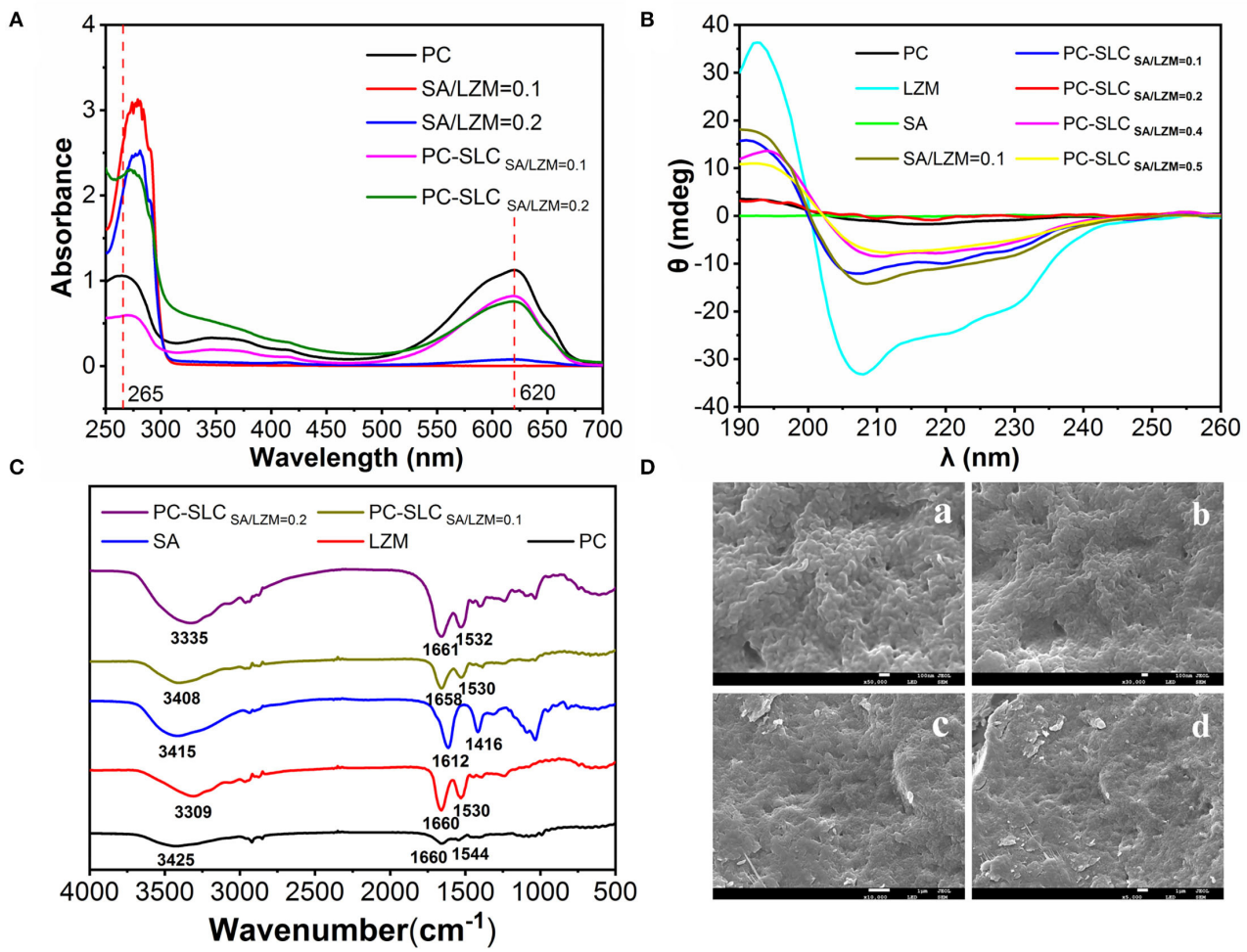

FIGURE 4 | UV spectra **(A)**, circular dichroism **(B)**, FT-IR spectra **(C)** of PC, LZM, SA, different weight ratios of SA/LZM and complex PC-SLC containing different weight ratios of SA/LZM, and different magnifications [50,000x (a), 30,000x (b), 10,000x (c), and 5,000x (d)] of complex PC-SLC Scanning electron micrographs **(D)**.

structure of PC. The combination of SA and LZM resulted in a 25.9% decrease in α-helix deflection, 7.6% increase in β-fold deflection, 1.6% increase in β-turn angle deflection, and 16.7% increase in radon deflection of PC. The β-folding is more flexible, which can improve the flexibility properties and expansion of the protein (25). Comparison with PC shows that the β-folding of the complexes formed by different weight ratios of SA/LZM all changed. And when the weight ratio of SA/LZM was 0.1, the corresponding complexes underwent the greatest increase in deflection of β-folding. The results suggest that the presence of SA and LZM may cause the greatest structural expansion of PC.

FT-IR Analysis

FTIR spectroscopy is used to detect the emergence of new interactions, marked by the appearance of new wave number shifts. As shown in **Figure 4C**, the strong absorption vibration peak at 3,414 cm^{-1} is attributed to the -OH stretching vibration of SA, and the smaller absorption peak at 2,936 cm^{-1} is attributed to the C-H stretching vibration absorption peak. 1,612 and 1,416 cm^{-1} are the asymmetric and symmetric stretching vibration of -COO-, which is the characteristic absorption peak of SA. 1,034 cm^{-1} is the C-O-C stretching vibration peak of pyran ring of SA. The broad absorption peak of LZM at 3,308 cm^{-1} is attributed to the stretching vibration peaks of the functional groups O-H and N-H. The characteristic absorption peaks of LZM at 1,660 cm^{-1} and 1,530 cm^{-1} are the amide I and amide II bands, respectively. The absorption peak at 1,642 cm^{-1} is caused by the -C=O stretching vibration or N-H bending vibration, while the absorption peak at 1,536 cm^{-1} is caused by the N-H stretching vibration. The main changes observed in the PC-SLC complex spectra compared to SA, LZM and PC are the O-H and amide bond stretching vibrational peaks located in the 1,500-1,660 cm^{-1} region. It is noteworthy that the formation of PC-SLC complexes was accompanied by a shift in the peak wave number of the hydrogen bonds, along with a shift change in the amide I and amide II bonds. The precise vibration of the carboxyl group (1,612 cm^{-1}) in SA can no longer be observed, which may be attributed to the electrostatic interaction between the amino and

TABLE 1 | The secondary structure composition of PC, LZM, SA, SA/LZM with a weight ratio of 0.1, and PC-SLC formed by different weight ratios of SA/LZM (0.1, 0.2, 0.4, 0.5).

	HELIX	BETA	TURN	RANDOM
PC	50.8 ± 1.8^{a}	29.9 ± 1.0^{ab}	1.9 ± 2.0^{de}	17.4 ± 3.6^{c}
LZM	22.5 ± 0.8^{cd}	39.9 ± 1.2^{a}	9.6 ± 1.6^{c}	28 ± 1.3^{ab}
SA	18.6 ± 4.5^{d}	40.4 ± 11.5^{a}	12.5 ± 5.8^{bc}	28.5 ± 5.7^{ab}
$PC\text{-}SLC_{SA/LZM=0.1}$	24.9 ± 0.4^{cd}	37.5 ± 1.9^{a}	3.5 ± 0.2^{de}	34.1 ± 2^{a}
$PC\text{-}SLC_{SA/LZM=0.2}$	35.9 ± 7.5^{b}	31.9 ± 5.3^{a}	0.9 ± 1.3^{e}	31.3 ± 5.2^{a}
$PC\text{-}SLC_{SA/LZM=0.4}$	40.9 ± 1.8^{b}	17.9 ± 2.1^{c}	18.2 ± 1.2^{ab}	23 ± 2.1^{bc}
$PC\text{-}SLC_{SA/LZM=0.5}$	40.1 ± 0.8^{b}	19.4 ± 1.6^{bc}	20.1 ± 1.1^{a}	20.4 ± 1.2^{bc}
SA/LZM = 0.1	27.6 ± 0.8^{c}	37.6 ± 0.9^{a}	7 ± 1.1^{cd}	27.8 ± 2.8^{ab}

Values are expressed as means ± standard deviation; (n = 3); Superscript (a–e) values with different letters indicate significant differences at the same concentration ($p < 0.05$).

carboxylate groups, leading to the merger of the two vibrations. These results all suggest that electrostatic interactions are the main force that enables the formation of the complex PC-SLC. Chang et al. (26) studied the IR spectra of Zein/NaCas/pectin complexes and found that the O-H vibrations and the amide bond region undergo major IR band changes in the formed complexes, and the carboxyl group vibrations of pectin disappear, all of which indicate that the formation of the complexes is driven by electrostatic driving force of the interaction.

SEM Analysis

The apparent morphology of PC-SLC complexes was observed using scanning electron microscopy and the results are shown in **Figure 4D**. The PC-SLC complex shows an irregular spherical structure and the spheres are clustered together. Yue et al. (27) showed that the ideal structure to form a complex is one with a uniform, smooth spherical surface with fewer cracks and collapses in the walls. It has also been shown that complex with rough surfaces are more sensitive to oxidation reactions due to the large surface area they possess, while complex with smooth surfaces are less susceptible to oxidation reactions (28). Therefore, it is assumed that the aggregated spheres may also increase the stability due to the reduction of surface area. The reason for the aggregation may be that the pressure during the freeze-drying process causes the spheres to squeeze each other together. Kurniasih et al. (29) microencapsulated chlorophyll with maltodextrin-fish gelatin and showed the formation of ice crystals during freeze-drying while generating porous forms due to sublimation processes.

Stability of PC-SLC

pH Stability Analysis

Figure 5A shows the cumulative release rate of PC from complex PC-SLC in disodium hydrogen phosphate-citrate buffer solution at pH 3-8. The pH stability was evaluated by monitoring the change of PC release rate with time (0-12 h). The release of PC from the complexes under all pH conditions showed a two-step release profile, including a burst release within 2 h and a continuous slow release for 10 h. The reason for this may be due to the physical adsorption to the PC of PC-SLC and almost 90% of the PC has been released within 12 h. Zhang et al. (30) prepared polysaccharide supramolecular hydrogels based on carboxymethyl β-cyclodextrin/chitosan inclusion complexes and EDTA-chitosan constructs by electrostatic interactions. The system loading of BSA resulted in a continuous slow release of BSA in a buffer solution at pH 7.4 for 12 h, after which stability was achieved. The sustained release behavior may be attributed to the fact that PC-SLC form a barrier to protect the PC (31). Similar results were obtained from Khan et al. (8) by studying the controlled release in CA/NaAlg polyelectrolyte complexes (PEC). PC was essentially not released at pH = 3, while the highest release rate was observed at pH = 8. This indicates that the closer the pH value of the system is to alkalinity, the more unstable the complex is and the faster release of PC. This is because the isoelectric points of PC and LZM are 3.4 and 11, respectively, and both are positively charged at pH = 3 so that they cannot be bound by electrostatic force. PC and LZM, one negatively charged and one positively charged, form complex with SA in aqueous solution when the pH increases. PC is unstable under strong alkaline conditions, which may be responsible for the increased release rate. The efficacy of complexes generated by protein-polysaccharide interactions for nutrient encapsulation and colloidal stability was preliminarily demonstrated by Hosseini et al. by electrostatic interaction forces under changing pH conditions (32).

Thermal Stability Analysis

Xu et al. (33) studied the stability of PC at 30-70°C, and the general denaturation temperature of PC is 45°C. Therefore, this experiment investigated the release of PC and PC-SLC complexes in disodium hydrogen phosphate-citrate buffer solution at different temperature conditions, and the results are shown in **Figure 5B**. The results showed that the stability of PC decreased significantly above 53°C, while the prepared PC-SLC complexes showed higher stability than PC. This may be due to the protective effect on the stability of PC after the formation of complex. As Alehosseini et al. (34) studied the stabilization of Pickering emulsions by CSNPs to improve the thermal stability of D-limonene. Suzery et al. (35) prepared microencapsulated PC using sodium alginate as coating material by extrusion method. Microspheres with high encapsulation efficiency were prepared by varying the amount of sodium alginate. The stability of the microspheres was observed at hot air drying (43°C) and freezing (−2°C) conditions. It was found that the stability of the prepared microspheres was greatly influenced by different temperature conditions.

Photostability Analysis

PC is unstable under light conditions (36). In order to determine whether the complexes can increase the stability of PC under light conditions, this study investigated the stability of PC and PC-SLC in disodium hydrogen phosphate-citrate buffer solution at pH = 7.4 using UVB light. As shown in **Figure 5C**, the release of PC-SLC was faster under light conditions than under non-light conditions, and there was a tendency to lose PC. The end point of release was reached when the release lasted for 4 h. The cumulative release rate of the complexes with light at this

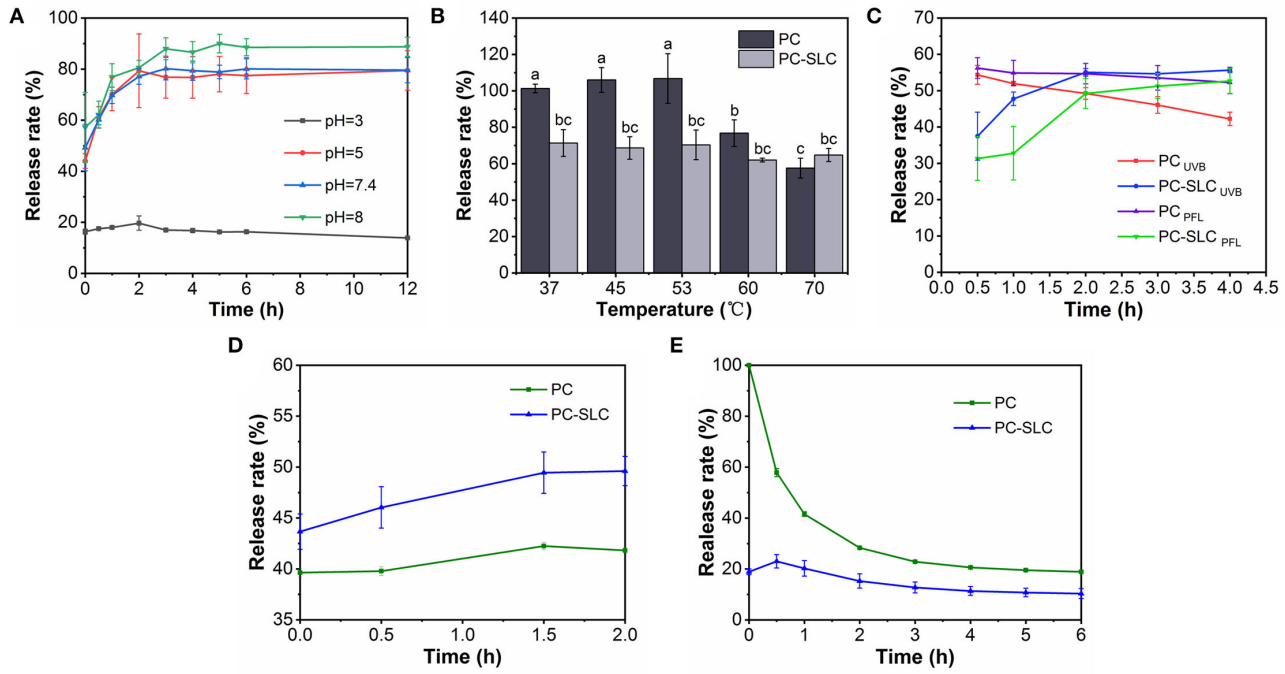

FIGURE 5 | Stability of PC-SLC under pH **(A)**, temperature **(B)**, light **(C)**, simulated gastric fluid, **(D)** and simulated intestinal fluid **(E)** conditions.

endpoint was higher than that of the samples without light. This suggests that light accelerates the release of PC-SLC and has an effect on the stability of PC-SLC. The effect of epigallocatechin gallate (EGCG) on the physicochemical properties of PC was investigated by Yang et al. (37). Under 8 days of light storage conditions, the structure of PC changed from α-helical structure to β-sheeted structure. Combining PC with EGCG to form a complex improved the stability of PC. It can be seen that SA-LZM can encapsulate PC so that PC will not be degraded under UVB light conditions, thus protecting and improving the stability of PC.

In vitro Simulated Digestion Stability Analysis of PC-SLC

The stability of the complexes under simulated gastrointestinal fluid conditions was assessed by measuring the release rate of PC (**Figures 5D,E**). The samples PC and PC-SLC showed good stability with 42.24 ± 0.37 and 49.45 ± 2.03% release rates of PC in SGF, respectively. The relative release rate of PC-SLC remained stable within 2 h in SGF. When PC-SLC was incubated in SIF, the release rate increased rapidly to 23% within 30 min and remained relatively stable thereafter. This may be due to the fact that the formed PC-SLC protects the PC from pepsin digestion in the simulated gastric juice to some extent and is digested by trypsin in the simulated intestinal juice (38). Barbosa et al. (39) used the formation of composite gels of carboxymethylcellulose and whey protein isolated complex to encapsulate sachainchioil containing β-carotene (β-C), and the prepared microcapsules could be preserved under SGF conditions and showed higher release during *in vitro* simulated intestinal digestion. The complex is stabilized in the gastric juice and slowly digested in the intestinal juice, which is usually the most ideal situation (40). The above study showed that PC-SLC have the ability to deliver PC to the intestine.

Analysis of Antioxidant Activity of PC-SLC

The antioxidant activity of PC is related to its unique structure (41). In this study, the antioxidant activity of PC-SLC was evaluated by ABTS and DPPH free radical scavenging. **Figures 6A,B** show the antioxidant capacity results of different samples at various concentrations. The results indicated that all samples showed significant antioxidant capacity. Schmatz et al. (42) prepared a novel nanofiber material, PC/polyvinyl alcohol nanoparticles (PC-PVAn), using electrostatic spinning and electrospraying techniques. Polymer nanofibers containing PC-PVAn showed antioxidant capacity in all methods used (ABTS, DPPH and reducing power). However, the antioxidant activity of the free PC-PVAn in the medium was significantly higher than that of the PC-PVAn incorporated into the nanofibers. This result was expected because using the same sample mass, the phycocyanin concentration present was at higher proportions in the nanoparticles compared to the nanofibers, and this may have been reflected in the quantification of the antioxidant capacity of phycocyanin. Similarly, the antioxidant capacity of PC-SLC obtained by adding the same concentration of sample solution in this study was slightly lower than that of free PC. In conclusion, the ABTS radical scavenging ability of PC-SLC was slightly better or not much different at the same sample concentration, but at the same time we observed that SA-LZM complex without PC also had certain antioxidant activity (43, 44). Therefore, it can be

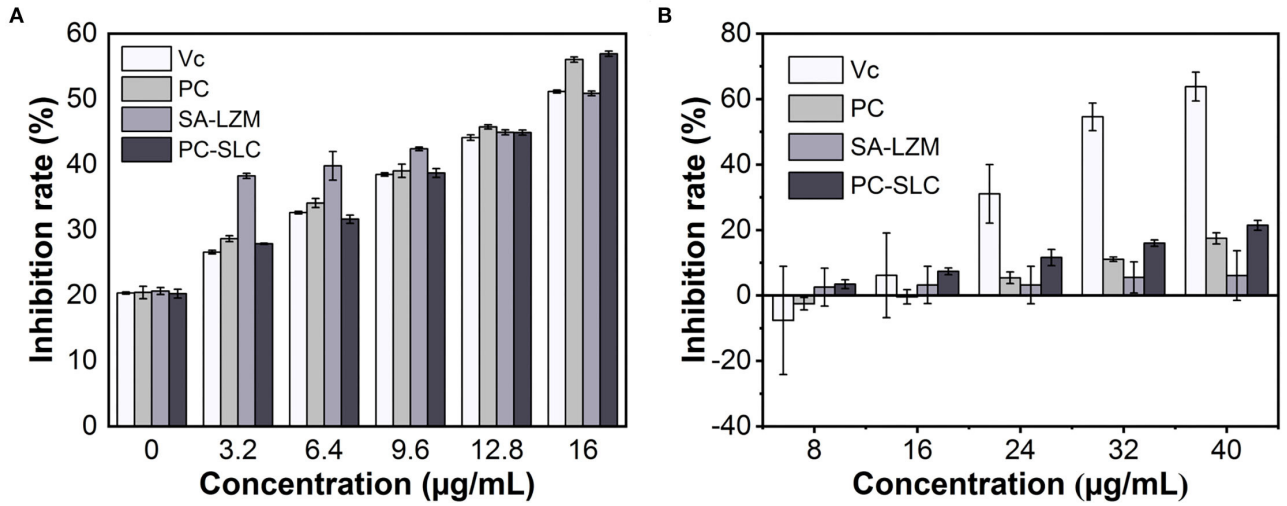

FIGURE 6 | Determination of DPPH **(A)** and ABTS **(B)** radical scavenging capacity of the complex PC-SLC.

inferred that due to the addition of SA and LAM, the antioxidant activity of PC-SLC may be higher than that of PC.

As shown in **Figure 6B**, the DPPH radical scavenging ability of each sample increased gradually with the increase of the sample concentration. Generally, the DPPH radical scavenging ability of PC-SLC was higher than that of PC. The results showed that the formed complex PC-SLC had good DPPH radical scavenging ability.

The above antioxidant experimental results show that PC-SLC is a powerful natural antioxidant that can be better applied in various fields.

CONCLUSION

In this study, PC-SLC complex were successfully prepared by electrostatic interactions between SA and LZM. The complexes formed at a mass ratio of 0.1 for SA-LZM showed the highest PC encapsulation efficiency (89.9 ± 0.374%). Then the stability and antioxidant activity of the complexes were explored. It was found that the formed complex PC-SLC has a protective effect on PC and can improve the stability of PC by studying the stability of the complex at different pH, temperature, light and simulated gastrointestinal fluid conditions. The good antioxidant activity of the complex PC-SLC was demonstrated by the ABTS and DPPH radical scavenging ability tests. These findings may expand the application of polysaccharide-protein complexes as new carriers of bioactive substances in drug delivery systems, as well as broaden the range of PC applications.

DATA AVAILABILITY STATEMENT

The original contributions presented in the study are included in the article/supplementary material, further inquiries can be directed to the corresponding author/s.

AUTHOR CONTRIBUTIONS

B-WQ: conceptualization, investigation, writing—original draft, and writing—review and editing. X-TL: investigation and writing—original draft. C-XW: data curation and investigation. SS and C-QA: conceptualization, methodology, and supervision. Y-HF: conceptualization, investigation, project administration, resources, software, and writing—review and editing. All authors contributed to the article and approved the submitted version.

FUNDING

This research was supported by the National Natural Science Foundation of China (Grant No. 31501431) and the National Key Research and Development Program of China (2018YFD0901106).

REFERENCES

1. Abalde J, Betancourt L, Torres E, Cid A, Barwell C. Purification and characterization of phycocyanin from the marine Cyanobacterium Synechococcus Sp. Io9201. *Plant Sci.* (1998) 136:109-20. doi: 10.1016/S0168-9452(98)00113-7
2. Martínez-Galero E, Pérez-Pastén R, Perez-Juarez A, Fabila-Castillo L, Gutiérrez-Salmeán G, Chamorro G. Preclinical antitoxic properties of spirulina (Arthrospira). *Pharmaceut Biol.* (2015) 54:1345-53. doi: 10.3109/13880209.2015.1077464
3. Bellahcen TO, Aamiri A, Touam I, Hmimid F, Amrani AE, Cherif A, et al. Evaluation of moroccan microalgae: spirulina platensis as a potential source of natural antioxidants. *J Complement Integr Med.* (2020) 17:20190036. doi: 10.1515/jcim-2019-0036
4. Estrada JEP, Bescós PB, Fresno A. Antioxidant activity of different fractions of spirulina platensis protean extract.

Farmaco. (2001) 56:497-500. doi: 10.1016/S0014-827X(01)01084-9
5. Ferraro G, Imbimbo P, Marseglia A, Illiano A, Fontanarosa C, Amoresano A, et al. A thermophilic C-phycocyanin with unprecedented biophysical and biochemical properties - sciencedirect. *Int J Biol Macromol.* (2020) 150:38-51. doi: 10.1016/j.ijbiomac.2020.02.045
6. Silveira ST, Burkert J, Costa J, Burkert C, Kalil SJ. Optimization of phycocyanin extraction from spirulina platensis using factorial design - sciencedirect. *Bioresour Technol.* (2007) 98:1629-34. doi: 10.1016/j.biortech.2006.05.050
7. Jung KH, Park JO, Park JH, Choi WS, Seo YC, Lee HY. Stable isolation of phycocyanin from spirulina platensis associated with high-pressure extraction process. *Int J Mol Sci.* (2013) 14:1778-87. doi: 10.3390/ijms14011778
8. Khan M, Varadharaj S, Shobha JC, Naidu MU, Parinandi NL, Kutala VK, et al. C-Phycocyanin ameliorates doxorubicin-induced oxidative stress and apoptosis in adult rat cardiomyocytes. *J Cardiovasc Pharmacol.* (2006) 47:9-20. doi: 10.1097/01.fjc.0000191520.48404.27
9. HN P, Chetan AN. Enhanced stability of C-phycocyanin colorant by extrusion encapsulation. *J Food Sci Technol.* (2019) 56:4526–34. doi: 10.1007/s13197-019-03955-8
10. Wu HL, Wang GH, Xiang WZ, Li T. Stability and antioxidant activity of food-grade phycocyanin isolated from spirulina platensis. *Int J Food Prop.* (2015) 19:2349-62. doi: 10.1080/10942912.2015.1038564
11. Petersen SB, Jonson V, Fojan P, Wimmer R, Pedersen S. Sorbitol prevents the self-aggregation of unfolded lysozyme leading to and up to 13 degrees C stabilisation of the folded form. *J Biotechnol.* (2004) 114:269-78. doi: 10.1016/j.jbiotec.2004.07.004
12. Faieta M, Neri L, Sacchetti G, Michele AD, Pittia P. Role of saccharides on thermal stability of phycocyanin in aqueous solutions. *Food Res Int.* (2020) 132:109093. doi: 10.1016/j.foodres.2020.109093
13. Das A, Djdsm A, Javc B, Mgdm A. Encapsulation of phycocyanin by electrospraying: a promising approach for the protection of sensitive compounds. *Food Bioprod Process.* (2020) 119:206-15. doi: 10.1016/j.fbp.2019.07.008
14. Harnsilawat T, Pongsawatmanit R, Mcclements DJ. Characterization of B-lactoglobulin–sodium alginate interactions in aqueous solutions: a calorimetry, light scattering, electrophoretic mobility and solubility study. *Food Hydrocolloids.* (2006) 20:577-85. doi: 10.1016/j.foodhyd.2005.05.005
15. Zhao M, Zacharia NS. Protein encapsulation *via* polyelectrolyte complex coacervation: protection against protein denaturation. *J Chem Phys.* (2018) 149:163326. doi: 10.1063/1.5040346
16. Bennett A, Bogorad L. Complementary chromatic adaptation in a filamentous blue-green alga. *J Cell Biol.* (1973) 58:419-35. doi: 10.1083/jcb.58.2.419
17. Fan Y, Liu Y, Gao L, Zhang Y, Yi J. Improved chemical stability and cellular antioxidant activity of resveratrol in zein nanoparticle with bovine serum albumin-caffeic acid conjugate. *Food Chem.* (2018) 261:283-91. doi: 10.1016/j.foodchem.2018.04.055
18. Wei X, Dai J, Zhong Y, Zhang D, Wang Q. Caffeic acid phenethyl ester loaded in nano-targeted delivery system with casein: physicochemical characterization, *in vitro* release, and binding mechanisms. *Lebensmittel-Wissenschaft und-Technologie.* (2021) 150:111938. doi: 10.1016/j.lwt.2021.111938
19. Li Y, Yang D, Wang Y, Li Z, Zhu C. Co-delivery doxorubicin and silybin for anti-hepatoma *via* enhanced oral hepatic-targeted efficiency. *Int J Nanomed.* (2018) 14:301-15. doi: 10.2147/IJN.S187888
20. Wang T, Zhao H, Bi Y, Fan X. Preparation and antioxidant activity of selenium nanoparticles decorated by polysaccharides from sargassum fusiforme. *J Food Sci.* (2021) 86:977-86. doi: 10.1111/1750-3841.15605
21. Liang X, Cao K, Li W, Li X, Hu K. Tannic acid-fortified zein-pectin nanoparticles: stability, properties, antioxidant activity, and *in vitro* digestion. *Food Res Int.* (2021) 145:110425. doi: 10.1016/j.foodres.2021.110425
22. Wang X, Lee J, Wang YW, Huang Q. Composition and rheological properties of beta-lactoglobulin/pectin coacervates: effects of salt concentration and initial protein/polysaccharide ratio. *Biomacromol.* (2007) 8:992-7. doi: 10.1021/bm060902d
23. Chaiklahan R, Chirasuwan N, Bunnag B. Stability of phycocyanin extracted from *spirulina* sp.: influence of temperature, Ph and preservatives. *Process Biochem.* (2012) 47:659-64. doi: 10.1016/j.procbio.2012.01.010
24. Zhang X, Li M, Lv Y, Sun X, Huang X. Probing gold nanoparticles for the desensitization to β-lactoglobulin from binding mechanism, structure and Ige binding changes. *Food Chem.* (2020) 342:128329. doi: 10.1016/j.foodchem.2020.128329
25. Chen L, Chen J, Ren J, Zhao M. Effects of ultrasound pretreatment on the enzymatic hydrolysis of soy protein isolates and on the emulsifying properties of hydrolysates. *J Agricult Food Chem.* (2011) 59:2600-9. doi: 10.1021/jf103771x
26. Chang C, Wang T, Hu Q, Luo Y. Zein/Caseinate/Pectin complex nanoparticles: formation and characterization. *Int J Biol Macromol.* (2017) 104:117-24. doi: 10.1016/j.ijbiomac.2017.05.178
27. Yue H, Qiu B, Jia M, Liu J, Wang J, Huang F, et al. Development and optimization of spray-dried functional oil microcapsules: oxidation stability and release kinetics. *Food Sci Nutr.* (2020) 8:4730-8. doi: 10.1002/fsn3.1684
28. Tolun A, Altintas Z, Artik N. Microencapsulation of grape polyphenols using maltodextrin and gum arabic as two alternative coating materials: development and characterization. *J Biotechnol.* (2016) 239:23-33. doi: 10.1016/j.jbiotec.2016.10.001
29. Kurniasih RA, Dewi EN, Purnamayati L. Effect of different coating materials on the characteristics of chlorophyll microcapsules from caulerpa racemosa. *IOP Confer Ser Earth Environ Sci.* (2018) 116:012030. doi: 10.1088/1755-1315/116/1/012030
30. Zhang WC, Wang Y, Guo J, Huang C, Hu Y. Polysaccharide supramolecular hydrogel microparticles based on carboxymethyl β-cyclodextrin/chitosan complex and edta-chitosan for controlled release of protein drugs. *Polymer Bull.* (2021) 1–11. doi: 10.1007/s00289-021-03807-6
31. Yuliani S, Torley PJ, D'Arcy B, Nicholson T, Bhandari B. Extrusion of mixtures of starch and D-limonene encapsulated with B-cyclodextrin: flavour retention and physical properties. *Food Res Int.* (2006) 39:318-31. doi: 10.1016/j.foodres.2005.08.005
32. Hosseini S, Emam D Jomeh Z, Sabatino P, Paul VDM. Nanocomplexes arising from protein-polysaccharide electrostatic interaction as a promising carrier for nutraceutical compounds. *Food Hydrocoll.* (2015) 50:16-26. doi: 10.1016/j.foodhyd.2015.04.006
33. Xu J, Zhu S, Zhang M, Cao P, Adhikari B. Combined radio frequency and hot water pasteurization of nostoc sphaeroides: effect on temperature uniformity, nutrients content, and phycocyanin stability. *LWT Food Sci Technol.* (2021) 141:110880. doi: 10.1016/j.lwt.2021.110880
34. Alehosseini E, Jafari SM, Tabarestani HS. Production of D-limonene-loaded pickering emulsions stabilized by chitosan nanoparticles. *Food Chem.* (2021) 354:129591. doi: 10.1016/j.foodchem.2021.129591
35. Suzery M, Hadiyanto Sutanto H, Soetrisnanto D, Azizah N, editors. The Improvement of phycocyanin stability extracted from spirulina sp using extrusion encapsulation technique. In: *International Conference of Chemical and Material Engineering* (2015).
36. Aoki J, Sasaki D, Asayama M. Development of a method for phycocyanin recovery from filamentous cyanobacteria and evaluation of its stability and antioxidant capacity. *BMC Biotechnol.* (2021) 21:1-10. doi: 10.1186/s12896-021-00692-9
37. Yang R, Ma T, Shi L, Wang Q, Zhang L, Zhang F, et al. The formation of phycocyanin-egcg complex for improving the color protection stability exposing to light. *Food Chem.* (2021) 370:130985. doi: 10.1016/j.foodchem.2021.130985
38. Li D, Wu G, Zhang H, Qi X. Preparation of crocin nanocomplex in order to increase its physical stability. *Food Hydrocoll.* (2020) 2:106415. doi: 10.1016/j.foodhyd.2020.106415
39. Barbosa A, Bastos L, Garcia-Rojas EE. Complex coacervates formed between whey protein isolate and carboxymethylcellulose for encapsulation of B-Carotene from sacha inchi oil: stability, *in vitro* digestion and release kinetics. *Food Biophys.* (2021) 16:293–305. doi: 10.1007/s11483-021-09670-2
40. Ni Y, Gu Q, Li J, Fan L. Modulating *in vitro* gastrointestinal digestion of nanocellulose-stabilized pickering emulsions by altering cellulose lengths. *Food Hydrocoll.* (2021) 118:106738. doi: 10.1016/j.foodhyd.2021.106738
41. Carrillo W, Gómez-Ruiz JA, Miralles B, Ramos M, Barrio D, Recio I. Identification of antioxidant peptides of hen egg-white lysozyme and evaluation of inhibition of lipid peroxidation and cytotoxicity in the zebrafish model. *Eur Food Res Technol.* (2016) 242:1777-85. doi: 10.1007/s00217-016-2677-1

42. Schmatz DA, Costa J, Morais M. A novel nanocomposite for food packaging developed by electrospinning and electrospraying. *Food Packag Shelf Life.* (2019) 20:100314. doi: 10.1016/j.fpsl.2019.100314
43. Frenot A, Chronakis IS. Polymer nanofibers assembled by electrospinning. *Curr Opin Colloid Interface Sci.* (2003) 8:64-75. doi: 10.1016/S1359-0294(03)00004-9
44. Sen M. Effects of molecular weight and ratio of guluronic acid to mannuronic acid on the antioxidant properties of sodium alginate fractions prepared by radiation-induced degradation. *Appl Radiat Isotopes Includ Data Instrument Methods Use Agri Industry Med.* (2011) 69:126-9. doi: 10.1016/j.apradiso.2010.08.017

Conflict of Interest: The authors declare that the research was conducted in the absence of any commercial or financial relationships that could be construed as a potential conflict of interest.

Publisher's Note: All claims expressed in this article are solely those of the authors and do not necessarily represent those of their affiliated organizations, or those of the publisher, the editors and the reviewers. Any product that may be evaluated in this article, or claim that may be made by its manufacturer, is not guaranteed or endorsed by the publisher.

Copyright © 2022 Qiao, Liu, Wang, Song, Ai and Fu. This is an open-access article distributed under the terms of the Creative Commons Attribution License (CC BY). The use, distribution or reproduction in other forums is permitted, provided the original author(s) and the copyright owner(s) are credited and that the original publication in this journal is cited, in accordance with accepted academic practice. No use, distribution or reproduction is permitted which does not comply with these terms.

frontiers | Frontiers in Nutrition

ORIGINAL RESEARCH
published: 24 May 2022
doi: 10.3389/fnut.2022.887064

The Effect of Glycosylated Soy Protein Isolate on the Stability of Lutein and Their Interaction Characteristics

Xia Wang[1], Shaojia Wang[1], Duoxia Xu[1], Jingwei Peng[2], Wei Gao[2]* and Yanping Cao[1]**

[1] Beijing Advanced Innovation Center for Food Nutrition and Human Health (BTBU), School of Food and Health, Beijing Higher Institution Engineering Research Center of Food Additives and Ingredients, Beijing Technology and Business University (BTBU), Beijing, China, [2] Chenguang Biotech Group Co., Ltd., Handan, China

OPEN ACCESS

Edited by:
Biao Yuan,
China Pharmaceutical University, China

Reviewed by:
Qian Zha,
Shanghai Academy of Agricultural Sciences, China
Zufei Xiao,
Bavarian Office for Forest Seeding and Planting, Germany

***Correspondence:**
Shaojia Wang
wangshaojia@btbu.edu.cn
Wei Gao
gw@cn-cg.com
Yanping Cao
caoyp@th.btbu.edu.cn

Specialty section:
This article was submitted to Food Chemistry, a section of the journal Frontiers in Nutrition

Received: 01 March 2022
Accepted: 11 April 2022
Published: 24 May 2022

Citation:
Wang X, Wang S, Xu D, Peng J, Gao W and Cao Y (2022) The Effect of Glycosylated Soy Protein Isolate on the Stability of Lutein and Their Interaction Characteristics. Front. Nutr. 9:887064. doi: 10.3389/fnut.2022.887064

Lutein is a natural fat-soluble carotenoid with various physiological functions. However, its poor water solubility and stability restrict its application in functional foods. The present study sought to analyze the stability and interaction mechanism of the complex glycosylated soy protein isolate (SPI) prepared using SPI and inulin-type fructans and lutein. The results showed that glycosylation reduced the fluorescence intensity and surface hydrophobicity of SPI but improved the emulsification process and solubility. Fluorescence intensity and ultraviolet–visible (UV–Vis) absorption spectroscopy results showed that the fluorescence quenching of the glycosylated soybean protein isolate by lutein was static. Through thermodynamic parameter analysis, it was found that lutein and glycosylated SPI were bound spontaneously through hydrophobic interaction, and the binding stoichiometry was 1:1. The X-ray diffraction analysis results showed that lutein existed in the glycosylated soybean protein isolate in an amorphous form. The Fourier transform infrared spectroscopy analysis results revealed that lutein had no effect on the secondary structure of glycosylated soy protein isolate. Meanwhile, the combination of lutein and glycosylated SPI improved the water solubility of lutein and the stability of light and heat.

Keywords: soy protein isolate, inulin-type fructans, lutein, stability, interaction

INTRODUCTION

Lutein, an oxygen-containing fat-soluble carotenoid, is widely distributed in flowers, vegetables (1), fruits, egg yolks (2), algae, grains (3), etc. and is mainly derived from marigolds (4). Lutein is also present in the macular pigment of human eyes and plays an indispensable role in preventing eye diseases, such as age-related macular degeneration (AMD) (5). However, it cannot be synthesized within the human body and should be supplied from external sources, such as food (6). Lutein possesses a carbon skeleton and a polyolefin chain (7), a major chromophore group (8). The carbon chain is supported by hydroxyl-containing ionone rings on each side with three stereocenters, β-ionone ring containing a stereo center (3R), and ε-ionone ring containing two stereocenters (3′R and 6′R) (9). The eight conjugated olefins in the carbon chain of the lutein molecule make lutein susceptible to degradation by the external environment (10).

The encapsulation systems, including liposomes, emulsions, gels, and molecular complexes, are often used to inhibit the degradation and improve the stability of biologically active substances, such as lutein (11). Of them, the macromolecules' cavity (such as protein) has attracted increasing interest in the encapsulation of biologically active substances. It is reported that egg white albumin improves the stability of marigold lutein ester extract during storage, and lutein dipalmitate binds spontaneously to egg protein through van der Waals forces and hydrogen bonding (12). Yi et al. (13) found that the stability of lutein increased with the increase of milk protein content, the protective effect of sodium caseinate (SC) on lutein was stronger than the whey protein isolate (WPI), and the milk protein interacted with lutein through hydrophobic bond.

Soy protein isolate (SPI) is a plant protein (about 90% protein) with high nutritional value and is widely used in the food industry (14, 15). It is mainly composed of β-conglycinin (7S, 180–210 kDa) and glycinin (11S, approximately 360 kDa) and accounts for about 70% of the total protein. The 11S component consists of 6 acidic and 6 basic polypeptide chains linked together by disulfide bonds, whereas the 7S is stabilized by hydrophobic interactions (16). In recent years, SPI has been used as a carrier in food-grade delivery systems to improve the stability of biologically active substances. Cao et al. (17) found that SPI could improve the thermal stability of chlorophyll. Tapal and Tiku (18) improved water solubility and bioavailability of curcumin using SPI. Wan et al. (19) also showed that SPI could be used as a carrier of resveratrol (RES) in functional foods, which could improve the water solubility and stability of RES. However, the functional properties of SPI, such as solubility in neutral and mildly acidic environments, severely limit its use as an encapsulation wall material. As such, the physical, chemical, and enzymatic properties of SPI are often modified (16). Physical modification mainly relies on high temperature and high pressure or shearing, making the equipment requirements relatively high and large-scale production difficult. Enzymatic modification is expensive, and protein hydrolysis can make the taste worse. Chemical modification has a high effect on the functional properties of the protein, mainly by introducing food-grade ingredients (20). Glycosylation is a typical chemical modification, which modifies the structure of the protein and improves the functional properties of the protein through a covalent bond between the amino groups of protein and the carbonyl group of the reducing sugar (21). The glycosylation of glucan and protein improves the freeze–thaw stability of SPI hydrolysate (SPIH) emulsion (22), the binding and transporting ability of casein phosphopeptide to calcium (23), the solubility, emulsifying, and foaming ability of peanut protein isolate (24). The emulsifying properties and emulsifying stability of the conjugates of inulin and WPI were significantly higher than the WPI at a pH of 3–7 (25). Inulin-type fructans (ITFs) are linear fructose polymers with predominantly or only β-(2→ 1) fructosyl–fructose linkages (26). Stabilizing the intestinal mucosal barrier, reducing the risk of colon cancer, promoting calcium absorption, and improving constipation are the physiological functions of ITFs (27–33). ITFs are widely used as a prebiotic food ingredient (34). However, the modification effects of ITFs on SPI and ITF-modified SPI on the stability of lutein are still unknown.

Therefore, the present study aimed to study the modification effect of ITFs on SPI and ITF-modified SPI (glycosylated soybean protein isolate, GSPI) on the stability of lutein and the interaction between GSPI and lutein. The study results will provide insights into the preparation of protein-encapsulating systems for embedding lutein and other similar biologically active compounds.

MATERIALS AND METHODS

Materials

Soy protein isolate was purchased from Shanghai Yuanye Bio-Technology Co., Ltd. (Shanghai, China). ITFs and lutein extract were provided by Chenguang Biotech Group Co., Ltd. (Hebei, China). Phosphates were purchased from Shanghai Aladdin Biochemical Technology Co., Ltd. (Shanghai, China). Lutein (97%) was purchased from ChromaDex, USA. Bovine serum albumin (BSA, purity 97%) was obtained from Beijing Solarbio Science and Technology Co., Ltd. (Beijing, China). Sodium 8-naphthalenesulfonate-1-anilino (ANS) ≥97% was purchased from Shanghai Macklin Biochemical Technology Co., Ltd. (Shanghai, China). G250 Coomassie Brilliant Blue Ultra pure grade was purchased from Beijing Boao Tuoda Science and Technology Co., Ltd.

Absolute ethanol (chromatographic grade), methyl tert-butyl ether (chromatographic grade), methanol (chromatographic grade), cyclohexane (chromatographic grade), and N-hexane (chromatographic grade) were purchased from Beijing Merida Technology Co., Ltd. (Beijing, China). Ethyl acetate (analytical grade) and potassium hydroxide (KOH) (analytical grade) were purchased from Tianjin Fuchen Chemical Reagent Company (Tianjin, China). 2, 6-Di-tert-butyl-*p*-cresol (BHT) (analytical grade) was purchased from Shanghai Macklin Biochemical Technology Co., Ltd. (Shanghai, China).

Sample Preparation

Soy protein isolate and ITFs (mass ratio 1:1) were stirred overnight with 10 mM Na_2HPO_4 to make them fully hydrated and adjusted to pH 11 with 0.1 M NaOH to make the final protein concentration of 2% (w/v). The SPI/ITF mixtures were incubated in a water bath at 100°C for 4.7 h (previous research work has confirmed that the GSPI has the highest emulsification ability under this experimental condition). HSPI was the only heated SPI (100°C for 4.7 h), and G-SPI was the physical mixture of SPI and ITFs.

Lutein extract was dissolved in absolute ethanol and stored at 4°C protecting from light. The lutein content in the lutein ethanol solution was expressed as 10 mg/ml with 97% lutein standard product.

For stable analysis of protein and lutein complexes preparation, 15 ml of GSPI and SPI were adjusted to pH 7.0, and then 0.5 ml of lutein extract in absolute ethanol was added dropwise to GSPI and SPI, respectively. Finally, the volume was adjusted to 100 ml with 10 mM pH 7.0 phosphate-buffered saline (PBS) and incubated for 1 h at room temperature.

The complexes of different concentrations of 97% lutein (10, 20, 30, 40, 50, 60, and 70 μM) and GSPI (0.2 mg/ml) were also prepared to explore the interaction between lutein and protein.

Fourier Transform Infrared Spectroscopy

The freeze-dried sample was mixed with KBr at a ratio of 1:100 with KBr as the background. The wave number was 400–4,000 cm^{-1}, and the resolution was 4 cm^{-1} for 32 scans with IS5 infrared spectrometer (Thermo Fisher, USA).

The spectral range of 1,700–1,600 cm^{-1} (amide I) of GSPI and GSPI–lutein were subjected to Fourier deconvolution and second derivative analysis by PeakFit 4.12.

Fluorescence Spectrum

Later, 200 μl of all the samples were transferred to 96-well plates for fluorescence spectroscopy, and the intrinsic fluorescence spectrum was measured by M200 Pro TECAN Infinite multifunctional microplate reader (Tecan Inc., Switzerland).

Excitation Spectrum

The fluorescence excitation spectra of SPI, HSPI, G-SPI, and GSPI were measured at 293 K. The excitation wavelength was set from 250 to 380 nm and the emission wavelength was 420 nm (25).

Emission Spectrum

The fluorescence emission spectra of SPI, HSPI, G-SPI, and GSPI were measured at 293 K, and the fluorescence emission spectra of GSPI (0.2 mg/ml) and lutein (10, 20, 30, 40, 50, 60, and 70 μM) were measured at 293, 303, and 313 K. The emission wavelength was set from 310 to 460 nm, and the excitation wavelength was set at 280 nm, according to the method of Qi et al. (35).

The fluorescence quenching mechanism between GSPI and lutein was explored by the Stern–Volmer equation (1) (17):

$$\frac{F_0}{F} = 1 + K_{SV} \times [Q] = 1 + K_q \times \tau_0 \times [Q] \quad (1)$$

where, F_0 and F are the fluorescence intensity in the absence and presence of lutein. K_{SV} is the Stern–Volmer quenching constant. K_q is the bimolecular quenching rate constant. τ_0 is the average lifetime of the unquenched fluorophore, which is 10^{-8} s. [Q] is the concentration of lutein.

The double logarithmic Stern–Volmer equation was used to analyze the binding sites and binding constants of GSPI and lutein [Equation (2)]. The thermodynamic parameters of GSPI and lutein were determined by Equations (3, 4).

$$\log \frac{(F_0 - F)}{F} = log\, K_a + n\, log[Q] \quad (2)$$

where, n is the number of binding sites. K_a is the binding constant.

$$Ln\, K_a = -\frac{\Delta H}{RT} + \frac{\Delta S}{R} \quad (3)$$

$$\Delta G = \Delta H - T\Delta S = -RT\, Ln\, K_a \quad (4)$$

where, ΔH denotes the enthalpy change, ΔG denotes free energy change, and ΔS denotes entropy change. R denotes the gas constant 8.314 J/ (K mol). T (K) refers to different temperatures (20°C, 30°C, and 40°C).

Surface Hydrophobicity

The 1-anilino-8-naphthalenesulfonate (ANS) was used as a fluorescent probe to measure the surface hydrophobicity (H_0), according to the method of He et al. (20), with slight modifications. The sample was diluted with 10 mM pH 7.0 PBS to 0.01–0.09 mg/ml, then 2 ml of the protein sample was added with 40 μl ANS, and reacted for 10 min in the dark. Approximately 200 μl of each sample was transferred to a 96-well plate, and the fluorescence intensity was measured at 390 nm (excitation wavelength) and 470 nm (emission wavelength) using M200 Pro TECAN Infinite multifunctional microplate reader. The slope of the protein concentration and its corresponding fluorescence intensity were H_0.

Solubility and Emulsification

Solubility

The samples were centrifuged at 4,500 r/min for 15 min using an Avanti JXN-30 floor-standing centrifuge (Beckman, USA). The supernatant was diluted by 200 times, then 1 ml of the diluted solution was added with 5 ml of G250 Coomassie Brilliant Blue, mixed uniformly, and the absorbance was measured at 595 nm using an UVmini-1240 UV Spectrophotometer (Shimadzu, Japan). The samples were measured within 2–30 min. BSA was used as the standard curve to calculate the protein content.

Emulsification

Approximately 40 ml of GSPI and 10 ml of soybean oil were put into a 100-ml beaker, homogenized at a speed of 12,000 r/min for 2 min using T25 digital homogenizing and dispersing instrument (IKA, Germany) (36). Then, 50 μl was taken from the bottom and mixed with 5 ml of 0.1% SDS, and the absorbance values were measured at 500 nm. Afterward, 50 μl of deionized water and 5 ml of 0.1% SDS were adjusted to zero. The emulsifying activity index (EAI) was calculated by Equation (5).

$$EAI\ (m^2/g) = \frac{2 \cdot 2.303 \cdot A \cdot n}{C \cdot \left(1 - \text{“}\varphi''\right) \cdot 10^4} \quad (5)$$

where, A is the absorbance value at 500 nm, n is the dilution factor, C is the protein concentration (g/ml), and ϕ is the oil phase volume.

UV–Vis Absorption Spectroscopy

The mixtures of GSPI and lutein in 2.2 were diluted four times, namely GSPI (0.025 mg/ml) with lutein standards (2.5, 5.0, 7.5, 10, and 12.5 μM). The ultraviolet–visible (UV–Vis) spectra were measured in the wavelength range of 190–350 nm using a 10-mm quartz cell with TU-1900 Dual-Beam UV–Visible Spectrophotometer (Beijing Puxi General Instrument Co., Ltd., China.).

X-Ray Diffraction

The crystal of lutein, GSPI, and GSPI–utein was measured by a D8 Advance X-ray Diffractometer (Bruker Technology Co., Ltd., Germany) at a speed of approximately 2°/min and scanning at an angle (2θ) from 5° to 40°.

Stability of Lutein

Thermal stability: Around 8 ml of lutein, SPI–lutein, and GSPI–lutein were added into a pressure test tube, tightened the tube mouth, and then heated in an oil bath at 120°C for 50 min. The samples were taken every 10 min.

Light stability: Lutein, SPI–lutein, and GSPI–lutein were placed in a 100-ml sample bottle, irradiated under a 302-nm UV lamp for 12 h, and the samples were taken every 2 h for analysis. (The light was perpendicular to the sample, and the distance was about 2 cm.)

Color Measurements

The color characteristics were measured by a CR-800 Spectrophotometer under a reflection mode (Beijing Colorimeter Instrument Equipment Co., Ltd., China). The total color difference (ΔE) was calculated by Equation (6):

$$\Delta E = \sqrt{\left(L^* - L_0^*\right)^2 + \left(a^* - a_0^*\right)^2 + \left(b^* - b_0^*\right)^2} \quad (6)$$

where, ΔE means total color difference. L_0^*, a_0^*, and b_0^* mean the initial color values of the sample. L*, a*, and b* mean the color values of the sample at time *t*. L* means light and dark; a* means red and green, and b* means yellow and blue.

Content and Degradation Kinetics Analysis

Around 5 ml of the above sample was used for stability analysis. Then, 10 ml of absolute ethanol was mixed with 10 ml of 60% KOH, then shaken at room temperature for 3 h, and extracted with cyclohexane:*n*-hexane:ethyl acetate = 1:2:2. The extraction was repeated 3 times. The extracts were combined and rotary evaporated to near dryness in a 30°C water bath, then dissolved to 10 ml using a 0.1% BHT absolute ethanol for HPLC analysis. A standard curve was plotted using 97% lutein to characterize the content changes of lutein during the degradation process.

The change in lutein content was determined by Waters 2,695 HPLC (Waters Technology Co., Ltd., USA). The chromatographic column model was Venusil XBP C30 (5 μm, 250 mm × 4.6 mm). Phase A (methanol:water = 88:12), phase B (methyl tert-butyl ether). At 0–18 min, phase A changed from 100% to 10%; at 18.1 min, phase A changed from 10% to 100%, and kept it for 10 min. The flow rate was 1.0 ml/min, and the injection volume was 50 μl. The degradation rate was calculated by Equation (7), and the degradation kinetics was determined by Equations (8–10).

$$Degradation\ rate = \frac{C_0 - C_t}{C_0} 100\% \quad (7)$$

Kinetic equations (8–10) (37)

$$C_0 C_t = k_0 t \quad (8)$$

$$\mathrm{Ln}\,(C_t/C_0) = k_1 t \quad (9)$$

$$\frac{1}{C_t} - \frac{1}{C_0} = k_2 t \quad (10)$$

where, C_0 represents the initial content of lutein before stability analysis, and C_t represents lutein content at time *t* during stability analysis. k_0, k_1, and k_2 represent the kinetic constants.

Size Distribution

The particle size of lutein, GSPI, and GSPI–lutein was measured by an S3500 laser particle size analyzer (Microtrac, Germany). The sample was added dropwise to the sample cell until the screen showed ready, and then proceeded to the particle size distribution measurement.

Statistical Analysis

The images were generated by Origin 2021 software. The data were analyzed by one-way analysis of variance using IBM SPSS statistics 26. The significance analysis was done by LSD and Duncan's test ($p < 0.05$).

RESULTS AND DISCUSSION

Effect of Glycosylation on Protein Properties

Fourier Transform Infrared Spectroscopy

Fourier transform infrared (FTIR) could determine the occurrence of glycosylation reaction. The amide I bands (1,700–1,600 cm^{-1}) and amide II bands (1,600–1,500 cm^{-1}) of protein are the most sensitive regions related to protein conformation (38). The C=O stretching vibration of the peptide bond, the C–N stretching vibration of the amino group, and the N–H bending of the amino group are the characteristics of this amide zone (39). **Figure 1A** depicts the FTIR results of SPI, HSPI, ITFs, and GSPI under the range of 4,000–400 cm^{-1}. The amide I region of the GSPI absorption peak shifted from 1659.09 to 1658.38 cm^{-1}, and the absorption intensity was slightly reduced, which might be due to the decrease in the carbonyl content. The Schiff base and pyrazine formed during glycosylation showed an absorption at 1658.38 cm^{-1} (23). The amide II band shifted from 1536.99 to 1548.99 cm^{-1}, and the absorption peak of GSPI was stronger than SPI, indicating that the glycosylation product was formed by covalent bonds. This result was consistent with the results of glycosylated modified egg white protein pretreated by ball milling (40). The absorption intensity of GSPI was higher than SPI at the wavenumber of 1057.58 cm^{-1}, indicating that GSPI produces a new C–N covalent bond, which was consistent with the findings of WPI and inulin (25). Additionally, there was a

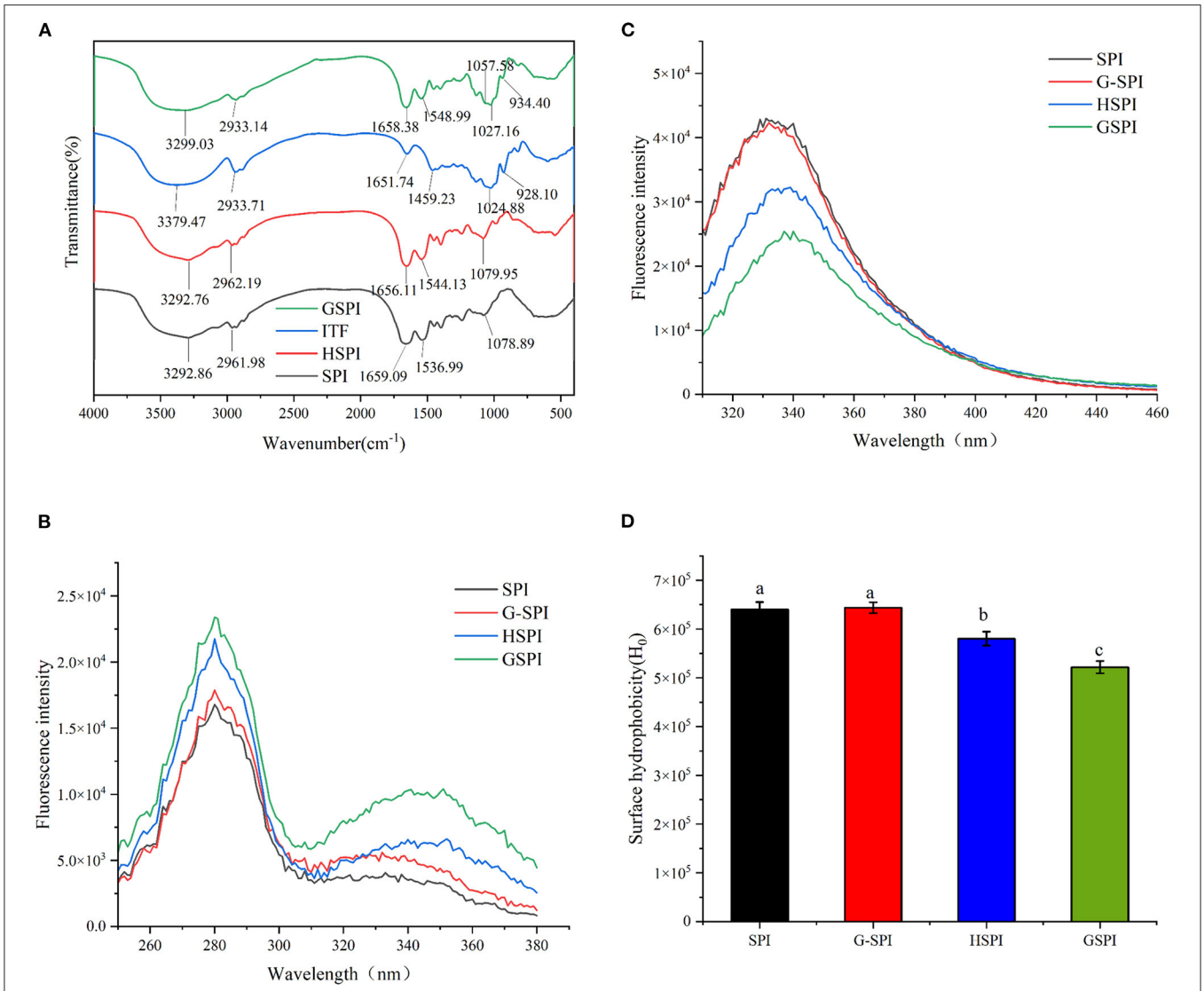

FIGURE 1 | (A) The Fourier transform infrared spectroscopy of SPI, HSPI, ITFs, and GSPI. **(B)** Fluorescence excitation spectroscopy of 0.1 mg/ml SPI, HSPI, G-SPI, GSPI, $T = 293$ K, pH = 7.0, $\lambda_{ex} = 280$ nm, and $\lambda_{em} = 310$–460 nm. **(C)** Fluorescence emission spectroscopy of 0.1 mg/ml SPI, HSPI, G-SPI, GSPI, $T = 293$ K, pH = 7.0, $\lambda_{em} = 420$ nm, and $\lambda_{ex} = 250$–380 nm. **(D)** Surface hydrophobicity of 0.01–0.09 mg/ml SPI, HSPI, G-SPI, GSPI, $T = 293$ K, pH = 7.0, $\lambda_{em} = 470$ nm, and $\lambda_{ex} = 390$ nm. Different letters indicate significant differences.

broad stretching vibration peak at 3,700–3,200 cm^{-1}, intimating the existence of hydrogen bonds and the increase of free hydroxyl content. This result was consistent with the Maillard reaction products of whey protein and flaxseed gum (41).

Fluorescence Intensity

Glycosylation is a chemical method for modifying proteins by covalent bonding between the proteins and sugars (40). The fluorescent substances with characteristic peaks between 340 and 370 nm are produced during a reaction (42). As depicted in **Figure 1B**, SPI, HSPI, G-SPI, and GSPI had a characteristic protein excitation wavelength at 280 nm, whereas GSPI had another maximum excitation wavelength at 351 nm. These results confirmed the occurrence of the Maillard reaction and the production of fluorescent substances. This was consistent with the previous research result showing that WPI and inulin had a maximum fluorescence excitation wavelength of 344 nm (25). **Figure 1C** depicts the fluorescence emission spectrum, indicating that the fluorescence intensity of SPI and G-SPI had not much difference. The fluorescence intensity of GSPI was less than SPI, suggesting that ITFs had a shielding effect on the fluorescence of SPI. Some previous studies had also manifested that the fluorescence intensity of glycosylated protein was less than the original protein (43), and this effect increased with the decrease of dextran molecular weight. Notably, heating increased the fluorescence intensity of the protein, and the fluorescence intensity of WPI increased by dry heat treatment (44). However, in this study, the fluorescence intensity of HSPI was less than

SPI. Therefore, it was speculated that this phenomenon was caused by extreme pH. Zhao et al. (45) revealed that extreme alkaline pH treatment of PSE-like chicken proteins had the same result.

Surface Hydrophobicity

Surface hydrophobicity is one of the essential functional properties of the protein, reflecting protein conformation and structure (46). ANS is commonly used as a probe to determine H_0 of proteins, which binds to the hydrophobicity of proteins efficiently (47). **Figure 1D** depicts the change in H_0 of SPI, G-SPI, HSPI, and GSPI, indicating that the physical mixture of SPI and ITFs was not significantly different from the H_0 of SPI. Compared with SPI, the H_0 of HSPI was significantly lower, which might be due to the fact that the alkaline conditions could make the protein fold and reduce the exposure of the SPI hydrophobic group. The H_0 decreased significantly after glycosylation and the exposed hydrophobic groups of SPI bound to ITFs, resulting in a decrease in H_0. In previous studies, the same results were obtained after glycosylation of SPI with *Pleurotus eryngii* polysaccharide (PEP) or dextran (DX) (20, 43). H_0 was consistent with the fluorescence emission spectroscopy results, and similar results were obtained under extremely acidic pH excursions and mild heating conditions for SPI (48).

Emulsification and Solubility

The EAI of protein is involved in several parameters, such as solubility, hydrophobicity, and structural flexibility (49). EAI is often used to indicate the emulsification of protein. As shown in **Figure 2A**, The EAI of SPI and GSPI were measured at different pH conditions, and the results showed that the emulsifying ability of GSPI was greater than SPI under the pH range of 5.5–7.5. Compared with GSPI, the EAI values of SPI were much more affected by pH. The poor solubility of SPI limits its application. The solubility of glycosylation significantly increased, and the protein content of GSPI diluted by centrifugation was 56.29 ± 0.96–59.30 ± 1.85 μg/ml, with no significant change in pH 5.5–7.5, whereas SPI had poor solubility in neutral and weakly acidic conditions (**Figure 2B**).

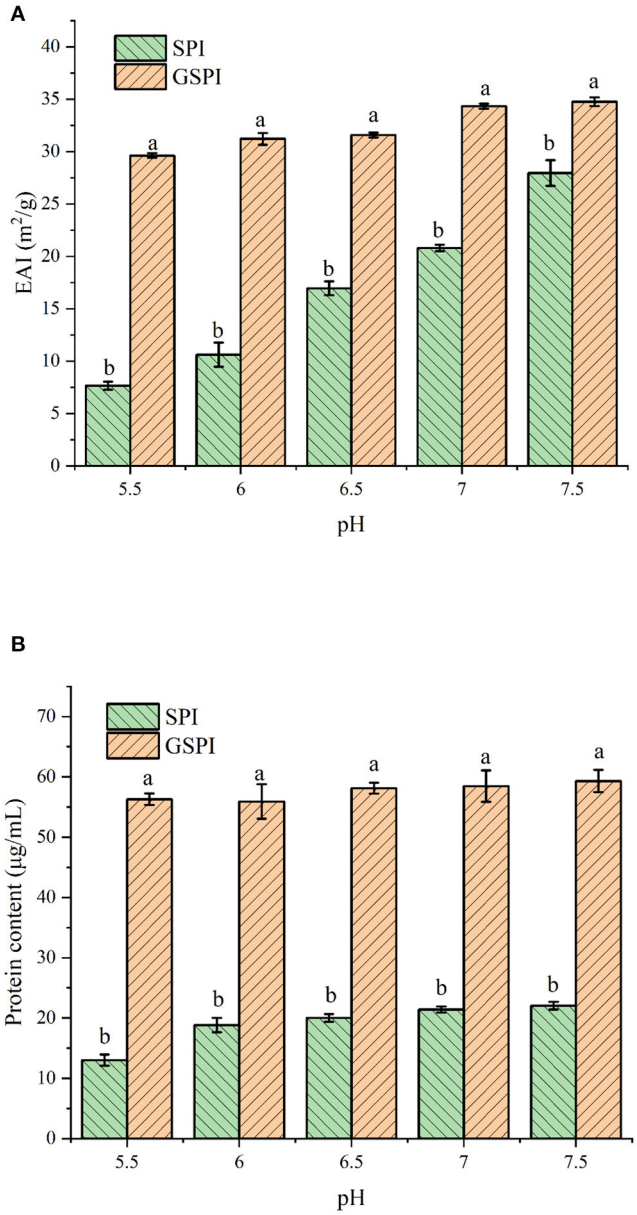

FIGURE 2 | (A) Emulsification of SPI and GSPI at pH 5.5–7.5. **(B)** Solubility of SPI and GSPI at pH 5.5–7.5. Different letters indicate significant differences between SPI and GSPI at the same pH.

Interaction Between GSPI and Lutein

Fluorescence Quenching

Fluorescence quenching methods could reveal the protein conformation and/or dynamic changes in the macromolecular systems. The Stern–Volmer equation is the easiest method to determine the quenching pattern (50). Quenching occurs when the quencher is located near or in contact with the fluorophore (51). Protein fluorescence arises from the presence of multiple fluorophores, mainly including three aromatic amino acids—Phe, Tyr, and Trp (52). The changes in the amino acid environment change the fluorescence intensity. As depicted in **Figure 3A**, with the increase of lutein (10, 20, 30, 40, and 50 μM), the fluorescence intensity of GSPI continued to decrease, accompanied by a red shift, indicating an interaction between lutein and GSPI, which changed the microenvironment of the fluorophore (53).

Fluorescence quenching includes static quenching, dynamic quenching, and combined static and dynamic quenching. Static quenching is caused by the formation of complexes, whereas dynamic quenching is caused by intermolecular collisions. The dynamic and static combination quenching is caused by the formation of complexes and intermolecular collisions. As shown in **Figure 3B** and **Table 1**, the slope (K_{SV}) of 303 and 313 K was >293 K, indicating that the fluorescence quenching of GSPI was caused by the collision of lutein and GSPI, which was a sign of dynamic quenching. However, the value of K_q

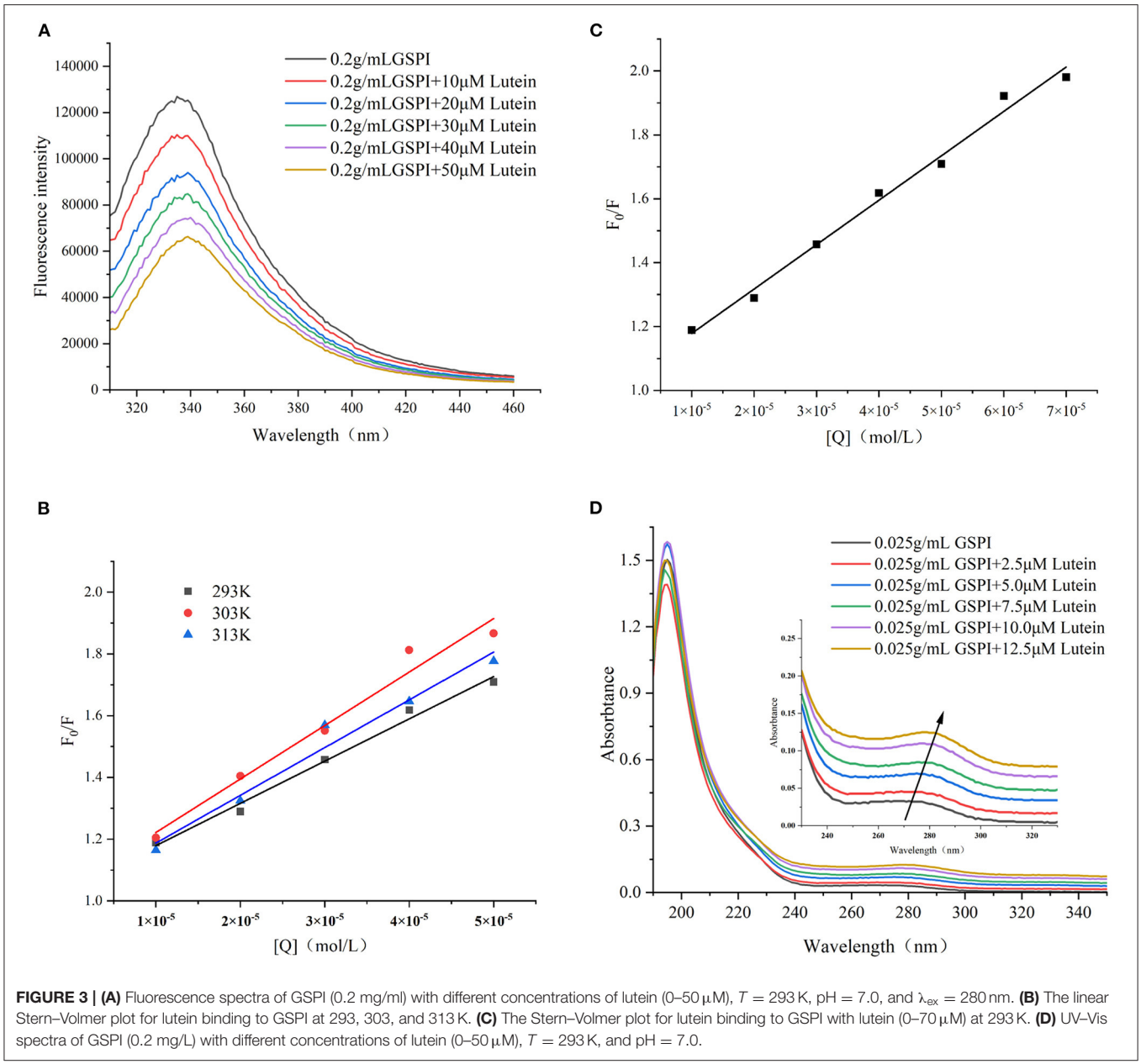

FIGURE 3 | (A) Fluorescence spectra of GSPI (0.2 mg/ml) with different concentrations of lutein (0–50 μM), $T = 293$ K, pH = 7.0, and $\lambda_{ex} = 280$ nm. **(B)** The linear Stern–Volmer plot for lutein binding to GSPI at 293, 303, and 313 K. **(C)** The Stern–Volmer plot for lutein binding to GSPI with lutein (0–70 μM) at 293 K. **(D)** UV–Vis spectra of GSPI (0.2 mg/L) with different concentrations of lutein (0–50 μM), $T = 293$ K, and pH = 7.0.

far exceeded the maximum value of the dynamic quenching rate constant [10^{10}/(mol s)], indicating that the quenching was static. Thus, it could not be concluded if it is a static or dynamic quenching.

The quenching effects of high lutein concentration on GSPI fluorescence and UV–Vis were studied to evaluate the type of quenching between GSPI and lutein. In the case of dynamic quenching, the relationship between F_0/F and high-lutein concentration might concave toward the Y-axis (54). **Figure 3C** depicts a good linear relationship between increasing lutein concentration and F_0/F ($R^2 = 0.9901$), with no concave to the Y-axis (55). It also confirmed that there was no dynamic quenching between lutein and GSPI.

TABLE 1 | Lutein induces the Stern–Volmer quenching constant (K_{SV}) and bimolecular quenching rate (K_q) of GSPI at different temperatures (293, 303, and 313 K).

T (K)	K_{SV} (10^4/mol)	K_q (10^{12}/(mol s))	R^2
293	1.3689	1.3689	0.9899
303	1.7122	1.7122	0.9739
313	1.5495	2.7171	0.9715

Ultraviolet–visible is a simple and effective method for the interaction between small molecules and proteins (56). Dynamic quenching does not change the absorption spectrum of the

fluorophore, whereas complex formation (static quenching) changes the absorption spectrum of the fluorophore (57, 58). As depicted in **Figure 3D**, with the addition of lutein, the absorption intensity of the ultraviolet spectrum increased, which was accompanied by a significant red shift ($\Delta\lambda$ = 10 nm). This indicated that lutein formed a complex with GSPI (59), leading to a red shift in the spectrum (60, 61). Therefore, lutein quenched the fluorescence of GSPI by static quenching.

Binding Forces and Thermodynamic Parameters

The binding constant (K_a value) reflects the strength of the binding force (62). As depicted in **Figure 4**, the lg $[(F_0\text{-}F)/F]$ and lg[Q] presented a good linear relationship ($R^2 > 0.98$). The n-values of the three different temperatures at 293, 303, and 313 K were 0.8551, 0.9237, and 0.9861, respectively, indicating that there was only one binding site. The K_a values of lutein and GSPI interaction at 293, 303, and 313 K showed an increasing trend with the increase in temperature (**Table 2**), suggesting that the GSPI–lutein complex was relatively stable at higher temperatures (63).

The thermodynamic parameters, such as ΔG, ΔH, and ΔS, could reveal the GSPI–lutein interaction (64). The value and sign of ΔH and ΔS could reflect the interaction force between small molecules and proteins (65). The forces between the biologically active substances and proteins mainly include hydrophobic interaction, hydrogen bonding, van der Waals force, electrostatic attraction, etc. (66). The interaction force could be divided into four types: for $\Delta H > 0$ and $\Delta S > 0$, the main force is hydrophobic interaction; for $\Delta H > 0$ and $\Delta S < 0$, the main force is electrostatic and hydrophobic interaction; for $\Delta H < 0$ and $\Delta S < 0$, hydrogen bonding and van der Waals force play a major role; and for $\Delta H < 0$ and $\Delta S > 0$, electrostatic interaction plays a principal role (67). As summarized in **Table 2**, $\Delta H > 0$ and $\Delta S > 0$ demonstrated that the interaction force between lutein and GSPI was mainly hydrophobic interaction. Yi et al. (13) reported similar results for WPI and SC (13). Furthermore, the values of ΔG (−20.09, −22.85, and −24.91 kJ mol^{-1}) were negative at 293, 303, and 313 K, indicating spontaneous binding of lutein with GSPI.

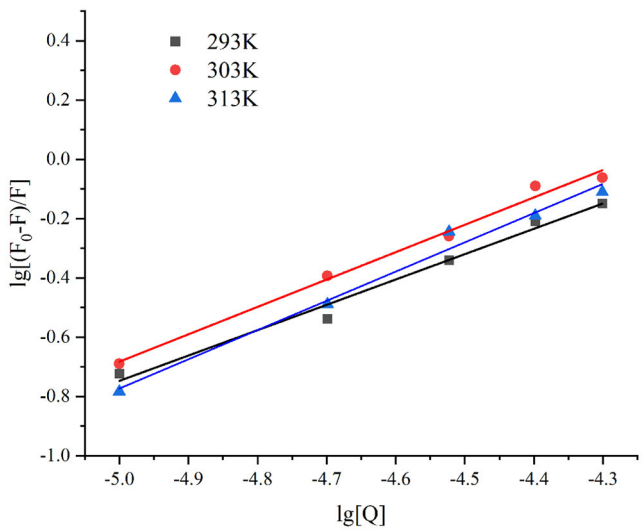

FIGURE 4 | The linear plot of lg $[(F_0\text{-}F)/F]$ against lg [Q] at different temperatures, T = 293, 303, and 313 K.

X-Ray Diffraction

The crystal analysis of the sample was performed by XRD. **Figure 5** depicts the diffraction patterns of lutein, GSPI, and GSPI–lutein. Lutein showed a strong diffraction peak within 10°-25° (2θ), suggesting that lutein had a highly crystalline structure. After the combination of lutein and GSPI, the frontal characteristic diffraction peak of lutein did not appear, showing the presence of lutein in GSPI in an amorphous form (68).

Secondary Structure Analysis

The combined effect of lutein on the structural changes of GSPI was studied by an FTIR. GSPI was used as a control. As described in Section 3.1.2, the amide I region was the most sensitive region related to protein conformation. The amide I region in the FTIR spectra of GSPI and GSPI–lutein was analyzed, and the secondary structural data were obtained by calculating the integrated area of each sub-peak in the 1,600–1,700 cm^{-1} spectrum. The ratio of each secondary structure of GSPI and GSPI–lutein is depicted in **Figure 6**. The FTIR spectra indicated that GSPI–lutein was bound through hydrophobic interaction and had little effect on its secondary structure. These results were consistent with the previous study results reporting that SPIHs interacting with cyanin-3-O-glucoside (Cy3G) (60) and SPI (unheated and heated) combined with curcumin (69) had no significant effect on the secondary structure of the protein.

Effect of GSPI on the Stability of Lutein

Color Analysis

In addition to physiological functions, lutein is also popular as a coloring agent. Therefore, studying its color changes has high significance. The smaller the total color difference (ΔE), the more stable the lutein (70). $\Delta E > 3$ indicated a very significant

TABLE 2 | Binding parameters and thermodynamic parameters of GSPI–lutein system at different temperatures.

T (K)	K_a (10^4 L /mol)	n	R^2	ΔH (kJ mol^{-1})	ΔS (kJ mol^{-1})	ΔG (kJ mol^{-1})
293	0.3189	0.8551	0.9846	50.64	241.79	−20.09
303	0.8701	0.9237	0.9908			−22.85
313	1.4315	0.9861	0.9854			−24.91

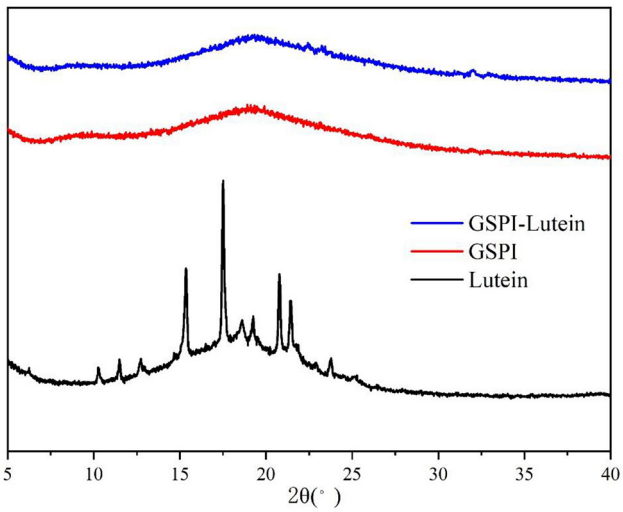

FIGURE 5 | X-ray diffraction of lutein, GSPI, and GSPI–lutein.

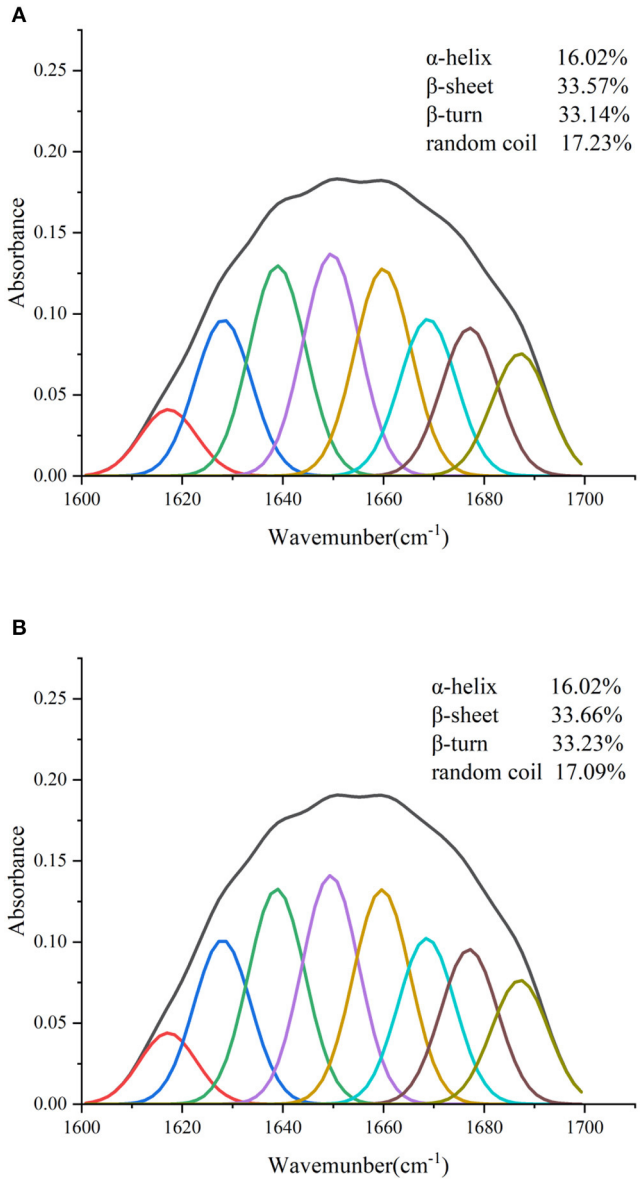

FIGURE 6 | Fourier transform infrared spectrogram of GSPI and GSPI–lutein in the region of 1,600–1,700 cm^{-1}. **(A)** GSPI and **(B)** GSPI–lutein.

difference, $1.5 < \Delta E < 3$ indicated a significant difference, $\Delta E < 1.5$ indicated a small difference (71). As depicted in **Figure 7A**, ΔE of lutein reached 11.83 ± 0.18 at 5 h of light exposure. At this time, the ΔE of SPI–lutein and GSPI–lutein was lower, accounting for 1.04 ± 0.06 and 0.41 ± 0.74, respectively. This result indicated that protein had a positive effect on the photostability of lutein. The difference between SPI–lutein and GSPI–lutein appeared with the prolongation of light time. When the light time was 12 h, the ΔE of SPI–lutein and GSPI–lutein was significantly different, accounting for 7.65 ± 1.34 and 1.91 ± 0.18, respectively. GSPI–lutein exhibited better light stability than lutein and SPI–lutein. However, the advantage of thermal stability was not good as light stability (**Figure 7B**). At 120°C oil bath for 50 min, the ΔE of lutein was 9.42 ± 0.52, the ΔE of SPI–lutein was 6.20 ± 0.08, and the ΔE of GSPI–lutein was 5.58 ± 0.08. Overall, GSPI had a better effect on the color stability of lutein than SPI.

Degradation Rate

Lutein is sensitive to environmental factors, such as light and heat, due to its high degree of unsaturation. **Figure 7C** depicts the degradation rates of lutein, SPI–lutein, and GSPI–lutein under the influence of light and heat, respectively. The degradation rate and total color difference showed the same trend. When lutein was exposed to light for 4 h, the degradation rate reached as high as 95.41% ± 0.34. At this time, the degradation rates of SPI–lutein and GSPI–lutein were 15.78% ± 5.56 and 9.40% ± 2.13, respectively. Compared with lutein, the degradation rate of GSPI–lutein was reduced by about 86.01%. Lutein was completely degraded at 5 h (not shown). With the increase in light time, the degradation rate of GSPI–lutein was always lower than SPI–lutein. Thermal degradation for 10 min showed a significant protective effect of the protein, but there was no significant difference in the protective effect of SPI and GSPI. After 50 min, the degradation rate of lutein was 89.46% ± 0.21, the degradation rate of SPI–lutein was 77.48% ± 0.94, and the degradation rate of GSPI–lutein was 65.96% ± 0.82 (**Figure 7D**). Overall, GSPI–lutein has excellent light stability and fine stability at high temperatures and short time. Additionally, lutein (with or without protein) followed the first-order degradation kinetics at 120°C and zero-order degradation kinetics under UV light at 25°C (**Table 3**).

Particle Size Analysis

The particle size affects the stability of the lutein system (32, 72). The smaller the particle size, the greater the stability in the aqueous solution. As depicted in **Figure 8**, the average particle

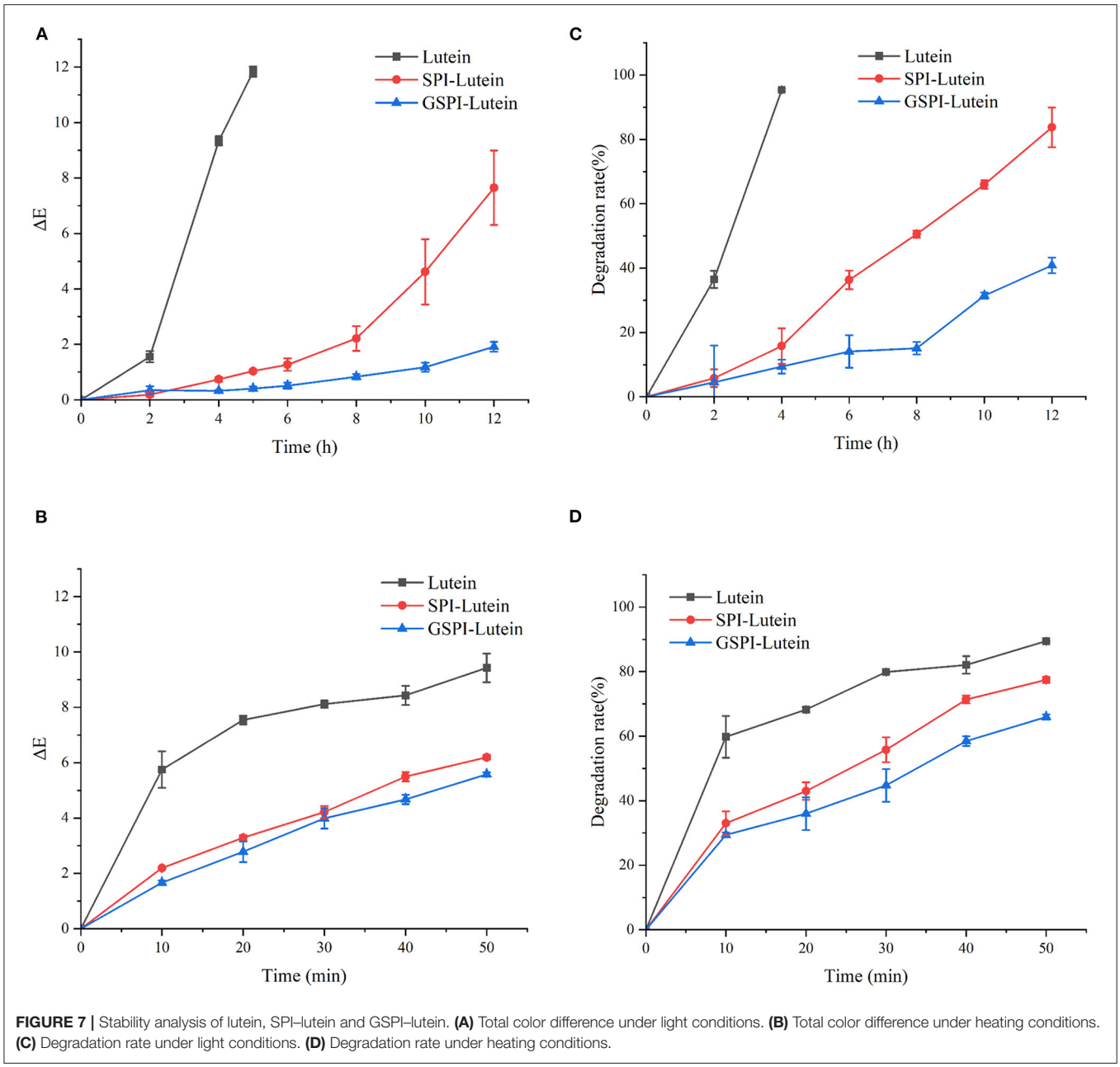

FIGURE 7 | Stability analysis of lutein, SPI–lutein and GSPI–lutein. **(A)** Total color difference under light conditions. **(B)** Total color difference under heating conditions. **(C)** Degradation rate under light conditions. **(D)** Degradation rate under heating conditions.

TABLE 3 | Correlation coefficients of zero-order, first-order, and second-order kinetic models for the lutein degradation.

Correlation coefficient	R_0	R_1	R_2
120°C	0.9676	0.9923	0.9792
25°C UV light	0.9826	0.9677	0.9477

size of lutein in the aqueous solution was about 2 μm. The average particle sizes of SPI and SPI–lutein were about 83.34 and 84.15 μm, respectively. The average particle sizes of GSPI and GSPI–lutein were about 212 and 219 nm, respectively. GSPI and GSPI–lutein had lower particle sizes, indicating that they were more stable in the aqueous solutions.

CONCLUSION

In this study, the effects of glycosylation on the structure and stability of SPI were investigated by fluorescence spectroscopy, FTIR, emulsification, and solubility. The results showed that the glycosylation reaction occurred, and GSPI had better emulsification and solubility than SPI. Then, the interaction between GSPI and lutein was investigated by fluorescence quenching, thermodynamic binding parameters, UV–Vis, and

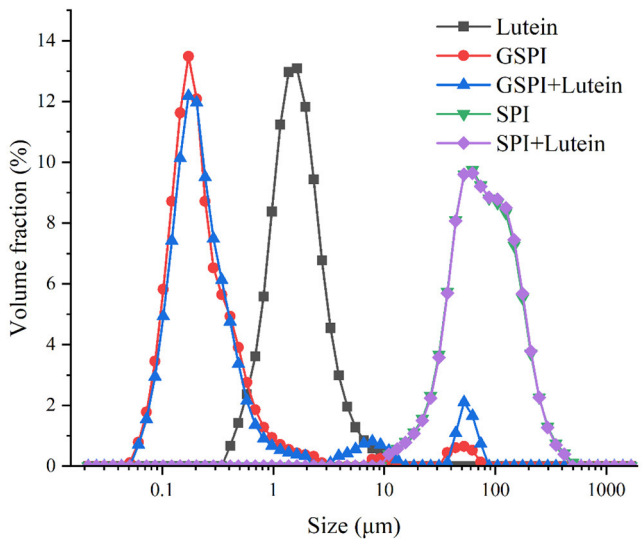

FIGURE 8 | Particle size distribution of lutein, GSPI, GSPI–lutein, SPI, and SPI–lutein.

XRD. The results indicated that lutein was spontaneously bound to GSPI at a stoichiometric of 1:1. The fluorescence of GSPI was quenched by static quenching during the binding process, which slightly affected the secondary structure of GSPI. Finally, the total color difference and degradation rate results showed that GSPI had a better stabilization effect on lutein.

DATA AVAILABILITY STATEMENT

The datasets presented in this study can be found in online repositories. The names of the repository/repositories and accession number(s) can be found in the article/supplementary material.

AUTHOR CONTRIBUTIONS

XW: data management, investigation, validation, and writing—original draft. SW: methodology, project management, and writing—review and editing. DX: fund acquisition and supervision. JP: resources, concepts, and supervision. WG: project management, resources, and capital acquisition. YC: conceptualization, project management, and supervision. All authors contributed to the article and approved the submitted version.

FUNDING

This research was supported by the National Natural Science Foundation of China (31871808), the School Level Cultivation Fund of Beijing Technology and Business University for Distinguished and Excellent Young Scholars (BTBUYP2020), the Construction of Service Capability of Scientific and Technological Innovation (PXM2019_014213_000010, PXM2018_014213_000033, PXM2018_014213_000014, PXM2018_0142 13_000041, and 19005857058), and the Cultivation and Development of Innovation Base (Z171100002217019).

ACKNOWLEDGMENTS

We would like to thank MogoEdit (https://www.mogoedit.com) for its English editing during the preparation of this manuscript.

REFERENCES

1. Chung RWS, Leanderson P, Gustafsson N, Jonasson L. Liberation of lutein from spinach: Effects of heating time, microwavereheating and liquefaction. *Food Chem.* (2019) 277:573–8. doi: 10.1016/j.foodchem.2018.11.023
2. Youjia F, Jingde Y, Longwei J, Lili R, Jiang Z. Encapsulation of lutein into starch nanoparticles to improve its dispersity in water and enhance stability of chemical oxidation. *Starch/Staerke.* (2019) 71:1800248. doi: 10.1002/star.201800248
3. Ziegler JU, Wahl S, Wurschum T, Longin CF, Carle R, Schweiggert RM. Lutein and lutein esters in whole grain flours made from 75 genotypes of 5 triticum species grown at multiple sites. *J Agric Food Chem.* (2015) 63:5061–71. doi: 10.1021/acs.jafc.5b01477
4. Cheng X, Zhao XZ, Huang CL, Zhang XH Lyu YM. Lutein content in petals and leaves of marigold and analysis of lutein synthesis gene expression. *Acta Physiologiae Plantarum.* (2019) 41:128. doi: 10.1007/s11738-019-2913-y
5. Hentschel V, Kranl K, Hollmann J, Lindhauer MG, Bohm V, Bitsch R. Spectrophotometric determination of yellow pigment content and evaluation of carotenoids by high-performance liquid chromatography in durum wheat grain. *J Agric Food Chem.* (2002) 50:6663–8. doi: 10.1021/jf025701p
6. Yoshizako H, Hara K, Takai Y, Kaidzu S, Obana A, Ohira A. Comparison of macular pigment and serum lutein concentration changes between free lutein and lutein esters supplements in Japanese subjects. *Acta Ophthalmol.* (2016) 94:e411–e6. doi: 10.1111/aos.13106
7. Lyu ZJ, Wang F, Liu P, Zhang K, Sun Q, Bai X, et al. One-pot preparation of lutein block methoxy polyethylene glycol copolymer-coated lutein nanoemulsion. *Colloid Polym Sci.* (2021) 299:1055–62. doi: 10.1007/s00396-021-04824-7
8. Rodriguez-Concepcion M, Avalos J, Luisa Bonet M, Boronat A, Gomez-Gomez L, Hornero-Mendez D, et al. A global perspective on carotenoids: Metabolism, biotechnology, and benefits for nutrition and health. *Prog Lipid Res.* (2018) 70:62–93. doi: 10.1016/j.plipres.2018.04.004
9. Horvath MP, George EW, Tran QT, Baumgardner K, Zharov G, Lee S. et al. Structure of the lutein-binding domain of human StARD3 at 174 angstrom resolution and model of a complex with lutein. *Acta Crystallogr F Struct Biol Commun.* (2016) 72:609–18. doi: 10.1107/S2053230X16010694
10. Huang J, Bai F, Wu Y, Ye Q, Liang D, Shi C, et al. Development and evaluation of lutein-loaded alginate microspheres with improved stability and antioxidant. *J Sci Food Agric.* (2019) 99:5195–201. doi: 10.1002/jsfa.9766
11. Steiner BM, McClements DJ, Davidov-Pardo G. Encapsulation systems for lutein: a review. *Trends Food Sci Technol.* (2018) 82:71–81. doi: 10.1016/j.tifs.2018.10.003
12. Qi X, Xu DX, Zhu JJ, Wang SJ, Peng JW, Gao W, et al. Interaction of ovalbumin with lutein dipalmitate and their effects on the color

stability of marigold lutein esters extracts. *Food Chem.* (2022) 372:131211. doi: 10.1016/j.foodchem.2021.131211
13. Yi J, Fan Y, Yokoyama W, Zhang Y, Zhao L. Characterization of milk proteins-lutein complexes and the impact on lutein chemical stability. *Food Chem.* (2016) 200:91–7. doi: 10.1016/j.foodchem.2016.01.035
14. Chee-Yuen G, Wen-Hwei O, Lee-Min W, Azhar Mat E. Effects of ribose, microbial transglutaminase and soy protein isolate on physical properties and in-vitro starch digestibility of yellow noodles. *LWT – Food Sci Technol.* (2009) 42:174–9. doi: 10.1016/j.lwt.2008.05.004
15. Zhang Y, Chen S, Qi B, Sui X, Jiang L. Complexation of thermally-denatured soybean protein isolate with anthocyanins and its effect on the protein structure and in vitro digestibility. *Food Res Int.* (2018) 106:619–25. doi: 10.1016/j.foodres.2018.01.040
16. Sharif HR, Williams PA, Sharif MK, Abbas S, Majeed H, Masamba KG, et al. Current progress in the utilization of native and modified legume proteins as emulsifiers and encapsulants - a review. *Food Hydrocoll.* (2018) 76:2–16. doi: 10.1016/j.foodhyd.2017.01.002
17. Cao JR Li FW, Li YY, Chen HP, Liao XJ, Zhang Y. Hydrophobic interaction driving the binding of soybean protein isolate and chlorophyll: Improvements to the thermal stability of chlorophyll. *Food Hydrocoll.* (2021) 113:106465. doi: 10.1016/j.foodhyd.2020.106465
18. Tapal A, Tiku PK. Complexation of curcumin with soy protein isolate and its implications on solubility and stability of curcumin. *Food Chem.* (2012) 130:960–5. doi: 10.1016/j.foodchem.2011.08.025
19. Wan ZL, Wang JM, Wang LY, Yuan Y, Yang XQ. Complexation of resveratrol with soy protein and its improvement on oxidative stability of corn oil/water emulsions. *Food Chem.* (2014) 161:324–31. doi: 10.1016/j.foodchem.2014.04.028
20. He M. Y., Li L, Wu C, Zheng L, Jiang L, Huang Y, et al. Effects of glycation and acylation on the structural characteristics and physicochemical properties of soy protein isolate. *J Food Sci.* (2021) 86:1737–50. doi: 10.1111/1750-3841.15688
21. Zhang H, Chi Y. Modified soy protein isolate with improved gelling stability by glycosylation under the conditions of ocean shipping. *Int J Food Sci Technol.* (2011) 46:14–22. doi: 10.1111/j.1365-2621.2010.02355.x
22. Zhang Z, Wang X, Yu J, Chen S, Ge H, Jiang L. Freeze-thaw stability of oil-in-water emulsions stabilized by soy protein isolate-dextran conjugates. *Lwt-Food Sci Technol.* (2017) 78:241–9. doi: 10.1016/j.lwt.2016.12.051
23. Jiang L, Li S, Wang N, Zhao S, Chen Y, Chen Y. Preparation of dextran-casein phosphopeptide conjugates, evaluation of its calcium binding capacity and digestion *in vitro*. *Food Chem.* (2021) 352:129332. doi: 10.1016/j.foodchem.2021.129332
24. Liu Y, Zhao GL, Zhao MM, Ren JY, Yang B. Improvement of functional properties of peanut protein isolate by conjugation with dextran through Maillard reaction. *Food Chem.* (2012) 131:901–6. doi: 10.1016/j.foodchem.2011.09.074
25. Wang W, Li C, Bin Z, Huang Q, You L, Chen C, et al. Physicochemical properties and bioactivity of whey protein isolate-inulin conjugates obtained by Maillard reaction. *Int J Biol Macromol.* (2020) 150:326–35. doi: 10.1016/j.ijbiomac.2020.02.086
26. Apolinario AC, Goulart de. Lima Damasceno BP, de Macedo Beltrao NE, Pessoa A, Converti A, da Silva JA. Inulin-type fructans: a review on different aspects of biochemical and pharmaceutical technology. *Carbohydrate Polymers.* (2014) 101:368–78. doi: 10.1016/j.carbpol.2013.09.081
27. Closa-Monasterolo R, Ferre N, Castillejo-DeVillasante G, Luque V, Gispert-Llaurado M, Zaragoza-Jordana M, et al. The use of inulin-type fructans improves stool consistency in constipated children. a randomised clinical trial: pilot study. *Int J Food Sci Nutr.* (2017) 68:587–94. doi: 10.1080/09637486.2016.1263605
28. Coxam V. Current data with inulin-type fructans and calcium, targeting bone health in adults. *J Nutr.* (2007) 137:2527S—33S. doi: 10.1093/jn/137.11.2527S
29. Kleessen B, Blaut M. Modulation of gut mucosal biofilms. *Br J Nutr.* (2005) 93:S35–40. doi: 10.1079/BJN20041346
30. Pool-Zobel BL. Inulin-type fructans and reduction in colon cancer risk: review of experimental and human data. *Br J Nutr.* (2005) 93:S73–90. doi: 10.1079/BJN20041349
31. Roberfroid MB. Introducing inulin-type fructans. *Br J Nutr.* (2005) 93:S13–25. doi: 10.1079/BJN20041350
32. Roberfroid MB. Inulin-type fructans: Functional food ingredients. *J Nutr.* (2007) 137:2493S—502. doi: 10.1093/jn/137.11.2493S
33. Scholz-Ahrens KE, Schrezenmeir J. Inulin and oligofructose and mineral metabolism: The evidence from animal trials. *J Nutr.* (2007) 137:2513S—23. doi: 10.1093/jn/137.11.2513S
34. Boehm A, Kaiser I, Henle T. Heat-induced degradation of inulin. *Eur Food Res Technol.* (2005) 220:466–71. doi: 10.1007/s00217-004-1098-8
35. Qi X, Xu DX, Zhu JJ, Wang SJ, Peng JW, Gao W, et al. Studying the interaction mechanism between bovine serum albumin and lutein dipalmitate: multi-spectroscopic and molecular docking techniques. *Food Hydrocoll.* (2021) 113:106513. doi: 10.1016/j.foodhyd.2020.106513
36. He M, Wu C, Li L, Zheng L, Tian T, Jiang L, et al. Effects of cavitation Jet treatment on the structure and emulsification properties of oxidized Soy Protein Isolate. *Foods.* (2020) 10:2. doi: 10.3390/foods10010002
37. Song JF Li DJ, Pang HL, Liu CQ. Effect of ultrasonic waves on the stability of all-trans lutein and its degradation kinetics. *Ultrason Sonochem.* (2015) 27:602–8. doi: 10.1016/j.ultsonch.2015.04.020
38. Sharafodin H, Soltanizadeh N. Potential application of DBD Plasma Technique for modifying structural and physicochemical properties of Soy Protein Isolate. *Food Hydrocoll.* (2022) 122:107077. doi: 10.1016/j.foodhyd.2021.107077
39. Dursun Capar T, Yalcin H. Protein/polysaccharide conjugation via Maillard reactions in an aqueous media: impact of protein type, reaction time and temperature. *LWT – Food Sci Technol.* (2021) 152:112252. doi: 10.1016/j.lwt.2021.112252
40. Wu Y, Zhang Y, Duan W, Wang Q, An F, Luo P, et al. Ball-milling is an effective pretreatment of glycosylation modified the foaming and gel properties of egg white protein. *J Food Eng.* (2022) 319:110908. doi: 10.1016/j.jfoodeng.2021.110908
41. Zhang Z, Chen W, Zhou X, Deng Q, Dong X, Yang C, et al. Astaxanthin-loaded emulsion gels stabilized by Maillard reaction products of whey protein and flaxseed gum: Physicochemical characterization and in vitro digestibility. *Food Res Int.* (2021) 144:110321. doi: 10.1016/j.foodres.2021.110321
42. Matiacevich SB, Buera MP, A. critical evaluation of fluorescence as a potential marker for the Maillard reaction. *Food Chem.* (2006) 95:423–30. doi: 10.1016/j.foodchem.2005.01.027
43. Hu QH, Wu YL, Zhong L, Ma N, Zhao LY, Ma GX, et al. *In vitro* digestion and cellular antioxidant activity of β-carotene-loaded emulsion stabilized by soy protein isolate-Pleurotus eryngii polysaccharide conjugates. *Food Hydrocoll.* (2021) 112:106340. doi: 10.1016/j.foodhyd.2020.106340
44. Spotti MJ, Martinez MJ, Pilosof AMR, Candioti M, Rubiolo AC, Carrara CR. Influence of Maillard conjugation on structural characteristics and rheological properties of whey protein/dextran systems. *Food Hydrocoll.* (2014) 39:223–30. doi: 10.1016/j.foodhyd.2014.01.014
45. Zhao X, Xing T, Xu X, Zhou G. Influence of extreme alkaline pH induced unfolding and aggregation on PSE-like chicken protein edible film formation. *Food Chem.* (2020) 319:126574. doi: 10.1016/j.foodchem.2020.126574
46. Kang ZL, Bai R, Lu F, Zhang T, Gao ZS, Zhao SM, et al. Effects of high pressure homogenization on the solubility, foaming, and gel properties of soy 11S globulin. *Food Hydrocoll.* (2022) 124:107261. doi: 10.1016/j.foodhyd.2021.107261
47. Xiao H, Huang L, Zhang W, Yin Z. Damage of proteins at the air/water interface: Surface tension characterizes globulin interface stability. *Int J Pharm.* (2020) 584:119445. doi: 10.1016/j.ijpharm.2020.119445
48. Liu Q, Geng R, Zhao J, Chen Q, Kong B. Structural and gel textural properties of Soy Protein Isolate when subjected to extreme acid pH-shifting and mild heating processes. *J Agric Food Chem.* (2015) 63:4853–61. doi: 10.1021/acs.jafc.5b01331
49. Hu YY, Wu Z, Sun YY, Cao JX, He J, Dang YL, et al. Insight into ultrasound-assisted phosphorylation on the structural and emulsifying properties of goose liver protein. *Food Chem.* (2022) 373:131598. doi: 10.1016/j.foodchem.2021.131598
50. Matyus L, Szollosi J, Jenei A. Steady-state fluorescence quenching applications for studying protein structure and dynamics. *J Photochem Photobiol B.* (2006) 83:223–36. doi: 10.1016/j.jphotobiol.2005.12.017
51. Pandit S, Kundu S. Fluorescence quenching and related interactions among globular proteins (BSA and lysozyme) in presence of titanium dioxide

nanoparticles. *Colloids Surfaces a-Physicochem Engineer Aspects.* (2021) 628. doi: 10.1016/j.colsurfa.2021.127253. [Epub ahead of print].
52. Hinderink EBA, Berton-Carabin CC, Schroen K, Riaublanc A, Houinsou-Houssou B, Boire A, et al. Conformational changes of whey and pea proteins upon emulsification approached by front-surface fluorescence. *J Agric Food Chem.* (2021) 69:6601–12. doi: 10.1021/acs.jafc.1c01005
53. Bayraktutan T, Onganer Y. Biophysical influence of coumarin 35 on bovine serum albumin: Spectroscopic study. *Spectrochim Acta A Mol Biomol Spectrosc.* (2017) 171:90–6. doi: 10.1016/j.saa.2016.07.043
54. Wang BL, Pan DQ, Zhou KL, Lou YY, Shi JH. Multi-spectroscopic approaches and molecular simulation research of the intermolecular interaction between the angiotensin-converting enzyme inhibitor (ACE inhibitor) benazepril and bovine serum albumin (BSA). *Spectrochim Acta A Mol Biomol Spectrosc.* (2019) 212:15–24. doi: 10.1016/j.saa.2018.12.040
55. Zhang YF, Zhou KL, Lou YY. Pan Dq, Shi JH. Investigation of the binding interaction between estazolam and bovine serum albumin: multi-spectroscopic methods and molecular docking technique. *J Biomol Struct Dyn.* (2017) 35:3605–14. doi: 10.1080/07391102.2016.1264889
56. You Y, Yang L, Chen H, Xiong L, Yang F. Effects of (–)-Epigallocatechin-3-gallate on the functional and structural properties of Soybean Protein Isolate. *J Agric Food Chem.* (2021) 69:2306–15. doi: 10.1021/acs.jafc.0c07337
57. Zhang D, Zhang X, Liu Y-C, Huang S-C, Ouyang Y, Hu Y-J. Investigations of the molecular interactions between nisoldipine and human serum albumin in vitro using multi-spectroscopy, electrochemistry and docking studies. *J Mol Liq.* (2018) 258:155–62. doi: 10.1016/j.molliq.2018.03.010
58. Tantimongcolwat T, Prachayasittikul S, Prachayasittikul V. Unravelling the interaction mechanism between clioquinol and bovine serum albumin by multi-spectroscopic and molecular docking approaches. *Spectrochim Acta A Mol Biomol Spectrosc.* (2019) 216:25–34. doi: 10.1016/j.saa.2019.03.004
59. Yue Y, Yin C, Huo F, Chao J, Zhang Y. The application of natural drug-curcumin in the detection hypochlorous acid of real sample and its bioimaging. *Sensors Actuators B-Chem.* (2014) 202:551–6. doi: 10.1016/j.snb.2014.05.119
60. Chen Z, Wang C, Gao X, Chen Y, Kumar Santhanam R, Wang C, et al. Interaction characterization of preheated soy protein isolate with cyanidin-3-O-glucoside and their effects on the stability of black soybean seed coat anthocyanins extracts. *Food Chem.* (2019) 271:266–73. doi: 10.1016/j.foodchem.2018.07.170
61. Wang YX, Zhang L, Wang P, Xu XL, Zhou GH. pH-shifting encapsulation of curcumin in egg white protein isolate for improved dispersity, antioxidant capacity and thermal stability. *Food Res Int.* (2020) 137:109366. doi: 10.1016/j.foodres.2020.109366
62. Chen YS, Zhou YF, Chen M, Xie BJ, Yang JF, Chen JG, et al. Isorenieratene interaction with human serum albumin: Multi-spectroscopic analyses and docking simulation. *Food Chem.* (2018) 258:393–9. doi: 10.1016/j.foodchem.2018.02.105
63. Yang L, Baohua L, Lianzhou J, Regenstein JM, Nan J, Poias V, et al. Interaction of soybean protein isolate and phosphatidylcholine in nanoemulsions: a fluorescence analysis. *Food Hydrocoll.* (2019) 87:814–29. doi: 10.1016/j.foodhyd.2018.09.006
64. Lelis CA, Nunes NM, de Paula HMC, Coelho YL, da Silva LHM, Pires ACD. Insights into protein-curcumin interactions: kinetics and thermodynamics of curcumin and lactoferrin binding. *Food Hydrocoll.* (2020) 105:105825. doi: 10.1016/j.foodhyd.2020.105825
65. Mohammadi F, Moeeni M. Study on the interactions of trans-resveratrol and curcumin with bovine alpha-lactalbumin by spectroscopic analysis and molecular docking. *Mater Sci Eng C Mater Biol Appl.* (2015) 50:358–66. doi: 10.1016/j.msec.2015.02.007
66. Song Z, Yuan W, Zhu R, Wang S, Zhang C, Yang B. Study on the interaction between curcumin and CopC by spectroscopic and docking methods. *Int J Macromolecules.* (2017) 96:192–9. doi: 10.1016/j.ijbiomac.2016.11.099
67. Wang C, Xie Y. Interaction of protein isolate with anthocyanin extracted from black Soybean and its effect on the anthocyanin stability. *J Food Sci.* (2019) 84:3140–6. doi: 10.1111/1750-3841.14816
68. Zhao C, Cheng H, Jiang P, Yao Y, Han J. Preparation of lutein-loaded particles for improving solubility and stability by Polyvinylpyrrolidone (PVP) as an emulsion-stabilizer. *Food Chem.* (2014) 156:123–8. doi: 10.1016/j.foodchem.2014.01.086
69. Chen FP Li BS, Tang CH. Nanocomplexation between curcumin and soy protein isolate: influence on curcumin stability/bioaccessibility and in vitro protein digestibility. *J Agric Food Chem.* (2015) 63:3559–69. doi: 10.1021/acs.jafc.5b00448
70. Jimenez-Aguilar DM, Ortega-Regules AE, Lozada-Ramirez JD, Perez-Perez MCI, Vernon-Carter EJ, Welti-Chanes J. Color and chemical stability of spray-dried blueberry extract using mesquite gum as wall material. *J Food Composition Analysis.* (2011) 24:889–94. doi: 10.1016/j.jfca.2011.04.012
71. Bellary AN, Indiramma AR, Prakash M, Baskaran R, Rastogi NK. Anthocyanin infused watermelon rind and its stability during storage. *Innovative Food Sci Emerg Technol.* (2016) 33:554–62. doi: 10.1016/j.ifset.2015.10.010
72. Mengyao L, Fuli W, Chuanfen P, Wenting T, Qingjie S. Nanoencapsulation of lutein within lipid-based delivery systems: characterization and comparison of zein peptide stabilized nano-emulsion, solid lipid nanoparticle, and nano-structured lipid carrier. *Food Chem.* (2021) 358:129840. doi: 10.1016/j.foodchem.2021.129840

Conflict of Interest: JP and WG were employed by Chenguang Biotech Group Co., Ltd.

The remaining authors declare that the research was conducted in the absence of any commercial or financial relationships that could be construed as a potential conflict of interest.

Publisher's Note: All claims expressed in this article are solely those of the authors and do not necessarily represent those of their affiliated organizations, or those of the publisher, the editors and the reviewers. Any product that may be evaluated in this article, or claim that may be made by its manufacturer, is not guaranteed or endorsed by the publisher.

Copyright © 2022 Wang, Wang, Xu, Peng, Gao and Cao. This is an open-access article distributed under the terms of the Creative Commons Attribution License (CC BY). The use, distribution or reproduction in other forums is permitted, provided the original author(s) and the copyright owner(s) are credited and that the original publication in this journal is cited, in accordance with accepted academic practice. No use, distribution or reproduction is permitted which does not comply with these terms.

frontiers | Frontiers in Nutrition

ORIGINAL RESEARCH
published: 15 June 2022
doi: 10.3389/fnut.2022.852433

DHA Ameliorates Cognitive Ability, Reduces Amyloid Deposition, and Nerve Fiber Production in Alzheimer's Disease

*Min Xiao[1,2], Wei Xiang[2], Yashu Chen[3], Nan Peng[1], Xiubo Du[4], Shuhuan Lu[2], Yao Zuo[2], Boling Li[2], Yonggang Hu[1] and Xiangyu Li[2]**

[1] College of Life Science and Technology, Huazhong Agricultural University, Wuhan, China, [2] CABIO Biotech (Wuhan) Co., Ltd., Wuhan, China, [3] Key Laboratory of Oil Crop Biology and Genetic Breeding, Oil Crops Research Institute, Ministry of Agriculture, Chinese Academy of Agricultural Sciences, Wuhan, China, [4] Shenzhen Key Laboratory of Microbial Genetic Engineering, College of Life Sciences and Oceanography, Shenzhen University, Shenzhen, China

OPEN ACCESS

Edited by:
Shuai Chen,
Wuhan University, China

Reviewed by:
Xinglong Yang,
The First Affiliated Hospital of Kunming Medical University, China
Taotao Dai,
Guangxi Academy of Agricultural Science, China
Long Chen,
Jiangnan University, China

***Correspondence:**
Xiangyu Li
neal_lee@cabio.cn

Specialty section:
This article was submitted to Food Chemistry, a section of the journal Frontiers in Nutrition

Received: 11 January 2022
Accepted: 30 May 2022
Published: 15 June 2022

Citation:
Xiao M, Xiang W, Chen Y, Peng N, Du X, Lu S, Zuo Y, Li B, Hu Y and Li X (2022) DHA Ameliorates Cognitive Ability, Reduces Amyloid Deposition, and Nerve Fiber Production in Alzheimer's Disease. Front. Nutr. 9:852433. doi: 10.3389/fnut.2022.852433

Background: The etiology of Alzheimer's disease (AD) is very complex. Docosahexaenoic acid (DHA) is important in cognitive ability and nervous system development. A limited number of studies have evaluated the efficacy of DHA in the treatment of AD.

Introduction: We detected neurofibrillary tangles (NFT) in the hippocampus and cortex of transgenic mice brain through silver glycine staining. We determined the activity of neurons by staining Nissl bodies, used liquid NMR to detect metabolites in the brain, and functional magnetic resonance imaging results to observe the connection signal value between brain regions.

Materials and Methods: We fed 3-month-old APP/PS1 double transgenic mice with DHA mixed feeds for 4 months to assess the effects of DHA on cognitive ability in AD mice through the Morris water maze and open field tests. To evaluate its effects with AD pathology, continuous feeding was done until the mice reached 9 months of age.

Results: Compared to AD mice, escape latency significantly decreased on the fifth day while swimming speed, target quadrant stay time, and the crossing number of platforms increased by varying degrees after DHA treatment. Brain tissue section staining revealed that DHA significantly reduced Aβ and nerve fibers in the brain of AD mice.

Conclusion: DHA significantly reduced the deposition of Aβ in the brain and inhibited the production of nerve fibers, thereby increasing cognitive abilities in AD mice. In addition, DHA suppressed blood lipid levels, and restored uric acid and urea levels, implying that DHA is a potential therapeutic option for early AD.

Keywords: Alzheimer's disease, docosahexaenoic acid, omega-3, PUFAs, neurodegenerative disease, Aβ, NFT, liquid NMR

INTRODUCTION

Alzheimer's disease (AD) is a progressive neurodegenerative disease that is characterized by cognitive difficulties, reduced language abilities, weakened learning and memory abilities, and motor dysfunctions (1). Not only does it cause great harm to the patients, it is also associated with a heavy socio-economic burden on the family and society. Currently, senile plaques (SP) formed by Amyloid β-peptide (Aβ) deposition and nerve fiber tangles (NFT) formed by aggregation of hyperphosphorylated tau proteins are two key pathological factors associated with AD (2). As the aging population increases, so will the number of AD patients in the world. However, there is no effective therapeutic option for AD.

The etiologies for most AD cases is unknown, except for 1–5% of cases where genetic differences have been identified. Several competing hypotheses have been proposed to explain the etiology of this disease. They include genetic, cholinergic hypothesis, amyloid hypothesis, and Tau hypothesis among others. In the last decade, more than 50 drug candidates have successfully passed phase II clinical trials, but none has passed phase III (3). The main challenge in the fight against Alzheimer's disease is the absence of drugs that are capable of slowing disease progression. Since 2003, no new drugs have been approved for the treatment of Alzheimer's disease. There are only limited studies of some dietary components improving AD conditions.

Long chain omega-3 polyunsaturated fatty acids (n-3 LC PUFAs) are long-chain fatty acids (20 or more carbons) whose first double bond is located at the methyl end after the third carbon. Docosahexaenoic acid (DHA), an omega-3 essential fatty acid, is a polyunsaturated fatty acid ($C_{22}H_{32}O_2$) with six double bonds at positions 4, 7, 10, 13, 16, and 19. DHA and its derivatives have been shown to regulate gene expression levels of inflammatory mediators, as well as enzymes involved in lipid metabolism and Aβ processing. They are also important in preventing or retarding inflammatory aspects of AD pathology (4). Twenty-four week supplementation with 900 mg/day DHA was found to improve learning and memory functions in age-related cognitive decline. Therefore, it is a beneficial supplement for improving cognitive health with aging (5). Studies have reported potential therapeutic effects of DHA in preventing, regulating or improving AD progression.

Studies on the effects of DHA on AD pathology focused on behavioral aspects, which could not be associated with AD-related pathological indicators, and could not further explore the underlying mechanisms. Based on previous research findings, we used various comprehensive research methods to study the effects of DHA-rich mixed feeds on PS1/APP double transgenic AD mice models through behavioral experiments, *in vivo* NMR detection, liquid NMR detection and other methods. Learning and memory abilities, anxiety, Aβ formation and Tau hyperphosphorylation were evaluated.

The purpose of this study is to explore how DHA improves the symptoms of AD and try to discover the mechanism of treatment. The results of this study have certain guiding significance for the follow-up in-depth research on effective means of treating AD.

MATERIALS AND METHODS

Animals and Treatment

Double transgenic AD mice models (2 × Tg-AD) carrying human gene mutants APPswePSEN1dE9/Nju and B6C3F1 WT mice were purchased from GemPharma Tech Co., Ltd. (Nanjing, China). Animals were raised in an animal facility under the conditions of 12-h light/12-h dark cycle at 22 ± 2°C with free access to food and water. The SPF grade standard feed and docosahexaenoic acid mixed feed were provided by CABIO Biotech (Wuhan) Co., Ltd. The 3-month-old 2 × Tg-AD male mice were randomly allocated into three groups: (i) AD control group; (ii) The 50 mg/kg DHA-treated AD group; (iii) The 300 mg/kg DHA-treated AD group, while age/gender-matched WT mice were allocated into two groups, which were the WT control and the 300 mg/kg DHA-treated WT groups. There were 12 mice in each group. The AD control and WT control mice groups were fed with the standard feed. For behavioral testing, all mice were fed to 7 months of age. Feeding was continued until 9 months of age (6 months of dosing), some mice were obtained for liquid nuclear magnetic resonance and functional magnetic resonance experiments while the remaining mice were euthanized and brain tissues as well as serum obtained for various biochemical and pathological experiments. Ethical approval was obtained from the Animal Ethical and Welfare Committee of Shenzhen University, China. All animal experiments were performed according to the animal experiment guidelines and regulations of Shenzhen University, China.

The low concentration of DHA is determined with reference to the new resource food 2010 No. 3 announcement issued by the China Food and Drug Administration, and the high concentration is determined with reference to the Chinese health food functional evaluation method (2020).

Behavioral Tests

Morris Water Maze

The Morris water maze task was performed as previously described with some modifications (6) to assess spatial memory performance of the 9-month-old mice. The water maze was a blue tank (160 cm diameter, 50 cm height) filled with water (21–23°C) to a depth of 26 cm. At this temperature, mice are eager to find an opening through which they can escape from the water because they do not like swimming. The circular water pool was artificially divided into four equal areas, the first to fourth quadrant, and separated using an invisible platform (12 cm diameter, 1–2 cm below the water surface) in the middle of the third quadrant. During the five consecutive days of training, mice were gently released into the water in the first quadrant to start the test and were allowed up to 1 min to find the submerged platform. In case they could not mount the platform within 1 min, they would be guided to the platform for 10 s before being returned back to the cage. The escape latency and swimming speeds for the mice were recorded. After 24 and 72 h of training sessions, probe trials were performed in which the platform was removed. Each mouse was gently released into the first quadrant and searched freely for 2 m. Time that mice spent in the target

quadrant (third quadrant) and the number of mice crossing the previous platform position were recorded. The trials were recorded using a video monitor connected to a computer. The test was run using a water maze software (Water Maze MT-200, Chengdu, China).

Open Field Test

The open field equipment was a 1.2 m × 1.2 m square PVC box, and the bottom of it was divided into 25 grids (5 × 5). The test was performed as previously described with some modifications (6). Briefly, a single mouse was placed in the middle grid of the box and timed for 3 mins. The number of grids that the mouse crossed and the number of rearing (the two front legs were raised at the same time) were recorded. To avoid affecting the experimental results, the smells were wiped off using ethanol before the next mouse experiment.

Tissue and Serum Preparation

Mice were anesthetized using isoflurane and their brain tissues rapidly collected. The left hemisphere was fixed in 4% phosphate-buffered paraformaldehyde, while the right one was dissected into the hippocampus and cortex and stored at −80°C for the subsequent biochemical analyses. Blood samples were obtained by removing eyeballs of the mice. Blood was left to stand for 3–4 h and centrifuged at 15 × rpm for 30 min. Then, the supernatant was aspirated to obtain mice serum.

Serum Biochemical Analysis

Biochemical analyses were performed using a fully automatic biochemical analyzer (iMagic-M7, ICUBIO). Test kits were manufactured by ICUBIO (Shenzhen, China), include Glutamate Pyruvate Transaminase (ALT) Assay Kit, Glutamate Oxaloacetate Transaminase (AST) Assay Kit, Low density lipoprotein cholesterol (LDL-C) Assay Kit, High density lipoprotein cholesterol (HDL-C) Assay Kit, Urea Assay Kit, Triglycerides (TG) Assay Kit. All procedures were performed according to the manufacturer's instructions.

Thioflavin T Staining

Brain sections were washed several times using ddH_2O after which they were immersed in 0.001 g/mL ThT working solution (Sigma Aldrich, St. Louis, MO, United States) and stained at room temperature for 30 mins. Subsequently, sections were washed using ddH_2O for 5 s and mounted with the anti-fluorescence quenching medium. Finally, sections were imaged using a confocal microscope (OLYMPUS FV1000).

Silver Staining

After being washed several times using ddH_2O, brain sections were treated with formic acid for 5 mins and washed three times again. Then, sections were placed in silver glycine solution (preheated at 37°C in advance) for 3–5 min, removed and the residual glycine silver solution on the sections quickly shaken off. Sections were put into reducing solution I (warmed to 45°C in advance), removed after a few seconds, quickly shaken, placed in reducing solution II for a few seconds (preheated to 45°C in advance) and cleaned using ddH_2O. In case the staining background was too deep, it was treated using sodium thiosulfate solution and washed three times using ddH_2O. The slides were mounted with anti-fluorescence quenching sealers and imaged by confocal microscopy (OLYMPUS FV1000, Olympus Corporation, Made in Japan).

Statistical Analysis

Data were analyzed using GraphPad Prism software and presented as mean ± standard error of the mean (S.E.M.). Statistical significance were considered at $^{*}p < 0.05$; $^{**}p < 0.01$; $^{***}p < 0.001$. Statistical analyses were performed by one-way ANOVA followed by the Student's *t*-test.

RESULTS

DHA Treatment Ameliorated Cognitive Impairment and Depression/Anxiety Behaviors in Alzheimer's Disease Mice

The Morris water maze (MWM) was used to evaluate the effects of DHA treatment on spatial memory and learning abilities in 2 × Tg AD mice (6). After 4 months of DHA treatment, some mice groups exhibited progressively shorter escape latencies, while the WT mice treated with high DHA reached the shortest escape latency significantly on the fifth day (**Figure 1A**). Swimming speeds of mice in the WT, AD + DHA-L, and AD + DHA-L groups were significantly different from those of the AD group (**Figure 1B**), implying that DHA partially restored exercise and spatial learning abilities of AD mice. After 24 h of the detection period, target quadrant retention time of the WT, AD + DHA-L, and AD + DHA-L groups were significantly higher than those of the AD group, while there were no significant differences in the other groups (**Figure 1C**). Platform crossing numbers of DHA -treated mice group were not significantly higher than those of the other groups after 24 and 72 h. Similarly, DHA did not result in a significant increase in crossing numbers of mice in other groups (**Figures 1D,F**), implying that DHA could partially improve short-term memory of AD mice, but not their long-term memories. These findings show that feeding DHA for 4 months partially restored motor functions of AD mice and improved some of their learning and memory impairments.

The open field test (OFT) was performed to investigate the effects of DHA on depression- and anxiety-related behaviors of AD mice (6). After 4 months of DHA feeding, compared to WT mice, AD mice exhibited typical depression/anxiety behaviors, including significant reductions in the frequencies of grid crossing and rearing (**Figures 2A,B**). Compared to AD mice, the DHA treatment mice group exhibited significantly improved depression/anxiety behaviors, which was associated with a significant increase in grid crossing and feeding frequencies (**Figures 2A,B**). These behavioral MWM and OFT findings

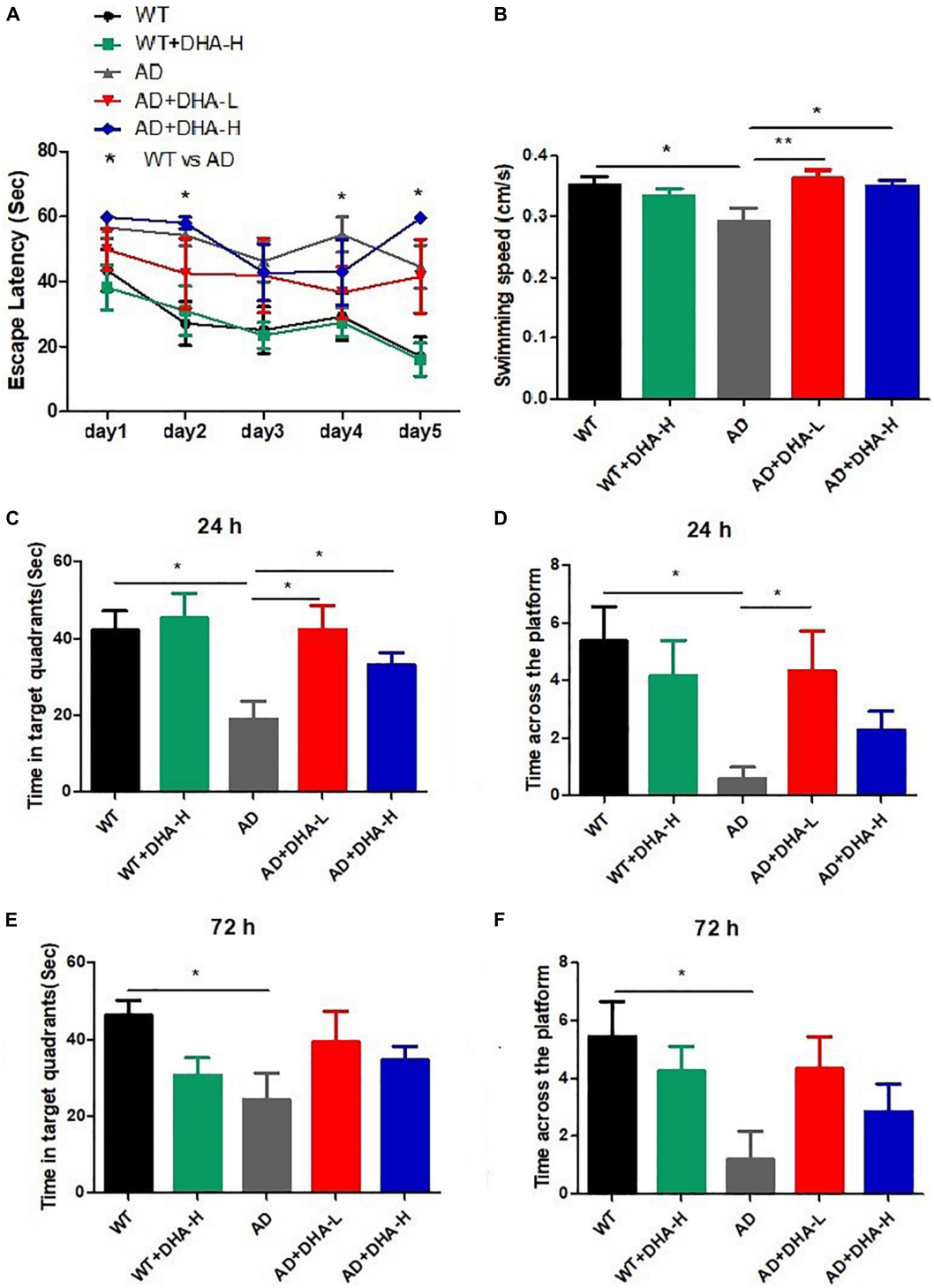

FIGURE 1 | Effect of DHA treatment for 4 months on spatial memory and learning ability in 2 × Tg AD mice. **(A)** Escape latency; **(B)** average swimming speed; **(C)** time in target quadrant 24 h after 5-day training; **(D)** times crossing platform 24 h after 5-day training; **(E)** time in target quadrant 72 h after 5-day training; **(F)** times crossing platform 72 h after 5-day training (*$p < 0.05$; **$p < 0.01$). Student's *t* test was used for statistical analysis. Error bars represent mean ± S.E.M. ($n = 12$).

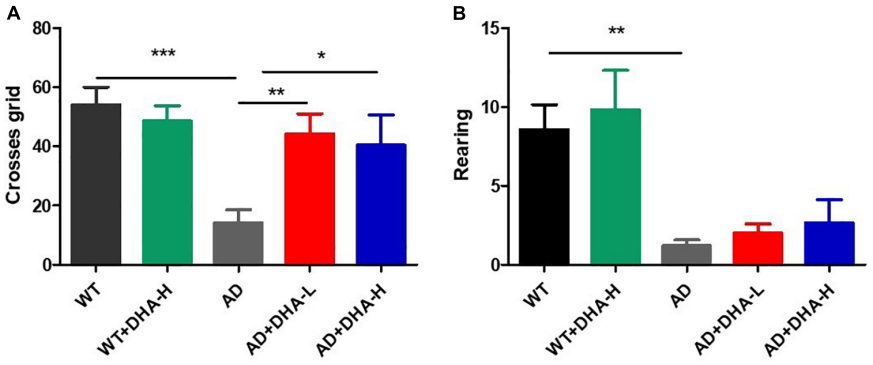

FIGURE 2 | Effect of DHA treatment for 4 months on depression- and anxiety-related behaviors in 2 × Tg AD mice. **(A)** Times of crossing grids; **(B)** times of standing (*$p < 0.05$; **$p < 0.01$; ***$p < 0.001$). Student's *t* test was used for statistical analysis. Error bars represent mean ± S.E.M. ($n = 12$).

(**Figures 1**, **2**) show that DHA treatment (including moderate or high DHA concentration) effectively improved some cognitive decline and depression/anxiety behaviors in AD mice.

DHA Significantly Suppressed the Pathological Hallmarks of Alzheimer's Disease Mice

Western blot was used to detect the expression levels of Aβ oligomers and APP protein in the hippocampus of mice. It can be seen from the results that the expression levels of Aβ protein and APP protein in AD group mice were significantly increased compared with WT group mice, and DHA administration for 4 months significantly decreased the AD + DHA-L and AD + DHA-H groups. The Aβ protein expression level and APP protein expression level of mice were not significantly different (**Figure 3**).

Interactions between Aβ and tau may be central to the development of Alzheimer's disease (7) while APP/PS1 transgenic mice develop age-related accumulation of plaques and tangles in the brain (8). Detection of plaques in the hippocampus and cortex of mouse brain through thioflavin T staining, to some extent, reflects the accumulation and distribution of Aβ in the brain. From the findings, the areas occupied by Aβ plaques of WT mice were all reduced significantly in both the cortex and hippocampus, compared to AD mice. Compared to AD mice as control group, low or high DHA treatments reduced Aβ plaque aggregations in CA3, CA1, DG, and Cor of AD mice (**Figure 4**).

The results of Western blot showed that total Tau (Tau5) and Tau phosphorylation sites (S202, S404, and S422) had no significant changes in all groups of mice (**Figure 5**).

Glycine silver staining was used to detect neurofibrillary tangles (NFTs) in the hippocampus and cortex of mouse brains. Formation of NFT was due to excessive phosphorylation of the tau protein, which caused it to entangle with each other after falling off the microtubule tangle of nerve fibers (9, 10). From the results, the NFTs of WT and DHA treated mice were significantly less than those of the AD group in CA3, CA1, DG, and Cor. However, DHA treated mice exhibited slightly worse outcomes than the WT group (**Figure 6**).

DHA Had No Obvious Improvement Effect on Liver Functions, Kidney Functions, and Blood Lipid Levels in Experimental Mice

Apolipoprotein A1 (ApoA1) and apolipoprotein B (ApoB) are lipid-related indicators (11, 12). ApoA1 is a high-density lipoprotein whose main role is to transport lipids from tissues and organs to the liver, and the liver decomposes the lipids (13). ApoA1 is negatively correlated with atherosclerotic cardiovascular disease. ApoB exists on the surface of low-density lipoprotein and is used to detect and take up low-density lipoproteins, increasing coronary atherosclerotic heart disease incidences even at low levels (12). Triglyceride (TG), also known as neutral fat, is the main source of energy in the body. Its content increases with age, especially for middle-aged and elderly people whose weight exceeds the standard. High triglyceride levels can easily result in thick blood and thrombosis leading to high blood pressure, gallstones, pancreatitis, and Alzheimer's. Apolipoprotein A1 (ApoA1) is mainly present in form of HDL and is the main apolipoprotein of HDL. It is mainly synthesized in the liver and small intestines. Under normal circumstances, high levels of HDL are better than low levels, which helps prevent hyperlipidemia, fat deposition and arterial Atherosclerosis. As the main apolipoprotein of LDL, Apolipoprotein B (ApoB) has various physiological functions, including the synthesis, assembly and secretion of VLDL rich in triglycerides. Clinically prescribed ApoB refers to ApoB100, which is better at low levels under normal conditions. We found that DHA had no significant effects on the levels of triglycerides, HDL, and LDL in each group of mice.

Aspartate transferase (AST) and alanine aminotransferase (ALT) are used to evaluate liver functions (14). Alanine aminotransferase (ALT) is an enzyme involved in the metabolism of human proteins. When liver cells are damaged, ALT is released from cells. We found that liver functions of AD mice in the WT group were significantly impaired. Cell damage can cause serum ALT activity to double, therefore, determination of ALT activity is one of the most sensitive indicators of liver cell damage. After adding DHA, serum ALT activities of AD + DHA-L and

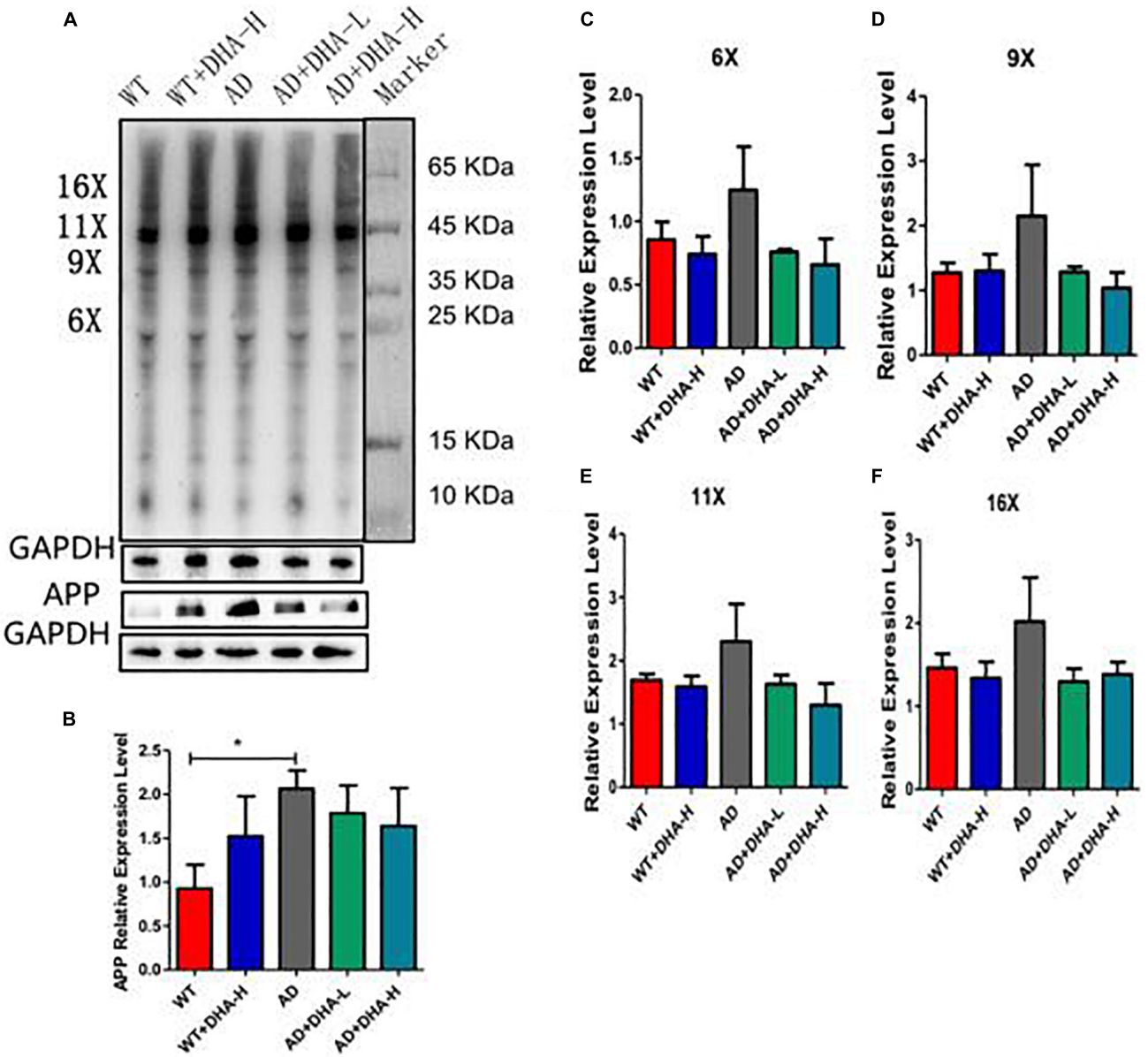

FIGURE 3 | Detection of Aβ protein levels in mouse cortex tissue (n = 4). **(A)** Western blot detection of the expression levels of Aβ oligomers and APP in hippocampus; **(B)** Quantitative analysis of gray value of APP protein expression level; **(C)** Quantitative analysis of gray value of 6-fold oligomer of Aβ protein; **(D)** Aβ protein 9 Gray value quantitative analysis of fold oligomers; **(E)** Gray value quantitative analysis of Aβ protein 11-fold oligomers; **(F)** Gray value quantitative analysis of Aβ protein 16-fold oligomers (*$p < 0.05$).

AD + DHA-H groups were significantly suppressed, which was basically the same as that of the WT group. Serum ALT activities of the WT + DHA-H and WT mice groups were significantly altered. Therefore, high-dose DHA had no toxic effects on WT mice, while low-dose DHA had a certain protective effect on the livers of AD mice (**Figure 5A**). Aspartate aminotransferase (AST) was formerly known as glutamic oxaloacetic transaminase (GOT). AST has two isoenzymes, ASTs and ASTm, which exist in soluble cytoplasm and mitochondria, respectively. When liver cells are mildly damaged, ASTs increase significantly, and in severe injuries ASTm appear in the serum in large quantities. We found that there were no significant differences in AST levels among the WT, AD, and DHA treatment groups, implying that drug treatment had no toxic and side effects on mice livers (**Figures 7A,B**).

For kidney functions, uric acid (UA) and urea are very important. UA is the final product of purine metabolism. Alterations in UA levels can fully reflect the body's metabolic, immune and other functions (15). Urea is a product of human protein catabolism (16). Excessive uric acid and urea levels

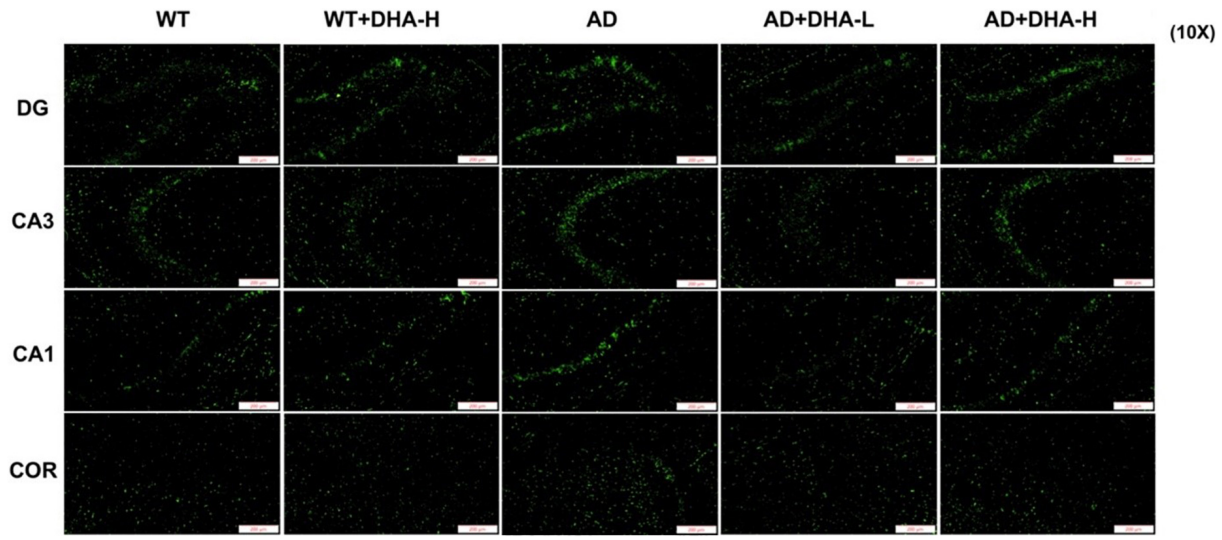

FIGURE 4 | Effect of DHA treatment on deposition of Aβ in the hippocampus and cortex of 2 × Tg AD mice. CA3:CA3 area of mouse hippocampus; CA1, CA1 area of mouse hippocampus; Cor, cortical area; DG, dentate gyrus area of hippocampus (n = 4).

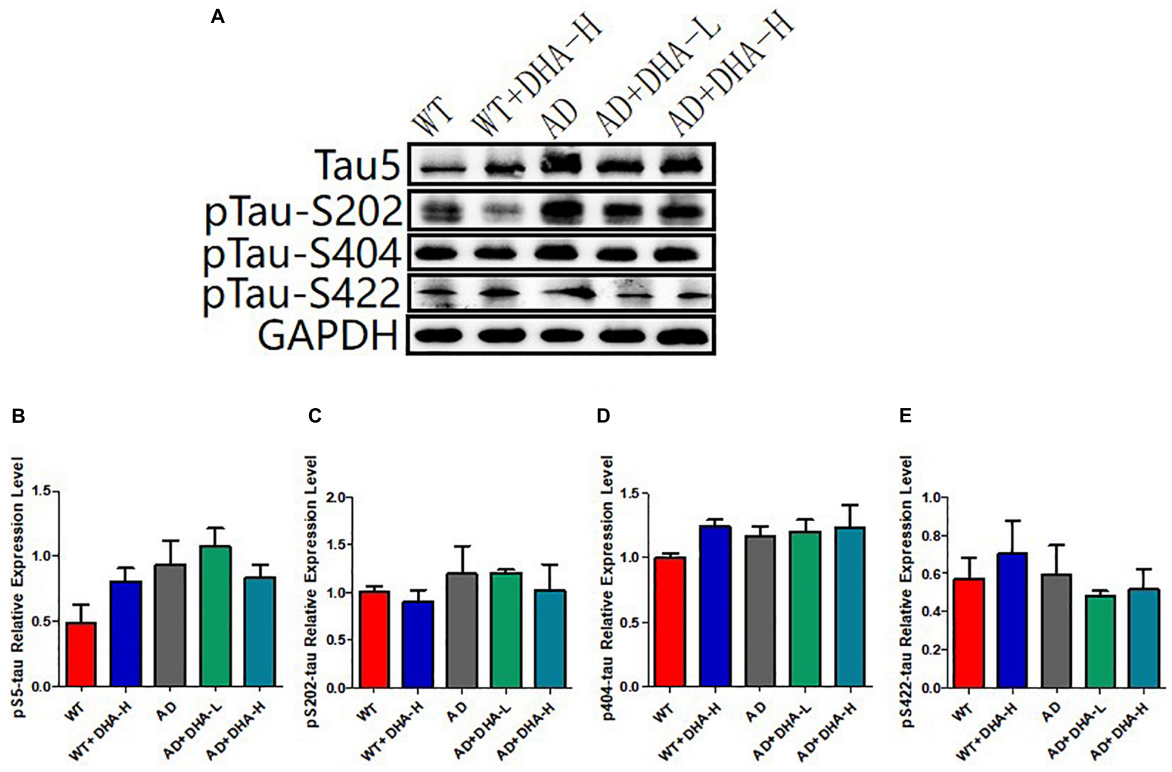

FIGURE 5 | Detection of expression levels of total tau and phosphorylated tau protein in mouse hippocampus (n = 4). **(A)** Western blot detection of the expression levels of total tau and phosphorylated tau protein in the hippocampus of mouse brain; **(B)** Quantitative analysis of the gray value of total tau protein. **(C)** The expression level of phosphorylated protein at S202 of Tau. **(D)** Tau at the S202 site; the expression level of phosphorylated protein at S404; the expression level of phosphorylated protein at S422 of **(E)** Tau.

indicate liver and kidney damage, while an increase in UA levels but within the normal range can hinder the onset of AD (17). In this study, there were no significant differences in UA and urea levels among the WT, AD, and DHA groups, implying that drug treatment had no toxic or protective effects on kidney functions (**Figure 8**).

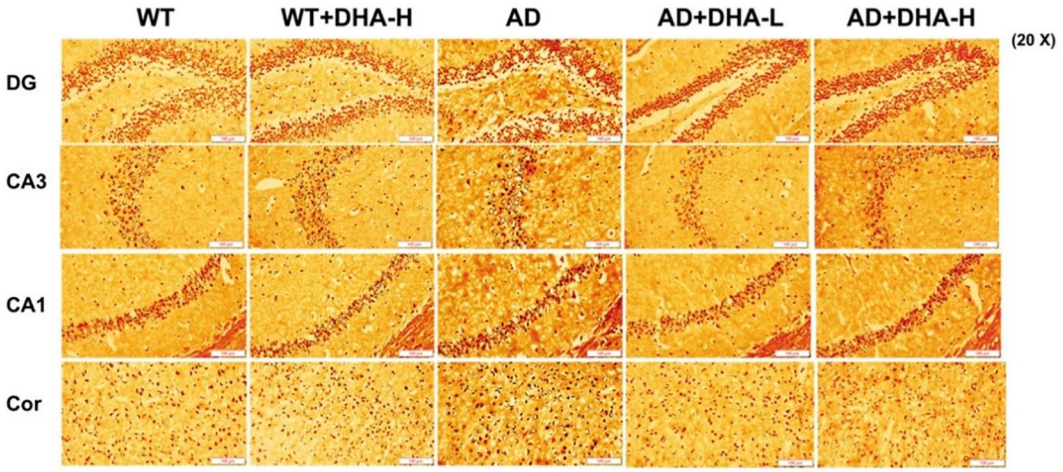

FIGURE 6 | Effect of DHA treatment on neurofibrillary tangles in the hippocampus and cortex of 2 × Tg AD mice (n = 4).

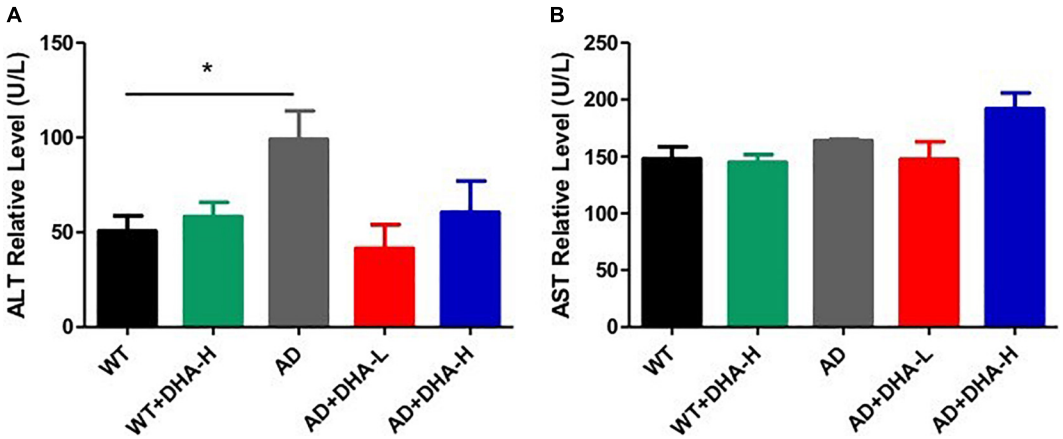

FIGURE 7 | Effects of DHA treatment on liver - indicators in 2 × Tg AD mice. **(A)** Alanine aminotransferase; **(B)** aspartate transferase (*$p < 0.05$). The student's t test was used for statistical analyses. Error bars represent mean ± S.E.M. (n = 6).

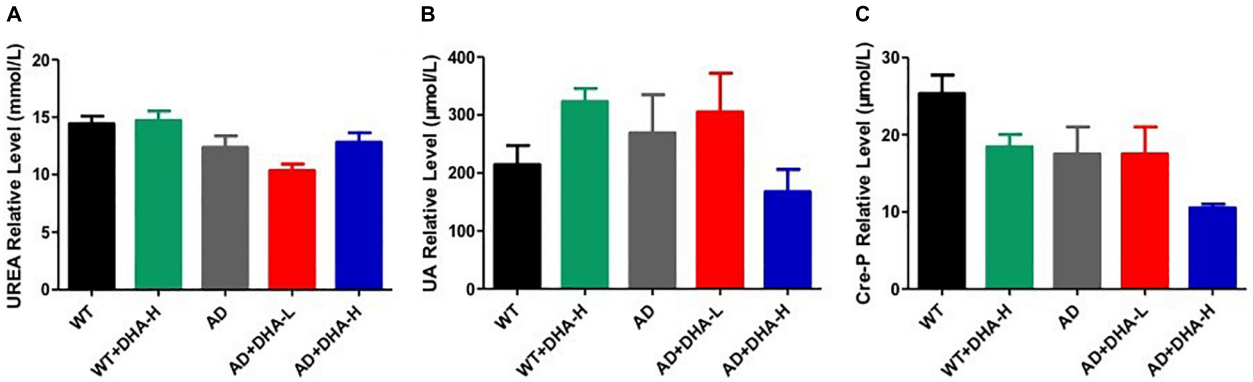

FIGURE 8 | Effect of DHA treatment on kidney- indicators in 2 × Tg AD mice. **(A)** Urea; **(B)** auric acid; **(C)** Cre-P. Student's t test was used for statistical analyses. Error bars represent mean ± S.E.M. (n = 6).

From the analysis of serum biochemical indicators, DHA did not improve liver as well as kidney functions and neither did it affect blood lipid levels of experimental mice. In addition, it had no toxic effects on experimental mice.

DHA Had Little Effects on Inositol, Glycine, and Taurine

Inositol, glycine, and taurine are common small molecules in the brain. They are associated with brain development, neurotransmission among others (18–20). The results of the concentration of Myo-instal in different brain regions showed that the WT group did not change significantly compared with the WT + DHA-H group, and the concentration of Myo-instal in the WT group showed an upward trend compared with the AD group. For mice in the AD + DHA-L, AD + DHA-H, and AD groups, they were concentration of Myo-instal down-regulated in the striatum, cortex and epithalamus, with significant differences. Since the specific role of concentration of Myo-instal is not yet clear, the result needs further verification.

Concentrations of glycine in different brain regions and the ratio of WT group to WT + DHA-H were all down-regulated. Moreover, the concentration of glycine in AD mice were also down-regulated. There was almost no change in glycine levels in the AD + DHA-L and AD groups, but the content of AD + DHA-H group has changed. These findings indicate that high-dose DHA may not have much effect on normal mice, but it can improve glycine levels in the brains of AD mice.

Compared to the WT group, the WT + DHA-H group exhibited significantly decreased concentrations of taurine in the striatum. The concentration of taurine results in other brain regions were different from the wild type group. WT group compared to the AD group, taurine in the HYP area was significantly up-regulated. After feeding with DHA, mice in the AD + DHA-L group exhibited significantly down-regulated taurine levels in the cortical area, while significant effects were not observed in mice in the AD + DHA-H group (**Figure 9**). Detection of neurofibrillary tangles (NFTs) in the hippocampus and cortex of mouse brain by silver glycinate staining. The NFT positive areas were evaluated using Image-Pro Plus Software. Western blot detection of Aβ protein expression in hippocampus of mouse brain. The pictures represent NFT level (**Figure 10**) and Aβ level (**Figure 11**) in the mice brain.

DISCUSSION

Alzheimer's disease is a progressive neurodegenerative disorder that is commonly associated with the onset of dementia in elderly people. The main clinical symptoms for AD include progressive memory loss and cognitive impairments (21). Typical pathological features include accumulation of Aβ plaques in brain tissues, nerve fiber tangles in brain cells, and neuronal loss among others, resulting in inflammation, oxidative stress, impairments in vasorelaxation, and progressive brain atrophy (1, 7, 22, 23). DHA has been shown to enhance brain development, cognition, and learning behaviors (24). After DHA digestion, it can bypass tight junctions of the blood brain barrier (BBB) and enter the brain through inner membrane lobules. Therefore, improving Alzheimer's disease outcomes through dietary intake of DHA is safe and effective. Free DHA in dietary is transported across the outer membrane leaflet of the blood-brain barrier (BBB) *via* passive diffusion, attenuates the brain inflammatory response that leads to AD. A limited number of studies have evaluated the mechanisms through which DHA interferes with Alzheimer's disease progression. In this study, we used APP/PS1 transgenic mice model that developed age-related accumulation of plaques and tangles in the brain, showing some relatable symptoms of Alzheimer's disease to test the hypothesis that DHA is effective in treating Alzheimer's disease. Compared to AD control mice group, DHA improved spatial learning, memory ability and anxiety of mice. It also suppressed the accumulation of some Aβ oligomers and the formation of neurofibrillary tangles. In mice models, DHA did not interfere with liver and kidney functions, and it improved AD symptoms by improving blood lipid functions and preventing cardiovascular and cerebrovascular diseases.

Not only is DHA an essential factor for the healthy growth and development of infants and young children, it is also involved in improving cardiovascular health, reducing the symptoms associated with rheumatoid arthritis and depression, and improving human cognition. Large amounts of DHA are contained in the cerebral cortex and retina, especially in the gray matter and photoreceptor cells of the cerebral cortex. These DHAs are mainly in the form of phospholipids (25). DHA is very important in brain development (26). With cell membrane formation, neurons continue to form axons and dendrites. The growing cell membrane must be relatively fluid, and DHA is very fluid. Moreover, synapses of the most important functional units in the brain circuit are preferentially composed of DHA-rich cell membranes (27). DHA is an essential factor for the differentiation and migration of neurons as well as glial cells during brain development. It is also important in stimulating myelination and synapse. In addition, DHA is involved in neural cell differentiation (28), neural development (29) and in preventing synapse loss (30). Alzheimer's disease is prevalent in Western countries. Due to the association between DHA and brain development, and the relatively low intake of omega-3 fatty acids in these countries, there is a need to determine whether increasing DHA intake can reduce AD risks and improve cognitive repair in patients with mild AD. After death, in death patients, DHA levels decrease in specific areas of the brain, such as the pons, white matter, and especially in the frontal gray matter and hippocampus (31). In addition, since DHA contains six double bonds, it is very sensitive to lipid peroxidation. Elevations in peroxidation products of DHA in the brains of AD patients assumes that the loss of DHA can be attributed to the increase in oxidative stress (32). This lipid change occurs in the latter stages of AD, but also in the early stages of the disease (33). PUFA plays important roles in the prevention of AD, other types of dementia, and cognitive impairment (34). The prevention of AD by DHA is mostly based on the amyloid hypothesis (3, 35). Dietary DHA was shown to be involved in improving learning-related memory deficiencies in Aβ peptide-infused AD rat models. DHA pre-administration ameliorated the deterioration of learning ability-related memory in AD rat models (36). Moreover, dietary DHA is protective against

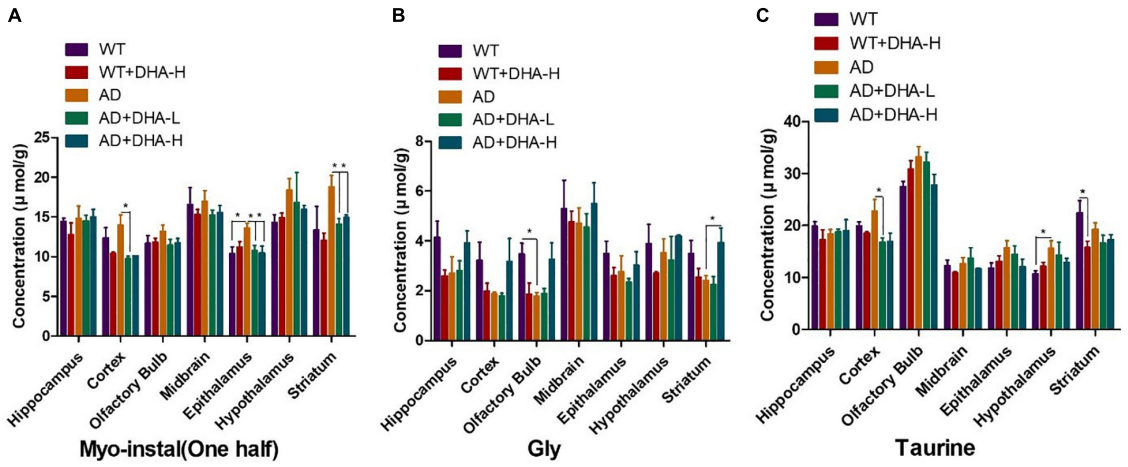

FIGURE 9 | Effects of DHA treatment on common small molecules in the brain in 2 × Tg AD mice. **(A)** Myo-Inositol, **(B)** glycine, **(C)** taurine. Student's *t* test was used for statistical analyses. Error bars represent mean ± S.E.M. ($n = 4$). $^*P < 0.05$.

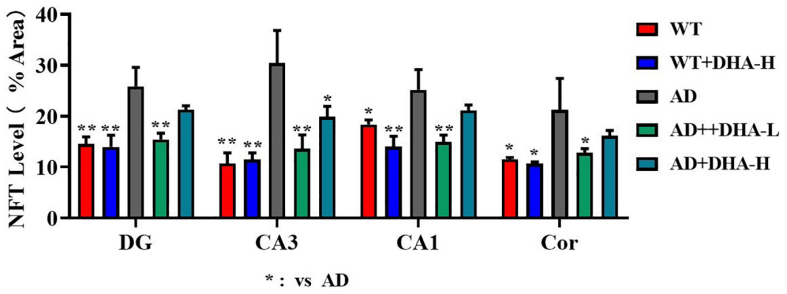

FIGURE 10 | Effects of DHA treatment on NFT level in the brain in 2 × Tg AD mice. $^*p < 0.05$, $^{**}p < 0.01$. Error bars represent mean ± S.E.M. ($n = 6$).

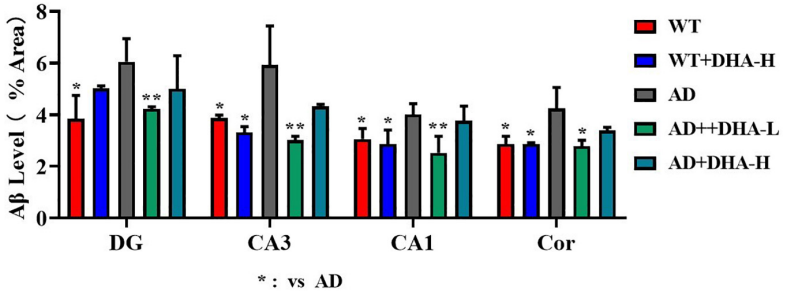

FIGURE 11 | Effects of DHA treatment on Aβ level in the brain in 2 × Tg AD mice. $^*p < 0.05$, $^{**}p < 0.01$. Error bars represent mean ± S.E.M. ($n = 6$).

Aβ production, accumulation, and its potential downstream toxic effects (37). Cell cultivation experiments revealed that DHA down regulates the secretion of Aβ peptides in aging human neural cells (38). Dietary DHA was associated with significantly increased levels of memory in the hippocampus and frontal cortex, which was associated with the protection of synaptic proteins. Both parameters were strongly correlated with learning as well as memory capacities and were implicated in the prevention of Aβ oligomer-induced impairments. Therefore, DHA is important in AD prevention (39). DHA was shown to protect against and ameliorate learning ability impairments in Aβ1–40 infused AD rat models, with concurrent increases in DHA levels and decreases in lipid peroxide levels and reactive oxygen species in the cortico-hippocampal tissues (40).

The mechanisms through which DHA affects AD symptoms may involve indirectly influencing blood vessels to prevent Aβ production. A diet rich in DHA altered the behaviors and cognitive abilities, cerebral hemodynamics [relative cerebral blood volume (rCBV)] as well as Aβ deposition levels in APPswe/PS1dE9 mice at 8 and 15 months of age (41). The

study found that DHA altered rCBV in 8-month-old APP/PS1 and wild-type mice [AU1]. In 15-month-old APP/PS1 mice, DHA supplementation improved spatial memory, reduced Aβ deposition, and slightly increased rCBV, implying that a diet rich in DHA can reduce the pathological symptoms associated with AD. Therefore, long-term consumption of DHA-rich foods can improve AD symptoms. The Framingham Heart study showed that high plasma DHA levels can reduce the risk of AD development (42).

Moreover, adequate DHA intakes can reduce the risk of AD development (43–45) while dietary intake of n-3 PUFA may suppress cognitive declines (46, 47). Freund-Levi (48) performed a trial and proved the positive effects of DHA supplementation on cognition of very mild AD patients. In APP transgenic mice, brain Aβ levels were found to be decreased after dietary DHA supplementation (37, 49). It has been postulated that DHA supplementation increases the amounts of neuron sorting protein LR11, which regulates the processing of APP and the subsequent reduction in Aβ production (50). In addition, DHA supplementation in tg2576 AD mice depleted of DHA improved memory acquisition (30). The study by Hooijmans corroborates these findings (51). In their study, they used open-air experiments to determine exploratory behaviors and used the Morris water maze (MWM) and 8- and 15-month-old wild-type and double-transgenic APPswe/PS1dE9 mice. The 12 circular orifice plates were used for spatial learning and memory assessments (41).

The water maze experiment is the most classic experiment to test spatial learning and memory abilities of mice (51). The escape latency of the 5 days' spatial training, swimming speed, time in target quadrant and the number of crossing platform reflects learning abilities, movement abilities, and spatio-memory abilities (52). In this study, the escape latency for mice in each group was shortened day by day. However, some mice in the same cage were injured in a fight, mice in the AD + DHA-H group took more time to find the platform on the 5th day than in the previous 4 days due to injuries in some mice. At 24 and 72 h after training, the time spent in the platform quadrant of the mice in each DHA treatment group was significantly increased compared to WT and AD mice. Compared to 72 h, residence time of mice in the 24 h treatment group and the AD group was significantly increased. The WT + DHA-H group exhibited an increasing trend compared to the WT group, however, the difference was not significant. The number of times mice in each treatment group crossed the platform was also better at 24 h than at 72 h. Compared to the AD group, the number of times mice in the WT group crossed the platform was significantly high. Finally, 24 and 72 h after training, the number of times mice in each treatment group crossed the platform was also better at 24 h than at 72 h. Results for mice in the WT group were more significant than those in the AD group. Compared to AD group mice, the number of times that mice in the AD + DHA-L group crossed the platform was significantly increased. In this study, low-dose DHA improved memory and learning abilities of AD mice, without significant changes in other groups.

The open field experiment, which exploits mice innate avoidance to open fields and exploration of new things, is used to evaluate spontaneous activities and anxiety in mice (6). In this study, we found that long-term DHA supplementation increased the number of rearing and crossing grids of AD mice, implying that the spontaneous activity and anxiety of AD mice were improved by DHA treatment. Combining the results from the water maze experiment and the open field experiment, long-term DHA supplementation had a certain therapeutic effect on impaired cognitive and motor abilities of AD mice.

As earlier mentioned, Aβ and hyperphosphorylated tau are two major toxic proteins of Alzheimer's disease (7). Aβ is attributed to continuous shearing of APP proteins by β-amylase and γ-secretase. Large amounts of Aβ precipitate outside neurons to form senile plaques (SP) (7, 22, 53). Tau promotes the assembly of microtubules and maintains cytoskeleton functions. Over-phosphorylated tau not only loses its biological functions but also dissociates from the microtubules and aggregates with each other, eventually forming a large number of NFTs (9, 54). Aβ has strong toxic effects and induces tau hyperphosphorylation, which leads to neuronal degeneration, dysfunction, and death (55, 56). In this study, through brain section thioflavin and silver staining, we found that the number or area of beta amyloid in DHA-fed AD mice was reduced in certain brain regions, showing the Aβ clearance effect of DHA. The number of NFTs in AD mice was also decreased with increasing DHA concentrations. Neuronal damage and death, especially in brain learning and memory-related areas, are pathological features of AD (1). Therefore, DHA suppressed neuronal damage by reducing Aβ and inhibiting tau protein hyperphosphorylation, which improved cognitive abilities and mobility of AD mice.

Obesity, hypertension, cardiovascular and cerebrovascular diseases increase the risk of AD (57–59). Lipoproteins are complexes of different lipids and proteins that act on the transport and clearance of lipids or lipid-related molecules from circulation (60). Lipoproteins also play a vital role in brain functions. High-density lipoproteins (HDL) and their main protein component, ApoA1, are directly involved in the outflow of cholesterol from the brain (12, 61). Overexpression of human ApoA1 in circulation was shown to prevent learning and memory impairments in APP/PS1 transgenic mice, partly by suppressing neuroinflammation and cerebral amyloid angiopathy (12). In addition, ApoB was found to be elevated in AD plasma and serum, and over expression of ApoB in transgenic mice triggered apoptosis and neurodegeneration in the brain (62–64). In this study, there were no significant differences in ApoA1 and ApoB levels between the WT and AD groups. Moreover, after DHA supplementation, differences in ApoA1 and ApoB levels were not significant, implying that DHA had no effect on the apolipoproteins.

Analysis of serum biochemical indicators showed that DHA had no effects on blood lipid levels, kidney functions and liver functions of experimental mice. AST and ALT are the most sensitive indicators of liver cell damage. When liver cells are severely damaged, AST and ALT levels are significantly elevated in serum (14). In this study, neither DHA supplemented AD mice nor WT mice had significantly elevated AST and ALT levels, and there were no differences between the groups, implying that DHA did not impair liver functions.

Among the possible markers for age-related cognitive decline, UA is controversial because it has antioxidant properties.

However, elevated UA levels increases the risk of gout and cardiovascular disease and affects kidney functions. Serum UA levels in AD patients were found to be significantly low than in healthy controls (14, 65). In this study, there were no significant differences in renal function indices in WT, AD and DHA treatment groups, implying that DHA had no toxic effects on kidney functions, and no obvious protective effects.

Inositol is associated with signal transduction, and its imbalance leads to neurological disorders (18). Inositol was shown to improve pathological characteristics of Alzheimer's disease animal models and reversed cognitive impairments (66, 67). However, we found that inositol was stably expressed in different groups. Glycine is a neurotransmitter with anti-inflammatory, signaling, and cellular immunity functions (19). Inhibition of glycine transporter-1 (GlyT1) elevated glycine levels, thereby inhibiting cognitive impairments in Alzheimer's disease animal models (68). We also found that high-dose DHA may not have a significant effect in normal mice, but it improved glycine levels in the brains of AD mice, which may be a good phenomenon. Due to aging, taurine levels in mammalian brain decrease, affecting memory ability (69).

In this study, taurine levels in the brains of AD mice fed with DHA did not significantly improve.

CONCLUSION

(1) DHA suppressed neuronal damage by reducing Aβ and inhibiting tau protein hyperphosphorylation, which improved cognitive abilities and mobility of AD mice.

(2) DHA has a certain effect on lowering blood lipid levels and may have a positive effect on the prevention of vascular diseases, which may improve Alzheimer's disease outcomes.

DATA AVAILABILITY STATEMENT

The original contributions presented in the study are included in the article/supplementary material, further inquiries can be directed to the corresponding author.

ETHICS STATEMENT

The animal study was reviewed and approved by Animal Ethical and Welfare Committee of Shenzhen University.

AUTHOR CONTRIBUTIONS

MX: conceptualization, methodology, project administration, and writing – review and editing. WX: data curation, writing – original draft preparation, and formal analysis. YC: writing – review and editing and investigation. NP, SL, and YZ: writing – review and editing. XD: resources, data curation, and formal analysis. BL: project administration. YH and XL: supervision. All authors contributed to the article and approved the submitted version.

REFERENCES

1. Villemagne VL, Burnham S, Bourgeat P, Brown B, Ellis KA, Salvado O, et al. Amyloid β deposition, neurodegeneration, and cognitive decline in sporadic Alzheimer's disease: a prospective cohort study. *Lancet Neurol.* (2013) 12:357–67. doi: 10.1016/S1474-4422(13)70044-9
2. Penke B, Bogár F, Paragi G, Gera J, Fülp L. Key peptides and proteins in Alzheimer's disease. *Curr Protein Pept Sci.* (2019) 20:577–99. doi: 10.2174/1389203720666190103123434
3. Bachurin SO, Bovina EV, Ustyugov AA. Drugs in clinical trials for Alzheimer's disease: the major trends. *Med Res Rev.* (2017) 37:1186–225. doi: 10.1002/med.21434
4. Heras-Sandoval D, Pedraza-Chaverri J, Pérez-Rojas J. Role of docosahexaenoic acid in the modulation of glial cells in Alzheimer's disease. *J Neuroinflamm.* (2016) 13:61. doi: 10.1186/s12974-016-0525-7
5. Yurko-Mauro K, Mccarthy D, Rom D, Nelson EB, Ryan AS, Blackwell A, et al. Beneficial effects of docosahexaenoic acid on cognition in age-related cognitive decline. *Alzheimers Dement.* (2010) 6:456–64. doi: 10.1016/j.jalz.2010.01.013
6. Morris R. Developments of a water-maze procedure for studying spatial learning in the rat - sciencedirect. *J Neurosci Methods.* (1984) 11:47–60. doi: 10.1016/0165-0270(84)90007-4
7. Vorhees CV, Williams MT. Morris water maze: procedures for assessing spatial and related forms of learning and memory. *Nat Protoco.* (2006) 1:848–58. doi: 10.1038/nprot.2006.116
8. Bloom GS. Amyloid-β and tau: the trigger and bullet in Alzheimer disease pathogenesis. *JAMA Neurol.* (2014) 71:505–8. doi: 10.1001/jamaneurol.2013.5847
9. Howlett DR, Bowler K, Soden PE, Riddell D, Davis JB, Richardson JC, et al. Abeta deposition and related pathology in an APP x PS1 transgenic mouse model of Alzheimer's disease. *Histol Histopathol.* (2008) 23:67–76. doi: 10.14670/HH-23.67
10. Hanger DP, Anderton BH, Noble W. Tau phosphorylation: the therapeutic challenge for neurodegenerative disease. *Trends Mol Med.* (2009) 15:112–9. doi: 10.1016/j.molmed.2009.01.003
11. Stieler JT, Bullmann T, Kohl F, Tøien Ø, Brückner M, Härtig W, et al. The physiological link between metabolic rate depression and tau phosphorylation in mammalian hibernation. *PLoS One.* (2011) 6:e14530. doi: 10.1371/journal.pone.0014530
12. Millán J, Pintó X, Muñoz A, Zúñiga M, Pedro-Botet J. Lipoprotein ratios: physiological significance and clinical usefulness in cardiovascular prevention. *Vasc Health Risk Manag.* (2009) 5:757–65.
13. Walldius G, Jungner I. Is there a better marker of cardiovascular risk than LDL cholesterol? Apolipoproteins B and AI–new risk factors and targets for therapy. *Nutr Metab Cardiovasc Dis.* (2007) 17:565–71. doi: 10.1016/j.numecd.2007.02.010
14. Wang X, Rader DJ. Molecular regulation of macrophage reverse cholesterol transport. *Curr Opin Cardiol.* (2007) 22:368. doi: 10.1097/HCO.0b013e3281ec5113
15. Giambattistelli F, Bucossi S, Salustri C, Panetta V, Mariani S, Siotto M, et al. Effects of hemochromatosis and transferrin gene mutations on iron dyshomeostasis, liver dysfunction and on the risk of Alzheimer's disease. *Neurobiol Aging.* (2012) 33:1633–41. doi: 10.1016/j.neurobiolaging.2011.03.005
16. Gjin N. Uric acid and cardiovascular disease. *Clin Chim Acta.* (2018) 484:150.
17. Wang H, Ran J, Jiang T. Urea. *Urea Transporters.* (2014) 73:7–29.
18. Al-Khateeb E, Althaher A, Al-Khateeb M, Al-Musawi H, Shafagoj Y. Relation between uric acid and alzheimer's disease in elderly jordanians. *J. Alzheimers Dis.* (2015) 44:859–65. doi: 10.3233/JAD-142037

19. Frej AD, Otto GP, Williams RS. Tipping the scales: lessons from simple model systems on inositol imbalance in neurological disorders. *Eur J Cell Biol.* (2017) 96:154–63. doi: 10.1016/j.ejcb.2017.01.007
20. Gundersen RY, Vaagenes P, Breivik T, Fonnum F, Opstad PK. Glycine–an important neurotransmitter and cytoprotective agent. *Acta Anaesthesiol Scand.* (2005) 49:1108–16. doi: 10.1111/j.1399-6576.2005.00786.x
21. Menzie J, Pan C, Prentice H, Wu J-Y. Taurine and central nervous system disorders. *Amino Acids.* (2014) 46:31–46. doi: 10.1007/s00726-012-1382-z
22. Sadhu A, Upadhyay P, Agrawal A, Ilango K, Karmakar D, Singh GPI, et al. Management of cognitive determinants in senile dementia of Alzheimer's type: therapeutic potential of a novel polyherbal drug product. *Clin Drug Invest.* (2014) 34:857–69. doi: 10.1007/s40261-014-0235-9
23. Palop JJ, Mucke L. Amyloid-beta-induced neuronal dysfunction in Alzheimer's disease: from synapses toward neural networks. *Nat Neurosci.* (2010) 13:812–8. doi: 10.1038/nn.2583
24. Wenk GL. Neuropathologic changes in Alzheimer's disease. *J Clin Psychiatry.* (2006) 64(Suppl. 9):7–10.
25. Lauritzen L, Hansen HS, Jorgensen MH, Michaelsen KF. The essentiality of long chain n-3 fatty acids in relation to development and function of the brain and retina. *Prog Lipid Res.* (2001) 40:1–94. doi: 10.1016/s0163-7827(00)00017-5
26. Mccann JC, Ames BN. Is docosahexaenoic acid, an n-3 long-chain polyunsaturated fatty acid, required for development of normal brain function? An overview of evidence from cognitive and behavioral tests in humans and animals. *Am J Clin Nutr.* (2005) 82:281–95. doi: 10.1093/ajcn.82.2.281
27. Breckenridge WC. The lipid composition of adult rat brain synaptosomal plasma membranes. *Biochim Biophys Acta.* (1972) 266:695–707. doi: 10.1016/0006-3002(72)90012-1
28. Katakura M, Hashimoto M, Shahdat HM, Gamoh S, Shido O. Docosahexaenoic acid promotes neuronal differentiation by regulating basic helix–loop–helix transcription factors and cell cycle in neural stem cells. *Neuroscience* (2012) 160:1–9. doi: 10.1016/j.neuroscience.2009.02.057
29. Dagai L, Peri-Naor R, Birk RZ. Docosahexaenoic acid significantly stimulates immediate early response genes and neurite outgrowth. *Neurochem Res.* (2009) 34:867–75. doi: 10.1007/s11064-008-9845-z
30. Calon F, Lim GP, Yang F, Morihara T, Cole GM. Docosahexaenoic acid protects from dendritic pathology in an Alzheimer's disease mouse model. *Neuron.* (2004) 43:633–45.
31. Sderberg M, Edlund C, Kristensson K, Dallner G. Fatty acid composition of brain phospholipids in aging and in Alzheimer's disease. *Lipids.* (1991) 26:421–5. doi: 10.1007/BF02536067
32. Montine TJ, Morrow JD. Fatty acid oxidation in the pathogenesis of Alzheimer's disease. *Am J Pathol.* (2005) 166:1283–9. doi: 10.1016/S0002-9440(10)62347-4
33. Markesbery WR, Kryscio RJ, Lovell MA, Morrow JD. Lipid peroxidation is an early event in the brain in amnestic mild cognitive impairment. *Ann Neurol.* (2010) 58:730–5. doi: 10.1002/ana.20629
34. Conquer JA, Tierney MC, Zecevic J, Bettger WJ, Fisher RH. Fatty acid analysis of blood plasma of patients with alzheimer's disease, other types of dementia, and cognitive impairment. *Lipids.* (2000) 35:1305–12. doi: 10.1007/s11745-000-0646-3
35. Vassar R. BACE1 inhibitor drugs in clinical trials for Alzheimer's disease. *Alzheimers Res Ther.* (2014) 6:89. doi: 10.1186/s13195-014-0089-7
36. Hashimoto M, Hossain S. Neuroprotective and ameliorative actions of polyunsaturated fatty acids against neuronal diseases: beneficial effect of docosahexaenoic acid on cognitive decline in Alzheimer's disease. *J Pharmacol Sci.* (2011) 116:150–62. doi: 10.1254/jphs.10r33fm
37. Lim GP, Calon F, Morihara T, Yang F, Teter B, Ubeda O, et al. A diet enriched with the omega-3 fatty acid docosahexaenoic acid reduces amyloid burden in an aged Alzheimer mouse model. *J Neurosci.* (2005) 25:3032. doi: 10.1523/JNEUROSCI.4225-04.2005
38. Lukiw WJ, Cui JG, Marcheselli VL, Bodker M, Botkjaer A, Gotlinger K, et al. A role for docosahexaenoic acid–derived neuroprotectin D1 in neural cell survival and Alzheimer disease. *J Clin Invest.* (2005) 115:2774–83. doi: 10.1172/JCI25420
39. Oster T, Florent-Béchard S, Allouche A, Garcia P, Malaplate-Armand C, Kriem B, et al. Dietary DHA supplementation leads to synaptic protection and cognitive preservation in an Alzheimer's disease mouse model. *Alzheimers Dement.* (2009) 5:181–2.
40. Hashimoto M, Hossain S, Shimada T, Sugioka K, Yamasaki H, Fujii Y, et al. Docosahexaenoic acid provides protection from impairment of learning ability in Alzheimer's disease model rats. *J Neurochem.* (2010) 81:1084–91. doi: 10.1046/j.1471-4159.2002.00905.x
41. Hooijmans CR, Van der Zee CE, Dederen PJ, Brouwer KM, Reijmer YD, Groen TV, et al. DHA and cholesterol containing diets influence Alzheimer-like pathology, cognition and cerebral vasculature in APPswe/PS1dE9 mice. *Neurobiol Dis.* (2009) 33:482–98. doi: 10.1016/j.nbd.2008.12.002
42. Schaefer EJ, Bongard V, Beiser AS, Lamon-Fava S, Wolf PA. Plasma phosphatidylcholine docosahexaenoic acid content and risk of dementia and Alzheimer disease: the Framingham Heart Study. *Arch Neurol.* (2006) 63:1545–50. doi: 10.1001/archneur.63.11.1545
43. Barberger-Gateau P, Letenneur L, De Schamps V, Peres K, Dartigues JF, Renaud S. Fish, meat, and risk of dementia: cohort study. *BMJ Br Med J.* (2002) 325:932–3. doi: 10.1136/bmj.325.7370.932
44. Kalmijn S, Launer LJ, Ott A, Witteman JC, Hofman A, Breteler MM. Dietary fat intake and the risk of incident dementia in the Rotterdam study. *Ann Neurol.* (2010) 42:776–82. doi: 10.1002/ana.410420514
45. Morris MC, Evans DA, Bienias JL, Tangney CC, Bennett DA, Wilson RS, et al. Consumption of fish and n-3 fatty acids and risk of incident Alzheimer disease. *Arch Neurol.* (2003) 60:940–6. doi: 10.1001/archneur.60.7.940
46. Kotani S, Sakaguchi E, Warashina S, Matsukawa N, Yamashima T. Dietary supplementation of arachidonic and docosahexaenoic acids improves cognitive dysfunction. *Neurosci Res.* (2006) 56:159–64. doi: 10.1016/j.neures.2006.06.010
47. Gelder BV, Tijhuis M, Kalmijn S, Kromhout D. Fish consumption, n-3 fatty acids, and subsequent 5-y cognitive decline in elderly men: the Zutphen elderly study. *Am J Clin Nutr.* (2007) 85:1142–7. doi: 10.1093/ajcn/85.4.1142
48. Freund-Levi Y, Eriksdotter-Jnhagen M, Cederholm T, Basun H, Palmblad J. ??-3 Fatty acid treatment in 174 patients with mild to moderate Alzheimer disease: omeGad study. *JAMA Neurol.* (2006) 63:1402–8. doi: 10.1001/archneur.63.10.1402
49. Oksman M, Iivonen H, Hogyes E, Amtul Z, Penke B, Leenders I, et al. Impact of different saturated fatty acid, polyunsaturated fatty acid and cholesterol containing diets on beta-amyloid accumulation in APP/PS1 transgenic mice. *Neurobiol Dis.* (2006) 23:563–72. doi: 10.1016/j.nbd.2006.04.013
50. Ma QL, Teter B, Ubeda OJ, Morihara T, Dhoot D, Nyby M, et al. Omega-3 fatty acid docosahexaenoic acid increases SorLA/LR11, a sorting protein with reduced expression in sporadic Alzheimer's disease (AD): relevance to AD prevention. *J Neurosci.* (2011) 27:14299–307. doi: 10.1523/JNEUROSCI.3593-07.2007
51. Hooijmans CR, Rutters F, Dederen PJ, Gambarota G, Veltien A, Groen TV, et al. Changes in cerebral blood volume and amyloid pathology in aged Alzheimer APP/PS1 mice on a docosahexaenoic acid (DHA) diet or cholesterol enriched typical western diet (TWD). *Neurobiol Dis.* (2007) 28:16–29. doi: 10.1016/j.nbd.2007.06.007
52. Sarkadinagy E, Wijendran V, Diau GY, Chao AC, Hsieh AT, Turpeinen A, et al. The influence of prematurity and long chain polyunsaturate supplementation in 4-week adjusted age baboon neonate brain and related tissues. *Pediatr Res.* (2003) 54:244–52.
53. Dawkins E, Small DH. Insights into the physiological function of the beta-amyloid precursor protein: beyond Alzheimer's disease. *J Neurochem.* (2014) 129:756–69. doi: 10.1111/jnc.12675
54. Strooper BD, Annaert W. Proteolytic processing and cell biological functions of the amyloid precursor protein. *J Cell Sci.* (2000) 113:1857–70. doi: 10.1242/jcs.113.11.1857
55. Avila J. Tau phosphorylation and aggregation in Alzheimer's disease pathology. *FEBS Lett.* (2006) 580:2922–7. doi: 10.1016/j.febslet.2006.02.067
56. Karr JW, Szalai VA. Cu(II) binding to monomeric, oligomeric, and fibrillar forms of the Alzheimer's disease amyloid-beta peptide. *Biochemistry.* (2008) 47:5006–16. doi: 10.1021/bi702423h
57. Prohovnik I, Perl DP, Davis KL, Libow L, Lesser G, Haroutunian V. Dissociation of neuropathology from severity of dementia in late-onset Alzheimer disease. *Neurology.* (2006) 66:49–55. doi: 10.1212/01.wnl.0000191298.68045.50

58. Barnes DE, Yaffe K. The projected effect of risk factor reduction on Alzheimer's disease prevalence. *Lancet Neurol.* (2011) 10:819–28. doi: 10.1016/S1474-4422(11)70072-2
59. Baumgart M, Snyder HM, Carrillo MC, Fazio S, Kim H, Johns H. Summary of the evidence on modifiable risk factors for cognitive decline and dementia: a population-based perspective. *Alzheimers Dement J Alzheimers Assoc.* (2015) 11:718–26.
60. De Reuck J, Maurage CA, Deramecourt V, Pasquier F, Cordonnier C, Leys D, et al. Aging and cerebrovascular lesions in pure and in mixed neurodegenerative and vascular dementia brains: a neuropathological study. *Folia Neuropathol.* (2018) 56:81–7. doi: 10.5114/fn.2018.76610
61. Lewis TL, Cao D, Lu H, Mans RA, Su YR, Jungbauer L, et al. Overexpression of Human Apolipoprotein A-I Preserves cognitive function and attenuates neuroinflammation and cerebral amyloid angiopathy in a mouse model of Alzheimer Disease. *J Biol Chem.* (2010) 285:36958–68. doi: 10.1074/jbc.M110.127829
62. Sherman C, Peterson SJ, Frishman WH. Apolipoprotein A-I mimetic peptides: a potential new therapy for the prevention of atherosclerosis. *Cardiol Rev.* (2010) 18:141–7.
63. Bereczki E, Berna G, Csont T, Ferdinandy P, Scheich H, Santha M. Overexpression of human apolipoprotein B-100 induces severe neurodegeneration in transgenic mice. *J Proteome Res.* (2008) 7:2246–52. doi: 10.1021/pr7006329
64. Caramelli P, Nitrini R, Maranhão R, Lourenço A, Caramelli B. Increased apolipoprotein B serum concentration in Alzheimer's disease. *Acta Neurol Scand.* (2010) 100:61–3. doi: 10.1111/j.1600-0404.1999.tb00724.x
65. Takechi R, Galloway S, Pallebage-Gamarallage M, Wellington CL, Mamo J. Differential effects of dietary fatty acids on the cerebral distribution of plasma-derived apo B lipoproteins with amyloid-beta. *Br J Nutr.* (2009) 103:652–62. doi: 10.1017/S0007114509992194
66. Al-khateeb E, Al-dalahmah O, Al-zayadneh E, Alawadi Z, khatib F, Naffa R, et al. Relation between copper, lipid profile, and cognition in elderly Jordanians. *J Alzheimers Dis.* (2014) 41:203–11. doi: 10.3233/JAD-132180
67. Fenili D, Brown M, Rappaport R, Mclaurin JA. Properties of scyllo–inositol as a therapeutic treatment of AD-like pathology. *J Mol Med.* (2007) 85:603–11. doi: 10.1007/s00109-007-0156-7
68. Mclaurin JA, Kierstead ME, Brown ME, Hawkes CA, Lambermon M, Phinney AL, et al. Cyclohexanehexol inhibitors of Abeta aggregation prevent and reverse Alzheimer phenotype in a mouse model. *Nat Med.* (2006) 12:801–8. doi: 10.1038/nm1423
69. Harada K, Nakato K, Yarimizu J, Yamazaki M, Morita M, Takahashi S, et al. A novel glycine transporter-1 (GlyT1) inhibitor, ASP2535 (4-[3-isopropyl-5-(6-phenyl-3-pyridyl)-4H-1,2,4-triazol-4-yl]-2,1,3-benzoxadiazole), improves cognition in animal models of cognitive impairment in schizophrenia and Alzheimer's disease. *Eur J Pharmacol.* (2012) 685:59–69. doi: 10.1016/j.ejphar.2012.04.013

Conflict of Interest: MX, WX, SL, YZ, BL, and XL were employed by CABIO Biotech (Wuhan) Co., Ltd.

The remaining authors declare that the research was conducted in the absence of any commercial or financial relationships that could be construed as a potential conflict of interest.

Publisher's Note: All claims expressed in this article are solely those of the authors and do not necessarily represent those of their affiliated organizations, or those of the publisher, the editors and the reviewers. Any product that may be evaluated in this article, or claim that may be made by its manufacturer, is not guaranteed or endorsed by the publisher.

Copyright © 2022 Xiao, Xiang, Chen, Peng, Du, Lu, Zuo, Li, Hu and Li. This is an open-access article distributed under the terms of the Creative Commons Attribution License (CC BY). The use, distribution or reproduction in other forums is permitted, provided the original author(s) and the copyright owner(s) are credited and that the original publication in this journal is cited, in accordance with accepted academic practice. No use, distribution or reproduction is permitted which does not comply with these terms.

frontiers | Frontiers in Nutrition

ORIGINAL RESEARCH
published: 07 July 2022
doi: 10.3389/fnut.2022.878229

Pea Peptide Supplementation in Conjunction With Resistance Exercise Promotes Gains in Muscle Mass and Strength

Shaohui Jia[1], Qiming Wu[2], Shue Wang[3], Juntao Kan[2], Zhao Zhang[4], Xiping Zhang[4], Xuejun Zhang[4], Jie Li[4], Wenhan Xu[5], Jun Du[2] and Wei Wei[4]**

[1] Hubei Collaborative Innovation Center for Sports Intervention and Health Promotion, Wuhan Sports University, Wuhan, China, [2] Amway (Shanghai) Innovation & Science Co., Ltd., Shanghai, China, [3] School of Public Health, Shandong University, Jinan, China, [4] Zhong Shi Du Qing (Shandong) Biotechnology Company, Heze, China, [5] College of Food Science and Engineering, Northwest A&F University, Yangling, China

OPEN ACCESS

Edited by:
Biao Yuan,
China Pharmaceutical University, China

Reviewed by:
Fan Yao,
Huazhong Agricultural University, China
Gong Jianke,
Huazhong University of Science and Technology, China

***Correspondence:**
Jun Du
Eric.Du@amway.com
Wei Wei
zhongshiweiwei@163.com

Specialty section:
This article was submitted to Food Chemistry, a section of the journal Frontiers in Nutrition

Received: 17 February 2022
Accepted: 21 March 2022
Published: 07 July 2022

Citation:
Jia S, Wu Q, Wang S, Kan J, Zhang Z, Zhang X, Zhang X, Li J, Xu W, Du J and Wei W (2022) Pea Peptide Supplementation in Conjunction With Resistance Exercise Promotes Gains in Muscle Mass and Strength. Front. Nutr. 9:878229. doi: 10.3389/fnut.2022.878229

It is generally considered that protein supplementation and resistance exercise significantly increase muscle mass and muscle growth. As the hydrolysis products of proteins, peptides may play the crucial role on muscle growth. In this study, male rats were orally administrated 0.4 g/kg body weight of pea peptide combined with 8 weeks of moderate intensity resistance exercise training. After treatment, the body gains, upper limb grip, muscle thickness, and wet weight of biceps brachii were tested, and the cross-sectional area of biceps brachii muscle fiber and the types of muscle fibers were determined by HE staining, immunofluorescence staining, and lactate dehydrogenase activity, respectively. Western blot analysis was used to investigate the level of growth-signaling pathway-related proteins. The results showed that pea peptide supplementation combined with resistance exercise training significantly increased body weight, upper limb grip, muscle thickness, wet weight of biceps brachii, and cross-sectional area of muscle fiber. Meanwhile, pea peptide supplementation obviously elevated the ratio of fast-twitch fiber (type II) and the expression of muscle growth-signaling pathway-related proteins. In addition, the PP2 oligopeptide in pea peptide with the amino acid sequence of LDLPVL induced a more significant promotion on C2C12 cell growth than other oligopeptides.

Keywords: pea peptide, resistance exercise, muscle mass, muscle strength, muscle growth

INTRODUCTION

Skeletal muscle mass is an integral body tissue playing the key roles in strength, performance, and metabolic regulation. Skeletal muscle mass is the product of continuous and simultaneous processes of muscle protein synthesis (MPS) and muscle protein breakdown (MPB) and the net balance between these two processes determines whether muscle mass increases, decreases, or remains constant (1).

It is well known that protein supplementation including animal protein such as meat, fish, dairy products, eggs, and plant protein such as tofu, legumes, and quinoa is necessary for muscle growth in responsible to resistance exercise. A general view within the sport nutrition community is that animal proteins and whey protein, in particular, are more effective in building muscle in response to

resistance exercise training (2). Whereas some researchers regarded that plant proteins such as soy protein may have a number of advantages over animal protein including lowering blood cholesterol levels (3), other researchers also suggested that any nutritional supplement that could increase protein accretion in muscle would maximize resistance training effects by enhancing muscle anabolism (4). At the same time, studies have also shown that there are no differences not only between plant protein and whey protein, but also between soy protein and general animal protein when it comes to building muscle (5). Soy protein is often considered to be the quintessential plant protein and plays a positive role on increasing muscle mass (6). Pea protein is another important plant protein, and one study has confirmed that pea protein supplementation induced a greater increase on muscle thickness as compared to placebo (7).

It is reported that the intake of essential amino acids (EAAs) such as leucine, isoleucine, lysine, methionine, phenylalanine, threonine, tryptophan, and valine after physical exercise can ensure the optimal protein synthesis, and the net protein synthesis increases when EAAs are consumed before and after resistance exercise (8, 9). In the recent years, oligopeptides have attracted more and more attention in many fields owing to their high biological activity and absorbability (10–12). Unfortunately, more studies are still needed to determine the role of oligopeptides in promoting muscle growth.

Despite supplementation with plant derived proteins has been confirmed to promote muscle growth in response to resistance exercise training, few studies have focused on the effect of pea peptides on skeletal muscle growth. Therefore, in this study, pea oligopeptide (PP) was first obtained by enzymatic hydrolysis of pea protein. Then, 2-month-old rats were orally administrated pea oligopeptide and performed 8 weeks of resistance exercise training to evaluate the effect of pea oligopeptide supplementation combined with resistance exercise on skeletal muscle growth and explore new functional substances for combating muscle atrophy.

MATERIALS AND METHODS

Pea Oligopeptide Preparation

The pea protein was diluted to 7.5% solution with free ionic water and rise the temperature to 55°C. Then, the solution was adjusted to pH 8.5 with 1 mol/L NaOH and added into 1.2% alkaline protease to hydrolyze the proteins for 6 h. After treatment, the enzyme was inactivated at 100°C for 20 min. Subsequently, the hydrolysate was filtered through a regenerated cellulose dialysis membrane with a molecular weight of 1,000 Dalton. Finally, the filtrate was collected and freeze-dried to obtain pea oligopeptide.

Determination of Amino Acid Composition of Pea Peptide

The above-obtained sample was further purified by a high-performance liquid chromatograph (HPLC, Agilent 1100, Tokyo, Japan), and then, the purified products of RP-HPLC were collected to determine the amino acid composition of pea peptide using Hitachi Amino Acid Analyzer (LA8900, Hitachi, Japan).

TABLE 1 | Amino acid composition of pea peptide (g / 100 g peptide).

Retention time	Amino acid	Area	Percentage (%)
4.733	Asp	5332554	12.12
5.380	Thr	1700427	3.67
5.973	Glu	2601175	7.02
6.673	Ser	7574282	13.20
7.293	Pro	783389	4.77
9.513	Gly	2478635	3.94
10.280	Ala	1866356	4.07
11.667	Cys	155165	0.59
12.273	Val	2869568	5.93
13.500	Met	436951	0.94
15.800	Ile	1926054	4.28
16.987	Leu	3430418	9.25
18.300	Tyr	646207	2.46
19.507	Phe	1746753	4.59
22.000	Lys	3693258	7.06
24.200	His	879921	2.00
28.240	Arg	2723907	7.19

Separation of Pea Peptides by HPLC

The above peptides were further separated and purified by reverse HPLC under the following conditions: the mobile phase consisted of 95% acetonitrile and 5% water containing 0.1% trifluoroacetic, and the flow rate was 1.0 ml/min. After separation, the peak tip solution was collected to determine the amino acid sequence.

Animals Grouping and Treatment

A total of 30 male Sprague-Dawley (SD) rats at the age of 8 weeks were obtained from Hubei Provincial Center for Disease Control and Prevention (license no. scxk (E) 2011-0012). All animals were first acclimated for at least 1 week and then kept under the following conditions: specific pathogen free, 12-h light–dark cycles at 22–24°C, and free access to food and water except when fasting tests were required. All experiments were conducted under the institutional guidelines of the Institutional Animal Care and Use Committee at Wuhan Sports University for the humane treatment of laboratory animals. Finally, the rats were randomly divided into control group (CN), resistance exercise training group (RT), and pea peptide combined with resistance training group (PP+RT), and 10 rats were fed in each group. The rats in RT group were carried out 8 weeks of resistance exercise training, the rats in PP + RT group were daily intragastrically administered with 0.4 g/kg body weight of pea peptides and then performed resistance exercise training for 8 weeks, and the rats in CN group were daily intragastrically administered with same volume of saline. The detailed exercise protocol is as follows: after a week of familiarization with the ladder, the rats of RT and PP +RT group were performed 8 weeks of ladder climbing exercise on a 1-m ladder with a 2-cm grid ladder inclined at 85° with weights attached to their tails. The maximum load carried successfully throughout the length

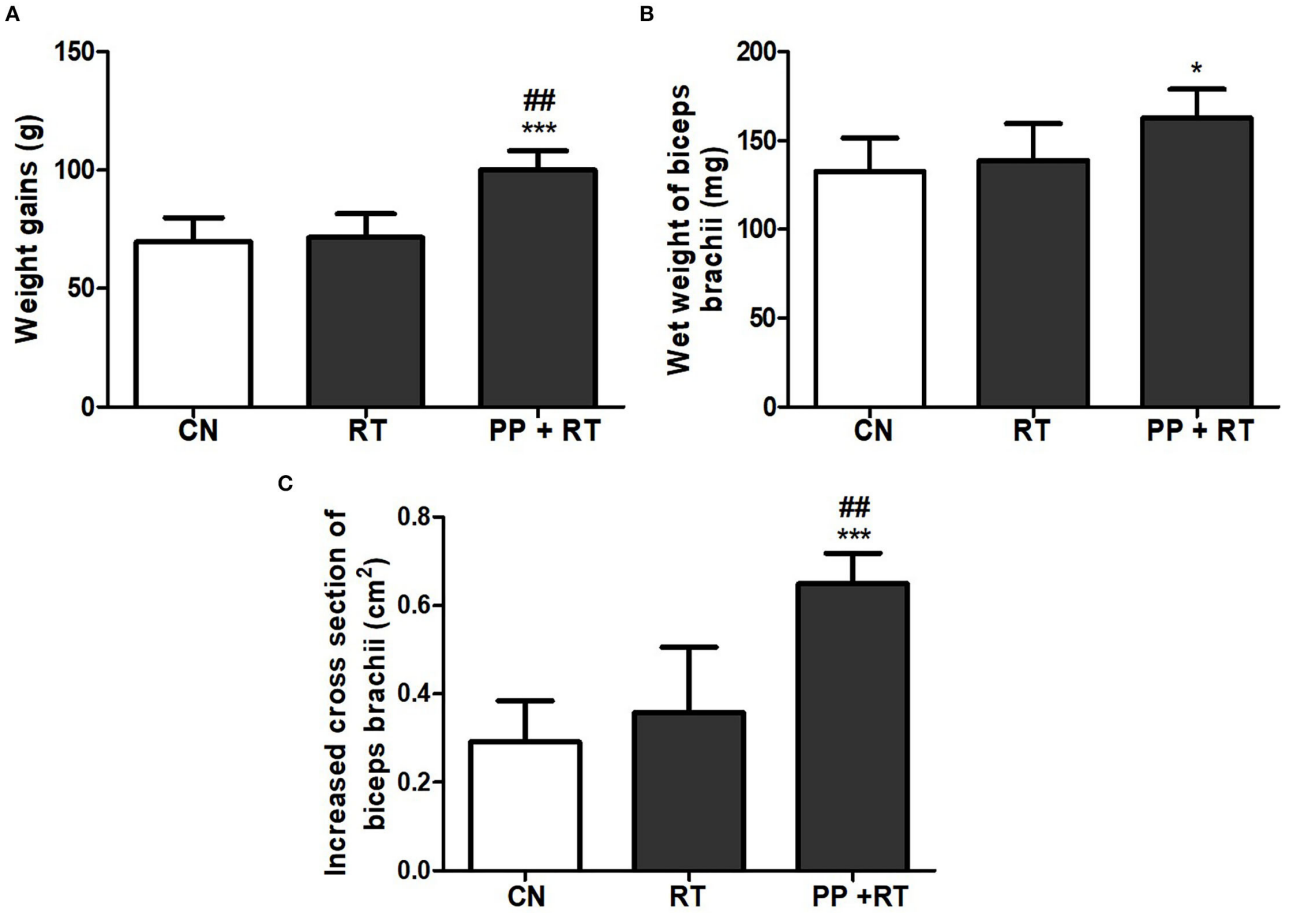

FIGURE 1 | Pea peptide supplementation combined with resistance exercise induced elevated muscle thickness and weight gains. **(A)** Body weight gains of the rats in CN, RT, and PP+RT group. **(B)** Wet weight of biceps brachii in the rats of CN, RT, and PP+RT group. **(C)** Increased cross-section of biceps brachii in the rats of CN, RT, and PP+RT group. CN: Control group, the rats were intragastrically administered with same volume of saline; RT: Resistance training group, the rats were carried out 3 times each week of resistance exercise training; PP+RT: Pea peptide supplementation combined with resistance exercise training group, the rats were daily intragastrically administered with 0.4 g/kg body weight of pea peptides and performed three times each week of resistance exercise training. The significant difference between groups was validated with one-way ANOVA using GraphPad Prism 6, $^{*}p < 0.05$, $^{***}p < 0.01$ vs. CN group, and $^{\#\#}p < 0.01$ vs. RT group (n = 5/group). Data are presented as mean ± standard deviation (M ± SD).

of the ladder was considered to be the maximum load capacity for the training session, and the maximum load capacity was detected at weeks 1, 2, 4, 6, and 8. Each rat carried a load that was 50% of its body mass at the first training week and exercise load added to 100% of its body weight until the end of the 8th week with the frequency of three times per week, and 60 s of rest interval between repetitions and 5 min of rest interval between sets.

HE Staining

Biceps brachii muscle tissues of rats were harvested from the rats and fixed with 4% paraformaldehyde (PFA) overnight. The tissues embedded in paraffin were sectioned into 4 μm thickness, followed by deparaffinization and rehydration, and finally stained with hematoxylin and eosin following the manufacturer's introductions (Solarbio, Beijing, G1121).

Cell Culture and Treatment

C2C12 cell line was purchased from China Center for Type Culture Collection (CCTCC) and cultured with DMEM (Gibco, C11995500BT) containing 10% fetal bovine serum, 100 U/ml penicillin, and 100 mg/ml streptomycin in six well plates at 37°C. When the cells grew to 70% of the culture plate, 0.1 mg/ml of pea peptide components 1, 2, 3, 4, and 5 prepared by HPLC was added and incubated for 48 h. After treatment, the cells were harvested to perform western blot analysis.

Immunofluorescence Staining

Biceps brachii muscle tissues of rats were fixed with 4% PFA (Solarbio, Beijing, P1110) and embedded in paraffin. The 4-μm sections were prepared, followed by deparaffinization, rehydration, and quenching endogenous peroxidases with 0.3% H_2O_2 (in PBS) for 10 min. Then, the tissue sections were incubated with antigen retrieval buffer (Solarbio, C1032) at 95°C

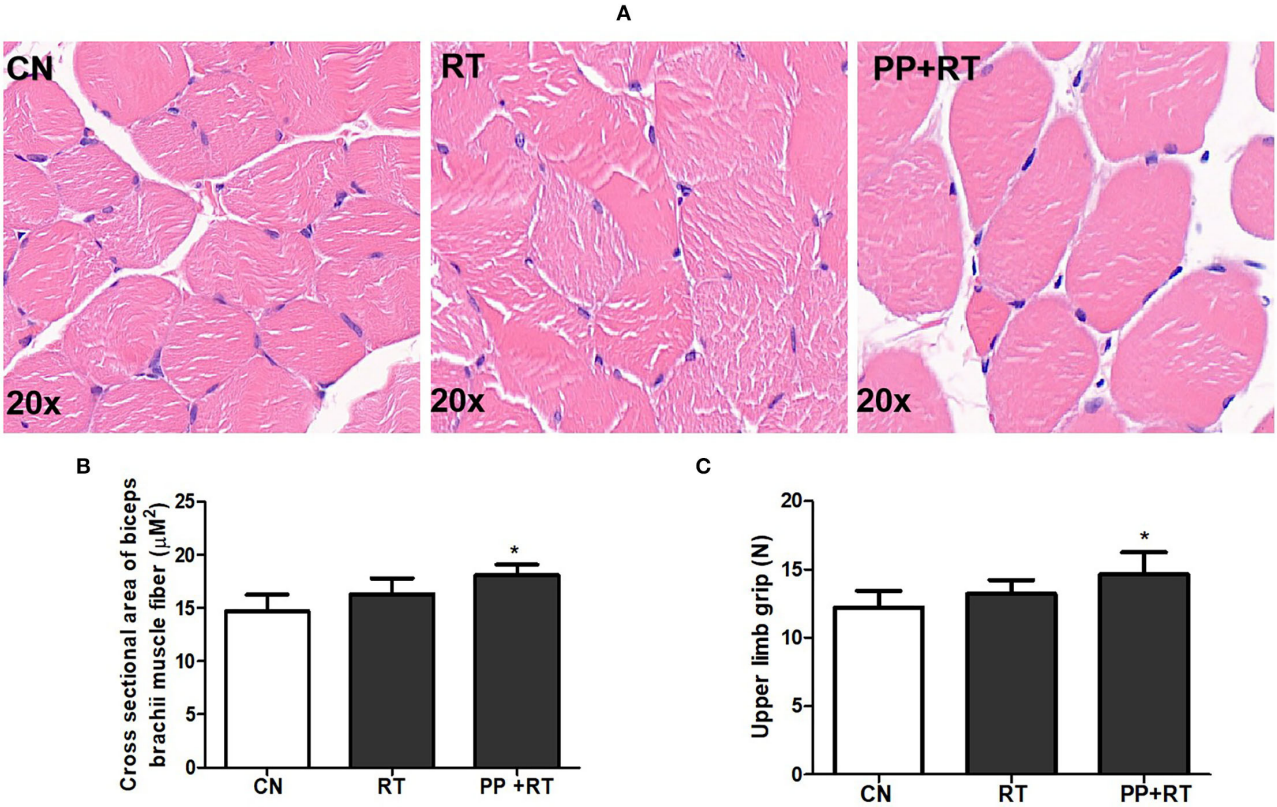

FIGURE 2 | Pea peptide supplementation combined with resistance exercise increased cross-section of muscle fiber and forelimb grip in rats. **(A)** HE staining of biceps brachii in the rats of CN, RT, and PP+RT group (20 x); **(B)** Statistical analysis of **(A)**; **(C)** Upper limb grip of rats in CN, RT and PP+RT group; CN, Control group; RT, Resistance training group; PP+RT: Pea peptide supplementation combined with resistance training. The significant difference between groups was validated with one-way ANOVA using GraphPad Prism 6, $^*p < 0.05$ vs. CN group (n=5/group). Data are presented as mean ± standard deviation (M ± SD).

for 20 min, permeabilized by 0.1% Triton X-100, and incubated with anti-fast skeletal myosin heavy chain antibody (MYH1, Abcam, 1:100, ab133567) and anti-slow skeletal myosin heavy chain antibody (MYH7, Abcam, 1: 500, ab234431) overnight at 4°C, followed by incubating with a secondary antibody goat anti-rat IgG H&L with FITC label (Alexa Fluor® 488) and goat anti-rabbit IgG H&L with CY3 label (Alexa Fluor® 647) for 60 min. After treatment, micromorphology was detected by Fluorescent Microscopy (IX83, Olympus). FITC glows green by excitation wavelength 465–495 nm and emission wavelength 515–555 nm; CY3 glows red by excitation wavelength 510–560 nm and emission wavelength 590 nm.

Determination of Lactate Dehydrogenase Activity

The lactate dehydrogenase activity of skeletal muscle was determined by enzyme-linked immunosorbent assay (ELISA) analysis. Briefly, 0.1 g of biceps brachii muscle tissues was cut and added into 1 ml of extracting solution, then, the tissues were homogenized for 3 min at 65 Hz in a pre-cooled homogenizer at 4°C, and the homogenate was centrifuged at 4°C for 10 min with the speed of 8,000 *g*. After treatment, the supernatant was collected to detect the activity of lactate dehydrogenase according to the instructions (Solarbio, bc0685).

Western Blot Analysis

Muscle tissue or cell lines were put into the pre-cooled saline solution to remove blood and connective tissues. After the tissues were cut, the cell lysis buffer and protease inhibitor (PMSF) were added into the centrifuged tube according to the ratio of 100:1 and then homogenized for 5 min at 65 Hz in a pre-cooled homogenizer at 4°C. The homogenized samples were treated with ultrasonic for 5 min and centrifuged at 4°C for 10 min, and then, the supernatant was collected to measure the protein concentration using BCA kit (Beyotime Institute of Biotechnology, China). The prepared total protein was separated by sodium dodecyl sulfate–polyacrylamide gel electrophoresis (SDS-PAGE) at 80 V and transferred onto a PVDF membrane for 2.5 h at 350 mA. The PVDF membrane was blocked for 2 h at room temperature with 5% nonfat milk and then washed three times with Tris Buffered Saline with 0.5% of Tween (TBST). Subsequently, the membrane was incubated with primary antibody including IGF-1R, myostatin, CDK6, cyclin D1, t-AMPK, and p-AMPK (Cell Signaling Technology, Danvers, MA, USA) overnight at 4°C, respectively, and the primary

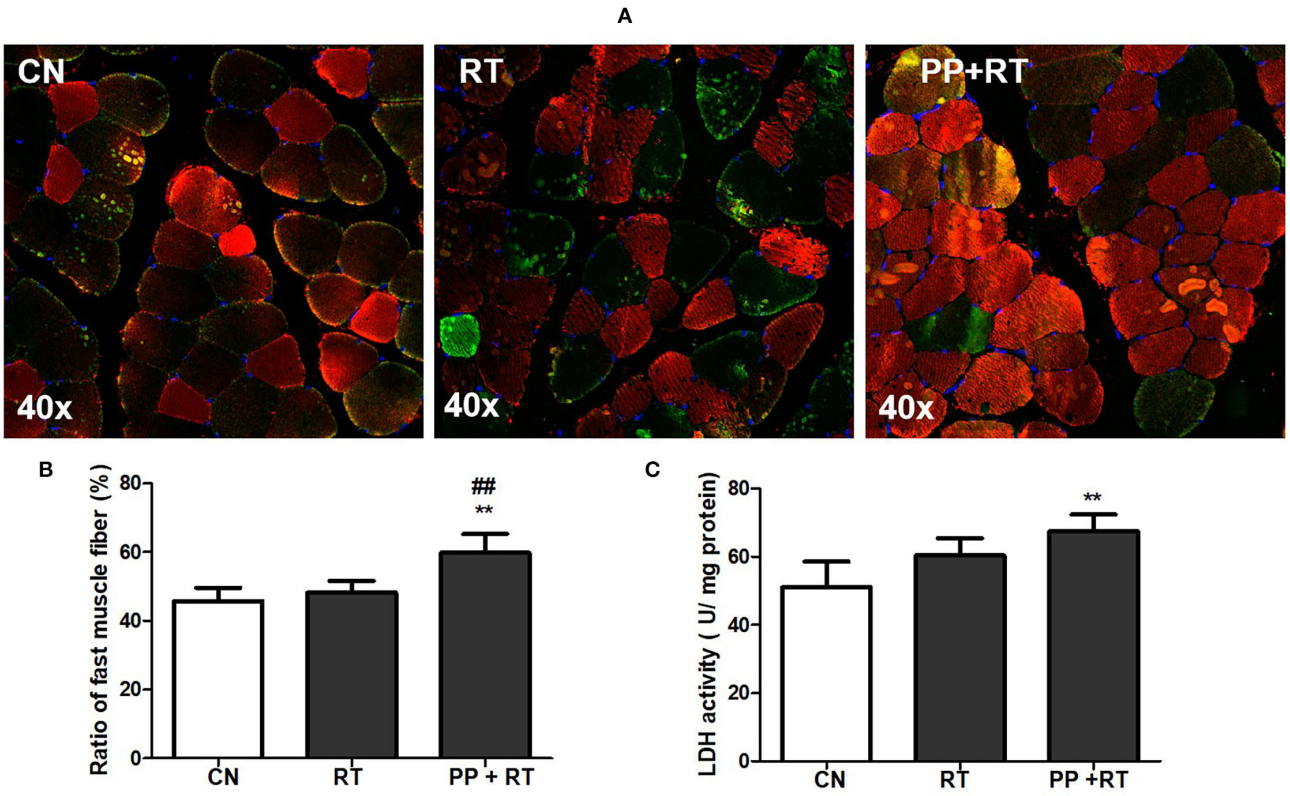

FIGURE 3 | Pea peptide supplementation enhanced the proportion of type 2 muscle fiber. **(A)** Immunofluorescence staining of biceps brachii in the rats of CN, RT, PP+RT group (40 x). Fast muscle fibers were labeled with red fluorescence and slow muscle fibers were labeled with green fluorescence; **(B)** statistical analysis of **(A)**; **(C)** upper limb grip of rats in CN, RT, PP+RT group. CN: Control group; RT: resistance training group; PP+RT: pea peptide supplementation combined with resistance training. The significant difference between groups was validated with one-way ANOVA using GraphPad Prism 6, $^{**}p < 0.01$ vs. CN group, and $^{\#\#}p < 0.01$ vs. RT group ($n = 5$/group). Data are presented as mean ± standard deviation (M ± SD).

antibody GAPDH (all from Cell Signaling Technology, Danvers, MA, USA) was used as the reference antibodies, respectively. Following incubation, the membrane was washed with TBST and incubated with secondary antibody (Abcam, UK) for 1 h at room temperature. Finally, the membranes were developed using an enhanced chemiluminescence (ECL) reagent (Pierce Biotechnology, Rock-ford, IL, USA). All blots were quantified using ImageJ software (National Institutes of Health, USA).

Cell Proliferation Assay

Cell proliferation was evaluated by MTT assay. C2C12 cells were seeded in a 96-well cell culture plate at a density of 1×10^4 cells/well and incubated with pea peptide (10 μg/ml) for 12, 24, or 48 h. Untreated cells served as the control group. After treatment, MTT was added into each well at a final concentration of 5 mg/ml, and the cells were further incubated at 37°C for 4 h. Dimethyl sulfoxide (100 μl) was added into each well after removing the medium. After shaking the plates for 5 min, the absorbance of the mixture was measured at 490 nm using a microplate ELISA reader (SpecterMax i3x, Austria).

Statistical Analysis

All values were performed using GraphPad prism 6.0 (GraphPad Software, Inc. San Diego, CA, USA) software. Data were presented as mean ± standard deviation (M ± SD). Statistical analysis was performed using one-way ANOVA between groups. Tukey's *post hoc* test was performed to express the mean difference between groups. The statistically significant difference was considered at $p < 0.05$.

RESULTS

The Amino Acid Composition of Pea Peptide

The amino acid content of pea peptide is up to 93.08%. The content of Ser was 13.20%, which is the most abundant amino acids in pea peptide. Moreover, pea peptide is also rich in the branched chain amino acids (Val, Ile, and Leu) and account for 19.46%. In addition, pea peptide contains abundant hydrophobic amino acids, including Ala, Val, Leu, Gly, Phe, and Met, accounting for about 28.72% (**Table 1**).

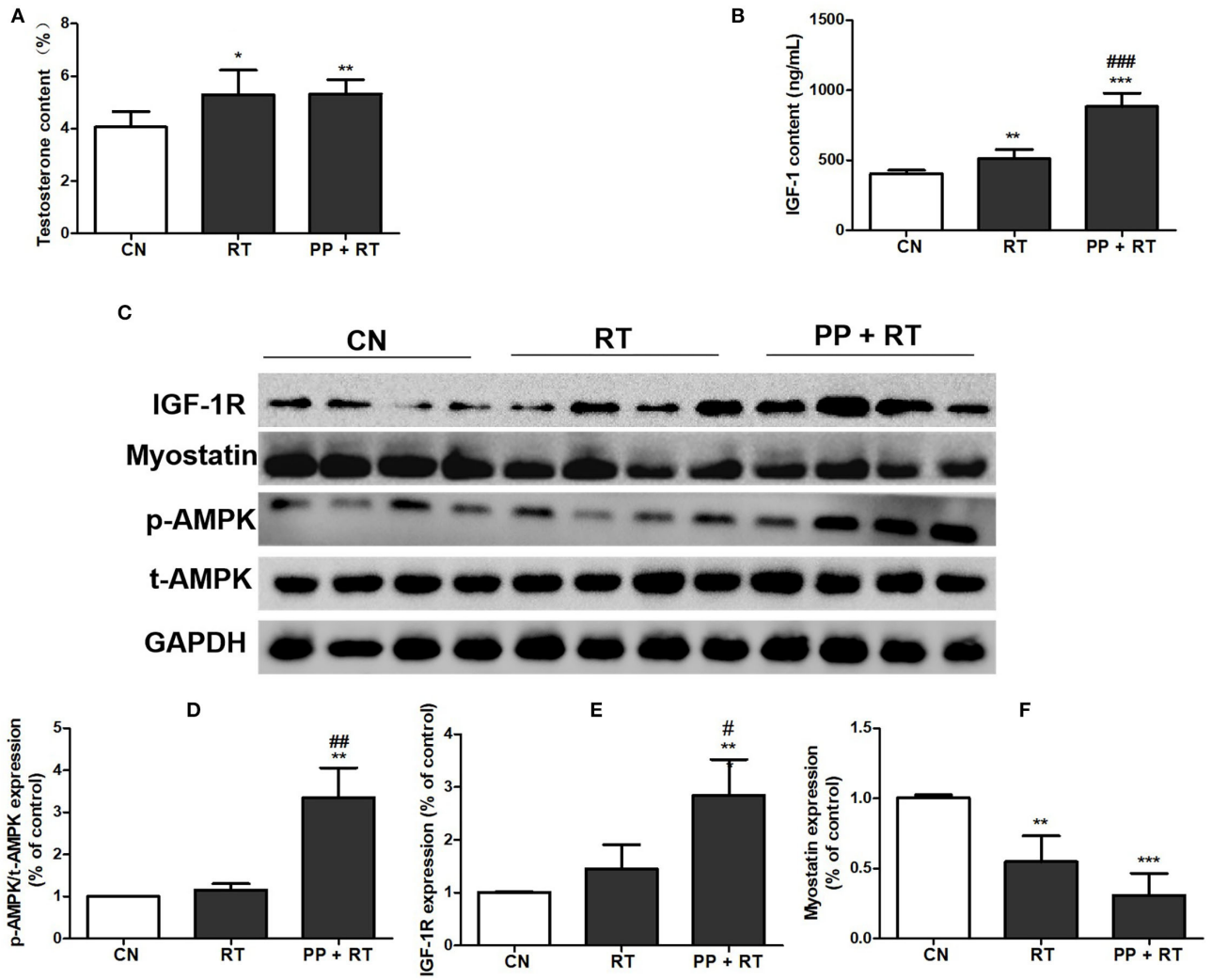

FIGURE 4 | Pea peptide supplementation activated muscle growth-signaling pathway. **(A)** Circulating testosterone content of the rats in CN, RT, and PP + RT group; **(B)** circulating IGF-1 content of the rats in CN, RT, and PP + RT group; **(C)** p-AMPK, t-AMPK, IGF-1R, and myostatin expression of skeletal muscle detected by western blots analysis; **(D)** statistical analysis of p-AMPK expression; **(E)** statistical analysis of IGF-1R expression; **(F)** statistical analysis of myostatin expression. CN: Control group; RT: resistance training group; PP+RT: pea peptide supplementation combined with resistance training. The significant difference between groups was validated with one-way ANOVA using GraphPad Prism 6, $^{*}p < 0.05$, $^{**}p < 0.01$, $^{***}p < 0.001$ vs. CN group, and $^{\#}p < 0.05$, $^{\#\#}p < 0.01$, $^{\#\#\#}p < 0.001$ vs. RT group ($n = 5$/group). Data are presented as mean ± standard deviation (M ± SD).

Pea Peptide Supplementation Combined With Resistance Exercise Induced Elevated Muscle Thickness and Body Weight Gains

As shown in **Figure 1**, compared with control and resistance training, treatment with pea peptide supplementation combined with resistance training resulted in an obvious increase on the body weight gains and the cross-section of biceps brachii (**Figures 1A,C**). We also observed that resistance exercise failed to enhance the wet weight of biceps brachii, whereas pea peptide combined with resistance exercise induced a significant increase on the wet weight of biceps brachii (**Figure 1B**).

Pea Peptide Supplementation Combined With Resistance Exercise Increased Forelimb Grip and Muscle Cross-Section

We subsequently investigated the effect of pea peptide supplementation on muscle strength, and the results showed that the cross-sectional area of biceps brachii muscle fiber in PP+RT group was significantly higher than that in CN and RT group (**Figures 2A,B**) ($p < 0.05$). Correspondingly, the upper limb grip also presented an obvious elevation in the rats of PP+RT group compared to CN and RT group (**Figure 2C**) ($p < 0.05$).

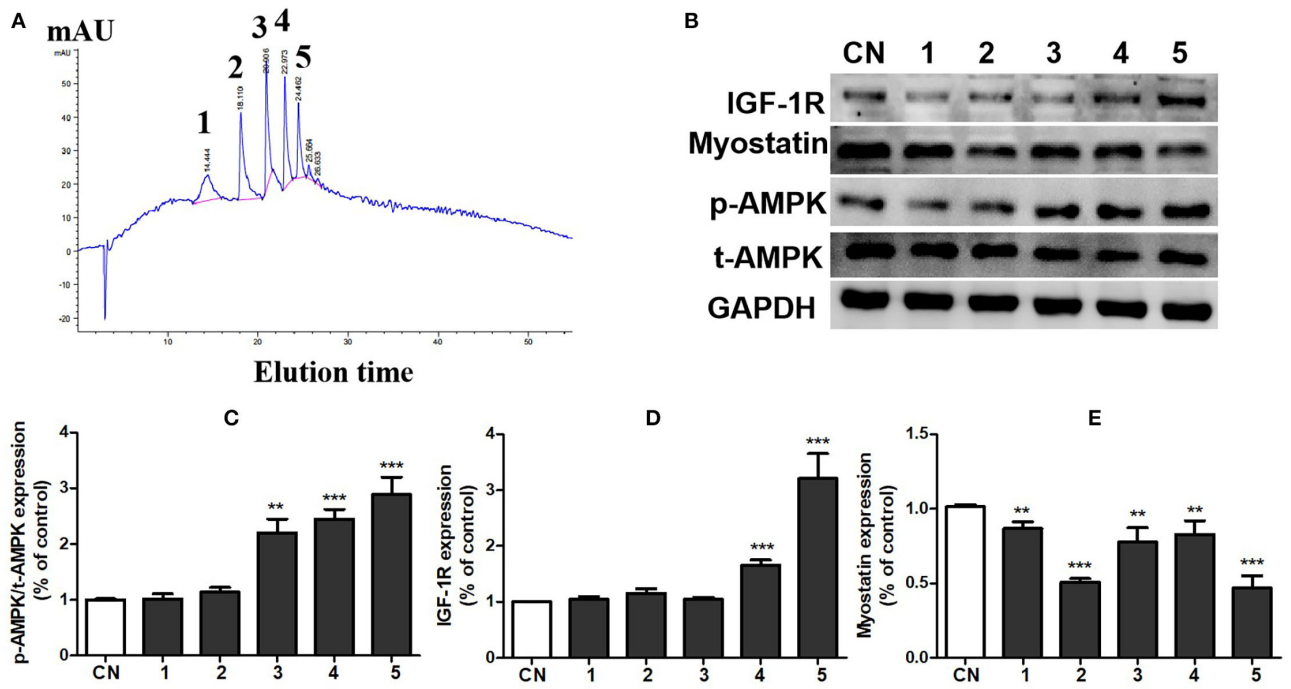

FIGURE 5 | Component 5 of pea peptide significantly activated muscle growth-signaling pathway. **(A)** Separation of pea peptides by HPLC; **(B)** expression of t-AMPK, p-AMPK, myostatin, and IGF-1R investigated by western blots; **(C)** statistical analysis of p-AMPK and t-AMPK expression; **(D)** statistical analysis of IGF-1R expression; **(E)** statistical analysis of myostatin expression. CN: Control group; RT: resistance training group; PP+RT: pea peptide supplementation combined with resistance training. The significant difference between groups was validated with one-way ANOVA using GraphPad Prism 6, $^{**}p < 0.01$, $^{***}p < 0.001$ vs. CN group (n = 5/group). Data are presented as mean ± standard deviation (M±SD).

Pea Peptide Supplementation Combined With Resistance Exercise Enhanced the Ration of Type 2 Muscle Fiber

Immunofluorescence staining indicated that resistance exercise alone failed to alter the ratio of fast-twitch muscular fiber in biceps brachii muscle. Whereas pea peptide supplementation combined with resistance exercise induced a great increase on the ratio of fast-twitch muscular fiber (**Figures 3A,B**), meanwhile, the LDH activity of biceps brachii muscle in PP + RT group showed a significant elevation compared with CN and RT group (**Figure 3C**).

Pea Peptide Supplementation Combined With Resistance Exercise Activated Muscle Growth-Signaling Pathway

A significant improvement in muscle mass and muscle strength induced by pea peptide supplementation has been observed in this study, we subsequently investigated the effect of pea peptide supplementation on muscle growth-signaling pathway. The results showed that testosterone content of the rats in RT and PP+RT group was significantly higher than that in CN group (**Figure 4A**). We also observed a significant elevation on the concentration of circulating IGF-1 in RT group compared with CN group and a more significant increase on the concentration of circulating IGF-1 in PP+RT group compared with CN and RT group (**Figure 4B**). Western blot analysis also indicated that pea peptide supplementation combined with resistance exercise significantly enhanced the expression of IGF-1R and p-AMPK, while obviously reduced myostatin expression in skeletal muscle (**Figures 4C–F**).

Component 5 of Pea Peptide Significantly Activated Muscle Growth-Signaling Pathway

To further clarify the substances with muscle enhancing effect in pea peptide, we divided soybean peptides into five components by HPLC (**Figure 5A**) and then detected the effects of each component on the activation of growth-signaling pathway in C2C12 cells. The results showed that all of five components obviously inhibited myostatin expression ($p < 0.05$); whereas the 3th, 4th, and 5th components significantly improved the phosphorylation of AMPK, and the 4th and 5th components tremendously elevated the expression of IGF-1R (**Figures 5B–E**). On the whole, the 5th component is likely superior to other components on the activation of growth-signaling pathway.

Pea Oligopeptide 2 Largely Promoted the Proliferation of C2C12 Cells

We subsequently determined the amino acid sequence of the peptides in component 5 of pea peptides by mass spectrometry and found that the 5th component contained five oligopeptides

TABLE 2 | Amino acid sequence of oligopeptide in pea peptide.

Oligopeptide in pea peptide	Amino acid sequence
1 (PP1)	Glu-Gly-Ser-Leu-Leu-Leu-Pro-His (EGSLLLPH)
2 (PP2)	Leu-Asp-Leu-Pro-Val-Leu (LDLPVL)
3 (PP3)	Leu-Leu-Tyr-Val-Ile-Arg (LLYVIR)
4 (PP4)	Thr-Asn-Tyr-Glu-Glu-Ile-Glu-Lys-Val-Leu-Leu (TNYEEIEKVLL)
5 (PP5)	Asn-Thr-Asn-Tyr-Glu-Glu-Ile-Glu-Lys-Val-Leu (NTNYEEIEKVL)

(**Table 2**). Then, we synthesized these five oligopeptides and co-incubated with C2C12 cells. After treatment for 48 h, the five pea oligopeptides all significantly promoted the proliferation of C2C12 cells when compared to control (**Figures 6B–F**). Notably, co-incubation of PP2 resulted in a more conspicuous proliferation of C2C12 cells in comparison with other oligopeptides and presented an obvious cell growth promoting effect even at 24 h (**Figure 6A**). Correspondingly, western blot analysis also showed that co-culture PP2 significantly elevated the expression of IGF-1R, cyclin D1, CDK6, and p-AMPK when compared to control.

DISCUSSION

Nowadays, much evidence has confirmed that plant protein supplementation produces similar gains in muscle thickness and strength as animal proteins in response to resistance exercise (4, 13–15). In this study, we observed that compared to placebo, pea peptide supplementation combined with resistance exercise markedly increased the muscle thickness of biceps brachii and the muscle strength of upper limb. Meanwhile, we found that pea peptide combined with resistance exercise significantly increased the cross-sectional area of muscle fibers. These above results demonstrated that pea peptide plays a crucial role in the promotion of muscle growth in response to resistance exercise training. Skeletal muscle is broadly characterized by the presence of two distinct categories of muscle fibers named slow-twitch fibers (type I) and fast-twitch fiber (type II). Fast-twitch fibers have higher LDH activity and display a stronger contractility in contrast with slow-twitch fibers (4). In our study, immunofluorescence staining as well as LDH detection revealed that pea peptide supplementation combined with resistance exercise obviously enhanced the ration of fast muscle fiber.

In addition, we investigated the effect of pea peptide on muscle growth-signaling pathway. The results indicated that pea peptide supplementation combined with resistance exercise largely increased the expression of IGF-1R and the ration of p-AMPK/t-AMPK and conversely decreased myostatin expression. We also found that pea peptide supplementation combined with resistance exercise significantly elevated the concentration of circulating testosterone and IGF-1. IGF-1/IGF-1R signal axis plays a key role on muscle growth. It is reported that resistance exercise training effectively alleviated skeletal muscle atrophy by activating IGF-1/IGF-1R-PI3K/Akt pathway and resulted in the decrease of protein degradation and cell apoptosis (16). Myostatin, a member of the transforming growth factor-β superfamily, is a potent negative regulator of skeletal muscle growth and is conserved in many species, from rodents to humans. Myostatin is also known as growth differentiation factor 8. Myostatin inactivation can induce skeletal muscle hypertrophy, whereas its overexpression or systemic administration causes muscle atrophy (17). AMPK has also been considered to play an important role in regulating muscle mass and regeneration due to their effects on anabolic and catabolic cellular processes (18, 19).

To further explore the effect of pea peptide on the promotion of muscle growth, we obtained 5 components from pea peptides by HPLC and then incubated them with C2C12 cells to investigate the effect of various components on cell growth-signaling pathway. We observed that co-cultured with the 5th component of pea peptide significantly elevated the expression of p-AMPK and IGF-1R, while decreased myostatin expression. Subsequently, we harvested peak solution of the 5th component to determine the amino acid sequence using mass spectrometer. Additionally then, these five oligopeptides were synthesized and incubated with C2C12 cells to evaluate the effect of these five oligopeptides on cell proliferation. We found that all these five oligopeptides induced a significant proliferation of C2C12 cells after incubated for 48 h; moreover, PP2 incubation likely resulted in a more obvious increase in the number of cells than other oligopeptides. Further study indicated that PP2 induced the more conscious elevation on the expression of p-AMPK, IGF-1R, cyclin D1, and CDK6. Muscle regeneration is a rapid and extensive self-renewal process relying on the presence of satellite cells. These cells are activated and then proliferated to provide a myoblast population that either fuses to each other to create new myofibers or fuses to existing damaged myofibers for repair (20). According to a latest cell cycle study, an excessively activated CDK/cyclin D1 would cause the growth and development of cells. As a cell cycle regulator, cyclin D1 is necessary for the G1 phase progress (21). In the G1 phase, retinoblastoma is hyperphosphorylated by the cyclin DCDK4/CDK6 complex, causing the release and activation of the E2F-DP transcription factor complex, which in turn activates the expression of the genes required for S-phase progression (22). People have always been concerned about whether plant protein supplement can promote muscle growth as animal protein supplement in response to resistance exercise. Similar to other findings, our research provides strong evidence that pea protein can significantly promote muscle growth. In addition, this study also determines an optimal oligopeptide promoting muscle growth from pea protein. Of course, our results cannot resolve the debate between proteins and oligopeptides on the promotion of muscle growth.

In the recent years, muscle atrophy is a public health issue that causes a growing concern around the world, which imposes a huge burden on life quality of patients (23). Skeletal muscle is the largest organ in mammals and plays the vital roles in mobility and metabolism. Excessive loss of muscle mass is associated with poor prognosis in several diseases, including myopathies

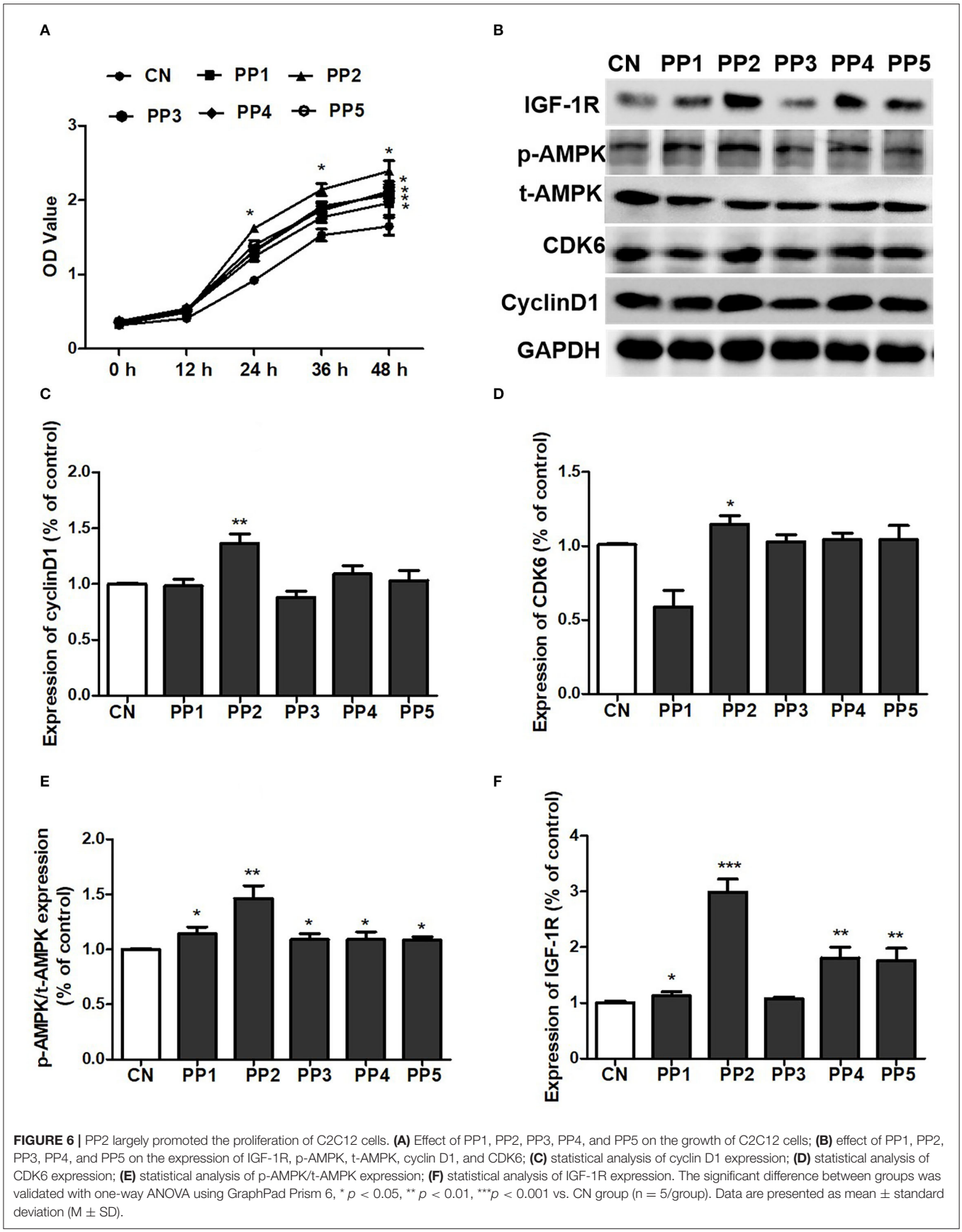

FIGURE 6 | PP2 largely promoted the proliferation of C2C12 cells. **(A)** Effect of PP1, PP2, PP3, PP4, and PP5 on the growth of C2C12 cells; **(B)** effect of PP1, PP2, PP3, PP4, and PP5 on the expression of IGF-1R, p-AMPK, t-AMPK, cyclin D1, and CDK6; **(C)** statistical analysis of cyclin D1 expression; **(D)** statistical analysis of CDK6 expression; **(E)** statistical analysis of p-AMPK/t-AMPK expression; **(F)** statistical analysis of IGF-1R expression. The significant difference between groups was validated with one-way ANOVA using GraphPad Prism 6, * $p < 0.05$, ** $p < 0.01$, ***$p < 0.001$ vs. CN group (n = 5/group). Data are presented as mean ± standard deviation (M ± SD).

and muscular dystrophies, as well as in systemic disorders such as cancer, diabetes, sepsis, and heart failure (24), and thus, maintenance of muscle mass is crucial for preventing metabolic disorders. It is reported that an inadequate diet and especially a low diet in protein appear to be associated with a decrease in muscle mass and muscle strength (25, 26). To alleviate muscle atrophy, several researchers have even suggested that elderly individuals should consume more protein than recommended daily allowance (27–29). Resistance training is widely recognized to increase muscle mass and muscle tension strength. Therefore, it is now recommended to incorporate resistance training programs and an adequate protein intake for the maintenance of muscle mass and muscle strength (30, 31). In our study, we demonstrated that pea peptide supplementation combined with resistance exercise significantly promoted muscle growth. Based on other researches (32) and our results, we regarded that pea peptide supplementation combined with resistance exercise may be a good strategy for the prevention and treatment of muscle atrophy.

Taken together, our study demonstrated that pea peptide combined with resistance exercise training markedly promoted skeletal muscle growth. Furthermore, the oligopeptide with amino acid sequence of LDLPVL presented a more significant proliferation of C2C12 cells than other oligopeptides.

DATA AVAILABILITY STATEMENT

The raw data supporting the conclusions of this article will be made available by the authors, without undue reservation.

ETHICS STATEMENT

The animal study was reviewed and approved by Animal Care and Use Committee at Wuhan Sports University.

AUTHOR CONTRIBUTIONS

WW and QW participated in the peptide purification and Western blots analysis. JK participated in HE and ELISA analysis. All authors contributed to the article and approved the submitted version.

REFERENCES

1. Devries MC, Phillips SM. Supplemental protein in support of muscle mass and health: advantage whey. *J Food Sci.* (2015) A8–A15. doi: 10.1111/1750-3841.12802
2. van Vliet S, Burd NA, van Loon LJ. The skeletal muscle anabolic response to plant- versus animal-based protein consumption. *J Nutr.* (2015) 145:1981–91. doi: 10.3945/jn.114.204305
3. Tokede OA, Onabanjo TA, Yansane A, Gaziano JM, Djousse L. Soya products and serum lipids: A meta-analysis of randomised controlled trials. *Br J Nutrit.* (2015) 114:831–43. doi: 10.1017/S0007114515002603
4. Messina M, Lynch H, Dickinson JM, Reed KE. No difference between the effects of supplementing with soy protein versus animal protein on gains in muscle mass and strength in response to resistance exercise. *Int J Sport Nutr Exerc Metab.* (2018) 28:674–85. doi: 10.1123/ijsnem.2018-0071
5. Babault N, Païzis C, Deley G, Guérin-Deremaux L, Saniez M-H, Lefranc-Millot C, et al. Pea proteins oral supplementation promotes muscle thickness gains during resistance training: a double-blind, randomized, Placebo-controlled clinical trial vs. whey protein. *J Int Soc Sports Nutr.* (2015) 12:3. doi: 10.1186/s12970-014-0064-5
6. Lee MC, Hsu YJ, Yang LH, Huang CC, Ho CS. Ergogenic effects of Green Tea combined with isolated soy protein on increasing muscle mass and exercise performance in resistance-trained mice. *Nutrients.* (2021) 13:4547. doi: 10.3390/nu13124547
7. Rutherfurd SM, Fanning AC, Miller BJ, Moughan PJ. Protein digestibility-corrected amino acid scores and digestible indispensable amino acid scores differentially describe protein quality in growing male rats. *J Nutr.* (2015) 145:372–9. doi: 10.3945/jn.114.195438
8. Richter CK, Skulas-Ray AC, Champagne CM, Kris-Etherton PM. Plant protein and animal proteins: Do they differentially affect cardiovascular disease risk? *Adv Nutrit.* (2015) 6:712–28. doi: 10.3945/an.115.009654
9. Wolfe RR. Effects of amino acid intake on anabolic processes, *Can J Appl. Physiol.* (2001) 26:S220–7. doi: 10.1139/h2001-056
10. Walker D K, Dickinson JM, Timmerman KL, Drummond MJ, Reidy PT, Fry CS, et al. Exercise, amino acids, and aging in the control of human muscle protein synthesis. *Med Sci Sports Exerc.* (2011) 43:2249–58. doi: 10.1249/MSS.0b013e318223b037
11. Zamyatnin AA. Structural-functional diversity of the natural oligopeptides. *Prog Biophys Mol Biol.* (2018) 133:1–8. doi: 10.1016/j.pbiomolbio.2017.09.024
12. Hashizume K, Ito T, Nagae Y, Tokiwano T. Quantitation and sensory properties of three newly identified pyroglutamyl oligopeptides in sake. *Biosci Biotechnol Biochem.* (2019) 83:357–64. doi: 10.1080/09168451.2018.1530095
13. Zheng ZQ, Geng ZH, Liu JX, Guo ST. Compressed food with added functional oligopeptides improves performance during military endurance training. *Asia Pac J Clin Nutr.* (2017) 26:1066–75.
14. Morton RW, Murphy KT, McKellar SR, Schoenfeld BJ, Henselmans M, Helms E, et al. systematic review, meta-analysis and meta-regression of the effect of protein supplementation on resistance training-induced gains in muscle mass and strength in healthy adults. *Br J Sports Med.* (2017) 52:376–84. doi: 10.1136/bjsports-2017-097608
15. Lynch HM, Buman MP, Dickinson JM, Ransdell LB, Johnston CS, Wharton CM. No significant differences in muscle growth and strength development when consuming soy and whey protein supplements matched for leucine following a 12 week resistance training program in men and women: a randomized trial. *Int J Environ Res Public Health.* (2020) 17:3871. doi: 10.3390/ijerph17113871
16. Chen X, Liang D, Huang Z, Jia G, Zhao H, Liu G. Quercetin regulates skeletal muscle fiber type switching via adiponectin signaling. *Food Funct.* (2021) 12:2693–702. doi: 10.1039/D1FO00031D
17. Feng L, Li B, Xi Y, Cai M, Tian Z. Aerobic exercise and resistance exercise alleviate skeletal muscle atrophy through IGF-1/IGF-1R-PI3K/Akt pathway in mice with myocardial infarction. *Am J Physiol Cell Physiol.* (2022) 322:C164–76. doi: 10.1152/ajpcell.00344.2021
18. Rodriguez J, Vernus B, Chelh I, Cassar-Malek I, Gabillard JC, Hadj Sassi A, et al. Myostatin and the skeletal muscle atrophy and hypertrophy signaling pathways. *Cell Mol Life Sci.* (2014) 71:4361–71. doi: 10.1007/s00018-014-1689-x
19. Thomson DM. The role of AMPK in the regulation of skeletal muscle size, hypertrophy, and regeneration. *Int J Mol Sci.* (2018) 19:3125. doi: 10.3390/ijms19103125
20. Frangos SM, DesOrmeaux GJ, Petrick HL. Skeletal muscle AMPK activation: mounting evidence against a role in substrate utilization during acute exercise. *J Physiol.* (2020) 598:5017–9. doi: 10.1113/JP280447
21. Ciciliot S, Schiaffino S. Regeneration of mammalian skeletal muscle. Basic mechanisms and clinical implications. *Curr Pharm Des.* (2010) 16:906–14. doi: 10.2174/138161210790883453
22. Wang Y, Zhu JF, Liu YY, Han GP. An analysis of cyclin D1, cytokeratin 5/6 and cytokeratin 8/18 expression in breast papillomas and papillary carcinomas. *Diagn Pathol.* (2013) 8:8. doi: 10.1186/1746-1596-8-8

23. Ezhevsky SA, Nagahara H, Vocero-Akbani AM, Gius DR, Wei MC, Dowdy SF. Hypo-phosphorylation of the retinoblastoma protein (pRb) by cyclin D:Cdk4/6 complexes results in active pRb. *Proc Natl Acad Sci U S A.* (1997) 94:10699–704. doi: 10.1073/pnas.94.20.10699
24. He N, Ye H. Exercise and muscle atrophy. *Adv Exp Med Biol.* (2020) 1228:255–67. doi: 10.1007/978-981-15-1792-1_17
25. Bonaldo P, Sandri M. Cellular and molecular mechanisms of muscle atrophy. *Dis Model Mech.* (2013) 6:25–39. doi: 10.1242/dmm.010389
26. McLean RR, Mangano KM, Hannan MT, Kiel DP, Sahni S. Dietary protein intake is protective against loss of grip strength among older adults in the framingham offspring cohort. *J Gerontol A Biol Sci Med Sci.* (2016) 71:356–61. doi: 10.1093/gerona/glv184
27. Lord C, Chaput JP, Aubertin-Leheudre M, Labonte M, Dionne IJ. Dietary animal protein intake: association with muscle mass index in older women. *J Nutr Health Aging.* (2007) 11:383–7.
28. Morais JA, Chevalier S, Gougeon R. Protein turnover and requirements in the healthy and frail elderly. *J Nutr Health Aging.* (2006) 10:272–83. doi: 10.1002/gps.1534
29. Lemieux FC, Filion ME, Barbat-Artigas S, Karelis AD, Aubertin-Leheudre M. Relationship between different protein intake recommendations with muscle mass and muscle strength. *Climacteric.* (2014) 17:294–300. doi: 10.3109/13697137.2013.829440
30. Paddon-Jones D, Rasmussen BB. Dietary protein recommendations and the prevention of sarcopenia. *Curr Opin Clin Nutr Metab Care.* (2009) 12:86–90. doi: 10.1097/MCO.0b013e32831cef8b
31. Beaudart C, Dawson A, Shaw SC, Harvey NC, Kanis JA, Binkley N, et al. Nutrition and physical activity in the prevention and treatment of sarcopenia: systematic review. *Osteoporos Int.* (2017) 28:1817–33. doi: 10.1007/s00198-017-3980-9
32. Liao CD, Chen HC, Huang SW, Liou TH. The Role of muscle mass gain following protein supplementation plus exercise therapy in older adults with sarcopenia and frailty risks: a systematic review and meta-regression analysis of randomized trials. *Nutrients.* (2019) 11:1713. doi: 10.3390/nu11081713

Conflict of Interest: WW, ZZ, XiZ, XuZ, and JL were employed by Zhong Shi Du Qing (Shandong) Biotechnology Company. QW, JK, and JD were employed by Amway (Shanghai) Innovation & Science Co., Ltd.

The remaining authors declare that the research was conducted in the absence of any commercial or financial relationships that could be construed as a potential conflict of interest.

Publisher's Note: All claims expressed in this article are solely those of the authors and do not necessarily represent those of their affiliated organizations, or those of the publisher, the editors and the reviewers. Any product that may be evaluated in this article, or claim that may be made by its manufacturer, is not guaranteed or endorsed by the publisher.

Copyright © 2022 Jia, Wu, Wang, Kan, Zhang, Zhang, Zhang, Li, Xu, Du and Wei. This is an open-access article distributed under the terms of the Creative Commons Attribution License (CC BY). The use, distribution or reproduction in other forums is permitted, provided the original author(s) and the copyright owner(s) are credited and that the original publication in this journal is cited, in accordance with accepted academic practice. No use, distribution or reproduction is permitted which does not comply with these terms.

frontiers | Frontiers in Nutrition

TYPE Methods
PUBLISHED 22 July 2022
DOI 10.3389/fnut.2022.879518

Check for updates

OPEN ACCESS

EDITED BY
Biao Yuan,
China Pharmaceutical
University, China

REVIEWED BY
Wang Ying Yu,
China Agricultural University, China
Alaa Kareem Niamah,
University of Basrah, Iraq
Xiao Xu,
Shaoxing University, China

*CORRESPONDENCE
Lianfeng Ai
ai_lianfeng@126.com
Yan Zhang
snowwinglv@126.com

SPECIALTY SECTION
This article was submitted to
Food Chemistry,
a section of the journal
Frontiers in Nutrition

RECEIVED 19 February 2022
ACCEPTED 30 June 2022
PUBLISHED 22 July 2022

CITATION
Guo XJ, Tian H, Yang F, Fan SF, Zhang JW, Ma JM, Ai LF and Zhang Y (2022) Rapid determination of 103 common veterinary drug residues in milk and dairy products by ultra performance liquid chromatography tandem mass spectrometry. *Front. Nutr.* 9:879518. doi: 10.3389/fnut.2022.879518

COPYRIGHT
© 2022 Guo, Tian, Yang, Fan, Zhang, Ma, Ai and Zhang. This is an open-access article distributed under the terms of the Creative Commons Attribution License (CC BY). The use, distribution or reproduction in other forums is permitted, provided the original author(s) and the copyright owner(s) are credited and that the original publication in this journal is cited, in accordance with accepted academic practice. No use, distribution or reproduction is permitted which does not comply with these terms.

Rapid determination of 103 common veterinary drug residues in milk and dairy products by ultra performance liquid chromatography tandem mass spectrometry

Xiujuan Guo[1], Hao Tian[2], Fan Yang[3], Sufang Fan[3], Jingwen Zhang[3], Junmei Ma[3], Lianfeng Ai[2]* and Yan Zhang[3,4]*

[1]Fourth Hospital of Hebei Medical University, Shijiazhuang, China, [2]Technology Center of Shijiazhuang Customs District, Shijiazhuang, China, [3]Hebei Food Inspection and Research Institute, Shijiazhuang, China, [4]Hebei Key Laboratory of Forensic Medicine, College of Forensic Medicine, Hebei Medical University, Shijiazhuang, China

A multi-residue method has been developed for the identification and quantification of 103 common veterinary drug residues in milk and dairy Products. This method was based on QuEChERS with dispersive solid-phase where C18 sorbent and anhydrous sodium sulfate were used to sample purification. After evaporation and reconstitution, the samples were analyzed by ultra-performance liquid chromatography-tandem mass spectrometry. The mean recovery results were all higher than 60% except ampicillin, pipemidic acid, enoxacin, and estriol, and the relative standard deviation was <20.0%. The limit of quantification ranged between 0.1 and 5 μg/kg for milk and between 0.5 and 25 μg/kg for milk powder. It was successfully used to detect residues of veterinary drug in real samples. This study proposes a simple and fast analytical method for monitoring multi-class veterinary drug residues to ensure food safety.

KEYWORDS

rapid detection, veterinary drug residues, milk, dairy products, UPLC-MS/MS

Introduction

Milk and dairy products already enter thousands of households for their sweet and delicious taste, rich nutrition, easy digestion and absorption, and suitable for all ages in China. To protect milk consumers' health, it is essential to ensure that the products marketed are suitable. Because veterinary drugs are widely and sometimes incorrectly used in livestock breeding, residues of antibiotics, hormones, and anticoccidials, have been the main potential threats for the safety of milk and dairy products either

as original compounds or metabolites. The presence of veterinary drug residues in food poses potential health risk to consumers as they could cause allergic reactions, present carcinogenic or teratogenic mechanisms, or induce antimicrobial resistance (1). Consequently, the highest residue of sulfonamides, quinolones, lincoamides, macrolides, β-lactam antibiotics, benzimidazoles, and triazines in the relevant laws and regulations formulated by many countries and regions such as China, European, and United States were at the μg/kg level (2–5). Chloramphenicol, nitroimidazole drugs and their metabolites, as well as some hormones, have potential animal carcinogenesis, teratogenicity, mutagenicity and genotoxicity, which have been listed as prohibited drugs or banned in dairy animals in many countries. Therefore, it is essential to monitor the drug residue in dairy products.

At present, the main methods for the determination of veterinary drug residues in animal-derived foods are high-performance liquid chromatography tandem mass spectrometry (HPLC-MS/MS) (6). The method for the determination of veterinary drug residue in a single category has been more mature. However, because most of the animal diseases are mixed infection, two or more different kinds of drugs are often used in clinical treatment. Therefore, the simultaneous detection of multiple residues of veterinary drugs is a new method studied in recent years (7–15). In sample preparation, most of the commonly used methods for the analysis of veterinary drug residue in foods were liquid-liquid extraction, solid phase extraction, but the operations were complicated and time-consuming. Quick, Easy, Cheap, Effective, Rugged, and Safe is a rapid pre-treatment method developed in recent years, which can be used to extract the target compound from the samples by a convenient, economical and rapid way (16–18). The main applications of quantitative multi-analyte methods in determination of veterinary drug residues in milk and other animal derived foods are presented in Table 1. In this work, 103 veterinary drugs, including sulfonamides, (fluoro)quinolones, nitroimidazoles and their metabolites, lincoamides, macrolides, β-lactams, benzimidazoles and their metabolites, exogenous estrogens, chloramphenicols, glucocorticoids, and triazines were simultaneously determined by QuEChERS combined with ultra-high performance liquid chromatography (UPLC) and tandem mass spectrometry (MS/MS). Compared with previous literatures, this work is more targeted and covers almost all possible veterinary drug contaminants in animal husbandry in China; isotope internal standard method is as much as possible used to qualify the analytes, then the result is more accurate; and the extraction and purification of target analytes with different chemical properties were realized by the simplest sample pretreatment method. This simple method, including sample extraction and data processing, allowed for high-throughput testing of milk samples to monitor veterinary drug residues.

Materials and methods

Instruments and reagents

WATERS ACQUITY UPLC, WATERS XEVO TQ-S tandem quadrupole mass spectrometry (Waters Corporation, USA); ACQUITY UPLC HSS T3 column (100 * 2.1 mm, 1.7 μm, Waters Corporation, USA), TDL-5-A centrifuge, water bath nitrogen blow-drying device, PT2100 type homogenizer, Vortex-Gene 2 scroll oscillator (United States Scientific Industries), 0.22. μm filter (Merck, Germany).

Among 103 common veterinary drug standards, including 22 sulfonamides, 20 (Fluoro)quinolones, 9 nitroimidazoles and metabolites, 9 β-lactams, 2 linconamides, 10 macrolides (species), 8 benzimidazoles and metabolites, 4 exogenous estrogens, 3 chloramphenicols, 8 glucocorticoids, 4 endogenous hormones, 4 triazines, and metabolites. Isotopic internal standards (sulfadimidine-D4, sulfathiazole-D6, sulfonamethoxazole-D6, sulfadimethoxypyrimidine-D4, sulfaquinoxane-D6, metronidazole-D4, hydroxymetronidazole-D2, hydroxymetronidazole-D3, metronidazole-D3, lonidazole-D3, hydroxyisopronidazole-D3, isoprolozole-D3norfloxacin-D5, ciprofloxacin-D8, enrofloxacin-D3, lonitrazole-D3, hydroxyisopronidazole-D3, isoprodazol-D3, norfloxacin-D5, ciprofloxacin-D8, enrofloxacin-D3 Chloramphenicol-D5, methyl prednisone-D4, 17-β-Estradiol-D4), the purity of standard compounds (seeing Table 3 for details) ≥ 98%, all purchased by Dr Ehrenstorfer GmbH Company of Germany. N-propyl ethylenediamine adsorbents (PSA), octadecyl bonded silica gel adsorbents (C18) purchased from Waters Company of the United States. Methanol (HPLC grade), acetonitrile (HPLC grade), ethyl acetate (HPLC grade), formic acid (HPLC grade), anhydrous sodium sulfate (analytical regent), anhydrous magnesium sulfate (analytical regent), ultra-pure water were treated by Milli-Q water purification system (Millipore company). The constant volume solution was 0.1% formic acid water-acetonitrile solution (87 + 13, V/V) in positive mode and methanol aqueous solution (50 + 50, V/V) in negative mode. Preparation of standard storage solution and working liquid: the standard products were dissolved with methanol (β-lactam drugs in acetonitrile-water) and transferred to 100 mL brown capacity bottle for 10 mg, respectively. Dilute to 100 ml with methanol (or acetonitrile-water) and stored at −20°C. When used, the above standard stock solutions were mixed and diluted with acetonitrile into different concentrations of standard working solution.

Sample preparation

The liquid milk was weighed 5.0 g, the precision was 0.01 g, and the milk powder sample was 1.0 g, mixed with 4.0 g water

TABLE 1 Comparison with other methods.

Compounds	Matrix	Sample preparation	Detection identification	Quantitative method	Recoveries	Reference
33 antibiotics: Sulfonamides (13), Tetracyclines (4), Macrolides (4), Quinolones (11), and Amphenicols (1)	Milk	Extraction and protein precipitation with ACN	LC-ESI-MS/MS (+) and (−)	Internal standard	–	(20)
18 veterinary drugs: Sulfonamides (4), Quinolones (2), Coccidiostats (7), Corticosteroids (3), Trimethoprim, and other contaminants (1)	Milk	Extraction with CAN–cleanup with SPE (Strata-X)	LC-ESI-MS/MS (+)	Internal standard and matrix external standard	65–119%	(21)
143 veterinary drugs and pharmaceuticals	Milk	Extraction with TCA 5% (w/v)–ACN (3:1, v/v), cleanup with HLB SPE	LC-ESI-Q/TOF (+)	External standard	>60%	(22)
	Fish	Extraction with 0.1% formic acid (v/v)/0.1% EDTA solution-MeOH-ACN, cleanup with hexane partitioning				
52 veterinary drugs, encompassing 12 classes: Aminocoumarins (1), amphenicols (2), anthelmintics (1), avermectins (4), imidazoles (9), lincosamides (2), macrolides (6), Non-steroidal anti inflammatory drugs (7), quinolones (2), β-lactams (8), sulfonamides (6), tetracyclines (2), and 2 unclassified compounds	Milk powders	Extraction with ACN, cleanup with Waters Oasis PRiME HLB	LC-ESI-MS/MS (+)	Internal standard	70–120%	(23)
84 veterinary drugs: Quinolones (14), Tetracyclines (4), Macrolides (7), β-Lactames (8), Sulfonamides (22), Trimethoprimethoprim, Tiamulin, Dapsone, Ormetoprim, Anthelmintics (21), and other contaminants (4)	Chicken muscle	Solid–liquid extraction with EDTA-succinate buffer and acetonitrile	LC-ESI-MS/MS (+)		29% (ofloxacin) to 98% (erythromycin)	(24)
155 veterinary drugs of 21 different classes	Animal source foods	Extraction with ACN–FA solution, cleanup with Waters Oasis PRiME HLB	LC-ESI-Q/Orbitrap (±)	External standard, add standard solution before purification	79.2–118.5%	(14)
103 veterinary drugs residuces: Nitroimidazoles (9), β-lactams (9), Licoamides (2), Macrolides (10), 20 (Fluoro)quinolones (20), Sulfonamides (22), Benzimidazoles (8), Exogenous estrogens (8), 3 Chloramphenicols (3), 8 Glucocorticoids (8), 4 triazines (4)	Milk and milk powder	Extraction with ACN, cleanup with improved QuEChERS	LC-ESI-MS/MS (+) and (−)	Internal standard and matrix external standard	>60% except ampicillin, pipemidic acid, enoxacin, and estriol	This work

vortex and placed in a 50 mL centrifugal tube. After adding 25 μL 1.0 μg/mL internal standard solution (sulfonamides, quinolones, and nitroimidazole drugs using isotopic internal standard), 15.0 mL acetonitrile and 5 g anhydrous sodium sulfate were added accurately, the vortex was rotated rapidly for 2 min, and centrifuged at 4°C for 5 min for 5,000 r/min. The remaining

TABLE 2 The conditions of gradient elution in ESI (+).

Time (min)	Flow rate (mL/min)	A (%)	B (%)	Gradient curve number
0.0	0.3	95	5	6
4.5	0.3	85	15	6
5.0	0.3	85	15	6
6.0	0.3	80	20	6
6.5	0.3	75	25	8
8.5	0.3	50	50	6
10.0	0.3	5	95	6
10.5	0.3	0	100	6
10.6	0.3	95	5	6
12.6	0.3	95	5	6

TABLE 3 The conditions of gradient elution in ESI (−).

Time (min)	Flow rate (mL/min)	A (%)	B (%)	Gradient curve number
0.00	0.4	80	20	–
0.50	0.4	85	15	6
2.00	0.4	85	15	6
4.00	0.4	80	20	6
9.50	0.4	75	25	8
11.00	0.4	50	50	6
11.10	0.4	5	95	6
11.60	0.4	95	5	1
13.00	0.4	95	5	1

part was added 10.00 mL acetonitrile, extracted at high speed with 10,000 r/min homogenizer for 2 min, centrifuged at 4°C for 5 min at 5,000 r/min, and combined with the liquid to be purified.

The sample was purified and removed at 6.00 mL in a 10 mL plug scale centrifugal tube. After adding 100 mg C18, 300 mg anhydrous sodium sulfate at one time, the vortex dispersed, and after centrifuging 5 min at 10,000 r/min, the 5.00 mL extract was accurately separated and blown to near dry at 45°C on the water bath nitrogen blowing dryer, and the concentrate was dissolved in 1.0 mL 0.1% formic acid water-acetonitrile. The solution filtered with 0.22 μm membrane, and used for UPLC-MS/MS analysis. According to the above steps, the blank extract of the sample was prepared.

Instrument conditions

The UPLC conditions were column temperature of 40°C, injection volume of 5 μL; the positive ion scanning mode: flow rate of 0.3 mL/min. The mobile phase A is 0.1% formic acid solution, mobile phase B is acetonitrile, and the gradient elution conditions are shown in Table 2; the negative ion scanning mode: flow rate of 0.4 ml/min. The mobile phase A is pure water, mobile phase B is acetonitrile, and the gradient elution conditions are shown in Table 3.

The MS/MS conditions were electrospray ion source (ESI) including two methods. one was multi-reaction monitoring (MRM) mode scanning positive: electrospray voltage 3.0 kV, cone hole voltage 20 V, solvent removal gas temperature 450 °C, solvent removal gas flow rate 1,000 L/H, cone hole reverse blowing velocity 150 L/H, atomization gas pressure 7 Bar, ion source temperature 150°C. The other was MRM negative scanning mode: the electrospray voltage is 2.5 kV, cone hole voltage 30 V, the solvent removal gas temperature is 500°C, the solvent removal gas flow rate is 1,000 L/H, the cone hole reverse blowing velocity is 150 L/H, and the atomization gas pressure seven Bar, ion source temperature is 150°C. The parameters such as retention time and collision energy in positive and negative modes are shown in Table 4.

Results

Selection of extraction solvents

For the simultaneous determination of veterinary drug residues in milk and milk powder, the extraction method is the key. According to the different chemical properties of each compound, the recovery rates of each target substance were investigated when methanol, acetonitrile, ethyl acetate, and methanol-acetonitrile (1:1) were used as extractants, respectively. It was found that when extracted with ethyl acetate and methanol solution, the fat was too much, the effect of removing impurities was not good, and the recovery rate of penicillin drugs was not easy to be concentrated by nitrogen blowing, and the recovery rate of penicillin drugs was not easy to be controlled when extracted with methanol-acetonitrile (1:1), only nitroimidazole drugs and some sulfonamides and (fluoro)quinolones were recovered in the positive mode, and the protein precipitation was not complete. When acetonitrile is a polar solvent, it can avoid extracting too much fat from the tissue and has a good protein deposition effect at the same time. Therefore, it was preliminarily determined that acetonitrile was used as extraction solvent. Because sulfonamides, nitroimidazoles, and quinolones are amphoteric substances, they are more easily extracted in acidic extraction solvents. Macrolides, lincosamides drugs and benzimidazole drugs belong to weak basic substances, and the pKa values of all kinds of drugs are quite different. In this study, the extraction efficiency of pure acetonitrile, 1% formic acid and 1% acetic

TABLE 4 Information and optimized mass spectrometry parameters of 103 standard veterinary drugs in ESI$^+$ (1–80) and ESI$^-$ (81–103).

No.	Compounds	RT (min)	Parent (m/z)	Product (m/z)	Collision energy (V)	Scan time range (min)
9 Nitroimidazoles						
1	Dimetridazole	3.64	142.1	81.0	22	0.10–4.30
				96.1*	14	
	Dimetridazole-IS	3.58	145.2	99.2	15	0.10–4.30
2	HMMNI	2.93	158.1	55.0	20	0.10–4.30
				140.1*	13	
	HMMNI-IS	2.92	161.2	143.1	11	0.10–4.30
3	Metronidazole	2.94	172.2	82.1	22	0.10–4.30
				128.0*	15	
	Metronidazole-IS	2.94	176.2	86.0	22	0.10–4.30
4	Metronidazole-OH	2.31	188.2	123.1*	12	0.10–4.30
				126.0	22	
	Metronidazole-OH-IS	2.37	190.2	128.0	19	0.10–4.30
5	Ronidazole	3.66	201.1	140.1*	12	0.10–4.30
	Ronidazole-IS	3.66	204.2	143.1	10	0.10–4.30
	Ipronuidazole	8.14	170.1	109.0	23	7.50–8.90
6				124.2*	17	
	Ipronidazole-IS	8.13	173.2	127.2	18	7.50–8.90
7	Ipronidazole-OH	6.43	186.2	122.0	18	6.10–8.00
				168.2*	14	
	Ipronidazole-OH-IS	6.4	189.2	125.2	18	6.10–8.00
8	Ornidazole	6.68	220.1	82.1	28	6.10–8.00
				128.0*	14	
9	Tinidazole	5.42	248.2	121.1*	16	5.20–6.50
				128.0	20	
1 Cephalosporin						
10	Ceftiofur	8.44	524.2	125.2	60	8.22–9.35
				241.1*	14	
8 Penicillins						
11	Penicillin V	9.34	351.2	114.1	32	9.10–11.20
				160.0*	12	
12	Oxacillin	9.58	402.2	160.1*	12	9.10–11.20
				243.2	12	
13	Nafcillin	9.86	415.2	171.1	38	9.10–11.20
				199.1*	14	
14	Cloxacillin	9.76	436.0	159.8*	20	9.10–11.20
				277.0	16	
15	Dicioxacillin	10.02	470.2	159.8*	16	9.10–11.20
				311.1	13	
16	Penicillin G	5.85	335.2	91.0*	40	5.20–6.50
				128.0	26	
17	Ampicillin	4.92	350.2	106.1*	16	4.20–5.50
				160.1	10	

(Continued)

10.3389/fnut.2022.879518

TABLE 4 Continued

No.	Compounds	RT (min)	Parent (m/z)	Product (m/z)	Collision energy (V)	Scan time range (min)
18	Piperacillin	8.78	518.3	143.1*	19	8.35–9.70
				160.1	10	
2 Licoamides						
19	Clindamycin	8.02	425.1	125.9*	27	7.50–8.90
				377.1	17	
20	Lincomycin	4.38	407.1	125.9*	29	4.20–5.50
				359.2	17	
10 Macrolides						
21	Tilmicosin	8.11	869.6	174.0*	42	7.50–8.90
				696.6	41	
22	Josamycin	9.45	828.8	109.1	35	9.10–11.20
				174.2*	32	
23	Tamulin	9.11	494.4	119.0	32	8.35–9.70
				192.1*	20	
24	Oleandomycin	9.14	688.7	158.2*	27	8.35–9.70
				544.6	16	
25	Erythromycin	8.69	734.4	158.0*	30	8.35–9.70
				576.5	17	
26	Stereomycin	9.1	772.4	108.8*	37	8.35–9.70
				215.0	28	
27	Roxithromycin	9.29	837.6	158.2*	33	8.35–9.70
				679.5	22	
28	Tylosin	8.84	916.5	100.8	43	8.35–9.70
				174.0*	38	
29	Azithromycub	7.81	749.5	158.0*	40	7.05–8.20
				591.5	29	
30	Spriamycin	7.76	843.5	141.9	33	7.05–8.20
				174.0*	35	
20 (Fluoro)quinolones						
31	Cinoxacin	8.09	263.0	189.0	26	7.50–8.90
				245.0*	15	
32	Lomefloxaxin	6.6	352.1	208.2	22	6.10–7.60
				265.0*	16	
33	Danofloxacin	6.7	358.2	314.1*	17	6.10–7.60
				340.1	22	
34	Enrofloxacin	6.95	360.1	245.0	26	6.10–7.60
				316.2*	18	
	Enrofloxacin-IS	6.93	364.9	321.0	20	6.10–7.60
35	Orbifloxacin	7.1	396.3	295.2*	24	6.10–7.60
				352.6	17	
36	Nalidixic acid	9.25	233.0	186.9	24	9.10–11.20
				215.0	14	
37	Flumequine	9.39	262.1	202.0	32	9.10–11.20
				244.0*	21	
38	Norfloxaxin	5.81	320.0	233.0	22	5.20–6.50
				276.2*	15	

(Continued)

TABLE 4 Continued

No.	Compounds	RT (min)	Parent (m/z)	Product (m/z)	Collision energy (V)	Scan time range (min)
	Norfloxaxin-IS	5.81	324.9	281.0	16	5.20–6.50
39	Enoxacin	5.52	321.1	232.0	36	5.20–6.50
				303.1*	15	
40	Ciprofloxacin	6.13	332.0	245.0	21	5.20–6.50
				288.2*	16	
	Ciprofloxacin-IS	6.13	339.9	296.0	18	5.20–6.50
41	Pefloxacin	6.03	334.1	290.1*	17	5.20–6.50
				316.1	19	
42	Ofloxacin	5.89	362.1	261.1	25	5.20–6.50
				318.1*	19	
43	Marbofloxacin	5.43	363.1	71.8	20	5.20–6.50
				320.0*	15	
44	Flerofloxacin	5.78	370.1	269.1	25	5.20–6.50
				326.1*	19	
45	Pipemidic acid	4.53	304.0	217.0*	21	4.20–5.50
				286.1	18	
46	Oxolinic acid	8.46	262.0	216.0	30	8.20–9.35
				244.0*	19	
47	Gatifloxacin	7.33	376.1	289.1	28	7.05–8.20
				332.1*	19	
48	Sarafloxacin	7.47	386.1	299.1	26	7.05–8.20
				342.2*	16	
49	Sparfloxaxin	7.59	393.1	292.1	24	7.05–8.20
				349.2*	20	
50	Difloxaxin	7.54	400.1	299.1	26	7.05–8.20
				356.2*	18	
22 Sulfonamides						
51	Sulphanilamide	1.71	173.8	65.6	30	0.10–4.30
				92.8*	22	
52	Sulfaguanidine	1.42	214.8	91.8*	24	0.10–4.30
				155.8	14	
53	Sulfacetamid	3.23	215.0	107.8*	18	0.10–4.30
				155.8	8	
54	Sulfadiazine	3.85	251.0	91.8	27	0.10–4.30
				155.8*	15	
	Sulfadiazine-IS	3.85	156.8	161.8	14	0.10–4.30
55	Sulfamethoxazole	7.96	254.0	91.8	26	7.70–8.50
				155.8*	16	
	Sulfamethoxazole-IS	7.96	259.8	161.8	14	7.70–8.50
56	Sulfamoxole	8.21	268.0	91.8	23	7.70–8.50
				155.8*	15	
57	Sulfadoxine	7.95	311.0	91.8	32	7.70–8.50
				155.8*	15	
58	Sulfamethizole	6.23	271.0	91.8	30	5.95–7.15
				155.8*	15	

(Continued)

10.3389/fnut.2022.879518

TABLE 4 Continued

No.	Compounds	RT (min)	Parent (m/z)	Product (m/z)	Collision energy (V)	Scan time range (min)
59	Sulfadimidine	6.25	279.0	91.8*	30	5.95–7.15
				124.0	20	
60	Sulfameter	6.43	281.0	125.8	20	5.95–7.15
				155.8*	16	
61	Sulfamethoxypyridazine	6.55	281.0	125.8	20	5.95–7.15
				155.8*	16	
62	Sulfisoxazole	5.79	268.0	91.8	25	5.05–6.35
				155.8*	13	
63	Sulfapyridine	4.59	250.0	107.8	22	4.0–5.35
				155.8*	14	
64	Sulfathiazole	4.35	256.0	91.8	25	4.0–5.35
				155.8*	15	
	Sulfathiazole-IS	4.34	261.8	161.8	14	4.0–5.35
65	Sulfamerazine	5.06	265.0	91.8*	28	4.0–5.35
				155.8	15	
66	Trimethoprim	5.22	291.0	122.8*	27	4.0–5.35
				229.8	25	
67	Sulfabenzamide	8.54	277.0	107.8	22	8.2–9.35
				155.8*	15	
68	Sulfaquinoxaline	8.73	301.1	91.8	27	8.2–9.35
				155.8*	15	
	Sulfaquinoxaline-IS	8.73	306.9	161.8	16	8.2–9.35
69	Sulfadimethoxine	8.72	311.1	91.8	32	8.2–9.35
				155.8*	20	
	Sulfadimethoxine-IS	8.66	316.9	161.9	22	8.2–9.35
70	Sulfaphenazole	8.78	315.0	155.8	19	8.2–9.35
				159.8*	20	
71	Sulfamonomethoxine	7.37	281.0	125.8	20	7.0–8.0
				155.8*	16	
72	Sulfachloropyridazine	7.6	285.1	91.8	28	7.0–8.0
				155.8*	15	
8 Benzimidazoles						
73	Albendazole sulfone	8.3	298.0	159.0*	25	7.5–8.9
				266.0	18	
74	Oxfendazole	8.21	316.2	159.1*	32	7.5–8.9
				191.2	20	
75	Albendazole S-oxide	7.32	282.3	159.2	32	6.1–8.00
				208.1*	20	
76	Fenbendazole	9.87	300.2	159.2	20	9.10–11.2
				268.8*	20	
77	Flubendazole	9.45	314.1	122.9	33	9.10–11.2
				282.1*	22	
78	Fenbendazole sulfone	9.07	332.2	159.1	42	8.5–9.7
				300.2*	20	
79	Mebendazole	8.99	296.3	105.1	34	8.5–9.7
				264.2*	20	

(Continued)

10.3389/fnut.2022.879518

TABLE 4 Continued

No.	Compounds	RT (min)	Parent (m/z)	Product (m/z)	Collision energy (V)	Scan time range (min)
80	Albendazole	9.23	266.2	191.3	32	8.5–9.7
				234.2*	20	
4 Exogenous estrogens						
81	Zeranol	8.25	321.3	161.0	−32	8.05–10.50
				277.3*	−24	
82	Hexestrol	9.91	269.2	119.0*	−40	8.05–10.50
				134.1	−14	
83	Diethyatibestrol	9.02	267.2	237.1	−30	8.05–10.50
				251.2*	−26	
	Diethyatibestrol-D8	9	275.2	245.1*	−28	8.05–10.50
84	Dienestrol	9.08	265.2	93.0*	−24	8.05–10.50
				235.2	−40	
3 Chloramphenicols						
85	Chloramphenicol	3.47	321.0	152.1*	−18	0.10–4.00
				257.1	−12	
	Chloramphenicol-D5	3.51	326.1	157.1	−18	0.10–4.00
86	Thiamphenicol	1.56	354.0	184.9*	−24	0.10–4.00
				227.0	−14	
87	Florfeniol	2.91	356.0	184.9	−20	0.10–4.00
				336.0*	−8	
8 Glucocorticoids						
88	Hydrocortisone	4.82	407.1	297.1	−28	4.10–7.60
				331.1*	−16	
89	Prednisolone	4.64	403.1	295.0	−28	4.10–7.60
				329.1*	−11	
90	Prednisone	4.62	430.1	299.1	−18	4.10–7.60
				327.1*	−13	
91	Beclomethasone	7.17	453.1	377.1*	−13	4.10–7.60
				407.1	−11	
92	Betamethasone	6.56	437.1	307.0	−30	4.10–7.60
				361.1*	−18	
93	Dexamethasone	6.73	437.1	307.0	−30	4.10–7.60
				361.1*	−18	
94	Fludrocortisone	4.9	425.5	295.1	−33	4.10–7.60
				349.1*	−20	
95	Methylprednisolone	6.35	419.1	309.0	−32	4.10–7.60
				343.1*	−18	
	Methylprednisolone-D4	6.34	422.4	346.3	−14	4.10–7.60
4 Endogenous estrogens						
96	Ethinylestradiol	8.68	295.2	145.1	−40	7.80–9.00
				267.2	−25	
97	Estriol	3.54	287.2	145.1	−42	7.80–9.00
				171.1	−36	
98	17-α-estradiol	8.51	271.2	145.1	−40	7.80–9.00
				183.1	−38	

(Continued)

TABLE 4 Continued

No.	Compounds	RT (min)	Parent (m/z)	Product (m/z)	Collision energy (V)	Scan time range (min)
99	17-β-estradiol	8.24	271.2	145.1	−40	7.80–9.00
				183.1	−38	
	17-β-estradiol-D4	8.19	275.2	187.2	−38	7.80–9.00
4 triazines						
100	Toltrazuril	9.59	424.3	424.3*	−4	8.20–10.0
	Toltrazuril-D3	9.58	427.0	427.0*	−4	8.20–10.0
101	Toltrazuril sulfoxide	8.55	440.2	371.2*	−17	8.20–10.0
				383.2	−13	
102	Toltrazuril sulfone	9.19	456.0	456.0*	−4	8.20–10.0
103	Diclazuril	9.41	405.0	334.0*	−19	8.20–10.0

* is a quantitative ion.

acid were compared. The effect of 1% formic acid and 1% acetic acid on the extraction efficiency of all kinds of drugs was not consistent. The extraction efficiency of (fluoro)quinolones with acidic acetonitrile was better, but the extraction rate of erythromycin decreased under acidic acetonitrile, which may be due to the hydrolysis of glycoside bonds. However, considering that the same pretreatment method should be shared with the negative model, acidity has a great influence on the substance of the negative mode. Considering the factors affecting the extraction efficiency and protein removal of all kinds of drugs, especially the effect on the stability of drugs under acidic and alkaline conditions, acetonitrile was used to extract all kinds of drugs without adding acid. Supplementary Figure 1 showed the results of typical compounds with different chemical properties using different extractions. When the sample is extracted, proper amount of anhydrous sodium sulfate can effectively prevent the moisture and water-soluble impurities in the sample from entering the extract solution. Sodium sulfate also has salting out effect, which is helpful to improve the extraction efficiency. Then, in the extraction add 5 g anhydrous sodium sulfate and extract twice with acetonitrile.

Selection of purification conditions

Two purification methods, liquid-liquid partition extraction and solid phase extraction, were compared. Waters HLB column, MCX column and MAX column were used to purify the compounds, but because there were too many kinds of veterinary drugs, the properties of the compounds varied greatly and were not easy to be controlled (see Supplementary Figure 2). For example, sulfonamides were easy to be lost after solid phase extraction column, and the recovery rate was on the low side. The results of SPE Therefore, in this experiment, the purification method of SPE was abandoned, and the dispersed solid phase extraction (QuEChERS) with less time consuming and low analysis cost was selected. The general rapid pretreatment method of 103 compounds should not only consider the recoveries, but also effectively purify the matrix and reduce the influence of impurities. However, the existing commercial QuEChERS adsorbents or purification tubes are not suitable for the pretreatment of various drug residue with different physical and chemical properties. Commonly used adsorbents include C18, primary secondary amine (PSA), Flori silica, and graphitized carbon black (GCB). When adsorbing impurities, the adsorbents may also adsorb the target compounds, which may affect the recovery rate of the target compounds. Therefore, when selecting the adsorbents, we should try our best to select the adsorbents which have little influence on the target compounds. As a strong polar absorbent, Flori silica cannot remove lipid and carbohydrate impurities; GCB is usually used to remove pigment components from plant extract, because it can adsorb strong drugs with benzene ring functional groups, which has a great impact on the recovery of most penicillin, quinolones, sulfonamides and benzimidazoles; PSA can effectively remove fatty acids and sterols from the matrix, but there are fat residue in the purified extract, and PSA can adsorb acidic drugs as alkaline adsorption fillers. C18 can effectively remove lipophilic impurities such as lipids and carbohydrates, but excessive C18 can also adsorb lipophilic drugs. Therefore, combined with the above factors, the purification effect of C18 and anhydrous sodium sulfate was investigated. The C18 of 20, 50, 100, 200, 500 mg was used for purification, and it was found that when the amount of C18 powder was added, the solution was mixed into a yellowish clear solution. Although the amount of C18 powder was too much, the purification effect was good, but some of the target substances

were adsorbed (see Supplementary Figure 3). Therefore, a good balance between purification effect and recovery can be obtained by using mixed adsorbents of 100 mg C18 and 300 mg anhydrous sodium sulfate per gram of sample. The extract optimized by QuEChERS was yellowish and transparent, and the overall recovery was 31.1–120.7%.

HPLC conditions

The optimization of the separation condition mainly considers the influence of the matrix, the separation effect, and the response strength. The ACQUITY UPLC BEH C18 column (100 * 2.1 mm, 1.7 μm) was compared when the column was

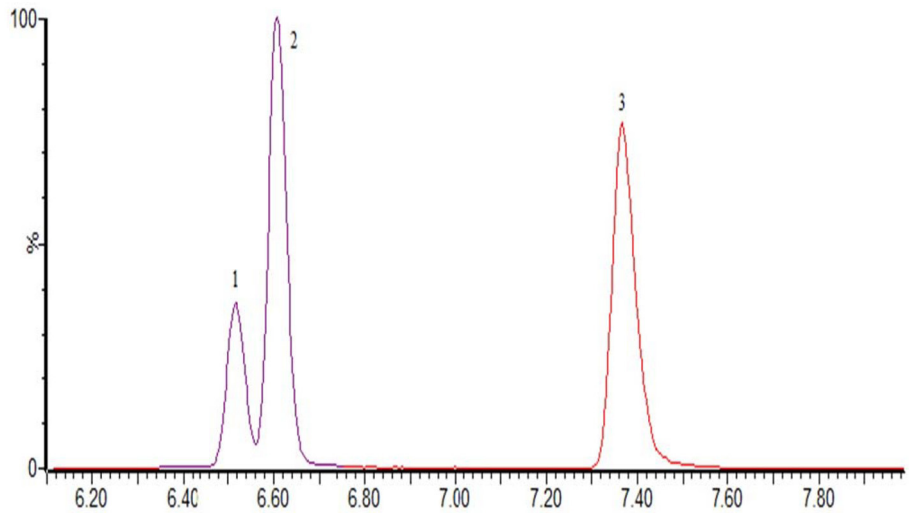

FIGURE 1
The MRM of sulfameter (1), sulfamethoxypyridazine (2), and sulfamonomethoxine (3) in positive mode.

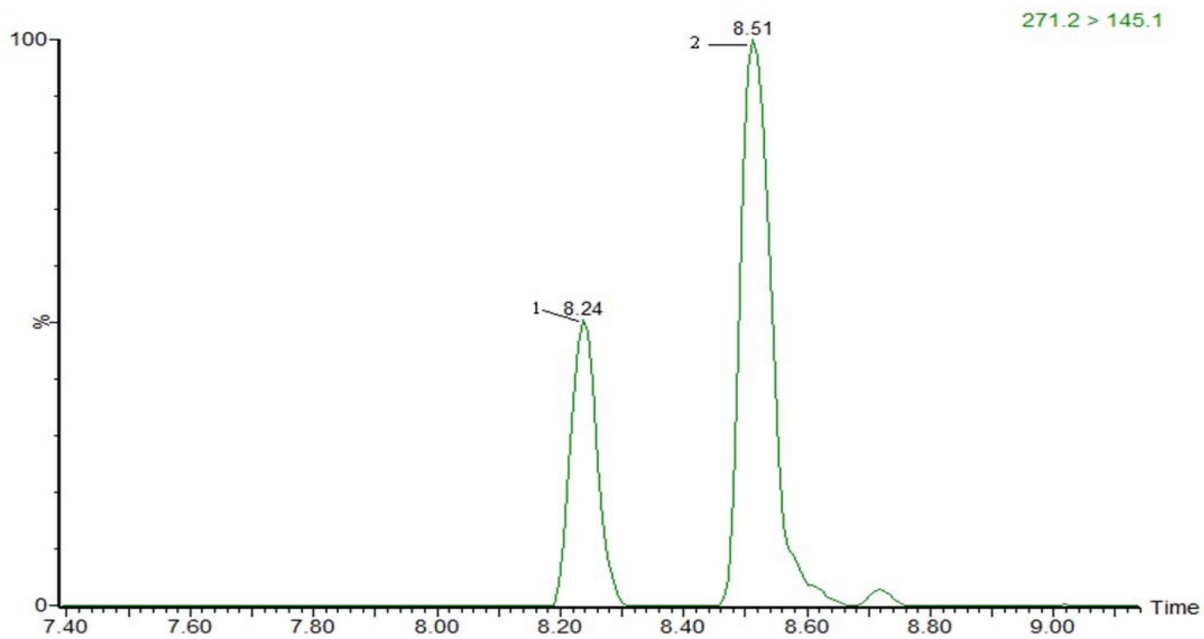

FIGURE 2
The MRM of 17-α-estradiol (2) and 17-β-estradiol (1) in negative mode.

selected. and HSS T3 (100 * 2.1 mm, 1.8 μm). In the positive mode, the separation condition can be met by changing the elution condition of the mobile phase by continuously changing the elution condition of the mobile phase. However, because of the large polarity of some substances in the penicillins, the stability and the linearity of this kind of substance have obvious advantages when using T3 column. Therefore, HSS T3 is selected as analytical column, and the co-isomer of the positive mode scanning is taken as an example for the separation of sulfameter, sulfamethoxypyridazine, and sulfamonomethoxine. The separation chromatograms were shown in Figure 1; the negative pattern can be separated from the isomer by the HSS T3 column, and the separation degree can be maintained. Take estradiol as an example, seeing Figure 2.

In the mobile phase selection, methanol and acetonitrile were selected as the strong eluting mobile phase. The experimental results show that when methanol is used as mobile phase, the ionization of some drugs is inhibited to varying degrees, the peak shape widens, the abundance decreases obviously, and the sensitivity decreases, while the ionization efficiency of acetonitrile is obviously better than that of methanol, so the mobile phase is strongly eluted with acetonitrile. In positive mode, 0.1% formic acid solution, aqueous solution and 5 mmol/L amine acetate (containing 0.1% acetic acid) were selected as aqueous phase (A), acetonitrile as organic phase (B). The mobile phase selection of UPLC was carried out. The results showed that the peak shape of sulfonamides and quinolones was wide when aqueous solution was used as phase A, penicillin was unstable and some substances were poor when 5 mmol/L acetic acid (containing 0.1% acetic acid) was used as phase A when 0.1% formic acid solution was used as phase A, most of the substances such as sulfonamides quinolones were in ion state, the peak shape was sharp symmetry, and the signal response of mass spectrometry was enhanced. In negative mode, water, 0.1% ammonia aqueous solution and 0.5 mmol/mL ammonium acetate solution were selected as aqueous phase (A), acetonitrile as organic phase (B) to select UPLC mobile phase. Because some compounds in the

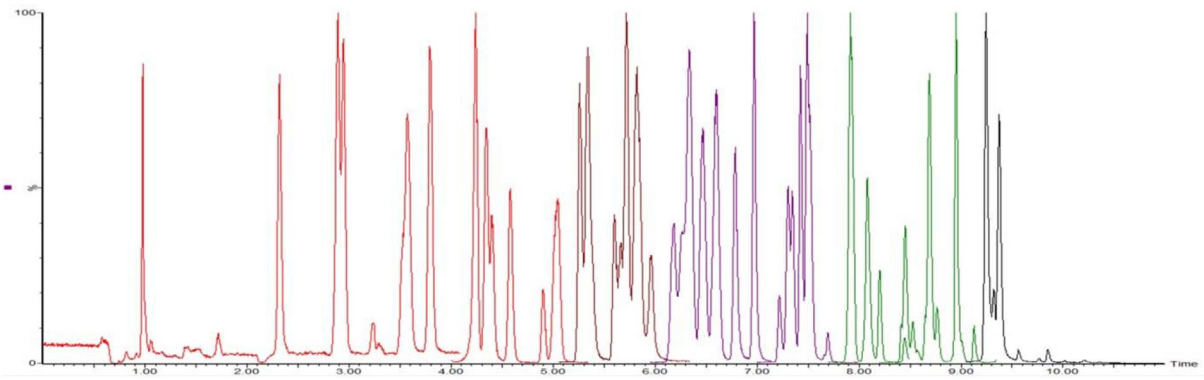

FIGURE 3
The TIC of 80 analytes mixed drugs standard solution in milk (ES+).

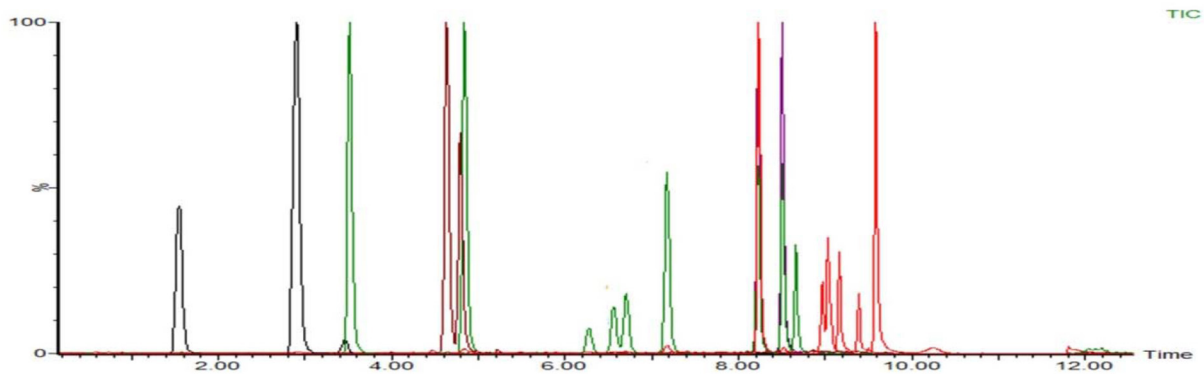

FIGURE 4
The TIC of 23 analytes mixed drugs standard solution in milk (ES−).

TABLE 5 Calibration curve, linear ranges, correlation coefficients, LODs, and LOQs.

No.	Compound	Matrix	ng/mL	Calibration curve	R	LOD μg/kg	LOQ μg/kg
9 Nitroimidazoles							
1	Dimetridazole	Milk	0.5–100	Y = 0.639X + 0.122	0.9959	0.25	0.5
		Milk powder	0.5–100	Y = 0.720X + 0.043	0.9995	1.25	2.5
2	HMMNI	Milk	1.0–200	Y = 0.696X + 0.301	0.9967	0.5	1
		Milk powder	1.0–200	Y = 0.686X + 0.088	0.9979	2.5	5
3	Metronidazole	Milk	0.5–100	Y = 1.788X + 0.361	0.9957	0.25	0.5
		Milk powder	0.5–100	Y = 1.812X + 0.040	0.9992	1.25	2.5
4	Metronidazole-OH	Milk	1.0–200	Y = 1.105X + 0.540	0.9968	0.5	1
		Milk powder	1.0–200	Y = 1.419X + 0.311	0.9964	2.5	5
5	Ronidazole	Milk	0.5–100	Y = 0.767X + 0.158	0.9959	0.25	0.5
		Milk powder	0.5–100	Y = 0.843X + 0.013	0.9993	1.25	2.5
6	Ipronidazole	Milk	0.5–100	Y = 0.819X + 0.146	0.9982	0.25	0.5
		Milk powder	0.5–100	Y = 0.793X + 0.156	0.9956	1.25	2.5
7	Ipronidazole-OH	Milk	0.5–100	Y = 2.152X + 0.359	0.9976	0.25	0.5
		Milk powder	0.5–100	Y = 2.279X + 0.527	0.9956	1.25	2.5
8	Ornidazole*	Milk	0.5–100	Y = 92,308X + 6,667	0.9962	0.25	0.5
		Milk powder	0.5–100	Y = 80,354X + 11,838	0.9969	1.25	2.5
9	Tinidazole*	Milk	0.5–100	Y = 86,108X + 6,759	0.9956	0.25	0.5
		Milk powder	0.5–100	Y = 80,354X + 11,838	0.9969	1.25	2.5
9 β-lactams							
10	Ceftiofur*	Milk	10–100	Y = 213.5X + 42.82	0.9990	2.5	10
		Milk powder	10–100	Y = 423.1X−6.541	0.9982	12.5	50
11	Penicillin V*	Milk	10–100	Y = 272.1X + 467.5	0.9943	2.5	10
		Milk powder	10–100	Y = 4,806X + 4,720	0.9943	12.5	50
12	Oxacillin*	Milk	10–100	Y = 1,381X−191.4	0.9976	2.5	10
		Milk powder	10–100	Y = 2,096X + 3,707	0.9936	12.5	50
13	Nafcillin*	Milk	10–100	Y = 1749X−58.15	0.9964	2.5	10
		Milk powder	10–100	Y = 3,077X + 6,349	0.9933	12.5	50
14	Cloxacillin*	Milk	10–100	Y = 390.7X−24.30	0.9974	2.5	10
		Milk powder	10–100	Y = 692.2X + 1,425	0.9911	12.5	50
15	Dicioxacillin*	Milk	10–100	Y = 168.9X−35.42	0.9941	2.5	10
		Milk powder	10–100	Y = 413.5X + 790.1	0.9978	12.5	50
16	Penicillin G*	Milk	10–100	Y = 4806X + 4,720	0.9972	2.5	10
		Milk powder	10–100	Y = 2,530X−686.9	0.9926	12.5	50
17	Ampicillin*	Milk	10–100	Y = 19,085X + 2,353	0.9963	2.5	10
		Milk powder	10–100	Y = 16,238X−2,682	0.9912	12.5	50
18	Piperacillin*	Milk	10–100	Y = 2,925X + 2.353	0.9993	2.5	10
		Milk powder	10–100	Y = 2,456X−221.0	0.9966	12.5	50
2 Lincosamides							
19	Clindamycin*	Milk	0.25–50	Y = 76,561X + 15,921	0.9972	0.25	0.25
		Milk powder	0.25–50	Y = 102,009X + 68.8	0.9929	1.25	1.25
20	Lincomycin*	Milk	0.25–50	Y = 97,200X + 17,976	0.9963	0.25	0.25
		Milk powder	0.25–50	Y = 137,158X−2,470	0.9972	1.25	1.25
10 Metabolites							
21	Tilmicosin*	Milk	0.5–100	Y = 1,446X + 202.1	0.9965	0.25	0.5
		Milk powder	0.5–100	Y = 1,699X−93.10	0.9979	1.25	2.5

(Continued)

TABLE 5 Continued

No.	Compound	Matrix	ng/mL	Calibration curve	R	LOD μg/kg	LOQ μg/kg
22	Josamycin*	Milk	0.5–100	Y = 18,323X + 2,412	0.9951	0.25	0.5
		Milk powder	0.5–100	Y = 19,955X + 679.9	0.9992	1.25	2.5
23	Tamulin*	Milk	0.25–30	Y = 1,446X + 202.1	0.9944	0.25	0.25
		Milk powder	0.25–30	Y = 19,001X−12,352	0.9978	1.25	1.25
24	Oleandomycin*	Milk	0.5–100	Y = 16,339X + 28,48	0.9965	0.25	0.5
		Milk powder	0.5–100	Y = 17,984X + 1,238	0.9947	1.25	2.5
25	Erythromycin*	Milk	2.0–100	Y = 1,646X + 207.9	0.9915	0.5	2
		Milk powder	2.0–100	Y = 3,349X + 1,521	0.9918	2.5	10
26	Stereomycin*	Milk	0.5–100	Y = 6,124X + 1,213	0.9961	0.25	0.5
		Milk powder	0.5–100	Y = 8,190X + 5.480	0.9946	1.25	2.5
27	Roxithromycin*	Milk	0.5–100	Y = 15,726X + 2,810	0.9958	0.25	0.5
		Milk powder	0.5–100	Y = 15,638X + 283.1	0.9955	1.25	2.5
28	Tylosin*	Milk	0.5–100	Y = 9,936X + 1,637	0.9942	0.25	0.5
		Milk powder	0.5–100	Y = 12,202X + 71.16	0.9967	1.25	2.5
29	Azithromycub*	Milk	0.5–100	Y = 2,486X + 0.9926	0.9926	0.25	0.5
		Milk powder	0.5–100	Y = 2,985X−105.8	0.9978	1.25	2.5
30	Spriamycin*	Milk	0.5–100	Y = 1,208X + 144.6	0.9951	0.25	0.5
		Milk powder	0.5–100	Y = 1,347X−44.71	0.9971	1.25	2.5
20 (Fluoro)quinolones							
31	Cinoxacin	Milk	1.0–100	Y = 2.336X + 0.426	0.9968	0.25	1
		Milk powder	1.0–100	Y = 2.559X + 0.479	0.9954	1.25	5
32	Lomefloxaxin	Milk	1.0–100	Y = 1.231X + 0.154	0.9976	0.25	1
		Milk powder	1.0–100	Y = 1.298X−0.131	0.9943	1.25	5
33	Danofloxacin	Milk	1.0–100	Y = 0.415X + 0.072	0.9975	0.25	1
		Milk powder	1.0–100	Y = 0.482X−0.059	0.9949	1.25	5
34	Enrofloxacin	Milk	1.0–100	Y = 2.404X + 0.432	0.9959	0.25	1
		Milk powder	1.0–100	Y = 2.319X−0.024	0.9955	1.25	5
35	Orbifloxacin	Milk	1.0–100	Y = 2.563X + 0.476	0.9954	0.25	1
		Milk powder	1.0–100	Y = 2.498X + 0.083	0.9956	1.25	5
36	Nalidixic acid	Milk	1.0–100	Y = 7.482X + 1.548	0.9986	0.25	1
		Milk powder	1.0–100	Y = 6.737X + 0.745	0.9958	1.25	5
37	Flumequine	Milk	0.5–50	Y = 5.187X + 0.998	0.9976	0.25	0.5
		Milk powder	0.5–50	Y = 6.015X + 1.438	0.9947	1.25	5
38	Norfloxaxin	Milk	1.0–100	Y = 2.337X + 0.393	0.9957	0.25	1
		Milk powder	1.0–100	Y = 2.139X−0.281	0.9984	1.25	5
39	Enoxacin	Milk	1.0–100	Y = 0.667X + 0.064	0.9986	0.25	1
		Milk powder	1.0–100	Y = 0.733X−0.112	0.9945	1.25	5
40	Ciprofloxacin	Milk	1.0–100	Y = 2.749X + 0.514	0.9959	0.25	1
		Milk powder	1.0–100	Y = 2.322X−0.193	0.9991	1.25	5
41	Pefloxacin	Milk	1.0–100	Y = 1.693X + 0.305	0.9983	0.25	1
		Milk powder	1.0–100	Y = 1.548X−0.064	0.9951	1.25	5
42	Ofloxacin	Milk	1.0–100	Y = 2.534X + 0.455	0.9982	0.25	1
		Milk powder	1.0–100	Y = 2.572X−0.064	0.9956	1.25	5
43	Marbofloxacin	Milk	1.0–100	Y = 0.968X + 0.171	0.9987	0.25	1
		Milk powder	1.0–100	Y = 1.046X−0.053	0.9947	1.25	5
44	Flerofloxacin	Milk	1.0–100	Y = 1.430X + 0.230	0.9977	0.25	1

(Continued)

TABLE 5 Continued

No.	Compound	Matrix	ng/mL	Calibration curve	R	LOD μg/kg	LOQ μg/kg
		Milk powder	1.0–100	Y = 1.750X−0.116	0.9950	1.25	5
45	Pipemidic acid	Milk	1.0–100	Y = 1.793X−0.257	0.9966	0.25	1
		Milk powder	1.0–100	Y = 1.809X + 0.238	0.9968	1.25	5
46	Oxolinic acid	Milk	1.0–100	Y = 5.431X + 1.046	0.9975	0.25	1
		Milk powder	1.0–100	Y = 5.536X + 0.109	0.9968	1.25	5
47	Gatifloxacin	Milk	1.0–100	Y = 0.703X + 0.114	0.9962	0.25	1
		Milk powder	1.0–100	Y = 0.761X−0.084	0.9957	1.25	5
48	Sarafloxacin	Milk	1.0–100	Y = 1.079X−0.073	0.9985	0.25	1
		Milk powder	1.0–100	Y = 1.102X + 0.159	0.9962	1.25	5
49	Sparfloxaxin	Milk	1.0–100	Y = 1.772X + 0.060	0.9990	0.25	1
		Milk powder	1.0–100	Y = 1.888X + 0.041	0.9983	1.25	5
50	Difloxaxin	Milk	1.0–100	Y = 2.449X + 0.488	0.9979	0.25	1
		Milk powder	1.0–100	Y = 2.081X + 0.037	0.9983	1.25	5
22 Sulfonamides							
51	Sulphanilamide	Milk	0.5–100	Y = 0.104X−0.003	0.9988	0.25	0.5
		Milk powder	0.5–100	Y = 0.153X−0.031	0.9966	1.25	2.5
52	Sulfaguanidine	Milk	1.0–100	Y = 0.034X−0.004	0.9990	0.5	1
		Milk powder	1.0–100	Y = 0.047X−0.019	0.9938	2.5	5
53	Sulfacetamide	Milk	0.5–100	Y = 0.026X−0.001	0.9987	0.25	0.5
		Milk powder	0.5–100	Y = 0.033X−0.010	0.9952	1.25	2.5
54	Sulfadiazine	Milk	0.5–100	Y = 0.754X−0.010	0.9994	0.25	0.5
		Milk powder	0.5–100	Y = 1.107X−0.380	0.9959	1.25	2.5
55	Sulfamethoxazole	Milk	0.5–50	Y = 0.643X + 0.020	0.9990	0.25	0.5
		Milk powder	0.5–50	Y = 0.903X−0.209	0.9974	1.25	2.5
56	Sulfamoxole	Milk	0.5–100	Y = 1.026X + 0.473	0.9977	0.25	0.5
		Milk powder	0.5–100	Y = 1.650X−0.512	0.9967	1.25	2.5
57	Sulfadoxine	Milk	0.25–50	Y = 1.282X−0.286	0.9969	0.25	0.25
		Milk powder	0.25–50	Y = 2.720X + 0.053	0.9988	1.25	1.25
58	Sulfamethizole	Milk	0.5–100	Y = 1.087X + 0.062	0.9975	0.25	0.5
		Milk powder	0.5–100	Y = 1.775X−0.573	0.9955	1.25	2.5
59	Sulfadimidine	Milk	0.5–100	Y = 1.083X + 0.096	0.9942	0.25	0.5
		Milk powder	0.5–100	Y = 1.976X−0.587	0.9957	1.25	2.5
60	Sulfameter	Milk	0.5–100	Y = 0.771X + 0.044	0.9980	0.25	0.5
		Milk powder	0.5–100	Y = 1.090X−0.308	0.9963	1.25	2.5
61	Sulfamethoxypyridazine	Milk	0.5–100	Y = 1.532X + 0.140	0.9942	0.25	0.5
		Milk powder	0.5–100	Y = 2.519X−0.595	0.9966	1.25	2.5
62	Sulfisoxazole	Milk	0.5–100	Y = 1.308X + 0.112	0.9950	0.25	0.5
		Milk powder	0.5–100	Y = 2.477X−0.671	0.9970	1.25	2.5
63	Sulfapyridine	Milk	0.5–100	Y = 1.457X + 0.162	0.9939	0.25	0.5
		Milk powder	0.5–100	Y = 2.353X−0.767	0.9961	1.25	2.5
64	Sulfathiazole	Milk	0.5–100	Y = 0.615X + 0.030	0.9991	0.25	0.5
65	Sulfamerazine	Milk	0.5–100	Y = 1.013X + 0.109	0.9946	0.25	0.5
		Milk powder	0.5–100	Y = 1.793X−0.517	0.9978	1.25	2.5
66	Trimethoprim	Milk	0.5–100	Y = 0.952X + 0.170	0.9917	0.25	0.5
		Milk powder	0.5–100	Y = 1.057X−0.650	0.9954	1.25	2.5
67	Sulfabenzamide	Milk	0.5–100	Y = 0.376X−0.010	0.9991	0.25	0.5

(Continued)

TABLE 5 Continued

No.	Compound	Matrix	ng/mL	Calibration curve	R	LOD μg/kg	LOQ μg/kg
		Milk powder	0.5–100	Y = 0.475X−0.183	0.9955	1.25	2.5
68	Sulfaquinoxaline	Milk	0.5–100	Y = 0.715X + 0.002	0.9991	0.25	0.5
		Milk powder	0.5–100	Y = 0.937X−0.231	0.9977	1.25	2.5
69	Sulfadimethoxine	Milk	0.25–50	Y = 1.422X + 0.011	0.9981	0.25	0.25
		Milk powder	0.25–50	Y = 1.705X−0.241	0.9975	1.25	1.25
70	Sulfaphenazole	Milk	0.5–100	Y = 0.293X + 0.006	0.9980	0.25	0.5
		Milk powder	0.5–100	Y = 0.383X−0.071	0.9980	1.25	2.5
71	Sulfamonomethoxine	Milk	0.5–100	Y = 1.218X + 0.085	0.9965	0.25	0.5
		Milk powder	0.5–100	Y = 2.087X−0.573	0.9953	1.25	2.5
72	Sulfachloropyridazine	Milk	0.5–100	Y = 1.110X + 0.084	0.9962	0.25	0.5
		Milk powder	0.5–100	Y = 1.890X−0.493	0.9962	1.25	2.5
8 Benzimidazoles							
73	Albendazole sulfone*	Milk	0.5–50	Y = 8,1371X + 531.7	0.9972	0.5	1
		Milk powder	0.5–50	Y = 74,424X−710.1	0.9984	2.5	5
74	Oxfendazole*	Milk	0.5–50	Y = 89,002X + 1,207	0.9972	0.5	1
		Milk powder	0.5–50	Y = 79,036X + 1,958	0.9991	2.5	5
75	Albendazole S-oxide*	Milk	0.5–50	Y = 60,846X + 160.1	0.9974	0.5	1
		Milk powder	0.5–50	Y = 53,345X + 31.79	0.9984	2.5	5
76	Fenbendazole*	Milk	0.5–50	Y = 6,277X + 782.37	0.9952	0.5	1
		Milk powder	0.5–50	Y = 4,096X + 1,411.5	0.9937	2.5	5
77	Flubendazole*	Milk	0.5–50	Y = 53,388X + 1,303	0.9995	0.5	1
		Milk powder	0.5–50	Y = 38,169X + 1,464	0.9947	2.5	5
78	Fenbendazole sulfone*	Milk	0.5–50	Y = 57,550X + 396.3	0.9967	0.5	1
		Milk powder	0.5–50	Y = 4,257X + 106.2	0.9938	2.5	5
79	Mebendazole*	Milk	0.5–50	Y = 61,256X + 404.9	0.9969	0.5	1
		Milk powder	0.5–50	Y = 58,564X + 315.2	0.9952	2.5	5
80	Albendazole*	Milk	0.5–50	Y = 29,005X + 1,633	0.9965	0.5	1
		Milk powder	0.5–50	Y = 27,227X + 2,098	0.9961	2.5	5
4 Exogenous hormones							
81	Zeranol	Milk	1.0–50	Y = 14.45X + 3.849	0.9974	0.5	1
		Milk powder	5.0–250	Y = 14.75X + 5.401	0.9989	2.5	5
82	Hexestrol	Milk	1.0–50	Y = 0.426X + 0.082	0.9994	0.5	1
		Milk powder	5.0–250	Y = 0.526X−0.011	0.9985	2.5	5
83	Diethyatibestrol	Milk	1.0–50	Y = 1.141X + 0.443	0.9971	0.5	1
		Milk powder	5.0–250	Y = 1.278X−0.192	0.9996	2.5	5
84	Dienestrol	Milk	1.0–50	Y = 2.482X + 0.644	0.9986	0.3	1
		Milk powder	5.0–250	Y = 2.911X + 0.308	0.9988	1.5	5
3 Chloramphenicol							
85	Chloramphenicol	Milk	0.1–5.0	Y = 3.097X + 0.003	0.9937	0.05	0.1
		Milk powder	0.5–2.5	Y = 3.122X−0.064	0.9911	0.25	0.5
86	Thiamphenicol	Milk	1.0–100	Y = 0.727X + 0.833	0.9932	0.5	2
		Milk powder	5.0–500	Y = 1.081X + 0.501	0.9968	2.5	10
87	Florfeniol	Milk	1.0–100	Y = 2.784X + 0.788	0.9994	0.5	2
		Milk powder	5.0–500	Y = 3.437X + 1.753	0.9963	2.5	10
8 glucocorticoids							
88	Hydrocortisone	Milk	0.5–20	Y = 1.254X + 0.378	0.9902	0.2	0.5

(Continued)

TABLE 5 Continued

No.	Compound	Matrix	ng/mL	Calibration curve	R	LOD μg/kg	LOQ μg/kg
		Milk powder	2.5–100	Y = 1.295X + 0.358	0.9979	1	2.5
89	Prednisolone	Milk	0.5–20	Y = 1.573X + 0.103	0.9933	0.2	0.5
		Milk powder	2.5–100	Y = 1.638X + 0.356	0.9971	1	2.5
90	Prednisone	Milk	0.5–20	Y = 0.340X−0.016	0.9926	0.2	0.5
		Milk powder	2.5–100	Y = 0.330X + 0.085	0.9909	1	2.5
91	Beclomethasone	Milk	0.5–20	Y = 6.838X + 1.531	0.9930	0.2	0.5
		Milk powder	2.5–100	Y = 6.925X + 2.035	0.9936	1	2.5
92	Betamethasone	Milk	0.5–20	Y = 1.653X−0.219	0.9970	0.2	0.5
		Milk powder	2.5–100	Y = 1.656X + 0.205	0.9923	1	2.5
93	Dexamethasone	Milk	0.5–20	Y = 1.959X + 0.261	0.9921	0.2	0.5
		Milk powder	2.5–100	Y = 1.814X + 0.128	0.9964	1	2.5
94	Fludrocortisone	Milk	0.5–20	Y = 21.89X + 2.653	0.9945	0.2	0.5
		Milk powder	2.5–100	Y = 23.11X + 5.674	0.9967	1	2.5
95	Methylprednisolone	Milk	0.5–20	Y = 2.476X + 0.328	0.9965	0.2	0.5
		Milk powder	2.5–100	Y = 2.245X + 0.369	0.9948	1	2.5
4 Endogenous estrogens							
96	Ethinylestradiol	Milk	5.0–200	Y = 2.711X−6.517	0.9971	2.5	10
		Milk powder	25.0–1,000	Y = 1.842X−0.683	0.9963	12.5	50
97	Estriol	Milk	5.0–200	Y = 10.86X−35.08	0.9987	1.5	5
		Milk powder	25.0–1,000	Y = 8.440X−6.388	0.9959	12.5	25
98	17-α-estradiol	Milk	5.0–200	Y = 7.897X−19.83	0.9993	1.5	5
		Milk powder	25.0–1,000	Y = 4.247X−1.891	0.9983	12.5	25
99	17-β-estradiol	Milk	5.0–200	Y = 1.860X−8.540	0.9907	2.5	10
		Milk powder	25.0–1,000	Y = 1.424X−3.214	0.9998	12.5	50
4 Triazines							
100	Toltrazuril	Milk	1.0–50	Y = 0.266X + 0.042	0.9994	0.3	1
		Milk powder	5.0–250	Y = 0.285X + 0.027	0.9998	1.5	5
101	Toltrazuril sulfoxide	Milk	1.0–50	Y = 0.104X−0.058	0.9966	0.3	1
		Milk powder	5.0–250	Y = 0.255X−0.008	0.9964	1.5	5
102	Toltrazuril sulfone	Milk	1.0–50	Y = 1.494X−0.213	0.9992	0.3	1
		Milk powder	5.0–250	Y = 0.906X + 0.080	0.9986	1.5	5
103	Diclazuril	Milk	1.0–50	Y = 0.528X + 0.999	0.9986	0.3	1
		Milk powder	5.0–250	Y = 0.816X + 0.014	0.9996	1.5	5

*Used external standard method.

negative model, especially the above factors, were selected as the mobile phase of the method, 0.1% formic acid water and acetonitrile were selected as the mobile phase and eluted under gradient conditions.

Mass spectrometry conditions

According to the chemical structure of the analytes to be tested, these 12 kinds of analytes are suitable for ionization in the positive ion mode of ESI source. One hundred three kinds of standards were diluted with acetonitrile into a mixed solution of 0.1 μg/mL and injected into peristaltic pump. The responses of 80 analytes in positive ion scanning modes were higher than in the negative ion scanning modes, and for the other 23 analytes were the reverse. The all parent ions were all molecular ion of [M+H] + or [M–H]–, except glucocorticoids, for which the ions of [M+HCOOH-H]- have the best responses. The daughter ions were analyzed by full scan, and two characteristic daughter ions were selected, in which the ion pairs with high signal to noise ratio, good peak shape, and small interference were used as quantitative ions. The total ion chromatograms (TIC) current of 103 drugs in added milk are illustrated in Figures 3, 4 under the conditions of positive and negative mode, respectively.

TABLE 6 Recoveries and *RSD*s of analytes of milk and milk powder.

No.	Analyte	Milk				Milk powder			
		Spiked (μg/kg)	Average recovery (%)	Intra-day RSD, % ($n = 6$)	Inter-day RSD, % ($n = 18$)	Spiked (μg/kg)	Average recovery (%)	Intra-day RSD, % ($n = 6$)	Inter-day RSD, % ($n = 18$)
1	Dimetridazole	0.5/1/5	95.4/97.4/96.9	3.7/4.7/4.5	4.7/5.2/5.3	2.5/5/25	83.2/93.2/96.7	6.0/5.1/4.8	6.5/5.4/5.0
2	HMMNI	1/2/10	108.8/104.6/97.7	7.3/6.9/7.9	7.7/7.6/8.7	5/10/50	86.4/93.2/101.7	6.9/4.1/5.7	7.4/5.7/6.1
3	Metronidazole	0.5/1/5	107.9/103.7/105.7	7.1/6.9/5.6	7.8/7.7/6.3	2.5/5/25	92.3/94.3/98.2	3.7/2.9/3.1	5.6/3.1/4.3
4	Metronidazole-OH	1/2/10	97.3/98.7/103.4	6.8/6.1/5.4	7.6/6.8/6.2	5/10/50	95.2/99.7/101.3	7.4/4.6/5.7	8.3/5.4/4.6
5	Ronidazole	0.5/1/5	93.1/94.7/99.2	5.5/4.1/3.4	6.2/4.6/4.6	2.5/5/25	76.4/89.3/97.4	4.9/3.7/3.1	5.7/4.2/3.7
6	Ipronidazole	0.5/1/5	101.5/109.3/116.2	3.3/3.5/3.7	7.1/6.6/4.7	2.5/5/25	85.6/95.1/96.7	5.1/4.8/3.6	6.1/5.2/4.2
7	Ipronidazole-OH	0.5/1/5	100.6/102.4/105.9	2.5/3.6/4.2	3.8/5.2/4.3	2.5/5/25	88.3/97.3/98.9	6.8/4.8/5.2	8.1/6.2/5.6
8	Ornidazole	0.5/1/5	103.7/101.3/102.9	10.2/9.4/8.1	11.8/10.9/9.4	2.5/5/25	98.3/97.6/94.3	7.9/6.3/6.7	8.9/7.1/6.9
9	Tinidazole	0.5/1/5	100.6/105/107.6	7.7/7.0/7.2	9.3/7.6/6.8	2.5/5/25	86.3/96.3/92.6	8.3/6.4/6.3	9.3/6.9/6.8
10	Ceftiofur	10/20/50	63.9/57.4/68.3	7.0/6.0/5.5	9.7/6.9/7.1	50/100/200	68.6/59/74.2	9.2/8.3/8.7	9.4/9.2/9.6
11	Penicillin V	10/20/50	67.7/80.9/86.2	9.2/8.1/7.6	10.5/9.2/8.7	50/100/200	79.9/83.2/93.1	10.3/8.1/8	11.4/9.3/8.9
12	Oxacillin	10/20/50	71.4/82/92.6	9.2/6.0/4.7	10.5/6.8/7.8	50/100/200	74.5/89.3/94.2	8.9/8.0/6.3	9.9/9.1/7.3
13	Nafcillin	10/20/50	72.8/85.9/93.3	12.5/10.2/11.5	13.3/11.6/9.9	50/100/200	81.7/93.7/89.2	9.2/7.8/6.5	10.2/8.1/7.2
14	Cloxacillin	10/20/50	72.1/87.9/97.8	11.3/9.4/9.3	12.4/9.9/9.5	50/100/200	87.9/89.7/93.5	12.8/9.0/9.2	13.1/9.3/10.2
15	Dicioxacillin	10/20/50	70.7/83.1/94	12.5/9.6/9.2	14.2/9.7.2/9.4	50/100/200	88.9/78.9/98.6	14.9/12.8/8.1	16.1/13.8/8.7
16	Penicillin G	10/20/50	88.5/90/92.1	11.5/8.8/5.6	13.1/9.6/8.7	50/100/200	78.9/90.2/96.9	10.6/8.0/7.4	11.4/8.6/8.2
17	Ampicillin	10/20/50	37.1/46.5/50.2	11.3/7.9/6.9	12.1/8.4/7.7	50/100/200	46.7/55.2/52.1	10.3/8.4/8.3	11.1/9.3/9.2
18	Piperacillin	10/20/50	61/82.5/86.1	10.1/6.1/5.5	10.9/7.8/6.7	50/100/200	79.1/80.2/84.3	9.4/8.5/7.5	10.1/9.2/8.1
19	Clindamycin	1/5/10	89.4/92.2/96.7	4.8/3.8/3.4	6.5/5.5/4.3	5/25/50	84/96.2/94.7	6.7/4.4/5.2	7.2/4.7/5.6
20	Lincomycin	1/5/10	104.3/107.3/109.8	4.2/3.7/4.1	5,7/4.6/4.3	5/25/50	93.2/96/94.6	5.1/4.1/4.9	6.5/4.4/5.3
21	Tilmicosin	5/10/20	105.1/106/108.7	4.7/3.9/5.2	6.3/4.7/4.8	25/50/100	84.1/85.4/96.1	5.4/4.2/7.5	6.8/4.7/8.4
22	Josamycin	5/10/20	95.9/100.1/105.3	10.2/6.3/7.5	10.8/7.5/6.8	25/50/100	82.3/92.4/89.4	7.8/8.3/6.4	8.7/9.3/7.1
23	Tamulin	5/10/20	109.3/106.8/102.1	5.0/4.8/4.0	5.7/5.5/5.7	25/50/100	99/94.2/96.2	5.2/5.2/4.6	7.8/5.8/5.1
24	Oleandomycin	5/10/20	102.5/104.8/99.8	4.7/4.5/6.3	5.4/5.2/7.2	25/50/100	85.4/93.2/96.4	7.9/5.5/6.8	8.8/6.1/7.5
25	Erythromycin	5/10/20	95.1/92.7/94.2	9.2/4.2/4.1	10.5/4.8/4.7	25/50/100	79.1/84.8/86.7	11.8/10.4/8.2	12.9/11.4/9
26	Stereomycin	5/10/20	83.7/93.8/97	8.3/6.6/4.9	9.4/7.1/5.2	25/50/100	74.3/85.7/88.3	7.4/7.3/6.9	8.1/8/7.6
27	Roxithromycin	5/10/20	113.5/99.2/101.1	5.7/4.4/4.7	6.1/4.7/5.2	25/50/100	80.2/89.4/87.6	5.6/5.1/4.7	6.1/5.6/5.1
28	Tylosin	5/10/20	76.6/82.5/74.6	7.6/6.3/5.2	8.7/7.2/6.2	25/50/100	62.4/68.5/77.5	7.6/6.6/8.0	8.3/7.3/8.9
29	Azithromycin	5/10/20	90.4/98.6/109.8	10.6/9.0/9.2	12.2/10.3/10.6	25/50/100	84.6/86.4/98.4	8.8/7.5/7.6	9.8/8.3/8.0
30	Spriamycin	5/10/20	91.7/95.6/98.7	5.6/3.5/4.6	7.7/7.4/6.1	25/50/100	70.3/74.1/80.3	7.7/8.1/7.6	8.5/9.2/8.0

(Continued)

10.3389/fnut.2022.879518

TABLE 6 Continued

No.	Analyte	Milk				Milk powder			
		Spiked (μg/kg)	Average recovery (%)	Intra-day RSD, % ($n = 6$)	Inter-day RSD, % ($n = 18$)	Spiked (μg/kg)	Average recovery (%)	Intra-day RSD, % ($n = 6$)	Inter-day RSD, % ($n = 18$)
31	Cinoxacin	1/5/10	96.1/116.1/109.6	3.1/4.2/3.9	7.3/6.6/5.8	5/25/50	80.3/87.4/94.3	5.8/6.7/4.0	6.4/7.4/4.4
32	Lomefloxaxin	1/5/10	107.8/112.7/105	5.1/4.1/6.3	5.9/4.4/6.7	5/25/50	78.7/85.9/94.2	5.4/6.5/6.0	6.9/7.2/6.7
33	Danofloxacin	1/5/10	86.8/112/106.5	6.0/5.9.0/9.7	6.4/6.3/10.3	5/25/50	75.6/88.2/80.8	7.3/6.7/8.4	8.1/7.4/8.9
34	Enrofloxacin	1/5/10	107.6/110.1/118.8	3.6/3.0/4.3	4.8/3.2/4.5	5/25/50	96.4/99.1/99.5	6.4/4.3/5.1	6.8/4.5/5.4
35	Orbifloxacin	1/5/10	115.8/113/107.7	3.7/3.4/4.1	5.9/3.6/4.3	5/25/50	84.2/88.7/88.5	5.5/5.6/6.9	7.8/5.9/7.3
36	Nalidixic acid	1/5/10	102.1/114.5/115.6	4.8/3.4/4.1	6.1/3.6/4.3	5/25/50	94.7/98.3/99.4	5.7/6.5/7.6	6.3/6.9/6.7
37	Flumequine	1/5/10	85.2/88.4/93.3	3.6/3.3/4.9	5.8/3.5/5.2	5/25/50	77.6/85.7/85	8.0/7.1/7.2	8.5/7.5/6.8
38	Norfloxaxin	1/5/10	81.6/90.4/101.2	7.5/5.3/4.8	7.9/5.6/5.1	5/25/50	77.2/89.8/97.3	7.8/5.4/6.1	8.6/6.9/6.8
39	Enoxacin	1/5/10	53.4/62.3/67.7	6.1/5.9/5.7	7.9/6.6/6.4	5/25/50	54.2/66.6/65.3	7.5/5.7/6.2	8.3/6.3/6.4
40	Ciprofloxacin	1/5/10	115.3/105.6/103.9	8.0/5.8/5.3	9.3/6.5/6.6	5/25/50	89.4/97.4/99.7	10.3/8.9/7.4	11.2/9.7/8.1
41	Pefloxacin	1/5/10	94.5/99.8/93.3	5.2/3.6/4.7	5.8/4.4/5.3	5/25/50	83.7/94.2/89.3	8.5/5.6/6.0	9.3/6.1/6.5
42	Ofloxacin	1/5/10	79.3/87.2/99.2	5.3/4.8/5.0	7.4/5.5/5.7	5/25/50	78.2/85.5/98.4	6.9/5.9/6.0	7.5/6.4/6.5
43	Marbofloxacin	1/5/10	87.3/94.4/99.6	4.9/4.6/5.4	5.6/5.2/6.1	5/25/50	86.3/87.8/99.1	8.4/6.3/5.6	9.0/6.8/6.1
44	Flerofloxacin	1/5/10	100.7/104.9/110.7	3.6/5.0/5.4	6.1/5.7/6.1	5/25/50	90.1/95.3/96.9	8.1/6.2/6.0	8.8/6.5/6.5
45	Pipemidic acid	1/5/10	43.1/57.1/55.4	5.1/5.3/4.9	6.8/6.1/5.6	5/25/50	45.6/53.9/48.9	9.3/10.1/10.1	10.1/9.9/10.0
46	Oxolinic acid	1/5/10	112.4/106.3/112.5	4.8/4.0/3.5	5.9/4.5/4.0	5/25/50	106.2/102.9/104.3	5.6/5.9/5.2	6.7/6.4/5.8
47	Gatifloxacin	1/5/10	91.4/101.1/102.7	3.6/4.0/3.1	6.1/4.4/4.4	5/25/50	90.7/83.3/89.4	5.6/4.9/6.1	6.2/5.4/6.8
48	Sarafloxacin	1/5/10	92.7/98.8/105.5	4.0/4.6/5.2	4.4/5.1/5.7	5/25/50	75.7/85.7/83.8	4.6/3.4/5.8	6.5/4.5/6.2
49	Sparfloxaxin	1/5/10	92.2/95.7/93.8	5.6/5.6/4.8	6.2/6.2/5.3	5/25/50	86.8/93.1/92	4.6/5.2/4.4	4.9/5.6/4.7
50	Difloxaxin	1/5/10	104.2/101.8/103.4	4.5/4.1/3.5	4.9/4.5/3.8	5/25/50	83.3/97/99.1	4.4/4.6/3.5	4.7/4.9/4.6
51	Sulphanilamide	1/5/10	108.3/102.7/105.5	7.8/5.5/5.1	8.6/6.3/5.7	5/25/50	87.6/92.7/96.7	7.1/6.8/7.4	7.6/7.4/7.9
52	Sulfaguanidine	1/5/10	97.8/103.7/114.6	5.4/5.5/4.7	7.8/6.1/5.2	5/25/50	92.6/96.8/100.4	5.2/5.7/6.1	5.8/6.3/6.8
53	Sulfacetamide	1/5/10	100.4/101.2/93.6	5.8/6.9/5.7	6.5/7.7/6.3	5/25/50	85.2/91.1/95.1	6.9/5.8/5.8	7.6/6.4/6.8
54	Sulfadiazine	1/5/10	91.5/95.1/97.7	6.7/5.8/5.4	7.5/6.5/6.3	5/25/50	97.2/108.2/98.9	7.8/7.9/6.1	9.6/8.8/7.8
55	Sulfamethoxazole	1/5/10	102.1/106.5/103.1	4.2/4.0/3.7	7.7/4.5/4.2	5/25/50	99.4/101.5/105.5	6.0/5.3/5.3	6.6/5.9/4.9
56	Sulfamoxole	1/5/10	103.5/106.3/109.1	4.8/3.9/3.4	5.4/4.4/3.9	5/25/50	89.9/98.3/103.5	4.6/8.4/7.3	5.1/9.3/8.1
57	Sulfadoxine	1/5/10	96.5/100.6/111.2	5.7/4.6/5.1	6.5/5.2/5.8	5/25/50	97.4/100.7/107.3	8.7/4.7/4.7	9.6/6.7/5.2
58	Sulfamethizole	1/5/10	96.8/90.2/100.5	6.5/5.4/4.6	7.4/6.1/5.2	5/25/50	98.5/105.6/104.6	4.3/5.3/5.9	4.8/5.9/6.5
59	Sulfadimidine	1/5/10	101.3/108.2/102.7	5.3/5.2/4.8	5.8/5.7/5.3	5/25/50	101.6/108.5/111.1	6.1/5.5/4.5	6.8/6.1/6.1
60	Sulfameter	1/5/10	101.7/109.2/107.1	4.1/3.2/3.3	4.5/3.8/3.6	5/25/50	91.6/98.6/101.1	6.1/5.4/6.9	7.8/6.4/7.9

(Continued)

10.3389/fnut.2022.879518

TABLE 6 Continued

No.	Analyte	Milk				Milk powder			
		Spiked (μg/kg)	Average recovery (%)	Intra-day RSD, % ($n = 6$)	Inter-day RSD, % ($n = 18$)	Spiked (μg/kg)	Average recovery (%)	Intra-day RSD, % ($n = 6$)	Inter-day RSD, % ($n = 18$)
61	Sulfamethoxypyridazine	1/5/10	98.1/100.3/94.5	6.0/5.3/5.4	6.6/6.3/5.9	5/25/50	100.9/101.1/101.9	5.3/4.8/6.0	6.1/5.5/6.9
62	Sulfisoxazole	1/5/10	93.1/101.4/96.5	6.1/7.2/6.0	6.7/7.9/5.6	5/25/50	98.9/120.7/115.9	6.4/7.5/5.7	7.3/8.6/6.5
63	Sulfapyridine	1/5/10	99.2/102.8/110.1	4.0/2.3/2.9	4.4/2.8/3.5	5/25/50	101.1/107.8/117	4.8/5.3/5.4	5.5/6.1/6.2
64	Sulfathiazole	1/5/10	106.6/109.4/100.9	6.4/5.2/4.1	7.7/6.2/4.9	5/25/50	99.3/110.1/115.6	5.4/4.8/4.8	7.2/5.5/5.3
65	Sulfamerazine	1/5/10	103.5/103.9/101.1	11.3/11.0/10.6	13.5/12.2/11.1	5/25/50	105.3/114.7/115.4	10.5/12/9.9	11.6/13.5/11.1
66	Trimethoprim	1/5/10	99.4/98.9/101.6	5.6/4.9/4.5	5.9/5.1/4.7	5/25/50	102.5/116.4/117.7	3.6/4.8/5.2	4.9/5.4/5.8
67	Sulfabenzamide	1/5/10	97.9/102.2/105.8	7.2/5.8/5.7	7.6/6.1/6.4	5/25/50	96.1/92.9/104.3	6.2/5.9/5.8	7.9/6.8/6.5
68	Sulfaquinoxaline	1/5/10	101/100.4/96	4.6/6.3/6.4	4.8/6.6/6.7	5/25/50	89.1/97.4/105.1	6.6/6.2/6.8	7.4/7.0/7.6
69	Sulfadimethoxine	1/5/10	108.3/103.1/105.4	5.8/5.8/6.3	7.1/6.3/6.6	5/25/50	99/105.3/115.3	6.1/5.6/6.8	6.8/6.3/8.3
70	Sulfaphenazole	1/5/10	104.1/95.3/101.2	6.7/7.1/6.2	7.3/7.6/7.4	5/25/50	94.4/91.2/100.3	8.2/7.7/7.8	9.2/8.6/7.4
71	Sulfamonomethoxine	1/5/10	99.6/94.9/98.5	5.1/4.8/4.1	5.4/5.1/4.4	5/25/50	90.5/92.6/101.9	5.2/4.5/7.0	5.8/5.5/7.8
72	Sulfachloropyridazine	1/5/10	100.6/102.8/105.8	6.4/6.3/8.5	7.8/6.7/9.1	5/25/50	97.3/97.7/101	7.4/6.8/6.0	8.3/7.3/6.7
73	Albendazole sulfone	1/5/10	103.8/116.8/117.3	6.1/6.3/5.5	8.5/6.7/5.9	5/25/50	92.3/98.8/102.4	6.5/5.9/3.8	7.3/6.6/5.3
74	Oxfendazole	1/5/10	89.8/91.5/93.7	7.2/7.0/6.0	7.9/7.5/6.4	5/25/50	86.1/96.3/93.4	5.6/5.7/6.1	7.3/6.4/6.8
75	Albendazole S-oxide	1/5/10	102.2/107.3/105	10.7/10.8/8.4	11.2/11.3/8.8	5/25/50	94.7/102.2/101.2	8.1/7.1/7.8	9.3/8.1/8.9
76	Fenbendazole	1/5/10	97.3/104.8/105.1	9.4/10.1/9.7	9.8/10.6/10.2	5/25/50	103.8/95.4/94	7.5/7.6/5.5	8.5/8.6/6.2
77	Flubendazole	1/5/10	103.8/105.4/102.9	5.6/4.2/4.1	5.9/4.4/4.3	5/25/50	95.1/97.6/101.2	6.7/6.5/5.5	7.6/7.4/6.0
78	Fenbendazole sulfone	1/5/10	100.4/104.4/102.7	8.1/7.2/7.3	8.5/7.5/7.6	5/25/50	94.3/92.3/91.3	9.8/6.8/6.7	11.1/7.8/7.7
79	Mebendazole	1/5/10	97.4/113.4/107.7	11.1/7.2/7.1	11.6/7.5/6.4	5/25/50	101.5/89.5/97.6	7.5/6.5/6.5	8.6/8.0/7.5
80	Albendazole	1/5/10	99.4/98.3/97.8	6.1/4.3/4.7	6.5/4.6/5.3	5/25/50	93.2/82.5/92.1	8.2/7.2/7.9	9.4/8.2/9.0
81	Zeranol	1/5/10	73.7/89/83.1	14.5/8.3/8.1	15.5/8.9/8.7	5/25/50	79.3/85.4/87.2	11.3/10.2/11.2	12.9/11.7/10.8
82	Hexestrol	1/5/10	57.6/89.4/92.6	15.5/13.7/12.9	16.6/14.6/13.8	5/25/50	53.1/86.5/103.7	13.2/10.4/9.5	15.1/110/10.9
83	Diethyatibestrol	1/5/10	61.7/77.1/83.8	11.3/7.4/5.8	12.1/7.9/6.2	5/25/50	62.1/74.7/89.8	12.3/8.4/6.9	14.1/9.6/8.5
84	Dienestrol	1/5/10	75.8/84.2/101.1	11.2/4.8/8.5	10.9/5.2/9.2	5/25/50	79.1/86.5/97.7	13.6/6.7/11.0	14.5/12.4/10.9
85	Chloramphenicol	0.2/1/5	95.9/95.3/91.5	8.1/10.4/4.3	8.8/11.3/4.7	1/5/25	90.2/92.6/92.3	10.7/11.4/5.2	13.2/12.8/8.9
86	Thiamphenicol	2/5/20	64.4/91/106.1	6.9/3.6/5.9	7.5/3.9/6.4	10/25/100	61.8/95.1/104.4	7.8/4.8/6.1	8.9/5.5/6.2
87	Florfeniol	2/5/20	83.4/90.3/110.4	4.9/5.2/7.1	5.3/5.7/7.7	10/25/100	82.7/89.1/104.1	7.6/4.8/5.2	8.0/6.5/5.9
88	Hydrocortisone	1/5/10	78.3/96.5/85.4	10.4/9.4/5.3	11.3/10.2/5.8	5/25/50	75.1/95.3/89.7	10.9/9.8/6.7	12.5/11.2/7.7
89	Prednisolone	1/5/10	61/96.9/83.9	10.9/5.2/14.1	11.8/9.7/15.3	5/25/50	64.1/98.3/87.1	9.4/7.2/15.0	10.7/8.2/7.8
90	Prednisone	1/5/10	90.1/96.1/83.9	11.8/12.8/14.1	12.8/13.9/10.3	5/25/50	87.9/94/89.8	9.5/13.2/11.9	13.5/13.4/12.6

(Continued)

10.3389/fnut.2022.879518

TABLE 6 Continued

No.	Analyte	Milk				Milk powder			
		Spiked (μg/kg)	Average recovery (%)	Intra-day RSD, % ($n = 6$)	Inter-day RSD, % ($n = 18$)	Spiked (μg/kg)	Average recovery (%)	Intra-day RSD, % ($n = 6$)	Inter-day RSD, % ($n = 18$)
91	Beclomethasone	1/5/10	86.3/108.1/99.7	12.5/7.8/8.7	13.6/8.5/9.5	5/25/50	82.5/110.5/98.1	10.3/8.2/8.0	11.8/9.4/9.1
92	Betamethasone	1/5/10	79.1/104.4/69.8	15.3/8.4/9.4	16.6/9.1/10.2	5/25/50	65.8/101.2/68.2	8.9/9.2/8.3	11.3/10.5/8.5
93	Dexamethasone	1/5/10	78.8/95.5/91.3	9.6/5.7/4.1	10.4/6.2/5.6	5/25/50	81.2/99.3/87.3	9.1/6.0/4.5	10.4/7.4/6.5
94	Fludrocortisone	1/5/10	72.2/100.7/97.1	6.8/5.7/14.6	7.4/6.2/10.2	5/25/50	76.3/97.9/98.6	9.8/6.2/12.2	11.2/7.1/7.9
95	Methylprednisolone	1/5/10	72.3/102.3/96	13.0/6.3/9.7	14.1/6.8/10.5	5/25/50	71.1/101/74.7	14.8/7.1/8.6	15.2/8.1/8.5
96	Ethinylestradiol	10/20/50	60.8/62.6/71.6	10.1/7.2/11.9	11.5/7.8/12.9	50/100/250	61.8/64.3/68.9	13.0/8.0/10.4	13.9/9.1/7.9
97	Estriol	5/10/50	49.8/44.5/73.6	19.1/19.2/11.8	19.5/18.6/12.1	25/50/250	54.1/42.9/71.4	10.3/18.4/11.0	11.8/12.5/12.3
98	17-α-estradiol	5/10/50	64.5/65.1/62.3	17.8/11.6/9.4	19.3/12.6/10.2	25/50/250	67.7/67.8/63.3	15.4/10.5/8.5	17.6/11.8/9.5
99	17-β-estradiol	10/20/50	90.3/72.3/73.7	11.2/14.4/7.1	12.1/15.5/8.8	50/100/250	86.8/68.2/73.4	14.1/12.2/8.5	15.8/13.9/9.2
100	Toltrazuril	1/2/10	83.9/93/98.4	7.9/10.0/3.2	8.5/10.8/9.8	5/10/50	78.8/101.3/97.6	6.8/8.7/5.2	9.8/9.9/6.7
101	Toltrazuril sulfoxide	1/2/10	107.2/97.9/78.6	8.0/3.5/7.9	8.3/7.6/8.6	5/10/50	102.7/92/76.6	8.4/6.2/8.2	9.6/7.4/8.6
102	Toltrazuril sulfone	1/2/10	83.3/94.3/77.8	4.7/8.1/6.8	5.3/8.6/7.3	5/10/50	78.8/90.2/70.9	6.8/8.4/5.4	7.8/9.3/7.6
103	Diclazuril	1/2/10	105.1/99.1/74.1	2.7/11.4/8.1	9.8/10.4/8.7	5/10/50	102.3/87.2/72.4	5.2/6.3/5.1	8.7/8.4/8.6

The MRM chromatograms of every compound were showed in Supplementary Figure 4.

Method validation

Linear range, linear equation, and detection limit

The six levels of the series of mixed matrix working solutions were determined under the selected chromatographic separation conditions and mass spectrometry parameters. the ratio of the peak area of the target to the peak area of the internal standard substance is the vertical coordinate (Y), and the mass concentration (ng/mL) of the target substance is the abscissa (X) as the quantitative working curve; The of the matrix was obtained, the linear correlation coefficients linear regression equation ranged from 0.9902 to 0.9998, indicating that the compound has a good linear relationship within the corresponding concentration range. The detection limit of the compound (LOD) and the limit of quantitation (LOQ) were determined according to the 3 and 10 signal-to-noise (S/N) ratio. The LODs of 103 drugs in the milk were 0.1–10 μg /kg, and the LOQs were 0.5–25 μg /kg; the LODs in the milk powder matrix are 0.5–25 μg /kg, and the LOQs are 0.5–50 μg/kg. The results are shown in Table 5.

Recovery and precision

The blank milk and milk powder samples were selected, and the recovery and precision experiments were carried out according to the above pretreatment methods. Recovery experiments were carried out at three levels, and six parallel tests were made for each level. The results showed that the recoveries in milk was from 31.1 to 118.8%, the relative standard deviations (intra-day RSD) ranged from 2.34 to 19.2%, and the recovery of milk powder was in the range of 42.9–120.7%, and the range of intra-day RSDs were 4.5–18.4%. Ampicillin achieved the lowest results of recovery of 37.1–50.2%, and estriol had the largest RSD of 19.2%. The recovery results of all drugs were shown in Table 6. The recovery of some drugs in this study needs to be improved compared with the detection method of a single or single kind of veterinary drug, but as a rapid screening method, it is applicable to the latest announcement issued by the Food and Drug Administration (Food and Drug Administration, FDA) on March 22, 2012: if the screening purpose of veterinary drug residue in food proves that the drug to be tested can be detected, The recovery rate can be relaxed to an appropriate extent (19).

Analysis of market samples

Twenty cow Milk Samples and 10 Milk Powder Samples Obtained From Local Supermarkets Were Analyzed. The

Analysis Was Completed in Just 2 Days. And Lincomycin Was Found 10.2 ± 1.5 μg/kg in Only one Milk Sample, but the Concentration Was Below the Current MRL (0.15 ppm).

Conclusions

A method based on QuEChERS and UPLC-MS/MS for the determination of common veterinary drug residues was investigated. One hundred three analytes were quantified and validated using selected daughter ions under optimized MRM condition with ESI (+) or ESI (–) mode. The clean-up with QuEChERS consist of C18, and anhydrous sodium sulfate was suitable for simultaneous analysis of multi-class in milk and milk powder. The method is accurate, simple, rapid, and economic, and can be applied as a screening method in the determination of drug residues in milk and dairy products.

Data availability statement

The original contributions presented in the study are included in the article/supplementary material, further inquiries can be directed to the corresponding author/s.

Author contributions

LFA and YZ conceived and designed the experiments. XJG, HT, and FY performed the experiments. SFF and JWZ analyzed the data. JMM wrote the original draft. All authors have read and approved the manuscript.

Funding

This work was supported by the Science and Technology project of Hebei Province (21475501D) and Science and Technology project of general Administration of China (2019HK112).

Conflict of interest

The authors declare that the research was conducted in the absence of any commercial or financial relationships that could be construed as a potential conflict of interest.

Publisher's note

All claims expressed in this article are solely those of the authors and do not necessarily represent those of their affiliated organizations, or those of the publisher, the editors and the reviewers. Any product that may be evaluated in this article, or claim that may be made by its manufacturer, is not guaranteed or endorsed by the publisher.

Supplementary material

The Supplementary Material for this article can be found online at: https://www.frontiersin.org/articles/10.3389/fnut.2022.879518/full#supplementary-material

References

1. Baynes RE, Dedonder K, Kissell L, Mzyk D, Marmulak T, Smith G, et al. Health concerns and management of select veterinary drug residues. *Food Chem. Toxicol.* (2016) 88:112–122. doi: 10.1016/j.fct.2015.12.020

2. Chinese Ministry of Agriculture. *GB 31650-2019 National Food Safety Standard Maximum Residue Limits for Veterinary Drugs in Foods.* Beijing: Chinese Ministry of Agriculture (2019).

3. Codex Alimentarius. *Maximum Residue Limits (MRLs) and Risk Management Recommendations (RMRs) for Residues of Veterinary Drugs in Foods.* Rome: Codex Alimentarius (2018).

4. US FDA. *Milk Drug Residue Sampling Survey* (2015). US FDA. Available online at: https://www.fda.gov/media/91217/download

5. EFSA. *Report for 2017 on the Results From the Monitoring of Veterinary Medicinal Product Residues and Other Substances in Live Animals and Animal Products.* EFSA (2019). Available online at: https://efsa.onlinelibrary.wiley.com/doi/epdf/10.2903/sp.efsa.2019.EN-1578

6. Li S, Zhang Q, Chen M, Zhang X, Liu P. Determination of veterinary drug residues in food of animal origin: sample preparation methods and analytical techniques. *J Liq Chromatogr Relat Technol.* (2020) 43:701–24. doi: 10.1080/10826076.2020.1798247

7. Desmarchelier A, Bessaire T, Savoy MC, Tarres A, Mujahid C, Beck A, et al. Screening of 154 veterinary drug residues in foods of animal origin using LC–MS/MS: first action 2020.04. *J AOAC Int.* (2021)104:650–81. doi: 10.1093/jaoacint/qsaa168

8. Wong MH. Zheng C. Trace analysis of multiclass antibiotics in food products by liquid chromatography-tandem mass spectrometry: method development. *J Agric Food Chem.* (2021) 69:1656–66. doi: 10.1021/acs.jafc.0c05778

9. Mehl A, Schmidt LJ, Schmidt L, Morlock GE. High-throughput planar solid-phase extraction coupled to orbitrap high-resolution mass spectrometry via the auto TLC-MS interface for screening of 66 multi-class antibiotic residues in food of animal origin. *Food Chem.* (2021) 351:129211. doi: 10.1016/j.foodchem.2021.129211

10. Chen J, Ying GG, Deng WJ. Antibiotic residues in food: extraction, analysis, and human health concerns. *Agric Food Chem.* (2019) 67:7569–86. doi: 10.1021/acs.jafc.9b01334

11. Casey CR, Andersen WC, Williams NT, Nickel TJ, Ayres PR. Multiclass, multiresidue method for the quantification and confirmation of 112 veterinary drugs in game meat (Bison, Deer, Elk, and Rabbit) by rapid polarity switching liquid chromatography–tandem mass spectrometry. *Agric Food Chem.* (2021) 69:1175–86. doi: 10.1021/acs.jafc.0c01422

12. Moga A, Vergara BM, Lerma-García MJ, Carrasco-Correa EJ, Herrero-Martínez JM, Simó-Alfonso EF. Determination of antibiotics in meat samples using analytical methodologies: a review. *Compr Rev Food Sci Food Saf.* (2021) 20:1681–716. doi: 10.1111/1541-4337.12702

13. Zhao L, Lucas D, Long D, Richter B, Stevens J. Multi-class multi-residue analysis of veterinary drugs in meat using enhanced matrix removal lipid cleanup

and liquid chromatography-tandem mass spectrometry. *J Chromatogr A*. (2018) 1549:14–24. doi: 10.1016/j.chroma.2018.03.033

14. Zhao W, Jiang R, Guo W, Guo C, Li S, Wang J, et al. Screening and analysis of multiclass veterinary drug residues in animal source foods using UPLC-Q-Exactive orbitrap/MS. *Bull Environ Contam Tox*. (2021) 107:228–38. doi: 10.1007/s00128-021-03273-w

15. Zhou W, Ling Y, Liu T, Zhang Y, Li J, Li H, et al. Simultaneous determination of 16 macrolide antibiotics and 4 metabolites in milk by using quick, easy, cheap, effective, rugged, and safe extraction (QuEChERS) and high-performance liquid chromatography tandem mass spectrometry. *J Chromatogr B*. (2017) 1061:411–20. doi: 10.1016/j.jchromb.2017.07.046

16. Khatibi SA, Hamidi S, Siahi-Shadbad MR. Current trends in sample preparation by solid-phase extraction techniques for the determination of antibiotic residues in foodstuffs: a review. *Crit Rev Food Sci Nutr*. (2020) 61:3361–82. doi: 10.1080/10408398.2020.1798349

17. Zhang C, Deng Y, Zheng J, Zhang Y, Yang L, Liao C, et al. The application of the QuEChERS methodology in the determination of antibiotics in food: a review. *Trends Anal Chem*. (2019)118:517–37. doi: 10.1016/j.trac.2019.06.012

18. Kim L, Lee D, Cho HK, Choi SD, Choi SD. Review of the QuEChERS method for the analysis of organic pollutants: persistent organic pollutants, polycyclic aromatic hydrocarbons, and pharmaceuticals. *Trends Environ Anal Chem*. (2019) 22:e00063. doi: 10.1016/j.teac.2019.e00063

19. Food and Drug Administration. *Guidelines for the Validation of Chemical Methods for the FDA Foods Program*. Food and Drug Administration. Available online at: http://www.fda.gov/downloads/ScienceResearch/FieldScience/UCM298730.pdf

20. Freitas A, Barbosa J, Ramos F. Development and validation of a multi-residue and multiclass ultra-high-pressure liquid chromatography–tandem mass spectrometry screening of antibiotics in milk. *Int Dairy J*. (2013) 33:38–43. doi: 10.1016/j.idairyj.2013.05.019

21. Nebot C, Iglesias A, Regal P, Miranda J, Cepeda A, Fente C. Development of a multi-class method for the identification and quantification of residues of antibiotics, coccidiostats and corticosteroids in milk by liquid chromatography–tandem mass spectrometry. *Int Dairy J*. (2012) 22:78–85. doi: 10.1016/j.idairyj.2011.09.001

22. Dasenaki ME, Bletsou AA. Koulis GA, Thomaidis NS. Qualitative multiresidue screening method for 143 veterinary drugs and pharmaceuticals in milk and fish tissue using liquid chromatography quadrupole-time-of-flight mass spectrometry. *J Agric Food Chem*. (2015) 63:4493–508. doi: 10.1021/acs.jafc.5b00962

23. Wittenberg JB, Simon KA, Wong JW. Targeted multiresidue analysis of veterinary drugs in milk-based powders using liquid chromatography-tandem mass spectrometry (LC-MS/MS). *J Agric Food Chem*. (2017) 65:7288–93. doi: 10.1021/acs.jafc.6b05263

24. Biselli S, Schwalb U, Meyer A, Hartig L. A multi-class, multi-analyte method for routine analysis of 84 veterinary drugs in chicken muscle using simple extraction and LC-MS/MS. *Food Addit Contam*. (2013) 30:921–39. doi: 10.1080/19440049.2013.777976

Advantages of publishing in Frontiers

OPEN ACCESS
Articles are free to read for greatest visibility and readership

FAST PUBLICATION
Around 90 days from submission to decision

HIGH QUALITY PEER-REVIEW
Rigorous, collaborative, and constructive peer-review

TRANSPARENT PEER-REVIEW
Editors and reviewers acknowledged by name on published articles

Frontiers
Avenue du Tribunal-Fédéral 34
1005 Lausanne | Switzerland

Visit us: www.frontiersin.org
Contact us: frontiersin.org/about/contact

REPRODUCIBILITY OF RESEARCH
Support open data and methods to enhance research reproducibility

DIGITAL PUBLISHING
Articles designed for optimal readership across devices

FOLLOW US
@frontiersin

IMPACT METRICS
Advanced article metrics track visibility across digital media

EXTENSIVE PROMOTION
Marketing and promotion of impactful research

LOOP RESEARCH NETWORK
Our network increases your article's readership